CHAPTER

1

Renewable Hydrogen Energy: An Overview

Luis M. Gandía, Gurutze Arzamendi, Pedro M. Diéguez

Escuela Técnica Superior de Ingenieros Industriales y de Telecomunicación, Universidad Pública de Navarra, Campus de Arrosadía, E-31006 Pamplona, Spain

OUTLINE

1.1 Setting the Context: Climate Change and Energy Security 1
1.1.1 International Energy Outlook 2
1.1.1.1 Oil and Liquid Fuels 2
1.1.1.2 Natural Gas and Coal 3
1.1.1.3 Electricity 4
1.1.1.4 CO_2 Emissions 4
1.1.2 Toward Decarbonization 4
1.2 Is A New Energy Carrier Necessary? 6
1.2.1 The Hydrogen Economy 6
1.2.2 The Efficiency Issue 7
1.2.3 Hydrogen Contribution to Transportation and the Electric Grid 9
1.2.3.1 Hydrogen in Transportation 10
1.2.3.2 Hydrogen and the Electric Grid 10
1.3 Hydrogen Production 11
1.3.1 Pathways 11
1.3.1.1 Nonrenewable Hydrogen 11
1.3.1.2 Renewable Hydrogen 13
1.3.2 Status and Prospects of Renewables 14
1.4 Hydrogen Today 15
Acknowledgments 16
References 16

1.1 SETTING THE CONTEXT: CLIMATE CHANGE AND ENERGY SECURITY

The experience gained from over a decade of sustained research, development and demonstration projects corroborates that hydrogen and fuel cell technologies have strong potential to play a significant role in the new energy system that must be defined in the coming years. This energy system should provide adequate and prompt responses to the threats posed by the climate change and energy security issues.

The leaders of the Group of Eight (G8) recognized during the summit held in L'Aquila (Italy), July 2009 that, as for the dangers of climate change, the costs of inaction far outweigh the costs of moving toward low-carbon societies. But at the same time, it is obvious that secure energy availability is indispensable for social and economic development, so it is essential to ensure global energy access. It was also recognized, in agreement with the work of the United Nations (UN) Intergovernmental Panel on Climate Change,[1] that the increase in global average temperature above preindustrial levels should not exceed 2 °C. To this end, global CO_2 emissions must peak and then start to decline rapidly within the next 5–10 years to have a reasonable chance of avoiding the worst impact of climate change. The global atmospheric CO_2 concentration was about 330 ppm in 1970 and after 40 years it has increased at least 60 ppm, reaching over 390 ppm by the end of 2010. It has been projected that if atmospheric CO_2 levels increase up to about 450 ppm, a critical point could be reached at which warming exacerbated by strong positive feedbacks will seriously disrupt climate.[2] At the rate at which CO_2 emissions are currently growing, the critical point could be attained well before the next 40 years. In response to this serious threat, the G8 leaders expressed their willingness to share with all countries the goal of achieving at least a 50% reduction of global emissions by 2050 and to support

http://dx.doi.org/10.1016/B978-0-444-56352-1.00001-5

a goal of developed countries reducing greenhouse gas (GHG) emissions by 80% or more by 2050 compared to 1990.

Regrettably, results from the most recent studies lead to discouraging perspectives. The International Energy Agency (IEA) has estimated that 80% of the total CO_2 emissions permissible by 2035 in order to achieve a stabilization in 450 ppm are already "locked-in" by our current energy-related infrastructure.[3] In the IEA central scenario, the so-called New Policies Scenario, in which the governments' commitments are assumed to be implemented in a cautious manner, the trend of global emissions is consistent with a long-term average temperature increase of more than 3.5 °C. But the situation could even become much worse under the IEA Current Policies Scenario, which assumes that no new policies are added to those in force as of mid-2011. In this case, we would run the dangerous risk that the mean temperature rises 6 °C or more.[3] Despite the almost generalized concern about the consequences of climate change, it is disappointing that policy makers are often faced with continuous difficulties in reaching clear compromises on the reduction of GHG emissions. The most recent demonstration occurred during the UN Climate Change Conference 2011 held in Durban (South Africa). Fortunately in this occasion, the world's three largest pollutant emitters (United States, China and India) have agreed for the first time to sign up to a legal treaty to reduce GHG emissions. To elaborate an instrument with legal force applicable to all parties, it has been decided to create the so-called Ad Hoc Working Group on the Durban Platform for Enhanced Action.[4] The problem is that it has been scheduled that the Working Group completes its mission no later than 2015 and that the resulting legal instrument comes into effect from 2020. This may be too late. In fact, in the absence of stringent new actions by 2017, the energy-related infrastructure in place by that year will it make impossible to accomplish the CO_2 stabilization objective without extremely high costs.[3]

Previous analysis gives an idea of the risks associated to the difficulties of reaching international agreements on the reduction of GHG emissions. However, to better appreciate the magnitude of the challenge posed by the energy security issue and the need of transforming the energy system, a brief international energy outlook and a summary of the milestones that have to be achieved by a decarbonized economy are presented in the following subsections. Regrettably, we will see that the role assigned to hydrogen in the current energy policies is, at least in Europe, little relevant at the moment.

1.1.1 International Energy Outlook

According to the U.S. Energy Information Administration (EIA), under the conditions of a reference case that does not contemplate the incorporation of legislation or policies affecting energy markets, the world marketed energy consumption grows by 53% from 2008 to 2035.[5] This means that the world primary energy consumption increases from 12,726 Mtoe in 2008 to 15,599 Mtoe in 2020 and 19,404 Mtoe in 2035[a]. The projected increase is modest in the case of the countries that are part of the Organization for Economic Cooperation and Development (OECD) (18%). Much of the growth takes place in non-OECD nations that increase by 85% their primary energy use during that period. The reason for this big difference mainly lies in the very different economic growth pace of these world regions. The recovery from the 2008 to 2009 worldwide economic recession makes uneven progresses. In the developed countries, the recovery is slow compared with previous economic crises; it seems that this situation will continue, at least in the short term, as suggested by the high unemployment figures and debt levels of some economies as well as financial turbulences existing within the OECD. In contrast, economic growth will remain robust in the main emerging economies due to strong capital incomes. According to the U.S. EIA reference case, China and India will continue to lead the world economic growth and the growth of the energy demand. The projected average annual gross domestic product (GDP) increase of the OECD countries during the 2008–2035 period is 2.1%, led by the OECD Americas with 2.6%. The annual energy consumption growth for the whole OECD region is 0.6% over this 27-year period. In the case of the non-OECD nations, the average annual GDP increase is much higher, up to 4.6%, led by the non-OECD Asia with a mean 5.3% GDP growth. This impressive sustained economic development is consistent with the projected average annual energy consumption growth for the non-OECD nations of 2.3% and 2.9% for the non-OECD Asia region.[5] It is very relevant that the combined energy use of China and India more than doubles over the 2008–2035 period, reaching 31% of the world energy consumption, whereas the percentage of the OECD region amounts up to 37.4%.

In the following subsections, a more detailed outlook by energy sources as well as prospects for electricity and the energy-related CO_2 emissions will be presented.

1.1.1.1 Oil and Liquid Fuels

The U.S. EIA projections show that liquid fuels, mainly from fossil origin, will remain the largest

[a]1 Mtoe = 10^7 Gcal = 3.968×10^7 MBtu = 4.1868×10^7 GJ = 0.04,187 EJ = 11,630 GWh.

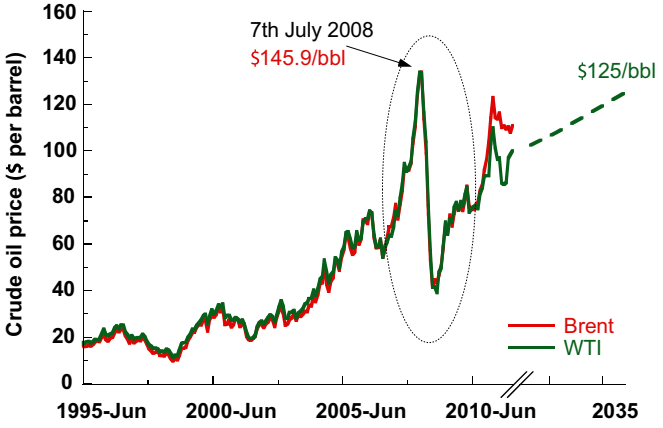

FIGURE 1.1 Evolution of the monthly average prices of the Brent and WTI crude oils since June 1995. (For color version of this figure, the reader is referred to the online version of this book.)

primary energy source with a market share that decreases from 34% to 29% between 2008 and 2035. Global consumption of petroleum-derived fuels and other liquids as biodiesel, bioethanol and synthetic fuels obtained from coal and gas increase altogether from 85.7 million barrels per day (bpd) in 2008 to 112.2 million bpd in 2035. Great part of this important increase corresponds to the transport sector which, in the absence of significant technological advances and despite the rising oil prices, increases the use of liquid fuels by 46%.[5] The evolution of the monthly average prices of the Brent and West Texas Intermediate (WTI) crude oils since June 1995 is shown in Fig. 1.1. As can be seen, Brent crude oil price peaked at U.S. $145.9 per barrel (bbl) on 7th July 2008 and then decreased abruptly to initiate again a progressive increase characterized by a marked volatility, reaching $111/bbl by the end of January 2012. The average annual price in 2011 was $113/bbl, which almost coincided with that of 2008 ($112/bbl). Similarly, the WTI crude oil price peaked at $145/bbl in July 2008, and then decreased markedly to increase again reaching $98.5/bbl by the end of January 2012. Annual average prices for WTI oil crude were $98.3, $38.9 and $90.7 per barrel in 2008, 2009 and 2011, respectively. According to the EIA reference case projections, the average WTI oil crude price will reach $125/bbl in 2035. In a recent and thorough study, Sorrell et al.[6] report that, as a result of a series of geological, technological and even definitional aspects, there is a real increase of the global average oil reserve that can be observed since 1995. The reserve growth is higher for the older (discovered before 1986) and larger onshore fields and the main contributions to this growth come from Saudi Arabia (37%), Iran (15%), Venezuela (12%) and Qatar (9%). Despite this positive finding from the point of view of the future global oil supply, as the decline rate of all currently producing fields is at least 4% per year, more than two thirds of the current oil production capacity may need to be replaced by 2030 simply in order to keep the production constant.[6] Within this context, it is expected that during the coming decades, an important development of the exploitation of unconventional resources of liquid fuels as oil sands, extraheavy oil, shale oil, biofuels, and coal-to-liquids and gas-to-liquids technologies takes place. Global production of unconventional liquid fuels reached 3.9 million bpd in 2008 and it is projected that it increases up to 13.1 million bpd by 2035, accounting for 12% of the world's fuel liquids supply. Main future contributions are expected to come from Canadian oil sands (4.8 million bpd), biofuels from the USA and Brazil (2.2 and 1.7 million bpd, respectively) and extraheavy oil from Venezuela (1.4 million bpd).[5] Despite the good perspectives for this sector, especially for the Canadian oil sands (over 7 million bpd of capacity), it should be noted that these unconventional resources are characterized by significantly higher energy intensity and GHG emissions than conventional light oil.[7]

1.1.1.2 *Natural Gas and Coal*

World consumption of natural increases by 52% according to the EIA projections, that is, from 3.141×10^6 million m^3 in 2008 to 4.783×10^6 million m^3 in 2035. It is expected that natural gas continues being the preferred fuel for electric power production due to its advantages in terms of relatively low capital costs and energy efficiency associated to the use of combined cycle gas turbines. The strong position of natural gas within the energy market will be reinforced by the growth of liquefied natural gas production capacity and the recent advances in drilling technologies such as horizontal drilling and hydraulic fracturing that make now profitable to exploit many sources of unconventional natural gas as shale gas basins. It is expected that the natural gas reserve growth helps to control the gas price and increases the demand for this energy source likely above the projections. Initial estimates rise the shale gas reserve above 187 trillion m^3. This figure is very significant taking into account that world-proven gas natural reserve and world technically recoverable gas resources (excluding shale oil) were 189 trillion m^3 and 453 trillion m^3, respectively, by January 2011.[5] Coinciding with the shale gas production boom, concern has arisen about the environmental impact of the new drilling techniques. In a recent life cycle analysis, Burnham et al.,[8] from the Argonne National Laboratory (IL, USA) found similar GHG emissions from shale gas and conventional natural gas production and use, which were 23% and 33% lower than for gasoline and coal, respectively. This study has alerted to the

importance of controlling the upstream methane leakage and venting, which are key contributors to the total GHG from natural gas (conventional or unconventional) and can significantly reduce its benefits compared to oil or coal from the point of view of GHG emissions.

Regarding coal, world consumption increases by 50% according to the EIA reference case projections from 3502 Mtoe in 2008 to 5289 Mtoe in 2035. This remarkable consumption growth corresponds to that in the non-OECD Asia countries because the use of coal in the rest of the world remains almost unchanged. Especially China and India, having large domestic reserves of coal, increase its use for power generation and industrial sector by 70−100%. World projections of coal consumption are subjected to significant uncertainty in relation with the final feasibility and deployment of carbon capture and storage (CCS). This subject is treated with more detail in Section 1.3.1.1.

1.1.1.3 Electricity

World net generation of electricity increases by 84% in the EIA reference case, from 19.1 million GWh in 2008 to 35.2 million GWh in 2035.[5] This impressive growth is led by the non-OECD Asia region with an annual average increase of 4.0% from 2008 to 2035, whereas it is only 1.2% per year for the OECD region due to the maturity of the market in the developed countries. Coal remains the main primary energy source for electricity generation although its share decreases from 40% in 2008 to 36.6% in 2035. Natural gas shows an opposite trend, with its share increasing from 21.8% to 23.8%. However, the most important growth corresponds to power generation from renewables with a share rising from 19.3% in 2008 to 23.4% in 2035. More than 82% of this increase is due to hydroelectric and wind energy which, by the end of the projection period, contribute with further 2.5 million GWh and 1.3 million GWh, respectively. Electricity from nuclear power maintains an almost constant share of about 14%, with a generation that increases from 2.6 million GWh in 2008 to 4.9 million GWh in 2035. Nuclear energy is considered a key piece of the future energy mix because it can contribute significantly to achieving a high degree of decarbonization of the energy system. However, the possible long-term implications of the incidents that occurred at the Fukushima Daiichi (Japan) nuclear power plant in March 2011 have given rise to considerable uncertainty about the future evolution of nuclear power generation. It is then likely that the projected figures are somewhat overestimated. The EIA projections show that 75% of the nuclear power-installed capacity growth takes place in non-OECD countries, led by China, Russia and India, which add 106, 28 and 24 GW, respectively, of new generation capacity.

1.1.1.4 CO_2 Emissions

Under the current policies assumption, global energy-related CO_2 emissions are projected to increase by 43% over the period between 2008 and 2035.[5] This implies passing from 30,200 million metric tons in 2008 to 43,200 million metric tons in 2035. Much of this big increase is associated to the robust economic growth exhibited by the largest non-OECD developing nations. Coal accounts for the main share of CO_2 emissions that increases slightly from 44.1% in 2008 to 44.9% in 2035. On the other hand, whereas the share of liquid fuels decreases from 35.3% to 33.2%, that of natural gas increases from 20.6% to 21.9% over the 27-year projection period. With regard to carbon intensity, whereas it improves (decreases) worldwide when referred to the unit of economic output due to more efficient energy transformation processes, different trends arise when considering CO_2 emissions per capita. In this case, emissions from the OECD countries fall slightly from 11.1 metric tons per person in 2008 to 10.6 metric tons per person in 2035. In contrast, the emissions intensity increases in the non-OECD countries, especially China, where the increase is from 5.1 to 9.3 metric tons per person during the 2008−2035 period. This gives an idea of the magnitude of the expected energy consumption increase in the most populated country on earth.

1.1.2 Toward Decarbonization

The international energy outlook presented in the previous section makes it clear that under a scenario dominated by the current policies, the energy-related CO_2 emissions increase remarkably, just the opposite to what is needed in order to possibly limit the increase in global average temperature below 2 °C. Strongly determined policies are required to remedy this situation. First and foremost, the overall energy consumption has to be reduced. Forecasts by the IEA according to the 450 PS scenario (based on a plausible post-2012 climate policy framework to stabilize the GHG concentration at 450 ppm CO_2-equivalent) projects a global primary energy consumption of 14,920 Mtoe by 2035.[9] This figure contrasts clearly with the above-mentioned 19,404 Mtoe projected by the U.S. EIA for 2035 under current policies assumption. The gap should be even higher because the U.S. EIA forecasts include only marketed energy, whereas those by the IEA also include biomass, such as fuelwood, charcoal and agricultural waste used for cooking and heating in developing countries, that accounts for about 10% of world primary energy demand. In Fig. 1.2, the world consumption of primary energy by sources in 2009 and in 2035 according to the IEA 450 PS scenario is compared. It can be seen that the achievement of the GHG concentration stabilization

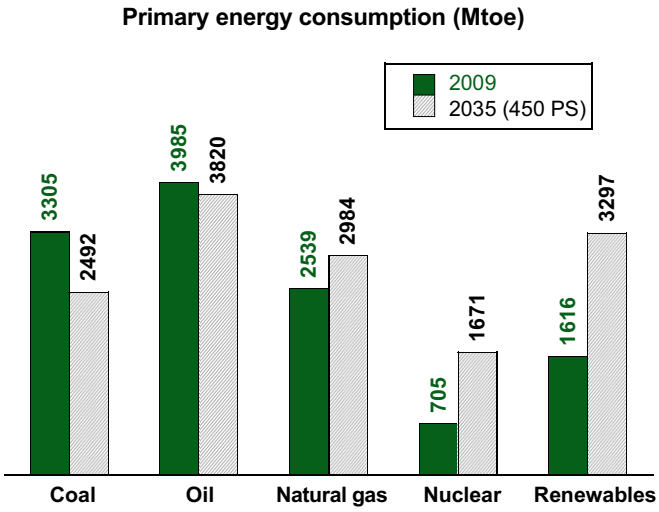

FIGURE 1.2 Primary energy consumption by source in 2009 and in 2035 according to the projections of the IEA 450 PS scenario compatible with the stabilization of the GHG concentration at 450 ppm CO_2-equivalent. (For color version of this figure, the reader is referred to the online version of this book.)

goal (450 PS) requires doubling the contribution of both renewables and nuclear power in the energy mix. Their share should increase from 13.2% in 2009 to 26.8% in 2035 in the case of renewables and from 5.8% in 2009 to 11.2% in 2035 for nuclear power. According to the 450 PS scenario, the combined share of fossil fuels should decrease from 81% in 2009 to 62% in 2035; nevertheless, the natural gas consumption increases by 17%. On the other hand, whereas the required oil consumption decreases is small, that of coal is about 25%. This constitutes a very challenging goal owing to the strong implantation of coal use for electricity generation, especially in the USA, China and India that have large domestic reserves.

The European Union (EU), in response to the commitment expressed by the G8 leaders in 2009 in order to achieve a significant reduction of the GHG emissions by 2050, has launched a series of ambitious initiatives. In support of the European Council's abatement objectives for Europe, the European Climate Foundation (ECF) has elaborated the *Roadmap 2050: a practical guide to a prosperous, low-carbon Europe*.[10] This document outlines plausible ways to achieve a reduction target of GHG emissions of at least 80% compared to 1990 levels. Among the findings of this study it can be emphasized that the GHG emission reduction objectives will be hard to realize if a transition to a new energy system both in the way the energy is used and in the way it is produced is not started before 2015. This has also important implications from the economic point of view. Having begun the transition in 2010, the capital spent in the power sector would have increased from €30 000 million in the first year to €65 000 million in 2025. If delayed by 10 years, the capital spent in 2035 would increase up to €90 000 million. However, apart from technical and economic issues, the feasibility of implementation of the decarbonization pathways is considered the biggest challenge. The following milestones have to be achieved by a European decarbonized economy between now and 2050[10]:

1. Installation of about 5000 km^2 of solar panels over 40 years is required; this means equaling 0.1% of the EU area assuming that half of the new capacity corresponds to rooftop panels. Installation and replacement of close to 100,000 wind turbines (of which half could be offshore) is also required. This implies between 2000 and 4000 new turbines per year, a pace similar to that exhibited by the wind energy sector in the last years although the new turbines should be significantly larger (up to 7−10 MW).
2. An overall expansion of electric grid interconnection between and across regions in Europe that is an increase of factor three from today's level of transmission capacity is needed. Moreover, between 190 and 270 GW of backup generation capacity is required to maintain the reliability of the electric system, of which 120 GW is already in the baseline. This represents 10−15% of total generation capacity by 2050 that would be run at load factors between less than 5% up to a maximum of 8% depending of the degree of penetration of renewables.
3. The implementation of CCS for power generation and the industrial sector is required. This implies building the corresponding infrastructure for transporting and storing the captured CO_2. It should be noted that the ECF's roadmap has been designed under the assumption of a carbon tax of at least € 20−30 per metric ton of CO_2 over 40 years.
4. Under the assumption of a penetration of renewables of 40%, about 1.5 million GWh per year of nuclear power is required, compared with approximately 1 million GWh per year today. About 200 GW of new nuclear power would be required, representing over a 100 of new nuclear plants entering into operation. In contrast, a degree of penetration of renewables of 80% would lead to the replacement of half the current level of nuclear power production.
5. Potentially up to 200 million electric and fuel cell vehicles and around 100 million heat pumps for buildings and city districts need to be deployed.

Along the lines of the ECF work, on 15 December 2011 the European Commission (EC) adopted the Communication *Energy Roadmap 2050*[11] where the EC explores the challenges posed by delivering the EU's

decarbonization objective of reducing GHG emissions to 80–95% below 1990 levels by 2050 while ensuring security of energy supply and competitiveness. Within this context, it should be noted that the EU has as the starting point the *Directive on the Promotion of the Use of Energy from Renewable Sources*.[12] This Directive establishes as general objectives to achieve a 20% share of energy from renewable sources in the EU's gross final consumption of energy and a 10% share of energy from renewables in each member state's transport energy consumption by 2020. These objectives are ambitious but insufficient because they would lead to less than half of the decarbonization goal for 2050. The Energy Roadmap 2050 is the basis for developing a long-term European framework in order to guarantee a high degree of decarbonization of the European economy. According to this document, a secure, competitive and decarbonized energy system in 2050 is possible.[11] To this end, a transition is necessary from the current system, characterized by high fuel and operational costs, to a system based on higher capital expenditure but lower fuel costs. Cumulative grid investment costs alone could amount to €1.5×10^6 to 2.2×10^6 million between 2011 and 2050. These large figures result from the fact that electricity will have to play an increasingly important role, doubling its share in final demand energy to 36–39% in 2050, and contributing to the decarbonization of transport and heating/cooling needs. It should be taken into account that in the coming few years an important number of power plants will reach the end of their useful life. This can be viewed as an opportunity for performing the structural change that needs the power generation system. Another key point is the need for reducing the primary energy demand through energy saving and improved efficiency strategies. Primary energy demand should decrease by 16–20% by 2030 and 32–41% by 2050 as compared to consumption peaks in 2005–2006.

However, as important as the above objectives is the need to transmit a new sense of urgency and collective responsibility to the public and private sectors as well as to the general public in order to suitably address the challenges posed by the climate change and the transformation of our energy system.

1.2 IS A NEW ENERGY CARRIER NECESSARY?

At this point, the reader will have perceived the minor role assigned to hydrogen in the current energy policies. The same conclusion was reached by Bleischwitz and Bader after a thorough review of the EU energy and regulatory and spending policies.[13] It can be said that the current EU policy framework does not hinder hydrogen development but it does not constitute a strong push factor either.

In the *European Energy Roadmap 2050*, probably the world's most ambitious decarbonization strategy designed until now, hydrogen appears only in the section entitled *Smart technology, storage and alternative fuels*.[11] Regarding alternative fuels and electric vehicles, it is mentioned that they have to be supported by regulatory developments, standardization, infrastructure policy and further research and demonstration efforts, particularly on batteries, fuel cells and hydrogen, which together with smart grids can multiply the benefits of electromobility both for decarbonization of transport and development of renewable energy.

The fact that the role assigned to hydrogen in the current policies is little relevant despite the progresses made in the recent years suggests that perhaps we have to ask the question: Is a new energy carrier really necessary?

In the following subsections, we will try to answer this question discussing on the evolution of the *Hydrogen Economy* concept, the issue of the energy efficiency and the interactions between hydrogen and electricity.

1.2.1 The Hydrogen Economy

The roots of the hydrogen economy concept have been established by Dunn in his *History of Hydrogen*.[14] It should be remembered that hydrogen has traditionally important applications in the chemical industry such as ammonia and methanol syntheses, oil refining and several petrochemical processes. However, a series of cases can be found that illustrate the interest for other uses of hydrogen from the start of the twentieth century. At that time, for example, the first big commercial units of water electrolysis were built and put into operation in Canada taking advantage of its large hydroelectric resources. Hydrogen and oxygen were mainly used in steel-cutting procedures. The German zeppelins used hydrogen for air travel during the 1920s and 1930s. During World War II, numerous cars, delivery vans and trucks were adapted to run on hydrogen in Germany and England. The U.S. space program led to the start of the development of fuel cells in the 1950s and 1960s. But the origin of the concept of a hydrogen economy corresponds to the electrochemist John Bockris in 1970. At that time, Bockris was a consultant to General Motors (GM) and, in his book *Energy: The Solar Hydrogen Alternative* (1975), he traces the coining of the term to a discussion at GM about possible alternatives to gasoline where it was agreed that hydrogen would be the eventual fuel for all types of transport in the future. Along with Bockris,[15] T. Nejat Veziroglu, who has been president

of the International Association for Hydrogen Energy (IAHE) since its beginning in 1974, has also had a prominent role in the development and dissemination of the hydrogen economy concept.[16,17] It seems no coincidence that the birth of the hydrogen economy concept in the 1970s coincides with the first oil crisis that marked the beginning of the end of cheap oil. The hydrogen economy pursues the final objective of a new energy system where human civilization is primarily powered by hydrogen. However, hydrogen is not an alternative fuel but an energy carrier that has to be produced consuming primary energy. This constitutes the central, but not unique, problem of the hydrogen economy.[18]

McDowall and Eames carried out an extensive review of the literature available until 2005 with the aim of capturing the diversity of published studies dealing with the future of hydrogen as an energy carrier and the hydrogen economy.[19] Despite divergent views on the factors that will shape the future of hydrogen energy, four main issues stand out in the early studies as the drivers of a hydrogen economy: climate change, energy security, local air quality and international competitiveness. A series of barriers to the development of a hydrogen economy have also been identified. Among the most outstanding are the difficulties involved in establishing a market for hydrogen and fuel cells in the absence of a hydrogen distribution and refueling infrastructure, and vice versa, without a market for hydrogen, there are no incentives for investments in very expensive new infrastructures. There is also agreement that the high cost of fuel cells as well as of hydrogen produced from low-carbon routes is a big hurdle for the deployment of hydrogen as an energy carrier in the sustainable future. A series of technological barriers are also recognized: difficulties for onboard storage of hydrogen, which limits the driving range of fuel cell vehicles, limited lifetime and reliability of fuel cells, uncertainty over the feasibility, costs and environmental impact of CCS, safety issues, public acceptance and the lack of specific legislation, codes and standards. Under these circumstances, the exploratory studies project that the hydrogen economy emerges very slowly, or not at all, in *business as usual* scenarios. However, a rapid deployment is predicted under conditions of strong governmental support combined, or as a result, of technological breakthroughs that allow greatly reducing costs, marked oil price increases, shifts in social values, or a rapid intensification of the problems associated to climate change. Several policy measures are usually recommended to support the hydrogen economy: increased R&D funding, infrastructure development, tax incentives for hydrogen fuel production and fuel cell vehicles purchase, support for renewables and targets for low carbon vehicles.

Taking the transition to fuel cell vehicles as the key step toward a hydrogen economy introduction, as it is usually considered in the early hydrogen futures studies, one can find a broad temporal distribution covering the period between 2010 and 2050 when the hydrogen economy emerges; this illustrates the diversity of views in this regard.[19] Once emerged, there is considerable agreement that the evolution of the hydrogen economy is from decentralized to centralized schemes. At first, a decentralized scheme based on the local (onsite) production of hydrogen from water electrolysis and biomass processing or steam reforming of natural gas facilitates overcoming the big barrier posed by the lack of a suitable infrastructure to the transition to hydrogen. Later, a gradual shift to centralized architectures allows introducing a wider variety of energy sources as coal and nuclear thermal energy for hydrogen generation at large scale and lower costs provided that a dedicated hydrogen distribution infrastructure is available. There is also agreement that in the short to medium term hydrogen production will rely on methane steam reforming, preferably with CCS, whereas the ultimate hydrogen economy is based on renewables. Fossil fuels as natural gas and coal and nuclear energy are frequently considered as transitional technologies.

McDowall and Eames identified a series of problems with the majority of the early literature.[19] Many of the studies make assumptions about the effects of policies on innovation and diffusion of new technologies but without a theoretical background or making explicit the basis of the assumptions. Predictions, forecasts and targets are recycled, deployed as arguments to confirm particular views of the future. Many of the descriptive futures display a prohydrogen bias, and there is also a tendency to analyze the prospective developments in hydrogen relatively isolated rather than integrated in a global and dynamic energy system.

In our opinion, another important weakness of many studies related to hydrogen energy is that the key issue of the efficiency, that is, the overall energy balance of hydrogen use is very often not clearly addressed.

1.2.2 The Efficiency Issue

Primary energy is consumed in all the steps of the hydrogen economy chain: production, storage, distribution, delivery and end use. Bossel[20] and Bossel et al.[21] have performed an analysis of the energy losses associated to these steps adopting water electrolysis for hydrogen production, as it allows the direct use of renewable sources as hydroelectric, wind or solar energy. Starting from 100 kWh of AC renewable electricity, Bossel estimated and compared the overall

efficiency between the electricity source and wheel motion for two types of cars: a hydrogen fuel cell electric vehicle (FCEV) and a battery electric vehicle (BEV) with regenerative braking.[20] The results for the FCEV case when hydrogen is distributed, stored and transferred to the vehicle as compressed gas are summarized in Fig. 1.3A. As can be seen, there is a cascade of energy losses that begins with the AC−DC conversion of electricity to feed the water electrolyzer. Bossel assumed efficiencies for these steps of 95 and 75%, respectively. As for the electrolysis, the figure seems reasonable in view of the performance of the modern alkaline bipolar filter press-type water electrolyzers, although it is significantly lower (50−65%) for the polymer electrolyte membrane (PEM) electrolyzers.[22,23] Transmission electricity losses were not present, in accordance with a plant for hydrogen production directly from the renewable electricity source. Regarding hydrogen delivery, in this example, it was considered that hydrogen was first compressed to 20 MPa and distributed by road to filling stations where it was stored at 10 MPa, and finally compressed to 40 MPa for rapid transfer to vehicles where it is stored at 35 MPa. The aggregate efficiency of this delivery scheme is 72%. As for the fuel cell, 50% efficiency was assumed that along with a 90% efficiency for the rest of the vehicle system yields an efficiency of the fuel cell-based powertrain of 45%. This results in 23 kWh of final useful energy, that is, an estimated overall efficiency of only 23%. The 50% efficiency assigned for the fuel cell seems today to be somewhat low. According to the Fuel Cells Technology Program of the U.S. Department of Energy, a PEM fuel cell yields 60% efficiency for transportation. Taking this value into account, the overall efficiency would increase up to about 28% (27.7 kWh of final energy available). Obviously, the final result is also dependent on the way hydrogen is stored and delivered. Presently, compressed and liquefied hydrogen are the only options commercially available. According to Bossel, the energy efficiency of the delivery scheme based on liquid hydrogen is 65% for the liquefaction process and 90% for its road transport, storage and vehicle transfer steps resulting in an aggregate 58%. In this case, the useful energy finally available, 22.5 kWh (22.5% overall efficiency assuming 60% efficiency for the fuel cell), is lower than when considering the use of hydrogen as compressed gas.

In the case of the BEV (Figure 1.3B), the losses correspond to the electricity transmission through the grid (90%), AC−DC conversion and battery charging (85%) and the electric powertrain (90%). The final overall efficiency of the BEV, 69%, is much higher than that for the FCEV. Obviously, the production of hydrogen from electricity (and water) to reconvert it back to electricity in a hydrogen fuel cell will be always much less efficient that the direct use of the original electric resource regardless of the way hydrogen is stored and delivered. From this example, it can be said that about one fourth of

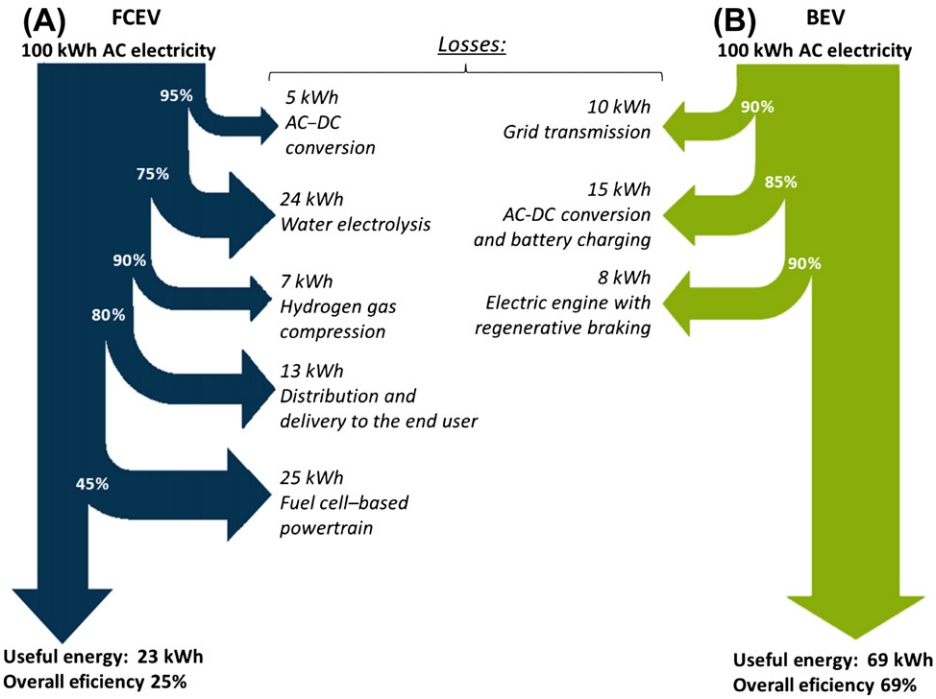

FIGURE 1.3 Energy losses for an FCEV fueled with hydrogen from water electrolysis and a BEV. (For color version of this figure, the reader is referred to the online version of this book.) *Source: Data taken from Bossel.*[20]

the electric power obtained from a renewable resource is finally put to service when using hydrogen produced from water electrolysis as energy carrier. It should be noted that water electrolysis has the advantage that produces very pure hydrogen, suitable for direct use in a PEM fuel cell. This is in contrast with the hydrogen production pathways from biomass, natural gas or coal that produce a mixture of hydrogen and carbon oxides (CO and CO_2). As PEM fuel cells do not tolerate CO concentrations in the feed above 10−50 ppm, it is necessary to further process the hydrogen stream to convert CO into CO_2 and then separate the carbon dioxide. Although the reforming of natural gas is a very efficient process that can achieve 90% for large-scale centralized plants, the need for hydrogen purification represents a significant energy penalty. Methane can be obtained from renewables resources as biomass gasification or the anaerobic digestion of organic wastes to produce biogas to further produce hydrogen, but at the expense of additional energy losses. It is interesting to mention at this point that hydrogen can be used in internal combustion engines (ICEs). Of course the efficiency is low compared with a fuel cell, although thermal efficiencies up to 35% can be achieved, which are better than the typical values for gasoline engines. However, ICEs do not require high-purity hydrogen that can offset to some extent the lower efficiency. Hydrogen-fueled ICE vehicles can be considered a transitional or bridging technology that would allow a faster introduction of hydrogen in the transport sector. This is mainly due to their lower cost, immediate availability and the possibility of using the current manufacture infrastructure of the automotive industry.[24]

The analysis of the parasitic energy losses led Bossel to state that a hydrogen economy will never make sense because it is an extremely inefficient proposition for the distribution of electricity from renewables. He also affirmed that, despite some niche markets tolerating high energy losses, it is unlikely that hydrogen will ever become a relevant energy carrier in an energy system relying on renewables and energy efficiency.[20] Although much less categorical in their conclusions, Rand and Dell also indicated that it would be very inefficient and uneconomic under most conditions to convert renewable electricity to a chemical fuel to be used in an ICE or reconverted back to electricity in a fuel cell.[25] According to these authors, it would be generally better to utilize directly renewable electricity since energy losses during electricity distribution are comparatively small. Two possible exceptions are highlighted. On the one hand is the case of islands or isolated communities with large renewable resources but without storing means that could produce hydrogen with surplus energy and reconvert it to electricity during periods of peak demand or insufficient renewable resource. On the other hand are countries such as Iceland or Norway that have abundant and cheap geothermal or hydroelectricity that could be used to produce hydrogen for use in transport. Rand and Dell also mentioned that without taking account of the losses incurred in compressing and distributing hydrogen, about 45% of the original electricity used to generate hydrogen by water electrolysis may be recovered with fuel cells. This figure is in line with the previous analysis of energy losses of an FCEV if one considers 75% efficiency for water electrolysis and 60% efficiency for the fuel cell.

Armaroli and Balzani also expressed a critical view.[18] Due to the environmental issues posed by the production of hydrogen from the currently available procedures, these authors described that talking about a hydrogen economy is *at least in part a futile exercise* before having developed the exploitation of renewables. They also described as irrational the use of water electrolysis to produce hydrogen that will be used in fuel cells to generate electricity again. The only reason to do it would be related to the capacity of hydrogen to store energy, but this practice is far from the dream of a global energy economy because it may become only a part of a future new energy system.

As discussed previously (see Section 1.1.2), the reduction of the primary energy consumption should be one of the pillars supporting this system. Energy efficiency will play a key role to achieve this goal. In fact, it should be noted that current energy losses during the whole energy conversion process amount to about two thirds of the primary energy used in power plants, kilns, thermal engines, high-temperature chemical processes, etc.[26] Electrolysis and fuel cell combinations may be employed for temporary storage of energy but only in situations where convenience outweighs inefficiency, as in the case of the FCEVs. In the very long term, when renewable electricity may be the main source of energy, efficiency considerations will dictate that it should be transmitted directly and not by chemical carriers as hydrogen. A sustainable energy system cannot be built on the basis of inefficiency, and this principle has to also be applied to the hydrogen economy. Therefore, the original hydrogen energy concept needs to be redesigned.

1.2.3 Hydrogen Contribution to Transportation and the Electric Grid

In a recent essay by Andrews and Shabani, it is affirmed that the time for a vision of the future in which hydrogen is the exclusive fuel has passed because the trend is toward the extensive use of electricity and batteries.[27] This does not imply that its future role has to be irrelevant. There are important areas of application in which hydrogen can still make significant

contributions, but in cooperation with electricity, not as competitors. This is the case of the use of hydrogen in the transportation sector and as energy storage means for the support of electric grids relying extensively on renewables.[27] These applications will be briefly commented on in the next subsections.

1.2.3.1 Hydrogen in Transportation

Our standard of living is in great part due to an easy access to the effective and fast transport of passengers, raw materials and manufactured goods. For this reason, as well as due to the strong implications of transport from the environmental and energy security points of view, this sector will continue playing a key role in the future energy system.[28,29]

Contrary to what happens today, that oil-derived fuels cover almost 95% of the energy demand of the transport sector, it is expected that in the coming decades there is a remarkable diversification of the energy sources used for transportation. Although the share of oil (including unconventional resources) will presumably continue to be predominant until at least 2035–2050, it seems reasonable that synthetic fuels from natural gas and coal, compressed and liquefied natural gas as well as biofuels gradually increase their contribution. Nevertheless, these options should also face their own challenges. This is the case, for example, of biofuels, which due to the possible negative impact of their extensive production on sustainability, have a maximum estimated future share of 20–30%.[29] All the alternatives mentioned so far are fuels for ICEs (note that methane can also feed some high-temperature fuel cells suitable for stationary applications). But what may lead to a revolution of the transport sector is its electrification, a revolution that perhaps has already started. Several car manufacturers are now commercializing a series of electric vehicles that, although with a small market share at the moment, are expected to grow their sales at a rapid pace in the coming years. These vehicles can be ranked according to an increased involvement of the battery in the powertrain, and thus extended electric driving range, as follows[29]: hybrid electric vehicles (HEVs), plug-in hybrid electric vehicles (PHEVs) and pure BEVs. Both HEVs and PHEVs incorporate an ICE whereas the BEVs include an electric engine. The FCEVs can be considered an alternative to the PHEVs and HEVs. Electrification has important advantages:

1. It is an effective way of decarbonizing the transport sector provided that electricity from renewables is used to recharge the batteries.
2. The energy efficiency is much higher compared to the use of liquid fuels or even FCEVs; nevertheless, further development of batteries technology is still required.
3. There is only need for a network of recharging stations but, in contrast to hydrogen, the distribution infrastructure already exists, the electric grid. Of course, a transformation of the grid management system will be required to permit a high degree of penetration of renewables in the electricity mix.

Despite the optimistic perspectives for the electric vehicles, perhaps the main challenge they have to face is that of customer acceptance regarding their limited driving range, as well as the availability, accessibility and user convenience of the recharging stations. According to the current status of the battery technology, it seems that BEV will be suitable only for short-distance transport, for example in urban areas, due to their limited driving range. In order to increase the range to large distances PHEVs can be used, but they depend on the availability of liquid fuels. This is where the hydrogen FCEVs become more competitive because these vehicles cover the entire driving range; moreover, refueling is much faster than in the case of the electric vehicles.[29] The drawbacks are the higher cost of FCEVs and the complexity and cost of a completely new hydrogen distribution infrastructure.

The degree of success of the BEVs and FCEVs will depend to a great extent on the future technological progress and cost evolution of batteries and fuel cells. A significant breakthrough in battery technology allowing BEVs to cover the entire driving range would likely make the FCEVs largely unnecessary. In contrast, the consequences of a breakthrough in fuel cells technology leading to a substantial reduction of the FCEV cost is much less clear due to the uncertainties about the feasibility of a supporting hydrogen infrastructure. It may also happen that BEVs and FCEVs reach their corresponding market shares that can differ depending on different regional or national determining factors such as the grid characteristics, hydrogen costs, renewables deployment and liquid fuels availability.

Finally, the potential of the hydrogen-fueled ICE vehicles to dynamize an early hydrogen market that can catalyze the integration of hydrogen in the transport sector should not be forgotten.

1.2.3.2 Hydrogen and the Electric Grid

The electric grid accumulates over a century of reliable service but aging of the infrastructure is challenging the ability of the electric grid to continue performing suitably. One of the main challenges is the management of an increasing share of intermittent generation capacity associated to renewables as wind and solar energy. The fluctuations of these sources are more pronounced than fluctuations in electricity demand and compensating for these variations is complex.

The smart grid concept is very promising regarding the solution of these problems.[30] A smart grid consists in the application of modern communications infrastructure to various segments of the electric grid. This enables the system operator to better monitor the high-voltage transmission grid and control the energy flows more precisely. The load control capacity offered by a smart grid could help to compensate for wind and solar variability by managing energy storage systems, as for example, thermal storage units based on electric water heaters, compressed air facilities or hydropumping. Hydrogen produced from water electrolysis offers also the possibility of storing renewable energy during overgeneration periods. The Spanish case constitutes a good example of the potential of hydrogen to balance the grid loads.[31] The current power generation capacity in Spain is over 90 GW while the peak demand reaches about 45 GW. Clearly, the Spanish power system is dramatically underutilized. Part of this overcapacity, even those corresponding to nonrenewable energy sources, could be considered for hydrogen production, as suggested for other world regions.[32] Moreover, an analysis of the data from the Spanish power operator shows that annual power generation exceeds the electricity demand in an amount that in 2009 reached 3.25% (8170 GWh), with a daily average surplus of 22.4 GW. The study carried out by Gutiérrez-Martín and Guerrero-Hernández is based on the analysis of the deployment of 53 water electrolysis plants of a rated capacity of 50 MW each during the period 2011–2020.[31] It was concluded that, by starting the operation in 2011 with 23 electrolysis units, a positive cash flow is obtained from 2014 with net income of €1863 million in the whole period considered. It is possible in this way to attain up to 42.2% share of renewable power generation in Spain by 2020. The total surplus energy would amount up to 126,013 GWh, being about 61% off-peak generated energy. The energy back generated with hydrogen would be 11,674 GWh ≈ 1 Mtoe, or the energy content equivalent of about 297,000 tons of hydrogen. The study serves to illustrate that it is technically and economically feasible to improve the management of the electric grid using the excess power during overgeneration periods for producing hydrogen from water electrolysis.

1.3 HYDROGEN PRODUCTION

Hydrogen is an energy carrier so its production is the first step of its possible contribution to the energy system. Moreover, this step greatly influences its environmental and carbon footprints because hydrogen can be obtained whatever the type (fossil, nuclear or renewable) of primary energy used.

This section will start with a series of simple calculations with the aim of illustrating the order of magnitude that represents the amount of hydrogen that can be needed in the future. The analysis is limited to the foreseeable needs for transportation since, as discussed previously, the transport sector is one of the most likely areas of application of hydrogen. According to the U.S. EIA reference case, the primary energy demanded by the transport sector will increase from 2470 Mtoe in 2008 to 3578 Mtoe in 2035.[5] This is equivalent to an increase from 103 to 150 EJ. It should be noted these enormous amounts of energy include all transport means (road, rail, air, water and even pipeline). As a first approximation, only road transport with light-duty vehicles will be considered. Even with a significant electrification of the transportation, the share attained by the FCEVs could reach 30–70%.[29] Therefore, the energy that would be demanded in the form of hydrogen in 2035 can be estimated between 6 and 14 EJ. The higher heating value of hydrogen is 141.6 MJ/kg so the amount of hydrogen required would be between 42.4 and 98.9 million tons. The current annual world production of hydrogen is about 60 million tons that are mainly used for ammonia synthesis (51%), oil refining (35%) and methanol synthesis (8%).[33] This implies that by 2035, the global production capacity of hydrogen would have to be between two and three times the current one. Achieving this figure looks challenging but not impossible, especially if there is a dynamic market stimulating the production and consumption of hydrogen. These calculations can be considered conservative compared to what would be the hydrogen-equivalent of the total world energy demanded by the transportation sector. One can realize in this way the unattainable implications of a hydrogen economy fully powered with hydrogen.

In the following subsections, the main routes for hydrogen production will be presented, with emphasis on the use of renewables.

1.3.1 Pathways

One of the attractive features of hydrogen as an energy carrier is that it can be obtained from virtually any energy source. This topic has been profusely treated in the literature so here we will limit to provide a general overview distinguishing between routes leading to the production of nonrenewable and renewable hydrogen.[33–35]

1.3.1.1 Nonrenewable Hydrogen

The main pathways for hydrogen from nonrenewable energy sources are schematized in Fig. 1.4. Nuclear power has been included in this category because the available nuclear fuel reserves are limited. These routes

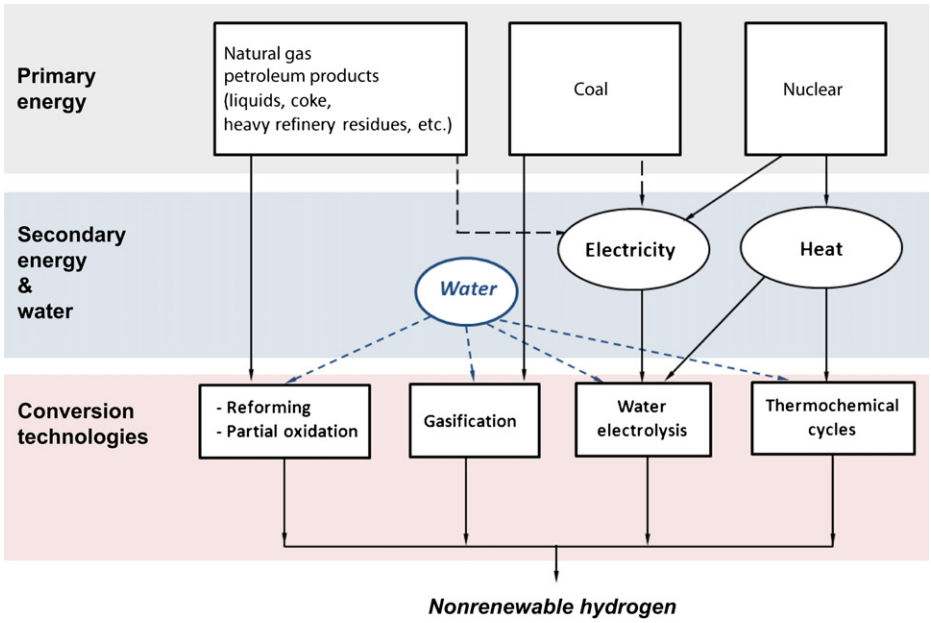

FIGURE 1.4 Scheme of the main hydrogen production pathways from fossil fuels and nuclear power. (For color version of this figure, the reader is referred to the online version of this book.)

have great importance because they are currently used to produce over 96% of the total hydrogen. About 48% is obtained from methane, mainly by steam reforming, 30% from petroleum fractions in refineries (through steam reforming and partial oxidation) and 18% from coal gasification.[18,33] The share of water electrolysis to hydrogen production is 4% and only the contribution of renewables to the electricity mix could be considered capable of producing renewable hydrogen. This contribution was about 20% in 2010.[36]

Hydrogen production from fossil fuels is carried out through a series of thermochemical processes involving several catalytic steps. These processes are commercially available and, in the case of the steam reforming of methane (SRM), especially mature. As long as natural gas remains at moderate prices, even including a carbon tax, SRM will prevail as the technology of choice for massive hydrogen production.[37] There is almost general agreement that the huge amounts of hydrogen required for its introduction in the transportation sector could only be obtained in the short and medium terms by means of SRM. Recent developments in the field of coal gasification such as the entrained flow gasifiers used in the Integrated Gasification Combined Cycle (IGCC) systems indicate that this technology will play an increasingly important role for hydrogen production.[38–40] Power plants based on IGCC could efficiently coproduce hydrogen and electricity. However, in order that fossil fuels can contribute to hydrogen production within an energy system compatible with the stabilization of the GHG concentration in the atmosphere, the development and deployment of CCS technologies are indispensable.

Regarding CO_2 and CCS, Benson and Surles made an interesting analogy with other environmental problems.[41] In the same manner as pollutants such as SO_2 or NO_x from power plants or municipal wastes are no longer released into the environment, these authors wonder whether it could be the same with the CO_2 emissions from fossil fuels. In previous occasions, avoiding pollutant emissions was initially believed to be too costly. However, once the requirements to limit the emissions are established, technological innovation in competitive markets resulted in effective solutions at acceptable costs. This is also expected for CCS, also known as carbon sequestration. The process starts with the separation and concentration to a nearly pure form of the CO_2 contained in flue gases at the industrial source. Then it is compressed to about 10 MPa and pumped as liquid into deep geological formations where it is stored. Suitable underground formations are depleted oil and gas wells, brine-filled formations or deep unmineable coal beds. Consideration was also given to the injection and storage of CO_2 in the ocean, but concerns about possible unknown environmental impacts have led to loss of interest in this option. Potential storage capacity is estimated to be over 3×10^6 million tons of CO_2 and a few industrial-scale projects have been operated.[41] There are different types of CCS systems: postcombustion, precombustion and oxyfuel combustion. The flue gas pressure, its CO_2 content and the type of fuel (solid or gas) are important factors in selecting the capture system. There is relatively little experience in combining CO_2

capture, transport and storage into a fully integrated system.[42] In addition to the technological challenges that still remain, numerous life cycle assessment studies are being performed in order that the decision to deploy CCS at a large scale is based on robust information on its overall costs and benefits.[43]

As mentioned earlier, water electrolysis constitutes a minority pathway to hydrogen production. The technology is mature; moreover, there are commercial units available with rated powers up to 3.5 MW that are capable of producing up to about 600 hydrogen tons per year.[23] The main drawbacks are economic; the operating costs are especially much higher than for the thermochemical routes. High-temperature heat available, for example, at nuclear power plants could be used in conjunction with electricity to perform the electrolysis of steam with the advantage that at high temperature it is thermodynamically feasible to lower the fraction of energy supplied to the electrolyzer in the form of electricity, thus reducing production costs. This technology is not commercially available yet, although promising progresses have been made in recent years.

As indicated in Fig.1.4, high-temperature heat can be used to obtain hydrogen from water by means of thermochemical cycles. This pathway consists in a series of chemical reactions forming a closed cycle in which water is decomposed and all other chemical compounds are recycled. Typically, thermochemical cycles require heat at temperatures of at least 850–900 °C. For this reason, the feasibility of these cycles is typically linked to nuclear power, although the concept also shows potential to be performed with geothermal resources.[44] At present, the most promising cycles are the so-called sulfur–iodine (S–I), Br–Ca–Fe and copper-chloride (Cu-Cl). None of them is commercially available yet.

The cost of hydrogen is obviously a key factor that will markedly influence the role a given technology will play for future hydrogen production. Bartels et al. performed a literature review on this issue.[45] Even including CCS, the cheapest hydrogen can be obtained from coal (U.S. $1.05–1.83/kg) and natural gas ($2.48–3.17/kg). Although the initial capital cost of the coal plants are much higher than that fueled with natural gas, the coal ones benefit from a significantly cheaper and more abundant feedstock.

Hydrogen costs are much higher for the remaining production routes. Regarding, for example, water electrolysis combined with the current nuclear reactors technology, the cost of hydrogen is within the $4.36–7.36/kg range. These figures can be compared with the price of gasoline taking into account that 1 kg of hydrogen has approximately the same energy content as a U.S. gallon (3.78 l) of gasoline.

1.3.1.2 *Renewable Hydrogen*

The main pathways for hydrogen from renewable energy sources are schematized in Fig. 1.5. Biomass can be used for hydrogen production through thermochemical processes. Among the several possible options, gasification is expected to be commercially available in the near future with very attractive hydrogen costs (U.S. $1.44–2.83/kg).[33,45] Anaerobic digestion is also

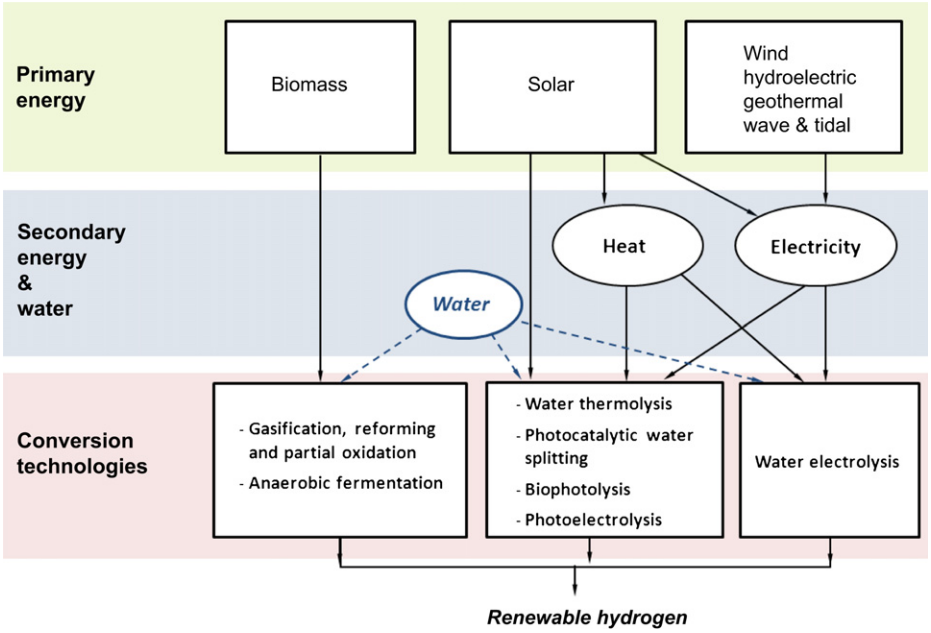

FIGURE 1.5 Scheme of the main hydrogen production pathways from renewables. (For color version of this figure, the reader is referred to the online version of this book.)

an appealing route to hydrogen production because it allows the valorization of organic wastes. Low production rate is one of the main challenges of this process.[46] In Fig. 1.5, wind, hydroelectric, geothermal, wave and tidal energies have been grouped because their contribution to hydrogen production would be almost exclusively based on water electrolysis. Hydrogen from wind power and water electrolysis could be obtained at prices of $5.55–6.77/kg. Of course, solar photovoltaic (PV) energy can also be used to obtain hydrogen from water electrolysis. PV panels have experienced remarkable cost reductions in the last years; however, hydrogen produced from water electrolysis driven with PV electricity is still much more expensive ($23.27/kg) than hydrogen from wind power.[45] Nevertheless, the evolution is favorable and it is expected that in the future the costs of hydrogen produced from both solar PV and wind power are similar. Concentrated solar power also allows generating electricity that can be used for water electrolysis; hydrogen costs are estimated at $6.46/kg.[45]

It is apparent from Fig. 1.5 that solar energy is the most versatile form of renewable energy regarding hydrogen production. In fact, in addition to solar electricity-driven water electrolysis, there are many other options.[46–48] Solar–thermal water splitting, also known as solar thermolysis, is receiving considerable attention. The idea of the direct decomposition of water driven by concentrated solar heat is attractive. However, the process is unfavored thermodynamically; at temperatures as high as 2200 °C, a maximum water (steam) dissociation of 25% can be achieved. Moreover, the necessity of separating hydrogen of the coproduced oxygen, radiation losses and challenges associated to the availability of materials for reactor construction capable of withstanding these extremely high temperatures are issues that may make this process technically and economically unfeasible. As a result, the interest is now placed on the thermochemical cycles that, as discussed in the previous section, can operate at much lower temperatures.[49,50]

Photocatalytic water splitting under visible light irradiation allows obtaining hydrogen from the irradiation of sunlight on water in the presence of a suitable catalyst that reduces the high activation energy of the decomposition reaction.[51,52] The process can be carried out more easily by an indirect route, using water in combination with a so-called sacrificial reducing agent, typically, and alcohol such as methanol. Noble metals such as Pd, Pt, Ir and Au supported on a semiconductor such as TiO_2 are active catalysts for this process. The use of a sacrificial agent compromises the sustainability of the indirect route since whereas hydrogen gas is liberated, oxygen from water forms CO_2 by the reaction with the alcohol. Although renewable alcohols such as bioethanol and glycerol can be used instead of methanol, the direct pathway is more appealing and also more challenging. This process can be carried out in a photoelectrochemical cell in which one of the electrodes (anode) is a photocatalyst (e.g. TiO_2) exposed to sunlight and the other (cathode) is made of Pt. Under a suitable pH gradient provided by the electrolytes in each chamber, oxygen and hydrogen evolve separately from the anode and cathode, respectively. Another possibility is to irradiate with sunlight a slurry of the photocatalyst in water leading to the coproduction of hydrogen and oxygen that have to be subsequently separated. Typical photocatalysts are semiconductor metal oxides and sulfides such as TiO_2, NiO, $SrTiO_3$ and ZnS.[52] Issues such as the need for absorbing a wide range of solar radiation, low production rate and catalyst stability require considerable research effort before photocatalytic water splitting can significantly contribute to hydrogen production.[51]

Photoelectrolysis is another hydrogen production process in which both sunlight and electricity are used. Main difference with conventional water electrolysis is that one of the electrodes contains a photocatalyst that is exposed to light. However, a photoelectrochemical cell is more compact. Finally, in biophotolysis, microorganisms such as microalgae that are sensible to light and exhibit hydrogen evolution capacity are cultured in a photobioreactor. The process can be carried out at room temperature and pressure and it has now been demonstrated at the laboratory scale only.[46]

Before concluding this section, it would be convenient to highlight that water is as necessary as renewable energy to produce hydrogen. This is obvious for the routes based on water electrolysis, photolysis or thermolysis, but the reforming and gasification of fossil fuels and biomass also require water, that in many cases should be of very high purity. It is also frequent that regions rich in renewable energy resources are arid or semiarid. In these situations, onsite hydrogen production will not be possible. Globally speaking, water is a resource under pressure, and massive hydrogen production would likely increase this pressure. This key issue should be taken into account when considering the impact of the deployment of hydrogen as an energy carrier.

1.3.2 Status and Prospects of Renewables

The availability of renewable hydrogen depends on the deployment of renewables. Renewables are being developed at a rapid pace, but these resources are only allocated to power generation, not as fuels, biofuels being the only exception. The conclusion is that an even stronger implantation of renewables would be

required in the future to satisfy both electricity and hydrogen production.

According to REN21, between 2005 and 2010, total global capacity of solar PV, wind power, concentrating solar thermal power, solar water heating systems and biofuels grew at average annual rates ranging from 15% to 50%. Continued strong growth is expected in all renewable energy sectors in the coming years.[36] Total investment in renewables exceeded U.S. $226 000 million in 2010, with an additional $40000−45000 million in large hydropower. For the first time, the investment in developing countries surpassed that in developed countries. More than a third of the investment corresponds to China, making it the world leader for the second year. Global hydropower production represented about 16% of global electricity production in 2010. An estimated 30 GW of capacity was added to reach a total of 1010 GW worldwide. China and Brazil are the most active countries for new hydroelectric generation. Wind power added 38 GW during 2010 reaching a total of about 198 GW. The trends include an increasingly more relevant role of the emerging markets, driven primarily by China, as well as continued offshore development and growing popularity of community-based projects and distributed small-scale grid-connected turbines. Regarding solar PV, global production and markets more than doubled in 2010. About 17 GW of capacity were added worldwide reaching a total of 40 GW. In this case, the market was dominated by Europe, particularly Germany. In contrast, cell manufacturing shifted to Asia, with 10 of the top 15 manufacturers located in the region. Remarkable cost reductions of solar PV are challenging the development of concentrating thermal solar power. On the other hand, solar heating capacity increased by an estimated 25 GWth in 2010 to reach approximately 185 GW_{th} that are used for both water and space heating. Geothermal power plants reached over 11 GW experiencing a significant acceleration that is expected to continue.

With regard to biomass, 62 GW of power capacity were in operation by the end of 2010. Trends of this sector include an increasing demand of biomass pellets for heat and power and the use of biomass in combined heat and power plants and in centralized district heating systems. Methane obtained from biogas is increasingly being injected into natural gas pipelines, particularly in Europe. Liquid biofuels (bioethanol and biodiesel) provided about 2.7% of global road transport fuels in 2010.[36]

1.4 HYDROGEN TODAY

There exists an enthusiastic and active community integrated by national and international associations and official agencies, some governments, research and education institutions, private companies and even individuals working in pursuit of the development and deployment of hydrogen as an energy carrier. To conclude this chapter, a selection of the main activities promoted by this community will be briefly presented. The future role of hydrogen in our energy system greatly depends on their success.

As it has been demonstrated for the renewables, the deployment of hydrogen will likely fail without governmental support. Main initiatives in this regard correspond to the European and U.S. authorities. *HyWays* is the name of the European hydrogen energy roadmap.[53] This roadmap was designed with the aim of helping to overcome the economic, technological and institutional barriers that make the introduction of hydrogen in the energy system difficult. One of its drivers is the fact that the possibility of taking a leader position in the worldwide market for hydrogen technologies would provide new economic opportunities and strengthen European competitiveness. The main challenges were identified as the need for cost reduction, which requires a substantial increase in R&D investments, and policy support, because hydrogen is generally not on the agenda of the ministries responsible for environment protection and energy security. The roadmap objectives for 2050 include 80% of light-duty vehicles and city buses fueled with CO_2-free hydrogen, reaching more than 80% CO_2 reduction in passenger car transport and the use of hydrogen in stationary end-use applications in remote locations and island grids. As a consequence of this roadmap, a Fuel Cells and Hydrogen Join Technology Initiative was established as a European public−private partnership for hydrogen and its end-use applications.[54]

The *Hydrogen and Fuel Cells Program Plan* outlines the strategy, activities and plans of the U.S. Department of Energy Hydrogen and Fuel Cells Program.[55] This document was completely revised in September 2011 after its previous update in 2006; by that year, it was known as the *Hydrogen Posture Plan*. The new program seeks to act as a catalyst in the transition from R&D to demonstration and early deployment of hydrogen by integrating real-world technology demonstrations, public outreach and education and market transformation activities. To this end, a detailed technology development timeline and key milestones are established between 2010 and 2020 in the areas of fuel cell R&D, hydrogen production, delivery and storage, manufacturing R&D, technology validation, education, safety, codes and standards, market transformation and system analysis.

Regarding international cooperation, the most outstanding initiative is the International Partnership for Hydrogen and Fuel Cells in the Economy (IPHE) that includes 17 member countries and the EC and the IEA Implementing Agreements.[56] This organization has recently published the *IPHE Renewable Hydrogen*

Report that contains a collection of project overviews outlining past and current demonstrations, including R&D projects involving hydrogen that is produced from renewable sources.[57] Another relevant example of international cooperation is the Partnership for Advancing the Transition to Hydrogen (PATH).[58] This is a not-for-profit international coalition of hydrogen associations (up to 20) established in 2002 that seeks international cooperation to help advance the transition to hydrogen as potential energy carrier. PATH has recently published the *Annual Report on World Progress in Hydrogen* that is intended to provide a broad level picture of the current state of the global hydrogen and fuel cell industry. The issues addressed include hydrogen and fuel cell development projects, government funding and initiatives, production, manufacturing, technology deployment, education, public perception, employment data, international partnerships and status of PATH associations.

The role of international associations in the development of hydrogen energy is of great importance. The IAHE was pioneering in this regard.[16,59] The work of the IAHE is particularly relevant with regard to the dissemination of the scientific knowledge and technology progresses in the hydrogen energy field through its official scientific journal, the *International Journal of Hydrogen Energy*, and the organization of the World Hydrogen Energy Conferences.

Acknowledgments

The financial support by the Spanish Ministry of Science and Innovation and Ministry of Economy and Competitiveness (ENE2009-14522-C04 and ENE2012-37431-C03 grants, respectively) is gratefully acknowledged.

References

1. IPCC. In *Climate Change 2007: Synthesis Report. Contribution of Working Groups I, II and III to the Fourth Assessment Report of the Intergovernmental Panel on Climate Change;* Pachauri, R. K., Reisinger, A., Eds.; IPCC: Geneva, 2007.
2. Ritter, S. K. Global Warming and Climate Change. *Chem. Eng. News December* **2009,** *21,* 11.
3. International Energy Agency. *World Energy Outlook 2011: Executive Summary;* OECD/IEA: Paris, 2011.
4. United Nations, Framework Convention on Climate Change, Draft Decision -/CP.17 Establishment of an Ad Hoc Working Group on the Durban Platform for Enhanced Action. Available at http://unfccc.int/resource/docs/2011/cop17/eng/l01.pdf (accessed February 6, 2012).
5. U.S. Energy Information Administration (EIA). *International Energy Outlook 2011, DOE/EIA-0484.* September 2011, Available at: http://www.eia.gov/forecasts/ieo/pdf/0484(2011).pdf (accessed February 6, 2012).
6. Sorrell, S.; Speirs, J.; Bentley, R.; Miller, R.; Thompson, E. Shaping the Global Oil Peak: A Review of the Evidence on Field Sizes, Reserve Growth, Decline Rates and Depletion Rates. *Energy* **2012,** *37,* 709.
7. Brandt, A. R. Variability and Uncertainty in Life Cycle Assessment Models for Greenhouse Gas Emissions from Canadian Oil Sands Production. *Environ. Sci. Technol.* **2012,** *46,* 1253.
8. Burnham, A.; Han, J.; Clark, C. E.; Wang, M.; Dunn, J. B.; Palou-Rivera, I. Life-Cycle Greenhouse Gas Emissions of Shale Gas, Natural Gas, Coal, and Petroleum. *Environ. Sci. Technol.* **2012,** *46,* 619.
9. International Energy Agency. *Key World Energy Statistics 2011;* OECD/IEA: Paris, 2011.
10. European Climate Foundation. *Roadmap 2050: A Practical Guide to a Prosperous, Low-Carbon Europe*. April 2010, Available at: http://www.roadmap2050.eu/attachments/files/Volume1_fullreport_PressPack.pdf (accessed February 6, 2012).
11. European Commission. *Communication COM(2011) 885/2 from the Commission to the European Parliament, the Council, the European Economic and Social Committee and the Committee of the Regions: Energy Roadmap 2050, Brussels*. December 2011, Available at http://ec.europa.eu/energy/energy2020/roadmap/doc/com_2011_8852_en.pdf (accessed February 6, 2012).
12. Directive 2009/28/EC of the European Parliament and of the Council of 23 April 2009 on the Promotion of the Use of Energy from Renewable Sources. *Official Journal of the European Union* 5.6.2009:L140/16−62.
13. Bleischwitz, R.; Bader, N. Policies for the Transition Towards a Hydrogen Economy: The EU Case. *Energy Policy* **2010,** *38,* 5388.
14. Dunn, S. History of Hydrogen. In *Encyclopedia of Energy,* Vol. 3; Elsevier-Academic Press: San Diego (CA), 2004; 241.
15. Bockris, J. O.' M. Hydrogen Economy in the Future. *Int. J. Hydrogen Energy* **1999,** *24,* 1.
16. Veziroglu, T. N. Quarter Century of Hydrogen Movement 1974−2000. *Int. J. Hydrogen Energy* **2000,** *25,* 1143.
17. Momirlan, M.; Veziroglu, T. N. Current Status of Hydrogen Energy. *Renew. Sust. Energ. Rev.* **2002,** *6,* 141.
18. Armaroli, N.; Balzani, V. The Hydrogen Issue. *ChemSusChem* **2011,** *4,* 21.
19. McDowall, W.; Eames, M. Forecasts, Scenarios, Visions, Backcasts and Roadmaps to the Hydrogen Economy: A Review of the Hydrogen Futures Literature. *Energy Policy* **2006,** *34,* 1236.
20. Bossel, U. Does a Hydrogen Economy Make Sense? *Proc. IEEE* **2006,** *94,* 1826.
21. Bossel, U.; Eliasson, B.; Taylor, G. The Future of the Hydrogen Economy: Bright or Bleak? *Proc. Eur. Fuel Cell Forum* April **2003**. Available at: http://planetforlife.com/pdffiles/h2report.pdf (accessed February 6, 2012).
22. Gandía, L. M.; Oroz, R.; Ursúa, A.; Sanchis, P.; Diéguez, P. M. Renewable Hydrogen Production: Performance of an Alkaline Water Electrolyzer Working under Emulated Wind Conditions. *Energy Fuels* **2007,** *21,* 1699.
23. Ursúa, A.; Gandía, L. M.; Sanchis, P. Hydrogen Production from Water Electrolysis: Current Status and Future Trends. *Proc. IEEE* **2012,** *100,* 410.
24. Sáinz, D.; Diéguez, P. M.; Sopena, C.; Urroz, J. C.; Gandía, L. M. Conversion of a Commercial Gasoline Vehicle to Run Bi-Fuel (Hydrogen-Gasoline). *Int. J. Hydrogen Energy* **2012,** *37,* 1781.
25. Rand, D. A. J.; Dell, R. M. *Hydrogen Energy. Challenges and Prospects, RSC Energy Series;* RSC Publishing, The Royal Society of Chemistry: Cambridge (UK), 2008.
26. Jochem, E. Energy-Efficient Solutions Needed—Paving the Way for Hydrogen. In *The Hydrogen Economy. Opportunities and Challenges;* Ball, M., Wietschel, M., Eds.; Cambridge University Press: Cambridge (UK), 2009; p 599.
27. Andrews, J.; Shabani, B. Re-envisioning the Role of Hydrogen in a Sustainable Energy Economy. *Int. J. Hydrogen Energy* **2012,** *37,* 1184.

28. Wietschel, M.; Doll, C. Sustainable Transport Visions: The Role of Hydrogen. In *The Hydrogen Economy. Opportunities and Challenges;* Ball, M., Wietschel, M., Eds.; Cambridge University Press: Cambridge (UK), 2009; p 563.
29. Wietschel, M.; Ball, M. The Future of Hydrogen—Opportunities and Challenges. In *The Hydrogen Economy. Opportunities and Challenges;* Ball, M., Wietschel, M., Eds.; Cambridge University Press: Cambridge (UK), 2009; p 613.
30. Blumsack, S.; Fernandez, A. Ready or Not, Here Comes the Smart Grid!. *Energy* **2012,** *37,* 61.
31. Gutiérrez-Martín, F.; Guerrero-Hernández, I. Balancing the Grid Loads by Large Scale Integration of Hydrogen Technologies: The Case of the Spanish Power System. *Int. J. Hydrogen Energy* **2012,** *37,* 1151.
32. Felder, F. A.; Hajos, A. Using Restructured Electricity Markets in the Hydrogen Transition: The PJM Case. *Proc. IEEE* **2006,** *94,* 1864.
33. Ball, M.; Weindorf, W.; Bünger, U. Hydrogen Production. In *The Hydrogen Economy. Opportunities and Challenges;* Ball, M., Wietschel, M., Eds.; Cambridge University Press: Cambridge (UK), 2009; p 277.
34. Gupta, R. B., Ed. *Hydrogen Fuel—Production, Transport, and Storage;* CRC Press—Taylor & Francis Group: Boca Raton (FL), 2009.
35. Stolten, D., Ed. *Hydrogen and Fuel Cells—Fundamentals, Technologies and Applications;* Wiley-VCH: Weinheim, 2010.
36. REN21. *Renewables 2011 Global Status Report;* REN21 Secretariat: Paris, 2011.
37. Navarro, R. M.; Peña, M. A.; Fierro, J. L. G. Hydrogen Production Reactions from Carbon Feedstocks: Fossil Fuels and Biomass. *Chem. Rev.* **2007,** *107,* 3952.
38. Cormos, C.-C.; Starr, F.; Tzimas, E.; Peteves, S. Innovative Concepts for Hydrogen Production Processes Based on Coal Gasification with CO_2 Capture. *Int. J. Hydrogen Energy* **2008,** *33,* 1286.
39. Cormos, C.-C.; Starr, F.; Tzimas, E. Use of Lower Grade Coals in IGCC Plants with Carbon Capture for the Co-production of Hydrogen and Electricity. *Int. J. Hydrogen Energy* **2010,** *35,* 556.
40. Wei, W.; Kulkarni, P.; Liu, K. Integration of H_2/Syngas Production Technologies with Future Energy Systems. In *Hydrogen and Syngas Production and Purification Technologies;* Liu, K., Song, C., Subramani, V., Eds.; AIChE—John Wiley & Sons: Hoboken (NJ), 2010; p 451.
41. Benson, S. M.; Surles, T. Carbon Dioxide Capture and Storage: An Overview with Emphasis on Capture and Storage in Deep Geological Formations. *Proc. IEEE* **2006,** *94,* 1795.
42. Metz, B., Davidson, O., de Coninck, H., Loos, M., Meyer, L., Eds. *IPCC Special Report on Carbon Dioxide Capture and Storage;* Cambridge University Press: New York (NY), 2005.
43. Sathre, R.; Chester, M.; Cain, J.; Masanet, E. A Framework for Environmental Assessment of CO_2 Capture and Storage Systems. *Energy* **2012,** *37,* 540.
44. Balta, M. T.; Dincer, I.; Hepbasli, A. Thermodynamic Assessment of Geothermal Energy Use in Hydrogen Production. *Int. J. Hydrogen Energy* **2009,** *34,* 2925.
45. Bartels, J. R.; Pate, M. B.; Olson, N. K. An Economic Survey of Hydrogen Production from Conventional and Alternative Energy Sources. *Int. J. Hydrogen Energy* **2010,** *35,* 8371.
46. Dincer, I. Green Methods for Hydrogen Production. *Int. J. Hydrogen Energy* **2012,** *37,* 1954.
47. Rajeshwar, K., McConnell, R., Licht, S., Eds. *Solar Hydrogen Generation—Toward a Renewable Energy Future;* Springer: New York (NY), 2008.
48. Vayssieres, L., Ed. *On Solar Hydrogen & Nanotechnology;* John Wiley & Sons (Asia): Singapore, 2009.
49. Perkins, C.; Weimer, A. W. Likely Near-Term Solar-Thermal Water Splitting Technologies. *Int. J. Hydrogen Energy* **2004,** *29,* 1587.
50. Agrafiotis, C.; Roeb, M.; Konstandopoulos, A. G.; Nalbandian, L.; Zaspalis, V. T.; Sattler, C.; Stobbe, P.; Steele, A. M. Solar Water Splitting for Hydrogen Production with Monolithic Reactors. *Solar Energy* **2005,** *79,* 409.
51. Bowker, M. Sustainable Hydrogen Production by the Application of Ambient Temperature Photocatalysis. *Green Chem.* **2011,** *13,* 2235.
52. Navarro, R. M.; Consuelo Alvarez-Galván, M.; Villoria de la Mano, J. A.; Al-Zahrani, S. M.; Fierro, J. L. G. A Framework for Visible-Light Water Splitting. *Energy Environ. Sci.* **2010,** *3,* 1865.
53. HyWays, The European Hydrogen Energy Roadmap, ftp://ftp.cordis.europa.eu/pub/fp7/energy/docs/hyways-roadmap_en.pdf
54. Fuel Cells and Hydrogen Joint Technology Initiative, http://www.fch-ju.eu/.
55. The Department of Energy Hydrogen and Fuel Cells Program Plan, Available at http://www.hydrogen.energy.gov/pdfs/program_plan2011.pdf
56. International Partnership for Hydrogen and Fuel Cells in the Economy, http://www.iphe.net/.
57. IPHE Renewable Hydrogen Report, March 2011. Available at, http://www.iphe.net/docs/Renewable_H2_Rpt_040411.pdf.
58. Partnership for Advancing the Transition to Hydrogen, http://www.hpath.org/.
59. International Association for Hydrogen Energy, http://www.iahe.org/.

CHAPTER

2

Water Electrolysis Technologies

Pierre Millet [*], *Sergey Grigoriev* [†]

[*]University of Paris (XI), France, [†]National Research Center "Kurchatov Institute", Moscow, Russian Federation

OUTLINE

2.1 Introduction to Water Electrolysis 19
2.1.1 Brief Historical Review 19
2.1.2 Thermodynamics 20
2.1.3 Kinetics and Efficiencies 22
2.1.4 Main Water Electrolysis Technologies 22

2.2 Alkaline Water Electrolysis 25
2.2.1 Principles 25
2.2.2 Cell Components and Stack Structure 26
2.2.3 Performances 26
2.2.4 Technology Developments and Applications 26
2.2.5 Limitations, Recent Advances and Perspectives 28

2.3 Proton-Exchange Membrane Water Electrolysis 29
2.3.1 Principles 29
2.3.2 Cell Components 30
2.3.3 Performances 31
2.3.4 Technology Developments and Applications 31
2.3.5 Limitations, Recent Advances and Perspectives 32
2.3.5.1 Reduced PGM Contents 33
2.3.5.2 Non-PGM Catalysts 34
2.3.5.3 Higher Operating Current Densities 35
2.3.5.4 Higher Operating Temperature 35
2.3.5.5 Higher Pressure Operation 35
2.3.5.6 Other Cell Components 35
2.3.5.7 Extended Lifetime of Operation 36

2.4 High-Temperature Water Electrolysis 36
2.4.1 Principles 36
2.4.2 Cell Components 37
2.4.3 Performances 37
2.4.4 Technology Developments and Applications 38
2.4.5 Limitations, Recent Advances and Perspectives 39

2.5 Conclusion 39

References 40

2.1 INTRODUCTION TO WATER ELECTROLYSIS

2.1.1 Brief Historical Review

It is reported in the literature[1] that water electrolysis (the electricity-driven $H_2O \rightarrow H_2 + 1/2\,O_2$ reaction) was performed for the first time in 1800 by the English scientists William Nicholson (1753–1815) and Anthony Carlisle (1768–1842). Thus doing, they initiated the science of electrochemistry. It is also reported in the literature that the German scientist Johann Ritter repeated these experiments one month later and was the first able to collect evolving hydrogen and oxygen separately.[2]

The laws of electrolysis were discovered later and reported in 1833–1834 by the English scientist Michael Faraday. He established the quantitative relationship between the amount of electricity q passing through the electrode/electrolyte interface and the mass m of substances involved in the electrolysis (redox) process:

$$m = k_e q, \tag{2.1}$$

where $k_e = M/nF$ is the electrochemical equivalent in kg/C ≡ kg/(Amps × s); M in kg/mole is the molar mass of substance produced at the interface; n is the number of electrons involved in the electrochemical reaction; $F = 96{,}485.3$ C/mole is the Faraday's constant.

Renewable Hydrogen Technologies
http://dx.doi.org/10.1016/B978-0-444-56352-1.00002-7

Faraday's law is a law of mass conservation and is therefore strictly verified. A practical condition is that new species formed at both interfaces (anode and cathode) are fully separated and do not spontaneously react with each other. Concerning water electrolysis, when the steady (stationary) electric current I and time period t are known, the theoretical (maximum) amount of hydrogen (or oxygen) produced can be calculated using:

$$V_{\text{theor.}} = \frac{k_e I t}{\rho} \tag{2.2}$$

where $V_{\text{theor.}}$ in m^3 is the theoretical volume of gas evolved, I in A is the total current, t in s is time; ρ in kg/m^3 is the gas density.

Although the principles of water electrolysis were discovered at the very early nineteenth century, it took almost a 100 years before electrolyzers of industrial scale were developed for hydrogen production in countries where hydropower was cheap and abundant. At that time, industrial applications were targeting chemical markets. In 1902, more than 400 industrial electrolyzers were in operation worldwide. In 1927, the Norwegian company Norsk Hydro Electrolyzers developed the first water–alkaline electrolyzer for the synthesis of ammonia and in 1939, the first 10,000 Nm^3/h H_2 plant was in operation. Later, a unit delivering 60,000 Nm^3/h H_2 was put in operation. In 1948, the first pressurized water electrolyzer was built and operated by Zdansky/Lonza. In 1966, the first solid polymer electrolyte (SPE) electrolyzer was built by General Electric Co. In 1972 and 1978, the development of solid-oxide water electrolysis (SOWE) and advanced alkaline water electrolysis was started, respectively. Over the last decades, new applications of hydrogen as an energy carrier, for example, in the storage of energy obtained from renewable energy sources, were found. Water electrolysis can be used for the regulation of electrical grids (peak shaving). The coupling of large-scale high-temperature water electrolyzers with nuclear power plants (using electrical power and waste heat of high-temperature helium reactor) is regarded as one of the key technologies for hydrogen production within the framework of hydrogen–nuclear energy. In addition, the production of hydrogen by electrolysis is suitable for systems based on renewable energy (solar, wind, surges, tides, etc.) that are not integrated into the network. In such cases, hydrogen can accumulate the energy to produce electricity and heat for the time periods when the renewable source does not produce electricity. Electrolyzers are also used in miscellaneous applications such as the analytical instruments (equipment for gas chromatographs), correction systems for water-chemistry mode of nuclear reactors, high-purity metals and alloys metallurgy, the production of high-purity materials for the electronics industry and hydrogen welding. It should finally be noted that electrolysis allows the concentration of heavy hydrogen isotopes in the liquid phase. This is one of the technologies used in the production of hydrogen isotopes. This is based on the fact that different isotopes undergo reactions at different rates. When deuterated water is electrolyzed, hydrogen evolves at a higher rate than deuterium relative to their concentrations. As a result, the deuterium to hydrogen ratio increases in the remaining water.[3]

2.1.2 Thermodynamics

In standard conditions (298 K, 1 bar), the water splitting reaction is as follows:

$$H_2O_{(l)} \rightarrow H_{2(g)} + \frac{1}{2}O_{2(g)} \tag{2.3}$$

Assuming that the chemical reaction is performed along a reversible path under isothermal conditions, then:

$$\Delta G(T) = \Delta H(T) - T\Delta S(T) \tag{2.4}$$

where $\Delta H(T)$ in J/mol is the enthalpy change associated with reaction (a); $\Delta H(T)$ is positive up to $\approx$2250 °C (the water splitting reaction is endothermic); $\Delta H(T)$ is the total amount of energy that must be supplied to the electrolysis cell to dissociate water into H_2 and O_2. $\Delta S(T)$ in J/mol/K is the entropy change; $\Delta S(T)$ is positive because 1 mol of water dissociates into 1.5 mol of gases. T in K is the absolute temperature. $T\Delta S(T)$ is positive. $\Delta G(T)$ in J/mol is the Gibbs free energy change; $\Delta G(T)$ is positive (reaction (a) is a nonspontaneous process) up to $\approx$2250 °C because over this temperature range, the enthalpy term is predominant over the entropic change. $\Delta G(T)$ represents the amount of electricity that must be supplied to the electrolysis cell in addition to the $T\Delta S(T)$ amount of heat to dissociate water. In standard conditions (25 °C), $\Delta G^0 = 237.23$ kJ/mol (2.94 kWh/Nm^3 H_2), $\Delta H^0 = 285.83$ kJ/mol (3.54 kWh/Nm^3 H_2), $\Delta S^0 = 163.09$ J/mol/K.

The electrolysis of water vapor is as follows:

$$H_2O_{(g)} \rightarrow H_{2(g)} + \frac{1}{2}O_{2(g)} \tag{2.5}$$

For the electrolysis of water vapor, $\Delta G^0 = 228.61$ kJ/mol (2.84 kWh/Nm^3 H_2), $\Delta H^0 = 241.81$ kJ/mol (3.00 kWh/m^3 of hydrogen) and $\Delta S^0 = 44.32$ J/mol/K. The enthalpy difference between reactions 2.3 and 2.5 is the enthalpy of water vaporization.

The electrical work required for the electrolysis of 1 mol of water in standard conditions is:

$$\Delta G_T^0 = nFE^0 \tag{2.6}$$

where E^0 in V is the standard thermodynamic voltage (for liquid water $E^0 = 1.229$ V at 25 °C). However, it is also possible to define another electrolysis voltage,

the so-called thermoneutral voltage, which is the voltage required for water electrolysis to occur at constant temperature, without exchange of heat to the surroundings:

$$E_{TN}(T) = \frac{\Delta H(T)}{nF} \tag{2.7}$$

At temperatures less than 100 °C, $E_{TN} = \Delta H^0/2F \approx 1.48$ V and slightly depends upon pressure. When a cell voltage less than E^0 volt is applied to the electrolysis cell, nothing occurs because there is not enough energy supplied to the cell to perform the nonspontaneous reaction (3). When a cell voltage U such as $E^0 < U < E_{TN}$ is applied to the electrolysis cell, electrolysis is possible but heat is required from the surrounding. If no heat is supplied, then the temperature of the electrolysis cell will decrease. At the thermoneutral cell voltage, the water dissociation reaction will take place at constant temperature, without any exchange of heat (absorption or release) to the surroundings. At voltages above the thermoneutral voltage, the electrolysis process is exothermic and heat is released to the surroundings.

Main thermodynamic functions associated with the water splitting reaction are plotted in Fig. 2.1. Abrupt changes of ΔH and $T\Delta S$ at 373 K are due to the vaporization of liquid water into vapor.

The dimensionless term η_{TD} defined as the ratio of the Gibbs free energy change to the enthalpy change can be used to express the fraction of electrical energy required for the water splitting. Since both $\Delta G(T)$ and $\Delta H(T)$ are functions of operating temperature, η_{TD} is also a function of operating temperature:

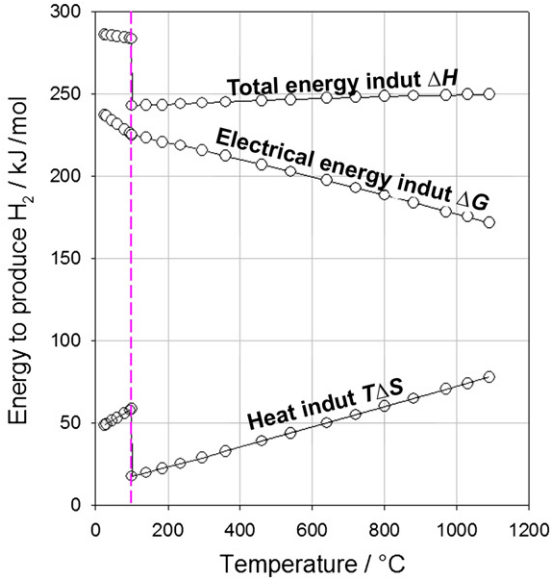

FIGURE 2.1 Temperature dependence of main thermodynamic parameters for water electrolysis. (For color version of this figure, the reader is referred to the online version of this book.)

$$\eta_{TD}(T) = \frac{\Delta G(T)}{\Delta H(T)} = \frac{E(T)}{E_{TN}(T)} \tag{2.8}$$

As can be seen from Fig. 2.1, the enthalpy of water dissociation does not change significantly with operating temperature. On the contrary, the significant change of the entropic term leads to a significant decrease in Gibbs free energy and corresponding electrolysis voltage. Therefore, the percentage η_{TD} of electricity required to split water also decreases with temperature (Table 2.1).

In the high operating temperature range (800–1000 °C), approximately two thirds of the energy required for the dissociation reaction must be supplied as electricity and one third as heat. Since the cost of the kWh of heat is usually significantly less than the cost of the kWh of electricity, the energy cost required to split water is less expensive at higher operating temperatures.

A quantitative expression of the thermodynamic cell voltage required to split water into hydrogen and oxygen can be derived from the general Nernst formula. $E(T)$ is a function of operating temperature, partial pressures of reactants and water activity in the electrolyte:

$$E = E^0 + \frac{RT}{nF}\ln\frac{P_{O_2}^{1/2}P_{H_2}}{a_{H_2O}} \tag{2.9}$$

In Eqn (2.9), E^0 is the standard value of the equilibrium cell voltage ($E^0 = \Delta G^0/2F = 1.229$ V at 25 °C for liquid water); R in J/mol/K is the absolute gas constant; T is the absolute temperature; P_{O_2} and P_{H_2} in atm are the partial pressure of the reaction products and a_{H_2O} is the activity of water in the electrolyte (close to unity in a first approximation). According to Eqn (2.9), an increase in operating pressure yields an increase in E. Nevertheless, pressurized water electrolysis is interesting because there is a need to compress hydrogen for storage and transportation, and pressurized water electrolysis can compete with electrolysis followed by mechanical compression. An additional benefit of pressurized water electrolysis is that the water vapor content of gases released from the pressurized electrolyzer is less significant than at atmospheric pressure (approximately 20–30 times lower) and the cost of the drying process is therefore reduced.

TABLE 2.1 Thermodynamic Voltage $E(T)$ and Percentage η_{TD} of Energy Required in the Form of Electricity to Split Water at Atmospheric Pressure and Different Operating Temperatures

T (°C)	25	90	800	1000
E (V)	1.229	1.176	0.978	0.920
η_{TD} (%)	83	80	66	62

2.1.3 Kinetics and Efficiencies

At equilibrium, the water splitting reaction occurs at an infinitely small rate, a situation of no practical interest. To split water into hydrogen and oxygen, the cell voltage U applied to the electrolysis cell must be significantly larger than the thermodynamic voltage in order to let a significant current density flow across the cell and reduce capital expenses. Main resistances to current flow are (1) charge transfer overvoltages at both anode/electrolyte (η_a) and cathode/electrolyte (η_c) interfaces and (2) the resistivity of the electrolyte. In industrial system, parasite ohmic losses are also encountered in electrodes and cable wiring to the electrolyzer. During water electrolysis, the anodic overvoltage is due to the charge transfer associated to the oxygen evolution reaction (OER) and the cathodic overvoltage is due to the charge transfer associated to the hydrogen evolution reaction (HER). Both terms are a function of operating current density according to the Butler–Volmer theory of charge transfer. At a current density j, the cell voltage $U(j)$ is given by:

$$U(j) = E + \eta_c(j) + \eta_a(j) + JR_{el}(j), \tag{2.10}$$

where J in A is current; R_{el} in Ohm is electrolyte resistivity.

When no mass transport limitations take place (this is usually the case in water electrolysis because of highly concentrated electrolytes and mobile charge carriers are used), values of η_c and η_a are related to the current density through the Tafel equation:

$$\eta = a + b \cdot \ln I \tag{2.11}$$

where $a = -RT/(\alpha \cdot n \cdot F) \ln i_0$ and $b = 2.303 \times RT/(\alpha \cdot n \cdot F)$, α is a transfer coefficient, i.e. the number of electrons transferred due to electrochemical reaction ($\alpha \approx 0.5$).

It can be seen from Eqn (2.11) that overvoltages decrease when the operating temperature increases. Hence, when the operating temperature of the electrolysis cell increases, less electricity is required because (1) ΔG (and η_{TD}) decrease (thermodynamic factor) and (2) the overall kinetics improves (kinetic factor). However, charge transfer overvoltages increase when the current density increases. The enthalpy efficiency of a water electrolysis cell operating at current density j and temperature T with a cell voltage $U(T,j)$ is defined as:

$$\eta_{\Delta H}(T,j) = \frac{n\,F\,E_{TN}(T,j)}{n\,F\,U(T,j)} = \frac{E_{TN}(T,j)}{U(T,j)} \tag{2.12}$$

At low current density ($j \approx 0$), $U \approx E_{TD}$ and $\eta_{\Delta H} \approx 1$. In the literature, the energy consumption per unit of mass (with units of kWh/kg) or unit of volume (with units of kWh/Nm^3) is commonly used to compare the efficiency of different electrolyzers. It should be noted, however, that both expressions are functions of the operating current density j.

Another important electrolysis cell characteristic is the current (faradic) efficiency. It is defined as the ratio of the volume of gas produced over a given time interval to the theoretical volume that should be produced during that time in accordance with Faraday's laws:

$$\eta_F = \frac{V_{actual}}{V_{theor.}} \tag{2.13}$$

Usually, $\eta_F \approx 1$ but significantly lower values are sometimes obtained. There are several reasons for such deviations, mainly (1) the energy consumption used for the electrolysis of impurities present in the electrolyte; (2) the spontaneous recombination of reaction products that are not appropriately separated during operation ($H_2 + 1/2\ O_2 \rightarrow H_2O$ in the case of water electrolysis); and (3) the formation of stray currents in the electrolysis stack when liquid electrolytes are used (alkaline process). In the alkaline and polymer electrolyte processes, the overall efficiency of the electrolysis cells is usually in the 75–85% range. In the high-temperature SOWE, even higher efficiencies (close to unity) can be reached to the high kinetics of charge transfer and to the excellent conductivity of the electrolyte at such elevated temperatures. However, the calculation of the overall efficiency of an electrolyzer should take into account the efficiency of the electrical source. The efficiency of thermal power stations is usually less than 50%, and therefore, the overall efficiency of the hydrogen production process is approximately 40%.

2.1.4 Main Water Electrolysis Technologies

There are two main experimental parameters to carry out water electrolysis: temperature and electrolyte pH. The temperature dependence of thermodynamic and enthalpy water dissociation voltage is plotted in Fig. 2.2. Whereas the enthalpy voltage remains constant almost over the entire range of practical operating temperatures (i.e. the enthalpy change ΔH does not vary significantly with operating temperature as shown in Fig. 2.1), the thermodynamic voltage significantly decreases, following the temperature dependence of the Gibbs free energy change (Fig. 2.1). Water electrolysis technologies can be classified into low-temperature processes ($T < 150\,^\circ$C), medium-temperature processes ($200\,^\circ\text{C} < T < 600\,^\circ$C) and high-temperature processes ($>600\,^\circ$C). Concerning the pH, as indicated in the previous sections, the half-cell reactions differ with the pH of the electrolyte. In acidic media, protons carry the current in the electrolyte and the following reactions take place:

$$\text{Anode}(+): H_2O(\text{liq}) \rightarrow \frac{1}{2}O_2(g) + 2H^+ + 2e^- \tag{2.14}$$

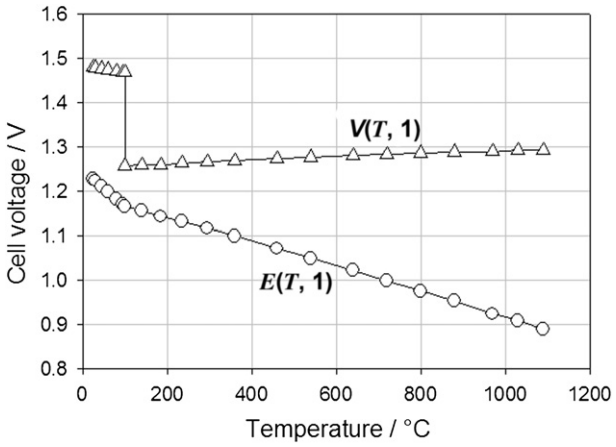

FIGURE 2.2 Thermodynamic and enthalpy water splitting voltages as a function of operating temperature.

$$\text{Cathode}\,(-): 2H^+ + 2e^- \rightarrow H_2(g) \tag{2.15}$$

$$\text{Fullreaction}: H_2O(\text{liq}) \rightarrow H_2(g) + \frac{1}{2}O_2(g) \tag{2.16}$$

Using the Nernst equation, the potential of the anode is:

$$E^+ = E^0_{H_2O/O_2} + \frac{RT}{nF} Ln \frac{\left(a^2_{H^+}\right)\left(f^{1/2}_{O_2}\right)}{a_{H_2O}} \tag{2.17}$$

At 298 K, when the pressure of oxygen is 1 bar (ideal gas), $E^+ \approx 1.23 - 0.06$ pH. Using the Nernst equation, the potential of the cathode is:

$$E^- = E^0_{H_2/H^+} + \frac{RT}{nF} Ln \frac{a^2_{H^+}}{f_{H_2}} \approx -0.06 \text{ pH} \tag{2.18}$$

At 298 K, when the pressure of hydrogen is 1 bar (ideal gas), $E^- \approx -0.06$ pH. Therefore, when the anode and cathode are immerged in the same electrolyte, the cell voltage is $E_{cell} = E^+ - E^- = 1.23$ V.

In alkaline electrolyte, different half-cell reactions take place:

$$\text{Anode}(+): 2OH^- \rightarrow H_2O + \frac{1}{2}O_2(g) + 2e^- \tag{2.19}$$

$$\text{Cathode}(-): 2H_2O + 2e^- \rightarrow H_2(g) + 2OH^- \tag{2.20}$$

$$\text{Fullreaction}: H_2O(\text{liq}) \rightarrow H_2(g) + \frac{1}{2}O_2(g) \tag{2.21}$$

Using the Nernst equation, the potential of the anode can be derived:

$$E^+ = E^0_{H_2O/O_2} + \frac{RT}{nF} Ln \frac{\left(a_{H_2O}\right)\left(f^{1/2}_{O_2}\right)}{a^2_{HO^-}} \tag{2.22}$$

At 25 °C, when the pressure of oxygen is 1 bar (ideal gas), $E^+ \approx 1.23 + \text{pKe} - 0.06$ pH. Using the Nernst equation, the potential of the cathode is:

$$E^- = E^0_{H_2O/H_2} + \frac{RT}{nF} Ln \frac{a^2_{H_2O}}{f_{H_2} a^2_{HO^-}} \tag{2.23}$$

At 25 °C, when the pressure of hydrogen is 1 bar (ideal gas), $E^- \approx \text{pKe} - 0.06$ pH.

Therefore, when the anode and cathode are immerged in the same electrolyte, the cell voltage is $E_{cell} = E^+ - E^- = 1.23$ V. From these results, it can be concluded that the thermodynamic voltage required to split water into hydrogen and oxygen is the same, whatever the pH of the electrolyte (Fig. 2.3). The only difference between alkaline and acidic water electrolysis is that the potential of each electrode is shifted along the potential axis, as a function of electrolyte pH.

Protons and hydroxyl ions are the most mobile ionic species. Concentrated solutions are required to avoid concentration overvoltages. Consequences are mostly on electrode material stability. From a historical perspective, alkaline water electrolyzers were first developed because in alkaline media, many metals are passivated and corrosion is prevented. Electrolyzers using liquid acidic electrolyte are seldom found because of severe corrosion issues. Acid water electrolysis technology developed in the late 1960s when SPEs (protons remain confined into the membrane electrolyte) became commercially available. More recently, ceramics have been used as solid electrolyte for operation at higher temperatures. For temperature above 800 °C, oxide ion (O^{2-}) conductors are preferred. In the intermediate temperature range (250–600 °C), some proton-conducting ceramics can also be used. The main features of the different water electrolysis technologies are compiled in Table 2.2.

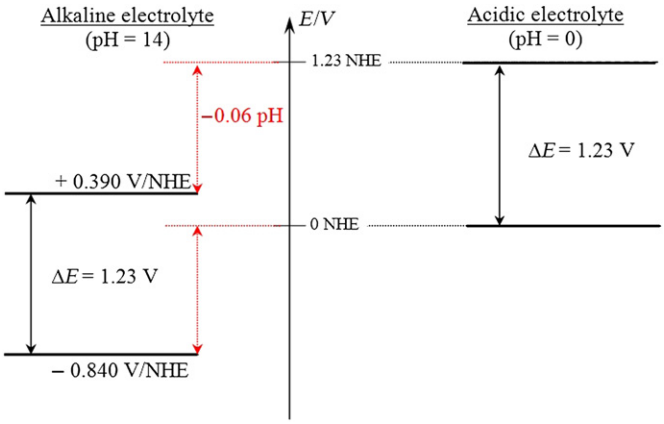

FIGURE 2.3 Electrode potential versus pH for the water splitting reaction (NHE, normal hydrogen electrode). (For color version of this figure, the reader is referred to the online version of this book.)

TABLE 2.2 Comparison of Main Water Electrolysis Technologies[4]

Technology status	Mature technology		Lab-scale, R&D	
	Alkaline	**PEM**	**Medium *T***	**Solid oxide**
T range (°C)	Ambient/120	Ambient/90	250/600	800/1000
Electrolyte/pH	25−30 wt% $(KOH)_{aq}$	PFSA*	Polymer or $Sr[Ce_xZr_{1-x}]_{0.95}$ $Yb_{0.05}O_3$,[5] $La_{0.6}Ba_{0.4}ScO_{2.8}$	Y_2O_3−ZrO_2, Sc_2O_3−ZrO_2, MgO−ZrO_2, CaO−ZrO_2
Mobile species	OH^-	H_3O^+	H_3O^+	O^{2-}
Cathode catalyst	Nickel foam/Ni-SS†	Platinum	Ni−YSZ or Ni-GDC Cermet with proton-conducting electrolyte	Ni−YSZ or Ni-GDC Cermet
Cathode carrier	Nickel foam/Ni-SS; Ni−Mo/ZrO_2−TiO_2	Carbon		
Anode catalyst	Ni_2CoO_4, La−Sr−CoO_3, Co_3O_4	Ir/Ru oxide	(La,Sr)MnO_3, (La,Sr)(Co,Fe)O_3	(La,Sr)MnO_3, (La,Sr)(Co,Fe)O_3
Anode carrier	–	–	–	Gd-doped ceria
Separator	Asbestos, PAM,‡ ZrO_2-PPS,§ NiO, Sb_2O_5-PS¶	Electrolyte membrane	Electrolyte membrane	Electrolyte membrane
Sealant	Metallic	Synthetic rubber or fluoroelastomer	Glass and vitro-ceramics	Glass and vitro-ceramics
Current distributor	Ni	Titanium		Ferritic SS (Crofer APU**)
Containment material	Nickel-plated steel	Stainless steel	Stainless steel	Stainless steel
P range (bar)	1−200	1−350 (700)	1	1−5
Conventional current density (A/cm^2)	0.2−0.5	0−3	0−0.1	0−2
Efficiency (%) (at *i* $A/cm^2/U_{cell}$ V/*T*°C)	60−80; 0.2−0.5/2.0/80	80; 1.0/1.8/90	Lab-scale tests	100; 3.6/1.48/950
Capacity (Nm^3/h)	1−500	1−230	1	1
Durability (h)	100,000	10,000−50,000	500	500−2000
H_2O specification	Liquid	$\rho > 10\,M\Omega\,cm$	Steam	Steam
Load cycling	Medium	Good	No data av.	No data av.
Stop/go cycling	Weak	Good	No data av.	Weak

* *Perfluorosulfonic acid.*
** *Auxiliary power unit.*
† *Stainless steel.*
‡ *Polysulfone-bonded polyantimonic acid.*
§ *ZrO_2-PPS—ZrO_2 on polyphenylsulfone.*
¶ *Sb_2O_5-PS—polysulfone impregnated with Sb_2O_5 polyoxide.*

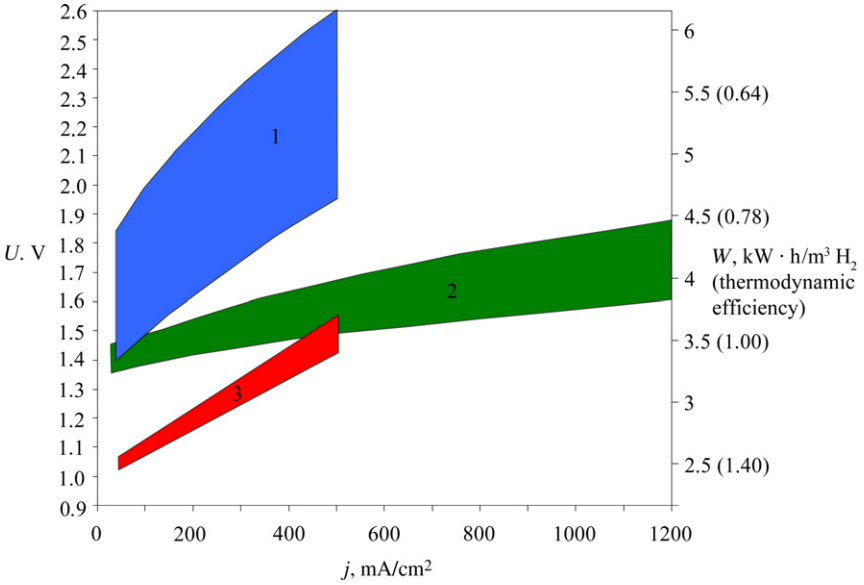

FIGURE 2.4 Polarization curves ($U-j$) and specific energy consumption of main water electrolysis technologies: 1, industrial alkaline electrolyzers (70–95 °C); 2, solid polymer electrolyzers (90–110 °C; 0–3.0 MPa); 3, high-temperature solid-oxide electrolyzers (900 °C) with additional heat supply. (For color version of this figure, the reader is referred to the online version of this book.)

The voltage–current density relationships and electricity consumption of the main water electrolysis technologies are compared in Fig. 2.4. Detailed principles and main characteristics are discussed in the next sections.

2.2 ALKALINE WATER ELECTROLYSIS

2.2.1 Principles

The general features of alkaline water electrolysis cells are pictured in Fig. 2.5.

Two metallic electrodes are immersed in a liquid electrolyte. Aqueous solutions of KOH or NaOH are usually used for that purpose. The concentration of the electrolyte solution is usually up to 40 wt% to provide maximum electrical conductivity at temperatures up to 90 °C. Specific conductivity of KOH solution is $54.3 \times 10^{-2}/\Omega/\text{cm}$ at 25 °C.[6] Water reduction takes place at the cathode of the electrolyzer according to:

$$2H_2O + 2e^- \rightarrow H_2 + 2OH^- \left(E_C^0 = -0.828\ \text{V}\right), \quad (2.24)$$

and the oxidation of hydroxyl ions takes place at the anode according to:

$$2OH^- \rightarrow \frac{1}{2}O_2 + H_2O + 2e^- \left(E_A^0 = +0.401\ \text{V}\right). \quad (2.25)$$

Only water is consumed during the process and therefore water has to be supplied to the cell to feed the reaction and maintain the concentration of the electrolyte to an optimum value. At usual operating temperature (60–80 °C), water vapor and traces of electrolyte are also carried away by gas products. On a dry basis, hydrogen purity is usually ≈99.9%.

As can be seen from Fig. 2.5, a cell separator (usually a porous and electrolyte-impregnated material) is placed between the two electrodes to avoid the spontaneous back recombination of H_2 and O_2 into water. In a gap-cell configuration, the two massive electrodes are placed face to face, allowing a small (a few mm thick) electrolyte gap between the electrodes and the separator where gaseous H_2 and O_2 are evolved. As the current density increases, gas bubbles tend to form a continuous and highly resistive film at the surface of both electrodes and as a result, operating current densities are limited to values up to a few 100 mA/cm^2. In the more-efficient zero-gap cell configuration, the two electrodes are porous and pressed against the cell separator. Thus, the interpolar distance is lower and gases are evolved at the back of the electrodes, allowing higher current density values to be reached.

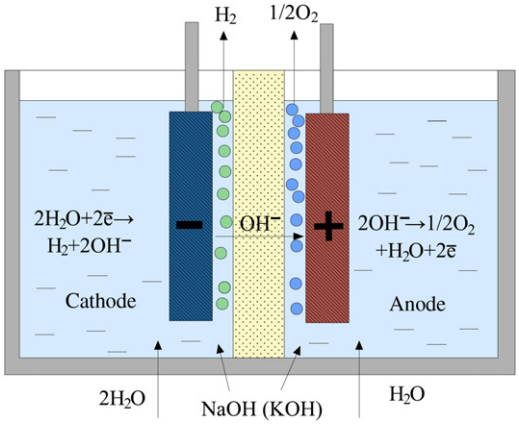

FIGURE 2.5 Schematic diagram of the alkaline electrolysis cell. (For color version of this figure, the reader is referred to the online version of this book.)

2.2.2 Cell Components and Stack Structure

Steel grids are usually used as electrode materials. In some cases, in order to improve the charge transfer kinetics, these grids are covered with a layer of porous nickel produced by leaching of zinc from the Ni–Zn alloy (Raney nickel). For several decades, asbestos (natural silicate mineral) has been used for the porous diaphragm-separating anode and cathode. But due to the toxicity of the material (the inhalation of asbestos fibers can cause lung cancer), the need for harmless materials has led to the development of a large variety of alternative solutions, in particular to the development of polymer-based composite materials.[7] It should be mentioned that the presence of a porous diaphragm generates some specific operating problems. In particular, safety issues may become critical, especially at elevated pressures, because of the possible mixing of product gases. Moreover, gas purity tends to decrease when operating pressure is raised. The advantages of alkaline water electrolysis over other water electrolysis processes are as follows: (1) relatively lower capital expenses due to the use of cheap cell materials (electrodes and separators), (2) proven technology with well-established operational costs; (3) demonstration of large capacity units; and (4) raw water can be used directly in the process without the need for specific purification procedures. On the less positive side, the quality of hydrogen (and oxygen) is quite low (hydrogen contains impurities of oxygen, water vapor with alkali) and higher hydrogen purity requires additional purification steps. Most alkaline water electrolyzers are built using a filter-press configuration. The stack is made by the series connection of up to several hundred elementary cells. Each individual cell shares a common metallic plate (so-called bipolar plates) with the neighboring cells.

2.2.3 Performances

As discussed in Section 2.1, the cell efficiency is a function of the operating current density. Higher operating current densities are required to reduce capital expenses but at the same time, lower current densities are required to reduce operational costs (in particular, the electricity consumption per mass unit). A compromise has to be found. The typical polarization curve of an alkaline water electrolysis cell is plotted in Fig. 2.6. Usually, operating current densities are limited to the 400–500 mA/cm^2 range and volumetric stack densities to ca. 15–20 L/Nm^3 H_2 are achieved. The different contributions to the total electrolysis voltage are also plotted in Fig. 2.6. The ohmic drop across the electrolyte and the oxygen (OER) and hydrogen (HER) evolution reaction overvoltages equally contribute to power losses.

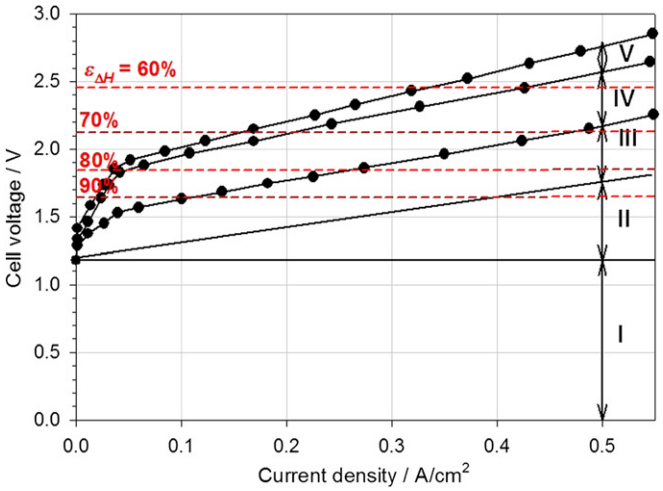

FIGURE 2.6 Electrochemical performances of a conventional alkaline water electrolysis cell. I, thermodynamic voltage; II, ohmic drop in the electrolyte; III, anodic overvoltage associated with the OER; IV, cathodic overvoltage associated with the HER; V, ohmic drop in the main power line. $\varepsilon_{\Delta H}$ = enthalpy efficiency. (For color version of this figure, the reader is referred to the online version of this book.)

The specific energy consumption to produce hydrogen ranges from 4.1 to 4.5 kWh/Nm^3 H_2 at 0.45 A/cm^2.

2.2.4 Technology Developments and Applications

Alkaline water electrolysis is known as the main process for the water-splitting reaction. Military applications related to the use of hydrogen isotopes boosted the development of the technology. The first plants for the electrolysis of heavy water and the production of deuterium were built in Norway. Nowadays, several companies are manufacturing alkaline electrolyzers for the production of hydrogen of electrolytic grade: NEL Hydrogen (a former department of Norsk Hydro Co., Norway)[8]; Hydrogenics Corporation[9] (which acquired Stuart Energy Systems Corp. in 2005); Teledyne[10] (Teledyne Energy Systems, Inc. is a subsidiary of Teledyne Technologies Inc, Maryland, USA); the Russian company "Uralkhimmash"[11]; De Nora (Italy), whose main products are electrolytic cells for chlorine production. The production capacity of industrial systems is usually in the 5–500 Nm^3 H_2/h.

Uralkhimmash produces a range of alkaline electrolyzers (Fig. 2.7). Main characteristics are compiled in Table 2.3. The electrodes of all electrolyzers are made of profiled steel coated with nickel. Diaphragms are still made of asbestos. The table shows that the specific weight and size characteristics of electrolyzers are very high and do not vary greatly with productivity growth. Thus, the electrolyzer mass of FV-250M is about 60 tons, and the

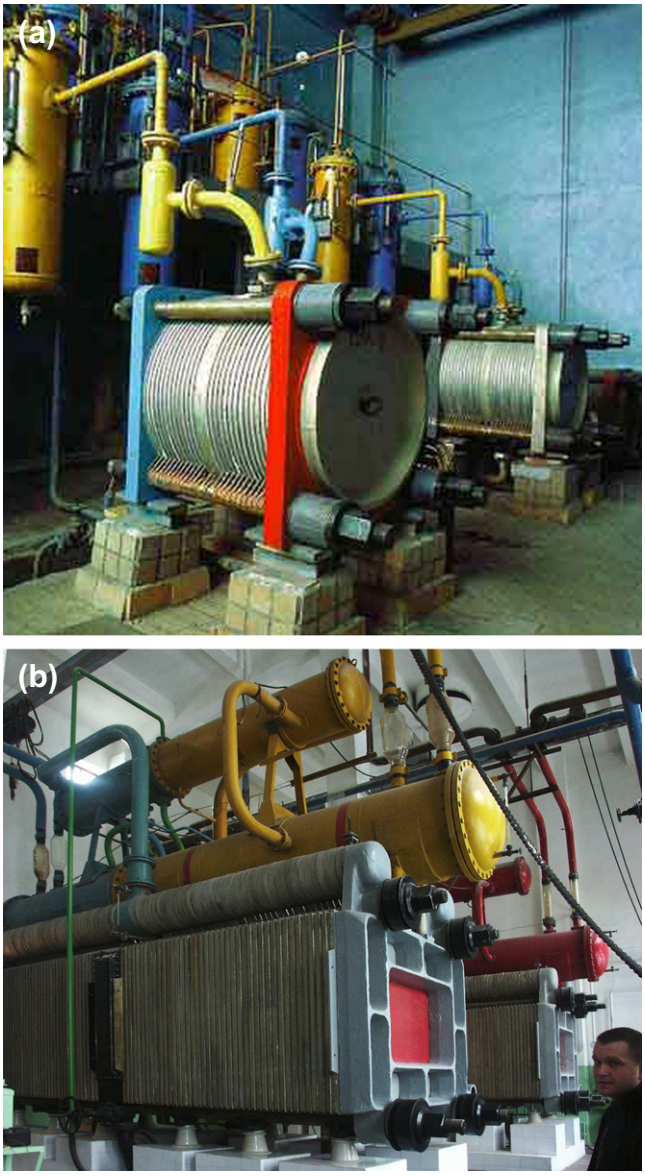

FIGURE 2.7 Electrolysis modules by JSC "Uralkhimmash" (a) SEU-40 and FV-500 (b). (Figures included in electrolyzers' names indicate hydrogen delivery rate in Nm^3/h.) (For color version of this figure, the reader is referred to the online version of this book.)

size is $7.95 \times 3.64 \times 6.54\,m^3$. The size and weight of analogs from other companies are usually 20–30% less.

NEL Hydrogen (Norway) is a world producer of electrolytic systems (Fig. 2.8). Electrolyzers operating at atmospheric pressure can deliver 50–485 Nm^3/h. Energy consumption is usually 4.1–4.3 $kWh/H_2\,Nm^3$ at current densities up to $0.3\,A/cm^2$. Line current is up to 5150 A. Hydrogen purity is 99.9%, operating temperature is 80 °C, and the electrolyte is a 25% solution of KOH. The area of $4 \times 13.5\,m^2$ is needed to install the electrolyzer that produced 485 Nm^3/h. Pressurized electrolyzers operating at 1.2 MPa and delivering up to 65 Nm^3/h are also commercially available.

The Canadian company Stuart Energy Systems Corp. (now Hydrogenics)[9] produced bipolar and monopolar systems. Monopolar electrolyzers are easy to design and require low maintenance, but they are much heavier and larger and this reduces the application field. Technical characteristics of monopolar cell type EI-250 manufactured over many years by Electrolyzer Company (subdivision of Stuart Energy Systems Corp.) are compiled in Table 2.4.

The applications of water electrolyzers by the Electrolyzer Company are in ammonia synthesis, hydrogen peroxide synthesis, oxygen production and hydrogen isotope separation. The company manufactures self-contained electrolysis systems for meteorological stations. Electrolyzer Company developed one of the first pilot stations for filling 200 buses per day, fueled by hydrogen compressed up to 400 bar.

In 2005, Stuart Energy Systems Inc. (Canada) and Vandenborre Hydrogen Systems (Belgium) formed Hydrogenics Corporation that manufactures electrolysis systems with hydrogen productivity up to 120 Nm^3/h (Fig. 2.9). Operating pressure is up to 25 bar, hydrogen purity is 99.9% and oxygen purity is 99.5%. Specific energy consumption is 4.8–4.9 $kWh/m^3\ H_2$, taking into account the energy required for the operation of supporting systems. The Teledyne Company produces electrolyzers that can deliver up to 150 m^3/h (Fig. 2.10). The water electrolysis stack is positioned at the bottom of the case. Two cylindrical liquid–gas separators (water–H_2 and water–O_2) are installed above. Ancillary equipment includes water circulation, water purity, electricity and heat management sensors for remote monitoring. The compression system and hydrogen storage units are included.

Alkaline water electrolyzers are manufactured for a wide range of market applications. Industrial hydrogen markets are growing fast. Major industrial gas-consuming industries are (1) electric power generator cooling in power plants (it is estimated that over 16,000 hydrogen-cooled generators are installed worldwide) and the addressable market is estimated at $2000 million with payback typically less than 1 year; (2) semiconductor manufacturing; (3) flat panel computers and TV screen producing units; (4) heat treatment plants and (5) analytical chemistry laboratories. Laboratory markets are also significant: (1) laboratory gas generators represent an estimated $60.0 million market worldwide and (2) hydrogen can potentially be used in place of helium as gas carrier in gas analyzers (or as fuel gas for flame detectors). Other industrial markets are glass manufacturing; food processing; meteorology; heat treating and welding industry. Hydrogen as an energy carrier is opening the way to new applications such as management of smart grids for more energy flexibility; chemical storage of renewable energy

TABLE 2.3 Technical Characteristics of Electrolyzers SEU and FV

	Electrolyzer				
Parameters	**SEU-4M-10**	**SEU-3M-10**	**SEU-20**	**SEU-40**	**FV-250M**
Operating pressure, MPa	1	1	1	1	0.1
Operating temperature, °C	80	85	85	90	85
Voltage, V	72	78	100	200	180.4
Gas purity, %					
Hydrogen	99.0	99.0	99.7	99.7	99.5
Oxygen	98.0	98.0	99.5	99.5	98.5
Volumetric efficiency, m^3/h					
Hydrogen	4	8 (max 12)	20.5	41	260
Oxygen	2	4 (max 6)	10.25	20.5	130
Size characteristics, mm					
Length	1700	2050	2400	4100	7950
Width	610	915	1060	1060	3640
Height	830	1080	1780	1785	6540
Weight, kg	1290	3032	4720	7435	59,420
Time to failure, h	11,500	11,500	11,500	11,500	11,500
Established resource to overhaul, h	25,500	25,500	25,500	25,500	25,500
Service life, years	10	10	10	10	10

sources and hydrogen refueling stations for automotive applications.

2.2.5 Limitations, Recent Advances and Perspectives

Alkaline water electrolysis is a mature technology. Several megawatt industrial electrolyzers are used in the industry for the large-scale production of hydrogen in view of different end-uses. The industry has developed electrolyzers that can deliver up to approximately 60 kg/h ($\approx$670 Nm^3/h). From an economic viewpoint, the lifetime of these systems (several tens of thousands of hours of operation) can be considered as satisfactory for continuous operation and is profitable. However, current alkaline electrolysis cells can hardly operate at very low current density, a limit in view of emerging markets of great potential. In particular, this is a limit in terms of flexibility in load-following operation, which will be required for operation with renewable energy sources. From the material viewpoint, major research efforts concern the development of advanced diaphragms with adapted electrodes/catalysts. Most efficient diaphragms used to be made of asbestos that is now forbidden in most countries. The replacement of asbestos by composite ceramic/polymer materials is proposed but there is still room for improvement.[12] Enhanced electrocatalysis is also an issue. Attempts have been made to identify alternative electrocatalysts, and the electrocatalytic properties of some transition metal macrocycles have received attention.[13] From the performance viewpoint, higher efficiencies can be obtained using advanced alkaline water electrolyzers. Prototypes delivering up to 25 Nm^3 H_2/h have been developed over the last decades.

FIGURE 2.8 Alkaline water electrolysis modules developed by NEL Hydrogen. (For color version of this figure, the reader is referred to the online version of this book.)

TABLE 2.4 EI-250 Type Cell Characteristics

Parameters	Value
Productivity of hydrogen, m^3/h	42
Electrolysis temperature, °C	70
Nominal current density, kA/m^2	2.5
Nominal voltage, V	1.85
Energy efficiency, %	81
Energy consumption, kW/m^3 H_2	4.4
Overall dimensions of the electrolyzer, m	$1.1 \times 1.8 \times 2.1$
Weight of the electrolyzer, tons	6.6

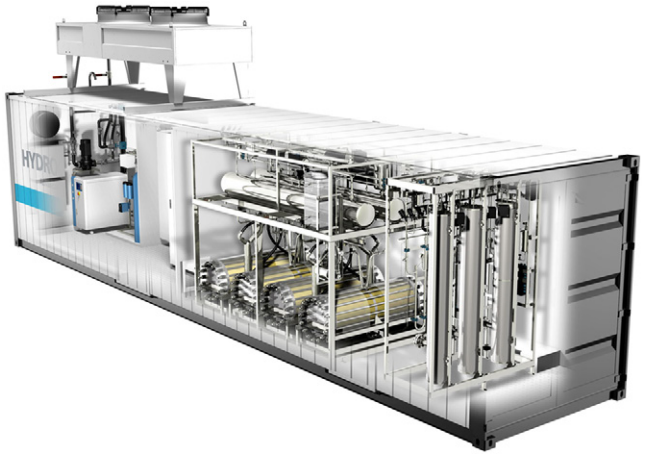

FIGURE 2.9 Alkaline hydrogen generator HySTAT by Hydrogenics Corporation. Productivity is 24 kg of hydrogen per day. (For color version of this figure, the reader is referred to the online version of this book.)

Such units using the zero-gap configuration are reported to operate at higher current densities $1.25\,A/cm^2$, 120 °C, 5–40 bars. The electrical power consumption (at $200\,mA/cm^2$) is $3.81\,kWh/Nm^3$ H_2 at 90 °C (≈78% efficiency) and $3.65\,kWh/Nm^3$ H_2 at 120 °C (≈80% efficiency) (stainless steel).

FIGURE 2.10 "Titan" electrolyzer by Teledyne Company. (For color version of this figure, the reader is referred to the online version of this book.)

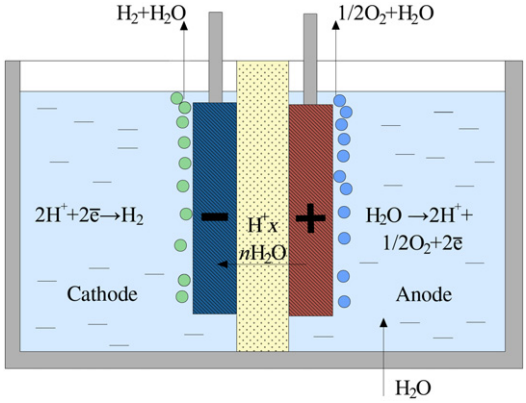

FIGURE 2.11 Schematic diagram of PEM electrolysis cell. (For color version of this figure, the reader is referred to the online version of this book.)

2.3 PROTON-EXCHANGE MEMBRANE WATER ELECTROLYSIS

2.3.1 Principles

The general features of proton-exchange membrane (PEM) water electrolysis cells are pictured in Fig. 2.11. Two electrodes are pressed against a proton-conducting polymer electrolyte thus forming a so-called membrane electrode assembly (MEA). The MEA is immersed in pure (18 MΩ cm) water. Mobile protons species remain confined inside the polymer membrane.

Oxygen evolution tales place at the anode:

$$H_2O \rightarrow \frac{1}{2}O_2 + 2e^- + 2H^+ \quad (E^0 = 1.229\ V \text{ at } 25^\circ C) \tag{2.26}$$

The hydrogen ions are transported across the ion-exchange membrane (SPE) and hydrogen is generated at the cathode:

$$H^+ + 2e^- \rightarrow H_2 \quad (E^0 = 0\ V \text{ at } 25^\circ C) \tag{2.27}$$

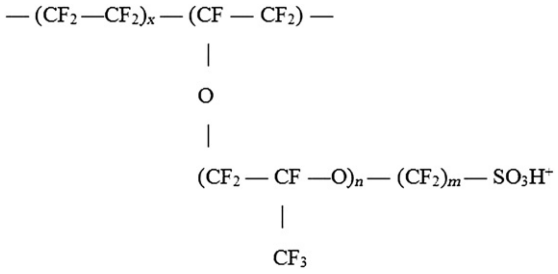

FIGURE 2.12 The structural formula of Nafion® membrane by DuPont de Nemours.

The overall reaction is:

$$H_2O \rightarrow H_2 + \frac{1}{2}O_2 \quad \left(E^0 = 1.229\ \text{V at } 25^\circ\text{C}\right) \qquad (2.28)$$

From a historical perspective, the development of PEM water electrolyzers started in the 1960s at General Electric Co. (USA) when appropriate proton-conducting polymers became commercially available.[14] The most famous one is Nafion® developed by DuPont de Nemours Co.[15] This is a perfluorinated polymer with functional sulfonic acid end-groups (Fig. 2.12).

Although protons remain inside the membrane, the acidy is very high (similar to that of a 1M sulfuric acid solution). Therefore, only noble metal catalysts that can sustain such acidity are required at both the anode and cathode. PEM water electrolysis is an expensive technology and the first electrolyzers for space vehicles and oxygen generation in submersibles were developed.

2.3.2 Cell Components

SPE water electrolyzers, also called PEM electrolyzers in modern literature, are considered the safest and most effective technology to produce hydrogen from water.[16] A key component of SPE systems is the ion-exchange membrane. In 1959, W. Grubb was the first to propose the use of organic cation-exchange membrane as solid electrolyte in electrochemical cells, in particular, for fuel cells in view of the US space program. First attempts were made using sulfonated polystyrene. However, its chemical stability was not sufficient for practical applications and the performances of fuel cells using this kind of membrane were significantly lower than those obtained with water–alkaline fuel cells.[17,18]

Today, new SPE materials made of perfluorinated phosphonic acid copolymers have appropriate properties (relatively low resistance, high mechanical strength and good chemical stability) for operation in fuel cells and water electrolyzers. As already mentioned, the most famous brand of this kind of membranes is Nafion® by DuPont de Nemours Co. (USA).[19] Ion-exchange perfluorinated membranes are elastic and transparent films, several tens to several hundreds micrometers thick, with a smooth surface. From the chemical viewpoint, the material is a copolymer of tetrafluoroethylene containing grafted sulfonic functional groups. The material has a high chemical stability, in particular, in the presence of native oxygen at high potential values, thus offering a resource for several tens of thousand hours of operation. However, even today, the problem of chemical stability of these materials is not completely solved. In particular during fuel cell operation, it has been shown that the incomplete (two electrons) reduction of oxygen can lead to the formation of hydrogen peroxide which, although formed in small amounts, can lead to a gradual degradation of the membrane.[20] The consequence is an increasing gas permeability during operation and a decrease in cell efficiency (the cell voltage and fuel efficiency tend to decrease with time). Hydrogen peroxide can also be formed during water electrolysis.

In contact with water, membrane swelling and dissociation of the ion-exchange groups occurs. As a result, protons can move freely in the volume of the polymer from one electrode to another through a system of fixed sulfonic acid groups. The acidity of these materials is equivalent to that of 10% sulfuric acid aqueous solutions. The resistivity of the membrane is significantly larger than the resistance of aqueous solutions of alkalis (11–12 Ohm cm at 20 °C and 5–6 Ohm cm at 80–90 °C). It is therefore necessary to use thin (100–300 μm thick) membranes to reduce ohmic losses during electrolysis but the use of smaller thicknesses is not appropriate because the permeability of gases through the membrane becomes too important.

There is no liquid electrolyte, so the electrodes should be held tightly to the membrane (the so-called zero-gap configuration), and to provide high surface contact between the catalyst (electronic conductor) and the electrolyte, the catalyst is deposited on the surface of the membrane with the ion-exchange electrolyte.[21] The resulting electrocatalytic composition has mixed electronic–ionic conductivity and has the porosity (30%) required for removal of gaseous reaction products. Porous current collectors are pressed firmly against catalytic layers and adjacent electrolysis cells are separated by metallic bipolar plates. It should be noted that zero-gap cells were also used in water–alkaline electrolyzers to reduce ohmic losses, but the increasing rate of mutual products' transport through the membrane, especially at high pressures, is problematic.

Highly dispersed catalysts based on platinum group metals (PGM) are used in PEM water electrolyzers. Ruthenium has the highest catalytic activity in the reaction of oxygen evolution, but Ru is not stable at the anode potentials of 1.23 V in acidic media. Currently,

the most widely used anode catalyst is Ir (or oxide), as well as mixed oxide compositions, such as $Ru_xIr_ySn_{1-x-y}O_2$ and $Ru_xIr_yTi_{1-x-y}O_2$ with catalyst loadings of ca. 2.0 mg/cm^2. Pt or Pd can be used at the cathode, including the carbon carrier. Pt can also be used as an anode catalyst, but in this case, the cell voltage is 100–200 mV higher. Porous titanium is usually used for the current collectors, the thickness is 600–1000 μm, porosity is >30%. The current collector is used to apply the required potential to the catalyst, supply reagent to the interfaces and remove reaction products. It should be noted that PGMs are also used to protect current collectors against surface oxidation (e.g. Pt coatings of ≈1 mg/cm^2).

The main advantages of PEM water electrolysis are as follows:

1. possibility of operating the cells at high (several A/cm^2) current density;
2. High efficiencies can be obtained, even at high current densities; this is because a PEM cell is a thin zero-gap cell and thus, ohmic losses are minimized and the overall efficiency is improved due to a lack of screening of the electrodes by gas bubbles; also, highly dispersed catalyst particles are used; they offer a large specific surface area and overvoltages are significantly low;
3. De-ionized water is used as sole reactant; as a result, high-purity gases are produced;
4. High dynamic range (0–100% production range reached within less than 50 ms).

The main drawbacks of PEM water electrolysis are as follows:

1. Capital expenses of not only MEA materials (catalysts and SPE) but also of other cell components (titanium is commonly used) are still too high;
2. Need for high-purity water and therefore expensive purification units;
3. Large-scale systems (>100 Nm^3/h H^2) still need to be developed.

2.3.3 Performances

Typical polarization curves measured on PEM water electrolysis stacks are plotted in Fig. 2.13. State-of-the-art range of operation of commercial PEM water electrolyzers is delineated by the gray rectangle. An enthalpy efficiency of 80% is commonly achieved at 1.0–1.5 A/cm^2 using platinum for the HER at the cathode and iridium oxide at the anode for the OER. As can be seen from Fig. 2.13, the membrane thickness provides a significant contribution to the cell efficiency. These electrolyzers deliver high-purity hydrogen (≥99.99% after drying), oxygen from the anode being the main impurity. Operation

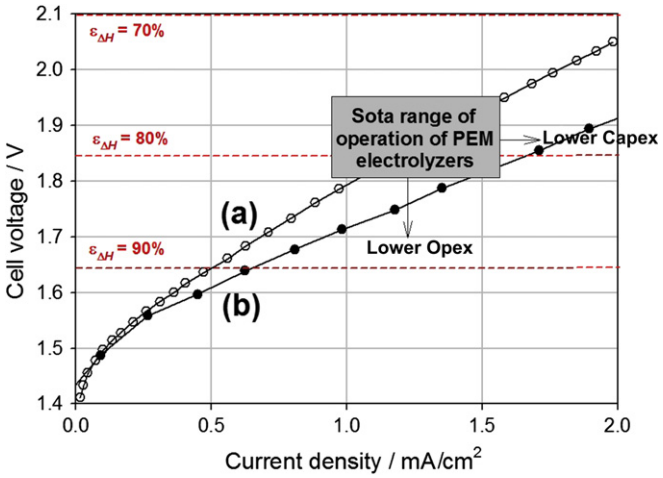

FIGURE 2.13 Current–voltage polarization curves of conventional PEM water electrolysis cells at 80 °C using platinum for the HER and iridium oxide for the OER. $P = 1$ bar: (a) membrane thickness = 200 μm; (b) membrane thickness = 150 μm. (For color version of this figure, the reader is referred to the online version of this book.)

lifetime of 10,000 h and longer is a common good practice. Reduced maintenance operations are required when high-purity water is fed to the electrolyzer. The energy consumption is usually low (≈3.9 kWh/m^3 at 1 A/cm^2) and the technology offers the possibility of delivering hydrogen at high pressure (up to 3 MPa and more) directly in the cell[21,22] in order to favor the direct storage of compressed hydrogen and reduce gas-drying costs. R&D programs are aimed at decreasing both operational and capital expenses. Reduction of cell voltage at constant current density is an important goal. This can be achieved by using more efficient electrocatalysts and can reduce the system Opex (operational expenses). Higher operating current densities at constant cell voltage is another important goal. This can be achieved by using thinner membranes and can reduce the system Capex (capital expenses).

2.3.4 Technology Developments and Applications

Currently, the major manufacturers of industrial water PEM electrolyzers are Hamilton Sundstrand (USA),[23] Proton OnSite (USA)[24] and Yara (Norway).[25] These companies have created electrolyzers operating under pressures up to 2.8 MPa with capacity up to 26 m^3/h, and it is possible to combine electrolysis installations with capacity of 260 m^3/h (Figs 2.14 and 2.15).

The German company H-tec[26] produces small demonstration samples of water PEM electrolyzers for educational purposes. Researches and developments of PEM electrolyzers are conducted in many countries, for example, in France, Japan, and India.[27,28] The

FIGURE 2.14 PEM electrolyzer HOGEN S Series by Proton OnSite. Productivity, 1 m^3H_2/h; electric power consumption, 5.6–9.0 kWh/m^3; electrolysis voltage, 2.3–3.8 V; output pressure, 1.4 MPa; size, $97 \times 78 \times 10^6$ cm^3; weight, 215 kg. (For color version of this figure, the reader is referred to the online version of this book.)

FIGURE 2.15 PEM electrolyzer by Yara (Norsk Hydro Electrolysers). Productivity, 10 Nm^3 H_2/h; electric power consumption, 4.4 kWh/m^3; output pressure, 3.0 MPa; hydrogen purity, 99.9% (O_2 as main impurity). (For color version of this figure, the reader is referred to the online version of this book.)

possibility of significant progress in this area has been demonstrated through the Japanese WE-NET program, where a cell was developed and successfully tested with surface area of 2500 cm^2, operating voltage of 1.556 V at 80 °C, current density of 1 A/cm^2 and an energy conversion efficiency of 95.1%. This efficiency is explained by the proximity of the electrolysis voltage to the thermoneutral voltage (ca. 1.48 V). Development of advanced PEM electrolyzers with elevated pressure (up to 5.0 MPa) has been successfully implemented in the project GenHyPEM of 6th Framework European Program.[29] The objectives of this project were development of new gas-tight membranes, high-performance nanocatalysts (including nonplatinum) and biporous current collectors to improve the efficiency of mass transfer processes. In Russia, researches and developments of water PEM electrolysis systems for more than 20 years are conducted in the National Research Center "Kurchatov Institute", Federal State Unitary Enterprise "Red Star" and other organizations. Currently, PEM electrolyzers have been created with capacity from a few milliliters to several cubic meters of hydrogen per hour (Fig. 2.16) for various purposes.[30]

Potentially, market applications of PEM water electrolyzers are similar to those of their alkaline counterparts although commercially available systems have lower production capacities than the alkaline systems.

2.3.5 Limitations, Recent Advances and Perspectives

As indicated in the previous section, an increasing number of private companies are active in the field and PEM technology offers a number of advantages. A brief comparison of PEM and alkaline water electrolysis technologies is provided in Table 2.5.

The main difference between the two technologies is that the alkaline process is well established, with impressive track records in terms of market assessment. Capital expenses are more favorable, even though alkaline electrolyzers operate at much lower current densities (at least two times lower), and thus, operational costs (in particular energy costs) are also more favorable. Moreover, the technical know-how gained over almost a century of operation in the development of large-scale systems also speaks in favor of alkaline systems. However, PEM electrolysis offers more significant perspectives in terms of improvement. It can be

FIGURE 2.16 PEM electrolysis stacks developed by NRC "Kurchatov Institute". (a) Stack with productivity of 25 l/h, (b) Stack with productivity of 125 l/h and operating pressure of 30 bar, (c) Stack with productivity of 1.5 m^3 and operating pressure of 30 bar, (d) Electrolysis module with bi-stack configuration with productivity of 2.5 m^3 and operating pressure of 130 bar. (For color version of this figure, the reader is referred to the online version of this book.)

TABLE 2.5 Comparison of Alkaline and PEM Water Electrolysis Technologies

	Alkaline electrolysis	**PEM electrolysis**
Electrolyte	Caustic solution	Polymer electrolyte
Nominal current density	0.45 A/cm^2	1.0 A/cm^2
Energy consumption	4.35 kWh/Nm^3 at 0.45 A/cm^2	4.35 kWh/Nm^3 at 1.0 A/cm^2
Maximum current density	0.8 A/cm^2	10 A/cm^2
H_2 delivery pressure	Up to 30 bar	Up to 700 bar
H_2 purity (dry basis)	≥99.9%	≥99.99%
Lifetime	≥60,000 h	≥25,000 h
Dynamic range	0–100%	0–100%
Volumetric stack density	16 L per Nm^3/h H_2	0.5 L per Nm^3/h H_2

said that in terms of market applications, PEM electrolyzers will probably become a serious competitor of the alkaline technology in the coming years, even for the large-scale production of hydrogen. To reach this goal, cost is of course the main issue and substantial progresses are needed to reduce capital expenses (a simplified cost analysis is provided in Fig. 2.17). MEA cost (approximately two thirds for the SPE and one third for the PGM catalysts including platting process) accounts for only 12% of the entire system cost. Cost of bipolar plates and flow fields is two times larger than MEA cost.

Some significant advances have been made during the last years and there is still room for further improvements. They are the subjects of many international R&D programs, in the public sector and in the industry.

2.3.5.1 *Reduced PGM Contents*

A first option to bring cost down was to reduce PGM contents. This can be achieved by dispersing

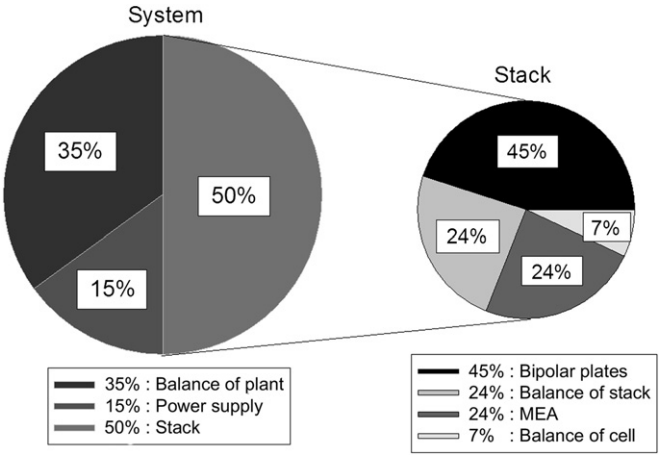

FIGURE 2.17 Cost analysis of PEM water electrolyzers.

nanoparticles at the surface of electronic carriers of large surface area. Similar to PEM fuel cell technology, carbon-supported platinum nanoparticles are commonly used now at the cathode of PEM electrolyzers for the HER. At the anode, mixed oxides (e.g. RuO_2–IrO_2–SnO_2) are increasingly used for the OER. PGM loadings have been significantly reduced. Pt loadings at cathodes are now in the 0.3–0.5 mg/cm^2 range (Fig. 2.18). Palladium (which is significantly less expensive than platinum and even more active) can also be used for that purpose. Like platinum, palladium can be deposited at the surface of carbon carriers.[21]

2.3.5.2 Non-PGM Catalysts

Another option to reduce MEA costs is to develop non-PGM electrocatalysts. Some advances have been made in this field over the last years.[31] Some typical polarization curves measured on a PEM water electrolyzer operating at 80 °C are plotted in Fig.2.19. The overall efficiency differs significantly from one curve to the other, highlighting the role of electrocatalysts. A first reference curve (Pt/Pt) is obtained using pure platinum particles for both the OER and the HER. As can be seen from Fig. 2.19, an enthalpy efficiency of ≈65% is obtained at 1 A/cm^2. More efficient results are obtained when pure iridium particles are used at the anode for the OER (Pt/Ir): an efficiency of ≈82% is obtained at 1 A/cm^2. Because of the increasing cost of noble metals, there is a need to find cheaper materials. Over the last years, several non-PGM catalysts have been identified and used at the cathode of PEM water electrolysis cells in place of platinum. For example, polyoxometalates can be used for that purpose. In Fig. 2.19, three additional curves (red circles, curves labeled 1, 2, 3) were obtained with increasing loadings of α-$H_4SiW_{12}O_{40}$ for the HER and iridium metal for the OER. Although the electrochemical performances are not as good as those obtained with the Pt/Ir reference curve, results are encouraging: an enthalpy efficiency close to 70% has been obtained at 1 A/cm^2. Another example is provided by cobalt-based clathrochelates.[32] These results offer new and interesting perspectives for application in the industry.

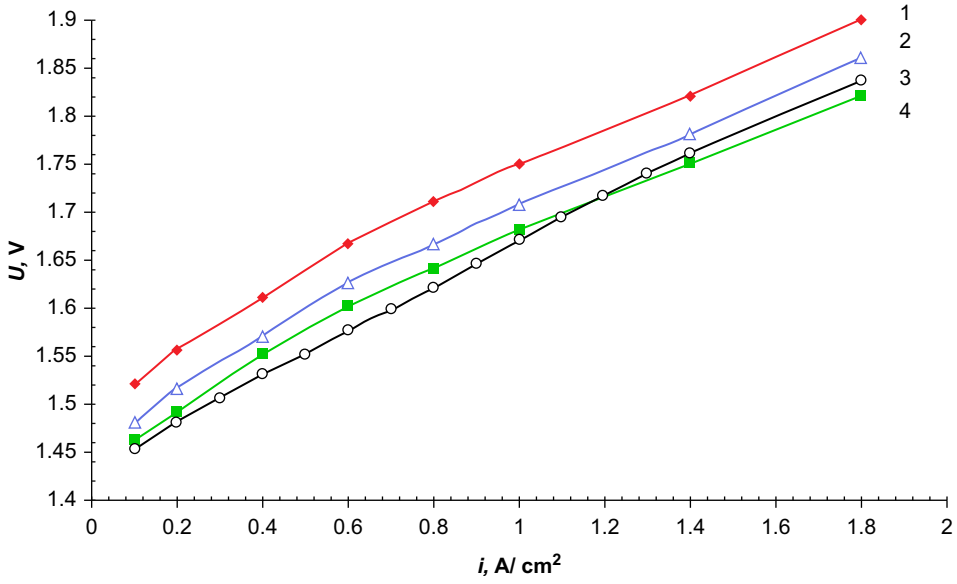

FIGURE 2.18 Current–voltage polarization curves measured at 90 °C on PEM water electrolysis cells with different catalysts. 1, cathode: Pt30/C—2.0 mg/cm^2; anode: Ir—2.4 mg/cm^2; 2, cathode: Pt30/C—2.0 mg/cm^2, anode: RuO_2(30%)–IrO_2(32%)–SnO_2(38%)—2.0 mg/cm^2; 3, cathode: Pd40/C—2.4 mg/cm^2, anode: Ir—2.4 mg/cm^2; 4, cathode: Pt30/C—2.0 mg/cm^2, anode: RuO_2(50%)–IrO_2(50%)—2.0 mg/cm^2 (Pt30/C is 30 wt% Pt on carbon carrier). (For color version of this figure, the reader is referred to the online version of this book.)

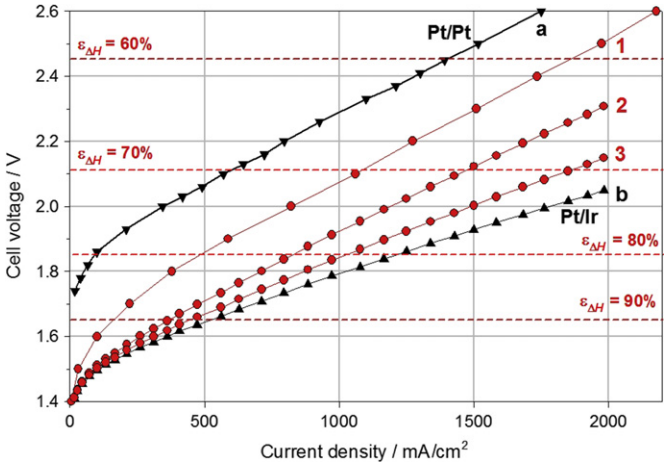

FIGURE 2.19 Current-voltage characteristics of PEM water electrolysis cells (7 cm^2) at 90 °C; (a) reference curve with Pt for both HER and OER; (b) reference curve with Pt for the HER and Ir for the OER; (•) Ir for the OER (2.5 mg/cm^2) and a-$H_4SiW_{12}O_{40}$ (at different concentrations) for the HER: (1): 0.2 mg/cm^2; (2): 0.5 mg/cm^2; (3): 0.8 mg/cm^2. (For color version of this figure, the reader is referred to the online version of this book.)

Such approaches, however, require additional R&D efforts. They could also have some positive side effects since the replacement of platinum would release the constraints on feed-water resistivity (Pt is highly sensitive to metal underpotential deposition).

2.3.5.3 Higher Operating Current Densities

To further reduce expenses, it is also necessary to develop new materials in order to increase current density (lower capital expenses) and to increase operating temperature (lower operational costs). These fields of material science are of growing interest, also driven by potential applications in the PEM fuel cell industry. Whereas in PEM fuel cells, maximum operating current densities come from mass transfer limitations (transport of gaseous reactant to the reactive centers), there is no such limitations in water electrolysis cells. Significantly high current densities (10 A/cm^2) have been demonstrated. The main problem comes from the insufficient conductivity of the electrolyte and inappropriate ohmic losses. Better efficiencies can be obtained by using thinner membranes but in turn, gas cross-permeation effects tend to reduce faradic efficiency and reduce gas purity.

2.3.5.4 Higher Operating Temperature

Concerning the SPE, there is a need to develop polymer proton conductors for operation at more elevated temperatures. Research in this field is driven by potential applications in the H_2/O_2 fuel cell industry for automotive applications. Significant progresses have been made in the development of improved perfluorinated polymer materials operating in the 120–150 °C temperature range (e.g. using materials such as Aquivon® products from Solvay Solexis Co.). Some of these materials have been successfully tested in PEM water electrolysis cells. Also, polybenzimidazole materials operating at temperatures ca. 200 °C have been developed. They may offer in the future some interesting possibilities to operate water electrolysis cells in this very interesting temperature range.

2.3.5.5 Higher Pressure Operation

PEM water electrolysis technology offers the possibility to increase operating pressure for the direct storage of hydrogen in pressurized vessels. This is a very attractive prospect for stationary systems with relatively small (up to 100 kW) power capacity. This is a challenging field of research. The main problem is to reduce the rate of gas cross-permeation by diffusion through the membrane which, in turn, can reduce the current efficiency and lead to the formation of hazardous H_2/O_2 explosive gas mixtures. Over the last years, several experiments have been reported in the literature. A PEM electrolyzer that can deliver 10 Nm^3/h H_2 at a pressure up to 13.0 MPa has been developed and tested at the Kurchatov Institute within the frame of a Federal R&D project. Typical polarization curves measured at different operating temperatures and pressures are plotted in Fig. 2.20.

It can be seen that temperature is the parameter that has the most significant effect on the process efficiency. Pressure has a less pronounced effect. From a thermodynamic viewpoint, an increase of pressure tends to increase the electrolysis voltage. But at high current densities, this effect is balanced by a better kinetics (transport of gas bubbles away from the interfaces) and as a result, higher operating pressures do not negatively impact cell performances. Increased operating pressure is also necessary to perform water electrolysis at temperatures above 100 °C.

At this stage, it is worth mentioning the development of so-called reversible systems or unitized regenerative fuel cells, i.e. electrochemical devices that can operate either like a fuel cell or an electrolyzer (a kind of H_2/O_2 battery).[33] Reversible PEM systems are interesting to create a stand-alone (decentralized) energy system based on intermittent power sources, such as renewable energy sources.

2.3.5.6 Other Cell Components

As shown in Fig. 2.17, the MEA is not the sole component responsible for the expensive capital costs in PEM water electrolyzers. Other cell components also add significant contributions. Bipolar plates, flow fields and current distributors are two times

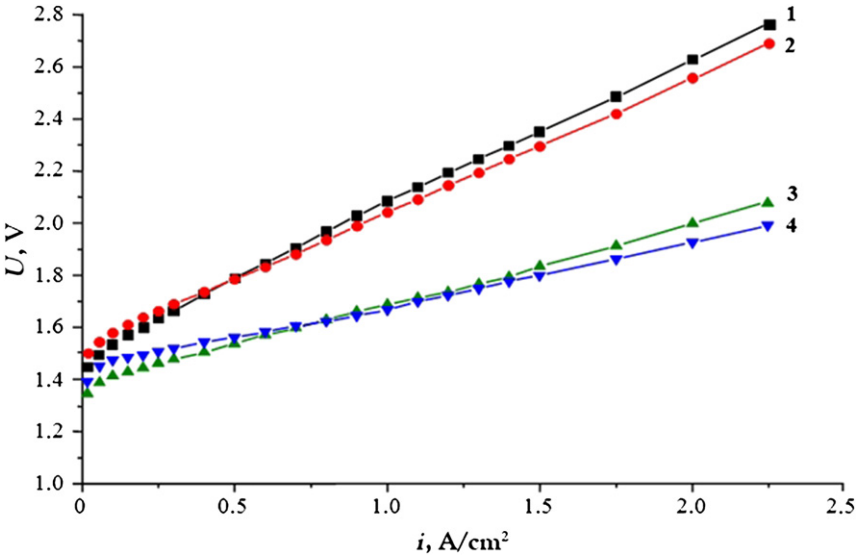

FIGURE 2.20 The current–voltage characteristics of PEM electrolysis cell at different operating temperatures and pressures. 1, $T = 30\,^{\circ}C$, $P = 1$ bar; 2, $T = 30\,^{\circ}C$, $P = 25$ bar, 3, $T = 90\,^{\circ}C$, $P = 1$ bar, 4, $T = 90\,^{\circ}C$, $P = 25$ bar. (For color version of this figure, the reader is referred to the online version of this book.)

more expensive. This includes raw material costs and surface treatment (titanium bipolar plates and current collectors) to reduce contact resistance (Pt coatings are expensive, nitrides, carbides, etc.). Main challenges for PEM water electrolysis are to identify and synthesize alternative materials with performances similar to those used in state-of-the-art technology.

2.3.5.7 *Extended Lifetime of Operation*

In the industry, PEM electrolyzers have demonstrated their ability to operate during several tens of thousand hours. Extending the lifetime of operation offers the possibility to further bring capital expenses down. Lifetime operation in the upper 10,000–100,000 h time range is the target. PEM water electrolysis is well suited for dynamic operation. Several studies have shown that performances remain stable and that the electrolyzers can provide rapid response time to current signals. Therefore, high dynamic ranges (0–100% production range reached within less than 50 ms) are accessible. This is of particular interest when transient renewable energy sources are used as power sources. PEM water electrolyzers can add flexibility to the management of smart grids.

2.4 HIGH-TEMPERATURE WATER ELECTROLYSIS

2.4.1 Principles

The general features of SOWE cells are pictured in Fig. 2.21. Oxide-ion conducting ceramics is used as solid electrolyte and cell separator. Water molecules are reduced at the cathode according to:

$$H_2O_{(g)} + 2e^- \rightarrow H_{2(g)} + O^{2-} \tag{2.29}$$

The resulting oxygen ions O^{2-} migrate to the anode, where oxygen evolves according to:

$$2O^{2-} - 2e^- \rightarrow O_2 \tag{2.30}$$

Such solid-oxide electrolysis cells usually operate in the 800–1000 °C temperature range. The most common electrolyte (like in solid-oxide fuel cell (SOFC) technology) is zirconia ZrO_2 stabilized with yttrium and scandium oxides.[34–37]

The transport of oxide ions across zirconia is a diffusion process throughout the defects of the crystal structure. The resistivity of the solid electrolyte is larger than the resistance of alkaline solutions and ion-exchange

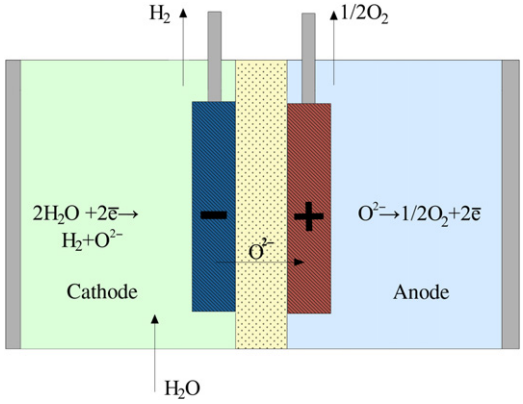

FIGURE 2.21 Schematic diagram of solid-oxide electrolysis cell. (For color version of this figure, the reader is referred to the online version of this book.)

TABLE 2.6 Ionic Conductivity of Several Solid Electrolytes at Different Temperatures

Electrolyte	Conductivity, Ohm/cm		
	880 °C	650 °C	500 °C
$(Bi_2O_3)_{0.8}(SrO)_{0.2}$	2.7×10^{-1}	5.0×10^{-2}	6.0×10^{-3}
$(Bi_2O_3)_{0.8}(BaO)_{0.2}$	–	7.0×10^{-1}	1.1×10^{-2}
$(Bi_2O_3)_{0.75}(Y_2O_3)_{0.25}$	3.5×10^{-1}	1.1×10^{-1}	1.3×10^{-2}
$(Bi_2O_3)_{0.65}(Gd_2O_3)_{0.35}$	2.6×10^{-1}	5.6×10^{-2}	3.5×10^{-3}
$(Bi_2O_3)_{0.85}(Nb_2O_5)_{0.15}$	5.0×10^{-1}	1.1×10^{-1}	1.1×10^{-2}
$(Bi_2O_3)_{0.80}(Ta_2O_5)_{0.20}$	7.3×10^{-2}	1.0×10^{-2}	5.0×10^{-3}
$(Bi_2O_3)_{0.78}(MoO_3)_{0.22}$	1.1×10^{-1}	1.7×10^{-2}	2.6×10^{-3}
$(Bi_2O_3)_{0.78}(WO_3)_{0.22}$	1.5×10^{-1}	4.1×10^{-2}	1.0×10^{-3}
$(ZrO_2)_{0.91}(Y_2O_3)_{0.09}$	2.0×10^{-2}	3.8×10^{-3}	4.6×10^{-4}

membranes (≈30 Ohm·cm even at 900–1000 °C, Table 2.6). Therefore, thin ceramic membranes (30–150 μm) are required for the electrolysis process to reduce ohmic losses as much as possible.

2.4.2 Cell Components

In conventional technology, the main SOWE cell components are stainless steel bipolar plates and manganite-coated stabilized zirconia as solid electrolyte (Fig. 2.22).

2.4.3 Performances

The development of SOWE technology in view of applications in the industry started in the early 1970s. Prototypes using tubular cells and delivering up to 1 Nm^3/h H_2 at 1000 °C have been developed and tested at Dornier Systems Co. Similar developments have been made in parallel by Westinghouse. According to the literature, in spite of encouraging lifetimes and high cell efficiencies (operations for 500 h and efficiencies close to 100% have been reported[38]), experiments have been stopped because of prohibitive costs and lack of short-term commercial applications. Since then, because of the world energy crisis, the situation became gradually more favorable and new R&D programs have been launched.[39,40] Possibility of operation at high current densities with efficiencies close to 100% have been confirmed (e.g. a current density of 3.6 A/cm^2 has been reported at 1.48 V and 950 °C[41]). In addition, the overall efficiency of these solid-oxide cells can be further improved by co-electrolyzing water vapor and carbon dioxide to produce syngas ($H_2 + CO$), that is of great industrial interest, for example for the production of synthetic fuels. Some typical polarization curves measured for these systems are plotted in Fig. 2.23. At such operating temperatures, electrochemical processes are fully reversible and the electrochemical cells can operate either as a fuel cell or as an electrolysis cell. The cell resistance (the slope of the polarization curves) decreases significantly when the temperature increases and current densities of several A/cm^2 can be obtained during the co-electrolysis of water vapor and CO_2. The composition of the syngas can be adjusted by monitoring the composition of the water–CO_2 gas mixtures introduced in the electrolyzer.

High-temperature water electrolyzers using solid-oxide electrolyte[42] was successfully developed in the 1980s at the Institute of the High-Temperature Electrochemistry of the Ural Branch of the Russian Academy of Sciences. The heat balance during electrolysis was more specifically analyzed in order to determine the conditions for which the electrolysis cell does not exchange heat with the surrounding. When the electrolysis cell was operated at constant temperature, it was

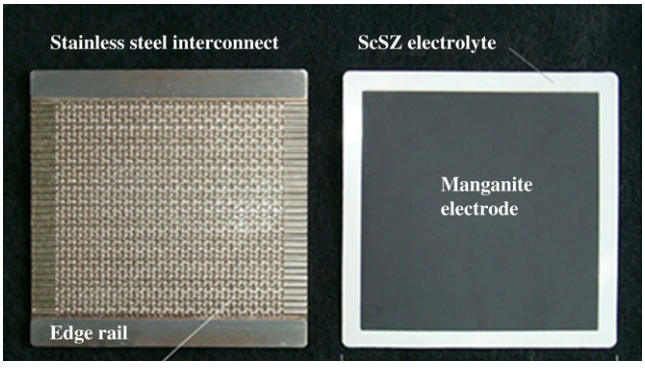

FIGURE 2.22 Photographs of bipolar plates and MEAs used in SOFC technology. (For color version of this figure, the reader is referred to the online version of this book.) *Source: CERAMATEC Co.*

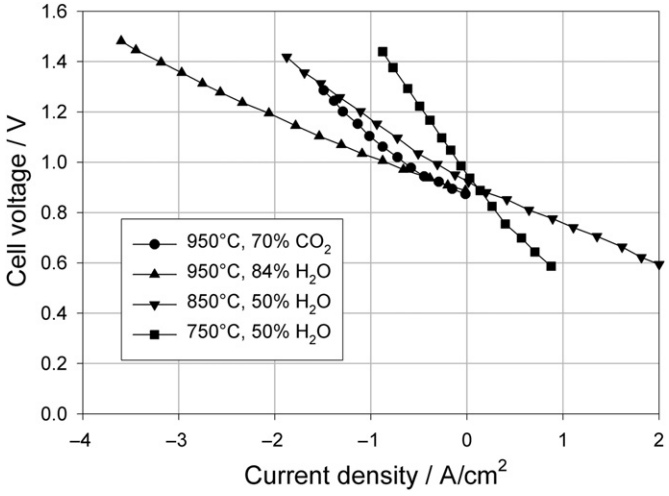

FIGURE 2.23 Polarization curves measured on a 5 × 5 cm^2 SOFC cell.[38]

found that operation at low current density (corresponding to cell voltage less than 1.29 V) without the supply of external heat led to a significant temperature drop inside the stack. The maximum temperature difference between the cell and the environment was found to be ca. 20 °C at a current density of 0.3 A/cm^2. As the operating current density was increased, the temperature difference gradually decreased and at 0.6 A/cm^2 the temperature of the electrolyzer became similar to that of the environment. These results demonstrated that the energy consumption of the water splitting reaction conducted at high temperature requires less electricity compared to low-temperature electrolysis and that the remaining energy requirements can be provided by additional heat supply (for example from high-temperature gas-cooled reactor or solar concentrators).

2.4.4 Technology Developments and Applications

High-temperature water electrolysis cells using ceramic membranes are developed by several companies and research centers: Siemens–Westinghouse (USA–Germany), Institute of the High-Temperature Electrochemistry of Ural Branch of Russian Academy of Sciences (Russia) (Fig. 2.24), National Research Center "Kurchatov Institute" (Russia) and State Scientific Center "AI Leypunsky Physics and Power Engineering Institute" (Russia).

Electrodes are deposited on both surfaces of a thin ceramic membrane used as electrolyte. SOWE cells can have different geometries: planar geometries (similar to cells of other electrolytic cell types), tubular (the electrolyte is in the form of a thin-walled tube), and even more complex configurations such as "honeycomb" shapes (Fig. 2.25). At such elevated temperatures of operation, the need for electrocatalysts is less significant compared to the requirements at lower operating temperatures. It is therefore possible to operate such cells with non-PGM catalysts. The usual material used at the cathode for the HER is a ceramic-metal (cermet) alloy containing Ni and Zr. The usual material used at the anode for the OER is platinum- or strontium-doped lanthanum manganite. However, it is difficult to completely eliminate the use of precious metals; in state-of-the-art technology, they are used to assure appropriate electrical contacts between the cells.

R&D programs were carried out by a group of national laboratories in the USA (supported by the U.S. Department of Energy) in 2006. A demonstration electrolyzer containing 25 planar cells with a hydrogen production capacity of 160 L/h (800 °C) has been developed. The electrolyzer has been tested for 1000 h. During the test, it was found that electrochemical performances tend to decrease significantly, leading to a final loss of

FIGURE 2.24 High-temperature electrolysis for 100 L of hydrogen per hour developed by the Institute of High-Temperature Electrochemistry of Ural Branch of Russian Academy of Sciences. (For color version of this figure, the reader is referred to the online version of this book.)

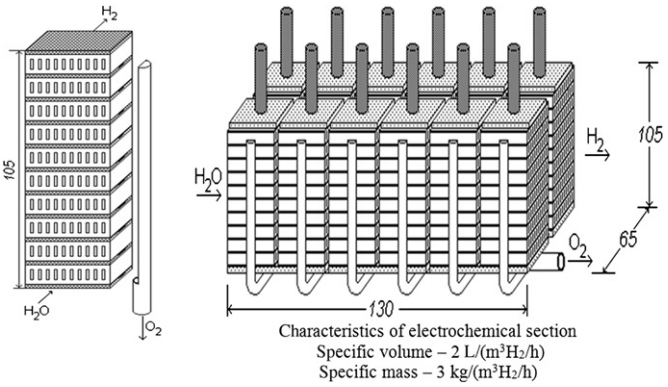

FIGURE 2.25 Schematic diagram of a solid-oxide water electrolyzer developed at the Institute of High-Temperature Electrochemistry of Russian Academy of Sciences.

almost 30%. It was shown that the stability of electrode materials, in particular hydrogen electrode based on nickel and zirconium oxide stabilized with yttrium and scandium (for mixed electronic−ionic conductivity) is not sufficient at high concentrations of water vapor and can lead to the oxidation of the nickel surface. However, work is continuing in this direction and it is planned to build electrolyzers having an input power of 200−1000 kW.

High-temperature solid-oxide electrolysis cells offer the possibility to simultaneously decompose water vapor and carbon dioxide. It can be used to develop effective life support systems, for example, for space and submarine operation. The thermodynamic voltage required at 900−1000 °C in the SOWE cell is less than 1 V and a typical cell voltage of 1.2−1.3 V is commonly used. This corresponds to an electricity consumption of 2.8−3.0 kWh/Nm^3 H_2. However, about 0.4−0.5 kWh/Nm^3 H_2 of heat is required to maintain the operating temperature at constant values. Usually, heat is supplied directly to the electrolyzer and to the evaporator. The advantage of SOWE becomes determinant when heat sources (e.g. high-temperature nuclear reactors or concentrated solar power) are available. In this case, the formal conversion efficiency of electrical energy into thermal energy of hydrogen is about 1.3−1.4. On a less positive side, high operating temperatures and use of thin-walled ceramic solid electrolyte films create some problems. A very promising trend is to develop SOWE cells that can operate at significantly lower temperatures (e.g. 500−700 °C). However, solid electrolyte materials operating in this temperature range (e.g. Bi_2O_3)[43] lack stability and suffer from the onset of mixed (electronic + ionic) conductivity, which reduces the output current. Thus, high-temperature solid-oxide electrolysis cells are attractive from the standpoint of thermodynamics (the equilibrium potential difference is less than 1 V at 900 °C) and kinetics (low overvoltage, low levels of diffusion limitations). This type of electrolyzer does not require precious metal catalysts and is not sensitive to impurities in the feed water. However, the problem of structural materials and design for high temperature is not fully resolved, and the development process of these electrolyzers is quite slow. Synergies with SOFC are expecting to improve the situation.

2.4.5 Limitations, Recent Advances and Perspectives

Cell components in solid-oxide water electrolyzers are similar to those used in SOFC technology. There are also strong synergies in terms of perspectives. However, even though solid-oxide cells can be operated either in fuel cell or electrolysis modes, operation in electrolysis mode adds some specific challenges to the materials. In particular, corrosion issues (especially at the anode during oxygen evolution) due to the high operating temperature are critical. In state-of-the-art technology, the rate of performance degradation under high steam contents remains too high for practical applications. Degradation processes are further accelerated by the corrosion of interconnects. The purity of the feed steam is known to have a large influence on the degradation rate. Cell tightness is generally obtained using glass seals or vitro-ceramic seals that cannot survive thermal cycling. The degradation rate expressed in %/h or μV/h has become a key performance indicator for that technology, even more significant that the cell efficiency. Performance tests made on a five-cell stack operating at 800 °C and 0.3 A/cm^2 revealed a degradation rate of cell voltage close to 15%/1000 h.[44] The problem has been confirmed by the developments made at Ceramatec Co. (USA) and Idaho National Laboratory[45]: even at low current densities, a degradation rate close to 20%/1000 h has been observed at 800−900 °C. But improvements are being made. Results obtained in the course of the recent EU-FP7 RelHy project showed a degradation rate less than 5%/1000 h at 800 °C and 0.6 A/cm^2.[46] The exact nature of these degradation mechanisms is unknown and is asking for additional R&D.[47] It looks as if a compromise has to be found between performance and lifetime. Among various causes for performance degradation, the highly corrosive environment in the electrolyzer and mechanical and thermal constraints are responsible for most losses. Operation at lower temperatures (down to the 700−800 °C range) is expected to solve the problem. However, at such "low" temperatures, the ionic conductivity of best oxide-ion conductors (e.g. yttrium-stabilized ZrO_2) becomes insufficient. Some scandia-doped zirconium and some nickelates have been proposed[48] in replacement but there is a need for new solid materials. Finally, it should be mentioned that an interesting extension of steam electrolysis is the co-electrolysis of water vapor and carbon dioxide. It can be used to reduce steam contents in the feed gas and somewhat reduce corrosion issues. Also, it can improve the efficiency of the process and lead to the formation of a valuable syngas ($H_2 + CO$).[49]

2.5 CONCLUSION

Water electrolysis is a well-established technology that has been used for almost one century for miscellaneous application in the industry (food industry, power plants, metallurgy, etc.). Nowadays, it is also considered as a key process that can be used for the production of high-purity hydrogen from water and renewable energy sources. It is expected that in the near future, water electrolyzers will occupy an increasingly prominent place

for the decentralized production of hydrogen, for example, in hydrogen-fueling stations. Thus, in spite of its long industrial history, this is still the focus of several ambitious R&D programs and investments worldwide. There are different water electrolysis technologies. The difference between them comes from the temperature of operation and the pH of the electrolyte. The alkaline process is the oldest and a more mature one. But SPE water electrolysis has been making very significant progresses over the last years and because of its large potential for further improvement, it is expected to play a significant role in view of the so-called hydrogen economy and the large production of hydrogen of electrolytic grade from renewable energy sources. The high-temperature water electrolysis process is probably more efficient. However, it is faced with critical challenges (especially, in material science). Such challenges will have to be overcome before any market application can be considered.

References

1. Trasatti, S. Water Electrolysis: Who First? J. Electroanal. Chem. **1999**, *476*, 90–91.
2. Wetzels, Walter D. Johann Wilhelm Ritter: Romantic Physics in Germany In *Romanticism and the Sciences*; Cunningham, Andrew, Jardine, Nicholas, Eds.; Cambridge University Press: Cambridge; 1990, pp 199–212.
3. Fateev, V. N.; Porembsky, V. I.; Samoilov, D. I. *Electrochemical Method for Deuteroxide and Hydrogen Isotopes Producing in the Book "Isotopes"*; Fizmatlit: Moscow; 2005, 277–289.
4. Cerri, I. Lefebvre-Joud, F. Holtappels, P. Honegger, K. Stubos, T. Millet, P. In: Hydrogen and Fuel Cells', Scientific Assessment in support of the Materials Roadmap enabling Low Carbon Energy Technologies, JRC Scientific and Technical Reports, May 2012.
5. Sata, N. Proton Conduction in Mixed Perovskite-Type Oxides; Solid State Ionics **1999**, *125*, 383–387.
6. Kuleshov, N. V.; Korovin, N. V.; Terentyev, A. A.; Ryzhikov, A. V. Domestic Electrolysis—a Necessary Component of Hydrogen Energy in Russia. In *Proceedings of International Symposium of Hydrogen Energy. Moscow, November 1–2, 2005*; Publishing House of MPEI; pp. 156–162.
7. Rosa, V. M.; Santos, M. B. F.; Da Silva, E. P. New Materials for Water Electrolysis Diaphragms; Int. J. Hydrogen Energy **1995**, *20* (9), 697–700.
8. http://www.hydro.com.
9. http://www.hydrogenics.com.
10. http://www.teledynees.com.
11. http://www.uralhimmash.ru.
12. Divisek, J.; Murgen, J. Diaphragms for Alkaline Water Electrolysis and Method for Production of the Same as well as Utilization Thereof, U. S. Patent 4,394,244, 1983.
13. Pile, D.L.; Doughty, D.H.; Sandia National Laboratory, Report on DOE Contract DE-AC04-94AL85000 (2005).
14. Davenport, R. J.; Schubert, F. H. Space Water Electrolysis: Space Station through Advanced Missions; J. Power Sources **1991**, *36*, 235–250.
15. Mosdale, R.; Srinivasan, S. Analysis of Performance and of Water and Thermal Management in Proton Exchange Membrane Fuel Cells; Electrochim. Acta **1995**, *40* (4), 413–421.
16. Grigoriev, S. A.; Porembsky, V. I.; Fateev, V. N. Pure Hydrogen Production by PEM Electrolysis for Hydrogen Energy; Int. J. Hydrogen Energy **2006**, *31* (2), 171–175.
17. Timonov, A. M. Solid Polymer Electrolytes: Structure, Properties and Applications; Soros Educat. J. **2000**, *6* (8), 69–75.
18. Grubb, W.T. United States Patent No 2913511, 1959.
19. www2.dupont.com.
20. Kinumoto, T.; Inaba, M.; Nakayama, Y.; Ogata, K.; Umebayashi, R.; Tasaka, A.; Iriyama, Y.; Abe, T.; Ogumi, Z. Durability of Perfluorinated Ionomer Membrane Against Hydrogen Peroxide; J. Power Sources **2006**, *158*, 1222–1228.
21. Grigoriev, S. A.; Millet, P.; Fateev, V. N. Evaluation of Carbon-Supported Pt and Pd Nanoparticles for the Hydrogen Evolution Reaction in PEM Water Electrolysers; J. Power Sources **March 2008**, *177* (2), 281–285.
22. Grigoriev, S. A.; Khaliullin, M. M.; Kuleshov, N. V.; Fateev, V. N. Water Electrolysis in the System with a Solid Polymer Electrolyte; Russian J. Electrochemistry **2001**, *37* (8), 953–957.
23. http://www.hamiltonsundstrand.com.
24. http://www.protononsite.com.
25. http://www.yara.com.
26. http://www.h-tec.com.
27. Millet, P.; Andolfatto, F.; Durand, R. Design and Performance of a Solid Polymer Electrolyte Water Electrolyzer; Int. J. Hydrogen Energy **February 1996**, *21* (2), 87–93.
28. Yamaguchi, M.; Horiguchi, M.; Nakanori, T. Development of Large-Scale Water Electrolyzer Using Solid Polymer Electrolyte in WE-NET. *Proceedings of the 13th World Hydrogen Energy Conference*, Beijing, China, June 12–15, 2000, Vol. 1, pp. 274–281.
29. http://www.genhypem.u-psud.fr.
30. Fateev, V. N.; Archakov, O. V.; Lyutikova, E. K.; Kulikova, L. N.; Porembsky, V. I. Water Electrolysis in Systems with a Solid Polymer Electrolyte; Electrochemistry **1993**, 551–557; T. 29. P. 551. No 4.
31. Millet, P.; Ngameni, R.; Grigoriev, S. A.; Mbemba, N.; Brisset, F.; Ranjbari, A.; Etiévant, C. PEM Water Electrolyzers: from Electrocatalysis to Stack Development; Int. J. Hydrogen Energy **2010**, *35*, 5043–5052.
32. Dinh Nguyen, M-T.; Ranjbari, A.; Catala, L.; Brisset, F.; Millet, P.; Aukauloo, A. Implementing Molecular Catalysts for Hydrogen Production in Proton Exchange Membrane Water Electrolysers; Coord. Chem. Rev. **2012**, *256*, 2435–2444.
33. Grigoriev, S. A.; Millet, P.; Porembsky, V. I.; Fateev, V. N. Development and Preliminary Testing of a Unitized Regenerative Fuel Cell Based on PEM Technology; Int. J. Hydrogen Energy **March 2011**, *36* (6), 4164–4168.
34. Perfiliev, M. V.; Demin, A. K.; Kuzin, B. L.; Lipilin, A. *High-Temperature Gases Electrolysis*; Science: Moscow; 232.
35. Korobtsev, S.V. *Development of Fundamental Technologies of Production and Use of Hydrogen based on Solid Oxide Electrochemical Reversible High-Temperature Systems*; Report on Round-Table Meeting "Russian Research and Development in the Field of Hydrogen Technologies": Moscow, February 8, 2006.
36. Hauch, A.; Jensen, S.H.; Mogensen, M. Ni/YSZ Electrodes in Solid Oxide Electrolyzer cells, *Proceedings of the 26th Risø International Symposium on Materials Science: Solid State Electrochemistry*, Roskilde, Denmark, 2005, pp. 203–208.
37. O'Brien, J. E.; Stoots, C. M.; Herrings, J. S., et al. Hydrogen Production Performance of 10-Cell Planar Solid Oxide Electrolysis Stack; J. Fuel Cell Sci. Technol. **May, 2006**.
38. Quandt, K. H.; Streicher, R. Concept and Design of a 3.5 MW Pilot Plant for High Temperature Electrolysis of Water Vapor; Int. J. Hydrogen Energy **1985**, *11*, 309–315.

39. Mogensen, M.; Jensen, S.H.; Hauch, A.; Chorkendorff, I.; Jacobsen, T. *Proceedings 7th European SOFC Forum (2006)*, Lucerne, Switzerland, July 2008.
40. Stoots, C.; O'Brien, J.E.; Hawkes, G.L.; Herring, J.S.; Hartvigsen, J.J. High Temperature Steam and Carbon Dioxide Electrolysis Experiments at INL, Workshop on High Temperature Electrolysis, Roskilde, Denmark, September 18−19, 2006.
41. Jensen, S. H.; Larsen, P. H.; Mogensen, M. Hydrogen and Synthetic Fuel Production from Renewable Energy Sources; Int. J. Hydrogen Energy **2007**, *32*, 3253−3257.
42. Dyomin, A. K.; Kuzin, B. L.; Lipilin, A. S. A Pilot Study of a Thermal Mode of a High-Temperature Electrolyser for Water Decomposition; Electrochemistry **1987**, *23*, 1258−1260.
43. Zhuravlev, V.D.; Lobachevsky, N.I.; Bamburov, V.G.; Kozhevnikov, V.L. Investigation of the Conductivity of Solid Solutions based on Bi_2O_3, *The 8th International Workshop "Fundamental Problems of Solid Body Ionics*." Chernogolovka, 2006, p. 217.
44. Brisse, A.; Schefold, J.; Zahid, M. High Temperature Water Electrolysis in Solid Oxide Cells; Int. J. Hydrogen Energy **2008**, *33*, 5375−5382.
45. Herring, S.; O'Brien, J. E.; Stoots, C. M.; Hawkes, G. L.; Hartvigsen, J. J.; Shahnam, M. Progress in High Temperature Electrolysis for H_2 Production Using Planar SOFC Technology; Int. J. Hydrogen Energy **2007**, *32*, 440−450.
46. Schefold, J.; Brisse, A.; Zahid, M. *Proceeding of the 217th ECS Meeting*, Vancouver, Canada, April 25−30, 2010.
47. Sohal, S. *Manohar Degradation in Solid Oxide Cells During High Temperature Electrolysis*; Idaho 83415; Idaho National Laboratory: Idaho Falls; http://www.inl.gov; Prepared for the U.S. Department of Energy Office of Nuclear Energy Under DOE Idaho Operations Office Contract DE AC07-05ID14517.
48. Stevens, P.; Bassat, J-M.; Mauvy, F.; Grenier, J-C.; Lalanne, C. Matériaux d'anode pour SOEC, French Patent EDF/CNRS WO 2006/008390.
49. Zhan, Z.; Kobsiriphat, W.; Wilson, J. R.; Pillai, M.; Kim, I.; Barnett, S. A. Syngas Production by Coelectrolysis of CO_2/H_2O: The Basis for a Renewable Energy Cycle; Energy Fuels **2009**, *23*, 3089−3096.

CHAPTER

3

Hydrogen Production from Water Splitting Using Photo-Semiconductor Catalysts

Rufino Manuel Navarro Yerga, María Consuelo Alvarez-Galván, Fernando Vaquero, Javier Arenales, José Luis García Fierro

Grupo de Energía y Química Sostenibles, Instituto de Catálisis y Petroleoquímica (CSIC), Marie Curie 2, Madrid, Spain

OUTLINE

3.1 Introduction 43

3.2 Principles of Water Splitting on Photo-Semiconductor Catalysts 44
- *3.2.1 Concept* 44
- *3.2.2 Energy Requirements* 45
- *3.2.3 Semiconducting and Electrochemical Properties of Photo-Semiconductor Catalysts* 46

3.3 Photo-Semiconductor Materials for Water Splitting 47
- *3.3.1 Photocatalysts Active under UV Irradiation* 47
  - 3.3.1.1 TiO_2 and Titanates 48
  - 3.3.1.2 Tantalates and Niobates 48
  - 3.3.1.3 d^{10} Metal Oxides 48
  - 3.3.1.4 Nonoxide Materials 48
- *3.3.2 Photocatalysts Active under Visible Irradiation* 48
  - 3.3.2.1 Oxides 48
  - 3.3.2.2 Sulfides 49
  - 3.3.2.3 Other Materials 49

3.4 Strategies to Improve the Visible Response of UV-Active Photocatalysts 49
- *3.4.1 Band Gap Engineering* 50
  - 3.4.1.1 Cation or Anion Doping 50
  - 3.4.1.2 Composite Systems 52
  - 3.4.1.3 Solid Solutions 52
- *3.4.2 Dye Sensitization* 54

3.5 Strategies to Improve the Photogenerated Charge Separation 55
- *3.5.1 Nanodesign: Controlling the Size and Form* 55
  - 3.5.1.1 Advanced Synthesis Approaches 55
  - 3.5.1.2 Anisotropic Photocatalysts and Other Structures 56
- *3.5.2 Loading of Co-catalysts* 57

3.6 Challenges and Opportunities 58

Acknowledgments 59

References 59

3.1 INTRODUCTION

Sunlight radiates a large amount of energy and intensity that would contribute significantly to our electrical and chemical needs. Approximately 120,000 TW of solar energy continuously reaches the Earth,[1] with 5% of this radiation at wavelengths less than 400 nm, in the ultraviolet (UV) range, and 49% within the visible spectrum, in the 400–750 nm wavelength.[2] However, the utilization of sunlight as an energy source depends on its capture, conversion, storage and distribution. The fundamental discrepancies in the times and places of solar energy supply and human energy demands can be overcome by converting solar radiation into an energy carrier such as hydrogen. The conversion of solar radiation into hydrogen offers the advantages of being transportable as well as

http://dx.doi.org/10.1016/B978-0-444-56352-1.00003-9

storable for extended periods of time. Additionally, the chemical energy stored in the H–H bond is easily released when it combines with oxygen, yielding only water as a reaction product (Fig. 3.1). Solar energy can be used to produce hydrogen in the form of heat (thermochemical[3,4]), light (photoelectrochemical (PEC),[5] photosynthetic[6] or photocatalytic[7]) or electricity (electrolysis[8]). Among them, the most efficient is the production of hydrogen by water splitting (Eqn (3.1)) using solar light because it does not have the inefficiencies associated with thermal transformations or with the conversion of solar energy to electricity followed by electrolysis:

$$H_2O \rightarrow \text{sunlight} \rightarrow H_2 + \frac{1}{2}O_2 \qquad (3.1)$$

The reaction involves the standard Gibbs free energy change (ΔG^0) greater than 237 kJ/mol, equivalent to 2.46 eV per molecule (1 eV/molecule = 96.1 kJ/mol). This energy is equivalent to the energy of photons with wavelengths between 1010 and 500 nm. As pure water does not absorb solar radiation, the water splitting needs a photo-semiconductor capable of efficiently absorbing solar energy and then splitting the molecule in an indirect way. Because the electrochemical decomposition of water to hydrogen and oxygen is a two-electron stepwise process, it is possible to use photo-semiconductor surfaces capable of absorbing solar energy to generate electrons and holes that can, respectively, reduce and oxidize the water molecules adsorbed on photocatalysts.

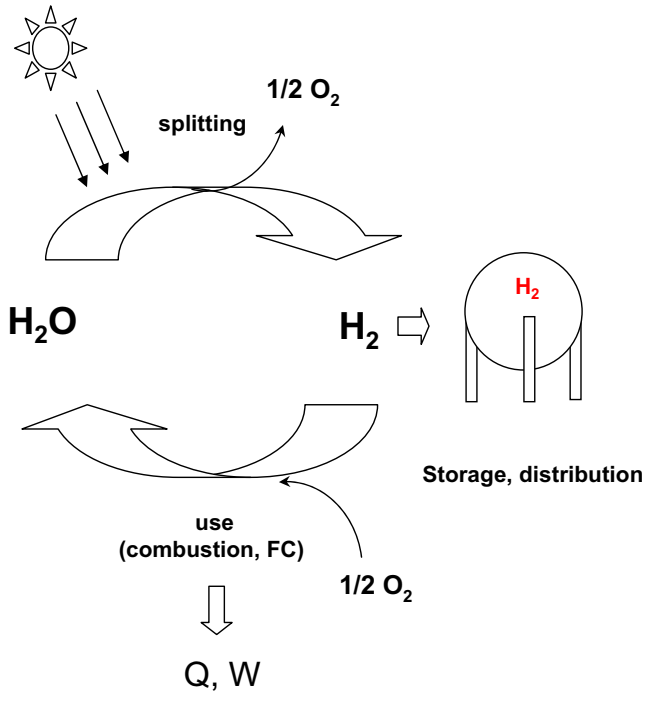

FIGURE 3.1 Scheme of generation and use of solar hydrogen as energy carrier. (For color version of this figure, the reader is referred to the online version of this book.)

Research in this field was initiated by the pioneering work conducted by Honda and Fujishima in 1972[5] in a PEC cell that demonstrated that hydrogen generation via splitting of water was possible using photocatalysts based on n-type TiO_2 semiconductor capable of absorbing light energy. This work stimulated the research for water splitting using particulate photocatalysts, which was first realized in 1980 by Lehn et al.,[9] Sato and White[10] and Domen et al.[11] Over the last 40 years, many types of photo-semiconductors, with more than 130 materials including oxides, nitrides, sulfides, carbides and phosphides have been reported to act as efficient particle photocatalysts for hydrogen evolution via water splitting. Unfortunately, most of the photocatalysts are only active under UV light irradiation (ca. 4% of solar irradiation) and the activity under visible light is quite limited. So far, the maximum apparent quantum efficiency (hydrogen yield per number of incident photons) for overall water splitting over visible light-driven particle photocatalysts records only a few percent (5.9%) apparent quantum efficiency over $Rh_{2-y}Cr_yO_3/(Ga_{1-x}Zn_x)(N_{1-x}Zn_x)$ photocatalysts applied to pure water under visible irradiation.[12] The low quantum efficiency is still the current "bottleneck" of the hydrogen production from solar light. The efficiency values achieved is still far from the quantum efficiency of 10% marked as the initial starting point for practical application. Consequently, progress in material science and engineering applied to the development of efficient semiconductors used as photocatalysts is still a major issue, the design of efficient photo-semiconductor systems for production of molecular hydrogen from water splitting being one of the foremost challenges in the development of a solar hydrogen economy.[1,12–20]

This chapter reports the most significant advances made in H_2 production via water splitting and the challenges that need to be addressed over the next coming years to verify the feasibility of hydrogen production by inorganic semiconductors as a competitive process in the hydrogen economy. Particular attention is given to the new materials and strategies reported in the literature over the past years for developing efficient particulate photocatalysts for water splitting.

3.2 PRINCIPLES OF WATER SPLITTING ON PHOTO-SEMICONDUCTOR CATALYSTS

3.2.1 Concept

Water splitting into H_2 and O_2 is classified as an "uphill" photocatalytic reaction because it is accompanied by a large positive change in the Gibbs free energy ($\Delta G^0 = +237$ kJ/mol, 2.46 eV per molecule). In this

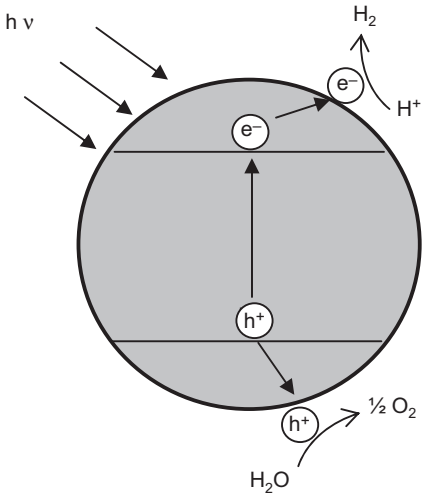

FIGURE 3.2 Sketch diagram showing the basic principle of overall water splitting on a photocatalyst. Irradiation with an energy greater than the band gap (E_g) of the semiconductor photocatalyst; the electrons (e^-) of the valence band are excited into the conduction band (CB) whereas the holes (h^+) are left in VB.

reaction, photon energy is converted into chemical energy, as seen in the photosynthesis of green plants. This reaction is therefore sometimes referred to as artificial photosynthesis:

$$H_2O(l) \rightarrow H_2(g) + \frac{1}{2}O_2(g) \tag{3.2}$$

Figure 3.2 depicts the basic principle of overall water splitting on a solid photocatalyst. Under irradiation with energy greater than the band gap (E_g) of the semiconductor photocatalyst, the electrons (e^-) of the valence band (VB) are excited into the conduction band (CB) whereas the holes (h^+) are left in VB. The electrons and holes that did not suffer recombination migrate toward the surface of the semiconductor where they, respectively, reduce and oxidize the water molecules adsorbed on the semiconductor surface.

Photocatalysts for photochemical water splitting can be used for this purpose according to two types of configurations: PEC cells and particulate photocatalytic systems. The PEC cell for water decomposition involves two electrodes immersed in an aqueous electrolyte, of which one is a photocatalyst exposed to light. In particulate photocatalytic systems, the photocatalysts are in the form of particles or powders suspended in aqueous solution in which each particle acts as microphotoelectrode that performs both oxidation and the reduction reactions of water on its surface (Fig. 3.3). This eliminates the need for a conducting substrate so that conventional synthesis routes can be used; therefore they are much simpler and less expensive to develop and use than PEC cells. However, particulate photocatalytic systems have disadvantages in comparison with PEC cells with regard to the separation of charge carriers; the separation is not as efficient as with a photoelectrode system, and there are difficulties associated with the effective separation of the stoichiometric mixture of oxygen and hydrogen to avoid backward reaction.

This work is focused on particulate photocatalytic systems excluding work on photoanodes used for PEC H_2 generation, which has been reviewed elsewhere.[21,22]

3.2.2 Energy Requirements

To achieve overall water splitting, the energy requirements imply that the bottom of the CB must be located at a more negative potential than the reduction potential of

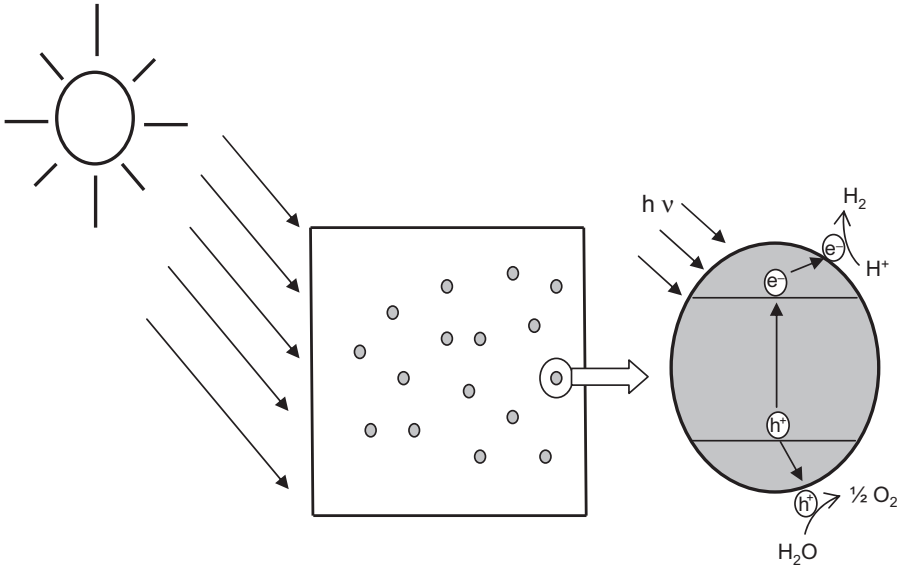

FIGURE 3.3 Scheme of the photocatalyst particulate suspension system for water splitting.

H^+/H_2 (0 V vs. normal hydrogen electrode (NHE) at pH = 0), whereas the top of the VB must be positioned more positively than the oxidation potential of H_2O/O_2 (1.23 V vs. NHE). Accordingly, water-splitting reaction can only be conducted if the photon energy is superior to 1.23 eV. This energy is equivalent to the energy of a photon with a wavelength of around 1010 nm, indicating that visible light possesses energy enough for the decomposition of water. In addition to the band structure of the semiconductor, there is an activation barrier in the charge-transfer process between photocatalyst and water molecules derived from the energy losses (transport of electron/hole, kinetic losses, electron/hole recombination) associated with solar energy conversion. As a consequence of this energy loss, the optimal band gap for high-performance photocatalyst increases from the theoretical value of 1.23 to 2.0−2.2 eV.

Factors other than band gap energy such as charge separation, mobility and the lifetime of photogenerated electrons and holes also play an important role on the photocatalytic activity of semiconductors. The generation and separation of electrons and holes strongly depend on both the presence of co-catalysts on the surface of the photocatalysts and their structural and electronic properties. As a general rule, highly crystalline materials with a low density of defects, which act as recombination centers of electrons and holes, are beneficial for water-splitting reaction. Loading of appropriate co-catalysts onto the photocatalysts also facilitates the redox reactions taking place on their surfaces.[23−25] The co-catalysts are typically a noble metal (e.g. Pt, Rh) or metal oxide (e.g. NiO, RuO_2) loaded on the surface as nanoparticles whose principal role is to reduce the electron−hole recombination and to reduce the activation energy for gas evolution.

As overall water splitting is generally difficult to achieve due to the uphill nature of the reaction, the photocatalytic activities of photocatalysts have sometimes been examined in the presence of reducing reagents (alcohols, sulfides, sulfites, EDTA etc.) or oxidizing ones (persulfate, Ag^+, Fe^{3+} etc.) to facilitate either water reduction or oxidation. When the photocatalytic reaction is carried out in aqueous solutions including easily reducing reagents such as alcohols and sulfides, photogenerated holes irreversibly oxidize the reducing reagent instead of water, thus facilitating water reduction by CB electrons. On the other hand, electron acceptors such as Ag^+ or Fe^{3+} consume the photogenerated electrons in the CB and the O_2 evolution reaction is enhanced. The reactions using redox reagents are not "overall" water-splitting reactions but are often carried out as test reactions for photocatalytic H_2 or O_2 evolution. However, one should realize that the results obtained using redox reagents do not guarantee activity for overall water splitting using pure water.

3.2.3 Semiconducting and Electrochemical Properties of Photo-Semiconductor Catalysts

The photocatalysts used for the water-splitting reaction must satisfy several functional requirements with respect to semiconducting and electrochemical properties[2]: (1) appropriate visible light absorption with band gap around 2.0−2.2 eV and band edge potentials suitable for overall water splitting; (2) ability to separate photo-excited electrons from reactive holes once formed; (3) minimization of energy losses related to charge transport and electron−hole recombination; (4) chemical stability to corrosion and photo-corrosion in aqueous environments; (5) kinetically suitable electron transfer properties from photocatalysts' surface to water; and (6) low production cost.

The electronic structure is doubtless the principal parameter that decides the light-harvesting ability of the photocatalyst. Figure 3.4 depicts the band positions of various semiconductors respect to the potentials (NHE) for water oxidation/reduction processes.[26] Among the semiconductors represented in Fig. 3.4, only $KTaO_3$, $SrTiO_3$, TiO_2, ZnS, CdS and SiC fulfill the thermodynamic requirements for overall water splitting.

As stated above, chemical stability against photocorrosion and dissolution processes is another essential requirement to be met by the photocatalyst. A number of photocatalysts that exhibit suitable semiconducting properties for solar energy conversion (CdS, GaP, TaON) are not stable in the water oxidation reaction because the anions of these salts or oxy-salts become more easily oxidized than water causing their degradation upon formation of an oxide layer at the surface.[27]

Water oxidation/reduction reactions at the photocatalyst surface may only happen if separate charge carriers (electrons and holes) generated by absorbed light can reach the solid−liquid interface during their life time and are capable of finding suitable reaction partners, protons for electrons and water molecules for holes. To achieve this, both generation and separation of photoexcited electrons and holes with low recombination rate is also an essential condition to be fulfilled by the photocatalysts. Transport of electrons and holes toward the catalyst surface strongly depends on the microstructure and surface properties of photocatalysts. As a general rule, the photoactivity increases in highly crystalline photocatalysts because the density of defects caused by grain boundaries, which act as recombination centers of electrons and holes, decreases when increasing crystallinity of particles.[28] Surface area, determined by the size of the photocatalyst particles, also influences the efficiency of carrier transport. An efficient charge transport implies necessarily diffusion lengths longer than the size of the particles. Therefore, the possibility for the charge carrier to reach the surface increases upon decreasing the particle size of

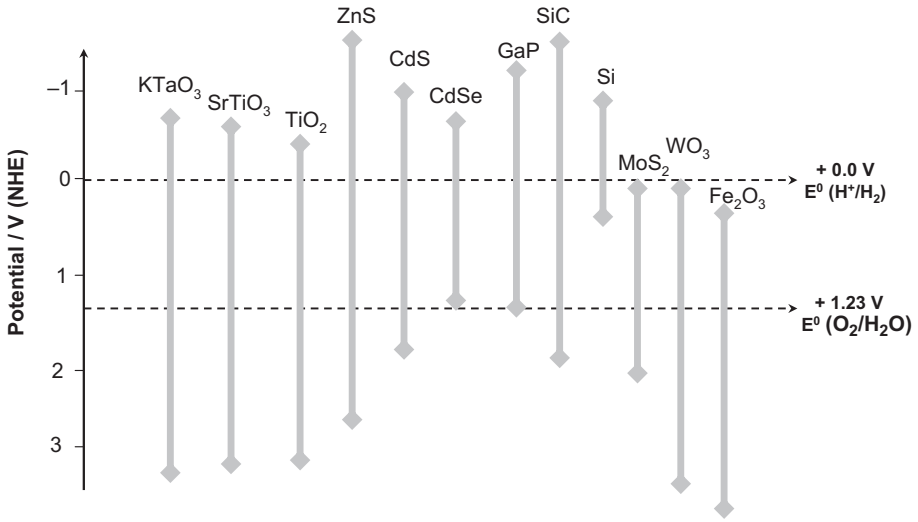

FIGURE 3.4 Band gap energy and relative band position of different photocatalysts with respect to the potentials (NHE) for water oxidation/reduction reactions.

photocatalysts.[29] Nevertheless, the improvement on the efficiency associated to a high crystalline degree of the photocatalyst has much larger effect on the efficiency than that associated with low crystal sizes.[30]

3.3 PHOTO-SEMICONDUCTOR MATERIALS FOR WATER SPLITTING

The number of elements whose compounds display photocatalytic activity for water splitting is limited. Elements included in photocatalysts for water splitting are summarized in Fig. 3.5. The photocatalysts are made of metal oxides, metal sulfides, oxysulfides, oxynitrides and composites thereof. Most metal oxide, sulfide and nitride photocatalysts consist of metal cations with d^0 and d^{10} configurations. Unfortunately, most of the photo-semiconductor materials are only active under UV light and those active under visible light are quite limited.

3.3.1 Photocatalysts Active under UV Irradiation

Various kinds of semiconducting metal oxides have been reported to act as efficient photocatalysts to split

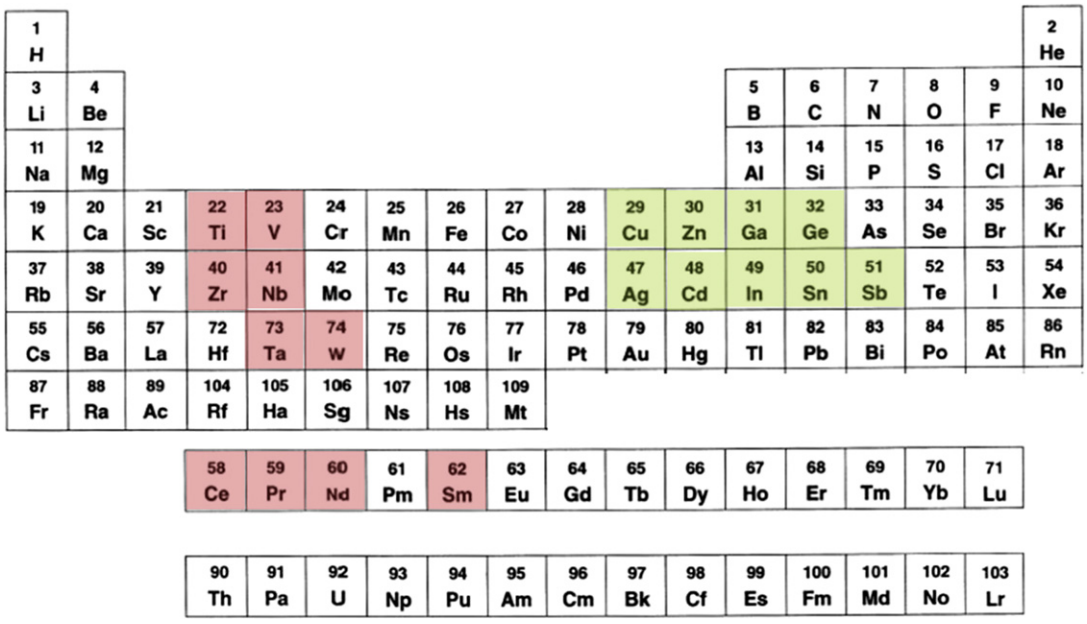

FIGURE 3.5 Elements included in photocatalysts for water splitting: elements with d^{10} configuration (red) and elements with d^0 configuration (light green). (For interpretation of the references to color in this figure legend, the reader is referred to the online version of this book.)

gaseous or liquid phase water into H_2 and O_2 under UV light irradiation. The UV-active photocatalysts can be divided into four groups: TiO_2 and titanates; tantalates and niobates; d^{10} metal oxides and non-oxide materials.

3.3.1.1 TiO_2 and Titanates

Overall water splitting using particulate TiO_2[10] and $SrTiO_3$[11] under UV light was reported for the first time in 1980. Other titanates are known to work as efficient photocatalysts for water splitting under UV irradiation. When TiO_2 is fused with metal oxides, e.g. La_2O_3, Sm_2O_3, metal titanates with intermediate band gaps can be obtained. Shibata et al.[31] reported that layered titanates ($Na_2Ti_3O_7$, $K_2Ti_2O_5$ and $K_2Ti_4O_9$) were active in photocatalytic H_2 evolution from aqueous methanol solutions. Perovskite titanates, La_2TiO_5, La_2TiO_3 and $La_2Ti_2O_7$, with layered structures have been also described as materials with high photocatalytic activities under UV irradiation.[32] Titanates with cubic-pyrochlore structure $R_2Ti_2O_7$ (R = Y, Eu, Ga, La) showed a fairly high activity for overall water-splitting reaction.[33,34]

3.3.1.2 Tantalates and Niobates

Oxides with layered and tunneling structures are considered as promising materials to perform efficient water photodecomposition. According to this fact, tantalates and niobates oxides with corner-sharing of MO_6 (M = Ta, Nb) octahedra structure have been considered as photocatalysts for water splitting. Tantalates and niobates oxides are highly active for pure water splitting even without co-catalysts but only under UV light because of their high energy band gap (4.0–4.7 eV).[35–39] The high activity of this layered compounds are related with the easy migration and separation of the photogenerated electron–holes through the corner-shared framework of MO_6 units.[40]

3.3.1.3 d^{10} Metal Oxides

Various metal oxides with d^{10} configuration (In^{3+}, Ga^{3+}, Ge^{4+}, Sn^{4+}, Sb^{5+}) have been shown to be effective for water splitting under UV light. B-Ga_2O_3 with a band gap of 4.5 eV has been reported as promising photocatalysts for water splitting under UV–visible irradiation.[41] Inoue and co-workers investigated photocatalytic properties for water splitting of different indates.[42,43] The photocatalytic activity for water decomposition under UV irradiation was considerably large for $CaIn_2O_4$, $SrIn_2O_4$ and $BaIn_2O_4$, which show distorted InO_6 octahedra with dipole moment. Metal oxides with d^{10} configurations have distorted octahedral and/or tetrahedral structures ($CaSb_2O_6$[44] Zn_2GeO_4,[45] $ZnGa_2O_4$[46] were also reported to show activity for water splitting under UV irradiation).

3.3.1.4 Nonoxide Materials

Sulfides, nitrides and phosphide photocatalysts that have wide band gap and VB at relatively negative potentials compared to oxides have also been reported as semiconductors for UV-driven photocatalysis. ZnS has been reported as high-active photocatalyst for hydrogen production from SO_3^{2-} solutions under UV irradiation.[47] InP was the sole reported phosphide capable of producing hydrogen from aqueous sulfite solutions.[48] Nitrides of transition metal-cations with d^{10} electronic configuration (Ga^{3+}, Ge^{4+}) are another type of photocatalysts that can split water efficiently under UV light.[49,50]

3.3.2 Photocatalysts Active under Visible Irradiation

The number of single-phase materials active under visible irradiation for water splitting is quite limited. The photocatalysts active under visible light can be divided into three groups: oxides, sulfides and other materials.

3.3.2.1 Oxides

Valence band-controlled photocatalysts having a continuous VB formed by atomic orbitals of the constituent elements have been reported by many researchers as materials capable of producing H_2 from aqueous solutions under visible light. $BiVO_4$ with scheelite structure and Ag_3VO_4 with perovskite structure were found to show photocatalytic activities for O_2 evolution from aqueous silver nitrate solution under visible light irradiation.[51–53] These oxides possess steep absorption edges in the visible light region. The steep edges indicate that the visible light absorption of these oxides is due to a band–band transition. In contrast with other oxides, the VB of $BiVO_4$ and Ag_3VO_4 consist of Bi and Ag orbitals mixed with O2p states that result in the increase of the VB potentials and the decrease in the band gap energy. Therefore, $BiVO_4$ and Ag_3VO_4 have the ability to absorb visible light. However, these catalysts did not have potential for H_2 production because the CB potentials of the photocatalysts do not have sufficient overpotential for the reduction potential of water.

Lee and co-workers[54] reported that $PbBi_2Nb_2O_9$, an Aurivillius-phase perovskite, acts as photocatalyst capable of producing H_2 or O_2 from aqueous solutions containing sacrificial reagents under visible light. Lv et al.[55] developed a new LiCr-$(WO_4)_2$ single-phase oxide photocatalyst that showed photocatalytic activity for H_2 production under visible light irradiation. $RbPb_2Nd_3O_{10}$ Dian-Jacobson phase layered perovskite is also a single-phase oxide that showed photocatalytic

activity under visible light. Domen and co-workers[56] reported visible light response of $RbPb_2Nd_3O_{10}$ with capacity to produce H_2 or O_2 from aqueous solutions under visible light. Li and Ye[57] developed binary lead niobates $Pb_3Nb_2O_8$ and $Pb_3Nb_4O_{13}$, which are visible light-sensitive photocatalysts. The hybridization of the Pb6s and O2p orbitals in these niobates is responsible for the observed visible light response.

3.3.2.2 Sulfides

Sulfide photocatalysts, which have narrow band gap and VB at relatively negative potentials compared to oxides, are good candidates for visible light-driven photocatalysts. Metal sulfide photocatalysts, however, are not stable in the water oxidation reaction under visible light because the S^{2-} anions are more susceptible to oxidation than water causing the photo-degradation of the photocatalyst.[27,58] For that reason, sulfide photocatalysts are not suitable for water splitting unless appropriate strategies are designed to minimize the photo-degradation. A common method for reducing the photo-corrosion of the sulfides under irradiation is by means of the use of suitable sacrificial reagents. Photo-corrosion may be effectively suppressed by using a Na_2S/Na_2SO_3 mixture as electron donor.[59] Using this mixed solution, the photocatalytic reaction should proceed as follows, avoiding the degradation of sulfide photocatalyst:

$$\text{Photocatalysts} + hv \rightarrow e^-(CB) + h^+(VB) \quad (3.3)$$

$$2H_2O + 2e^-(CB) \rightarrow H_2 + 2OH^- \quad (3.4)$$

$$SO_3^{2-} + H_2O + 2h^+(VB) \rightarrow SO_4^{2-} + 2H^+ \quad (3.5)$$

$$2S^{2-} + 2h^+(VB) \rightarrow S_2^{2-} \quad (3.6)$$

$$S_2^{2-} + SO_3^{2-} \rightarrow S_2O_3^{2-} + S^{2-} \quad (3.7)$$

$$SO_3^{2-} + S^{2-} + 2h^+(VB) \rightarrow S_2O_3^{2-} \quad (3.8)$$

Among the available sulfide semiconductors, nanosized CdS is an interesting photocatalyst, since it has a narrow band gap (2.4 eV) and a suitable CB potential to effectively reduce the H^+.[59,60] CdS loaded with Pt co-catalyst shows very high efficiency in light absorption and hydrogen production under visible light (apparent quantum efficiency = 25%[61]).

3.3.2.3 Other Materials

A new class of titanium semiconductor, titanium disilicide ($TiSi_2$), which absorbs a wide range of the solar spectrum, has been proposed as a prototype photocatalyst for the water-splitting reaction.[62] This photocatalyst presents two phases of hydrogen evolution when the reaction is conducted under specific conditions. At short reaction times, the system shows a nonlinear dependence for H_2 evolution, whereas a nearly linear dependence takes place at longer reaction times. The first part of the H_2 evolution–time curve was interpreted in terms of the surface oxidation of $TiSi_2$ whereas the linear part observed at longer illumination times was attributed to water splitting.

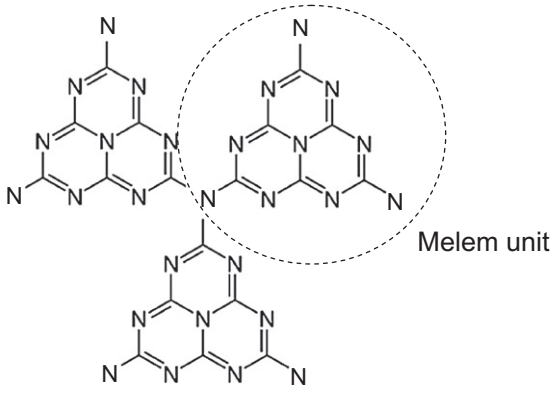

FIGURE 3.6 Schematic structure of a perfect graphitic carbon nitride sheet constructed from melem units. *Source: Adapted from Ref. 63.*

Graphitic carbon nitride (g-C_3N_4, Fig. 3.6) with a band gap of 2.7 eV was developed as a promising photocatalyst for hydrogen or oxygen production from water under visible-light irradiation with the assistance of sacrificial reagents.[63] The prepared g-C_3N_4 achieved steady H_2 production from water containing triethanolamine as a sacrificial electron donor on visible light illumination.

Some phosphate semiconductors were also reported as active photocatalysts for water splitting under visible light. $Li_9Fe_3(P_2O_7)_3(PO_4)_2$ was proven to be an active photocatalyst for H_2 production under visible light irradiation using I^- ions as electron donor.[64]

Graphene oxide semiconductor photocatalyst (Fig. 3.7) with a band gap of 2.4–4.3 eV can also steadily produce H_2 from an aqueous methanol solution or pure water under visible light irradiation as reported recently by Yeh et al.[65]

3.4 STRATEGIES TO IMPROVE THE VISIBLE RESPONSE OF UV-ACTIVE PHOTOCATALYSTS

As shown in Section 3.3.1, various kinds of semiconducting metal oxides have been reported to act as efficient photocatalysts to split gaseous or liquid phase water into H_2 and O_2 under UV light irradiation. However, most of metal oxide photocatalysts are unable to split pure water under visible light. This is mainly due to the fact that as the band gap energy of the metal oxide becomes smaller, the CB edge shifts more positively.[66] To overcome this difficulty, suitable band engineering is

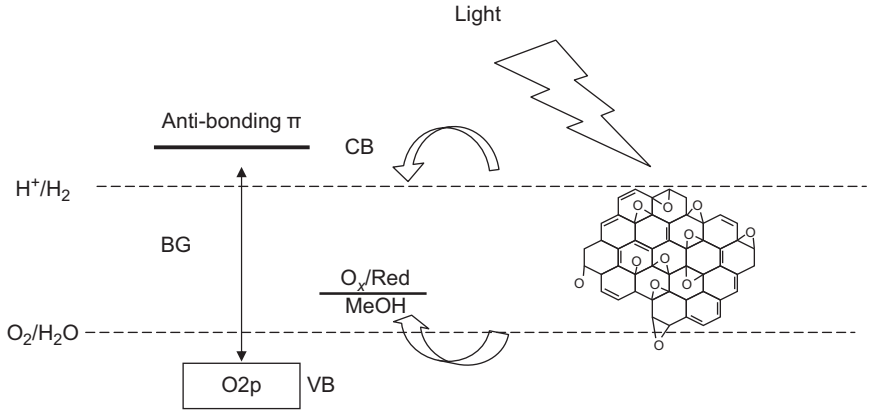

FIGURE 3.7 Energy-level diagram of semiconducting graphene oxide. *Source: Adapted from Ref. 65.*

required in order to develop new photocatalysts for water splitting under visible light irradiation when starting with wide band semiconductors.

3.4.1 Band Gap Engineering

The ability to adjust and fine-tune band gap and band positions is essential in developing visible light-responsive photocatalysts for H_2 production. Three approaches toward band engineering have been reported: cation or anion doping; VB modification; and solid solution formation.

3.4.1.1 Cation or Anion Doping

The replacement of cations or anions in the lattice of a wide band gap semiconductor has often been used for enhancing the visible light response of wide band gap photocatalysts (UV-active).

The replacement of cations in the crystal lattice of a wide band gap semiconductor may create impurity energy levels within the band gap of the photocatalyst that facilitates absorption in the visible range, as depicted in Fig. 3.8. Although a cation-doped photocatalyst can induce visible light response, most of these photocatalysts do not record photoactivity because dopants in the photocatalysts act not only as visible light absorption centers, with an absorption coefficient dependent on the density of dopants, but also as recombination sites between photogenerated electrons and holes.[67] Furthermore, the impurity levels created by dopants in the photocatalysts are usually discrete, which would appear disadvantageous for the migration of the photo-generated holes.[68] Therefore, it is important to fine-tune both the content and depth of the cation substitution in the structure of the host photocatalysts to develop visible light-driven water-splitting photocatalysts. Metal ions may be incorporated into the photocatalysts by chemical methods such as impregnation and precipitation or by the advanced ion-implantation technique that allows for the incorporation of cations by the impact of high-energy ions accelerated by high voltage (50–200 keV).[69–71]

Anion doping is another approach undertaken to enhance the visible light response of wide band gap (UV-active) semiconductors. As in wide band gap oxide semiconductors, the top of the VB consists of O2p atomic orbitals and partial replacement of oxide anions by other anions such as nitrogen,[72,73] sulfur[74] or carbon[75] has

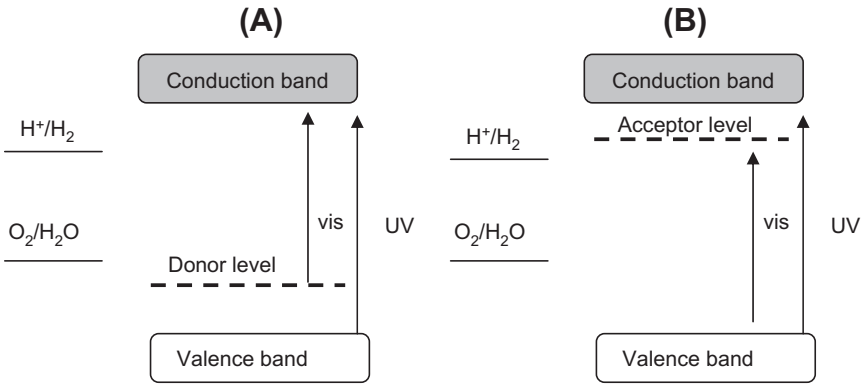

FIGURE 3.8 Band structure of cation-doped photocatalyst with visible light response from a photocatalyst with UV response (donor level (A) or acceptor level (B) former by ion doping).

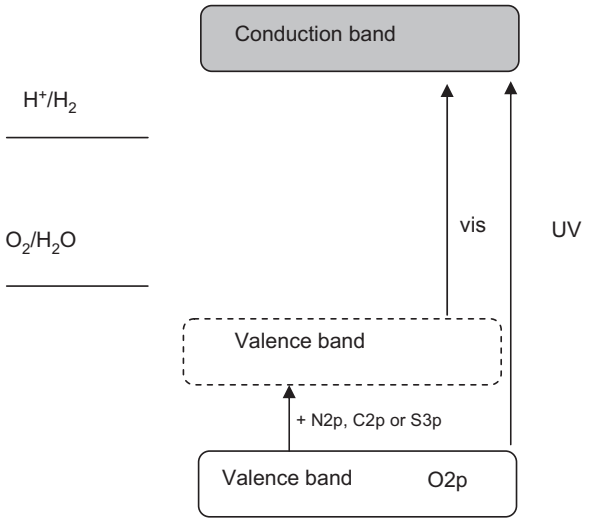

FIGURE 3.9 Band structure of anion-doped photocatalyst with visible light response from a semiconductor with UV response.

often been practiced. In all these anion-doped semiconductors, the mixing of the p orbitals of the doping anion (N, S or C) with the O2p orbitals results in a shift of the VB edge upward and in a narrowing of the band gap energy as illustrated in Fig. 3.9. In contrast with the cation doping technique, the anionic replacement usually forms less electron–hole recombination centers, and therefore these doped oxide semiconductors exhibit better photocatalytic activity. Nevertheless, the control of the oxygen defects, originated by difference in the formal oxidation state of oxygen and dopant element, is essential as these defects act as recombination centers that may reduce the efficiency of the anion-doped photocatalyst.

3.4.1.1.1 DOPED TiO_2 AND TITANATES

Kato and Kudo reported that TiO_2 co-doped with a combination of Sb^{5+} and Cr^{3+} are active for O_2 evolution under visible light irradiation ($\lambda > 440$ nm) from an aqueous solution using $AgNO_3$ as sacrificial reagent.[76] In this system, doped Cr^{3+} ions form electron donor level within the band gap of TiO_2 that allows this semiconductor to absorb visible light. Co-doping with Sb^{5+} was necessary to maintain the charge balance, resulting in the suppression of the formation of Cr^{6+} ions and oxygen defects in the lattice.

Doping of transition metal ions into TiO_2 by advanced ion-implantation technique has been shown to enable modified-TiO_2 to work under visible light.[23,77] The Cr^{3+} or V^{5+} ion-implanted TiO_2 films display photoactivity under visible light for H_2 evolution from aqueous solution involving methanol as sacrificial reagent with a quantum yield (QY) of 1.25.[78] Although the ion-implantation method provides a way of modifying the optical properties of TiO_2, it was not practical for mass production due to the high cost of the ion-implantation equipment used to develop these TiO_2 modified photocatalysts.

The doping of foreign metal ions into $SrTiO_3$ and La_2TiO_7 is a conventional method for the development of visible light-driven photocatalysts based on these titanates. A survey of dopants for $SrTiO_3$ revealed that the doping of Rh or the co-doping of Cr^{3+}–Ta^{5+} or Cr^{3+}–Sb^{5+} were effective in making $SrTiO_3$ visible light responsive.[76,79,80] These doped $SrTiO_3$ samples loaded with Pt co-catalysts have shown activity for H_2 production from aqueous methanol solutions under visible light irradiation.

Doping of $La_2Ti_2O_7$ with Cr^{3+} or Fe^{3+} ions allows the visible light absorption above 400 nm by the excitation of the electrons in the Cr3d or Fe3d band to the CB.[81,82] However, these doped-$La_2Ti_2O_7$ samples do not show activity for pure water splitting under visible light irradiation. Only in the presence of methanol as sacrificial electron donor, the doped-$La_2Ti_2O_7$ samples are active for H_2 evolution under visible light.

N-doped TiO_2 has been tested for photocatalytic water splitting.[83] Under visible light, this Pt-modified photocatalyst evolves O_2 from aqueous $AgNO_3$ as sacrificial electron acceptor and traces of H_2 from aqueous solutions of methanol as sacrificial electron donor.

The visible light response of layered $Ln_2Ti_2O_7$ (Ln = lanthanides) improved with the partial substitution of oxygen by sulfur anions in the $Ln_2Ti_2O_7$ lattice. This is illustrated by $Sm_2Ti_2S_2O_5$, which has been demonstrated to be responsive to visible light excitation at wavelengths up to ca. 650 nm.[84] S3p atomic orbitals constitute the upper part of the VB of $Sm_2Ti_2S_2O_5$ and contribute to lowering the band gap energy (2.0 eV) from that of the corresponding $Sm_2Ti_2O_7$ (3.5 eV). Under visible light irradiation, the $Sm_2Ti_2S_2O_5$ works as a stable photocatalyst for the reduction of H^+ to H_2 or oxidation of H_2O to O_2 in the presence of a sacrificial electron donor (Na_2S–Na_2SO_3 or methanol) or acceptor (Ag^+).

3.4.1.1.2 DOPED TANTALATES AND NIOBATES

Tantalates and niobates can form oxynitride compounds to reduce the band gap of these materials. In these compounds, O atoms are partially substituted for N atoms in metal oxide causing the VB to shift to higher potential energy as a result of the hybridization of the O2p orbitals with the N2p orbitals. Following this strategy, $MTaO_2N$ (M = Ca, Sr, Ba), TaON and $Sr_2Nb_2O_{7-x}N_x$ ($x = 1.5$–2.8) have been studied as photocatalysts for water splitting under visible light irradiation.[73,85,86] TaON and MTa_2N (M = Ca, Sr, Ba) have small band energies (2.5 eV for TaON and 2.5–2.0 eV for $MTaO_2N$) and are capable of absorbing visible light at 500–630 nm.[85] TaON samples show photocatalytic activity under visible light for H_2 production

from aqueous solutions using methanol as sacrificial reagent and also for O_2 production from aqueous solutions with $AgNO_3$ as electron acceptor. On the other hand, $MTaO_2N$ samples are capable of producing H_2 under visible light in the presence of methanol as sacrificial electron donor though they did not have sufficient potential to oxidize water using $AgNO_3$ as electron acceptor.

Nitrogen substitution on $Sr_2Nb_2O_7$ oxides also enables the absorption of the oxynitride in the visible range as result of the mixing of N2p with O2p states near of the VB. $Sr_2Nb_2O_{7-x}N_x$ samples with different N substitution ($x = 1.5-2.8$) show photocatalytic activity under visible light for H_2 evolution from aqueous methanol solutions.[86] The most active photocatalysts were those that achieve the higher nitrogen substitution maintaining the original layered structure of $Sr_2Nb_2O_7$. An excess of nitrogen substitution facilitates the collapse of the layered structure of the parent oxide and turns into the less-active nonlayered $SrNbO_2N$.

3.4.1.1.3 DOPED SULFIDES

Studies have been carried out to improve the visible light sensitivity of ZnS-based photocatalysts. One of the strategies for inducing visible light response in ZnS was the chemical doping of ZnS with metal ions (Cu^{2+},[87] Ni^{2+}[88] and Pb^{2+}[89]). The doped-ZnS materials are capable of absorbing visible light as a result of the transitions from M^{n+} (M = Cu, Ni, Pb) levels to the CB of ZnS. These doped-ZnS photocatalysts showed high photocatalytic activity under visible light for H_2 production from aqueous solutions using SO_3^{2-}/S^{2-} as electron donor reagents.

3.4.1.2 *Composite Systems*

Use of composite semiconductors is another strategy to develop photocatalysts with visible light response by starting with wide band gap photocatalysts. This strategy consists in the coupling of a wide band gap semiconductor with a narrow band semiconductor with a more negative CB level. According to this, CB electrons can be injected from the small band gap semiconductor to the large band semiconductor allowing the extent in the absorption capacity of the mixed photocatalyst (Fig. 3.10). In the photocatalyst composites, the semiconductor particles are in electronic contact without any mixing at molecular level that mitigates the carrier recombination by means of the inter-particle electron transfer. For successful coupling of semiconductors, the following conditions are necessary to be met: (1) the CB level of the semiconductor of the narrow band gap should be more negative than that of the semiconductor with wide band gap; (2) the CB level of the semiconductor with wide band gap should be more negative than the water reduction potential, and (3) electron injection should be fast and efficient.

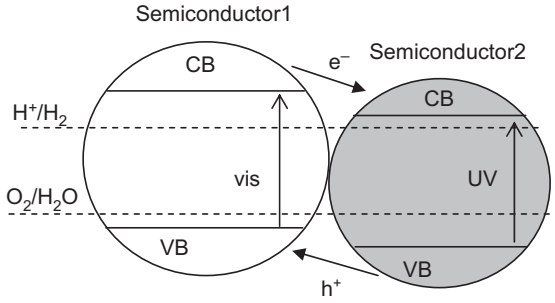

FIGURE 3.10 Band structure of photocatalyst composite with enhanced visible light response made from the mixture between wide and narrow band gap photocatalysts.

Improvement of visible light response of TiO_2 and ZnO can be achieved by their combination with CdS.[90–92] In these composite systems, the photogenerated electrons move from CdS to the attached semiconductors, whereas photogenerated holes remain in CdS. This charge-carrier separation stops charge recombination, therefore improving the photocatalytic activity of TiO_2 and ZnO under visible light. Similarly, the TiO_2/SnO_2 mixed oxide showed enhanced photocatalytic activity for hydrogen generation compared to bare TiO_2.[93]

The incorporation of a guest photocatalyst into the interlayers of a lamellar semiconductor has also been considered as a way of enhancement of the photocatalytic activity. In this guest–host semiconductor, the recombination between photoinduced charges is suppressed due to the quick charge transfer from the guest to the host semiconductor. Wu et al.[94] reported the intercalation of nanosized TiO_2 into the interlayer of various layered metal oxides ($H_4Nb_6O_{17}$, HNb(Ta)WO_6 or $HLaNb_2O_7$). These intercalated composited photocatalysts possessed high activity for hydrogen production in the presence of methanol as sacrificial reagent under visible light irradiation.

The encapsulation of guest photocatalyst into micro/mesostructured semiconductors is another composite alternative for the effective separation of the photogenerated charges. Narrow band gap semiconductors, such as CdS, have been incorporated into nanotubular TiO_2 obtaining composite photocatalysts with high efficiency for hydrogen production (43.4% at 420 nm) from water solutions containing sulfide and sulfite ions as hole scavengers.[95]

3.4.1.3 *Solid Solutions*

The third approach to span the visible light response of wide band gap photocatalysts is by means of making solid solutions between wide and narrow band gap

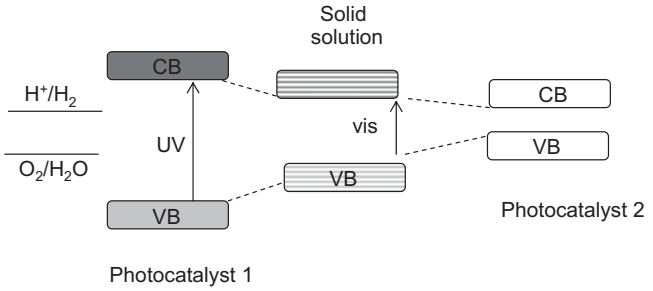

FIGURE 3.11 Band structure of solid solution photocatalyst made from the mixture between wide and narrow band gap photocatalysts.

semiconductors with similar lattice structure as depicted in Fig. 3.11. Solid solutions of two or more semiconductors are formed where the lattice sites are interdispersed with the solid solution components.

3.4.1.3.1 METAL OXIDE SOLID SOLUTIONS

A certain class of oxide solid solutions has recently been proposed as active photocatalysts for the overall water-splitting reaction under visible light. The solid solution of Y_2WO_6 and Bi_2WO_6 ($BiYWO_6$) was found by Liu et al.[96] to have photocatalytic ability to split water into H_2 and O_2 under visible light. It was suggested that the Bi6s and Y4d orbitals contributed to the creation of new valence and CB, respectively. The solid solution $BiYWO_6$ responds to visible light up to 470 nm. In this case, the efficiency for water splitting under visible light so far achieved is also very low. For example, a quantum efficiency of only 0.17% at 420 nm was reported for $BiYWO_6$ solid solution with RuO_2 as co-catalyst. Nevertheless, the activity of this type of photocatalysts can be expected to be promoted feasibly by changing the ratio of Bi/Y/W in the flexible structure of the solid solution. The solid solution composed of $BiVO_4$ and $DyVO_4$ ($Bi_{0.5}Dy_{0.5}VO_4$) was also reported as active under visible light splitting water into H_2 and O_2.[97] However, the activity so far achieved over this type of photocatalysts is very low (H_2 production of 34.5 μmol/h over 0.1 g of $Bi_{0.5}Dy_{0.5}VO_4$ with Pt−Cr_2O_3 co-catalyst). $Bi_xIn_{1-x}TaO_4$ ($0 < x < 1$) solid solutions were also reported as semiconductor materials with activity under visible light for H_2 and O_2 production from aqueous solution containing sacrificial reagents.[98] It was suggested that the band structure consisted of a CB of mainly Ta5d, In5p and In5s orbitals, whereas the VB was principally O2p, Bi6s and B6p orbitals.

3.4.1.3.2 METAL (OXY)NITRIDE SOLID SOLUTIONS

The solid solution between GaN and ZnO (($Ga_{1-x}Zn_x$)($N_{1-x}O_x$)) was tested first.[69] GaN and ZnO have wurtzite structures with similar lattice parameters and therefore they can form solid solutions. Whereas GaN and ZnO have band gap energies greater than 3 eV and therefore do not absorb visible light, the ($Ga_{1-x}Zn_x$)($N_{1-x}O_x$) solid solution has absorption edges in the visible region with band energies of 2.4−2.8 eV. Density functional calculations indicated that the visible light response of the solid solution originates from the presence of Zn3d and N2p electrons in the upper VB that provide p−d repulsion for the VB resulting in the narrowing of the band gap. The ($Ga_{1-x}Zn_x$)($N_{1-x}O_x$) solid solution exhibits low phtotocatalytic activity even under UV irradiation. However, its activity under visible light increases remarkably by the modification of ($Ga_{1-x}Zn_x$)($N_{1-x}O_x$) solid solution by superficial deposition of co-catalyst nanoparticles. Different transition metal and oxides have been examined as co-catalysts to promote activity of ($Ga_{1-x}Zn_x$)($N_{1-x}O_x$) solid solutions.[99,100] Among the various co-catalysts examined, the largest improvement in activity was obtained when ($Ga_{1-x}Zn_x$)($N_{1-x}O_x$) was loaded with a mixed oxide of Rh and Cr. From this sample, it is observed that H_2 and O_2 evolve steadily and stoichiometrically under visible light from pure water without sacrificial reagents. The quantum efficiency of the Rh−Cr loaded ($Ga_{1-x}Zn_x$)($N_{1-x}O_x$) photocatalyst for overall water splitting reaches ca. 2.5% at 420−440 nm.[99,100] These photocatalysts based on ($Ga_{1-x}Zn_x$)($N_{1-x}O_x$) solid solutions were the first particulate photocatalyst systems capable of performing the overall water splitting by one-step photo-excitation under visible light.

The solid solution between ZnO and $ZnGeN_2$ (($Zn_{1+x}Ge$)(N_2O_x)) has also been found to be an active oxynitride photocatalyst for pure water splitting under visible light.[101] The solid solutions ($Zn_{1+x}Ge$)(N_2O_x) present absorption in the visible region with a band gap energy of ca. 2.7 eV, which is smaller than the band gaps of Ge_3N_4 (3.8 eV), $ZnGeN_2$ (3.3 eV) and ZnO (3.2 eV). The visible light response of this solid solution originates from the p−d repulsion between Zn3d and N2p and O2p electrons in the upper part of the VB that narrows the band gap. Neither $ZnGeN_2$ nor ZnO alone exhibit photocatalytic activity for overall water splitting under UV irradiation. However, the solid solution ($Zn_{1+x}Ge$)(N_2O_x) loaded with nanoparticulate RuO_2 co-catalyst becomes active under visible irradiation generating H_2 and O_2 stoichiometrically from pure water.

3.4.1.3.3 SULFIDE SOLID SOLUTIONS

Insertion of foreign elements in the structure of CdS forming solid solutions (Cd1-xMxS) is the basis of an interesting strategy for improving the photocatalytic properties of CdS. ZnS is interesting as a semiconductor for combining with CdS. CdS and Zn made a continuous series of solid solutions ($Cd_{1-x}Zn_xS$) where metal atoms are mutually substituted in the same crystal lattice.[102,103] Valle et al.[104] investigated the photophysical and

photocatalytic properties of $Cd_{1-x}Zn_xS$ solid solutions with different Zn concentration ($0.2 < x < 0.35$). The solid solution between CdS and ZnS showed a blue shift of the absorption edge with the increase in Zn concentration. The photocatalytic activity of samples increases gradually when the Zn concentration increases from 0.2 to 0.3. The change in activity for H_2 production for these samples arises mainly from the modification of the energy level of the CB as the concentration of Zn increased in the solid solution photocatalyst.

Combination of ZnS with $AgInS_2$ and $CuInS_2$ to produce solid solutions $(CuAgIn)_xZn_{2(1-x)}S_2$ is other strategy followed to improve the optical absorption of ZnS in the visible range.[105–107] The optical absorption of these materials can be adjusted between 400 and 800 nm depending on solid solution composition. $(CuAgIn)_xZn_{2(1-x)}S_2$ solid solutions showed high photocatalytic activities for H_2 evolution from aqueous solutions containing sacrificial reagents, SO_3^{2-} and S^{2-}, under visible light irradiation. Loading solid solutions with co-catalyst improved the photocatalytic activity. Pt loaded on $(AgIn)_{0.22}Zn_{1.56}S_2$ showed the highest activity for H_2 evolution with an apparent QY of 20% at 420 nm.

Other ternary sulfides comprising In^{3+} and one type of transition metal cation (Cd^{2+}, Zn^{2+}, Mn^{2+}, Cu^{+}) are also investigated as photocatalysts for water splitting under visible light. However, up to now, the efficiency achieved over these photocatalyst is very low. For example, a quantum efficiency of only 3.7% at 420 nm was reported for the most active $Na_{14}In_{17}Cu_3S_{35}$ photocatalyst.[108] Recently,[109] a solid solution was reported to be formed from AGa_5S_8 and AIn_5S_8 (A = Cu or Ag), which are active under visible light, with relatively high QY (15%). They were active from aqueous solutions containing electron donors.

3.4.2 Dye Sensitization

An effective strategy for populating the CB of UV photocatalyst is by excitation of a chromophore such as an organic dye. However, the development of efficient dye-sensitized solar cells using single-crystal semiconductor electrodes was precluded by poor light harvesting efficiencies and low photocurrent densities.

The photosensitization of wide band gap semiconductors such as TiO_2 by adsorbed dyes has been studied since the late 1960s.[110,111] The earlier photo-electrochemical studies focused on flat electrodes, but these systems were facing an intrinsic problem. Only the first monolayer of adsorbed dye results in efficient electron injection into the semiconductor, but the light harvesting efficiency of a single dye monolayer is very small. In a porous film consisting of nanometer-sized TiO_2 particles, the effective surface area can be enhanced 1000-fold, thus making light absorption efficient even with only a dye monolayer on each particle. Nature, in fact, uses a similar means of absorption enhancement by stacking the chlorophyll-containing thyalkoid membranes of the chloroplast to form the grana structures. An intriguing feature in the nanocrystalline TiO_2 films is that the charge transport of the photoinjected electrons passing through all the particles and grain boundaries is highly efficient, the QY being practically unity.

Whereas much pertinent information has been gathered over the years on the overall performance of dye sensitized semiconductor systems, more precise data about the details of the electron injection and recapture process are required. The rapid nature of these reactions requires application of fast kinetic techniques which, in the case of solid semiconductor powders, is very difficult. Similar effects have been observed with a number of different sensitizers such as porphyrins and $Ru(bipy)_3^{2+}$ derivatives or $Fe(CN)_6^{4-}$ [112] surface-derivatized TiO_2 particles. In all these cases, the back-electron transfer from the semiconductor particle to the oxidized sensitizer occurred with a rate that was several orders of magnitude slower than the forward injection. Thus, the combination of a sensitizer with a colloidal semiconductor particle affords a molecular device for light-induced charge separation. The question should be addressed why in this system the rate of the back-reaction is so much smaller than that of the forward electron transfer. One might assume the fact that recapture of the CB electron has a large driving force placing this reaction in the inverted region where the rate drops with increasing heat release. In addition, entropic factors should be considered. If there is only one sensitizer cation available at the surface, the back-reaction is associated with a significant entropy decrease which amounts to ca. 67 J/K mol.

Light harvesting can also be improved by incorporating a multicomponent system possessing several chromophoric molecular components. This kind of antenna system absorbs the incident light and channels the excitation energy to a common acceptor-reaction center. Porphyrins, the main chromophores of natural photosynthesis, have been the obvious candidates for the design of artificial antenna systems. Another interesting series of polynuclear species of large nuclearity, which because of their shape can be called "dendrimers" or "arborols", has been obtained using Ru(II) and/or Os(II) as metal centers, bis-bipyridine-type ligands as bridging groups and bipyridine-type terminal ligands.[113,114] Following a modular synthetic strategy known as "complexes-as-metals/complexes-as-ligands", such polynuclear species can be obtained with a high degree of synthetic control in terms of the nature and position of metal centers, bridging ligands, and terminal ligands. The energy of

the metal-to-ligand charge transfer excited state of each unit depends on metal and ligands in a well-known and predictable way. Thus, synthetic control translates into control on the direction of energy flow within these molecules.

For some practical purposes (e.g. to bind at an interface with good surface coverage), one-dimensional (1D) antenna systems might be more convenient than highly branched ones. A 1D antenna requires stepwise energy transfer along a chain of molecular components, and the maximum length of the system (i.e. number of components) depends critically on the driving force demand of each energy-transfer step. The possibility to obtain efficient energy migration along chain-like systems has been checked with the cyano-bridged pentanuclear species. These results suggest that in strongly coupled systems of this type, energy migration between isoenergetic adjacent molecular components takes place efficiently. The presence of a higher-energy "stopper" on one end and a lower-energy "trap" at the other end is sufficient to give directionality to the overall process.

3.5 STRATEGIES TO IMPROVE THE PHOTOGENERATED CHARGE SEPARATION

Apart of the electronic properties of the photosemiconductors, the precise design of the bulk and surface properties from the semiconductor is essential to control the interrelation between its electronic, microstructural and surface properties. In the search for more efficient photocatalysts for water splitting, the control of the synthesis of the material to tailor its crystallinity and morphology at the nanometric scale is very important, because these properties have a major influence on the rate of water-splitting reaction. All these approaches have been nicely discussed in a recent review by Best and Dunstan.[115]

3.5.1 Nanodesign: Controlling the Size and Form

The water-splitting reaction at the photocatalyst interface occurs if charge carriers (electrons and holes) generated in the bulk of the semiconductor by absorbed light can reach the surface during their lifetime and manage to find suitable reaction partners, protons for electrons and water molecules for holes. The transport of photo-excited carriers is determined by the crystal size, the crystalline structure, the nature and number of structural defects and the surface properties of photocatalysts. To have an efficient charge-carrier dynamics, the diffusion length of charge carriers must be longer than the particle size. High crystalline degree of the photocatalyst has a positive effect on transport of photo-excited carriers, as the density of defects caused by grain boundaries, which act as recombination centers of electrons and holes, decreases when particle crystallinity increases. Apart from that, crystalline size also influences the electronic properties of the photocatalyst. It has been reported that the band gap of a crystalline semiconductor is a function of the particle size, increasing the band gap of photocatalysts with the decrease in particle size to nanometer range.

Taking into account the effects of particle size on light absorption, charge-carrier dynamics and surface area, much effort has been made to control the synthesis of materials in order to optimize the particle size, crystallinity morphology and defects of photocatalysts at the nanometric scale.

3.5.1.1 *Advanced Synthesis Approaches*

Nanostructured photocatalysts have the potential to reduce the extent of electron–hole recombination due to short charge transfer distances, and reactant adsorption and product desorption can be enhanced due to the high surface area offered by nanostructures. A critical issue of aqueous dispersions of semiconductor powders conductive to visible light excitation is stability.

Taking into account the importance of the structural characteristics (crystalline phase, crystalline size and geometrical surface area) in the control of band structure and in the concentration and mobility of photocatalyst charges, studies have been conducted on the influence of preparation methods on the photophysical properties of CdS.[116,117] Improvement in CdS photoactivity is observed from preparation methods that lead CdS phases with good crystallinity and few crystal defects.

Different approaches have been undertaken over the last two decades to synthesize semiconductor systems. Salt precursors like $Cd(NO_3)_2$, $Cd(ClO_4)_2$ and Na_2S have often been used for synthesis of II–IV nanoparticles in aqueous media.[118] Some other organometallic or TOP/TOPO (tri-*n*-octylphosphine/tri-*n*-octylphosphine oxide)-based synthesis have been used for preparing Cd-calcogenides (CdX, X = S, Se, Te).[119] The particle diameter of II–IV nanoparticles can be adjusted by using a combination of the cation, calcogenide precursor and stabilizing agents. Among the stabilizing agents, thiols,[120,121] surfactants,[122,123] phosphates,[124] zeolites and microporous oxide films[125] remain prominent. A somewhat different approach must be followed to synthesize the other class of III–V semiconductors due to the increase in covalent bond strength in III–V lattices.[126] Molecular beam epitaxy,[127] colloidal methods based upon TOP/TOPO[128,129] along with the more widely employed dehalosilylation reactions have often been used to synthesize GaP, InP, GaP and GaAs nanoparticles.[130]

Oxide semiconductors can be synthesized relatively easily due to their stability in an aqueous media. The most common method involves a metal salt or alkoxide combined with an acid or base catalyst to seed crystal growth and maintain particle size at about 5 nm.[131] This is similar to the sol–gel based technique, where particle growth drops before the formation of a gel. This method can be used to synthesize several oxide nanoparticles, e.g. TiO_2, ZnO, and films, where a slightly different sol–gel method is used for pellet preparation.

3.5.1.2 *Anisotropic Photocatalysts and Other Structures*

Generating anisotropic photocatalysts particularly with 1-D or longitudinal structures such as nanotubes, nanorods, nanowires and nanoribons has been widely explored. Physically, these structures may offer exploitable advantages such as higher surface-area-to-volume ratio compared with spherical particles, aligned pores, and wavelength-specific light trapping.

Compared to powder and planar systems, nanotubes and nanowires enhance charge separation and photocurrent response. It was demonstrated that photoconversion efficiency of TiO_2 nanowires is almost twice that of spherical nanoparticles.[133] The aspect ratio also plays a key role on the performance. Photon absorption and photocurrent density increase with the aspect ratio of the nanotube. Therefore, the charge transfer at the semiconductor–electrolyte interface is enhanced, limiting electron–hole recombination processes at the tube surface and in the bulk.[134] This observation opens the door for new designs of efficient photo-catalysts for water splitting. Following this line, Mahajan et al. recently showed that TiO_2 nanotube arrays are highly stable with respect to activity and morphology and can yield H_2 without any noticeable decrease in rate for at least one month.[132]

Doping of nanotubes is also common practice to harvest the fraction of visible light. Modified tubular arrays have been shown to produce eight times the photocurrent density of un-modified arrays,[135] and 20 times the current density of nanoparticulate films.[136] Similar work has been reported for ZnO nanotubes and wires through Cd doping to reduce the band gap from 3.4 to 3.0 eV.[62] TiO_2 nanotube arrays formed by anodic oxidation of titanium[137] have very high surface areas,[138] comparable to porous titania nanoparticle films, and proven photocatalytic properties. Although the TiO_2 band gap, 3.0 and 3.2 eV for rutile and anatase, respectively, restricts excitation wavelengths to less than about 400 nm, Varghese et al.[139] have succeeded in incorporating nitrogen into the nanotubes during anodization, with a subsequent heat treatment resulting in crystallized nanotubes with N2p states formed above the titania VB that shifts the absorption edge of titania to around 540 nm. The nitrogen-doped titania nanotube arrays were synthesized by anodizing titanium foil in an NH_4F/H_2O water electrolyte containing ethylene glycol at 55 V.[140] Nanotube array samples up to about 130 μm in length and average pore diameter of 95 ± 13 nm with wall thickness of 20 ± 5 nm were prepared by changing the anodization time. Ti anodization in fluorine-containing electrolytes yields amorphous nanotube arrays, hence elevated temperature oxygen annealing is needed to maintain titania stoichiometry and reduce lattice defects. However, annealing the nitrogen-incorporated samples at high temperatures in an oxygen-rich environment generally removes the nitrogen by oxidation. Therefore, incorporated nitrogen within the nanotube sample can be maintained by limiting the oxygen flow across the sample during annealing.

Decorating nanorods or wires with nanoparticles or thin layers is another recent approach to develop efficient photocatalysts for water splitting. Jang et al.[141] reported optimized H_2 production on decorated CdS nanowires with TiO_2 nanoparticles in the presence of hole scavengers and a Pt co-catalyst. Effective charge separation was found to occur in the 1D CdS system and this led to improved photo-catalytic activity. Similar ideas have been investigated by many groups, including CdS-decorated TiO_2 nanowires,[142,143] Au nanoparticles on TiO_2,[144] and CdS nanorods.[145]

Synthesis of photocatalysts possessing alternate morphologies such as cube, pyramid and fractals has also been extensively reported in recent years. Compared with the anisotropic design, these 3D structures are bound by their facets, each of which is energetically unique. In principle, the photocatalytic redox sites as well as sites for preferential adsorption of reactants are dictated by the facets. For TiO_2, different groups have reported the tailored synthesis of anatase single crystals with a high percentage of the highly reactive {001} facets.[146,147] Nanostructured anatase TiO_2 with a large percentage of other exposed high-energy facets {010} and {100}, respectively, exhibited much higher activities than that of commercial anatase powders. In the same way, Shen et al.[148] found that the photocatalytic activity of $ZnIn_2S_4$ was greatly affected by the crystal plane space along the *c*-axis, the increasing d (001) space greatly improved the photocatalytic activity. A similar effect of the surface nanostructured was also observed on La-doped $NaTaO_3$.[149]

Ordered mesoporous materials have also been explored as photocatalysts. The mesoporous photocatalysts possess two major beneficial characteristics: high surface area and nanoscale channel wall of mesopores that can facilitate the transfer of photogenerated electrons and holes to the surface, avoiding their

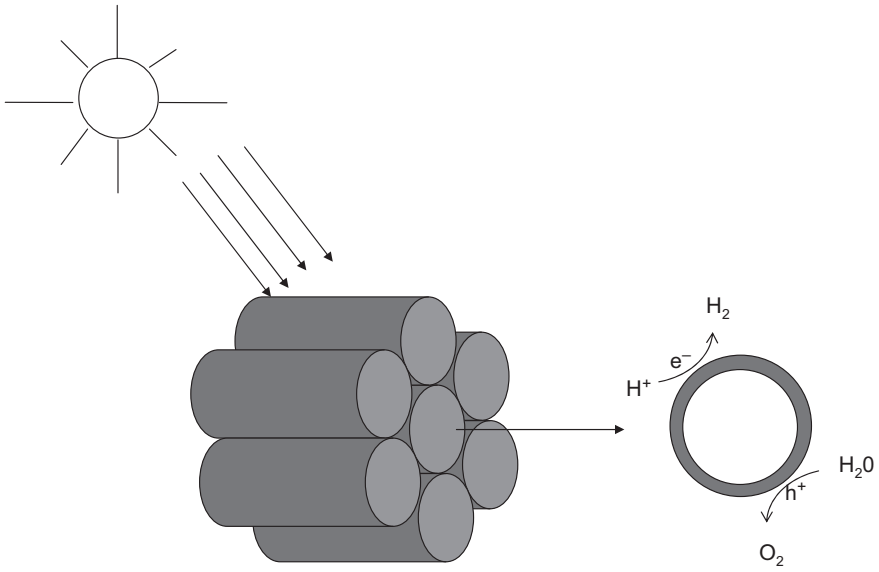

FIGURE 3.12 Scheme of photogenerated charge separation on mesoporous photocatalysts.

recombination in the bulk (Fig. 3.12). Mesoporous tantalum oxide,[150] tantalum nitride[151] and g-C_3N_4[152] have been reported as mesoporous structures with higher photoactivity than bulk counterparts.

Metal oxide nanosheets are another class of materials studied as photocatalysts[110,153,154] because of their morphological characteristics (Fig. 3.13). These compounds consists on negatively charged corner- and/or edge-shared MO_6 (M = Ti, Nb, Ta) octahedral units that stack to form a two-dimensional (2D) layered structure interleaved with alkaline cations to compensate for the negative charge of the sheets. Upon photoexcitation, electrons and holes generated in the sheets cause redox reactions with water molecules adjacent to the layers.

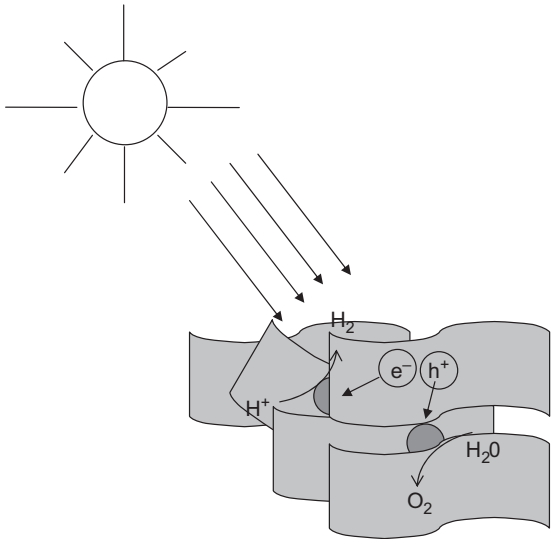

FIGURE 3.13 Scheme of photogenerated charge separation on metal oxide nanosheets.

3.5.2 Loading of Co-catalysts

Although some of the photocatalysts developed to date (CdS, tantalates, layered compounds) can decompose water without co-catalysts, most require the loading of a suitable co-catalyst to obtain a high activity and reasonable reaction rates. The deposition of noble metals (e.g. Pt, Rh) or metal oxides (e.g. NiO, RuO_2) onto photocatalyst surfaces is an effective way of enhancing photocatalyst activity.[23–25] The co-catalyst improves the efficiency of photocatalysts, as shown in Fig. 3.14, as a result of the following: (1) the capture of CB electrons or VB holes from the photocatalysts,[155] thereby reducing the possibility of electron–hole recombination and (2) the transference of electrons and holes to surface water molecules, thereby reducing the activation energy for the reduction (Fig. 3.14(A))/oxidation (Fig. 3.14(B)) of water.[156] The activity of the co-catalysts is found to be strongly dependent on the quantity of co-catalysts deposited on the photocatalyst surface. When the amount exceeds a critical limit, the co-catalysts act as electron–hole recombination centers, reducing the efficiency of the host photocatalyst.

Noble metals such as Pt and Rh are excellent promoters for H_2 evolution but can also catalyze a backward reaction, forming water from H_2 and O_2, limiting their usefulness as co-catalysts for photocatalytic overall water splitting. To avoid the backward reaction,

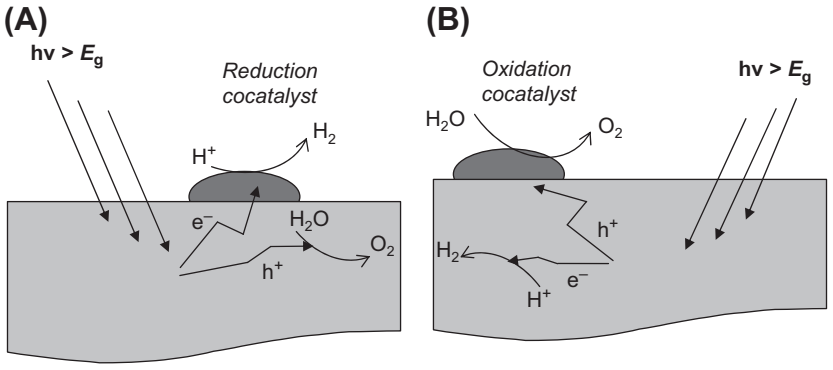

FIGURE 3.14 Photocatalyst surface modification by addition of co-catalyst to facilitate the hydrogen (A) or oxygen (B) evolution in water splitting.

transition-metal oxides that do not exhibit activity for water formation from H_2 and O_2 are usually applied as co-catalysts for overall water splitting. NiO_x was successfully applied as an H_2 evolution co-catalyst when loaded on the surface of $SrTiO_3$.[11] RuO_2 was also applied as co-catalyst for overall water splitting over KTi_4O_9,[157] $Na_2Ti_3O_7$,[158] and β-Ge_3N_4.[159]

Mixed Ni−Cr and Rh−Cr oxides were used as co-catalysts on $(Ga_{1-x}Zn_x)(N_{1-x}O_x)$ for photocatalytic overall water splitting.[99] Core-shell structured nanoparticles (with a noble metal or metal oxide core and Cr_2O_3 shell) were presented as a new type of co-catalysts for overall water splitting.[160] In these core−shell structured nanoparticles, the Cr_2O_3 shell can suppress water formation being permeable to the evolution of H_2 (Fig. 3.15). Among the noble metals and metal oxides examined as nanoparticulated cores, Rh was the most effective in enhancing photoactivity.

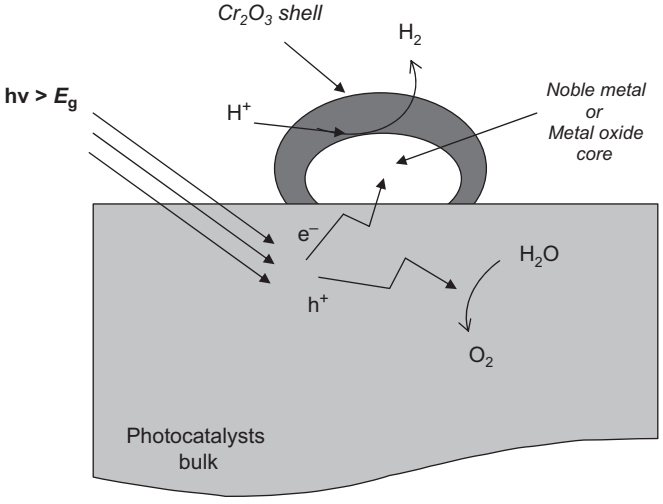

FIGURE 3.15 Scheme of hydrogen evolution on core/shell nanostructured nanoparticles as co-catalyst.

3.6 CHALLENGES AND OPPORTUNITIES

Photocatalytic H_2 production via water photolysis offers unique opportunities to develop a C-free fuel and sustainable energy system. As shown in the preceding sections, the structural and electronic structure of photocatalyst material is the core of the photocatalytic H_2 production technology. Significant advances have been achieved in the design and development of unique photocatalysts that can split water into H_2 and O_2. Several types of semiconductors including oxides, nitrides and sulfides have been reported to act as efficient photocatalysts for photolysis of water. Among these photocatalysts, higher QY are reported under UV light for $NiO/NaTaO_3$ (56% QY).[38] Although this yield is very high, results have only a limited value for practical H_2 production because UV light accounts for only about 3−4% of solar radiation energy. Therefore, utilization of solar energy on a large scale requires the development of photocatalysts capable of splitting water efficiently under visible light (λ ~ 600 nm).

Currently, the number of visible light-driven photocatalysts is limited. However, many oxides, sulfides, oxynitrides and oxysulfides have recently been found to be active for H_2 and O_2 evolution under visible light irradiation. So far, the maximum quantum efficiency over visible light-driven photocatalysts achieves only a few percent at wavelengths as long as 500 nm Cr/Rh−GaN/ZnO (2.5% QY).[160] This value is still far from the QY of 10% marked as the initial starting point for practical application.[161] Thus, the development of new photocatalysts is still a major issue.

Novel photocatalysts are expected to be developed, whereas the existing ones should be optimized. Nanostructured photocatalysts are expected to be a future trend, since these nanostructures display much better performance than their bulk counterparts. There is no general rule to say what kind of material is more appropriate, because there is no existing photocatalyst

that meets all the requirements, and all candidates have their own virtues and drawbacks. Definitely, metal oxide photocatalysts are considered promising candidates as they are cheap and display good resistance to corrosion even though they show low photonic efficiency. Among the metal oxides, TiO_2 has been and will be one of the most important photocatalysts for H_2 production. Its major disadvantage is the low utilization of visible light, as a consequence of its wide band gap. Osterloh[162] reviewed not only simple but also complex metal oxide structures as active photocatalysts for the water-splitting reaction. Some of these complex oxides have suitable band structures for visible light water splitting, since more metal elements can contribute to the construction of VB and/or CB. Moreover, a few of them display nest-like nanostructures, which are suitable for nanosized co-catalyst loading.

Metal sulfides can be applied in practical photocatalytic H_2 production systems if sulfur by-products such as hydrogen sulfide from natural gas wells and oil desulfurization are available. Solid solutions from two or more semiconductors are ideal photocatalytic systems driven by visible light, in which the optical and photocatalytic properties can be properly adjusted by suitable choice of the constituents and loading level. Oxynitrides and oxysulfides have been found to be stable photocatalysts for water reduction and oxidation under visible irradiation. This finding provides good clues to fine-tuning the VB position.

1D and 2D structures with high aspect ratio and well-defined morphology will attract more attention, as they favor charge and mass transport, respectively. Understanding of the interfacial and local properties of photocatalysts, such as the interfaces between photocatalysts, co-catalyst and water, and the location of grain edges and boundaries, is needed. The charge and mass transport processes in these areas, which often dominate in structured systems, are different from those involved in the bulk phase. In most cases, photocatalytic H_2 production can be increased dramatically by incorporating co-catalysts. Hence, appropriate design of photocatalyst structures is important in order to host co-catalysts in well-defined and tailored locations. The reaction kinetics in photocatalytic H_2 production has to be emphasized to a greater extent if maximum efficiency is expected. Theoretical and modeling work is useful and imperative in better understanding of the process and mechanism of photocatalytic H_2 production as well as designing new photocatalysts and photoreactor systems. Theoretical work at a molecular level will help to construct the picture of H_2 production on catalytic surfaces, which may allow us to design such catalytic surfaces on the basis of insight.

Acknowledgments

The present work was performed within the research programs supported by the CAM and MICINN (Spain) under Projects S2009ENE-1743 and PIB2010Z-00531. F.V. would also like to acknowledge financial support from the MICINN (Spain) through the FPI Program.

References

1. Lewis, N. S.; Nocera, D. G. *Proc. Natl. Acad. Sci. U.S.A.* **2006,** *103* (43), 15729.
2. Navarro, R. M.; del Valle, F.; Villoria, J. A.; Fierro, J. L. G. In Serrano, B., de Lasa, H., Eds., Vol. 36; Elsevier Science Publishers, 2009; p 111. (Chapter 4).
3. Funk, J. *Int. J. Hydrogen Energy* **2001,** *26,* 185.
4. Kogan, A.; Splieger, E.; Wolfshtein, M. *Int. J. Hydrogen Energy* **2000,** *25,* 739.
5. Fujishima, A.; Honda, K. *Nature* **1972,** *238,* 37.
6. Miyake, J.; Miyake, M.; Adsada, Y. *J. Biotechnol.* **1999,** *70,* 89.
7. Bard, A. J. *Science* **1980,** *207,* 139.
8. Levene, J.; Ramsden, T. *Summary of Electrolytic Hydrogen Production;* NREL: Golden, CO, 2007. MP-560-41099.
9. Lehn, J. M.; Sauvage, J. P.; Ziessel, R. *Nouv. J. Chim.* **1980,** *4,* 623.
10. Sato, S.; White, J. M. *Chem. Phys. Lett.* **1980,** *72,* 83.
11. Domen, K.; Naito, S.; Soma, M.; Onishi, T.; Tamaru, K. *J. Chem. Soc. Chem. Commun.* **1980,** 543.
12. Hisatomi, T.; Maeda, K.; Takanabe, K.; Kubota, J.; Sakata, Y.; Domen, K. *J. Phys. Chem. C* **2009,** *113,* 21458.
13. Kodama, T.; Gokon, N. *Chem. Rev.* **2007,** *107,* 4048.
14. Esswein, A. J.; Nocera, D. G. *Chem. Rev.* **2007,** *107,* 4022.
15. Yang, X.; Baik, M. H. *J. Am. Chem. Soc.* **2008,** *130,* 16231.
16. Kanan, M. W.; Nocera, D. G. *Science* **2008,** *321,* 1072.
17. Kudo, A.; Miseki, Y. *Chem. Soc. Rev.* **2009,** *38,* 253.
18. Sala, X.; Romero, I.; Rodríguez, M.; Escriche, L.; Llobet, A. *Angew. Chem. Int. Ed.* **2009,** *48,* 2842.
19. Navarro, R. M.; Sanchez-Sanchez, M. C.; Alvarez-Galvan, M. C.; del Valle, F.; Fierro, J. L. G. *Energy Env. Sci.* **2009,** *2,* 35.
20. Navarro, R. M.; Alvarez-Galvan, M. C.; del Valle, F.; Villoria, J. A.; Fierro, J. L. G. *Chem. Sust. Chem.* **2009,** *2,* 471.
21. Currao, A. *Chimia* **2007,** *61,* 815.
22. Aroutiounian, V. M.; Arakelyan, V. M.; Shanhnazaryan, G. E. *Solar Energy* **2005,** *78,* 581.
23. Anpo, M.; Takeuchi, M. *J. Catal.* **2003,** *216,* 505.
24. Iwase, A.; Kato, H.; Kudo, A. *Catal. Lett.* **2006,** *108,* 7.
25. Inoue, Y.; Hayashi, O.; Sato, K. *J. Chem. Soc. Faraday Trans.* **1990,** *86,* 2277.
26. Xu, Y.; Schoonen, M. A. A. *Am. Mineral.* **2000,** *85,* 543.
27. Ellis, A. B.; Kaiser, S. W.; Bolts, J. M.; Wrighton, M. S. *J. Am. Chem. Soc.* **1977,** *99,* 2839.
28. Ikeda, S.; Tanaka, A.; Shinohara, K.; Hara, M.; Kondo, J. N.; Maruya, K.; Domen, K. *Microporous Mater.* **1997,** *9,* 253.
29. Ashokkumar, M. *Int. J. Hydrogen Energy* **1998,** *23,* 427.
30. Kudo, A.; Kato, H.; Tsuji, I. *Chem. Lett.* **2004,** *33,* 1534.
31. Shibata, M.; Kudo, A.; Tanaka, A.; Domen, K.; Maruya, K.; Ohishi, T. *Chem. Lett.* **1987,** *16,* 1017.
32. Kim., J.; Hwang, D. W.; Kim, H. G.; Bae, S. W.; Ji, S. M.; Lee, J. S. *Chem. Commun.* **2002,** *21,* 2488.
33. Abe, R.; Higashi, M.; Zhou, Z.; Sayama, K.; Abe, Y. *Chem. Lett.* **2004,** *33,* 954.
34. Abe, R.; Higashi, M.; Sayama, K.; Abe, Y.; Sugihara, H. *J. Phys. Chem. B* **2006,** *110,* 2219.
35. Takata, T.; Tanaka, A.; Hara, M.; Kondo, J. N.; Domen, K. *Catal. Today* **1998,** *44,* 17.
36. Kato, H.; Kudo, A. *Chem. Lett.* **1999,** 1207.
37. Kato, H.; Kudo, A. *J. Phys. Chem. B* **2001,** *105,* 4285.

38. Kato, H.; Asakura, K.; Kudo, A. *J. Am. Chem. Soc.* **2003,** *125,* 3082.
39. Kim, J.; Huang, D. W.; Kim, H. G.; Lee, J. S.; Li, W.; Oh, S. H. *Top. Catal.* **2005,** *35* (3–4), 295.
40. Kurihara, T.; Okutomi, H.; Miseki, Y.; Kato, H.; Kudo, A. *Chem. Lett.* **2006,** *35,* 274.
41. Yanagida, T.; Sakata, Y.; Imamura, H. *Chem. Lett.* **2004,** *33,* 726.
42. Sato, J.; Saito, S.; Nishiyama, H.; Inoue, Y. *J. Phys. Chem. B* **2003,** *107,* 7965.
43. Sato, J.; Kobayashi, H.; Inoue, Y. *J. Phys. Chem. B* **2003,** *107,* 7970.
44. Sato, J.; Saito, S.; Nishiyama, H.; Inoue, Y. *J. Photochem. Photobiol. A* **2002,** *148,* 85.
45. Sato, J.; Kobayashi, H.; Ikarashi, K.; Saito, N.; Nishiyama, H.; Inoue, Y. J. *J. Phys. Chem. B* **2004,** *108,* 4369.
46. Ikarashi, K.; Sato, J.; Kobayashi, H.; Saito, N.; Nishiyama, H.; Inous, Y. *J. Phys. Chem. B* **2002,** *106,* 9048.
47. Reber, J. F.; Meier, K. *J. Phys. Chem.* **1984,** *88,* 5903.
48. Ohmori, T.; Mametsuka, H.; Suzuki, E. *Int. J. Hydrogen Energy* **2000,** *25,* 953.
49. Arai, N.; Saito, N.; Nishiyama, H.; Inoue, Y.; Domen, K.; Sato, K. *Chem. Lett.* **2006,** *35,* 796.
50. Maeda, K.; Saito, N.; Inoue, Y.; Domen, K. *Chem. Mater.* **2007,** *19,* 40929.
51. Kudo, A.; Ueda, K.; Kato, H.; Mikami, I. *Catal. Lett.* **1998,** *53,* 229.
52. Kudo, A.; Omori, K.; Kato, H. *J. Am. Chem. Soc.* **1999,** *121,* 11459.
53. Konta, R.; Kato, H.; Kobayashi, H.; Kudo, A. *Phys. Chem. Chem. Phys.* **2003,** *5,* 3061.
54. Kim, H. G.; Hwang, D. W.; Lee, J. S. *J. Am. Chem. Soc.* **2004,** *126,* 8912.
55. Lv, J.; Zhao, Z.; Li, Z.; Ye, J.; Zou, Z. *J. Alloys Compd.* **2009,** *485,* 346.
56. Yoshimura, J.; Ebina, Y.; Kondo, J.; Domen, K.; Tanaka, A. *J. Phys. Chem.* **1993,** *97,* 1970.
57. Li, X.; Ye, J. *J. Phys. Chem. C* **2007,** *111,* 13109.
58. Williams, R. *J. Chem. Phys.* **1960,** *32,* 1505.
59. Reber, J. F.; Meier, K. *J. Phys. Chem.* **1986,** *90,* 824.
60. Darwent, J. R.; Porter, G. *J. Chem. Soc. Chem. Commun.* **1981,** *4,* 145.
61. Bühler, N.; Meier, K.; Reber, J. F. *J. Phys. Chem.* **1984,** *88* (15), 3261.
62. Ritterskamp, P.; Kuklya, A.; Wüstkamp, M. A.; Kerpen, K.; Weidenthaler, C.; Demuth, M. *Angew. Chem. Int. Ed.* **2007,** *46,* 7770.
63. Wang, X.; Maeda, K.; Thomas, A.; Takanabe, K.; Xin, G.; Carlsson, J. M.; Domen, K.; Antonietti, M. *Nat. Mater.* **2009,** *8,* 76.
64. Ji, F.; Li, C.; Zhang, J. *ACS Appl. Mater. Interface* **2010,** *2,* 1674.
65. Yeh, T. F.; Syu, J. M.; Cheng, C.; Chang, T. H.; Teng, H. S. *Adv. Funct. Mater.* **2010,** *20,* 2255.
66. Scaife, D. E. *Solar Energy* **1980,** *25,* 41.
67. Sung Lee, J. *Catal. Surv. Asia* **2005,** *9* (4), 217.
68. Li, Y.; Chen, G.; Zhou, C.; Sun, J. *Chem. Commun.* **2009,** 2020.
69. Maeda, K.; Takata, T.; Hara, M.; Saito, M.; Inoue, Y.; Kobayashi, H.; Domen, K. *J. Am. Chem. Soc.* **2005,** *127,* 8286.
70. Tsuji, I.; Kato, H.; Kobayashi, H.; Kudo, A. *J. Am. Chem. Soc.* **2004,** *126,* 13406.
71. Kambe, S.; Fujii, M.; Kawai, T.; Kawai, S. *Chem. Phys. Lett.* **1984,** *109,* 105.
72. Asahi, R.; Morikawa, T.; Ohwaki, T.; Aoki, K.; Taga, Y. *Science* **2001,** *293,* 269.
73. Hitoki, G.; Takata, T.; Kondo, J. N.; Hara, M.; Kobayashi, H.; Domen, K. *Chem. Commun.* **2002,** 1698.
74. Umebayashi, T.; Yamaki, T.; Itoh, H.; Asai, K. *Appl. Phys. Lett.* **2002,** *81,* 454.
75. Khan, S. U. M.; Al-Shahry, M.; Ingler, W. B. *Science* **2002,** *297,* 2243.
76. Kato, H.; Kudo, A. *J. Phys. Chem. B* **2002,** *106,* 5029.
77. Anpo, M. *Pure Appl. Chem.* **2000,** *72,* 1265.
78. Matsuoka, M.; Kitano, M.; Takeuchi, M.; Tsujimaru, K.; Anpo, M.; Thomas, J. M. *Catal. Today* **2007,** *122,* 51.
79. Ishii, T.; Kato, H.; Kudo, A. *J. Photochem. Photobiol. A* **2004,** *163,* 181.
80. Konta, R.; Ishii, T.; Kato, H.; Kudo, A. *J. Phys. Chem. B* **2004,** *108,* 8992.
81. Hwang, D. W.; Kim, H. G.; Jang, J. S.; Bae, S. W.; Ji, S. M.; Lee, J. S. *Catal. Today* **2004,** *93,* 845.
82. Hwang, D. W.; Kim, H. G.; Lee, J. S.; Kim, J.; Li, W.; Oh, S. H. *J. Phys. Chem. B* **2005,** *109,* 2093.
83. Kim, H. G.; Hwang, D. W.; Lee, J. S. *J. Am. Chem. Soc.* **2004,** *126* (29), 8912.
84. Ishikawa, A.; Takata, T.; Kondo, J. N.; Hara, M.; Kobayashi, H.; Domen, K. *J. Am. Chem. Soc.* **2002,** *124,* 13547.
85. Yamashita, H.; Takata, T.; Hara, M.; Kondo, J. N.; Domen, K. *Solid State Ion.* **2004,** *172,* 591.
86. Ji, S. M.; Borse, P. H.; Kim, H. G.; Hwang, D. W.; Jang, J. S.; Bae, S. W.; Lee, J. S. *Phys. Chem. Chem. Phys.* **2005,** *7,* 1315.
87. Kudo, A.; Sekizawa, M. *Catal. Lett.* **1999,** *58,* 241.
88. Kudo, A.; Sekizawa, M. *Chem. Commun.* **2000,** *15,* 1371.
89. Tsuji, I.; Kudo, A. *J. Photochem. Photobiol. A* **2003,** *156* (1–3), 249.
90. Spanhel, L.; Weller, H.; Henglein, A. *J. Am. Chem. Soc.* **1987,** *109,* 6632.
91. Navarro, R. M.; Del Valle, F.; Fierro, J. L. G. *Int. J. Hydrogen Energy* **2008,** *33,* 4265.
92. Fujii, H.; Ohtaki, M.; Eguchi, K.; Arai, H. *J. Electrochem. Soc.* **1975,** *122,* 1487.
93. Sasikala, R.; Shirole, A.; Sudarsan, V.; Sakuntala, T.; Sudakar, C.; Naik, R.; Bharadwaj, S. R. *Int. J. Hydrogen Energy* **2009,** *34,* 3621.
94. Wu, J.; Cheng, Y.; Lin, J.; Huang, Y.; Huang, M.; Hao, S. *J. Phys. Chem. C* **2007,** *111,* 3624.
95. Li, C.; Yuan, J.; Han, B.; Jiang, L.; Shangguan, W. *Int. J. Hydrogen Energy* **2010,** *35,* 7073.
96. Liu, H.; Yuan, J.; Shangguan, W.; Teraoka, Y. *J. Phys. Chem. C* **2008,** *112,* 8521.
97. Wang, Q.; Liu, H.; Jiang, L.; Yuan, J.; Shangguan, W. *Catal. Lett.* **2009,** *131,* 160.
98. Luan, J.; Zou, Z.; Lu, M.; Chen, Y. *Mater. Chem. Phys.* **2006,** *98,* 434.
99. Maeda, K.; Teramura, K.; Lu, D.; Takata, T.; Saito, N.; Inue, Y.; Domen, K. *Nature* **2006,** *440* (7082), 295.
100. Maeda, K.; Teramura, K.; Saito, N.; Inoue, Y.; Domen, K. *J. Catal.* **2006,** *243,* 303.
101. Lee, Y.; Terashima, H.; Shimodaira, Y.; Teramura, K.; Hara, M.; Kobayashi, H.; Levene, J.; Ramsden, T. *Summary of Electrolytic Hydrogen Production;* National Renewable Energy Laboratory, 2007. MP-560-41099.
102. Fedorov, V. A.; Ganshing, V. A.; Norkeshko, Y. U. N. *Mater. Res. Bull.* **1993,** *28,* 50.
103. Nayeem, A.; Yadaiah, K.; Vajralingam, G.; Mahesh, P.; Nagbhoosshanam, M. *Int. J. Mod. Phys. B* **2001,** *15* (7), 2387.
104. Valle F.; Navarro R. M.; Ishikawa A.; Domen K.; Fierro J. L. G. In *Int. Symp. on Catalysis for Clean Energy and Sustainable Chemistry*; Madrid, Spain, 2008.
105. Kudo, A.; Tsuji, I.; Kato, H. *Chem. Commun.* **2002,** 1958.
106. Tsuji, I.; Kato, H.; Kudo, A. *Angew. Chem.-Int. Ed.* **2005,** *44,* 3565.
107. Tsuji, I.; Kato, H.; Kobayashi, H.; Kudo, A. *J. Phys. Chem. B* **2005,** *109,* 7329.
108. Zheng, N.; Bu, X.; Vu, H.; Feng, P. *Angew. Chem.-Int. Ed.* **2005,** *44,* 5299.
109. Kaga, H.; Saito, K.; Kudo, A. *Chem. Commun.* **2010,** *46,* 3779.
110. Gerischer, H. *Photochem. Photobiol.* **1972,** *16,* 243.
111. Jana, A. K. *J. Photochem. Photobiol. A: Chem.* **2000,** *132,* 1.
112. Abe, R.; Sayama, K.; Arakawa, H. *Chem. Phys. Lett.* **2002,** *362,* 441.
113. Gurunathan, K. *J. Mol. Cat. A: Chem.* **2000,** *156,* 59.
114. Yum, J. H.; Walter, P.; Huber, S.; Rentsch, D.; Geiger, T.; Neusch, F.; DeAngelis, F.; Graetzel, M.; Nazeeruddin, M. K. *J. Am. Chem. Soc.* **2007,** *129,* 10320.
115. Best, J. P.; Dunstan, D. E. *Int. J. Hydrogen Energy* **2009,** *34,* 7562.
116. Arora, M. K.; Shinha, A. S. K.; Updhyay, S. N. *Ind. Eng. Chem. Res.* **1998,** *37* (10), 3950.

117. Jing, D. W.; Guo, L. J. *J. Phys. Chem. B* **2006,** *110* (23), 11139.
118. Murray, C. B.; Norris, D. J.; Bawendi, M. G. *J. Am. Chem. Soc.* **1993,** *115,* 8706.
119. Rogach, A. L.; Harrison, M.; Kershaw, S. V.; Kornovski, A.; Burt, M.; Eychmuller, A.; Weller, H. *Phys. Status Solidi B* **2001,** *224,* 153.
120. Hoppe, K.; Geidel, E.; Weller, H.; Eychmuller, A. *Phys. Chem. Chem. Phys.* **2002,** *4,* 1704.
121. Tricot, Y. M.; Fendler, J. H. *J. Phys. Chem.* **1986,** *90,* 3369.
122. Herron, N.; Calabrese, J. C.; Farneth, W. E.; Wang, Y. *Science* **1993,** *259,* 1426.
123. Nozik, A. J.; Williams, F.; Nenadovic, M. T.; Rajh, T.; Micic, O. I. *J. Phys. Chem.* **1985,** *89,* 397.
124. Elliot, D. J.; Grieve, K.; Furlong, D. N.; Grieser, F. *Adv. Colloid Interface Sci.* **2001,** *91,* 113.
125. Banin, U. In *Nanoparticles. From Theory to Application;* Schmid, G., Ed.; Wiley-VCH Verlag GmbH: Weinheim, 2004.
126. Leon, R.; Petroff, P. M.; Leonard, D.; Fafard, S. *Science* **1995,** *267,* 1966.
127. Cao, Y. W.; Banin, U. *J. Am. Chem. Soc.* **2000,** *122,* 9692.
128. Peng, X.; Wickham, J.; Alivisatos, A. P. *J. Am. Chem. Soc.* **1998,** *120,* 5343.
129. Uchida, H.; Curtis, C. J.; Nozik, A. J. *J. Phys. Chem.* **1991,** *95,* 5382.
130. Oskam, G. *J. Sol−Gel Sci. Technol.* **2006,** *37,* 161.
131. Liz-Marzan, L. M.; Mulvaney, P. *J. Phys. Chem. B* **2003,** *107,* 7312.
132. Mahajan, V. K.; Mohapatra, S. K.; Misra, M. *Int. J. Hydrogen Energy* **2008,** *33,* 5369.
133. Sahaym, U.; Norton, M. G. *J. Mater. Sci.* **2008,** *43,* 5395.
134. Vucemilovic, M. I.; Vukelic, N.; Rajh, T. *J. Photochem. Photobiol. A: Chem.* **1988,** *42,* 157.
135. Sarathy, K. V.; Thomas, P. J.; Kulkarni, G. U.; Rao, C. N. R. *J. Phys. Chem. B* **1999,** *103,* 399.
136. Liang, H.; Zhang, H.; Hu, J.; Guo, Y.; Wan, L.; Bai, C. *Angew. Chem. Int. Ed.* **2004,** *43,* 1540.
137. Liu, H.; Owen, J. S.; Alivisatos, A. P. *J. Am. Chem. Soc.* **2007,** *129,* 305.
138. Bullen, C.; Mulvaney, P. *Langmuir* **2006,** *22,* 3007.
139. Varghese, O. K.; Paulose, M.; Latempa, T. J.; Grimes, C. A. *Nano Lett.* **2009,** *9* (2), 731.
140. Paulose, M.; Shankar, K.; Yoriya, S.; Prakasam, H. E.; Varghese, O. K.; Mor, G. K.; Latempa, T. A.; Fitzgerald, A.; Grimes, C. A. *J. Phys. Chem. B* **2006,** *110,* 16179.
141. Kim, J. C.; Choi, J.; Lee, Y. B.; Hong, J. H.; Lee, J.; Yang, J. W. *Chem. Commun.* **2006,** 5024.
142. Jang, J. S.; Kim, H. G.; Joshi, U. A.; Jang, J. W.; Lee, J. S. *Int. J. Hyd. Energy* **2008,** *33,* 5975.
143. Li, H.; Zhu, B.; Feng, Y.; Wang, S.; Zhang, S.; Huang, W. *J. Solid State Chem.* **2007,** *180,* 2136.
144. Misra, M.; Raja, K. S.; Majan, V. K.; Mohapatra, S. K. *Proc. of SPIE* **2006,** 6340.
145. Saunders, A. E.; Popov, I.; Banin, U. *J. Phys. Chem. B.* **2006,** *110,* 25421.
146. Wu, B.; Guo, C.; Zheng, N.; Xie, Z.; Stucky, G. D. *J. Am. Chem. Soc.* **2008,** *130,* 17563.
147. Li, J.; Xu, D. *Chem. Commun.* **2010,** *46,* 2301.
148. Shen, S.; Zhao, L.; Guo, L. *Int. J. Hydrogen Energy* **2008,** *33,* 4501.
149. Yamakata, A.; Ishibashi, T.; Kato, H.; Kudo, A.; Onishi, H. *J. Phys. Chem. B* **2003,** *107,* 14383.
150. Takahara, Y.; Kondo, J. N.; Takata, T.; Lu, D.; Domen, K. *Chem. Mater.* **2001,** *13,* 1194.
151. Hisatomi, T.; Otani, M.; Nakajima, K.; Teramura, K.; Kako, Y.; Lu, D.; Takat, T.; Kondo, J. N.; Domen, K. *Chem. Mater.* **2010,** *22,* 3854.
152. Chen, X.; Jun, Y. S.; Takanabe, K.; Maeda, K.; Domen, K.; Fu, X.; Antoinetti, M. *J. Am. Chem. Soc.* **2009,** *131,* 168.
153. Ebina, Y.; Sakai, N.; Sasaki, T. *J. Phys. Chem. B* **2005,** *109,* 17212.
154. Ikeda, S.; Hara, M.; Kondo, J. N.; Domen, K.; Takahashi, H.; Okubo, T.; Kakihana, M. *Chem. Mater.* **1998,** *10,* 72.
155. Maruthamuthu, P.; Ashokkumar, M. *Int. J. Hydrogen Energy* **1988,** *13, 677*.
156. Maruthamuthu, P.; Ashokkumar, M. *Int. J. Hydrogen Energy* **1989,** *14,* 275.
157. Ogura, S.; Sato, K.; Inoue, I. *Phys. Chem. Chem. Phys.* **2000,** *2,* 2449.
158. Ogura, S.; Kohno, M.; Sato, K.; Inoue, Y. *J. Mater. Chem.* **1998,** *8,* 2335.
159. Maeda, K.; Saito, N.; Lu, D.; Inoue, Y.; Domen, K. *J. Phys. Chem. C* **2007,** *111,* 4749.
160. Maeda, K.; Teramura, K.; Lu, D.; Saito, N.; Inoue, Y.; Domen, K. *Angew. Chem. Int. Ed.* **2006,** *45,* 7806.
161. Turner, J.; Sverdrup, G.; Mann, M. K.; Maness, P. C.; Kroposki, B.; Ghirardi, M.; Umebayashi, T.; Yamaki, T.; Itoh, H.; Asai, K. *Appl. Phys. Lett.* **2002,** *81,* 454.
162. Osterloh, J. E. *Chem. Mater.* **2008,** *20,* 35.

CHAPTER

4

Solar Thermal Water Splitting

Martin Roeb, Nathalie Monnerie, Anis Houaijia, Dennis Thomey, Christian Sattler

Deutsches Zentrum für Luft und Raumfahrt e.V., Institute of Solar Research, Linder Höhe, Köln, Germany

OUTLINE

4.1 Introduction 63

4.2 Direct Water Splitting 64

4.3 Thermochemical Cycles 65

4.3.1 Redox Cycles 65

4.3.2 Sulfur-Based Cycles 73

4.3.2.1 Solar Decomposition of Sulfuric Acid 73

4.3.2.2 Sulfur–Iodine Cycle 75

4.3.2.3 HyS Cycle 77

4.3.3 Other Cycles 78

4.4 High-Temperature Electrolysis 80

4.4.1 Thermodynamics of High-Temperature Electrolysis 80

4.4.1.1 Configuration of the Electrolyzer 80

4.4.1.2 Materials of the Electrolyzer 81

4.4.2 Energy Sources 81

4.4.3 Operation Modes 83

4.5 Conclusions 83

References 84

4.1 INTRODUCTION

Today's energy economy is mainly based on the usage of fossil fuels like hard coal, lignite coal, petroleum oil and natural gas. Electricity and fuel production from those resources emits greenhouse gases and other pollutants. This creates the need to develop more sustainable and thus cleaner energy systems. Renewable energy sources like biomass, wind, geothermal and solar energy are cleaner options.

The potential of wind energy is high but daily and seasonal fluctuations are immense and statistical. Hydroelectric power is limited due to the availability of suitable sites and due to environmental impact on aquatic ecosystems and fishery. Geothermal is only available at certain sites, the wells are often located kilometers below the surface. The land available for biomass and, in particular, energy crop production is limited since it creates competition with food production. Solar energy has the greatest potential to cover the future energy demand since it is a safe, clean and unlimited resource. Nevertheless, there are challenges of using solar energy for electricity and fuel production. The availability of sunlight on the earth's surface depends much on the locations. Beyond this, it is an intermittent energy source because it is not available at night and on cloudy days. Therefore, it is advantageous to have means in hand to store and transport the solar energy collected on daytime or in regions rich in sunlight.

One promising method to overcome the intermittency is storing solar energy in the form of chemicals like hydrogen or hydrocarbons. Such products are useful as storage medium, as energy carrier, as a "solar fuel" or as an intermediate for chemical commodities. If looking at fuels, hydrogen is of specific interest since the only product of hydrogen combustion is water, which in turn is the feed to produce hydrogen with solar energy. Using hydrogen as a fuel offers great potentials. It was reported that the efficiency of a hydrogen internal combustion engine could be 20% higher than a gasoline engine.[1] The hybrid electric motor and fuel cell vehicle

http://dx.doi.org/10.1016/B978-0-444-56352-1.00004-0

could even be two to three times more efficient than an internal gasoline combustion engine.[2]

When looking at already established markets, hydrogen plays a central role in the upgrading of petroleum products. Beyond this, hydrogen is one of the main pillars of the production of fertilizers in the agricultural industry. Population growth in many areas of the world and the depletion of easy accessible sources of fossil fuels cause a significantly rising need of hydrogen by modern agriculture and petroleum products.[3]

The hydrogen demand in those fields is nowadays mostly covered by hydrogen produced from fossil fuels, e.g. from steam methane reforming, from refinery off-gases, and from coal gasification. This kind of production causes high amounts of greenhouse gases and is not sustainable. Only 4% of the annual production is from water—mainly alkaline or PEM electrolysis is used for this kind of production. Even this hydrogen is not entirely produced in a sustainable way because the electricity stems from a broad variety of primary energy sources including coal. Contrary to this, a sustainable hydrogen production should be rather based on the use of renewable energy sources and on abundant raw materials.

Numerous methods for hydrogen production from water splitting with solar energy are available. The most important ones are thermolysis, thermochemical cycles, water electrolysis, steam electrolysis, photochemical, photoeletrochemical, photocatalytic, and hybrid methods. The latter low-temperature methods based on the use of photons are not considered in this chapter. Only thermal and thermoelectrical methods for hydrogen production from water splitting are examined. All these methods require the integration of a chemical process and a concentrating solar system like solar towers, solar troughs, linear Fresnel system or dish systems. The most important techniques will be described in terms of their technical merits, of the status of their development and of technical and economic prospects. Representative projects at different stages of maturity will be introduced exemplarily, in which research and development targets have already been addressed and which still need further effort.

4.2 DIRECT WATER SPLITTING

Direct water splitting involves the single-step dissociation of water. At elevated temperatures, water molecules split into their components hydrogen and oxygen according to the next reaction:

$$H_2O \rightarrow H_2 + \frac{1}{2} O_2 \tag{4.1}$$

In order to achieve a considerable dissociation degree, higher temperature at above 2500 K is required. The degree of dissociation increases by increasing the temperature and decreasing the pressure. The following figure shows the degree of dissociation and the composition of the reacting mixture as a function of the reaction temperature at a pressure of 1 bar.[4]

The product gas contains not only H_2 and O_2 but also other species such as H and OH as shown in Fig. 4.1.

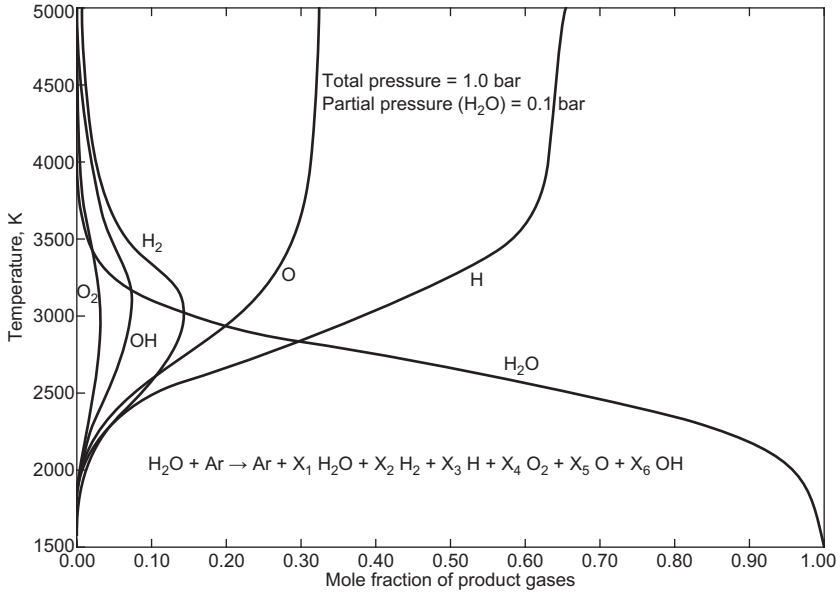

FIGURE 4.1 Dissociation degree of water and composition of the reacting mixture.[4]

A very important issue of the direct water splitting is to avoid the recombination of the main species in the product H_2 and O_2. Therefore, an effective separation of hydrogen strategy is required. Depending on the temperature level, there are two kinds of separation:

- Separation at low temperature: The recombination of hydrogen and oxygen can be avoided if the product gas will be cooled. In this case, a rapid cooling is necessary. Generally, the cooling time has to be shorter than the time constant of the reaction. This type of rapid cooling is known as *quenching*.[5] During the quench process, the temperature of the gas mixture has to decrease very quickly. The temperature change of the quench agent is normally in the range of 400−450 K with a residence time of milliseconds. Possible quench agents are steam or inert gas like Argon.[6] After the quenching process, separation of hydrogen from the product gas can take place in solid membrane. Palladium membranes have been successfully demonstrated for such applications, which can operate at 650 K with a pressure drop in the range of 10−30 atm. Other membranes such as polymeric membranes can be used at lower operating temperatures. Experiments using this separation strategy have been successfully carried out with the 2 kW solar furnace in Odeillo (France)[7] and the 1 kW solar furnace in Montreal (Canada).[5] Expecting problems, which are related to the degradation of the materials of the membrane, quenching with steam was successful and palladium membrane at 670 K has been used for the separation of hydrogen. A hydrogen purity of 99% has been achieved.
- Separation at high temperature: The separation of hydrogen can take place in the reactor. This method has the advantage that exergy losses due to quenching in the case of separation at low temperature can be avoided. As a result, the efficiency of the process will increase. This kind of separation needs a modification of the reactor and materials must be used, which can resist the high temperatures. Currently, there is no membrane available that can be integrated in the solar reactor due to the possible degradation of the membrane and catalytic effects on the metal, which can lead to the recombination of the hydrogen and oxygen. The palladium membrane already mentioned has the best chance to be developed for the separation at high temperatures. Microporous refractory membranes are currently under development but subatmospheric operating pressure is required in the reactor.

Figure 4.2 shows the schematic of a process for hydrogen production, which uses a solar reactor and a quenching unit.[8] The reactor is designed as a cavity receiver, which concentrates solar energy. The water steam enters the reactor and will be heated up to the reaction temperature. After leaving the reactor, the product gas enters the quench unit, where the rapid cooling within milliseconds will take place.

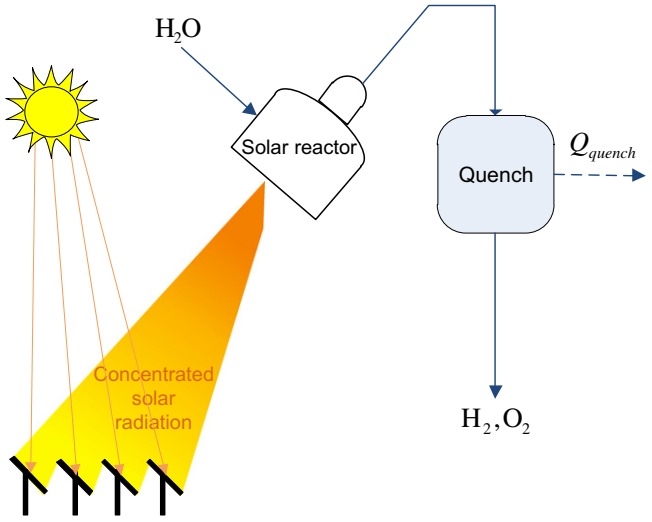

FIGURE 4.2 Schematic of the direct water-splitting process. (For color version of this figure, the reader is reffered to the online version of this book.)

4.3 THERMOCHEMICAL CYCLES

4.3.1 Redox Cycles

Thermochemical cycles are processes that decompose water into hydrogen and oxygen via chemical reactions using intermediate reactions and substances. They are very promising processes for "clean" hydrogen mass production. In the literature, up to 3000 thermochemical cycles are reported but only very few are proven to be relevant for the bulk production of hydrogen. These thermochemical cycles require heat for the water-splitting process. This heat can be provided by concentrated solar energy in a central receiver system (CRS). The CRS consists of mirrors, so-called *heliostats*, which concentrate the sunlight onto the receiver. The receiver located on the top of the tower is made up of honeycomb-structured ceramics acting as an absorber for the solar radiation and as a chemical reactor.

With the oil crisis in the late 1970s and early 1980s, the interest in the thermochemical water splitting increased a lot but then research slowed down all over the world except in Japan because of the national concern about the foreign energy dependence. However, the integration of such thermochemical cycles with a solar CRS is quite new.

One process for thermochemical hydrogen production is based on metal oxides (MOs). MO cycles offer a unique alternative to the direct splitting of water and recent solar thermochemical research has focused on them. The MO cycles are attractive because they involve fewer and less complex chemical steps than lower temperature processes and have, thus, the possibility to reach higher cycle efficiency. The reaction scheme is as follows:

$$MO_{reduced} + H_2O \rightarrow MO_{oxidized} + H_2 \quad \text{(splitting)} \tag{4.2}$$

$$MO_{oxidized} \rightarrow MO_{reduced} + O_2 \quad \text{(regeneration)} \tag{4.3}$$

During the first step of the cycle (water-splitting step), the reduced and, therefore, activated material is oxidized by abstracting oxygen from water and producing hydrogen. In the next step (the reduction step), the material is reduced again, setting some of its lattice oxygen free. Major advantages are that pure hydrogen is produced and that hydrogen and oxygen are produced in separate steps, i.e. no separation of hydrogen and oxygen is needed.

Several redox materials consisting of oxide pairs of multivalent metals (e.g. Fe_3O_4/FeO[9,10] and Mn_3O_4/MnO[11]) or systems of MO/metal (e.g. ZnO/Zn[12]) have been evaluated for such applications. A lot of MO redox systems need a too high temperature for the solar reduction step ($\Delta G < 0$ for $T > 2500$ K), which is the case of the cycles based on MoO_2/Mo, SnO_2/Sn, TiO_2/TiO_{2-x}, MgO/Mg or CaO/Ca redox pairs. For some other redox-pair cycles, the splitting step (production of H_2) is not feasible, as predicted by thermodynamics in the case of Co_3O_4/CoO and Mn_3O_4/MnO cycles.

Concerning the redox material Mn_3O_4/MnO, it can be reduced at 1900 K but the hydrogen yield in the water-splitting step of the process using this redox material is too low to be considered of any practical interest.[13]

A solution is to make react together the solar produced MnO with NaOH and to consider the Mn_2O_3/MnO cycle. This cycle was proposed relatively recently:

$$MnO + NaOH \rightarrow NaMnO_2 + \frac{1}{2} H_2 \tag{4.4}$$

$$NaMnO_2 + \frac{1}{2} H_2O \rightarrow \frac{1}{2} Mn_2O_3 + NaOH \tag{4.5}$$

$$\frac{1}{2} Mn_2O_3 \rightarrow MnO + \frac{1}{4} O_2 \tag{4.6}$$

H_2 may be produced by reacting MnO with NaOH at above 900 K. The solar thermal reduction (third step) occurs at above 1835 K.[14] In fact, it occurs as a series of reactions where Mn_2O_3 decomposes to Mn_3O_4 at a temperature of around 1255 K and then Mn_3O_4 decomposes into MnO and oxygen. The maximum efficiency was calculated to be 74% for the overall cycle but with a process scheme including conservative and ideal assumptions, more realistic efficiencies were calculated of 26–51% without the separation steps and of 16–21% when considering all steps, including separation.[11] However, this cycle has three steps, and so its maximum theoretical efficiency will be lesser than that of a two-step cycle, the efficiency in each of the steps has to be evaluated and this three-step cycle can eventually be more easily achieved than any of the two-step cycles.[14] Thus, a study was realized in 2005 to simulate a solar water-splitting process working with Mn_2O_3/MnO and to determine its economic feasibility. A simplified flow sheet of this process is shown in Fig. 4.3.

It was calculated that for a plant producing 55.8 million Kg/year of hydrogen, the selling price of hydrogen is 9.04 $/kg.[15] An economical problem is the excess water needed to recover NaOH in the second reaction step. Thus, it would be interesting to investigate further this step and to determine if there are conditions requiring less water.

Studies about the two-step cycles at temperatures of about 2300 K were related to CdO/Cd. This cycle is closely related to the zinc oxide cycle but cadmium, being toxic, makes its use in a technical application very unlikely. It produces hydrogen with solar energy at 1723 K.

$$CdO(s) \rightarrow Cd(g) + \frac{1}{2} O_2 \tag{4.7}$$

$$Cd(l) + H_2O(g) \rightarrow CdO_2(s) + H_2(g) \tag{4.8}$$

Both reactions have been demonstrated in laboratory studies but, until here, no feasibility evaluation of the closed cycle operation was made. However, this cycle stays interesting and recently, an economic study was realized and estimated the hydrogen cost as <4.5 $/kg.[16] The thermal efficiency of the CdO cycle was estimated to be 59% and a rotating kiln counter flow hydrolysis reactor was designed for increasing the hydrolysis yield. Moreover, it was proposed to integrate the cycle with solar power using a beam down collector design and a fluidized-bed decomposition receiver-reactor (Fig. 4.4) but the proposed molten cadmium quench process has not been demonstrated.[17]

Another interesting MO cycle is based on SnO/SnO_2. It was recently demonstrated using solar energy.

$$SnO_2(s) \rightarrow SnO(g) + \frac{1}{2} O_2 \tag{4.9}$$

$$SnO(s) + H_2O(g) \rightarrow SnO_2(s) + H_2(g) \tag{4.10}$$

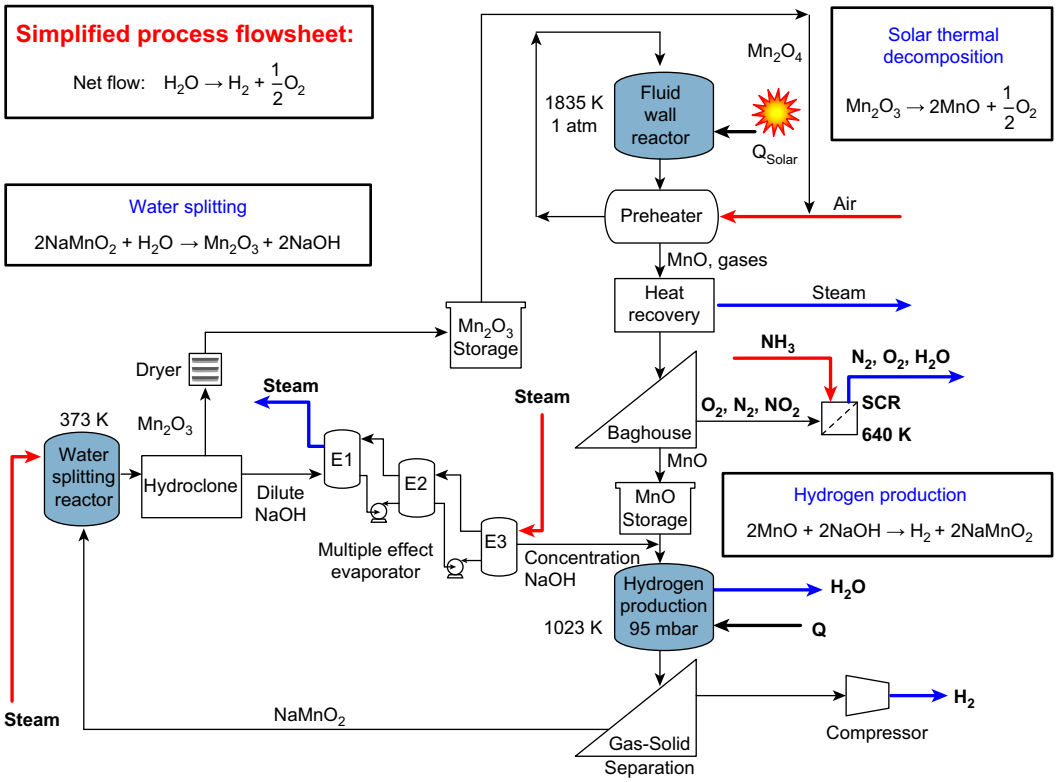

FIGURE 4.3 Simplified manganese process flowsheet.[15] (For color version of this figure, the reader is reffered to the online version of this book.) *Source: Published by M. Kerins, J. Martinek and J. Wyss (2005). The authors are grateful for Mr Alan Weimer's permission to reprint the material here.*

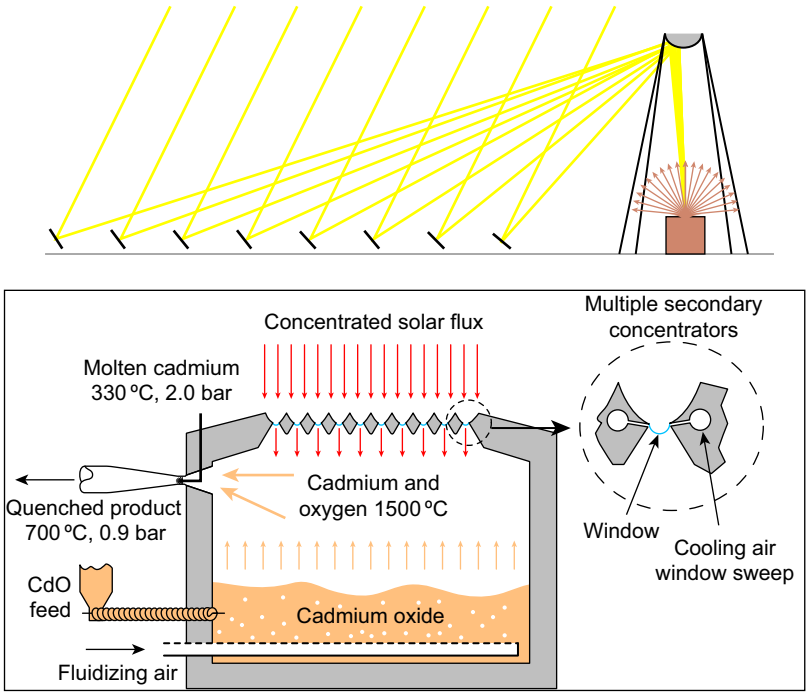

FIGURE 4.4 Beam down collector integrated with fluidized-bed decomposition receiver/reactor.[17] (For color version of this figure, the reader is reffered to the online version of this book.)

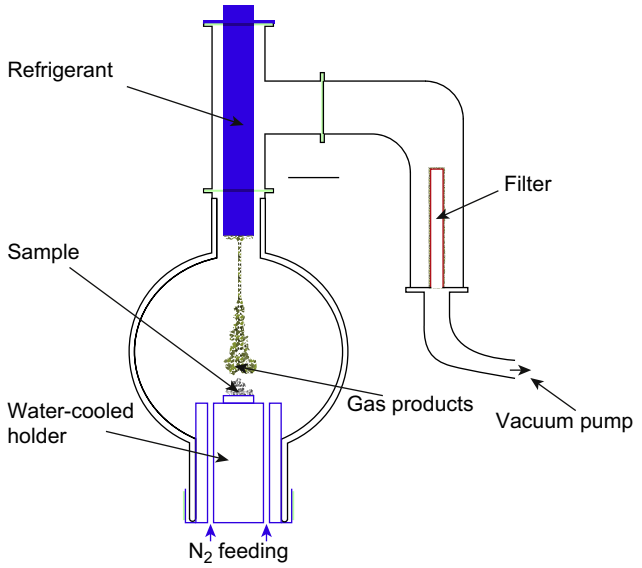

FIGURE 4.5 Experimental setup for solar reduction of volatile metal oxide.[18] (For color version of this figure, the reader is reffered to the online version of this book.)

The reduction step was tested in a glass solar reactor represented in Fig. 4.5. The sample was directly heated by concentrated solar energy supplied by a solar furnace.

A 1-kWth solar reactor prototype was successfully tested for continuous operation and showed that the SnO_2 reduction can be performed efficiently at 1873 K and the SnO hydrolysis at 823 K with a yield of hydrogen over 90%. Exergy and energy efficiencies of the cycle are 30 and 36%, respectively. The first design of the hydrogen production process was proposed to operate the cycle continuously. This process could be considered as an alternative cycle given its attractive characteristics such as relatively low temperature, high chemical yields and rapid kinetics for both the dissociation and hydrolysis reactions. It is still necessary to develop innovative reactor technologies with materials stable at such temperature and upon successive cycling.[18]

Actually, the thermochemical hydrogen production process based on MOs was originally proposed by Nakamura in 1977 using Fe_3O_4/FeO as redox material. It consists of two steps, which are as follows:

$$Fe_3O_4 \rightarrow 3FeO + \frac{1}{2}O_2 \tag{4.11}$$

$$3FeO + H_2O \rightarrow Fe_3O_4 + H_2 \tag{4.12}$$

The thermal dissociation of magnetite to wüstite at 2300 K was experimentally studied in a solar furnace by Sibieude in 1982.[19] It was found necessary to quench the products in order to avoid reoxidation, but quenching introduces an energy penalty of up to 80% of the solar energy input.[20] This leads to some material problems, including loss of oxide by vaporization. However, the feasibility of such solar thermochemical water splitting has been demonstrated by using a prototypical counter-rotating-ring receiver/reactor/recuperator, called CR5 (Fig. 4.6).[22] This reactor uses a stack of counter-rotating rings with fins along the perimeter, which contain the ferrite reactant, presumably on a support. The reactant fin is heated by the concentrated solar radiations, which provide the necessary heat for the oxygen-producing reaction. A vacuum pump removes the evolved oxygen. On the opposite side of the stack, the hydrolysis reaction takes place: steam oxidizes the ferrite and produces hydrogen. The CR5 facilitates continuous removal and sweeping of the product gases and the isolated reaction zones established allow the separation of the solid and gas products. The analyses suggest that thermal efficiencies of about 50% are possible.[22]

In order to solve the problem encountered with the pure Fe_3O_4/FeO as redox material, a system using mixed-metal ferrites has been researched in recent years and proposed. Partial substitution of iron in Fe_3O_4 by other metals (e.g. Mn, Ni, Co and Zn) forms mixed MOs of the type $(Fe_{1-x}M_x)_3O_4$ that may be reducible at lower temperatures than those required for the reduction of Fe_3O_4, while the reduced-phase $(Fe_{1-x}M_x)_{1-y}O$ remains capable of splitting water.[23] To minimize

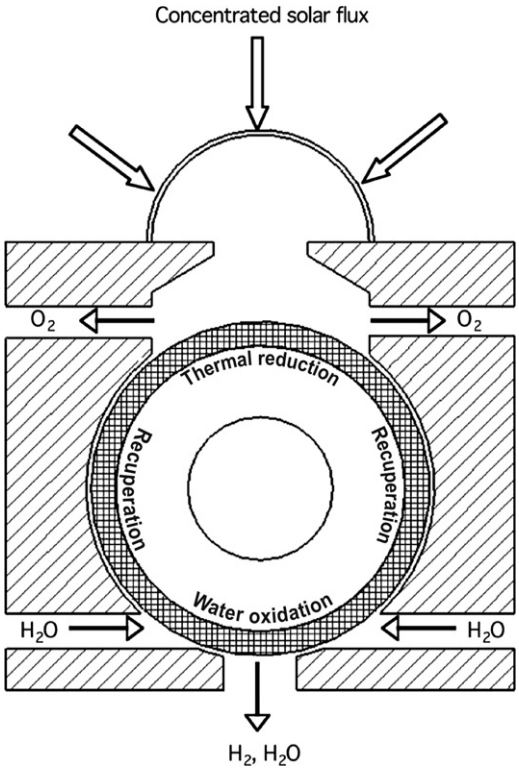

FIGURE 4.6 Schematic representation of CR5.[21]

sintering and deactivation of the oxide, it is possible to stabilize these mixed MOs on yttria-stabilized zirconia (YSZ).[24] The ferrite cycles enable the production of hydrogen using water and an iron-based MO. They involve a minimum number of steps and reactants and involve solid−gas reactions. Moreover, they can avoid the recombination reactions and irreversibility associated with quenching needed with volatile MOs such as zinc or cadmium oxides.[22] That's why they are very attractive.

Some experiments were also made with CR5, a new kind of reactant material in which ferrite particles are dispersed in a monolithic zirconia structure was developed and appeared to enhance reactivity and kinetics. The ferrite spinel/zirconia mixtures were evaluated to establish the feasibility of the CR5 concept, which appears to provide an integrated approach for potentially efficient and low-cost solar hydrogen.[22]

The achievement of solar water splitting at 1373 K over thermally reduced (1673 K) cobalt-substituted ferrites on YSZ was recently proved in the CR5, but is quite slow. Reaction times of more than 3 h were required for complete reduction or oxidation.[25]

In Japan, a concept for a windowed reactor using an internally circulating fluidized bed of $NiFe_2O_4/m\text{-}ZrO_2$ (Ni-ferrite supported on zirconia) particles was developed and demonstrated in laboratory scale for the solar thermochemical water splitting. About 45% of the $NiFe_2O_4$ was converted and was then completely reoxidized with steam at 1000 °C to generate hydrogen.[26]

Among feasible cycles, the Zn/Fe_3O_4 system was able to react with water to form hydrogen and $ZnFe_2O_4$ at 873 K.[27]

$$\frac{3}{4}\,ZnFe_2O_4 \;\rightarrow\; \frac{1}{2}\,O_2 + \frac{3}{4}\,Zn + \frac{1}{2}\,Fe_3O_4 \qquad (4.13)$$

$$H_2O + \frac{3}{4}\,Zn + \frac{1}{2}\,Fe_3O_4 \;\rightarrow\; H_2 + \frac{3}{4}\,ZnFe_2O_4 \qquad (4.14)$$

Figure 4.7 represents the dispositive used in laboratory scale for this cycle.

First, thermodynamic evaluation indicated that the Zn/Fe_3O_4 system may not proceed since H_2O/Zn system may react more spontaneously but the experimental results showed the production of $ZnFe_2O_4$, which is produced when the Zn/Fe_3O_4 system reacts with water. The yield of H_2 was 93.4%, and the reaction ratio for $H_2O/Zn/Fe_3O_4$ system was calculated to be 74%.[27]

The mixed iron oxides were also investigated recently within the EU-Project Hydrosol-2.[28,29] In this project, a two-step thermochemical cycle for solar hydrogen production from water has been developed.

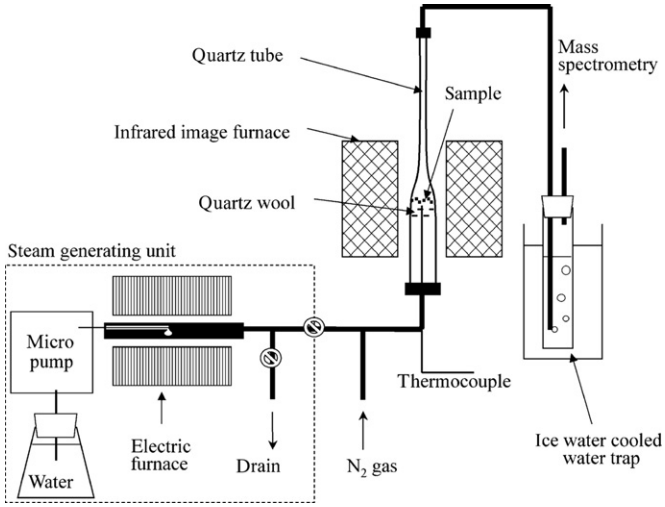

FIGURE 4.7 Experimental setup for hydrogen generation reaction.[27]

The redox systems favored are zinc- and nickel/zinc-based ferrites. The reaction scheme in the case of zinc can be written as follows:

$$ZnFe_y^{2+}\,Fe_{2-y}^{3+}\,O_{4-y/2} + x\,H_2O \;\rightarrow\; ZnFe_{y-x/2}^{2+}\,Fe_{2-y+x/2}^{3+}\,O_{4-y/2+x} + x\,H_2 \quad \text{(water splitting)} \qquad (4.15)$$

$$ZnFe_{y-x/2}^{2+}\,Fe_{2-y+x/2}^{3+}\,O_{4-y/2+x} \;\rightarrow\; ZnFe_y^{2+}\,Fe_{2-y}^{3+}\,O_{4-y/2} + \frac{x}{2}\,O_2 \quad \text{(reduction)} \qquad (4.16)$$

To realize the continuous supply of hydrogen, a quasi-continuous operating reactor was built at the Deutsches Zentrum für Luft- und Raumfahrt (DLR) in Germany. This monolithic solar receiver reactor consists of two separate chambers with fixed honeycomb absorbers in both chambers, as shown in Fig. 4.8. The honeycomb-structured ceramics were coated with a thin layer of the mixed iron-oxide redox system and placed inside a solar receiver.

At the beginning, the MO is present in a reduced form. By adding water vapor at 1073 K, oxygen is abstracted from the water molecules and hydrogen is produced. When the MO system is saturated, it is heated up for regeneration at 1473 K. The oxygen is exhausted from the redox system using nitrogen as flushing gas.[28] The product gas passes through heat exchangers and is cooled down before residual water is separated. The concept features a closed receiver-reactor constructed from ceramic multichanneled monoliths. The receiver surface is divided into several square apertures, two of which making up one receiver pair. One aperture

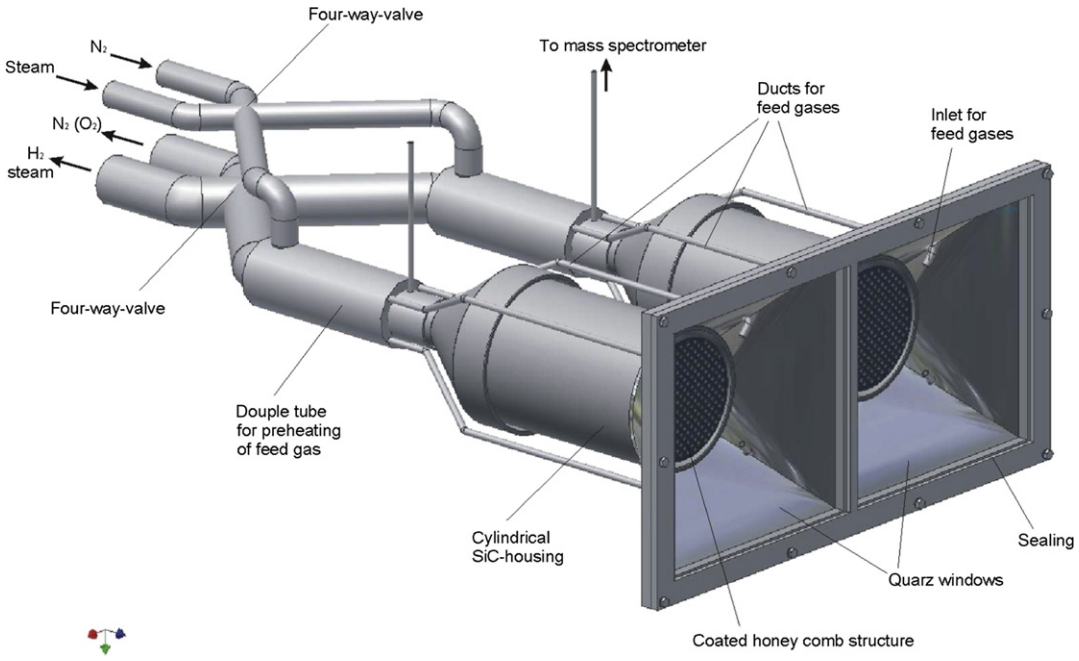

FIGURE 4.8 Schematic of the solar hydrosol reactor. (For color version of this figure, the reader is reffered to the online version of this book.)

is applied for the dissociation of the water vapor, while the other one is used for the regeneration of the catalyst. Their individual temperature levels are controlled by focusing and defocusing heliostats. Thus, hydrogen can be produced continuously by alternating the reaction steps. This technique avoids the need of continuous powder feeding and collection (no solid flow).

After successful experiments in the solar furnace of DLR in Cologne, hydrogen production using ferrites are now in the demonstration state. In fact, the temperature level of up to 1473 K in order to reach a mass production of hydrogen can only be realized by using a solar tower system, which consists of a set of tracked mirrors, tower and receiver. Within the EU-project Hydrosol II, a-100 kWth pilot plant has been installed on a solar tower at Plataforma Solar de Almería in Spain and is in operation since 2008 (Fig. 4.9). The multichamber arrangement of the reactor enables a quasicontinuous solar hydrogen production. Significant amounts of hydrogen were produced with a steam conversion of up to 30%.

Zn/ZnO has been studied extensively and is one promising candidate of the metal−MO-type cycles:

$$\mathrm{ZnO(s)} \rightarrow \mathrm{Zn(g)} + \frac{1}{2}\,\mathrm{O_2} \tag{4.17}$$

$$\mathrm{Zn(l)} + \mathrm{H_2O} \rightarrow \mathrm{H_2} + \mathrm{ZnO(s)} \tag{4.18}$$

The production of solar hydrogen via the Zn/ZnO water-splitting thermochemical cycle consists of

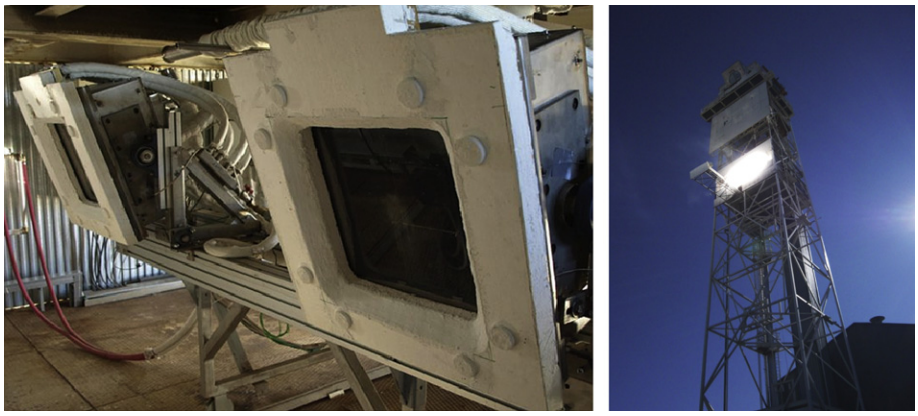

FIGURE 4.9 Hydrosol pilot plant in operation at Plataforma Solar de Almería in Spain. (For color version of this figure, the reader is reffered to the online version of this book.)

a first-step solar endothermic dissociation of ZnO and a second-step nonsolar exothermic oxidation of Zn.[30] Thermodynamically, the Zn/ZnO cycle is one of the most efficient and the water splitting takes place at temperature below 900 K, but the ZnO decomposition reaction takes place at very high temperatures (~2300 K) and engenders the formation of a mixture of Zn and O_2, which must be quenched to avoid their recombination and this influences the efficiency and the safety of the process.

In fact, the recombination of Zn and O_2 is a parasitic reverse reaction limiting the Zn yield after the solar step. The gas quenching to minimize Zn recombination (e.g. by adding large amounts of inert gas) constitutes the major challenge of this cycle.[18]

Nevertheless, the process requires further basic research to achieve fundamental knowledge on how to deal with extreme conditions.[30,31] The thermal decomposition of ZnO has been investigated and exploratory tests were carried out in a solar furnace since 1977.[20] A prototype laboratory-scale reactor was fabricated in the form of a tubular aerosol flow reactor featuring Zn evaporation, steam quenching, and Zn/H_2O-reaction zones. An average of 60% and 45% H_2 yield was achieved at temperatures 1023 and 1073 K, respectively. The H_2 yield decreases with increasing temperature. In fact, lower temperature leads to the formation of smaller Zn particles, due to the lower Zn evaporation rates. These smaller Zn particles have a higher specific surface area resulting in a better conversion and thus, a higher H_2 yield. The estimated solar-to-fuel efficiency of this cycle is 36% without heat recovery from the quench process.[32] A solar chemical reactor laden with ZnO particles serving as radiation absorbers was developed and experimentally demonstrated at a power level of 10 kW in 1999.[31] Using Zn nanoparticles for the splitting reaction improves the reaction kinetics, the heat and mass transfer, which permits operating at short residence times and, consequently, with smaller reactor volumes. Thus, a combined process was developed, consisting of the formation of Zn nanoparticles by steam quenching a Zn(g) flow, followed by their in situ steam splitting for generating H_2. Figure 4.10 shows the solar chemical reactor concept developed at the Paul Scherrer Institute (PSI) in Switzerland and using a windowed rotating cavity receiver lined with ZnO particles, which are held by centrifugal force. A secondary concentrator in front of the aperture augments the solar flux. Solar tests were carried out in a solar furnace with this 10 kW prototype subjected to mean solar concentration of 3500 suns and cavity surface temperature reaching 1973 K[33] and have proved the low thermal inertia of the reactor and its resistance to thermal shocks.[20] The feasibility of the solar chemical reactor technology for the thermal dissociation of ZnO is now being demonstrated in a 100-kWth pilot plant.[32]

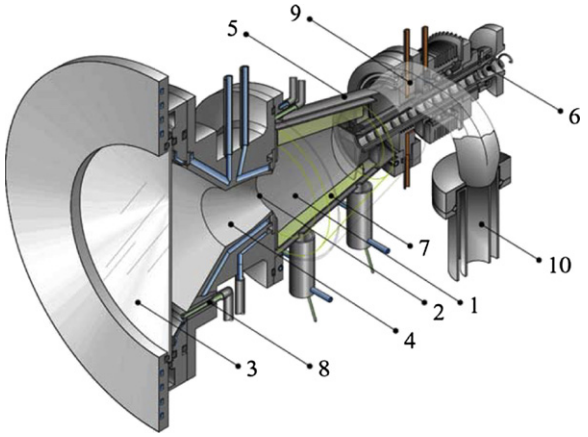

FIGURE 4.10 Schematic of the solar reactor concept for the thermal dissociation of ZnO to Zn and O_2 at 2300 K. 1: rotating cavity-receiver, 2: aperture, 3: quartz window, 4: compound parabolic concentrator (CPC), 5: outside conical shell, 6: reactant's feeder, 7: ZnO layer, 8: purge gas inlet, 9: product's outlet port, 10: quench device. (For color version of this figure, the reader is reffered to the online version of this book.) *Source: PSI Switzerland.*

The carbothermal reduction of ZnO was actively studied and demonstrated in a 300-kWth reactor in the frame of the EU-project Solzinc at the solar tower research facility of WIS in Israel.[30,31] The solar chemical reactor showed in Fig. 4.11 is made of two cavities. The upper one is functioning as the solar absorber and the lower one as the reaction chamber containing a ZnO/C-packed bed and subjected to thermal radiation from the upper cavity. With this arrangement, the upper cavity protects the quartz window against particles and condensable gases coming from the reaction

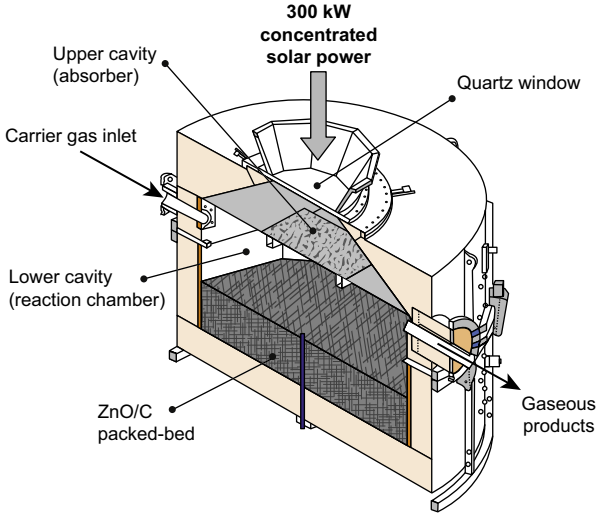

FIGURE 4.11 Two-cavity solar reactor concept for the carbothermal reduction of ZnO.[34] (For color version of this figure, the reader is reffered to the online version of this book.)

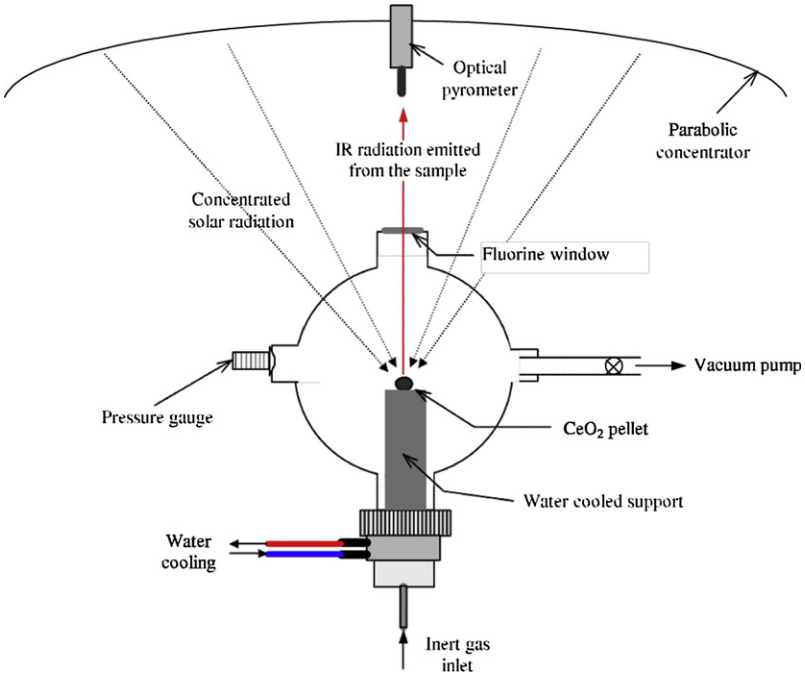

FIGURE 4.12 Solar reactor used to reduce CeO_2.[35] (For color version of this figure, the reader is reffered to the online version of this book.)

chamber. The reactor was batch-operated in the 1300−1500 K range and yielded 50 Kg/h of 95% purity Zn. The solar-to-fuel energy conversion efficiency was 30%. Zinc can react with water to form high-purity hydrogen.

A new MO cycle to consider for hydrogen production is the CeO_2/Ce_2O_3 cycle. This redox material is very attractive because of its rapid fuel production kinetics and its high selectivity. The cycle consists of two chemical steps:

$$2CeO_2 \rightarrow Ce_2O_3 + \frac{1}{2}O_2 \quad \text{(reduction)} \qquad (4.19)$$

$$Ce_2O_3 + H_2O \rightarrow 2CeO_2 + H_2 \quad \text{(hydrolysis)} \qquad (4.20)$$

This process is simple and uses available, nontoxic and low-cost chemical compounds. Its feasibility was recently demonstrated in a lab-scale solar reactor (Fig. 4.12) at 2273 K under inert atmosphere at reduced pressure (10−20 KPa) for the reduction step and in a fixed-bed reactor at 673−873 K for the hydrogen generation step, where the water-splitting reaction was completed with fast kinetics. In fact, complete hydrolysis of Ce(III) oxide with 100% conversion is reached after <5 min. Moreover, the size of the particles has no influence about the efficiency of the hydrolysis.[35] The results have shown that the cerium oxide cycle is a promising process for hydrogen production.

This cycle is still investigated also by the ETH and the California Institute of Technology. A prototype reactor (Fig. 4.13) was built and tested in a high-flux solar simulator.

A high-rate solar fuel production from H_2O was thus demonstrated in terms of materials, reaction rates, cyclability (over 500 thermochemical cycles) and reactor technology, using a solar reactor comprising a porous ceria cylinder directly exposed to the concentrated solar radiation.[37] The first thermodynamic analysis indicates an efficiency value between 16% and 19%. If taking account the sensible heat recovery, the reactor optimization and the system integration, some increase in efficiency is expected.

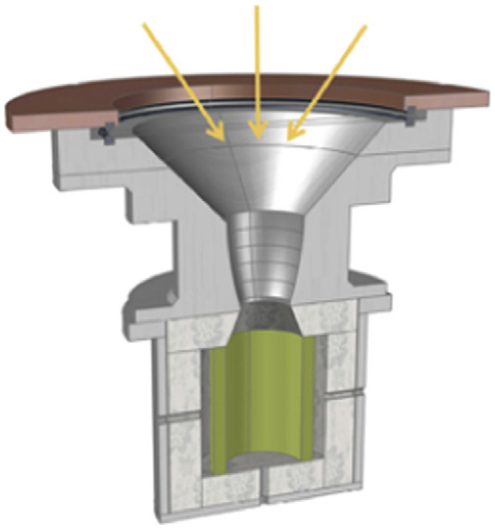

FIGURE 4.13 The ETH-Caltech solar reactor for producing H_2 from H_2O via the thermochemical cycle with ceria redox reactions.[36] (For color version of this figure, the reader is reffered to the online version of this book.)

The high reactivity of Ce_2O_3 with steam is very interesting and encourages searching new family of mixed-oxide cycles containing cerium oxides, in order to decrease the temperature of the reduction step, similarly to the ferrite family. Aim in the future is thus to low the reaction temperature and to reengineer the reactor to improve its efficiency.

Actually only ZnO/Zn and Fe_3O_4/FeO—and associated ferrite systems—cycles have been studied extensively and proved in a demonstration scale. Moreover, the cerium oxide family presents several significant advantages for hydrogen production and seems to represent a new challenging possibility for the future.

4.3.2 Sulfur-Based Cycles

Originally, sulfur-based cycles were developed to produce hydrogen by high-temperature heat from nuclear very high-temperature reactors (VHTRs). However, the required temperature level can also be provided by solar thermal towers and, as VHTRs are still in an early stage of development, they are currently the only applicable energy source available.

Thermochemical cycles of the sulfur family have in common the decomposition of sulfuric acid—a high-temperature, endothermic reaction step. Sulfur as the central element is recycled in these processes appearing in different compounds at changing oxidation state. Several cycles of the sulfur family have been studied during the past decades. Most prominent are the Mark 13 cycle, the sulfur–iodine (SI) cycle and the hybrid sulfur cycle (HyS). The Mark 13 operates with the toxic and corrosive halogen bromide[38] and, in the view of the authors, is not qualified for technical realization. Hence, in the following, the focus is on the other two processes. The SI cycle is a three-step process introducing iodine, which is less critical than bromide. While all reactions of the SI are chemical, meaning that chemical affinity and heat are the only driving forces, the two-step HyS includes an electrochemical reaction. Before these cycles are presented in detail, the sulfuric acid decomposition reaction is described as it allows introducing solar energy into sulfur-based water-splitting processes.

4.3.2.1 Solar Decomposition of Sulfuric Acid

Sulfuric acid is one of the most important primary products of the chemical industry with a global consumption of about 165 million tons in 2001.[39] Its decomposition is a well-known process proposed in the first half of the twentieth century[40,41] and is widely applied in industrial facilities to regenerate waste sulfuric acid. This reaction as the energy consuming process step is crucial for all sulfur-based cycles. It can be divided into four process steps, which partly proceed progressively as sulfuric acid is being heated. First, diluted sulfuric acid is concentrated by evaporating the water dissolved in the acid. Then, the concentrated and still-liquid sulfuric acid is evaporated. Subsequently, the gaseous acid is dissociated forming sulfur trioxide:[42]

$$H_2SO_{4(g)} \rightarrow SO_{3(g)} + H_2O_{(g)} \quad \Delta H^\circ = +98\ \text{kJ/mol} \tag{4.21}$$

Finally, the sulfur trioxide is decomposed to sulfur dioxide:[42]

$$SO_{3(g)} \rightarrow SO_{2(g)} + \frac{1}{2}\,O_{2(g)} \quad \Delta H^\circ = +99\ \text{kJ/mol} \tag{4.22}$$

The given subreactions are strongly endothermic. While the first one is fast and takes place spontaneously, the reduction of SO_3 proceeds at a low reaction rate and, hence, requires the use of catalysts. In Fig. 4.14, the equilibrium molar fractions of all the chemical components involved are presented. Accordingly, the dissociation of H_2SO_4 is completed at about 820 K while temperatures of up to 1120 K are needed to decompose about 80% of the SO_3.

In chemical plants, for treatment of waste sulfuric acid, fossil fuels are burned to achieve the required temperature level. This technology, however, is not applicable to thermochemical cycles driven by concentrated solar power where energy is provided by either radiating the reaction zone or heating the reactor with hot inert fluid from a solar receiver. Hence, innovative heat exchanger technology is required as an interface in order to introduce solar energy into the sulfuric acid decomposition reaction.

Several research groups developed decomposer designs during the past 30 years. In the 1980s, the first

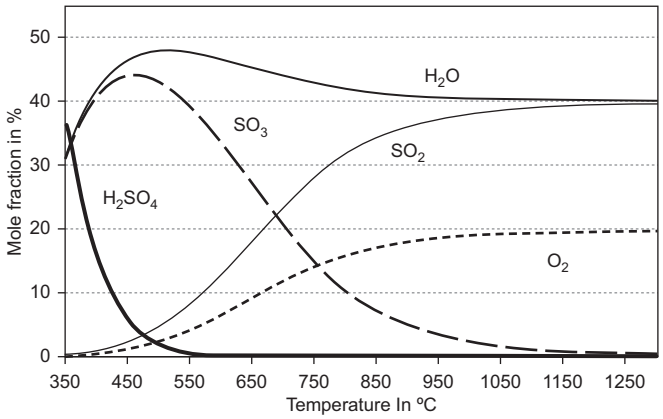

FIGURE 4.14 Thermodynamic equilibrium of the H_2SO_4- and SO_3-decomposition depending on the temperature at 1 bar.[43]

prototypes of heat exchangers for decomposition of sulfuric acid were constructed by the European Commission Joint Research Council (JRC-Ispra) in Italy and General Atomics (GA) in the USA. During the years 2000–2010, new concepts have been developed with silicon carbide (SiC) as construction material by Sandia National Laboratory (SNL) in USA, the Japanese Atomic Energy Agency (JAEA), the Korean Atomic Energy Research Institute (KAERI) and the German Aerospace Center (DLR). Although only GA and DLR powered their systems by solar energy, also the other designs originally developed for nuclear VHTRs could be operated by inert gas heated in a solar-power tower.

Among these designs, four different concepts can be identified:

(1) Hot inert gas is produced in a separate heat exchanger and brought into direct contact with the process gas. The design of JRC-Ispra foresees air as the heat vector.
(2) The heat of an inert-gas stream is transferred to the acidic gases in a corrosion-resistant heat exchanger. SNL and JAEA designed reactors made of SiC while KAERI uses steel with an SiC coating.
(3) A reactor absorbing solar radiation on one side of a wall and transferring the heat to the other side where the process gas flows. GA applied this concept using steel as construction material.
(4) Solar radiation is absorbed by a porous structure while process gas flows through the open volume of the absorber. This concept of a receiver-reactor is applied by DLR using SiSiC as absorber material.

Most of these systems are designed to operate with gaseous H_2SO_4 and/or SO_3. Only JRC-Ispra and DLR have developed concepts to vaporize liquid sulfuric acid.

The JRC-Ispra program on thermochemical splitting of water for the production of hydrogen started in 1970 and ended in 1983 with an extension of 15 months to help conclude experimental testing of the decomposer. In 1980, the design of the so-called CRISTINA process was initiated.[44] The basic idea is to avoid the use of high-alloyed steels by introducing air as energy vector. The air is superheated by high-temperature helium from a nuclear high-temperature gas-cooled reactor and is then brought into direct contact with sulfuric acid. Adiabatic reactors have been designed for concentration, evaporation and decomposition. The SO_3 cracking tower is the only part of the CRISTINA process, which was constructed and tested.[45] Decomposition of SO_3 proceeds inside a steel tube made of Incoloy 800 that is filled with catalytic iron rings. This reaction chamber, with a maximum operating pressure of 25 bars, is located inside a pressure vessel of AISI 316 steel where the gap between chamber and vessel is filled with refractory silica bricks. While passing through the reactive zone, the temperature of the fluid drops from 1180 to 1100 K as a result of the adiabatic operation. The experiments were carried out in an electrically heated test loop, with SO_3 produced in a synthesis reactor by oxidization of SO_2. During testing, a maximum SO_3 conversion of 51% corresponding to 73% of the maximum theoretical value was reached. The experiments proved that the cracking tower can be constructed and operated under design conditions.

GA designed and constructed a catalytic metal reactor to decompose sulfuric acid at the beginning of the 1980s funded by the US Department of Energy (DOE). The experimental system was tested atop the solar tower at the Georgia Institute of Technology (GIT) in Atlanta.[46] The solar reactor (Fig. 4.15) was constructed with 40 vertical tubes of Incoloy 800H in a circular configuration and designed to operate at 1173 K and ambient pressure. It was mounted in an insulated cavity with an aperture at the bottom side through which the solar flux entered the system. Sulfuric acid vapor from a feed system was decomposed inside the tubes containing an iron-oxide catalyst. The maximum conversion of 83% (94% of theoretical maximum) was obtained at the maximum flow rate of 84 mol/h H_2SO_4, and operating temperature of 1143 K. After on sun testing, the reactor was modified to carry out experiments at higher pressure using electrical heating elements to simulate solar radiation.[47] This modified decomposer was operated at a pressure of up to 12 bars and a maximum flow rate of 153 mol/h H_2SO_4 using iron oxide and platinum as catalysts and reaching a conversion of 70% (96% of theoretical maximum). Overall, experimental testing of the two systems was

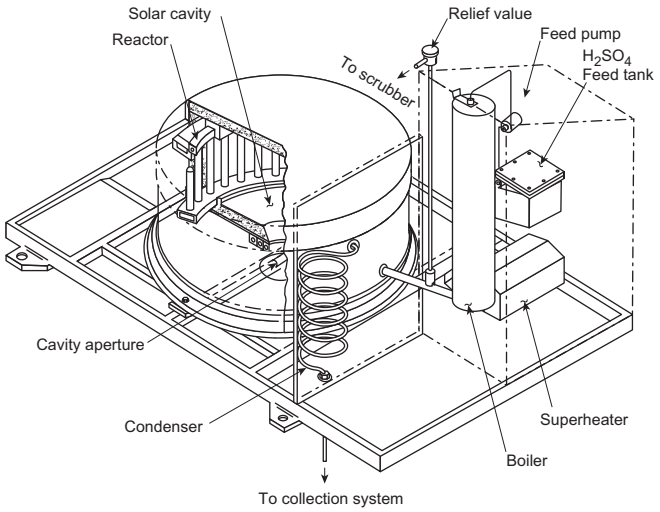

FIGURE 4.15 Catalytic solar reactor of GA. *Source: Reprinted courtesy of the National Technical Information Service, GA Technologies Report GA-A17573, UC-62C (February 1985).*

successful proving the suitability of the engineering materials Incoloy 800H, Hastelloy C-276, and Inconel 825 and of the catalysts platinum and iron oxide.

During the Integrated Laboratory Scale experiment of DOE's Nuclear Hydrogen Initiative, SNL was responsible for construction and testing of the sulfuric acid decomposition section of the SI cycle.[48] The so-called *bayonet sulfuric acid decomposer* was constructed of an outer and an inner SiC tube powered by electrical heaters. The open end of the bayonet was mounted in a polytetrafluorethylene (PTFE) manifold inside a steel block with connectors for the inlet and outlet streams. Sulfuric acid flows upward through the annulus and is heated to the operating temperature before reaching the catalyst bed in the upper part of the annulus, where decomposition of SO_3 takes place. At the top of the bayonet, the flow is redirected downward through the inner tube so that heat of the product gas is recuperated. During testing, the temperature of the catalyst was kept constant at 1123 K reaching pressures of up to 3 bars and acid flow rates of up to 7.1 mol/h H_2SO_4. The maximum conversion fraction was 84% corresponding to 86% of the value at thermodynamic equilibrium. The concept proved to be qualified fulfilling all design objectives.

From 2004 to 2007, DLR developed the first prototype of a directly absorbing receiver-reactors for the decomposition of sulfuric acid as part of the European research project HYTHEC.[49] Subsequently, from 2008 to 2011, DLR constructed a second reactor in the EU project HycycleS.[50] This optimized system has two separate reaction chambers for the vaporization of liquid sulfuric acid at about 673 K and subsequent dissociation of SO_3 at about 1123 K (Fig. 4.16). Both compartments are made of high-alloyed steel 316 Ti and closed by a quartz glass window at the front side to avoid discharge of acidic gases and, at the same time, allow solar radiation to enter the system. SiSiC structures (i.e. foam vaporizer in evaporator and honeycomb in decomposer chamber) are used to absorb solar radiation and transfer heat to the reaction gases. The honeycomb is catalytically activated with iron oxide and mixed oxide (i.e. $CuFe_2O_4$) coatings. During testing between 2009 and 2010, a maximum SO_3 conversion of 80% (89% of theoretical maximum) was reached at flow rates of up to 6.5 mol/h H_2SO_4 and ambient pressure. Operation of the system was successful and is ongoing in follow-up projects.

JAEA and KAERI separately developed heat exchangers to decompose sulfuric acid by heat of a nuclear VHTR. JAEA test fabricated a system made of SiC without operating it with sulfuric acid.[51] KAERI constructed and tested a heat exchanger made of steel with an SiC coating.[52] Both systems exhibited some manufacturing problems. JAEA stopped its program while the development of the Korean heat exchanger is still ongoing.

In conclusion, various sulfuric acid evaporators and decomposers have been developed and demonstrated in the 1980s and during 2000–2010. Some decomposers (cf. concepts of JRC-Ispra, SNL, JAEA and KAERI) were not specifically designed for solar application. None of these designs can be irradiated directly on the top of a solar tower and, hence, require at least one additional heat exchanger in order to drive them by solar energy. As a result, the performance of a process incorporating one of these reactors would be limited by the thermal efficiency of the solar receiver. The directly absorbing systems of GA and DLR allow for higher overall process thermal efficiency, as only one heat-exchanging step is required. Some systems have been successfully tested at laboratory scale. The next development step would be the construction of a pilot plant.

4.3.2.2 *Sulfur–Iodine Cycle*

The SI water-splitting process (Fig. 4.17), also known as ISPRA Mark 16 SI thermochemical cycle, is a promising cycle for efficient production of hydrogen.

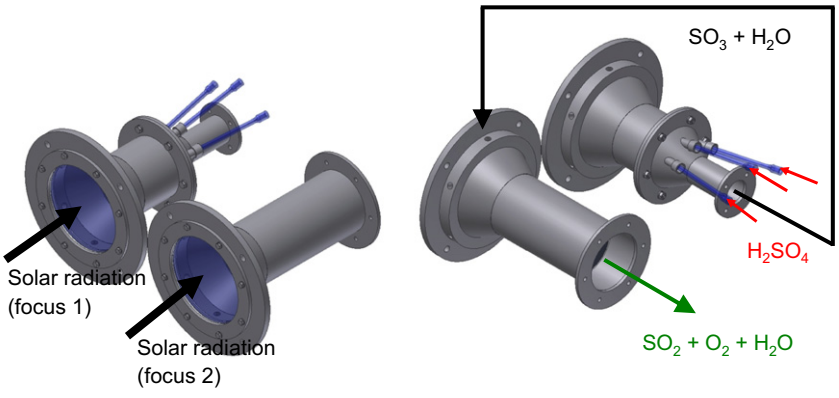

FIGURE 4.16 DLR solar receiver-reactor with two chambers for evaporation and decomposition.[50] (For color version of this figure, the reader is reffered to the online version of this book.)

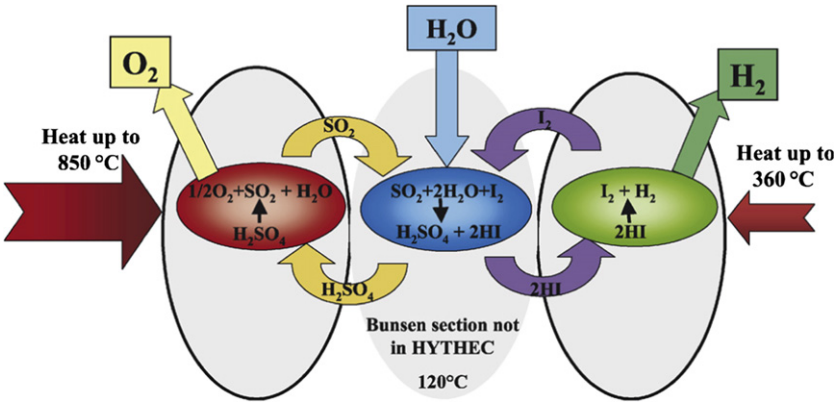

FIGURE 4.17 The sulfur–iodine cycle.[53] (For color version of this figure, the reader is reffered to the online version of this book.)

It was originally proposed and developed in the USA by GA in the mid-1970s.[54] The three basic reactions are:

$$2H_2O + SO_2 + xI_2 \rightarrow H_2SO_4 + 2HI_x \quad (300-400\ \text{K}) \tag{4.23}$$

$$2HI_x \rightarrow xI_2 + H_2 \quad (400-1000\ \text{K}) \tag{4.24}$$

$$H_2SO_4 \rightarrow H_2O + SO_2 + \frac{1}{2}O_2 \quad (1120-1200\ \text{K}) \tag{4.25}$$

Figure 4.18 shows the mains step of the SI process. Originally, this cycle was developed to be coupled to a nuclear heat source, but more recently, the coupling to a solar thermal plant was designed.[46]

The first reaction is exothermic and known as the *Bunsen section*. The Bunsen reaction can be split into four elementary reactions:

$$SO_2 + 2H_2O \rightarrow H_2SO_4 + H_2 \tag{4.26}$$

$$I_2 + H_2 \rightarrow 2HI \tag{4.27}$$

$$H_2SO_4 + 4H_2O \rightarrow H_2SO_4 \cdot 4H_2O \tag{4.28}$$

$$2HI + 8I_2 + 10H_2O \rightarrow 2HI \cdot 5H_2O + 8I_2 \tag{4.29}$$

The Bunsen reaction requires surplus of water and iodine in order to proceed. The separation of the two acids produced in this step is one difficulty of the SI cycle. The removal by distillation of the two acids requires a lot of energy, which has a direct influence on the efficiency of the cycle. One of the major challenges of this cycle is to reduce the excess of water and iodine and to find separation processes that consume less energy than distillation.

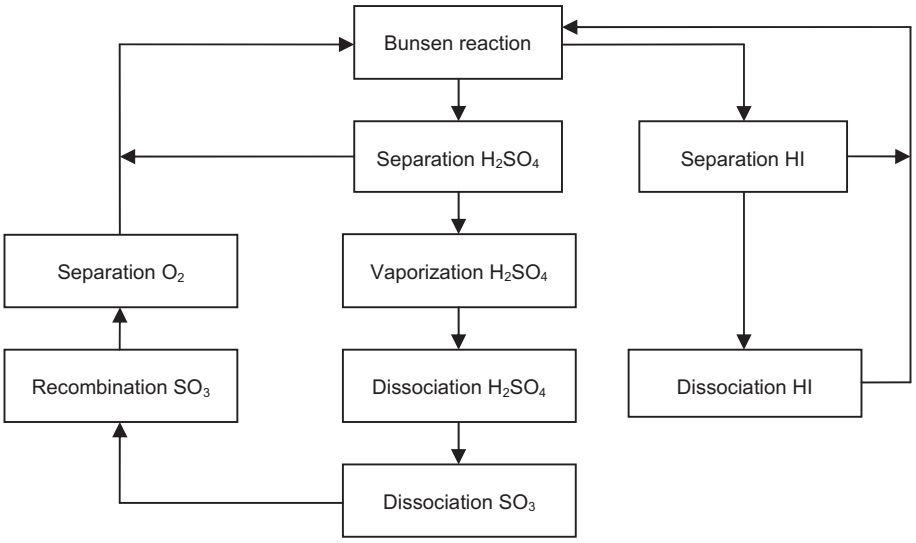

FIGURE 4.18 Main steps of the sulphur–iodine process.

Following the Bunsen reaction, HI and H_2SO_4 are decomposed according to the reactions shown in Eqns (4.24) and (4.25). Equation (4.24) is the HI decomposition step with a small endothermic heat of reaction. The direct decomposition of HI involves the circulation of large amounts of products and requires the evaporation of large water quantities. The reaction takes place in a catalytic reactor.

Equation (4.25) is the major endothermic reaction and takes place in the vapor phase in a catalytic reactor at about 1200 K (Section 4.3.2.1). H_2SO_4 decomposition is carried out in three steps: first, a partial distillation of sulfuric acid takes place in a multistage evaporator, then H_2SO_4 is decomposed in SO_3 and H_2O and finally SO_3 is decomposed in SO_2 and O_2.

Each reaction has been successfully conducted at laboratory scale and small process development units have been operated. The thermal decomposition of H_2SO_4 is the reaction that requires the greatest heat input, typically at temperatures in the range of 1120 K.

GA has done a great effort of research and development on this process.[55,56] A bench-scale system was constructed and used to demonstrate the operation of the cycle and test components. The feasibility of this cycle was successfully demonstrated in a glass, quartz and Teflon lab-scale apparatus,[57] on the solar power tower of the GIT[58] and in the solar furnace of DLR in Cologne, Germany.[59]

Cost studies were carried out to indicate which parts of the process have the greatest influence on the hydrogen-production cost. The decomposition of H_2SO_4 and HI were found to be costly procedures causing severe corrosion problems. However, work on improvements to this process has been continued at various locations, like in the Technical University at Aachen in Germany[60], or in Japan, by JAERI who developed a pilot test plan[61] and by JAEA, who has successfully demonstrated "continuous" hydrogen production at a rate of about 32 l/h for 20 h.[62]

Recently, it is again in the focus of intensive research and the European project Hythec has investigated the effective potential for massive hydrogen production of the SI thermochemical cycle. There was also collaboration between SNL, GA and Commissariat à l'énergie atomique to build a water-splitting test apparatus featuring the extractive distillation with a designed hydrogen production rate of 100–200 l/h.[51]

Some flowsheets were developed to interface the process with a solar central receiver. Based on these flowsheets, the first overall efficiency estimation published by GA in 1981 was estimated to be about 47%[63]. A real efficiency of the SI cycle is now given with 35%.[53,63]

The SI cycle requires some corrosion-resistant materials because of the use of corrosive chemicals such as H_2SO_4, HI, and I_2 at high temperatures. Refractory alloys such as Hastelloy has a certain corrosion resistance in the gas-phase environments but in the liquid-phase environments, only specific materials, e.g. glass, ceramics, and rare metals showed resistance to corrosion. However, these materials have a great impact on the cost of produced hydrogen and their use has to be limited.[64] Concerning the components in contact with HI_x at high temperature, some materials were tested and Ta- and Nb-based refractory metals as well as ceramic mullite are capable to tolerate the extreme HI_x environment.[65]

4.3.2.3 *HyS Cycle*

The HyS, also known as Westinghouse sulfur cycle or Ispra Mark 11 cycle, was originally proposed by Brecher et al.[66] in 1975. It is the first demonstrated thermochemical water-splitting process with only two reactions. After thermal decomposition of sulfuric acid (Section 4.3.2.1), this hybrid cycle is closed by an electrochemical step:

$$\text{Anode:} \quad SO_2 + 2H_2O \rightarrow H_2SO_4 + 2H^+ + 2e^- \tag{4.30}$$

$$\text{Cathode:} \quad 2H^+ + 2e^- \rightarrow H_2 \tag{4.31}$$

In this electrolysis, sulfur dioxide and water form sulfurous acid, which is used to depolarize the anode. Sulfuric acid is produced yielding two protons and two electrons, which pass through the electrolyte separator and are conducted via an external circuit, respectively, toward the cathode. There they are recombined forming hydrogen. The theoretical cell potential is only about 14% of conventional water electrolysis with a theoretical voltage of 1.23 V.[67] Hence, this sulfur dioxide-depolarized electrolyzer (SDE) has the potential to significantly reduce the amount of electrical power required. Therefore, the HyS compares favorably to water electrolysis as most of the electrical energy is replaced by thermal heat introduced in the sulfuric acid decomposition reaction.

In Fig. 4.19, a simplified process flow sheet of the HyS is presented. The SDE typically operates at temperatures of about 100 °C converting SO_2 and H_2O to sulfuric acid, which is recycled to the decomposition section, and the desired product hydrogen. There the acid is vaporized at about 400–600 °C by low-temperature heat from the external heat source and partly by internal heat recuperation. Subsequently, the acidic gases are superheated to temperatures in excess of 800 °C catalytically forming SO_2 (Section 4.3.2.1). The product gas mainly contains SO_2, H_2O and O_2 with traces of SO_3 and H_2SO_4. After heat recuperation and condensation of water, which is recycled to the SDE, the by-product oxygen is

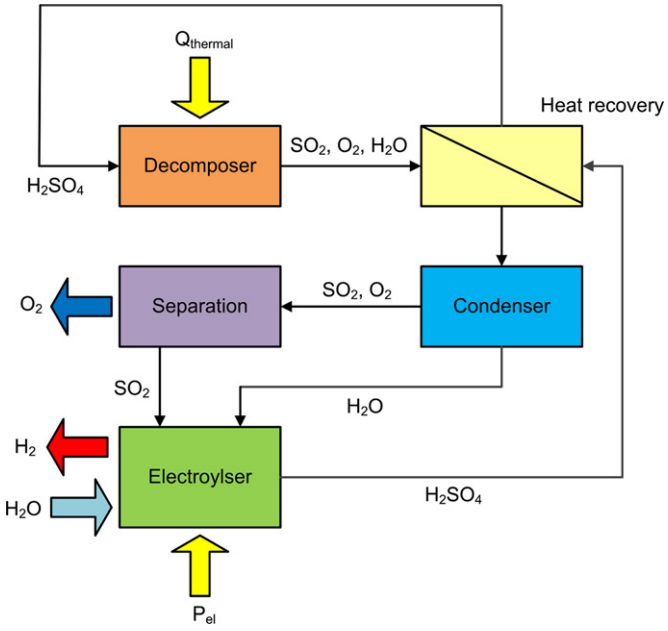

FIGURE 4.19 Simplified process flow diagram of the hybrid sulfur cycle. (For color version of this figure, the reader is reffered to the online version of this book.)

separated from the SO_2, which is conveyed back to the electrolysis.

According to the study made by Bilgen,[68] the overall thermal efficiency of the process, given by the following equation, has been assumed to be in the range of 37%.

$$\eta = \frac{HHV(H_2)}{\sum Q_i}$$

Where $HHV(H_2)$ is the higher heating value of H_2 and $\sum Q_i$ is the total thermal energy consumed by the process.

The cycle efficiency can be optimized by adjusting the flow sheet and operating conditions of the process components.[69] High pressure in the decomposer will decrease the SO_2 production, due to Le Chatelier's principle (Eqn (4.22)), but allows for a more compact design of the system. On the other hand, a low decomposition pressure will possibly result in higher compression work for the oxygen separation. Operating the decomposer at higher temperature will yield more SO_2; however, this parameter is limited by material constraints and, in terms of solar applications, will increase the heat losses due to reradiation. A low acid concentration is beneficial for the SDE but increases the heat load of the decomposition section. Considering these effects, Jeong et al.[69] assuming a nuclear heat source found an optimal efficiency of 47% (LHV)[2] (lower heating value) for 10 bar and 1200 K in the decomposer and an acid concentration of 70 wt.% in the electrolyzer. For a different flow sheet considering a solar heat source, Corgnale et al. [70] derived an annual average efficiency of 32% (LHV) with a potential to reach 39% (LHV) after technological improvements in the future. In this analysis, the decomposer operates at a peak temperature of 1193 K and an inlet pressure of 40 bars while the SDE processes SO_2 dissolved in sulfuric acid with an inlet concentration of 43 wt.%. With these considerations, specific hydrogen production costs of 4 $/kg in 2015 and 2.85 $/kg in 2025 are estimated. In a comparison of different thermochemical processes by Graf et al. in 2008,[71] the lowest specific hydrogen cost was predicted for the HyS in the range of 3.90–5.40 €/kg.

The electrolysis cell consists of two electrodes and a proton-exchange membrane, which allows the hydrogen ions to pass through. The electrodes are usually prepared with catalysts, which are mainly made from carbon-supported platinum. Lu[72] investigated four designs of electrodes by using different types of catalysts. The first configuration consists of electrodes, which are made from a mixture of catalyzed carbon powder and phenolic resin. In the second design, the platinum particles were directly coated on the carbon by using the ion-exchange method. The operation of the electrolyzer using the mentioned configurations shows that the electrodes had a low performance. This fact is related to the low, specific surface areas of the used catalyst. In the two following configurations, the electrodes were so modified that an increase of the electrochemical activity was achieved. The electrodes of the third configuration are characterized with a layer of carbon-supported platinum catalysts on a sheet of conducting carbon cloth, which uses PTFE as a binder. In the last layout of the electrodes, the platinum loading has been decreased from 10 g/cm^2 to 1 mg/cm^2 with no penalty of the cell performance reaching cell potentials of 680 and 910 mV at 200 and 400 mA/cm^2. About 20 years later in experiments carried out by the Savannah River National Laboratory, a significantly lower cell potential of −600 mV was achieved at a current density of 500 mA/cm^2.[70]

These results are promising and indicate the technical feasibility of the HyS. Next, the development of a pilot plant in the range of several hundred kilowatts combining the sulfuric acid decomposer and the SDE would be required in order to approach the estimated specific costs given above. After further improvements in the future, the HyS has the potential for highly efficient and economic production of hydrogen.

4.3.3 Other Cycles

In the copper–chlorine cycle, the water is decomposed into hydrogen and oxygen through intermediate copper–chlorine components. This thermochemical cycle requires process heat at lower temperature as

compared to the other thermochemical cycles using Zn/ZnO and Mg/MgO redox pairs. The overall water-splitting reaction is given by Eqn (4.1).

The copper–chlorine cycle has been analyzed as a promising pathway for hydrogen production at the Argonne National Laboratory (ANL) by Lewis et al.[73] This cycle has also been investigated by the Atomic Energy of Canada Ltd.[74]

The overall process given consists of four chemical reactions. Other studies considered a five-step thermochemical cycle.[75] In addition to the advantage of using heat at low temperatures, the electrochemical step of this cycle requires low voltage. The four steps in the copper–chlorine cycle are given by the following reactions:[76]

- *Hydrogen production step*: This is the main step of the cycle and the hydrogen chloride gas HCl and the solid Cu react together to form liquid cupric chloride CuCl and hydrogen gas. This step is given by the following reaction:

$$2Cu(s) + 2HCl\,(g) \rightarrow 2CuCl(l) + H_2(g) \tag{4.32}$$

The reaction is exothermic and takes place at a temperature in the range of 430–475 °C. Experiments of the H_2 production step have been carried out at the ANL in a furnace.[77] A very important aspect of this step is that the temperature, at which the reaction takes place, has to be above 430 °C in order to avoid the formation of solid CuCl.[78]

- *Hydrolysis step*: This step is endothermic and temperatures in the range of 375–400 °C are required to run the reaction. The reaction takes place between solid copper chloride $CuCl_2$ and water steam. The products of this step, namely hydrochloric gas HCl and solid Cu_2OCl_2, are given by the following reaction:

$$2CuCl_2(s) + H_2O(g) \rightarrow Cu_2OCl_2(s) + 2HCl(g) \tag{4.33}$$

- *Electrolysis step*: This step consists of the electrolysis of liquid CuCl at ambient temperature according to the next reaction:

$$2CuCl(l) \rightarrow CuCl_2(aq) + Cu(s) \tag{4.34}$$

The voltage needed to run this electrolysis step is assumed to be between 0.4 and 0.6 V.[79]

- *Oxygen production step*: Solid Cu_2OCl_2 decomposes under heat supply to oxygen gas O_2 and liquid cupric chloride CuCl according to the following reaction:

$$2Cu_2OCl_2(s) \rightarrow 4CuCl(l) + O_2(g) \tag{4.35}$$

The oxygen-production step is the most important one since it has the highest temperature of the different steps, which is estimated to be at 500 °C. This reaction is endothermic and the heat required can be divided into two parts:[79]

- The reactants have to be heated up from 375 °C to 500 °C with a heat requirement of about 20.2 KJ/mol H_2.
- The heat of the reaction at 500 °C is approximately 129.2 KJ/mol H_2.

The heat for the oxygen-production step can be supplied by the molten salt central receiver. Figure 4.20 shows the schematic of the central receiver coupled to

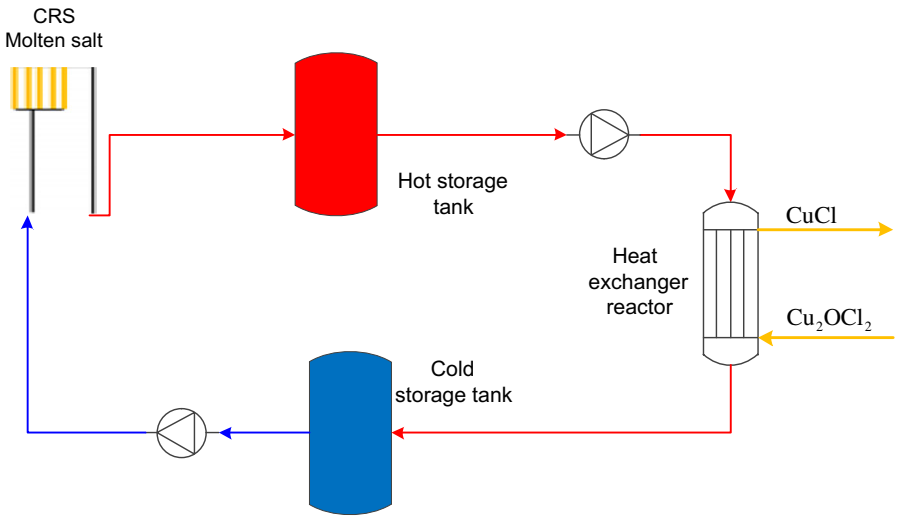

FIGURE 4.20 Schematic of the molten-salt central receiver. (For color version of this figure, the reader is reffered to the online version of this book.)

the oxygen-production step. The working fluid is molten salt and it has been successfully demonstrated in solar power plants.

The molten-salt plant coupled to the copper–chlorine cycle consists of a central receiver, two storage tanks, two pumps and a heat exchanger reactor. The cold, molten salt from the cold tank will be heated in the central receiver mounted on the top of the tower. The hot salt will be delivered to the heat exchanger reactor, where the chemical reaction will take place. The heat exchanger reactor is normally a shell and tube heat exchanger. The molten salt is fed on the shell side and the reacting Cu_2OCl_2 on the tube side. The hot molten salt has usually a temperature of 550 °C and cools down by heat transfer to the Cu_2OCl_2.

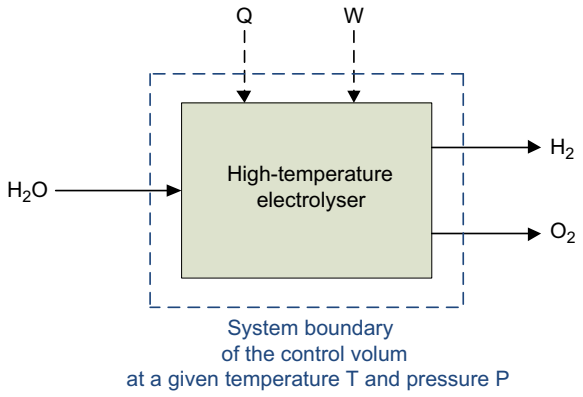

FIGURE 4.21 Schematic of the water electrolysis process. (For color version of this figure, the reader is reffered to the online version of this book.)

4.4 HIGH-TEMPERATURE ELECTROLYSIS

The splitting of water can be achieved through electrolysis, which uses electricity in order to split water into hydrogen and oxygen in an electrolysis cell that consists of an anode and a cathode. The conventional process of water splitting is the alkaline electrolysis, which has been realized and demonstrated for more than 80 years. High-temperature electrolysis differs from the conventional alkaline electrolysis. A part of the energy required for the water splitting will be provided as high-temperature heat at around 800–1000 °C. As a consequence, the electric power will be reduced.

4.4.1 Thermodynamics of High-Temperature Electrolysis

Steam is fed to the cathode side of the electrolyzer where it is reduced to hydrogen. The oxide ions pass through the electrolyte to the anode where they recombine to oxygen by releasing two electrons.

The following reactions describe the chemical reactions, which take place on both sides of the electrolyzer:

$$\text{On the cathode side: } H_2O + 2e \rightarrow H_2 + O^{2-} \quad (4.36)$$

$$\text{On the anode side: } O^{2-} \rightarrow \frac{1}{2}O_2 + 2e \quad (4.37)$$

The total reaction of the water splitting is written as follows:

$$H_2O \rightarrow H_2 + \frac{1}{2}O_2 \quad (4.38)$$

In order to estimate the energy needs (heat and electricity demand) of the electrolyzer, an analysis from a thermodynamic point of view is necessary. We consider the electrolyzer as a control volume, as shown in Fig. 4.21. Q is the heat input and W is the electrical energy.

The first law of thermodynamics for this process is given by the following equation:

$$Q + W = \Delta H_R \quad (4.39)$$

where ΔH_R is the enthalpy change of the reaction (It can also be considered as the total energy demand for the water-splitting process.), W, the electricity demand and Q, the heat demand. For reversible operation:

$$Q_{rev} = T\Delta S_R \quad (4.40)$$

where ΔS_R is the entropy change of the reaction at the operating temperature T of the electrolyzer. Equations (4.39) and (4.40) give the following equation:

$$W_{rev} = \Delta H_R - T\Delta S_R = \Delta G_R \quad (4.41)$$

where ΔG_R represents the Gibbs free-energy change of the reaction. Equation (4.41) is plotted in the following figure for temperatures in the range of 0–1000 °C at a pressure of 1 bar.[80]

Figure 4.22 shows that the electricity demand decreases with the temperature because some of the energy will be supplied as heat.

4.4.1.1 Configuration of the Electrolyzer

The water-splitting reaction will take place in a solid-oxide electrolysis cell. The solid-oxide cell consists of two main components:

- An electrolyte
- Two electrodes (anode and cathode).

Figure 4.23 shows the configuration of the solid-oxide cell.

The electrolyte is a gas-tight ceramic membrane which can conduct ions and is located between two porous electrodes that can conduct electrons: steam/hydrogen

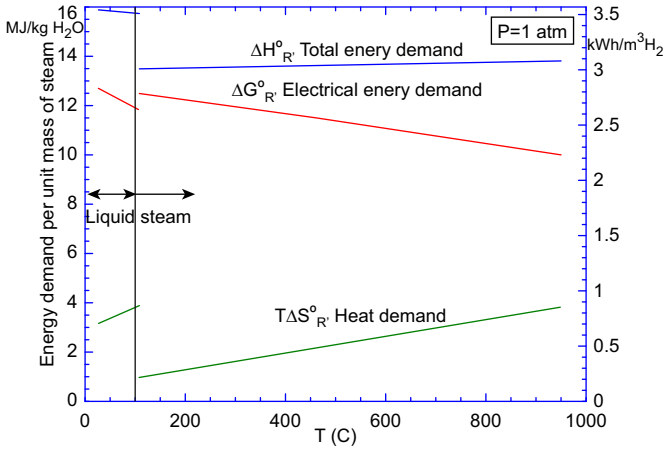

FIGURE 4.22 Energy demand of the electrolysis process.[80] (For color version of this figure, the reader is reffered to the online version of this book.)

electrode (anode) and the air/oxygen electrode (cathode). The design of the solid-oxide cell includes the use of a sweep gas in order to avoid the degradation of the electrode. Possible sweep gases are air, steam and oxygen. The steam, mixed with hydrogen in order to maintain reducing conditions on the anode side, is fed to the cathode. The water molecules dissociate to form hydrogen and oxygen ions. The oxygen ions are transported through the electrolyte on the anode where they are oxidized to form oxygen gas.

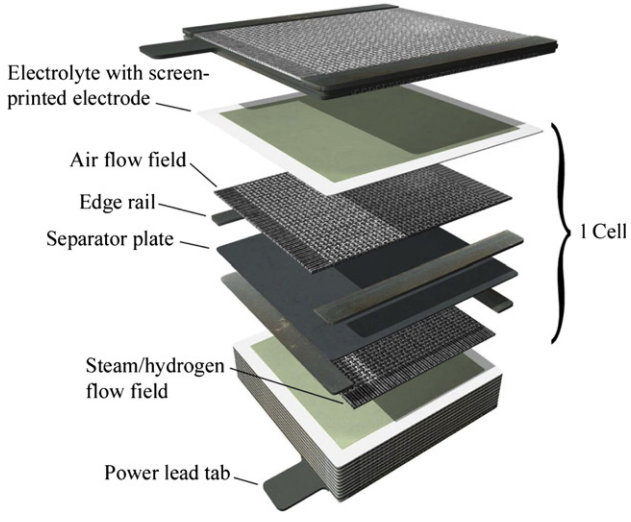

FIGURE 4.23 Configuration of the solid-oxide cell. (For color version of this figure, the reader is reffered to the online version of this book.) *Source: The figure presented in this chapter was first published by O'Brien, J. E.; Stoots, C. M.; McKellar, M. G.; Harvego, E. A.; Condie, K. G.; Housley, G. K.; Herring, J. S. and Hartvigsen, J. J. In: "Status of the INL High Temperature Electrolysis Research Program—Experimental and Modeling,"* Proceedings, Fourth Information Exchange Meeting on Nuclear Hydrogen, NEA. *Oakbrook, IL, April 14—16, 2009. The authors are grateful for Mr James O'Brien's permission to reprint the material here.*

4.4.1.2 *Materials of the Electrolyzer*

The materials of the main components of the electrolyzerelectrolyzer, namely the electrolyte and the electrodes, have to satisfy some requirements. The electrolyte should have good ion conductivity and its chemical stability is a key issue for the safe operation of the electrolyzer. In the following sections, the state of the art of the electrolyzer materials will be presented.

- *The electrolyte*: The common material is YSZ, which has a good chemical stability and high conductivity for ions. YSZ has a melting point of 2973 K.[81] The zirconia material is normally doped with other components in order to improve the oxygen conductivity. Many studies have shown that a higher conductivity can be achieved if the zirconia will be doped with Y_2O_3, Yb_2O_3 and Sc_2O_3.[82,83] Other dopants decrease the ionic conductivity of the electrolyte.[84]
- *The cathode*: Noble metals such as Pt and nonprecious metals such as Ni and Co are the most suitable materials for the cathode. The main disadvantage of those materials is related to its high cost.[85] Ni is the most common material, which can be mixed with other ionic particles, in order to increase the area of the reacting zone, where the reduction takes place. This kind of electrode is called *cermet electrode* (Ni-YSZ cermet).[86] Alternative material for the cermet electrode is the samaria-doped ceria, which is still in development.[87]
- *The anode*: Noble materials can also be used for the anode, but due to its high costs, electronic conducting oxides represent the best alternative, such as the lanthanum strontium manganate (LSM). An overdoping of the LSM with MnO_x is required due to the fact that MnO_x can diffuse from the anode to the electrolyte and, as a consequence, a reaction of La_2O_3 or SrO with YSZ will take place leading to the formation of poorly conducting $La_2Zr_2O_7$ or $SrZrO_3$.[88]

4.4.2 Energy Sources

Several solar thermal technologies can be coupled to the high-temperature electrolyzer. Two main aspects have to be considered:

- Capability of electricity supply for the electroyser
- Capability to serve as heat source.

Other aspects have to be taken into consideration such as sweep gas generation and the quality of water, which will be fed into the electrolyzer. The solar tower technology appears to be the best candidate to be coupled to the high-temperature electrolyzer. This technology has been demonstrated in the solar Tower of

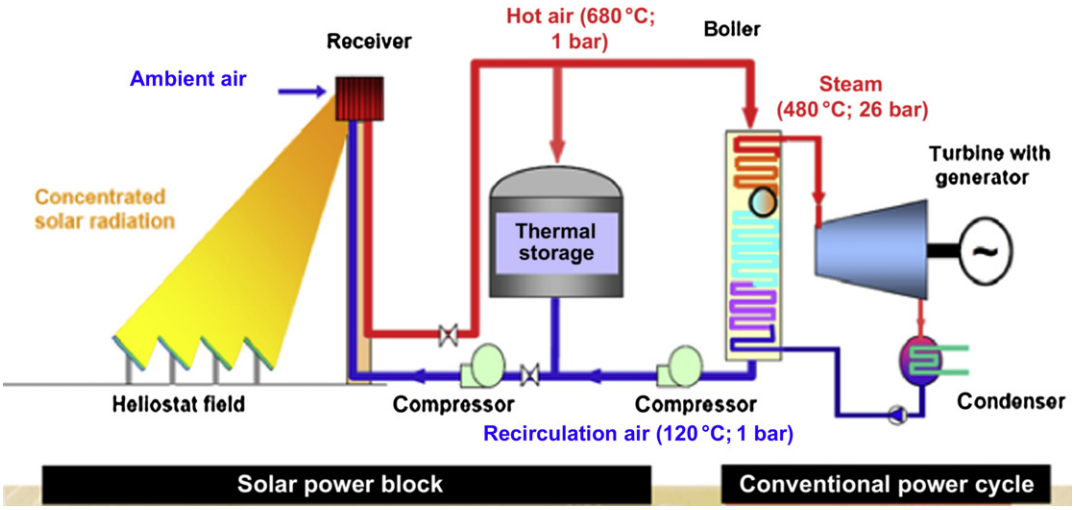

FIGURE 4.24 The air solar power tower of Jülich.[89] For color version of this figure, the reader is reffered to the online version of this book.

Jülich (Germany), which is currently operated by the German Aerospace Center (DLR).[89] The receiver is installed on the top of the Tower and is made of porous ceramic elements through which incoming ambient air flows. The heated air will be delivered to a water–steam cycle in a heat recovery boiler, where steam will be generated. The steam then drives a turbine, which produces electricity. Figure 4.24 shows the solar tower of Jülich using air as working fluid.

Other solar tower technologies use molten salt as heat transfer fluid. The molten salt used in these systems is a mixture (by weight) of 60% sodium nitrate and 40% potassium nitrate. The molten salt heated in the receiver is delivered to a thermal storage system; the hot salt is extracted from the storage system for generation of steam in the steam generator, which will be used to produce electricity. In this configuration, the thermal storage system buffers the steam generator from solar transients and also supplies energy during periods of no insolation. The largest demonstration of this technology was the Solar Two project, a 10 MWt power tower located near Barstow, CA. Figure 4.25 shows the Gemasolar solar tower in Seville (Spain), which is operated by Torresol Energy.

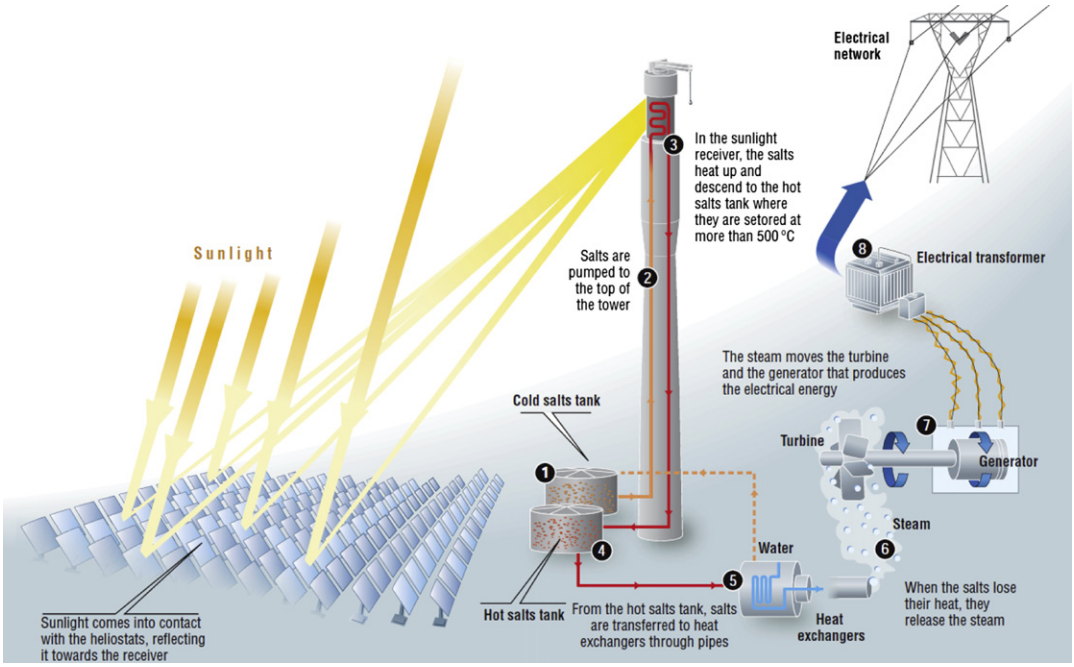

FIGURE 4.25 The Gemasolar solar power tower. (For color version of this figure, the reader is reffered to the online version of this book.)
Source: © Gemasolar plant, property of Torresol Energy.

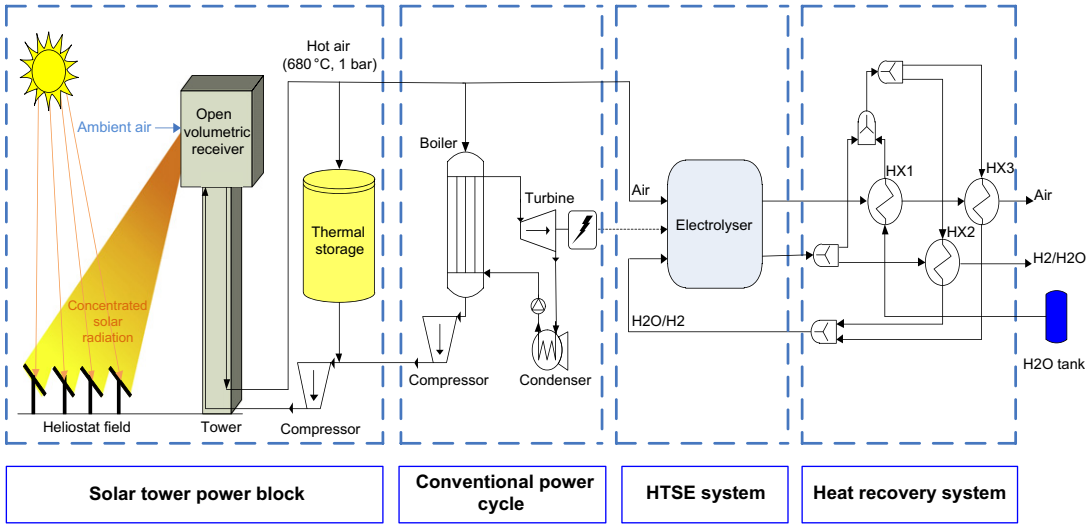

FIGURE 4.26 Flow diagram of the solar tower coupled to the high-temperature electrolyzer. (For color version of this figure, the reader is reffered to the online version of this book.)

The solar Tower plant uses an open volumetric receiver, where the air will be heated up to a temperature at about 700 °C. A part of the solar heat powers a steam generator, while the other part of the heated air is used as sweep gas in the electrolyzer. A thermal storage system is integrated into the power cycle in order to run the electrolyzer, which can be used to balance energy demand between daytime and night time. Figure 4.26 shows the flow diagram of the solar Tower technology coupled to the high-temperature electrolyzer.

The steam used for the electrolysis process has to respond to some quality requirements. Therefore, the steam used for the electricity generation cannot be used in the electrolyzer.

The heat recovery system consists of two medium heat exchangers. The water stream from the tank will be divided into two substreams in order to increase the operating temperature of the electrolyzer. The heat of the oxygen stream leaving the electrolyzer will be used to evaporate the water from the tank. Then, the evaporated water stream will be divided into two substreams. The first substream will be overheated in the heat exchanger HX2 by the O_2 stream leaving the heat exchanger HX1.

4.4.3 Operation Modes

There are three possible modes for the operation of the high-temperature electrolyzer:

- Exothermal mode: the outlet gases have a higher temperature than the inlet gases. This operation mode is characterized by a cell voltage, which is higher than the thermoneutral voltage.
- Isothermal mode: the outlet gases have the same temperature as the inlet gases.
- Endothermal mode: the temperature of the outlet streams is less than the one of the inlet streams.

4.5 CONCLUSIONS

While developing solar high-temperature processes, several challenges regarding materials, components, separation issues and operational strategies are being addressed to make such processes practicable and commercially available. Other challenges are the temporal change of load and spatial temperature gradients. Selection, qualification and certification of suitable construction, catalyst and redox materials for key components are major objectives of research. Commercial plants with more than 100 MWth are envisaged in the long term. Almost all carbon-free solar thermal hydrogen production processes are in an early development stage. First commercial plants for mass production are expected to be available after 2020.

High-temperature electrolysis of water is one interesting candidate for solar thermal water splitting due to its higher efficiency compared to room temperature alkaline or PEM electrolysis. But still major effort is necessary to avoid or at least to significantly reduce the degradation of the materials caused by the high operating temperature.

The main challenge of the direct water splitting consists of the separation of hydrogen from the product gas. Two main separation strategies have been presented at different temperature levels. The separation at high temperature level appears to be the most relevant separation strategy but requires materials of the reactor, which can resist the high temperatures and which are not state-of the-art, yet.

The copper–chlorine cycle, which consists of four steps, is a promising thermochemical cycle due to the fact that the hydrogen production step takes place at low temperatures. In addition to that, the electrochemical step of this cycle is an electrochemical step with low voltage requirement. Challenges still have to be addressed concerning reaction selectivities and product separation.

Sulfur-based cycles represent processes that comprise as one central step, the industrially and widely established process, of decomposition of sulfuric acid. This is the process step that couples in concentrated solar energy at temperatures significantly below 1200 K. As the most prominent examples of sulfur-based cycles, the SI cycle and the two-step HyS are particularly promising since they exhibit low, specific hydrogen costs at high efficiencies. All reaction steps have been successfully demonstrated and reached a level of maturity sufficient for the development of a pilot plant. Future improvements of catalyst and construction materials need to be addressed for an industrial realization.

So-called redox cycles based on metal–MO pairs are extensively investigated by many groups today. The most promising material families are based on rare-earth metals or ferrites. A number of process concepts have been introduced to integrate such cycle in a solar plant. Some are based on particle technologies, others use monolithic bodies made of or coated by the active redox material. The main challenge of those processes remains the availability of sufficiently active and stable redox materials.

Nevertheless, estimated hydrogen costs for long-term carbon-free solar water-splitting processes based on current process designs predict a very high potential. Nevertheless, aspects concerning market penetration and mass production of materials and components should be considered along with research and development work. When considering energy losses and additional costs by the long-distance transport of hydrogen as a fuel, thermal processes seem only viable if fuel prices rise significantly compared to the current level in Europe. But here again, other already established and existing sectors need to be taken into account. The increasing industrial hydrogen demand in countries with high direct solar radiation will be the most important driver for the development of solar thermal processes and the realization of pilot plants in the short- to mid-term. There is potential to cover the estimated hydrogen demand of around 2 EJ by numerous commercial solar thermal plants in the future. Sites for pilot plants on commercial scale require a high direct solar radiation above 2000 kWh/m^2 yr and the large-scale availability of water. Solar cleaning and desalination of seawater (e.g. by multieffect distillation or reverse osmosis) appears to be an obligatory complementary in order to supply the water demand for hydrogen production. Solar thermal processes promise a huge potential for carbon-free and sustainable hydrogen production on large scale, using solar energy and water as clean and abundant sources for hydrogen.

References

1. Verhelst, S.; Wallner, T. Hydrogen-Fueled Internal Combustion Engines. *Progr. Energ. Combust. Sci.* **2009,** *35,* 490–527.
2. Ananthachar, V.; Duffy, J. J. Efficiencies of Hydrogen Storage Systems Onboard Fuel Cell Vehicles. *Sol. Energ.* **2005,** *78,* 687–694.
3. Boudriesa, R.; Dizene, R. Potentialities of Hydrogen Production in Algeria. *Int. J. Hydrogen Energ.* **2008,** *33,* 4476–4487.
4. Baykara, S. Z. Experimental Solar Water Thermolysis. *Int. J. Hydrogen Energ.* **2004,** 1459–1469.
5. Bilgen, E.; Galindo, J.; Baykara, S. Z. "Experimental Study of Hydrogen Production by Direct Decomposition of Water," presented at the Proceedings of the 18th IECEC. Orlando, USA, 1983.
6. Warner, J. Hydrogen Separation and the Direct High-Temperature Splitting of Water. *Int. J. Hydrogen Energ.* **1986,** 91–100.
7. Bilgen, E.; Ducarroir, M.; Foex, M.; Sibieude, F. Use of Solar Energy for Direct and Two-Step Water Decomposition Cycles. *Int. J. Hydrogen Energ.* **1977,** *2,* 251–257.
8. Steinfeld, A.; Meier, A. Solar Fuels and Materials *Encyclopedia of Energy,* Vol. 5; Elsevier, 2004.
9. Steinfeld, A.; Sanders, S.; Palumbo, R. Design Aspects of Solar Thermochemical Engineering—A Case Study: Two-Step Water-Splitting Cycle Using the Fe_3O_4/FeO Redox System. *Sol. Energ.* **1999,** *65,* 43–53.
10. Tsuji, M.; Togawa, T.; Wada, Y.; Sano, T.; Tamaura, Y. Kinetic Study of the Formation of Cation-Excess Magnetite. *J. Chem. Soc. Faraday Trans.* **1995,** *91,* 1533–1538.
11. Sturzenegger, M.; Nüesch, P. Efficiency Analysis for Manganese-Oxide-Based Thermochemical Cycle. *Energy* **1999,** *24,* 959–970.
12. Steinfeld, A. Solar Hydrogen Production via a Two-Step Water-Splitting Thermochemical Cycle Based on Zn/ZnO Redox Reactions. *Int. J. Hydrogen Energ.* **2002,** *27,* 611–619.
13. Lundberg, M. Model Calculations on Some Feasible Two-Step Water Splitting Processes. *Int. J. Hydrogen Energ.* **1993,** *18,* 369–376.
14. Perkins, C.; Weimer, A. W. Likely Near-Term Solar-Thermal Water Splitting Technologies. *Int. J. Hydrogen Energ.* **2004,** *29,* 1587–1599.
15. M. Kerins, J. Martinek,; J. Wyss, "Solar-Thermal Thermochemical Mn_2O_3/MnO Cycle to Split Water for Large Scale Hydrogen Production in the Desert Southwest," 2005.
16. L. C. Brown, B. Wong,; B. Buckingham, "Solar Production of Hydrogen Using a Cadmium Based Thermochemical Cycle," presented at the American Institute of Chemical Engineers. Salt Lake City, Utah. 2007.
17. Perret, R. Solar Thermochemical Hydrogen Production Research (STCH) Thermochemical Cycle Selection and Investment Priority. *SAND* **2011,** 3622.
18. Abanades, S.; Charvin, P.; Lemort, F.; Flamant, G. Novel Two-Step SnO_2/SnO Water-Splitting Cycle for Solar Thermochemical Production of Hydrogen. *Int. J. Hydrogen Energ.* **2008,** *33,* 6021–6030.
19. Sibieude, F.; Ducarroir, M.; Tofighi, A.; Ambriz, J. High Temperature Experiments with a Solar Furnace: the Decomposition of Fe_3O_4, Mn_3O_4, CdO. *Int. J. Hydrogen Energ.* **1982,** *7,* 79–88.

20. Steinfeld, A. Solar Thermochemical Production of Hydrogen—A Review. *Sol. Energ.* **2005,** *78,* 603−615.
21. Diver, R. B.; Miller, J. E.; Allendorf, M. D.; Siegel, N. P.; Hogan, R. E. Solar Thermochemical Water-Splitting Ferrite-Cycle Heat Engines. *J. Sol. Energ. Eng.* **2008,** *130,* 41001−41008.
22. Diver, R. B.; Siegel, N. P.; Moss, T. A.; Miller, J. E.; Evans, L. R.; Hogan, R. E.; Allendorf, M. D.; Stuecker, J. N.; James, D. L. *Innovative Solar Thermochemical Water Splitting;* SANDIA National Laboratories: Albuquerque, NM, 2008. SAND2008−0878.
23. Tamaura, Y.; Kojima, M.; Sano, T.; Ueda, Y.; Hasegawa, N.; Tsuji, M. Thermodynamic Evaluation of Water Splitting by a Cation-Excessive (Ni, Mn) Ferrite. *Int. J. Hydrogen Energ.* **1998,** *23,* 1185−1191.
24. Aoki, H.; Kaneko, H.; Hasegawa, N.; Ishihara, H.; Takahashi, Y.; Suzuki, A.; Tamaura, Y. *Two-Step Water Splitting with Ni-Ferrite System for Solar H_2 Production Using Concentrated Solar Radiation;* ISEC: Portland, Oregon, 2004.
25. Coker, E. N.; Rodriguez, M. A.; Ambrosini, A. and Miller, J. E. "Thermochemical Cycle for H_2 and CO Production: Some Fundamental Aspects." 15th Solar PACES International Symposium. 15−18 September 2009.
26. Gokon, N.; Takahashi, S.; Yamamoto, H.; Kodama, T. Thermochemical Two-Step Water-Splitting Reactor with Internally Circulating Fluidized Bed for Thermal Reduction of Ferrite Particles. *Int. J. Hydrogen Energ.* **2008,** *33,* 2189−2199.
27. Tamaura, Y.; Kojima, N.; Hasegawa, N.; Inoue, M.; Uehara, R.; Gokon, N.; Kaneko, H. Stoichiometric Studies of H_2 Generation Reaction for $H_2O/Zn/Fe_3O_4$ System. *Int. J. Hydrogen Energ.* **2001,** *26,* 917−922.
28. Roeb, M.; Sattler, C.; Klüser, R.; Monnerie, N.; Oliveira, L. d.; Konstandopoulos, A. G.; Agrafiotis, C.; Zaspalis, V. T.; Nalbandian, L.; Steele, A. M.; Stobbe, P. Solar Hydrogen Production by a Two-Step Cycle based on Mixed Iron Oxides. *J. Sol. Energ. Eng.* **2006,** *128,* 125−133.
29. Agrafiotis, C.; Roeb, M.; Konstandopoulos, A. G.; Nalbandian, L.; Zaspalis, V. T.; Sattler, C.; Stobbe, P.; Steele, A. M. Solar Water Splitting for Hydrogen Production with Monolithic Reactors. *Sol. Energ.* **2005,** *79,* 409−421.
30. Wegner, K.; Ly, H. C.; Weiss, R. J.; Pratsinis, S. E.; Steinfeld, A. In situ Formation and Hydrolysis of Zn Nanoparticles for H_2 Production by the 2-Step ZnO/Zn Water-Splitting Thermochemical Cycle. *Int. J. Hydrogen Energ.* **2006,** *31,* 55−61.
31. Palumbo, R.; Lede, J.; Boutin, O.; Ricart, E. E.; Steinfeld, A.; Möller, S.; Weidenkaff, A.; Fletcher, E. A.; Bielicki, J. The Production of Zn from ZnO in a High-Temperature Solar Decomposition Quench Process - I. The Scientific Framework for the Process. *Chem. Eng. Sci.* **1998,** *53,* 2503−2517.
32. Meier, A.; Steinfeld, A. Solar Thermochemical Production of Fuels. *Adv. Sci. Tech.* **2010,** *74,* 303−312.
33. Schunk, L. O.; Haeberling, P.; Wepf, S.; Wuillemin, D.; Meier, A.; Steinfeld, A. A Receiver-Reactor for the Solar Thermal Dissociation of Zinc Oxide. *J. Sol. Energ. Eng.* **2008,** *130,* 021009−021015.
34. Wieckert, C.; Frommherz, U.; Kräupl, S.; Guillot, E.; Olalde, G.; Epstein, M.; Santén, S.; Osinga, T.; Steinfeld, A. A 300 kW Solar Chemical Pilot Plant for the Carbothermic Production of Zinc. *J. Sol. Energ. Eng.* **2007,** *129,* 190−196.
35. Abanades, S.; Flamant, G. Thermochemical Hydrogen Production from a Two-Step Solar-Driven Water-Splitting Cycle Based on Cerium Oxides. *Sol. Energ.* **2006,** *80,* 1611−1623.
36. Haile, S. *New Reactor Paves the Way for Efficiently Producing Fuel from Sunlight*. 2011.
37. Chueh, W. C.; Falter, C.; Abbott, M.; Scipio, D.; Furler, P.; Haile, S. M.; Steinfeld, A. High-Flux Solar-Driven Thermochemical Dissociation of CO_2 and H_2O Using Nonstoichiometric Ceria. *Science* **2010,** *330,* 1797−1801.
38. Beghi, G. E. A Decade of Research on Thermochemical Hydrogen at the Joint Research Centre, ISPRA. *Int. J. Hydrogen Energ.* **1986,** *11,* 761−771.
39. Baerns, M.; Behr, A.; Brehm, A.; Gmehling, J.; Hofmann, H.; Onken, U.; Renken, A. *Technische Chemie,* 1st ed.; Wiley-VCH: Weinheim, 2006.
40. Debuch, C. P.; Markworth, E. "Method for the Treatment of Waste Sulphuric Acid." United States Patent. 1937.
41. Titlestad, N. "Sulphuric Acid Regeneration." United States Patent. 1946.
42. Barin, I. *Thermochemical Data of Pure Substances;* VCH, 1989.
43. Noglik, A.; Roeb, M.; Rzepczyk, T.; Hinkley, J.; Sattler, C.; Pitz-Paal, R. Solar Thermochemical Generation of Hydrogen: Development of a Receiver Reactor for the Decomposition of Sulfuric Acid. Transactions of the Asme. *J. Sol. Energ. Eng.* **2009,** *131*.
44. Broggi, A.; Joels, R. K.; Mertel, G.; Morbello, M.; Spelta, B. "Cristina—A Process for the Decomposition of Sulfuric Acid." in *3rd World Hydrogen Energy Conference*. Tokyo, Japan, 1980, pp. 1929−1937.
45. Broggi, A.; Langenkamp, H.; Mertel, G.; Velzen, D. V. "Decomposition of Sulfuric Acid by the CRISTINA Process—A Status Report." in *Hydrogen Energy Progress 2*, New York, 1982, pp. 611−621.
46. General Atomics. Decomposition of Sulfuric Acid Using Solar Thermal Energy, GA-A17573. *General Atomics GA-A17573* **1985**.
47. General Atomics. High-Pressure Catalytic Metal Reactor in a Simulated Solar Central Receiver, GA-A18285. *General Atomics GA-A18285* **1986**.
48. Gelbard, F.; Moore, R.; Parma, E. *Status of Initial Testing of the H2SO4 Section of the ILS Experiment;* Sandia National Laboratories, 2007.
49. Noglik, A.; Roeb, M.; Sattler, C.; Pitz-Paal, R. Experimental Study on Sulfur Trioxide Decomposition in a Volumetric Solar Receiver-Reactor. *Int. J. Energ. Res.* **2009,** *33,* 799−812.
50. Thomey, D.; de Oliveira, L.; Säck, J-P.; Roeb, M.; Sattler, C. "Development and Test of a Solar Reactor for Decomposition of Sulphuric Acid in Thermochemical Hydrogen Production." *Int. J. Hydrogen Energ.* **2012**, *37*, 16615−16622.
51. Onuki, K.; Kubo, S.; Terada, A.; Sakaba, N.; Hino, R. Thermochemical Water-Splitting Cycle Using Iodine and Sulfur. *Energ. Environ. Sci.* **2009,** *2,* 491−497.
52. Kim, C. S.; Hong, S.-D.; Kim, Y.-W.; Kim, J.-H.; Lee, W. J.; Chang, J. Thermal Design of a Laboratory—Scale SO_3 Decomposer for Nuclear Hydrogen Production. *Int. J. Hydrogen Energ.* **2008,** *33,* 3688−3699.
53. Le Duigou, A.; Borgard, J.-M.; Larousse, B.; Doizi, D.; Allen, R.; Ewan, B. C.; Priestman, G. H.; Elder, R.; Devonshire, R.; Ramos, V., et al. HYTHEC: An EC Funded Search for a Long Term Massive Hydrogen Production Route Using Solar and Nuclear Technologies. *Int. J. Hydrogen Energ.* **2007,** *32,* 1516−1529.
54. Norman, J. H. "Process for the Thermochemical Production of Hydrogen." US Patent 4089940, 1978.
55. Norman, J. H.; Mysels, K. J.; Sharp, R.; Williamson, D. Studies of the Sulfur−Iodine Thermochemical Water-Splitting Cycle. *Int. J. Hydrogen Energ.* **1982,** *7,* 545−556.
56. O'Keefe, D.; Allen, C.; Besenbruch, G.; Brown, L.; Norman, J.; Sharp, R.; McCorkle, K. Preliminary Results from Bench-Scale Testing of a Sulfur−Iodine Thermochemical Water-Splitting Cycle. *Int. J. Hydrogen Energ.* **1982,** *7,* 381−392.
57. I. A. E. Agency. *Hydrogen as an Energy Carrier and Its Production by Nuclear Power;* International Atomic Energy Agency, 1999.
58. Schultz, K. R. "Use of the Modular Helium Reactor," in *World Nuclear Association Annual Symposium*, London, 2003, pp. 1−11.

59. Roeb, M; Noglik, A.; Rietbrock, P. M.; Mohr, S.; Oliveira, L. D.; Sattler, C.; Cerri, G. G.; Maria, G. d.; Giovanelli, A.; Buenaventura, A.; et al. ""HYTHEC: Development of a Dedicated Solar Receiver-Reactor for the Decomposition of Sulphuric Acid," in *European Hydrogen Energy Conference EHEC 2005*: Zaragoza, Spain, 2005.
60. Roth, M.; Knoche, K. F. Thermochemical Water Splitting Through Direct Hi-Decomposition from $H_2O/HI/I_2$ Solutions. *Int. J. Hydrogen Energ.* **1989,** *14,* 545−549.
61. Kubo, S.; Kasahara, S.; Okuda, H.; Terada, A.; Tanaka, N.; Inaba, Y.; Ohashi, H.; Inagaki, Y.; Onuki, K.; Hino, R. A Pilot Test Plan of the Thermochemical Water-Splitting Iodine-Sulfur Process. *Nucl. Eng. Des.* **2004,** *233,* 355−362.
62. Yamawaki, M.; Nishihara, T.; Inagaki, Y.; Minato, K.; Oigawa, H.; Onuki, K.; Hino, R.; Ogawa, M. Application of Nuclear Energy for Environmentally Friendly Hydrogen Generation. *Int. J. Hydrogen Energ.* **2007,** *32,* 2719−2725.
63. Goldstein, S.; Borgard, J.-M.; Vitart, X. Upper Bound and Best Estimate of the Efficiency of the Iodine Sulphur Cycle. *Int. J. Hydrogen Energ.* **2005,** *30,* 619−626.
64. Kasahara, S.; Kubo, S.; Hino, R.; Onuki, K.; Nomura, M.; Nakao, S.-i. Flowsheet Study of the Thermochemical Water-Splitting Iodine-Sulfur Process for Effective Hydrogen Production. *Int. J. Hydrogen Energ.* **2007,** *32,* 489−496.
65. Wong, B.; Buckingham, R. T.; Brown, L. C.; Russ, B. E.; Besenbruch, G. E.; Kaiparambil, A.; Santhanakrishnan, R.; Roy, A. Construction Materials Development in Sulfur−Iodine Thermochemical Water-Splitting Process for Hydrogen Production. *Int. J. Hydrogen Energ.* **2007,** *32,* 497−504.
66. Brecher, L. E. and Wu, C. K. "Electrolytic Decomposition of Water." *United States Patent*, 1975.
67. Brecher, L. E.; Spewock, S.; Warde, C. J. "The Westinghouse Sulfur Cycle for the Thermochemical Decomposition of Water." in *1st World Hydrogen Energy Conference, Conference Proceedings*, Miami Beach, Florida. 1976, pp. 9A-1-9A-16.
68. Bilgen, E. Solar Hydrogen Production by Hybrid Thermochemical Processes. *Sol. Energ.* **1988,** *41,* 199−206.
69. Jeong, Y. H.; Kazimi, M. S.; Hohnholt, K. J.; Yildiz, B. *Optimization of the Hybrid Sulfur Cycle for Hydrogen Generation;* Massachusetts Institute of Technology, Center for Advanced Nuclear Energy Systems: Cambridge, MA, 2005.
70. Corgnale, C.; Summers, W. A. Solar Hydrogen Production by the Hybrid Sulfur Process. *Int. J. Hydrogen Energ.* **2011,** *36,* 11604−11619.
71. Graf, D.; Monnerie, N.; Roeb, M.; Schmitz, M.; Sattler, C. Economic Comparison of Solar Hydrogen Generation by Means of Thermochemical Cycles and Electrolysis. *Int. J. Hydrogen Energ.* **2008,** *33,* 4511−4519.
72. Lu, P. W. T. Technological Aspects of Sulfur Dioxide Depolarized Electrolysis for Hydrogen Production. *Int. J. Hydrogen Energ.* **1983,** *8,* 773−781.
73. Lewis, M. A.; Serban, M. and Basco, J. K. "Hydrogen Production at <550 °C Using a Low Temperature Thermochemical Cycle." *Presented at the ANS/ENS Exposition New Orleans*, USA, 2003.
74. Sadhankar, R.; Li, H.; Ryland, D. K.; Suppiah, S. "Future Hydrogen Production Using Nuclear Reactors," Presented at the *Climate Change Technology Conference*, Ottawa, Canada, 2006.
75. Orhan, M.; Dincer, I.; Rosen, M. A. Energy and Exergy Assessments of the Hydrogen Production Step of a Copper−Chlorine Thermochemical Water Splitting Cycle Driven by Nucleus-Based Heat. *Int. J. Hydrogen Energ.* **2008,** *33,* 6456−6466.
76. Rosen, M.; Naterer, G.; Suppiah, S. "Nuclear-Based Hydrogen Production with a Thermochemical Copper−Chlorine Cycle and Supercritical Water Reactor," Presented at the *Canadian Hydrogen Association Workshop*, Quebec, Canada, 2006.
77. M. A. Lewis, M. Serban,; J. K. Basco, "Kinetic Study of the Hydrogen and Oxygen Production Reactions in the Copper-Chloride Thermochemical Cycle," in AIChE Spring National Meeting, 2004.
78. Lewis, M. A.; Masin, J. G.; Vilim, R. B. *Development of the Low Temperature Cu-Cl Thermochemical Cycle;* International Congress on Advances in Nuclear Power Plants: Seoul, Korea, 2005.
79. Naterer, G.; Gabriel, K.; Wang, Z.; Daggupati, V.; Gravelsins, R. Thermochemical Hydrogen Production with a Copper−Chlorine Cycle. *Int. J. Hydrogen Energ.* **2008,** *33,* 5439−5489.
80. O'Brien, J. E. Thermodynamics and Transport Phenomena in High Temperature Steam Electrolysis Cells. *J. Heat Tran.* **2012,** *134,* 1−11.
81. Strickler, D. W.; Carlson, W. G. Ionic Conductivity of Cubic Solid Solutions in the System $CaO-Y_2O_3-ZrO_2$. *J. Am. Ceram. Soc.* **1964,** *3,* 122−130.
82. Badwal, S.; Ciacchi, F.; Milosevic, D. Scandia-Zirconia Electrolytes for Intermediate Temperature Solid Oxide Fuel Cell Operation. *Solid State Ionics* **2000,** 91−100.
83. Hirano, M.; Inagaki, M.; Mizutani, Y.; Nomura, K.; Kawai, M.; Nakamura, Y. Mechanical and Electrical Properties of Sc_2O_3-Doped Zirconia Ceramics Improved by Postinterning with HIP. *Solid State Ionics* **2000,** 1−9.
84. Etsell, T.; Flengas, S. Electrical Properties of Solid Oxide Electrolytes. *Chem. Rev.* **1970,** 339−415.
85. Iwahara, H.; Uchida, H.; Yamasaki, I. High-Temperature Steam Electrolysis Using $SrCeO_3$-Based Proton Conductive Solid Electrolyte. *Int. J. Hydrogen Energ.* **1987,** 79−80.
86. Jiang, S.; Chan, S. A Review of Anode Materials Development in Solid Oxide Fuel Cells. *J. Mat. Sci.* **2004,** 4405−4444.
87. Uchida, H.; Osada, N.; Watanabe, M. High-Performance Electrode for Steam Electrolysis Mixed Conducting Ceria-Based Cathode with Highly-Dispersed Ni Electrocatalysts. *Electrochem. Solid State Lett.* **2004,** 500−502.
88. Mogensen, M.; Primdahl, S.; Jorgensen, M.; Bagger, C. Composite Electrodes in Solid Oxide Fuel cells and Similar Solid State Devices. *J. Electroceram.* **2000,** 141−193.
89. Koll, G.; Schwarzbözl, P.; Hennecke, K.; Schmitz, M. and Hoffschmidt, B. "The Solar Tower Jülich—A Research and Demonstration Plant for Central Receiver Systems." in *Proceedings of the 15th Solar PACES Symposium*, Berlin, Germany, 2009.

CHAPTER

5

Biomass Sources for Hydrogen Production

Víctor Martínez-Merino, María José Gil, Alfonso Cornejo

Dept. Química Aplicada, Universidad Pública de Navarra, Pamplona, Spain

OUTLINE

5.1 Introduction 87

5.2 Biomass Composition and Properties 89

5.3 Biomass Resource Potential 92

5.4 Pretreatment of Biomass Feedstocks 94
- *5.4.1 Physical and Thermal Pretreatments* 94
  - 5.4.1.1 Particle Size Reduction 94
  - 5.4.1.2 Irradiation 94
  - 5.4.1.3 Drying 95
  - 5.4.1.4 Steam Pretreatment 95
  - 5.4.1.5 Liquid Hot Water Pretreatment 95
- *5.4.2 Chemical Pretreatments* 95
  - 5.4.2.1 Acidic Pretreatments 95
  - 5.4.2.2 Alkali Pretreatments 96
  - 5.4.2.3 Ammonia Pretreatments 96
  - 5.4.2.4 IL Pretreatments 96
- *5.4.3 Biological Pretreatments* 97

5.5 Methodologies for the Production of Hydrogen from Biomass 98
- *5.5.1 Thermochemical Gasification Coupled with Water–Gas Shift* 98
- *5.5.2 Fast Pyrolysis Followed by Reforming of Bio-oil* 101
- *5.5.3 Aqueous Phase Reforming* 102
- *5.5.4 Supercritical Water-Mediated Transformations of Biomass* 103
- *5.5.5 Microbial Conversion of Biomass* 104
  - 5.5.5.1 Dark Fermentation 104
  - 5.5.5.2 Photofermentation 105

5.6 Life Cycle Assessment and Hydrogen Production Costs 105

References 107

5.1 INTRODUCTION

Nowadays, commercial hydrogen is being mainly produced by using nonrenewable raw materials: nearly 90% of hydrogen is obtained by steam reforming either from natural gas or naphtha fractions from oil, whereas gasification of coal and electrolysis of water are industrially used in a minor extent. On one hand these processes are highly energy intensive and not always environmentally friendly; on the other hand fossil fuel reserves worldwide are depleting at an alarming rate. Therefore, sustainable production of hydrogen by exploiting alternative sources seems imperative for the developing of a true hydrogen economy. Biomass is abundant, environmental friendly and renewable, hence, the production of hydrogen from biomass represents a promising approach. Biomass-derived hydrogen is likely to become a fuel for a more sustainable future.

Biomass, mainly in the form of wood, is the oldest source of energy that has been used by humans, traditionally by direct combustion in a very inefficient process. Alternatively, converting biomass into gaseous and liquid fuels, electricity and especially hydrogen, is undoubtedly a more efficient way of biomass utilization. Within this context, and although not fully developed yet, there are some competitive processes for obtaining hydrogen from biomass,[1,2] thus the use of biomass as a major feedstock is gaining considerable attention. Hydrogen from biomass presents many advantages such as independence from oil imports, net product

http://dx.doi.org/10.1016/B978-0-444-56352-1.00005-2

remains within the country, stable pricing level, peace keeping, and also an improvement of the CO_2 balance that can be around 30%.[3]

Biomass is the plant material derived from the reaction between CO_2 in the air, water and sunlight, by means of the photosynthesis to produce mainly carbohydrates ($C_nH_{2n}O_n$), that are building blocks of biomass that efficiently store chemical energy.[4]

The list of plant species, byproducts and waste materials that can be potentially used as feedstock is almost endless.[5] Hence, biomass is the most versatile renewable resource that can be used for the sustainable production of hydrogen. Last but not least, biomass is renewable and consumes atmospheric CO_2 during plant growth; after the biomass treatment for extracting the chemical energy stored in its chemical bonds the carbon is oxidized to produce CO_2 and water, releasing the previously "trapped" CO_2 that is again available to produce new biomass. Consequently, if biomass was processed efficiently, the production of hydrogen may have a small net CO_2 impact when compared to fossil fuels.

Despite the versatility of biomass, most of the energy produced from biomass comes nowadays from wood and wood wastes (64%), followed by municipal solid waste (MSW) (24%), agricultural waste (5%) and landfill gases (5%). Biomass resources can be roughly divided into four general categories[6]:

- *Energy crops*: herbaceous energy crops, woody energy crops, industrial crops, agricultural crops and aquatic crops.
- *Agricultural residues (AR) and waste*: crop and animal waste.
- *Forestry waste and residues*: mill wood waste, logging residues, trees and shrub residues.
- *Industrial and municipal wastes*: MSW, sewage sludge and industrial waste.

Energy crops[7] are those annual and perennial species that are specifically cultivated to produce solid, liquid or gaseous forms of energy. The main characteristics that an energy crop must fulfill are the following: high yield (maximum production of dry matter per hectare), low energy input to produce biomass, low cost, low contaminant matter composition and low nutrient requirements. Potential energy crops include woody crops and grasses/herbaceous plants, sweet sorghum, starch and sugar crops as well as oilseeds that can be used as raw material for hydrogen production.[4]

Currently, commercial production of biofuels comes from conversion of sugar (sucrose), starch or oil crops, termed "first generation feedstock".[8] The production processes for these biofuels are technologies developed mainly for liquid biofuels.[9] Nevertheless, using food crops to produce fuels raises a number of problems: their costs can be high, particularly in Europe, compared to the net energy balance that is still low; furthermore the use of high quality arable land for biofuels production competes with the requirements for food production.

Biofuels can also be produced from other raw materials of the so-called "second generation feedstock". In particular, lignocellulosic resources have potential benefits as better environmental performance, low life-cycle carbon emissions, no associated land-use changes and huge potential. These feedstocks are in particularly short rotation coppices (poplar, willow, and eucalyptus) and many herbaceous lignocellulosic crops (miscanthus, switchgrass or reed canary grass).

Alternatively, moderately dried wastes such as wood residue, wood scrap and urban garbage can be directly burned as fuel. Water-containing biomass such as sewage sludge, agricultural and livestock effluents as well as animal excreta is processed mainly by microbial fermentation. Agricultural and forestry wastes, as well as industrial effluents from sources such as the pulp/paper and food industries, are mainly constituted by lignocellulosic material that can offer an economic, environmental-friendly way for renewable hydrogen production (Table 5.1).

Microalgal farming has been also described as a big challenge and opportunity for the biofuels industry.[10] Microalgae present a simple cellular structure, rapid rate of reproduction together with a high photosynthetic efficiency. Moreover, many microalgal strains can be grown under harsh conditions. Indeed, microalgae can be grown with almost no need of soil (e.g. 49 or 132 times less soil requirement than commonly used rapeseed or soybean crops) and they show a big ability for capturing CO_2 and other greenhouse gases, together with a short harvesting cycle.[11] Undoubtedly, these are evident

TABLE 5.1 List of Some Biomass Wastes Used for Hydrogen Production

Biomass species	Main conversion process
Bio-nut shell	Steam gasification
Olive husk	Pyrolysis
Tea waste	Pyrolysis
Crop straw	Pyrolysis
Black liquor	Steam gasification
Municipal solid waste	Supercritical water extraction
Crop grain residue	Supercritical fluid extraction
Pulp and paper waste	Microbial fermentation
Manure slurry	Microbial fermentation
Petroleum basis plastic waste	Supercritical fluid extraction

Source: From Ref. 7.

advantages over first and second generation feedstocks and therefore microalgae are emerging as the "third generation feedstock" for biofuels production.

Microalgae species can be adapted to live in a variety of environmental conditions. Thus, it is possible to find the species that suits better to specific growth characteristics (i.e. less soil requirements), which is not possible with other current biofuel feedstocks as soybean, rapeseed, sunflower or palm oil.[12]

The efficiency of microalgal biomass production is influenced by the cultivation systems: open versus closed pond systems, photobioreactors and by environmental conditions such as light intensity and wavelength, temperature, CO_2 concentration, nutrient composition, salinities and mixing conditions.

Microalgae have high carbohydrate and lipid contents, so they can be used to produce various biofuels. Biodiesel production needs microalgae which have a higher lipid content; bioethanol and biohydrogen production needs more carbohydrate (i.e. some microalgae contain over 30% of carbohydrate content such as *Scenedesmus dimorphus*, *Spirogyra* sp., *Prymnesium parvum*, *Porphyridium cruentum* and *Anabaena cylindrica*).[11] In addition, the residual microalgae biomass (e.g. *Scenedesmus*) derived from oil extraction processes has been also used to produce hydrogen.[13] Some studies have already demonstrated the viability of the production of hydrogen from *Cladophora fracta* and *Chlorella protothecoides* through pyrolysis and steam gasification.[14] A large number of unicellular, filamentous, fresh water, and marine cyanobacterial species and strains have been reported to produce large amounts of hydrogen (i.e. *Gloeocapsa alpicola*, *Anabaena variabilis*, *Anabaena azollae*, *Arthrospira (Spirulina) platensis*, *A. cylindrica*, *Cyanothece* or *Nostoc muscorum*).[15] *Anabaena* sp. has been reported to produce extraordinarily significant amount of hydrogen, particularly, nitrogen starved cells of *A. cylindrica* produces highest amount of hydrogen (30 ml $H_2/L \cdot h$).[16] Nevertheless, in order to establish the third generation feedstock as a major source of biomass some drawbacks as the high requirements in cost and energy, particularly in agitation, harvesting and drying of biomass must be overcome.

5.2 BIOMASS COMPOSITION AND PROPERTIES

The value of a particular type of biomass for the production of hydrogen depends on its chemical and physical properties that are a function of its chemical composition and structure. The main components of biomass are cellulose, hemicelluloses, lignin, extractives, lipids, proteins, simple sugars, starch, water, hydrocarbons, ashes, and other compounds. Woody plants are composed of fibers closely intertwined, forming a hard outer surface, while herbaceous plants have a lower proportion of lignin compared to cellulose fibers. The "green" parts of plants and the seeds are rich in proteins, starch and/or oil.

According to the composition of biomass, it can be classified into three general classes of feedstocks that could be appropriate for the production of hydrogen: (1) triglyceride feedstocks, (2) carbohydrates and (3) lignocellulosic feedstocks.

Triglyceride feedstocks are comprised of fatty acids and glycerol derived from both vegetal and animal origin. Sources of triglycerides include various vegetable oils, waste oil products (e.g. yellowgrease, trap grease), and algal sources.[17] Although triglycerides are promising feedstocks for the production of hydrogen because of their low O/C ratio,[18] nowadays, vegetable oils are being used mainly for the production of biodiesel by transesterification. Production of biodiesel affords glycerol as a byproduct in large amounts that is a promising feedstock for the hydrogen production by thermochemical and biological processes (see sections 5.5.2, 5.5.3 and 5.5.4).

Regarding the hydrogen production from biomass, carbohydrates are widely used in the form of monomeric glucose or xylose, sucrose (a disaccharide of α-D-glucopyranose and β-D-fructofuranose) and starch (a glucose polysaccharide that consists in a mixture of 10−20% wt amylose, a linear polymer formed by α-1,4 glycoside bonds between glucose units, and 80−90 wt% amylopectin that is a nonlinear polymer where branching takes place with α-1,6 glycoside linkages (Fig. 5.1(A)).

Sucrose and starch crops have been utilized for fuel production due to the relative easiness for their hydrolysis and subsequent fermentation. Amylopectine is water insoluble whereas amylose from starch can be easily hydrolyzed into their constituent sugar monomers (mainly glucose) by the use of inexpensive enzymes, mainly α-amylase and gluco-amylase, in mild reaction conditions.

Lignocelluloses are the fibrous materials forming the cell walls and hence being essential building blocks in plants structure. Lignocellulose consists of three basic polymers: cellulose (≈40% wt, $[C_6H_{10}O_5]_x$), hemicelluloses (≈25% wt, such as xylan $[C_5H_8O_4]_m$), and lignin (≈20% wt $[C_9H_{10}O_3\ (OCH_3)_{0.9-1.7}]_n$). The remaining 15% are minor components that mainly consist of proteins, terpenic oils, fatty acid esters, and small amounts of inorganic compounds commonly known as ashes.

Cellulose is the most plentiful biogenic polymer on earth with an estimated availability of up to 324 000 million m^3 and an annual production of 100 000 million tonnes, a large fraction coming from domestic and

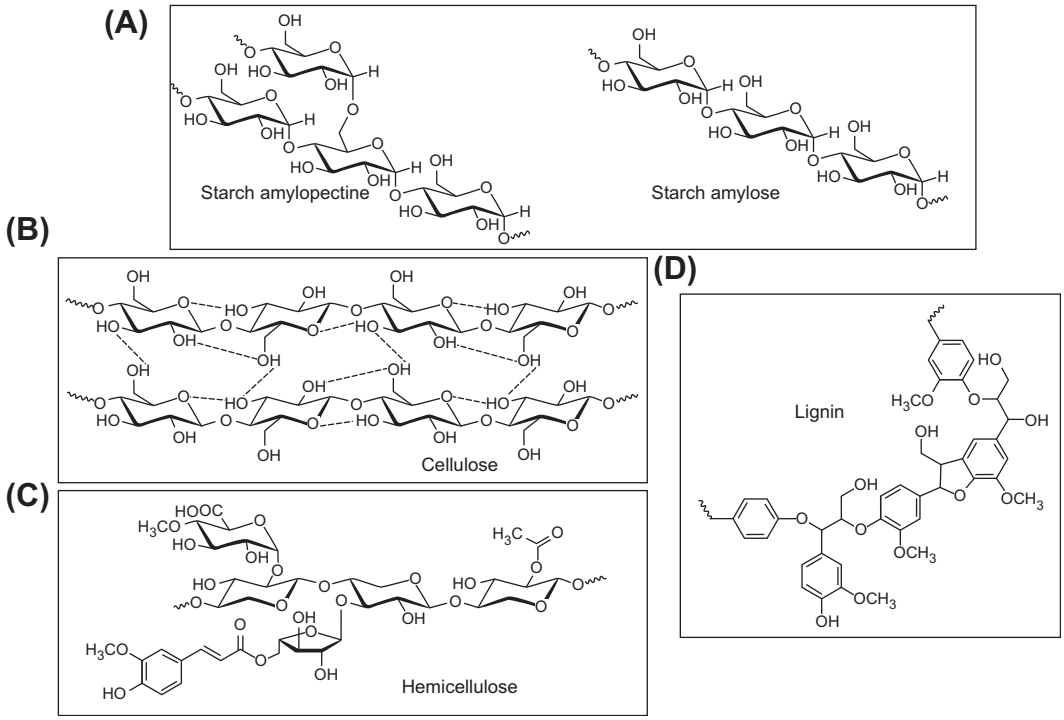

FIGURE 5.1 Chemical structure of biomass derived compounds including: (A) Starches, (B) cellulose, (C) hemicellulose and (D) lignin.

industrial wastes. Cellulose typically accounts for 40–50 wt% of the biomass being an abundant component in plants and wood that appears in different forms. Cellulose is a polymer of glucose whose molecular structure is built up from linearly connected β-D-glucopyranose units (Fig. 5.1(B)). Cellulose chains typically contain around 300–1700 units in wood pulp, and 800–10,000 units in cotton or other plant fibers[19] affording molecular weights ranging from 50 to 2000 kDa. Alternating glucose units within the polymer are rotated by 180° around the axis of the polymer to accommodate optimal bond angles in the acetal oxygen bridges.

Hydroxyl groups are the most abundant functional groups in cellulose and, as a consequence, hydrogen bonding is the main cohesive force in the polymer that is in the origin of the formation of sheets of cellulose chains that are stacked together forming a crystalline material that is recalcitrantly water insoluble.

Crystallinity also hinders the accessibility of catalysts to the acetal groups and hence renders cellulose less easily hydrolyzable. At least seven allomorphic forms have been described for cellulose, but the most relevant polymorphs from an industrial point of view are cellulose I (α and β) and cellulose II.

Hemicellulose is the second major wood chemical constituent accounting for 25–35% of the mass of dry wood, 28% in softwoods, and 35% in hardwoods. From a chemical point of view, hemicelluloses consist of heteropolymeric sugars and sugar acids with a backbone of 1,4-linked β-D-pyranosyl units in which O_4 is in equatorial orientation (Fig. 5.1(C)). The most important component is xylose with small amounts of other hexoses such as D-glucose, D-mannose, D-galactose, pentoses as L-arabinose, and some uronic acids as 4-O-methyl glucuronic acid or galacturonic acid. Typical chains contain about 200 sugar units with a molecular weight around 30 kDa. Hemicelluloses act as the cement material holding together the cellulose micelles and fiber.[20] Contrary to cellulose, their higher chemical complexity does not allow hemicelluloses to form semicrystalline domains; hence random contacts with other structures like cellulose are easier. The hemicelluloses are mostly not extractable by hot water or by treatments with chelating agents but, unlike cellulose, they are extractable in aqueous alkali.

Lignin is an amorphous aromatic polymer (Fig. 5.1(D)) produced from phenylpropanoic precursors[21] that provide plants structural rigidity and a hydrophobic vascular system for the transportation of water and solutes.[22] Natural occurrence of lignin in biomass decreases in order from softwoods (27–33%) > hardwoods (18–25%) > grasses (17–24%).[23] Lignins are produced by the enzymatic dehydrogenative polymerization of coniferyl alcohol (common in softwoods), syringyl alcohol (common in hardwoods) and coumaryl alcohol (common in grasses). All the proposed structures for lignin are approximations since lignin structure is not identical within the complex world of plants.

TABLE 5.2 Chemical Composition of Some Biomass Feedstocks and Two Solid Fossil Fuels (wt%)

Material	Moisture (%)	VM* (% dry)	FC† (% dry)	Ash (% dry)	HHV‡ (MJ/kg)
Wood	20	82	17	1	18.6
Miscanthus	11.5	81.2	15.8	3	18.5
Wheat straw	16	70.2	25	4.8	17.3
Bagasse	45–50	–	–	3.5	19.4
Sewage sludge	6.4	48	5.7	46.3	–
Marine algae	10.7	50.5	25.9	23.6	–
Lignite	10.5	36.7	28.7	34.6	26.8
Bituminous coal	3.1	39.3	50.6	10.1	34

* *Volatile matter.*
† *Fixed carbon content.*
‡ *High heating value.*

Moreover, native lignin undergoes profound structural changes and dramatic modification of molecular weight profiles depending on the isolation technology employed. The basic chemical phenylpropane units of lignin (primarily syringyl, guaiacyl and *p*-hydroxy phenol) are bonded together by a set of intramolecular linkages to form a very complex matrix that comprises a variety of functional groups, such as hydroxyl, methoxy and carbonyl, which give a high polarity to the lignin macromolecule. This complex structure renders lignin the more difficult to hydrolyze constituent of lignocellulosic materials.

The biomass composition determines its properties, quality and potential applications and consequently, the choice of conversion process and any subsequent processing difficulties that may arise. The actual composition of the biomass as an energy source can be determined using different analysis:

- *Proximate analysis*: namely fixed carbon (FC), volatile matter (VM), ash yield, and moisture.
- *Ultimate analysis*: determines the amount of organic elements within the biomass sample (C, O, H, S, N).
- *Ash analysis*: determines the amount of inorganic elements of the biomass sample (Si, Al, Fe, Ca, S, Mg, K, Ti, Na, P, and occasionally Mn, Cl as well as trace elements).

An extensive overview of the chemical composition of biomass was conducted by Vassilev.[24] Data for 86 biomass varieties (woody, grass, straw, shells, pits, agricultural and animal biomass, algae, refuse and contaminated biomass, etc.) were analyzed and compared to fossil fuels. At first sight, the chemical composition of biomass and especially the ash components are highly variable, due to the extremely high variations of moisture, bulk ash yield, and different types of inorganic matter in biomass. However, when the proximate and ultimate analyses are recalculated on dry and dry ash-free bases the compositions are within a quite narrow range (Table 5.2). The order of abundance in decreasing order of the most common elements in biomass is the following: C, O, H, N, Ca, K, Si, Mg, Al, S, Fe, P, Cl, Na, Mn, and Ti. The correlation analysis amongst the elemental composition found five important associations, namely C–H, N–S–Cl, Si–Al–Fe–Na–Ti, Ca–Mg–Mn and K–P–S–Cl. This classification system can be important for the utilization and the processing of biomass to energy and biofuels. For example, the system could help to predict the composition and behavior of inorganic residues, (i.e. ashes formed during combustion and gasification of biomass mixtures).

The moisture content is one of the main properties that determines the technology for the biomass treatment, as well as inorganic materials content and the relative proportion of cellulose and lignin.[25,26]

The *moisture* (M) content of biomass is a relevant property given that thermal conversion processes require low moisture content feedstocks (<50%) whereas microorganisms can efficiently convert wet biomass. The moisture content in biomass usually ranges in the values 3–63% although it can reach even 80% for some raw species.

The VM content of biomass is that portion of biomass that can be driven-off as a gas (including moisture) by heating (1223 K, 7 min). VM commonly includes light hydrocarbons, CO, CO_2, H_2, moisture, and tars. VM is usually about 48–86% that is noticeably higher than in solid fossil fuels (e.g. coal ranges from 12% to 68%).

FC content represents the solid carbon in the biomass that remains in the char after devolatilization in the pyrolysis process. FC includes either elemental carbon in the original fuel, as well as any carbonaceous residue formed upon heating in the determination of the VM. VM and FC provide a measure of the ease to ignite the

biomass, which is related with the ease in gasification or oxidation processes.

Ash is the inorganic solid residue left after the fuel is completely burned. Its major components in the analyzed biomass are silica, aluminum, iron, and calcium together with small amounts of magnesium, titanium, sodium, and potassium. The ash content affects both the handling and processing costs that have a high impact in the overall cost of the biomass conversion to energy. Indeed, the bigger the magnitude of ash, the lower the amount of net biomass that can be converted to energy. For instance, in a biochemical transformation this solid residue represents the quantity of nonbiodegradable matter present in the biomass. Last but not least, ashes can represent operational problems as they can give rise to the formation of liquid phases that can lead to blockages of airways in the furnace and can cause formation of slags, fouling, clogging, and corrosion.

Alkali metal content, the presence of alkali metals (i.e. Na, K, Mg and Ca) can produce side reactions with silica present in the ash, especially in thermochemical processes, affording liquid phases.

Relative proportion of lignocellulosic components. The relative proportion of cellulose, hemicellulose, and lignin can predict the behavior of biomass during pyrolysis. Moreover the cellulose/lignin ratio is a determining factor when selecting biomass for biochemical conversion processes (see section 5.4) given that the biodegradability of cellulose is much higher than that of lignin.[4]

Heating value is the amount of heat that is released by the unit of mass or volume of fuel initially at 25 °C once it is combusted and the products have returned to a temperature of 25 °C (MJ/kg for solids, MJ/l for liquids, or MJ/Nm^3 for gases). It can be expressed in two forms, higher heating value (HHV) that includes the latent heat contained in the water vapor and the lower heating value.[27]

The heating value of biomass is relatively low, especially on a volume basis, because its density is very low. The heating value is strongly dependent on the composition of the biomass, mainly the oxygen to carbon (O/C) and the hydrogen to carbon (H/C) ratios. Biomass presents much higher O/C ratios than those of fossil fuels. The HHV of biomass correlates well with its high O/C and H/C ratios. Indeed, when O/C ratio increases from 0.1 to 0.7, HHV decreases from 38 MJ/kg to about 15 MJ/kg. Nevertheless, when the H/C ratio increases, the effective heating value of the fuel increases (e.g. HHV for methane, ethane and propane are 55.50, 51.90 and 50.35 MJ/kg respectively according to NIST Chemistry Webbook).[28]

Bulk density is defined for the overall space occupied by a given amount of biomass particles (ρ_{bulk} = Total mass of biomass/bulk volume occupied by biomass). This parameter is relevant for transport and storage costs. The low bulk density of biomass makes transportation and handling more difficult and costly. Therefore, long-distance transportation reduces economic and environmental attractiveness of biomass.

5.3 BIOMASS RESOURCE POTENTIAL

The potential of biomass as a renewable energy source, can be envisaged as theoretical, technical, or economic. The theoretical potential describes the amount of biomass that could be grown annually (estimated at 3500 EJ/year worldwide),[29] technical potential depends on the available technologies and therefore is steadily increasing whereas the economic potential is the most variable because economic conditions vary, sometimes drastically, over time when compared to other feedstocks.

Global primary energy consumption in 2002 was estimated in 431 EJ (10 300 million ton oil eq.) and is expected to rise to at least 690 EJ in 2030. Nowadays, conventional biomass (mostly used for heating and cooking in developing countries) covers more than 10% of global primary energy in terms of heating value (50 EJ).[30] Many studies[29–32] have been undertaken to assess the possible contribution of biomass to the future global energy supply. These studies offered very different results (there is almost an order of magnitude of difference between the highest and the lowest estimates for the year 2050) being the major reason three crucial parameters that are uncertain: land availability, yields of energy crops and availability of forest woods and wastes. Furthermore, comparisons are difficult as a consequence of different terminology and systematization of categories as well as insufficient documentation of approaches and scenario assumptions. Nevertheless, most of these studies concluded that biomass has a great potential as a reliable source for the future production of fuels.[33]

Indeed, Bauen[34] estimates that biomass could theoretically provide between 25% and 33% of the global primary energy supply by 2030 (Table 5.3).

However, Smeets, using the Quicksand modeling and including three types of biomass, estimated the possible 2050 technical bioenergy production in 215–1272 EJ/year from energy crops on surplus agricultural land, 76–96 EJ/year from agricultural and forestry residues and wastes and 74 EJ/year from surplus forest growth.[32] Other studies, as that reported by Fischer,[29] estimated the global bioenergy potential in 225 EJ for 1990, although only 46 EJ was actually used, with a potential grow to 370–450 EJ in 2050.

More geographically restricted studies have assessed the biomass resource potential in Europe[35,36] but the

TABLE 5.3 Estimated of Global Biomass Potential by 2030

Region	Energy crops (M ha)	Dry matter (Gt/year)	EJ/year*
Europe	25–90	0.4–1.5	6.3–23.8
USA 2005 BTS	30	1.1	17.5
USA 2011 BTS	25	1.4	22.3
Latin America	121	1.5	23.8
China and India	86	1.7	27.0
Australia	–	<0.004	<0.07

** Million dry tons (Mdt) of biomass account for 1 EJ.*
Source: Adapted from Ref. 34.

outcomes were different because of the heterogeneous approaches and scopes. One thorough estimation about the cost and supply potential of bioenergy crops was reported by De Witt covering EU27 and Ukraine which was based on land availability assessment and a detailed one-by-one kilometer grid size modeling.[37,38] Within the model, agricultural land could increase from 360×10^3 to 600×10^3 km^2 of arable land and from 50×10^3 to 240×10^3 km^2 of grassland and pastures. The study considered several crops: lignocellulosic (poplar, willow, eucalyptus), herbaceous lignocellulosic (miscanthus, switchgrass, reed canary grass), oil crops (sunflower, rapeseed), sugar crops (sugar beet) and starch crops (wheat, rye, triticale, corn). Another important variable was feedstock production costs, that in Europe were in the range of 5.0–15.0 €/GJ for 1st generation feedstocks and 1.5–4.5 €/GJ for 2nd generation feedstocks, whereas AR costs were in the range of 1.0–4.0 €/GJ and forestry residue supply costs lay between 2.0 and 4.0 €/GJ. Estimated primary energy content of the biomass was 1.7–12.2 EJ/year on arable land while herbaceous lignocellulose crops could contribute an additional 1.6–3.6 EJ/year, AR with 3.1–3.9 EJ/year and forestry could add up to 1.4–5.4 EJ/year. Hence, the maximum amount for all resources in EU27 + Ukraine by 2030 was estimated in 27.7 EJ/year.

The Biomass Energy Europe (BEE) project of the European Community (Table 5.4) obtained somehow similar estimated values, after 55 biomass resource assessments were analyzed with the aim of harmonizing data and calculations that will improve the accuracy and comparability of future biomass resource assessments for energy.[39]

Similar studies have also been developed in the US to evaluate the replacement of 30% petroleum consumption in the US by sustainable biomass being the most relevant "The reports Billion-Ton Study" (2005 BTS) and the posterior "US Billion-Ton update" (2011 BTS).[41,42] 2011 BTS attempts to estimate biomass supplies (costs and quantities) and treats environmental sustainability in a more comprehensive and rigorous way than 2005 BTS. The applied POLYSYS simulation estimated that land-use and biomass production will change in time depending on the farmgate prices and yields, as shown in Fig. 5.2 for the highest simulated farmgate price of 60 US $ per dry ton and 3% annual energy crop yield growth. In this scenario, the available bioenergy from US biomass should increase from 5.4 EJ (2012) to 18.5 EJ (2030), considering 1 EJ per 63 million dry ton of biomass.

Biomass production for energy purposes can be particularly suitable for regional or local application where sufficient and affordable biomass resources are available, especially in countries with few fossil energy sources. Biomass can valorize marginal land, bringing socioeconomic benefits in these regions but overexploitation of biomass resources in developing countries should be avoided, in order to reduce the competition between potential food production and feedstock for the production of biomass.[43] Furthermore, equipment and services for the exploitation of biomass from forestry, agriculture, or dedicated crops, can have considerable positive impact on employment, especially in rural areas.[44] Nevertheless, risks on biodiversity conservation associated with widespread use of biomass intensive farming, fertilizers and chemicals may appear upon biomass intensive production for energy. Therefore, certifications that biomass feedstocks are produced in a sustainable way should be necessary.

The main barriers to spread the use of biomass for the production of fuels and power are cost and low

TABLE 5.4 Summary of Bioenergy Potentials at EU27 (EJ/year)

EU27	2000	2010	2020	2030	2050
Energy crops	0.1–1.6	0.3–9.6	0.5–14.7	2.0–18.4	15.4–19.9
Forestry and forestry residues	0.7–4.5	1.6–4.4	0.8–4.2	1.6–3.7	1.7–2.2
Agricultural and organic waste	0.5–3.9	1.0–3.9	1.5–4.4	1.1–3.1	0.7
Total	1.3–10.0	2.8–17.9	2.8–23.3	4.8–25.2	17.8–22.8

Source: Adapted from Ref. 40.

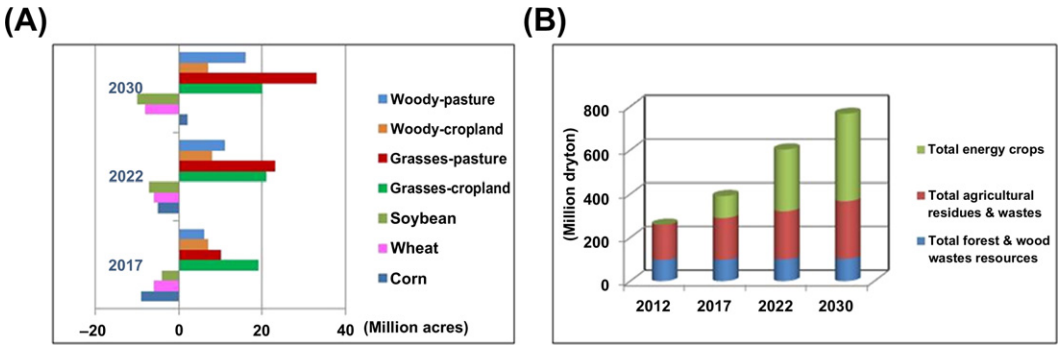

FIGURE 5.2 (A) US land-use change 2017–2030, at $60 per day ton under high-yield (3%) assumptions. (B) Summary of available biomass in US at the same scenario. (For color version of this figure, the reader is referred to the online version of this book.) *Source: Adapted from Refs 41,42.*

conversion efficiency. In the long term, bio-power potential will depend on technology advances and on the competition to produce food in arable land use. However, efficient agricultural systems combined with the geographic optimization of land use patterns could reduce the area of land needed to cover the global food demand in 2050 by as much as 72% of the currently used area. Other improvements, as the in situ conversion of biomass into pellets or bio-oil, could increase energy efficiency and also facilitate international trade as well as reduce transportation and handling costs.

5.4 PRETREATMENT OF BIOMASS FEEDSTOCKS

Biomass usually needs to be pretreated prior to be converted to fuels[45] either by thermochemical or biochemical processes.[8,9,46–49] Most thermal conversion processes demand a finely divided and substantially dry feed, and most microorganisms cannot directly use natural lignocellulosic materials to grow and produce biofuels neither. Therefore pretreatment is required to match the feedstock to the process.[50] The main pretreatment operations are:

- Tailoring and screening of the feedstock to keep particle sizes within appropriate limits and prevent contamination of the feedstock by metals or rocks.
- Drying of the feedstock to moisture contents suitable for the conversion technology.
- Depolymerization of lignocellulosic matrices in order to obtain smaller molecules that can be used, or further converted to platform chemicals and biofuels.

Pretreatment is one of the main associated economic costs (about 20% of the total cost) in the production of biofuels from lignocellulose, so the number of preconditioning steps should be minimized when possible.[51] Moreover, pretreatment must be effective on a wide range of lignocellulosic materials and feedstock loadings affording high yield of fractions for hydrogen production.

Pretreatment operations comprise physical and thermal, chemical and/or biological methods.[51] In any case, the selected pretreatment must have a low energy cost, either by low demand or by energy recovery at the end of the process.[51–53]

5.4.1 Physical and Thermal Pretreatments

Particle size reduction, irradiation, drying, steam or liquid hot water pretreatments (LHWs) are usually applied to set up biomass for the production of hydrogen.

5.4.1.1 Particle Size Reduction

Smaller particles have larger surface areas per unit mass and larger pore sizes that facilitate heat transfer and gasification. For instance, a reduction in the particle size from 1.2 to 0.075 mm can noticeably increase the conversion and the hydrogen yield (by a factor of 2) as well as reduce tars formation.[50] Several techniques have been reported for the reduction of particle size in the feedstock including dry, wet and vibratory ball milling and compression milling. In the lowest particle size demanding processes, such as in acidic pretreatments or entrained flow gasifiers, the energetic costs of size reduction processes can reach up to one third of the overall energy demand. Hence, milling is not feasible in an industrial scale,[54] although it has been recently shown that chemical pretreatment prior to milling reduced significantly the energy consumption and also the cost of solid–liquid separation.[51]

5.4.1.2 Irradiation

Lignocellulosic structure can also be broken using irradiation processes such as gamma rays, electron rays, microwaves or sonication. High energy irradiation with gamma or electron rays promotes changes in the crystalline structure of cellulose and therefore in its

physical and chemical properties.[55] Electron beam irradiation has been used in the pretreatment of rice straw[56] or combined with hot water or NaOH solutions in the pretreatment of hemp (1% NaOH, 450 kGray, 48 h hydrolysis) affording an increase in the yield of the as obtained xylose (from 8% to 29%) and glucose (from 18% to 37%) yields.[55]

Microwaves can efficiently destruct the structure of plants cell walls, due to their high heating efficiency and because of its ease operation. Microwave-assisted acid pretreatment (MAP) is advantageous against traditional lignocellulosic thermal acid pretreatment because of its shorter duration and higher efficiency in hydrolysis.[57] Indeed, MAP applied to corn stover (700 W, 0.3 N H_2SO_4, 45 min) increased the hydrogen production in more than 40% after fermentation and reaching up to 1.53 mol H_2/mol of glucose.[57]

Sonication with temperature control (303 K, 20 min, 79 kJ/gTS) has also been proved to be efficient in the pretreatment of seed sludge, as shown by hydrogen yields of 1.55 mol H_2/mol of glucose and a volumetric increase in hydrogen production of 40% and 120% over acid pretreated and untreated sludge respectively.[58]

5.4.1.3 Drying

Gasification processes are only efficient over dry biomass. Therefore, high moisture containing biomass collected from farm and forest lands need to be dried to obtain the desired range of water content. Drying is an energy intensive process, which decreases the overall energy efficiency of the process that can be, however optimized reusing the waste heat from the gasification process in the drying step.[59]

5.4.1.4 Steam Pretreatment

The steam pretreatment (SP), commonly referred as steam explosion, is a process that combines steam heating and hydrolysis of the glycosidic bonds of the lignocellulose, by the combined action of the acids formed upon the breakdown of the lignocellulosic structural components and by shearing forces due to the expansion promoted by moisture.[60] In this process, partially comminuted biomass is subjected to high-pressure steam (0.7–4.8 MPa at 433–513 K) for several minutes. Rapid venting results in an explosive decompression together with flash cooling of the biomass. Outstreams materials result in two separate phases: an aqueous phase where products from the acidic hydrolysis of lignocellulose can be found being xylose the major component together with some glucose, mannose, arabinose, and galactose. The second fraction consists of wet solid lignocellulose that is enriched in lignin and cellulose which is now more accessible and therefore easily hydrolyzable. Because of the relative harsh conditions some toxic byproducts as furfural and 5-hydroxymethylfural that can affect the following fermentation steps are generated.

The SP is an attractive process because it makes limited use of chemicals, it requires relatively low energy inputs with almost no environmental cost and it does not result in excessive dilution of the resulting sugars. The SP efficiency can be further enhanced by addition of an acidic catalyst, such as H_2SO_4, CO_2 or SO_2, that increases the recovery of hemicellulose sugars while decreasing the production of inhibitory compounds and improving the enzymatic hydrolysis on the solid residue. SP technology has been used for ethanol production from a wide range of raw materials, as poplar[61] and herbaceous residues as wheat straw.[62] The method has been successfully applied on hardwoods and AR or herbaceous biomass. However, it is not very effective for softwoods due to the low content of acetyl groups in the hemicellulose, in which case, the use of an acid catalyst is especially important.[63]

5.4.1.5 Liquid Hot Water Pretreatment

LHW consists of treating biomass with liquid pressurized superheated water (573–603 K) during short times in countercurrent, co-current or flow through reactor configurations. The experimental results show that high degrees of biomass solubilization are possible using LHW; however, the yield of undesired degradation products increases with treatment severity as well.[64] Further degradation of the resulting monosaccharides can be reduced by keeping pH between 4 and 7[65] avoiding the need of both a final neutralization and a washing step as water is the solvent, which is an additional advantage because of its low cost. LHW pretreatment is nowadays considered for large-scale pretreatment of corn fiber.

5.4.2 Chemical Pretreatments

The chemical pretreatment breaks down some of the constituents of the biomass mainly by reaction in acid, alkali, ammonia or ionic liquid (IL) media.

5.4.2.1 Acidic Pretreatments

The hemicellulosic fraction of the biomass can be solubilized in acidic media to make cellulose more accessible to enzymes.[52] Nitric acid, hydrochloric acid, and phosphoric acid have been tested [66–69] although the most widely used approach is based on treatment with dilute sulfuric acid (DA).[67] Typically, an aqueous suspension of the substrate (10% w/w) is mixed with a dilute H_2SO_4 solution (1.5%) and heated at 394 K with residence times of 60 min.[70] High yields of soluble sugars can be obtained (80–90% of theoretical yield

from hemicellulose and 50–60% of theoretical yield from cellulose) by a two-stage DA pretreatment process alternating mild and harsh conditions: High soluble sugar yield from the hemicellulose is obtained upon the first stage whereas hydrolysis in harsh conditions affords high glucose yield from the remaining cellulose upon the second stage.[71] Nevertheless, depending on the process temperature, some inhibiting compounds for further fermentation treatments, as furfural and 5-hydroxymethylfurfural, may appear as degradation compounds from aromatic lignin.

5.4.2.2 Alkali Pretreatments

In contrast to acidic treatments, alkaline treatments are focused on the solubilization and removal of lignin from the biomass.[72] Typical hydroxides, as NaOH or KOH can be used for alkali pretreatments but, they present high cost and low recovery because of the formation of some salts (i.e. from fatty acids). Alternatively, lime (CaO or $Ca(OH)_2$) pretreatment has low reagent cost,[73] is safer, and presents easier recovery of the calcium salts as calcium carbonate after reaction with CO_2.[74] Lime pretreatments utilize aqueous $Ca(OH)_2$ at low temperatures (298–403 K) achieving the removal of amorphous substances such as lignin, hydrolyzing the acetyl groups of hemicelluloses and reducing steric hindrance, and thus enhancing cellulose digestibility[67] (e.g. lime pretreatment of switchgrass, solubilizes 26% of xylan and 29%–33% of lignin).[75]

The addition of an oxidizing agent as oxygen at high pressures or H_2O_2, promotes better removal of lignin (wet oxidation process, WO). Indeed, the combined action of alkali and oxygen removes about 80% of lignin in hardwoods (poplar woods).[76] WO is also an appropriate method for fractionating sugarcane bagasse and for enhancing further enzymatic hydrolysis. Alkaline WO of sugarcane at 468 K during 15 min afforded good results, yielding a solid material with nearly 70% cellulose content, a solubilization of approximately 93% of hemicelluloses and 50% of lignin, and an enzymatic convertibility of cellulose of around 75%.[77]

However lime pretreatment is less effective when applied to softwood, requiring larger volumes of water (5–10 g H_2O/g biomass) in downstream processing as well as neutralization agents. Moreover, the oxidation of lignin to other water-soluble aromatic compounds is a risk, again due to the possibility of the formation of inhibitors.[54]

5.4.2.3 Ammonia Pretreatments

Ammonia pretreatments of lignocellulosic materials have also shown good performances in the cellulose digestion. The ammonia fiber/freeze explosion (AFEX) treatment consists of subjecting the biomass to the contact with liquid ammonia at 333–373 K in a pressure vessel for periods of up to an hour. Then pressure is released promoting rapid expansion of the ammonia gas (that can be then recovered) and hence, swelling and physical disruption of biomass fibers occurs, although only a small amount of the solid is solubilized. The gas expansion causes a phase change in the crystalline structure of the cellulose switching from cellulose I to cellulose III which has enhanced solubility and reactivity.[67] In addition, ammonia can form strong hydrogen bonds, penetrating into cellulose fibers pulling at the flexible hydroxymethyl groups causing conversion into cellulose I, decreasing intra-sheet hydrogen bonding, and introducing inter-sheet hydrogen bonding. These rearrangements increase the number of hydrogen bonds that surface cellulose chains can make with water, resulting in enhanced solubility together with some small amount of hemicellulose that is solubilized in the oligomeric form.[47] In spite of some deacetylation process only small amounts of byproducts from degradation appear being a good substrate for further enzymatic hydrolysis.

The AFEX pretreatment is highly effective on AR and herbaceous crops, with limited effectiveness on woody biomass and other high lignin content feedstocks.[78,79] AFEX combined with DA pretreatments can afford more than 80% of total sugar yield in the enzymatic hydrolysis of washed pretreated solids.[80] AFEX-centered cellulosic technology simplifies production steps, reduces the requirement for nutrient supplementation, increases the diversity of byproducts and potentially enhances the environmental benefits beyond the direct impact of the pretreatment processes. However, ammonia recovery and recycle is complex and expensive because of its high volatility, which is significant with regards to the commercial potential of the AFEX pretreatment.[81]

Ammonia recycle percolation (ARP) is another highly effective process in delignifying biomass and also in increasing the enzymatic digestibility.[82] An aqueous solution of ammonia (5–15%) is circulated through a reactor with a packed bed of biomass at elevated temperatures (423–473 K)[63,83] where the ammonia outstreams can be either recirculated or recycled. ARP is very selective in delignification, achieving a reduction of 70–85% of the content of lignin in corn stover within the first 20 min of pretreatment. Hemicellulose (40–60%) can be also solubilized by ARP, whereas cellulose remains intact.[84] The most important challenge for ARP processes is reducing the energy costs by a reduction in the liquid loading. Similar processes at moderate temperatures (298–333 K) like soaking in aqueous ammonia are currently under development.[82]

5.4.2.4 IL Pretreatments

ILs are organic salts with a melting point lower than 373 K and are considered as green solvents, due to their

negligible vapor pressure, nonflammability, chemical and thermal stability, non-explosiveness, high polarities and their recyclability. ILs can be considered as a promising new approach to pretreatment for biomass because they are non-derivatizing agents and do not produce fermentation inhibitors. Pretreatment with ILs not only disrupts the plant cell walls and separates cellulosic, hemicellulosic, and lignin components, but also disrupts the crystallinity of cellulose making it more readily hydrolizable. Nevertheless, ILs present some drawbacks such as nonbiodegradability, high cost and that their toxicity is still controversial.

ILs properties can be easily tuned by changing the structures of the cations or anions. Cellulose was only solubilized with BMIM (1-butyl-3-methylimidazole) derived ILs when the anions were Cl^-, Br^- or SCN^- whereas no solubility was observed with PF_6^- and BF_4^- counteranions.[85] Indeed, cellulose was dissolved more effectively in ILs whose anions were good hydrogen bond acceptors, such as OAc^-, $HCOO^-$, $(MeO)_2PO_2^-$ or Cl^-. In contrast, ILs containing low-basicity anions, such as dicyanamide, or non-coordinating anions, such as BF_4^- or PF_6^-, were not so efficient in dissolving cellulose. NMR studies on the mechanism of dissolution of cellulose in chloride-based IL suggested that the solvation of cellulose by (BMIM)Cl involves stoichiometric hydrogen bonding between the hydroxyl protons of the solute and the chloride ions of the IL.[85] However, the role of the cation in the cellulose dissolution by ILs remains still uncertain. Cellulose can be dissolved in ILs containing imidazolium, pyridinium ammonium and phosphonium cations, showing better solubility in short alkyl chain ($n < 6$) substituted cations with an even number of carbon atoms.[85] Additional solubility of cellulose in ILs can be achieved by microwave heating, as expected.

5.4.3 Biological Pretreatments

Chemical and thermal pretreatments usually require high energy, corrosion-resistant high-pressure reactors, as well as extensive washing of the resulting products, which increase the costs. Moreover, because of harsh reaction conditions, toxic substances interfering with the microbial fermentation and large volumes of waste stream may be produced.[86] Consequently, from both economic and environmental perspectives, biological pretreatment has attracted interest because of its potential advantages such as low energy requirements, mild environmental conditions and simple operation techniques.

Fungal pretreatment had been previously explored to upgrade lignocellulosic materials for food and paper applications. Recently, this environmentally friendly approach has received renewed attention as a pretreatment method for enhancing enzymatic saccharification of lignocellulosic biomass in bioethanol production processes.[52] Fungi that are active in the biodegradation of wood can be roughly classified into three main groups according to their methods of degrading biomass: white-rot, brown-rot and soft-rot fungi.

White-rot fungi such as *Ceriporiopsis subvermispora*, *Dichomitus squalens*, *Phanerochaete chrysosporium*, and *Phlebia radiata* are the most effective in delignification of biomass for fuels due to their unique ligninolytic systems. White-rot fungi have been studied for pretreatment of a wide range of biomass feedstocks (cotton stalk, corn stover, rice straw, wheat straw, aspenwood) showing high delignification efficiency and affording woods with a white fibrous appearance that have selectively degraded lignin and hemicellulose fractions while cellulose fraction is essentially unaffected. Moisture and particle size of the feedstock, aeration, and pretreatment time are critical for fungal metabolism and growth to achieve good performance.[87] Analysis of white-rot degraded woods indicated that lignin degradation involves oxidant agents such as singlet oxygen and hydroxyl radicals that produce oxidative demethylation or demethoxylation, side-chain oxidation and propyl side-chain cleavage reactions. Ligninolytic enzymes such as lignin peroxidase, manganese peroxidase, H_2O_2-forming enzymes and *laccase* are responsible for oxidation of lignin and related compounds.

Pretreatment of corn stover with white-rot fungi, *Pleurotus ostreatus BP2*, *Echinodontium taxodii 2538* and *Irpex lacteus CD2*, during 30 days before pyrolysis, accelerated the thermal degradation of lignocellulose, decreasing the required operating temperature and made the pyrolysis more efficient and energy saving. The content of sulphur decreased up to 46% upon pretreatment making the lignocellulose pyrolysis more environmentally friendly, with less SO_x emission.[88] Pretreatment of rice straw with SP prior to biological treatment using *P. ostreatus*, reduced the treatment time required for obtaining a 33% net glucose yield from 60 to 36 days.[89] Biological pretreatment of corn straw for 15 days using *E. taxodii* followed by alkali/oxidative pretreatment led to an increase of 51% in reducing sugars.[90] Similar results were also reported by Ma et al. who observed that acid pretreatment (0.25% H_2SO_4, 301−373 K for 15−60 min) followed by 15 days fungal pretreatment improved the hydrolysis by 1−2 times over acid pretreatment alone.[91]

The main drawback for biological pretreatment is the slow rate for industrial purposes. Large amounts of space, careful growth conditions, and large residence times are required. These drawbacks can be overcome by combination of fungal pretreatments with other physicochemical methods that can help to improve enzymatic digestibility.

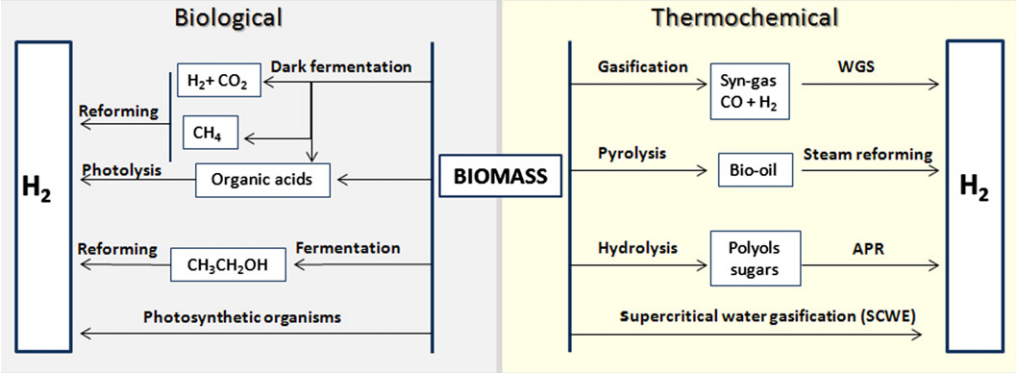

SCHEME 5.1 Different process routes for the production of hydrogen from biomass. (For color version of this figure, the reader is referred to the online version of this book.)

5.5 METHODOLOGIES FOR THE PRODUCTION OF HYDROGEN FROM BIOMASS

Several processes are currently available for the production of hydrogen from biomass that can be roughly classified into biological and thermochemical routes (Scheme 5.1). Thermochemical routes are discussed in detail in Chapter 6, whereas biological routes are discussed in Chapter 8. In this chapter, the different routes of hydrogen production from biomass will be briefly outlined.

5.5.1 Thermochemical Gasification Coupled with Water–Gas Shift

Gasification roughly consists of a partial thermal oxidation in an atmosphere with low oxygen content that affords a high proportion of gaseous products (CO_2, water steam, CO, hydrogen and gaseous hydrocarbons as methane), small quantities of char, ashes, and condensable compounds (tars and oils). Hydrocarbons in the outstreams can be further used in a combined gas cycle either to provide energy for the gasification or for the production of electricity, increasing the overall energetic efficiency. Nowadays, gasification coupled with water–gas shift reaction (WGS) is the most widely used process for the production of hydrogen starting from biomass.[17,25,27] Biomass gasification is similar to coal gasification except that biomass gasification is conducted at much lower temperature to avoid side processes.

Biomass gasification can be seen as a way of pyrolysis that takes place at high temperatures, and produces a mixture of gases with a hydrogen content ranging 6–6.5%[92] with an overall yield ranging from 12% to 20% based on the biomass weight depending on the feedstock (Table 5.5). Gasification coupled with WGS is usually carried within the range of 873–1273 K in the presence of oxygen/air and/or steam.[3,25] The whole process can be deemed as neutral regarding CO_2 emissions (Scheme 5.2).[1]

Gasification processes can be carried either in the presence or in the absence of catalysts in entrained flow gasifiers, fixed bed (updraft and downdraft fixed bed) gasifiers, entrained flow gasifiers and fluidized-bed reactors (Scheme 5.3).[3]

Because of the high reactivity of biomass, air is sufficient as oxidizing medium and fluidized-bed processes are preferred (either bubbling or circulating).[94] Addition of steam as the gasification agent results in steam reforming of the produced hydrocarbons, mainly methane, yielding a syn-gas that can be further used in WGS. These processes are simultaneously run in the gasifier affording higher yields of hydrogen in the gaseous outstreams (Table 5.6). Steam reforming after gas purification also allows production of hydrogen from the methane byproduct that appears upon gasification. Finally pressure swing absorption (PSA), which is the most widely used technology to purify the gaseous outstreams (Scheme 5.4), removes the traces of CO that are harmful for fuel cells and catalysts (Table 5.6).

TABLE 5.5 Typical Producer-Gas Composition for Downdraft Gasifiers Operated on Low-to-Medium-Moisture (20% for Wood, 7% for Coal) Content Fuels

Component in the outstreams	Wood gas (vol%)	Charcoal gas (vol%)
Nitrogen	50–54	55–65
Carbon monoxide	17–22	28–32
Carbon dioxide	9–15	1–3
Hydrogen	12–20	4–10
Methane	2–3	0–2
Heating value (MJ/m^3)	5–5.9	4.5–5.6

Source: Adapted from Ref. 93.

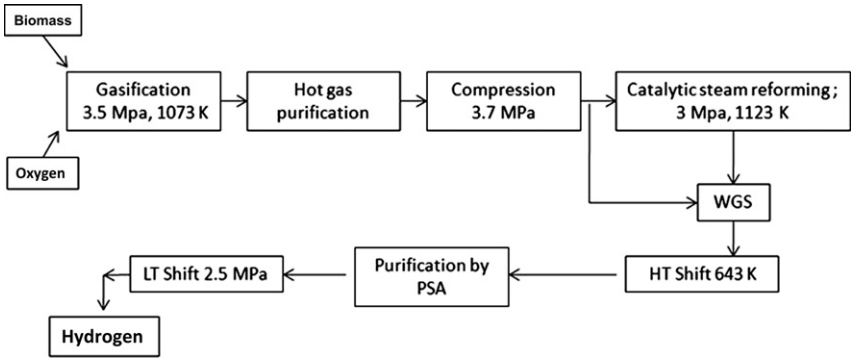

SCHEME 5.2 Overall flow diagram for hydrogen production from biomass. *Adapted from Ref. 7.*

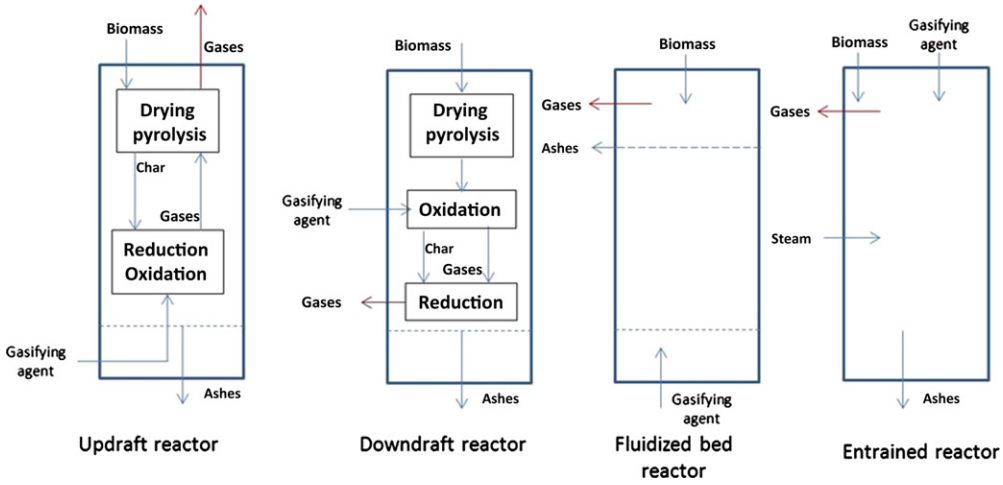

SCHEME 5.3 Typical designs for gasifiers. (For color version of this figure, the reader is referred to the online version of this book.) *Source: Adapted from Ref. 94.*

TABLE 5.6 Hydrogen Yields from Different Feedstocks and Processes

Feedstock	Catalyst	T (K)	Gasifying agent	H_2 (% in the gas phase)	References
Cellulose	Ni-Dolomite	1173	Air	33	95
Cellulose	$Rh/CeO_2/SiO_2$ (50%)	773	Air	31	95
Cellulose	$Rh/CeO_2/Al_2O_3$ (20%)	773	Air	22	95
Unknown		1053–1103	Air	5–16	93
Pine sawdust	Dolomite	1073	Steam	52	96
Unknown		1023–1073	Steam	38–56	93
Unknown		975	Steam	38	97
Unknown		1325	Steam	50	97
Hazelnut shell		1225	Steam	60	98
Woodchips		1473	Steam	58	99
Almond shell	La-Ni-Fe-Perovskite	1173	Steam	64	100
Cellulose	JRC-SIO6	623	Steam (pressured)	29	101
Unknown		1058–1108	Steam-O_2	14–32	93
Sawdust	Na_2CO_3	1285		15	6

The chemistry of biomass gasification is quite complex because of the heterogeneity of the starting materials. Properties such as moisture content, mineral fraction, density or chemical composition widely differ depending on the source of biomass requiring the specific design of the gasifier for each specific feed. A combination of pyrolysis, partial oxidation and/or steam reforming of gaseous alkanes and char takes place under the described conditions that are gathered in Scheme 5.4.[1,93]

The yield of hydrogen that can be directly generated from biomass gasification is relatively low, in the range of 16%–18%.[102] Nevertheless, the gaseous fractions can be further used for the production of hydrogen by means of the steam reforming (2) of hydrocarbons and the WGS reaction of CO (3).[94] Pyrolysis (4)–(6) includes endothermic processes that usually occur in the range of 473–573 K. The VM of the biomass is reduced resulting in the release of hydrocarbon gases that can be further condensed forming liquid tars, and the formation of solid carbonized biomass or char. The oxidation reactions taking place in the gasifier can be summarized in partial oxidation processes (7)–(10), char complete oxidation (11) and the water reaction of char (12).[17] Reduction step occurs in the 1073–1273 K range in the absence of oxygen as result of different reductive processes as the water reaction (12), the Boudouard reaction (13), the methane reaction (14) and hydrogenation/polymerization processes (15) that produce more hydrocarbons.

Gasification can also be explained following the flow of the oxidizing agent in the gasifier (Scheme 5.3). First, partial oxidation of the carbonaceous residue from biomass takes place in an exothermic process, which raises the temperature (8)–(9). In a second step, the lack of oxygen together with the availability of carbon, CO_2 and steam produces recombination to molecular hydrogen and CO (syn-gas). Then, the gas stream is enriched by the biomass pyrolysis products and finally, the warm gases help to evaporate the incoming biomass moisture. Inorganic compounds are converted to ashes that are collected at the bottom of the reactor or entrained in the gas stream. An additional pretreatment step to reduce moisture content below 5% in biomass is also needed, that has a high impact in the overall operation costs.

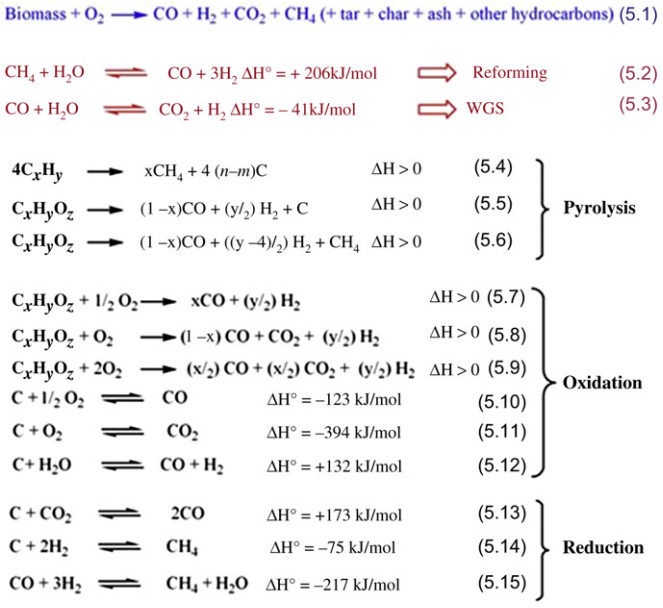

SCHEME 5.4 Chemical reactions involved in gasification process. (For color version of this figure, the reader is referred to the online version of this book.)

Major issues in biomass gasification are the formation of tar and the high operation temperatures. The undesired tar polymerizes at the operating conditions to more complex structures that are not prone to hydrogen production. Nowadays, three methodologies can be envisaged for minimizing tar formation and optimize the gaseous outstreams[103]: (1) proper gasifier design; (2) incorporation of catalysts to gasification; (3) improved control of operating variables.

Operating parameters such as the gasifying agent, the temperature and the residence time are key factors in the formation and decomposition of tar. Indeed, tar can be thermally cracked using temperatures above 1273 K.[103] Catalysts not only reduce tar formation, but are also particularly effective for improving gas product quality and conversion. In this regard, dolomite-loaded nickel catalysts, alkaline metal oxides as $Rh/CeO_2/SiO_2$ and $Rh/CeO_2/Al_2O_3$[95] are successfully used as gasification catalysts. The yields of hydrogen from biomass with the use of dolomite in a fluidized-bed gasifier and the use of nickel-based catalyst in a fluidized-bed gasifier downstream from the gasifier afforded up to 130 g H_2/kg of biomass operating at 925–1125 K (Table 5.6).[96] It has also been observed that the addition of inorganic salts as chlorides, carbonates and chromates have a beneficial effect on the reaction. Another option to overcome tar formation and energetic cost associated with high operating temperature consists of using direct solar thermal gasification technologies that are appearing as an appealing alternative to classical gasification methodologies.[104] Enhancements in overall conversion, product composition ratios, and tar reduction are achievable at temperatures greater than 1273 K that can be reached in solar furnaces. Furthermore, the utilization of concentrated solar energy to drive these reactions eliminates the need to consume a portion of the product stream for heating.[2]

WGS reaction (3) reforms the CO produced upon gasification using water to produce CO_2 and hydrogen. The WGS is a thermodynamically spontaneous equilibrium that involves all the gases that are present in the reduction process. The production of hydrogen is

therefore increased in an excess of steam, decreasing the reaction temperature as much as possible or removing the hydrogen from the mixture (i.e. using membrane reactors that allow the separation of hydrogen).[105] Consequently, the composition of the gas corresponds to a number of parameters such as fuel composition, gasifying medium, operating pressure, temperature, moisture contents of the fuel or mode of bringing the reactants in contact with the gasifier.

WGS reaction (3) has been traditionally carried out in a separate reactor in the presence of CuO−ZnO, Cr_2O_3 or Fe_2O_3 catalysts depending on the reaction temperature. High temperature reaction (623−773 K) is carried out using Cr_2O_3 and/or Fe_2O_3 [1]; addition of cocatalysts such as Rh to Fe_2O_3−Cr_2O_3 catalysts enhances the activity by a factor of 4.[106] WGS can also be conducted in the presence of Zn and Cu oxides at lower temperatures (473−523 K). Alternatively, WGS can be replaced by the transformation of CO to electricity and CO_2 using aqueous polyoxometalates and gold catalysts at room temperature.[107]

Dry biomass has been successfully used as raw material for the production of hydrogen by gasification either as an additive to the feed of a coal gasification plant or as the sole feed (i.e. pine sawdust, hazelnut shell, paper, yellow pine woodchips, wood sawdust, wheat straw and waste wood).[92]

5.5.2 Fast Pyrolysis Followed by Reforming of Bio-oil

Pyrolysis consists of heating biomass in the absence of air or oxygen at a specified rate to a maximum temperature and holding it for a specified residence time. Pyrolysis can be classified in to carbonization (≈673 K, several days), slow or conventional (≈873 K, 5−30 min), fast (≈773 K, <2 s), flash (<923 K, <1 s) and ultra-rapid pyrolysis (≈1273 K, <0.5 s).[27] The nature of the products depends on a number of factors such as temperature and heating rate. Amongst them, fast pyrolysis yields the biggest proportion of *bio-oil*, whereas higher amount of char is obtained in slow pyrolysis and more chemicals and gases are produced in flash pyrolysis. Biomass must be fed as small size particles in order to allow rapid heat transfer.[1]

Virtually, any form of biomass can be considered for fast pyrolysis ranging from agricultural wastes such as straw, olive pits and nut shells to energy crops such as miscanthus and sorghum, forestry or solid wastes; nevertheless, most of the work has been carried out on wood because of the supposed consistency and compatibility between different tests.[46] Fast pyrolysis of biomass is usually carried out in the absence of air at atmospheric pressure at 623−823 K, under high heating range (10^3−10^4 K/s) and short gas residence time (<2 s).[7] Fast pyrolysis produces vapors that are rapidly cooled outside the reactor producing *bio-oils* achieving 70−80% effective biomass conversion. The pyrolysis overall reaction (5.16) can be described as follows[92]:

$$Biomass \rightarrow H_2 + CO + CH_4 + bio\text{-}oil \quad \Delta H > 0 \qquad (5.16)$$

Chemical composition of *bio-oil* is not the result of a thermodynamic equilibrium and so the composition of *bio-oil* tends to the composition of equilibrium upon storage.[108] *Bio-oils* are sometimes corrosive because of the presence of alkalis. Furthermore, char and ashes are also present in these *bio-oils* as well as some water that is produced in the pyrolysis reaction.[109] The heating value of *bio-oil* is relative low (16−19 MJ/kg) as its oxygen content (30−40%) is very high, usually present as water content (10−30%).[1,110] The other major groups of compounds identified are hydroxyaldehydes, hydroxyketones, sugars, carboxylic acids, and phenolic compounds that appear as oligomer fractions having molecular weights ranging from 900 to 2500.[110] Hence, the pyrolysis oil can be separated into two fractions based on water solubility. The water-soluble fraction can be used for hydrogen production while the water-insoluble fraction mainly consisting of lignin-derived compounds may be used for adhesive formulations that help to improve the overall process economics.[6]

The aqueous fraction of *bio-oil* is further transformed (or transported elsewhere) via catalytic steam reforming (5.17) at 1025−1125 K over a Ni-based catalyst in a two steps process whose overall stoichiometry, coupled with the WGS [5.3 in Scheme 5.4], gives a maximum yield of 0.172 kg H_2/kg *bio-oil* (11.2% based on $CH_{1.9}O_{0.7}$ wood).[7]

$$bio\text{-}oil + H_2O \rightarrow CO + H_2 \qquad (5.17)$$

Catalytic steam reforming process can be applied for the reforming of *bio-oil* from biomass pyrolysis (5.17) and hydrocarbons, mainly methane, from biomass gasification, increasing the overall hydrogen yield. The most relevant parameters in catalytic steam reforming are the steam to carbon ratio (S/C) in the reactor feed together with unsaturation of the starting *bio-oil* components (Table 5.7). Although the catalyst for steam reforming of *bio-oil* and methane are essentially similar, in this chapter the discussion will be only focused on the reforming of *bio-oil*.

The main hurdle of catalytic steam reforming is catalyst deactivation due to coke deposition, although the Ni/NiO, Cr_2O_3 or MgO packed with amorphous silica have shown high efficiency. Catalysts further pre-reduced with hydrogen have also been reported for the steam reforming of glycerol producing up to 6.2 mol H_2/mol glycerol (89% yield at 853 K and 0.1 MPa).[115]

TABLE 5.7 Hydrogen Yield after Steam Bio-oil Reforming from Biomass

Feedstock	Catalyst	T (K)	S/C*	% H_2 (yield)	References
Bio-oil	C12A7-O^-	1023	4	18	111
	C12A7-O^-/18%Mg	1023	4	80	
Bio-oil (pine wood)	Ni(Mg)/Al_2O_3	923	7.6	63†	112
	Ni(Ca)/Al_2O_3	923	7.6	61†	
Bio-oil BTg	Ni/Al_2O_3	1223	5	65	113
	Ni(Ru)/Al_2O_3	1223	5	85	
	Ni(Mg)/Al_2O_3	1123	5	62	
	Ni/Al_2O_3	1123	5	54	
Bio-oil (poplar wood)	Ni/Al_2O_3	1100	4.92	65‡	114
	Ni/MgO-Al_2O_3	1100	4.92	80‡	
	Ni/MgO-La_2O_3-Al_2O_3	1100	4.92	75‡	
	Ni-Cr/MgO-La_2O_3-Al_2O_3	1100	4.92	82‡	
	Ni-Co/MgO-La_2O_3-Al_2O_3	1100	4.92	87‡	
	G-91	1100	4.92	80‡	
	C11-NK	1100	4.92	87‡	
	46-1	1100	4.92	80‡	
	46-4	1100	4.92	80‡	
Glycerol	Ni/SiO_2	853	9.0	89	115

* *Steam to carbon ratio.*
† *% in gas content.*
‡ *After 5 min stream.*

Despite these promising results, the conversion of biomass for hydrogen production using pyrolysis followed by steam reforming still poses great technical challenges as the hydrogen purity and yield as well as environmental concerns that could be overcome by integrating in situ CO_2 capture in the steam reforming reaction.[116,117]

5.5.3 Aqueous Phase Reforming

Biomass-derived polyols and sugars with a C/O ratio of 1:1, such as methanol, ethylene glycol, glycerol, glucose or sorbitol, can be converted to hydrogen, CO, alkanes and CO_2 using the aqueous phase reforming (APR) reaction on supported catalysts.[1] The APR process combines C–C bond cleavage with WGS in a single reactor at relatively mild conditions (<540 K, <3 MPa).[118] Water does not need to be evaporated and low levels of CO (<1000 ppm) are produced so that the hydrogen-rich effluent can be purified either by PSA or by using membranes (Scheme 5.4).[119,120]

Because of the chemical structure of polyols, the reaction can follow different pathways (Scheme 5.5 for the case of ethylene glycol). The C–C cleavage pathway produces CO that is adsorbed on the catalyst surface and undergoes WGS to give CO_2 and hydrogen. Nevertheless, CO and CO_2 can undergo methanation and/or Fischer–Tropsch reactions with the previously formed

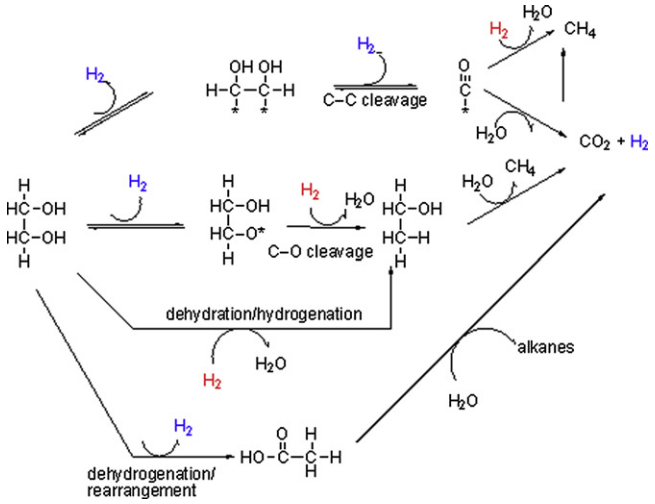

SCHEME 5.5 Reaction pathways for APR process of ethylenglycol. (*) represents surface metal sites. (For color version of this figure, the reader is referred to the online version of this book.) *Source: Adapted from Ref. 118.*

hydrogen yielding water and alkanes, and so diminishing overall hydrogen selectivity of the process. The cleavage of C−O bonds, the dehydratation/hydrogenation route, as well as the dehydrogenation/rearrangement route also provide CO_2 and hydrogen together with higher alkanes yields. Hence, good catalyst for hydrogen production by APR reaction must be selective toward C−C bond cleavage as well as not very active for CO adsorption and inactive for methanation, which is thermodynamically favorable, and Fischer−Tropsch reactions. Most research has been focused on Group VIII catalysts,[121] mainly Pt-supported catalysts[122] although Sn-promoted Raney-nickel catalysts[123] have also demonstrated to be very active. Rh and Ru catalysts showed lower selectivity for production of hydrogen and high selectivity for alkane production.[121,124] Ce, Mg or La catalysts also yielded low hydrogen selectivity.[125]

Selectivity of the APR reforming of polyols with a C/O ratio of 1:1 over Pt/Al_2O_3 (498 K, 2.9 MPa) increased with decreasing number of C atoms in the polyols (glucose 50% selectivity < sorbitol < glycerol < ethylene glycol 96% selectivity).[118] The APR of methanol was even more effective, reaching 99% selectivity and 75% yield. The use of harsher conditions (538 K and 5.6 MPa) diminished both selectivities and yield (i.e. 88% and 69% respectively for ethylene glycol). The support also influences the activity and selectivity of Pt catalysts in the APR being TiO_2 the best support followed by, carbon and Al_2O_3,[121] although MgO, ZrO_2 or CeO_2 also gave promising results.[126] Indeed, APR of cellulose using Pt/C catalysts afforded quantitative conversion of cellulose and 70% overall hydrogen yield.[90]

The APR reaction has been demonstrated to be a promising pathway to produce hydrogen from biomass, although further improvements in catalysts activity and stability should be done prior to scale-up in view of a commercial application.

5.5.4 Supercritical Water-Mediated Transformations of Biomass

Supercritical water (SCW, critical point of water: Pc = 22.09 MPa, Tc = 647.29 K)[127] shows intermediate properties between the liquid and the gaseous state. SCW presents a decrease in its dielectric constant and thus, some of its hydrogen bonding is lost with regards to the liquid state. Consequently, SCW can dissolve organic compounds under certain conditions. Last, but not least, the autoionization constant, K_w, is increased reaching the value of 10^{-11} near its critical point, making SCW an excellent medium for acid or base catalyzed reactions even on organic compounds. Gasification of wet biomass is highly inefficient but gasification in high-pressure hot water is an attractive process for wet biomass like aquatic biomass and raw sewage.[27] Tar precursors are completely soluble in SCW and so can be reformed directly and the production of hydrogen and CO_2 is preferred instead of CO.[128]

Supercritical water gasification (SCWG) of biomass typically occurs between 773 and 1023 K at about 25−40 MPa.[27,129] Ideally, steam reforming of a polysaccharide, as cellulose $(C_6H_{10}O_5)_n$, should yield 12 mol H_2/mol C_6 (5.18a). Nevertheless, when biomass is subjected to these conditions it is decomposed into char, tar, gas and other compounds that are in situ reformed into hydrogen, CO, CO_2, and short hydrocarbons (CH_4 mainly) (5.18b):

$$(C_6H_{10}O_5)_n + 7n\cdot H_2O \rightarrow 12n\cdot H_2 + 6n\cdot CO_2 \quad (5.18a)$$

$$x\cdot C_6H_{12}O_6 + y\cdot H_2O \rightarrow n\cdot H_2 + m\cdot CH_4 + w\cdot CO + z\cdot CO_2 \quad (5.18b)$$

The basic reaction pathways of biomass SCWG and the impact of salts, proteins, and lignin are well known and they have been reviewed.[27,129,130] The overall process can be roughly divided in to carbohydrate steam reforming and CO methanation and WGS, as well as other reactions that render the effluents acidic.[27] At the chemical equilibrium state, H_2 and CO_2 yields sharply increased with increasing temperature, whereas the CH_4 yield decreased.[130] Contrary to this, CH_4 yield increased and H_2 decreased with increasing feedstock concentration. In both cases, the CO yield was very low because of the simultaneous WGS reaction.[130,131] Moreover, the hydrogen yield from biomass SCWG increased as the polyols chain length decreased (glycerol > glucose > corn or potato starch).[132] Tar formation in model compounds such as glucose became significant at relatively high feed concentrations (>5 wt%).[133]

By means of full factorial experiments, Guo et al.[134] optimized the reactor operation parameters of corn cob SCWG and found that the order of influence of the different operating parameters on H_2 yield was temperature > pressure >> feedstock concentration >> residence time. Highest H_2 yield (26.3 mol H_2/kg of biomass, ≈4.4 mol H_2/mol C_6) and carbon efficiencies (95%) were obtained at higher temperatures (≈1048 K) and lower feedstock concentrations (≈3%). Hydrogen yield also increased by 29% with the acid hydrolysis pretreatment of the feedstock. The addition of an oxidizing agent caused a decrease in the hydrogen yield but promoted the carbon gasification efficiency.

Catalysts can improve hydrogen yields (Table 5.8). Thus, Ru/Al_2O_3 promoted an increase in the yield of glucose SCWG from 6.5 to the stoichiometric limit of 12 mol H_2/mol C_6 in a continuous flow process (glucose 1 wt%).[133] The addition of an alkali, such as KOH, to model glucose also improved H_2 yields but this effect on real feedstock (straw, wood, sewage) was less

TABLE 5.8 Selected Examples and Catalyst Effect on H_2 Yield from Biomass SCWG

Feedstock	Catalyst	T (K)	P (Mpa)	mol H_2/mol C_6	References
Glucose 0.1 M	–	923	30	4.3	137
Glucose 0.6 M	–	1023	28	4.8	131
Glucose (1 wt%)	–	973	25	6.5	133
	Ru/Al_2O_3 (5%)	973	25	12	
Glucose 0.1 M	KOH 0.002 M	873	25	9.1	135
Cathecol	KOH 0.002 M	873	20–30	10.6	
Glucose (9 wt%)	–	923	35	0.2	136
	$Ni/\gamma Al_2O_3$ (2%)	923	35	1.9	
	Ni/CeO_2-γAl_2O_3 (2%)	923	35	2.3	
Corn cob (3 wt%)	–	1048	>22	4.4	134
Sawdust	–	1123	–	9.6	138

noticeable [135] and unfortunately, the addition of alkali salts may cause corrosion, plugging, or fouling.[129] Other catalysts, such as $Ni/\gamma Al_2O_3$ and Ni/CeO_2-γAl_2O_3, also improved yields and selectivity of H_2 production from the glucose SCWG (35 MPa, 923 K, 9 wt% feed), although intense metal leaching was observed and they were readily deactivated by coke deposition.[136] The high feed concentration (9 wt%) can be responsible for the low H_2 yield and coke deposition, as it has been observed with model molecules (glucose > 5 wt%).[133]

Even if SCWG has been reported to be the most efficient conversion technology of biomass with a high moisture content (>40%),[139] the costs of this process, including solar-driven SCWG, doubles the cost of biomass gasification/pyrolysis methods.[140] Furthermore, SCWG processes are highly determined by the chemical kinetics, which is still not fully understood. Hence, a lot of research has still to be done to design efficient plants. Probably the drop in gasification efficiency and gas yield with an increase in the feed dry solids concentration may be a major obstacle to commercial SCW gasification.[27]

5.5.5 Microbial Conversion of Biomass

Microorganisms usually work in mild conditions using biomass or wastewater for feeding. The production of hydrogen by microorganisms is usually carried out by enzymes, commonly nitrogenase, Fe-hydrogenase or NiFe-hydrogenase.[141] Thus, microorganisms containing these enzymes can be seen as a sustainable alternative for the production of hydrogen from biomass. The main biological processes to produce hydrogen are dark fermentation and photofermentation of biomass, water biophotolysis (direct or indirect) and water–gas shift. All of them will be presented in Chapter 8, but now we will briefly summarize the microbial conversion of biomass (dark and photo fermentations).

5.5.5.1 *Dark Fermentation*

Hydrogen production by dark fermentation uses anaerobic bacteria as well as some microalgae, such as green algae, at temperatures ranging from 303 to 353 K, being carbohydrates the main potential fermentable substrates.[6] Pure simple sugars, such as glucose and fructose, are preferable but relatively expensive, so starch waste, cellulose, waste sludge and carbohydrate-rich industrial waste subjected to the corresponding pretreatment could be adequate.[122] The amount and purity of the produced hydrogen are strongly dependent on the metabolic pathway followed by the microorganisms. Indeed, if glucose is chosen as the model substrate, up to 4 mol of hydrogen could be produced per mole of glucose if acetic acid was the final metabolite (5.19), whereas only two hydrogen moles would be produced if butyric acid was the end metabolite (5.20). *Clostridium pasterianum, Clostridium butyricum and Clostridium beijerinkii* are high hydrogen producers,[92] yielding 2.4–3.2 mol H_2/mol glucose.[122]

$$C_6H_{12}O_6 + H_2O \rightarrow 2CH_3COOH + 2CO_2 + 4H_2 \quad (5.19)$$

$$C_6H_{12}O_6 + H_2O \rightarrow CH_3CH_2CH_2COOH + 2CO_2 + 2H_2 \quad (5.20)$$

Important parameters in dark fermentation are hydraulic retention time and pH that should be maintained between 5 and 6[6] in order to prevent diverting the metabolic pathway toward the production of organic

compounds. Partial pressure of hydrogen is another important factor that affects the yield, and so hydrogen should be removed to increase its production and to prevent obtaining reduced substrates. Apart from hydrogen, other gases such as carbon dioxide, carbon monoxide, methane and hydrogen sulfide are produced by the metabolic conversion of biomass. Therefore, a purification step for the hydrogen is required as well as for the produced wastewater prior to its reuse.

Hydrogen production via *dark anaerobic fermentation* leads to a negative net energy balance.[142] Nevertheless, the introduction of a second methanogenic step leads to a positive net energy production (9%).[142] Indeed, in a typical two-step test conducted at 35 °C, H_2 was first produced from glucose (acidogenesis step, yielding 11% of the glucose energy content) and then biogas was obtained from the volatile fatty acids resulting from the first step (methanogenesis step, 44% of the energy content) (5.21).

$$C_6H_{12}O_6 + 2H_2O \rightarrow 4H_2 + 4CO_2 + 2CH_4(9\%\ \text{useful energy}) \quad (5.21)$$

Given that dark fermentation is neither land demanding nor affected by weather conditions, it is being considered as a topic of growing interest in fuel production.

5.5.5.2 Photofermentation

Three different groups of phototroph microorganisms are involved in biological hydrogen production processes: aerobic green algae (eukaryotes), cyanobacteria (blue-green algae), and anaerobic photosynthetic bacteria (mostly Gram negative prokaryotes).[143] Within this group photosynthetic purple bacteria have been considered the best for photobiological hydrogen production because they can use either industrial wastes or byproducts from dark fermentation (as organic acids), through nitrogenase enzymes (5.22).[6,122,144,145]

$$CH_3COOH + 2H_2O \rightarrow 4H_2 + 2CO_2 \quad (5.22)$$

Organic acids are used as electron donor and transported to the nitrogenase which, in the absence of nitrogen, transfers the electron to one proton.[92] The process is done under deficient nitrogen conditions using infrared light. Microorganisms can be immobilized on agar gel, porous glass, activated glass or polyurethane foam so they can be used either in batch or continuous processes. Nevertheless, the photofermentation is still limited by the high energy demand of nitrogenase enzymes, low light conversion efficiencies (<10%), reoxidation as well as other side metabolic processes. Contrary to dark fermentation, the photofermentation needs anaerobic photobioreactors covering large areas. Moreover, reported scale laboratory photofermentation experiments only yielded near 10% of the theoretically possible hydrogen production (>0.1 kg H_2/kg glucose or 9 mol H_2/mol glucose).[146]

As it has been pointed before, dark fermentation produces large amounts of acetic and/or butyric acids that can be further used as supply for a photo fermentative process. Therefore the integration of the two processes could maximize the hydrogen production (5.23).[122,147,148]

$$C_6H_{12}O_6 + 6H_2O \rightarrow 12H_2 + 6CO_2 \quad (5.23)$$

Typical reported yields for integrated processes were about 7.2 mol H_2/mol C_6 from starch-manufacturing wastes[149] or 5.3 mol H_2/mol C_6 from glucose.[150] Nevertheless, when sugarcane was used as feedstock in the two-step integrated process, the hydrogen yield was slightly improved although greenhouse gases (GHC) emissions balance with regard to photofermentation was slightly worse.[141] Some of these processes yield up to 9 mol H_2/mol C_6 and are expected to become very competitive. Bioengineering of these microorganisms might help to adapt the metabolic processes to the future production of hydrogen.

5.6 LIFE CYCLE ASSESSMENT AND HYDROGEN PRODUCTION COSTS

Life Cycle Assessment analysis (LCA) is a standardized protocol (ISO 14040, 2006)[148] that consists of a systematical method that helps to identify and evaluate the environmental impacts of a specific process or competing processes. Resources and energy consumption as well as emissions within the process must be evaluated together with material and energy balances in a "*cradle-to-grave*" manner in all the operations.[151] Thus LCA can be used to compare the goodness of different hydrogen production methods.[152] The LCA methodology consists of four interrelated components[147]:

- Goal definition and scoping (must encompass all the processes necessary from the extraction of the biomass to the final application)
- Inventory analysis (involves the collection and compilation of the required data to quantify the relevant inputs and outputs of the process)
- Impact assessment
- Global interpretation and evaluation.

A hot spot within an LCA corresponds to the decision process, where different strategies can be adopted.[153,154] Extrapolation of an LCA study to other one must be carefully done. In the case of the transformation of biomass to hydrogen, LCA should at least count on[155,156]:

- Biomass acquisition, manufacturing and transportation
- Spends and impacts of hydrogen production

- Liquefaction and storage of hydrogen
- Human health and environmental aspects as well as waste management.

There are extensive reports comparing LCA for classical hydrogen production methodologies as steam reforming of natural gas, coal gasification, thermochemical water splitting or wind electrolysis.[151,157,158] In the previous years some LCA studies for the hydrogen production from biomass feedstocks (named biohydrogen) have also been published. One of the first comparing LCA reports pointed that biohydrogen production could be competitive against traditional hydrogen production, because primary energy ratio (expressed as $E_{\text{fuel product}}/(E_{\text{fossil}} + E_{\text{biomass energy consumed}})$) from biomass (0.35–0.71) was comparable to that from natural gas (0.66) and better than that from coal (0.39).[159]

A more specific LCA on woody biomass gasification for the hydrogen production reflected that the biomass gasification-steam reforming-PSA (Scheme 5.4) route was more energy efficient than the biomass gasification-electricity generation-electrolysis route.[155] Nevertheless, the LCA also indicated that the biomass gasification-electricity-electrolysis route had a better environmental performance, because the as-employed energy for electrolysis could be obtained via a combined cycle coupled to the gasifier.

Another LCA compared different technologies for biohydrogen production regarding gasification or fast pyrolysis, and different biomass feedstocks as whole forest, forest residues (FR), and AR.[160] Gasification was more efficient than fast pyrolysis, and the maximum net energy ratio (NER = 9.3) arose from the FR-based pathway using the Gas Technology Institute gasifier, whereas the minimum NER (1.3) came from the AR-based pathway using fast pyrolysis. The GHG emissions lied in the range of 1.2–8.1 kg CO_2 eq/kg H_2.

Similar LCA studies have also been reported comparing the energetic efficiency of hydrogen production by thermophilic and photoheterotrophic fermentation from waste raw materials (wheat straw, steam potato peels and sweet sorgum stalk).[148] All the variables of the processes were evaluated for the different raw materials, starting from the collection and transport of the waste, the corresponding pretreatment of the biomass, treatment of the effluents, and gas recovery and compression. The production of biohydrogen resulted advantageous against other fossil hydrogen production pathways in terms of GHG emissions and yielding similar energy ratios than those from the steam reforming of methane.

The utilization of biomass for the production of energy is gaining increasing attention. Hence, it would be highly desirable that LCA reached more realistic predictions[161,162] in order to assure a really sustainable energy production.

Since the viability of new processes will be decisive in order to implement these new methodologies for the hydrogen production, LCAs should provide a rigorous estimation of the cost of the hydrogen production from biomass. Studies comparing the cost of the production of hydrogen must include all the associated costs to the production (equipment, construction, building, engineering and supervision costs) as well as the raw materials prices. With this aim, some spreadsheets are available from the DOE (US Department of Energy) Webpage that allow calculating the cost of delivered hydrogen by some production routes (biomass gasification, coal gasification, natural gas reforming, nuclear gas electrolysis) changing raw materials costs and all operating variables.[163] The specific cost parameters relevant to biofuel production as well as the basic approach based on the annuity model are presented in Scheme 5.6.

Given the huge number of studies and their heterogeneity, the costs are usually normalized to an economic situation (i.e. 2011 €, 2007 US $, etc.). The cost of a kilogram of hydrogen could be a very convenient unit to estimate the economic viability compared to fossil fuels, because of the energy contained by 1 kg of hydrogen (119 MJ) is almost equivalent to the energy contained

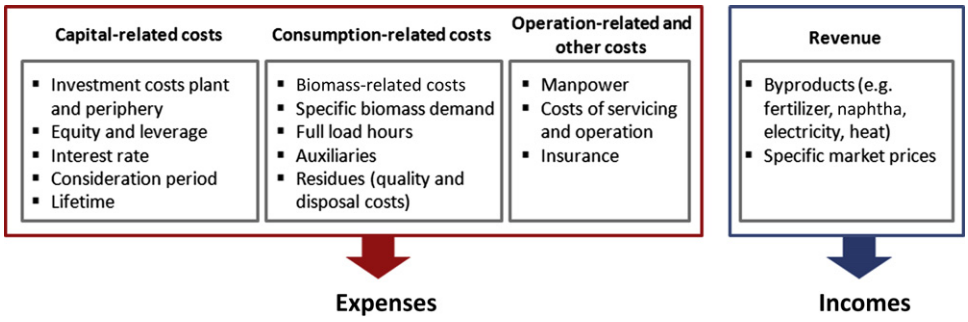

SCHEME 5.6 Specific cost parameters relevant to biofuel production. (For color version of this figure, the reader is referred to the online version of this book.) *Source: Adapted from Ref. 120.*

in one gallon (3.785 l) of gasoline (121.7 MJ).[31] Therefore, any source of hydrogen with a $/kg cost below that of the gasoline gallon may represent an economic advantage.

Recently, Bartels[31] presented an excellent report gathering the economic costs for the hydrogen production using available technologies from both conventional and alternative energy resources, normalized to 2007 US $ and using the Chemical Engineering Plan Cost Index. The results of the analysis showed that the most economical sources of hydrogen were coal (0.36−1.83 $/kg) and natural gas (2.48−3.17 $/kg), whose estimated cost was near gasoline (2.00−4.00 $/gallon). However, in the case of fast pyrolysis of biomass,[31] apart from hydrogen production, other valuable substances in the nonaqueous soluble fraction of the *bio-oil* are useful as adhesive resins[5,164] and reduce the hydrogen cost to 1.47−2.57 $/kg (2007 US $). The gasification of biomass at higher temperature than that of pyrolysis could produce hydrogen in the range of 1.44−2.83 $/kg H_2, depending on factors such as the size of the facility and the cost of feedstock.[165] For instance, the cost of hydrogen based on a plant production of 140 ton H_2/day will increase from 1.99 $/kg H_2 at 46 $/biomass dry ton (bdt) to 2.30 $/kg H_2 at 80 $/bdt.[31] An independent study by the DOE estimated a similar hydrogen production cost (2.40−3.40$/kg H_2 in 2009 US $) using biomass gasification for a plant production of 135 ton H_2/day (from 40 to 120 $/bdt).[166] More optimistic studies assessed hydrogen production cost in 1.34 $/kg H_2 (2005 US $) processing 2000 bdt/day under optimized gasification methodology[167] and in 1.25 $/kg H_2 (2009 US $) from a 234 ton H_2/day plant.[38]

Studies gathered by Balat[7] about the costs of hydrogen production in 2005 US $ estimated 0.78 $/kg H_2 from steam methane reforming, 1.41 $/kg H_2 from coal gasification, 1.24 $/kg H_2 from biomass gasification, 1.26 $/kg H_2 from biomass pyrolysis and 3.77 $/kg H_2 from biomass photofermentation.[168] Older reports, as that of Abbasi,[169] set 1.03 $/kg H_2 (2003 US $) from natural gas reforming, 0.96 $/kg H_2 from coal gasification, 4.63 $/kg H_2 from biomass gasification and 3.8 $/kg H_2 from biomass pyrolysis, respectively compared with 0.93 $/gallon of gasoline. Above evolution of the biohydrogen costs seems a consequence of the achieved improvements in the biomass processing technologies.

An important factor in the economic evaluation for the production of hydrogen reflected by the available estimations is the sensitivity of the final cost to the price of the raw materials. Worldwide reserves for natural gas are estimated to last about 60 years whereas the coal reserves are estimated to last about 133 years.[170] It is worth noting that the cost of natural gas contributes with up to 52−68% to the cost of hydrogen produced by methane steam reforming.[7] Major costs in coal gasification are however attributed to the plant construction (an increase of 25% in coal price changes only 0.05 $/kg of the final hydrogen).[7] Even in the case of a lower influence of the relatively inexpensive coal, depleting of the corresponding reserves approach should largely increase the feedstock-associated cost.[171,172] Nevertheless, the cost for the hydrogen production from biomass mainly comes from operating, distribution and blending costs (harvest and pretreatments)[73,173] as well as capital costs.[7,174,175] Dedicated cellulosic crops are more expensive (ca. 60 $/ton)[174] than the collection and transportation cost of cellulosic waste (i.e. corn stover, wheat straw, or rice straw) that is estimated at 35 $/ton[174] and more costly than coal (based on energy content). Concerning pretreatments, according to Eggeman study of process models for the production of bioethanol, lime and AFEX process seemed to be the most cost advantageous pretreatments.[73]

Therefore, it can be said that biomass provides a promising economically viable pathway to hydrogen, being the main issue to solve the land availability to produce all the required biomass. The implementation of biohydrogen as an energy carrier will probably come from reduction of costs through development and commercialization technologies,[175] valorization of municipal wastes, crops wastes and industrial wastes (such as glycerol from biodiesel production) as alternative feedstocks, as well as new applications for the byproducts derived from the hydrogen production.

References

1. Tanksale, A.; Beltramini, J. N.; Lu, G.-Q. M. *Renew. Sustain. Energy Rev.* **2010,** *14,* 166.
2. Turner, J.; Sverdrup, G.; Mann, M. K.; Maness, P.-C.; Kroposki, B.; Ghirardi, M.; Evans, R. J.; Blake, D. *Int. J. Energy Res.* **2008,** *32,* 379.
3. Balat, M. *Energ. Source Part A* **2010,** *32,* 1388.
4. McKendry, P. *Bioresour. Technol.* **2002,** *83,* 37.
5. Nath, K.; Das, D. *Curr. Sci.* **2003,** *85,* 265.
6. Ni, M.; Leung, D. Y. C.; Leung, M. K. H.; Sumathy, K. *Fuel Process. Technol.* **2006,** *87,* 461.
7. Balat, M.; Balat, M. *Int. J. Hydrogen Energy* **2009,** *34,* 3589.
8. Hayes, D. J. *Catal. Today* **2009,** *145,* 138.
9. Cheng, C.-L.; Lo, Y.-C.; Lee, K.-S.; Lee, D.-J.; Lin, C.-Y.; Chang, J.-S. *Bioresour. Technol.* **2011,** *102,* 8514.
10. Wijffels, R. H.; Barbosa, M. J. *Science* **2010,** *329,* 796.
11. Harun, R.; Singh, M.; Forde, G. M.; Danquah, M. K. *Renew. Sustain. Energy Rev.* **2010,** *14,* 1037.
12. Mata, T. M.; Martins, A. A.; Caetano, N. S. *Renew. Sustain. Energy Rev.* **2010,** *14,* 217.
13. Yang, Z.; Guo, R.; Xu, X.; Fan, X.; Li, X. *Int. J. Hydrogen Energy* **2010,** *35,* 9618.
14. Demirbas, A. *Energy Convers. Manag.* **2010,** *51,* 2738.
15. Singh, N. K.; Dhar, D. W. *Agron. Sustain. Dev.* **2011,** *31,* 605.
16. Tredici, M. R.; Margheri, M. C.; Dephilippis, R.; Materassi, R. *J. Gen. Microbiol.* **1990,** *136,* 1009.
17. Huber, G. W.; Iborra, S.; Corma, A. *Chem. Rev.* **2006,** *106,* 4044.

18. Milne, T. A.; Elam, C. C.; Evans, R. J. *Hydrogen from Biomass. State of the Art and Research Challenges;* National Renewable Energy Laboratory: Golden, Co, USA, 2001.
19. Van De Vyver, S.; Geboers, J.; Jacobs, P. A.; Sels, B. F. *ChemCatChem* **2011,** *3,* 82.
20. Lange, J.-P. *Catalysis for Renewables;* Wiley-VCH Verlag GmbH & Co. KGaA, 2007; p 21.
21. Balat, H.; Kirtay, E. *Int. J. Hydrogen Energy, 35,* 7416.
22. Alonso, D. M.; Bond, J. Q.; Dumesic, J. A. *Green Chem.* **2010,** *12,* 1493.
23. Holladay, J. E.; Bozell, J. J.; White, J. F.; Johnson, D. *Top Value-Added Chemicals from Biomass. Volume II-Results of Screening for Potential Candidates from Biorefinery Lignin;* U.S. Department of Energy, 2007.
24. Vassilev, S. V.; Baxter, D.; Andersen, L. K.; Vassileva, C. G. *Fuel* **2010,** *89,* 913.
25. de Lasa, H.; Salaices, E.; Mazumder, J.; Lucky, R. *Chem. Rev.* **2011,** *111,* 5404.
26. Saidur, R.; Abdelaziz, E. A.; Demirbas, A.; Hossain, M. S.; Mekhilef, S. *Renew. Sustain. Energy Rev.* **2011,** *15,* 2262.
27. Basu, P. *Biomass Gasification and Pyrolysis. Practical Design and Theory;* Elsevier Kidlington: Oxford, UK, 2010.
28. *U. D. o. c. National Institute of Standards and Technology.*
29. Fischer, G.; Schrattenholzer, L. *Biomass Bioenergy* **2001,** *20,* 151.
30. Hoogwijk, M.; Faaija, A.; van den Broek, R.; Berndes, G.; Gielen, D.; Turkenburg, W. *Biomass Bioenergy* **2003,** *25,* 119.
31. Bartels, J. R.; Pate, M. B.; Olson, N. K. *Int. J. Hydrogen Energy* **2010,** *35,* 8371.
32. Smeets, E. M. W.; Faaij, A. P. C.; Lewandowski, I. M.; Turkenburg, W. C. *Prog. Energy Combust. Sci.* **2007,** *33,* 56.
33. Berndes, G.; Hoogwijk, M.; van den Broek, R. *Biomass Bioenergy* **2003,** *25,* 1.
34. Bauen, A.; Berndes, G.; Junginger, M.; Londo, M.; Vuille, F.; Ball, R.; Bole, T.; Chudziak, C.; Faaij, A.; Mozaffarian, H. *Bioenergy — A Sustainable and Reliable Energy Source — A Review of Status and Prospects,* EA Bioenergy: ExCo:2009:06IEA, 2009.
35. de Wit, M.; Faaij, A. *Biomass Bioenergy* **2010,** *34,* 188.
36. Ericsson, K.; Nilsson, L. J. *Biomass Bioenergy* **2006,** *30,* 1.
37. Fischer, G.; Prieler, S.; van Velthuizen, H.; Lensink, S. M.; Londo, M.; de Wit, M. *Biomass Bioenergy* **2010,** *34,* 159.
38. *PEP Yearbook, Process Economics Program;* SRI Consulting, 2009.
39. Torén, J. *Biomass Energy Europe, (BEE). Executive Summary, Evaluation and Recommendations;* European Commission, 2011. FP7 GRANT AGREEMENT N° 213417.
40. Vesterinen, P. *Harmonization of Biomass Resource Assessments* In: *Data Sources Handbook,* Vol. 2; European Commission, 2010. Biomass Energy Europe (BEE). FP7 GRANT AGREEMENT N°: 213417.
41. Perlack, R. D.; Stokes, B. J. *U.S. Billion-Ton Update: Biomass Supply for a Bioenergy and Bioproducts Industry;* Oak Ridge National Laboratory, Department of Energy: Oak Ridge, TN, U.S, 2011. ORNL/TM-2011/224.
42. Perlack, R. D.; Wright, L. L.; Graham, R. L.; Turhollow, A.; Stokes, B. *Biomass as Feedstock for a Bioenergy and Bioproducts Industry: The Technical Feasibility of a Billion-Ton Annual Supply;* USDA Agricultural Research Service, Oak Ridge National Laboratory, 2005. ORNL/TM-2005/66, DOE/GO-102005-2135.
43. *Biomass for Heat and Power. Opportunity and Economics;* European Climate Foundation, Sodra, Sveaskog, Vattenfall, 2010.
44. *Prospects for Hydrogen from Biomass;* International Energy Agency: Paris, 2006. IEA-HIA Task 16, Subtask 16B.
45. Yoo, C. G.; Nghiem, N. P.; Hicks, K. B.; Kim, T. H. *Bioresour. Technol.* **2011,** *102,* 10028.
46. Bridgwater, T. *J. Sci. Food Agric.* **2006,** *86,* 1755.
47. Langan, P.; Gnanakaran, S.; Rector, K. D.; Pawley, N.; Fox, D. T.; Cho, D. W.; Hammel, K. E. *Energy Environ. Sci.* **2011,** *4,* 3820.
48. Bin, Y.; Wyman, C. E. *Biofuels Bioproducts Biorefining* **2008,** *2.*
49. Yang, B.; Wyman, C. E. *Bioresour. Technol.* **2008,** *99,* 5756.
50. Luo, S.; Xiao, B.; Guo, X.; Hu, Z.; Liu, S.; He, M. *Int. J. Hydrogen Energy* **2009,** *34,* 1260.
51. Agbor, V. B.; Cicek, N.; Sparling, R.; Berlin, A.; Levin, D. B. *Biotechnol. Adv.* **2011,** *29,* 675.
52. Alvira, P.; Tomas-Pejo, E.; Ballesteros, M.; Negro, M. J. *Bioresour. Technol.* **2010,** *101,* 4851.
53. Amidon, T. E.; Wood, C. D.; Shupe, A. M.; Wang, Y.; Graves, M.; Liu, S. *J. Biobased Mater. Bioenergy* **2008,** *2,* 100.
54. Hendriks, A. T. W. M.; Zeeman, G. *Bioresour. Technol.* **2009,** *100,* 10.
55. Shin, S.-J.; Sung, Y. J. *Radiat. Phys. Chem.* **2008,** *77,* 1034.
56. Bak, J. S.; Ko, J. K.; Han, Y. H.; Lee, B. C.; Choi, I.-G.; Kim, K. H. *Bioresour. Technol.* **2009,** *100,* 1285.
57. Chun-Zhao, L.; Xi-Yu, C. *Int. J. Hydrogen Energy* **2010,** *35.*
58. Elbeshbishy, E.; Hafez, H.; Nakhla, G. *Int. J. Hydrogen Energy* **2010,** *35,* 6184.
59. Brammer, J. G.; Bridgwater, A. *Biomass Bioenergy* **2002,** *22,* 271.
60. Datar, R.; Huang, J.; Maness, P. C.; Mohagheghi, A.; Czemik, S.; Chornet, E. *Int. J. Hydrogen Energy* **2007,** *32,* 932.
61. Negro, M. J.; Manzanares, P.; Ballesteros, I.; Oliva, J. M.; Cabanas, A.; Ballesteros, M. *Appl. Biochem. Biotechnol.* **2003,** *105,* 87.
62. Horn, S. J.; Nguyen, Q. D.; Westereng, B.; Nilsen, P. J.; Eijsink, V. G. H. *Biomass Bioenergy* **2011,** *35,* 4879.
63. Sun, Y.; Cheng, J. Y. *Bioresour. Technol.* **2002,** *83,* 1.
64. Rogalinski, T.; Ingram, T.; Brunner, G. *J. Supercrit. Fluids* **2008,** *47,* 54.
65. Cara, C.; Romero, I.; Miguel Oliva, J.; Saez, F.; Castro, E. *Appl. Biochem. Biotechnol.* **2007,** *137,* 379.
66. Mosier, N. S.; Hendrickson, R.; Brewer, M.; Ho, N.; Sedlak, M.; Dreshel, R.; Welch, G.; Dien, B. S.; Aden, A.; Ladisch, M. R. *Appl. Biochem. Biotechnol.* **2005,** *125,* 77.
67. Mosier, N.; Wyman, C.; Dale, B.; Elander, R.; Lee, Y. Y.; Holtzapple, M.; Ladisch, M. *Bioresour. Technol.* **2005,** *96,* 673.
68. Mosier, N.; Hendrickson, R.; Ho, N.; Sedlak, M.; Ladisch, M. R. *Bioresour. Technol.* **2005,** *96,* 1986.
69. Kim, Y.; Hendrickson, R.; Mosier, N.; Ladisch, M. R. *Energy Fuels* **2005,** *19,* 2189.
70. Pan, C.-M.; Ma, H.-C.; Fan, Y.-T.; Hou, H.-W. *Int. J. Hydrogen Energy* **2011,** *36,* 4852.
71. Nguyen, Q.; Tucker, M.; Keller, F.; Eddy, F. *Appl. Biochem. Biotechnol.* **2000,** *84—86,* 561.
72. Hamelinck, C. N.; Suurs, R. A. A.; Faaij, A. P. C. *Biomass Bioenergy* **2005,** *29,* 114.
73. Eggeman, T.; Elander, R. T. *Bioresour. Technol.* **2005,** *96,* 2019.
74. Gandi, J.; Holtzapple, M. T.; Ferrer, A.; Byers, F. M.; Turner, N. D.; Nagwani, M.; Chang, S. *Anim. Feed Sci. Technol.* **1997,** *68,* 195.
75. Chang, V. S.; Burr, B.; Holtzapple, M. T. *Appl. Biochem. Biotechnol.* **1997,** *63—5,* 3.
76. Chang, V. S.; Nagwani, M.; Kim, C. H.; Holtzapple, M. T. *Appl. Biochem. Biotechnol.* **2001,** *94,* 1.
77. Martin, C.; Klinke, H. B.; Thomsen, A. B. *Enzyme Microb. Technol.* **2007,** *40,* 426.
78. McMillan, J. D. In Himmel, M. E., Baker, J. O., Overend, R. P., Eds. **1994,** *Vol. 566; p 292.*
79. Wyman, C. E.; Dale, B. E.; Elander, R. T.; Holtzapple, M.; Ladisch, M. R.; Lee, Y. Y. *Bioresour. Technol.* **2005,** *96,* 2026.
80. Lau, M. W.; Gunawan, C.; Dale, B. E. *Biotechnol. Biofuels* **2009,** *2.*
81. Eggeman, T.; Verser, D. *Appl. Biochem. Biotechnol.* **2005,** *121,* 605.
82. Kim, T. H.; Lee, Y. Y. *Bioresour. Technol.* **2005,** *96,* 2007.
83. Kim, T. H.; Taylor, F.; Hicks, K. B. *Bioresour. Technol.* **2008,** *99,* 5694.
84. Kim, T. H.; Kim, J. S.; Sunwoo, C.; Lee, Y. Y. *Bioresour. Technol.* **2003,** *90,* 39.
85. Swatloski, R. P.; Spear, S. K.; Holbrey, J. D.; Rogers, R. D. *J. Am. Chem. Soc.* **2002,** *124,* 4974.

86. Shi, J.; Chinn, M. S.; Sharma-Shivappa, R. R. *Bioresour. Technol.* **2008,** *99,* 6556.
87. Wan, C.; Li, Y. *Bioresour. Technol.* **2011,** *102,* 7507.
88. Yang, X.; Zeng, Y.; Ma, F.; Zhang, X.; Yu, H. *Bioresour. Technol.* **2010,** *101,* 5475.
89. Taniguchi, M.; Suzuki, H.; Watanabe, D.; Sakai, K.; Hoshino, K.; Tanaka, T. *J. Biosci. Bioeng.* **2005,** *100,* 637.
90. Wen, G.; Xu, Y.; Xu, Z.; Tian, Z. *Catal. Commun.* **2010,** *11,* 522.
91. Ma, F.; Yang, N.; Xu, C.; Yu, H.; Wu, J.; Zhang, X. *Bioresour. Technol.* **2010,** *101,* 9600.
92. Kirtay, E. *Energy Convers. Manag.* **2011,** *52,* 1778.
93. Puig-Arnavat, M.; Carles Bruno, J.; Coronas, A. *Renew. Sustain. Energy Rev.* **2010,** *14,* 2841.
94. *Biomasa: Gasificación;* BESEL, S.A., IDAE (Instituto para la Diversificación y Ahorro de la Energía): Madrid, 2007.
95. Asadullah, M.; Ito, S. I.; Kunimori, K.; Yamada, M.; Tomishige, K. *Environ. Sci. Technol.* **2002,** *36,* 4476.
96. Lv, P. M.; Chang, J.; Wang, T. J.; Fu, Y.; Chen, Y.; Zhu, J. X. *Energy Fuels* **2004,** *18,* 228.
97. Demirbas, A. *Energy Convers. Manag.* **2002,** *43,* 877.
98. Demirbas, A. *Energy Sources* **2005,** *27,* 339.
99. Kriengsak, S. N.; Buczynski, R.; Gmurczyk, J.; Gupta, A. K. *Environ. Eng. Sci.* **2009,** *26,* 739.
100. Rapagna, S.; Provendier, H.; Petit, C.; Kiennemann, A.; Foscolo, P. U. *Biomass Bioenergy* **2002,** *22,* 377.
101. Minowa, T.; Inoue, S. *Renew. Energy* **1999,** *16,* 1114.
102. Demirbas, A. *Fuel* **2001,** *80,* 1885.
103. Navarro, R. M.; Sanchez-Sanchez, M. C.; Alvarez-Galvan, M. C.; del Valle, F.; Fierro, J. L. G. *Energy Environ. Sci.* **2009,** *2,* 35.
104. Midilli, A.; Rzayev, P.; Olgun, H.; Ayhan, T. *Int. J. Hydrogen Energy* **2000,** *25,* 723.
105. Knoeff, H. A. M. *BTG biomass technology group, BV,* Enschede, The Netherlands, 2008 <http://www.btgworld.com>.
106. Lei, Y.; Cant, N. W.; Trimm, D. L. *J. Catal.* **2006,** *239,* 227.
107. Kim, W. B.; Voitl, T.; Rodriguez-Rivera, G. J.; Dumesic, J. A. *Science* **2004,** *305,* 1280.
108. Zhang, Q.; Chang, J.; Wang, T.; Xu, Y. *Energy Convers. Manag.* **2007,** *48,* 87.
109. Balat, M.; Balat, M.; Kirtay, E.; Balat, H. *Energy Convers. Manag.* **2009,** *50,* 3158.
110. Czernik, S.; Bridgwater, A. V. *Energy Fuels* **2004,** *18,* 590.
111. Wang, Z.; Pan, Y.; Dong, T.; Zhu, X.; Kan, T.; Yuan, L.; Torimoto, Y.; Sadakata, M.; Li, Q. *Appl. Catal. A Gen.* **2007,** *320,* 24.
112. Medrano, J. A.; Oliva, M.; Ruiz, J.; Garcia, L.; Arauzo, J. *Energy* **2011,** *36,* 2215.
113. Salehi, E.; Azad, F. S.; Harding, T.; Abedi, J. *Fuel Process. Technol.* **2011,** *92,* 2203.
114. Garcia, L.; French, R.; Czernik, S.; Chornet, E. *Appl. Catal. A Gen.* **2000,** *201,* 225.
115. Chen, H.; Ding, Y.; Cong, N. T.; Dou, B.; Dupont, V.; Ghadiri, M.; Williams, P. T. *Renew. Energy* **2011,** *36,* 779.
116. He, L.; Chen, D. *ChemSusChem* **2012,** *5,* 587.
117. Chen, D.; He, L. *ChemCatChem* **2011,** *3,* 490.
118. Cortright, R. D.; Davda, R. R.; Dumesic, J. A. *Nature* **2002,** *418,* 964.
119. Huber, G. W.; Shabaker, J. W.; Evans, S. T.; Dumesic, J. A. *Appl. Catal. B Environ.* **2006,** *62,* 226.
120. Zinoviev, S.; Muller-Langer, F.; Das, P.; Bertero, N.; Fornasiero, P.; Kaltschmitt, M.; Centi, G.; Miertus, S. *ChemSusChem* **2010,** *3,* 1106.
121. Huber, G. W.; Dumesic, J. A. *Catal. Today* **2006,** *111,* 119.
122. Holladay, J. D.; Hu, J.; King, D. L.; Wang, Y. *Catal. Today* **2009,** *139,* 244.
123. Huber, G. W.; Shabaker, J. W.; Dumesic, J. A. *Science* **2003,** *300,* 2075.
124. Chun-Hui, Z.; Xi, X.; Chun-Xiang, L.; Dong-Shen, T.; Jorge, B. *Chem. Soc. Rev.* **2011,** *40,* 5588.
125. Iriondo, A.; Barrio, V. L.; Cambra, J. F.; Arias, P. L.; Gueemez, M. B.; Navarro, R. M.; Sanchez-Sanchez, M. C.; Fierro, J. L. G. *Top. Catal.* **2008,** *49,* 46.
126. Menezes, A. O.; Rodrigues, M. T.; Zimmaro, A.; Borges, L. E. P.; Fraga, M. A. *Renew. Energy* **2011,** *36,* 595.
127. Demirbas, A. *Energy Convers. Manag.* **2009,** *50,* 2782.
128. Kruse, A.; Meier, D.; Rimbrecht, P.; Schacht, M. *Ind. Eng. Chem. Res.* **2000,** *39,* 4842.
129. Kruse, A. *Biofuels Bioproducts Biorefining* **2008,** *2,* 415.
130. Guo, L. J.; Lu, Y. J.; Zhang, X. M.; Ji, C. M.; Guan, Y.; Pei, A. X. *Catal. Today* **2007,** *129,* 275.
131. Lee, I. G.; Kim, M. S.; Ihm, S. K. *Ind. Eng. Chem. Res.* **2002,** *41,* 1182.
132. Antal, M. J.; Allen, S. G.; Schulman, D.; Xu, X.; Divilio, R. J. *Ind. Eng. Chem. Res.* **2000,** *39,* 4040.
133. Byrd, A. J.; Pant, K. K.; Gupta, R. B. *Ind. Eng. Chem. Res.* **2007,** *46,* 3574.
134. Guo, Y.; Liu, X.; Azmat, M. U.; Xu, W.; Ren, J.; Wang, Y.; Lu, G. *Int. J. Hydrogen Energy* **2012,** *37,* 227.
135. Schmieder, H.; Abeln, J.; Boukis, N.; Dinjus, E.; Kruse, A.; Kluth, M.; Petrich, G.; Sadri, E.; Schacht, M. *J. Supercrit. Fluids* **2000,** *17,* 145.
136. Youjun, L.; Sha, L.; Liejin, G.; Ximin, Z. *Int. J. Hydrogen Energy* **2010,** *35.*
137. Hao, X. H.; Guo, L. J.; Mao, X.; Zhang, X. M.; Chen, X. J. *Int. J. Hydrogen Energy* **2003,** *28,* 55.
138. Turn, S.; Kinoshita, C.; Zhang, Z.; Ishimura, D.; Zhou, J. *Int. J. Hydrogen Energy* **1998,** *23,* 641.
139. Yoshida, Y.; Dowaki, K.; Matsumura, Y.; Matsuhashi, R.; Li, D.; Ishitani, H.; Komiyama, H. *Biomass Bioenergy* **2003,** *25,* 257.
140. Lu, Y.; Zhao, L.; Guo, L. *Int. J. Hydrogen Energy* **2011,** *36,* 14349.
141. Manish, S.; Banerjee, R. *Int. J. Hydrogen Energy* **2008,** *33,* 279.
142. Tommasi, T.; Ruggeri, B.; Sanfilippo, S. *J. Clean. Prod.* **2012**.
143. Dasgupta, C. N.; Gilbert, J. J.; Lindblad, P.; Heidorn, S. A.; Skjanes, K.; Das, D. *Int. J. Hydrogen Energy* **2010,** *35,* 10218.
144. Das, D.; Veziroglu, T. N. *Int. J. Hydrogen Energy* **2001,** *26,* 13.
145. Yetis, M.; Gunduz, U.; Eroglu, I.; Yucel, M.; Turker, L. *Int. J. Hydrogen Energy* **2000,** *25.*
146. Ferreira, A. F.; Marques, A. C.; Batista, A. P.; Marques, P. A. S. S.; Gouveia, L.; Silva, C. M. *Int. J. Hydrogen Energy* **2012,** *37,* 179.
147. Claassen, P. A. M.; de Vrije, T. *Int. J. Hydrogen Energy* **2006,** *31,* 1416.
148. Djomo, S. N.; Blumberga, D. *Bioresour. Technol.* **2011,** *102,* 2684.
149. Yokoi, H.; Maki, R.; Hirose, J.; Hayashi, S. *Biomass Bioenergy* **2002,** *22,* 389.
150. Nath, K.; Kumar, A.; Das, D. *Appl. Microbiol. Biotechnol.* **2005,** *68,* 533.
151. Spath, P. L.; Mann, M. K. *LifeCycle Assessment of Hydrogen Production via Natural Gas Steam Reforming;* National Renewable Energy Laboratory: Golden, Colorado US, 2001.
152. Ferreira, A. F.; Ribau, J. P.; Silva, C. M. *Int. J. Hydrogen Energy* **2011,** *36,* 13547.
153. Benoit, V.; Rousseaux, P. *Int. J. Life Cycle Assess.* **2003,** *8,* 74.
154. Gasafi, E.; Weil, M. *J. Clean. Prod.* **2011,** *19,* 1590.
155. Koroneos, C.; Dompros, A.; Roumbas, G. *Chem. Eng. Process.* **2008,** *47,* 1267.
156. Koroneos, C.; Dompros, A.; Roumbas, G.; Moussiopoulos, N. *Int. J. Hydrogen Energy* **2004,** *29,* 1443.
157. Cetinkaya, E.; Dincer, I.; Naterer, G. F. *Int. J. Hydrogen Energy* **2012,** *37,* 2071.
158. Dufour, J.; Serrano, D. P.; Galvez, J. L.; Moreno, J.; Garcia, C. *Int. J. Hydrogen Energy* **2009,** *34,* 1370.
159. Spath, P. L.; Mann, M. K.; Amos, W. A. *Update of Hydrogen from Biomass-Determination of the Delivered Cost of Hydrogen;* NREL: Golden Colorado, 2003.

160. Kabir, M. R.; Kumar, A. *Bioresour. Technol.* **2011,** *102,* 8972.
161. Lee, D.-H.; Lee, D.-J.; Veziroglu, A. *Bioresour. Technol.* **2011,** *102,* 8475.
162. Cucek, L.; Varbanov, P. S.; Klemes, J. ÃJ.; Kravanja, Z. *Energy* **2012**.
163. Mann, M.K. <http://www.hydrogen.energy.gov/h2a_prod_studies.html>.
164. Demirbas, M. F. *Energ. Source Part A* **2006,** *28,* 245.
165. Padro, C. E. G.; Putsche, V. *Survey of the Economics of Hydrogen Technologies* 1999.
166. Parks, G. D.; Curry-Nkansah, M.; Hughes, E.; Sterzinger, G. *Hydrogen Production Cost Estimate Using Biomass Gasification;* U.S. Department of Energy: Golden, Colorado, USA, 2011.
167. Spath, P.; Aden, A.; Eggeman, T.; Ringer, M.; Wallace, B.; Jechura, J. *Biomass to Hydrogen Production Detailed Design and Economics Utilizing the Battelle Columbus Laboratory Indirectly-Heated Gasifier;* U.S. Department of Energy Golden: Colorado, USA, 2005.
168. Norman, K. *Interim Report: Feasibility of Microscale Glucose Reforming for Renewable Hydrogen. SANDIA Report No. SAND2007-1713,* Sandia National Laboratories, New Mexico, California, 2007.
169. Abbasi, T.; Abbasi, S. A. *Renew. Sustain. Energy Rev.* **2011,** *15,* 3034.
170. BP Statistical Review of World Energy 2008, B. P. Company, London, 2008.
171. Penner, S. S. *Energy* **2006,** *31,* 33.
172. Kreutz, T.; Williams, R.; Consonni, S.; Chiesa, P. *Int. J. Hydrogen Energy* **2005,** *30,* 769.
173. Kim, S. D.; Dale, B. E. *J. Ind. Ecol.* **2003,** *7,* 147.
174. Zhang, Y. H. P. *Process Biochem.* **2011,** *46,* 2091.
175. Orecchini, F.; Bocci, E. *Energy* **2007,** *32,* 1006.

CHAPTER

6

Hydrogen from Biomass: Advances in Thermochemical Processes

Li He, Jia Yang, De Chen

Department of Chemical Engineering, Norwegian University of Science and Technology, Trondheim, Norway

OUTLINE

6.1 Introduction 111

6.2 Steam Reforming of Biomass-Derived Chemicals 113
- *6.2.1 Challenges in Steam Reforming of Biomass-Derived Chemicals* 113
- *6.2.2 Steam Reforming of Biomass-Derived Ethanol and Carbohydrates* 114
- *6.2.3 Steam Reforming of Bio-Oil Produced by Fast Pyrolysis* 115
- *6.2.4 Catalysis in Reforming Reactions of Biomass-Derived Oxygenates* 116
  - 6.2.4.1 General Reaction Mechanism of Reforming Reactions 116
  - 6.2.4.2 Reforming Catalysts for H_2 Production 117
  - 6.2.4.3 High-Temperature WGS Reaction 119
- *6.2.5 Coke Formation in Reforming of Biomass-Derived Chemicals* 119
- *6.2.6 Steam Reforming Thermal Efficiency* 120
- *6.2.7 Reactors for Steam Reforming of Biomass* 121

6.3 Aqueous-Phase Reforming 121

6.4 Supercritical Reforming 123

6.5 Sorption-Enhanced Reforming of Biomass-Derived Chemicals 123
- *6.5.1 Strategies for Sorption-Enhanced H_2 Production* 123
- *6.5.2 SESR of Biogas* 124
- *6.5.3 SESR of Ethanol and Polyols* 124
- *6.5.4 SESR of Sugars* 125
- *6.5.5 SESR of the Aqueous Phase of Bio-Oil* 125
- *6.5.6 Catalyst in SEHP* 126
- *6.5.7 CO_2 Acceptor in Thermal Chemical Conversion of Biomass* 126

6.6 H_2 Production by Biomass Gasification 126
- *6.6.1 Catalysts for Gasification of Biomass* 127
- *6.6.2 Sorption-Enhanced Biomass Gasification* 128
- *6.6.3 Sorption-Enhanced Water Gas Shift Reaction* 128

6.7 Conclusions and Perspectives 129

Acknowledgments 130

References 130

6.1 INTRODUCTION

The emerging H_2 energy economy and the increasing demand of H_2 by refineries lead to a large demand for new H_2 production capacity.[1] Currently, most H_2 is produced by the steam reforming of fossil fuels.[2] With the consideration of increasing global concern about climate change and CO_2 emission, it is imperative to produce H_2 in a CO_2 neutral manner. Currently, there are two major ways to obtain CO_2 neutral production of H_2: the first one is the utilization of the existing technologies for the production of H_2 by means of steam reforming or partial oxidation of nonrenewable fossil fuels, combined with CO_2

http://dx.doi.org/10.1016/B978-0-444-56352-1.00006-4

sequestration, whereas the second one is the H_2 production from renewable resources such as water (e.g. by the action of sunlight) or biomass (e.g. by catalytic conversion). With advantages of their renewability, availability, diversity and easy-to-transport (solid or liquid), biomass or biomass-derived chemicals have been considered as alternative feedstocks for H_2 generation.[3–6] The recent works in this field have demonstrated specific benefits of steam reforming biomass or biomass-derived compounds for H_2 production.[6,7]

Although renewable biomass is an attractive alternative to fossil fuel feedstock, the effectiveness of biomass as H_2 source depends critically on the discovery of new generations of heterogeneous catalysts, as well as process designs which improve largely the utilization of biomass and the energy efficiency in the conversion of biomass or biomass-derived chemicals to H_2. The conversion technologies from biomass to H_2 can be divided into two categories: (1) direct production routes and (2) conversion of storable intermediates or biomass-derived chemicals. Both conversion routes can be carried out by means of thermochemical and biological processes. This chapter focuses only on the progresses in thermochemical processes.

Figure 6.1 represents the scheme for H_2 production from lignocellulosic biomass by thermochemical processes. Similar to the production of biofuels from biomass, three routes can be found in the biomass conversion to H_2: gasification, pyrolysis and hydrolysis-sugar.[9] Lignocellulosic biomass differs greatly in its physical, chemical and morphological properties, affecting the gasification process. Gasification of lignocellulosic biomass as a direct route presents not many requirements in relation to the biomass pretreatment and is considered as a simple process for a diversity of feedstocks. However, lignocellulosic biomass has a low H_2 content and, in general, gives, therefore, a low H_2 yield. The focus of gasification performance has been on the improvement in the product gas composition (H_2, CO, CO_2, CH_4, and C_nH_m), minimization of tar and char content in the effluent stream and enhancement in the gas yield, cold-gas efficiency and carbon conversion. To overcome the problems associated to the gasification process, the indirect routes, as shown in Fig. 6.1, can be promising alternatives to biomass conversion for H_2 production. Additional production steps in the hydrolysis-sugar and pyrolysis routes help to improve the overall H_2 yield in biomass conversion. Another advantage of the additional steps or production of intermediates is that transportation costs might be reduced by a distributed conversion of large-volume biomass to intermediates such as sugars, alcohols or bio-oils. In the hydrolysis-sugar route, biomass is decomposed to relatively simple chemical forms such as glucose, that is, the main monomer which the lignocellulosic biomass is composed of. Afterward, H_2 is produced either by directly reforming sugars or by fermentation of the sugars to ethanol[10] and other polyols,[11] followed by the reforming process. Pyrolysis is mainly referred to conversion of biomass into liquids at a temperature of 377–527 °C at 1–5 atm in the absence of air.[12] The slow pyrolysis mainly produces charcoal and is considered not suitable for H_2 production. The products of the fast pyrolysis are distributed in all the gas, liquid and solid phases.[13] Various properties of bio-oil such as low heating value due to high moisture content (15–30%), highly corrosive (pH about 2.5), incompatibility with conventional fuels, high ash content, high viscosity, incomplete volatility and chemical instability (high contents of aldehydes, ketones and carboxyl acids) all have an adverse effect on the quality of bio-oil as a transportation fuel.[12] Upgrading process is necessary to convert bio-oil into a ready alternative to petroleum fuel within the transportation industry. There have been intensive studies on the conversion of the bio-oil aqueous fraction to synthesis gas or H_2 by steam reforming.

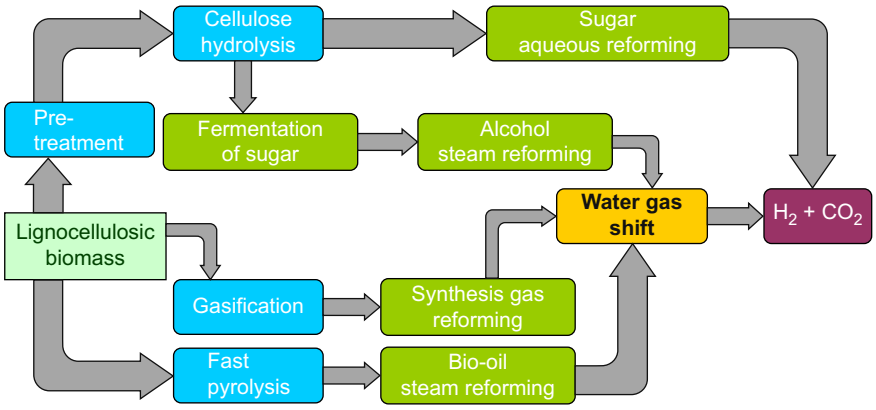

FIGURE 6.1 Schematic presentation of biomass conversion routes for H_2 production by thermochemical processes.[8] (For color version of this figure, the reader is referred to the online version of this book.)

As seen in Fig. 6.1, all three routes for conversion of biomass to H_2 involve reforming and/or the water gas shift (WGS) reaction to enrich H_2 content in the gas product. Since the WGS of the effluent from reforming of biomass-derived compounds is not particularly different from that used in reforming of methane, it is not discussed here.

Currently, the predominant technology for H_2 production is still steam reforming of natural gas, where Ni is the most commonly used catalyst. Steam reforming of natural gas is considered a mature industrial process. There has been particular interest in applying current knowledge and facility of the natural gas reforming process to the conversion of biomass or biomass-derived chemicals in order to reach a competitive hydrogen production. Fossil and biomass-derived fuels can be represented by a generic formula: $C_nH_mO_k$. The reforming or gasification of biomass or biomass-derived chemicals in the presence of steam can be described by following reactions[14]:

$$C_nH_mO_k + (n-k)H_2O = nCO + (n + m/2 - k)H_2 \quad (6.1)$$

The WGS reaction occurs to refine the product distribution.

$$CO + H_2O = CO_2 + H_2 \quad (6.2)$$

Combining Eqns (6.1) and (6.2), the complete reforming reaction of the hydrocarbon oxygenates with steam for H_2 production can be represented as the following:

$$C_nH_mO_k + (2n-k)H_2O = nCO_2 + (2n + m/2 - k)H_2 \quad (6.3)$$

Various reforming technologies have been developed with a potential for industrial H_2 production. The reaction in Eqn (6.3) can be used as a general guide to simply describe the desired H_2 production by reforming of oxygenates or hydrocarbons. Reforming of biomass-derived chemicals is generally classified by the reaction conditions, in particular, by the water phase, namely steam reforming, aqueous reforming and supercritical reforming (SCR). Steam reforming is conducted at high temperature and water reacts on the catalytic surface as steam. In aqueous reforming or SCR, higher pressure and lower temperature are applied. They involve water at high density and gas effluent contains H_2, CO, CO_2, methane, and so on.

In this chapter, H_2 production from biomass will be discussed in terms of production processes such as steam reforming (Section 6.2), aqueous reforming (Section 6.3), SCR (Section 6.4), sorption-enhanced steam reforming (SESR) (Section 6.5) and gasification (Section 6.6). Particular attention will be given to new progresses in reforming and sorption-enhanced reforming of biomass-derived chemicals. Catalyst development, feedstock selection, process evaluation and theoretical limitations will be addressed in detail.

6.2 STEAM REFORMING OF BIOMASS-DERIVED CHEMICALS

Although steam reforming of biomass-derived chemicals is an extension of the conventional steam reforming of methane, we will first look at additional challenges in the H_2 production from steam reforming of highly functionalized chemicals derived from biomass. Then we will discuss general technical concerns in steam reforming of biomass-derived chemicals, such as feedstocks using carbohydrates from hydrolysis, bio-oils production from fast pyrolysis of biomass, catalytic reactions and process development challenges. Moreover, with acknowledging dissimilarity in reforming by using steam and aqueous water, there are many general features commonly shared by various types of reforming reactions. This section will also discuss common features in reforming reactions such as catalysis and criteria for catalyst development in production of H_2. In addition, H_2 production should be optimized with the consideration of the process development. The reforming efficiency and process design are presented with focus on economical production of H_2 and energy reduction at the end of this section.

6.2.1 Challenges in Steam Reforming of Biomass-Derived Chemicals

Compared with conventional feedstocks for H_2 production, additional challenges are encountered in conversion of bio-based chemicals, mainly summarized as following:

- Complexity of feedstocks. The origin of biomass and the chemistries in its decomposition to monomer products lead to a mixture of oxygenated hydrocarbons with distinct chemical and physical properties,[15] which have profound impact on the steam reforming processes.[16]
- High risk of coking. Compared to conventional fuels, biomass-derived compounds are often characterized with low hydrogen-to-carbon ratio, indicating potential high risk of coke formation in gasification processes.[17] The carbon formation can be reduced with the addition of excess steam, which alters the hydrogen-to-carbon ratio in the reaction system. Besides the intrinsic strong tendency to coke formation, the low thermal stability and high

functionality of many oxygenated hydrocarbons lead to thermal decomposition or homogeneous polymerization before or when they go through the reforming catalyst bed. The high risk of solid deposition has substantially limited the choice of feedstocks for steam reforming. The model compounds such as C_1–C_3 oxygenated hydrocarbons are often used in the study of the steam reforming of bio-based feedstocks.[18] However, recent results have showed the difficulties in gasifying heavy feedstocks by steam reforming.[19,20] Steam reforming of glucose has been studied in a comparative study. The results showed that glucose reforming suffered from severe thermal decomposition, producing tars and chars at temperatures where steam reforming reactions were not yet effective.[21]

- Difficulty in sulfur removal. The hydrogenation of alkyl thiol compounds and the subsequent adsorption/absorption of H_2S can remove sulfur in natural gas quantitatively.[22] In contrast, desulfurization of dibenzothiophene derivatives, which are representative to the organic sulfur-containing compounds present in liquid hydrocarbon fuels, can only partly remove sulfur, even using novel hydrotreating catalysts or by deep adsorptive desulfurization.[23] The challenge in the removal of sulfur in biomass can pose problems in the reforming processes, where the candidate catalysts, typically from group 8–10, are prone to sulfur poisoning.
- Low selectivity. Biomass-derived molecules are highly reactive due to their high degree of functionality.[24] Consequently, processing such feedstocks can generate a broad range of products, challenging the selective conversion to H_2, particularly with biomass-derived polyols such as glycerol and sorbitol as well as sugar compounds. It is often necessary to have additional multiple reaction steps for elevating H_2 content to meet application requirement. Such complex processing makes the production uneconomical at present.

6.2.2 Steam Reforming of Biomass-Derived Ethanol and Carbohydrates

Steam reforming of biomass-derived carbohydrates produces synthesis gas or H_2-rich gas. The high purity of H_2 is obtained with further unit operation on synthesis gas such as the WGS reaction and pressure swing adsorption. The steam reforming of bioethanol, glycerol, sorbitol and glucose has been extensively studied. There has been a large body of study on steam reforming of bioethanol, which has also been intensively reviewed by many groups in terms of reaction mechanism and catalyst deactivation,[25] catalysts development[4,7,18,26] and system integration with fuel cells.[27]

The reaction pathways in ethanol reforming are summarized in Table 6.1, showing a complex feature in product formation and distribution. Ethanol decomposition, dehydrogenation to aldehyde and its subsequent steam reforming or decompositions occur concurrently or subsequently with ethanol steam reforming, which leads to by-products formation and lowers H_2 selectivity. It represents also a high potential of coke formation by means of condensation of unsaturated oxygenates and polymerization of olefins. It is essential to gain a better understanding of reaction mechanism and design better catalysts to control the reactions pathways. The strategy to achieve high activity, selectivity and stability of catalysts will be discussed in Section 6.2.4.

Thermodynamic analysis predicts that temperature higher than 600 °C and steam-to-carbon ratio higher than 3 are necessary to avoid carbon formation.[28] The reaction routes for H_2 production from ethanol such as steam reforming, partial oxidation and oxidative steam reforming have a great impact on the product distribution.[25] Although steam reforming provides a high H_2 yield, partial oxidation makes reactor more compact due to fast reaction in the presence of oxygen. Oxidative steam reforming could make the H_2 production autothermal. Glycerol is a 10% by-product of manufactured biodiesel and also a by-product from the hydrolysis and transesterification of triglycerides that produce long-chain acids.[29] The excess of glycerol produced has made its price low on the current market. Therefore, it is interesting to convert glycerol to clean energy carrier such as H_2. The recent progresses in the research on glycerol steam reforming have been reviewed by several groups,[4,30–32] including reaction mechanism and development of different catalysts.

Zhou et al.[29] compared the steam reforming of ethanol and glycerol with sugars, which can often be represented by glucose, xylose and sucrose. It was found that sugars are difficult to be processed as reforming feedstocks. It was attributed to their high functionality and low thermal stability. They were readily decomposed or transformed to solid carbonaceous species upon injection and in the reactor freeboard, leading to difficulty in process operability and a low H_2 yield. To avoid formation of solid carbonaceous species, reforming sugars need a very high steam-to-carbon ratio (>14). The high content of water in the feed was found to reduce sugar decomposition by shortening the residence time of the sugar feed in the high-temperature

TABLE 6.1 The Reaction Pathway in Ethanol Reforming[18]

Reaction	Equation	Remarks
Sufficient steam supply	$C_2H_5OH + 3H_2O \rightarrow 2CO_2 + 6H_2$	Ideal pathway, the highest hydrogen production
Insufficient steam supply	$C_2H_5OH + H_2O \rightarrow 2CO + 4H_2$ $C_2H_5OH + 2H_2 \rightarrow 2CH_4 + H_2O$	Undesirable products, lower hydrogen production
Dehydrogenation	$C_2H_5OH \rightarrow C_2H_4O + H_2$	Reaction pathways for hydrogen production in practice
Acetaldehyde decomposition	$C_2H_4O \rightarrow CH_4 + CO$	
Acetaldehyde steam reforming	$C_2H_4O + H_2O \rightarrow 3H_2 + 2CO$	
Dehydration	$C_2H_5OH \rightarrow C_2H_4 + H_2O$	Undesired pathway, main source of coke formation
Coke formation	$C_2H_4 \rightarrow$ polymeric deposits(coke)	
Decomposition	$C_2H_5OH \rightarrow CO + CH_4 + H_2$ $2C_2H_5OH \rightarrow C_3H_6O + CO + 3H_2$ $C_2H_5OH \rightarrow 0.5CO_2 + 1.5CH_4$	Coke formation, low hydrogen production
Reaction of decomposition products		
Methanation	$CO + 3H_2 \rightarrow CH_4 + H_2O$ $CO_2 + 4H_2 \rightarrow CH_4 + 2H_2O$	
Methane decomposition	$CH_4 \rightarrow 2H_2 + C$	
Boudouard reaction	$2CO \rightarrow CO_2 + C$	
Water gas shift reaction (WGSR)	$CO + H_2O \rightarrow CO_2 + H_2$	Reduce coke formation, enhance hydrogen production

freeboard above the catalyst bed.[16] On the other hand, aqueous-phase reforming (APR),[3] gasification in supercritical water (SCW)[33] and sorption-enhanced reforming[8] provide better opportunity for H_2 production from sugars and sugar-derived carbohydrates in terms of high H_2 yield and low coke formation. This will be discussed in Sections 6.3–6.5.

6.2.3 Steam Reforming of Bio-Oil Produced by Fast Pyrolysis

Fast pyrolysis can effectively convert biomass into liquid oil by heating, and lignocellulosic biomass is liquefied to bio-oil with a typical yield of *ca* 70%. Bio-oil is a mixture containing widely ranged compounds. Upon the addition of water, bio-oil separates into: (1) an aqueous phase containing mostly carbohydrate-derived compounds and (2) a hydrophobic phase, composed mainly of lignin-derived oligomers.[12] The aqueous, carbohydrate-derived fraction is often used for H_2 production by steam reforming.

There have been intensive studies on the conversion of bio-oil aqueous fraction to synthesis gas or H_2 by steam reforming. Model compounds are often used to gain a better understanding of chemistry in bio-oil steam reforming and to develop efficient catalysts of the reforming reactions. Acetic acid[16,34–56] is often used as a model compound of bio-oil. There are also other model compounds, including methanol,[57] acetone,[19,47,50,53,58–62] ethanol,[19,47,48,62–64] ethyl acetate,[51] *m*-xylene,[51] *m*-cresol,[65] dibenzyl ether,[16] *m*-cresol, glucose,[16,19] xylose[16] and phenol.[61,66,67] Oxygenated aromatics (e.g. *m*-cresol and dibenzyl ether) are found to have much lower reactivity in steam reforming for H_2 production in comparison to acetic acid at low temperatures.[16,19] Critical temperature is an important parameter for gas production. At a temperature lower than the critical level, a large amount of carbonaceous deposits is easily formed on the catalyst surfaces, leading to low gas production and low catalyst activity. High rate of coke formation is a result of high potential of polymerization and condensation reactions at low temperatures. At temperatures higher than the critical temperature, the reactivity of oxygenated aromatics is higher than acetic acid toward H_2 formation.

Steam reforming of the actual bio-oil aqueous phase has also been studied by many groups.[14,47,48,55,68–70] High H_2 yield was obtained often at high operation temperatures. For instance, H_2 yields as high as 85% of the stoichiometric values can be achieved at 750 °C, a gas hourly space velocity of 1100/h, a steam-to-carbon ratio of 5 on a commercial Ni catalyst.[14,69] Although Ni

catalysts are often developed for steam reforming of natural gas and crude oil fractions, it was found out that they still had a good activity to promote H_2 formation in steam reforming of the actual bio-oil aqueous phase. This was explained by its high WGS activity.[14] As mentioned previously, Ni catalyst suffers from coke formation. Therefore, in the steam reforming of bio-oil, high steam-to-carbon ratio was recommended to avoid deteriorate catalyst performance by suppressing coke formation.[71] In general, steam reforming of bio-oil is an extension of the steam reforming of natural gas. In principle, some of the compounds in the aqueous phase can be reformed at a temperature range (<650 °C) much lower than steam reforming of methane, which is typically between 700 and 900 °C depending on the pressure and steam-to-carbon ratio. But in practice, the operation of steam reforming of bio-oil is often conducted at temperature even higher than 650 °C in order to suppress coke formation. Indeed, coke formation is more severe in the reforming of bio-oils because some of bio-oil components are thermally unstable and easily decompose in the temperature range relevant to steam reforming reaction.[68] Clearly, steam reforming of bio-oils requires catalysts with high resistance to coke formation.

Besides the above-mentioned challenges posed by the nature of biofuel, possible thermal efficiency needs to be addressed. Companied by low H_2 content, most of biofuels are characterized by high contents of oxygen. As a result, H_2 yield from biomass is low and becomes an intrinsic limitation of the process efficiency. However, the low yield of H_2 on a weight basis cannot be the only criterion to assess the viability of the biofuel conversion. The energy efficiency of the conversion process might outweigh the drawback of the low H_2 yield.[72]

6.2.4 Catalysis in Reforming Reactions of Biomass-Derived Oxygenates

6.2.4.1 General Reaction Mechanism of Reforming Reactions

Reaction mechanisms of the steam reforming of oxygenates are far more complex than those of the methane reforming. The oxygenates have distinct chemical properties, which are often represented by various functional groups. Although the alcohol groups are most common among the bio-based oxygenates, different ways of biomass processing lead to generation of various groups, such as carbonyl, aldehyde, ester, carboxyl, ether and so on. Reaction mechanism of ethanol reforming has been intensively studied, which has been recently reviewed,[25] and summarized in Fig. 6.2.

The steam reforming of ethanol is composed of a bifunctional mechanism. Dehydrogenation and

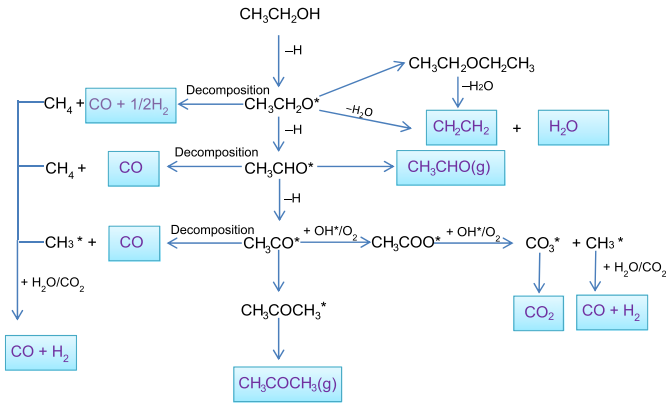

FIGURE 6.2 Mechanism for ethanol conversion on oxides or supported metal catalyst, summarized based on discussion in Ref. 25. Products are highlighted in blue. (For interpretation of the references to color in this figure legend, the reader is referred to the online version of this book.)

dehydration reactions take place mainly on the support, and the dehydrogenation reactions are promoted at the metal and metal–support interface.[3] Ethanol adsorbs in a dissociative manner to produce ethoxy species, mostly on the oxide supports. Ethoxy species either dehydrate to produce ethylene on acidic sites or dehydrogenate to adsorbed acetaldehyde on the metal particle and support interface, following a further H_2 abstraction and leading to the formation of acetyl species (Fig. 6.2). The acetyl species can also be oxidized to acetate species by hydroxyl groups, which can be further oxidized to carbonate species that decompose to give CO_2. In parallel, the ethoxy species, the dehydrogenated species (acetaldehyde, acetyl species), and the acetate species can all decompose to CO, CH_x, and H_2. The CH_x species can be hydrogenated and desorb as methane. Alternatively, the CH_x species and CH_4 can react with water, oxygen, and/or CO_2 to produce H_2 and CO. The decomposition reactions occur in the temperature range 300–500 °C, whereas the steam reforming, partial oxidation, and dry reforming of methane reactions are favored at higher temperatures (above 500 °C).

The oxygenates, which can be used as feedstock in reforming reaction, are normally monomers of biomass or decomposition products from biomass processing. Compared to direct conversion of biomass, it is less difficult to suppress undesirable reactions in conversion of oxygenates such as glucose, sorbitol, glycerol, ethylene glycol, methanol, and so on. The reaction path and corresponding product distribution greatly depend on the chemical nature of the feedstock. Experimental results from APR of glucose, sorbitol, glycerol, ethylene glycol and methanol over a Pt/Al_2O_3 catalyst at 225 and 265 °C revealed that the molecular identity had a great influence on C–C and C–O cleavage.[73] The turnover

frequency of H_2 formation from APR of 10 wt% glucose, sorbitol, glycerol, ethylene glycol and methanol at 225 °C over a 3 wt% Pt/Al_2O_3 catalyst under conditions to minimize transport limitations and at low conversions of the reactant have been measured to be 0.5, 1.0, 3.5, 7.0 and 7.0/min, respectively. The selectivity for H_2 production was in the order of glucose < sorbitol < glycerol < ethylene glycol < methanol, whereas the selectivity for alkane production took the opposite trend.[73] It seems as if the more reduced molecules (i.e. less OH groups) were easier to undergo C−C cleavage, although the effect of the molecule length could not be excluded.

The above experimental results also indicated a general trend that the C−C cleavage reactivity of oxygenates is much higher than alkanes. This trend is further supported by a density functional theory (DFT) calculation on the C−C bond in the species derived from the adsorption of ethanol and ethane on Pt (1 1 1).[74] The results suggest that ethanol should undergo a faster C−C cleavage than ethane. The electronic energy associated with the formation of the transition state, which controls the rate of the C−C cleavage, is equal to 125 kJ/mol for ethane.[3] This value is much higher than the energy of 4 kJ/mol for the transition state of ethanol.[74]

The discussed trend is also valid for the steam reforming of oxygenates at high temperatures. In the steam reforming of the bio-oil aqueous fraction, the reactivity of oxygenates is much higher than CH_4 and C_2H_4, which are the main intermediates formed on the Ru reforming catalysts.[70] Therefore, a high residence time is needed in order to completely convert CH_4 and C_2H_4 for a higher H_2 selectivity.

Under the reforming conditions, biomass or biomass-derived compounds usually yield H_2 with methane as a main byproduct, due to the low reactivity of methane with water. The energy carried by methane reduces the energy efficiency for H_2 production. It is desirable to reduce the formation of methane in biomass conversion. Methane can be formed by the methanation of CO or by the decomposition of the feed chemical via the C−O cleavage. Suppressing the methanation reactions by selectively removing H_2 or CO, reducing the C−O cleavage by enhancing the C−C cleavage and increasing the catalytic activity for methane reforming are the three major principles for obtaining a low content of methane in the product gas from biomass steam reforming reaction.

6.2.4.2 *Reforming Catalysts for H_2 Production*

Based on above analysis of reaction mechanism, catalysts should be rationally designed to have a high activity of C−C bond cleavage and high-temperature WGS reactions to achieve high activity and high selectivity to H_2 as well as good stability. A low activity of C−O scission is beneficial for suppressing alkene formation reactions, which are often followed by hydrogenation or coke formation.[3,63] It should also have low activity of methanation, polymerization and condensation reactions.[75]

Mavrikakis et al. applied the DFT calculation to design catalysts in oxygenate conversion.[76] They generated the entire potential energy surface for ethanol decomposition on the transition metals by combining Brønsted−Evans−Polanyi correlation developed for C−C and C−O cleavage[74] and the scaling relation proposed by Abild-Pedersen et al.[77] CH−CO cleavage was identified as the rate-determining step on various metals. The developed simple kinetic model predicted well the experimental observations that five metals (Pt, Pd, Ir, Rh and Ru) provide high selectivity to C−C cleavage, which was attributed to the weak bonding of the O atom to the metal surface relative to the C atom.

On a close-packed surface, DFT calculations suggested that the order of the O-binding energy followed W > Co > Ir > Ru > Ni > Rh > Cu > Pd > Pt > Ag > Au, whereas the order of the C-binding energy followed Ir > Rh > Ru > Pt > Co > Pd > Ni > Cu > Au > Ag.[77] Furthermore, Cu, Au and Ag were estimated to have a much lower C-binding energy than the other transition metals. These metals have very low activity for C−C cleavage, which are not expected to be active for catalyzing the steam reforming of oxygenates for H_2 production.[76]

These results explain quite well the experimental observed effects of the metal identity on the C−C cleavage activity. Rh, Ir, Ru, Co and Ni exhibited a good activity for C−C cleavage among Ru, Ir, Fe, Rh, Co, Pt, Ni, Pd and Cu catalysts supported on silica in the hydrogenolysis of ethane.[78] It should be noted that such catalytic property can vary differently with the type of catalyst support, addition of promoters, operating conditions, etc. For example, in the steam reforming of ethanol over MgO-supported catalysts, a kinetic measurement showed that the Rh sites were 2.2, 3.7 and 5.8 times more active for converting ethanol to gaseous products than Pd, Co and Ni, respectively.[79] In the case of CeO_2-supported catalysts, the activity of ethanol conversion decreased in the following order: Ir > Pt > Pd > Rh ≥ Ru.[80]

The order of the catalyst activity in ethanol decomposition was found to generally follow the order of the C-binding energy, and a metal with a high C-binding energy was expected to have a high activity. This may explain why Rh generally possesses a superior activity for C−C cleavage.[18] Rh was found to be very active in ethanol decomposition[76] as well as the steam reforming of glycerol,[81] bio-oil,[55] phenol[66] and palm fatty acid.[82] The high C-binding energy of Rh is also expected to promote tar removal by favoring C−C cleavage in the steam reforming of the heavy compounds in tar.[66] For the same reason, Ru with a high C−C cleavage activity

TABLE 6.2 Kinetic Models and Activation Energies of Steam Reforming of Methanol, Ethanol, Glycerol and 1-Hydroxy-2-Propanone on Different Catalysts. The Reactor Types Used for Kinetic Study Are Also Indicated

Feed	Catalysts	Activation energy (kJ/mol)	Rate expression	Reactor	References
Methanol	Pd/ZnO	94.8	$2.9047 * 10^{10} e^{\frac{-94800}{RT}} p_{MeOH}^{0.715} p_{H_2O}^{0.08a}$ Power-law	Microchannel	85
Ethanol	Ni/Al_2O_3		$\frac{kN_A}{(1+K_A N_A)}$	Fixed bed	86
	Ni−Al	145.8	$\frac{kK_A K_W P_A P_W C_t^2}{(1+K_A P_A + K_W P_W)^2}$	Fixed bed	87
	Co−Na/ZnO	46	$7.1 * 10^{-6} e^{\frac{-45.81}{RT}} p_{EtOH}^{0.36}$ Power-law	Membrane reactor	88
	$Rh/CeO_2/Al_2O_3$	110.3	$\frac{kP_A P_W}{(1+K_A P_A + K_W P_W + K_M P_M)^2}$	Microchannel	89
	Pt/C	N.A.	Power-law	Fixed bed	90
Glycerol	Pt/C Pt−Re(1:1)/C Pt−Re(1:2)/C	90 60 70	Power-law	Fixed bed	91
	Ru/Al_2O_3	21.2	Power-law	Fixed bed	92
	Ru/Al_2O_3	55.9	$\frac{kP_A}{(1+bP_A)}$	Fixed bed	93
	Ni/CeO_2	103.4	Power-law	Fixed bed	94
	$Ni-ZrO_2/CeO_2$	43.4	Power-law	Fixed bed	95
	Ni/Al_2O_3	60.2	Power-law	Fixed bed	96
	Co/Al_2O_3	66.7	Power-law	Fixed bed	97
	Co-Ni/Al_2O_3	63.3	$\frac{kP_A P_W}{(1+K_A P_A)(1+K_W P_W)}$	Fixed bed	98
1-Hydroxy-2-propanone	Pt/C	N.A.	$\frac{kp_A}{(1+K_A P_A)}$	Fixed bed	99

A: alcohol, W: water, M: methane, *P*: partial pressure, *K*: equilibrium constant, *k*: rate constant, N_A: flow rate of alcohol (kmol/s), C_t: total concentration of active sites, b: lumped parameter for rate constants.

is also a very active catalyst for the steam reforming of oxygenates.[49,52,83,84] The C- and O-binding energy on the metal surface is a useful index in screening for a catalyst with a selective activity for C−C or C−O cleavage.

Both the experimental and modeling results revealed that Mavrikakis's work can be useful to guide the selection of a catalyst for H_2 production by reforming of oxygenates. A high C-binding energy and a low O-binding energy are expected to result in high activity and high selectivity to C−C cleavage. Such principle for catalyst selection could be common in the steam reforming, APR and gasification reaction of biomass and biomass-derived compounds.

Kinetic modeling is valuable for reactor design and for better understanding of the reaction mechanism. Kinetic models and activation energies of steam reforming of methanol, ethanol and glycerol on different catalysts are summarized in Table 6.2. The results indicate that the activation energy varies very much with the catalyst composition and supports. However, it should be noted that no exclusive conclusion can be drawn from the comparison. Steam reforming is a fast and highly endothermic reaction. It is difficult to eliminate mass and heat transport in practice. Microchannel reactor may be a good solution for the kinetic study of such reactions. Anyhow, work on more rigorous kinetic study and modeling is highly desired.

Catalyst supports have a significant effect on the steam reforming of biomass-derived oxygenates. The basic support is the superior one to suppress the acidic sites catalyzed dehydration reactions to form olefins, which can sequentially polymerize to form coke on the support.[3] In this regard, basic supports such as Mg−Al mixed oxides can suppress the dehydration reactions.[82,100−102] MgO-supported catalysts often appear to have a better stability.[102] The sintered Ni catalysts

were found to be redispersed during the reduction and regenerate through the formation of NiO−MgO solid solution as an intermediate. The support effect on the selectivity in the steam reforming of palm fatty acid distillate over Rh catalysts was studied on $MgO-Al_2O_3$, Al_2O_3 and $Ce-ZrO_2$ (with a Ce/Zr ratio of 3/1, 1/1 and 1/3) supports.[82] At 750 °C, H_2, CO, CO_2 and CH_4 are the major products, together with small amounts of alkanes and alkenes, i.e. C_2H_4, C_2H_6 and C_3H_6. Among all the catalysts, $Rh/MgO-Al_2O_3$ yielded the highest H_2 yield with the greatest resistance to carbon deposition and the lowest amounts of alkane and alkene compounds.

In addition to the influence of supports on the catalyst stability, the contribution of the interface between the metal particles and supports to the reactions has also been recognized by fundamental studies.[25] The dissociation of ethanol to ethoxy species can occur on the support. Dehydrogenation of the ethoxy species to acetaldehyde is very likely assisted by the metal particles on the support. The support also appears to provide oxygen for nucleophilic attack of the acetaldehyde species in their conversion to acetate.

6.2.4.3 *High-Temperature WGS Reaction*

A high activity for the WGS reaction, which improves H_2 production by converting CO to CO_2, is also an important criterion in the selection of a catalyst for H_2 production. Compared with other noble metal catalysts, Rh is very active to C−C rupture.[3] However, Rh has low activity for the WGS reaction. Pt promotes the WGS reaction, but its activity for C−C rupture is limited.[103] It is therefore anticipated that H_2 production could be enhanced by using Rh−Pt. In addition, Ru-based catalyst exhibits higher activity for C−C bond rupture over Rh and comparable activity to Cu for the WGS reaction. However, Ru might reduce H_2 selectivity by facilitating methanation reaction or induce dehydration of oxygenates to form ethylene, leading to coke formation via polymerization.[18]

In an examination of the kinetics of the WGS reaction catalyzed by alumina-supported Group VIIB, VIII and IB metals, it was found that the activity for the WGS reaction decreased in the following order: Cu > Re > Co > Ru > Ni > Pt > Os > Au > Fe > Pd > Rh > Ir.[104] Although Pt and Ni have a lower activity for C−C cleavage than Rh, they have a better activity for the WGS reaction.[103] This could explain a different CO_2 production activity order in the reforming of ethylene glycerol: Pt ~ Ni > Ru > Rh ~ Pd > Ir.[63] The good performance of Pt in the WGS reaction has been observed in many studies. As one example, the catalytic activity of noble metals (Pt, Rh, Ru and Pd) for the WGS reaction was investigated in terms of the physicochemical properties of the metallic phase and the supports.[83] Pt was reported with a superior activity over the tested metals, particularly, when Pt was supported on a "reducible" support (i.e. TiO_2, CeO_2, La_2O_3 and Yttria-stabilized zirconia) rather than on an "irreducible" support (i.e. Al_2O_3, MgO and SiO_2). Although the appreciable activity for C−C cleavage and the high activity for the WGS reaction might make Pt a potentially good candidate for being a catalyst in reforming and sorption-enhanced reforming, it is worth noting that most of the reports on the WGS reaction activity of Pt were at a temperature lower than 400 °C, which are not suitable conditions for steam reforming. Evaluation of the WGS activity at temperatures above 500 °C is expected to help the selection of a catalyst for improving H_2 production by gaseous reforming reaction. A special effort was made to study the performance of noble metal (Rh, Pt, Pd, Ir, Ru and Ag) and Ni catalysts supported on $CeO_2-Al_2O_3$ for the WGS reaction at temperatures of 500 and 700 °C.[105] The Pd catalyst showed the highest conversion of CO to CO_2 at a temperature of 500 °C, whereas the highest conversion was observed with the Pt catalyst at a temperature of 700 °C.

6.2.5 Coke Formation in Reforming of Biomass-Derived Chemicals

Compared to conventional fossil fuels, biomass-based compounds often have a low ratio of H_2 to carbon, indicating a potential high risk of coke formation in reforming and gasification reactions. In addition, biomass-based feedstocks have a low thermal stability and, therefore, a strong tendency to decompose under the conditions employed for steam reforming. Species such as ethylene produced during decomposition or dehydration induce coke formation.[106] By investigating steam reforming of a series of biomass-based model compounds, the rate of coke formation was found to decrease in the following order: glucose >> *m*-xylene > acetone > ethylene glycol > acetic acid.[51] The severe coke formation in the conversion of oxygenates with a high reactivity poses a challenge in realizing efficient H_2 production from biomass-based feedstocks.

The reaction mechanism of carbon formation and principles for designing a catalyst with a high resistance to carbon formation have been intensively studied in the steam reforming of methane,[107] natural gas,[106] liquid hydrocarbons[108] and alcohols.[109] A simple reaction mechanism of hydrocarbon steam reforming, including filamentous carbon formation, was investigated under the prereforming conditions, namely low-temperature (480−550 °C) steam reforming.[106] Two strategies have been suggested to improve the performance of the catalysts for H_2 production by bio-oil steam reforming.[14] The first approach is aimed to enhance steam adsorption and facilitate partial oxidation of the precursors of coke. The second one is to slow the surface reactions such as cracking, deoxygenation and dehydration of the adsorbed intermediates.

Co- and Ni-based catalysts often suffer from filamentous carbon formation in the steam reforming reactions, due to a high solubility of carbon in the metals. The driving force for coke formation can be reduced by modifying the surface property of the metal phase, such as forming surface alloy with Au or selectively poisoning the metal surface with H_2S.[110] Coke formation can also be reduced by decreasing the size of the metal particles.[111]

In addition, coke formation can be accelerated through the acidic sites of the support, which induce the production of coke precursors. Such an adverse effect has been reduced by neutralizing the acidity of support material with alkali metal dopants or by using a basic support such as MgO, CeO_2 and ZnO.[100,101,112,113]

As a summary, suppressing or avoiding coke formation is an important issue in the development of a process for reforming biomass or biomass-derived compounds. A fast C–C cleavage of the species adsorbed on the catalyst is expected to decrease the decomposition and polymerization of the feed chemicals for reforming reactions.

6.2.6 Steam Reforming Thermal Efficiency

Thermal management is crucial since it has direct impact on the economy and feasibility of a process. Even though enthalpy balances are often applied to identify where energy is lost and how to improve the system thermal efficiency, exergy analysis has been proved to be a more effective method.[83–85] Exergy concerns the quality of energy apart from the quantity available. It offers more practical meaning for assessing different forms of energy, fuels and process efficiencies. For example, the enthalpy analysis has shown 100% efficiency possible for a methanol reforming, while, with exergy analysis, <50% efficiency has been predicted as a maximum due to the unrecovered latent heat of steam and the low quality of the heat.[114]

The thermal efficiency for H_2 production can be evaluated with the following equations[115]:

$$\text{Efficiency } \eta\% = \frac{\text{Lower heating value of hydrogen produced}}{\text{Lower heating value of fuel used}} \times 100 \tag{6.4}$$

In the process with steam addition, Eqn (6.4) is rewritten as Eqn (6.5).

$$\text{Efficiency } \eta\% = \frac{\text{Lower heating value of hydrogen produced}}{\text{Lower heating value of fuel used} + \text{latent energy of steam}} \times 100 \tag{6.5}$$

As seen in Fig. 6.3, dot line indicates the results predicted for reforming of glycerol in the presence of steam. The H_2 yield and process thermal efficiency are obtained at reaction equilibrium conditions. The thermal efficiency of reforming of glycerol is calculated according to the above equations. As seen in the figure, reforming of glycerol has optimum conditions for thermal efficiency at temperature ranging from 600 to 700 °C. More interestingly, Fig. 6.3 also presents a comparison of H_2 yield and thermal efficiency for reforming of glycerol with and without

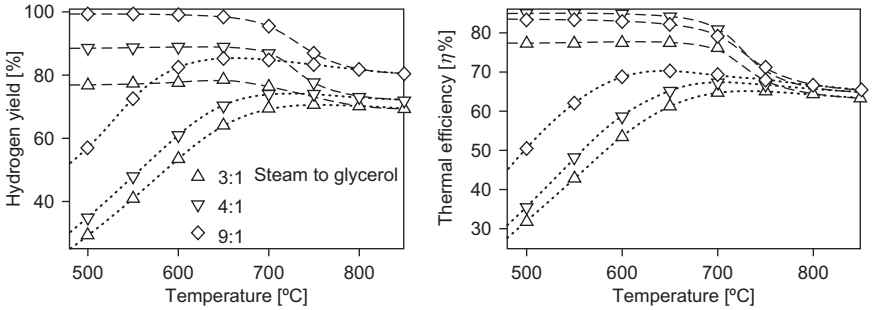

FIGURE 6.3 Hydrogen productivity and thermal efficiency of the steam reforming processes as a function of temperature and steam-to-glycerol ratio at pressure of 1 atm. The lines (– – –) and (* * * * * *) represent for steam reforming of glycerol with and without in situ CO_2 capture, respectively.[116]

CO_2 sorption. The integration of CO_2 sorption in H_2 production via reforming reaction is discussed in detail in Section 6.5.

6.2.7 Reactors for Steam Reforming of Biomass

Most of the model systems and experimental studies in reforming reaction were conducted with fixed-bed reactor. Performance of a reaction system based on a fixed-bed reactor can be adversely influenced by uneven temperature distribution in the reactor, low heat transfer efficiency from the utility to the reactor, difficulty in realization of a continuous operation, and so on. To overcome such problems, a fluidized bed can be utilized as an alternative to a fixed-bed reactor.[117] One strategy for lowering the requirement of the steam-to-carbon ratio is to improve the contact between the nonvolatile molecules and catalyst surfaces in a fluidized-bed reactor, which could largely improve the H_2 yield and reduce the coke formation.[67]

As early as in 1997, Czernik et al. suggested that steam reforming of the pyroligneous oil from lignocellulose could be economically competitive with the conventional means of H_2 production in terms of production cost.[118] They proposed a regionalized system of H_2 production, where small- and medium-sized pyrolysis units (<500 Mg/day) provide bio-oil to a central reforming unit for producing H_2 and CO_2. A thermodynamic modeling of the major constituents of bio-oil has shown that the reforming is possible within a wide range of temperature and steam-to-carbon ratios. Initially through microscale tests[118] and then with bench-scale fixed-bed reactor experiments,[69] they demonstrated the reforming of bio-oil by using bio-oil model compounds such as methanol, acetic acid, hydroxyacetaldehyde and 4-allyl-2,6-dimethoxyphenol, as well as carbohydrate-derived fraction from bio-oil. Employing process conditions similar to those used for the steam reforming of natural gas (fixed-bed, commercial nickel catalysts), they obtained H_2 yields exceeding 80% of those theoretically possible. However, the formation of carbonaceous deposits, especially in the upper layer of the catalyst bed and the reactor freeboard, limited the reforming time to 3–4 h. Czernik et al. developed a fluidized-bed reactor for the steam reforming of bio-oil.[67] The catalysts were more stable in the fluidized-bed reactor than in the fixed-bed reactor due to a better contact of the catalyst particles with steam.[67] The H_2 yield obtained in a fluidized-bed reactor from the carbohydrate-derived fraction of wood pyrolysis oil was about 80%, which corresponds to approximately 6 kg of H_2 from 100 kg of wood used for pyrolysis. This fraction of the bio-oil was also coreformed with natural gas. The H_2 yield from the coreforming was about 80% of the stoichiometric limit. These results suggest that the steam reforming of complex hydrocarbons in a fluidized-bed reactor is a promising solution to improve H_2 production.

6.3 AQUEOUS-PHASE REFORMING

APR is a process where hydrocarbons or oxygenates are dissolved in water and react with water molecules in aqueous phase at low temperatures and high pressures to form H_2 and hydrocarbons.[73] H_2 can be produced by the APR of various oxygenated hydrocarbons derived from biomass, such as ethanol,[119–123] ethylene glycol,[63,124–127] polyols (glycerol,[128–132] sorbitols[133–136] and glucose[137,138]), cellulose[139,140] and woody biomass.[141] The catalytic issues and process conditions for renewable H_2 and alkane production by APR of oxygenated hydrocarbons over supported metal catalysts were reviewed by Dumesic et al.[3] The selectivity of the reforming process depends on various factors such as nature of the catalytically active metal, support, solution pH, feed and process conditions.

A representative reaction pathway in APR of ethylene glycol is illustrated in Fig. 6.4, including the reaction pathways leading to the formation of H_2 and alkanes from oxygenated hydrocarbon $C_nH_mO_k$ ($n \geq 2$) (ethylene glycol as an example here) over a metal catalyst. Ethylene glycol is first adsorbed on the metal surface through two C atoms or one C and one O atom on which a dehydrogenation step occurs. On the transition metal catalysts (M), the species bonded to the surface by the formation of M–C bonds which are more stable than the species through M–O bonds,[154–156] due to the weak bonding of O atom to the metal surface in relation to that of the C atom.[77] In the ideal dehydrogenation pathway (the pathway I in Fig. 6.4), H_2 and CO are formed through the cleavage of the C–C bond in the species derived from the oxygenate, followed by

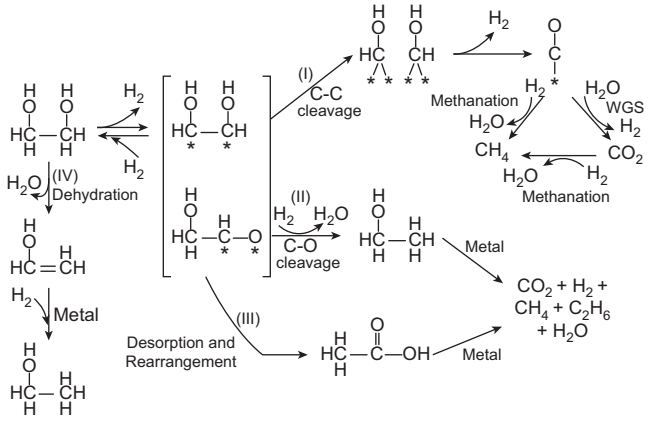

FIGURE 6.4 Reaction pathways and selectivity challenges for the production of H_2 from the reaction of ethylene glycol with water (* represents a metal surface site).[3]

the WGS reaction to convert CO into CO_2 and H_2. The pathway II leads to the formation of an alcohol on the catalytic site by breaking the C−O bond, followed by hydrogenation. The alcohol is further converted to CO_2 and H_2 through the C−C cleavage or to alkanes (e.g. CH_4 and C_2H_6) through the C−O cleavage. The pathway III involves a rearrangement to generate an acid, which then decomposes to alkanes (CH_4, C_2H_6 and so on), CO_2, CO, H_2 and H_2O.[3] The dehydration reaction in the pathway IV is often catalyzed on the acidic sites to form alkenes. In order to enhance H_2 production and suppress the formation of alkanes and alkenes, it is preferable to have the dehydrogenation of the oxygenate and the sequential C−C cleavage presented in the pathway I rather than the dehydration and C−O cleavage.

Similar to steam reforming process, hydrogen, carbon oxides, methane or hydrocarbon derivatives are generated as products in APR. In fact, both aqueous and steam reforming share the common features of the reaction mechanism, where C−C cleavage is the preferred path while the formation of alkanes and alkenes should be suppressed for the H_2 production. Different from steam reforming, H_2 and other light gas compounds are bubbled out from the reactant mixture. APR does not need to vaporize both water and the feedstocks and requires less energy for producing H_2. Due to the low operation temperature and high pressure, WGS reaction is favored by thermodynamics. One of the benefits with APR is that H_2 is generated at high concentration and with low concentration of CO. Moreover, it is possible to operate the APR process to achieve very low CO levels in the product by using an ultra-shift-zone downstream of the reactor. In addition, the low operation temperature results in a less chance to thermal decomposition of oxygenates, which are typical chemicals in most biomass-derived feedstocks for H_2 production. Such features make APR a good alternative to solve coking-related problems. However, as mentioned above, the feedstocks need to be dissolved in water. There are only limited number of the biomass-derived oxygenates or hydrocarbons that can be completely miscible with water or with high solubility in water. This can be a major drawback to extend application of APR to a broad feedstock range. APR has been applied to polyols as feedstocks.[73] Reforming of simple alcohols, such as ethanol and glycerol, yields a good production of H_2-rich gas with low level of CO content. However, similar to steam reforming reaction, APR is challenged by using large molecules or heavy oxygenates such as glucose. APR of glucose gives a very low H_2 yield. This is attributed to homogeneous decomposition of glucose which competes with reforming reactions. To suppress producing alkenes as by-products and coke formation in APR, compromise is made by using very high water/carbon ratios or low concentrations of glucose.[3] In such cases, conversion of glucose to H_2 can be compared to other polyols. Obviously, direct conversion of glucose to H_2 by APR is not economically viable. A preferable approach for producing H_2 from glucose is to convert glucose to sorbitol through hydrogenation, followed by the APR of sorbitol. Sorbitol is considered as a better feedstock due to less thermal decomposition in APR.[137,142,143] In general, APR is a new technology which has shown a great potential for conversion of water-soluble feedstocks, particularly for light compounds. APR has less feedstock flexibility compared to conventional steam reforming reaction.

As mentioned above, steam reforming and APR share the common features in reaction mechanism in terms of oxygenates activation and surface reactions leading to CO, CO_2 and H_2 formation. Therefore, the requirement for the catalysts could be similar for these reactions. Catalysts with high activity to C−C and C−H bond cleavage and high activity to the WGS reaction are preferred. Ni, Pd, Pt, Ru, Rh and Ir catalysts have been reported to be active in aqueous reforming of biomass-derived oxygenated hydrocarbons. The activity decreases in the following order for silica-supported metals in ethylene glycol aqueous reforming: Pt ≈ Ni > Ru > Rh ≈ Pd > Ir. Silica-supported Rh, Ru and Ni showed a low selectivity for production of H_2 and a high selectivity for alkane production. It appears that catalysts based on Pt and Pd may be more promising materials for the selective production of H_2 by APR of oxygenated hydrocarbons, such as ethylene glycol.[63] However, their high price is the main drawback for the large-scale application. The Ni, Co,[144,145] and their bimetallic catalyst[135,144,146−150] have drawn a great attention in APR of oxygenated hydrocarbons.

The selectivity of the reforming process depends on various factors such as nature of the catalytically active metal, support, solution pH, feed and process conditions.[3] By manipulating these factors, the APR can be tailored to selective H_2 production. Pt, Pd and Ni−Sn alloys show high activity to formation of H_2 and low activity to the formation of alkanes, while supported Ni catalysts is more selective to the formation of alkanes. The more basic/neutral supports are better than the acidic supports (e.g. silica−alumina), in terms of selective H_2 production. Also, gaseous carbon dioxide dissolved in the solution at high pressures makes a slightly acidic solution (pH = 4−5). However, neutral and basic solutions favor the H_2 production, high H_2 selectivity and low alkane selectivities. The identity of the feed plays also a role in the reaction selectivity. In general, polyols (e.g. sorbitol) have a higher selectivity for H_2 production than sugars (e.g. glucose).

6.4 SUPERCRITICAL REFORMING

SCR is operated under the conditions where water is in supercritical state (i.e. temperatures above 375 °C and pressures above 217 atm). H_2 production by SCR or gasification of biomass has been reviewed by Guo et al.[151] and Peterson et al.[152] The reaction mechanism of SCR is similar to APR, but SCR can realize a better control over thermal decomposition of heavy oxygenates such as glucose.[153–155] The required water-to-carbon ratio is much lower than APR or the concentration of hydrocarbon feedstocks can be higher than APR. In addition, SCR reactions can be considered as a good alternative to APR for processing different types of biomass (even with high moisture) or biomass-derived compounds. The selectivity to H_2 is not sensitive to the types of biomass compounds used, meaning less deviation caused by feedstock variation and better flexibility in feedstock selection. It is a promising alternative for H_2 production directly from woody biomass,[33,156] biomass wastes,[154] cellulose and sugars.[153–155] However, a comparative study on the hydrothermal gasification and steam reforming of glucose suggests that steam reforming is more competitive in energy and H_2 production capacity.[157] Voll et al. provided a thermodynamic analysis of biomass gasification via SCR using methanol, ethanol, glycerol, glucose and cellulose as a model molecule.[158] The gas product consisted primarily of H_2 and carbon dioxide as well as small amounts of methane and carbon monoxide.

In general, rigorous reaction conditions are required by reforming of hydrocarbons in aqueous phase, particularly with SCR. This is a limiting factor for application of SCR.

6.5 SORPTION-ENHANCED REFORMING OF BIOMASS-DERIVED CHEMICALS

As seen above (Fig. 6.3), the effectiveness of glycerol as a H_2 source can be largely improved by integration of CO_2 sorption into reforming reaction. The key feature of the concept is that reforming, WGS and CO_2 removal reactions occur simultaneously in one reactor with a mixture of reforming catalysts and CO_2 acceptors achieving sorption-enhanced H_2 production (SEHP). SESR was initially used to improve the productivity of H_2 from methane steam reforming.[159] The removal of CO_2 from the gas mixture in the reformer during the catalytic reactions shifts the equilibrium boundary of H_2 concentration and drives the reactions toward H_2 production. The application of the SEHP concept can be extended to the conversion of biomass-derived chemicals or complex feedstocks, similar to the gasification of heavy oil and coal in the presence of steam.[5,160,161] As has been demonstrated in Fig. 6.3, SEHP has great potential for high thermal energy efficiency with 85% for SER of glycerol compared to 70% for reforming of glycerol.[116] SEHP could achieve a target cost for H_2 at \$2–4/kg (energy equivalent of 1 gallon of gasoline) from the Department of Energy (USA).[162]

In addition to glycerol,[116,163] thermodynamic analysis of SEHP has been performed on methane,[164,165] a mixture of methane and carbon dioxide (land-fill gas),[166] ethanol,[116,167] sorbitol,[168] glucose[168] and bio-oil.[169] It is found that SEHP has potential for obtaining a high concentration of H_2 from biomass-derived compounds and thus achieving a high efficiency in the conversion of biomass to H_2. The improvement in H_2 production greatly depends on in situ removal of CO_2.

$$\mathrm{CaO(s)} + \mathrm{CO_2} \rightleftharpoons \mathrm{CaCO_3(s)} \tag{6.6}$$

$$\mathrm{C_nH_mO_k} + (2n-k)\mathrm{H_2O} + n\mathrm{CaO(s)} = n\mathrm{CaCO_3(s)} + (2n + \mathrm{m}/2 - k)\mathrm{H_2} \tag{6.7}$$

It is important to point out that the extension of the reaction in Eqn (6.6) is limited by the equilibrium pressure of CO_2, as defined by Eqn (6.8).[170]

$$K_\mathrm{a} = 1/P^{\mathrm{eq}}_{\mathrm{CO_2}} = \exp\left(-\Delta G^{\mathrm{o}}_{\mathrm{rxn}}(T)/\mathrm{RT}\right) \tag{6.8}$$

The H_2 partial pressure in the gas phase in reforming of hydrocarbon oxygenates can be derived in the following form by using Eqns (6.6)–(6.8). According to Eqn (6.9), as the CO_2 produced in reforming reaction is removed to a very low concentration, a high concentration of H_2 can be achieved.

$$p_{\mathrm{H_2}} = \left(\frac{Kp_{\mathrm{C_nH_MO_K}}p^{2n-k}_{\mathrm{H_2O}}}{p^{n}_{\mathrm{CO_2}}}\right)^{\frac{1}{2n+\frac{m}{2}-k}} \tag{6.9}$$

6.5.1 Strategies for Sorption-Enhanced H_2 Production

The application of SEHP in processing biomass or biomass-derived chemicals can be realized as shown in Fig. 6.5. Comparing to APR or SCR, much more flexibility in feedstock makes SEHP more attractive. SEHP can be used in many stages of biomass conversion for value-added products, e.g. in the gasification of biomass, reforming of the aqueous fraction of bio-oil or biomass-derived oxygenates, the conversion of carbohydrates in waste-water or low-valued liquid by-products from biomass processing, upgrading or conditioning the gaseous mixture from biomass gasification, the utilization of biomass-derived methane-rich gases (BMGs), and so on.

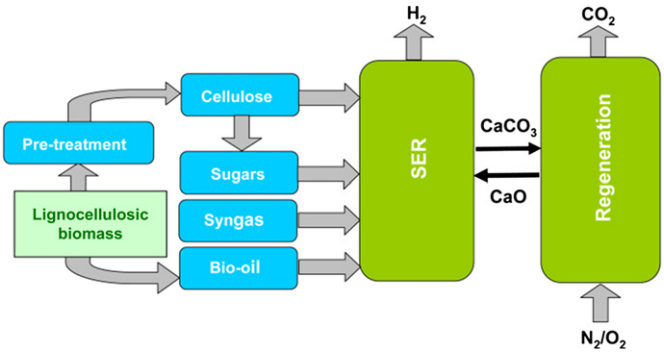

FIGURE 6.5 Strategy for H_2 production from lignocellulosic biomass using sorption-enhanced reactions (SER).[8] (For color version of this figure, the reader is referred to the online version of this book.)

Another advantage associated to the SEHP process is that the production of a highly concentrated H_2 as a product gas from biomass-derived chemicals can be accomplished in a compact process since WGS reaction unit and H_2 purification unit can be eliminated or reduced. In addition, CO_2-rich effluent is released during the regeneration of CO_2 acceptor and thereby can be considered as a convenient separation for its sequestration or use as a chemical. Moreover, a very high conversion of CO to CO_2 is promoted by the CO_2 capture at the temperature range of 500–650 °C for SEHP. This may avoid the need of a separate WGS reaction step and avoid the use of the WGS catalyst, which is often sulfur-sensitive.[171] This can be an important concern in biomass processing where desulfurization of biomass-based organics is more difficult than that for conventional fossil fuels.[23]

However, catalysts and operating conditions should be manipulated for each biomass-derived chemicals used in SEHP. Additionally, the thermal decomposition of some organic compounds can be significant and accelerate coking and catalyst deactivation. Such problems should be studied particularly in the context of the integration of reforming and CO_2 capture reactions for biomass conversion. In the following sections, H_2 production from biomass will be discussed in terms of chemicals used in SEHP, such as biogas, polyols, sugars, and bio-oil. The developments of catalysts and CO_2 acceptors will also be briefly presented.

6.5.2 SESR of Biogas

BMGs such as landfill gas, biogas and digester gas are potentially important renewable resources for near-future H_2 production. Coupling CO_2 capture into reforming of BMG is, in nature, similar to that for methane steam reforming. The main reactions can be compared to SEHP from methane. Methane reforming with in situ CO_2 capture has been studied intensively. The process and material development for integration of in situ CO_2 capture in the methane reforming process have been intensively discussed in a recently published book.[172] The SEHP of methane is often performed by using a mixture of a commercial reforming catalyst and CaO obtained upon the calcination of $CaCO_3$.[173] The purity of the produced H_2 can be higher than 90%. The reaction system can be optimized by finding the temperature range which favors both the catalytic reactions and CO_2 removal reactions. The H_2 concentration is determined by the kinetics of sorption and catalyst performance. On the other hand, BMG has different characteristics from methane for H_2 production. BMG has a lower content of methane, in some cases, even <45%.[174] Therefore, different processes should be developed according to methane content in order to achieve high H_2 production efficiency.[166] It is suggested that autothermal SEHP by using a mixture of biogas and bio-oil can have a comparable efficiency with the system using conventional fossil fuels.[169]

6.5.3 SESR of Ethanol and Polyols

Even though APR, SCR, gasification or steam reforming can selectively produce H_2 and CO_2, SEHP has been demonstrated experimentally to have high selectivity to H_2 and improved H_2 yield.

SEHP using ethanol has been featured with a high H_2 yield and a high purity from one single reaction unit.[28,167] New reaction process with a great potential for realizing a sustainable H_2 production has also been demonstrated experimentally. An interesting feature resulting from coupling CO_2 capture to reforming of ethanol is the reduction of the risk of carbon formation. Thermodynamic analysis has revealed that a much lower steam-to-carbon ratio can be used in reforming of ethanol in the presence of CO_2 capture for carbon-free operation than in the conventional steam reforming. No obvious carbon formation was found in the experimental process testing for SEHP from ethanol with a mixture of hydrotalcite-like (HTls) material-derived Co–Ni (Co–Ni/HTls) catalysts and calcined dolomite as acceptor.[28] H_2 was produced with purity fairly close to the theoretical prediction at a steam-to-carbon ratio of 3 and temperatures ranging from 500 to 650 °C. It is worth noting that the applied steam-to-carbon ratio in the studied case for ethanol is lower than the typical values for APR and SCR. The catalyst selection can also affect the SEHP. The best result with a composition of more than 99 mol% H_2, *ca* 0.4 mol% CH_4, 0.1 mol% CO and 0.2 mol% CO_2 was obtained over 40 Ni and 20 Co–20 Ni/HTls at 550 °C. Different catalysts and acceptors have also been used by Iwasaki et al.[175] The mixture of 1 wt% Rh/CeO_2 catalyst and Li_4SiO_4 as the

sorbent promoted H_2 production with the highest H_2 purity of 96%. A commercial 58 wt% Ni/Al_2O_3 catalyst and Li_4SiO_4 as sorbent material yielded a concentration of H_2 above 99%, together with CO concentration less than 0.12%.[176] Various hydrocarbon fuels such as a propane–butane mixture and methanol were compared with ethanol in SEHP over a mixture of $CaCO_3$-calcined acceptors and commercial Ni catalysts.[177] Ethanol was reported with the best performance at a steam-to-carbon ratio of 2.5 and a pressure of 3 atm, obtaining a H_2 purity of 98–99 vol% with both CO and CO_2 impurities of about 10–20 ppm. More interestingly, H_2 produced from the reforming of ethanol was fed to a proton exchange membrane fuel cells fuel cell stack without any loss of efficiency.

A high H_2 purity (>90%) was obtained by the catalytic steam reforming of glycerol with a commercial Ni-based catalyst and dolomite as the sorbent under atmospheric pressure within a temperature range of 400–700 °C.[178] An optimal temperature with 97% H_2 purity was indicated at *ca* 500 °C for SEHP with glycerol as feedstock. Steam conversion was suggested to reflect the glycerol reforming efficiency in addition to glycerol conversion.

The SEHP with glycerol was conducted with Co–Ni/HTls catalysts and dolomite as the CO_2 acceptor.[116] H_2 production approached the theoretical boundary at temperatures above 575 °C or a steam-to-carbon ratio not less than 1.3. The best performance of the developed process was obtained at a steam-to-carbon ratio of 3 where the H_2 purity and yield were at *ca* 99%. Thermal decomposition-related problems which are confronted in traditional reforming, APR or SCR were also observed in SEHP by using glycerol as feedstock, but to a lesser extent. The results revealed that elimination of the non-catalytic reactions, sufficient methane steam reforming and WGS reaction are crucial for obtaining high H_2 yield and production efficiency.

Most studies on reforming of glycerol are conducted on refined glycerol with high purity. It has recently been reported that high-purity H_2 (>99%) can be produced directly by SESR of crude glycerol.[179] The composition of crude glycerol varies depending on the biomass feedstock and the biodiesel production process. Up to date, crude glycerol market price is in a range of 25–46 $/ton, which is much lower than refined glycerol (55–78 $/ton). It is reasonable to believe that the use of crude glycerol can decrease the cost of H_2 production.[179,180] A thermodynamic analysis suggests that all the impurities in crude glycerol such as methanol linoleic ($C_{19}H_{34}O_2$), palmitic ($C_{17}H_{34}O_2$), oleic ($C_{19}H_{36}O_2$) and stearic acid methyl esters ($C_{19}H_{38}O_2$) can be fully converted under the studied conditions.[181] However, the experimental results indicated that H_2 yield was still lower than corresponding theoretical value.[179] The inferior performance of crude glycerol to refined glycerol was attributed to the thermal decomposition of the heavier compounds indicated in the analysis. To enhance the C–C cleavage on the catalyst surface and to avoid the homogenous thermal decomposition of the feed, a water-cooled injection nozzle was used to spray liquids into the catalyst bed.[67] In addition to a new design of the reforming reactor, a catalyst with a high C–C cleavage activity should be considered to improve H_2 yield.

6.5.4 SESR of Sugars

As mentioned above, the conversion of glucose for H_2 production poses great technical challenges due to its high functionality and low thermal stability. SEHP has been recently applied to the H_2 production from glucose.[21] In the same study, sorbitol was used to compare with glucose and reforming of sorbitol exhibited a relatively easy processing ability. The experimental assessment was conducted at a steam-to-carbon ratio of 1.8 for sorbitol and 6 for glucose from 450 to 625 °C. Values of 98.8 mol% H_2 from sorbitol and 99.9 mol% H_2 from glucose were obtained by integrating in situ CO_2 capture into the reforming reaction. However, selection of optimal reaction temperature was not straightforward. High reforming temperature improved the glucose conversion and in turn produced high H_2 yield. On the other hand, very high H_2 purity was obtained at low-temperature regime which was associated with carbonaceous deposition. The experimental results yet confirm again that coupling CO_2 capture reduced the risk in coke formation during the reforming of glucose. Similar to glycerol reforming, a new reactor design is required to improve heat transfer or alternatively reconstructing the reactor.

6.5.5 SESR of the Aqueous Phase of Bio-Oil

Numerous studies on wood thermochemical conversion have focused on the production of biofuels. Bio-oil or biomass-derived pyrolysis oil contains a group of highly oxygenated chemicals and unstable upon storage, requiring further upgrading such as deoxygenation for fuel application. Thermodynamic analysis has indicated that the aqueous phase of bio-oil can be alternatively used for H_2 production. Thermodynamic simulation on SESR of bio-oil was conducted with dextrose ($C_6H_{12}O_6$) as the model compound.[182] H_2 was produced as high as 95 mol%. Another thermodynamic analysis on the bio-oil aqueous fraction in SEHP was carried out with a mixture of compounds, which represented a real composition of bio-oil.[169] The mixture contained

acetic acid 15%, acetaldehyde 15%, acetone 15%, ethylene glycol 15%, ethanol 5%, formic acid 15%, formaldehyde 10% and methanol 10%. The SEHP was predicted with H_2 concentration higher than 95% in a temperature range of 550–700 °C, at a steam-to-carbon ratio of 4 and a pressure of 10 atm.

The experimental testing of SEHP with an actual bio-oil aqueous fraction was found to be difficult, but still better results were obtained than without in situ CO_2 capture.[183] The H_2 concentration (about 70–80%) in the gas product without CO_2 capture was much lower than the value predicted by thermodynamics. The optimization of SEHP was also found to be complicated with a necessary trade-off between H_2 purity and yield since the H_2 purity was favored at low-temperature regime of 500–700 °C, whereas a higher H_2 yield was obtained at a higher temperature.

Similar to the bio-oil aqueous fraction, sunflower oil is a mixture of heavy fatty compounds, which have a strong pyrolytic tendency at the temperatures relevant to the operation of the catalytic reforming reactions. A substantial amount of carbonaceous species was found to be deposited in the catalyst-acceptor bed, causing a serious problem in the operation of the SEHP.[184] SESR of a sunflower oil and methane mixture generated H_2 at a high concentration (*ca* 90%) in comparison to conventional steam reforming (67%).

6.5.6 Catalyst in SEHP

One of the major obstacles in the conversion of oxygenates to H_2 by catalytic reforming reaction is coke formation, which destroys the catalyst structure and reduces catalyst activity. The integration of in situ CO_2 capture to the reforming process is expected to reduce solid carbon formation.[28] In the context of screening a catalyst for SEHP, it should be noted that the catalyst behavior can be different in the reforming reactions with and without CO_2 capture. However, there are very few studies on the evaluation of a catalyst in relation to the circumstance of in situ CO_2 capture. A series of Ni–Co/HTls catalysts was designed and tested in the steam reforming of ethanol with and without in situ CO_2 capture.[185] The best performance for H_2 production was given by 40 Ni and 40 Co/HTls at 550 °C in SESR, whereas 30 Co–10 Ni/HTls was found to be the best in terms of H_2 yield and selectivity in the reforming reaction without CO_2 capture. Clearly, there is a merit in identifying a good catalyst by testing catalysts in SESR.

As a summary, a good catalyst for SEHP from biomass-related feedstocks should possess such properties as being active to both high-temperature WGS reaction and low-temperature reforming reaction, promoting the decomposition of the feed through C–C cleavage and having a high resistance to coke formation.

6.5.7 CO_2 Acceptor in Thermal Chemical Conversion of Biomass

The CaO-based CO_2 acceptor has found interesting applications in thermal chemical conversion of biomass for H_2 production. CaO-based CO_2 acceptor can be used for tar reduction in biomass gasification or for enhancing H_2 production in gasification and gaseous reforming. Particularly, the integration of CaO-based CO_2 acceptor with reforming catalyst has shown a great potential to realize a sustainable H_2 production. Currently, most of the experimental studies on SEHP are conducted with dolomite or limestone as the CO_2 acceptor. Efforts have been made to improve the cyclic activity of the acceptor such as using part of the carbonation capacity or shortening the carbonation time.[186] The hydration of fresh or spent CaO materials at mild temperatures,[187–189] which have been reviewed by many groups.[190–192]

In addition to the above methods, developing new synthetic materials as CO_2 acceptors is often considered for obtaining a better CO_2 capture performance.[190,193] Nanostructured CaO,[194] $LiZrO_3$,[195] and $NaZrO_3$[196] have improved cyclic conversion of CaO and stability.

6.6 H_2 PRODUCTION BY BIOMASS GASIFICATION

Biomass gasification is a process to convert solid biomass or liquid biomass-derived compounds for the production of synthesis gas in the presence of air, steam or SCW. The overall reforming reaction of $C_nH_mO_k$ for H_2 production in the presence of oxygen or air can be written as follows[197]:

$$\begin{aligned} C_nH_mO_k + y(O_2 + 3.76N_2) \\ + (2n - 2y - k)H_2O(1) \;\rightarrow\; nCO_2 \\ + (2n - 2y - k + m/2)H_2 + 3.76yN_2 \end{aligned} \qquad (6.10)$$

According to Ahmed,[115] a maximum thermal efficiency can be achieved only when the reforming process is operated thermoneutrally or under slightly exothermic conditions. Namely, the enthalpy change in the overall reaction represented in Eqn (6.10) is zero or slightly above zero. From thermodynamic perspective, the amounts of steam and O_2 added to the fuel process system for obtaining thermoneutrality are only a function of the elemental composition of the fuel in use,

given that the standard formation enthalpy changes of water and CO_2 are constants.

The products of biomass gasification are in fact fairly complicated, including water, charcoal, oils or tars, and gases containing methane, hydrogen, carbon monoxide, and carbon dioxide. The gasification, steam gasification (SG) and supercritical gasification of biomass or sugars, followed by steam reforming (removing hydrocarbons and tar), WGS and CO_2/H_2 separation steps, are the widely practiced process routes for converting biomass to a gas mixture of H_2 and CO_2 (see the conventional SG route in Fig. 6.6). Figure 6.6 only represents a simplified process without gas cleaning units for removing solid particles, H_2S and NH_3, which are common impurities from gasifiers. The actual gas product composition depends largely on the history and type of biomass such as the contents of cellulose, hemicellulose and lignin, elemental composition, inherent mineral content, amount of volatile matters or moisture content.

Due to high functionality and reactivity of the chemicals or monomer in biomass, gasification of biomass is a complex process, involving pyrolysis, partial oxidation and/or steam reforming of gaseous alkanes and char, the WGS reaction, etc.[9] The formation of tar, which is the higher molecular weight condensate, is the most cumbersome and problematic parameter in the commercialization of biomass gasification. Catalytic reduction of tar is an important task in conversion of biomass for H_2 production.[198] Tar reduction has been performed on calcined dolomites, magnesites, zeolites and olivine, in addition to metallic catalysts based on nickel, cobalt and iron. Catalyst deactivation is reported as a common problem due to coke deposition on the surface of the catalyst and material sintering in harsh working conditions (e.g. high temperatures and steam content). Some catalysts have been reported with improved resistance to deactivation, including Co/MgO[199] and $Ni/CeO_2/Al_2O_3$ with Pt as a promoter.[102]

Another challenge for H_2 production by biomass gasification is the low yield of H_2 since H_2 concentration in the product gas from a gasifier has been reported at a level from 18 to 59 vol%.[5] Such concentrations are far too low to realize a profitable production of H_2.

To overcome the above problems and improve H_2 production in the biomass gasification process, it is proposed to integrate CO_2 capture into biomass conversion. There are two alternatives to apply SEHP in the biomass gasification as shown in Fig. 6.6. One of them is the in situ CO_2 removal by using the solid CO_2 acceptors directly in the gasifier, referred to as sorption-enhanced steam gasification (SESG).[5,161,200] Another possibility is the post-sorption-enhanced WGS (SEWGS) reaction, in which the CO_2 capture is incorporated in the WGS step as shown in Fig. 6.6.[201]

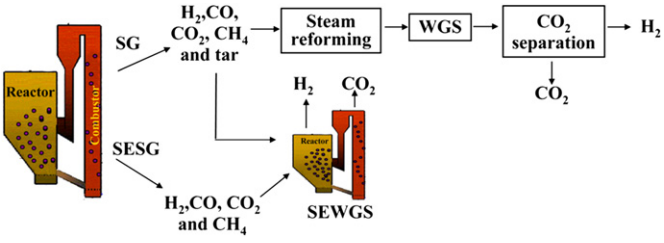

FIGURE 6.6 Strategy of H_2 production from biomass by steam gasification (SG) or sorption-enhanced steam gasification (SESG).[8] (For color version of this figure, the reader is referred to the online version of this book.)

6.6.1 Catalysts for Gasification of Biomass

Low-temperature gasification is an attractive alternative to high-temperature gasification (>700 °C) in terms of energy efficiency and also particularly interesting for promoting H_2 production by integrating CO_2 capture into the conversion of biomass or biomass-derived compounds. However, low-temperature gasification usually yields a higher amount of tar at the expense of gas yield than gasification at high temperatures. The use of a catalyst in a gasifier is helpful for eliminating tar production and increasing gas yield. The gas yield and product distribution in the catalytic SG process are mainly influenced by the properties of the used catalyst and less by the properties of the biomass.[202] In this context, it is considered to be of interest the development of a catalyst which is capable of promoting both the WGS reaction and reforming reactions of the pyrolyzed products from biomass (gaseous species, tar, char, etc.) in a low-temperature gasification process. In a previous investigation for the gasification of cedar wood, the order in the activity at 550 °C in the reforming of tar to synthesis gas was observed as the following: Rh > Pt > Pd > Ni = Ru, whereas Rh and Ni exhibited a higher performance at 650 °C in terms of the activity of tar reforming and the yield of gas.[203] With the objective of developing a low-temperature gasification process, a commercial Ni catalyst, dolomite and an Rh catalyst were examined and compared in the SG of cellulose.[204] At 500−600 °C, only the Rh catalyst was able to convert cellulose and no tar or char was detected in the effluent gas. Despite being less effective than Rh catalyst, Ni catalyst is also a promising candidate for promoting SG reactions. The performance of an Ni catalyst can be promoted by choosing suitable support material. Ni catalysts supported on the mixed oxides of CeO_2 and Al_2O_3 at various ratios were studied in the SG of cedar wood at temperatures of 550 and 650 °C.[113] The addition of CeO_2 to the support was found to improve the catalyst performance for tar elimination and coke resistance.

Moreover, in the gasification of cellulose at 500 and 600 °C, the Ni catalyst supported on CeO_2/zeolite did not show a noticeable difference in the rate of gas production in comparison to an Rh/Ce/SiO_2 catalyst.[205] Cobalt is also used in the catalytic SG of biomass. The performance of Co and Ni catalysts supported on MgO for tar reduction was compared in the steam reforming of naphthalene at 600 °C.[199] The Co/MgO catalyst was found to be more active than the Ni catalysts tested in the study. The oxidation of the Ni metal by steam was considered to be responsible for its lower activity with respect to the Co catalyst. A high and stable activity was also observed on the Co/MgO catalyst in the SG of real biomass (Radiata pine) at 600 °C.[199] The good performance of Co/MgO for gasification was attributed to the high surface area of the Co metal and a small amount of coke deposited on the metal surface.

Several metal catalysts were tested for H_2 production from lignin under the SCR conditions.[156] The order of the catalyst activity for gasification was as the following: ruthenium > rhodium > platinum > palladium > nickel. This follows again the previously discussed principle that a catalyst with a higher C−C cleavage activity is more active for gasification. The H_2 production decreased in the following order: palladium > ruthenium > platinum > rhodium > nickel. The high yield of H_2 on Pd was considered to be associated with its high activity for the WGS reaction.

6.6.2 Sorption-Enhanced Biomass Gasification

Similar to SESR, SESG has a great advantage over conventional SG. SESG reaction can be operated at a lower temperature in the gasifier (650−700 °C in SESG vs 850−900 °C in SG) as well as in the combustor (850 °C in SESG vs 950 °C in SG), but it yields a much higher H_2 content (50−65% for SESG vs 40−50% for SG).[161,200] However, the H_2 content is still very low and a WGS step after the SESG step is needed to enrich H_2 content. SEWGS is able to give fuel cell-grade H_2 at 200−400 °C using a low-temperature acceptor.[206−208]

The SESG of woody biomass (Japanese oak, volatile content of 82.4 wt%) was conducted by using CaO as the CO_2 sorbent in a pressurized batch reactor.[209] The removal of CO_2 increased the conversion of solid biomass to synthesis gas (40% without CaO vs 80% with CaO) and the H_2 content (50% without CaO vs 80% with CaO) at 650 °C and 6 atm. The CaO-to-carbon ratio was reported to have a great influence on the H_2 yield. The best H_2 content was obtained at 80.7% with CaO-to-carbon ratio of 2.

CaO can be used not only as an acceptor but also as a catalyst for the tar reduction.[210] With the objective of tar elimination, CaO-based materials are often used at temperature above 800 °C in biomass gasification. If temperature is at a low-medium level (<800 °C), CaO tends to remove CO_2 due to favorable removal equilibrium. The dual role of CaO as both catalyst and acceptor was examined in the gasification of a wet biomass, revealing that the presence of the acceptor greatly promoted H_2 production from both biomass gasification and CO_2 capture at an optimal temperature of 650−700 °C.[211] It was also concluded that CaO had a stronger catalytic effect on the WGS reaction than on the steam reforming of methane.

Recently, a large progress has been made for production of almost pure H_2 directly from raw, solid lignocellulosic biomass by sorption-enhanced catalytic steam gasification in a combined downdraft flow fluidized-bed and fixed-bed reactor.[212] A Pd/Co−Ni catalyst and dolomite as a CO_2 acceptor were fed together with the biomass (chestnut wood sawdust). Almost pure H_2 (>99.9 vol%) and high H_2 yields (up to 90%) can be achieved by this process, which combines conventional gasification/steam reforming, WGS reaction and H_2 separation by CO_2 capture in one step. The in situ removal of CO_2 by the carbonation reaction of dolomite shifts the equilibrium of steam reforming and WGS reactions toward H_2 production. The hydrotalcite-derived Pd/Co−Ni catalyst has shown high activity in the cleavage of C−C and C−H bonds during the conversion of tars and hydrocarbons, which resulted from fast pyrolysis and catalytic SG. The promotion of Co−Ni catalysts with Pd allows the cofeed of the catalysts together with the biomass and also the oxidative autothermal regeneration of the CO_2 acceptors, since no prereduction was required for Pd/Co−Ni catalysts.

6.6.3 Sorption-Enhanced Water Gas Shift Reaction

As shown in Fig. 6.6, SEWGS reaction can combine conditioning, steam reforming, WGS reaction and CO_2 separation into one stage for high-purity H_2 production after the biomass gasification. It will largely simplify the process and cut down the production cost. The synthesis gas composition of 5% C_2H_4, 12% CH_4, 23% CO, 25% CO_2 and 35% H_2 on a molar basis was chosen to resemble the synthesis gas produced in steam biomass gasification plant in Güssing, Austria.[201] SEHP with such gas mixture yielded 98% H_2 in a temperature range of 500−575 °C with Ni−Co catalysts and dolomite as the sorbent. The results suggested that SEWGS of the synthesis gas promoted the steam reforming of the hydrocarbons, WGS reaction and CO_2 removal in parallel. The produced gas was also featured with a very low level of CO (i.e. 0.2 mol%). This might be an opportunity to cut down a large cost in energy consumption. The product gas from gasifier often needs

to be cooled to approximately 500 °C to condense the alkaline compounds and then needs to be heated up again before it enters the reformer.[213] This reheating step may be eliminated by using the SEHP since it is capable of yielding high conversion of hydrocarbons and, therefore, high H_2 concentration in the gas effluent from gasifier at a temperature level of 500 °C.

SEHP can also be integrated in the post-biomass gasification step to refine the produced gas from gasifier. A mixture of methane, toluene and 1-methyl naphthalene, the last two being representative to tar species from gasifier, was used as model gas for H_2 production in biomass gasification.[214] A nearly 100% conversion of the hydrocarbons and a 97 mol% H_2 concentration in the product gas were achieved over a mixture of Ni-based catalyst and calcined dolomite at a tar concentration of 30 g/Nm^3 and a temperature of 640 °C. A similar study with toluene as tar model compound in gas production also demonstrated an effective conversion of hydrocarbons to H_2. A unique feature in the study is the pellets with cores made of calcium and magnesium oxides and shells mainly comprised alumina impregnated with a nickel catalyst.[215]

6.7 CONCLUSIONS AND PERSPECTIVES

H_2 production from renewable biomass provides an attractive opportunity for realizing the full environmental benefit of H_2 as a clean energy carrier. A number of processes have been carried out for an efficient conversion of biomass to H_2, where steam reforming, APR, SCR and gasification were reviewed in this chapter. The selection of the process depends on the availability of biomass or biomass-derived chemicals and the properties of the feedstocks. For relatively light oxygenates such as ethanol, ethylene glycol and glycerol, steam reforming is an effective route for H_2 production. To convert polyols such as sorbitol and glycerol, even sugars to H_2, APR is a promising alternative. However, there is still a challenge in controlling the conversion selectively toward H_2.

Sorption-enhanced reaction can be a promising route for H_2 production from biomass-derived chemicals, due to its high energy efficiency, simplicity of the process, high purity of H_2 produced, as well as excellent flexibility in terms of feedstock. It offers a great opportunity for sustainable production of H_2 from a diversity of lignocellulosic biomass-derived chemicals, including solid biomass, biomass-derived chemicals, bio-oil, biogas, synthesis gas from biomass gasification, organic wastes, etc. Apart from the availability, other factors such as price, transportation, toxicity, energy density, value of H_2 content, solubility in water should be taken into account in the selection of the feedstock for H_2 production.

The feasibility of H_2 production from biomass resources relies on many factors. The H_2 cost per unit is considered to be the most important criterion in cost–benefit analysis. The vast majority of reactors and system demonstrations found in literature have dealt with H_2 production from methane as fuel. With regards to the impact factors on H_2 cost, there are certain similarities in using methane or biomass resources as H_2 source. For example, strict requirement to H_2 purity of the produced gas is expected to increase the cost of H_2 production. However, more concerns are involved in the production from biomass-based sources, including the cost of biomass pretreatment or intermediates, transportation convenience, possibility, localization, and so on. H_2 productivity, which is defined as the amount of H_2 produced divided by the amount of fuel fed into the reformer, is an important factor to H_2 production cost, particularly as biomass-based chemicals are usually more expensive than methane. A high H_2 productivity from biomass-based chemicals is often preferred. To improve H_2 productivity and purity by thermal conversion of biomass and biomass-derived compounds, more work has to be conducted on reforming at low temperatures, enhancing product selectivity, lowering coking potential and boosting process energy efficiency. However, detailed technoeconomic analysis of these processes is necessary.

An important factor for improving H_2 purity and productivity is the choice of the used catalyst. Catalyst properties should be tuned for the preferred chemistry to happen between the catalyst surface and reactants. A preferential activation of C–C bond over C–O bond is desirable. The binding energy of C and O with the metal surface is a fundamental parameter for the rational design of catalysts for H_2 production from biomass. There is a great need for catalysts especially with a high activity for both the high-temperature WGS and low-temperature reforming reaction. Catalyst development should be conducted with acknowledging the general chemical features of biomass-derived chemicals and possible reaction conditions for converting a wide range of chemicals.

In the sorption-enhanced processes, approximately 90% of the total energy contained in the starting lignocellulosic biomass or carbohydrate can be transferred to the final product, namely the cleanest energy carrier H_2. Therefore, this technology offers an opportunity to develop a competitive process of energy production based on lignocellulosic biomass, as a good supplement to today's fossil fuel-based energy system. In particular, efficient H_2 production from biomass by sorption-enhanced processes might be a good alternative to current H_2 sources, supplying renewable H_2 in future refineries.

Acknowledgments

The financial support of Research Council of Norway (NFR) is gratefully acknowledged.

References

1. Kothari, R.; Buddhi, D.; Sawhney, R. L. *Renew. Sustain. Energy Rev.* **2008,** *12,* 553–563.
2. Rostrup-Nielsen, T. *Catal. Today* **2005,** *106,* 293–296.
3. Davda, R. R.; Shabaker, J. W.; Huber, G. W.; Cortright, R. D.; Dumesic, J. A. *Appl. Catal. B Environ.* **2005,** *56,* 171–186.
4. de la Piscina, P. R.; Homs, N. *Chem. Soc. Rev.* **2008,** *37,* 2459–2467.
5. Florin, N. H.; Harris, A. T. *Chem. Eng. Sci.* **2008,** *63,* 287–316.
6. Saxena, R. C.; Seal, D.; Kumar, S.; Goyal, H. B. *Renew. Sustain. Energy Rev.* **2008,** *12,* 1909–1927.
7. Haryanto, A.; Fernando, S.; Murali, N.; Adhikari, S. *Energy Fuels* **2005,** *19,* 2098–2106.
8. Chen, D.; He, L. *ChemCatChem* **2011,** *3,* 490–511.
9. Huber, G. W.; Iborra, S.; Corma, A. *Chem. Rev.* **2006,** *106,* 4044–4098.
10. Brethauer, S.; Wyman, C. E. *Bioresour. Technol.* **2010,** *101,* 4862–4874.
11. Monedero, V.; Perez-Martinez, G.; Yebra, M. J. *Appl. Microbiol. Biotechnol.* **2010,** *86,* 1003–1015.
12. Yan, N.; Zhao, C.; Gan, W.; Kou, Y. *Chinese Journal of Catalysis* **2006,** *27* (12), 1159–1163.
13. Mohan, D.; Pittman, C. U.; Steele, P. H. *Energy Fuels* **2006,** *20,* 848–889.
14. Garcia, L.; French, R.; Czernik, S.; Chornet, E. *Appl. Catal. A Gener.* **2000,** *201,* 225–239.
15. Lin, Y.-C.; Huber, G. W. *Energy Environ. Sci.* **2009,** *2,* 68–80.
16. Marquevich, M.; Czernik, S.; Chornet, E.; Montane, D. *Energy Fuels* **1999,** *13,* 1160–1166.
17. Prins, M. J.; Ptasinski, K. J.; Janssen, F. J. J. G. *Chem. Eng. Sci.* **2003,** *58,* 1003–1011.
18. Ni, M.; Leung, D. Y. C.; Leung, M. K. H. *Int. J. Hydrog. Energy* **2007,** *32,* 3238–3247.
19. Hu, X.; Lu, G. X. *Appl. Catal. B Environ.* **2009,** *88,* 376–385.
20. Wu, C.; Sui, M.; Yan, Y. J. *Chem. Eng. Technol.* **2008,** *31,* 1748–1753.
21. He, L.; Chen, D. *ChemSusChem* **2012,** *5,* 587–595.
22. Navarro, R. M.; Pena, M. A.; Fierro, J. L. G. *Chem. Rev.* **2007,** *107,* 3952–3991.
23. Tye, C. T.; Smith, K. J. *Catal. Today* **2006,** *116,* 461–468.
24. Simonetti, D. A.; Dumesic, J. A. *Catal. Rev. Sci. Eng.* **2009,** *51,* 441–484.
25. Mattos, L. V.; Jacobs, G.; Davis, B. H.; Noronha, F. B. *Chem. Rev.* **2012,** *112,* 4094–4123.
26. Piscina, P. R. D. L.; Homs, N. *Chem. Soc. Rev.* **2008,** *37,* 2459–2467.
27. Silveira, J. L.; Braga, L. B.; de Souza, A. C. C.; Antunes, J. S.; Zanzi, R. *Renew. Sustain. Energy Rev.* **2009,** *13,* 2525–2534.
28. He, L.; Berntsen, H.; Chen, D. *J. Phys. Chem. A* **2009,** *114,* 3834–3844.
29. Zhou, C. H. C.; Beltramini, J. N.; Fan, Y. X.; Lu, G. Q. M. *Chem. Soc. Rev.* **2008,** *37,* 527–549.
30. Briens, C.; Piskorz, J.; Berruti, F. *Int. J. Chem. React. Eng.* **2008,** *6*.
31. Nahar, G.; Dupont, V. *Biofuels* **2012,** *3,* 167–191.
32. Vaidya, P. D.; Rodrigues, A. E. *Chem. Eng. Technol.* **2009,** *32,* 1463–1469.
33. Cheng, L.; Ye, X. P. *Biofuels* **2010,** *1,* 109–128.
34. Iulianelli, A.; Longo, T.; Basile, A. *Int. J. Hydrog. Energy* **2008,** *33,* 4091–4096.
35. Iwasa, N.; Yamane, T.; Takei, M.; Ozaki, J. I.; Arai, M. *Int. J. Hydrog. Energy* **2010,** *35,* 110–117.
36. Medrano, J. A.; Oliva, M.; Ruiz, J.; Garcia, L.; Arauzo, J. *Int. J. Hydrog. Energy* **2008,** *33,* 4387–4396.
37. Medrano, J. A.; Oliva, M.; Ruiz, J.; Garcia, L.; Arauzo, J. *Int. J. Hydrog. Energy* **2009,** *34,* 7065–7074.
38. Bimbela, F.; Oliva, M.; Ruiz, J.; Garcia, L.; Arauzo, J.; Anal, J. *Appl. Pyrolysis* **2007,** *79,* 112–120.
39. Takanabe, K.; Aika, K.; Inazu, K.; Baba, T.; Seshan, K.; Lefferts, L. *J. Catal.* **2006,** *243,* 263–269.
40. Takanabe, K.; Aika, K.; Seshan, K.; Lefferts, L. *J. Catal.* **2004,** *227,* 101–108.
41. Basile, A.; Gallucci, F.; Iulianelli, A.; Borgognoni, F.; Tosti, S. *J. Membr. Sci.* **2008,** *311,* 46–52.
42. Hu, X.; Lu, G. X. *J. Mol. Catal. A Chem.* **2007,** *261,* 43–48.
43. Alcala, R.; Shabaker, J. W.; Huber, G. W.; Sanchez-Castillo, M. A.; Dumesic, J. A. *J. Phys. Chem. B* **2005,** *109,* 2074–2085.
44. Takanabe, K.; Aika, K. I.; Seshan, K.; Lefferts, L. *Top. Catal.* **2008,** *49,* 68–72.
45. Hu, X.; Lu, G. X. *Chem. Lett.* **2006,** *35,* 452–453.
46. Galdamez, J. R.; Garcia, L.; Bilbao, R. *Energy Fuels* **2005,** *19,* 1133–1142.
47. Kechagiopoulos, P. N.; Voutetakis, S. S.; Lemonidou, A. A.; Vasalos, I. A. *Energy Fuels* **2006,** *20,* 2155–2163.
48. Kechagiopoulos, P. N.; Voutetakis, S. S.; Lemonidou, A. A.; Vasalos, I. A. *Ind. Eng. Chem. Res.* **2009,** *48,* 1400–1408.
49. Basagiannis, A. C.; Verykios, X. E. *Int. J. Hydrog. Energy* **2007,** *32,* 3343–3355.
50. Vagia, E. C.; Lemonidou, A. A. *Appl. Catal. A Gener.* **2008,** *351,* 111–121.
51. Hu, X.; Lu, G. *Appl. Catal. B: Environ.* **2009,** *88,* 376–385.
52. Basagiannis, A. C.; Verykios, X. E. *Appl. Catal. B Environ.* **2008,** *82,* 77–88.
53. Guell, B. M.; Babich, I.; Nichols, K. P.; Gardeniers, J. G. E.; Lefferts, L.; Seshan, K. *Appl. Catal. B Environ.* **2009,** *90,* 38–44.
54. Guell, B. M.; da Silva, I. M. T.; Seshan, K.; Lefferts, L. *Appl. Catal. B Environ.* **2009,** *88,* 59–65.
55. Ortiz-Toral, P. J.; Satrio, J.; Brown, R. C.; Shanks, B. H. *Energy and Fuels* **2011,** *25* (7), 3289–3297.
56. Basagiannis, A. C.; Verykios, X. E. *Appl. Catal. A Gener.* **2006,** *308,* 182–193.
57. Takezawa, N.; Iwasa, N. *Catal. Today* **1997,** *36,* 45–56.
58. Takanabe, K.; Aika, K.; Seshan, K.; Lefferts, L. *Chem. Eng. J. (Lausanne)* **2006,** *120,* 133–137.
59. Bimbela, F.; Oliva, M.; Ruiz, J.; Garcia, L.; Arauzo, J. *J. Anal. Appl. Pyrolysis* **2009,** *85,* 204–213.
60. Medrano, J. A.; Oliva, M.; Ruiz, J.; Garcia, L.; Afauzo, J. *J. Anal. Appl. Pyrolysis* **2009,** *85,* 214–225.
61. Rioche, C.; Kulkarni, S.; Meunier, F. C.; Breen, J. P.; Burch, R. *Appl. Catal. B* **2005,** *61,* 130–139.
62. Vagia, E. C.; Lemonidou, A. A. *Int. J. Hydrog. Energy* **2008,** *33,* 2489–2500.
63. Davda, R. R.; Shabaker, J. W.; Huber, G. W.; Cortright, R. D.; Dumesic, J. A. *Appl. Catal. B: Environ.* **2003,** *43,* 13–26.
64. Kechagiopoulos, P. N.; Voutetakis, S. S.; Lemonidou, A. A.; Vasalos, I. A. *Catal. Today* **2007,** *127,* 246–255.
65. Wu, C.; Liu, R. H. *Int. J. Hydrog. Energy* **2010,** *35,* 7386–7398.
66. Constantinou, D. A.; Efstathiou, A. M. *Appl. Catal. B Environ.* **2010,** *96,* 276–289.
67. Czernik, S.; French, R.; Feik, C.; Chornet, E. *Ind. Eng. Chem. Res.* **2002,** *41,* 4209–4215.
68. Huang, L.; Zhu, Y.; Zheng, H.; Ding, G.; Li, Y. *Catal. Lett.* **2009,** *131,* 312–320.

69. Wang, D. N.; Czernik, S.; Chornet, E. *Energy Fuels* **1998,** *12,* 19−24.
70. Basagiannis, A. C.; Verykios, X. E. *Catal. Today* **2007,** *127,* 256−264.
71. Li, H. Y.; Xu, Q. L.; Xue, H. S.; Yan, Y. J. *Renew. Energy* **2009,** *34,* 2872−2877.
72. Turn, S.; Kinoshita, C.; Zhang, Z.; Ishimura, D.; Zhou, J. *Int. J. Hydrog. Energy* **1998,** *23,* 641−648.
73. Cortright, R. D.; Davda, R. R.; Dumesic, J. A. *Nature* **2002,** *418,* 964−967.
74. Alcala, R.; Mavrikakis, M.; Dumesic, J. A. *J. Catal.* **2003,** *218,* 178−190.
75. Armor, J. N. *Appl. Catal. A* **1999,** *176,* 159−176.
76. Ferrin, P.; Simonetti, D.; Kandoi, S.; Kunkes, E.; Dumesic, J. A.; Norskov, J. K.; Mavrikakis, M.; Am, J. *Chem. Soc.* **2009,** *131,* 5809−5815.
77. Abild-Pedersen, F.; Greeley, J.; Studt, F.; Rossmeisl, J.; Munter, T. R.; Moses, P. G.; Skúlason, E.; Bligaard, T.; Nørskov, J. K. *Phys. Rev. Lett.* **2007,** *99,* 016105.
78. Sinfelt, J. H.; Yates, D. J. C. *J. Catal.* **1967,** *8,* 82−90.
79. Frusteri, F.; Freni, S.; Spadaro, L.; Chiodo, V.; Bonura, G.; Donato, S.; Cavallaro, S. *Catal. Commun* **2004,** *5,* 611−615.
80. Erdohelyi, A.; Rask, J.; Kecskes, T.; Toth, M.; Dömök, M.; Baan, K. *Catal. Today* **2006,** *116,* 367−376.
81. Hirai, T.; Ikenaga, N.-o; Miyake, T.; Suzuki, T. *Energy Fuels* **2005,** *19,* 1761−1762.
82. Laosiripojana, N.; Kiatkittipong, W.; Charojrochkul, S.; Assabumrungrat, S. *Appl. Catal. A* **2010,** *383,* 50−57.
83. Panagiotopoulou, P.; Kondarides, D. I. *Catal. Today* **2006,** *112,* 49−52.
84. Yamazaki, T.; Matsuki, K. *J. Jpn. Pet. Inst.* **2006,** *49,* 246−255.
85. Cao, C.; Xia, G.; Holladay, J.; Jones, E.; Wang, Y. *Appl. Catal. A* **2004,** *262,* 19−29.
86. Akande, A.; Aboudheir, A.; Idem, R.; Dalai, A. *Int. J. Hydrog. Energy* **2006,** *31,* 1707−1715.
87. Mas, V.; Bergamini, M.; Baronetti, G.; Amadeo, N.; Laborde, M. *Top Catal.* **2008,** *51,* 39−48.
88. Yun, S.; Lim, H.; Ted Oyama, S. *J. Membr. Sci.* **2012,** *409*−*410,* 222−231.
89. Peela, N. R.; Kunzru, D. *Ind. Eng. Chem. Res.* **2011,** *50,* 12881−12894.
90. Sutar, P. N.; Vaidya, P. D.; Rodrigues, A. E. *Chem. Eng. Technol.* **2010,** *33,* 1645−1649.
91. Simonetti, D. A.; Kunkes, E. L.; Dumesic, J. A. *J. Catal.* **2007,** *247,* 298−306.
92. Sundari, R.; Vaidya, P. D. *Energy Fuel* **2012,** *26,* 4195−4204.
93. Byrd, A. J.; Pant, K. K.; Gupta, R. B. *Fuel* **2008,** *87,* 2956−2960.
94. Adhikari, S.; Fernando, S. D.; Haryanto, A. *Chem. Eng. Technol.* **2009,** *32,* 541−547.
95. Dave, C. D.; Pant, K. K. *Renew. Energy* **2011,** *36,* 3195−3202.
96. Cheng, C. K.; Foo, S. Y.; Adesina, A. A. *Catal. Today* **2011,** *178,* 25−33.
97. Cheng, C. K.; Foo, S. Y.; Adesina, A. A. *Catal. Comm.* **2010,** *12,* 292−298.
98. Cheng, C. K.; Foo, S. Y.; Adesina, A. A. *Ind. Eng. Chem. Res.* **2010,** *49,* 10804−10817.
99. Dubey, V. R.; Vaidya, P. D. *Chem. Eng. J.* **2012,** *180,* 263−269.
100. Frusteri, F.; Freni, S.; Chiodo, V.; Donato, S.; Bonura, G.; Cavallaro, S. *Int. J. Hydrog. Energy* **2006,** *31,* 2193−2199.
101. Biswas, P.; Kunzru, D. *Catalysis Letters* **2007,** *118* (1−2), 36−49.
102. Nakamura, K.; Miyazawa, T.; Sakurai, T.; Miyao, T.; Naito, S.; Begum, N.; Kunimori, K.; Tomishige, K. *Appl. Catal. B Environ.* **2009,** *86,* 36−44.
103. Liguras, D. K.; Kondarides, D. I.; Verykios, X. E. *Appl. Catal. B Environ.* **2003,** *43,* 345−354.
104. Grenoble, D. C.; Estadt, M. M.; Ollis, D. F. *J. Catal.* **1981,** *67,* 90−102.
105. Haryanto, A.; Fernando, S.; Adhikari, S. *Catal. Today* **2007,** *129,* 269−274.
106. Sperle, T.; Chen, D.; Lødeng, R.; Holmen, A. *Appl. Catal. A Gener.* **2005,** *282,* 195−204.
107. Rostrup-Nielsen, J. R.; Sehested, J. In *Catalyst Deactivation 2001, Proceedings;* Spivey, J. J., Roberts, G. W., Davis, B. H., Eds.; pp 1−12.
108. Rostrup-Nielsen, J. R.; Christensen, T. S.; Dybkjaer, I. In *Recent Advances in Basic and Applied Aspects of Industrial Catalysis;* Rao, T. S. R., Dhar, G. M., Eds.; pp 81−95.
109. Rostrup-Nielsen, J. R. *Phys. Chem. Chem. Phys.* **2001,** *3,* 283−288.
110. Rostrup-Nielsen, J. R.; Nielsen, R. *Catal. Rev. Sci. Eng.* **2004,** *46,* 247−270.
111. Chen, D.; Christensen, K. O.; Ochoa-Fernandez, E.; Yu, Z. X.; Totdal, B.; Latorre, N.; Monzon, A.; Holmen, A. *J. Catal.* **2005,** *229,* 82−96.
112. Haga, F.; Nakajima, T.; Miya, H.; Mishima, S. *Catal. Lett.* **1997,** *48,* 223−227.
113. Kimura, T.; Miyazawa, T.; Nishikawa, J.; Kado, S.; Okumura, K.; Miyao, T.; Naito, S.; Kunimori, K.; Tomishige, K. *Appl. Catal. B: Environ.* **2006,** *68,* 160−170.
114. Palo, D. R.; Dagle, R. A.; Holladay, J. D. *Chem. Rev.* **2007,** *107,* 3992−4021.
115. Toonssen, R.; Woudstra, N.; Verkooijen, A. H. M. *Int. J. Hydrog. Energy* **2008,** *33,* 4074−4082.
116. He, L.; Parra, J. M. S.; Blekkan, E. A.; Chen, D. *Energy Environ. Sci.* **2010,** *3,* 1046−1056.
117. Abanades, J. C.; Anthony, E. J.; Wang, J.; Oakey, J. E. *Environ. Sci. Technol.* **2005,** *39,* 2861−2866.
118. Wang, D.; Czernik, S.; Montane, D.; Mann, M.; Chornet, E. *Ind. Eng. Chem. Res.* **1997,** *36,* 1507−1518.
119. Cruz, I. O.; Ribeiro, N. F. P.; Aranda, D. A. G.; Souza, M. M. V. M. *Catal. Comm.* **2008,** *9,* 2606−2611.
120. Roy, B.; Martinez, U.; Loganathan, K.; Datye, A. K.; Leclerc, C. A. *Int. J. Hydrog. Energy* **2012,** *37,* 8143−8153.
121. Saville, S.; Boydelatour, A.; Leclerc, C. *Abstr. Pap. Am. Chem. Soc.* **2011,** *241*.
122. Tang, Z.; Monroe, J.; Dong, J.; Nenoff, T.; Weinkauf, D. *Ind. Eng. Chem. Res.* **2009,** *48,* 2728−2733.
123. Tokarev, A. V.; Kirilin, A. V.; Murzina, E. V.; Eranen, K.; Kustov, L. M.; Murzin, D. Y.; Mikkola, J. P. *Int. J. Hydrog. Energy* **2010,** *35,* 12642−12649.
124. Huber, G. W.; Shabaker, J. W.; Evans, S. T.; Dumesic, J. A. *Appl. Catal. B Environ.* **2006,** *62,* 226−235.
125. Kim, H.-D.; Park, H. J.; Kim, T.-W.; Jeong, K.-E.; Chae, H.-J.; Jeong, S.-Y.; Lee, C.-H.; Kim, C.-U. *Int. J. Hydrog. Energy* **2012,** *37,* 8310−8317.
126. Liu, J.; Sun, B.; Hu, J.; Pei, Y.; Li, H.; Qiao, M. *J. Catal.* **2010,** *274,* 287−295.
127. Shabaker, J. W.; Davda, R. R.; Huber, G. W.; Cortright, R. D.; Dumesic, J. A. *J. Catal.* **2003,** *215,* 344−352.
128. Guo, Y.; Liu, X.; Azmat, M. U.; Xu, W.; Ren, J.; Wang, Y.; Lu, G. *Int. J. Hydrog. Energy* **2012,** *37,* 227−234.
129. Lehnert, K.; Claus, P. *Catal. Comm.* **2008,** *9,* 2543−2546.
130. Meryemoglu, B.; Kaya, B.; Irmak, S.; Hesenov, A.; Erbatur, O. *Fuel* **2012,** *97,* 241−244.
131. Wen, G.; Xu, Y.; Ma, H.; Xu, Z.; Tian, Z. *Int. J. Hydrog. Energy* **2008,** *33,* 6657−6666.
132. Zhang, L.; Karim, A. M.; Engelhard, M. H.; Wei, Z.; King, D. L.; Wang, Y. *J. Catal.* **2012,** *287,* 37−43.

133. Kirilin, A. V.; Tokarev, A. V.; Kustov, L. M.; Salmi, T.; Mikkola, J. P.; Murzin, D. Y. *Appl. Catal. A Gener.* **2012,** *435,* 172−180.
134. Kirilin, A. V.; Tokarev, A. V.; Murzina, E. V.; Kustov, L. M.; Mikkola, J.-P.; Murzin, D. Y. *ChemSusChem* **2010,** *3,* 708−718.
135. Tanksale, A.; Zhou, C. H.; Beltramini, J. N.; Lu, G. Q. *J. Incl. Phenom. Macrocycl. Chem.* **2009,** *65,* 83−88.
136. Zhang, Q.; Wang, T.; Li, B.; Jiang, T.; Ma, L.; Zhang, X.; Liu, Q. *Appl. Energy* **2012,** *97,* 509−513.
137. Davda, R. R.; Dumesic, J. A. *Chem. Comm.* **2004,** 36−37.
138. Wen, G.; Xu, Y.; Xu, Z.; Tian, Z. *Catal. Lett.* **2009,** *129,* 250−257.
139. Wen, G.; Xu, Y.; Liu, Q.; Wang, C.; Liu, H.; Tian, Z. *Catal. Lett.* **2011,** *141,* 1851−1858.
140. Wen, G.; Xu, Y.; Xu, Z.; Tian, Z. *Catal. Comm.* **2010,** *11,* 522−526.
141. Valenzuela, M. B.; Jones, C. W.; Agrawal, P. K. *Energy Fuels* **2006,** *20,* 1744−1752.
142. Huber, G. W.; Dumesic, J. A. An Overview of Aqueous-Phase Catalytic Processes for Production of Hydrogen and Alkanes in a Biorefinery. *Catal. Today* **2006,** 119−132.
143. Shabaker, J. W.; Huber, G. W.; Dumesic, J. A. *J. Catal.* **2004,** *222,* 180−191.
144. Huber, G. W.; Shabaker, J. W.; Dumesic, J. A. *Science* **2003,** *300,* 2075−2077.
145. Zhu, L.-J.; Guo, P.-J.; Chu, X.-W.; Yan, S.-R.; Qiao, M.-H.; Fan, K.-N.; Zhang, X.-X.; Zong, B.-N. *Green Chem.* **2008,** *10,* 1323−1330.
146. Luo, N.; Ouyang, K.; Cao, F.; Xiao, T. *Biomass Bioenerg.* **2010,** *34,* 489−495.
147. Iriondo, A.; Cambra, J. F.; Barrio, V. L.; Guemez, M. B.; Arias, P. L.; Sanchez-Sanchez, M. C.; Navarro, R. M.; Fierro, J. L. G. *Appl. Catal. B Environ.* **2011,** *106,* 83−93.
148. Wang, X.; Li, N.; Pfefferle, L. D.; Haller, G. L. *Catal. Today* **2009,** *146,* 160−165.
149. Wang, X.; Li, N.; Pfefferle, L. D.; Haller, G. L. *J. Phys. Chem. C* **2010,** *114,* 16996−17002.
150. Wang, X.; Li, N.; Zhang, Z.; Wang, C.; Pfefferle, L. D.; Haller, G. L. *ACS Catal.* **2012,** *2,* 1480−1486.
151. Guo, Y.; Wang, S. Z.; Xu, D. H.; Gong, Y. M.; Ma, H. H.; Tang, X. Y. *Renew. Sustain. Energy Rev.* **2010,** *14,* 334−343.
152. Peterson, A. A.; Vogel, F.; Lachance, R. P.; Froeling, M.; Antal, M. J., Jr.; Tester, J. W. *Energy Environ. Sci.* **2008,** *1,* 32−65.
153. Yu, D.; Aihara, M.; Antal, M. J. *Energy Fuels* **1993,** *7,* 574−577.
154. Williams, P. T.; Onwudili, J. *Energy Fuels* **2006,** *20,* 1259−1265.
155. Fang, Z.; Minowa, T.; Fang, C.; Smith, J. R. L.; Inomata, H.; Kozinski, J. A. *Int. J. Hydrog. Energy* **2008,** *33,* 981−990.
156. Yamaguchi, A.; Hiyoshi, N.; Sato, O.; Bando, K. K.; Osada, M.; Shirai, M. *Catal. Today* **2009,** *146,* 192−195.
157. Azadi, P.; Otomo, J.; Hatano, H.; Oshima, Y.; Farnood, R. *Int. J. Hydrog. Energy* **2010,** *35,* 3406−3414.
158. Voll, F. A. P.; Rossi, C.; Silva, C.; Guirardello, R.; Souza, R.; Cabral, V. F.; Cardozo, L. *Int. J. Hydrog. Energy* **2009,** *34,* 9737−9744.
159. Harrison, D. P. *Ind. Eng. Chem. Res.* **2008,** *47,* 6486−6501.
160. Florin, N.; Harris, A. *Environmentalist* **2007,** *27,* 207−215.
161. Koppatz, S.; Pfeifer, C.; Rauch, R.; Hofbauer, H.; Marquard-Moellenstedt, T.; Specht, M. *Fuel Process. Technol.* **2009,** *90,* 914−921.
162. Satyapal, S. *2009 Annual Progress Report*, 2009.
163. Chen, H. S.; Zhang, T. F.; Dou, B. L.; Dupont, V.; Williams, P.; Ghadiri, M.; Ding, Y. L. *Int. J. Hydrog. Energy* **2009,** *34,* 7208−7222.
164. Ochoa-Fernandez, E.; Haugen, G.; Zhao, T.; Ronning, M.; Aartun, I.; Borresen, B.; Rytter, E.; Ronnekleiv, M.; Chen, D. *Green Chem.* **2007,** *9,* 654−662.
165. Cobden, P. D.; van Beurden, P.; Reijers, H. T. J.; Elzinga, G. D.; Kluiters, S. C. A.; Dijkstra, J. W.; Jansen, D.; van den Brink, R. W. *Int. J. Greenh. Gas Control* **2007,** *1,* 170−179.
166. Barelli, L.; Bidini, G.; Corradetti, A.; Desideri, U. *Energy* **2007,** *32,* 834−843.
167. Li, M. *Int. J. Hydrog. Energy* **2009,** *34,* 9362−9372.
168. He, L. *Sorption Enhanced Reforming of Biomass Derived Compunds: Proceses and Materials;* Norwegian Univeristy of Science and technology: Trondheim, 2009.
169. Iordanidis, A. A.; Kechagiopoulos, P. N.; Voutetakis, S. S.; Lemonidou, A. A.; Vasalos, I. A. *Int. J. Hydrog. Energy* **2006,** *31,* 1058−1065.
170. Sandler, S. I., Ed. *Chemical and Engineering Thermodynamics;* Wiley: New York, 1999.
171. Rase, H. F., Ed. *Handbook of Commercial Catalysts: Heterogeneous Catalysts;* CRC Press LLC, 2000.
172. Sircar, K. B. L. S. *Sorption Enhanced Reaction Concepts from Hydrogen Productions, Materials & Processes;* Research Signpost: Karala, India, 2010.
173. Balasubramanian, B.; Lopez Ortiz, A.; Kaytakoglu, S.; Harrison, D. P. *Chem. Eng. Sci.* **1999,** *54,* 3543−3552.
174. Spiegel, R. J.; Preston, J. L. *Energy* **2003,** *28,* 397−409.
175. Iwasaki, Y.; Suzuki, Y.; Kitajima, T.; Sakurai, M.; Kameyama, H. *J. Chem. Eng. Jpn.* **2007,** *40,* 178−185.
176. Essaki, K.; Muramatsu, T.; Kato, M. *Int. J. Hydrog. Energy* **2008,** *33,* 6612−6618.
177. Lysikov, A. I.; Trukhan, S. N.; Okunev, A. G. *Int. J. Hydrog. Energy* **2008,** *33,* 3061−3066.
178. Dou, B.; Dupont, V.; Rickett, G.; Blakeman, N.; Williams, P. T.; Chen, H.; Ding, Y.; Ghadiri, M. *Bioresour. Technol.* **2009,** *100,* 3540−3547.
179. Fermoso, J.; He, L.; Chen, D. *Int. J. Hydrog. Energy* **2012,** *37,* 14047−14054.
180. Pricing, I. Chemical Price Reports: Glycerol. In *Reed Business Information Limited;* Taylor, J., Ed.; 2011; 2011. http://www.icis.com/bioresources.
181. Dou, B.; Rickett, G. L.; Dupont, V.; Williams, P. T.; Chen, H.; Ding, Y.; Ghadiri, M. *Bioresour. Technol.* **2010,** *101,* 2436−2442.
182. Kinoshita, C. M.; Turn, S. Q. *Int. J. Hydrog. Energy* **2003,** *28,* 1065−1071.
183. Yan, C. F.; Hu, E. Y.; Cai, C. L. *Int. J. Hydrog. Energy* **2010,** *35,* 2612−2616.
184. Dupont, V.; Ross, A. B.; Hanley, I.; Twigg, M. V. *Int. J. Hydrog. Energy* **2007,** *32,* 67−79.
185. He, L.; Berntsen, H.; Ochoa-Fernández, E.; Walmsley, J.; Blekkan, E.; Chen, D. *Top. Catal.* **2009,** *52,* 206−217.
186. Manovic, V.; Anthony, E. J. *Energy Fuels* **2008,** *22,* 1851−1857.
187. Hughes, R. W.; Lu, D.; Anthony, E. J.; Wu, Y. H. *Ind. Eng. Chem. Res.* **2004,** *43,* 5529−5539.
188. Li, Y. J.; Zhao, C. S.; Qu, C. R.; Duan, L. B.; Li, Q. Z.; Liang, C. *Chem. Eng. Technol.* **2008,** *31,* 237−244.
189. Manovic, V.; Lu, D.; Anthony, E. J. *Fuel* **2008,** *87,* 3344−3352.
190. Choi, S.; Drese, J. H.; Jones, C. W. *ChemSusChem* **2009,** *2,* 796−854.
191. MacDowell, N.; Florin, N.; Buchard, A.; Hallett, J.; Galindo, A.; Jackson, G.; Adjiman, C. S.; Williams, C. K.; Shah, N.; Fennell, P. *Energy Environ. Sci.* **2010,** *3,* 1645−1669.
192. Feng, B.; An, H.; Tan, E. *Energy Fuels* **2007,** *21,* 426−434.
193. Wang, Q.; Luo, J.; Zhong, Z.; Borgna, A. *Energy Environ. Sci.* **2011,** *4,* 42−55.
194. Sultana, K. S.; Chen, D. *Catal. Today* **2011,** *171,* 43−51.
195. Ochoa-Fernandez, E.; Ronning, M.; Grande, T.; Chen, D. *Chem. Mater.* **2006,** *18,* 1383−1385.

196. Zhao, T. J.; Ochoa-Fernandez, E.; Ronning, M.; Chen, D. *Chem. Mater.* **2007,** *19,* 3294−3301.
197. Qi, A. D.; Peppley, B.; Karan, K. *Fuel Process. Technol.* **2007,** *88,* 3−22.
198. Devi, L.; Ptasinski, K. J.; Janssen, F. *Biomass Bioenerg.* **2003,** *24,* 125−140.
199. Furusawa, T.; Tsutsumi, A. *Appl. Catal. A Gener.* **2005,** *278,* 207−212.
200. Pfeifer, B. P. C.; Hofbauer, H. *Int. J. Chem. React. Eng.* **2007,** *5.* A9.
201. He, L.; Chen, D. *ChemSusChem* **2010,** *3,* 1169−1171.
202. Rei, M.-H.; Yang, S. J.; Hong, C. H. *Agric. Wastes* **1986,** *18,* 269−281.
203. Tomishige, K.; Miyazawa, T.; Asadullah, M.; Ito, S.; Kunimori, K. *Green Chem.* **2003,** *5,* 399−403.
204. Asadullah, M.; Ito, S.-i.; Kunimori, K.; Yamada, M.; Tomishige, K. *Environ. Sci. Technol.* **2002,** *36,* 4476−4481.
205. Inaba, M.; Murata, K.; Saito, M.; Takahara, I. *Energy Fuels* **2006,** *20,* 432−438.
206. Beaver, M. G.; Caram, H. S.; Sircar, S. *Int. J. Hydrog. Energy* **2009,** *34,* 2972−2978.
207. Lee, K. B.; Beaver, M. G.; Caram, H. S.; Sircar, S. *J. Power Sources* **2008,** *176,* 312−319.
208. van Selow, E. R.; Cobden, P. D.; Verbraeken, P. A.; Hufton, J. R.; van den Brink, R. W. *Ind. Eng. Chem. Res.* **2009,** *48,* 4184−4193.
209. Hanaoka, T.; Yoshida, T.; Fujimoto, S.; Kamei, K.; Harada, M.; Suzuki, Y.; Hatano, H.; Yokoyama, S.-y.; Minowa, T. *Biomass Bioenerg.* **2005,** *28,* 63−68.
210. Han, L.; Wang, Q.; Ma, Q.; Yu, C.; Luo, Z.; Cen, K. *J. Anal. Appl. Pyrolysis* **2010,** *88,* 199−206.
211. Guoxin, H.; Hao, H. *Biomass Bioenerg.* **2009,** *33,* 899−906.
212. Fermoso, J.; Rubiera, F.; Chen, D. *Energy Environ. Sci.* **2012,** *5,* 6358−6367.
213. McKendry, P. *Bioresour. Technol.* **2002,** *83,* 47−54.
214. Di Felice, L.; Courson, C.; Jand, N.; Gallucci, K.; Foscolo, P. U.; Kiennemann, A. *Chem. Eng. J. (Lausanne)* **2009,** *154,* 375−383.
215. Satrio, J. A.; Shanks, B. H.; Wheelock, T. D. *Energy Fuels* **2006,** *21,* 322−326.

CHAPTER

7

Hydrogen from Bioethanol

Jordi Llorca [*], *Vicente Cortés Corberán* [†], *Núria J. Divins* [*], *Raquel Olivera Fraile* [†], *Elena Taboada* [*]

[*]Institute of Energy Technologies, Technical University of Catalonia—BarcelonaTECH, Barcelona, Spain, [†]Institute of Catalysis and Petroleumchemistry (ICP), Spanish Council for Scientific Research (CSIC), Marie Curie 2, Madrid, Spain

OUTLINE

7.1 Introduction 135
7.1.1 Bioethanol Manufacture 136
7.1.2 Catalytic Routes to Hydrogen Production: The Pros and Cons 136
7.1.3 Reaction Pathways and Thermodynamics 138
7.2 Steam Reforming of Ethanol 141
7.2.1 Noble Metal Catalysts 141
7.2.2 Nickel Catalysts 143
7.2.3 Cobalt Catalysts 145
7.3 Partial Oxidation of Ethanol 147
7.3.1 Preliminary Overview 147
7.3.2 Reaction Mechanism 147
7.3.3 Noble Metal Catalysts 148
7.3.4 Non-noble Metals and Structured Catalysts 149
7.3.5 Autothermal Oxidation 150
7.4 Autothermal Reforming of Ethanol 151
7.4.1 Noble Metal Catalysts 151
7.4.2 Nickel Catalysts 152
7.4.3 Other Catalytic Systems 154
7.5 Ethanol Reforming in Catalytic Membrane Reactors 155
7.6 Ethanol Reforming in Miniaturized Systems 158
7.7 Photocatalytic Production of Hydrogen from Ethanol 159
7.8 Concluding Remarks 161
Acknowledgments 162
References 162

7.1 INTRODUCTION

Ethanol is probably the first product ever obtained by a catalytic (enzymatic) process in mankind history: as a beverage, it has been produced since almost 5000 years in the Ancient Egypt. Since then, most human cultures and societies have been producing it, using practically any natural resource suitable for fermentation. Apart from its use as a beverage, ethanol is one of the most versatile organic chemicals because of its unique properties as a solvent, an antifreezing agent, a germicide, a fuel and especially as a chemical intermediate for other organic chemicals. Under ordinary conditions, it is a volatile, flammable, transparent and colorless liquid with a pleasant and characteristic odor. The physical and chemical properties of ethanol are primarily dependent on the reactivity of the hydroxyl group, which makes it a polar compound and gives rise to intermolecular hydrogen bonding. A very peculiar property of ethanol is the volume shrinkage that occurs when mixed with water and the volume expansion when mixed with gasoline.[1] As a fuel, ethanol has a high octane rating: 109 RON (Research Octane Number), 90 MON (Motor Octane Number), and it is currently used in fuel blends for spark ignition engines.

The term *bioethanol* is currently used to refer the ethanol produced from biomass resources by biological processes (fermentation, enzymatic catalysis). The term is also applied, in a broader sense, to all alcoholic liquors

produced by fermentation of sugars from plants, where the alcohol-to-water ratio on a molar basis is between 1:7 and 1:12. Ethanol is therefore considered a renewable resource, due to its easy and broadly implemented production from a variety of plants. Ethanol has high hydrogen-to-carbon ratio of 3 and a high hydrogen content per unit volume in the liquid state. In addition, ethanol distribution networks are already available in many countries. All these factors make it a very attractive raw material for hydrogen production, especially for mobile applications.

There has been considerable discussion on the global energy efficiency obtained when fuel bioethanol is produced from agriculture products (for instance, from corn) because of the energy used in planting and harvesting, fertilizer, transportation, and processing into ethanol. It has been reported that the energy output in the fuel ethanol is at least 1.34 times (1.53 under a best-case scenario) the energy used in its production from corn.[2,3] Most of this energy consumed in processing is used to remove all water after fermentation. Then, the global energy balance would be considerably improved when bioethanol is used in processes using water as reactant (such as reforming) to produce hydrogen for fuel cell, instead of using it as a fuel mixed with gasoline.[4]

7.1.1 Bioethanol Manufacture

Though industrial ethanol can be produced synthetically by hydration of ethylene or as a by-product of certain industrial operations, most of it is produced by fermentation of sugar, starch or cellulose. For instance, fermentation processes share of total production in US, Western Europe and Japan increased from 83% in 1997 to 90% in 2001.[1] Bioethanol is produced by anaerobic fermentation of sugars in aqueous solution by yeasts, which produces beverage-grade alcohol containing about 14% ethanol. However, to obtain pure ethanol to use as a gasoline additive, the aqueous ethanol obtained from fermentation process needs to be distilled. This is an energy-intensive process and contributes over 50% to the total cost of ethanol production.[5] Due to the first oil crisis of 1973, Brazil started in 1975 the ProAlcohol program to produce fermentation alcohol from sugar cane for its use as fuel in gasohols. Since then, the increasing demand of ethanol as fuel component, and as a substitute for methyl tertiary butyl ether (MTBE), has rocketed the world production. Thus, in spite of the economical crisis, it increased from 40,164 million l in 2004 to 86,714 million l in 2011.[6] The United States, where most fuel alcohol is currently made mainly from grains, mostly corn, is currently the world's first producer of ethanol, followed by Brazil; together, they represent nearly 86% of the world's total production.

The use of edible plants (especially corn) as a source of fuel ethanol has increased their price in such a way that has opened a conflict of interests between their use as a source of food vs. a source of fuel. This has generated the need of researching the use of nonedible natural resources (grasses, straw, etc.) to produce bioethanol. This biomass is lignocellulosic and accounts for about half of the world biomass. The use of lignocellulosics increases greatly the availability of raw materials for ethanol production and reduces the production price markedly. However, the complex molecular structures of lignocellulosics make production of ethanol from them more difficult than from sugar cane or starch-rich materials.[7] All processes for ethanol production from lignocellulosics consist of two main steps: hydrolysis of cellulose and hemicellulose to monomeric sugars, and subsequent fermentation to produce bioethanol. A more detailed description can be found in Ref. 8.

7.1.2 Catalytic Routes to Hydrogen Production: The Pros and Cons

There are three main reactive pathways for producing hydrogen directly from ethanol, all of them are catalytic, that differ by the coreactant used, the process chemistry and the maximum hydrogen yield reachable, namely, steam reforming, partial oxidation and its combination, and autothermal reforming (ATR).

The highest hydrogen production can be obtained by ethanol steam reforming (ESR) where ethanol reacts with water steam to give carbon dioxide and hydrogen. The overall reaction can be formally written as:

$$CH_3CH_2OH(g) + 3H_2O(g) \rightarrow 2CO_2(g) + 6H_2(g)$$
$$\Delta H^0_{298\ K} = 173.3\ \text{kJ/mol} \quad (7.1)$$

Though reaction stoichiometry determines a steam-to-ethanol molar ratio $S/E = 3$, rather higher ratios can be used. This is advantageous as it allows using directly the bioethanol produced by fermentation, where the S/E ratio is about 13, without any need of distillation.

Its main disadvantage is its high endothermicity, which brings along two drawbacks: (1) a high energy input is needed to run the reaction, in addition to the energy needed to evaporate both liquid reactants and to heat the steam; and (2) hydrogen formation is limited by thermodynamic equilibrium. The latter can be improved by increasing the S/E:[9] reported equilibrium H_2 yields of 5.5 mol/mol of ethanol at around 773−873 K with $S/E > 20$. However, the increase of S/E ratio worsens the energy input drawback, increasing the energy needed for water evaporation, which adds to the relatively high temperatures (600−1073 K) needed to reach practical conversions.

Another important issue is that reaction conditions may lead to formation of carbon monoxide,

$$\begin{gathered}\mathrm{CH_3CH_2OH(g) + H_2O(g) \;\rightarrow\; 2CO(g) + 4H_2(g)} \\ \Delta H^0_{298\ \mathrm{K}} = 255.5\ \mathrm{kJ/mol}\end{gathered} \tag{7.2}$$

thus reducing the hydrogen yield to 4 mol/mol of ethanol. This reaction introduces another problem because carbon monoxide is a poison for polymer electrolyte membrane fuel cell (PEMFC) electrocatalysts: high CO content in the ESR product current makes unavoidable a further purification step to reduce it to levels below few parts per million in the feed to the fuel cell.[10] In this case, the water gas shift (WGS) reaction can be used to recover additional hydrogen:

$$\begin{gathered}\mathrm{CO(g) + H_2O(g) \;\rightarrow\; H_2(g) + CO_2(g)} \\ \Delta H^0_{298\ \mathrm{K}} = -40.4\ \mathrm{kJ/mol}\end{gathered} \tag{7.3}$$

(in fact, Reaction (7.1) is the result of Reaction (7.2) followed by Reaction (7.3)).

Partial oxidation of ethanol (POE), the reaction of ethanol with oxygen to produce hydrogen and carbon dioxide, overcomes these drawbacks, but the maximum hydrogen yield is 3 mol/mol of ethanol:

$$\begin{gathered}\mathrm{CH_3CH_2OH(g) + \frac{3}{2}O_2(g) \;\rightarrow\; 3H_2(g) + 2CO_2(g)} \\ \Delta H^0_{298\ \mathrm{K}} = -552\ \mathrm{kJ/mol}\end{gathered} \tag{7.4}$$

However, for low oxygen-to-ethanol (O/E) molar ratios, carbon monoxide can be also produced, but the reaction is thermodynamically unfavored:

$$\begin{gathered}\mathrm{CH_3CH_2OH(g) + \frac{1}{2}O_2(g) \;\rightarrow\; 3H_2(g) + 2CO(g)} \\ \Delta H^0_{298\ \mathrm{K}} = 14.0\ \mathrm{kJ/mol}\end{gathered} \tag{7.5}$$

Though the maximum hydrogen yield is lower than in ESR, POE presents the advantages brought by its exothermicity: (1) there is no need of external energy input, what simplifies the process scheme by avoiding the heating units; (2) there are no equilibrium limitations, what allow to operate at temperatures markedly lower than those used for ESR, say, between 473 and 873 K; and (3) reaction is much faster, and then, the reactor needed is smaller than for ESR. All these factors contribute to make the process setup much more compact. Moreover, the coreactant (oxygen) is a gas (no need to evaporate it), which can be substituted by air directly taken from the atmosphere. Both features are of great interest for on-board hydrogen production for mobile applications of fuel cells. The presence of oxygen can also contribute to decrease the formation of carbonaceous residues on the catalyst surface, thus keeping the catalytic activity for longer periods.

The main drawback of POE is common to all selective or partial oxidation processes in the gas phase: the competing total oxidation (combustion) reaction is much more favored thermodynamically:

$$\begin{gathered}\mathrm{CH_3CH_2OH(g) + 3O_2}(E) \;\rightarrow\; \mathrm{2CO_2(g) + 3H_2O(g)} \\ \Delta H^0_{298\ \mathrm{K}} = -1293\ \mathrm{kJ/mol}\end{gathered} \tag{7.6}$$

The oxidation of hydrogen is also very exothermic (and hence thermodynamically favored):

$$\begin{gathered}\mathrm{H_2(g) + \frac{1}{2}O_2(g) \;\rightarrow\; H_2O(g)} \\ \Delta H^0_{298\ \mathrm{K}} = -241.0\ \mathrm{kJ/mol}\end{gathered} \tag{7.7}$$

As a result, hydrogen selectivity is usually low. Moreover, the mixture of a fuel (ethanol) with oxygen entails the risks of explosion and the need to operate outside the explosion (flammability) range, i.e. from 3.5 (lower) to 19 (upper)%v/v in air.[11]

ATR, also known as oxidative steam reforming (OSR), seeks to contribute the heat released by the partial oxidation reaction to the steam reforming reaction. The feed consists of a mixture of water, ethanol and oxygen whose concentrations should be adjusted correctly to ensure that the net enthalpy of the reaction is close to thermal neutrality, producing predominantly hydrogen and carbon dioxide:

$$\begin{gathered}\mathrm{CH_3CH_2OH(l) + (3-2}x\mathrm{)H_2O(l) + }x\mathrm{O_2(g) \;\rightarrow\; 2CO_2(g)} \\ \mathrm{+ (6-2}x\mathrm{)H_2(g)} \quad \Delta H^0_{298\ \mathrm{K}} = (173.3 - 483.6x)\ \mathrm{kJ/mol}\end{gathered} \tag{7.8}$$

where x stands for the ethanol-to-oxygen molar ratio. Due to this thermal near-neutrality, ATR avoids the drawbacks of ESR because it does not need an external supply of heat if the concentrations of water, ethanol and oxygen are properly adjusted, and may be operated at much lower temperatures than ESR. For instance, by using $x = 0.6$, Reaction (7.8) becomes thermally near-neutral: $\Delta H^0_{298\ \mathrm{K}} = +4.4$ kJ/mol, with $\Delta G^0_{298\ \mathrm{K}} = -187.2$ kJ/mol.[12] But adjustment can be made in various ways. If one keeps S/E = 3 at 973 K, 0.482 mol of oxygen per mole of ethanol are required to achieve zero enthalpy. Moreover, the presence of water in the feed inhibits the flammability and explosion risks of the oxygen–ethanol mixtures, decreases combustion selectivity and retards the carbonaceous residue deposition on the catalyst surface. However, it is difficult to control the working conditions for a steady-state operation, and to optimize catalysts with the needed functionalities in the adequate proportion. As an alternative, the coupling of both ESR and POE reactions in separate but integrated reactors has been investigated,[13] as shown in Section 7.6. In this case, the complexity of the control of the reaction

conditions to keep thermal neutrality remains, but catalysts for each reaction can be optimized separately.

Thermodynamic equilibrium of ESR, POE and ATR was studied by Gibbs free energy minimization including the possibility of solid coke formation for the ranges of S/E = 0−10, O/E = 0−3 and reaction temperatures (T_R) of 473−1273 K.[14] The main conclusions were the following:

1. Ethanol processed with steam and/or air will yield to the decomposition of ethanol over the whole T_R range studied, to methane and CO_2 at low T_R, but at $T_R > 673$ K, methane is reduced, hydrogen content rises strongly and CO also evolves.
2. A higher hydrogen yield is possible in ESR than in POE; in the favorable operation window, i.e. $T_R = 823-923$ K and S/E > 4, a hydrogen yield of 4 mol/mol of ethanol, with CO molar fraction <0.1 and without danger of coke formation, is possible.
3. In POE, high hydrogen content appears jointly with high CO content, and reasonable hydrogen yields can be achieved at O/E < 1.5 and $T_R > 873$ K but avoiding coke formation requires O/E > 0.8; this makes POE an unfavorable choice for hydrogen-rich feeds for fuel cells due to high CO content, but useful for gas production.
4. The main advantage of ATR, besides reducing the energy demand for ESR, is to reduce coke formation rate; over the whole S/E ratio range, increasing O/E ratio from 0 to 0.75 in ATR shows no strong effect on the hydrogen and carbon monoxide formation at $T_R < 873$ K.

Despite the higher process energy required by ESR due to its endothermicity, the total energy demand (that also considers the lower heating value of ethanol) per mole of hydrogen produced follows the order POE > ATR ≥ ESR.

Nevertheless, the higher hydrogen yield attainable by ESR and the technological maturity of other steam reforming processes make that, in practice, most research is devoted to ESR.

The techniques of hydrogen production from ethanol have been the aim of several reviews in the literature, but most of them are devoted to ESR,[15−17] a few review and compare the three alternative routes[5,7,18] and just one is devoted to POE (and partial oxidation of methanol).[19]

It should be noted that the apparent simplicity of Eqns (7.1), (7.4) and (7.7) represent just overall stoichiometric reactions, respectively, for ESR, POE and ATR, but the real reactive systems are very complex. Due to the high intrinsic reactivity of ethanol, and that of the reaction intermediates and products among them and with the water and/or oxygen in the feed, there are many reactions occurring simultaneously. They result in a lower hydrogen yield[5] and processes leading to catalyst deactivation. For these reasons, they are described in detail in the next section.

7.1.3 Reaction Pathways and Thermodynamics

In the absence of any other reactant, the main reactions of ethanol itself, as a typical alcohol, are dehydrogenation to acetaldehyde (Reaction (7.9)) and dehydration to ethylene (Reaction (7.10)):

$$\begin{aligned} &CH_3CH_2OH(g) \rightarrow CH_3CHO(g) + H_2(g) \\ &\Delta H^0_{298\ K} = 68.4\ kJ/mol \end{aligned} \quad (7.9)$$

$$\begin{aligned} &CH_3CH_2OH(g) \rightarrow CH_2{=}CH_2(g) + H_2O(g) \\ &\Delta H^0_{298\ K} = 45\ kJ/mol \end{aligned} \quad (7.10)$$

Ethanol may also decompose to methane and carbon oxides:

$$\begin{aligned} &CH_3CH_2OH(g) \rightarrow \frac{1}{2}CO_2(g) + \frac{3}{2}CH_4(g) \\ &\Delta H^0_{298\ K} = -74\ kJ/mol \end{aligned} \quad (7.11)$$

$$\begin{aligned} &CH_3CH_2OH(g) \rightarrow CO(g) + CH_4(g) + H_2(g) \\ &\Delta H^0_{298\ K} = 49\ kJ/mol \end{aligned} \quad (7.12)$$

Both acetaldehyde and ethylene are important intermediates that might be formed even at low temperatures, before the formation of hydrogen and carbon oxides through ESR Reactions (7.1) and (7.2). While ethylene is a precursor of coke formation, acetaldehyde plays an important role in the pathways leading to hydrogen formation. Acetaldehyde may decompose into methane and CO or condensate to produce acetone:

$$\begin{aligned} &CH_3CHO(g) \rightarrow CO(g) + CH_4(g) \\ &\Delta H^0_{298\ K} = -18.8\ kJ/mol \end{aligned} \quad (7.13)$$

$$\begin{aligned} &2CH_3CHO(g) \rightarrow CH_3COCH_3(g) + CO(g) + H_2(g) \\ &\Delta H^0_{298\ K} = 5.1\ kJ/mol \end{aligned} \quad (7.14)$$

This condensation can be very favored by the presence of water:

$$\begin{aligned} &2CH_3CHO(g) + H_2O(g) \rightarrow CH_3COCH_3(g) + 2H_2(g) \\ &+ CO_2(g)\ \ \Delta H^0_{298\ K} = -35.9\ kJ/mol \end{aligned} \quad (7.15)$$

When water is present, either introduced in the feed for ESR or as a reaction product in POE, it may react with ethanol (Reactions (7.1) and (7.2)), but also with the products evolved from ethanol in reforming reactions:

$$\begin{aligned} &CH_3CHO(g) + 3H_2O(g) \rightarrow 2CO_2(g) + 5H_2(g) \\ &\Delta H^0_{298\ K} = 104.8\ kJ/mol \end{aligned} \quad (7.16)$$

$$CH_3CHO(g) + H_2O(g) \rightarrow 2CO(g) + 3H_2(g)$$
$$\Delta H^0_{298\ K} = 187.1\ kJ/mol \quad (7.17)$$

$$CH_2{=}CH_2(g) + 4H_2O(g) \rightarrow 6H_2(g) + 2CO_2(g)$$
$$\Delta H^0_{298\ K} = 127.6\ kJ/mol \quad (7.18)$$

$$CH_4 + 2H_2O \rightarrow CO_2(g) + 4H_2(g)$$
$$\Delta H^0_{298\ K} = 164.4\ kJ/mol \quad (7.19)$$

and the WGS reaction:

$$CO(g) + H_2O(g) \rightarrow H_2(g) + CO_2(g)$$
$$\Delta H^0_{298\ K} = -40.4\ kJ/mol \quad (7.20)$$

The final result is a higher yield to CO, CO_2 and hydrogen than in absence of water. Note that all reactions that give methane are exothermic and favored at low temperatures and tend to reduce hydrogen production. Then, the formation of methane should be avoided in the ESR.[18] Furthermore, the hydrogen formed may, in turn, produce other hydrogenation reactions:

$$CH_3CH_2OH(g) + 2H_2(g) \rightarrow 2CH_4(g) + H_2O(g)$$
$$\Delta H^0_{298\ K} = -157\ kJ/mol \quad (7.21)$$

$$CH_2{=}CH_2(g) + H_2(g) \rightarrow CH_3CH_3(g)$$
$$\Delta H^0_{298\ K} = -136.5\ kJ/mol \quad (7.22)$$

$$CO(g) + 3H_2(g) \rightarrow CH_4(g) + H_2O(g)$$
$$\Delta H^0_{298\ K} = -205.5\ kJ/mol \quad (7.23)$$

$$CO_2(g) + 4H_2(g) \rightarrow CH_4(g) + 2H_2O(g)$$
$$\Delta H^0_{298\ K} = -164.4\ kJ/mol \quad (7.24)$$

These reactions are all exothermic and attention should be paid in the catalyst design to limit the hydrogenation function to minimize the hydrogen consumption by these reactions.

Coke formation on the catalysts surface is very often observed in the ethanol processing reactions. The mechanism of deposit formation seems to be common to both ESR and POE, and includes several reactions:

$$2CO(g) \rightarrow C(s) + CO_2(g)$$
$$\Delta H^0_{298\ K} = -171.5\ kJ/mol \quad (7.25)$$

$$2CO(g) \rightarrow C(s) + CO_2(g)$$
$$\Delta H^0_{298\ K} = -171.5\ kJ/mol \quad (7.26)$$

$$CH_2{=}CH_2(g) \rightarrow [polymers] \rightarrow 2C(s) + 2H_2(g)$$
$$\Delta H^0_{298\ K} = -52.1\ kJ/mol \quad (7.27)$$

$$CO(g) + H_2(g) \rightarrow C(s) + H_2O(g)$$
$$\Delta H^0_{298\ K} = -131.0\ kJ/mol \quad (7.28)$$

$$CO_2(g) + 2H_2(g) \rightarrow C(s) + 2H_2O(g)$$
$$\Delta H^0_{298\ K} = -89.8\ kJ/mol \quad (7.29)$$

All these reactions form a fairly complex reactive network that is outlined in Fig. 7.1.

Thermodynamic equilibrium calculations performed at different S/E ratios and different pressures indicate that formation of undesirable byproducts, such as methane

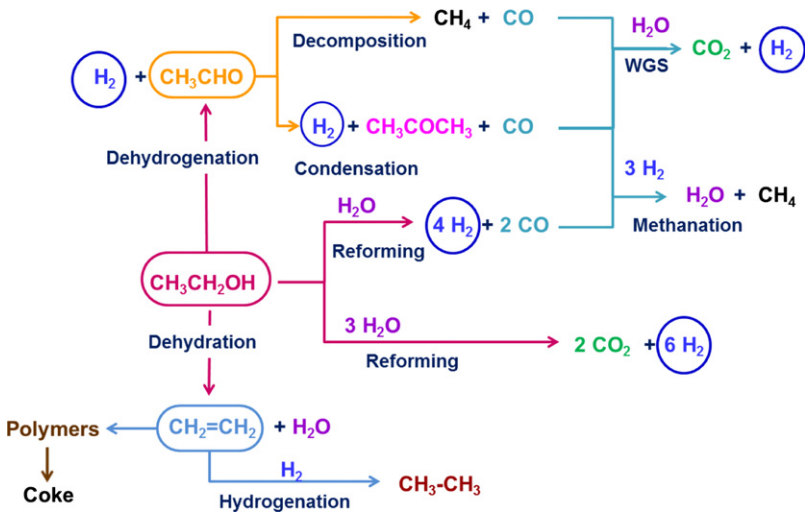

FIGURE 7.1 Reaction scheme of the steam reforming of ethanol (ESR). (For color version of this figure, the reader is referred to the online version of this book.)

and CO, could be minimized by using higher S/E ratios and low pressure, preferably at 1 atm.[5,20] On increasing the total pressure, the H_2 and CO_2 yields decrease, while the methane equilibrium concentration increases.

When oxygen is present, its high oxidizing power causes the oxidation reactions to become predominant. In the POE process, besides the main reactions, namely, ethanol partial oxidations (Reactions (7.4) and (7.5)) and combustion (Reaction (7.6)), ethanol may undergo oxydehydrogenation to acetaldehyde:

$$CH_3CH_2OH(g) + \frac{1}{2}O_2(g) \rightarrow CH_3CHO(g) + H_2O(g)$$
$$\Delta H^0_{298\ K} = -153\ kJ/mol \quad (7.30)$$

and, depending on the oxygen concentration, all intermediate products can be either partially oxidized

$$CH_3CHO(g) + \frac{3}{2}O_2(g) \rightarrow 2H_2(g) + 2CO_2(g)$$
$$\Delta H^0_{298\ K} = -620.7\ kJ/mol \quad (7.31)$$

$$CH_3CHO(g) + \frac{1}{2}O_2(g) \rightarrow 2H_2(g) + 2CO(g)$$
$$\Delta H^0_{298\ K} = -54.7\ kJ/mol \quad (7.32)$$

$$CH_4(g) + \frac{1}{2}O_2(g) \rightarrow 2H_2(g) + CO(g)$$
$$\Delta H^0_{298\ K} = -35.9\ kJ/mol \quad (7.33)$$

or totally oxidized (combustion reactions):

$$CH_3CHO(g) + \frac{5}{2}O_2(g) \rightarrow 2H_2O(g) + 2CO_2(g)$$
$$\Delta H^0_{298\ K} = -1167\ kJ/mol \quad (7.34)$$

$$CH_4(g) + 2O_2(g) \rightarrow 2H_2O(g) + CO_2(g)$$
$$\Delta H^0_{298\ K} = -799.6\ kJ/mol \quad (7.35)$$

$$CO(g) + \frac{1}{2}O_2(g) \rightarrow CO_2(g)$$
$$\Delta H^0_{298\ K} = -283.0\ kJ/mol \quad (7.36)$$

As water is the main byproduct in all oxidation reactions, it becomes the main coreactant when oxygen is consumed, and all the reforming reactions indicated for ESR are also involved in POE, increasing the complexity of the overall reaction network. The simplified reaction network in the POE process is outlined in Fig. 7.2, where reforming secondary reactions have been omitted for clarity.

A comparison of the equilibrium compositions calculated for ESR with those for POE shows that the absence of steam in the feed decreases the H_2 concentration from >70% in the ESR reaction to ~50% in the POE reaction, and that to achieve a maximum H_2 yield, temperatures above 873 K would be required for either ESR or POE, as long as CH_4 is considered in the calculation as one of the present species. If it is excluded, a high H_2 yield could be obtained at lower temperatures. This means that catalysts with low selectivity to decomposition into CH_4 could produce high yields of H_2 at temperatures around 573 K.[5]

ATR reaction network is equivalent to the one depicted for POE, but including all the reforming reactions depicted for ESR. The main difference lies on the different contribution of each reaction involved, due to the simultaneous presence of oxygen and steam in the feed.

Summarizing, the reaction networks for the three processes that convert ethanol into hydrogen are extremely complex, both from the mechanistic and the thermodynamic points of view. The intermediate steps involved include a variety of reaction types (dehydration, dehydrogenation, reforming, total and selective oxidation, WGS, etc.). They show different dependency

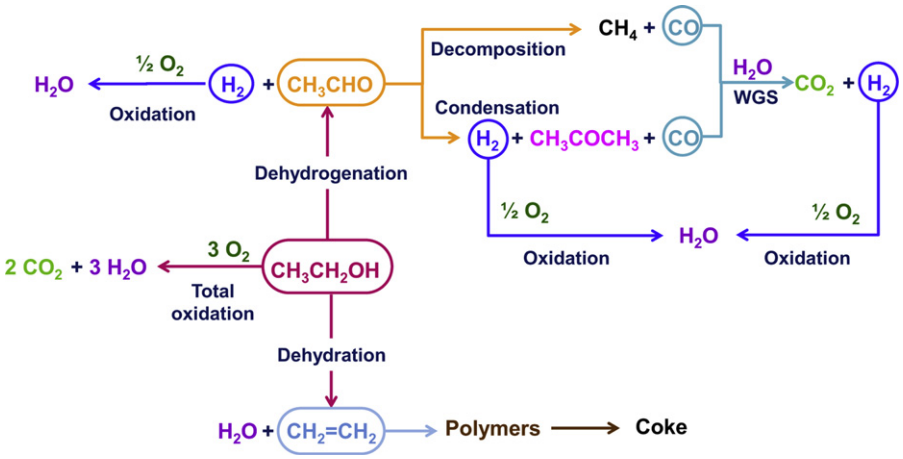

FIGURE 7.2 Reaction scheme of the partial oxidation of ethanol (POE). For clarity, the reforming reactions with the water produced (equivalent to those in ESR in Fig. 7.1) are not shown. (For color version of this figure, the reader is referred to the online version of this book.)

relationships on reaction conditions and their promotion depends on different functionalities of the catalyst. In addition, formation of coke precursors from several of the compounds involved makes deactivation an important issue for the practical application of these processes. All these factors explain the need for extensive research of catalysts, as well as of reactor and process engineering, to optimize hydrogen production and process performance. The catalytic systems and the more recent developments for each of these three alternative routes will be discussed in detail in Sections 7.2–7.6.

7.2 STEAM REFORMING OF ETHANOL

7.2.1 Noble Metal Catalysts

Many studies have been focused on the ESR using supported nickel, cobalt and noble metal catalysts. An efficient catalyst for hydrogen production from ethanol has to dissociate the C–C bond (at reasonably low temperatures), maintain the CO concentration low and be stable under catalytic operation. Deactivation, related to coke and carbonaceous compounds deposition, is the major drawback of the catalytic systems based on transition metals. Among transition metals, noble metals, and in particular, Rh and Ru,[21] are known to successfully break the C–C bond leading to less coke deposition and thus to more stable catalysts.

As explained above, the ESR reaction mechanism over noble metals involves a complex set of reactions. In an early work by Cavallaro,[22] he explored the performance of different Rh-containing catalysts supported on Al_2O_3 for the ESR under steam-to-carbon ratio $S/C = 4.2$. At a preliminary stage, he found that the reaction mechanism starts with the dehydrogenation and/or dehydration of the ethanol which are assisted by the acid support, followed by the rapid conversion of the products into CH_4, CO and CO_2, catalyzed by Rh. He noticed that the presence of Rh at high temperatures ($T = 923$ K) prevents coke formation and the catalyst maintains its activity for several hours. Auprêtre et al.[23] and Breen et al.[24] tested a wide range of catalysts in order to elucidate the best catalytic system. The former studied different active phases (Rh, Pt, Pd, Ru, Ni, Cu, Zn, Fe) as well as supports (Al_2O_3, CeO_2–Al_2O_3, CeO_2, CeO_2–ZrO_2, ZrO_2) in order to obtain highly active catalysts for the ESR rendering high H_2 yields and selective toward the formation of CO_2 both in the ESR and the WGS. They found that the most active and selective catalysts were the Rh- and Ni-based ones, achieving the highest H_2 yield with the $Rh/CeZrO_2$ catalyst. Breen et al.[24] studied Rh, Pt, Pd and Ni catalysts supported over Al_2O_3 and CeO_2–ZrO_2 and obtained that Rh and Pt exhibited better performance and were more active when supported over ceria–zirconia mixed oxides.

Since these initial works, considerable effort has been done in the research of the ESR over noble metals, and Rh, Pt, Pd, Ru, Ir and Ag-based catalysts have been investigated. In more than 40% of the published works, Rh-based catalysts have been used as this metal is most effective with respect to ethanol conversion and hydrogen selectivity, due to its strong capacity to successfully dissociate the C–C bond of the ethanol molecule.[25,26] Nearly 30% correspond to Pt-based catalysts taking advantage of the strong oxidation activity and the Water Gas Shift Reaction (WGSR) promotion of Pt and its high activity and selectivity toward H_2 production.[27] To a lesser extent, Pd-based catalysts have been used due to its known dehydrogenation and steam reforming of methane catalytic activity. Also, some works report on the use of Ru-based catalysts because their H_2 production is comparable to that of Rh only at high Ru loading. Whereas Rh catalysts are stable, Ru induces dehydration of ethanol to form ethylene, leading to coke formation via polymerization.[28,29] Iridium has been tested in few works[30,31] and it was found that Ir particles are responsible for the C–C bond cleavage in acetaldehyde which mainly decomposes to CO and CH_4, at temperatures above 673 K or is converted to acetone at lower temperatures. Finally, Ramos et al.[29] also tested Ag/CeO_2 for the ESR obtaining poor activity of the catalyst being the main products H_2 and acetaldehyde between 373 and 873 K.

Bimetallic catalysts have synergetic effects; they show higher activity than the metals alone in bond dissociation, dehydrogenation and oxidation processes but few authors have studied them.[32] Idriss et al.[21] and Scott et al.[33] studied $Rh–Pd/CeO_2$, obtaining that the direct oxidation route to acetate over CeO_2 is suppressed by the presence of the metals and the dehydrogenation reaction temperature is lowered by about 100 K in comparison with CeO_2 alone. Additionally, by in-situ IR studies, they inferred that the bimetallic catalysts break the C–C bond of ethanol at temperatures below 400 K. Rh–Pt and Pt–Pd supported over CeO_2 were studied by Idriss.[34] Rh–Pt was also tested by Simson et al.[35] for SR of 85% pure ethanol and 15% gasoline (E85).

One problem in the elucidation of the reaction mechanism is that most of the ethanol reaction mechanisms proposed in the literature rely on infrared spectroscopy (IR) results not measured under realistic reaction conditions.[36,37] It should be stressed that the nature of the support may strongly influence the catalytic performance of ESR catalysts and even participate in the reaction. Furthermore, the strong metal–support interaction prevents metal particle sintering and diminishes the formation of carbonaceous deposits and, thus, catalyst deactivation. De Lima et al.[37] and Idriss et al.,[21] among others, examined the reaction mechanism over Pt/CeO_2 and $Rh–Pd/CeO_2$, respectively. The main reaction

mechanism was found to proceed firstly by a dissociative adsorption of ethanol to ethoxy species which react with the surface and undergo dehydrogenation to form adsorbed acetaldehyde. Acetaldehyde may be then oxidized in the presence of hydroxyl groups to adsorbed acetate/acetyl intermediates. Finally, the acetates suffer demethanation to CH_x groups and carbonate species, which decompose to CO_2, following C−C bond cleavage. These CH_x groups may then hydrogenate to CH_4 and a fraction decomposes to adsorb C and H. High- and low-surface area CeO_2-supported Rh catalysts were investigated by da Silva et al.[38] using Diffuse Reflectance Infrared Fourier Transform Spectroscopy (DRIFTS). Although catalyst deactivation occurred by carbon deposition during ESR, they did not observe carbon formation on the Rh/CeO_2 high surface area, due to higher fugacity of oxygen.

Noble metals supported over alumina are often used because of its chemical and mechanical resistance under reaction conditions, although it is known that acid supports assist ethanol dehydration to ethylene at low temperatures, which in turn facilitates the formation of C deposits.[22,39] Ciambelli et al.[40] carried out temperature programmed desorption (TPD) experiments concluding that under reaction conditions, Al_2O_3 is not able to promote the desorption of the secondary reaction products, poisoning the surface catalyst and hindering the decomposition process which finally leads to a marked decay in H_2 and CO_2 selectivity. TPO studies allowed them to investigate the C formation; they found stable carbonaceous species and coke residues on both Al_2O_3 and Pt/Al_2O_3. Erdohelyi et al. (2006)[41] carried out IR and TPD measurements on Pt, Rh, Pd, Ir and Ru supported over Al_2O_3 and reported that the accumulation of surface acetate species may deactivate the catalytic systems.

Although CeO_2 and Al_2O_3 are the most used oxides, other supports have been explored. ZrO_2, SiO_2, Y_2O_3, C, Nb_2O_5, $MgAl_2O_4$, MgO, TiO_2 and also zeolites have been tested as noble metal supports. Among these, ZrO_2 is the most frequently used due to its large oxygen storage capacity (OSC), high oxygen mobility and steam activation. Ce−Zr solid solutions have been widely used because the addition of ZrO_2 to the ceria lattice results in enhancing ceria redox properties, its basicity is reduced as the ZrO_2 content increases, its thermal resistance is improved and it also helps to increase metal dispersion.[42−44] Roh et al.[43] designed Rh/CeO_2ZrO_2 catalysts in order to attempt to kinetically control H_2 selectivity against CH_4 formation by increasing the metal−support interaction. Diagne et al.[25] investigated the performance of Rh supported over CeO_2, ZrO_2 and Ce−Zr solid solutions for the ESR under $S/C = 4$. At 673 and 773 K, the catalysts showed similar behavior with respect to H_2 production with values close to thermodynamic equilibrium; the main difference was in CO_2 and CO distribution which was found to be sensitive to reaction temperature and to the relative amount of ZrO_2 and CeO_2. Interestingly, they performed TPR experiments finding large variations of Rh dispersion between all catalysts concluding that this had a small effect on H_2 production. Birot et al.[41] achieved the best performance (highest hydrogen yield and less coke deposition) for an $Rh/Ce_{0.5}Zr_{0.5}O_2$ for ESR under $S/C = 2$ without carrier gas at 873 K achieving 3.63 $mol_{H_2}/mol_{ethanol}$.

Noble metals supported over Al_2O_3−ZrO_2 have been also tested. The introduction of ZrO_2 to alumina supports leads to the detection of smaller amounts of acetate. The formation of H_2, CO_2 and CH_4 increased with the zirconia content of the catalyst as concluded by Dömök et al.[27] after performing DRIFT and TPD experiments. Supports based on CeO_2/Al_2O_3 and CeO_2−ZrO_2/Al_2O_3 have been utilized, too. Peela et al.[45] obtained that $Rh/CeO_2/Al_2O_3$ showed higher activity and selectivity than Rh/Al_2O_3 alone for ESR under $S/C = 3$ at 673−873 K. De Rogatis et al.[46] synthesized $Rh/Ce_{0.2}Zr_{0.8}O_2/Al_2O_3$ nanocomposites and characterized and tested them against ESR. These materials favored methane formation at moderated temperatures while they also inhibited the formation of ethylene and acetaldehyde, contrary to the behavior of their counterpart without the ceria−zirconia solid solution.

Liguras et al.[28] examined the performance for the ESR in the temperature range of 873−1123 K of Rh, Ru, Pt and Pd supported over Al_2O_3, MgO and TiO_2 changing the metal loading between 0 and 5 wt.%. They concluded that for low-loaded catalysts, Rh is the most active and selective toward hydrogen production. Ru, particularly, and Rh performance improved increasing the metal content leading to higher ethanol conversions and H_2 selectivity. Gucciardi et al.[47] tested Rh/Al_2O_3 catalysts with different metal loading (0, 0.2 and 2 wt.% Rh) for the ESR at 823 and 923 K under $S/C = 3$ and diluted conditions. The H_2 yield obtained was maximum for the highest Rh-content being nearly negligible for the low-content Rh catalyst, but the conversion decayed faster on the former (mainly at low temperatures), ascribed to deposition of coke on the reactive sites. Moura et al.[48] tested Rh supported over alumina, magnesia and Mg−Al oxide obtained from hydrotalcite, attaining that the magnesium-containing catalysts showed low ethane selectivity and high H_2 selectivity. Roh et al.[49] studied Rh-based catalysts over various supports, as well. 1 wt.% Rh over Al_2O_3, $MgAl_2O_4$, ZrO_2, and ZrO_2−CeO_2 was used for ESR at $T < 723$ K and the activity followed the order: Rh/ZrO_2−$CeO_2 > Rh/Al_2O_3 > Rh/MgAl_2O_4 > Rh/ZrO_2$. De Lima et al.[36,37] studied Pt/CeO_2 and $Pt/CeZrO_2$ catalysts, respectively. The presence of the metal improved the ethanol conversion and resulted in high selectivity to H_2, CO and CO_2, but the Pt−support interfaces were quickly lost due to

the formation of carbonaceous species which led to the catalyst deactivation. Chen et al.[50] performed ESR at 623−823 K over $Pt/Ce_xZr_{1-x}O_2$ catalysts ($x = 0.2$, 0.4, 0.6 or 0.8). The catalysts showed good initial stability and were highly active at lower temperatures, only yielding H_2, CO, CH_4 and CO_2 as products. At 723−823 K, the selectivity of products was close to the thermodynamic control.

Biomass-derived ESR over a commercial alumina supported 5 wt.% Pd catalyst was investigated by Goula et al.[51] for ethanol/water mixtures = 3, 4.5, 9 and 15 at different load and temperatures ranging between 493 and 973 K. They attained full ethanol conversion at temperatures higher than 573 K. At temperatures close to 923 K, hydrogen selectivity up to 95% was obtained; indeed, they noticed that in this temperature region, the products mixture was controlled by the methane steam reforming and the WGSR. During their experiments, only traces of acetaldehyde and ethylene were detected and no carbon formation was found, achieving a stable catalyst. Galvita et al.[52,53] studied the ESR over 1 wt.% Pd supported on a porous carbonaceous material. For S/C = 4.05 and atmospheric pressure, the catalyst exhibited full ethanol conversion at 600 K and high activity and long-term stability for the decomposition of ethanol into CO, CO_2, CH_4 and H_2.

To improve the performance of the catalysts and block coking, different dopants have been tested. Dömök et al.[54] incorporated K (up to 0.4 wt.%) into Pt/Al_2O_3 which was found to destabilize surface acetate groups; the ESR activity and stability were improved in proportion with the K content. De Lima et al.[55] incorporated Sn into Pt/CeO_2 achieving improved stability. Yaseneva et al.[56] modified the support by introducing La, Pr and Sm into Ru and Pt supported catalysts: $Ce_xZr_{1-x}(La,Pr,Sm)_{1-2x}O_2/Al_2O_3$, as it is expected that the incorporation of low-valence cations (such as La, Gd, Pr) into the lattice of ceria−zirconia solutions stabilizes it and improves the lattice oxygen mobility.[57] Their results showed that Ru-containing catalysts doped by Sm were the most effective while among the Pt-based ones, La-doping led to the most active catalyst. Can et al.[58] and Le Valant et al.[59] added 10 wt.% of Sc, Y, La, Er and Gd to 1 wt.% Rh/Al_2O_3 catalysts. On these modified supports, the dehydration reaction, leading to olefins which are coke precursors, is disfavored and consequently, the ethanol conversion and the hydrogen yield are increased. Le Valant et al.[59] emphasize that the addition of rare earth elements instead of magnesium to alumina supports leads to a rearrangement of the acidity and basicity of the alumina. The higher hydrogen production was achieved with $Rh/Y{-}Al_2O_3$, which was found to be the less acidic support and one of the most basic supports performing IR spectroscopy of adsorbed pyridine and CO_2.

The Duprez's group[59,60] has done extensive research on the addition of impurities to pure ethanol−water mixtures in order to simulate raw bioethanol, which is of major importance for a cost-effective industrial application. Raw bioethanol contains higher alcohols and also aldehydes, amines, acids and esters. Over $Rh/MgAl_2O_4$, esters, ethers, acetic acid, ethyl acetate, C_4 alcohols and branched alcohols had a poisoning effect on the catalyst which was strongly deactivated after only 2 h on-stream due to coke production. Simson et al.[35] studied 4 wt.% Rh-Pt on a zirconia-based support for the SR of E85 with and without sulfur. The tests performed showed that full ethanol and gasoline conversion and equilibrium concentrations of H_2, CO_2, CO and CH_4 could be achieved with the sulfur-free mixture for at least 110 h of performance. In the presence of only 5 ppm of sulfur, after 22 h on-stream, the catalyst underwent a strong deactivation. After TPO analysis, they concluded that large carbon deposits were formed, demonstrating that sulfur promotes C formation.

7.2.2 Nickel Catalysts

Nickel-based catalysts are the most frequently used in reforming reactions due to C−C bond rupture capability. Nickel has been generally supported onto alumina because of its ability to withstand reaction conditions.[61] However, due to the alumina acid sites, this support tends to favor carbon deposition, for what other supports have also been tested. On the contrary to noble metals, ESR over nickel catalysts takes place at moderate temperatures. It has been generally observed that the selectivity to hydrogen is increased with the increase in temperature, water-to-ethanol molar ratio and nickel loading.[62−64] The reaction mechanism over nickel-based catalysts follows the same steps than over noble metal-based catalysts.[65,66]

In contrast to noble metals, the particles of nickel species tend to sinter under ESR reaction conditions. Besides, acid sites on alumina favor the dehydration of ethanol to ethylene, competing with the dehydrogenation to acetaldehyde. Both facts, nickel particle sintering and alumina acidity generate carbon deposits, which deactivate the catalyst. To avoid these inconveniences, different promoters have been added to nickel-based catalysts. Copper is the most efficient promoter for the production of hydrogen.[61] Copper species are active in the WGS reaction to produce hydrogen and avoid the growth of nickel particles.[67] Youn et al. also studied the effects of adding molybdenum to Ni/Al_2O_3. They observed that Mo reduces the interaction between Ni and alumina, increasing the reducibility of nickel species, and also prevents the growth of nickel particles.[68] Calcium, as well as Mg, is an efficient promoter to neutralize aluminum acid sites. Vizcaino et al. modified

Ni/Al_2O_3 catalysts with Mg, obtaining an increase in the catalytic activity due to lower ethylene formation.[69] They also modified Cu−Ni/SBA-15 catalysts with magnesium and calcium. The dispersion of the Cu−Ni phase was improved and its interaction with the support was strengthened.[70] The same group of authors studied the effect of Mg and Ca addition on coke deposition over $Cu-Ni/SiO_2$. They observed reduction of the metallic Cu−Ni particle size and strengthening of the metal−support interaction. Moreover, Mg- and Ca-promoted catalysts favored the formation of defective carbon, which is more reactive and thermodynamically easier to be removed during ESR.[71] Magnesium produces less carbon deposition when added to Ni/CeO_2 catalysts, too. Zhang et al.[72] increased OSC and oxygen mobility of CeO_2 supports by adding magnesium into the lattice of Ni/CeO_2. The insertion of Mg into CeO_2 lattice efficiently promotes the reduction of Ce^{4+}. Mg-modified Ni/CeO_2 catalysts have larger OSC and smaller Ni crystallite size compared with bare Ni/CeO_2. Choong et al.[73] also observed that the addition of calcium on Ni/Al_2O_3 greatly reduces the acidity of Al_2O_3. Calcium also increased water adsorption, providing nickel catalyst the proximity and abundance of adsorbed OH groups.

Other supports as well as other promoters have also been used with success. Ni has been supported onto perovskite-type oxides ($LaAlO_3$, $SrTiO_3$ and $BaTiO_3$), where lattice oxygen may play a possible role in hindering coke formation.[74] Chen et al. obtained highly dispersed surface nickel particles formed during the reduction of the perovskite $La_{1-x}Ca_xFe_{0.7}Ni_{0.3}O_3$. With oxygen in the feed, these particles could be oxidized and restored back into the perovskite bulk, as well as the deposited carbon could be eliminated.[75] Layered double hydroxides (LDH) are also useful supports due to their high surface area. Busca et al. synthesized Ni−Co−Zn−Al LDH to be used as precursors of mixed oxide catalysts. After calcination, the LDH converts into a mixture of a rock salt phase (NiO), a wurtzite phase (ZnO) and a spinel phase.[76] Yu et al. synthesized Cu-promoted NiMgAl catalysts derived from hydrotalcites. The addition of small amounts of copper to NiMgAl catalysts led to the increase of surface Ni species and the enhancement of Ni^{2+} reducibility. They obtained catalysts with strong resistance to coke formation and the sintering of nickel particles.[77] Multiple works deal with simple and multiple oxides as supports in order to avoid the high acidity of alumina and, consequently, the formation of coke. Zhang et al. synthesized Ni-based catalysts doped with Cu additives and supported onto $Al_2O_3-SiO_2$, Al_2O_3-MgO, Al_2O_3-ZnO and $Al_2O_3-La_2O_3$. The catalysts modified with MgO and ZnO had much higher hydrogen selectivity than the ones modified with SiO_2, as well as good coke resistance.[78] Chen et al. studied the effect of Cu/Ni ratio over $Cu-Ni/SiO_2$ catalysts. The catalysts with $Cu/Ni \geq 1$ showed higher ethanol and acetaldehyde conversion, higher selectivity of acetaldehyde steam reforming and lower coking at temperatures below 673 K than the Ni-rich catalysts. Analysis by X-ray diffraction (XRD), X-ray Photoelectron Spectroscopy (XPS) and Extended X-ray Absorption Fine Structure (EXAFS) indicated that the Cu-rich catalysts had formed an alloy structure with Ni-enriched surface.[79] A singular work was published by Therdthianwong et al.[80] since they reformed bioethanol in supercritical water at 773 K and 25 MPa on Ni/Al_2O_3 and $Ni/CeZrO_2/Al_2O_3$. Under supercritical water and in a noncatalytic environment, ethanol was reformed to H_2, CO_2 and CH_4 with small amounts of CO and C_2 gas and liquid products. The presence of the catalysts led to more than three- to four-fold increase in ethanol conversion and hydrogen yield than that of noncatalytic condition. The ceria−zirconia promoted catalyst was more active than the unpromoted one. On the promoted catalyst, complete ethanol conversion was achieved and no coke formation was found. Different results on catalytic activity were obtained by Li et al. after testing two polymorphs of zirconia. The decrease in particle size of zirconia resulted in enhanced metal−support interaction, which accounted for the high activity of the catalyst. Tetragonal zirconia yielded a higher activity in WGS reaction but a lower activity in methane steam reforming than that of monoclinic zirconia.[81] Ternary mixed oxides have been tested with success as well. NiMgN (N = La, Ce) samples deactivate faster than NiMAl (M = Mg, Ca, Zn) having smaller Ni crystallites. In particular, the presence of Ca produced an important dispersing effect over the Ni species, favoring hydrogen production while keeping moderate coke formation.[82] Another example of ternary mixed oxides are the nickel-based catalysts with nominal composition $5Ni/Ce_{0.5}Zr_{0.33}M_{0.17}O_{2-\delta}$, where M is the promoter element(s) selected from Mg, Ca, Y, La, CaMg or Gd. The authors found that the catalytic activity increased with an increase in the active metal reducibility, ratio of pore volume/surface area and active metal dispersion, but decreased with an increase in the carbon propensity factor.[83] Iriondo et al. synthesized nickel and platinum catalysts supported on bare Al_2O_3 and La_2O_3- and CeO_2-modified Al_2O_3. La_2O_3 doping of the Ni/Al_2O_3 catalyst improved the metal dispersion (Iriondo et al., 2012).[84] Seelam et al.[85] compared metal and metal oxide nanoparticle catalysts (Ni, Co, Pt and Rh) supported on carbon nanotubes (CNTs) and compared to a commercial catalyst (Ni/Al_2O_3). The Co/CNT and Ni/CNT catalysts were found to have the highest activity and selectivity toward hydrogen. Almost complete ethanol conversion was achieved over the Ni/CNT catalyst at 673 K. Active carbon as a support for Ni, Ni/Cu and Ni/Cu/Pd has

been tested at a temperature range of 423–973 K by Ozkan et al.[86]; Ni/Cu/Pd catalyst gave the highest selectivity toward hydrogen.

Vizcaino et al. have used ordered mesoporous silica as support of copper and nickel, and promoted with Mg, Ca, Ce and La.[70,87] The addition of the promoters strengthened metal–support interaction, enhanced metallic dispersion and therefore, improved the catalytic performance of the materials. Inokawa et al. increased the basicity of Na–Y zeolites impregnated with Ni by an ion-exchange process with aqueous solutions including Na^+, K^+ and Cs^+. Increase of the zeolite basicity was effective for selective acceleration of the dehydrogenation reaction with ethanol, inhibition of coke deposition and the promotion of hydrogen production.[88] Kwak et al. also worked over a zeolite Y, synthesized together with MgO and promoted with Ni and Gd (Kwak et al., 2011).[89]

7.2.3 Cobalt Catalysts

Low-cost cobalt-based catalysts are less active for ESR than catalysts that contain noble metals, but they are very selective to H_2 and CO_2 because the reforming temperature can be as low as 623 K in such a way that the WGS occurs simultaneously with steam reforming and, consequently, CO concentration is kept low. In addition, methane is not an intermediate of the reforming process over cobalt-based catalysts and, consequently, high hydrogen yields are easy to achieve. The first work on ESR over cobalt catalysts was reported by Haga et al.,[90] where the catalytic performance of cobalt supported over Al_2O_3, SiO_2, MgO, ZrO_2 and C was described. This pioneering work was followed by those of Cavallaro et al.[91] and Llorca et al.[92] Cavallaro et al.[91] reported on the ESR over Co/Al_2O_3 and Co/MgO under $S/C \sim 4.2$ aimed to simulate the composition of biomass-derived ethanol/water mixtures. They noticed that Co/Al_2O_3 decayed in short time because of coke deposition, whereas Co/MgO was found more stable. Llorca et al.[92] studied cobalt supported over a great variety of supports with different acidity and redox properties (MgO, Al_2O_3, SiO_2, TiO_2, V_2O_5, ZnO, La_2O_3, CeO_2 and Sm_2O_3) under $S/C = 6.5$ to simulate bio-ESR. Supports with strongly acidic properties favored the dehydration of ethanol into ethylene whereas supports with basic properties favored dehydrogenation of ethanol into acetaldehyde, which was recognized to be the first step of the reforming process over cobalt. The same conclusion was reached by Kaddouri and Mazzocchia[93] and by Batista et al.[94] on Co/SiO_2 and Co/Al_2O_3 catalysts. On the other hand, supports with redox properties showed better properties for ESR because they favored suppression of coke and reduction of cobalt. ZnO-supported cobalt showed the best catalytic performance. In-situ magnetic measurements coupled to ESR over the above cobalt catalysts allowed[95,96] to demonstrate that metallic cobalt is a highly active species for the reforming of ethanol. Under reaction conditions, the Co/ZnO catalyst showed 92% of reduced cobalt, mainly as small superparamagnetic nanoparticles. On the other hand, in-situ FTIR with CO as a probe molecule revealed that in addition to metallic cobalt, oxidized Co species were also present at the surface, thus suggesting that the redox pair $Co^0 \leftrightarrows Co^{2+}$ is responsible for the activity of cobalt in ESR.[97] This has been recently supported by the combined XPS–TPD work of Martono et al.[98] over model Co/ZnO(0001) catalysts. The catalytic role of Co^0 and Co^{2+} during ESR has also been investigated by Karim et al.[99] over Co/MgO, who concluded that Co^0 is much more active for C–C cleavage and WGS, and by Hyman and Vohs[100] over metallic and oxidized cobalt model surfaces. Over cobalt-based catalysts, ethanol is first adsorbed to yield ethoxy species, which undergo dehydrogenation and transform into acyl species (rate-determined step[101]) which, in turn, react with activated water to yield hydrogen and carbon oxides. CH_4 is a secondary product formed through the methanation reaction.[102] Carbonates are formed at the surface of the catalyst and carboxylates are detected, which are believed to be spectator species. Dimethyl ketone can also be formed via condensation of acetaldehyde. A complete network of reactions can be found in Song et al.[103] The mechanism of the ethanol reforming reaction is accompanied by a simultaneous transformation of the cobalt phase. High Resolution Transmission Electron Microscopy (HRTEM), XRD, Raman spectroscopy and in-situ magnetic measurements show that Co_3O_4 is active for ethanol dehydrogenation and, subsequently, is progressively reduced by the hydrogen generated during the first step of the reaction into CoO and metallic Co.[104] The same transformation has shown to occur over Co/CeO_2 by using in-situ XRD, controlled-atmosphere X-ray Absorption Fine Structure (XAFS) and XPS.[105] Lin et al.[106] reported by in-situ XRD that hcp Co possess higher activity than fcc Co for ESR. Once metallic cobalt is formed, the catalyst becomes very active for the ESR and the hydrogen yield increases sharply. However, a consequence of this reaction scheme is that extensive carbon deposition occurs under reaction conditions upon formation of metallic cobalt nanoparticles,[107] which certainly constitutes the major drawback of cobalt-based catalysts for ESR, although Karim et al.[102] claimed that catalysts can be regenerated with mild oxidation. It is important to highlight that most of the work reported in the literature concerning ESR over Co-based catalysts has been conducted at high S/C ratio or under diluted conditions (i.e. using inert gas as carrier), and only a few studies have been carried out directly with ethanol–water mixtures under realistic conditions, which obviously have a great impact on coke formation. Carbon deposition occurs in various geometries, including CNTs, fibers, platelets and onion shell-type.[108]

Several strategies have been attempted to minimize coke formation over Co-based catalysts under ESR conditions. Llorca et al.[109] incorporated Na^+ promoter into Co/ZnO (up to 1% w/w) and obtained an important decrease of coke deposition during ESR, as evidenced by XPS and HRTEM, due to blocking of strong acidic sites of the support, which leads to the formation of ethylene, a well-known coke precursor. The same catalysts were studied by Kim et al.[110] by EXAFS and concluded that Na^+ promoter enhanced the reducibility of Co phase on ZnO, thus resulting in a stable and active catalyst for ESR. Galetti et al.[111] used a similar approach adding K^+ to a CuCoZnAl oxide, which resulted in a stable catalyst for ESR at 873 K. On the other hand, it has been demonstrated that alloying of cobalt with more electronegative elements such as Ni or Cu results in worse catalytic performance, whereas alloying of cobalt with the less electronegative elements Fe[112] and Mn[113,114] promotes the redox pair $Co^0 \leftrightarrows Co^{2+}$, both in terms of lower cobalt reduction temperature as well as fast reoxidation, which in turn results in a better catalytic stability. The promoter, low coke deposition effect of Fe has also been pointed out by Sekine et al.[115] and Kazama et al.[116] with cobalt catalysts supported over Al_2O_3 and $SrTiO_3$.

Considerable efforts have been addressed toward the Co/CeO_2 and Co/ZrO_2 systems for ESR due to the large OSC and high oxygen mobility exhibited by ceria and ceria–zirconia solid solutions that are able to oxidize carbon residues and prevent extensive carbon deposition. Song and Ozkan[117] and Song et al.[118] used DRIFT and isotopic labeling to show the mechanism of carbon removal and the involvement of water in the reaction network over these catalysts during ESR. De Lima et al.[119] showed that high S/C ratios and the presence of oxygen promoted cleaning of the Co surface under ESR for Co/CeO_2, as expected. Avila-Neto et al.[120] have used in-situ temperature and spatial resolved X-ray Absorption Near-Edge Structure (XANES) to show that the Co^{2+}/Co^0 ratio in Co/Al_2O_3 modified with La_2O_3 and CeO_2 can be tuned by choosing appropriate water and oxygen partial pressures to obtain stable catalysts for ESR operation. Rybak et al.[121] pointed out that the ZrO_2/CeO_2 ratio exerts significant influence on the coke formation. Lebarbier et al.[122] studied the effect of Zn promotion in Co/ZrO_2 catalysts and noted that addition of Zn inhibited the oxidation of metallic cobalt particles under ESR. Enhanced oxygen mobility in CeO_2 was achieved by Ca^{2+} incorporation, which originated unit cell expansion in the ceria lattice and improved catalytic performance in ESR as well.[123] The influence of the preparation method on the reducibility of Co/Ce–Zr–O catalysts was reported by Lin et al.[124] and Song et al.[125] A proper metal–support interaction allows only partial reduction of cobalt and leads to a superior catalytic performance for the production of hydrogen through ESR. Long-term catalytic runs exceeding 750 h were reported by Benito et al.[126]

Noble metal (Pt, Pd, Rh, Ru, Ir)-promoted cobalt catalysts have also been investigated for ESR.[127,128] The effects of the noble metals include a marked lowering of the reduction temperature of the cobalt surface species interacting with the support due to hydrogen spillover and the stabilization of Co sites in the reduced state throughout the reaction. This causes an enhancement of catalytic activity but, in most cases, causes rapid deactivation by coke deposition. The best catalytic performance for ESR was obtained for the CoRu formulation.

Cobalt hydrotalcite-derived catalysts have been used for ESR as well. Contreras et al.[129,130] evaluated Co hydrotalcites with basic sites and noted a promoting effect of W on catalytic activity, which was related to changes in the pore morphology of the support. He et al.[131] studied Co–Ni catalysts prepared from hydrotalcites and reported high hydrogen yields during ESR for a molar Co:Ni ratio of 3:1. Lucredio et al.[132] studied catalysts derived from Co/Mg/Al hydrotalcites modified with La and Ce. Recently, Espinal et al.[133] have performed detailed in-situ XPS and magnetic characterization of catalysts derived from Co/Mg/Al hydrotalcites and found that no metallic cobalt is formed under ESR at 823 K. This interesting result allows designing catalysts containing cobalt for ESR without coke deposition (no metallic cobalt) by placing in appropriate environments Co^{2+} active species. A similar conclusion has been reached by Da Costa-Serra and Chica[134] using delaminated zeolite as Co support. Long-term catalytic tests (300 h) under high loads of commercial bioethanol have shown stable operation over hydrotalcite-derived cobalt catalysts promoted with potassium.[135] In contrast, Domínguez et al.[136] used cobalt talc for ESR and encountered an outstanding activity due to the segregation of metallic Co nanoparticles at the surface of the talc nanolayers, as determined by in-situ XPS and magnetic measurements, which was accompanied by coke deposition.

Most ESR studies for hydrogen production have used conventional packed bed reactors but the use of structured catalytic wall reactors offers important advantages in terms of efficiency, such as rapid mass and heat transport, low pressure drop and no reactor blocking, good structural and thermal stability, and precise control of process conditions with higher hydrogen yields. In addition, they are robust, easy to scale up and replace, and offer homogeneous flow distribution patterns. Regarding ESR over Co-based catalytic walls, Casanovas et al.[137] reported the preparation of cordierite honeycombs coated with Co/ZnO catalysts and their catalytic performance for ESR. Monoliths loaded with cobalt talc in SiO_2 aerogel host were prepared under supercritical conditions by Domínguez et al.[138]; they exhibited fast start-up and were about four times more active for hydrogen

generation under ESR at 623 K than monoliths loaded with Co/SiO_2, which was related to the better mass transfer characteristics of the aerogel support. Metal plates coated with CoFe/ZnO and CoMn/ZnO catalysts by electrophoretic deposition were described by Nedyalkova et al.[139]

7.3 PARTIAL OXIDATION OF ETHANOL

7.3.1 Preliminary Overview

There are very few publications in the open literature, around 35 according to our knowledge, specific on the POE to hydrogen, and most of them have appeared in the past 8 years. This underlines that, until relatively recently, all efforts to obtain hydrogen from ethanol focused on steam reforming. Besides scarce, some reported results are partial (incomplete in relevant details), unclear, and sometimes contradictory. For instance, very few papers report on oxygen conversion data, despite the presence or absence of oxygen in the reaction medium plays a critical role for production of hydrogen, as it will be shown below. This could explain why, using the same catalyst, hydrogen formation is sometimes reported at 473 K while in other cases, it is not detected until 773 K. Other relevant result usually missing in the reports is the amount of water formed, also critical for hydrogen formation and selectivity. Despite the data might be good and the experiments well carried out, cautions should then be taken on the interpretation given to these data and the conclusions reached.

Broadly speaking, catalytic systems investigated for POE are those that have provided good results in similar reactions, such as partial oxidation of methanol or ESR. Most POE catalysts contain one or more metals (Pt, Pd, Rh, Co, Ni) supported on oxides, mainly those exhibiting redox properties. Criteria for selecting the metal are their specific catalytic features, already depicted in Section 7.2.1. Briefly, rhodium is the most effective one for ethanol conversion, due to its strong ability to successfully dissociate the C−C bond.[25,26] Platinum possesses a strong oxidation activity and promotes the WGS reaction.[27] Palladium is active for dehydrogenation and steam reforming of methane. Ruthenium can be as efficient as rhodium for H_2 formation but is not stable because it induces dehydration of ethanol to ethylene, leading to coke formation via polymerization.[28] Nickel shows C−C bond rupture capability, but it is very active in coke formation and tends to sintering. Copper is active in the WGS reaction and inhibits growth of nickel particles.[67]

7.3.2 Reaction Mechanism

The earliest works, from the Idriss group,[140−142] focused on understanding ethanol decomposition at a molecular level, by studying its reactions with metal oxides and with noble metals supported on cerium oxide in the presence of oxygen by TPD and IR. Ethanol adsorbed dissociatively to form ethoxy ($CH_3CH_2O(a)$) species on any surface. The main product of the reaction of ethanol over a series of oxides (Fe_2O_3, Fe_2O_3−CaO, Fe_3O_4, TiO_2, CaO, and SiO_2) was always acetaldehyde, with secondary products acetone and ethyl acetate, but no hydrogen.[143] CeO_2 was four orders of magnitude more active than these oxides and generated acetate species and no dehydration products. The addition of Pd, Pt, or Rh to CeO_2 partially reduced its surface, as evidenced by the absence of carboxylate bands in the IR spectra.[140−142] The mechanism is the same on the three metals supported on ceria, but unlike Pd/CeO_2 and Pt/CeO_2, Rh/CeO_2 readily dissociates the C−C bond to produce adsorbed CO and CH_4.[144]

The Noronha group[145] also studied the mechanism of ethanol conversion on Pt/CeO_2, but concentrated on the reaction under oxidative conditions. They agree with Idriss group that the first step was formation of ethoxy species. Under an oxygen-free atmosphere (TPD conditions), these species decompose; but in the presence of oxygen, the simultaneous oxidation of ethoxy and its derivatives leads to oxidative dehydrogenation to acetaldehyde (Reaction (7.30)), and when the temperature is increased, a fraction of the ethoxy species migrates to the metal particle and decomposes, forming methane, hydrogen and CO.[146,147] The common feature of the mechanisms of POE over Pt, Pd, Rh, Pt−Rh and Co-based catalysts is the initial ethanol adsorption and ethoxy formation. The difference among the metal catalysts lies on the pathways of the intermediates evolved from ethoxy. So, dehydrogenation of ethoxy gives rise to acetaldehyde on Pt, Pd and Co, while five-membered ring oxametallacycle groups are formed on Rh-containing catalysts.[148] Further transformation of adsorbed ethoxy species and the oxametallacycle lead to different product selectivities. On Pt and Pd, acetaldehyde can desorb or dehydrogenate further to acetyl and later oxidize to acetate adsorbed species, which finally decompose to methane, hydrogen and CO. On Rh-based catalysts, the oxametallacycle decomposes to adsorbed CH_x and CO species, which desorb as methane and CO/CO_2 on Rh; methane is not desorbed from Rh−Pt, due to the oxidation of the CH_x species.[19]

It is worth noting that the extension of homogeneous reaction (in the absence of any catalyst) of the usual ethanol−oxygen reacting mixtures for POE is important, especially at high temperatures. For instance, the reaction of a mixture with an $O/E = 0.4$ diluted in nitrogen (72 mol%) becomes significant above 673 K, reaching conversion values of 76% at 973 K.[146] The main products are acetaldehyde and methane, whose yields decrease for the former and increase for the latter with the

increase in reaction temperature. The gas phase formation of acetaldehyde, a key intermediate in the catalytic reaction, adds complexity to the overall reaction network, but this factor is usually overlooked in literature.

7.3.3 Noble Metal Catalysts

The Noronha group, the most active in the POE research, has studied intensively noble metal catalysts for POE. To avoid gas phase homogeneous reaction, they tested Pt/CeO_2 catalysts at 573 K with various residence times (W/Q).[146] Catalyst stability depended on preparation method of the support, and was related with its OSC. Main products were acetaldehyde and methane for all W/Q values studied: selectivity of the former decreased and that to methane increased with the increase of W/Q. CO and CO_2 were the subproducts; the CO_2/CO ratio decreased with the increase of W/Q. Hydrogen formation was observed only for W/Q >1.5 g s/cm^3, for which yields of acetaldehyde and methane (not quantified) remained constant. This effect was not discussed, and data of oxygen conversion and water formation were not provided. Experiments conducted with similar Pt/CeO_2 catalyst and reaction conditions have evidenced that hydrogen is only detected among the POE products once the oxygen fed is exhausted (i.e. 100% oxygen conversion).[149] So, the observed appearance of hydrogen above a certain W/Q value is because the total conversion of oxygen is achieved for such value.

The effect of the support nature on the performance of supported Pt catalysts was studied with Pt/Al_2O_3, Pt/CeO_2, Pt/ZrO_2 and $Pt/Ce_{0.5}Zr_{0.5}O_2$ catalysts. Acetic acid was the only product on Pt/Al_2O_3, what was related to the alumina acidic properties, with no hydrogen or CO formation. Acetaldehyde and methane were the main products on the three other catalysts, that showed approximately the same H_2 yield (0.7–0.8 H_2 mol/mol ethanol consumed) and CO yield (0.5–0.7 CO mol/mol ethanol consumed). The product distribution over these three catalysts was related to the redox properties of the supports. Pt/CeO_2 and $Pt/Ce_{0.5}Zr_{0.5}O_2$ catalysts, with a higher OSC, favored the formation of acetates, which could be decomposed to CH_4 and/or oxidized to CO_2. Pt/ZrO_2, led to dehydrogenation of the ethoxy species that could desorb as acetaldehyde. Then, the higher selectivity to acetaldehyde of this catalyst could be assigned to its lower OSC/oxygen release capacity.[147]

The Wang group studied POE at low temperatures (373–473 K), analyzing the effect of the O/E ratio and the reaction temperature (T_R) on the performance of 1.2% Pt/Al_2O_3 and 1.9% Pt/ZrO_2.[150] At 373 K, both Pt catalysts are active toward POE, reaching 50% ethanol conversion with a high hydrogen selectivity, S_{H_2} >90%, using an O/E = 0.75, i.e. oxygen deficient feed. At this temperature, a homologous catalyst supported on ZnO, 1.5% Pt/ZnO, produced no hydrogen nor CO, but both of them formed at higher T_R.[151] Oxygen was completely consumed in O/E ratio between 0.75 and 1.13, while S_{H_2} decreased drastically when increasing O/E molar ratio from 0.75 to 1.13, which may be attributed to hydrogen combustion (Reaction (7.7)). However, the results reported in these two papers show significant inconsistencies: for instance, for a ratio of O/E = 1, the S_{H_2} at 373 K reported for 1.2% Pt/Al_2O_3 and 1.9% Pt/ZrO_2 is either 5–20%[150] or 90–100%.[151] This makes it difficult to draw conclusions about this research. However, it should be noted that none of the authors indicate the degree of conversion of oxygen, which might determine the selectivity observed. The Al_2O_3 supported catalyst produces substantial amounts of CO (selectivity 60%). The much lower CO selectivity for 1.9% Pt/ZrO_2 than for Pt/Al_2O_3 was explained by oxidation of adsorbed CO to CO_2 by lattice oxygen from the reducible ZrO_2, oxygen species that are absent in Al_2O_3.

To analyze the effect of particle size of platinum crystallite on the POE reaction, catalysts with variable platinum loadings on the three supports were tested at 370 K with O/E = 1.0. The converse effect was found on ZnO-supported catalysts and those supported on zirconia or alumina: when the Pt crystallite size increased, conversion increased for the ZnO-supported samples (with no hydrogen formation) but it decreased for the alumina or zirconia supported samples, with a simultaneous slight decrease of S_{H_2}.[151]

Besides platinum, other noble metals have been studied as catalysts for POE. The influence of the nature of the metal supported on ceria was studied with Pt, Pd, Rh and Ru at temperatures between 573 and 1073 K.[147,148] The main differences are found in the mechanism, as discussed in Section 7.3.2. Rhodium was the most active but produced the highest CO yield, while platinum presented the lower formation of CO and the higher selectivity to methane. Neither sintering nor coke formation occurred on Rh/CeO_2.[152] Cai et al.[153] reported similar results with an Ir/CeO_2. The use of yttria instead of ceria as a support for palladium is deleterious: at low reaction temperature (<773 K), Pd/CeO_2 catalyst is more selective to H_2, CO_2 and acetaldehyde, whereas the CO formation is favored on Pd/Y_2O_3 catalyst.[154] Using yttria as a support, Ru/Y_2O_3 is more suitable system for H_2 production than Pd/Y_2O_3 by achieving a selectivity of about 59% (Silva et al., 2007).[155]

The activity trends are very similar in all those catalysts. The ethanol conversion increases with T_R up to 773–873 K where total conversion is achieved. In the conditions investigated, all catalysts require a minimum

temperature to produce hydrogen: 673 K for Pt/CeO_2, Rh/CeO_2 and Pd/CeO_2 and 773 K for Pd/Y_2O_3 and Ru/Y_2O_3. Above this minimum temperature, the hydrogen selectivity increases with T_R. The most selective catalyst for hydrogen is Ru/Y_2O_3 but others get quite similar results. In the absence of oxygen conversion data or detailed product yields, one may interpret these results by assuming that the observed minimum T_R for hydrogen formation is the one at which full conversion of oxygen is achieved on that specific catalyst. Once oxygen is exhausted, the water formed reacts in steam reforming reactions with the products or remaining ethanol present.[149,156,157]

Also gold has also been investigated for POE. Au/CeO_2 is an efficient catalyst for ethanol oxidation, with activity comparable to other supported noble metal catalyst, and high selectivity to CO_2 instead of CO. However, the product distribution is extremely dependent on the temperature, and the CO_2/CO ratio decreases with increasing T_R, and CO formation rate is higher than that of hydrogen. This indicates the limitation of Au/CeO_2 for an efficient H_2 production from ethanol (with low CO).[158]

Concerning bimetallic catalysts, the most selective catalyst for this product is a composite bimetallic $Pt-Rh/CeO_2$. The addition of platinum to rhodium decreases considerably or avoids the formation of secondary products resulting from acetaldehyde (such as benzene, ketene, and crotonaldehyde) observed with Rh/CeO_2. Using a ratio $O/E = 2$, a gas stream with 20.3% hydrogen is obtained at 973 K with this catalyst. At low T_R, the main reaction products were acetaldehyde and CO_2; for $T_R > 573$ K, CO_2, CO and methane.

One may conclude that, concerning activity, and despite the highest hydrogen selectivity of rhodium catalysts, the most practical catalyst seems to be based on platinum supported on an oxide with redox properties and high OSC. To overcome the problem of CO formation during POE over Rh catalysts, an integrated fuel processing system that combines POE over Rh/CeO_2 catalyst and subsequent WGS over a $Pt/V-CeO_2$ catalyst has been developed. Starting from a stream of 17% mol ethanol and using $O/E = 0.5$, it allows to obtain a final stream containing 17.7% H_2, 14.5% CO_2 and just 1.19% CO.[159]

7.3.4 Non-noble Metals and Structured Catalysts

Metallic nickel- and cobalt-based catalysts are frequently used in reforming reactions, but have deserved much less attention for POE. This is probably because under oxidative atmospheres, both metals can be easily oxidized, in an extent (surface or bulk) that depends on the reaction conditions, thus modifying their catalytic behavior. Moreover, the single oxide Co_3O_4 is one of the most active single oxides to catalyze total oxidation reactions.

Nickel–iron catalysts of variable composition, Ni_xFe_{100-x} ($x = 10-90$), show high activity for POE under various O/E ratios at 473–573 K.[160] At these conditions, pure nickel oxide NiO reaches a maximum selectivity to H_2 of 23% at 573 K, while pure Fe_2O_3 is hardly active for POE. Among the Ni-Fe catalysts, $Ni_{50}Fe_{50}$ had the best activity, and all catalysts showed similar activity and selectivity trends when the O/E ratio was varied. Ethanol conversion and selectivity to hydrogen and CO_2 markedly increased with the increase of O/E. This effect on hydrogen selectivity, namely, that the higher the amount of oxygen in the feed, the higher is selectivity to hydrogen, is the opposite of that observed with noble metal catalysts.[151] The catalysts were prepared by coprecipitation, calcination at 673 K and reduction with hydrogen at 573 K. Only the spinel $(Ni,Fe)Fe_2O_4$ and the $FeNi_3$ alloy phases were detected in all catalysts, their proportion varying with the metal composition; however, the surface consists mainly of oxidized species while the bulk consists mostly of the alloy. The highest hydrogen selectivity, 45%, was obtained with catalyst $Ni_{50}Fe_{50}$ at 573 K with $O/E = 1.5$.

The Schmal group investigated ethanol reactions, POE and ESR on a Cu/Nb_2O_5 catalyst at $T_R = 473-973$ K.[161] Its activity for ESR was comparable to that of Ni/Al_2O_3 but reaching the same level of hydrogen production at a temperature 200 K lower. Temperature-programmed reaction with 5% O_2/He flow after adsorption of ethanol shows that formation of acetaldehyde, H_2 and CO_2 starts at 503, 533 and 553 K, respectively. Under POE reaction conditions used, ethanol was fully converted at 573 K and hydrogen formation started at 473 K. In all cases, the formation of CO was very low. The maximum H_2 formation for the POE was 41% at $O/E = 0.8$, increasing to 50% at $O/E = 1.5$. Interestingly, the H_2/CO is around 10 for POE and 7 for ESR, which are excellent values compared to the Ni/Al_2O_3 catalyst.

The Schmal group has also investigated POE on a series of monolithic catalysts with copper,[162] cobalt,[163] and nickel oxides[164] as active components. Ethanol conversion becomes significant at 593 K on $CuO/\gamma\text{-}Al_2O_3$ washcoated cordierite honeycomb structured catalyst. Product distribution depended strongly on T_R. Below 743 K, main products were acetaldehyde and ethylene, with trace amounts of hydrogen (0.2% selectivity). Experiments at 743 K where hydrogen was introduced in the feed with various H_2/ethanol molar ratios showed that at the low T_R range, hydrogen is consumed in the reverse WGS. At higher T_R range (843–1043 K), ethanol conversion and hydrogen

selectivity (7−11.5%) increased with T_R, but methane and CO were the main products, with ratios $CH_4/H_2 = 2.6-3$ and $CO/H_2 = 3.6-5.6$, which makes the catalyst impractical.

Similar trends were found with $Co_3O_4/\gamma\text{-}Al_2O_3$ or $NiO/\gamma\text{-}Al_2O_3$ wash-coated cordierite honeycomb-structured catalysts, but both produced much less methane and CO than the CuO homolog at the same temperature. The cobalt catalyst showed the highest hydrogen selectivity values: up to 27.6%, and almost twofold of those of the other two catalysts at any T_R. To evaluate the water presence in the feed, pure ethanol was replaced by 95 vol.% hydrated ethanol (H_2O/ethanol molar ratio = 0.2). On both catalysts, the presence of water increased conversion and selectivity to hydrogen. The main difference between them was catalysts stability. At 693 K and with O/E = 0.3, the cobalt catalyst slightly activated during the first 10 h on stream, and then remained stable for other additional 30 h (though some carbon formation was observed after 30 h on stream). At the same reaction conditions, the nickel catalyst lost 40% activity after 96 h, showing changes in product distribution (formation of ethylene, CO and methane increased with time-on-stream). As expected, the nickel catalyst showed important carbon deposits after its use in reaction, with a 35% weight increase by carbon deposition. The catalyst deteriorates and crumbles turning to a black powder at the end of all experiments, due to the formation of well-defined filamentous carbon structures, which grow in most of Ni particles, causing the degradation of the monolithic structure.

7.3.5 Autothermal Oxidation

Structured catalyst supports, such as foams or monoliths, are also used for a completely different process strategy, autothermal oxidation, initiated by the group of Schmidt.[165] When the goal of POE is not CO-free hydrogen for fuel cell uses, but synthesis gas (H_2 and CO), the secondary oxidation of both (Reactions (7.7) and (7.36)), that is extremely fast, should be avoided. The rationale of this strategy is that if the contact time is short enough, secondary reactions can be avoided or minimized, and contact times of the order of milliseconds are used. To achieve these values, very high gas flows are used, which makes necessary the use of those open catalytic structures to reduce the pressure drop in the catalytic bed. At the same time, to achieve high conversion with so short contact times requires to operate the reaction at very high temperatures. As the formation of CO and H_2 by POE (Reaction (7.5)) is slightly endothermic, slight excess oxygen over its stoichiometry may be used to provide the needed heat by the strongly exothermic combustion of ethanol (Reaction (7.6)). In this way, once initiated, the reaction is self-maintained without external heat input (i.e. autothermal operation), and the actual T_R depends on the carbon-to-oxygen (C/O) ratio used. Note that a ratio C/O = 2 corresponds to pure ethanol, and C/O = 0.29 is the stoichiometry of ethanol combustion (Reaction (7.6)).

Deluga et al.[4] first reported that ethanol can be oxidized directly to H_2 with >80% selectivity and >95% conversion in an autothermal reformer, using Rh−Ce catalysts deposited on alumina foam with a catalyst contact time of 11 ms. The ethanol conversion remained at >95%, and that of oxygen >99% for all C/O ratios. The selectivity to both H_2 and CO peaked at ~80%, at C/O ~0.7. The study was later extended to various noble metals and metal plus ceria-coated alumina foams.[166] Rh, Pt, Pd, and Rh−Ru produced less H_2 than Rh−Ce catalysts, with Pt and Pd producing <50% H_2. Moreover, Pt, Pd, and Rh also produced more CH_4 and C_2H_4 than Rh−Ce. The order of effectiveness in syngas production is Rh−Ce > Rh−Al_2O_3 washcoat > Rh−Ru > Rh > Pd > Pt.

Other groups have also investigated POE at millisecond contact times over $Rh/\gamma\text{-}Al_2O_3$ wash-coated honeycomb monolith,[167] and Pt and PtSn catalysts supported on ceramic foams of $\alpha\text{-}Al_2O_3$ or partially stabilized zirconia (PSZ) (Loganathan and Leclerc, 2012).[168] Ethanol conversion, reaction temperature, and selectivity to hydrogen and CO increased for all catalysts with the increase of O/E ratio. The best results were obtained by the rhodium catalyst, that reached $S_{H_2} = 78\%$ and $S_{CO} = 70\%$ with contact time 11 ms and C/O ratio that produced no ethylene. Significant amounts of diethyl ether were formed at C/O > 1.20. Formation of ethylene follows opposite trends with increase of O/E ratio on the two catalytic systems: it decreased on Rh catalysts and increased on Pt catalysts. Among the latter, Pt/PSZ was the most active, while PtSn/PSZ showed the highest hydrogen selectivity (40% with O/E = 0.33), but also formed ethylene (not formed on the monometallic catalyst). However, when the bimetallic PtSn was supported on alumina, behaved as the monometallic Pt/PSZ, but formed more ethylene. The differences were attributed to the nature of the metallic phases, tin enriched in the PtSn supported on alumina. Though these catalysts do not achieve the same conversion as the rhodium based catalyst, they were stable over many hours without any signs of support disintegration.

Note that in some literature, this autothermal oxidation (where no water is introduced in the feed) is termed also ATR. To avoid the ambiguity of the term, in this chapter, we keep the term ATR for the reaction where ethanol is cofed with oxygen and water, and it is synonymous with OSR.

7.4 AUTOTHERMAL REFORMING OF ETHANOL

7.4.1 Noble Metal Catalysts

Most of the effective catalysts are noble metal catalysts and nickel-based catalysts. Looking for the thermal neutrality, the feed compositions explored are those fulfilling that criterion (Reaction (7.8)), with differences only in the use and contents of inert in the feed (nitrogen when air is used as oxidant).

The Mirodatos group explored a series of commercial 5 wt% noble metal (Pt, Pd, Ru, Rh)-based catalysts supported on Al_2O_3 at $T_R = 923-1073$ K, with $O/E = 0.68$ and $S/E = 1.6$.[169] At these conditions, the activity at 973 K increased in the order: $Pt < Pd << Ru < Rh$. Pt and Pd catalysts show similar performances with low selectivities to H_2, 20–23%, while Ru and Rh showed much higher S_{H_2} (75 and 90%, respectively). Aging experiments show that initial S_{H_2} of Rh/Al_2O_3 at optimal operation conditions decreased slightly and then stabilized (at 88%) in the first 10 h on stream and remained stable for at least 140 h. The effect of oxygen addition for a given S/E molar ratio was investigated on a similar 5 wt.% Rh/Al_2O_3 prepared by impregnation at 923 K varying O/E molar ratio between 0.2 and 1.1 and contact times between 12 and 655 ms.[170] Ethanol conversion was complete for $O/E > 0.4$, and enthalpy becomes zero for $O/E = 0.4$. Compared to pure SRE results at any S/E ratio, oxygen addition increased hydrogen yield up to a maximum for O/E molar ratio near 0.6, while S_{H_2} was little affected by O/E. Oxygen addition produces an appreciable improvement of catalyst life. In line with these results, ultrahigh vacuum TPD experiments of decomposition of ethanol over Rh(111) and (100) single-crystal surfaces showed that an oxidizing environment is required to avoid carbon poisoning and to promote C_2-molecules decomposition. On the contrary, excess of oxygen (for instance, oxygen coverage above 0.25 monolayer) leads to a strong reduction of hydrogen concentration due to water formation.[171]

ATR over Rh–Ce catalysts deposited on alumina foam, used in autothermal oxidation (Section 7.3.5), was first investigated feeding a 25% ethanol–aqueous mixture with a catalyst contact time of 11 ms.[4] The effect of the S/E ratio was studied at 973 K and contact time 7 ms with ethanol–water mixtures with 10–75% mol ethanol.[166] Water addition did not modify the ethanol conversion (>95%) but increased markedly S_{H_2}, reaching a maximum hydrogen yield of 3.3 mol/mol of ethanol for $O/E = 0.33$, while selectivity to CO decreased to values <50%, due to increased WGS and SR activity. Thus, the H_2/CO ratio rose to 6.3 and the CO_2/CO to 2.3 for 10% ethanol. Total amount of minor carbon-containing products was <3% at the H_2 maximum of $O/E \sim 1.5$. Contrary to its homolog Rh/Al_2O_3 catalyst, which deteriorated after 4–6 hours on stream, the $Rh–Ce/Al_2O_3$ was stable and its structure was not deteriorated.

The beneficial role of ceria as support was evidenced in the ATR on Rh/CeO_2 catalyst with stoichiometric feed (for Reaction (7.8), i.e. molar ratios $O/E = 0.6$, $S/E = 1.8$), at 823–923 K.[172] Ethanol was entirely converted to hydrogen and C_1 products at 673 K, and methane SR and reverse WGS were the major reactions above 823 K. The catalyst exhibited stable activity and selectivity during 70 h on-stream operation. Structural analysis of the used catalyst revealed that CeO_2 prevented effectively the highly dispersed Rh (particle sizes of 1–3 nm) from sintering and thus maintained sufficient $Rh–CeO_2$ interfacial areas, which facilitated coke gasification through its high oxygen storage–release capacities.

As rhodium is very expensive, attempts have been made to reduce the cost of Rh-based catalyst by reducing its load or substituting it for a less-expensive noble metal. Thus, mono- and bimetallic ZrO_2-supported Rh- and Pt-based catalysts (total metal loading 0.5 wt.%) were studied and compared in ethanol ATR, with $O/E = 0.2$ and $S/E = 1$ ratios at 973 K. As with other supports, the Rh-containing catalysts gave complete EtOH conversion at $T_R > 700$ C and were selective for H_2 production with minimal formation of side products. The interaction of Rh and Pt in the bimetallic $RhPt/ZrO_2$ catalyst improved the stability over that of the monometallic Rh/ZrO_2 catalyst.[173] However, over monometallic $Pt/CeZrO_2$, which is an efficient catalyst for ESR, less hydrogen and more acetaldehyde are formed in the presence of oxygen (ATR) than in its absence (ESR).[174]

Concerning other noble metals, Ru catalysts supported on cordierite monoliths, zirconia–alumina ceramic foams and γ-Al_2O_3 pellets are able to achieve ethanol conversion >95% and $S_{H_2} = 85–95\%$ in ATR at 873 K, with stoichiometric feed composition. Among them, the one supported on a cordierite monolith exhibited the better catalytic performance for a wide variety of process conditions and excellent long-term stability with low coke formation.[175]

Casanovas et al.[176] investigated Pd supported on ZnO and SiO_2 for ESR and ATR. Pd/SiO_2 showed lower ethanol conversion but similar S_{H_2} in ATR than in ESR. Performance of Pd/ZnO depended on the reduction pretreatment, due to the formation of a PdZn alloy, very active in the dehydrogenation of ethanol, thus facilitating the ulterior reforming.

The activity of iridium catalysts supported on oxide supports, including γ-Al_2O_3, ZrO_2, CeO_2, La_2O_3 and $La_2O_3–ZrO_2$, was systematically investigated.[153,177,178] The Ir/CeO_2 catalyst was highly active and stable for

the ESR, POE, and ATR. The outlet gas composition from ATR at 923 K of a stoichiometric feed ethanol−oxygen−water was 65% H_2, 18% CO_2, 15% CO, and 2% CH_4. The catalyst exhibited rather high stability for the reactions at 823−923 K with no apparent deactivation for 60 h on stream. The mean size of Ir particles (2−3 nm) was stable, while those of ceria sintered significantly from 6−8 to 14−27 nm. CeO_2 likely prevented the highly dispersed Ir particles from sintering and inhibited coke deposition through strong metal−support interactions.[153] The screening of several oxide supports (Al_2O_3, ZrO_2, CeO_2, La_2O_3) for supported Ir (1 wt.%) was conducted with a feed of molar ratios $S/E = 3$ and $O/E = 0.83$, between 673 and 973 K.[177] The highest ethanol conversion (90−100%) and S_{H_2} (36−48%) over a wide temperature range were obtained with Ir/La_2O_3. Unloaded ceria and lanthana are also active in ATR: La_2O_3 converted 73.4% ethanol with $S_{H_2} = 44.5\%$ at 923 K under the same reaction conditions. To explore the roles of Ir and these La species, a series of La_2O_3-supported 3 wt.% noble metal (Ir, Ru, Rh, Pd) catalysts were screened. The supported Ru, Ir and Rh catalysts showed similar activity and S_{H_2}. Taking the expense of Rh into account, Ir and Ru would be preferred to fabricate efficient ATR catalysts. The optimal Ir loading for Ir/La_2O_3 catalysts was 5 wt.%, which gave complete conversion of ethanol at milliseconds contact time and very high H_2 yield, close to the thermodynamic limit of the reaction, namely 3.4 mol per mole of ethanol, and remained stable for 40 h on stream. Recently, an autothermal reformer has been fabricated using this catalyst supported on ceramic foams.[79] The optimal catalytic activity and hydrogen selectivity were achieved over the ZrO_2 foam loaded catalyst. The strong interaction between the ceramic ZrO_2 foam and the catalyst results in the reduction of the Ir particle size, which significantly improves the ESR activity, S_{H_2} and catalyst stability. At continuous operation, the reformer produces a hydrogen flow enough to feed an O_2-H_2 fuel cell of around 765 W.

7.4.2 Nickel Catalysts

Nickel-based catalysts constitute probably the most studied system for ATR. Despite ESR over nickel catalysts takes place at moderate temperatures, usually a high reaction temperature and an excess amount of steam are required to prevent the carbon deposition and nickel sintering (Section 7.2.2). These two phenomena also justify the efforts required to develop efficient nickel-based catalysts with high activity and long durability for hydrogen production by low-temperature ATR. Two main strategies have been developed to reach these goals. One is to modulate the catalytic performance of nickel by the effect of support modification in monometallic catalysts. The other is to modify that performance by addition of a second active component in bimetallic catalysts. Indeed, the combination of both strategies has also been explored.

A broad variety of oxide supports have been explored for monometallic catalysts, analyzing the effect of their acidic, basic or redox properties and their metal−support interaction, on the activity and stability of nickel.

The Verykios group investigated ATR on a series of nickel-structured catalysts, using cordierite monoliths, ceramic foams made from mullite, zirconia−alumina and γ-Al_2O_3 pellets as supports for Ni/La_2O_3.[179] Catalysts were prepared on monoliths by adsorption and sol−gel techniques. All catalysts exhibit $S_{H_2} > 93\%$. Among them, slightly better results under adiabatic operation were obtained with the one supported on the $ZrO_2-Al_2O_3$ ceramic foam, prepared by wash-coating the active phase on the support, that showed the highest S_{H_2} (96−98%) and remarkable long-term stability. Though no significant changes were observed after 70 h on stream, carbon was continuously deposited onto the catalyst during operation (1.2 g C/l of ethanol processed), but catalyst could be fully regenerated by reoxidation.

Investigation of ATR of bioethanol (ethanol-to-water ratio = 11% by volume) in molten carbonate fuel cell (MCFC) simulated operative conditions (923 K, Gas Hourly Space Velocity (GHSV) = 5000−40,000/h referred to ethanol) over 21 wt.% Ni/MgO and 30% wt.% Ni/CeO_2 catalysts revealed that an optimum O/E ratio exists to enhance the performance of both catalysts.[180] Addition of oxygen to the feed was crucial in improving catalytic activity and stability of both catalytic systems (which significantly deactivate during ESR), at the expense of a small decrease of S_{H_2}, compared to ESR conditions. The composition of the ATR product stream, H_2:H_2O:CO_2:CO:CH_4 = 35:48:12:4.5:0.5 vol%, was adequate for feeding an MCFC operating at 923 K.

Yttria nanocrystals hydrothermally synthesized at different pH have been used as supports for nickel. Their different morphologies and crystal sizes, which depend on the pH used, have a limited effect on the ATR performance of Ni/Y_2O_3 catalysts. Nevertheless, the order of mobility of surface oxygen species on Y_2O_3 supports is similar with that of the catalytic performance of the corresponding Ni/Y_2O_3 catalysts, suggesting that the surface oxygen mobility of Y_2O_3 support is the key factor in causing the differences observed in catalytic performance.[181]

The Song group, from Seoul National University, has conducted an extensive research on the effect of a wide range of supports, including oxides (ZnO, MgO, TiO_2, ZrO_2, and γ-Al_2O_3) and oxide-stabilized mesoporous zirconias.[182] Catalysts were tested in ATR at 773 K with $S/E = 3$ and $O/E = 0.5$, and contact

time 175 g-catalyst/mol of ethanol. Total acidity of supporting single oxides increased in the order of $MgO < ZnO < TiO_2 < ZrO_2 < \gamma\text{-}Al_2O_3$, while their acid strength increased in the order of $ZrO_2 < TiO_2 < \gamma\text{-}Al_2O_3 < ZnO < MgO$. Hydrogen yield over nickel catalysts supported on them showed a volcano-shaped curve with respect to acidity of the supports. Among the catalysts tested, Ni/ZrO_2 with an intermediate acidity of support exhibited the best performance, followed by Ni/TiO_2. Nickel reducibility was also improved in these two catalysts, due to the weak interaction between nickel and support. However, main drawbacks of ZrO_2 as a support are its low surface area and weak mechanical stability at high T_R. Addition of lanthanide and alkaline-earth metal cations to zirconia network improves these properties, stabilizes the cubic or tetragonal phases of zirconia, and, if they are less electropositive than Zr^{4+}, causes oxygen vacancies, which eases oxygen mobility. 20 wt.% Ni catalysts supported on stabilized zirconias $M{-}ZrO_2$ ($M = Y_2O_3$, La_2O_3, CaO, and MgO) were investigated by the group. Hydrogen selectivity decreased in the order of $Ni/Y_2O_3{-}ZrO_2 > Ni/La_2O_3{-}ZrO_2 > Ni/CaO{-}ZrO_2 > Ni/MgO{-}ZrO_2 > Ni/ZrO_2$, in good agreement with the trend of their reducibility. The yttria-stabilized zirconias (YSZ), $Y_2O_3{-}ZrO_2$, with $Y/Zr = 0.1$, 0.2 and 0.3 were all mesoporous. The Ni catalysts supported on YSZ showed much higher S_{H_2} and more stable activity than Ni/ZrO_2. The best performance was shown by Ni/YSZ with $Y/Zr = 0.1$. A linear correlation was found between reducibility (reduction peak temperature) of supported nickel catalysts and their hydrogen yield in the ATR of ethanol.

On the basis of results for single metal oxide supports, Ni catalysts supported on a series of titania–zirconia mixed oxides $Ti_xZr_{1-x}O_2$ ($x = 0{-}1$) were tested for ATR.[183] Catalysts with partial metal substitution in the support formed more reducible nickel species and retained higher nickel dispersion than supported on the single titania or zirconia. The best performance was achieved with a Ti substitution degree $x = 0.2$, in coincidence with the optimal intermediate acidity.

Many metals have been explored as second component to modify nickel catalytic performance. Looking for reforming ethanol at low temperatures, Kugai et al.[66,184] explored its combination with the most efficient noble metal, Rh, and redox support, ceria. A series of $Ni{-}Rh/CeO_2$ catalysts, with variable Ni content and 1 wt.% Rh, and their corresponding monometallic catalysts with no Rh, were tested in ATR. The Rh-only catalyst was twice more active than the Ni-only one, but the more efficient was the bimetallic with 5 wt.% Ni, with about 100% ethanol conversion at 600 K with high selectivity to H_2 and CO_2 and low to CO, compared to ESR, which required a 75 K higher T_R to complete ethanol conversion. A higher Ni content decreased S_{H_2}. The role of Rh is mainly to cleave the C–C and C–H bonds of ethanol to produce H_2 and CO_x while Ni promoted WGS. The study of the effect of the CeO_2 support properties on the catalyst properties of the best bimetallic catalyst (5 wt.% Ni and 1 wt.% Rh) showed that with decreasing crystallite sizes of CeO_2 increased the Rh metal dispersion (and decreased that of Ni), thus increasing ethanol conversion and hydrogen selectivity.

However, most of the metals tested for combining with nickel are much less-expensive transition metals. The Mirodatos group first reported that an $Ni{-}Cu/SiO_2$ (1.8 wt.% Cu and 16.6 wt.% Ni) showed high activity and long-term stability for ATR of ethanol.[168,185,186] Operating under conditions corresponding to an on-board reformer, total conversion of ethanol and an $S_{H_2} = 97\%$ were achieved at 973 K with $S/E = 1.6$ and $O/E = 0.68$, thus producing a hydrogen-rich gas (33%). Compared with ESR, the presence of oxygen in the feed gas favors the production of hydrogen, while limiting the formation of methane and carbon deposition. Contrary to Ni/SiO_2 catalysts that deactivated and decreased S_{H_2} progressively due to coke formation, $Ni{-}Cu/SiO_2$ was stable for 140 h on stream. The catalytic performance of $Ni{-}Cu/SiO_2$ was similar to that of a 5 wt.% Rh/Al_2O_3 in terms of activity, S_{H_2} and long-term stability. So, it could be considered a less-expensive alternative to rhodium catalysts. The study of the effect of addition of small amounts (~0.6 wt.%) of Cu, Cr, Fe or Zn to Ni/Al_2O_3 catalyst (20 wt.%) showed that only Cu addition improved S_{H_2} over the whole temperature range 923–1073 K, especially at 923 K: 0.82 and 0.93 for monometallic Ni and Ni–Cu catalysts, respectively.[187] The increase of Cu content in the catalyst up to 3 wt.% reduces ethanol conversion and, more markedly, S_{H_2}, producing the lower values among the bimetallic catalysts. The different results obtained by increasing Cu content in Ni/SiO_2 and Ni/Al_2O_3 catalysts show that Ni–Cu interaction with the support plays an important role in the reaction network. Despite all these effects, the authors conclude that in terms of hydrogen production per mass of catalyst, monometallic Ni/Al_2O_3 showed the best performance in hydrogen production after that of $Rh(5)/Al_2O_3$ in the whole temperature range 923–1073 K, and outperformed their bimetallic combinations, their specific H_2 productivities being in the order: $Ni(20)/Al_2O_3 > Ni(16.7)Cu(2.1)/SiO_2 > Ni(19.4)Cu(0.6)/Al_2O_3 >> Ni(20.4)Cu(3.1)/Al_2O_3$ (numbers between brackets indicate the metal content, wt.%).

Song group also reported that copper is the most efficient promoter when comparing the effects of the addition of a higher amount (3 wt.%) of Ce, Co, Cu, Mg and Zn to $Ni(20)/Al_2O_3$ catalyst by a coimpregnation method.[67] At a variance of the results of Fierro et al. (2006)[187],

$Cu(3)Ni(20)/Al_2O_3$ gave an enhanced hydrogen yield and a suppressed CO yield compared with the monometallic $Ni(20)/Al_2O_3$ catalyst. In the absence of the characterization data of Fierro et al., one may hypothesize that the different results of the two groups could be due to the different procedures used by each group for calcination of precursors (15 h at 923 K (Fierro et al., 2006), or 8 h at 1173 K[67]) and catalyst prereduction (8 h at 923 K with pure H_2 for the former, or 3 h at 973 K with 50% H_2 in He for the latter), that could lead to different final states of the metals and their interaction with the support. Cu promoted WGS and inhibited the growth of Ni particles, and its catalytic effect depended on its content. The best performance for hydrogen production was found for a 5 wt.% Cu, for which the catalyst retains a Cu species state intermediate between copper aluminate and copper oxide. By contrast, if the Cu content is higher (7 wt.%), $Ni(20)Cu(7)/\gamma\text{-}Al_2O_3$ catalyst exhibited a rather low performance for hydrogen production, due to the suppressed gasification activity over the large Cu particles in the catalyst.

The same group investigated the effect of Mo addition in bimetallic $Ni(20)Mo(X)/\gamma\text{-}Al_2O_3$ catalysts with different Mo contents $X = 0-9$ wt.%.[68] The presence of Mo species impeded the incorporation of Ni species into the alumina lattice, thus increasing the reducibility of the supported catalysts, and, in contents up to 7 wt.%, suppressed coke formation. The best performance was obtained with 5 wt.% Mo. However, addition of excess Mo (9 wt.%) decreased the catalytic performance of the bimetallic catalyst, caused by both poor reducibility of Ni species and coverage of Ni sites by MoO_x species. In a similar way, addition of Co (1–6 wt.% CoO) to $Ni/\gamma\text{-}Al_2O_3$ system has a considerable effect on its metal–support interaction, increasing its reducibility with the increase of Co contents. This translates into higher hydrogen yields and increased catalyst stability.[188] Cerium and iron also promote the performance of alumina-supported nickel: a 5 wt.% Ce content improved markedly and stabilized (reducing its drop to <10% in 30 h on stream) selectivity to H_2 and CO_2 of the monometallic catalyst, and decreased markedly ethylene formation. A further improvement can be attained by the additional incorporation of 10 wt.% Fe. Thus, a hydrogen yield of 3.6 mol per mole of ethanol was obtained on $Ni–Ce–Fe/Al_2O_3$ at 873 K with $S/E = 3$ and $O/E = 0.5$.[189]

A quite different Ni–Ce catalytic system with exceptional properties for ATR at low temperature, nanooxyhydride $CeNiH_ZO_Y$, has been recently reported by Pirez et al.[190] The catalyst is obtained in situ by pretreatment of a nanostructured $NiCeO_x$ mixed oxide with H_2 at 523 K. Full ethanol conversion and a 50% H_2 content in the outlet gas were achieved at just 553 K using a feed with oxygen excess over the thermal neutrality stoichiometry, i.e. ethanol:water:oxygen:nitrogen = 1:3:1.6:1.3. Despite the formation of some solid carbon (0.063 g C per gram of catalyst and hour), activity is remarkably stable after 70 h on stream. At constant $S/E = 3$, variation of the O/E ratio had little effect in hydrogen formation, though ethanol conversion and reactor temperature increased with the increase of O/E. The active site has been modeled by an ensemble of two cations, one of Ce and one of Ni, in adjacent positions.

7.4.3 Other Catalytic Systems

Monometallic or noble metal-doped cobalt oxides supported on silica were tested for ATR at 623–673 K (Pereira et al., 2008)[191], but all of the catalysts deactivated under reaction conditions: decrease in ethanol conversion led to an increase in acetaldehyde selectivity and a decrease in S_{H_2}. This fact complicated selectivity comparison between catalysts. Activity of the monometallic Rh/SiO_2 and Ru/SiO_2 were lower than those obtained with Co/SiO_2 or bimetallic catalysts. Introduction of Rh or Ru to Co/SiO_2 decreased ethanol conversion, and had little effect on hydrogen production. However, it had a positive effect on the regenerability of deactivated catalysts as they facilitate the reduction of cobalt under the ATR experimental conditions. This makes it possible to use an oxidizing treatment to regenerate the used bimetallic catalysts.

The Noronha group has studied cobalt catalysts supported on ceria, with emphasis on the analysis of their stability under ESR, POE and ATR conditions[119,192] (Da Silva et al., 2010).[193] The most stable catalytic performance was observed under ATR conditions ($S/E = 3$, $O/E = 0.5$): total ethanol conversion and S_{H_2} near 60% were achieved at 773 K with $Q/W = 0.02$ g s/cm^3 and remained stable for 70 h. The reaction type, feed ratios, and T_R strongly influence the nature of the carbon deposits formed and their impact on catalyst stability. The results suggest that carbon filaments are formed lifting the Co particles from the support, but the presence of oxygen keeps accessible enough of the active surfaces. Changing the space time (W/Q) influences the deactivation rate by changing the relative rates of carbon removal and deposition. Analyses of postreaction samples indicate that higher space times favor the deposition of filamentous carbon, and that the amount of carbon exhibits a maximum as a function of space time. The decrease at the higher space times may be attributed to the oxygen mobility of the support that allows the cleaning of the surface. Studies made with Co/CeO_2 catalysts supported on two cerias with different surface areas and OSC evidenced that CeO_2 plays an active catalytic role in removing carbon from the catalyst by a support-mediated cleaning mechanism.

The higher oxygen/OH group mobility of high ceria surface area promoted the mechanism of carbon removal, which in turn contributes to the high stability of Co/CeO_2 catalyst. The effect of the cobalt particle size in the ATR of ethanol was investigated using cobalt on carbon nanofiber catalysts.[194] The smallest (<4 nm) particles showed a significantly larger amount of acetaldehyde and smaller amount of H_2 as compared to larger ones. This result indicated that under ATR conditions, the C−C cleavage is more difficult on small Co particles, due to a higher extent of surface oxidation of smaller particles in this reaction. The catalysts with larger Co particles (>4 nm) were quite stable during ATR reaction though significant carbon formation was detected.[194]

Some mixed oxides derived from layered double hydroxides (LDH), containing Ni, Cu or Co in their composition, have also been explored for ATR of ethanol. Velu et al.[12,195] investigated ATR over a series of LDH-derived CuNiZnAl mixed oxides, studying the effects of Cu/Ni ratio, temperature, O/E ratio, contact time, CO cofeed, and substitution of Cu/Ni by Co. In the conditions explored (S/E = 3, O/E = 0.4, ethanol space velocity = 107 mol/h Kg/(cat.)), total conversion of ethanol was achieved at 573 K over all the catalysts, with hydrogen yield between 2.5 and 3.5 mol per mole of ethanol converted depending on the catalyst used. The best performance was observed with Co−Ni catalysts (i.e. when Cu is fully substituted by Co), which exhibited the lower selectivity to undesirable products (acetaldehyde, methane and CO). Similar studies on LDH-derived Ni−Mg−Al−Fe−O catalysts found that partial substitution of aluminum by iron in the Ni−Mg−Al−O oxide improves its poor stability and low H_2 yield[196]: the tetracomponent $Ni_{0.35}Mg_{2.65}Al_{0.50}Fe_{0.50}O_{4.5\pm\delta}$ provided a high H_2 yield (near 3.7 mol H_2/mol ethanol), that remained stable during the 30 h test, improved the CH_4 reforming activity and made ethylene to disappear in product gases. Similar ex-LDH mixed oxides of Co−Al, Co−Zn−Al, Co−Mg−Al, Ni−Mg−Al and Cu−Mg−Al), have been studied in ATR with S/E = 2.28 and O/E = 0.36 at T_R = 848−948 K.[197] Apart from Cu catalyst, all reached the full ethanol conversion in this T_R range, and H_2 and CO_2 were the main reaction products. The highest S_{H_2} values (85−89%) were reached with Co-containing catalysts CoAl and CoMgAl.

Perovskite oxides $LaMO_3$ (M = Mn, Fe, Co, Ni) prepared by combustion method were used as precursors for ATR catalysts.[198] The prereduction treatment of the catalyst destroyed the perovskite structure of $LaNiO_3$ and $LaCoO_3$, generating highly dispersed metal particles, while the $LaMnO_3$ sample kept its structure well after reduction. The perovskite-derived Ni catalyst was the most active and showed higher S_{H_2} than the Ni/La_2O_3 catalyst of equal atomic composition prepared by impregnation. Moreover, no drop in conversion or selectivity with time on stream was detected, while the latter deactivated quickly, with a marked drop in S_{H_2}. These effects may be due to the formation of highly dispersed Ni nanoparticles from the perovskite precursor. Partial substitution (10%) of Ni by Fe in the perovskite precursor lead (after reduction) to catalyst with both Ni and Ni−Fe alloy with improved performance: hydrogen yield of 3.0 mol per mol of ethanol and stable activity in a 30 h test.[199]

7.5 ETHANOL REFORMING IN CATALYTIC MEMBRANE REACTORS

As discussed previously, the reaction temperature is an important operational parameter when conducting ethanol reforming reactions. High temperatures are necessary for C−C bond cleavage, but moderate temperatures are preferred for the WGS equilibrium to favor the formation of hydrogen and CO_2 at the expense of CO and water, thus maximizing the production of H_2 and avoiding the requirement of bulky WGS units at the reactor outlet. This condition considerably simplifies the fuel processor design, both in terms of number of catalytic stages required as well as heat transfer management. In this context, the use of catalytic membrane reactors (CMRs), where the generation and separation of hydrogen take place simultaneously, appears as an attractive approach to further simplify on-site/on-demand reformers (Fig. 7.3). In addition, the shift effect that occurs in CMR results in even higher hydrogen yields because the presence of a membrane selective to the hydrogen permits attaining very high conversion values in comparison with the traditional reactors operating under the same conditions.[200] In fact, the continuous removal of one of the reaction products, the hydrogen, promotes the reaction conversion beyond the equilibrium values. With respect to a classical configuration consisting of a reactor unit in series with a separation unit, CMR represents a modern configuration in

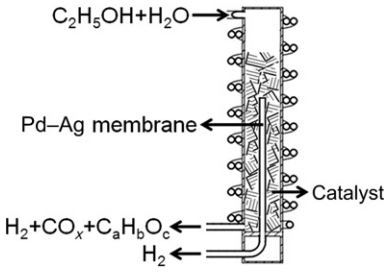

FIGURE 7.3 Scheme of a catalytic membrane reactor for generating PEMFC-grade hydrogen from ethanol steam reforming.

which an integrated reaction/separation unit has many potential advantages: reduced capital costs, improved yields and selectivities and drastically reduced downstream separation costs.[201,202]

Among CMRs, palladium-based membrane reactors fulfill the requirements to obtain an ultrapure hydrogen stream suitable for PEMFC feeding. Via innovative techniques, such as cold-rolling and diffusion welding developed at several laboratories and companies, robust Pd-based thin wall tubes <0.05 mm wall thickness have been produced[203] and their complete hydrogen selectivity and durability have been demonstrated in long-term tests.[204] The hydrogen flux through the membrane increases with decreasing membrane thickness, and the overall cost decreases. Also, submicron-thick Pd-based membranes have been manufactured using microfabrication technology.[205] Today, numerous CMR designs are available containing a bundle of Pd-based tubes or fingers.[206,207] These devices are capable for producing higher hydrogen throughputs than single-tube membrane modules and can be used in compact reforming systems. In addition, the reject gas from the membrane can be used as a fuel source for a catalytic combustor to provide a self-sustainable operation.[208] Autothermal ESR operation in a fluidized membrane bed reactor with intrinsic CO_2 capture has also been proposed.[209]

Commercial applications of Pd-based permeators for producing very pure hydrogen have been studied for more than 50 years (i.e. in the fuel cycle of the fusion reactors). In fact, palladium membranes are among the oldest membranes studied for gas permeation and separation applications and are still the membranes with the highest hydrogen permeability and selectivity.[210] They are receiving renewed attention because of the prospect of the hydrogen economy. The most critical issue for practical applications of Pd membranes in CMR for hydrogen production is the chemical stability of the metal membranes (poisoning effects of the reaction mixture on hydrogen permeation, carbon deposition on the membrane, etc.). For a better chemical stability (poisoning) and physical stability (mechanical stress, hydrogen embrittlement), membrane reactors do not use pure Pd but various different types of Pd alloyed with other metals such as silver, copper, nickel, iron and platinum. Most Pd alloy membranes studied are of binary components, with a few of multicomponents. Pd−Ag (23 wt.% Ag) and Pd−Cu (38−42 wt.% Cu) alloy membranes are nowadays widely employed in CMR for hydrogen production. The Pd−Ag is a plastic alloy with a specific hydrogen permeability of $3.4\ nm^3\ mm/m^2\ h\ MPa^{0.5}$ at 873 K.[206] The hydrogen permeated depends not only on the membrane properties, but it is also a linear function of the driving force, which, in the case of Pd-based membranes, generally is given by the difference of the square roots of the H_2 partial pressure on each side of the membrane (Sieverts' law). The hydrogen permeation through dense Pd-based membranes follows a solution−diffusion transport mechanism, separation depending on the difference in diffusivity and solubility of hydrogen in the membrane. The membrane thickness plays an important role: as thin the membrane as high the hydrogen permeance, even affecting the membrane mechanical resistance. Therefore, for real applications to ensure the mechanical resistance and strength of the membrane, thicker membranes are necessary. They are generally deposited onto porous supports such as SiO_2, Al_2O_3, B_2O_3 and porous stainless steel (PSS).

Pd-alloy membranes have been used in CMRs mainly for WGS and steam reforming reactions of methane and methanol,[211] but their use in the ESR is relatively new.[211] The main aim of the scientists and engineers involved in this field is oriented to emphasizing the role of the membrane by analyzing the performances of the reaction system in terms of ethanol conversion, hydrogen yield and hydrogen recovery, that is, the amount of hydrogen collected in the permeate side vs. the total hydrogen produced during the reaction. A large piece of work on ESR with Pd−Ag membranes (wall thickness of 50 μm) using sweep-gas has been carried out at the University of Calabria, Italy. Gallucci et al.[212] studied both methanol and ESR over Ru/Al_2O_3 catalyst in three different Pd−Ag membrane reactors. For ESR, the highest conversion attained at 723 K was about 50% in counter-current mode, which was significantly higher than that attained in a traditional reactor. However, in the CMR, coke deposition occurred to a large extent with consequent deactivation of the catalyst. Basile et al.[213] used the same catalyst for performing ESR in a dense Pd−Ag CMR by varying the water:ethanol molar ratio between 3:1 and 9:1 at 573−673 K and 1.3 bar in counter-current mode. Hydrogen recovery values of 22% were reached as well as ethanol conversion higher than 99% with a 56% hydrogen yield, which represent a significant improvement over the performance obtained with conventional catalytic reactors according to the shift effect. Over the same catalyst, Tosti et al.[214] reached hydrogen yields as high as 80% working at 723 K and 2 bar using a dense thin-wall Pd−Ag tube. The same device was used by Tosti et al.[215] for studying Pt- and Ni-based catalysts, which showed a poor performance in terms of hydrogen yield with respect to the Ru-based catalyst ($Ru > Ni > Pt$ at low feed, while for higher feed flow ratios, the sequence was $Ru > Ni = Pt$). Tosti et al.[216] also obtained kinetic expressions and modeled the CMR operation with the Ru-, Ni- and Pt-based catalysts in order to optimize the membrane reformer by assessing the ratio between the reaction and permeation kinetics. The effect of pressure was

studied by Tosti et al.[217] in a Pd−Ag tube of 150 mm wall thickness in the range of 1−8 bar. At 723 K and 4 bar and a feed flow rate of 5 g/h, hydrogen recovery values close to 100% were measured. The Ru/Al_2O_3 catalyst was also studied for the OSR of ethanol in the CMR at 673 K, S/C = 5.5, GHSV = 2000/h and by using a sweep gas into the permeate side of the reactor,[218] being the maximum hydrogen recovery (c. 30%) achieved at O/C = 1.2. The OSR of ethanol was studied by Santucci et al.[219] over a Pt/Al_2O_3 catalyst in a membrane module with a finger-like configuration. The addition of oxygen had a positive effect on the performance of the CMR operating under pure ESR conditions. The behavior of the CMR for the POE over Rh/Al_2O_3 catalyst was studied by Iulianelli et al.[220] at 723 K, 1−3 bar, GHSV = 1300/h and O/C = 0.7−1.2. No carbon formation was detected and more than 40% hydrogen recovery was achieved. ESR over Co/Al_2O_3 catalyst was conducted by Iulianelli and Basile[221] and Iulianelli et al.[222] Several operational parameters such as temperature, pressure, sweep-gas flow and load were evaluated and hydrogen yield and recovery values as high as 60% and 95%, respectively, were reached at 673 K, 3 bar, SF = 25.2 (countercurrent flow) and Weight Hourly Space Velocity (WHSV) = 0.2/h. The same catalyst was tested at 673 K in a PSS-supported Pd membrane reactor with the aim of investigating the influence of the membrane characteristics as well as of the reaction pressure from 3 to 8 bar by Basile et al.[223] Hydrogen recovery of about 50% was reached under complete ethanol conversion. Co/Al_2O_3 and Ni/ZrO_2 catalysts have been recently used in the PSS membrane reactor at 673 K and 8−12 bar for simulating bio-ESR by using a mixture of water−ethanol−acetic acid and glycerol with 1:13:0.18:0.04 M ratio.[224] About 94% of bio-ethanol conversion was obtained at 12 bar and GHSV = 800/h over the Co/Al_2O_3 catalyst, with 40% hydrogen yield and 40% hydrogen recovery.

Lin et al. from Chienkuo Technology University, Taiwan studied the OSR of ethanol in a Pd−Ag/PSS membrane reactor (membrane thickness of 20 μm) loaded with $CuZn/Al_2O_3$ catalyst at 593−723 K and 3−10 bar.[225] The same study was conducted in an Ni−Pd−Ag ternary alloy membrane reactor with similar results.[226] Papadias et al.[227] at Argonne National Laboratory, USA, explored the benefits of high-pressure ESR for the production of hydrogen needed to refuel the high-pressure tanks of PEMFC vehicles. The experiments were conducted at 7−70 bar, 873−1023 K, S/C = 3−12 and GHSV = 8500−83,000/h in a Pd−Ag (30 μm) CMR loaded with $Rh/La_2O_3{-}Al_2O_3$ catalyst. As expected from thermodynamics, higher pressures showed inhibition of the hydrogen yield in favor of methane. In a recent work, Domínguez et al. from the Technical University of Catalonia, Spain studied the ESR in a similar CMR over cobalt talc at 598−673 K and 5−15 bar.[228] In addition to an improvement of the hydrogen yield, the CMR showed a rapid response to changes in the ethanol−water mixture load; a constant hydrogen flow was obtained after 2 s following variations of ±10%. The experiments of Papadias et al.[227] and Domínguez et al.[228] were performed without sweep gas, therefore, pure hydrogen was obtained in the permeate side of the membrane, ready to feed a PEMFC. In a similar configuration, López et al.[229] studied recently the ESR using a $Pd{-}Rh/CeO_2$ catalyst over cordierite monoliths in-series into a stainless-steel membrane reactor. Reaction yields of 3.1 mol hydrogen generated per mole ethanol in feed and total yields of 1.4 mol H_2 permeated per mole ethanol in feed were measured, with maximum hydrogen recuperation of 70%.

Although most of the ESR work in CMR has been done with Pd−Ag selective membranes, there are also some examples of ESR in different types of membrane reactors with the scope of reducing the cost. Yu et al. from the Korea Research Institute of Chemical Technology used Pt-impregnated Knudsen membranes to carry out simultaneously the ESR reaction and WGS.[230] The ethanol reforming membrane reactor showed ethanol conversion improvement up to c. 15% in comparison with a conventional reactor, with an improvement of hydrogen yield up to 10.5%. A similar experiment was performed with a CMR loaded with Pt/TiO_2 catalyst, which showed hydrogen recovery values of 78−87% in the temperature range 573−873 K.[231] Lim et al. from the Virginia Polytechnic Institute & State University, USA employed silica−alumina composite membranes with moderate hydrogen permeance for ESR over Na−Co/ZnO catalyst[232] and, more recently, Pd−Cu composite membranes over Al_2O_3.[233] High-effective hydrogen production from ethanol and water has been recently reported in a tubular dense mixed-conducting oxygen permeable membrane reactor, in which the water splitting takes place at the tube side of the membrane and the OSR of ethanol occurs at the shell side simultaneously.[234]

POE over Rh/Al_2O_3 in a dense Pd−Ag membrane reactor was evaluated working at 723 K, GHSV = 1300/h, O/E = 0.33−0.62 and reaction pressure range 1−3 bar (Lulianelli et al., 2010b).[220] Complete ethanol conversion was achieved in all the experimental tests, and in the best result, more than 40.0% CO_x-free hydrogen recovery was achieved. The comparison between the performances of Rh/CeO_2 catalyst in this reactor and in a fixed-bed reactor (FBR) highlights the benefits of using CMRs: using O/E = 0.5, full ethanol conversion and $S_{H_2} = 34\%$ were achieved at 723 K in CMR, compared to 85% ethanol conversion and $S_{H_2} = 60\%$ at much higher $T_R = 973$ K in FBR.[166] The activity of the Pd−Ag MR without catalyst was also tested. At stoichiometric O/E ratio, the CMR presented around 85% ethanol conversion

and around 11% H_2 selectivity (vs. 100% and 33%, respectively, in the presence of Rh catalyst). However, the main drawback was carbon deposition (not observed with catalyst), which covered the Pd−Ag membrane surface and lowered its hydrogen permeation capacity.

7.6 ETHANOL REFORMING IN MINIATURIZED SYSTEMS

The range of applications of hydrogen and fuel cells spans from stationary large power plants to automotive and other mobile devices as well as portable electronic gadgets requiring <1 W electrical output. Market analyses expect portable applications to enjoy widespread market success. This has moved researchers to investigate in the development of miniaturized fuel cell systems, including miniaturized reformers for the on-site generation of hydrogen.[235] At present, the tendency toward miniaturization and the wireless revolution is being restrained by battery life. Fuel cells last much longer than batteries and do not need to be replaced. However, fuel cell implementation in handheld electronics could be restrained if hydrogen feeding and/or refueling is not properly solved. As we have seen above, considerable work has been performed on hydrogen production via ESR using conventional reactors, but the scale reduction required for portable applications renders their utilization impractical. Furthermore, reforming reactions show strong thermal effects and conventional FBRs exhibit poor heat transfer characteristics. Microreactors assess both the problems of moving down the scale and increasing the heat transfer rate by the deposition of the catalyst directly on the reactor walls and the introduction of new manufacture techniques which permit, along with the miniaturization involved, the achievement of remarkable increases in the specific contact area.[236] The small dimensions attained for microchannels and their high reproducibility allow for better reaction control by achieving previously inaccessible residence times, short diffusional distances and flow pattern homogeneity, resulting in a considerable decrease in the amount of catalyst required with respect to conventional reactors. Also, microreaction technology provides enhanced safe operation in the management of hydrogen-producing reactions because large volumes are avoided, permitting the use of process parameters of otherwise explosive regimes. Therefore, microreactors appear as an invaluable technology for boosting the implementation of on-site and on-demand generation of hydrogen for portable applications, thus avoiding limitations imposed by hydrogen storage.

Numerous microdevices for the production of hydrogen from methanol steam reforming have been reported,[237] but the high temperatures required for ESR has prevented extensive work in this field.[238] Men et al. from the Institute of Microtechnology Mainz (IMM) tested several catalyst formulations based on Ni, Rh, Co, and Ni−Rh for ESR in a microchannel reactor (channels 500 μm width and 250 μm depth).[239] The best results were obtained over Ni−Rh/CeO_2, which showed no deactivation during a 100 h catalytic test at 923 K. Casanovas et al. from the Technical University of Catalonia (UPC) developed a microreactor for the generation of hydrogen from ethanol under an autothermal regime.[137] A two-sided platelet microreactor was designed for transferring the heat released during ethanol total catalytic oxidation over a $CuMnO_x$ catalyst in one side of the microreactor to the other side, where ESR occurred over a CoO_x−ZnO catalyst. Görke et al. from the Institute for Micro Process Engineering (Karlsruhe) used a microchannel reactor (channels 200 μm width and depth) to produce hydrogen by ESR over an Rh/CeO_2 catalyst.[240] For temperatures above 898 K, a space time yield four times higher than that obtained in conventional reactors was reached. Cai et al. from CNRS and the University of Lyon used a microreactor with channels 500 μm wide and deep, loaded with an Ir/CeO_2 catalyst, and hydrogen productivity was found significantly higher than in conventional FBRs, essentially due to better heat and mass transfers.[241] These are pioneering examples reported in the open literature concerning the generation of hydrogen from ethanol using microreactor technologies. More recently, Peela et al. from the Indian Institute of Technology (IIT) performed steam reforming and OSR of ethanol over Rh/CeO_2/Al_2O_3 in a microreactor with channels 500 μm wide and 400 μm deep and showed that microchannels produced hydrogen without diffusional effects in the catalyst layer with respect to a packed bed reactor.[45,242,272] Domínguez et al. from UPC coated a plate microreactor with cobalt talc, $Co_3[Si_2O_5]_2(OH)_2$, and performed ESR at low temperature (648 K) with trace CO formation.[243] Rahman et al. from the Imperial College London used a catalytic hollow fiber microreactor loaded with a Ni/MgO−CeO_2 to carry out ESR, with a flow rate of hydrogen three fold higher than that obtained in an FBR.[244,245] Finally, Kolb et al. from IMM in collaboration with Rosetti Marino company tested Rh−Ni and Rh−Co/Al_2O_3-based catalysts and developed a full microstructured ethanol fuel processor.[246]

To further reduce the hydrogen generation scale while maintaining system efficiency can hardly be attained by using conventional geometries and/or manufacture techniques of present-day microreactors. Therefore, the development of breakthrough technologies capable to provide higher hydrogen generation rates per unit volume and, at the same time, enable downscaling is required. In that sense, Llorca et al. from UPC reported

a novel approach to minimize systems for hydrogen production by using silicon micromonoliths with millions of parallel microchannels per square centimeter with a diameter of only ~3–4 μm.[247] Such geometry is achieved through photoassisted electrochemical etching in silicon wafers. The parallel channels show spectacular reproducibility, assuring excellent flow distribution. By means of precisely designed methods, the channels walls can be successfully coated with homogeneous thin layers of appropriate catalysts. With the resultant geometry, the specific contact area increases c. 100 times with respect to conventional microreactors, reaching fabulous values of $10^6\ M^2/m^3$. A silicon micromonolith coated with a Co_3O_4/ZnO catalyst was tested successfully for ESR[271] and used to build up a complete ethanol processor with in-series units comprising a total of c. 2×10^7 Channels.[248] Specific production rates exceeding 3.2 Nl of H_2 per cm^3 of liquid fed and cm^3 of micromonolith under residence times of the order of milliseconds were possible due to the great geometric area of the micromonoliths. Silicon micromonoliths coated with Au/TiO_2 have been tested also for CO preferential oxidation in the presence of excess hydrogen in order to simulate ethanol reformer outlet streams.[249]

7.7 PHOTOCATALYTIC PRODUCTION OF HYDROGEN FROM ETHANOL

Photocatalysis takes profit of light energy instead of heat. The main advantage vs. thermal catalysis is the possibility of working at room temperature. Photoreactions are initiated by excitation of a semiconductor photocatalyst, resulting in the promotion of an electron (e^-) from the valence band (VB) to the conduction band (CB) of the semiconductor (Fig. 7.4). Consequently, a hole (h^+) is created in the VB. The resulting electron/hole pair (e^-/h^+) can then migrate to the surface and initiate redox reactions with adsorbed organics. In the absence of suitable traps or scavengers of photogenerated carriers, electrons and holes recombine releasing heat. Recombination is mainly responsible for the generally low quantum efficiency of semiconductor-mediated photocatalytic processes. Electron–hole pairs that avoid recombination can migrate to the photocatalyst surface, where electrons may reduce protons to produce hydrogen and holes may oxidize water to produce oxygen. The ability of photogenerated charge carriers to split water depends on the relative positions of the energy levels of the CB and the VB of the semiconductor with respect to the hydrogen and oxygen evolution potentials of water respectively. In particular, water cleavage may occur in a cyclic manner only when $E_{CB} < E(H^+/H_2)$ and $E_{VB} > E(O_2/H_2O)$.

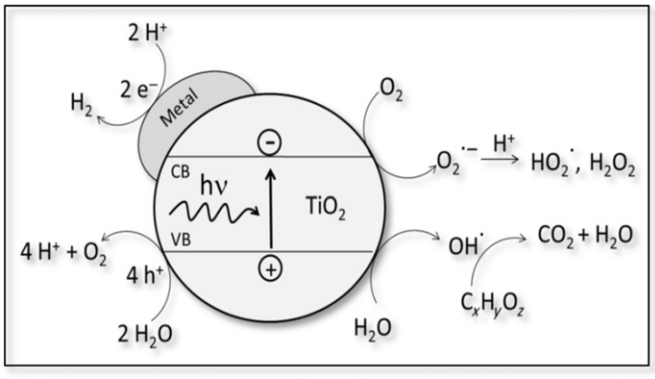

FIGURE 7.4 Schematic representation of water splitting, hydrogen generation and carbohydrate oxidation over an irradiated metal/TiO_2 photocatalyst.

Photoreactors for liquid phase reactions are typically based on slurry systems, where the solid catalyst is dispersed within the liquid reactant. Depending on the setup to illuminate the reactor, it can be (1) a top illumination slurry reactor, where the light source is directed to the dispersion from outside; (2) a side light fiber reactor, where the fibers are inside the dispersion; and (3) an annular slurry reactor, where the dispersion is around the light tube. On the other hand, the solid catalyst can be deposited onto the channels of a honeycomb support, being illuminated every channel with a side light fiber. This setup is defined as an internally illuminated monolith reactor.[250,251]

Among the semiconductor materials which fulfill $E_{CB} < E(H^+/H_2)$ and $E_{VB} > E(O_2/H_2O)$ (e.g. TiO_2, ZnO, ZnS, SiC, CdS, CdS, CdSe, $LaMnO_3$, $SrTiO_3$, WO_3, SnO_2, Fe_2O_3), titanium dioxide has attracted the most attention because of its chemical and photochemical stability, nontoxicity and low cost. It is the most active natural semiconductor known for photoreactions.[252] Among the polymorphs of titania, anatase is the most active because of its slowest electron–hole recombination rate. The major disadvantage of TiO_2 is that due to its relatively large energy band gap (3.2 eV for anatase), it can be activated only by photons in the near-UV region, and solar light has only 5% of UV-A light. Theoretically, the lowest energy required to split water into H_2 and O_2 is 1.23 eV. But, in the practice and due to energy losses, energies higher than 2.0 eV are necessary for efficient light-to-chemical energy conversion. However, semiconductors with band gap energies in the region of 2.0–2.5 eV are chemically/photochemically unstable, especially when used in aqueous media. For instance, cadmium sulfide (CdS) has a suitable band gap energy ($E_{BG} = 2.4$ eV) but it is susceptible to photocorrosion when dispersed in water. Pure titania is active for the photocatalysis of hydrogen production from water but the addition of metal atoms increases significantly the hydrogen yield. Several metals have been

used, such as Pt, Pd, Au, Cr, Ru, Rh, Ni, etc.[253] At the metal/semiconductor interface, a Schottky barrier is formed, which leads to electron trapping and decrease in the electron–hole recombination rate. Noble metals have high work functions; hence, tiny Schottky barriers are formed, favoring electron trapping. Metals also need to be efficient for adsorption of protons and their recombination into H_2. Moreover, they shouldn't be easily oxidized during the photocatalytic process. Doping of titania has also been deeply investigated in order to enhance its light absorption in the visible range. Doping N and B into TiO_2 improves its activity for hydrogen production because it favors the absorption of light of higher wavelength.[254] Another strategy is the incorporation of cations of valence higher than Ti^{4+} (W^{6+}, Ta^{5+}, Nb^{5+}) into the crystal matrix of titania. It results in enhanced rates of water cleavage while the opposite is observed upon doping with cations of lower valence (In^{3+}, Zn^{2+}, Li^{+}). The enhancement or reduction of photocatalytic activity is found to be dependent on the concentration and valence of the doping cations.[255] Park et al.[256] observed that vertically grown carbon-doped TiO_2 ($TiO_{2-x}C_x$) nanotube arrays with high aspect ratios showed much higher photocurrent densities and more efficient water splitting under visible-light illumination ($\lambda > 420$ nm) than pure TiO_2 nanotube arrays. TiO_2 has also been doped with CdS to broaden the absorption range. CdS is more efficient for the photodegradation of inorganics, while TiO_2 is more effective for the photodegradation of organic substances.[257] The photoactivity of Pt/TiO_2 system in the visible region can be improved by the addition of sensitizers, such as $[Ru(dcbpy)_2(dpq)]^{2+}$ (where dcbpy = 4,4′-dicarboxy 2,2′-bipyridine and dpq = 2,3-bis-(2′-pyridyl)-quinoxaline), leading to efficient water reduction. Sensitization enables using semiconductors that are not intrinsic absorbers of visible light and do not suffer destructive photodecomposition.[258]

Much work has been done on photocatalytic generation of hydrogen since Fujishima and Honda first reported in the early 1970s that hydrogen could be obtained from the photocatalytic splitting of water.[259] It has been widely confirmed that the hydrogen yield improves when an organic compound is added to the water. Because the organic compound acts as a sacrificial electron donor and consumes photogenerated holes and/or oxygen, the rates of electron–hole recombination and H_2–O_2 back reaction are decreased. Several fuels have been tested, such as aliphatic and aromatic hydrocarbons, alcohols, acids, esters, biomass, coal, tar sand, pitch, etc.[64,260–262] In the case of ethanol, it becomes a radical ethoxide under UV irradiation, which is then converted to the carbonyl compound. Metal sites trap electrons and reduce protons to molecular hydrogen. Hydrogen ions are generated by oxidation of water and alcohol.

Lianos et al. studied the activities of Au/TiO_2 and Pt/TiO_2 on the photogeneration of hydrogen using aqueous 5 M ethanol solutions. The main products were hydrogen, methane, carbon dioxide and acetaldehyde. They studied different parameters such as the method of metal deposition onto titania, the pretreatment calcination temperature, the metal loading and exposed surface area of metal and the initial pH of the suspension. They concluded that the overall activity of Au samples was generally about 30% lower than that of Pt samples.[263] The same group published on the photocatalytic hydrogen production from ethanol reforming employing highly efficient nanocrystalline titania films. Using a low-energy black-light source of only 16 W, they managed efficiencies of up to 74% active electron to incident photon ratio and 32% energy conversion efficiency for ethanol/water mixtures. They also tested other alcohols, such as iPrOH, *n*-BuOH and MeOH, but EtOH gave the best results.[264] In another publication, they stated that the size and distribution of platinum nanoparticles onto the titania affected directly the efficiency of the catalyst, being the smallest nanoparticles ($\approx$1 nm), fine distributed, the optimal.[265] Also in the University of Patras, Kondarides et al. reformed biomass for the generation of hydrogen over Pt/TiO_2 catalysts. They studied several isolated biomass compounds, such as glycerol, galactose, lactose, cellobiose, maltose, starch, cellulose and ethanol, and they concluded that the overall reforming reaction is nonselective with respect to the organic substrate employed and, therefore, practically all biomass-derived compounds in solution or in suspension may be used as feedstock.[262] Korzhak et al. studied the influence of the particle size in the efficiency of metal/titania catalysts, too. They used low-cost metals, such as Ag, Ni and Cu. They found that there was an optimal metal concentration range where the quantum yield of hydrogen production was maximal. A decrease in the photoreaction rate at further increment in the metal content was supposed to be connected with the enlargement of metal nanoparticles and deterioration of the intimate electron interaction between the components of the metal–semiconductor nanocomposites.[266]

Idriss et al. investigated the catalytic activity of anatase doped with Rh, Pd and Pt at 350 K over pure ethanol and other alcohols. They observed that in the absence of the metal, TiO_2 showed negligible production of hydrogen. The addition of Pd or Pt increased significantly the hydrogen production, reaching up to 10% of quantum yield. On the contrary, Rh-doped TiO_2 appeared to be much less active, despite all the samples had metallic particles with similar size, <10 nm. The authors completed the study testing other alcohols: methanol, propanol, isopropanol and *n*-butanol. The production of hydrogen was inversely proportional to the chain length.[64] Idriss et al. also investigated the

catalytic activity of Au/TiO_2 samples with different support particle size (10 nm vs. 150 nm). They observed that the production of hydrogen, defined as $l\,h_2/kg_{catal}$ - min, was equivalent in both samples when normalized by unit area, indicating the absence of a particle size effect of the semiconductor on the electron transfer reaction within this particle size range.[267] They obtained hydrogen production rates of $\approx 2\,l\,h_2/kg_{catal}$ min on 2 wt.% Au/TiO_2 anatase samples. Following with their research on Au/TiO_2, a new piece of work on gold loading and particle size was published in 2011. They tested that anatase is more active than rutile and surprisingly, it was also found that Au particle size did not affect the photoreaction rate over the 3−12 nm range.[268] The last piece of work of this group on ethanol photoreaction to hydrogen deals with the synergistic effect of the polymorph of the semiconductor. As previously stated, Au/TiO_2 anatase is about two orders of magnitude more active than Au/TiO_2 rutile. Yet, it was also found that when the anatase and rutile particles are present together, the reaction rate is higher than that observed over Au/TiO_2 anatase alone.[269]

Mizukoshi et al. made use of ultrasounds to deposit noble metals (Pt, Au and Pd) onto TiO_2. The photocatalytic activity was higher than for the conventional impregnated samples. They found a relationship between the catalytic activity and the work function of the metal: the higher the work function, the better activity. They also observed that smaller metallic particles led to more active catalysts.[270] The group of J.L. Falconer was interested not only in the photocatalytic decomposition of aliphatic alcohols, acids and esters to produce hydrogen but also in the mechanism of the reaction. They observed that when only alkyl groups were bonded to the carbon in a −C−O− group, alkanes formed but not hydrogen. Abstraction of a hydrogen atom appeared to be the first step in the photocatalytic decomposition of alcohols, acids and esters.[260]

7.8 CONCLUDING REMARKS

Ethanol is a renewable source of hydrogen with very important advantages such as worldwide availability, high hydrogen content, and handling safety. The manufacture of bioethanol is relatively simple and well-known. A lot of work has been carried out between 2000 and 2010 concerning thermally driven catalytic reactions aimed at hydrogen generation from ethanol−water mixtures over a great variety of catalysts. Assisted with modern catalyst preparation tools and strategies, several adequate catalyst formulations for ESR, partial oxidation and OSR do exist, in spite of the complex reaction networks that are inherent to all these processes. In general, noble metals supported over reducible oxides are the preferred catalysts due to their high activity and stability under high loads of ethanol although other promising formulations based on less-expensive transition metals may also play a role in the future.

However, several main issues for the implementation of these technologies remain hard to solve. One of them is catalyst robustness when raw bioethanol is directly used for hydrogen generation instead of model ethanol−water mixtures, which are used in most laboratories. As a natural resource, bioethanol contains a great variety of impurities, both inorganic and organic, embracing a wide range of functional groups that poses serious difficulties for catalyst stability under reforming conditions. Another critical aspect for ethanol implementation as a source of hydrogen for mobile and portable applications is ethanol reformer design. If ethanol reforming processes are intended to feed with hydrogen the anode of low-temperature fuel cells for on-site and/or on-board applications, much work is still required regarding engineering aspects related to microreactor technologies and hydrogen separation/purification methods adequate for such applications. Related to this, the development of CMRs, where the reforming of ethanol and separation of pure hydrogen through dense metallic membranes takes place simultaneously, appear as a valuable tool for drastically reducing downstream separation cost and complexity. Development of microchannel structured reactors also shows promise for the thermal integration of oxidation and reforming of ethanol, as well as for the compactness of the reformer for mobile applications.

The use of renewable energy sources, such as solar energy, is a way to improve the sustainability and the global energy balance of the hydrogen production. This is a driving force for making hydrogen from ethanol by photocatalytic processes using sunlight and appropriate catalysts, such as oxide semiconductors decorated with noble metal nanoparticles. Obviously, the photocatalytic route operating at room temperature is one of the most assertive dreams for the generation of hydrogen from renewable ethanol and some important advances have been accomplished very recently, but the yields attained are still quite low and much work related to both catalyst design and reactor engineering is needed.

Successful implementation of practical technologies for hydrogen production from ethanol still requires many efforts in several areas, such as catalyst design, in situ characterization and mechanism studies, reaction and process modeling, as well as engineering of catalyst, reactor and process. We may expect that convergent approaches from many disciplines and their mutual interactions will allow overcoming the currently remaining challenges.

Acknowledgments

VCC and ROF research work in this field is funded by the Spanish MICINN (projects MAT2006-12386-C05-03 and ENE2009-14522-C05-05). JL, NJD and ET acknowledge funding from MICINN (project CTQ2009-12520) and MINECO (project ENE2012-36368). JL is grateful to ICREA Academia program. NJD is grateful to UPC for a PhD grant.

References

1. Logsdon, J. E. Ethanol. In Seidel, A., Ed., Vol. 10; Wiley-Interscience: New York, 2004; pp. 527–567.
2. Shapouri, H.; Duffield, J. A.; Wang, M. *The Energy Balance of Corn Ethanol*. An Update. AER-814; USDA Office of the Chief Economist: Washington, D.C., 2002.
3. Shapouri, H.; Duffield, J. A.; Wang, M. The Energy Balance of Corn Ethanol Revisited. *Trans. ASAE* **2003,** *46,* 959–968.
4. Deluga, G. A.; Salge, J. R.; Schmidt, L. D.; Verykios, X. E. Renewable Hydrogen from Ethanol by Autothermal Reforming. *Science* **2004,** *303,* 993–997.
5. Subramani, V.; Song, C. Advances in Catalysis and Process for Hydrogen Production from Ethanol Reforming. *Catalysis* **2007,** *20,* 65–106.
6. Renewable Fuels Association. *World Fuel Ethanol Production*. http://ethanolrfa.org/pages/World-Fuel-Ethanol-Production, 2012 (accessed 30 July 2012).
7. Ni, M.; Leung, D. Y. C.; Leung, M. K. H. A Review on Reforming Bio-Ethanol for Hydrogen Production. *Int. J. Hydrogen Energy* **2007,** *32,* 3238–3247.
8. Galbe, M.; Zacchi, G. A. A Review of the Production of Ethanol from Softwood. *Appl. Microbiol. Biotechnol.* **2002,** *59,* 618–628.
9. Vasudeva, K.; Mitra, N.; Umasankar, P.; Dhingra, S. C. Steam Reforming of Ethanol for Hydrogen Production: Thermodynamic Analysis. *Int. J. Hydrogen Energy* **1996,** *21* (1), 13–18.
10. Brown, L. F. A Comparative Study of Fuels for On-Board Hydrogen Production for Fuel-Cell-Powered Automobiles. *Int. J. Hydrogen Energy* **2001,** *26,* 381–397.
11. Murtagh and Associates. *Material Safety Sheet Ethanol*. http://www.distill.com/materialsafety/msds-eu.html, 2012 (accessed June 2012).
12. Velu, S.; Satoh, N.; Gopinath, C. S.; Suzuki, K. Oxidative Reforming of Bio-Ethanol over CuNiZnAl Mixed Oxide Catalysts for Hydrogen Production. *Catal. Lett.* **2002,** *82,* 145–152.
13. Casanovas, A.; de Leitenburg, C.; Trovarelli, A.; Llorca, J. Catalytic Monoliths for Ethanol Steam Reforming. *Catal. Today* **2008,** *138,* 187–192.
14. Rabenstein, G.; Hacker, V. Hydrogen for Fuel Cells from Ethanol by Steam-Reforming, Partial-Oxidation and Combined Auto-Thermal Reforming: A Thermodynamic Analysis. *J. Power Sources* **2008,** *185,* 1293–1304.
15. Benito, M.; Sanz, J. L.; Isabel, R.; Padilla, R.; Arjona, R.; Daza, L. Bio-Ethanol Steam Reforming: Insights on the Mechanism for Hydrogen Production. *J Power Sources* **2005,** *151,* 11–17.
16. Haryanto, A.; Fernando, S.; Murali, N.; Adhikari, S. Current Status of Hydrogen Production Techniques by Steam Reforming of Ethanol: A Review. *Energy Fuels* **2005,** *19,* 2098–2106.
17. Vaidya, P. D.; Rodrigues, A. E. Insight into Steam Reforming of Ethanol to Produce Hydrogen for Fuel Cells. *Chem. Eng. J.* **2006,** *117,* 39–49.
18. Bion, N.; Duprez, D.; Epron, F. Design of Nanocatalysts for Green Hydrogen Production from Bioethanol. *ChemSusChem* **2012,** *5,* 76–84.
19. Hohn, K. L.; Lin, Y.-C. Catalytic Partial Oxidation of Methanol and Ethanol for Hydrogen Generation. *ChemSusChem* **2009,** *2,* 927–940.
20. Auprêtre, F.; Descorme, C.; Duprez, D.; Casanave, D.; Uzio, D. Ethanol Steam Reforming Over $Mg_xNi_{1-x}Al_2O_3$ Spinel Oxide-Supported Rh Catalysts. *J. Catal.* **2005,** *233,* 464–477.
21. Idriss, H.; Scott, M.; Llorca, J.; Chan, S.; Chiu, W.; Sheng, P.; Yee, A.; Blackford, M.; Pas, S.; Hill, A.; Alamgir, F.; Rettew, R.; Petersburg, C.; Senanayake, S.; Barteau, M. A Phenomenological Study of the Metal-Oxide Interface: The Role of Catalysis in Hydrogen Production from Renewable Resources. *ChemSusChem* **2008,** *1,* 905–910.
22. Cavallaro, S. Ethanol Steam Reforming on Rh/Al_2O_3 Catalysts. *Energy Fuels* **2000,** *14,* 1195–1199.
23. Auprêtre, F.; Descorme, C.; Duprez, D. Bio-Ethanol Catalytic Steam Reforming Over Supported Metal Catalysts. *Catal. Commun.* **2002,** *3,* 263–267.
24. Breen, J.; Burch, R.; Coleman, H. Metal-Catalyzed Steam Reforming of Ethanol in the Production of Hydrogen for Fuel Cell Applications. *Appl. Catal. B: Environ.* **2002,** *39,* 65–74.
25. Diagne, C.; Idriss, H.; Kiennemann, A. Hydrogen Production by Ethanol Reforming over $Rh/CeO_2–ZrO_2$ Catalysts. *Catal. Commun.* **2002,** *3,* 565–571.
26. Romero-Sarria, F.; Vargas, J. C.; Roger, A.-C.; Kiennemann, A. Hydrogen Production by Steam Reforming of Ethanol. *Catal. Today* **2008,** *133–135,* 149–153.
27. Dömök, M.; Oszko, A.; Baan, K.; Sarusi, I.; Erdohelyi, A. Reforming of Ethanol on $Pt/Al_2O_3–ZrO_2$ Catalyst. *Appl. Catal. A: Gen.* **2010,** *383,* 33–42.
28. Liguras, D. K.; Kondarides, D. I.; Verykios, X. E. Production of Hydrogen for Fuel Cells by Steam Reforming of Ethanol over Supported Noble Metal Catalysts. *Appl. Catal. B: Environ* **2003,** *43,* 345–354.
29. Ramos, I. A.; Montini, T.; Lorenzut, B.; Troiani, H.; Gennari, F.; Graziani, M.; Fornasiero, P. Hydrogen Production from Ethanol Steam Reforming on $M/CeO_2/YSZ$ (M = Ru, Pd, Ag) Nanocomposites. *Catal. Today* **2012,** *180,* 96–104.
30. Siang, J.-Y.; Lee, C.-C.; Wang, C.-H.; Wang, W.-T.; Deng, C.-Y.; Yeh, C.-T.; Wang, C.-B. Hydrogen Production from Steam Reforming of Ethanol Using Ceria-Supported Iridium Catalyst: Effect of Different Ceria Supports. *Int. J. Hydrogen Energy* **2010,** *35,* 3456–3462.
31. Zhang, B.; Cai, W.; Li, Y.; Xu, Y.; Shen, W. Hydrogen Production by Steam Reforming of Ethanol over an Ir/CeO_2 Catalyst: Reaction Mechanism and Stability of the Catalyst. *Int. J. Hydrogen Energy* **2008,** *33,* 4377–4386.
32. Sanchez-Sanchez, M. C.; Navarro Yerga, R.; Kondarides, D.; Verykios, X.; Fierro, J. L. G. Mechanistic Aspects of the Ethanol Steam Reforming on Pt, Ni and PtNi Catalysts Supported on γ-Al_2O_3. *J. Phys. Chem. A* **2010,** *114,* 3873–3882.
33. Scott, M.; Goeffrey, M.; Chiu, W.; Blackford, M. A.; Idriss, H. Hydrogen Production from Ethanol over $Rh–Pd/CeO_2$ Catalysts. *Top. Catal.* **2008,** *51,* 13–21.
34. Idriss, H. Ethanol Reactions over the Surfaces of Noble Metal/Cerium Oxide Catalysts. *Platin. Met. Rev.* **2004,** *48,* 105–115.
35. Simson, A.; Farrauto, R.; Castaldi, M. Steam Reforming of Ethanol/Gasoline Mixtures: Deactivation, Regeneration and Stable Performance. *Appl. Catal. B: Environ.* **2011,** *106,* 295–303.
36. De Lima, S.; Colman, R.; Jacobs, G.; Davis, B. H.; Souza, K. R.; de Lima, A. F. F.; Appel, L. G.; Mattos, L. V.; Noronha, F. B. Hydrogen Production from Ethanol for PEM Fuel Cells. An Integrated Fuel Processor Comprising Ethanol Reforming and Preferential Oxidation of CO. *Catal. Today* **2009a,** *146,* 110–123.
37. De Lima, S.; da Silva, A. M.; Graham, U. M.; Jacobs, G.; Davis, B. H.; Mattos, L. V.; Noronha, F. B. Ethanol Decomposition and Steam Reforming of Ethanol over $CeZrO_2$ and $Pt/CeZrO_2$ Catalyst: Reaction Mechanism and Deactivation. *Appl. Catal. A: Gen.* **2009b,** *352,* 95–113.

38. Da Silva, A. M.; de Souza, K. R.; Jacobs, G.; Graham, U. M.; Davis, B.; Mattos, L. V.; Noronha, F. B. Steam and CO_2 Reforming of Ethanol over Rh/CeO_2 Catalyst. *Appl. Catal. B: Environ.* **2011,** *102,* 94−109.
39. Scott, M. S.; Idriss, H. *Heterogeneous Catalysis for Hydrogen Production. Handbook of Green Chemistry,* 2010, pp 223−246.
40. Ciambelli, P.; Palma, V.; Ruggiero, A. Low Temperature Catalytic Steam Reforming of Ethanol. 2. Preliminary Kinetic Investigation of Pt/CeO_2 Catalysts. *Appl. Catal. B: Environ.* **2010,** *96,* 190−197.
41. Erdohelyi, A.; Rasko, J.; Kecskes, T.; Toth, M.; Domok, M.; Baan, K. Hydrogen formation in ethanol reforming on supported noble metal catalysts. *Catalysis Today* **2006,** 367−376.
42. Birot, A.; Epron, F.; Descorme, C.; Duprez, D. Ethanol Steam Reforming over Rh/$Ce_xZr_{1-x}O_2$ Catalysts: Impact of the CO−CO_2−CH_4 Interconversion Reactions on the H_2 Production. *Appl. Catal. B: Environ.* **2008,** *79,* 17−25.
43. Roh, H.-S.; Wang, Y.; King, D. L.; Platon, A.; Chin, Y.-H. Low Temperature and H_2 Selective Catalysts for Ethanol Steam Reforming. *Catal. Lett.* **2006,** *108,* 15−19.
44. Trovarelli, A. Catalytic Properties of Ceria and CeO_2-Containing Materials. *Catal. Rev. Sci. Eng.* **1996,** *38,* 439−520.
45. Peela, N. R.; Mubayi, A.; Kunzru, D. Steam Reforming over Rh/CeO_2/Al_2O_3 Catalysts in a Microchannel Reactor. *Chem. Eng. J.* **2011,** *167,* 578−587.
46. De Rogatis, L.; Montini, T.; Casula, M. F.; Fornasiero, P. Design of Rh/$Ce_{0.2}Zr_{0.8}O_2$/Al_2O_3 Nanocomposite for Ethanol Steam Reforming. *J. Alloys Compd.* **2008,** *451,* 516−520.
47. Gucciardi, E.; Chiodo, V.; Freni, S.; Cavallaro, S.; Galvano, A.; Bart, J. C. J. Ethanol and Dimethyl Ether Steam Reforming on Rh/Al_2O_3 Catalysts for High-Temperature Fuel-Cell Feeds. *React. Kinet. Mech. Catal.* **2011,** *104,* 75−87.
48. Moura, J. S.; Souza, M. O. G.; Bellido, J. D. A.; Assaf, E. M.; Opportus, M.; Reyes, P.; Rangel, M. C. Ethanol Steam Reforming over Rhodium and Cobalt-Based Catalysts: Effect of the Support. *Int. J. Hydrogen Energy* **2012,** *37,* 3213−3224.
49. Roh, H.-S.; Wang, Y.; King, D. L. Selective Production of H_2 from Ethanol at Low Temperatures over Rh/ZrO_2CeO_2 Catalysts. *Top. Catal.* **2008,** *49,* 32−37.
50. Chen, Y.; Shao, Z.; Xu, N. Ethanol Steam Reforming over Pt Catalysts Supported on $Ce_xZr_{1-x}O_2$ Prepared Via a Glycine Nitrate Process. *Energy Fuels* **2008,** *22,* 1873−1879.
51. Goula, M. A.; Kontou, S. K.; Tsiakaras, P. E. Hydrogen Production by Ethanol Steam Reforming over Commercial Pd/γ-Al_2O_3 Catalyst. *Appl. Catal. B: Environ.* **2004,** *49,* 135−144.
52. Galvita, V. V.; Semin, G. L.; Belyaev, V. D.; Semikolenov, V. A.; Tsikaras, P.; Sobyanin, V. A. Synthesis Gas Production by Steam Reforming of Ethanol. *Appl. Catal. A: Gen.* **2001,** *220,* 123−127.
53. Galvita, V. V.; Belyaev, V. D.; Semikolenov, V. A.; Tsikaras, P.; Frumin, A.; Sobyanin, V. A. Ethanol Decomposition over Pd-Based Catalyst in the Presence of Steam. *React. Kinet. Catal. Lett.* **2002,** *76,* 343−351.
54. Dömök, M.; Baán, K.; Kecskés, T.; Erdohelyi, A. Promoting Mechanism of Potassium in the Reforming of Ethanol on Pt/Al_2O_3 Catalyst. *Catal. Lett.* **2008,** *126,* 49−57.
55. De Lima, S.; da Silva, A. M.; Jacobs, G.; Davis, B. H.; Mattos, L. V.; Noronha, F. B. New Approaches to Improving Catalyst Stability over Pt/Ceria during Ethanol Steam Reforming: Sn Addition and CO_2 Co-Feeding. *Appl. Catal. B: Environ.* **2010,** *96,* 387−398.
56. Yaseneva, P.; PAvlova, S.; Sadykov, V.; Alikina, G.; Lykashevich, A.; Rogov, V.; Belochapkine; Ross, J. Combinatorial Approach to the Preparation and Characterization of Catalysts for Biomass Steam Reforming into Syngas. *Catal. Today* **2008,** *137,* 23−28.
57. Kaspar, J.; Fornasiero, P. Catalysis by Ceria and Related Materials. In Trovarelli, A., Ed., Vol. 2; Imperial College Press: London, UK, 2002; p 217.
58. Can, F.; Le Valant, A.; Bion, N.; Epron, F.; Duprez, D. New Active and Selective Rh−REO_x−Al_2O_3 Catalysts for Ethanol Steam Reforming. *J. Phys. Chem. C* **2008,** *112,* 14145−14153.
59. Le Valant, A.; Can, F.; Bion, N.; Duprez, D.; Epron, F. Hydrogen Production from Raw Bioethanol Steam Reforming: Optimization of Catalyst Composition with Improved Stability Against Various Impurities. *Int. J. Hydrogen Energy* **2010,** *35,* 5015−5020.
60. Le Valant, A.; Garron, A.; Bion, N.; Epron, F.; Duprez, D. Hydrogen Production from Raw Bioethanol over Rh/$MgAl_2O_4$ Catalyst. *Catal. Today* **2008,** *138,* 169−174.
61. Bshish, A.; Yahkkob, Z.; Narayanan, B.; Ramakrishnan, R.; Ebshish, A. Steam Reforming of Ethanol for Hydrogen Production. *Rev. Chem. Papers* **2011,** *65* (3), 251−266.
62. Li, M. S.; Wang, X. D.; Li, S. R.; Wang, S. P.; Ma, X. B. Hydrogen Production from Ethanol Steam Reforming over Nickel Based Catalyst Derived from Ni/Mg/Al Hydrotalcite-Like Compounds. *Int. J. Hydrogen Energy* **2010,** *35* (13), 6699−6708.
63. Wang, W. Production of Hydrogen by Steam Reforming of Bioethanol over Copper−Nickel Bimetallic Catalysts. *Int. J. Green Energy* **2009,** *6* (1), 92−103.
64. Yang, Y.; Ma, J.; Wu, F. Production of Hydrogen by Steam Reforming of Ethanol over a Ni/ZnO Catalyst. *Int. J. Hydrogen Energy* **2006,** *31* (7), 877−882.
65. Frusteri, F.; Freni, S.; Chiodo, V.; Spadaro, L.; Blasi, O. Di; Bonura, G.; Cavallaro, S. Steam Reforming of Bio-Ethanol on Alkali-Doped Ni/MgO Catalysts: Hydrogen Production for MC Fuel Cell. *Appl. Catal. A: Gen.* **2004,** *270,* 1−7.
66. Kugai, J.; Velu, S.; Song, C. Low-Temperature Reforming of Ethanol over CeO_2-Supported Ni−Rh Bimetallic Catalysts for Hydrogen Production. *Catal. Lett.* **2005,** *101* (3−4), 255−264.
67. Youn, M. H.; Seo, J. G.; Kim, P.; Kim, J. J.; Lee, H.; Song, I. K. Hydrogen Production by Auto-Thermal Reforming of Ethanol over Ni/γ-Al_2O_3 Catalysts: Effect of Second Metal Addition. *J. Power Sources* **2006,** *162,* 1270−1274.
68. Youn, M. H.; Seo, J. G.; Kim, P.; Song, I. K. Role and Effect of Molybdenum on the Performance of Ni−Mo/γ-Al_2O_3 Catalysts in the Hydrogen Production by Auto-Thermal Reforming of Ethanol. *J. Mol. Catal. A: Chem.* **2007,** *261,* 276−281.
69. Vizcaino, A. J.; Arena, P.; Baronetti, G.; Carrero, A.; Calles, J. A.; Laborde, M. A.; Amadeo, N. Ethanol Steam Reforming on Ni/Al_2O_3 Catalysts: Effect of Magnesium Addition. *Int. J. Hydrogen Energy* **2008,** *33* (13), 3489−3492.
70. Vizcaino, A. J.; Carrero, A.; Calles, J. A. Ethanol Steam Reforming on Mg- and Ca-Modified Cu-Ni/SBA-15 Catalysts. *Catal. Today* **2009,** *146* (1−2), 63−70.
71. Carrero, A.; Calles, J. A.; Vizcaino, A. J. Effect of Mg and Ca Addition on Coke Deposition over Cu−Ni/SiO_2 Catalysts for Ethanol Steam Reforming. *Chem. Eng. J.* **2010,** *63* (3), 395−402.
72. Zhang, C.; Li, S.; Li, M.; Wang, S.; Ma, X.; Gong, J. Enhanced Oxygen Mobility and Reactivity for Ethanol Steam Reforming. *AlChE J.* **2012,** *58* (2), 516−525.
73. Choong, C. K. S.; Huang, L.; Zhong, Z.; Jianyi, L.; Hong, L.; Chen, L. Effect of Calcium Addition on Catalytic Ethanol Steam Reforming of Ni/Al_2O_3. II. Acidity/Basicity, Water Adsorption and Catalytic Activity. *Appl. Catal. A: Gen.* **2011,** *407* (1−2), 155−162.
74. Urasaki, K.; Tokunaga, K.; Sekine, Y.; Matsukata, M.; Kikuchi, E. Production of Hydrogen by Steam Reforming of Ethanol over Cobalt and Nickel Catalysts Supported on Perovskite-Type Oxides. *Catal. Commun.* **2008,** *9* (5), 600−604.
75. Chen, S. Q.; Li, Y. D.; Liu, Y.; Bai, X. Regenerable and Durable Catalyst for Hydrogen Production from Ethanol Steam Reforming. *Int. J. Hydrogen Energy* **2011,** *36* (10), 5849−5856.
76. Busca, G.; Constantin, U.; Montanari, T.; Ramis, G.; Resini, C.; Sisani, M. Nickel Versus Cobalt Catalysts for Hydrogen

Production by Ethanol Steam Reforming: Ni–Co–Zn–Al Catalysts from Hydrotalcite-Like Precursors. *Int. J. Hydrogen Energy* **2010,** *35* (11), 5356–5366.
77. Yu, X.; Chu, W.; Wang, N.; Ma, F. Hydrogen Production by Ethanol Steam Reforming on NiCuMgAl Catalysts Derived from Hydrotalcite-Like Precursors. *Catal. Lett.* **2011,** *141* (8), 1228–1236.
78. Zhang, L.; Liu, J.; Li, W.; Guo, C.; Zhang, J. Ethanol Steam Reforming over Ni–Cu/Al_2O_3–MyOz (M = Si, La, Mg and Zn) Catalysts. *J. Nat. Gas Chem.* **2009,** *18* (1), 55–65.
79. Chen, L.; Lin, S. D. The Ethanol Steam Reforming over Cu–Ni/SiO_2 Catalysts: Effect of Cu/Ni Ratio. *Appl. Catal. B: Environ.* **2011b,** *106* (3–4), 639–649.
80. Therdthianwong, S.; Srisiriwat, N.; Therdthianwong, A.; Croiset, E. Reforming of Bioethanol over Ni/Al_2O_3 and Ni/$CeZrO_2$/Al_2O_3 Catalysts in Supercritical Water for Hydrogen Production. *Int. J. Hydrogen Energy* **2011,** *36* (4), 2877–2886.
81. Li, S.; Li, M.; Zhang, C.; Wang, S.; Ma, X.; Gong, J. Steam Reforming of Ethanol over Ni/ZrO_2 Catalysts: Effect of Support on Product Distribution. *Int. J. Hydrogen Energy* **2012,** *37* (3), 2940–2949.
82. Vizcaino, A. J.; Lindo, M.; Carrero, A.; Calles, J. A. Hydrogen Production by Steam Reforming of Ethanol Using Ni Catalysts Based on Ternary Mixed Oxides Prepared by Coprecipitation. *Int. J. Hydrogen Energy* **2012,** *37* (2), 1985–1992.
83. Sengupta, P.; Khan, A.; Zahid, M. A.; Ibrahim, H.; Idem, R. Evaluation of the Catalytic Activity of Various 5Ni/$Ce_{0.5}Zr_{0.33}M_{0.17}O_{2-\delta}$ Catalysts for Hydrogen Production by the Steam Reforming of a Mixture of Oxygenated Hydrocarbons. *Energy Fuels* **2012,** *26* (2), 816–828.
84. Iriondo, A.; Barrio, V. L.; El Doukkali, M.; Cambra, J. F.; Gueemez, M. B.; Requies, J.; Arias, P. L.; Sanchez-Sanchez, M. C.; Navarro, R.; Fierro, J. L. G. *International Journal of Hydrogen Energy* **2012,** *37* (2), 2028–2036.
85. Seelam, P. K.; Huuhtanen, M.; Sapi, A.; Szabo, M.; Kordas, K.; Turpeinen, E.; Toth, G.; Keiski, R. L. CNT-Based Catalysts for H_2 Production by Ethanol Reforming. *Int. J. Hydrogen Energy* **2010,** *35* (22), 12588–12595.
86. Ozkan, G.; Gok, S.; Ozkan, G. Active Carbon-Supported Ni, Ni/Cu and Ni/Cu/Pd Catalysed Steam Reforming of Ethanol for the Production of Hydrogen. *Chem. Eng. J.* **2011,** *171* (3), 1270–1275.
87. Calles, J. A.; Carrero, A.; Vizcaino, A. J. Ce and La Modification of Mesoporous Cu–Ni/SBA-15 Catalysts for Hydrogen Production through Ethanol Steam Reforming. *Microporous and Mesoporous Materials* **2009,** *119* (1–3), 200–207.
88. Inokawa, H.; Nishimoto, S.; Kameshima, Y.; Miyake, M. Promotion of H_2 Production from Ethanol Steam Reforming by Zeolite Basicity. *Int. J. Hydrogen Energy* **2011,** *36* (23), 15195–15202.
89. Kwak, Byeong Sub; Lee, Jun Su; Lee, Jun Sung; Choi, Byung-Hyun; Ji, Mi Jung; Kang, Misook *Applied Energy* **2011,** *88* (12), 4366–4375.
90. Haga, F.; Nakajima, T.; Miya, H.; Mishima, S. Catalytic Properties of Supported Cobalt Catalysts for Steam Reforming of Ethanol. *Catal. Lett.* **1997,** *48,* 223–227.
91. Cavallaro, S.; Mondello, N.; Freni, S. Hydrogen Produced from Ethanol for Internal Reforming Molten Carbonate Fuel Cell. *J. Power Sources* **2001,** *102,* 198–204.
92. Llorca, J.; Homs, N.; Sales, J.; Ramírez de la Piscina, P. Efficient Production of Hydrogen over Supported Cobalt Catalysts from Ethanol Steam Reforming. *J. Catal.* **2002,** *209,* 306–317.
93. Kaddouri, A.; Mazzocchia, C. A Study of the Influence of the Synthesis Conditions Upon The Catalytic Properties of Co/SiO_2 or Co/Al_2O_3 Catalysts used for Ethanol Steam Reforming. *Catal. Commun.* **2004,** *5,* 339–345.
94. Batista, M. S.; Santos, R. K. S.; Assaf, E. M.; Assaf, J. M.; Ticianelli, E. A. High Efficiency Steam Reforming of Ethanol by Cobalt-Based Catalysts. *J. Power Sources* **2004,** *134,* 27–32.
95. Llorca, J.; Dalmon, J. A.; Ramírez de la Piscina, P.; Homs, N. In Situ Magnetic Characterisation of Supported Cobalt Catalysts under Steam-Reforming of Ethanol. *Appl. Catal. A: Gen.* **2003,** *243,* 261.
96. Llorca, J.; Ramírez de la Piscina, P.; Dalmon, J. A.; Sales, J.; Homs, N. CO-Free Hydrogen from Steam-Reforming of Bioethanol over ZnO-Supported Cobalt Catalysts: Effect of the Metallic Precursor. *Appl. Catal. B: Environ.* **2003,** *43,* 355–369.
97. Llorca, J.; Homs, N.; Ramírez de la Piscina, P. In Situ DRIFT-Mass Spectrometry Study of the Ethanol Steam-Reforming Reaction over Carbonyl-Derived Co/ZnO Catalysts. *J. Catal.* **2004,** *227,* 556.
98. Martono, E.; Hyman, M. P.; Vohs, J. M. Reaction Pathways for Ethanol on Model Co/ZnO (0001) Catalysts. *Phys. Chem. Chem. Phys.* **2011,** *13,* 9880–9886.
99. Karim, A. M.; Su, Y.; Engelhard, M. H.; King, D. L.; Wang, Y. Catalytic Roles of Co^0 and Co^{2+} During Steam Reforming of Ethanol on Co/MgO Catalysts. *ACS Catal.* **2011,** *1,* 279–286.
100. Hyman, M. P.; Vohs, J. M. Reaction of Ethanol on Oxidized and Metallic Cobalt Surfaces. *Surf. Sci.* **2011,** *605,* 383–389.
101. Sahoo, D. R.; Vajpai, S.; Patel, S.; Pant, K. K. Kinetic Modeling of Steam Reforming of Ethanol for the Production of Hydrogen over Co/Al_2O_3 Catalyst. *Chem. Eng. J.* **2007,** *125,* 139–147.
102. Karim, A. M.; Su, Y.; Sun, J.; Yang, C.; Strohm, J. J.; King, D. L.; Wang, Y. A Comparative Study between Co and Rh for Steam Reforming of Ethanol. *Appl. Catal. B: Environ.* **2010,** *96,* 441–448.
103. Song, H.; Zhang, L.; Ozkan, U. S. Investigation of the reaction Network in Ethanol Steam Reforming over Supported Cobalt Catalysts. *Ind. Eng. Chem. Res.* **2010,** *49,* 8984–8989.
104. Llorca, J.; Ramírez de la Piscina, P.; Dalmon, J. A.; Homs, N. Transformation of Co_3O_4 during Ethanol Steam-Re-forming. Activation Process for Hydrogen Production. *Chem. Mater.* **2004,** *16,* 3573–3578.
105. Bayram, B.; Soykal, I. I.; von Deak, D.; Miller, J. T.; Ozkan. U.S. Ethanol Steam Reforming over Co-Based Catalysts: Investigation of Cobalt Coordination Environment under Reaction Conditions. *J. Catal.* **2011,** *284, 77*–89.
106. Lin, S. S. Y.; Kim, D. H.; Ha, S. Y. Metallic Phases of Cobalt-Based Catalysts in Ethanol Steam Reforming: The Effect of Cerium Oxide. *Appl. Catal. A: Gen.* **2009,** *355,* 69–77.
107. Bichon, P.; Haugom, G.; Venvik, H. J.; Holmen, A.; Blekkan, E. A. Steam Reforming of Ethanol over Supported Co and Ni Catalysts. *Top. Catal.* **2008,** *49,* 38–45.
108. Wang, H.; Liu, Y.; Wang, L.; Qin, Y. N. Study of the Carbon Deposition in Steam Reforming of Ethanol Over Co/CeO_2 Catalyst. *Chem. Eng. J.* **2008,** *145,* 25–31.
109. Llorca, J.; Homs, N.; Sales, J.; Fierro, J. L. G.; Ramírez de la Piscina, P. Effect of Sodium Addition on the Performance of Co–ZnO-Based Catalysts for Hydrogen Production from Bioethanol. *J. Catal.* **2004,** *222,* 470–480.
110. Kim, K. S.; Seo, H. R.; Lee, S. Y.; Ahn, J. G.; Shin, W. C.; Lee, Y. K. TPR and EXAFS Studies on Na-Promoted Co/ZnO Catalysts for Ethanol Steam Reforming. *Top. Catal.* **2010,** *53,* 615–620.
111. Galetti, A. E.; Gómez, M. F.; Arrua, L. A.; Marchi, A. J.; Abelló, M. C. Study of CuCoZnAl Oxide as Catalyst for the Hydrogen Production from Ethanol Reforming. *Catal. Commun.* **2008,** *9,* 1201–1208.
112. Torres, J. A.; Llorca, J.; Casanovas, A.; Domínguez, M.; Salvadó, J.; Montané, D. Mulitfactorial Design Analysis of Ni/La_2O_3–Al_2O_3, and Fe- and Mn-Promoted Co/ZnO Catalysts. *J. Power Sources* **2007,** *169,* 158–166.
113. Casanovas, A.; de Leitenburg, C.; Trovarelli, A.; Llorca, J. Ethanol Steam Reforming and Water Gas Shift Reaction over Co–Mn/ZnO Catalysts. *Chem. Eng. J.* **2009,** *154,* 267–273.
114. Casanovas, A.; Roig, M.; de Leitenburg, C.; Trovarelli, A.; Llorca, J. Ethanol Steam Reforming and Water Gas Shift over

Co/ZnO Catalytic Honeycombs Doped with Fe, Ni, Cu, Cr and Na. *Int. J. Hydrogen Energy* **2010,** *35,* 7690−7698.
115. Sekine, Y.; Kazama, A.; Izutsu, Y.; Matsukata, M.; Kikuchi, E. Steam Reforming of Ethanol over Cobalt Catalysts Modified with Small Amount of Iron. *Catal. Lett.* **2009,** *132,* 329−334.
116. Kazama, A.; Sekine, Y.; Oyama, K.; Matsukata, M.; Kikuchi, E. Promoting Effect of Small Amounts of Fe Addition onto Co Catalyst Supported on α-Al_2O_3 for Steam Reforming of Ethanol. *Appl. Catal. A: Gen.* **2010,** *383,* 96−101.
117. Song, H.; Ozkan, U. S. Ethanol Steam Reforming over Co-Based Catalysts: Role of Oxygen Mobility. *J. Catal.* **2009,** *261,* 66−74.
118. Song, H.; Bao, X.; Hadad, C. M.; Ozkan, U. S. Adsorption/Desorption Behavior of Ethanol Steam Reforming Reactants and Intermediates over Supported Cobalt Catalysts. *Catal. Lett.* **2011,** *141,* 43−54.
119. De Lima, S. M.; da Silva, A. M.; da Costa, L. O. O.; Graham, U. M.; Jacobs, G.; Davis, B. H.; Mattos, L. V.; Noronha, F. B. Study of Catalyst Deactivation and Reaction Mechanism of Steam Reforming, Partial Oxidation, and Oxidative Steam Reforming of Ethanol over Co/CeO_2 Catalyst. *J. Catal.* **2009,** *268,* 268−281.
120. Avila-Neto, C. N.; Liberatori, J. W. C.; da Silva, A. M.; Zanchet, D.; Hori, C. E.; Noronha, F. B.; Bueno, J. M. C. Understanding the Stability of Co-Supported Catalysts During Ethanol Reforming as Addressed by In Situ Temperature and Spatial Resolved XAFS Analysis. *J. Catal.* **2012,** *287,* 124−137.
121. Rybak, P.; Tomaszewska, B.; Machocki, A.; Grzegorczyk, W.; Denis, A. Conversion of Ethanol over Supported Cobalt Oxide Catalysts. *Catal. Today* **2011,** *176,* 14−20.
122. Lebarbier, V. M.; Karim, A. M.; Engelhard, M. H.; Wu, Y.; Xu, B. Q.; Petersen, E. J.; Datye, A. K.; Wang, Y. The Effect of Zinc Addition on the Oxidation State of Cobalt in Co/ZrO_2 Catalysts. *ChemSusChem* **2011,** *4,* 1679−1684.
123. Song, H.; Ozkan, U. S. Changing the Oxygen Mobility in Co/Ceria Catalysts by Ca Incorporation: Implications for Ethanol Steam Reforming. *J. Phys. Chem. A* **2010,** *114,* 3796−3801.
124. Lin, S. S. Y.; Daimon, H.; Ha, S. Y. Co/CeO_2−ZrO_2 Catalysts Prepared by Impregnation and Coprecipitation for Ethanol Steam Reforming. *Appl. Catal. A: Gen.* **2009,** *366,* 252−261.
125. Song, H.; Bing, T.; Ozkan, U. S. Novel Synthesis Techniques for Preparation of Co/CeO_2 as Ethanol Steam Reforming Catalysts. *Catal. Lett.* **2009,** *132,* 422−429.
126. Benito, M.; Padilla, R.; Serrano-Lotina, A.; Rodríguez, L.; Brey, J. J.; Daza, L. The Role of Surface Reactions on the Active and Selective Catalyst Design for Bioethanol Steam Reforming. *J. Power Sources* **2009,** *192,* 158−164.
127. Profeti, L. P. R.; Luciene, P. R.; Ticianelli, E. A.; Edson, A.; Assaf, E. M. Production of Hydrogen by Ethanol Steam Reforming on Co/Al_2O_3 Catalysts: Effect of Addition of Small Quantities of Noble Metals. *J. Power Sources* **2008,** *175,* 482−489.
128. Profeti, L. P. R.; Ticianelli, E. A.; Assaf, E. M. Ethanol Steam Reforming for Production of Hydrogen on Magnesium Aluminate-Supported Cobalt Catalysts Promoted by Noble Metals. *Appl. Catal. A: Gen.* **2009,** *360,* 17−25.
129. Contreras, J. L.; Salmones, J.; García, L. A.; Ponce, A.; Zeifert, B.; Fuentes, G. A. Hydrogen Production by Ethanol Steam Reforming over Co-Hydrotalcites Having Basic Sites. *J. New Mater. Electrochem. Systems* **2008,** *11,* 109−117.
130. Contreras, J. L.; Ortiz, M. A.; Fuentes, G. A.; Luna, R.; Salmones, J.; Zeifert, N.; Nuno, L.; Vázquez, A. Tungsten Effect over Co-Hydrotalcite Catalysts to Produce Hydrogen from Bio-Ethanol. *J. New Mater. Electrochem. Systems* **2010,** *13,* 253−259.
131. He, L.; Bernstsen, H.; Ochoa-Fernández, E.; Walmsley, J. C.; Blekkan, E. A.; Chen, D. Co−Ni Catalysts Derived from Hydrotalcite-Like Materials for Hydrogen Production by Ethanol Steam Reforming. *Top. Catal.* **2009,** *52,* 206−217.
132. Lucredio, A. F.; Bellido, J. A.; Assaf, E. M. Cobalt Catalysts Derived from Hydrotalcite-Type Precursors Applied to Steam Reforming of Ethanol. *Catal. Commun.* **2011,** *12,* 1286−1290.
133. Espinal, R.; Taboada, E.; Molins, E.; Chimentao, R. J.; Medina, F.; Llorca, J. Cobalt Hydrotalcite for the Steam Reforming of Ethanol with Scarce Carbon Production. *RSC Adv.* **2012,** *2,* 2946−2956.
134. Da Costa-Serra, J. F.; Chica, A. Bioethanol Steam Reforming on Co/ITQ-18 Catalyst: Effect of the Crystalline Structure of the Delaminated Zeolite ITQ-18. *Int. J. Hydrogen Energy* **2011,** *36,* 3862−3869.
135. Espinal, R.; Taboada, E.; Molins, E.; Chimentao, R. J.; Medina, F.; Llorca, J. Cobalt Hydrotalcites as Catalysts for Bioethanol Steam Reforming. The Promoting Effect of Potassium on Catalyst Activity and Long-Term Stability. *Appl. Catal. B: Environ.* **2012,** *127,* 59−67.
136. Domínguez, M.; Taboada, E.; Idriss, H.; Molins, E.; Llorca, J. Fast and Efficient Hydrogen Generation Catalyzed by Cobalt Talc Nanolayers Dispersed in Silica Aerogel. *J. Mater. Chem.* **2010,** *20,* 4875−4883.
137. Casanovas, A.; Saint-Gerons, M.; Griffon, F.; Llorca, J. Autothermal Generation of Hydrogen from Ethanol in a Microreactor. *Int. J. Hydrogen Energy* **2008,** *33,* 1827−1833.
138. Domínguez, M.; Taboada, E.; Molins, E.; Llorca, J. Co−SiO_2 Aerogel-Coated Catalytic Walls for the Generation of Hydrogen. *Catal. Today* **2008,** *138,* 193−197.
139. Nedyalkova, R.; Casanovas, A.; Llorca, J.; Montané, D. Electrophoretic Deposition of Co−Me/ZnO (Me = Mn, Fe) Ethanol Steam Reforming Catalysts on Stainless Steel Plates. *Int. J. Hydrogen Energy* **2009,** *34,* 2591−2599.
140. Yee, A.; Morrison, S. J.; Idriss, H. Study of the Reactions of Ethanol on CeO_2 and Pd/CeO_2 by Steady State Reactions, Temperature Programmed Desorption, and In Situ FT-IR. *J. Catal.* **1999,** *186,* 279−295.
141. Yee, A.; Morrison, S. J.; Idriss, H. A Study of Ethanol Reactions over Pt/CeO_2 by Temperature-Programmed Desorption and In Situ FT-IR Spectroscopy: Evidence of Benzene Formation. *J. Catal.* **2000,** *191,* 30−45.
142. Yee, A.; Morrison, S. J.; Idriss, H. The Reactions of Ethanol over M/CeO_2 Catalysts. Evidence of Carbon−Carbon Bond Dissociation at Low Temperatures over Rh/CeO_2. *Catal. Today* **2000,** *63,* 327−335.
143. Idriss, H.; Seebauer, E. G. Reactions of Ethanol over Metal Oxides. *J. Mol. Catal. A: Chem.* **2000,** *152,* 201−212.
144. Sheng, P.-Y.; Yee, A.; Bowmaker, G. A.; Idriss, H. H_2 Production from Ethanol over Rh−Pt/CeO_2 Catalysts: The Role of Rh for the Efficient Dissociation of the Carbon−Carbon Bond. *J. Catal.* **2002,** *208,* 393−403.
145. Mattos, L. V.; Noronha, F. B. Partial Oxidation of Ethanol on Supported Pt Catalysts. *J. Power Sources* **2005,** *145,* 10−15.
146. Mattos, L. V.; Noronha, F. B. Hydrogen Production for Fuel Cell Applications by Ethanol Partial Oxidation on Pt/CeO_2 Catalysts: the Effect of the Reaction Conditions and Reaction Mechanism. *J. Catal.* **2005,** *233,* 453−463.
147. Mattos, L. V.; Noronha, F. B. The Influence of the Nature of the Metal on the Performance of Cerium Oxide Supported Catalysts in the Partial Oxidation of Ethanol. *J. Power Sources* **2005,** *152,* 50−59.
148. Silva, A. M.; Barandas, A. P. M. G.; Costa, L. O. O.; Borges, L. E. P.; Mattos, L. V.; Noronha, F. B. Effect of the Metal Nature on the Reaction Mechanism of the Partial Oxidation of Ethanol over CeO_2-Supported Pt and Rh Catalysts. *Catal. Today* **2008,** *133*−*135*, 755−761. 27.
149. Olivera Fraile, R.; Cortés Corberán, V. Partial Oxidation of Ethanol to Hydrogen on Pt/CeO_2: the Role of Catalyst, Abstracts EuropaCat IX, Catalysis for a Sustainable World, Salamanca (Spain), 2009; P8−P96.

150. Bi, J.-L.; Hsu, S.-N.; Yeh, C.-T.; Wang, C. B. Low-Temperature Mild Partial Oxidation of Ethanol over Supported Platinum Catalysts. *Catal. Today* **2007,** *129,* 330–335.
151. Hsu, S. N.; Bi, J. L.; Wang, W. F.; Yeh, C. T.; Wang, C. B. Low-Temperature Partial Oxidation of Ethanol over Supported Platinum Catalysts for Hydrogen Production. *Int. J. Hydrogen Energy* **2008,** *33,* 693–699.
152. Costa, L. O. O.; Vasconcelos, S. M. R.; Pinto, A. L.; Silva, A. M.; Mattos, L. V.; Noronha, F. B.; Borges, L. E. P. Rh/CeO_2 Catalyst Preparation and Characterization for Hydrogen Production from Ethanol Partial Oxidation. *J. Mater. Sci.* **2008,** *43,* 440–449.
153. Cai, W.; Wang, F.; Zhan, E.; Van Veen, A. C.; Mirodatos, C.; Shen, W. Hydrogen Production from Ethanol over Ir/CeO_2 Catalysts: A Comparative Study of Steam Reforming, Partial Oxidation and Oxidative Steam Reforming. *J. Catal.* **2008,** *257,* 96–107.
154. Costa, L. O. O.; Silva, A. M.; Borges, L. E. P.; Mattos, L. V.; Noronha, F. B. Partial Oxidation of Ethanol over Pd/CeO_2 and Pd/Y_2O_3 Catalysts. *Catal. Today* **2008,** *138,* 147–151.
155. Silva, A. M.; Barandas, A. P. M. G.; Costa, L. O. O.; Borges, L. E. P.; Mattos, L. V.; Noronha, F. B. Partial oxidation of ethanol on Ru/Y_2O_3 and Pd/Y_2O_3 catalysts for hydrogen production. *Catal. Today* **2007,** *129,* 297–304.
156. Olivera Fraile, R. *Activity and Stability of Catalysts for Hydrogen Production by Partial Oxidation and Reforming of Ethanol*, PhD Thesis, UAM: Madrid, 2012 (in Spanish).
157. Olivera Fraile, R.; Cortés Corberán, V. *An Insight into the H_2 Production by Partial Oxidation of Ethanol over Pt/CeO_2–ZrO_2: Catalyst Role, Deactivation and Recovery, Book of abstracts 6th World Congress on Oxidation Catalysis;* Lille: France, 2009. poster 3C-1044.
158. Sheng, P.-Y.; Yee, A.; Bowmaker, G. A.; Idriss, H. The Reactions of Ethanol over Au/CeO_2. *Appl. Catal. A: Gen.* **2004,** *261,* 171–181.
159. Silva, A. M.; Duarte de Farias, A. M.; Costa, L. O. O.; Barandas, A. P. M. G.; Mattos, L. V.; Fraga, M. A.; Noronha, F. B. Partial Oxidation and Water–Gas Shift Reaction in an Integrated System for Hydrogen Production from Ethanol. *Appl. Catal. A: Gen.* **2008,** *334,* 179–186.
160. Wang, W.; Wang, Z.; Ding, Y.; Xi, J.; Lu, G. Partial Oxidation of Ethanol to Hydrogen over Ni–Fe Catalysts. *Catal. Lett.* **2002,** *81,* 63–68.
161. Guarido, C. E. M.; Cesar, D. V.; Souza, M. M. V. M.; Schmal, M. Ethanol Reforming and Partial Oxidation with Cu/Nb2O5 Catalyst. *Catal. Today* **2009,** *142,* 252–257.
162. Rodrigues, C. P.; Teixeira, V.; Schmal, M. Partial Oxidation of Ethanol on Cu/Alumina/Cordierite Monolith. *Catal. Commun.* **2009,** *10,* 1697–1701.
163. Rodrigues, C. P.; Teixeira, V.; Schmal, M. Partial Oxidation of Ethanol over Cobalt Oxide Based Cordierite Monolith Catalyst. *Appl. Catal. B: Environ.* **2010,** *96,* 1–9.
164. Rodrigues, C. P.; Schmal, M. Nickel–Alumina Wash Coating on Monoliths for the Partial Oxidation of Ethanol to Hydrogen Production. *Int. J. Hydrogen Energy* **2011,** *36,* 10709–10718.
165. Hickman, D. A.; Schmidt, L. D. Synthesis Gas Formation by Direct Oxidation of Methane over Pt Monoliths. *J. Catal.* **1992,** *138,* 267–282.
166. Salge, J. R.; Deluga, G. A.; Schmidt, L. D. Catalytic Partial Oxidation of Ethanol over Noble Metal Catalysts. *J. Catal.* **2005,** *235,* 69–78.
167. Hebben, N.; Diehm, C.; Deutschmann, O. Catalytic Partial Oxidation of Ethanol on Alumina-Supported Rhodium Catalysts: An Experimental Study. *Appl. Catal. A: Gen.* **2010,** *388,* 225–231.
168. Loganathan, K.; Leclerc, C. A. Partial oxidation of ethanol over platinum and platinum–tin catalysts at millisecond contact times for hydrogen production. *Fuel* **2012,** *96,* 434–439.
169. Fierro, V.; Klouz, V.; Akdim, O.; Mirodatos, C. Oxidative Reforming of Biomass Derived Ethanol for Hydrogen Production in Fuel Cell Applications. *Catal. Today* **2002,** *75,* 141–144.
170. Cavallaro, S.; Chiod, V.; Vita, A.; Freni, S. Hydrogen Production by Auto-Thermal Reforming of Ethanol on Rh/Al_2O_3 Catalyst. *J. Power Sources* **2003,** *123,* 10–16.
171. Vesselli, E.; Comelli, G.; Rosei, R.; Freni, S.; Fustrieri, F.; Cavallaro, S. Ethanol Auto-Thermal Reforming on Rhodium Catalysts and Initial Steps Simulation on Single Crystals Under UHV Conditions. *Appl. Catal. A: Gen.* **2005,** *281,* 139–147.
172. Cai, W.; Wang, F.; Zhan, E.; Van Veen, A. C.; Provendier, H.; Mirodatos, C.; Shen, W. Autothermal Reforming of Ethanol for Hydrogen Production over an Rh/CeO_2 Catalyst. *Catal. Today* **2008,** *138,* 152–156.
173. Gutierrez, A.; Karinen, R.; Airaksinen, S.; Kaila, R.; Krause, A. O. I. Autothermal Reforming of Ethanol on Noble Metal Catalysts. *Int. J. Hydrogen Energy* **2011,** *36,* 8967–8977.
174. De Lima, S.; da Cruz, I. O.; Jacobs, G.; Davis, B. H.; Mattos, L. V.; Noronha, F. B. Steam Reforming, Partial Oxidation, and Oxidative Steam Reforming of Ethanol over Pt/$CeZrO_2$ Catalyst. *J. Catal.* **2008,** *257,* 356–368.
175. Liguras, D. K.; Goundani, K.; Verykios, X. E. Production of Hydrogen for Fuel Cells by Catalytic Partial Oxidation of Ethanol over Structured Ru Catalysts. *Int. J. Hydrogen Energy* **2004,** *29,* 419–427.
176. Casanovas, A.; Llorca, J.; Homs, N.; Fierro, J. L. G.; Ramirez dela Piscina, P. Ethanol Reforming Processes over ZnO-Supported Palladium Catalysts: Effect of Alloy Formation. *J. Mol. Catal. A: Chem.* **2006,** *250,* 44–49.
177. Chen, H.; Yu, H.; Tang, Y.; Pan, M.; Yang, G.; Peng, F.; Wang, H.; Yang, J. Hydrogen Production via Autothermal Reforming of Ethanol over Noble Metal Catalysts Supported on Oxides. *J. Nat. Gas Chem.* **2009,** *18,* 191–198.
178. Chen, H.; Yu, H.; Yang, G.; Peng, F.; Wang, H.; Yang, J. Auto-Thermal Ethanol Micro-Reformer with a Structural Ir/La_2O_3/ZrO_2 Catalyst for Hydrogen Production. *Chem. Eng. J.* **2011,** *167,* 322–327.
179. Liguras, D. K.; Goundani, K.; Verykios, X. E. Production of Hydrogen for Fuel Cells by Catalytic Partial Oxidation of Ethanol over Structured Ni Catalysts. *J. Power Sources* **2004,** *130,* 30–37.
180. Frusteri, F.; Freni, S.; Chiodo, V.; Donato, S.; Bonura, G.; Bonura, G.; Cavallaro, S. Steam and Auto-Thermal Reforming of Bio-Ethanol over MgO and CeO_2 Ni Supported Catalysts. *Int. J. Hydrogen Energy* **2006,** *31,* 2193–2199.
181. Sun, G. B.; Hidajat, K.; Wu, X. S.; Kawi, S. A Crucial Role of Surface Oxygen Mobility on Nanocrystalline Y_2O_3 Support for Oxidative Steam Reforming of Ethanol to Hydrogen over Ni/Y_2O_3 Catalysts. *Appl. Catal. B: Environ.* **2008,** *81,* 303–312.
182. Youn, M. H.; Seo, J. G.; Jung, J. C.; Chung, J. S.; Song, I. K. Support Modification of Supported Nickel Catalysts for Hydrogen Production by Auto-thermal Reforming of Ethanol. *Catal. Surv. Asia* **2010,** *14,* 55–63. and publications by the authors referred therein.
183. Youn, M. H.; Jung, J. C.; Lee, H.; Bang, Y.; Chung, J. S.; Song, I. K. Hydrogen Production by Auto-Thermal Reforming of Ethanol over Nickel Catalysts Supported on Metal Oxides: Effect of Support Acidity. *Appl. Catal. B: Environ.* **2010,** *98,* 57–64.
184. Kugai, J.; Velu, S.; Song, C.; Engelhard, M. H.; Chin, Y.-H. Effects of Nanocrystalline CeO_2 Supports on the Properties and Performance of Ni–Rh Bimetallic Catalyst for Oxidative Steam Reforming of Ethanol. *J. Catal.* **2006,** *238,* 430–440.
185. Fierro, V.; Akdim, O.; Mirodatos, C. On-Board Hydrogen Production in a Hybrid Electric Vehicle by Bio-Ethanol Oxidative Steam Reforming over Ni and Noble Metal Based Catalysts. *Green Chem.* **2003,** *5,* 20–24.
186. Klouz, V.; Fierro, V.; Denton, P.; Katz, H.; Lisse, J. P.; Bouvot-Mauduit, S.; Mirodatos, C. Ethanol Reforming for Hydrogen

Production in a Hybrid Electric Vehicle: Process Optimization. *J. Power Sci.* **2002,** *105,* 26−34.
187. Fierro, V.; Akdim, O.; Provendier, H.; Mirodatos, C. Ethanol Oxidative Reforming over Ni-Based Catalysts. *J. Power Sources* **2005,** *145,* 659−666.
188. Andonova, S.; de Ávila, C. N.; Arishtirova, K.; Bueno, J. M. C.; Damyanova, S. Structure and Redox Properties of Co Promoted Ni/Al_2O_3 Catalysts for Oxidative Steam Reforming of Ethanol. *Appl. Catal. B: Environ.* **2011,** *105,* 346−360.
189. Huang, L.; Xie, J.; Chen, R.; Chu, D.; Hsu, A. T. Fe Promoted $Ni-Ce/Al_2O_3$ in Auto-Thermal Reforming of Ethanol for Hydrogen Production. *Catal. Lett.* **2009,** *130,* 432−439.
190. Pirez, C.; Capron, M.; Jobic, H.; Dumeignil, F.; Jalowiecki-Duhamel, L. Highly Efficient and Stable $CeNiH_ZO_Y$ Nano-Oxyhydride Catalyst for H_2 Production from Ethanol at Room Temperature. *Angew. Chem. Int. Ed.* **2011,** *50,* 10193−10197.
191. Pereira, E. B.; Homs, N.; Martí, S.; Fierro, J. L. G.; Ramírez de la Piscina, P. Oxidative steam-reforming of ethanol over Co/SiO_2, $Co-Rh/SiO_2$ and $Co-Ru/SiO_2$ catalysts: Catalytic behavior and deactivation/regeneration processes. *J. Catal.* **2008,** *257,* 206−214.
192. Da Silva, A. M.; de Souza, K. R.; Mattos, L. V.; Jacobs, G.; Davis, B. H.; Noronha, F. B. The Effect of Support Reducibility on the Stability of Co/CeO_2 for the Oxidative Steam Reforming of Ethanol. *Catal. Today* **2011,** *164,* 234−239.
193. Da Silva, A. M.; Costa, L. O. O.; Souza, K. R.; Mattos, L. V.; Noronha, F. B. The effect of space time on Co/CeO_2 catalyst deactivation during oxidative steam reforming of ethanol. *Catal. Commun.* **2010,** *11,* 736−740.
194. Da Silva, A. M.; Mattos, L. V.; den Breejen, J. P.; Bitter, J. H.; de Jong, K. P.; Noronha, F. B. Oxidative Steam Reforming of Ethanol over Carbon Nanofiber Supported Co Catalysts. *Catal. Today* **2011,** *164,* 262−267.
195. Velu, S.; Suzuki, K.; Vijayaraj, M.; Barman, S.; Gopinath, C. S. In Situ XPS Investigations of $Cu_{1-x}Ni_xZnAl$-Mixed Metal Oxide Catalysts Used in the Oxidative Reforming of Bio-Ethanol. *Appl. Catal. B: Environ.* **2005,** *55,* 287−299.
196. Huang, L.; Liu, Q.; Chen, R.; Hsu, A. T. Hydrogen Production via Auto-Thermal Reforming of Bio-Ethanol: The Role of Iron in Layered Double Hydroxide-Derived $Ni_{0.35}Mg_{2.65}AlO_{4.5\pm\delta}$ Catalysts. *Appl. Catal. A: Gen.* **2011,** *393,* 302−308.
197. Guil-López, R.; Navarro, R. M.; Peña, M. A.; Fierro, J. L. G. Hydrogen Production by Oxidative Ethanol Reforming on Co, Ni and Cu Ex-Hydrotalcite Catalysts. *Int. J. Hydrogen Energy* **2011,** *36,* 1512−1523.
198. Chen, H.; Yu, H.; Peng, F.; Yang, G.; Wang, H.; Yang, J.; Tang, Y. Autothermal Reforming of Ethanol for Hydrogen Production over Perovskite $LaNiO_3$. *Chem. Eng. J.* **2010,** *160,* 333−339.
199. Huang, L.; Zhang, F.; Wang, N.; Chen, R.; Hsu, A. T. Nickel-Based Perovskite Catalysts with Iron-Doping via Self-Combustion for Hydrogen Production in Auto-Thermal Reforming of Ethanol. *Int. J. Hydrogen Energy* **2012,** *37,* 1272−1279.
200. Gallucci, F.; Basile, A. Pd−Ag Membrane Reactor for Steam Reforming Reactions: A Comparison between Different Fuels. *Int. J. Hydrogen Energy* **2008,** *33,* 1671−1687.
201. Basile, A. Hydrogen Production Using Pd-Based Membrane Reactors for Fuel Cells. *Top. Catal.* **2008,** *51,* 107−122.
202. Mendes, D.; Tosti, S.; Borgognoni, F.; Mendes, A.; Madeira, L. M. Integrated Analysis of a Membrane-Based Process for Hydrogen Production from Ethanol Steam Reforming. *Catal. Today* **2010,** *156,* 107−117.
203. Tosti, S.; Bettinali, L. Diffusion Bonding of Pd−Ag Membranes. *J. Mater. Sci.* **2004,** *39,* 3041−3046.
204. Tosti, S.; Basile, A.; Bettinali, L.; Borgognoni, F.; Chiaravalloti, F.; Gallucci, F. Long-Term Tests of Pd−Ag Thin Wall Permeator Tube. *J. Membr. Sci.* **2006,** *284,* 393−397.
205. Tong, H. D.; Gielens, F. C.; Gardeniers, J. G. E.; Jansen, H. V.; van Rijn, C. J. M.; Elwenspoek, M. C.; Nijdam, W. Microfabricated Palladium−Silver Alloy Membranes and Their Application in Hydrogen Separation. *Ind. Eng. Chem. Res.* **2004,** *43,* 4182−4187.
206. Burkhanov, G. S.; Gorina, N. B.; Kolchugina, N. B.; Roshan, N. R. Palladium-Based Alloy Membranes for Separation of High Purity Hydrogen from Hydrogen-Containing Gas Mixtures. *Platin. Met. Rev.* **2011,** *55,* 3−12.
207. Tosti, S.; Basile, A.; Borgognoni, F.; Capaldo, V.; Cordiner, S.; Di Cave, S.; Gallucci, F.; Rizzello, C.; Santucci, A.; Traversa, E. Low Temperature Ethanol Steam Reforming in a Pd−Ag Membrane Reactor. Part 1: Pt-Based and Ni-Based Catalyst and General Comparison. *J. Membr. Sci.* **2008,** *308,* 258−263.
208. Montané, D.; Bolshak, E.; Abelló, S. Thermodynamic Analysis of Fuel Processors Based on Catalytic-Wall Reactors and Membrane Systems for Ethanol Steam Reforming. *Chem. Eng. J.* **2011,** *175,* 519−533.
209. Gallucci, F.; Van Sint Annaland, M.; Kuipers, J. A. M. Pure Hydrogen Production via Autothermal Reforming of Ethanol in a Fluidized Bed Membrane Reactor: A Simulation Study. *Int. J. Hydrogen Energy* **2010,** *35,* 1659−1668.
210. Gao, H.; Lin, Y. S.; Li, Y.; Zhang, B. Chemical Stability and Its Improvement of Palladium-Based Metallic Membranes. *Ind. Eng. Chem. Res.* **2004,** *43,* 6920−6930.
211. Iulianelli, A.; Basile, A. Hydrogen Production from Ethanol via Inorganic Membrane Reactors Technology: A Review. *Catal. Sci. Technol.* **2011,** *1,* 366−379.
212. Gallucci, F.; Basile, A.; Tosti, S.; Iulianelli, A.; Drioli, E. Methanol and Ethanol Steam Reforming in Membrane Reactors: An Experimental Study. *Int. J. Hydrogen Energy* **2007,** *32,* 1201−1210.
213. Basile, A.; Gallucci, F.; Iulianelli, A.; Tosti, S. CO-Free Hydrogen Production by Ethanol Steam Reforming in a Pd−Ag Membrane Reactor. *Fuel Cells* **2008,** *8,* 62−68.
214. Tosti, S.; Basile, A.; Bettinali, L.; Borgognoni, F.; Gallucci, F.; Rizello, C. Design and Process Study of Pd Membrane Reactors. *Int. J. Hydrogen Energy* **2008,** *33,* 5098−5105.
215. Tosti, S.; Basile, A.; Borgognoni, F.; Capaldo, V.; Cordiner, S.; Di Cave, S.; Gallucci, F.; Rizzello, C.; Santucci, A.; Traversa, E. Low Temperature Ethanol Steam Reforming in a Pd−Ag Membrane Reactor. Part 1: Ru-Based Catalyst. *J. Membr. Sci.* **2008,** *308,* 250−257.
216. Tosti, S.; Basile, A.; Borelli, R.; Borgognoni, F.; Castelli, S.; Fabbricino, M.; Gallucci, F.; Licusati, C. Ethanol Steam Reforming Kinetics of a Pd−Ag Membrane Reactor. *Int. J. Hydrogen Energy* **2009,** *34,* 4747−4754.
217. Tosti, S.; Fabbricino, M.; Moriani, A.; Agatiello, G.; Scudieri, C.; Borgognoni, F.; Santucci, A. Pressure Effect in Ethanol Steam Reforming via Dense Pd-Based Membranes. *J. Membr. Sci.* **2011,** *377,* 65−74.
218. Iulianelli, A.; Longo, T.; Liguori, S.; Seelam, P. K.; Keiski, R. L.; Basile, A. Oxidative Steam Reforming of Ethanol over Ru/Al_2O_3 Catalyst in a Dense Pd−Ag Membrane Reactor to Produce Hydrogen for PEM Fuel Cells. *Int. J. Hydrogen Energy* **2009,** *34,* 8558−8565.
219. Santucci, A.; Annesini, M. C.; Borgognoni, F.; Marrelli, L.; Rega, M.; Tosti, S. Oxidative Steam Reforming over a Pt/Al_2O_3 Catalyst in a Pd-Based Membrane Reactor. *Int. J. Hydrogen Energy* **2011,** *36,* 1503−1511.
220. Iulianelli, A.; Liguori, S.; Calabrò, V.; Pinacci, P.; Basile, A. Partial Oxidation of Ethanol in a Membrane Reactor for High Purity Hydrogen Production. *Int. J. Hydrogen Energy* **2010,** *35,* 12626−12634.
221. Iulianelli, A.; Basile, A. An Experimental Study on Bio-Ethanol Steam Reforming in a Catalytic Membrane Reactor. Part I: Temperature and Sweep-Gas Flow Configuration Effects. *Int. J. Hydrogen Energy* **2010,** *35,* 3170−3177.

222. Iulianelli, A.; Liguori, S.; Longo, T.; Tosti, S.; Pinacci, P.; Basile, A. An Experimental Study on Bio-Ethanol Steam Reforming in a Catalytic Membrane Reactor. Part II: Reaction Pressure, Sweep Factor and WHSV Effects. *Int. J. Hydrogen Energy* **2010,** *35,* 3159–3164.
223. Basile, A.; Pinacci, P.; Iulianelli, A.; Broglia, M.; Drago, F.; Liguori, S.; Longo, T.; Calabrò, V. Ethanol Steam Reforming Reaction in a Porous Stainless Steel Supported Palladium Membrane Reactor. *Int. J. Hydrogen Energy* **2011,** *36,* 2029–2037.
224. Seelam, P. K.; Liguori, S.; Iulianelli, A.; Pinacci, P.; Calabrà, V.; Huuhtanen, M.; Keiski, R.; Piemonte, V.; Tosti, S.; de Falco, M.; Basile, A. Hydrogen Production from Bio-Ethanol Steam Reforming in a Pd/PSS Membrane Reactor. *Catal. Today* **2012,** *193,* 42–48.
225. Lin, W. H.; Hsiao, C. S.; Chang, H. F. Effect of Oxygen Addition on the Hydrogen Production from Ethanol Steam Reforming in a Pd–Ag Membrane Reactor. *J. Membr. Sci.* **2008,** *322,* 360–367.
226. Lin, W. H.; Liu, Y. C.; Chang, H. F. Autothermal Reforming of Ethanol in a Pd–Ag/Ni Composite Membrane Reactor. *Int. J. Hydrogen Energy* **2010,** *35,* 12961–12969.
227. Papadias, D. D.; Lee, S. H. D.; Ferrandon, M.; Ahmed, S. An Analytical and Experimental Investigation of High-Pressure Catalytic Steam Reforming of Ethanol on a Hydrogen Selective Membrane Reactor. *Int. J. Hydrogen Energy* **2010,** *35,* 2004–2017.
228. Domínguez, M.; Taboada, E.; Molins, E.; Llorca, J. Ethanol Steam Reforming at Very Low Temperature over Cobalt Talc in a Membrane Reactor. *Catal. Today* **2012,** *193,* 101–106.
229. López, E.; Divins, N. J.; Llorca, J. Hydrogen Production from Ethanol over Pd–Rh/CeO_2 with a Metallic Membrane Reactor. *Catal. Today* **2012,** *193* (1), 145–150.
230. Yu, C. Y.; Lee, D. W.; Park, S. J.; Lee, K. Y.; Lee, K. H. Ethanol Steam Reforming in a Membrane Reactor with Pt-Impregnated Knudsen Membranes. *Appl. Catal. B: Environ.* **2009,** *86,* 121–126.
231. Yu, C. Y.; Lee, D. W.; Park, S. J.; Lee, K. Y.; Lee, K. H. Study on a Catalytic Membrane Reactor for Hydrogen Production from Ethanol Steam Reforming. *Int. J. Hydrogen Energy* **2009,** *34,* 2947–2954.
232. Lim, H.; Gu, Y.; Oyama, S. T. Reaction of Primary and Secondary Products in a Membrane Reactor: Studies of Ethanol Steam Reforming with a Silica-Alumina Composite Membrane. *J. Membr. Sci.* **2010,** *351,* 149–159.
233. Lim, H.; Gu, Y.; Oyama, S. T. Studies of the Effect of Pressure and Hydrogen Permeance on the Ethanol Steam Reforming Reaction with Palladium- and Silica-Based Membranes. *J. Membr. Sci.* **2012,** *396,* 119–127.
234. Zhu, N.; Dong, X.; Liu, Z.; Zhang, G.; Jin, W.; Xu, N. Toward High-Effective and Sustainable Hydrogen Production: Bio-Ethanol Oxidative Steam Reforming Coupled with Water Splitting in a Thin Tubular Membrane Reactor. *Chem. Comm.* **2012,** *48,* 7137–7139.
235. Kolb, G. *Fuel Processing for Fuel Cells;* Wiley-VCH, 2008.
236. Ehrfeld, W.; Hessel, V.; Löwe, H. *Microreactors: New Technology for Modern Chemistry;* Wiley-VCH, 2000.
237. Palo, D. R.; Dagle, R. A.; Holladay, J. D. Methanol Steam Reforming for Hydrogen Production. *Chem. Rev.* **2007,** *107,* 3992–4021.
238. Llorca, J. Microreactors for the Generation of Hydrogen from Ethanol (chapter 22). In *Handbook of Sustainable Energy;* Lee, W. H., Cho, V. G., Eds.; Nova Science Publishers, 2010; pp. 693–699.
239. Men, Y.; Kolb, G.; Zapf, R.; Hessel, V.; Löwe, H. Ethanol Steam Reforming in a Microchannel Reactor. *Process Saf. Environ. Prot.* **2007,** *85,* 413–418.
240. Görke, O.; Pfeifer, P.; Schubert, K. Kinetic Study of Ethanol Reforming in a Microreactor. *Appl. Catal. A: Gen.* **2009,** *360,* 232–241.
241. Cai, W.; Wang, F.; van Veen, A.; Descorme, C.; Schuurman, Y.; Shen, W.; Mirodatos, C. Hydrogen Production from Ethanol Steam Reforming in a Micro-Channel Reactor. *Int. J. Hydrogen Energy* **2010,** *35,* 1152–1159.
242. Peela, N. R.; Kunzru, D. Steam Reforming of Ethanol in a Microchannel Reactor: Kinetic Study and Reactor Simulation. *Ind. Eng. Chem. Res.* **2011,** *50,* 12881–12894.
243. Domínguez, M.; Cristiano, G.; López, E.; Llorca, J. Ethanol Steam Reforming over Cobalt Talc in a Plate Microreactor. *Chem. Eng. J.* **2011,** *176–177,* 280–285.
244. Rahman, M. A.; García-García, F. R.; Li, K. On-Board H_2 Generation by a Catalytic Hollow Fiber Microreactor for Portable Device Applications. *Catal. Commun.* **2011,** *16,* 128–132.
245. Rahman, M. A.; García-García, F. R.; Li, K. Development of a Catalytic Hollow Fiber Membrane Microreactor as a Microreformer Unit for Automotive Application. *J. Membr. Sci.* **2012,** *390–391,* 68–75.
246. Kolb, G.; Men, Y.; Schelhaas, K. P.; Tiemann, D.; Zapf, R.; Wilhelm, J. Development Work on a Microstructured 50 kW Ethanol Fuel Processor for a Small-Scale Stationary Hydrogen Supply System. *Ind. Eng. Chem. Res.* **2011,** *50,* 2554–2561.
247. Llorca, J.; Casanovas, A.; Trifonov, T.; Rodriguez, A.; Alcubilla, R. First Use of Macroporous Silicon Loaded with Catalyst Film for a Chemical Reaction: A Microreformer for Producing Hydrogen from Ethanol Steam Reforming. *J. Catal.* **2008,** *255,* 228–233.
248. López, E.; Irigoyen, A.; Trifonov, T.; Rodríguez, A.; Llorca, J. A Million-Channel Reformer on a Fingertip: Moving Down the Scale in Hydrogen Production. *Int. J. Hydrogen Energy* **2010,** *35,* 3472–3479.
249. Divins, N. J.; López, E.; Roig, M.; Trifonov, T.; Rodríguez, A.; González de Rivera, F.; Rodríguez, L. I.; Seco, M.; Rossell, O.; Llorca, J. A Million-Channel CO–PrO_x Microreactor on a Fingertip for Fuel Cell Application. *Chem. Eng. J.* **2010,** *167,* 597–602.
250. Carneiro, J.; Berger, R.; Moulijn, J. A.; Mul, G. An Internally Illuminated Monolith Reactor: Pros and Cons Relative to a Slurry Reactor. *Catal. Today* **2009,** *147S,* S324–S329.
251. Du, P.; Carneiro, J. T.; Moulijn, J. A.; Mul, G. A Novel Photocatalytic Monolith Reactor for Multiphase Heterogeneous Photocatalysis. *Appl. Catal. A: Gen.* **2008,** *334,* 119–128.
252. Yang, Y. Z.; Chang, C. H.; Idriss, H. Photo-Catalytic Production of Hydrogen from Ethanol over M/TiO_2 catalysts (M = Pd, Pt or Rh). *Appl. Catal. B: Environ.* **2006,** *67,* 217–222.
253. Kudo, A.; Miseki, Y. Heterogeneous Photocatalyst Materials for Water Splitting. *Chem. Soc. Rev.* **2009,** *38,* 253–278.
254. Luo, N.; Jiang, Z.; Shi, H.; Cao, F.; Xiao, T.; Edwards, P. P. Photo-Catalytic Conversion of Oxygenated Hydrocarbons to Hydrogen over Heteroatom-Doped TiO_2 Catalysts. *Int. J. Hydrogen Energy* **2009,** *34,* 125–129.
255. Karakitsou, K. E.; Verykios, X. E. Effects of Altervalent Cation Doping of TiO_2 on Its Performance as a Photocatalyst for Water Cleavage. *J. Phys. Chem.* **1993,** *1993* (97), 1184–1189.
256. Park, J. H.; Kim, S.; Bard, A. J. Novel Carbon-Doped TiO_2 Nanotube Arrays with High Aspect Ratios for Efficient Solar Water Splitting. *Nano Lett.* **2006,** *6,* 24–28.
257. Daskalaki, V. M.; Antoniadou, M.; Puma, G. L.; Kondarides, D. I.; Lianos, P. Solar Light-Responsive Pt/CdS/TiO_2 Photocatalysts for Hydrogen Production and Simultaneous Degradation of Inorganic or Organic Sacrificial Agents in Wastewater. *Environ. Sci. Technol.* **2010,** *44,* 7200–7205.
258. Dhanalakshmi, K. B.; Latha, S.; Anandan, S.; Maruthamuthu, P. Dye Sensitized Hydrogen Evolution from Water. *Int. J. Hydrogen Energy* **2001,** *26,* 669–674.

259. Fujishima, A.; Honda, K. Electrochemical Photolysis of Water at a Semiconductor Electrode. *Nature* **1972,** *238,* 37−38.
260. Blount, M. C.; Buchholz, J. A.; Falconer, J. L. Photocatalytic Decomposition of Aliphatic Alcohols, Acids and Esters. *J. Catal.* **2001,** *197,* 303−314.
261. Hashimoto, K.; Kawai, T.; Sakata, T. Photocatalytic Reactions of Hydrocarbons and Fossil Fuels with Water. Hydrogen Production and Oxidation. *J. Phys. Chem.* **1984,** *88,* 4083−4088.
262. Kondarides, D. I.; Daskalaki, V. M.; Patsoura, A.; Verykios, X. E. Hydrogen Production by Photo-Induced Reforming of Biomass Components and Derivatives at Ambient Conditions. *Catal. Lett.* **2008,** *122,* 26−32.
263. Bamwenda, G.; Tsubota, S.; Nakamura, T.; Haruta, M. Photo-assisted Hydrogen Production from a Water−Ethanol Solution: A Comparison of Activities of Au−TiO_2 and Pt−TiO_2. *J. Photochem. Photobio. A: Chem.* **1995,** *89,* 177−189.
264. Strataki, N.; Bekiari, V.; Kondarides, D.; Lianos, P. Hydrogen Production by Photocatalytic Alcohol Reforming Employing Highly Efficient Nanocrystalline Titania Films. *Appl. Catal. B: Environ.* **2007,** *77,* 184−189.
265. Strataki, N.; Boukos, N.; Paloukis, F.; Neophytides, S. G.; Lianos, P. Effect of the Conditions of Platinum Deposition on Titania Nanocrystalline Films on the Efficiency of Photocatalytic Oxidation of Ethanol and Production of Hydrogen. *Photochem. Photobio. Sci.* **2009,** *8,* 639−643.
266. Korzhak, A. V.; Ermokhina, N. I.; Stroyuk, A. L.; Bukhtiyarov, V. K.; Raevskaya, A. E.; Litvin, V. I.; Kuchmiy, S. Y.; Ilyin, V. G.; Manorik, P. A. Photocatalytic Hydrogen Evolution over Mesoporous TiO_2/Metal Nanocomposites. *J. Photochem. Photobio. A: Chem.* **2008,** *198,* 126−134.
267. Nadeem, M. A.; Murdoch, M.; Waterhouse, G. I. N.; Metson, J. B.; Keane, M. A.; Llorca, J.; Idriss, H. Photoreaction of Ethanol on Au/TiO_2 Anatase: Comparing the Micro to Nanoparticle Size Activities of the Support for Hydrogen Production. *J. Photochem. Photobio. A: Chem.* **2010,** *216,* 250−255.
268. Murdoch, M.; Waterhouse, G. I. N.; Nadeem, M. A.; Metson, J. B.; Keane, M. A.; Howe, R. F.; Llorca, J.; Idriss, H. The Effect of Gold Loading and Particle Size on Photocatalytic Hydrogen Production from Ethanol over Au/TiO_2. *Nat. Chem.* **2011,** *3,* 489−492.
269. Waterhouse, G. I. N.; Murdoch, M.; Llorca, J.; Idriss, H. Ethanol Photoreaction to Hydrogen over Au/TiO_2 Catalysts. Investigating the Synergistic Effect of Nanoparticles. *Int. J. Nanotechnol.* **2012,** *9,* 1/2.
270. Mizukoshi, Y.; Makise, Y.; Shuto, T.; Hu, J.; Tominaga, A.; Shironita, S.; Tanabe, S. Immobilization of Noble Metal Nanoparticles on the Surface of TiO_2 by the Sonochemical Methods: Photocatalytic Production of Hydrogen from an Aqueous Solution of Ethanol. *Ultrason. Sonochem.* **2007,** *14,* 387−392.
271. Casanovas, A.; Domínguez, M.; Ledesma, C.; Lopez, E.; Llorca, J. Catalytic Walls and Micro-Devices for Generating Hydrogen by low Temperature Steam Reforming of Ethanol. *Catal. Today* **2009,** *143,* 32−37.
272. Peela, N. R.; Kunzru, D. Oxidative Steam Reforming of Ethanol over Rh Based Catalysts in a Micro-Channel Reactor. *Int. J. Hydrogen Energy* **2011,** *36,* 3384−3396.

CHAPTER

8

Biological Hydrogen Production

Víctor Martínez-Merino, María José Gil, Alfonso Cornejo

Dept. Química Aplicada, Universidad Pública de Navarra, Pamplona, Spain

OUTLINE

8.1 Introduction 171

8.2 Dark Fermentation 173
- *8.2.1 Substrate* 175
- *8.2.2 Bioreactor Type* 176
- *8.2.3 Operational Parameters* 177

8.3 Photofermentation 178
- *8.3.1 Substrate* 180
- *8.3.2 Photobioreactor Type* 181
- *8.3.3 Operational Parameters* 182

8.4 Coupled Processes to Dark Fermentation 183
- *8.4.1 Co-cultivation Technologies* 183
- *8.4.2 Sequential Cultivation Technologies* 184

8.5 Biological Water Gas Shift Reaction 185
- *8.5.1 Substrate* 185
- *8.5.2 Reactor Design and Operating Conditions* 186

8.6 Biophotolysis of Water 186
- *8.6.1 Biophotolysis Using Green Algae* 187
  - 8.6.1.1 Substrate 187
  - 8.6.1.2 PhBRs and Operating Conditions 189
- *8.6.2 Biophotolysis Using Cyanobacteria* 190
  - 8.6.2.1 Substrate 191
  - 8.6.2.2 PhBRs and Operating Conditions 193

8.7 Life Cycle Assessment of the Biological H_2 Production 193

8.8 Conclusions 195

Acknowledgments 195

References 195

8.1 INTRODUCTION

Nowadays, the industrial production of hydrogen is mainly based on reforming of natural gas, as well as on coal gasification and water electrolysis[1] that are based on intensive energy processes. Alternatively, the biological production of hydrogen can be developed in processes mostly operated at near-ambient temperature[2] whose feedstocks come from renewable raw materials as well as waste materials.[3] Therefore, biohydrogen can be deemed as a promise for the development of a true environmentally friendly hydrogen economy, and therefore it is the subject of research for many Scientific Centers and Enterprises around the World.[4–9]

Hydrogen is a natural, though transient, fermentation by-product of several wild[2,10] and mutant[7,10] microorganisms. In addition, certain green algae and cyanobacteria (blue–green algae) contain enzymes that can produce hydrogen by splitting water into hydrogen and oxygen if a light source (i.e. sunlight) is provided.[4]

The main processes for the biological production of hydrogen[11] include dark-fermentative (Eqn (8.1)), photofermentative (Eqn (8.2)) processes, microbial water–gas shift (WGS, Eqn (8.3)) and water biophotolysis (Eqn (8.4)). Water biophotolysis is usually named direct or indirect biophotolysis. In the last one, electrons or energy to generate H_2 (Eqn (8.4.2a) or (8.4.2b)) come from the catabolism of compounds obtained from photosynthesis (Eqn (8.5)) and other carbon sources.

$$C_6H_{12}O_6 + 2H_2O \xrightarrow{\text{fermentative bacteria, archaea}} 2CH_3COOH + 2CO_2 + 4H_2 \quad \Delta_r G'^0 = -220.2\ \text{kJ/mol of glucose} \tag{8.1}$$

$$CH_3COOH + 2H_2O + h\nu \xrightarrow{\text{purple bacteria, microalgae}} 2CO_2 + 4H_2$$
$$\Delta_r G'^0 = +96.5\ \text{kJ/mol of acetate} \quad (8.2)$$

$$CO + H_2O \xrightarrow{\text{photosynthetic and fermentative, bacteria, microalgae}} CO_2 + H_2$$
$$\Delta_r G'^0 = -20.0\ \text{kJ/mol of CO} \quad (8.3)$$

$$2H_2O + h\nu \xrightarrow{\text{microalgae, cyanobacteria}} O_2 + 2H_2$$
$$\Delta_r G'^0 = +237.2\ \text{kJ/mol of } H_2O \quad (8.4)$$

$$\text{Steps: } 2H_2O + h\nu \rightarrow O_2 + 4H^+ + 4e^- \quad (8.4.1)$$

$$2H^+ + 2R^- \rightarrow H_2 \quad (8.4.2a)$$

$$N_2 + 8H^+ + 8R^- + ATP \rightarrow H_2 + 2NH_3 \quad (8.4.2b)$$

where $h\nu$ represents the energy from a photon in light, ATP the energy from biochemical sources, R^- represents electron donor species, $C_6H_{12}O_6$ represents glucose, a model compound for sugars, CH_3COOH a model for organic acids, and N_2 a model for nitrogen sources. A more detailed description of the microorganisms can be found in Ref. 12.

$$6H_2O + 6CO_2 + h\nu \rightarrow C_6H_{12}O_6 + 6O_2$$
$$\Delta_r G'^0 = +2873.4\ \text{kJ/mol of glucose} \quad (8.5)$$

The spontaneity of complete oxidation of glucose to CO_2 and H_2 (Eqn (8.6)) is controversial from a thermodynamic point of view:

$$C_6H_{12}O_6 + 6H_2O \rightarrow 6CO_2 + 12H_2$$
$$\Delta_r G'^0 = -27.1\ \text{kJ/mol of glucose} \quad (8.6)$$

Many authors,[1,6] based in a simplified method for the calculation of transformed Gibbs free energies in aqueous solutions, indicated that complete oxidation of glucose was not possible because it was not thermodynamically feasible, $\Delta_r G'^0 = +3.2$ kJ/mol of glucose.[13] However, transformed Gibbs free energies changed with temperature, pressure, pH, and ionic strength (I) mainly, and their values must be indicated in the calculations. Thus, in this work for general energy discussions, we will use calculated $\Delta_r G'^0$ from better estimated and tabulated $\Delta_f G'^0$ [14–16] at 298.15 K, 100 kPa, pH equal to 7.0, $I = 0.25$ M, as well as pMg = 3 for ATP, with CO_2 and H_2 in gas phase. At these conditions, the transformed Gibbs free energy for the complete oxidation of glucose in aqueous solution can be estimated as −27.1 kJ/mol. Obviously, both energy data (+3.2 and −27.1 kJ/mol) lead to opposite conclusions about the spontaneity of the process represented by Eqn (8.6) but anyway both values are low for Eqn (8.6). Therefore, it can be concluded that complete oxidation of glucose will need energy in the nature because of the intrinsic inefficiency of the metabolic pathways in transforming the energy that is estimated in a 50%.[17] Similarly, the G'^0 values for the partial oxidation of glucose to acetic acid (Eqn (8.1)) were again slightly different for both methods ($\Delta_r G'^0 = -220.2$ kJ/mol instead of $\Delta_r G'^0 = -206.3$ kJ/mol[13]).

Dark fermentations are the most spontaneous processes producing H_2 by microorganisms from biomass, mainly carbohydrates (Eqn (8.1), $\Delta_r G'^0 = -220.2$ kJ/mol), where the excess of energy is converted to ATP and heat. On the contrary, photofermentation produces H_2 from organic acids or volatile fat acids (VFAs) in a nonspontaneous process, (Eqn (8.2), $\Delta_r G'^0 = +96.5$ kJ/mol) being the energy partly taken from sunlight. Alternatively, carbon monoxide can be also oxidized by many microorganisms yielding H_2 through the exergonic microbial WGS reaction (Eqn (8.3), $\Delta_r G'^0 = -20.0$ kJ/mol). Moreover, some microorganisms are able to produce H_2 from water by direct photolysis (Eqn (8.4)) or indirect photolysis, coupling photosynthetic (Eqn (8.5)), and fermentative (Eqns (8.1) and (8.2)) processes. Water biophotolysis processes are nonspontaneous ($\Delta_r G'^0 = +237.2$ kJ/mol).

The previously mentioned methodologies can be coupled leading to optimized energy yields, as well as byproducts valorization. Thus, microbial WGS reaction can be coupled to thermal gasification of biomass (Chapter 5).[18] Similarly, acid products from dark fermentations can be also used to feed the cathode in microbial electrolysis cells (MECs).[19] Acidic products can be used as well as feedstocks for photofermentation processes leading to a net spontaneous "two-stage dark and photofermentative H_2 production"[5] whose overall catabolic process is slightly exergonic and offers the biggest theoretical H_2 yield, 12 mol H_2/mol glucose (Eqn (8.6) $\Delta_r G'^0 = = -27.1$ kJ/mol of glucose). Coupling of dark fermentation (Eqn (8.1)) with methanogenesis (Eqn (8.7) $\Delta_r G'^0 = -34.2$ kJ/mol of acetate) leads to the so-called "Biohythane" methodology (Eqn (8.8), $\Delta_r G'^0 = -288.6$ kJ/mol of glucose) that is the most exergonic process, although 4 mol H_2/mol glucose is not the best H_2 yield (Scheme 8.1).[20]

$$CH_3COOH \xrightarrow{\text{methanogenesis}} CH_4 + CO_2$$
$$\Delta_r G'^0 = -34.2\ \text{kJ/mol of acetate} \quad (8.7)$$

$$C_6H_{12}O_6 + 2H_2O \rightarrow 2CH_4 + 4CO_2 + 4H_2$$
$$\Delta_r G'^0 = -288.6\ \text{kJ/mol of glucose} \quad (8.8)$$

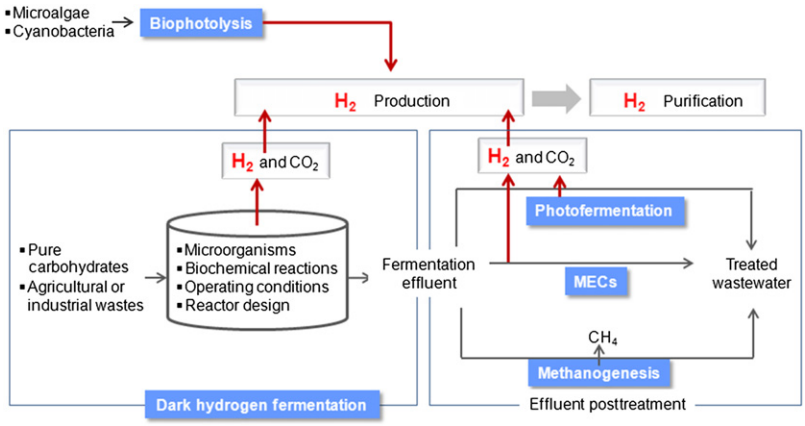

SCHEME 8.1 Flow chart of the dark biohydrogen system. (For color version of this figure, the reader is referred to the online version of this book.) *Source: Adapted from Refs. 21,22.*

8.2 DARK FERMENTATION

Fermentation can be deemed as a biological process in which energy is extracted from a carbon source.[23] Microorganisms that produce hydrogen upon fermentation can be classified as phototrophic (photo fermentation) or nonphototrophic (dark fermentation) depending on whether light is used or not, as an energy source.

Some bacteria that grow in the dark on carbohydrate-rich substrates produce hydrogen via dark fermentation under anoxic or anaerobic conditions[24] via the oxidation of an organic substrate that releases electrons that are transferred to H^+ under anaerobic conditions producing molecular hydrogen. Organic substrates are usually monosaccharides that come from acid or enzymatic hydrolysis of polysaccharides (e.g. starch or cellulose) previously generated upon photosynthesis.

Dark fermentation is mainly carried out by anaerobic bacteria, which can be described as *strict* or *facultative* anaerobes. *Strictly anaerobic bacteria* (e.g. *Clostridium*, *Desulfovibirio*, or *Ethanoligenens*) are the most common genus of bacteria that carry out dark fermentation using their ferredoxin oxidoreductase and hydrogenase enzymes, usually within an acidic pH range (4–7) and at different temperature intervals, 30–39 °C (i.e. mesophilic microorganisms) or 50–64 °C (i.e. thermophilic microorganisms). Some *facultative* anaerobes that possess hydrogenase enzymes (e.g. *Enterobacter aerogenes*, *Escherichia coli*, or *Klebsiella*) have been identified as hydrogen producers although with lower H_2 production rate than *strict* anaerobe. Finally, the hydrogen production was also found to be possible by some species of aerobic bacteria, such as *Alcaligenes* and *Bacillus*, although their hydrogen yields are low under anaerobic conditions (lower than 1.2 mol H_2/mol glucose).[10] Amongst these strains, *Clostridium* sp. and *Enterobacter* are the most widely studied.

Metabolic pathways in strict anaerobe dark fermentation: The well-known strictly anaerobes *Clostridia* are extremely sensitive to oxygen, which must be absent in solution to avoid cessation of the H_2 production. *Clostridia* can follow two major metabolic pathways, acidogenic and solventogenic pathways, during the fermentation of carbohydrates depending on ATP and NADH (an intracellular electron carrier) levels. Acidogenic pathway is characterized by rapid cell growth, high hydrogen production rates along with acetic and butyric acid production, whereas solventogenic pathway is characterized by slower growth, low hydrogen production rate, and production of reduced compounds (e.g. ethanol or butanol). Typically, one mol of glucose is transformed to 2 mol of pyruvate via the glycolysis step (or Embden–Meyerhoff–Parnas pathway) with concomitant formation of 2 NADH and 2 ATP units from NAD^+ and ADP respectively.[25] Then, pyruvate is oxidized into acetyl-CoA and CO_2. The last reaction requires the reduction of an oxidized ferredoxin (Fd^{ox}) unit by the pyruvate-*Fd* oxidoreductase to give the reduced Fd^{red}. The competition for Fd^{red} between NAD^+ and H^+ to give the corresponding NADH or H_2 will determine the metabolic pathway. Thus, the H_2 production arises from the oxidation of Fd^{red} by a [FeFe] hydrogenase regenerating Fd^{ox} and H_2 (Scheme 8.2A, acetate pathway). Additional H_2 can be produced from NADH by an NADH-hydrogenase when partial pressures of hydrogen are low (lower than 60 Pa).[26] The hydrolysis of acetyl-CoA to acetate will produce a new ATP unit. The overall process leading to the formation of acetate (Eqn (8.1), $\Delta_r G'^0 = -220.2$ kJ/mol) theoretically generates 4 mol H_2, venting a part of the produced energy in the production of 4 mol of ATP. However, the production of NADH from Fd^{red} and NAD^+ will boost reactions that consume NADH as the formation of butyrate, lactate, ethanol, etc.,[13] pulling the electrons away from the production of H_2.[25] Thus, in the butyrate pathway, one mol of NADH is consumed by

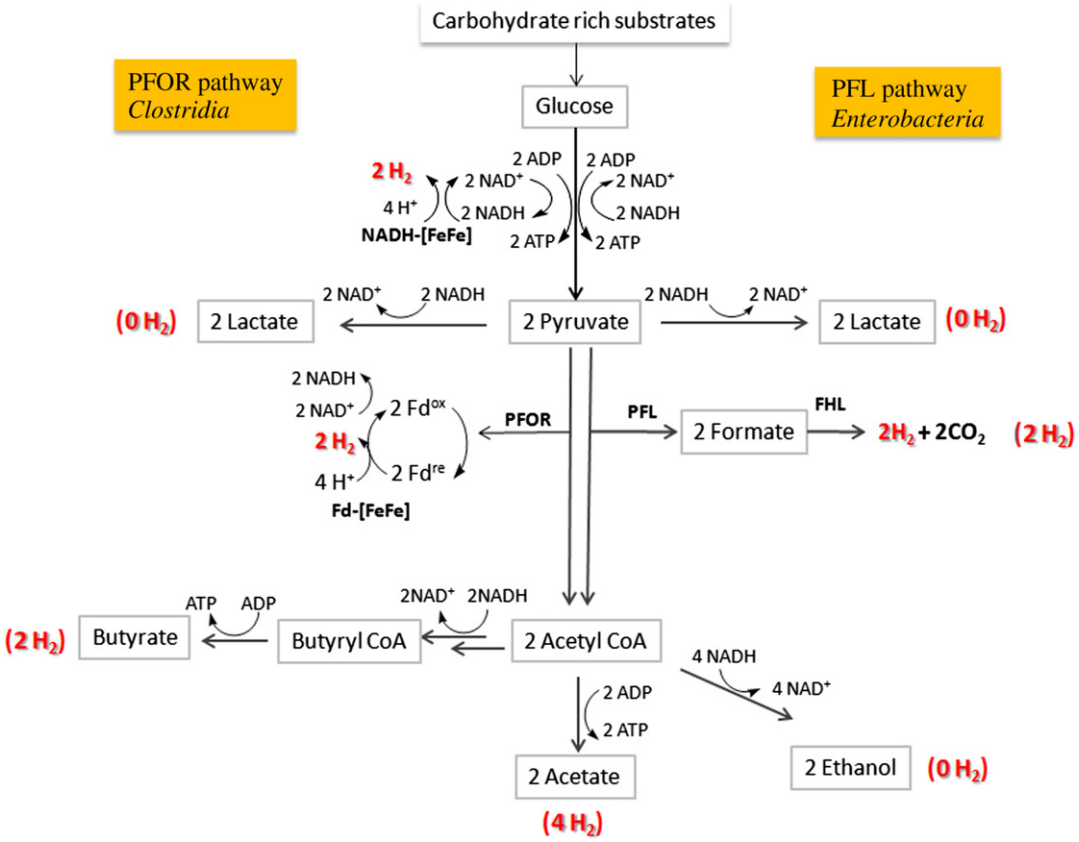

SCHEME 8.2 A) *Clostridia*-type fermentation. B) Enterobacteria-type fermentation. (For color version of this figure, the reader is referred to the online version of this book.) *Source: Adapted from Ref. 30.*

Acetyl-CoA to give 0.5 mol of butyrate, 0.5 mol of ATP together with 2 mol H_2 (Eqn (8.9), $\Delta_r G'^0 = -267.0$ kJ/mol).[25] A part of that energy is spent on the formation of 3 mol ATP. Other fermentative pathways, as the production of lactate via pyruvate (Eqn (8.10), $\Delta_r G'^0 = -200.7$ kJ/mol) or ethanol via acetyl-CoA (Eqn (8.11), $\Delta_r G'^0 = -271.3$ kJ/mol), produced 2 mol of ATP but hydrogen.[25]

$$\text{Glucose} \rightarrow \text{butyrate} + 2CO_2(g) + 2H_2(g)$$
$$\Delta_r G'^0 = -267.0 \text{ kJ/mol of glucose} \quad (8.9)$$

$$\text{Glucose} \rightarrow 2 \text{ lactate}$$
$$\Delta_r G'^0 = -200.7 \text{ kJ/mol of glucose} \quad (8.10)$$

$$\text{Glucose} \rightarrow 2 \text{ ethanol} + 2CO_2(g)$$
$$\Delta_r G'^0 = -271.3 \text{ kJ/mol of glucose} \quad (8.11)$$

Consequently, the hydrogen yield usually lies in the range of 1.1–2.6 mol H_2/mol hexose in *Clostridiaceae* pure cultures (e.g. *Clostridium paraputrificum*, *Clostridium lentocellum*, *Clostridium thermosuccinogenes*, *Clostridium bifermentans*, *Clostridium thermolacticum*, *Clostridium butyricum*, *Clostridium saccharoperbutylacetonicum*, *Clostridium acetobutylicum*, *Clostridium pasteurianum*).[10,27] The metabolic pathway will be determined by variables such as pH (low values stimulate the coupling of Fd^{red} and H^+ to form H_2),[28] hydrogen partial pressure, temperature, enzyme, and nutrient concentrations. In the case of hydrogen partial pressure, ferredoxin hydrogen production can continue as long as P_{H_2} is lower than 30 kPa, whereas from NADH the P_{H_2} must be lower than 60 Pa.[29]

The acetate pathway is almost the exclusive metabolic route from pyruvate in hyperthermophilic microbes (>65 °C), as it has been proposed for *Thermatoga maritime*[31] (eubacterium) or *Thermococcus kodakaraensis* KOD1[32] (archae). Hence, hyperthermophilic cultures can reach H_2 productions close to the theoretical maximum (4 mol H_2/mol glucose),[31–33] although with much lower H_2 production rates than mesophilic cultures together with low microbial growth and glucose utilization as well. Thermophiles (50–64 °C), typically *Thermoanaerobacterium* species, also prefer the acetate pathway against butyrate or ethanol pathways (≈5:2:1 mol).[34]

Metabolic pathways of facultative anaerobe dark fermentation: Facultative anaerobe microorganisms, especially *Enterobacteriaceae* (e.g. *E. coli*), are not sensitive to the presence of oxygen, and metabolize pyruvate to formic acid by pyruvate formate lyase producing acetyl-CoA. Overall processes are also strongly spontaneous (Eqn (8.12), $\Delta_r G'^0 = -257.7$ kJ/mol assuming that the acetyl-CoA produces mainly acetate). The produced formate is further broken down into hydrogen gas and carbon dioxide via formic hydrogenlyase (Scheme 8.2B, $\Delta_r G'^0 = -1.8$ kJ/mol of formate). Bacteria of the family *Enterobacteriaceae* have no specific coenzymes such as ferredoxin oxidoreductase, and therefore the NADH produced during anaerobic glycolysis is consumed by reduction of pyruvate and derivatives to give a mixture of acids and alcohols that will limit the hydrogen production of the fermentation.[10] Despite this limitation, *facultative* anaerobes can be easily grown, and thus, pure cultures of *Enterobactericeae* (e.g. *E. aerogenes* E. 82,005, *E. aerogenes* strain HO 39, *E. aerogenes* HU-101 AY2, and *Enterobacter cloacae* IIT-BT 08) have been evaluated in the hydrogen production,[10] yielding up to 2.2 mol H_2/mol glucose and 6.0 mol H_2/mol sucrose in the case of *E. cloacae*.[35]

$$\text{Glucose} + 2\text{NAD}^+ + 2\text{H}_2\text{O} \rightarrow 2\ \text{acetate} + 2\ \text{formate} + 2\text{NADH} + 2\text{H}^+ \quad \Delta_r G'^0 = -257.7\ \text{kJ/mol of glucose} \tag{8.12}$$

The H_2 yield can be improved by redirecting some metabolic pathways.[36] Thus, addition of NaBr and $NaBrO_3$ that blocks organic acid formation (proton-suicide techniques) on *E. cloacae* rises H_2 yield to 3.8 mol H_2/mol hexose.[37] *Escherichia* species can produce hydrogen in the range 0.2–1.8 mol H_2/mol hexose upon fermentation of starch hydrolysates[38] but a genetic modification of nonhydrogen producing *E. coli* BL-2, by *hydA* overexpressed recombinant gene (Fe-hydrogenase coded gene from *E. cloacae* IIT BT 08), can increase the H_2 production up to 3.1 mol H_2/mol glucose.[39]

Thermodynamic evaluation of the H_2 production by fermentation of glucose by mixed cultures in batch mode evidenced that the H_2 production from Fd^{red} electrons was inhibited by the NADH production at pH > 7.[25] On the contrary, the spontaneity of both processes was similar at pH < 7 and $P_{H_2} < 60$ kPa. At pH ≈ 4 butyrate pathway was preferred over acetate and ethanol pathways (≈12:3:1).[25] However, at pH ≈ 10, no hydrogen evolution was observed, and acid productive enzymes through Acetyl-CoA seemed to be repressed, leading to formation of lactate, formate, and ethanol (4:2:1 mol ratio).[25]

The hydrogen production can be improved using the so-called mixed cultures that are likely to contain a suite of necessary hydrolytic activities and are potentially more robust to changes in operation conditions. Some positive effects on the production of hydrogen have been found in *Clostridium*-mixed cultures, amongst them, the most relevant are granular formation/retention of biomass (*Streptococcus* sp.), oxygen depletion (*Klebsiella* or *Bacillus* in their lag phase), or breakdown of complex organic structures (e.g. *Bifidobacterium* sp., *Olsenella* sp., *Klebsiella oxytoca*, *Pseudomonas* sp., *Megasphaera* sp., *Bifidobacterium* sp.).[40] In spite of these positive effects, some drawbacks have been also found in mixed cultures as the competition for the substrate and the hydrogen consumption that can occur if one of the populations shifts to hydrogen-consuming activity. These drawbacks can be prevented either by the careful control of the design parameters or by operation techniques as heat-shock pretreatment (80–121 °C), acid pretreatment (pH 2–4), and alkaline pretreatment (pH 11) that can be applied to eliminate undesired hydrogen-consuming methanogens.[41]

The scale-up of the H_2 production by dark fermentation is highly dependent on the process conditions such as the kind of microorganism (mixed microbial cultures seem to be a more cost-effective and promising),[42] the substrate used as inoculum and feedstock respectively, bioreactor type and operational parameters (pH, temperature, gas partial pressure, hydraulic retention time (HRT), nutrient availability or presence of inhibitors) that must be optimized in each specific case. These variables are briefly discussed below.

8.2.1 Substrate

Although simple sugars such as glucose (Table 8.1, entry 1), cellobiose (entry 2), and sucrose (entry 3) are readily biodegraded and are hence preferential substrates, they are expensive raw materials.[43] Dark-fermentation processes can use a wide variety of organic wastes[3,44,45] whose interest depends on their availability, cost, carbohydrate content, and biodegradability.[3] The most interesting, starch- and cellulose-rich wastes, present complex structures (see Chapter 5), and therefore raw carbohydrates must be obtained by some pretreatments,[41] as grinding, delignification, and hydrolysis that also help to remove pathogens. Many wastes have been studied as feedstocks: Agricultural production (e.g. animal wastes and vegetal residues), food and beverage industries (e.g. slaughter houses and meat-processing, dairy, fish processing, starch-processing, sugar, edible oil, beverages, and distilleries), chemical industries (paper manufactures), and municipal or domestic sewage wastewater (as synthetic wastewater mainly). Some of them like molasses,[42] fruit and

TABLE 8.1 Biohydrogen Production by Dark Fermentation in Different Types of Reactor*

Entry	Reactor type	Seed (support)	Feed	H_2 yield (mol H_2/mol C_6)	H_2 rate (l H_2/l h)	Temp. (°C)	pH	Ref.
1	Batch	*E. cloacae* IIT-BT 08	Glucose	2.2	0.45	36	6.0	35
2	Batch	*E. cloacae* IIT-BT 08	Cellobiose	2.7	0.65	36	6.0	35
3	Batch	*E. cloacae* IIT-BT 08	Sucrose	3.0	0.66	36	6.0	35
4	CSTR	*E. aerogenes* HO39	Glucose	1.1	0.24	37	6.5	53
5	CSTR	*E. aerogenes* HO39 (glass)	Glucose	0.9	0.34 (0.85)†	37	6.5	53
6	CSTR	Mixed culture	Glucose	2.1	1.34	36	5.5	54
7	CSTR	Mixed culture (C-silicone)	Sucrose	1.6	15.1	40	6.0	55
8	CSTR pilot scale	Mixed culture	Molasses	3.0	0.23	35	4.5	42
9	Granule AFBR	Mixed culture	Glucose	1.7	6.6	37	5.5	56
10	Biofilm AFBR	Mixed culture (C)	Glucose	1.7	7.6	37	5.5	56
11	Granule UASB	Mixed culture	CDMW**	1.8	2.8	35	5.5	57
12	Granule UASB‡	Mixed culture (C)	Sucrose	1.5	(7.3)†	35	6.7	58
13	APBR	Mixed culture (C)	Glucose	2.9	(7.4)†	35	6.7	59
14	APBR	Mixed culture (C)	Glucose	3.9	(1.2)†	35	6.7	59
15	Batch	Mixed *Thermoanaerobacteriaceae*	Waste§	0.6	0.31	55	6.0	34
16	CSRT	*T. elfii*	Sucrose	3.3	0.07	65	7.4	33
17	CSRT	*C. saccharolyticus*	Sucrose	3.0	0.24	70	7.0	33

* *H_2 production yields and rates were transformed at the indicated units, when possible from reference data.*
** *CDMW = Coffee drink manufacturing wastewater.*
† *Maximum H_2 production rate.*
‡ *This bioreactor is also named carrier-induced granular sludge bioreactor (CIGSB).*
§ *Synthetic starch-based waste.*

vegetables,[46] brewery grains,[47] distillery effluents,[48] food waste treatment plants,[49] or synthetic wastewaters,[50,51] have been also investigated at a pilot scale.

8.2.2 Bioreactor Type

A wide variety of bioreactors have been evaluated in dark-fermentation processes,[22,41,52] but our discussion will be focused on those that are operated in continuous mode as they allow scaling-up for industrial application (Table 8.1). Two general systems have led to the good H_2 production rates and yields: continuous stirred tank reactors (CSTR, Table 8.1, entries 4–8) and anaerobic fluidized bed reactors (AFBR, Table 8.1, entries 9 and 10). The system performance is largely influenced by the reactor biomass retention, so that variables as biomass and cell granulation or immobilization must be also taken into account to improve H_2 production rate and yield.

CSTR have been widely used in the optimization of the continuous fermentative H_2 production from various substrates.[41] In classical CSTR, the biomass is suspended in a mixed liquor that has the same composition as the effluent (Table 8.1, entry 4). Complete mixing allows pH and temperature control, as well as intimate contact between the substrate and biomass. CSTR operating at high dilution rates or short residence times (usually measured as HRT) may cause washout of suspended cells provoking operational instability and also limiting the hydrogen production rate. Biomass retention (mass of volatile suspended solids by liter, g VSS/l) can be increased by formation of granules,[55,60,61] biofilms,[62] or gel-entrapped bioparticles (entry 7),[55,63] thus increasing the H_2 production rate (volume of H_2 by volume of mixture and time, l H_2/l h).[64] Indeed, a granular CSTR reactor seeded with silicone-immobilized sludge afforded the highest H_2 production rate, 15 l H_2/l h (from 0.5 h of HRT and 35.4 g VSS/l) with

an overall yield of 1.6 mol H_2/mol sucrose (entry 7).[55] AFBR showed worse performance than CSTR, indeed the H_2 production rate in granular-based AFBR was 6.5 l H_2/l h (entry 9) and biofilm-based AFBR produced 7.6 l H_2/l h (entry 10, from 0.25 h of HRT and 35 g VSS/l).[56]

A variety of cell supports has been successfully assayed in dark fermentations: granular activated carbon (entries 10, 12–14),[58,65,66] porous glass (entry 5),[53] silicone,[55] alginate,[53,67] polyvinyl alcohol,[68] as well as lignocellulosic material.[69,70] The retention of bacteria in membranes has been also studied, but this methodology is limited by the high capital costs for the membrane, membrane fouling, and high operating costs due to energy needed to push the water through the membrane.[71]

Other reactor configurations as upflow anaerobic sludge blanket (UASB) showed high and stable performance, but long start-up periods that can be reduced by using a CSRT reactor in their start-up stage (entries 11 and 12).[57,58] Anaerobic packed bed reactors (APBR,[59] entries 13 and 14) usually presented mass transfer resistance through the immobilized cultures, as well as a heterogeneous microbial activity, requiring recirculation and/or an increase of the turbulence.[22]

Although some pilot-scale plants have been already developed (entry 8),[42] bioH_2 industrial-scale reactors have not been set up yet. Design and reactor operational parameters must be carefully optimized by means of computational fluid dynamics tools[41,72] or computational neural networks models.[73]

8.2.3 Operational Parameters

As it has be pointed above, the *acidity of the media* affects metabolic pathways[44] as well as the activity of [FeFe] hydrogenase. Indeed, the H_2 production occurs upon the acidification stage of dark fermentation during the exponential growth of bacteria but the metabolism, unless the pH is careful controlled, can readily shift to the solvogenesis pathway during the stationary growth phase.[74] Optimal pH differs for each bacteria strain, however, some general conclusions can be outlined: for instance, optimum pH for the H_2 production by mesophiles (*Clostridium*-rich sludge,[75] *E. cloacae*[76]) and mixed cultures[77] is in the 5.0–6.0 range whereas lower pH values caused by high acid production can inhibit the hydrogen production unless substrate concentrations are carefully controlled.[78] Optimum pH for the H_2 production by thermophiles is higher (6.0–7.0 for *Thermoanaerobacteriaceae*)[34] than in mesophiles.

From an energetic point of view, the H_2 production at mesophilic *temperature* (30–40 °C) is preferred and affords moderate production rates (<1 l H_2/l h in batch mode,[10] up to 8 l H_2/l h for AFBR[56] and up to 15 l H_2/l h for CSRT[55]) and H_2 yields (usually < 3 mol H_2/mol hexose at highest production rates). The fermentation at high temperatures (50–55 °C) by thermophilic bacteria (e.g. *Thermoanaerobacterium* sp) afforded high H_2 overall yields (up to 3 mol H_2/mol hexose[79]) although with low rates[10,22] while hyper thermophiles (65–80 °C), as *Thermotoga elfii* (entry 16) and *Caldicellulosiruptor saccharolyticus* (entry 17) showed the biggest overall yields (close to 4 mol H_2/mol hexose[10,22,31,33]) but with very low production rates (<0.25 l/l h in batch mode).[10]

Hydraulic retention time (HRT) is related to the amount of organics that can be handled per unit of time and, it should be as low as possible to reach the highest H_2 production rates and yields. HRT optimum value depends on the rest of variables (bioreactor, substrate, pH, temperature, inoculums, etc.) and it must be optimized for each situation. Literature offers a wide rank of optimum HRTs values from 0.2 h to some days.[16,44]

Another important factor affecting the hydrogen production rate is the hydrogen partial pressure (P_{H_2}) since high H_2 pressures can shift [FeFe] hydrogenase activity. For instance, at $P_{H_2} < 60$ Pa, acetate pathway is the preferred for *Clostridia* but shifts to butyrate pathway at $P_{H_2} > 30$ kPa.[29] Both pathways can be suppressed at high P_{H_2} when NADH is redirected to the H_2 unproductive lactate-propionate pathway.[80] P_{H_2} can be reduced by sparging an external gas (CO_2 better than N_2) in the media with a noticeable increase in the H_2 production.[81,82] Furthermore, high P_{CO_2} has little effect on H_2-producing bacteria, but it had inhibitory effect on other microorganisms such as acetogens and lactic acid bacteria.[81] Vigorous mixing or using H_2 permeable membranes[83] represent alternative ways to avoid H_2 oversaturation. Other interesting option is the direct reduction of P_{H_2} by applying vacuum that led to significant improvement in the H_2 production.[84]

Besides a carbon source, fermentative bacteria require nutrients to carry out their metabolism, growth, and hydrogen production. Carbon and nitrogen availability as well as trace metals, growth factors, and vitamins are critical for process optimization and cost-effectiveness of each bacterial strain.

Nitrogen is an essential nutrient in the bacteria growth being the use of proper C/N ratios critical for the hydrogen production. Ammonia is the most widely used nitrogen source, although yeast extracts or peptones are the usual nitrogen sources too. Optimal ammonia concentration and C/N ratio depend on each strain, cell densities, etc. Indeed, excess of ammonia concentration was negative for the H_2 production: *E. coli* cultures working at 0.01 g N/l[85] yielded 1.7 mol H_2/mol hexose, whereas cultures at 7.0 g N/l[86] afforded only 1.1 mol H_2/mol hexose and cultures working at low cell densities and ammonia concentration ~1 mmol N/l reached up to 2 mol H_2/mol glucose.[85]

Optimal C/N ratios are usually large: C/N = 10 at 0.4 g N/l using yeast extracts,[87] or C/N = 47 at 0.9 g N/l gave the best H_2 yield (2.3 mol H_2/mol hexose) using anaerobic microflora.[88]

Phosphate plays a dual role both as nutrient (main source of ATP) and as buffer.[89] The best hydrogen yields were found at intermediate limiting phosphate concentrations, 0.2–0.5 mM.[85]

Trace metals are crucial at cellular level as they take part in cell growth, enzyme cofactors, transport processes and are constituents of dehydrogenases. Some authors pointed to magnesium, sodium, zinc, and iron as significant for the H_2 production, with magnesium being the most relevant.[88] Indeed, Mg^{2+} is an important cofactor that activates almost 10 enzymes that take part in glycolysis process; therefore, Mg^{2+} shortage may limit the growth anabolism of H_2-producing fermentative bacteria and thus their H_2-producing ability.[90] Iron (Fe^{2+}) is an essential constituent both for *Fd* and hydrogenase enzymes. Indeed, when fermentation is carried out in iron-limiting conditions, a decrease both in hydrogen and acetate-butyrate production is observed together with an increase in the production of alcohols and lactate.[91,92] The optimum Fe^{2+} concentration in a mixed culture diminishes as temperature increases: 800 mg Fe/l at 25 °C, 200 mg Fe/l at 30 °C, and 25 mg Fe/l at 35 °C.[93] Other heavy metals, such as cadmium, chromium, zinc, copper, nickel, and lead that may be present at significant concentrations in some industrial wastewater, can be toxic for some strains and so they may inhibit the H_2 production, although their relative toxicity depends on each strain, substrate, and biological process.[94–96] The CI_{50} (concentration in which biological activity was inhibited by 50% of control) relative to the H_2 production decreased in the following order for a granular sludge: copper (0.03 g Cu/l, most toxic) > nickel or zinc (1.6 g Ni or Zn/l) > chromiun (3.0 g Cr/l) > cadmium (3.5 g Cd/l) > lead (>5.0 g Pb/l).[94] Other sludges showed much higher sensitivity to heavy metals (CI_{50} < 0.005 g Zn/l,[95] 0.12 g Zn/l,[96] 0.072 g Cr/l[97]) or different order of toxicity (Zn < Cu < Cr).[95]

As conclusion, it can be stated that dark fermentation is a mature technology for the H_2 production. However, it is expensive and depends of multiple interrelated variables that should be optimized in each production system. Cost-effective processes can be achieved by coupling dark fermentation with other processes that use its wastewater as feedstock.[65]

8.3 PHOTOFERMENTATION

Hydrogen can be also produced by light-dependent fermentation in a process called photofermentation.[22] Anoxygenic phototrophs absorb sunlight and perform electron transport, which generates the proton motive force required for ATP synthesis. Photosynthetic bacteria like purple sulfur, purple nonsulfur (PNS), and green sulfur bacteria evolve molecular hydrogen under nitrogen-deficient conditions using light energy and reduced compounds as organic acids as proton source (Eqns (8.13)–(8.16)) in a process catalyzed by nitrogenase.[98,99] Purple and green sulfur bacteria are more sensitive to oxygen than PNS, showing also lower growth rates and nitrogenase activities.[12] PNS bacteria (e.g. *Rhodobacter spheroids*, *Rhodobacter capsulatus*, *Rhodovulum sulfidophilum*, *Rhodospirillum rubrum*, and *Rhodopseudomonas palustris*)[100,101] are not powerful enough to split water although, under anaerobic conditions, are able to use preferably organic acids, simple sugars, amino acids, alcohols, or industrial and agricultural effluents for the H_2 production.[102,103] Overall reactions for organic acids are strongly endoergic being the best substrates, from an energetic point of view, lactate (Eqn (8.13), $\Delta_r G'^0 = +14.4$ kJ/mol H_2) and malate (Eqn (8.14), $\Delta_r G'^0 = +10.3$ kJ/mol H_2)[104] followed by butyrate (Eqn (8.16), $\Delta_r G'^0 = +24.0$ kJ/mol H_2) and acetate (Eqn (8.2), $\Delta_r G'^0 = +24.1$ kJ/mol H_2), although the best substrate can change depending on the strain, being, for instance, succinate (Eqn (8.15), $\Delta_r G'^0 = +20.9$ kJ/mol H_2) the best substrate in some concrete strains of *Rhodobacter sphaeroides*, as ZX5.[105] Apart from thermodynamic considerations, different selectivities can be explained by substrate assimilation pathways and resulting redox status of the cell, as it has been proposed before.[103] It is worth to note that green sulfur bacteria are adapted to use H_2S, S, or thiosulfate as substrates.

$$\text{(Lactic acid)}\quad C_3H_6O_3 + 3H_2O \rightarrow 3CO_2 + 6H_2 \qquad \Delta_r G'^0 = +14.4\ \text{kJ/mol}\ H_2 \tag{8.13}$$

$$\text{(Malic acid)}\quad C_4H_6O_5 + 3H_2O \rightarrow 4CO_2 + 6H_2 \qquad \Delta_r G'^0 = +10.3\ \text{kJ/mol}\ H_2 \tag{8.14}$$

$$\text{(Succinic acid)}\quad C_4H_6O_4 + 4H_2O \rightarrow 4CO_2 + 7H_2 \qquad \Delta_r G'^0 = +20.9\ \text{kJ/mol}\ H_2 \tag{8.15}$$

$$\text{(Butyric acid)}\quad C_4H_8O_2 + 6H_2O \rightarrow 4CO_2 + 10H_2 \qquad \Delta_r G'^0 = +24.0\ \text{kJ/mol}\ H_2 \tag{8.16}$$

The photosynthetic system of purple bacteria is relatively simple comparing with the green algae and consists of only one photosystem, PSI, fixed in the intracellular membrane so there is no O_2 evolution in PSII. In the photofermentation process, the organic substrate is oxidized and the produced electrons are shuttled

through an electron transport in the membrane, which uses NAD^+/NADH and *Fd*, to a nitrogenase (*N_2ase*, Eqn (8.17)). Nitrogenases count with a dinitrogenase complex and a reductase subunit[7] that consists of a Fe−S-protein that is responsible for the transfer of electrons from the external electron donor to the dinitrogenase complex of the enzyme. The dinitrogenase complex is a Mo−Fe−S protein that catalyzes the stepwise reduction of the N_2 bonds leading to the formation of two molecules of ammonia[106,107] and H_2 (Eqn (8.17), $\Delta_r G'^0 = +38.3$ kJ/mol e^-). Thus, *N_2ase* convert naturally nitrogen into ammonia and hydrogen. However, the substrate reduction requires high-energy electrons and chemical energy input in the form of ATP. For each electron to pass from nitrogenase, two ATPs are used (2 ATP/e^-) and therefore 16 ATP for mol of H_2 (global Eqn (8.18)). In the absence of a nitrogen source, *N_2ase* acts as an ATP-dependent hydrogenase (Scheme 8.3).[103] The H_2 production by *N_2ase* from protons only (Eqn (8.19), $\Delta_r G'^0 = +40.8$ kJ/mol e^-) is slightly more endoergic than that from N_2 (Eqn (8.17), $\Delta_r G'^0 = +38.3$ kJ/mol e^-); it is irreversible and so interesting for the H_2 production. Concerning the standard transformed Gibbs energies, each mol of H_2 formed by *N_2ase* from protons only will consume 4 ATP[102] (−32.5 kJ from each mol of ATP) giving global Eqn (8.20). Equations (8.18) and (8.20) indicated that both *N_2ase* processes were energetically demanding. The presence of N_2 will favor ammonia production (Eqn (8.18)), and so decreasing H_2 production by mol e^-. PNS bacteria also have uptake hydrogenases that catalyze the conversion of molecular hydrogen into protons and electrons, and other alternative electrons sink such as production of poly-3-hydroxybutyrate (PHB) that therefore will reduce the H_2 production (Scheme 8.3). However, photofermentation process using nitrogenases bypass oxygen and hydrogen sensitivity showed by hydrogenases.

$$N_2 + 8H^+ + 8e^- \rightarrow H_2 + 2NH_3$$
$$\Delta_r G'^0 = +306.2 \text{ kJ/mol } H_2 = +38.3 \text{ kJ/mol } e^- \quad (8.17)$$

$$N_2 + 8H^+ + 8e^- + 16 \text{ ATP} \rightarrow H_2 + 2NH_3 + 16ADP + 16P_i \quad \Delta_r G'^0 = -26.7 \text{ kJ/mol } e^- \quad (8.18)$$

$$2H^+ + 2e^- \rightarrow H_2$$
$$\Delta_r G'^0 = +81.5 \text{ kJ/mol } H_2 = +40.8 \text{ kJ/mol } e^- \quad (8.19)$$

$$2H^+ + 2e^- + 4 \text{ ATP} \rightarrow H_2 + 4 \text{ ADP} + 4P_i$$
$$\Delta_r G'^0 = -24.2 \text{ kJ/mol } e^- \quad (8.20)$$

Reported H_2 production rates in photofermentation processes in suspended cultures[7,100] (lower than 0.2 l H_2/l h) are significantly lower than those from most dark-fermentation processes.[52] Furthermore, the H_2 yield from the same carbon source strongly varies amongst different PNS species, or even among different strains of the same species.[105] Most of non-mutant PNS bacteria yield low conversion efficiencies of H_2 from glucose (≈1 mol H_2/mol hexose), whereas mutant strains, with some of the competitive electron pathways blocked, can reach up to 3−7 mol H_2/mol hexose and a substrate conversion efficiency, CE^{su} (mol H_2 obtained/mol H_2 theoretical) in the interval 25−60% at 200 W/m^2,[108,109] although the H_2 production from

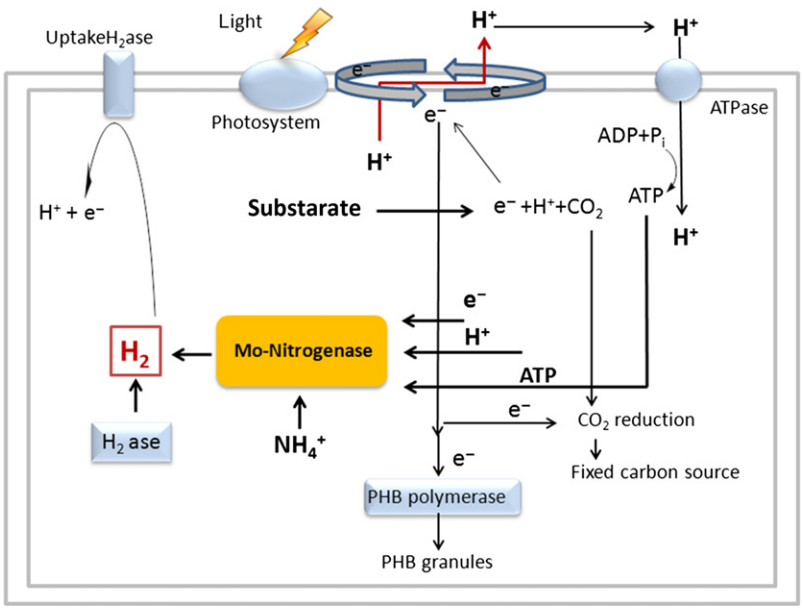

SCHEME 8.3 Metabolic pathways of photosynthetic bacteria (PNS) for H_2 production. (For color version of this figure, the reader is referred to the online version of this book.) *Source: Adapted from Ref. 103.*

VFA reached up efficiencies of 70–90% at 4 klux (~16 W/m^2).[105] It is worth noting the dual effect of the light intensity. In one hand, light strongly stimulates the expression and activity of nitrogenase as well as the photophosphorylation capacity in *R. capsulatus*, rendering the H_2 production activity higher.[110,111] On the other hand, light saturation may occur when the photosynthetic system supplies excess ATP and Fd^{red} compared to the capacity of nitrogenase[112] and the H_2 production can be inhibited as in cultures of *R. sphaeroides* ($I > 1.0$ kW/m^2).[113] Concerning the light intensity, some authors have proposed the reduction of pigment content of the bacteria by genetic manipulations to increase the light penetration, thereby increasing their H_2 production.[103,114]

In addition to those variables related with light absorption, the scale-up of photofermentation requires the optimization of similar variables to those commented for dark fermentation. Biotechnological approaches, as genetic engineering, can also improve photofermentation efficiency by means of inactivation of electron sink pathways (as uptake hydrogenase or PHB accumulation), truncating the light-harvesting antenna size of photosynthesis, enhancing PNS ammonia tolerance or electron and ATP flow to the nitrogenase, as it has been recently reviewed.[7,103] However, the main bottleneck in scale-up of phototrophic fermentation is the low efficiency of the light-energy conversion, CE^{en} (H_2 energy content/light energy content), which is caused by an excessive dissipation of light energy to heat, leading to efficiencies lower than 10%.[3,115,116] A resume of the main factors affecting the photofermentation is commented below.

8.3.1 Substrate

Although photosynthetic bacteria prefer organic acids (VFA) as substrates (Table 8.2), an adequate C/N ratio in the growth media is essential for the H_2 production, thus C/N = 7.5 yielded the highest H_2 production rate for *R. sphaeroides* O.U.001 from VFA.[117] Nitrogen sources as albumin, glutamate, or yeast extract were adequate to enhance the H_2 production.[3]

Utilization of industrial wastes (e.g. brewery,[126] olive mill,[127] sugar refinery,[109,128] tofu industry,[113] dairy industry,[126] or glycerol[129]) has been also reported and

TABLE 8.2 Substrate Conversion Efficiency and Rate of Hydrogen Production by Different PSN Bacterial Strains

Substrate (mM)	Photosynthetic bacteria	CE^{su} (%)	Max. H_2 rate (ml H_2/l h)	PhBR Mode	Ref.
Acetate (22)	*Rhodopseudomonas* sp.	73	25	Batch	118
Acetate (30)	*Rhodobacter capsulatus*	33	45	Batch	119
Acetate (35)	*Rhodobacter sphaeroides ZX-5*	69	90	Batch	105
Lactate (50)	*Rhodopseudomonas* sp.	10	11	Batch	118
Lactate (50)	*Rhodopseudomonas palustris*	13	9	Batch	118
Lactate (50)	*Rhodobacter sphaeroides ZX-5*	81	103	Batch	105
Lactate (100)	*Rhodobacter sphaeroides RV*	80	63	CSTR	120
Malate (7.5)	*Rhodobacter sphaeroides* OU001	35–45	5	Batch	121
Malate (17)	*Rhodobacter sphaeroides* OU001	75	7	Batch	122
Malate (30)	*Rhodobacter capsulatus ST410*	73	130	Batch	123
Malate (35)	*Rhodobacter sphaeroides ZX-5*	79	92	Batch	105
Butyrate (27)	*Rhodopseudomonas* sp.	8	8	Batch	118
Butyrate (50)	*Rhodobacter sphaeroides ZX-5*	72	118	Batch	105
Succinate (50)	*Rhodobacter sphaeroides ZX-5*	90	108	Batch	105
Succinate (50)	*Rhodovulum. sulfidophilum*	65	27	Batch	124
Glucose (10)	*Rhodobacter sphaeroides WT*	24	10*	Batch	125
Glucose (10)	*Rhodobacter sphaeroides* Glc^+	99	8*	Batch	125
Glucose (15)	*Rhodobacter sphaeroides ZX-5*	53	75	Batch	105
Sucrose (7)	*Rhodobacter sphaeroides ZX-5*	17	40	Batch	105

* ml H_2/h.g protein.
Source: Adapted from Ref. 105.

allows simultaneous waste treatment (Table 8.3).[102] Nevertheless, some problems are associated to the use of industrial effluents as high ammonia concentration (e.g. animal wastewaters), dark color of wastewaters (that reduces the light penetration), high organic matter or toxic compounds (e.g. heavy metals, phenolics, and poliaromatic hydrocarbons) content. Pretreatments are hence required before the H_2 gas production. Thus, in the case of the H_2 production from olive mill wastewater (OMW) by *R. sphaeroides* O.U.001, shadowing of the light absorption by substrate can be prevented by decoloration of the substrate, by mean of chemical oxidation with ozone or Fenton's reagent, as well as photodegradation by UV radiation, although these pretreatments gave unsuitable effluent for the H_2 production. Nevertheless, it was found that adsorption can be a good pretreatment. Using clay and zeolite as adsorbents production rates of 11 and 7 ml H_2/l h, respectively, were achieved from OMW at 4%[130] (alternatively, 9 ml H_2/l h from OMW at 1%).[127]

8.3.2 Photobioreactor Type

Unlike reactors for dark fermentation, photobioreactors (PhBRs) are still in the development phase.[132] The large-scale production of H_2 requires a proper design of the PhBR that depends on the selected strain and its light requirements (intensity and position of the light source) as well as hydrodynamics. The performance of a PhBR also depends on physical parameters (e.g. pH, temperature, light intensity, dissolved oxygen, dissolved CO_2, carbon, and nitrogen sources) that can affect the metabolic pathways.[133] The main criteria in the design of bioreactors are roughly surface to volume ratio (A/V), mass transfer of CO_2, oxygen removal, mixing, temperature control, and the material of construction.

The material of construction of the PhBR must be highly transparent, flexible, durable, nontoxic for the microorganisms, chemical and weather resistant. A detailed assessment of net energy ratio in the H_2 production from different reactor materials (LDPE, PMMA and glass) concluded that the only convenient material for panel reactors was LDPE.[132] Surface to volume ratio (A/V) determines the amount of light entering the system, therefore, the higher A/V ratio the higher the cell concentration and thus the greater volumetric productivities. Nevertheless, too high A/V ratios may produce an accumulation of oxygen that may cause inhibition of the photosynthesis.

Although fermentation-type reactors using internal illumination have been used for optimization studies,[134] predominant PhBR types for the H_2 production are tubular reactors, flat plate reactors, and alveolar panels.[133] *Tubular PhBR* consist of long transparent tube that usually provides high A/V ratios leading to high photosynthetic efficiencies, where the culture liquid is pumped mechanically or by airlift pumps. Vertical type reactors usually are constructed of glass or polyethylene and are jacketed with a water column that allows temperature control and light irradiation.[135] Horizontal tubular reactors are oriented toward sunlight affording higher light conversion efficiency but they lack of efficient temperature control. Finally, helical tubular are made by coiling straight tubes made of flexible plastic with an accurate inclination. *Flat panel PhBRs* present very high A/V ratio, and they usually consist of plates made with the minimal thickness that are arranged either in parallel vertical, tilted or horizontal dispositions and count with an open gas transfer area. *Alveolar panel PhBR* consists of transparent panels that are portioned to form rectangular channels called alveoli. This design present oxygen build-up because of the high photosynthetic activity and light saturation, and so photoinhibition is usually observed. In a comparative study at pilot scale, flat panel and tubular reactors yielded similar H_2 productivities by illuminated reactor surface area (3.3–3.7 l H_2/m^2 d), although flat panel needed only 0.12 m^2 ground space/m^2 reactor, whereas tubular reactors needed 1 m^2/m^2 reactor.[132]

TABLE 8.3 Production of H_2 by Photosynthetic Bacteria from Industrial Wastewaters

Entry	Photosynthetic bacteria	Carbon source	H_2 yield*	Ref.
1	*Rhodobacter sphaeroides* RV	Wheat starch	1.2	131
2	*Rhodobacter sphaeroides*	Brewery wastewater	5.4	126
3	*Rhodobacter sphaeroides*	Olive mill effluent	5.3	127
4	*Rhodobacter sphaeroides*	Dairy wastewater	6.3	126
5	*Rhodopseudomonas palustris*	Glycerol	10.4	129
6	*Rhodobacter capsulatus JP91*	Beet molasses	5.3	109
7	*Rhodobacter sphaeroides*	Tofu industry wastewater	1.8	113

* *mol H_2/mol C_6 or substrate in the case of glycerol.*
Source: Adapted from Ref. 102.

Mixing is another important parameter that prevents nutrient, light and temperature gradients. Inadequate mixing may cause settling of biomass, stagnant zones, cell aggregation as well as multiphase behavior. Air or inert gas bubbling at the bottom or the sides of the PhBR is the usual method of mixing,[7] although sometimes the evolved gas can be also recirculated.[136] Flat panel PhBRs lack of internal agitation and thus, several designs have been set up to overcome this fact, as a rocking motion with eccentric cam motion that provides sufficient homogenization.[137]

Most common PhBR operate in batch, continuous, or fed-batch modes.[100] Although in batch systems, the cumulative H_2 production ceases once the cells reach their stationary phase, it is possible to maintain the cell concentration of the exponential growth phase for longer periods maintaining a specific dilution rate by means of continuous systems.[138] Alternatively, in fed-batch processes, the substrate solution is added with a rate sufficient to support the bacterial community and to eliminate the substrate and product inhibitions with no effluent removal. Once the substrate consumption rate is equal to the feeding rate, the reactor substrate concentration reaches a quasi-steady-state level. Repeated cycles in fed-batch cultures evolve higher H_2 volumes and yields than in batch cultures.[139]

Although the H_2 production rates from suspended continuous cultures are relatively low as can be seen in Table 8.2, the H_2 production rates and yields can be increased by *immobilization of bacteria* in light-transmitting matrices (e.g. carrageenan, agar gel, polyvinyl alcohol, porous glass, activated glass, or polyurethane) with high A/V ratio.[98,99,102] Porous glass is stable, inert to microorganisms, does not present diffusion barriers for substrates and products (opposite to gels), and is transparent. Indeed, although most reported rates for immobilized cultures were lower than 0.2 l H_2/l h,[7,100,140] porous glass immobilized cultures of *R. sphaeroides* bacteria led to rates of 1.3 l H_2/l h[141] reaching up to 3.6–4.0 l H_2/l h.[98,142,143] An effective immobilized system is the best option for increasing the biomass concentration and consequently the light utilization efficiencies in the PhBR. This is the case of *R. palustris* that immobilized as biofilm in a flat panel or in glass beads yielded an energy efficiency of 8.9%[144] or a surprising 56%[145] (i.e. theoretical maximum CE^{en} calculated for photofermentation was 10%)[115,146] that was attributed to negligible loss of energy from 590 nm monochromatic LED source.

HRTs in PhBRs are usually longer (25–120 h), even for the best substrates (VFA).[100]

8.3.3 Operational Parameters

As it was mentioned before, process conditions in photofermentation require strict control of environmental conditions, nutritional requirements (glutamate, Fe, Mo, vitamins), and light intensities. Operational parameters must be optimized for each process: Optimal pH and temperature are in the range of 6.8–7.5 and 31–36 °C respectively,[147] whereas optimum VFA concentrations lie between 1.8 and 2.5 g/l.[100] Optimal wavelength and light intensity for PNS bacteria are in the range of visible and near-infrared spectrum (400–1000 nm)[121] and 4–10 klux (~6–50 W/m^2 depending on the irradiation source) respectively,[101,105] although an optimal intensity of 0.6–1.0 kW/m^2 has been reported for *R. Sphaeroides*.[148]

Light distribution inside PhBRs is one of the most important parameters affecting the H_2 production rate and reactor design,[115] and constitutes a great challenge in the photofermentation scale-up. Except for LED sources commented above, light-energy efficiencies typically vary between 0.2 and 9.3%.[115] Higher light-energy efficiencies can be found when photosynthetic bacteria cultures work at low light intensity and low H_2 production rates (e.g. photofermentation of glucose by *R. capsulatus* afforded 3 mol H_2/mol glucose with CE^{en} of 0.7%).[108] The use of alternating light/dark cycles can also lead to higher H_2 production than continuous illumination only[149] although the H_2 production by *R. sphaeroides* O.U.001 under dark conditions is lower than under illumination. PhBRs including light shade bands to avoid excessive sunlight at midday provided noticeable increases of conversion efficiency.[148] An alternative way to increase CE^{en} might be the reduction in the size of the photosynthetic antenna and reduction in pigment content of bacteria by genetic engineering (e.g. reduced pigment mutant of *R. sphaeroides* MTP4 produced H_2 more efficiently under high light intensity than the WT strain).[150]

High concentrations of fixed nitrogen, especially ammonium, and oxygen can inhibit the activity of nitrogenase.[102,133] Indeed, the H_2 production by *R. sphaeroides* is completely inhibited at ammonia concentrations above 2 μM, which also triggered excess biomass growth and reduction in light diffusion. Two-stage ammonia removal and the H_2 production process have been thus proposed for the H_2 production by *R. sphaeroides* from high-level ammonia containing wastewater.[151]

In spite of the intense investigations developed during the last few years, the production of H_2 by photofermentation is still in an early stage. It is expensive, energetically very inefficient and gives low H_2 production rates. However, it seems that genetic engineering could improve yields and production rates of H_2 as in the case of *R. capsulatus* JP91 yielded 7.4 mol H_2/mol hexose using sucrose as substrate or 5.2 mol H_2/mol hexose when substrate were beet molasses, although with low rates (0.06 l H_2/l h).[109]

8.4 COUPLED PROCESSES TO DARK FERMENTATION

A threshold of 8 mol H_2/mol hexose has been set to consider the production of bioH_2 by fermentative processes economically viable,[102] but none of the previously described single methods reaches such value nowadays. However, acidic effluents from dark fermentation could be adequate for other technologies as photofermentation or MECs (see below).

Two main methodologies have been described in coupled fermentation processes: co-cultivation (single stage) and sequential cultivation (two stages). The basic principle of a two-stage fermentation consists of a dark fermentation (Eqn (8.1)) of the substrate to produce H_2 and organic acids in the first stage, followed by photofermentation (Eqn (8.2)) of the acetate and other fermentation products (VFA) rich effluent. Overall yield of the integrated dark and photofermentation processes could afford theoretically up to 12 mol H_2/mol glucose (Eqn (8.6)).[30]

8.4.1 Co-cultivation Technologies

Co-cultivation methodologies (Table 8.4, entries 1–5), either in suspension or immobilized cultures, have shown to be feasible and provide noticeably higher H_2 yields (3.1–7.1 mol H_2/mol glucose) than the single processes alone.[12] Many microorganisms can be used for co-cultivation, although it is recommended that optimum pH and temperature of dark and photofermentation are similar. Thus, fermentation of starch by a suspension co-culture of *C. butryricum* and *Rhodobacter* sp M-19 afforded 6.4 mol H_2/mol glucose, whereas in a single dark fermentation yielded 1.9 mol H_2/mol of glucose. A separate two-step fermentation provided 3.7 mol H_2/mol of glucose[139] and similar co-cultures immobilized in agar gel afforded 7.0 mol H_2/mol of glucose.[152] Even higher H_2 yields (7.1 mol H_2/mol glucose) were obtained with an immobilized co-culture of *Lactobacillus delbrueckii* NBRC13953 and *R. sphaeroides*-RV (5:1, pH = 6.8, 30 °C, glucose = 4.5 g/l, Table 8.4, entry 2).[153] In spite of higher

TABLE 8.4 Selected Studies on Combined and Sequential Dark and Photofermentations for H_2 Production

Entry	Mode	Substrate	Dark fermentation microorganisms	H_2 yield*	Photofermentation microorganisms	Total H_2 yield*	Ref.
1	Co-cultivation	Starch	*C. butyricum*		*Rhodobacteracter* sp.	6.6	160
2		Glucose	*Lactobacillus debrueckki*		*R. sphaeroides RV*	7.1	153
3		Ground wheat starch	Anaerobic sludge		*R. sphaeroides NRLL-1727*	0.4	161
4		Alcohol distillery dregs	*Citrobacter freundii 01* *E. aerogenes E10*		*R.palustris P2*; cultivation in the dark	2.8	162
5		Cellulose	*Cellulomonas* sp.		*Rhodobacter capsulatus B100*	4.3	163
6	Batch	Glucose	*E. cloacae DM 11*	1.9	*Rhodobacter sphaeroides RV*	5.3	164
7		Glucose	*Clostridium butyricum*	1.7	*Rhodopseudomonas palustris*	5.5	165
8		Glucose	*E. harbinens B49*		*Rhodopseudomonas faecalis RLD-53*	3.1	166
9		Sucrose	*C. pasterianum CH4*	1.9	*R. palustris WP3–5*	5.1	167
10		Hydrolyzed cassava starch	Preheated activated sludge	2.1	*R. palustris*	2.9	168
11		Waste from yam processing	*C. butyricum* *E. aerogenes*	2.4	*Rhodobacter* sp.	7.0	160
12		Sucrose	Heat treated manure	1.8	*R. sphaeroides SH2C*	3.3	169
13		Beet molasses	*Caldicellulosiruptor saccharolyticus*	2.1	*Rhodobacter capsulatus YO3-hup⁻mutant*	6.9	166
14		Steamed ground wheat starch	Consortium	1.5	*R. sphaeroides RV*	4.6	170
15		Potato homogenate	Consortium	1.6	*Rhodobacter capsulatus B10*	5.6	171
16	Continuous	Sucrose	*C. butyricum CGS5*	3.3	*Rhodop. palustris WP3–5*	5.8	172

* *mol H_2/mol C_6.*

Source: Adapted from Refs. 12,100.

overall yields, H_2 production rates are much lower than in single-stage dark fermentation (<0.05 l H_2/l h).[100]

Co-cultivation presents some shortcomings in the coupling of dark and photofermentations that need further studies[12]: The shading of phototrophic cultures by suspended particles (bacterial cells, spores, and dense particles of solid wastes), the toxicity of substances released during dark-fermentation stage for PNS bacteria, as well as the concentration of VFA in the media from dark fermentation that can exceed 100 mM[154] while the recommended VFA concentrations for PNS bacteria are usually lower than 50 mM.[155]

8.4.2 Sequential Cultivation Technologies

Sequential dark and photofermentation (Table 8.4, entries 6–16), processes give overall H_2 yields higher than in the separate processes, although production rates are lower because photofermentation acts as bottleneck. Each process is carried out in different vessels allowing optimization of each separate stage but space requirements and operating costs to transfer material between the reactors are much higher than in single-step processes.[156] Operation parameters must be carefully controlled for both microbial systems. Thus, dark fermentation effluents (DFE) must be ammonia (lower than 0.04 g/l) and glucose-deficient and contain a desirable concentration of VFA (lower than 2.5 g/l) to promote effective photofermentation.[157] Dilution and neutralization of DFE have been used in most of the reported studies to adjust VFA and pH,[158] requiring large bioreactors that increase capital and expenditures reducing the overall energy efficiency. Other treatments of DFE such as denitrifying the substrate, centrifugation of efluents, or using semipermeable membranes have been also studied.[12]

The overall H_2 yield in these processes usually ranges between 1.6 and 7.2 mol H_2/mol glucose (Table 8.4).[100] Integration of dark fermentation of a waste medium containing sweet potato starch (10 g/l) by a mixed culture of *C. butyricum* and *E. aerogenes* HO-39 (fed-batch, 2.7 mol H_2/mol glucose) with the photofermentation of DFE by *Rhodobacter* sp. M-19 (4.5 mol H_2/mol glucose) produced up to 7.2 mol H_2/mol glucose, being pH control, and supplementation with $Na_2MoO_4 \cdot 2H_2O$ (20 μg/l) and EDTA (10 mg/l) critical parameters.[159]

A *three-stage system* (photosynthesis, dark, and photofermentation) has also been tested yielding the highest reported H_2 yields (7.1–8.3 mol H_2/mol hexose).[158,173] Microalgae, as *Dunaliella* and *Chlamydomonas*, produced a phototrophic accumulation of polysaccharides that were subsequently fermented by means of classical two-stage process. Pretreatment of algal biomass (frozen or cell concentration) prior to its transfer to the heterotrophic reactor is the main bottleneck of this method.[12]

DFE (with a pH increased from acidic to 7),[174] as acetate, can be also transformed into H_2 by MECs with consumption of an electric current.[175] MECs are emerging technologies that use electrohydrogenesis to directly convert biodegradable material into H_2.[176–178] MECs are basically modified microbial fuel cells (MFCs), oxygen is reduced at the cathode to give water and electricity, in which exoelectrogenic bacteria oxidize organic material on anode (Eqn (8.21)), and the electrons are further transferred to the cathode, where combine with protons evolved from the oxidation to produce H_2 (Eqn (8.22)).[179,180]

$$\text{Anode: } CH_3COOH + 2H_2O \rightarrow 2CO_2 + 8H^+ + 8e^- \qquad E'^0 = -0.28\ \text{V} \tag{8.21}$$

$$\text{Cathode: } 8H^+ + 8e^- \rightarrow 4H_2 \qquad \Delta_r G'^0 = +81.5\ \text{kJ/mol}\ H_2 \quad E'^0 = -0.41\ \text{V} \tag{8.22}$$

Although a circuit voltage greater than 0.13 V should produce H_2 at the cathode using acetate as organic material, typically voltages greater than 0.3 V are used, even with Pt catalysts, to increase gas production rates (0.001–0.063 l H_2/l h at 0.2–0.8 V) and yields (3.03–3.95 mol H_2/mol acetate at 0.3–0.8 V).[181] The energy efficiency ranges from 681 to 243% when evaluated in terms of only the voltage addition (0.2–0.8 V) as a result of the energy contributed by bacterial oxidation of the acetate.[181] Lactate, propionate, and butyrate or glucose are also good substrates for the H_2 production using MECs at 0.6 V achieving substrate efficiencies of 91, 89, and 80 or 71% respectively.[181]

Initial designs of MECs were pretty similar than those of fuel cells. Many microorganisms can act as anode in MECs or MFCs, although few individual strains produce power densities as high as strains from mixed communities.[182] Nowadays, anodes are made of graphite brush, stainless steel-Ni alloys, electrodeposited NiMo or NiW as well as Ni electrodeposited on carbon paper.[174] Membranes have been eliminated in MECs because they hinder proton diffusion between the electrodes and create substantial pH differences between the anode and cathode chambers. Thus, a single-chamber MEC (graphite brush anode, 0.8 V) can produce H_2 as fast as 0.13 l H_2/l h with the concomitant production of methane (3.5%).[174,183] An economic assessment of the H_2 production from wastewater of Napa Wine Company showed that MECs could be cost effective, although electricity production using MFCs was more effective than the H_2 production.[184]

8.5 BIOLOGICAL WATER GAS SHIFT REACTION

Microbial WGS reaction is an exergonic process ($\Delta_r G'^0 = -20.0$ kJ/mol CO) in which CO is oxidized to CO_2 by water, producing hydrogen (Eqn (8.3)). WGS reaction, a key step in the H_2 production from *syngas*, is catalyzed both by inorganic catalysts (Chapter 5) and carbon monoxide dehydrogenase (*CODH*) enzymes.[185–187] *CODH* is a membrane associated enzyme in anaerobes that contains non-heme Fe and Ni in the active site.[185] *CODH* provides electrons and protons for the electron transport as well as supply energy for cell growth (Eqn (8.23)). Monofunctional *CODH* only catalyzes the oxidation of CO to CO_2, and the electrons are transferred to an energy-converting hydrogenase (*ECH*) that reduces protons to molecular hydrogen (Eqn (8.19), Scheme 8.4).[188] Bifunctional *CODH*/acetyl-coenzyme A synthase can also form acetyl-CoA from CO_2 and CO, and subsequently reduced organic compounds as acetic acid (Eqn (8.24)), ethanol (Eqn (8.25)), methane (Eqn (8.26)), or hydrogen sulphide (Eqn (8.27)),[13] amongst others.[186]

$$\begin{gathered} CO + H_2O \rightarrow CO_2 + 2H^+ + 2e^- \\ \Delta_r G'^0 = -101.5 \text{ kJ/mol CO} \quad E'^0 = -0.52 \text{ V} \end{gathered} \tag{8.23}$$

$$\begin{gathered} 4CO + 2H_2O \rightarrow 2CO_2 + CH_3COOH \\ \Delta_r G'^0 = -44.1 \text{ kJ/mol CO} \end{gathered} \tag{8.24}$$

$$\begin{gathered} 6CO + 3H_2O \rightarrow 4CO_2 + CH_3CH_2OH \\ \Delta_r G'^0 = -37.4 \text{ kJ/mol CO} \end{gathered} \tag{8.25}$$

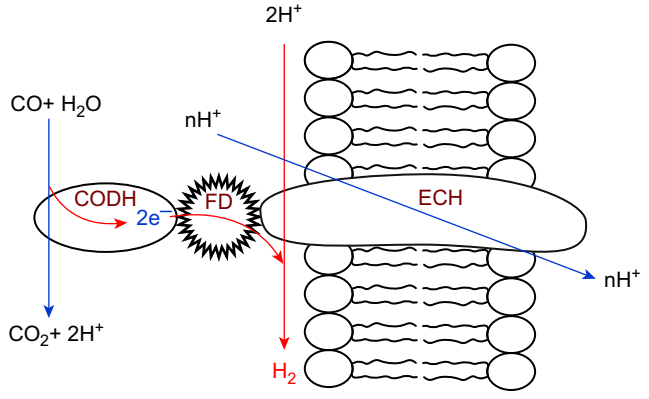

SCHEME 8.4 Hydrogen production by carbon monoxide dehydrogenase (*CODH*) coupled to an energy-converting hydrogenase (*ECH*). (For color version of this figure, the reader is referred to the online version of this book.) *Source: Adapted from Refs. 187,188.*

$$\begin{gathered} 4CO + 2H_2O \rightarrow 3CO_2 + CH_4 \\ \Delta_r G'^o = -52.7 \text{ kJ/mol CO} \end{gathered} \tag{8.26}$$

$$\begin{gathered} 4CO + SO_4^{2-} + H^+ \rightarrow 4CO_2 + HS^- \\ \Delta_r G'^0 = -58.0 \text{ kJ/mol CO} \end{gathered} \tag{8.27}$$

$$4CO + 2O_2 \rightarrow 4CO_2 \quad \Delta_r G'^0 = -257.2 \text{ kJ/mol CO} \tag{8.28}$$

Thermophilic bacteria (*Carboxydothermus hydrogenoformans*,[189] *Carboxydocella sporoproducens*,[190] *Thermosinus carboxydivorans*[191]) or acheae (*Thermococcus AM4*[192]) are examples of hydrogenic carboxydotrophs.[187] Nevertheless, *Citrobacter* sp Y19[193] and PNS bacteria *Rh. rubrum*[194] or *Rubrivivax gelatinosus*[195] are better candidates for the H_2 production via WGS as they afford CO conversions close to the theoretical H_2/CO value of 1.0 (Eqn (8.3)) under mesophilic conditions. However, given that the overall energy from WGS reaction is low, the cellular growth is slow requiring long times to reach the steady state when CO is the only substrate.[196]

Different strategies have been used to reach an adequate cell growth and the H_2 production – amongst them, alternating aerobic cell growth (Eqn (8.28)) and anaerobic H_2 production in darkness under CO/Ar atmosphere as in the case of *Citrobacter* sp Y19 that yielded up to 1 mol H_2/mol CO for 250 h at a rate of ~33 mmol H_2/g cell h.[193] Despite this high productivity, most of the studied bacteria have been cultured in anaerobic media. This is the case of *R. palustris* P4 (light, CO/Ar atm. and then dark) that afforded a rate of 21 mmol H_2/g cell h for 400 h[197] or 20 mmol H_2/g cell h using sucrose as nutrient for growing in an initial step in darkness.[198] Unfortunately, the last strain does not bear light–dark repeated cycles under CO.[198]

8.5.1 Substrate

The optimal substrate for the WGS reaction depends on the resistance of the strain. Thus, pure CO[199] and CO/(Ar,[193,197] N_2,[198] or H_2[195]) mixtures, including artificial *syngas*,[200,201] have been reported. Pure CO can be used either for thermophiles,[199] or PNS bacteria such as *Rx. gelatinosus*,[202] although 20% CO (v/v) mixtures are more commonly used. Other carbon sources, such as yeast extracts, VFA (acetate, malate), or sugars, are usually added to reach an adequate microorganism growth, as it was pointed above (e.g. *Rx. gelatinosus* CBS using malate–yeast extract as nutrient, produced up to 20 mmol H_2/g cell h[202]).

8.5.2 Reactor Design and Operating Conditions

Similar reactors than those described for fermentations can be used for microbial WGS although the mass transfer may limit CO conversion rates significantly. Hence, bioreactors for *syngas* fermentations may pursue longer gas/liquid contact time. Although CSTRs present high energy consumptions,[203] these are the most commonly employed[196] showing high gas/liquid mass transfer coefficients (K_La) at high impeller speeds because the as-generated small bubbles have lower rise velocities. K_La can be further improved incorporating baffles[203] or using Rushton-type impellers[204] as microbubble generators to the CSTR. However, it must be taken into account that excessive stirring can lead to foam formation and cell disruption, decreasing the H_2 production.[205]

The so-called trickle-bed reactors (TBR) are packed-bed reactors where the gas and the liquid phases trickle over the packing either in co-current or countercurrent mode. TBRs do not require mechanical agitation and present higher K_La than CSTRs, and thus, present higher efficiencies for *syngas* fermentation.[203] Bubble column reactors have been also successfully tested for WGS. However, their short residence times and high pressure drop make them impractical for commercial scale.[206] K_La can be also increased adding functionalized silica nanoparticles,[207] detergents, surfactants or cosolvents,[208] as well as increasing CO partial pressure.[206] A high pressure operation of the biological WGS reactor would allow reducing reactor size, although, due to CO inhibition, it would require higher cell mass to work properly.[206]

Most of the reviewed WGS processes were run at pH values close to 7, which balances *CODH* and *ECH* activities. CO content, feed rate of substrate, light, and gas flows are the key parameters being their optimal values strongly dependent on strain growth and CO uptake (e.g. the H_2 production from *syngas* in light by *Rh. rubrum* can be increased from 2[201] to 16 mmol H_2/g cell h just fixing the gas flow and the stirring rate[200]).

Despite the wide range of applications (i.e. valorization of photofermentation or steam methane reforming (SMR) byproducts), the H_2 production from *syngas* using biological WGS is not economic advantageous against catalytic methods because of the big size of bioreactors and the great demand of water and nutrients (estimated selling price for H_2 from *syngas* via WGS using *Rx. gelatinosus* in a countercurrent packed TBR reactor was greater than \$4.25/kg H_2 against \$1.00–1.50/kg H_2 for catalytic steam methane reforming),[206] although *syngas* fermentations to produce ethanol have demonstrated economic viability.[196]

8.6 BIOPHOTOLYSIS OF WATER

Cyanobacteria and green algae convert solar energy into chemical energy (carbohydrates, H_2, NAD(P)H, and ATP). Biophotolysis is the process in which light is used in biological systems to dissociate water into molecular oxygen and hydrogen. Nevertheless, some authors restrict biophotolysis of water to the process that happens through a photoautroph metabolism (i.e. sunlight, water, CO_2, and inorganic nutrients are the basic inputs). Scheme 8.5 describes "light reactions" of photosynthesis showing the electron transport chain

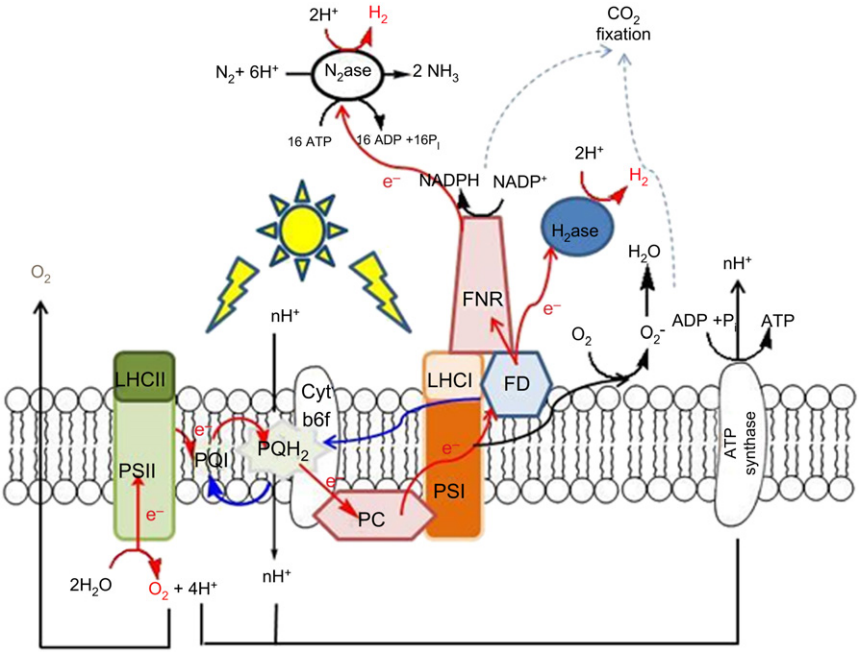

SCHEME 8.5 Electron transport chain in photosynthesis. Red arrows indicate electron flows that lead to H_2 production. Blue arrows indicate electron cyclic transports. Dotted arrows indicate electron flows that lead to CO_2 fixation. (For interpretation of the references to color in this figure legend, the reader is referred to the online version of this book.) *Source: Adapted from Ref. 209.*

embedded within the chloroplast thylakoid membrane (in green algae) or the photosynthetic membrane (in cyanobacteria).[209] Solar energy is captured by light harvesting complexes (LHCI/LHCII) at photosystems I and II (PSI/PSII). PSII is a protein complex found in plants, algae, and cyanobacteria, which mediates the light-dependent oxidation of water to yield protons, electrons, and oxygen (Eqn (8.29)). The resulting electrons are shuttled through a linear electron transport chain to the terminal electron acceptor of ferredoxin (*Fd*) via plastoquinone (*PQ*), cytochrome b6f complex (*Cyt b6f*), plastocyanin (*PC*), and PSI. *Fd* acts as a central hub of the electron flow, donating electrons to a number of biochemical pathways. Protons can be reduced by ATP-consuming nitrogenases (*N_2ase*, Eqn (8.18)), and by bidirectional or no-consuming ATP-reversible hydrogenases (*H_2ase*, Eqn (8.30), whose $D_rG'^0$ at pH = 6 is −19.1 kJ/mol H_2) giving rise to the H_2 production. Side processes include starch/glycogen biosynthesis (Calvin–Benson cycle) that is preferred under normal growth conditions or water regeneration by oxygen reduction (Mehler reaction).

$$N_2 + 8H^+ + 8e^- + 16ATP \rightarrow H_2 + 2NH_3 + 16ADP + 16P_i \quad \Delta_rG'^0 = -26.7\ \text{kJ/mol e}^- \tag{8.18}$$

$$2H_2O \rightarrow O_2 + 4H^+ + 4e^- \quad \Delta_rG'^0 = +155.7\ \text{kJ/mol } H_2O = +38.9\ \text{kJ/mol e}^- \tag{8.29}$$

$$2H^+ + 2Fd^- \rightarrow H_2 + 2Fd \quad \Delta_rG'^0 = +3.8\ \text{kJ/mol } H_2 = +1.9\ \text{kJ/mol e}^- \tag{8.30}$$

In addition, electrons can be also shuttled back to the *PQ* pool via PSI, (i.e. cyclic electron transfer). Both linear and cyclic electron transfers lead to the generation of a proton motive force within the lumen, which can be partially released through the production of ATP, or the transfer of protons to either the chloroplast stroma (algae) or the cytoplasm (cyanobacteria).[209]

Two different biophotolytic pathways can be roughly distinguished:

1. Direct biophotolysis: when electrons required for the H_2 production come from the water oxidation (PSII). It is generally performed by *green algae* under anaerobic conditions.[210]
2. Indirect biophotolysis: when electrons come from the catabolism of starch or lipids obtained during photosynthesis (Eqns (8.4.1–8.4.2),[26] and typically involves *cyanobacteria*. Indirect biophotolysis usually occurs when the photosynthetic electron transport chain is partially or fully inactive.

8.6.1 Biophotolysis Using Green Algae

Several green algae (*Scenedesmus obliquus*,[211] *Chlorella fusca*,[212] *Chlamydomonas reinhardtii*,[213,214] and *Platymonas subcordiformis*[215]) can use electrons both to metabolize H_2 in the CO_2-fixation process or to evolve H_2 in the light.[216,217]

Oxygen at concentrations higher than 0.1% acts as a transcriptional repressor and irreversible inhibitor of the [FeFe] hydrogenase catalytic activity hindering the H_2 production.[209] However, a lag of several minutes to hours is needed of anaerobic incubation in dark triggers for the synthesis and/or activation of reversible hydrogenases,[218] mainly [FeFe] hydrogenase in green algae and [NiFe] hydrogenase in cyanobacteria.[210] Anoxic conditions can be achieved either by oxygen removal (inert gases purging[219]) or by oxygen consumption through other metabolic pathways (i.e. mitochondrial respiration).

Green algae *C. reinhardtii* consume oxygen during its respiration and, under certain conditions (O_2 in the range of ppb in the liquid, low light intensity, absence of CO_2), synthesize hydrogenase enzymes and hence produce hydrogen.[220] Alternating 4 h periods of light/darkness on green algae cultures under argon atmosphere (as purging gas), H_2 was produced in a semicontinuous mode at values lower than 0.4 μmol/h.[221] Similarly, *Chlamydomonas* MGA 161 (light/dark 12:12) reached an average production rate of 1 ml H_2/l h during 84 h of darkness.[222]

Anoxic conditions and hence continuous H_2 photoproduction can be reached using sulfur deprived (-S) conditions (Table 8.5 entry 1).[223] In -S conditions, the D1 protein in PSII is not repaired, and therefore oxygen evolution is dramatically reduced by the reversible inhibition of PSII, driving the system to anaerobic conditions after a lag where cellular respiration consumes more oxygen than that is produced.[224,225] Nowadays, most H_2 production by water photolysis from green algae follow a two-stage process: First cells are grown under normal conditions, where carbon is accumulated, and then the cells are suspended on -S medium to establish anaerobiosis by consumption of cellular metabolites that triggers the H_2 production.[223] This methodology can be deemed as direct biophotolysis because the photosynthetic operations of the cells are still functioning and delivering electrons to the hydrogenases during anaerobiosis.[30] Anyway, the two-stage H_2 production by biophotolysis using green algae seems to be an attractive pathway (Table 8.5), although a detailed analysis of the variables afforded several limitations to reach up an economic viable production.

8.6.1.1 Substrate

Although green algae have been grown in many culture media, from seawater to synthetic media,

TABLE 8.5 Selected H_2 Production Rates from C. *reinhardtii* Cultures Using Two-stage Processes*

Entry	Strain (support)	Average production rate (ml H_2/l h)	Culture density† (mg Chl/l)	H_2 prod. time (h)	PhBR 1st/2nd stage	Substrate 1st/2nd stage	Ref.
1	*137c mt$^+$*	1.7	6	80	Batch	TAP/TAP-S, CO_2	223
2	*Dang 137c mt$^+$*	0.1–1.3	15	37–43	Batch/CS-PhBR	HS/HS-S, CO_2	224
3	*Dang 137c*	0.9 (2.8)**	15	30	Batch/CS-PhBR	HS/HS-S, CO_2	226
4		1.7 (4.0)**	15	15	Batch/CS-PhBR	TAP/TAP-S	226
5		3.0 (6.9)**	15	40	Batch/CS-PhBR	TAP/TAP-S, CO_2	226
6	*137c mt$^+$*	1.6–3.6 (3–7)**	23	150	Batch/CS-PhBR orbital	TAP/TAP-S-P,‡ CO_2	227
7	*137c mt$^+$(alginate)*	1.3 (4)**	18	200	Batch/Batch	TAP/TAP-S-P,‡ CO_2	227
8	*cc124*	0.6	11	4000	CS-PhBR	TAP-s§/TAP-S, CO_2	228
9		0.1–0.4	12	3048	Semicontinuous CS-PhBR	TAP/TAP-S, CO_2	225
10		0.9–1.1 (2.0)**	12	192	flat CS-PhBR	TAP/TAP-S, CO_2	229
11	*UTEX 90*	1.1–1.9	13.10^9 cells/l	79–116	Batch	TAP/TAP-S	230
12	*L159I-N230Y*	1.8 (5.8)**	12	285	Batch/flat CS-PhBR	TAP/TAP-S, CO_2	231
13	*cc124*	1.5 (2.1)**	12	53	Batch/flat CS-PhBR	TAP/TAP-S, CO_2	231
14	*WT*	0.3 (0.6)**	12	98	Batch/flat CS-PhBR	TAP/TAP-S, CO_2	231
15	*L159I-N230Y*	4.4 (9.0)**	18	160	Batch/cylinder CS-PhBR	TAP/TAP-S, CO_2	232
16	*Stm 6*	1.8 (2.6)**	26	300	Batch	TAP/TAP-S	233
17		1.0 (2.6)**	13	300	Batch	TAP/TAP-S	233
18	*cc1618*	0.2	13	100	Batch	TAP/TAP-S	233
19	*cc1036 pf18 mt$^+$(glass)*	4.3 (11.7)**	80	552	Batch/flat flow + Ar	TAP/TAP-S	234
20	*cc1036 pf18 mt$^+$(glass)*	1.6	80	2160	Batch/flat flow + Ar	TAP/TAP-s¶	235
21	From *NREL (silica)*	2.6	30	96	Batch/batch	TAP/TAP-S	236

* *H_2 production rates and culture densities were transformed at the indicated units, when possible from reference data.*
** *Initial H_2 production rate.*
† *Chl = chlorophyll.*
‡ *Phosphate buffer was also excluded from the TAP composition.*
§ *Culture-growth stage under limited sulfate conditions and sparged with 3% CO_2 in air.*
¶ *H_2 production stage under limited sulfate conditions 10–60 μM.*

most of the research has been developed using synthetic high salt content (HS)[237] media, Tris-Acetate-Phosphate (TAP) media[237] or sulfur limited/deprived media (-s/-S) where metal sulphates were substituted by chloride or citrate salts. Acetate is the carbon source in heterotrophic TAP, whereas a 2–3% CO_2 current was passed through the solution for autotrophic HS. *Chlorella pyrenoidosa* cultures were able to

produce H_2 at 0.2 ml H_2/l h under low light intensity (1.5 W/m^2) for 120 h in TAP media.[238] When the culture medium is switched from TAP to TAP-S, a typical lag of ~20 h under light irradiation is expected to reach anaerobiosis in *C. reinhardtii* cc124[218] or 137c (mt$^+$)[223] cultures, and the length of H_2 photoproduction phase is estimated in lower than 100 h, as Table 8.5 shows for 137c (mt$^+$). Heterotrophic cultures (Table 8.5, entry 1) usually present lower transition time to anaerobiosis phase and higher H_2 production than autotrophic ones (Table 8.5, entry 2).[226] A comparative experiment on the H_2 production from *C. reinhardtii* Dang 137c (Table 8.5, entries 3–5) showed that photomixotrophic cultures (entry 5) afforded better hydrogen photoproduction rates (average 3.0 ml H_2/l h) than autotrophic (entry 3) or heterotrophic (entry 4) cultures because while CO_2 is important for starch accumulation, acetate serves as the direct substrate for respiration during the aerobic phase of sulfur deprivation and, thus, contributes to the faster establishment of anaerobiosis in the PhBRs.[226] The deprivation of phosphate in TAP-S (TAP-S-P) cultures did not seem to be a decisive factor for the H_2 production, leading to similar yields (entry 6). Typically a final 87% hydrogen gas content in the headspace of the PhBR, with only 1% CO_2 and O_2 traces, can be obtained from the two-stage processes using *C. reinhardtii* 137c (mt$^+$) cultures (entry 1).

8.6.1.2 PhBRs and Operating Conditions

Cylinder or flat panel continuously stirred PhBR (CS-PhBR) are the most common PhBR for the H_2-producing stage using suspended cells (see Table 8.5). The change from growth stage (bubble column PhBR-I) to the sulfur-deprived stage (PhBR-II) is commonly accomplished by centrifugation of the growth media after a batch period in PhBR-I. However, continuous H_2 production could be achieved during 4000 h by means of two CS-PhBR: In the PhBR-I a *C. reinhardtii* cc124 culture grown under -s (TAP-s) conditions (50–75 μM sulfate) and was sparged with 3% CO_2 in air, and the resulting culture was used as continuously diluted cell feed of anaerobic PhBR-II, which ran under sulfur deprived conditions (TAP-S, Table 8.5, entry 8).[239] Long-term hydrogen production was ensured by a careful control of the operating conditions in PhBR-II (pH, light intensity, and feed rate). Sulfur-deprived cultures in PhBR-II were continuously diluted with sulfur-limited cells from PhBR-I, which quickly became sulfur deprived when cultivated anaerobically in PhBR-II and so they were competent in the H_2 production and could sustain a long-term H_2 production of 0.6 ml/l h.[228] Similarly, the *C. reinhardtii* cc124 culture from PhBR-I can be harvested by centrifugation and semicontinuously added, after dilution, to the PhBR-II (entry 9)[225] although the H_2 production rate was lower than in the previous case.

The *light intensity* and *frequency* on PhBR-I and II determines cell growth and density, PS operation and damage, as well as the H_2 production of each strain. The electron-transport chain can transport ~200 e$^-$/s that corresponds to a concentration of ~20 molecules of antenna chlorophyll/reaction center (Chl/rc), if full sunlight quanta were utilized.[221] The chlorophyll content is a function of light absorption at the photosynthetically active wavelengths of 645 nm and 663 nm,[240] although Chl concentration can be regulated by means of light intensity or genetic engineering. At average sunlight intensity, the concentration is estimated to be ~200 Chl/rc, and so only a 10% of absorbed radiation is photosynthetically active radiation (PAR) for the hydrogen production. Consequently, low absorbed light intensities (0.05–0.10 W/m^2) have been recommended for green algae to obtain up to 24% PAR.[221]

The rate for the production of hydrogen in 137c (Table 8.5, entry 2) ranges from 0.1 to 1.3 ml H_2/l h depending on the light intensity reaching its maximum at 22 W/m^2 of incident light during photosynthetic and early oxygen consumption stages and 4 W/m^2 thereafter.[224] Similar light intensities are optimum for cc124 (entry 10) for PhBR-I and II under mixotrophical conditions (2×14 W/m^2, both sides of a flat reactor) with slight variations on the production rate in the range 10–20 W/m^2.[229] The strain UTEX 90 showed an optimum light intensity at 40 W/m^2 (entry 11) for PhBR-I and II under heterotrophic conditions.[230] It is worth noting that simulation of circadian light/darkness cycles during cell growth of strain cc124 in PhBR-I yielded lower H_2 production in PhBR-II than when PhBR-I was continuously illuminated.[229]

The *mixing* in the PhBR is another important variable in the scaling-up the process as it is critical to provide uniform nutrient and light access and prevent mutual cell shading, dark zones, and even photoinhibition[241] and thus reaching higher PAR efficiencies.[242]

The PhBRs operation *temperatures* for *C. reinhardtii* strains gathered in Table 8.5 usually range from 25 to 28 °C, whereas the *optimum pH* was at about 7.2–7.6. The hydrogen partial pressure can shift hydrogenases from the hydrogen production to hydrogen uptake activities, and so decreasing the final H_2 yield.[227] This inverse relation between the hydrogen partial pressure in the headspace of the PhBR and the H_2 productivity has been evidenced in photomixotrophically cultured *C. reinhardtii* 137c mt$^+$ (entry 6).[227] Indeed, H_2 content in the PhBR headspace cannot exceed 5% to obtain higher H_2 yields, and therefore H_2 should be efficiently removed.[227]

Genetic modification of protein D1 can partially inhibit PSII, allowing hydrogenase and PSII work simultaneously affording continuous hydrogen production without the lag phases observed in -S processes.[133] D1

mutant *C. reinhardtii* L159I-N230Y can be obtained replacing L159 leucine and N230Y asparagine residues by isoleucine and tyrosine in *C. reinhardtii WT* (11/32b). As Table 8.5 shows, *C. reinhardtii* L159I-N230Y cultures (entry 12) gave significant better H_2 rates than cc124 strain (entry 13) and much better than WT (entry 14).[231] Hydrogen optimized production from *C. reinhardtii L159I-N230Y* reached up to 4.4 ml H_2/l h (18 mg Chl/l and 2×28 W/m^2, entry 15).[232]

Another promising genetic modification, *Stm6*, inhibited the cyclic electron transport around PSI of *C. reinhardtii* cc1618.[233] Entries 16–18 in Table 8.5 compare mutant vs WT (cc1618): H_2 production for the mutant is 5 times higher than that of the WT (entry 17 vs 18) and reaches up to 1.8 ml H_2/l h along 300 h (26 mg Chl/l, 20 W/m^2, entry 16).[233]

Another complementary approach to enhance the efficiency in the production of hydrogen by green algae consists of truncating the light-harvesting chlorophyll antenna by means of genetic modifications to prevent light over absorption and heat dissipation of energy.[209] Indeed, *Tla3* plasmid-modified *C. reinhardtii* strains showed up to 25% PAR efficiency from the solar light.[243]

The *immobilization of green algae* has been also studied. H_2 production was not improved by cells supported in Ca^{+2} alginate films when compared to suspended *C. reinhardtii* 137c mt$^+$ cells (Table 8.5, entry 6 vs. 7) because of diffusion limitations and poor stability under stirring, although the use of this support avoided the use of phosphate buffers.[227] Nonmotile *C. reinhardtii* mutant *CC-1036 pf18* mt$^+$ (entry 19) can be immobilized on glass fiber matrices[234] and produce H_2 (maximum rate 45 ml H_2/d) under constant TAP-S flow rate and argon bubbling up to 2.5 times faster than suspended cells (up to 11.7 ml H_2/l h referred to PhBR or 1.2 ml H_2/l h referred to TAP-S feeding, entry 19).[234] The process can be run continuously up to 90 days by keeping the 2nd stage at low sulfur concentration by adding 60–200 μM sulfate portions (entry 20).[235] The main disadvantages of this method are the long precolonization procedure (20–30 days) and the apparently irregular colonization of the glass matrix.[234] Fumed silica particles (CAB-O-SIL M-5, 200 m^2/g) have been also employed as support for the immobilization of *C. reinhardtii* (from NREL) under TAP/TAP-S media and 20 W/m^2 (entry 21).[236]

Photochemical efficiencies of 10% are generally targeted[243] to render the process viable, but current efficiencies are still far from fulfilling those requirements. Indeed, the parameter optimization of the two-stage TAP/TAP-S process using *C. reinhardtii* cc124 only yielded a photochemical efficiency in the order of 0.1%,[240] although higher efficiencies were reached by *C. reinhardtii L159I-N230YY* D1 mutant (3.2% PAR conversion efficiency). Additionally, the obtained H_2 production rates obtained by green algae biophotolysis were very low (~2 ml H_2/l·h), and so very big PhBRs (255 m^3) will be necessary to obtain moderate amounts of hydrogen continuously (1 kg H_2/d).

8.6.2 Biophotolysis Using Cyanobacteria

Cyanobacteria, also known as blue–green algae, cyanophyceae or cyanophites, have the unique property of using CO_2 as carbon source to produce cellular substances using solar energy that are further transformed to hydrogen using [NiFe] nitrogenases or bidirectional [NiFe] hydrogenases (*Hox*).[244] Cyanobacteria can produce hydrogen through indirect water-photolysis separating the photosynthetic processes from the H_2 production, either temporally or spatially.

In one hand, non-nitrogen fixing cyanobacteria (e.g. *Synechocystis*, *Synechococcus*, *Gloeobacter*, and *Gloeocapsa*)[7] can be used to produce hydrogen in a two-stages process similarly to the above described for green algae with temporal separation of photosynthesis products (glycogen accumulation) and the H_2 production. NAD(P)H produced during the dark fermentation of glycogen supplies the energy to bidirectional *Hox*,[245] which are induced under anaerobic conditions.[246] On the other hand, filamentous nitrogen-fixing cyanobacteria (e.g. the genus *Anabaena*, *Calothrix*, *Fischerella*, *Nodularia*, *Nostoc*, *Scytonema*, *Spirirestis*, and *Tolypothrix*, among others)[247] spatially separate the two processes by forming heterocysts. Heterocysts are specialized cells for nitrogen fixation (Eqn (8.18)) that are found within chains of photosynthetic cells and that are fed by neighboring photosynthetic cells, so they do not need their own photosynthetic system.[210] However, the H_2 production from [NiFe] nitrogenases (*Nif*) is limited by the uptake activity of [NiFe] hydrogenase (*Hup*).[248] Indeed, the H_2 photoproduction in N_2 fixers can be stimulated by genetic mutations that impair the activity of *Hup*[249] or inactivate the structural *hupSL* genes.[250]. Opposite to non-N_2 fixers, the hydrogen production from N_2 fixers (or diazotrophs) is usually accomplished in the two illuminated stage methods: a growth stage in the presence of CO_2 and N_2 at low light intensity followed by the H_2 photoproduction stage in inert gas. The optimal conditions for the H_2 production depend on each strain and bioreactor, but roughly light intensity, nitrogenase oxygen sensitivity of nitrogenase, uptake hydrogenase activity, temperature, as well as substrate and gas phase compositions are critical. Some reviews about the H_2 production rates from cyanobacteria have been reported.[135,251–253] Nevertheless, the comparison of these results is difficult because of the heterogeneity of units found within all the reviewed reports.

8.6.2.1 Substrate

Cyanobacteria can grow in entirely autotrophic media, being substrate or nutrient media composition one of the main factors influencing the H_2 production, see Table 8.6. Usual growth media in the H_2 production studies are: BG11[254] that contains nitrate and citrate salts; a more concentrated Allen−Arnon medium[255] (A&A) that contains vanadium salts and a higher molybdenum quantity but neither nitrate nor citrate salts; and Z8[256] that is the most concentrated medium and contains vanadium, molybdenum and nickel compounds besides nitrate and carbonate salts but not citrates. Other common growth media are ASP2[257] that contain many chlorides and higher concentration of monocationic than dicationic elements, and it was designed as marine synthetic medium. Zarrouk's medium[258] (pH > 9.5, $Na^+ > 0.4$ M) has been also used for extremophile *Arthrospira maxima*. Finally, $BG11_0$, $Zarrouk_0$, $ASP2_0$, and Z8x describe the corresponding media without any nitrate salts.

Non-nitrogen-fixing cyanobacteria (e.g. *Gloeocapsa alpicola* and *Synechocystis* PCC 6803) increase glycogen accumulation, and thus H_2 production, in nitrate-limited media.[246] Therefore, these species are usually cultured in nitrate-deprived media in two autotrophic stages: illuminated aerobic growth followed by the H_2 production under anoxic dark conditions. Similarly to green algae, the H_2 production by non-nitrogen-fixing cyanobacteria cultures also increases in -S media, (Table 8.6, entries 1−3). Methane addition also stimulated the H_2 production in *Synechocystis* sp. PCC 6803 cultures, probably due to an increase in the NAD(P)H generation.[259] When the medium was changed by addition of glucose from autotrophic to heterotrophic, the opposite effect was observed: the hydrogen production was higher in complete media ($BG11_0$ + glucose,[259] Zarrouk + glucose[260]) than in -S ($BG11_0$-S + glucose).[259] Nickel availability is essential in some strains of nonheterocystous cyanobacteria that do not possess *Hup* functionalities, as *Ar. maxima* CS-328 whose H_2 production was increased by 3.6 times when Ni concentration was raised to 1 μM.[260] In a full factorial analysis starving some elements from BG11 followed by a response surface modeling on *Synechocystis* sp. PCC 6803 cultures, it was concluded that optimum H_2 production (~0.3 ml H_2/l h) can be reached modifying BG11 with carbonate (46 mM) and low concentrations of ammonia (0.5 mM) and sulfate (0.02 mM).[261] In spite of above optimization,[135,252] the reported H_2 productions for non-nitrogen-fixing cyanobacteria are still lower than those of green algae (Table 8.5).

Nitrogen-fixing cyanobacteria are better hydrogen producers than nondiazotrophic cyanobacteria (Table 8.6, entries 5−25 vs. 1−4). The composition of the medium also influences the average specific H_2 production rate, and nitrate-deprived media are also recommended. Thus, *Anabaena variabilis* ATCC 29,413 cultures under A&A medium yielded a H_2 production rate five times larger than that under BG11 medium (Table 8.6, entries 5 and 6)[262] reaching good energy/H_2 conversion efficiency ($CE^{en} = 1.3\%$ for A&A, 0.3% for BG11). Those good results seem to be related to the expression of Vanadium-based nitrogenases and higher amounts of Mo-nitrogenases as well as the higher heterocystous frequency found in A&A than in BG11 medium.[262] It is worth noting that V-nitrogenases produce more hydrogen by mol N_2,[263] although their energy balance (Eqn (8.31)) is less favorable than Mo-nitrogenases (Eqn (8.18)).

$$N_2 + 12H^+ + 12e^- + 24ATP \rightarrow 3H_2 + 2NH_3 + 24ADP + 24P_i \quad \Delta_r G'^0 = -25.9\ \text{kJ/mol e}^- \qquad (8.31)$$

Mutant heterocystous cyanobacteria inactivating or limiting uptake hydrogenase (*Hup*-) activity, as *An. variabilis* ATCC 29,413 PK17K (Table 8.6, entry 8) and *Anabaena* PCC 7120 (entries 13−14) or/and reversible hydrogenase (*Hox*-, as *An. variabilis* ATCC 29,413 PK84, entries 8−10) showed increased H_2 production rates. Similarly, by limiting the *Hup* activity of non-N_2-fixing cyanobacteria, higher H_2 production rates than in WT strains are found, as it has been demonstrated for *ndhB*-defective *Synechocystis* PCC 6803 M55 mutant cultures.[264]

The composition of the gas phase in contact with the cultures can also condition the H_2 yield. Thus, during the growth phase, air, air enriched in CO_2, as well as Ar and/or N_2 with 2−6% CO_2 content are common gas phases, whereas anoxic gases as Ar or mixtures as Ar/2−6% CO_2 are commonly used during the H_2 production stage.[252] Methane can also stimulate the H_2 production in non-N_2 fixers.[259] The presence of CO_2 in the 2nd stage of N_2 fixers increases glycogen formation and so, fermentation products, leading to larger H_2 yields and also to higher heterocystous frequency (*Anabaena* sp. PCC 7120).[270] On the contrary, although cells remained viable for longer periods at 1% N_2, the presence of nitrogen decreases H_2 production rate[270], and indeed it is a much more potent inhibitor than oxygen (e.g. the H_2 production in heterocystous cyanobacteria is inhibited at 5% N_2 and severely at the N_2/O_2 ratio 4:1 found in air).[247] Concerning the oxygen concentration in the headspace, some N_2 fixers as *An. cylindrica* B629 show a steady loss of the H_2 production at oxygen levels greater than 1% whereas other strains, as *Nostoc commune* MFG-1, increase their H_2 production in the presence of 5−20% O_2.[247] *Calohrix* 336/3 cultures entrapped in alginate can produce H_2 even in the presence of 34% O_2 in the headspace (Table 8.6, entry 20).[268] Mutant

TABLE 8.6 Selected H_2 Production Rates from Cyanobacteria Cultures Using Two-stage Method*

Entry	Strain (support)	Average production rate (ml H_2/l h) [μmol/mg Chla h]	Culture density† (mg Chla/l)	H_2 prod. time (h)	PhBR 1st/2nd stage	Substrate 1st/2nd stage, gas	Ref.
1	*Synechocystis* PCC 6803	0.02	1.1	8	Batch	$BG11_0/BG11_0$, Ar	259
2	*Synechocystis* PCC 6803	0.10	1.1	8	Batch	$BG11_0$-S/$BG11_0$-S, Ar	259
3	*Gloeocapsa alpicola*	0.15	1.1	8	Batch	$BG11_0$-S/$BG11_0$-S, Ar	259
4	*Arthrospira maxima*	0.3–0.8	15‡	240	Shaken-PhBR	Zarrouk/$Zarrouk_0$, Ar	245
5	*An. variabilis* ATCC 29413	1.1 (1.5)**	1.1‡	190	Flat CS-PhBR	$BG11/BG11_0$, Ar	262
6	*An. variabilis* ATCC 29413	6.5 (9.0)**	1.2‡	190	Flat CS-PhBR	A&A/A&A, Ar	262
7	*An. variabilis* ATCC 29413	2.2 [45]	1.9	48	Shaken-PhBR	A&A/A&A, Ar-2% CO_2 5% N_2	265
8	*An. variabilis* 29413 PK17R Hup-	2.9 [59]	2.0	48	Shaken-PhBR	A&A/A&A, Ar-2% CO_2 5% N_2	265
9	*An. variabilis* 29413 PK84 Hup-Hox-	8.9 [168]	2.1	48	Shaken-PhBR	A&A/A&A, Ar-2% CO_2 5% N_2	265
10	*An. variabilis* 29413 PK84 Hup-Hox-	13.8 (24)**	17	3	Helical PhBR	A&A/A&A, Ar	266
11	*An. variabilis* 29413 PK84 Hup-Hox-	5.8 (10)**	3–17	25	Helical PhBR	A&A/A&A, Air-2% CO_2	266
12	*An. variabilis* 29413 PK84 Hup-Hox-	5.9	<2.5‡	960	PhBR outdoor	A&A/A&A, Air-2% CO_2	267
13	*Anabaena* PCC 7120	1.0 (1.6)** [13]**	5	96	Shaken-PhBR	Z8/Z8x, Ar-6% CO_2	268
14	*Anabaena* PCC 7120 Hup-	2.9 (3.7)** [30]**	5	120	Shaken-PhBR	Z8/Z8x, Ar-6% CO_2	268
15	*Anabaena* PCC 7120	[2]** [12]**,§	1–10	336	Batch	$BG11_0/BG11_0$, Ar	247
16	*An. cylindrica* UTEX B629	[32]** [49]**,§	1–10	336	batch	$BG11_0/BG11_0$, Ar	247
17	*Nostoc commune* MFG-1	[3]** [5]**,¶ [7]**,§	1–10	336	Batch	$BG11_0/BG11_0$, Ar	247
18	*Calothrix* 336/3	1.7 (3.1)** [25]**	5	96	Shaken-PhBR	Z8/Z8x, Ar-6% CO_2	268
19	*Calothrix* 336/3 (alginate)	0.2 (2.1)** 3 [35]**	2.4	720	Semicontin. 2nd	Z8/Z8x, Ar-6% CO_2	268
20	*Calothrix* 336/3 (alginate)	1.0 4	10	336	Continuous 2nd	Z8/Z8x, Ar-O_2, 2% CO_2	268
21	*Cyanothece* 51142	(6)** [152]**	0.5–2.0	12	12 h light/dark	$ASP2_0/ASP2_0$ Air	269
22	*Cyanothece* 51142	(20)** [230]**	2–5	12	12 h light/dark	$ASP2_0/ASP2_0$ Air 8% CO_2	269
23	*Cyanothece* 51142	(32)** [340] [373]**	2–5	12	12 h light/dark	$ASP2_0/ASP2_0$ Ar	269
24	*Cyanothece* 51142	(115)** [465]**	8–12	12	12 h light/dark	$ASP2_0/ASP2_0$-Gly‖ Ar	269
25	*Cyanothece* 51142	17	8–12	48	Shaken-PhBR	$ASP2_0/ASP2_0$-Gly‖ Air	269

* *H_2 production rates and culture densities were transformed at the indicated units, when possible from reference data.*
** *Initial H_2 or maximum production rate.*
† *Chla = chlorophyll* a.
‡ *g cell/l.*
§ *Including glucose 10 mM.*
¶ *5% Oxygen in the reactor headspace.*
‖ *Glycerol 50 mM.*

Hup-/Hox-, *An. variabilis* PK84 produced 6 ml H_2/l h for 40 days under enriched 2% CO_2 air (entry 12).

Because the H_2 production from nitrogenases is highly ATP demanding (Eqn (8.18)), an additional and limited source of carbon during 2nd stage, as CO_2,[268] glucose (entries 15–17),[247] or glycerol (entry 24 vs. 23),[269] usually increase H_2 rates and overall H_2 yields. Therefore, photomixotrophic cultures should be recommended for the H_2 production of N_2 fixers, although some nonheterocystous N_2 fixers showed a drop in H_2 rates as time goes by.[271]

Marine unicellular diazotrophs inhabiting ecological niches (such as deep oceans) with very low levels of nitrogenous nutrients, as *Cyanothece*, have developed effective strategies for collecting and storing solar energy, which can be used at night when the energy demands are high.[269] Indeed, *Cyanothece* 51,142 cultures presented the highest H_2 rates reported to date (Table 8.6, entries 21–24) probably due to their weak *Hup* activity under aerobic incubation[269] producing 17 ml H_2/l h during 2 days under air and using 50 mM glycerol as carbon source (entry 25).

Depending of each strain and mutation, hydrogen content in the reactor headspace is also conditioned by the hydrogenase-mediated H_2 uptake reaction[268,272] (e.g. 18% H_2 v/v for *Ar. maxima* cultures).[245] Moreover, the gas entrapped at the reactor headspace may consist of a dangerous H_2/O_2 mixture that should be extracted (e.g. through partial vacuum[273] or purging Ar[268]) to obtain longer H_2 production processes and higher yields.

8.6.2.2 PhBRs and Operating Conditions

PhBR useful for the H_2 production from cyanoacteria are similar to those described for green algae (tubular, flat panel, column PhBR). However, cyanobacteria are sensitive to stirring and consequently PhBR must be intermittently shaken, stirred at low speeds (80–130 rpm) or purged with gases. Last but not the least, cyanobacteria tend to form films at the PVC inner surface of the PhBR that must be cleaned when necessary (e.g. circulating polyurethane foam balls, Table 8.6, entry 12).[267]

The hydrogen production is also sensitive to the culture manipulation at the growth stage. Cultures first grown using 12 h light/dark periods and further subcultured in another media at low light intensity prior to incubation process showed a strong dependence of the H_2 production rate with the length of each step,[274] and also illumination during the growth. For instance in *Cyanothece* 51,142, 12 h light/dark periods yielded 340 μmol H_2/mg Chla·h[269] during 2nd stage whereas under continuous light only yielded 270 μmol H_2/mg Chla·h.[274] In other strains, as *Ar. maxima*, it has been demonstrated that the use of a day/night (12 h/12 h) cycle extended the viability of the culture.[245]

Similarly to green algae *C. reinhardtii*,[240] PAR of the heterocystous cyanobacteria *An. variabilis* lies in the range 400–700 nm with maxima at about 420, 610, and 680 nm.[262] *Light intensities* applied at the growth stage of cyanobacteria are generally low (5–25 W/m^2). However, during the photohydrogen stage production of N_2 fixers, the nitrogenase function is usually saturated at much higher light intensities than required for optimal growth.[251] Thus, intensities of 20–60 W/m^2 at the 2nd stage are frequent, and hydrogen production rates can be doubled within this range.[275] Higher intensities are recommended when chlorophyll concentrations are high. Similarly, increasing the *incubation temperature* from 23 to 30 °C in *Calothrix* 336/3 cultures provoked up two-fold increases in H_2 production rate.[275] Optimum temperature range for H_2 production rate usually lies in the range 30–40 °C,[135,251] although most experiments in Table 8.6 were run in the range 26–30 °C.

The *optimum pH* depended of each strain, although in most cases it is usually close to 7.0 during 1st stage and 7.5 during 2nd stage.[262] Some exceptions (e.g. the extremophile *Ar. maxima*) required pH greater than 9 at the growth stage (Table 8.6, entry 4).

Immobilization of cyanobacteria Calothrix 336/3 have been also assayed in alginate sticks, yielding prolonged H_2 productions (14 days) at moderate rates (1 ml H_2/l h) even in the presence of oxygen (Table 8.6, entry 20) although these results did not improve the productivity of outdoor PhBR using *An. variabilis PK84* mutant (6 ml H_2/l h for 40 days, entry 12).

The growth of cyanobacteria and the corresponding H_2 production can be developed entirely autotrophically with CO_2-enriched air, or even consuming the byproducts as glycerol (Table 8.6, entries 12, 22, 25). Therefore, cyanobacteria should be preferred to green algae as hydrogen producers by water photolysis. However, some challenges must be still resolved to spread this methodology being the low H_2 productions (a PhBR of 50 m^3 should be necessary to produce 1 kg H_2/day at 10 ml H_2/l h) the most relevant. It has been estimated that PhBRs producing 10 l H_2/l h (>20 times the best actual short term production) could provide 2.5 kW with a volume adequate for domestic purposes.[253]

8.7 LIFE CYCLE ASSESSMENT OF THE BIOLOGICAL H_2 PRODUCTION

It is expected that H_2 technologies will have a huge market penetration in the very next years. However, biological H_2 production is still under development hence, only few plants and operation data are available

making reliable impact evaluation by life cycle assessment(LCA) still a hard task. In this scenario, net energy analysis (NEA), as well as "out/(nonrenewable input)" net energy ratio (*NER*) can provide a tool for establishing the viability of different methods before scaling up.[1] It has been estimated that the H_2 production should take place at an efficiency of 7% under outdoor conditions to be economically viable and compete with fossil fuels.

Water biophotolysis is considered not suitable for practical application because of its low H_2 production rate and, hence, not many studies have been done about these processes.[1,99] Nevertheless, during the last few years, some LCA studies have evaluated the environmental impact of bioH_2 production and its use in the production of electricity. Assuming a 5% light-to-electricity conversion efficiency using green algae (*C. reinhardtii* in -S conditions) and a production of 164 MWh_e/year, the saved CO_2 emissions could be 25.5 t CO_2/year with respect to coal, 10.3 t CO_2/year vs. heavy fuel oil, and 8.4 t CO_2/year vs. natural gas.[276] Nevertheless, *NER* was lower than 0.1, four times less than from dark + photofermentation of potatoes peels.[276]

Water biophotolysis using cyanobacterium *Anabaena* sp. *PCC 7120* $HupL^-$ afforded 11.4 g H_2/kg biomass and 62.4 μmol H_2/mg Chla.h.[277] In spite of the relatively high H_2 production, the net energy ratio was very low ($NER < 0.001$, overall energy consumption 1538 MJ per MJ of produced H_2 and 115 kg CO_2/MJH_2). Even improving the method by elimination of the most energy-consuming steps (centrifugation accounts for 68% energy cost) and replacing artificial light (>18%) by sunlight, *NER* only rose to 0.06 ($18MJ_{expended}/MJH_2$ and 1.3 kg CO_2/MJH_2).[277] Therefore, *NER* values from biophotolysis were much less favorable than those reported for wheel to tank from natural gas steam reforming ($NER = 1.1$, 0.9 MJ_{ex}/MJH_2), electrolysis ($NER = 0.3$, 3.6 MJ_{ex}/MJH_2), as well as from dark + photofermentation of sugarcane ($NER = 3.1$, 0.3 MJ_{ex}/MJH_2) or potato peels residues ($NER = 1.8$, 0.5 MJ_{ex}/MJH_2).[278] Furthermore, greenhouse gas emissions from water biophotolysis were higher than those corresponding to natural gas steam reforming (0.1 kg CO_2/MJH_2), water electrolysis (0.2 kg CO_2/MJH_2), and dark + photofermentation of sugarcane (0.03 kg CO_2/MJH_2) or potato residues (0.1 kg CO_2/MJH_2).[278]

Alternatively, the generated cyanobacterium biomass during biophotolysis can be used as substrate in a subsequent dark-fermentation process by *E. aerogenes* to yield an overall production of 12.6 g H_2/kg biomass.[277] The integrated biophotolysis + dark-fermentation processes increased overall H_2 yield of biophotolysis by 10% but also increased the consumed energy (12%) and CO_2 emissions (10%).[277]

The production of H_2 by sugarcane dark, photofermentation, dark + photofermentation, and biocatalyzed electrolysis (MEC) has been also compared against steam methane reforming (SMR) by means of NEA and *NER*.[1] Reported *NER* values were as follows: dark 1.9, photo 3.0, dark + photo 3.1, MEC 1.8, and SMR 0.6. Net energy efficiency from SMR (64%) was clearly favorable against bioH_2 methods (10−27%) when the by-products were not considered. Nevertheless, when the by-products valorization was included within the balance, H_2 production afforded efficiencies favorable to bioH_2 processes (89% dark, 82% photo, 82% dark + photo, 77% MEC and 64% SMR).[1] Greenhouse gas emissions were greater than 0.03 kg CO_2/MJH_2 in all studied methods, but became negative for bioH_2 processes when the by-products valorization was considered (−0.73 kg CO_2/MJH_2 dark, −0.18 photo, −0.16 dark + photo, −0.15 MEC and +0.11 SMR).[1]

Another general comparison between H_2 production methods from corn silage, potato peels, or biowaste stated that H_2 from SMR offered better *NER* values (~0.75) than those from maize or potato biogas fermentation (~0.5), gasification of wood chips (~0.5), maize dark + photofermentation (0.4−0.5), or potato dark + biogas fermentation reforming (0.3−0.4).[170]

The LCA of H_2 production by dark + photofermentation processes using wheat straw, sweet sorghum stalk, and steam potato peels has been recently reported.[279] As it was pointed before, all the impacts (environmental, economic,…) were strongly dependent on whether the byproducts valorization was considered or not. Thus, when the co-product were not evaluated environmental impact was ~1.5 mPt/kg H_2[280] but when co-product were valorized values as low as 0.50, −0.03 and −1.12 mPt/kg H_2 for sorghum, wheat and potato were respectively obtained (low protein content of sorghum stalk hindered its use as fodder accounting for its positive value).[279] Fermentation stages accounted for the 41% of the impacts followed by compression and storage (25%) and the recovery stage (11−17%), whereas the hydrolysis (3%) and purification (0.5%) had minor impact. Concerning the *NER*, it was always greater than 1 reaching noticeably better values when the valorization of the by-products was considered 2.7 vs 1.2, 1.5 vs 1.1 and 1.4 vs 1.1 for potato, wheat and sorghum respectively. Moreover, greenhouse gas emissions were 56% lower in the case of potato peels than in SMR.

Technical developments combined with the use of coupled dark + photofermentation processes and the separation of particles for process heat production can lead to huge improvements in energy efficiency.[16] Food wastes have been also evaluated under integrated bioH_2 refinery point of view that includes hydrothermal hydrolysis and dark + photofermentation.[281] A previous

extractive fermentation applied to waste-derived substrates followed by hydrothermal pretreatment, achieved 83–99% of biowaste destruction. The selective separation of organic acids from waste-fed fermentations provided suitable substrate for the photofermentative H_2 production, which enhanced the gross energy generation up to 11-fold reducing the waste by 92% with a *NER* equal to 2.4.[281]

Similarly, LCA analysis on coupled dark + photofermentation process included in the *Hyvolution* project using pretreated potato peels was compared to SMR. In all the cases, Hyvolution had higher environmental impact. It must be noted that configurations without any recirculation and high buffer concentrations showed the highest impact (5.7 times higher than SMR, 98.3% of the impacts can be attributed to the inputs as buffers, base and fossil fuels for steam production) whereas the impact was reduced (2 times higher than SMR) when the sewage were recirculated.[282]

Fermentation temperature is the key factor in the energy balance in dark fermentation, accounting for ca. 80% of the energy consumption. Dark fermentation of glucose with yeasts extracts has been evaluated from an energy balance perspective in order to choose the most accurate operation parameters. H_2 production by batch dark fermentation afforded a positive net energy production in very restricted conditions (summer, small reactors, and energy recovery), but when methanation of the VFA by-products was coupled in the same reactor, the net energy balance was positive whatever be the conditions.[20]

Two-stage anaerobic digestion-MEC process[283] has been also evaluated. During the first stage, either methane or H_2 together with acetate and other VFAs were obtained from glucose by a microflora seed from Turin wastewater. More H_2 was obtained by means of an MEC using an acetate solution. The energy efficiency for the production of H_2 was very low during the first stage (11%) but the methanogenic step increased the overall energy efficiency (55%). The scale-up of the reactor (diameter beyond 2 m) rendered the energy return on investment viable. The MEC stage yielded 2.4 mol H_2/mol acetate (65%) meaning that the combination of processes can lead to increased overall yields.

All the gathered data confirm that valorization of by-products may be critical for the implementation of the biological H_2 production. Using renewable energies for the production of steam, heat integration and replacement of buffers and bases by sustainable produced ones is also necessary to reduce the environmental impact. Furthermore, the biological H_2 production is an emerging technology, thus it can be expected that process optimization might lead to further cost and greenhouse gas reductions.

8.8 CONCLUSIONS

Nowadays, nonphotosynthetic bacteria can produce 3.8 mol H_2/mol glucose and organic acids as by-products by fermentation. These acidic by-products can be further fermented by photosynthetic bacteria to reach an additional production of up to 3.6 mol H_2/mol acetate,[5] achieving an overall 91% of the theoretical maximum (12 mol H_2/mol glucose), although reported maximum yield was 69%.[173] The experimental results indicate that dark H_2 fermentation is a feasible option to produce H_2 from renewable biomass. BioH_2 can be produced at a high yield (4 mol H_2/mol hexose) or a high production rate (15 l/l h) from carbohydrates rich wastes, but not from protein and lipid-rich wastewaters and solid wastes.[10]

H_2 production via dark fermentation has the greatest potential as a pretreatment step of waste materials that can be followed by a suitable secondary process step, such as the additional H_2 production by photofermentation[3] or MECs,[1] bioconversion of volatile fatty acids to other products, (e.g. polyhydroxyalkanoates),[29] or conversion of the residual metabolites in methane by anaerobic fermentation.[20] In the last case, the net energy was calculated to be up to 80%, much higher than the yield of the H_2 production by dark fermentation alone (20%). Most LCA or *NER* analysis offered positive values for dark fermentation or two-stage methods (dark + photofermentations) of some biomass (i.e. sugarcane, potato peels or wheat straw) when valorization of co-products was considered. However, the environmental impact contribution of the dark + photofermentation processes was extremely high.

In spite of intensive research developed in the last decades, the rate of the H_2 production and *NER* values from water biophotolysis are still considerably lower than that obtained from dark or photofermentations. Biophotolysis processes need further screening or biotechnological approaches to find less sensitive strains to the loss of H_2 productivity induced by gases as N_2 or O_2.[247] Metabolic engineering of all competitive pathways may be the solution to improve the overall rates of H_2 photoproduction in microorganisms.[284]

Acknowledgments

We acknowledge Prof. Pedro M. Aparicio-Tejo for his kind comments and criticisms.

References

1. Manish, S.; Banerjee, R. *Int. J. Hydrogen Energy* **2008,** *33,* 279.
2. Das, D.; Veziroglu, T. N. *Int. J. Hydrogen Energy* **2001,** *26,* 13.
3. Kapdan, I. K.; Kargi, F. *Enzyme Microb. Technol.* **2006,** *38,* 569.

4. Reith, J. H., Wijffels, R. H., Barten, H., Eds. *Bio-methane & Bio-hydrogen. Status and Perspectives of Biological Methane and Hydrogen Production;* Dutch Biological Hydrogen Foundation: The Hague, The Netherlands, 2003.
5. Patel, S. K. S.; Kumar, P.; Kalia, V. C. *Int. J. Hydrogen Energy* **2012,** *37,* 10590.
6. Mudhoo, A.; Forster-Carneiro, T.; Sanchez, A. *Crit. Rev. Biotechnol.* **2011,** *31,* 250.
7. Eroglu, E.; Melis, A. *Bioresour. Technol.* **2011,** *102,* 8403.
8. Claassen, P. A. M.; de Vrije, T.; Koukios, E.; van Niel, E.; Eroglu, I.; Modigell, M.; Friedl, A.; Wukovits, W.; Ahrer, W. *J. Clean Prod.* **2010,** *18,* S4.
9. Najafpour, M. M.; Moghaddam, A. N.; Allakhverdiev, S. I.; Govindjee. *Biochim. Biophys. Acta Bioenerg.* **2012,** *1817,* 1110.
10. Lee, D.-J.; Show, K.-Y.; Su, A. *Bioresour. Technol.* **2011,** *102,* 8393.
11. Benemann, J. *Nat. Biotechnol.* **1996,** *14,* 1101.
12. Tekucheva, D. N.; Tsygankov, A. A. *Appl. Biochem. Microbiol.* **2012,** *48,* 319.
13. Thauer, R. K.; Jungermann, K.; Decker, K. *Bacteriol. Rev.* **1977,** *41,* 100.
14. Alberty, R. A. *Arch. Biochem. Biophys.* **1998,** *358,* 25.
15. Alberty, R. A. *Arch. Biochem. Biophys.* **1998,** *353,* 116.
16. Alberty, R. A. *Thermodynamics of Biochemical Reactions;* John Wiley & Sons, Inc.: Hoboken, N.J., USA, 2003.
17. Thauer, R. K.; Morris, J. G. *The Microbe 1984: Part II, Prokaryotes and Eukaryotes Soc. Gen. Microbiol. Symp,* Vol. 36; University Press: Cambridge, 1984.
18. Tirado-Acevedo, O.; Chinn, M. S.; Grunden, A. M.; Allen, I. L., Sima, S., Geoffrey, M. G., Eds., Vol. 70; Academic Press, 2010; p. 57.
19. Wrana, N.; Sparling, R.; Cicek, N.; Levin, D. B. *J. Clean Prod.* **2010,** *18* (Suppl. 1), S105.
20. Ruggeri, B.; Tommasi, T.; Sassi, G. *Int. J. Hydrogen Energy* **2010,** *35,* 10202.
21. Wang, A.-J.; Cao, G.-L.; Liu, W.-Z. *Adv. Biochem. Eng. Biotechnol.* **2012,** *128,* 143.
22. Show, K. Y.; Lee, D. J.; Tay, J. H.; Lin, C. Y; Chang, J. S. *Int. J. Hydrogen Energy* **2012**, in press.
23. Lee, H.-S.; Vermaas, W. F. J.; Rittmann, B. E. *Trends Biotechnol.* **2010,** *28,* 262.
24. Das, D.; Veziroglu, T. N. *Int. J. Hydrogen Energy* **2008,** *33,* 6046.
25. Lee, H.-S.; Salerno, M. B.; Rittmann, B. E. *Environ. Sci. Technol.* **2008,** *42,* 2401.
26. Mathews, J.; Wang, G. Y. *Int. J. Hydrogen Energy* **2009,** *34,* 7404.
27. Wang, J.; Wan, W. *Int. J. Hydrogen Energy* **2009,** *34,* 799.
28. Saint-Amans, S.; Girbal, L.; Andrade, J.; Ahrens, K.; Soucaille, P. *J. Bacteriol.* **2001,** *183,* 1748.
29. Angenent, L. T.; Karim, K.; Al-Dahhan, M. H.; Wrenn, B. A.; Domíguez-Espinosa, R. *Trends Biotechnol.* **2004,** *22,* 477.
30. Hallenbeck, P. C.; Ghosh, D. *Trends Biotechnol.* **2009,** *27,* 287.
31. Schröder, C.; Selig, M.; Schönheit, P. *Arch. Microbiol.* **1994,** *161,* 460.
32. Kanai, T.; Imanaka, H.; Nakajima, A.; Uwamori, K.; Omori, Y.; Fukui, T.; Atomi, H.; Imanaka, T. *J. Biotechnol.* **2005,** *116,* 271.
33. van Niel, E. W. J.; Budde, M. A. W.; de Haas, G. G.; van der Wal, F. J.; Claasen, P. A. M.; Stams, A. J. M. *Int. J. Hydrogen Energy* **2002,** *27,* 1391.
34. Zhang, T.; Liu, H.; Fang, H. H. P. *J. Environ. Manage.* **2003,** *69,* 149.
35. Kumar, N.; Das, D. *Process Biochem.* **2000,** *35,* 589.
36. Nath, K.; Das, D. *Appl. Microbiol. Biotechnol.* **2004,** *65,* 520.
37. Kumar, N.; Ghosh, A.; Das, D. *Biotechnol. Lett.* **2001,** *23,* 537.
38. Perego, P.; Fabiano, B.; Ponzano, G. P.; Palazzi, E. *Bioprocess. Eng.* **1998,** *19,* 205.
39. Chittibabu, G.; Nath, K.; Das, D. *Process Biochem.* **2006,** *41,* 682.
40. Hung, C.-H.; Chang, Y.-T.; Chang, Y.-J. *Bioresour. Technol.* **2011,** *102,* 8437.
41. Ren, N. Q.; Guo, W. Q.; Liu, B. F.; Cao, G. L.; Ding, J. *Curr. Opin. Biotechnol.* **2011,** *22,* 365.
42. Ren, N.; Li, J.; Li, B.; Wang, Y.; Liu, S. *Int. J. Hydrogen Energy* **2006,** *31,* 2147.
43. Kargi, F.; Eren, N. S.; Ozmihci, S. *Int. J. Hydrogen Energy* **2012,** *37,* 2260.
44. Kothari, R.; Singh, D. P.; Tyagi, V. V.; Tyagi, S. K. *Renew. Sust. Energy Rev.* **2012,** *16,* 2337.
45. Guo, X. M.; Trably, E.; Latrille, E.; Carrere, H.; Steyer, J.-P. *Int. J. Hydrogen Energy* **2010,** *35,* 10660.
46. La Licata, B.; Sagnelli, F.; Boulanger, A.; Lanzini, A.; Leone, P.; Zitella, P.; Santarelli, M. *Int. J. Hydrogen Energy* **2011,** *36,* 7861.
47. Chou, C.; Wang, C.; Huang, C.; Lay, J. *Int. J. Hydrogen Energy* **2008,** *33,* 1550.
48. Vatsala, T.; Mohan, R. S.; Manimaran, A. *Int. J. Hydrogen Energy* **2008,** *33,* 5404.
49. Lee, Y.-W.; Chung, J. *Int. J. Hydrogen Energy* **2010,** *35,* 11746.
50. Lin, C.-Y.; Wu, S.-Y.; Lin, P.-J.; Chang, J.-S.; Hung, C.-H.; Lee, K.-S.; Lay, C.-H.; Chu, C.-Y.; Cheng, C.-H.; Chang, A. C.; Wu, J.-H.; Chang, F.-Y.; Yang, L.-H.; Lee, C.-W.; Lin, Y.-C. *Int. J. Hydrogen Energy* **2011,** *36,* 8758.
51. Cavinato, C.; Giuliano, A.; Bolzonella, D.; Pavan, P.; Cecchi, F. *Int. J. Hydrogen Energy* **2012,** *37,* 11549.
52. Jung, K.-W.; Kim, D.-H.; Kim, S.-H.; Shin, H.-S. *Bioresour. Technol.* **2011,** *102,* 8612.
53. Yokoi, H.; Tokushige, T.; Hirose, J.; Hayashi, S.; Takasaki, Y. *J. Ferment. Bioeng.* **1997,** *83,* 481.
54. Fang, H. H. P.; Liu, H. *Bioresour. Technol.* **2002,** *82,* 87.
55. Wu, S.-Y.; Hung, C.-H.; Lin, C.-N.; Chen, H.-W.; Lee, A.-S.; Chang, J.-S. *Biotechnol. Bioeng.* **2006,** *93,* 934.
56. Zhang, Z. P.; Show, K. Y.; Tay, J. H.; David, T. L.; Lee, D. J. *Int. J. Hydrogen Energy* **2008,** *33,* 1559.
57. Jung, K.-W.; Kim, D.-H.; Shin, H.-S. *Int. J. Hydrogen Energy* **2011,** *36,* 1466.
58. Lee, K.-S.; Wu, J.-F.; Lo, Y.-S.; Lo, Y.-C.; Lin, P.-J.; Chang, J.-S. *Biotechnol. Bioeng.* **2004,** *87,* 648.
59. Lee, K. S.; Lo, Y. S.; Lo, Y. C.; Lin, P. J.; Chang, J. S. *Biotechnol. Lett.* **2003,** *25,* 133.
60. Show, K. Y.; Zhang, Z. P.; Tay, J. H.; Liang, T. D.; Lee, D. J.; Jiang, W. J. *Int. J. Hydrogen Energy* **2007,** *32,* 4744.
61. Lo, Y. C.; Lee, K. S.; Lin, P. J.; Chang, J. S. *Bioresour. Technol.* **2009,** *100,* 4381.
62. Zhang, Z.-P.; Show, K.-Y.; Tay, J.-H.; Liang, D. T.; Lee, D.-J.; Su, A. *Int. J. Hydrogen Energy* **2008,** *33,* 5151.
63. Lin, C. N.; Wu, S. Y.; Chang, J. S. *Int. J. Hydrogen Energy* **2006,** *31,* 2200.
64. Show, K.-Y.; Zhang, Z.-P.; Tay, J.-H.; Liang, D. T.; Lee, D.-J.; Ren, N.; Wang, A. *Int. J. Hydrogen Energy* **2010,** *35,* 13350.
65. Hawkes, F. R.; Hussy, I.; Kyazze, G.; Dinsdale, R.; Hawkes, D. L. *Int. J. Hydrogen Energy* **2007,** *32,* 172.
66. Ren, N.-Q.; Tang, J.; Liu, B.-F.; Guo, W.-Q. *Int. J. Hydrogen Energy* **2010,** *35,* 2807.
67. Wu, S.-Y.; Lin, C.-N.; Chang, J.-S. *Biotechnol. Prog.* **2003,** *19,* 828.
68. Kim, J. O.; Kim, Y. H.; Ryu, J. Y.; Song, B. K.; Kim, I. H.; Yeom, S. H. *Process Biochem.* **2005,** *40,* 1331.
69. Patel, S. K. S.; Purohit, H. J.; Kalia, V. C. *Int. J. Hydrogen Energy* **2010,** *35,* 10674.
70. Kumar, N.; Das, D. *Enzyme Microb. Technol.* **2001,** *29,* 280.
71. Lee, J.; Ahn, W.-Y.; Lee, C.-H. *Water Res.* **2001,** *35,* 2435.
72. Wang, X.; Ding, J.; Guo, W. Q.; Ren, N. Q. *Bioresour. Technol.* **2010,** *101,* 9749.
73. Horiuchi, J.; Kikuchi, S.; Kobayashi, M.; Kanno, T.; Shimizu, T. *Biochem. Eng. J.* **2001,** *9,* 199.
74. Bartacek, J.; Zabranska, J.; Lens, P. N. L. *Biofuels, Bioprod. Bioref.* **2007,** *1,* 201.

75. Lay, C.-H.; Lin, H.-C.; Sen, B.; Chu, C.-Y.; Lin, C.-Y. *J. Clean Prod.* **2012,** *27,* 155.
76. Kumar, N.; Das, D. *Process Biochem.* **1999,** *35,* 589.
77. Khanal, S. K.; Chen, W.-H.; Li, L.; Sung, S. *Int. J. Hydrogen Energy* **2004,** *29,* 1123.
78. Chong, M.-L.; Sabaratnam, V.; Shirai, Y.; Hassan, M. A. *Int. J. Hydrogen Energy* **2009,** *34,* 3277.
79. Valdez-Vazquez, I.; Ríos-Leal, E.; Esparza-García, F.; Cecchi, F.; Poggi-Varaldo, H. M. *Int. J. Hydrogen Energy* **2005,** *30,* 1383.
80. Ruzicka, M. *Water Res.* **2006,** *30,* 2447.
81. Kim, D.-H.; Han, S.-K.; Kim, S.-H.; Shin, H.-S. *Int. J. Hydrogen Energy* **2006,** *31,* 2158.
82. Mizuno, O.; Dinsdale, R.; Hawkes, F. R.; Hawkes, D. L.; Noike, T. *Bioresour. Technol.* **2000,** *73,* 59.
83. Liang, T.-M.; Cheng, S.-S.; Wu, K.-L. *Int. J. Hydrogen Energy* **2002,** *27,* 1157.
84. Lee, K.-S.; Tseng, T.-S.; Liu, Y.-W.; Hsiao, Y.-D. *Int. J. Hydrogen Energy* **2012**.
85. Bisaillon, A.; Turcot, J.; Hallenbeck, P. C. *Int. J. Hydrogen Energy* **2006,** *31,* 1504.
86. Salerno, M. B.; Park, W.; Zuo, Y.; Logan, B. E. *Water Res.* **2006,** *40,* 1167.
87. Morimoto, M.; Atsuko, M.; Atif, A. A. Y.; Ngan, M. A.; Fakhru'l-Razi, A.; Iyuke, S. E.; Bakir, A. M. *Int. J. Hydrogen Energy* **2004,** *29,* 709.
88. Lin, C. Y.; Lay, C. H. *Int. J. Hydrogen Energy* **2004,** *29,* 41.
89. Lin, C. Y.; Lay, C. H. *Int. J. Hydrogen Energy* **2004,** *29,* 275.
90. Liu, G.; Shen, J. *J. Biosci. Bioeng.* **2004,** *98,* 251.
91. Junelles, A. M.; Habatu-Idrissi, R.; Petitdemange, H.; Gay, R. *Curr. Microbiol.* **1988,** *17,* 299.
92. Lee, Y. J.; Miyahara, T.; Noike, T. *Bioresour. Technol.* **2001,** *80,* 227.
93. Zhang, Y.; Shen, J. *Int. J. Hydrogen Energy* **2006,** *31,* 441.
94. Li, C.; Fang, H. H. P. *Chemosphere* **2007,** *67,* 668.
95. Lin, C.-Y.; Shei, S.-H. *Int. J. Hydrogen Energy* **2008,** *33,* 587.
96. Yu, H. Q.; Fang, H. H. P. *Environ. Technol.* **2001,** *22,* 1459.
97. Yu, H. Q.; Fang, H. H. P. *Water Sci. Technol.* **2001,** *43,* 267.
98. Levin, D. B. *Int. J. Hydrogen Energy* **2004,** *29,* 1425.
99. Levin, D. B.; Pitt, L.; Love, M. *Int. J. Hydrogen Energy* **2004,** *29,* 173.
100. Argun, H.; Kargi, F. *Int. J. Hydrogen Energy* **2011,** *36,* 7443.
101. Basak, N.; Das, D. *World J. Microbiol. Biotechnol.* **2007,** *23,* 31.
102. Keskin, T.; Abo-Hashesh, M.; Hallenbeck, P. C. *Bioresour. Technol.* **2011,** *102,* 8557.
103. Kars, G.; Gunduz, U. *Int. J. Hydrogen Energy* **2010,** *35,* 6646.
104. Hustede, E.; Steinbüchel, A.; Schlegel, G. H. *Appl. Microbiol. Biotechnol.* **1993,** *39,* 87.
105. Tao, Y.; He, Y.; Wu, Y.; Liu, F.; Li, X.; Zong, W.; Zhou, Z. *Int. J. Hydrogen Energy* **2008,** *33,* 963.
106. Meyer, J.; Kelley, B. C.; Vignais, P. M. *J. Bacteriol.* **1978,** *136,* 201.
107. Allakhverdiev, S. I.; Thavasi, V.; Kreslavski, V. D.; Zharmukhamedov, S. K.; Klimov, V. V.; Ramakrishna, S.; Los, D. A.; Mimuro, M.; Nishihara, H.; Carpentier, R. *J. Photochem. Photobiol. C* **2010,** *11,* 87.
108. Abo-Hashesh, M.; Ghosh, D.; Tourigny, A.; Taous, A.; Hallenbeck, P. C. *Int. J. Hydrogen Energy* **2011,** *36,* 13889.
109. Keskin, T.; Hallenbeck, P. C. *Bioresour. Technol.* **2012,** *112,* 131.
110. Steinborn, B.; Oelze, J. *Arch. Microbiol.* **1989,** *152,* 100.
111. Jouanneau, Y.; Wong, B.; Vignais, P. M. *Biochim. Biophys. Acta, Bioenerg.* **1985,** *808,* 149.
112. Asada, Y.; Miyake, J. *J. Biosci. Bioeng.* **1999,** *88,* 1.
113. Zhu, H. G.; Suzuki, T.; Tsygankov, A. A.; Asada, Y.; Miyake, J. *Int. J. Hydrogen Energy* **1999,** *24,* 305.
114. Kim, N. J.; Lee, J. K.; Lee, C. G. *J. Microbiol. Biotechnol.* **2004,** *14,* 442.
115. Akkerman, I.; Janssen, M.; Rocha, J.; Wijffels, R. H. *Int. J. Hydrogen Energy* **2002,** *27,* 1195.
116. Hoekema, S.; Douma, R. D.; Janssen, M.; Tramper, J.; Wijffels, R. H. *Biotechnol. Bioeng.* **2006,** *95,* 613.
117. Eroglu, I.; Aslan, K.; Gunduz, U.; Yucel, M.; Turker, L. *J. Biotechnol.* **1999,** *70,* 103.
118. Barbosa, M. J.; Rocha, J. M. S.; Tramper, J.; Wijffels, R. H. *J. Biotechnol.* **2001,** *85,* 25.
119. Shi, X. Y.; Yu, H. Q. *Lett. Appl. Microbiol.* **2005,** *40,* 401.
120. Fascetti, E.; Todini, O. *Appl. Microbiol. Biotechnol.* **1995,** *44,* 300.
121. Koku, H.; Eroğlu, İ; Gündüz, U.; Yücel, M.; Türker, L. *Int. J. Hydrogen Energy* **2002,** *27,* 1315.
122. Basak, N.; Das, D. *Biomass Bioenerg.* **2009,** *33,* 911.
123. Ooshima, H.; Takakuwa, S.; Katsuda, T.; Okuda, M.; Shirasawa, T.; Azuma, M.; Kato, J. *J. Ferment. Bioeng.* **1998,** *85,* 470.
124. Maeda, I.; Miyasaka, H.; Umeda, F.; Kawase, M.; Yagi, K. *Biotechnol. Bioeng.* **2003,** *81,* 474.
125. Macler, B. A.; Pelroy, R. A.; Bassham, J. A. *J. Bacteriol.* **1979,** *138,* 446.
126. Seifert, K.; Waligorska, M.; Laniecki, M. *Int. J. Hydrogen Energy* **2010,** *35,* 9624.
127. Eroglu, E.; Gunduz, U.; Yucel, M.; Turker, L.; Eroglu, I. *Int. J. Hydrogen Energy* **2004,** *29,* 163.
128. Thangaraj, A.; Kulandaivelu, G. *Bioresour. Technol.* **1994,** *48,* 9.
129. Sabourin-Provost, G.; Hallenbeck, P. C. *Bioresour. Technol.* **2009,** *100,* 3513.
130. Eroglu, E.; Erolu, I.; Gunduz, U.; Yucel, M. *Biomass Bioenerg.* **2009,** *33,* 701.
131. Kapdan, I. K.; Kargi, F.; Oztekin, R.; Argun, H. *Int. J. Hydrogen Energy* **2009,** *34,* 2201.
132. Gebicki, J.; Modigell, M.; Schumacher, M.; van der Burg, J.; Roebroeck, E. *J. Clean Prod.* **2010,** *18* (Suppl. 1), S36.
133. Dasgupta, C. N.; Gilbert, J. J.; Lindblad, P.; Heidorn, S. A.; Skjanes, K.; Das, D. *Int. J. Hydrogen Energy* **2010,** *35,* 10218.
134. Chen, C. Y.; Chang, J. S. *Process Biochem.* **2006,** *41,* 2041.
135. Tiwari, A.; Pandey, A. *Int. J. Hydrogen Energy* **2012,** *37,* 139.
136. Hoekema, S.; Bijmans, M.; Janssen, M.; Tramper, J.; Wijffels, R. H. *Int. J. Hydrogen Energy* **2002,** *27,* 1331.
137. Gilbert, J. J.; Ray, S.; Das, D. *Int. J. Hydrogen Energy* **2011,** *36,* 3434.
138. Eroglu, I.; Aslan, K.; Gunduz, M.; Yucel, M.; Turker, L.; Zaborsky, O. R., Ed.; p. 143.
139. Yokoi, H.; Mori, S.; Hirose, J.; Hayashi, S.; Takasaki, Y. *Biotechnol. Lett.* **1998,** *20,* 895.
140. Laurinavichene, T. V.; Belokopytov, B. F.; Laurinavichius, K. S.; Khusnutdinova, A. N.; Seibert, M.; Tsygankov, A. A. *Int. J. Hydrogen Energy* **2012,** *37,* 8800.
141. Tsygankov, A. A.; Hirata, Y.; Miyake, M.; Asada, Y.; Miyake, J. *J. Ferment. Bioeng.* **1994,** *77,* 575.
142. Tsygankov, A. A.; Fedorov, A. S.; Talipova, I. V.; Laurinavichene, T. V.; Miyake, J.; Gogotov, I. N.; Rao, K. K.; Hall, D. O. *Appl. Biochem. Microbiol.* **1998,** *34,* 1.
143. Tsygankov, A. A.; Fedorov, A. S.; Talipova, I. V.; Laurinavichene, T. V.; Miyake, J.; Gogotov, I. N. *Appl. Biochem. Microbiol.* **1998,** *34,* 362.
144. Liao, Q.; Wang, Y. J.; Wang, Y. Z.; Zhu, X.; Tian, X.; Li, J. *Biores. Technol.* **2010,** *101,* 5315.
145. Tian, X.; Liao, Q.; Zhu, X.; Wang, Y.; Zhang, P.; Li, J.; Wang, H. *Bioresour. Technol.* **2010,** *101,* 977.
146. Bianchi, L.; Mannelli, F.; Viti, C.; Adessi, A.; Philippis, R. D. *Int. J. Hydrogen Energy* **2010,** *35,* 12216.
147. Ozmihci, S.; Kargi, F. *Int. J. Hydrogen Energy* **2010,** *35,* 6674.
148. Wakayama, T.; Miyake, J. *Int. J. Hydrogen Energy* **2002,** *27,* 1495.

149. Koku, H.; Eroğlu, İ; Gündüz, U.; Yücel, M.; Türker, L. *Int. J. Hydrogen Energy* **2003,** *28,* 381.
150. Kondo, T.; Arakawa, M.; Wakayama, T.; Miyake, J. *Int. J. Hydrogen Energy* **2002,** *27,* 1303.
151. Takabatake, H.; Suzuki, K.; Ko, I. B.; Noike, T. *Bioresour. Technol.* **2004,** *95,* 151.
152. Miyake, J.; Mao, X. Y.; Kawamura, S. *J. Ferment. Technol.* **1984,** *62,* 531.
153. Asada, Y.; Tokumoto, M.; Aihara, Y.; Oku, M.; Ishimi, K.; Wakayama, T.; Miyake, J.; Tomiyama, M.; Kohno, H. *Int. J. Hydrogen Energy* **2006,** *31,* 1509.
154. Özgür, E.; Afsar, N.; de Vrije, T.; Yücel, M.; Gündüz, U.; Claassen, P. A. M.; Eroglu, I. *J. Clean Prod.* **2010,** *18* (Suppl. 1), S23.
155. Lo, Y.-C.; Chen, C.-Y.; Lee, C.-M.; Chang, J.-S. *Int. J. Hydrogen Energy* **2011,** *36,* 14059.
156. Guwy, A. J.; Dinsdale, R. M.; Kim, J. R.; Massanet-Nicolau, J.; Premier, G. *Bioresour. Technol.* **2011,** *102,* 8534.
157. Lee, C. M.; Chen, P. C.; Wang, C. C.; Tung, Y. C. *Int. J. Hydrogen Energy* **2002,** *27,* 1309.
158. Kawaguchi, H.; Hashimoto, K.; Hirata, K.; Miyamoto, K. *J. Biosci. Bioeng.* **2001,** *91,* 277.
159. Yokoi, H.; Maki, R.; Hirose, J.; Hayashi, S. *Biomass Bioenerg.* **2002,** *22,* 389.
160. Yokoi, H.; Saitsu, A.; Uchida, H.; Hirose, J.; Hayashi, S.; Takasaki, Y. *J. Biosci. Bioeng.* **2001,** *91,* 58.
161. Ozmihci, S.; Kargi, F. *J. Ind. Microbiol. Biotechnol.* **2010,** *37,* 341.
162. Vatsala, T. M.; Raj, S. M.; Manimaran, A. *Int. J. Hydrogen Energy* **2008,** *33,* 5404.
163. Odom, J. M.; Peck, H. D. *Annu. Rev. Microbiol.* **1984,** *38,* 551.
164. Nath, K.; Kumar, A.; Das, D. *Appl. Microbiol. Biotechnol.* **2005,** *68,* 533.
165. Su, H.; Cheng, J.; Zhou, J.; Song, W.; Cen, K. *Int. J. Hydrogen Energy* **2009,** *34,* 8846.
166. Özgür, E.; Mars, A. E.; Peksel, B.; Louwerse, A.; Yücel, M.; Gündüz, U.; Claassen, P. A. M.; Eroğlu, İ *Int. J. Hydrogen Energy* **2010,** *35,* 511.
167. Chen, C.-Y.; Yeh, K.-L.; Lo, Y.-C.; Wang, H.-M.; Chang, J.-S. *Int. J. Hydrogen Energy* **2010,** *35,* 13356.
168. Su, H.; Cheng, J.; Zhou, J.; Song, W.; Cen, K. *Int. J. Hydrogen Energy* **2009,** *34,* 1780.
169. Phlips, E. J.; Mitsui, A. *Appl. Environ. Microbiol.* **1983,** *45,* 1212.
170. Miltner, A.; Wukovits, W.; Pröll, T.; Friedl, A. *J. Clean Prod.* **2010,** *18* (Suppl. 1), S51.
171. Laurinavichene, T. V.; Belokopytov, B. F.; Laurinavichius, K. S.; Tekucheva, D. N.; Seibert, M.; Tsygankov, A. A. *Int. J. Hydrogen Energy* **2010,** *35,* 8536.
172. Lo, Y. C.; Chen, C. Y.; Lee, C. M.; Chang, J. S. *Int. J. Hydrogen Energy* **2010,** *35,* 10944.
173. Kim, M.-S.; Baek, J.-S.; Yun, Y.-S.; Jun Sim, S.; Park, S.; Kim, S.-C. *Int. J. Hydrogen Energy* **2006,** *31,* 812.
174. Gomez, X.; Fernandez, C.; Fierro, J.; Sanchez, M. E.; Escapa, A.; Moran, A. *Bioresour. Technol.* **2011,** *102,* 8621.
175. Liu, H.; Grot, S.; Logan, B. E. *Environ. Sci. Technol.* **2005,** *39,* 4317.
176. Holladay, J. D.; Hu, J.; King, D. L.; Wang, Y. *Catal. Today* **2009,** *139,* 244.
177. Logan, B. E.; Call, D.; Cheng, S.; Hamelers, H. V. M.; Sleutels, T. H. J. A.; Jeremiasse, A. W.; Rozendal, R. A. *Environ. Sci. Technol.* **2008,** *42,* 8630.
178. Ditzig, J.; Liu, H.; Logan, B. E. *Int. J. Hydrogen Energy* **2007,** *32,* 2296.
179. Logan, B. E.; Rabaey, K. *Science* **2012,** *337,* 686.
180. Logan, B. E. *Microbial Fuel Cells;* Wiley: Hoboken, NJ, 2008.
181. Cheng, S.; Logan, B. E. *Proc. Natl. Acad. Sci. U.S.A.* **2007,** *104,* 18871.
182. Logan, B. E. *Nat. Rev. Microbiol.* **2009,** *7,* 375.
183. Call, D.; Logan, B. E. *Environ. Sci. Technol.* **2008,** *42,* 3401.
184. Cusick, R. D.; Kiely, P. D.; Logan, B. E. *Int. J. Hydrogen Energy* **2010,** *35,* 8855.
185. Ferry, J. G. *Annu. Rev. Microbiol.* **1995,** *49,* 305.
186. Oelgeschlager, E.; Rother, M. *Arch. Microbiol.* **2008,** *190,* 257.
187. Henstra, A. M.; Sipma, J.; Rinzema, A.; Stams, A. J. M. *Curr. Opin. Biotechnol.* **2007,** *18,* 200.
188. Hedderich, R. *J. Bioenerg. Biomembr.* **2004,** *36,* 65.
189. Svetlitchnyi, V.; Peschel, C.; Acker, G.; Meyer, O. *J. Bacteriol.* **2001,** *183,* 5134.
190. Slepova, T. V.; Sokolova, T. G.; Lysenko, A. M.; Tourova, T. P.; Kolganova, T. V.; Kamzolkina, O. V.; Karpov, G. A.; Bonch-Osmolovskaya, E. A. *Int. J. Syst. Evol. Microbiol.* **2006,** *56,* 797.
191. Sokolova, T. G.; Gonzalez, J. M.; Kostrikina, N. A.; Chernyh, N. A.; Slepova, T. V.; Bonch-Osmolovskaya, E. A.; Robb, F. T. *Int. J. Syst. Evol. Microbiol.* **2004,** *54,* 2353.
192. Sokolova, T. G.; Jeanthon, C.; Kostrikina, N. A.; Chernyh, N. A.; Lebedinsky, A. V.; Stackebrandt, E.; Bonch-Osmolovskaya, E. A. *Extremophiles* **2004,** *8,* 317.
193. Jung, G. Y.; Kim, J. R.; Jung, H. O.; Park, J.-Y.; Park, S. *Biotechnol. Lett.* **1999,** *21,* 869.
194. Kerby, R. L.; Ludden, P. W.; Roberts, G. P. *J. Bacteriol.* **1995,** *177,* 2241.
195. Uffen, R. L. *Proc. Natl. Acad. Sci. USA* **1976,** *73,* 3298.
196. Mohammadi, M.; Najafpour, G. D.; Younesi, H.; Lahijani, P.; Uzir, M. H.; Mohamed, A. R. *Renew. Sust. Energy Rev.* **2011,** *15,* 4255.
197. Jung, G. Y.; Jung, H. O.; Kim, J. R.; Ahn, Y.; Park, S. *Biotechnol. Lett.* **1999,** *21,* 525.
198. Lee, T. H.; Park, J.-y.; Park, S. *Biotechnol. Lett.* **2002,** *24,* 91.
199. Zhao, Y.; Cimpoia, R.; Liu, Z.; Guiot, S. R. *Int. J. Hydrogen Energy* **2011,** *36,* 10655.
200. Younesi, H.; Najafpour, G.; Ku Ismail, K. S.; Mohamed, A. R.; Kamaruddin, A. H. *Bioresour. Technol.* **2008,** *99,* 2612.
201. Najafpour, G.; Younesi, H.; Mohamed, A. R. *Biochem. Eng. J.* **2004,** *21,* 123.
202. Maness, P. C.; Weaver, P. F. *Int. J. Hydrogen Energy* **2002,** *27,* 1407.
203. Bredwell, M. D.; Srivastava, P.; Worden, R. M. *Biotechnol. Prog.* **1999,** *15,* 834.
204. Ungerman, A. J.; Heindel, T. J. *Biotechnol. Prog.* **2007,** *23,* 613.
205. Ismail, K. S. K.; Najafpour, G.; Younesi, H.; Mohamed, A. R.; Kamaruddin, A. H. *Biochem. Eng. J.* **2008,** *39,* 468.
206. Amos, A. Biological Water−Gas Shift Conversion of Carbon monoxide to Hydrogen, National Renewable Energy Laboratory (NREL). Milestone Completion Report. MP-560−35592, 2004.
207. Zhu, H.; Shanks, B. H.; Choi, D. W.; Heindel, T. J. *Biomass Bioenerg.* **2010,** *34,* 1624.
208. Gaddy, J. L; Chen, G. J. In US Patent 5,821,111, 1998.
209. Srirangan, K.; Pyne, M. E.; Perry Chou, C. *Bioresour. Technol.* **2011,** *102,* 8589.
210. Brentner, L. B.; Peccia, J.; Zimmerman, J. B. *Environ. Sci. Technol.* **2010,** *44,* 2243.
211. Gaffron, H.; Rubin, J. *J. Gen. Physiol.* **1942,** *26,* 219.
212. Kessler, E. *Arch. Microbiol.* **1973,** *93,* 91.
213. McBride, A. C.; Lien, S.; Togasaki, R. K.; San Pietro, A. *Mutational Analysis of Chlamydomonas Reinhardi: Application to Biological Solar Energy Conversion;* Academic Press: New York, 1977.
214. Greenbaum, E.; Guillard, R. R. L.; Sunda, W. G. *Photochem. Photobiol.* **1983,** *37,* 649.
215. Guan, Y.; Deng, M.; Yu, X.; Zhang, W. *Biochem. Eng. J.* **2004,** *19,* 69.
216. Melis, A. *Planta* **2007,** *226,* 1075.
217. Cinco, R. M.; Macinnis, J. M.; Greenbaum, E. *Photosynth. Res.* **1993,** *38,* 27.

218. Ghirardi, M. L.; Zhang, J. P.; Lee, J. W.; Flynn, T.; Seibert, M.; Greenbaum, E.; Melis, A. *Trends Biotechnol.* **2000,** *18,* 506.
219. Reeves, M. E.; Greenbaum, E. *Enzyme Microb. Technol.* **1985,** *10,* 169.
220. Kirtay, E. *Energy Conv. Manag.* **2011,** *52,* 1778.
221. Greenbaum, E. *Biophys. J.* **1988,** *54,* 365.
222. Miura, Y. *Process Biochem.* **1995,** *30,* 1.
223. Melis, A.; Zhang, L. P.; Forestier, M.; Ghirardi, M. L.; Seibert, M. *Plant Physiol.* **2000,** *122,* 127.
224. Tsygankov, A. A.; Kosourov, S. N.; Tolstygina, I. V.; Ghirardi, M. L.; Seibert, M. *Int. J. Hydrogen Energy* **2006,** *31,* 1574.
225. Oncel, S.; Vardar-Sukan, F. *Int. J. Hydrogen Energy* **2009,** *34,* 7592.
226. Kosourov, S.; Patrusheva, E.; Ghirardi, M. L.; Seibert, M.; Tsygankov, A. *J. Biotechnol.* **2007,** *128,* 776.
227. Kosourov, S. N.; Batyrova, K. A.; Petushkova, E.; Tsygankov, A.; Ghirardi, M. L.; Seibert, M. *Int. J. Hydrogen Energy* **2012,** *37,* 8850.
228. Fedorov, A. S.; Kosourov, S.; Ghirardi, M. L.; Seibert, M. *Appl. Biochem. Biotechnol.* **2005,** *121,* 403.
229. Oncel, S.; Sukan, F. V. *Biomass Bioenerg.* **2011,** *35,* 1066.
230. Kim, J. P.; Kang, C. D.; Park, T. H.; Kim, M. S.; Sim, S. J. *Int. J. Hydrogen Energy* **2006,** *31,* 1585.
231. Torzillo, G.; Scoma, A.; Faraloni, C.; Ena, A.; Johanningmeier, U. *Int. J. Hydrogen Energy* **2009,** *34,* 4529.
232. Scoma, A.; Krawietz, D.; Faraloni, C.; Giannelli, L.; Happe, T.; Torzillo, G. *J. Biotechnol.* **2012,** *157,* 613.
233. Kruse, O.; Rupprecht, J.; Bader, K. P.; Thomas-Hall, S.; Schenk, P. M.; Finazzi, G.; Hankamer, B. *J. Biol. Chem.* **2005,** *280,* 34170.
234. Laurinavichene, T. V.; Fedorov, A. S.; Ghirardi, M. L.; Seibert, M.; Tsygankov, A. A. *Int. J. Hydrogen Energy* **2006,** *31,* 659.
235. Laurinavichene, T. V.; Kosourov, S. N.; Ghirardi, M. L.; Seibert, M.; Tsygankov, A. A. *J. Biotechnol.* **2008,** *134,* 275.
236. Hahn, J. J.; Ghirardi, M. L.; Jacoby, W. A. *Biochem. Eng. J.* **2007,** *37,* 75.
237. Harris, E. H. *The Chlamydomonas Sourcebook: A Comprehensive Guide to Biology and Laboratory Use;* Academic Press: San Diego, 1989.
238. Wang, H.; Fan, X.; Zhang, Y.; Yang, D.; Guo, R. *Biotechnol. Lett.* **2011,** *33,* 1345.
239. Kosourov, S. N.; Tsygankov, A. A.; Seibert, M.; Ghirardi, M. L. *Biotechnol. Bioeng.* **2002,** *78,* 731.
240. Tamburic, B.; Zemichael, F. W.; Maitland, G. C.; Hellgardt, K. *Int. J. Hydrogen Energy* **2011,** *36,* 7872.
241. Pulz, O. *Appl. Microbiol. Biotechnol.* **2001,** *57,* 287.
242. Oncel, S.; Sabankay, M. *Bioresour. Technol.* **2012,** *121,* 228.
243. Melis, T. University of California, 2011.
244. Prince, R. C.; Kheshgi, H. S. *Crit. Rev. Microbiol.* **2005,** *31,* 19.
245. Ananyev, G.; Carrieri, D.; Dismukes, G. C. *Appl. Environ. Microbiol.* **2008,** *74,* 6102.
246. Troshina, O.; Serebryakova, L.; Sheremetieva, M.; Lindblad, P. *Int. J. Hydrogen Energy* **2002,** *27,* 1283.
247. Yeager, C. M.; Milliken, C. E.; Bagwell, C. E.; Staples, L.; Berseth, P. A.; Sessions, H. T. *Int. J. Hydrogen Energy* **2011,** *36,* 7487.
248. Tamagnini, P.; Axelsson, R.; Lindberg, P.; Oxelfelt, F.; Wünschiers, R.; Lindblad, P. *Microbiol. Mol. Biol. Rev.* **2002,** *66,* 1.
249. Mikheeva, L. E.; Schmitz, O.; Shestakov, S. V.; Bothe, H. *Z. Naturforsch. C* **1995,** *50,* 505.
250. Happe, T.; Schutz, K.; Bohme, H. *J. Bacteriol.* **2000,** *182,* 1624.
251. Dutta, D.; De, D.; Chaudhuri, S.; Bhattacharya, S. *Microb. Cell. Fact.* **2005,** *4,* 36.
252. Lopes Pinto, F. A.; Troshina, O.; Lindblad, P. *Int. J. Hydrogen Energy* **2002,** *27,* 1209.
253. Tsygankov, A. *Appl. Biochem. Microbiol.* **2007,** *43,* 250.
254. Allen, M. M. *J. Phycol.* **1968,** *4,* 1.
255. Allen, M. B.; Arnon, D. I. *Plant Physiol.* **1955,** *30,* 366.
256. Kotai, J. Norwegian Institute for Water Research, Publication B-11/69, 1972.
257. Provasoli, L.; McLaughlin, J. J. A.; Droop, M. R. *Arch. Microbiol.* **1957,** *25,* 392.
258. Zarrouk, C. Contribution a l'etude d'une Cyanophycee. Influence de divers facteurs physiques et chimiques sur la croissance et la photosynthese de Spirulina maxima. PhD Thesis. University of Paris (Paris, France), 1966.
259. Antal, T. K.; Lindblad, P. *J. Appl. Microbiol.* **2005,** *94,* 114.
260. Carrieri, D.; Ananyev, G.; Costas, A. M. G.; Bryant, D. A.; Dismukes, G. C. *Int. J. Hydrogen Energy* **2008,** *33,* 2014.
261. Burrows, E. H.; Chaplen, F. W. R.; Ely, R. L. *Int. J. Hydrogen Energy* **2008,** *33,* 6092.
262. Berberoglu, H.; Jay, J.; Pilon, L. *Int. J. Hydrogen Energy* **2008,** *33,* 1172.
263. Wall, J. D. *Nat. Biotechnol.* **2004,** *22,* 40.
264. Cournac, L.; Guedeney, G.; Peltier, G.; Vignais, P. M. *J. Bacteriol.* **2004,** *186,* 1737.
265. Sveshnikov, D. A.; Sveshnikova, N. V.; Rao, K. K.; Hall, D. O. *FEMS Microbiol. Lett.* **1997,** *147,* 297.
266. Tsygankov, A. A.; Borodin, V. B.; Rao, K. K.; Hall, D. O. *Biotechnol. Bioeng.* **1999,** *64,* 709.
267. Tsygankov, A. A.; Fedorov, A. S.; Kosourov, S. N.; Rao, K. K. *Biotechnol. Bioeng.* **2002,** *80,* 777.
268. Leino, H.; Kosourov, S. N.; Saari, L.; Sivonen, K.; Tsygankov, A. A.; Aro, E.-M.; Allahverdiyeva, Y. *Int. J. Hydrogen Energy* **2012,** *37,* 151.
269. Bandyopadhyay, A.; Stoeckel, J.; Min, H.; Sherman, L. A.; Pakrasi, H. B. *Nat. Commun.* **2010,** *1,* 139.
270. Marques, A. E.; Barbosa, A. T.; Jotta, J.; Coelho, M. C.; Tamagnini, P.; Gouveia, L. *Biomass Bioenerg.* **2011,** *35,* 4426.
271. Feng, X.; Bandyopadhyay, A.; Berla, B.; Page, L.; Wu, B.; Pakrasi, H. B.; Tang, Y. J. *Microbiology* **2010,** *156,* 2566.
272. Howarth, D. C.; Codd, G. A. *J. Gen. Microbiol.* **1985,** *131,* 1561.
273. Markov, S. A.; Thomas, A. D.; Bazin, M. J.; Hall, D. O. *Int. J. Hydrogen Energy* **1997,** *22,* 521.
274. Min, H.; Sherman, L. A. *Appl. Environ. Microbiol.* **2010,** *76,* 4293.
275. Allahverdiyeva, Y.; Leino, H.; Saari, L.; Fewer, D. P.; Shunmugam, S.; Sivonen, K.; Aro, E.-M. *Int. J. Hydrogen Energy* **2010,** *35,* 1117.
276. Romagnoli, F.; Blumberga, D.; Pilicka, I. *Int. J. Hydrogen Energy* **2011,** *36,* 7866.
277. Ferreira, A. F.; Marques, A. C.; Batista, A. P.; Marques, P. A. S. S.; Gouveia, L.; Silva, C. M. *Int. J. Hydrogen Energy* **2012,** *37,* 179.
278. Ferreira, A. F.; Ribau, J. P.; Silva, C. M. *Int. J. Hydrogen Energy* **2011,** *36,* 13547.
279. Djomo, S. N.; Blumberga, D. *Bioresour. Technol.* **2011,** *102,* 2684.
280. Pt is the Unit of Environmental Penalty Based on Impact 2002+. 1 Pt Represents 0.00071 DALY for Human Health, 9950 kg CO_{2eq} for Climate Change and 15200 MJ for Resources. Negative Values Account for Environmental Benign Processes.
281. Redwood, M. D.; Orozco, R. L.; Majewski, A. J.; Macaskie, L. E. *Bioresour. Technol.* **2012,** *119,* 384.
282. Ochs, D.; Wukovits, W.; Ahrer, W. *J. Clean Prod.* **2010,** *18,* S88.
283. Tommasi, T.; Ruggeri, B.; Sanfilippo, S. *J. Clean Prod.* **2012,** *34,* 91.
284. Turner, J.; Sverdrup, G.; Mann, M. K.; Maness, P.-C.; Kroposki, B.; Ghirardi, M.; Evans, R. J.; Blake, D. *Int. J. Energy Res.* **2008,** *32,* 379.

CHAPTER

9

Advances in Structured and Microstructured Catalytic Reactors for Hydrogen Production

Oihane Sanz[*], *Francisco J. Echave*[†], *Francisca Romero-Sarria*[‡], *José Antonio Odriozola*[‡], *Mario Montes*[*]

[*]Department of Applied Chemistry, UFI11/53, University of the Basque Country, UPV/EHU, San Sebastian, Spain, [†]Novargi-Nova-Synergy Industrial Solutions S.L, Vitoria-Gasteiz, Spain, [‡]Department of Inorganic Chemistry and Institute of Materials Science of Seville, University of Sevilla-CSIC, Sevilla, Spain

OUTLINE

9.1 Introduction 201
9.2 Structured Catalysts 202
9.3 Microstructured Reactors 202
9.4 Substrate Materials for Structured Catalysts and Microstructured Reactors 203
9.5 Catalyst Coating on Structured Substrate 205
9.5.1 Dip Coating or Washcoating 206
9.5.1.1 Slurry Properties 206
9.5.1.2 Washcoating Procedure 207
9.5.2 Surface Growing 208
9.5.3 Other Coating Methods 209
9.5.3.1 Methods from the Vapor Phase 209
9.6 Hydrogen Production from Biofuels 209
9.6.1 Dimethyl Ether 210
9.6.2 Biomethanol 211
9.6.2.1 Membranes 212
9.6.2.2 Foams 212
9.6.2.3 Felts 212
9.6.2.4 Microfibrous Networks 212
9.6.3 Biodiesel 213
9.6.4 Bioglycerol 213
9.6.5 Biogas 215
9.6.6 Producer Gas 215
9.6.7 Bioethanol 216
9.6.8 Bio-Oil 217
9.7 Combustion 217
Acknowledgments 218
References 218

9.1 INTRODUCTION

Fixed bed catalytic reactors are the most common chemical reactors but have certain limitations. On the one hand, it is impossible to simultaneously minimize the pressure drop and diffusional limitations in the pores, since both phenomena depend on catalyst particle size and the former requires very large sizes, while the second one requires very small sizes. The second problem is associated with the typical flow maldistribution that fixed beds produce. To solve these problems, the use of structured catalysts has been proposed, where the catalyst forms a thin film that coats the walls of the channels or pores of a structure, which allows for higher fluid flow with low pressure drop.[1]

However, in the case of fuel processors for the production of hydrogen there is a further limitation, which is the need of compact and lightweight systems for small-scale applications and transportation that are becoming increasingly frequent. To meet this need,

microchannel reactors have been recently developed, which also allow a remarkable integration of catalytic processes with the typical heat transfer from the fuel processing systems for the production of hydrogen.[2]

In this chapter, we will review the impact of structured and microstructured systems on renewable hydrogen production starting with sections in which these systems as well as some relevant aspects of their manufacture will be described.

9.2 STRUCTURED CATALYSTS

Structured catalysts are continuous unitary structures containing wide pores or channels allowing high flow with limited pressure drop. The catalytically active phase is dispersed in the ceramic structure (incorporated catalysts) or in a surface layer deposited on the walls of the structure channels (coated structured catalysts).[1] Considering the shape, structured catalysts can be classified into three groups: metal-gauze catalysts, foams and parallel longitudinal channel monoliths.

Metal gauzes are bulk-metal catalysts involving extremely short residence times and therefore are only suitable for extremely rapid reactions. Despite their important role in some industrial processes such as ammonia oxidation in nitric acid manufacture, they are not relevant in the production of renewable hydrogen and therefore will be not considered in this monograph.

Open-celled foams are three-dimensional (3D) cellular materials made of interconnected solid struts, forming a network. The unit cell in foams resembles a polyhedron with pentagonal or hexagonal faces that limit a spherical-like inner space. Each cell constitutes a pore, and the cell size is usually expressed in terms of pores per linear inch.[3] Tronconi et al., using a trade-off analysis between pressure drop and mass transfer, showed that foams show intermediate properties between fixed beds and parallel channel monoliths: the pressure drop is higher than in monoliths but far lower than in fixed bed and the flow pattern is not as laminar as in monoliths, favoring the gas–catalyst contact (increasing catalytic efficiency) and allowing radial flow.[3]

Parallel longitudinal channel monoliths are continuous unitary structures containing many narrow parallel straight or zigzag passages. In the case of ceramic monoliths, they are made by extrusion presenting square, triangular or hexagonal cells. The most frequent design in metallic monoliths is based on rolling or stacking alternate corrugated and flat strips. Multiple parallel channels are generated in between the corrugated strip. Crimping a metal foil on a pair of rollers having sinusoidal or triangular teeth produces corrugation. Variation in the number of cells per unit area is achieved by varying the pitch and width of the profile on the cramping rolls.[4] Avila et al. reviewed the different strategies proposed to prevent the telescopic effect and to increase the turbulence and radial flow.[4] Two parameters related to each characterize monoliths: the cell density (expressed in cells per square inch (cpsi) or cells per square centimeter) and the wall thickness. In the case of ceramic monoliths, usual values for cell density are between 50 and 400 cpsi and those for wall thickness are between 1 and 0.1 mm. For metallic monoliths, cell density can reach values as high as 1600 cpsi with wall thickness between 100 and 20 μm.[4]

9.3 MICROSTRUCTURED REACTORS

Through this past decade, there has been an enormous interest both in the academia and industry in the reactors of microchannels (sometimes called microreactors), as evidenced by the excellent monographs recently published.[5–10] Although a slight disagreement among different authors exists, the term reactors of microchannels is usually used to name the devices for chemical reaction in which the channels have at least one dimension smaller than 1 mm (submillimeter range).

They are characterized by a construction in "hierarchical" way, i.e. by assembly of compound units, themselves made of subunits, and so on. The basic unit is the microstructure that in most of the cases is a microchannel. A set of microstructures built together forms an element that together with connecting pipelines of fluids and a support or material base forms a unit. Units are usually grouped in the form of stacks (piling up), and when introduced into a housing with their corresponding connections, they form a device. The interconnection of several devices, either in parallel, series or any combination thereof, along with other elements or equipment, forms a plant or setup.

Due to size reduction, microchannels reactors provide a series of important advantages, among which the following stand out: (1) decrease in linear dimensions, (2) increase of the surface/volume ratio, (3) volume reduction, (4) fast and inexpensive tests for materials and processes, and (5) production flexibility. As a result, microchannels reactors show a series of benefits such as: (1) faster transfer of results from research to production; (2) faster start-up of production at lower costs; (3) easier scaling up of production; (4) smaller plant size; (5) lower materials, transport and energy costs; and (5) higher flexibility to market demands.

However, it must be realized that if production costs are related to economy of scale, the use of microchannels reactors will involve additional costs to conventional processes, as the higher costs due to micromachining, clearly higher than those of conventional equipments, must be added. Therefore, the use of microchannels

reactors will be justified only in those cases where it brings clear improvements to balance the unavoidable increases of cost of manufacture or operation. Some of these cases are related to areas such as[5] (1) substituting batch processes by continuous processes, (2) process intensification, (3) work safety, (5) changes in product quality, and (5) production delocalization.

The development of microchannel technology has advanced through independent evolution of reactor technology and catalyst technology. Three key aspects should be considered in the development of the technology of the reactor[11,12]: the manufacturing of the microchannels, the welding of the plates machined and chemical resistance to corrosion in the reaction atmosphere. Among the many different possibilities of producing microstructures (micromilling, microelectro discharge machining, embossing, laser micromachining, etc.), wet chemical etching is fast, leads to channels hemi cylindrical easily reproducible, is economical and is implemented industrially for most alloys of interest.[2,13] The reaction conditions are a point of paramount importance and will be discussed separately in the next section. The manufacturing of complex shape microreactors, moreover, must work under high pressures and temperatures, so it requires the use of unconventional bonding techniques. The most attractive among the possible techniques is diffusion welding with or without filler metal for which metallic low-melting point glasses are commonly used.[12,14,15]

9.4 SUBSTRATE MATERIALS FOR STRUCTURED CATALYSTS AND MICROSTRUCTURED REACTORS

The choice of the best substrate material depends on many properties that can be classified into three groups[4]:

- Properties related to the fabrication process such as adequate plasticity to permit their extrusion and immediate conformation into rigid structures with monolithic shape in the case of ceramics, or capability of rolling to thin foils and weldability in the case of metals.
- Properties related to the catalytic coating adhesion such as chemical compatibility or surface roughness.
- Properties related to the use of the catalyst or microreactor such as mechanical, thermal and chemical resistance under operation conditions.

In the case of ceramics, the most popular material is cordierite ($2MgO \cdot 2Al_2O_3 \cdot 5SiO_2$) due to its low thermal expansion coefficient,[16] high temperature resistance, good mechanical properties, chemical compatibility with most catalytic coatings and appropriate open porosity.[17] The fabrication of these ceramic monoliths can be carried out using cordierite as the starting material or a mixture of precursors and their posterior cordierisation.[4] Monoliths made from other ceramic materials needed for specific applications have been developed and have become commercially available, e.g. α- and γ-alumina, mullite, titania, zirconia, silicon nitride, silicon carbide, and the like, all of them doped with other compounds if necessary.[1]

Metals have important advantages over ceramic materials for their use as substrates for structured catalysts and microchannel reactors. First, they have greater mechanical strength and higher thermal conductivity. Second, they can be laminated to thickness much lower than those obtained by extrusion of ceramic pastes. This implies a greater open area in the case of monoliths, which means less pressure drop, and the possibility of manufacturing with much higher cell density. On the other hand, the lower wall thickness means less thermal inertia. Finally, metals are much easier to work, as they can be laminated, cut, embossed and machined, allowing manufacturing in more sophisticated shapes.

In the case of monoliths, it opens important opportunities for obtaining complex flow patterns that reduce the limitations of the highly laminar flow characteristic of the monoliths. Likewise, these capabilities of machining and welding are necessary in the manufacturing of microchannel reactors. On the other hand, the main drawback of metallic substrates for monoliths and microchannel reactors is the difficulty to obtain a good adherence between the catalytic coating and the metallic substrate. Catalyst adherence is hence of prime importance for the selection of the correct metallic alloy. Therefore, alloy selection depends on both the chemical resistance to reaction medium and the possibility of producing an adherent catalytic coating.

Many different metals and alloys have been used as substrate for monoliths and microchannel reactors,[18,19] but taking into account their mechanical and thermal properties, steels and aluminum are the most frequently used. Aluminum conducts the heat better and may be covered easily by alumina[20] but steel bears much higher working temperatures and pressures. Regarding steel, it is very important to consider the corrosion problems that can arise under extreme reaction conditions. Corrosion phenomena in an atmosphere with high (higher than unity) carbon activity, "metal dusting (MD)", is frequent in chemical industry, in particular in reforming and synthesis gas plants.[21] MD is a catastrophic carburizing phenomenon under high carbon activity atmospheres at temperatures between 450 and 800 °C producing a graphite and small metal particle layer and other compounds (carbides and oxides).[22] The corrosion degree of the alloy depends on its nature, the atmosphere and the temperature. All these commonly known problems, in particular for the case of iron-based alloys,[22] are less evidenced in the case of

nickel-based alloys[21] and some data are starting to be provided on the influence of the contact with ceramic materials. Catalytic phenomena leading to coke formation, which take place on oxidic catalysts considerably, decrease the induction period of the MD phenomenon.[23] Recently, Yin[24] discussed the thermodynamic aspects of the carburizing reaction in model atmospheres relevant to reforming $CO-CO_2$ and $CO-H_2O-H_2$ among others, considering pure metals and analyzing the influence of the gas-phase chemistry, temperature and pressure and found that the behavior is a function of the metallic nature, proving that Ni and Fe behave differently depending on the system's total pressure. Yin did not report, however, data for metal alloys as the free energy values of the involved reactions are not available. In general, carburizing phenomena, although severe, are less catastrophic in mixtures such as CH_4-H_2 than in mixtures such as $CO-H_2O-H_2$ in the case of alloys with high Ni content (AISI 310SS o Incoloy 800HT).[25,26]

Another aspect to be considered, that is becoming relevant in the past years, is the evidence that MD not only causes modifications in reactor wall but also affects gas-phase composition. Kempen and van Wortel[27] proved that water–gas shift (WGS) reaction is affected by carburizing of the reactor wall. Zeng and Natesan[28] studied the behavior of 14 high-temperature metal alloys, generally nickel base or high nickel content, at temperatures around 800 °C in $CO_2-CO-H_2O-H_2$ atmospheres and concluded that higher the nickel content, the less severe is the MD, which also decreased with high water concentrations and low pressures. High tungsten content in Fe–Cr alloys causes a clear improvement of the behavior of these alloys at working temperatures.[29]

In order to improve the adherence between the catalyst coating and the substrate alloy, different strategies have been proposed to intercalate an alumina interface, as recently reviewed by Avila et al.[4] But since the 1970s, when it was given a FeCrAl alloy with small amounts of Y shaped in thin sheets for the construction of metallic monoliths, Al-containing ferritic steels have become the reference alloy to prepare structured catalysts.[30,31] In the work by Avila et al. a complete review of the composition of the different commercial alloys in this family as well as their properties and the protection mechanism against high-temperature oxidation can be found.[4] These can be summarized as follows: (1) the main components are Fe 70–90%, Cr 10–25%, and Al 4–5% and the minor components (<1%) are Y, Ti, Zr, Ce, and Hf; (2) the high-temperature oxidation produces a protective alumina scale; (3) and minor components play very important roles such as reducing the oxygen permeability of the alumina protective scale and increasing the scale adherence during cyclic oxidation.

The adhesion of the catalyst to the alumina scale protecting FeCrAl alloys is related to chemical compatibility

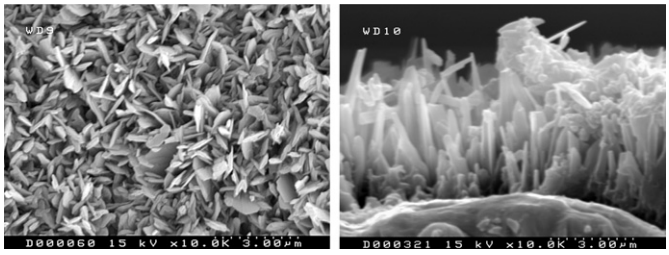

FIGURE 9.1 Top and lateral scanning electron micrographs of the alumina whiskers produced on Fecralloy® by calcination in air at 900 °C for 22 h.

(bond formation during thermal treatments) and the lack of important mismatch between their thermal expansion coefficients. However, in addition to that, several authors have reported that the mechanical anchoring when the surface roughness is wider than the catalyst particle size is even more important than the chemical bonding.[32–35]

This is another reason to explain the success of the FeCrAl alloys as metallic substrate for catalyst coating. Indeed, when these alloys are calcined in air at controlled temperature between 875 and 925 °C for long time (>12 h),[36,37] the aluminum migrating from the bulk oxidizes at the surface forming a very open structure of long randomly oriented whiskers (Fig. 9.1).

Austenitic steels such AISI 304 or AISI 316, have also been proposed as substrate for structured catalyst.[38] The oxidation of austenitic stainless steels results in the formation of a scale whose main constituents are mixed Cr–Fe and Cr–Fe–Mn oxides[39–41] in such a way that spinel-type oxides, $Mn_{1+x}Cr_{2-x}O_4$, having octahedral shape form the outermost part of the scale, while Cr_2O_3 platelets remain in the innermost part of the scale.[40] The thickness and exact composition of the scale depends on the temperature, time and atmosphere in which the oxidation treatment has been carried out.[41] The scale produced on AISI 304 monoliths by oxidation in air at 900 °C for 1 h has been shown to be suitable for coating with cryptomelane-like catalyst (manganese octahedral molecular sieve) both by washcoating and in situ grown coating.[38]

Aluminum and its alloys are also interesting substrates for medium-to-low temperature uses. Aluminum can be coated by anodization of an extremely adherent alumina layer, which can also provide textural properties on demand, depending on the parameters of the anodizing process. The choice of the electrolyte and the electrochemical parameters (temperature, time, electrolyte concentration, voltage and current density) allows one to control surface area and pore size of the alumina coating produced.[20,42,43] Figure 9.2 is the top view of the alumina produced with different operational conditions showing pores from 20 to 200 nm.

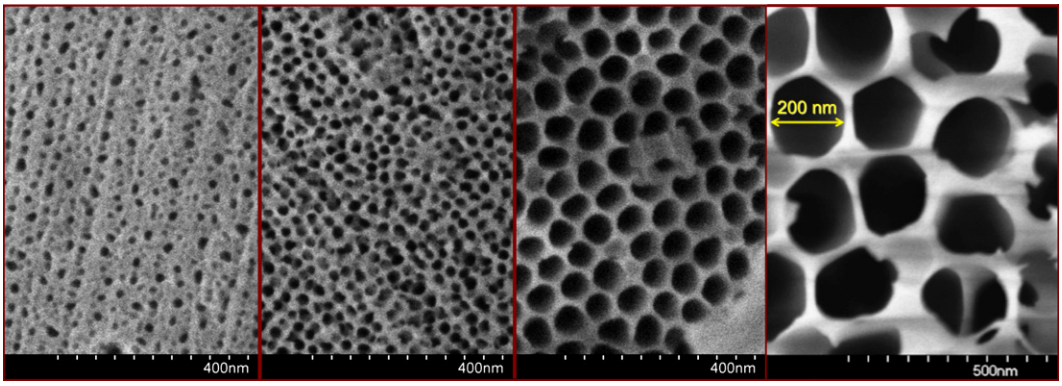

FIGURE 9.2 Top view of the porosity produced under different aluminum anodizing conditions. (For color version of this figure, the reader is referred to the online version of this book.)

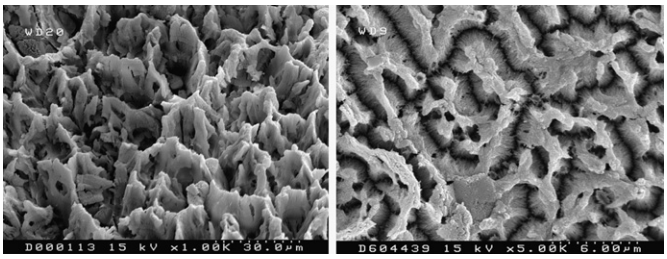

FIGURE 9.3 Surface roughness of the alumina scale produced by anodization under cracking conditions.

Furthermore, the anodizing process has been proposed by Sanz et al.[35,44] as a means of creating high surface roughness, which allows dramatic improvement in the adhesion of coatings made by washcoating. To do this, an anodizing process under severe experimental conditions is carried out, breaking or cracking the surface of alumina as shown in Fig. 9.3.

9.5 CATALYST COATING ON STRUCTURED SUBSTRATE

One of the simplest ways of obtaining structured catalysts is coating a structure previously made with the most suitable shape for the selected process with a thin layer of catalyst.[4,45,46] Therefore, a coated structured system consists of the structural material, the catalyst layer and between them, the interface in which the discontinuity occurs and will be ultimately responsible for the adhesion of the coating.

Among the features to that need to present in each of these three parts of the structured system, we can cite:

- Structural material
  - Mechanical and thermal properties suitable for the intended end use of the structured system and the coating processes to be used.
  - Ability to be manufactured with the necessary shape. In the case of the ceramic, it will be related to the possibility of being extruded or molded; for metals, it will be related to malleability, weldability, etc.
  - Ability to generate a scale chemically compatible with the catalyst coating and presenting a macroroughness that promotes the mechanical anchoring of the catalyst particles.
- Catalytic coating
  - Preserving the properties of the catalyst normally developed as a powder in the nature of the phases, the dispersion of the active phase and in the textural properties (specific surface area, porosity, etc.).
  - Presenting a compactness of the catalyst layer, which does not disintegrate during use.
  - Adhesion to the surface of the structural material ensuring that it does not peel with use. Lack of adhesion or compactness are usually difficult to discern because both produce the same effect, the loss of coating; however, in many cases, there are different problems in regard to be enhanced. In adhesion comes into play substrate surface that does not influence the compactness. This, however, is closely related to the layer thickness to be obtained.
- Interface
  - Suitable properties to assure that during the coating process a sufficiently thick and homogeneous layer is achieved, which results in a sufficient adhesion during subsequent use.
  - The adhesion is linked both to the chemical compatibility between the substrate and the coating layer and to the roughness of the surface that will favor the mechanical anchorage.
  - The chemical compatibility and roughness can be modified with thermochemical pretreatment of the substrate in the case of metals or with the addition of an intermediate layer or primer that can be used for both metals and ceramics.

From these general considerations arise the following three main features to assess the result of the catalytic coating of a structured material:

- The homogeneity of the coating on the entire surface of the structural material.
- The thickness or the load, i.e. the amount of catalyst deposited.
- The adhesion or peel strength during handling and use of structured system. Obviously, the adhesion to the substrate is as important as the compactness of the deposited catalyst layer.

After discussing the general aspects related to the components of structured systems and the main characteristics sought with these coatings, we will proceed to present the most important coating techniques. First, we will discuss the dip coating or washcoating from a liquid (suspension or sol mixture). Second, we will discuss the in situ growth techniques in which the catalyst is formed from a liquid solution by preferential growth of the new phase on the surface of the structural material. Finally, in the last section, we will discuss less-frequent techniques, but of some relevance for specific applications,[45] such as the methods from the vapor phase (physical vapor deposition (PVD), chemical vapor deposition (CVD)), electrophoretic or electrochemical deposits, etc.

9.5.1 Dip Coating or Washcoating

Dip coating consists of introducing the structure to be coated at a controlled rate within a liquid containing the catalyst or its precursor, keeping it submerged for a short time and then withdrawing it at a controlled rate. Subsequent steps are removing excess liquid, drying and calcinating to generate the solid layer adhered to the structural material. This method is often called "washcoating".

It is probably the most versatile of the methods because it can be applied to almost any suspension, colloid or sol containing the solid or precursors thereof. The result will depend on the properties of the solid (nature, shape, surface properties, etc.), those of the liquid (concentration, viscosity, surface tension, etc.) and those of the process (speed of immersion and emersion, time within the liquid, etc.).

Therefore, there are many parameters that control the final result and, as we shall see, these parameters are closely related so that it is difficult to modify one of them keeping the other unchanged. We will review below some of the most important ones.

9.5.1.1 Slurry Properties

Stable slurries (nonsettling) are obtained when the terminal velocity of the particles is very small. Small velocities are the result of canceling the gravity force by the drag force. Particle settling is well described in the creeping flow regime stated for Newtonian fluids in which the terminal velocity depends directly on the square of the particle size and the difference in density between the solid and the fluid and inversely on the viscosity. Therefore, for a particular catalyst and liquid (usually water) to increase the stability, it is convenient to reduce the particle size and increase the viscosity of the medium.[47] Let us analyze the two parameters particle size and viscosity.

9.5.1.1.1 CATALYST PARTICLE SIZE

Milling can reduce particle size, ball milling being the technique most frequently used in several studies on this parameter.[48–50] To obtain stable slurries of different solids, particle size distributions below 10 μm have been proposed.[32,51] Nevertheless, the positive effect of decreasing particle size has a limit since very small particles induce flocculation. Indeed, the smaller the particles size, the higher is the surface-to-volume ratio; therefore, the interaction between particles that produces gelling is favored.[47]

9.5.1.1.2 VISCOSITY

Assuming the Einstein model for the dilute dispersion of hard spheres, the viscosity of ideal water slurries (non-interacting spheres) only depends on the solid content, being higher as the solid content increases.[52] Nevertheless, when considering surface interactions, additives will play a fundamental role. First, we will consider pH modifiers since polarization of the surface of the oxide particles controls interparticle interactions. In the first approach, pH values far enough from the isoelectric point of the solid will assure that the particles mutually repel each other and cannot aggregate, since they will bear electric charges of the same sign. However, the pH controls not only the stability of the slurry via peptization-flocculation but also the viscosity because it controls the aggregate size.

Other additives may be used in order to promote slurry stability; long-chain surfactants containing hydrophilic and hydrophobic groups, for instance, adsorb on the catalyst surface leading to steric stabilization of the slurry.[52] Thickeners that increase the viscosity can be also used[4,53]; inorganic colloids (alumina, silica, etc.) or organic compounds (polyvinyl alcohol (PVOH), polyvinylpirrolidone, ammonium methacrylate, etc.) are examples of these additives. However, it has to be considered that surfactants, thickeners and other additives may present competitive and synergic mechanisms making it difficult to a priori predict the behavior of such complex mixtures.

9.5.1.2 Washcoating Procedure

In these procedures, monoliths or, in general, metallic structures are dipped into suitable slurries, kept in the particle dispersion for a certain period and finally withdrawn. Once the metallic monolith is withdrawn, it must be drained and the excess slurry eliminated. To form a thin oxide layer on the surface, the structured substrate has to be dried and calcined to suitable temperatures. The procedure ends by evaluating the produced washcoated material by measuring three characteristics: the specific obtained load (milligram per square centimeter), the homogeneity of the coating (by optical or electron microscopy) and the adherence (by the ultrasonic bath test). Relevant parameters controlling this procedure are discussed below.

9.5.1.2.1 DIPPING AND WITHDRAWING VELOCITY

This parameter is particularly important for both porous (ceramics) and nonporous (metals) substrates. To understand the role of this factor, it is important to consider the filling mechanism of the channels of a substrate vertically disposed in which there is a filling of the porosity of the wall with the solvent by a capillary mechanism, which produces a layer of the solid in suspension that is fixed to the wall as a thin filter cake.[54] The thickness of the cake will depend on the solid content of the suspension and the porosity of the substrate. If the immersion velocity is too slow, the solvent will rise by capillarity through the wall faster than the suspension front and no solid cake will be formed on the wall. If done too fast, it will not give time for the suspension to enter and rise in the channel. In this regard, it is noted that the rise or not of the suspension within a channel is governed by capillary rise. Therefore, the surface tension, the wetting angle with the solid substrate and the channel diameter will control this process. Once the suspension "wets" and therefore raises, the speed at which it does is controlled by the friction with the wall; therefore viscosity will control the rise rate. The velocity cannot therefore be fixed for all cases, but values between 2 and 6 cm/min are generally recommended.[55–57] The residence time in the liquid is usually between 1 and 6 min.

9.5.1.2.2 SUBSTRATE SURFACE

Passive layer, a protective oxide scale produced by the spontaneous oxidation in air or by a specific pretreatment, covers all nonnoble metals and alloys. The chemical nature and physical appearance of this scale influences relevant aspects of the washcoating process. The first one is the contact angle with the slurry, which is also affected by the surface roughness. For small contact angles, the capillary rise will allow a quick channel filling and the substrate will be well coated by the slurry. On the contrary, if the contact angle is large, slow channel filling must be expected, and at the limit, for contact angles higher than 90°, the substrate becomes hydrophobic, making it extremely difficult to fill the channels by dipping. The contact angle depends on the surface energies of both the solid and the liquid and hence, the surface nature and slurry additives modify the surface energy of both the solid and the liquid. For instance, surfactants, used as slurry additives, modify the liquid surface tension and therefore, the contact angle with the metallic substrate. The chemical nature of the oxide scale, in particular the chemical composition and hydroxylation degree, determines the oxide scale surface energy and controls the contact angle with the slurry. These surface energy modifications may result in wetting (hydrophilic) or nonwetting (hydrophobic) character of the slurry.

9.5.1.2.3 SIZE AND SHAPE OF THE CHANNELS

Capillary forces, both during immersion and drying, make the film of liquid, and hence the solid coats a little thicker at the corners. This phenomenon may be greater the more acute the angle of the corner. This accumulation is always produced by this technique and the relative importance depends on the coating thickness and the size and shape of the channel. Figure 9.4 schematizes these aspects and Fig. 9.5 shows two examples of corners accumulated by washcoating: one of ZSM-5 on Fecralloy® monoliths[58] and the other of $CoRe/Al_2O_3$ on a microchannel block.[59]

The size of the channels also influences the adhesion of the catalyst coating. Almeida et al.[47] studied the washcoating of different metallic substrates with $Ni/La_2O_3{-}Al_2O_3$ reforming catalyst and showed that the adhesion increased when the channel size decreased. They explained this result to be a consequence of the increasing geometrical constraints of the catalyst coating as the channel size decreased.

9.5.1.2.4 VISCOSITY

Viscosity is probably the main parameter controlling the result of washcoating.[47] Very small values ensure

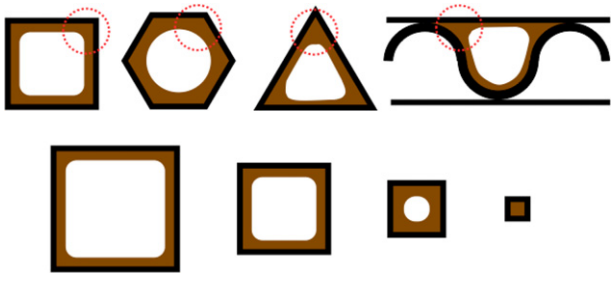

FIGURE 9.4 Effect of the shape and size on the accumulations in the corners produced by dip coating. (For color version of this figure, the reader is referred to the online version of this book.)

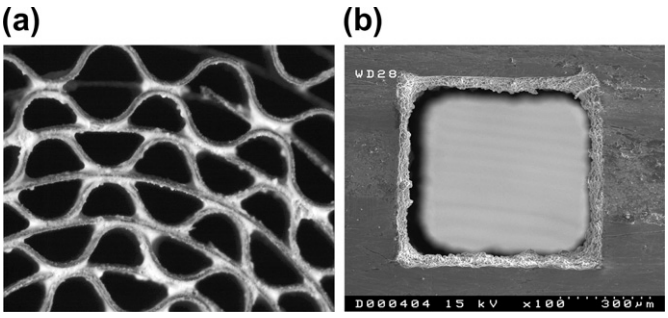

FIGURE 9.5 Micrographs showing catalyst accumulation in Fecralloy® substrates. (a) ZSM-5 deposited on 222 cells/cm^2 monoliths.[58] (b) CoRe/Al_2O_3 catalyst deposited on 700 × 700 μm microchannels.[59]

easy coating and homogeneity but give rise to extremely low loads, which would require numerous repeated coatings. Therefore, the trend is to increase viscosity, thereby increasing the load by coating. The upper limit is given by problems of entry into the channels of the structures and the difficulty of removing excess uniformly without giving rise to accumulations that may even plug the channels and mainly reduce the adhesion of the layer. The recommended values for good coverage are between 10 and 20 cp.[45,46,60–62] However, the non-Newtonian character of the slurries with high solid contents makes it difficult to compare the viscosity values obtained at different shear rates. This range can be extended in both directions due to the unique aspects such as diameter and length of the channel, porosity of the substrate or the conditions for removal of excess.

9.5.1.2.5 ELIMINATION OF THE SLURRY EXCESS

Usually, excess slurry is removed either by air blowing[4,32,45,46,54] or by centrifuging.[35,63] In general, by gravitational draining or by applying some form of pressure or vacuum to clear the channels of the slurry in excess, will leave a thin film that upon drying and calcination will produce the final adhered catalyst layer. Air blowing is easier, in particular when big-structured devices are considered but should be carefully executed to prevent heterogeneity.[64] The load obtained when the excess is removed by centrifugation is lower than when using air blowing, whatever the structure, microchannel or micromonolith considered.[47,63]

9.5.1.2.6 DRYING

During drying of slurries and colloids, strong capillary forces are generated contracting the solid coating. This can produce cracks and detachments from the substrate surface. When this phenomenon reduces the coating adherence, two strategies may be used.[47] The first one is the use of additives, such as PVOH or surfactants, to reduce surface tension. The second approach eliminates the capillary forces in using freeze-drying, but special care must be taken during freezing to prevent movement of the liquid phase. The freeze-dryer may allow keeping the monolith horizontal while continuously rotating it around its axis.[46]

9.5.2 Surface Growing

The surface growth is based on thermodynamic principles for the formation of a new phase. If we start from a homogeneous liquid phase and by varying the temperature or concentration we reach the solubility curve of that phase, thermodynamics indicate that a new solid phase should appear. The creation of this new phase produces the system stabilization due to a decrease in the total free energy that depends on the amount of the new phase formed, and thus it is a function of the particle-cubed radius. However, the creation of a new phase also entails a waste of energy associated with the creation of the interface (new surface), whose free energy depends on the squared radius. For very small sizes there is an energy cost that creates in the surface so little germs that they spontaneously tend to redissolve. The total free energy, sum of the two, passes through a maximum corresponding to the value of critical radius at which growth is favored. The sum of both free energies at this point involves an energy barrier (activation energy) that germs must overcome to continue growing. Therefore the system does not lead spontaneously to a new phase when reaching the solubility curve and it is necessary to reach that of supersolubility. When we introduce a preexisting surface (substrate), energy consumption to create the seed on the surface will be much smaller and therefore lower the activation barrier (ΔG surface growth). This causes the supersolubility curve to be much closer to the solubility one. So at this point, the surface growth will be favored over the formation of new germs within the liquid. Therefore, the surface allows in these conditions growth on it.

The methodology is thus to introduce the substrate into the medium that will produce the solid and to ensure that it is completely covered by the liquid medium with a good renewal of the liquid throughout the channels. This point can be complicated in the case of structured substrates, which have a multiplicity of channels of small diameter (monoliths and foams). So the agitation system must be carefully designed to ensure that the fluid flow lines pass through the interior of the structure. The second important point is to carry out the process slowly, trying to stay as close as possible to the line of supersaturation for surface growing to minimize the growth of crystals within the liquid.

So far we have considered only physical factors such as the presence of a surface (which also can be made

more active by increasing their surface roughness) or concentrations and renewal of the liquid medium. But there are other chemical factors of the surface also influencing the nucleation of surface growth. The first one is chemical compatibility, which makes it much easier when the phase of growth is similar to the substrate surface. Eleta et al.[58] showed that to grow purely siliceous ZSM-5 on Fecralloy® coated by alumina whiskers, the compatibility can be improved by pre-seeding by washcoating with submicron crystals of the same material or by using a primer with the structure-directing agent (TPABr) or colloidal silica. However, in this case, as it is necessary to carry out repeated synthesis to achieve an appropriate thickness, it was found that it is possible to start with the original surface of the Fecralloy® as the few crystals generated in the first synthesis act as seeds of the following, yielding equivalent results to the preseeding or the use of primers.

Finally, another interesting alternative has been reported by Frias et al.[38] when one of the elements in the substrate surface participates in the reaction producing the active phase to be deposited. Thus, the synthesis of cryptomelane, which is a phase of Mn- and K-forming nanofibers, a very active oxidation catalyst, can be carried out as a redox reaction between Mn^{2+} and Mn^{7+}. AISI 304 stainless steel has in its composition a small amount of Mn that is present on the mixed chromium oxide surface scale in the form of Mn^{2+}. If this properly pretreated alloy is introduced in the reaction medium producing cryptomelane, surface growth is favored by the presence of both the surface and the Mn^{2+} of that surface.

9.5.3 Other Coating Methods

9.5.3.1 Methods from the Vapor Phase

These include CVD and PVD. In CVD, precursors with high vapor pressure that decompose and deposit on the surface to be coated are used without using any solvent. At the vapor phase, it is possible to easily access complex geometries, obtaining very homogeneous coatings. The availability of volatile precursors that decompose on the surface is the key point of the method. Alkoxide precursors are used in this method. In PVD, mechanical (cathodic sputtering) or thermal methods (electron-evaporation beam) are used, typical of microelectronics industry. For the electrophoretic deposition, the starting material is a colloid or suspension of charged particles that is submitted to an electric field to direct the particles to the surface to be coated. The substrate to be coated acts as an electrode of the field. In the electrochemical deposit of an ionic solution, a current is applied so that ions are discharged at the electrodes of opposite sign. This method is used to deposit metals onto a conductive substrate, which must act as negative electrode to attract metal cations. A variant of this method is called "electroless plating" in which no electric current is used but a chemical reductant (redox reaction) generates the metallic coating.

9.6 HYDROGEN PRODUCTION FROM BIOFUELS

Xuan et al.[65] recently published a comprehensive review of biofuel processors including a diagram showing the main routes for the production of green hydrogen. Based on that picture, Fig. 9.6 presents an overview of the different possible ways of producing green hydrogen that we will follow throughout this chapter. There are several published studies suggesting that the direct conversion of wood or straw by thermochemical or biochemical processes is not suited for use in compact structured systems, so they will not be considered in this review. Comparatively, biomass-derived fuels in either liquid or gas form are more suitable to be used in compact stationary and mobile systems, because most of them are easy to transport and the infrastructures needed are readily available. Moreover, the production and utilization of biomass-derived fuels are much more technologically ready. Thus, the two-step utilization (biomass → biomass-derived fuels → hydrogen) is more favorable before the technologies of hydrogen storage and transportation are mature enough for cost-effective industrial use. Therefore, the scheme in Fig. 9.6 could be proposed as a summary of the two-step process to obtain hydrogen from fuels such as dimethyl ether (DME), biomethanol, biodiesel, bioglycerol, biogas, bioethanol and bio-oil.[65]

Different treatments can be used to produce hydrogen from biomass fuels such as steam reforming (SR), autothermal reforming (ATR) and partial oxidation (POX). The main products of these reactions are hydrogen, carbon dioxide, carbon monoxide and methane. After reforming process, CO elimination and CO_2 capture steps could follow if necessary (these processes will be described in the next chapter). POX is an exothermic process that offers advantages, such as fast start-up and compact design, whereas SR is an endothermic process that offers high efficiency for hydrogen production and lower by-product formation. POX can be used to obtain fast and dynamic systems, but the risk of hot spot formation is high and could deactivate the catalyst. ATR, also called oxidative steam reforming (OSR), can be considered a hybrid because it combines both oxidation and SR reactions to become a nearly thermally neutral process.

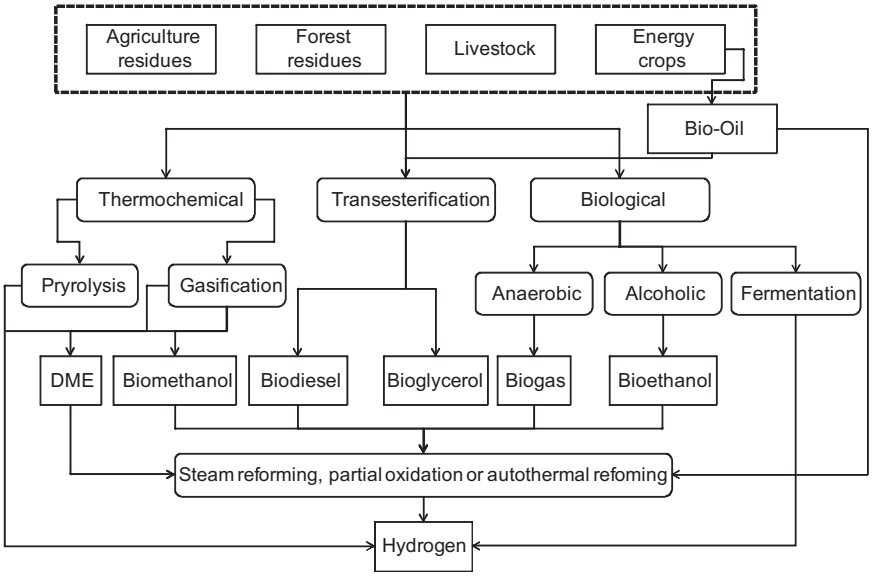

FIGURE 9.6 Scheme of the two-step process to obtain hydrogen from biomass-derived fuels. *Source: Figure adapted from Ref. 65.*

In the following sections, different types of biomass-derived fuels for hydrogen production will be reviewed with special emphasis on the use of structured and microstructured catalytic reactors.

9.6.1 Dimethyl Ether

DME has attracted much attention recently as a hydrogen source mainly because the well-developed infrastructure of liquefied petroleum gas can be readily adapted for DME use due to their similar physical properties.[66] Moreover, DME has a high hydrogen-to-carbon ratio and, therefore, high energy density. DME is easily liquefied at low pressure; corrosion-safe; easy to handle, store, transport; and less toxic than methanol.[67–69] DME can be obtained by a single-step production process from the product of the gasification of biomass (H_2/CO)[70,71] or by a two-step (indirect synthesis) process that starts with methanol synthesis and ends with DME synthesis (methanol dehydration).[72] The SR of DME proceeds via hydrolysis of DME followed by SR of methanol.[73] However, other reactions are involved, such as the WGS, DME decomposition and CO and CO_2 methanation. The overall reaction yields 6 mol of H_2 per mol of DME, and half the hydrogen comes from water.

There are only a few examples using catalytic monoliths for DME SR. Llorca et al.[74,75] used cordierite monolith cylinders ($\varnothing = 20$ mm, $L = 20$ mm, 400 cpsi) washcoated with $Cu{-}Zn/CeO_2{-}ZrO_2$ (with and without Pd) and $Cu{-}Zn/ZrO_2$ catalyst. Once the different oxide supports were bound to the monoliths walls, the active metals were loaded over the monoliths by incipient wetness impregnation. The $Cu{-}Zn/ZrO_2$ catalyst presents the highest selectivity toward the main products of the DME SR, H_2 (70%) and CO_2 (25%), whereas less than 4% of CO and 1% of CH_4 were produced. In addition to that, the Cu-Zn/ZrO2 catalyst showed high stability despite deactivation of the catalyst is one of the major drawbacks of reforming technologies.

DME hydrolysis is a slow reaction compared to methanol SR.[76] Therefore, the reaction is limited by chemical equilibrium but can be shifted further forward by continuous conversion of methanol to achieve high DME conversions. Oxygen is advantageous over steam as oxidant because the reaction rate is higher and is exothermic. The POX of DME has been shown to proceed through the oxidation of methyl species or the decomposition of methoxy species formed by dissociative adsorption of DME.[77] By combining the SR and the decomposition of methoxy species, a thermally neutral system can be obtained, where the heat needed for the SR reaction is supplied by POX. In practice, the ATR reaction is usually operated under slightly exothermic conditions to compensate for heat loss and to obtain a more dynamic system.

The ATR of DME in structured reactors has been barely studied. Nilsson et al.[76,78,79] studied a series of different Pd-based catalyst supported on cordierite monoliths. After preparation of the catalyst by impregnation or coprecipitation method, the catalyst powder was suspended in ethanol and ball-milled for 24 h. The cordierite monoliths ($\varnothing = 23$ mm, $L = 35$ mm, 400 cpsi) were dip-coated with the catalyst slurry. Alumina-supported Pd with Zn added showed high activity in ATR of DME at temperatures between 400 and 450 °C (at O_2:DME = 0.7; H_2O:DME = 2.5 and gas hourly space

velocity (GHSV) = 15,000/h). The presence of $ZnAl_2O_4$ and ZnO prevented interactions between Pd and Al_2O_3 avoiding Pd^0/Al_2O_3 sites.

The kinetic modeling[79] showed that the heat transport effects were very important when coupling the exothermic oxidation reactions with endothermic SR. During ATR conditions, several reactions may be competing on the catalyst surface.[76] The desired reactions are DME SR, DME POX and WGS, whereas decomposition reactions, which generate higher concentration of CO, are unwanted. As some of the reactions involved during DME ATR occur simultaneously, separate catalyst beds or segments, active for individual reaction, cannot be used.

9.6.2 Biomethanol

Before modern production technologies developed in the 1920s, methanol was obtained from wood as coproduct of charcoal production and, for this reason, was commonly known as wood alcohol. Methanol is currently made from natural gas but can also be made using biomass via POX and gasification reactions.[80] Biomass and coal can be considered as potential raw materials for gasification and further syngas production and methanol synthesis.

In principle, there are four routes available for catalytic hydrogen generation from methanol: decomposition, SR, POX and OSR. All four reactions can be carried out at moderate temperatures (200−400 °C) over transition metal catalysts, such as copper and palladium. Especially, Cu−ZnO-based catalysts have received considerable attention, because they are the reference catalysts for the reverse reaction, the methanol synthesis.

The major disadvantage with Cu-based catalysts is the sintering of metal at temperatures above 330 °C, which is difficult to avoid when part of the methanol is combusted to provide heat for the endothermic methanol SR. Pd/Zn alloy catalysts, on the other hand, exhibit excellent thermal stability and are nonpyrophoric, that is advantageous for portable hydrogen production.

Proper selection of the reforming reactor is especially critical for some applications such as production of hydrogen on board for vehicles or for use in the field of consumer electronics. The options are fixed bed reactor, monolithic reactor, wall-coated heat exchanger, microchannel reactor and metallic foam reactor. Among them, the microchannel reactors seem to be the most promising in portable electronics due to their fast response in transient regime, higher heat (which will lead to better temperature control inside reactor) and mass transfer characteristics, less channeling of reactants flow and less pressure drop.

One of the first steps in microreactor design, besides choosing the proper type of reactor, includes the decision of the appropriate structure of microreactor. Mathieu-Potvin et al.[81] presented an analysis to obtain the optimal catalytic microreactor geometry by taking into account fluid flow, mass transfer and heterogeneous chemical kinetics. They found analytically how the competition between diffusion, advection and kinetic phenomena dictate the optimal design of microreactors. The results showed that the optimal design of the microreactors depends on the Schmidt number, the Bejan number (pressure drop) and the catalyst number, which represents the amount of catalyst available. Multichannel catalytic wall microreactors are commonly used. Channels can be parallel or no parallel.[82−84] Other potential structures used are string reactor,[85] metallic grids [86] micro array,[87] and tree-shaped networks.[87] In a microstring reactor, microchannels are formed between catalytic parallel filaments or wires. In metallic grids, the microchannels are formed in the gaps inside the grids. In a microarray, the channels are formed between the micro pin-fin arrays.

The tree-shaped network for a methanol steam microreactor was developed in view of the optimization of the flow configuration. Some authors found that the methanol SR is enhanced in the tree-shaped microreactor, because it provides a reaction space with large surface-to-volume ratio and the reduction of the reactant velocities in the branches. The conversion rate was more than 10% higher than in serpentine reactors. The reduction of flow distance produced in the constructal microreactor almost the same pressure drop as in the corresponding serpentine reactor, despite the bifurcations and the reduction of the channel size in the branches.[86] On the other hand, the effect of the manifold structure in the SR of methanol was presented by Mei et al.[87] They found that reactor with small-scale cube post and acute triangle manifold offered better reforming performances at 260 °C than those of the large-scale cube posts and right triangle manifolds. However, their performances converged at high reaction temperature.

Before the beginning of microreactor fabrication, the reactor material and fabrication method should be decided. To build an efficient and compact microreactor, the fabrication technique must allow for 3D structures and the use of the appropriate materials and the technique should be low cost. Among the different techniques available to construct efficient and compact microreactors, such as, Lithographie, Galvanoformung, Abformung (LIGA), wet and dry etching processes, micromachining, lamination and soft lithography, the most widely used are micromachining and wet chemical etching.[88]

On the other hand, the fabrication materials must be chemically compatible, have the appropriate thermal properties, and be structurally sound. The microreactors

can be made of glass,[89] silicon based,[90] polydimethylsiloxane,[84] ceramic and metallic.[88] Polymeric materials would be of great interest in microreactors; however, no hydrogen-generating microreactors built of polymers were reported in the literature at the time of this review. Wang et al.[91] evaluated the effect of the heat transfer area and the thermal conductivity of the reactor materials: aluminum alloy, brass and stainless steel. They concluded that the use of a highly thermally conductive reactor material (Al-6061 aluminum alloy) and of sufficiently high volume fraction of solid mass are more critical than the high surface area for the effective heat transfer for the design of a methanol steam reformer to achieve homogeneous temperature distribution and high thermal efficiency of the reactor. This unique design enables the reactor mass to act as a secondary heat reservoir for heat transfer origin; thus, it simplifies the scale-up of reactor fabrications for the hydrogen production to meet different market needs without sacrificing the reactor efficiency.

Coating the walls of the microchannels by the washcoating method[92,93] is the most used technique, but other techniques are also used to deposit the catalyst in the microchannels, such as electroless plating,[94] packed beds by injecting a water-based suspension of catalyst particles at inlet point[94] and dual step methods depositing first the support followed by impregnation of the active phase.[95]

Beside microchannels, other types of structured systems have been used for methanol reforming, and they are briefly summarized below.

9.6.2.1 Membranes

Basile et al.[95–99] studied methanol SR and OSR to produce pure hydrogen in a Pd-Ag membrane reactor. Two types of membranes (flat and dense) and different types of catalyst were used. The results obtained from experimental studies were compared with those obtained in a conventional reactor (fixed bed reactor). They found that the best results are obtained with the dense membrane, high conversion, high hydrogen production and low carbon monoxide selectivity. On the other hand, Israni et al.[100] found in methanol SR using a Pd−Ag membrane reactor that high-purity hydrogen can be produced but that the low flux of H_2 through the membrane was the productivity-limiting step. The reason for the low membrane flux was the surface adsorption of the non-H_2 species, especially CO.

Sá et al.[101] studied the methanol SR in a carbon membrane reactor over a commercial CuO/ZnO/Al_2O_3 catalyst (Süd Chemie, G-66 MR). High methanol conversion and hydrogen recovery were obtained with low carbon monoxide permeate concentrations. The work of Papavasiliou et al.[102] presented an internal reforming methanol fuel cell that incorporates a methanol reforming catalyst into the anodic compartment of a high-temperature polymer electrolyte membrane fuel cell (HT-PEMFC). Authors examined application aspects of the cell, including operation temperature, type of catalyst pretreatment, phosphoric acid leaching effect and time-on-stream behavior of $CuMnO_x$ catalysts. Overall, the observed stability of the $CuMnO_x$ catalyst was satisfactory in the time frame of the presented experiments.

9.6.2.2 Foams

Foams of nickel, Raney nickel, alumina, FeCrAl and cellular SiC have been used as supports of microstructured reactors. However, only few reports have investigated the influence of substrate on the chemical reaction in terms of catalytic performances. Yu et al.[103] constructed a methanol steam microreformer, in which CuZnAlZr catalyst was supported on metal foams made on Ni, FeCrAl, Cu and CuZn. They found that the metal of the foams played an important role in the reaction. The metal atoms from the foam substrate tended to diffuse through the catalyst layer. The strong interaction between the Ni or FeCrAl metallic foams and catalyst resulted in the low activity for WGS reaction, increasing the CO selectivity.

9.6.2.3 Felts

Metal fiber sintered felts are a new type of functional and structural material, which has 3D reticulate structure, fully connected pores with highly accurate size and high porosity. Tang and coworkers[104–106] developed an innovative catalyst support, porous copper fiber sintered felt with high porosity and large pore size, by sintering copper fibers. The fibers were coated with copper-based catalyst and used in methanol SR. They studied the effect on the reactor performance of the porosity and manufacturing parameters by varying the GHSV and reaction temperature. Finally, the authors proposed a kind of oriented linear cutting sintered felt as an innovative catalyst support for methanol SR. The results showed that the structure of the sintered felt was the key influencing factor for the reaction performance in the condition of low GHSV or low reaction temperatures. On the other hand, they found that the oriented linear cutting fiber sintered felt presents better performance than the oriented linear copper wire sintered felt at low GHSV or low reaction temperature.

9.6.2.4 Microfibrous Networks

Tang et al.[107] presented a sinter-locked microfibrous networks consisting of 3 vol.% of 8-μm (diameter) nickel microfibers that have been utilized to entrap 30 vol.% of 100−200 μm porous Al_2O_3. ZnO and CaO were then highly dispersed onto the pore surface of the entrapped Al_2O_3 by the incipient wetness impregnation method.

Due to the unique combination of surface area, pore size/particle size, thermal conductivity, and void volume, the resulting microfibrous catalyst composites provided significant improvement of catalytic bed reactivity and utilization efficiency when used in methanol SR.

Ling et al.[108] investigated a microfibrous structured catalytic packing for miniature fuel processor consisting of a methanol steam reformer and subsequent CO cleanup train. The fuel processor was tested experimentally, and was capable of producing roughly 1700 sccm PEMFC-grade H_2 (163 W) in a long-term test. In this test, the Methanol Steam Reforming (MSR) reactors delivered above 97% methanol conversion throughout the entire 1200-h test. On the other hand, the CO cleanup train was placed on line after 800 h of MSR and illustrated the capability to decrease the CO concentration from around 3.5 to 1% at Preferential oxidation (PROX)-1 to less than 20 ppm at PROX-2 until to the end of test.

9.6.3 Biodiesel

Biodiesel is a mixture of esters obtained by the transesterification of vegetable oils (soybean, rapeseed, coconut, and even recycled cooking oils) with methanol or ethanol.[109] The reaction produces methyl or ethyl ester (biodiesel) and glycerol as by-products.[110] Biodiesel is also a promising biofuel for hydrogen production, because it has shorter carbon chains than the original oils and thus it is easier to reform to high-quality hydrogen-rich gas. Like other liquid hydrocarbons, biodiesel can be vaporized and reformed to produce H_2 and CO. Reforming of biodiesel does not possess the same challenges as conventional petrodiesel since it does not contain sulfur or aromatic species. Furthermore, there is a reduction in coke formation due to the presence of oxygen in the fuel itself.[65]

There are very few studies in the literature that report the reforming of biodiesel in structured reactors. Haynes and Shekhawat[111] have reviewed the latest developments in this area. The first results of the catalytic POX of methyl acetate, a model molecule for biodiesel, by Rh−Ce catalyst deposited on alumina foam monoliths were not too promising, because the primary products from the oxidation of methyl acetate were CO and H_2O, rather than CO_2 and H_2O.[112] Furthermore, methyl acetate produced less syngas than biodiesel as reported in another study, which used a soy oil-derived fuel.[113] Nevertheless, researchers at NETL (National Energy Technology Laboratory, USA) obtained excellent results using a structured catalyst consisting of Rh-based pyrochlore/zirconia-doped ceria/Al_2O_3 monolith.[114] A reforming unit was run on biodiesel (O/C = 0.6, steam-to-carbon ratio (S/C) = 0.5, 900 °C and 25,000/h) for over 100 h. In 2006, California InnovaTek and Seattle BioFuels announced the first successful production of hydrogen from 100% biodiesel in a microchannel steam reformer.[115] InnovaTek demonstrated the ability to generate hydrogen from pure biodiesel (B100) produced at the Seattle Biodiesel production facility. The microchannel reformer achieved a 100% conversion rate of the pure biodiesel (B100).

9.6.4 Bioglycerol

Glycerol surplus and the need for new renewable hydrogen sources have driven research studies on reforming of this alcohol, since H_2 production from glycerol provides a route for the massive use of this industrial by-product of the biodiesel synthesis.[116]

SR, POX, and OSR are the most studied catalytic processes for the production of hydrogen from glycerol. These processes are schematized in Eqns (9.1)−(9.3).

$$\text{SR:}\quad C_3H_8O_3 + 3H_2O \rightarrow 3CO_2 + 7H_2 \qquad \Delta H = +128\ \text{kJ/mol} \tag{9.1}$$

$$\text{POX:}\quad C_3H_8O_3 + \frac{3}{2}O_2 \rightarrow 3CO_2 + 4H_2 \qquad \Delta H = -603\ \text{kJ/mol} \tag{9.2}$$

$$\text{OSR:}\quad C_3H_8O_3 + \frac{3}{2}H_2O + \frac{3}{4}O_2 \rightarrow 3CO_2 + \frac{11}{2}H_2 \qquad \Delta H = -240\ \text{kJ/mol} \tag{9.3}$$

Thermodynamic studies of all these processes result in an optimal range for hydrogen production at atmospheric pressure and temperatures in the 600−750 °C range. SR is a quite effective reaction for hydrogen production since 7 mol of hydrogen per mol of reacted glycerol may be obtained. Adhikari et al.[117,118] found by direct minimization of Gibbs free energy that glycerol SR is favored at high temperature and atmospheric pressure. High S/C increase the glycerol conversion, decrease the methane formation and improve the stability of the catalyst (reduction of coking). According to these authors[118] the optimal conditions, from a theoretical point of view, are: atmospheric pressure, 627 °C and an S/C ratio of 3.

POX is an exothermic process (Eqn (9.2)) and consequently, the energetic cost is lower than in the previous case. However, only 4 mol of hydrogen per mol of reacted glycerol are obtained by POX. Wang[119] studied the thermodynamics of this process. Hydrogen production is maximized at atmospheric pressure, 750 °C and oxygen/glycerol ratio of 0.5. These conditions allow the complete conversion of glycerol, yielding 80% hydrogen and carbon monoxide. Besides this carbon formation is not favored in these conditions.

The third process might be considered a combination of the two previous processes in which the use of both water and oxygen as reactants results in a process known as OSR or ATR (Eqn (9.3)). This combination allows the energy required by the SR to be provided by the POX, which may result in a thermally neutral global process. The H_2O/O_2 ratio determines the thermal balance of the reaction. In the reaction depicted in Eqn (9.3), the hydrogen production per mol of glycerol is 5.5 and the reaction is slightly exothermic. Thermodynamic studies carried out by Yang et al.[120] pointed out that the hydrogen selectivity reaches a maximum when the process is carried out in the temperature range of 600–700 °C. An autothermal process is obtained by running the reaction at a carbon-to-oxygen ratio around 1.0. The presence of impurities in the glycerol feed stream reduces the catalyst performances for the autothermal process and alters the operational variables; the oxygen-to-crude glycerol ratio required to maintain an autothermal process is in the range of 0.4–0.7, being higher as the methanol content is lower.[121] In the autothermal process, water may be completely or partially replaced by carbon dioxide, the energy required for the reforming process being provided by oxidation of glycerol; however, according to thermodynamic calculations,[122] the syngas produced has a H_2/CO ratio very close to 1. For these authors, the autothermal process occurs at ~650 °C, oxygen-to-glycerol ratio equal to 0.9 and CO_2-to-glycerol ratio of 1. These reaction conditions allow one to obtain a reasonable hydrogen yield (2.67 mol of hydrogen) as well as very low amounts of methane and deposited carbon. The endothermic dry reforming also results in the formation of syngas, the optimum reaction conditions being close to those of the autothermal process but the reaction temperature being slightly higher, c. 730 °C.[123]

Cortright and Dumesic[124–129] developed a low-temperature high-pressure reforming process occurring in a condensed liquid phase called aqueous phase reforming (APR) that has been further implemented by other authors.[130–132] Some of the main advantages of the APR process are that costs are greatly reduced since the vaporization step is not required, the conditions at which the APR occurs favor the WGS reaction, the CO concentration in the reformate stream is decreased, and the hydrocarbon decomposition reactions are inhibited. In this process, hydrogen is obtained in a single step at high pressures and mild temperatures from a vast range of hydrocarbon sources (15–50 bar)[128] that may include oxygenated hydrocarbons derived from the biomass[129]; the resulting H_2-rich reformate contains a very low CO concentration. Although Pagliaro and Rossi indicated the use of microreactors for generating hydrogen on demand in a compact and highly efficient single-step reactor by Virent Inc., a detailed description either of the reactor or of the operating conditions was not found.[133]

The catalysts used in these processes for obtaining hydrogen from glycerol are similar to those proposed for the reforming of other alcohols; thus the catalytic properties of Ni, Pt, Ru, Re, Rh, Ir, Co and Pd in these reactions have been studied. However, the high cost of noble metals has driven extensive studies in Ni as active phase. Nevertheless, the main drawback of using nickel catalysts is the high carbon formation rate despite the activity in the WGS reaction. Ni is more active than Pt for this reaction; it also plays a role in hydrogen yield.[134,135] The SR of glycerol results in coke formation for most catalysts and temperatures investigated. The effect of different supports and promoters has been studied for the SR of glycerol. Despite the addition of noble metals, redox or basic additives, the Ni catalysts deactivate, although the rate of deactivation is slowed down with these modifications.[136–146] Conventional strategies to limit deactivation by carbon deposits consist either in promoting its gasification by adding alkaline components as MgO, K_2O, or lanthanide oxides to the support or in reducing carbon deposition rate by alloying the Ni metal with a group IV element.[147–155] The latter strategy has been used for designing catalysts for the APR process of glycerol.[127,156]

Noncatalytic pyrolysis or steam gasification of glycerol results in coke formation[145,146,154,155,157–159]; although the oxidation, gasification and reforming of carbon is possible for steam-to-carbon ratios higher than 4, this process is kinetically slow.[120,143]

According to Xuan et al.[65] the most studied fuel processors are tubular fixed bed configurations. Recent data suggest that catalytic reactions occur mainly in a thin layer of the catalyst particles, which evidences the importance of using monoliths and microreactors in the hydrogen production field. For instance, the POX of ethanol has been tested in monolithic reactors (cordierite), ceramic foams and pellets. The results evidenced the strong influence of the type of catalytic configuration on the hydrogen selectivity and stability. The best activity and selectivity were found in the monolithic reactor.[160,161] Few works treating these aspects in glycerol reforming are available in literature. However, in a recent work by Bobadilla et al.,[162] the influence of the shape of Ni catalysts in the glycerol SR has been studied. Diluted powders, eggshell pellets and monolithic catalysts were compared. Catalysts with the same composition and different shapes were tested in the glycerol SR in similar conditions. The authors observed that the activity was similar for all the solids (powders, eggshell and monolith) during the first hour of reaction, and then, eggshell and powder catalysts rapidly deactivated. On the contrary, the monolithic catalyst maintained its activity for 50 h. The analyses

of the solids after reaction indicate that the catalyst deactivation is due to the different degree of coking. In the case of monolithic reactor, the formation of coke is minimal while the blocking of the active sites by carbonaceous deposits in the conventional solids was evidenced. A correlation between the surface-to-volume ratio (related to the particle size) and the deactivation rate has been found: on decreasing the surface-to-volume ratio, the deactivation becomes faster. The effect of the surface-to-volume ratio on the catalytic gasification of carbon deposits has been argued as the key factor of the superior performance of the monolithic catalyst.

9.6.5 Biogas

Biogas is becoming increasingly interesting as an alternative to natural gas. It is especially useful because the composition is similar to that of natural gas, so the same reformers can be used for both fuels. Biogas is produced through the anaerobic degradation of organic materials in different environments. Biogas usually contains methane (60−70%), carbon dioxide (30−40%) and N_2 (1%). When used to produce syngas, since both CH_4 and CO_2 are the main greenhouse gas emissions, reforming of biogas not only reduces their emissions but also recycles them and increases their usability by producing hydrogen.[163] Besides SR and POX, biogas could be reformed by dry (CO_2) reforming.[163−165] Recently, ATR has attracted much attention because it requires low energy due to the balance of the endothermic reactions (SR and dry reforming) and the exothermic reaction (catalytic POX). ATR is considered suitable for producing hydrogen for small-scale applications such as distributed or small stationary fuel cell power systems because of high efficiency, easy start-up and rapid response.[166] The deposition of carbon on the catalyst producing deactivation is the major problem in dry reforming of biogas. The supply of oxygen prevents carbon deposition.[167] The most used catalysts are Ni-based [164,165,167,168] and Pt−Rh-based[163,169] catalyst.

The cordierite monoliths are the most used structured supports for biogas reforming.[163−165,167,168,170] Araki et al.[165] reported several advantages of using monoliths: higher geometric surface area, smaller pressure drop and fewer hot spots compared with conventional catalyst such as pellets or Raschig rings. The catalytic monoliths for biogas reforming were prepared by dipping the cordierite monolith into a slurry prepared with the catalyst in alcohol media.[164,165,167,168] FeCrAl metallic monoliths have been recently used by Lai et al.[169] Metallic monoliths were favorable to the transient response and cold starting.

No reference has been found using microstructured reactors for biogas reforming. Nevertheless, important progress has been made in the reforming of methane in microchannels reactors, technology that can be applied to biogas. To couple methane SR to fuel cell systems, many problems need to be overcome such as the large systems volume due to highly endothermic reactions, large heat requirement and the low heat-transfer problem in conventional fixed bed reactors.[171] Therefore, microchannel reactors have been recognized as promising candidates. Researchers from Velocys and Pacific Northwest National Laboratory (PNNL, USA) reported the development of millisecond microreactor concept for methane SR process with highly efficiency through channel walls.[11,172−174] Stainless steel is the most used material to fabricate microchannel plates for methane SR.[11,172−178] In spite of numerous studies that have been done with different catalysts (especially Ni-based catalyst and noble metal-based catalysts such as ruthenium, rhodium and platinum, among others[179,180]), the major impediment for the development of these devices is the deactivation of the catalyst due to coke formation during the reaction.

9.6.6 Producer Gas

Biomass gasification is an interesting possibility for expanding the utilization of biomass. Biomass gasification is a thermal conversion process where solid fuel is transformed into a fuel gas (producer gas) with a gasifying agent (air, steam, etc.).[181] The producer gas is normally a mixture of N_2, H_2, CO, CO_2, H_2O, CH_4 and light hydrocarbons whose use in advanced applications is hindered by the presence of contaminants such as tar, ammonia and particulates.[182] Tar as one of the contaminants in the producer gas is the main concern of many researchers. Before use as fuel or in chemical synthesis, the producer gas has to be purified. There are several types of catalysts for cracking tar of producer gas[181]: Ni-based catalyst, alkali metal catalyst, dolomite catalyst and noble metal catalyst. Ni-based catalysts are the most used and are very effective for tar as well as for simultaneous ammonia removal in coal or biomass gasification.[170,181−183] Ni-based catalyst can be found in two different forms: commercial particulate-shaped catalyst and home-made monoliths.[182] Most of the commercial Ni-based catalysts (rings) are very effective for tar elimination, but they are not good enough to eliminate particulates to an acceptable level and a hot filter is needed before the catalytic bed. During the reaction, some coke might be formed in filter pores plugging the filter. To overcome this problem, monolith catalysts and specially cordierite monoliths, were proposed.[170,182,184] In experiments by Ising et al.[183] and Corella et al.,[182] tar cracking efficiency was up to 95% at 900 °C with Ni-based monolith catalyst. Nevertheless, Corella et al.[182] observed some drawbacks. Most of the

reactions occurring in the monoliths were highly endothermic, and because the monolith has to operate in adiabatic form, significant longitudinal gradients of temperature in the monolith can be generated. Then, tar conversion in the monolith reactor was due to both thermal and catalytic routes.

9.6.7 Bioethanol

Traditionally, bioethanol is produced by fermentation of biomass sources, varying from agricultural crops to organic wastes. The generation of hydrogen through ethanol SR at low temperatures is currently being thoroughly investigated. The used catalysts are based on Ni, Ni/Cu, Co and noble metals (mostly Pd, Pt, Rh and Cu).

Men et al. from the Mainz Institute of Microtechnology (IMM) tested several catalyst formulations based on Ni, Rh, Co and Ni−Rh for the SR of ethanol in a microchannel reactor (channels 500 μm width and 250 μm depth).[185] Stainless steel microchannels were filled manually with the catalyst suspension and subsequently the excess was removed. The best results were obtained with Ni−Rh/CeO_2, which showed no deactivation during a 100-h catalytic test at 700 °C.

The group headed by Prof. Llorca from the Technical University of Catalonia (UPC) has a long experience in ethanol reforming. During the past years, they have been focused on the catalytic performance of structured reactors and microreactors coated with cobalt catalyst for ethanol processors.[186−196] They have shown that ethanol SR reaction can be effectively performed at low temperature over cobalt catalyst in a wide range of channel dimensions, ranging from conventional monoliths (cordierite monolith with a channel width of 0.9 mm[186,189,190,194]) to semicylindrical microchannels (AISI 304 stainless-steel plates with 0.35 mm radius[187,190−192]) and silicon micromonoliths (channel diameter of 3−4 mm[188,189,193]). All three systems coated with the same catalyst were tested under nondiluted and slightly diluted ethanol-water (S/C = 3) feed mixtures.[189] Maximum ethanol conversion of c. 70% and 90% were measured for monolith and microreactor operation, respectively. The Si micromonolithic reactor proved extremely promising for H_2 production in microfuel cell operation. Specific H_2 production rates exceeding 50 Nl of H_2 per ml of liquid and cm^3 of reactor were measured for c. 42% ethanol conversion and residence times in the order of milliseconds. Several methods for coating structured supports have been used by Llorca's group. They proposed the in situ urea precipitation method for the Si micromonolithic.[188,190,193] Catalytic coatings obtained by this method and by the in situ sol−gel method in cordierite monoliths and semicylindrical microchannels showed better mechanical stability than the coating obtained by washcoating.[190] Nevertheless, by changing the catalytic support of the catalyst slurry, they obtained very stable coatings on cordierite monoliths.[194] They also studied other coating methods for microchanneled plates such as the hydrothermal method[195] or the electrophoretic deposition.[191]

Görke et al. from the Institute for Micro Process Engineering (Karlsruhe) used a microchannel reactor (Nicrofer® plates with channels 200 μm width and depth) to produce hydrogen by ethanol SR over Rh/CeO_2 catalyst.[197] For temperatures above 675 °C, a space time yield four times higher than that obtained in conventional reactor was reported. Cai et al. from CNRS and the University of Lyon used stainless-steel microreactor with channels 500 μm wide and deep, loaded with an Ir/CeO_2 catalyst by injection of the slurry. Hydrogen productivity was found significantly higher than in conventional fixed bed reactor, essentially due to better heat and mass transfer.[198] Some authors have studied ceramic structured reactors for ethanol ATR. Nilsson et al.[199] designed an autothermal reformer using different fuels for a 1- to 5-kW fuel cell auxiliary power unit and Rh supported on Ce/La-doped γ-Al_2O_3 deposited on cordierite monolith. They concluded that the reformer design was most suitable for use with mixtures such as diesel, gasoline and E85 than with ethanol. Chen et al.[200] studied the effect of ceramic foam composition in the ATR of methanol. The employed ceramic foams (ZrO_2, Al_2O_3 and SiC) were coated with Ir/La_2O_3 catalyst by washcoating method. In terms of conversion and H_2 selectivity (3.1 mol H_2 per mol ethanol), the ZrO_2-foam-supported catalyst provided better performances, because ZrO_2 is active in adsorbing and dissociating steam.

Liguras et al.[160,161] from the University of Patras have not observed important differences in the catalytic POX of ethanol using different structured supports (foams and monoliths) with different composition (Al_2O_3−ZrO_2, mullite and cordierite) coated with the same catalyst (Ni/Al_2O_3 and Ru/Al_2O_3). However, they observed a difference in activity compared with the catalyst preparation method. The adsorption method produced the catalyst with the weakest performance, possibly due to active site inaccessibility. Sol−gel and washcoating methods presented similar results, but the author selected the washcoating method because it is the most well-established technique. Rodrigues et al.[201−203] from the Federal University of Rio de Janeiro also selected the method of washcoating to coat the cordierite monoliths (400 cpsi, $D = 12$ mm, $L = 8$ mm) with different catalyst. However, instead of preparing the catalyst first and then the catalyst slurry, they coated the monolith with the support (in this case alumina) and then deposited the active phase by impregnation.

9.6.8 Bio-Oil

By biomass pyrolysis (rapidly heating biomass in the absence of oxygen), bio-oils can be formed. Bio-oils show wide differences depending on the feedstock and the method of production used. However, elemental analysis of pyrolysis oil derived from different processes shows that its main components include the following groups: acids, alcohols, aldehydes, esters, ketones, sugars and phenols. The complexity of bio-oils makes it difficult to design catalysts based on kinetic and spectroscopic studies and to establish reaction mechanisms. Thus, model representative compounds such as acetic acid, ethylene glycol, and acetone are often used.

During the past decade, SR of bio-oil components has been persistently studied.[204,205] Acetic acid is considered to be the model compound of bio-oil, since its content in the oil mixture is relatively high.[206,207] Ni is the active phase most used for SR[204] and Pt- and Rh−Al_2O_3 catalyst are used for autothermal POX conditions.[207−210]

Up to now, most of the published studies have been limited to catalytic SR of bio-oils. Although the autothermal POX process is used by some researchers because this route offers shorter contact times and higher rates of heat transfer, they observed better results with SR due to the higher stability of the catalyst and increased yield of hydrogen due to WGS reaction.[211] The bio-oils reforming process presents some operating difficulties. Bio-oils could be treated directly as whole or using specific fractions, but it is only partly soluble in water and highly unstable on heating, polymerizing at temperatures below 80 °C.[210] On the other hand, a serious collateral effect of the reforming reaction of bio-oils is the formation of carbonaceous species on the catalyst surface.[205] Carbon deposits on the catalyst can be minimized by inhibiting the surface reactions leading to solid carbon formation via the presence of specific metals (Ru and Rh limit coke formation compared to Ni[210]) and by the use of specially designed reactors (preoxidation in excess steam,[211] cofeeding O_2 to the system,[205] cofeeding methane or methanol,[211] sequential cracking process,[210,212] etc.).

Structural supports used for reforming of bio-oils are ceramic: cordierite monoliths[206,210,212] and alumina foams.[206,207,209,212] The most used method to coat these structures with catalyst is washcoating. Structured supports are used to limit the pressure drop of conventional fixed bed reactors with powdered catalysts.[210] However, Basagiannis et al.[206] observed that the catalyst supported on pellets exhibited better performance than cordierite monoliths and alumina foams. This is attributed to a more efficient contact between the gas and the solid phases. The different structural forms affect mass transfer characteristic, which contribute to the alteration of catalytic activity and selectivity. However, the stability of the coated structured supports was higher than on pellets due to lower coke formation. Mirodatos' group is among the few that have been studying crude bio-oil (complex mixture of 200−300 compounds) reforming by catalyst deposited on cordierite monolith.[210,212] The best H_2 productivity obtained by Pt−CeO_2/ZrO_2 catalyst (provided by Johnson Matthey) was 18 mmol of H_2/g of bio-oil at 780 °C, but the formation of coke was still a drawback.

9.7 COMBUSTION

Due to the endothermic nature of some reactions involved in fuel processors, in particular SR, energy in the form of heat is required to be transferred from an external heat source to the reaction site. Taking into account that the reformer and external heat source form a heat exchanging system, the heat transfer from the external heat source to the reaction site plays a prominent role in fuel reforming performance.[213−216] The heat supply to the reformer can be achieved by several ways. The reformer may be heated externally[82,90] or internally by placing a heat source inside the reformer.[217] Actually, it has been proposed to integrate the reformer with a catalytic combustor as heat supplier.[218−220] Finally, instead of using a catalytic combustor, the reformer can be integrated with a homogeneous combustion chamber (noncatalytic combustion).

Microchannel reactors for coupling catalytic combustion with endothermic reforming processes have been manufactured of silicon,[221] silicon oxide,[89] stainless steel,[222] and cordierite ceramic.[223] Material selection for microreactor construction is guided by several factors, including thermal conductivity, easy introduction of catalyst, permselective properties in the case of membranes and of course, manufacture costs.

Factors affecting the overall performance when integrating a catalytic combustor with a reformer can be summarized as follows[224−229]: wall material and thickness of the channels, ratio of reforming to combustible mixture inlet velocities, gap sizes of the microchannels, external heat losses, type of fuel, reactor geometry, S/C ratio and reactor length. Finally, the type of catalyst and the amount of catalyst loaded in the microchannels also influence the overall process. Thus, low-conductivity materials (i.e. ceramics) are detrimental in terms of hot spot formation and axial temperature gradients. However, improved combustion and reforming overlap zone, via an appropriate choice of the catalyst loading and gap sizes, can mitigate this problem.

Stefanidis et al.,[225] compared the axial mass and heat transfer timescales, transverse mass and heat transfer timescale, and the reaction timescale of different

catalysts in the reforming channel and combustion channel of a coupled endo−exo microchannel reactor. They found that in the case of the reforming channel, the reaction timescale can become comparable or longer than the residence time. Overall, the timescales indicated that process intensification, in terms of external heat and mass transfer, in SR reaction was achieved. On the other hand, catalyst improvement (in loading or activity) of around one order of magnitude in the SR catalyst rate would be beneficial. In the case of the combustion channel, they found that the transverse mass and heat transfer and reaction timescales overlap, indicating that the combustion process operated in mixed reaction−transport controlled regime. Consequently, the process could be further intensified via decreasing the combustion channel gap size.

Recently, Moreno et al.,[230] presented a new class of integrated ceramic microchannel reactor for all-in-one reforming of hydrocarbons fuel. They reported a reactor having five methanol SR channels packed with Cu/Al_2O_3, interspersed with four methanol combustion channels washcoated with Pt/Al_2O_3, for autothermal hydrogen production.

On the other hand, Pan et al.,[231] developed a compact methanol reformer for hydrogen production that integrated one reforming chamber, one WGS reaction chamber, two preheating chambers and two combustion chambers. It could be started up at room temperature. The results indicated that this methanol reformer could provide a high concentration of hydrogen.

In the case of the homogenous combustion, there several studies have been published on the stability of homogeneous combustion in microscale and mainly in mesoscale. Kaisare et al.,[232] presented a review focusing on the question of choosing the appropriate reactor length, wall thickness, and opening size for self-sustained homogenous combustion in parallel channels. They found that increasing the reactor length results in shrinking of the region of self-sustained combustion due to increased heat loss through the reactor solid structure. An optimum gap width in the range of 600−1200 μm (transition from micro- to mesoscales) provided the largest region of self-sustained combustion. Size effects were stronger for methane than for propane combustion. The same authors[233] reviewed homogeneous, catalytic, homogeneous−heterogeneous and heat recirculating microburners.

Acknowledgments

Financial support by the Spanish Ministry of Science and Innovation and Ministry of Economy and Competitiveness (ENE2009-14522-C05 and ENE2012-37431-C03 grants, respectively) and UPV/EHU (GIU11/13) is gratefully acknowledged.

References

1. Cybulski, A.; Moulijn, J. A. *Structured Catalysts and Reactors;* Marcel Dekker, Inc.: New York, 1998.
2. Kolb, G. *Fuel Processing for Fuel Cells;* Wiley-VCH: Weinheim, 2008.
3. Giani, L.; Groppi, G.; Tronconi, E. Mass-Transfer Characterization of Metallic Foams as Supports for Structured Catalysts. *Ind. Eng. Chem. Res.* **2005,** *44,* 4993−5002.
4. Avila, P.; Montes, M.; Miro, E. E. Monolithic Reactors for Environmental Applications − A Review on Preparation Technologies. *Chem. Eng. J.* **2005,** *109,* 11−36.
5. Ehrfeld, W.; Hessel, V.; Löwe, H. *Microreactors: New Technology for Modern Chemistry,* 1st ed.; Wiley-VCH: Weinheim; New York, 2000.
6. Hessel, V.; Löwe, H.; Hardt, S. *Chemical Micro Process Engineering: Fundamentals, Modelling, and Reactions;* Wiley-VCH: Weinheim, 2004.
7. Jensen, K. F. Microreaction Engineering − Is Small Better? *Chem. Eng. Sci.* **2001,** *56,* 293−303.
8. Gavriilidis, A.; Angeli, P.; Cao, E.; Yeong, K. K.; Wan, Y. S. S. Technology and Applications of Microengineered Reactors. *Chem. Eng. Res. Des.* **2002,** *80,* 3−30.
9. Kolb, G.; Hessel, V. Micro-Structured Reactors for Gas Phase Reactions. *Chem. Eng. J.* **2004,** *98,* 1−38.
10. Hessel, V. *Micro Process Engineering: A Comprehensive Handbook;* Wiley-VCH: Weinhein, 2009.
11. Johnson, B. R.; Canfield, N. L.; Tran, D. N.; Dagle, R. A.; Li, X. S.; Holladay, J. D.; Wang, Y. Engineered SMR Catalysts Based on Hydrothermally Stable, Porous, Ceramic Supports for Microchannel Reactors. *Catal. Today* **2007,** *120,* 54−62.
12. Cruz, S.; Sanz, O.; Poyato, R.; Laguna, O. H.; Echave, F. J.; Almeida, L. C.; Centeno, M. A.; Arzamendi, G.; Gandia, L. M.; Souza-Aguiar, E. F.; Montes, M.; Odriozola, J. A. Design and Testing of a Microchannel Reactor for the PROX Reaction. *Chem. Eng. J.* **2011,** *167,* 634−642.
13. Madou, M. J. *Fundamentals of Microfabrication;* CRC Press: Boca Raton, Fla, 1997.
14. Tonkovich, A. L. M. (OH, US); Roberts, Gary L. (West Richland, WA, US); Perry, Steven T. (Galloway, OH, US); Fitzgerald, Sean P. (Columbus, OH, US). Methods of Conducting Simultaneous Exothermic and Endothermic Reactions. US Patent 6969506, 2005.
15. Khan, T. I.; Kabir, M. J.; Bulpett, R. Effect of Transient Liquid-Phase Bonding Variables on the Properties of a Micro-Duplex Stainless Steel. *Mat. Sci. Eng. A-Struct.* **2004,** *372,* 290−295.
16. Lachman, I. M.; Bagley, R. D.; Lewis, R. M. Thermal-Expansion of Extruded Cordierite Ceramics. *Am. Ceram. Soc. Bull.* **1981,** *60,* 202−205.
17. Williams, J. L. Monolith Structures, Materials, Properties and Uses. *Catal. Today* **2001,** *69,* 3−9.
18. Madou, M. J. *Fundamentals of Microfabrication;* CRC: Boca Raton, Florida, 1997.
19. Brandner, T. G. J. J.; Henning, T.; Kraut, M. Microfabrication in Metals and Polymers. In *Micro Process Engineering;* Kockmann, N., Ed.; Wiley-VCH: Weinheim, 2006; p 507.
20. Burgos, N.; Paulis, M. A.; Montes, M. Preparation of Al_2O_3/Al Monoliths by Anodisation of Aluminium as Structured Catalytic Supports. *J. Mater. Chem.* **2003,** *13,* 1458−1467.
21. Grabke, H. J. Thermodynamics, Mechanisms and Kinetics of Metal Dusting. *Mater. Corros.* **1998,** *49,* 303−308.
22. Grabke, H. J.; Guthrie, J. E. Points to be Considered in Carburization Testing of Alloys. *Mater. Corros.* **1998,** *49,* 278−281.
23. Di Gabriele, F.; Bernstein, J. R.; Al-Qhatani, M. M.; Liu, Z.; Jordan, M. P.; Richardson, J. A.; Stott, F. H. Study of the Metal

Dusting Behaviour of High-Temperature Alloys. *Mater. Corros.* **2003,** *54,* 854−859.
24. Yin, R. Thermodynamic Roles of Metallic Elements in Carburization and Metal Dusting. *Oxid. Met.* **2004,** *61,* 323−337.
25. Yin, R. C. Carburization Performance of Incoloy 800HT in CH_4/H_2 Gas Mixtures. *Mat. Sci. Eng. A-Struct.* **2004,** *380,* 281−289.
26. Yin, R. C. Cyclic and Isothermal Exposures of 310SS to 10%CH_4/H_2 Carburizing Gas Mixture at High Temperatures. *Mat. Sci. Eng. A-Struct.* **2005,** *391,* 19−28.
27. Kempen, A. T. W.; van Wortel, J. C. The Influence of Metal Dusting on Gas Reactions. *Mater. Corros.* **2004,** *55,* 249−258.
28. Zeng, Z.; Natesan, K. Corrosion of Metallic Interconnects for SOFC in Fuel Gases. *Solid State Ion.* **2004,** *167,* 9−16.
29. Horita, T.; Xiong, Y. P.; Kishimoto, H.; Yamaji, K.; Sakai, N.; Yokokawa, H. Application of Fe−Cr Alloys to Solid Oxide Fuel Cells for Cost-Reduction − Oxidation Behavior of Alloys in Methane Fuel. *J. Power Sources* **2004,** *131,* 293−298.
30 .Cairns, J. A.; Pugh, S. F. Catalyst, US Patent 3966645, 1976.
31. Cairns, J. A. Catalyst of a Coating on an Alloy Substrate, US Patent 4096095, 1978.
32. Agrafiotis, C.; Tsetsekou, A.; Ekonomakou, A. The effect of particle size on the adhesion properties of oxide washcoats on cordierite honeycombs. *J. Mater. Sci. Lett.* **1999,** *18,* 1421−1424.
33. Agrafiotis, C.; Tsetsekou, A. The Effect of Powder Characteristics on Washcoat Duality. Part I: Alumina Washcoats. *J. Eur. Ceram. Soc.* **2000,** *20,* 815−824.
34. Agrafiotis, C.; Tsetsekou, A. The Effect of Powder Characteristics on Washcoat Quality. Part II: Zirconia, Titania Washcoats − Multilayered Structures. *J. Eur. Ceram. Soc.* **2000,** *20,* 825−834.
35. Sanz, O.; Almeida, L. C.; Zamaro, J. M.; Ulla, M. A.; Miro, E. E.; Montes, M. Washcoating of Pt-ZSM5 onto Aluminium Foams. *Appl. Catal. B-Environ.* **2008,** *78,* 166−175.
36. Chapman, L. R.; Vigor, C. W.; Watton, J. F. Enhanced Oxide Whisker Growth on Peeled Al-Containing Stainless Steel Foil, US Patent 4331631, 1982.
37. Chapman, L. R.; Watton, J. F. Application of an Alumina Coating to Oxide Whisker-Covered Surface on Al-Containing Stainless Steel Foil, US Patent 4279782, 1981.
38. Frias, D. M.; Nousir, S.; Barrio, I.; Montes, M.; Martinez, L. M.; Centeno, M. A.; Odriozola, J. A. Nucleation and Growth of Manganese Oxides on Metallic Surfaces as a Tool to Prepare Metallic Monoliths. *Appl. Catal. A-Gen.* **2007,** *325,* 205−212.
39. Paul, A.; Odriozola, J. A.; San Miguel, M. A.; Sanz, J. F.; Alvarez, L. J. Experimental and Molecular Dynamics Simulation Analysis of $Lacro_3$ Precipitation in Chromia Scales. *Acta Mater.* **2000,** *48,* 2951−2958.
40. Paul, A.; Elmrabet, S.; Ager, F. J.; Odriozola, J. A.; Respaldiza, M. A.; da Silva, M. F.; Soares, J. C. Influence of Preoxidation and Annealing Treatments on the Isothermal Oxidation in Air at 1173 K of Cerium-Implanted EN-1.4301 Stainless Steel. *Oxid. Met.* **2002,** *57,* 33−51.
41. Paul, P.; Odriozola, J. A. Development of a Modified CVD Coating Process for the Enhancement of the High Temperature Oxidation Resistance of Cr_2O_3 and Al_2O_3 Forming Alloys. *Mat. Sci. Eng. A-Struct.* **2001,** *300,* 22−33.
42. Sanz, O.; Echave, F. J.; Odriozola, J. A.; Montes, M. Aluminum Anodization in Oxalic Acid: Controlling the Texture of Al_2O_3/Al Monoliths for Catalytic Aplications. *Ind. Eng. Chem. Res.* **2011,** *50,* 2117−2125.
43. Wiessmeier, G.; Honicke, D. Microfabricated Components for Heterogeneously Catalysed Reactions. *J. Micromech. Microeng.* **1996,** *6,* 285−289.
44. Sanz, O.; Echave, F. J.; Sanchez, M.; Monzon, A.; Montes, M. Aluminium Foams as Structured Supports for Volatile Organic Compounds (VOCs) Oxidation. *Appl. Catal. A-Gen.* **2008,** *340,* 125−132.
45. Meille, V. Review on Methods to Deposit Catalysts on Structured Surfaces. *Appl. Catal. A-Gen.* **2006,** *315,* 1−17.
46. Nijhuis, T. A.; Beers, A. E. W.; Vergunst, T.; Hoek, I.; Kapteijn, F.; Moulijn, J. A. Preparation of Monolithic Catalysts. *Catal. Rev.* **2001,** *43,* 345−380.
47. Almeida, L. C.; Echave, F. J.; Sanz, O.; Centeno, M. A.; Odriozola, J. A.; Montes, M. Washcoating of Metallic Monoliths and Microchannel Reactors. *Stud. Surf. Sci. Catal.* **2010,** *175,* 25−33.
48. He, M. Z.; Wang, Y. M.; Forssberg, E. Slurry Rheology in Wet Ultrafine Grinding of Industrial Minerals: a Review. *Powder Technol.* **2004,** *147,* 94−112.
49. Shi, F. N.; Napier-Munn, T. J. Effects of Slurry Rheology on Industrial Grinding Performance. *Int. J. Miner. Process.* **2002,** *65,* 125−140.
50. Tanaka, S.; Kato, Z.; Uchida, N.; Uematsu, K. Novel Examination of the Grinding Behavior of Alumina Powder. *Am. Ceram. Soc. Bull.* **2003,** *82,* 9301−9303.
51. Gonzalez-Velasco, J. R.; Gutierrez-Ortiz, M. A.; Marc, J. L.; Botas, J. A.; Gonzalez-Marcos, M. P.; Blanchard, G. Pt/$Ce_{0.68}Zr_{0.32}O_2$ Washcoated Monoliths for Automotive Emission Control. *Ind. Eng. Chem. Res.* **2003,** *42,* 311−317.
52. Patton, T. C. *Paint Flow and Pigment Dispersion: a Rheological Approach to Coating and Ink Technology,* 2nd ed; Wiley: New York; Chichester, 1979.
53. Agrafiotis, C.; Tsetsekou, A. The Effect of Processing Parameters on the Properties of Gamma-Alumina Washcoats Deposited on Ceramic Honeycombs. *J. Mater. Sci.* **2000,** *35,* 951−960.
54. Kolb, W. B.; Cerro, R. L. The Motion of Long Bubbles in Tubes of Square Cross-Section. *Phys. Fluids A-Fluid Dyn.* **1993,** *5,* 1549−1557.
55. Brinker, C. J.; Scherer, G. W. *Sol−Gel Science: the Physics and Chemistry of Sol−Gel Processing;* Academic Press: Boston, 1990.
56. Middleman, S. *Fundamentals of Polymer Processing;* McGraw-Hill: New York, 1977.
57. Valentini, M.; Groppi, G.; Cristiani, C.; Levi, M.; Tronconi, E.; Forzatti, P. The Deposition of Gamma-Al_2O_3 Layers on Ceramic and Metallic Supports for the Preparation of Structured Catalysts. *Catal. Today* **2001,** *69,* 307−314.
58. Eleta, A.; Navarro, P.; Costa, L.; Montes, M. Deposition of Zeolitic Coatings onto Fecralloy Microchannels: Washcoating vs. In Situ Growing. *Microporous Mesoporous Mater.* **2009,** *123,* 113−122.
59. Almeida, L. C.; Echave, F. J.; Sanz, O.; Centeno, M. A.; Arzamendi, G.; Gandia, L. M.; Sousa-Aguiar, E. F.; Odriozola, J. A.; Montes, M. Fischer−-Tropsch Synthesis in Microchannels. *Chem. Eng. J.* **2011,** *167,* 536−544.
60. Xu, X. D.; Moulijn, J. A. Preparation of Monolithic Catalysts by Dip Coating. *Prep. Catal. VII* **1998,** *118,* 845−854.
61. Liu, D. -J.; Winstead, D. R.; Van Den Bussche, N. Method of Preparing a Catalyst Layer Over a Metallic Surface of a Recuperator, US Patent 6540843, 2003.
62. Giani, L.; Cristiani, C.; Groppi, G.; Tronconi, E. Washcoating Method for Pd/-Gamma-Al_2O_3 Deposition on Metallic Foams. *Appl. Catal. B-Environ.* **2006,** *62,* 121−131.
63. Zwinkels, M. F. M.; Jaras, S. G.; Menon, P. G. Preparation of Combustion Catalysts by Washcoating Alumina Whiskers-Covered Metal Monoliths Using a Sol−Gel Method. *Prep. Catal. VI* **1995,** *91,* 85−94.
64. Tonkovich, A. L.; Yang, B. L.; Mazanec, T.; Daly, F. P.; Fitzgerald, S. P.; Arora, R.; Qiu, D.; Yang, B.; Perry, S. T.; Jarosh, K.; Neagle, P. W.; Hesse, D. J.; Taha, R.; Long, R.; Marco, J.; Yuschak, T. D.; Ramler, J. J.; Marchiando, M. Tailored and

Uniform Coatings in Microchannel Apparatus, US Patent 2005/0244304, 2005.
65. Xuan, J.; Leung, M. K. H.; Leung, D. Y. C.; Ni, M. A Review of Biomass-Derived Fuel Processors for Fuel Cell Systems. *Renew. Sust. Energ. Rev.* **2009,** *13,* 1301–1313.
66. Shimoda, N.; Faungnawakij, K.; Kikuchi, R.; Eguchi, K. Degradation and Regeneration of Copper–Iron Spinel and Zeolite Composite Catalysts in Steam Reforming of Dimethyl Ether. *Appl. Catal. A-Gen.* **2010,** *378,* 234–242.
67. Oka, K.; Nishiguchi, T.; Kanai, H.; Utani, K.; Imamura, S. Active State of Tungsten Oxides on WO_3/ZrO_2 Catalyst for Steam Reforming of Dimethyl Ether Combined with CuO/CeO_2. *Appl. Catal. A-Gen.* **2006,** *309,* 187–191.
68. Takeishi, K.; Suzuki, H. Steam Reforming of Dimethyl Ether. *Appl. Catal. A-Gen.* **2004,** *260,* 111–117.
69. Tanaka, Y.; Kikuchi, R.; Takeguchi, T.; Eguchi, K. Steam Reforming of Dimethyl Ether Over Composite Catalysts of Gamma-Al_2O_3 and Cu-Based Spinel. *Appl. Catal. B-Environ.* **2005,** *57,* 211–222.
70. Fukunaga, T.; Ryumon, N.; Shimazu, S. The Influence of Metals and Acidic Oxide Species on the Steam Reforming of Dimethyl Ether (DME). *Appl. Catal. A-Gen.* **2008,** *348,* 193–200.
71. Venugopal, A.; Palgunadi, J.; Jung, K. D.; Joo, O. S.; Shin, C. H. $Cu–Zn–Cr_2O_3$ Catalysts for Dimethyl Ether Synthesis: Structure and Activity Relationship. *Catal. Lett.* **2008,** *123,* 142–149.
72. Nilsson, M.; Pettersson, L. J.; Lindstrom, B. Hydrogen Generation from Dimethyl Ether for Fuel Cell Auxiliary Power Units. *Energy Fuel* **2006,** *20,* 2164–2169.
73. Faungnawakij, K.; Kikuchi, R.; Shimoda, N.; Fukunaga, T.; Eguchi, K. Effect of Thermal Treatment on Activity and Durability of $CuFe_2O_4–Al_2O_3$ Composite Catalysts for Steam Reforming of Dimethyl Ether. *Angew. Chem. Int. Ed.* **2008,** *47,* 9314–9317.
74. Ledesma, C.; Ozkan, U. S.; Llorca, J. Hydrogen Production by Steam Reforming of Dimethyl Ether Over Pd-Based Catalytic Monoliths. *Appl. Catal. B-Environ.* **2011,** *101,* 690–697.
75. Ledesma, C.; Llorca, J. Dimethyl Ether Steam Reforming over $Cu–Zn–Pd/CeO_2–ZrO_2$ Catalytic Monoliths. The Role of Cu Species on Catalyst Stability. *J. Phys. Chem. C* **2011,** *115,* 11624–11632.
76. Nilsson, M.; Jozsa, P.; Pettersson, L. J. Evaluation of Pd-Based Catalysts and the Influence of Operating Conditions for Autothermal Reforming of Dimethyl Ether. *Appl. Catal. B-Environ.* **2007,** *76,* 42–50.
77. Wang, S. Z.; Ishihara, T.; Takita, Y. Partial Oxidation of Dimethyl Ether Over Various Supported Metal Catalysts. *Appl. Catal. A-Gen.* **2002,** *228,* 167–176.
78. Nilsson, M.; Jansson, K.; Jozsa, P.; Pettersson, L. J. Catalytic Properties of Pd Supported on $ZnO/ZnAl_2O_4/Al_2O_3$ Mixtures in Dimethyl Ether Autothermal Reforming. *Appl. Catal. B-Environ.* **2009,** *86,* 18–26.
79. Creaser, D.; Nilsson, M.; Pettersson, L. J.; Dawody, J. Kinetic Modeling of Autothermal Reforming of Dimethyl Ether. *Ind. Eng. Chem. Res.* **2010,** *49,* 9712–9719.
80. Demirbas, A.; Gulu, D. Acetic Acid, Methanol and Acetone from Lignocellulosics by Pyrpolysis. *Energy Edu. Sci. Technol.* **1998,** *1,* 111–115.
81. Mathieu-Potvin, F.; Gosselin, L.; da Silva, A. K. Optimal Geometry of Catalytic Microreactors: Maximal Reaction Rate Density with Fixed Amount of Catalyst and Pressure Drop. *Chem. Eng. Sci.* **2012,** *73,* 249–260.
82. Kawamura, Y.; Ogura, N.; Yamamoto, T.; Igarashi, A. A Miniaturized Methanol Reformer with Si-Based Microreactor for a Small PEMFC. *Chem. Eng. Sci.* **2006,** *61,* 1092–1101.
83. Hao, Y. Z.; Du, X. Z.; Yang, L. J.; Shen, Y. Q.; Yang, Y. P. Numerical Simulation of Configuration and Catalyst-Layer Effects on Micro-Channel Steam Reforming of Methanol. *Int. J. Hydrogen Energy* **2011,** *36,* 15611–15621.
84. Ha, J. W.; Kundu, A.; Jang, J. H. Poly-Dimethylsiloxane (PDMS) Based Micro-Reactors for Steam Reforming of Methanol. *Fuel Process. Technol.* **2010,** *91,* 1725–1730.
85. Horny, C.; Kiwi-Minsker, L.; Renken, A. Micro-Structured String-Reactor for Autothermal Production of Hydrogen. *Chem. Eng. J.* **2004,** *101,* 3–9.
86. Chen, Y. P.; Zhang, C. B.; Wu, R.; Shi, M. H. Methanol Steam Reforming in Microreactor with Constructal Tree-Shaped Network. *J. Power Sources* **2011,** *196,* 6366–6373.
87. Mei, D.; Qian, M.; Liu, B.; Jin, B.; Yao, Z.; Chen, Z. A Micro-Reactor with Micro-Pin-Fin Arrays for Hydrogen Production Via Methanol Steam Reforming. *J. Power Sources* **2012,** *205,* 367–376.
88. Zapf, R.; Becker-Willinger, C.; Berresheim, K.; Bolz, H.; Gnaser, H.; Hessel, V.; Kolb, G.; Lob, P.; Pannwitt, A. K.; Ziogas, A. Detailed Characterization of Various Porous Alumina-Based Catalyst Coatings within Microchannels and Their Testing for Methanol Steam Reforming. *Chem. Eng. Res. Des.* **2003,** *81,* 721–729.
89. Terazaki, T.; Nomura, M.; Takeyama, K.; Nakamura, O.; Yamamoto, T. Development of Multi-Layered Microreactor with Methanol Reformer for Small PEMFC. *J. Power Sources* **2005,** *145,* 691–696.
90. Pattekar, A. V.; Kothare, M. V. A Microreactor for Hydrogen Production in Micro Fuel Cell Applications. *J. Microelectromech. Syst.* **2004,** *13,* 7–18.
91. Wang, H. H. F.; Chen, S. C.; Yang, S. Y.; Yeh, G. T.; Rei, M. H. Design of Compact Methanol Reformer for Hydrogen with Low CO for the Fuel Cell Power Generation. *Int. J. Hydrogen Energy* **2012,** *37,* 7487–7496.
92. Bravo, J.; Karim, A.; Conant, T.; Lopez, G. P.; Datye, A. Wall Coating of a $CuO/ZnO/AI_2O_3$ Methanol Steam Reforming Catalyst for Micro-Channel Reformers. *Chem. Eng. J.* **2004,** *101,* 113–121.
93. Jeong, H.; Kim, K. I.; Kim, T. H.; Ko, C. H.; Park, H. C.; Song, I. K. Hydrogen Production by Steam Reforming of Methanol in a Micro-Channel Reactor Coated with $Cu/ZnO/ZrO_2/Al_2O_3$ Catalyst. *J. Power Sources* **2006,** *159,* 1296–1299.
94. Fukuhara, C.; Ohkura, H.; Kamata, Y.; Murakami, Y.; Igarashi, A. Catalytic Properties of Plate-Type Copper-Based Catalysts, for Steam Reforming of Methanol, on an Aluminum Plate Prepared by Electroless Plating. *Appl. Catal. A-Gen.* **2004,** *273,* 125–132.
95. Pfeifer, P.; Kolbl, A.; Schubert, K. Kinetic Investigations on Methanol Steam Reforming on PdZn Catalysts in Microchannel Reactors and Model Transfer into the Pressure Gap Region. *Catal. Today* **2005,** *110,* 76–85.
96. Basile, A.; Tereschenko, G. F.; Orekhova, N. V.; Ermilova, M. M.; Gallucci, F.; Iulianelli, A. An experimental Investigation on Methanol Steam Reforming with Oxygen Addition in a Flat Pd–Ag Membrane Reactor. *Int. J. Hydrogen Energy* **2006,** *31,* 1615–1622.
97. Basile, A.; Tosti, S.; Capannelli, G.; Vitulli, G.; Iulianelli, A.; Gallucci, F.; Drioli, E. Co-Current and Counter-Current Modes for Methanol Steam Reforming Membrane Reactor: Experimental Study. *Catal. Today* **2006,** *118,* 237–245.
98. Basile, A.; Parmaliana, A.; Tosti, S.; Iulianelli, A.; Gallucci, F.; Espro, C.; Spooren, J. Hydrogen Production by Methanol Steam Reforming Carried Out in Membrane Reactor on Cu/Zn/Mg-Based Catalyst. *Catal. Today* **2008,** *137,* 17–22.
99. Iulianelli, A.; Longo, T.; Basile, A. Methanol Steam Reforming Reaction in a Pd–Ag Membrane Reactor for CO-Free Hydrogen Production. *Int. J. Hydrogen Energy* **2008,** *33,* 5583–5588.
100. Israni, S. H.; Harold, M. P. Methanol Steam Reforming in Single-Fiber Packed Bed Pd–Ag Membrane Reactor: Experiments and Modeling. *J. Membr. Sci.* **2011,** *369,* 375–387.
101. Sa, S.; Sousa, J. M.; Mendes, A. Steam Reforming of Methanol Over a $CuO/ZnO/Al_2O_3$ Catalyst Part II: A Carbon Membrane Reactor. *Chem. Eng. Sci.* **2011,** *66,* 5523–5530.

102. Papavasiliou, J.; Avgouropoulos, G.; Ioannides, T. $CuMnO_x$ Catalysts for Internal Reforming Methanol Fuel Cells: Application Aspects. Int. J. Hydrogen Energy.
103. Yu, H.; Chen, H. Q.; Pan, M. Q.; Tang, Y.; Zeng, K.; Peng, F.; Wang, H. J. Effect of the Metal Foam Materials on the Performance of Methanol Steam Micro-Reformer for Fuel Cells. *Appl. Catal. A-Gen.* **2007,** *327,* 106−113.
104. Tang, Y.; Zhou, W.; Pan, M. Q.; Chen, H. Q.; Liu, W. Y.; Yu, H. Porous Copper Fiber Sintered Felts: An Innovative Catalyst Support of Methanol Steam Reformer for Hydrogen Production. *Int. J. Hydrogen Energy* **2008,** *33,* 2950−2956.
105. Zhou, W.; Tang, Y.; Pan, M. Q.; Wei, X. L.; Chen, H. Q.; Xiang, J. H. A Performance Study of Methanol Steam Reforming Microreactor with Porous Copper Fiber Sintered Felt as Catalyst Support for Fuel Cells. *Int. J. Hydrogen Energy* **2009,** *34,* 9745−9753.
106. Pan, M. Q.; Tang, Y.; Wei, X. L.; Jiang, X. Oriented Linear Cutting Fiber Sintered Felt as an Innovative Catalyst Support for Methanol Steam Reforming. *Int. J. Hydrogen Energy* **2011,** *36,* 7066−7073.
107. Tang, Y.; Chen, L.; Wang, M. M.; Li, J. F.; Lu, Y. Microfibrous Entrapped $ZnO-CaO/Al_2O_3$ for High Efficiency Hydrogen Production Via Methanol Steam Reforming. *Particuology* **2010,** *8,* 225−230.
108. Ling, M.; Zhao, G. F.; Chen, W.; Wang, M. M.; Xue, Q. S.; Lu, Y. Microfibrous Structured Catalytic Packings for Miniature Methanol Fuel Processor: Methanol Steam Reforming and CO Preferential Oxidation. *Int. J. Hydrogen Energy* **2011,** *36,* 12833−12842.
109. Arzamendi, G.; Campo, I.; Arguinarena, E.; Sanchez, M.; Montes, M.; Gandia, L. M. Synthesis of Biodiesel with Heterogeneous NaOH/Alumina Catalysts: Comparison with Homogeneous NaOH. *Chem. Eng. J.* **2007,** *134,* 123−130.
110. Arzamendi, G.; Arguinarena, E.; Campo, I.; Gandia, L. M. Monitoring of Biodiesel Production: Simultaneous Analysis of the Transesterification Products Using Size-Exclusion Chromatography. *Chem. Eng. J.* **2006,** *122,* 31−40.
111. Haynes, D. J.; Shekhawat, D. Chapter 6 − Oxidative Steam Reforming. In *Fuel Cells: Technologies for Fuel Processing;* Shekhawat, D., Spivey, J. J., Berry, D. A., Eds.; Elsevier: Amsterdam, 2011; pp 129−190.
112. Nguyen, B. N. T.; Leclerc, C. A. Catalytic Partial Oxidation of Methyl Acetate as a Model to Investigate the Conversion of Methyl Esters to Hydrogen. *Int. J. Hydrogen Energy* **2008,** *33,* 1295−1303.
113. Subramanian, R.; Schmidt, L. D. Renewable Olefins from Biodiesel by Autothermal Reforming. *Angew. Chem. Int. Ed.* **2005,** *44,* 302−305.
114. Siefert, N.; Shekhawat, D.; Gemmen, R.; Berry, D.; Robey, E.; Bergen, R.; Haynes, D. J.; Moore, K.; Williams, M.; Smith, M. Operation of a Solid Fuel Cell on Biodiesel with a Partial Oxidation Reformer8th Interantional Conference on Fuel Cell Science, Engineering and Technology; ASME: Brooklyn, New York, 2010; pp 371−376.
115. InnovaTek, I. *InnovaTek Inc. and Seattle BioFuels, Inc. Announce the First Successful Production of Hydrogen from 100% Biodiesel in a Microchannel Steam Reformer.* http://innovatek.com/innovatek-inc-and-seattle-biofuels-inc-announce-first-successful-production-hydrogen-100-biodiesel-m, 2006.
116. Adhikari, S.; Fernando, S. D.; Haryanto, A. Kinetics and Reactor Modeling of Hydrogen Production from Glycerol via Steam Reforming Process over Ni/CeO_2 Catalysts. *Chem. Eng. Technol.* **2009,** *32,* 541−547.
117. Adhikari, S.; Fernando, S. D.; Haryanto, A. Hydrogen Production from Glycerol: An Update. *Energy Convers. Manag.* **2009,** *50,* 2600−2604.
118. Adhikari, S.; Fernando, S.; Gwaltney, S. R.; To, S. D. F.; Bricka, R. M.; Steele, P. H.; Haryanto, A. A Thermodynamic Analysis of Hydrogen Production by Steam Reforming of Glycerol. *Int. J. Hydrogen Energy* **2007,** *32,* 2875−2880.
119. Wang, W. J. Thermodynamic Analysis of Glycerol Partial Oxidation for Hydrogen Production. *Fuel Process. Technol.* **2010,** *91,* 1401−1408.
120. Yang, G.; Yu, H.; Peng, F.; Wang, H.; Yang, J.; Xie, D. Thermodynamic Analysis of Hydrogen Generation Via Oxidative Steam Reforming of Glycerol. *Renew. Energy* **2011,** *36,* 2120−2127.
121. Authayanun, S.; Arpornwichanop, A.; Paengjuntuek, W.; Assabumrungrat, S. Thermodynamic Study of Hydrogen Production from Crude Glycerol Autothermal Reforming for Fuel Cell Applications. *Int. J. Hydrogen Energy* **2010,** *35,* 6617−6623.
122. Kale, G. R.; Kulkarni, B. D. Thermodynamic Analysis of Dry Autothermal Reforming of Glycerol. *Fuel Process. Technol.* **2010,** *91,* 520−530.
123. Wang, X.; Li, M.; Wang, M.; Wang, H.; Li, S.; Wang, S.; Ma, X. Thermodynamic Analysis of Glycerol Dry Reforming for Hydrogen and Synthesis Gas Production. *Fuel* **2009,** *88,* 2148−2153.
124. Cortright, R. D. M. (WI, US); Dumesic, James A. (Verona, WI, US). Low-Temperature Hydrogen Production from Oxygenated Hydrocarbons, US 6964757, 2005.
125. Cortright, R. D. M. (WI, US); Dumesic, James A. (Verona, WI, US). Low-Temperature Hydrogen Production from Oxygenated Hydrocarbons, US 7618612, 2009.
126. Cortright, R. D. M. (WI); Dumesic, James A. (Verona, WI). Low-Temperature Hydrogen Production from Oxygenated Hydrocarbons, US 6699457, 2004.
127. Cortright, R. D.; Davda, R. R.; Dumesic, J. A. Hydrogen from Catalytic Reforming of Biomass-Derived Hydrocarbons in Liquid Water. *Nature* **2002,** *418,* 964−967.
128. Davda, R. R.; Shabaker, J. W.; Huber, G. W.; Cortright, R. D.; Dumesic, J. A. A Review of Catalytic Issues and Process Conditions for Renewable Hydrogen and Alkanes by Aqueous-Phase Reforming of Oxygenated Hydrocarbons Over Supported Metal Catalysts. *Appl. Catal. B-Environ.* **2005,** *56,* 171−186.
129. Huber, G. W.; Shabaker, J. W.; Dumesic, J. A. Raney Ni−Sn Catalyst for H_2 Production from Biomass-Derived Hydrocarbons. *Science* **2003,** *300,* 2075−2077.
130. Ozgur, D. O.; Uysal, B. Z. Hydrogen Production by Aqueous Phase Catalytic Reforming of Glycerine. *Biomass. Bioenerg.* **2011,** *35,* 822−826.
131. Luo, N. J.; Fu, X. W.; Cao, F. H.; Xiao, T. C.; Edwards, P. P. Glycerol Aqueous Phase Reforming for Hydrogen Generation Over Pt Catalyst − Effect of Catalyst Composition and Reaction Conditions. *Fuel* **2008,** *87,* 3483−3489.
132. King, D. L.; Zhang, L. A.; Xia, G.; Karim, A. M.; Heldebrant, D. J.; Wang, X. Q.; Peterson, T.; Wang, Y. Aqueous Phase Reforming of Glycerol for Hydrogen Production Over Pt−Re Supported on Carbon. *Appl. Catal. B-Environ.* **2010,** *99,* 206−213.
134. Pagliaro, M.; Rossi, M. *The Future of Glycerol: New Uses of a Versatile Raw Material;* Royal Society of Chemistry: Cambridge, 2008.
134. Buffoni, I. N.; Pompeo, F.; Santori, G. F.; Nichio, N. N. Nickel Catalysts Applied in Steam Reforming of Glycerol for Hydrogen Production. *Catal. Commun.* **2009,** *10,* 1656−1660.
135. Pompeo, F.; Santori, G. F.; Nichio, N. N. Hydrogen Production by Glycerol Steam Reforming with Pt/SiO_2 and Ni/SiO_2 Catalysts. *Catal. Today* **2011,** *172,* 183−188.
136. Sanchez, E. A.; D'Angelo, M. A.; Comelli, R.l. A. Hydrogen Production from Glycerol on Ni/Al_2O_3 Catalyst. *Int. J. Hydrogen Energy* **2010,** *35,* 5902−5907.
137. Profeti, L. P. R.; Ticianelli, E. A.; Assaf, E. M. Production of Hydrogen Via Steam Reforming of Biofuels on $Ni/CeO_2-Al_2O_3$

Catalysts Promoted by Noble Metals. *Int. J. Hydrogen Energy* **2009,** *34,* 5049−5060.
138. Adhikari, S.; Fernando, S. D.; To, S. D. F.; Bricka, R. M.; Steele, P. H.; Haryanto, A. Conversion of Glycerol to Hydrogen Via a Steam Reforming Process Over Nickel Catalysts. *Energy Fuel* **2008,** *22,* 1220−1226.
139. Nichele, V.; Signoretto, M.; Menegazzo, F.; Gallo, A.; Dal Santo, V.; Cruciani, G.; Cerrato, G. Glycerol Steam reforming for Hydrogen Production: Design of Ni Supported Catalysts. *Appl. Catal. B-Environ.* **2012,** *111,* 225−232.
140. Cui, Y.; Galvita, V.; Rihko-Struckmann, L.; Lorenz, H.; Sundmacher, K. Steam Reforming of Glycerol: The Experimental Activity of $La_{1-x}Ce_xNiO_3$ Catalyst in Comparison to the Thermodynamic Reaction Equilibrium. *Appl. Catal. B-Environ.* **2009,** *90,* 29−37.
141. Hirai, T.; Ikenaga, N.; Miyake, T.; Suzuki, T. Production of Hydrogen by Steam Reforming of Glycerin on Ruthenium Catalyst. *Energy Fuel* **2005,** *19,* 1761−1762.
142. Dave, C. D.; Pant, K. K. Renewable Hydrogen Generation by Steam Reforming of Glycerol Over Zirconia Promoted Ceria Supported Catalyst. *Renew. Energy* **2011,** *36,* 3195−3202.
143. Li, J.; Yu, H.; Yang, G.; Peng, F.; Xie, D.; Wang, H.; Yang, J. Steam Reforming of Oxygenate Fuels for Hydrogen Production: A Thermodynamic Study. *Energy Fuel* **2011,** *25,* 2643−2650.
144. Araque, M.; Martinez, L. M.; Vargas, J. C.; Roger, A. C. Hydrogen Production by Glycerol Steam Reforming over CeZrCo Fluorite Type Oxides. *Catal. Today* **2011,** *176,* 352−356.
145. Cheng, C. K.; Foo, S. Y.; Adesina, A. A. Glycerol Steam Reforming over Bimetallic Co−Ni/Al_2O_3. *Ind. Eng. Chem. Res.* **2010,** *49,* 10804−10817.
146. Chiodo, V.; Freni, S.; Galvagno, A.; Mondello, N.; Frusteri, F. Catalytic Features of Rh and Ni Supported Catalysts in the Steam Reforming of Glycerol to Produce Hydrogen. *Appl. Catal. A-Gen.* **2010,** *381,* 1−7.
147. Trimm, D. L. Catalysts for the Control of Coking During Steam Reforming. *Catal. Today* **1999,** *49,* 3−10.
148. Penkova, A.; Bobadilla, L.; Ivanova, S.; Dominguez, M. I.; Romero-Sarria, F.; Roger, A. C.; Centeno, M. A.; Odriozola, J. A. Hydrogen Production by Methanol Steam Reforming on NiSn/MgO−Al_2O_3 Catalysts: The Role of MgO Addition. *Appl. Catal. A-Gen.* **2011,** *392,* 184−191.
149. Zhang, Z. L.; Verykios, X. E. Carbon-Dioxide Reforming of Methane to Synthesis Gas over Supported Ni Catalysts. *Catal. Today* **1994,** *21,* 589−595.
150. Yamazaki, O.; Nozaki, T.; Omata, K.; Fujimoto, K. Reduction of Carbon-Dioxide by Methane with Ni−on−MgO−CaO Containing Catalysts. *Chem. Lett.* **1992,** 1953−1954.
151. Tomishige, K.; Chen, Y. G.; Fujimoto, K. Studies on Carbon Deposition in CO_2 Reforming of CH_4 over Nickel−Magnesia Solid Solution Catalysts. *J. Catal.* **1999,** *181,* 91−103.
152. Hufschmidt, D.; Bobadilla, L. F.; Romero-Sarria, F.; Centeno, M. A.; Odriozola, J. A.; Montes, M.; Falabella, E. Supported Nickel Catalysts with a Controlled Molecular Architecture for the Catalytic Reformation of Methane. *Catal. Today* **2010,** *149,* 394−400.
153. Trimm, D. L.; Onsan, Z. I. Onboard Fuel Conversion for Hydrogen-Fuel-Cell-Driven Vehicles. *Catal. Rev.* **2001,** *43,* 31−84.
154. Meeyoo, V.; Lee, J. H.; Trimm, D. L.; Cant, N. W. Hydrogen Sulphide Emission Control by Combined Adsorption and Catalytic Combustion. *Catal. Today* **1998,** *44,* 67−72.
155. Tsipouriari, V. A.; Zhang, Z.; Verykios, X. E. Catalytic Partial Oxidation of Methane to Synthesis Gas over Ni-Based Catalysts − I. Catalyst Performance Characteristics. *J. Catal.* **1998,** *179,* 283−291.
156. Shabaker, J. W.; Huber, G. W.; Dumesic, J. A. Aqueous-Phase Reforming of Oxygenated Hydrocarbons over Sn-Modified Ni Catalysts. *J. Catal.* **2004,** *222,* 180−191.
157. Valliyappan, T.; Bakhshi, N. N.; Dalai, A. K. Pyrolysis of Glycerol for the Production of Hydrogen or Syn Gas. *Bioresour. Technol.* **2008,** *99,* 4476−4483.
158. Valliyappan, T.; Ferdous, D.; Bakhshi, N. N.; Dalai, A. K. Production of Hydrogen and Syngas Via Steam Gasification of Glycerol in a Fixed-Bed Reactor. *Top. Catal.* **2008,** *49,* 59−67.
159. Stein, Y. S.; Antal, M. J.; Jones, M. A Study of the Gas-Phase Pyrolysis of Glycerol. *J. Anal. Appl. Pyrolysis* **1983,** *4,* 283−296.
160. Liguras, D. K.; Goundani, K.; Verykios, X. E. Production of Hydrogen for Fuel Cells by Catalytic Partial Oxidation of Ethanol Over Structured Ni Catalysts. *J. Power Sources* **2004,** *130,* 30−37.
161. Liguras, D. K.; Goundani, K.; Verykios, X. E. Production of Hydrogen for Fuel Cells by Catalytic Partial Oxidation of Ethanol Over Structured Ru Catalysts. *Int. J. Hydrogen Energy* **2004,** *29,* 419−427.
162. Bobadilla, L. F.; Alvarez, A.; Dominguez, M. I.; Romero-Sarria, F.; Centeno, M.A.; Montes, M.; Odriozola, J.A. Influence of the Shape of Ni Catalysts in the Glycerol Steam Reforming. *Appl. Catal. B-Environ.* DOI:org/10.1016/j.apcatb.2012.1005.1004.
163. Lau, C. S.; Tsolakis, A.; Wyszynski, M. L. Biogas Upgrade to Syn-Gas (H_2−CO) Via Dry and Oxidative Reforming. *Int. J. Hydrogen Energy* **2011,** *36,* 397−404.
164. Araki, S.; Hino, N.; Mori, T.; Hikazudani, S. Durability of a Ni Based Monolithic Catalyst in the Autothermal Reforming of Biogas. *Int. J. Hydrogen Energy* **2009,** *34,* 4727−4734.
165. Araki, S.; Hino, N.; Mori, T.; Shimizu, T.; Hikazudani, S. Reforming Reactions of Model Biogas over Honeycomb Supported Ni Catalysts. *J. Jpn. Petrol. Inst.* **2009,** *52,* 120−127.
166. Yuan, Z. S.; Ni, C. J.; Zhang, C. X.; Gao, D. N.; Wang, S. D.; Xie, Y. M.; Okada, A. Rh/MgO/$Ce_{0.5}Zr_{0.5}O_2$ Supported Catalyst for Autothermal Reforming of Methane: The Effects of Ceria−Zirconia Doping. *Catal. Today* **2009,** *146,* 124−131.
167. Araki, S.; Hino, N.; Mori, T.; Hikazudani, S. Start-Up Procedures in Autothermal Reforming of Biogas over a Ni Based Catalytic Monolith. *Catal. Commun.* **2009,** *10,* 1300−1304.
168. Araki, S.; Hino, N.; Mori, T.; Hikazudani, S. Autothermal Reforming of Biogas over a Monolithic Catalyst. *J. Nat. Gas Chem.* **2010,** *19,* 477−481.
169. Lai, W.; Lai, M.; Horng, R. Study on Hydrogen-Rich Syngas Production by Dry Autothermal Reforming from Biomass Derived Gas. *Int. J. Hydrogen Energy* **2012;** http://dx.doi.org/10.1016/j.ijhydene.2012.1003.1076.
170. Wang, C. G.; Wang, T. J.; Ma, L. L.; Gao, Y.; Wu, C. Z. Steam Reforming of Biomass Raw Fuel Gas over NiO−MgO Solid Solution Cordierite Monolith Catalyst. *Energy Convers. Manag.* **2010,** *51,* 446−451.
171. Barelli, L.; Bidini, G.; Gallorini, F.; Servili, S. Hydrogen Production Through Sorption-Enhanced Steam Methane Reforming and Membrane Technology: A Review. *Energy* **2008,** *33,* 554−570.
172. Tonkovich, A. L. Y.; Yang, B.; Perry, S. T.; Fitzgerald, S. P.; Wang, Y. From Seconds to Milliseconds to Microseconds Through Tailored Microchannel Reactor Design of a Steam Methane Reformer. *Catal. Today* **2007,** *120,* 21−29.
173. Tonkovich, A. Y.; Perry, S.; Wang, Y.; Qiu, D.; LaPlante, T.; Rogers, W. A. Microchannel Process Technology for Compact Methane Steam Reforming. *Chem. Eng. Sci.* **2004,** *59,* 4819−4824.
174. Wang, Y.; Chin, Y. H.; Rozmiarek, R. T.; Johnson, B. R.; Gao, Y.; Watson, J.; Tonkovich, A. Y. L.; Vander Wiel, D. P. Highly Active and Stable Rh/MgO−Al_2O_3 Catalysts for Methane Steam Reforming. *Catal. Today* **2004,** *98,* 575−581.

175. Zhai, X. L.; Cheng, Y. H.; Zhang, Z. T.; Jin, Y.; Cheng, Y. Steam Reforming of Methane over Ni Catalyst in Micro-Channel Reactor. *Int. J. Hydrogen Energy* **2011,** *36,* 7105−7113.
176. Izquierdo, U.; Barrio, V. L.; Cambra, J. F.; Requies, J.; Güemez, M. B.; Arias, P. L.; Kolb, G.; Zapf, R.; Gutiérrez, A. M.; Arraibi, J. R. Hydrogen Production from Methane and Natural Gas Steam Reforming in Conventional and Microreactor Reaction Systems. *Int. J. Hydrogen Energy* **2012,** *37,* 7026−7033.
177. Ryi, S. K.; Park, J. S.; Choi, S. H.; Cho, S. H.; Kim, S. H. Novel Micro Fuel Processor for PEMFCs with Heat Generation by Catalytic Combustion. *Chem. Eng. J.* **2005,** *113,* 47−53.
178. Ryi, S. K.; Park, J. S.; Cho, S. H.; Kim, S. H. Fast Start-Up of Microchannel Fuel Processor Integrated with an Igniter for Hydrogen Combustion. *J. Power Sources* **2006,** *161,* 1234−1240.
179. Zhai, X. L.; Ding, S.; Liu, Z. H.; Jin, Y.; Cheng, Y. Catalytic Performance of Ni Catalysts for Steam Reforming of Methane at High Space Velocity. *Int. J. Hydrogen Energy* **2011,** *36,* 482−489.
180. Acha, E.; Requies, J.; Barrio, V. L.; Cambra, J. F.; Guemez, M. B.; Arias, P. L. Water Effect in Hydrogen Production from Methane. *Int. J. Hydrogen Energy* **2010,** *35,* 11525−11532.
181. Anis, S.; Zainal, Z. A. Tar Reduction in Biomass Producer Gas Via Mechanical, Catalytic and Thermal Methods: A Review. *Renew. Sust. Energ. Rev.* **2011,** *15,* 2355−2377.
182. Corella, J.; Toledo, M.; Padilla, R. Catalytic Hot Gas Cleaning with Monoliths in Biomass Gasification in Fluidized Beds. 1. Their Effectiveness for Tar Elimination. *Ind. Eng. Chem. Res.* **2004,** *43,* 2433−2445.
183. Ising, M.; Gil, J.; Unger, C. Gasification of Biomass in a Circulating Fluidized Bed with Special Respect to Tar Reduction. In *1st World Conference and Exhibition on Biomass for Energy and Industry, Sevilla, Spain*; 2000; pp. 1755−1758.
184. Cybulski, A.; Moulijn, J. A. Monoliths in Heterogeneous Catalysis. *Catal. Rev.* **1994,** *36,* 179−270.
185. Men, Y.; Kolb, G.; Zapf, R.; Hessel, V.; Lowe, H. Ethanol Steam Reforming in a Microchannel Reactor. *Process. Saf. Environ.* **2007,** *85,* 413−418.
186. Casanovas, A.; de Leitenburg, C.; Trovarelli, A.; Llorca, J. Catalytic Monoliths for Ethanol Steam Reforming. *Catal. Today* **2008,** *138,* 187−192.
187. Casanovas, A.; Saint-Gerons, M.; Griffon, F.; Llorca, J. Autothermal Generation of Hydrogen from Ethanol in a Microreactor. *Int. J. Hydrogen Energy* **2008,** *33,* 1827−1833.
188. Llorca, J.; Casanovas, A.; Trifonov, T.; Rodriguez, A.; Alcubilla, R. First Use of Macroporous Silicon Loaded with Catalyst Film for a Chemical Reaction: A Microreformer for Producing Hydrogen from Ethanol Steam Reforming. *J. Catal.* **2008,** *255,* 228−233.
189. Dominguez, M.; Taboada, E.; Molins, E.; Llorca, J. Co−SiO_2 Aerogel-Coated Catalytic Walls for the Generation of Hydrogen. *Catal. Today* **2008,** *138,* 193−197.
190. Casanovas, A.; Dominguez, M.; Ledesma, C.; Lopez, E.; Llorca, J. Catalytic Walls and Micro-Devices for Generating Hydrogen by Low Temperature Steam Reforming of Ethanol. *Catal. Today* **2009,** *143,* 32−37.
191. Nedyalkova, R.; Casanovas, A.; Llorca, J.; Montane, D. Electrophoretic Deposition of Co−Me/ZnO (Me = Mn, Fe) Ethanol Steam Reforming Catalysts on Stainless Steel Plates. *Int. J. Hydrogen Energy* **2009,** *34,* 2591−2599.
192. Casanovas, A.; de Leitenburg, C.; Trovarelli, A.; Llorca, J. Ethanol Steam Reforming and Water-Gas Shift Reaction over Co−Mn/ZnO Catalysts. *Chem. Eng. J.* **2009,** *154,* 267−273.
193. Lopez, E.; Irigoyen, A.; Trifonov, T.; Rodriguez, A.; Llorca, J. A Million-Channel Reformer on a Fingertip: Moving Down the Scale in Hydrogen Production. *Int. J. Hydrogen Energy* **2010,** *35,* 3472−3479.
194. Casanovas, A.; Roig, M.; de Leitenburg, C.; Trovarelli, A.; Llorca, J. Ethanol Steam Reforming and Water-Gas Shift over Co/ZnO Catalytic Honeycombs Doped with Fe, Ni, Cu, Cr and Na. *Int. J. Hydrogen Energy* **2010,** *35,* 7690−7698.
195. Dominguez, M.; Cristiano, G.; Lopez, E.; Llorca, J. Ethanol Steam Reforming over Cobalt Talc in a Plate Microreactor. *Chem. Eng. J.* **2011,** *176-77,* 280−285.
196. Dominguez, M.; Taboada, E.; Molins, E.; Llorca, J. Ethanol Steam Reforming at Very Low Temperature over Cobalt Talc in a Membrane Reactor. *Catal. Today,* DOI:10.1016/j.cattod.2012.02004.
197. Gorke, O.; Pfeifer, P.; Schubert, K. Kinetic Study of Ethanol Reforming in a Microreactor. *Appl. Catal. A-Gen.* **2009,** *360,* 232−241.
198. Cai, W. J.; Wang, F. G.; van Veen, A.; Descorme, C.; Schuurman, Y.; Shen, W. J.; Mirodatos, C. Hydrogen Production from Ethanol Steam Reforming in a Micro-Channel Reactor. *Int. J. Hydrogen Energy* **2010,** *35,* 1152−1159.
199. Nilsson, M.; Karatzas, X.; Lindstrom, B.; Pettersson, L. J. Assessing the Adaptability to Varying Fuel Supply of an Autothermal Reformer. *Chem. Eng. J.* **2008,** *142,* 309−317.
200. Chen, H. Q.; Yu, H.; Yang, G. X.; Peng, F.; Wang, H. J.; Yang, J. A. Auto-Thermal Ethanol Micro-Reformer with a Structural Ir/La_2O_3/ZrO_2 Catalyst for Hydrogen Production. *Chem. Eng. J.* **2011,** *167,* 322−327.
201. Rodrigues, C. P.; da Silva, V. T.; Schmal, M. Partial Oxidation of Ethanol on Cu/Alumina/Cordierite Monolith. *Catal. Commun.* **2009,** *10,* 1697−1701.
202. Rodrigues, C. P.; da Silva, V. T.; Schmal, M. Partial Oxidation of Ethanol over Cobalt Oxide Based Cordierite Monolith Catalyst. *Appl. Catal. B-Environ.* **2010,** *96,* 1−9.
203. Rodrigues, C. P.; Schmal, M. Nickel−Alumina Washcoating on Monoliths for the Partial Oxidation of Ethanol to Hydrogen Production. *Int. J. Hydrogen Energy* **2011,** *36,* 10709−10718.
204. Kalinci, Y.; Hepbasli, A.; Dincer, I. Biomass-Based Hydrogen Production: A Review and Analysis. *Int. J. Hydrogen Energy* **2009,** *34,* 8799−8817.
205. Trane, R.; Dahl, S.; Skjøth-Rasmussen, M. S.; Jensen, A. D. Catalytic Steam Reforming of Bio-Oil. *Int. J. Hydrogen Energy* **2012,** *37,* 6447−6472.
206. Basagiannis, A. C.; Verykios, X. E. Steam Reforming of the Aqueous Fraction of Bio-Oil over Structured Ru/MgO/Al_2O_3 Catalysts. *Catal. Today* **2007,** *127,* 256−264.
207. Kruger, J. S.; Rennard, D. C.; Josephson, T. R.; Schmidt, L. D. Effect of Functional Groups on Autothermal Partial Oxidation of Bio-Oil. Part 1: Role of Catalyst Surface and Molecular Oxygen. *Energy Fuel* **2011,** *25,* 3157−3171.
208. Kruger, J. S.; Rennard, D. C.; Josephson, T. R.; Schmidt, L. D. Effect of Functional Groups on Autothermal Partial Oxidation of Bio-Oil. Part 2: Role of Homogeneous and Support-Mediated Reactions. *Energy Fuel* **2011,** *25,* 3172−3185.
209. Rennard, D. C.; Dauenhauer, P. J.; Tupy, S. A.; Schmidt, L. D. Autothermal Catalytic Partial Oxidation of Bio-Oil Functional Groups: Esters and Acids. *Energy Fuel* **2008,** *22,* 1318−1327.
210. Domine, M. E.; Iojoiu, E. E.; Davidian, T.; Guilhaume, N.; Mirodatos, C. Hydrogen Production from Biomass-Derived Oil over Monolithic Pt- and Rh-Based Catalysts Using Steam Reforming and Sequential Cracking Processes. *Catal. Today* **2008,** *133,* 565−573.
211. Rennard, D.; French, R.; Czernik, S.; Josephson, T.; Schmidt, L. Production of Synthesis Gas by Partial Oxidation and Steam Reforming of Biomass Pyrolysis Oils. *Int. J. Hydrogen Energy* **2010,** *35,* 4048−4059.
212. Iojoiu, E. E.; Domine, M. E.; Davidian, T.; Guilhaume, N.; Mirodatos, C. Hydrogen Production by Sequential Cracking of

Biomass-Derived Pyrolysis Oil over Noble Metal Catalysts Supported on Ceria–Zirconia. *Appl. Catal. A-Gen.* **2007,** *323,* 147–161.
213. Karim, A.; Bravo, J.; Datye, A. Nonisothermality in Packed Bed Reactors for Steam Reforming of Methanol. *Appl. Catal. A-Gen.* **2005,** *282,* 101–109.
214. Erickson, P. A.; Liao, C. H. Heat Transfer Enhancement of Steam Reformation by Passive Flow Disturbance Inside, the Catalyst Bed. *J. Heat. Trans-T ASME* **2007,** *129,* 995–1003.
215. Shah, K.; Besser, R. S. Understanding Thermal Integration Issues and Heat Loss Pathways in a Planar Microscale Fuel Processor: Demonstration of an Integrated Silicon Microreactor-Based Methanol Steam Reformer. *Chem. Eng. J.* **2008,** *135,* S46–S56.
216. Chein, R. Y.; Chen, L. C.; Chen, Y. C.; Chung, J. N. Heat Transfer Effects on the Methanol-Steam Reforming with Partially Filled Catalyst Layers. *Int. J. Hydrogen Energy* **2009,** *34,* 5398–5408.
217. Suh, J. S.; Lee, M. T.; Greif, R.; Grigoropoulos, C. P. Transport Phenomena in a Steam-Methanol Reforming Microreactor with Internal Heating. *Int. J. Hydrogen Energy* **2009,** *34,* 314–322.
218. Won, J. Y.; Jun, H. K.; Jeon, M. K.; Woo, S. I. Performance of Microchannel Reactor Combined with Combustor for Methanol Steam Reforming. *Catal. Today* **2006,** *111,* 158–163.
219. Kim, T. Micro Methanol Reformer Combined with a Catalytic Combustor for a PEM Fuel Cell. *Int. J. Hydrogen Energy* **2009,** *34,* 6790–6798.
220. Lee, J. H.; Do, G. S.; Moon, H. J.; Kwon, O. C. An Annulus-Type Micro Reforming System Integrated with a Two-Staged Micro-Combustor. *Int. J. Hydrogen Energy* **2010,** *35,* 1819–1828.
221. Kwon, O. J.; Yoon, D. H.; Kim, J. J. Silicon-Based Miniaturized Reformer with Methanol Catalytic Burner. *Chem. Eng. J.* **2008,** *140,* 466–472.
222. Delsman, E. R.; de Croon, M. H. J. M.; Kramer, G. J.; Cobden, P. D.; Hofmann, C.; Cominos, V.; Schouten, J. C. Experiments and Modelling of an Integrated Preferential Oxidation-Heat Exchanger Microdevice. *Chem. Eng. J.* **2004,** *101,* 123–131.
223. Kolios, G.; Frauhammer, J.; Eigenberger, G. Efficient Reactor Concepts for Coupling of Endothermic and Exothermic Reactions. *Chem. Eng. Sci.* **2002,** *57,* 1505–1510.
224. Stefanidis, G. D.; Vlachos, D. G. High vs. Low Temperature Reforming for Hydrogen Production Via Microtechnology. *Chem. Eng. Sci.* **2009,** *64,* 4856–4865.
225. Stefanidis, G. D.; Vlachos, D. G. Intensification of Steam Reforming of Natural Gas: Choosing Combustible Fuel and Reforming Catalyst. *Chem. Eng. Sci.* **2010,** *65,* 398–404.
226. Chein, R. Y.; Chen, Y. C.; Chung, J. N. Thermal Resistance Effect on Methanol-Steam Reforming Performance in Micro-Scale Reformers. *Int. J. Hydrogen Energy* **2012,** *37,* 250–262.
227. Chein, R. Y.; Chen, Y. C.; Lin, Y. S.; Chung, J. N. Hydrogen Production Using Integrated Methanol-Steam Reforming Reactor with Various Reformer Designs for PEM Fuel Cells. *Int. J. Energ. Res.* **2012,** *36,* 466–476.
228. Tadbir, M. A.; Akbari, M. H. Integrated Methanol Reforming and Oxidation in Wash-Coated Microreactors: A Three-Dimensional Simulation. *Int. J. Hydrogen Energy* **2012,** *37,* 2287–2297.
229. Tadbir, M. A.; Akbari, M. H. Methanol Steam Reforming in a Planar Wash Coated Microreactor Integrated with a Micro-Combustor. *Int. J. Hydrogen Energy* **2011,** *36,* 12822–12832.
230. Moreno, A. M.; Wilhite, B. A. Autothermal Hydrogen Generation from Methanol in a Ceramic Microchannel Network. *J. Power Sources* **2010,** *195,* 1964–1970.
231. Pan, L. W.; Ni, C. J.; Zhang, X. B.; Yuan, Z. S.; Zhang, C. X.; Wang, S. D. Study on a Compact Methanol Reformer for a Miniature Fuel Cell. *Int. J. Hydrogen Energy* **2011,** *36,* 319–325.
232. Kaisare, N. S.; Vlachos, D. G. Optimal Reactor Dimensions for Homogeneous Combustion in Small Channels. *Catal. Today* **2007,** *120,* 96–106.
233. Kaisare, N. S.; Vlachos, D. G. A Review on Microcombustion: Fundamentals, Devices and Applications. *Prog. Energ. Combust.* **2012,** *38,* 321–359.

CHAPTER

10

Microprocess Technology for Hydrogen Purification

Svetlana Ivanova [*], *Oscar Hernando Laguna* [†], *Miguel Ángel Centeno* [*], *Asier Eleta* [§], *Mario Montes* [†], *José Antonio Odriozola* [*]

[*]Department of Inorganic Chemistry and Institute of Materials Science of Seville, University of Sevilla-CSIC, Sevilla, Spain, [†]Department of Applied Chemistry, UFI11/53, University of the Basque Country, UPV/EHU, San Sebastian, Spain, [§]NOVARGI-Nova Synergy Industrial Solutions, Vitoria-Gasteiz, Spain

OUTLINE

10.1 Introduction 225
10.2 CO Cleanup Fundamentals 226
10.2.1 WGS: The First Stage of CO Cleanup 226
10.2.2 Fine Cleanup: PROX and Selective Methanation Reactions 227
10.3 Structured Reactors for CO Cleanup 229
10.4 Hydrogen Cleanup Processors 230
Acknowledgments 239
References 239

10.1 INTRODUCTION

Portable electronic devices are behind the interest in fuel cell (FC) technology to replace or supplement batteries in portable applications. FCs generate electrical power in an environmentally clean and safe way; they provide instant power having very high energy densities (four to six times larger) as compared to Li-ion batteries. However, they have limited power capacity and cannot respond to the sudden changes in the load that may occur in some applications. The design of hybrid FC–battery systems as well as the development of strategy for management of the energy may solve among others the problem of oversizing of the FC associated with the changes in the load. For these hybrid systems, the polymer electrolyte membrane fuel cells (PEMFCs) have been considered to enhance the energy density of batteries. However, relevant challenges such as H_2 storage and water and thermal management are still unresolved for PEMFCs.

Safety issues are usually raised for H_2 storage, especially when applied for use in vehicles' power traction and auxiliary power units (APUs). To reduce safety problems, one option is to produce H_2 on demand using small reactors whose characteristic dimensions are in the range of microscale (typically <1000 μm) or mesoscale (1000 μm to a few centimeters), often called microreactors.[1] Consequently, the interest for the development of such systems has grown and in the years between 2000 and 2010 there has been a considerable increment in the number of patents[2,3] and scientific papers devoted to the microtechnology that is involved in manufacturing individual microreactors[4–6] and even complete fuel processor devices.[7–10]

H_2 may be produced from hydrogen-containing compounds such as hydrocarbons, ammonia or chemical hydrides, depending on the power requirements of the FC. Hydrocarbon reforming is the most viable H_2 production technique, among others such as ammonia cracking, pyrolysis and aqueous-phase reforming.

Nowadays, hydrogen is mainly produced by steam reforming, especially if the ultimate objective is the generation of pure hydrogen since it provides the highest hydrogen–carbon monoxide (H_2–CO) molar ratio ($H_2/CO = 3$).[11] Although the fuel processing reactors are designed to maximize H_2 production through steam reforming, partial oxidation or autothermal reforming reactions, hydrocarbons as a source of hydrogen also produce other compounds such as H_2O, CO, CO_2 and some other molecules coming from their incomplete transformation. In chapter nine, the use of structured and microstructured catalytic reactors for hydrogen production has been reviewed.[12]

While CO_2 could be easily removed and does not affect the FC performances, the presence of CO in the reformate gas, produced mainly from natural gas or liquefied petroleum gas,[13] is a major drawback for the PEMFCs, because the anode, which is commonly manufactured in Pt or Pt–Ru, may be poisoned by the strong irreversible adsorption of CO molecules over the anode surface. In this sense, the CO levels in the hydrogen stream must be as low as possible, typically less than 50 ppm in the case of Pt–Ru anodes and less than 10 ppm for Pt ones.[14] Otherwise, the lifetime of the PEMFCs anode will be dramatically reduced. This indicates that in the FC processors, the H_2 purification steps are as important as the production step itself. Therefore, fuel processor developments must consider the finest possible cleanup reactors for ensuring the life of the PEMFCs.

10.2 CO CLEANUP FUNDAMENTALS

Commonly, the reforming out-gassing flow presents CO contents around 10 vol.% and passes through the first stage of purification by the water-gas shift (WGS) reaction.[15–21] This process, which can be carried out at high or low temperature allows decreasing the CO levels up to 0.5–1% depending on the outlet temperature. Nevertheless, these CO contents are still very high for feeding a PEMFC, and additional purification steps are required.

To further reduce carbon monoxide levels, selective methanation, preferential oxidation of CO reactions or both can be used. Although CO methanation is viable, the preferential oxidation of CO in the presence of H_2 (PROX) is usually the chosen technology.[22–28]

10.2.1 WGS: The First Stage of CO Cleanup

The typical 6–15 vol.% of CO present in the reformate gas can be easily converted and the hydrogen yield increased via the water-gas shift reaction (WGS)

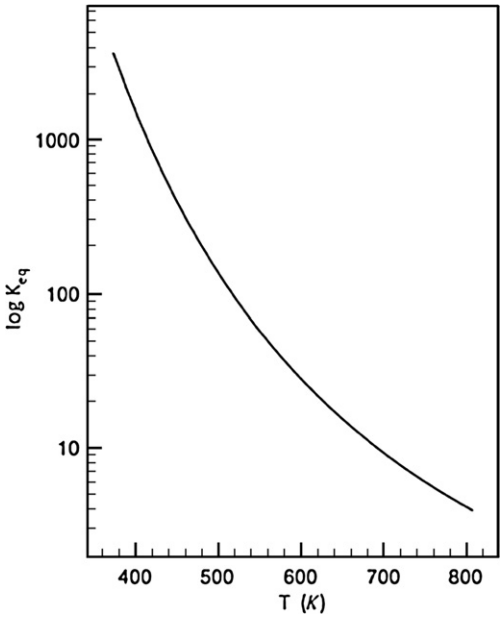

FIGURE 10.1 Variation of the equilibrium constant for the WGS with temperature. *Source: Adapted from Zalc et al.*[29]

$$CO + H_2O \Leftrightarrow CO_2 + H_2 \quad \Delta H^0_{298} = -41.1 \ \text{kJ/mol} \tag{10.1}$$

Since there is no volume change associated with the reaction, the equilibrium constant minimally depends on the pressure. However, WGS is an exothermic equilibrium reaction and the equilibrium conversion decreases with increasing temperature as shown in Fig. 10.1. When operated in adiabatic conditions, the exothermicity causes an increase in the catalytic bed temperature and CO conversion is partially inhibited. Therefore, a significantly better performance can be achieved by operating at a relatively high temperature, thereby exploiting the reaction kinetics when the gas composition is far from equilibrium, and then lowering the temperature as thermodynamics begin to limit the CO conversion.[29–31] Hence, the lowest temperature at which maximum CO conversion can be achieved is determined by the catalyst's kinetics and the dew point of the gas.[32]

The industrial plant processes for H_2 production are well established and optimized from the economic point of view and the possibilities for modification are scarce. The industrial WGS process takes place in a series of fixed bed adiabatic converters where the reformate gas goes through two WGS reactors, high temperature shift (HTS) and low temperature shift (LTS) converters, with the LTS reactor at significantly lower temperatures in order to shift the equilibrium toward maximal hydrogen production.[11]

The well-established industrial WGS processes may not be appropriate for small-scale applications such as residential FCs or on-board hydrogen generators. An alternative to this is the design of reactors allowing optimized temperature profiles for small-scale hydrogen generators. The most appropriate and cost-effective technology for small-scale fuel processors combines on-board reforming of hydrocarbon with a FC to form an integrated power plant. These plants must include catalytic CO cleanup stages since CO produced in the reforming process poisons the PEMFC catalyst. The WGS reaction reduces the CO concentration to levels below 1 vol.% and increases the H_2 yield, but the WGS catalyst requirements for integrated FC power plants are quite different from those of the traditional Fe_2O_3–Cr_2O_3-based (HTS) or Cu–ZnO-based (LTS) catalysts. First, the catalyst should demonstrate sufficient activity over a reasonable temperature window, be durable enough (at least 5000 h) and support rapid start-up and shutdown conditions. In addition, the catalyst must be nonpyrophoric and in situ prereduction procedures should be avoided. In addition, reduced volume and weight of the catalyst bed becomes an economical requisite.

The thoroughly described traditional catalysts[11,33,34] are generally considered inappropriate for application in fuel processors for FC applications. In an excellent review, Farrauto et al.[35] carefully detail the main drawbacks associated with the use of the traditional WGS catalysts, mainly associated with operational variables. The large volume and heat capacity of these catalysts results in a slow response to transient operation of flow rate and temperature that is intrinsic to on-demand power requirements. In response to these limitations, noble metal-based WGS catalysts are under intense development worldwide for FC applications. Despite the extensive research in the past 10 years on oxide-supported gold catalysts,[17,36–42] other noble metals have also found their place in the development of the WGS low-temperature catalysts as Pt,[43–46] Ru,[47,48] Pd[47,49] or Ir[47,50] supported on mineral oxide or mixed oxides carriers. Nevertheless, the diverse catalytic system reported as active in WGS, Pt- and Au-based catalysts appears the most promising to substitute the traditional catalysts especially for small-scale application.

10.2.2 Fine Cleanup: PROX and Selective Methanation Reactions

The PROX reaction is a cheap and viable alternative to achieve the desired low levels of CO. In the years between 2000 and 2010, several works have been devoted to the study of many catalysts for such reaction[51] that can be classified into three groups:[52]

- Supported platinum metal-based (Pt, Ru, Rh) catalysts,[53–67]
- Gold-supported catalysts, and[68–84]
- Copper–cerium oxide-based catalysts,[23,25,26,28,63,85–113] which are the most studied

The last group of catalysts presents a considerable higher selectivity for the CO oxidation than Pt-supported catalysts at similar conversion levels. The stability of copper–cerium oxide-based catalysts is also higher than that of gold catalysts.

The selectivity and stability of copper–ceria catalysts has focused research on the improvement of its catalytic performances. Several synthesis procedures have been tried including the modification of copper loading or the inclusion of transition metal additives. Snytnikov et al.[52] summarizing open literature data and their own experimental observations conclude that the more active copper–cerium oxide systems have copper contents around 2–6 wt.% Cu. The formation of large copper oxide particles above 6 wt.% Cu reduces the availability of Cu^0 during the reaction, which is detrimental for the catalytic activity.

Whatever the catalyst, the operating temperature window for the maximal CO oxidation (Eqn (10.2)) is quite narrow. After this window, the CO conversion decreases with temperature as a result of oxygen consumption in the oxidation of hydrogen (Eqn (10.3)). Moreover, the heat released in these two oxidation reactions favors the slightly endothermic reverse water-gas shift reaction (R-WGS) (Eqn (10.4)).

$$CO + \frac{1}{2}O_2 \rightarrow CO_2 \quad \Delta H^0_{298} = -286.3 \text{ kJ/mol} \tag{10.2}$$

$$H_2 + \frac{1}{2}O_2 \rightarrow H_2O \quad \Delta H^0_{298} = -243.5 \text{ kJ/mol} \tag{10.3}$$

$$CO + H_2 \Leftrightarrow CO + H_2O \quad \Delta H^0_{298} = -41.1 \text{ kJ/mol} \tag{10.4}$$

These two side reactions determine the loss of selectivity to the desired CO oxidation reaction and consequently the lowering of the overall process yield. Adiabatic fixed bed reactors suffer loss of selectivity as the temperature increases at the reactor exit as a result of lower CO coverages that favor hydrogen oxidation and favorable conditions for the R-WGS. Oversized adiabatic reactors also favor the latter reaction, which usually results in designing two-stage PROX reactors.[114] Therefore, the strict control of the optimal operating temperature for the PROX reaction becomes a capital challenge.

The methanation reaction is a well-known process widely employed in the chemical industry for producing synthetic natural gas[115] or to remove carbon oxides from feeding streams in hydrogen or ammonia plants[116] as well as in processes related to Fischer–Tropsch synthesis.[13] A well-known technology together with safety issues has driven the proposal of the CO methanation reaction (Eqn (10.5)) for the fine cleanup of reformate gases as an alternative to PROX in the final purification step.[117]

$$CO + 3H_2 \Leftrightarrow CH_4 + H_2O \quad \Delta H^0_{298} = -206.2 \text{ kJ/mol} \tag{10.5}$$

$$CO_2 + 4H_2 \Leftrightarrow CH_4 + 2H_2O \quad \Delta H^0_{298} = -164.9 \text{ kJ/mol} \tag{10.6}$$

Some advantages of the methanation of CO with respect to the PROX reaction have been reported.[119–123] An O_2-free process drives most of these advantages. Hydrogen oxidation to water is completely avoided, safety problems are drastically reduced, and H_2 dilution by nitrogen accompanying the injected oxygen is eliminated. Moreover, on avoiding the highly exothermic hydrogen oxidation, the suitable working temperature window widens as the operating conditions do. A better temperature control of the reaction is expected since the methanation reactions of carbon oxides (Eqns (10.5) and (10.6)) are less exothermic than the oxidations of CO and H_2 (Eqns (10.2) and (10.3)). The significant consumption of hydrogen (3 mol/mol of CO abated, Eqn (10.5)), the simultaneous methanation of CO and CO_2[124,125] and the activity of the catalyst in the R-WGS are the main drawbacks of the methanation reaction. Therefore, even in the case of 100% selective catalyst for CO methanation, the hydrogen lost on reaction is only suitable if the initial CO concentration is rather small. Hence, methanation is proposed only as the final step of the hydrogen purification process, sometimes even after the PROX step.

The combination of PROX and methanation reactions for ensuring CO levels at the reactor outlet well below 10 ppm has been explored by the BASF Corporation.[126] The catalytic device combines different layers of Pt/Fe/alumina and Ru/alumina catalysts. These catalytic wall monoliths or foams are prepared in such a way that they include an upstream zone coated with the PROX catalyst and a downstream zone, accounting for between 10% and 70% of the reactor length, coated with the same PROX catalyst and overcoated with the methanation catalyst. The authors argue that this coating architecture allows the oxidation and methanation of CO to occur simultaneously and therefore the process effectiveness is higher than that obtained by doing separate treatments.

Fortunately, methane is an inert molecule for the PEMFCs and can be reused by recirculating the outlet gas of the FC into the reformer as a feedstock or as a fuel burnt for heating. Since the H_2 efficiency of the FCs is only 80–90%,[127] they are normally equipped with such a recirculation line in order to recover the unreacted H_2. Thus, assuming that two of the three H_2 moles spent in the CO methanation can be recovered through the profit of the methane produced, only 1 mol of H_2 (that converted into H_2O) per mol of removed CO can be considered lost. Of course, such calculations imply that methanation of CO_2 does not occur (Eqn (10.6)).

The key problem for CO abatement in H_2 streams by the methanation reaction is selectivity, since reformate gases contain high amounts of CO_2 (15–20 vol.%). The simultaneous[128,129] and competitive[124,125] methanation of carbon oxides is sensitive to temperature, pressure and composition of reactants.[130–132] Then, the operating conditions (gas space velocity, stream composition, temperature and so on) greatly influence the CO methanation activity and selectivity, since at temperatures high enough the methanation of CO and CO_2 as well as the R-WGS take place simultaneously, decreasing the selectivity of the process.

Despite the increasing interest and the extensive research efforts undertaken in the past 10 years, ruthenium-based and nickel-based catalysts remain the most frequently used on the basis of their efficiency and selectivity.[14,119,121–123,125,133–135] The Ni-based catalysts are less expensive than the ruthenium-based ones, but they are pyrophoric, need long pretreatment in reducing atmosphere and rapidly lose activity in contact with air. Also, Rh seems to be very active, while Pt tends to catalyze the R-WGS.[118] Doping of a conventional nickel catalyst with Pt and Re resulted in larger operating temperature windows and slower deactivation rates than the conventional Ru/TiO_2 catalyst.[136] The methanation activity and selectivity seems to markedly depend on the type of active metal, the metal loadings, the metal particle size, the existence of promoters and the nature of the support.[117,137,138] Crystallite sizes above 10 nm are desirable since Ru crystallite size controls the selectivity to CO_2 methanation.[139] The increase in ruthenium improves CO selectivity, because Ru blocks the sites where CO_2 methanation proceed.[140] Panagiotopoulou et al.[118] reported that for a similar Ru content and comparable crystallite size, the nature of the metal oxide support significantly affects the catalytic performances, the activity for the CO/CO_2 methanation of ruthenium centers being improved when supported on TiO_2 compared to when supported on Al_2O_3, CeO_2, YSZ or SiO_2.

Most articles deal with powder catalysts in a single-step fixed bed reactor, although the use of two-stage methanation reactors[141] as well as multiple reaction zone reactors with decreasing temperature profiles have also been proposed.[123] These point to the

importance of temperature control of these exothermic reactions to design highly selective processes. In general, these powder-based CO methanation reactors have been reported as effective to abate CO until the desired levels, even when integrated in a miniature hydrogen production reactor.[142]

10.3 STRUCTURED REACTORS FOR CO CLEANUP

The advances in design of catalysts, which are not the subject of this chapter, and the management of the heat of reaction are key issues in all the processes that may be involved in the cleanup of the H_2-rich reformate gases. A promising solution for solving the practical problems arising in the employment of catalytic technologies for FC applications could be provided by a successful design at reactor level. The desired performance criteria for the catalysts bed design are

- Low pressure drop
- High catalyst loading per reactor volume
- High external mass transfer rate from bulk fluid onto catalyst surface and high internal mass transfer rate within the catalyst
- Heat transfer management, generally assured by the reactor design

In this scenario, microreactors fulfill all the criteria for reactor design, providing an optimal heat control during exothermic and endothermic reactions.[1,143] The high surface-to-volume ratios attainable for the catalyst in microreactors improves thermal management by fast heat and mass transfer and suggests that microfabricated multiphase systems could have performance advantages relative to conventional macroscopic systems for at least small-scale production. Shorter space–time yields are enabled in microchannel systems due to the reduction of the transport limitations.[144] These advantages may even be improved if the microreactor is built using metallic materials, which have inherent high thermal conductivities. All these advantages that results in low volumes and weights associated with the microreactors systems dictate their mandatory use in residential cogenerators, vehicles applications and portable devices.[145,146]

In the years between 2000 and 2010, Forschungszentrum Karlsruhe and the Institute for Microtechnology Mainz have been the pioneers in driving multichannel microreactors, micromixers, and micro heat exchangers manufactured in metal by using lithography, electroplating, and molding.[147]

Goerke et al.[148] published one of the first studies on the use of microreactors for both WGS and PROX reactions. They probed three catalysts (Au/CeO_2, Au/α-Fe_2O_3, and CuO/CeO_2) in microreactors built by stacking 25 stainless steel-coated foils in a clamping device. Every foil was previously micromechanized for generating 38 parallel grooves on one of its faces, resulting in square sections of $200 \times 70\ \mu m^2$ and a total channel volume of $266\ mm^3$. Prior to clamping the stack, the foils were coated with the catalyst in the mechanized side in order to cover the walls of the grooves, resulting in a coated surface of $6460\ mm^2$. The joining of the foils resulted in the formation of channels with three of the four walls covered by the catalyst, as can be observed in Fig. 10.2. The clamped device slightly leaks. Despite these leaks, this microreactor coated with a CuO/CeO_2 catalyst allows, for a CO inlet concentration of 1 vol.%, a CO conversion that even exceeds 99% at temperatures below 150 °C in the PROX reaction. The main conclusion of these authors deals with the superior temperature control and the feasibility of dynamic operation of microreactors extending the operation temperature window. This is associated with the high heat transfer coefficients of the microreactor system that allows a better control of the isothermicity during the process.

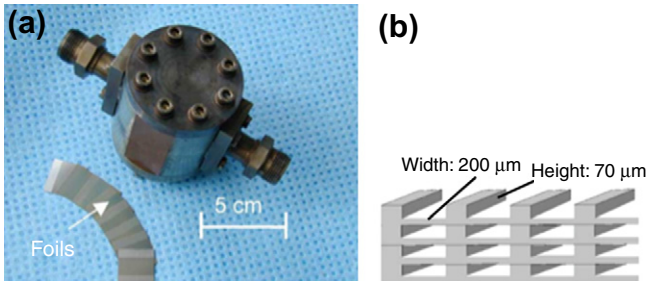

FIGURE 10.2 (a) Clamping device for testing the coated foils concerning the WGS and PROX reaction, (b) scheme of stacked foils. (For color version of this figure, the reader is referred to the online version of this book.) *Source: With permission from Goerke et al.*[148]

The observation of leaks points out the need for an effective, cheap, available and reproducible technique for joining metallic foils, in such a way that the joining (welding) temperatures do not affect the coated catalyst performances or do allow the load of the catalyst in the joined device. This may become one of the bottleneck stages in developing microreactors since welding of the block may require expensive techniques that complicate the scaling up of the microreactor production.

Manufacturing microdevices brings to the scene the nature of metallic materials. Steels are the choice materials for manufacturing microreactors and, in particular, ferritic alloys in the case of parallel microchannel monoliths.[149] Metal dusting (MD) is a dramatic corrosion phenomenon frequent in the chemical industry, occurring in atmospheres with high carbon activity, above unity, in particular in reforming and synthesis gas plants.[150,151] The corrosion degree of the alloy depends

on its nature, the atmosphere and the mixture temperature. Catalytic phenomena leading to coke formation, which take place on oxidic catalysts, decrease considerably the induction period of the MD phenomenon.[152] In a previous work, Yin[153] discussed the thermodynamic aspects of the carburizing reaction in model atmospheres relevant to reforming, such as CO-CO_2 and CO-H_2O-H_2 among others, considering pure metals and analyzing the influence of the gas-phase chemistry, temperature and pressure, and found that the behavior is a function of the nature of the metal, Ni and Fe behaving differently. This different behavior depends on the system's total pressure. In general, carburizing phenomena, although severe, are less catastrophic in CH_4-H_2 mixtures than in CO-H_2O-H_2 mixtures in the case of alloys with high Ni content (AISI 310 SS or Incoloy 800HT).[154–156]

Oxide layers formed on chromia-forming stainless steels protect the base alloy against MD but at chromia layer defects MD is observed. [157–159] In very low oxygen partial pressure environments, alumina-former alloys are more effective against MD.[160,161] Figure 10.3 demonstrates the MD phenomenon in AISI 316 stainless steel submitted for 15 days to 250 °C in an atmosphere with carbon activity above unity. The corrosion depth is in the order of the microreactor wall thickness. Unfortunately, prolonged high temperature treatments of aluminum-alloyed ferritic steels results in the formation of a brittle phase that rapidly deteriorates the mechanical properties of the microstructured device. The nature of the metallic surface also affects the catalyst performances since the carburization/oxidation processes that occur on the metallic surface result in metallic oxides coexisting with the catalytic phase, which may alter the activity and selectivity of the catalyst.[162,163] Thus the use of metallic alloys with high nickel content or even nickel-based alloys have been proposed for manufacturing microreactors provided their surfaces are coated prior to reaction with metallic aluminides in order to form inert alumina layers on the metallic surface.[164,165]

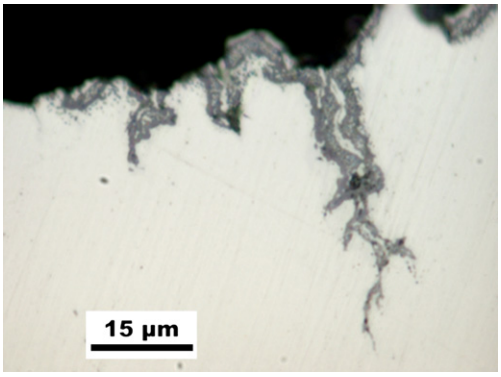

FIGURE 10.3 Backscattered electron detector image of the surface of an AISI 316 stainless steel subjected for 15 days to 250 °C in an atmosphere with carbon activity above unity. The dark areas correspond to metallic carbides with bright areas inside corresponding to the particles of trapped metals. The surface roughness indicates a heavily corroded metal.

Some key issues of the microfabrication process for PROX microreactors have been recently analyzed and the design tested using a washcoated CuO_x/CeO_2 catalyst.[111]

10.4 HYDROGEN CLEANUP PROCESSORS

The combination of the noble metal catalyst with structured reactors (monoliths or micro-reactors) can present significant advances in FC technology.

In the years between 2000 and 2010, the Engelhard Corp. reported[33,34,166] the development of precious metals monolith catalysts for use in automotive and residential fuel processors. The best catalyst can operate at space velocities as high as 30,000/h achieving 1% CO at the outlet of the WGS section.

The characteristics and performance parameters of one of the proposed catalyst compared to traditional WGS catalyst are presented in Table 10.1.

In the WGS reaction, which is usually kinetically limited, the reaction time scale is long compared to that for diffusion. This means that the conversion is directly proportional to the coated surface area. The washcoating procedures appear then to be essential for the good catalytic performance of the coated monoliths. The effects of the preparation parameters of monolithic Pt/$Ce_{0.8}Zr_{0.2}O_2$/cordierite catalyst on its catalytic performances in WGS were thoroughly investigated by Du et al.[167] They found an optimum of 50 wt.% for $Ce_{0.8}Zr_{0.2}O_2$ loading, 0.68 wt.% for Pt loading and a value of three for Pt/Re weight ratio. Teo et al.[168] studied Au-supported catalysts washcoated on cordierite monolith. They reported protocols for optimum washcoating procedures that resulted in excellent catalyst performances in the low-temperature WGS, although the catalysts quickly deactivated. For improving the catalyst stability, the authors proposed the addition of ZrO_2 and, once deactivated, regeneration of the catalyst by thermal treatment at 300 °C in the presence of air. Casanovas et al.[169] reported a strong influence of the preparation route on the homogeneity and stability of Co/ZnO catalyst coatings as well as the effect of promoting with Mn the previously optimized Co/ZnO monolith catalyst.[170]

Although scarcely studied, the metallic substrate may influence the catalytic performances of monolithic devices. Using AISI 304 stainless steel as metallic substrate, monoliths washcoated with CeO_2 or Au/CeO_2 catalysts were prepared. Catalyst deposition

TABLE 10.1 Comparison of the Characteristics and Performances of Traditional WGS Catalysts and Engelhard Corp. Monoliths[34]

	HTS catalyst (FeCr)	LTS catalyst (CuZn)	Precious Metal catalyst
Form	3–10 mm pellets	3–6 mm pellets	Monolith supported
Activity	Not active below ~350 °C	High activity starting below 200 °C	Highly active above 250–300 °C
Thermal stability	Stable to ~500 °C	Loss of activity above ~260–280 °C	Stable to >~400 °C
Space velocity	<8000/h	<6000/h	>20,000/h
Poisons	Low sensitivity to sulfur	Deactivated on exposure to sulfur and halogens	Tolerant to some poisons
Other considerations	Self-heating material in the reduced state Cr(VI) may be present Inexpensive material Insensitive to sulfur; used to polish sulfur at very low levels	Needs to be carefully reduced Self-heating material in the active reduced state Deactivates by water condensation and air exposure Needs careful discharge from the reactor (pyrophoric catalyst) Reaction is diffusion limited	Insensitive to start–stop and air exposure No need for prereduction Kinetics limits the usefulness of the catalyst below 250 °C

on the stainless steel surface resulted in modifications of the catalyst, the oxide scale and the oxide scale/alloy interface through the interaction between the coating and the steel oxidation layer. Besides this, oxidation of the alloy is also detected. As a result of these modifications, CO oxidation on Au/CeO_2 catalysts is enhanced and gold surface dynamics is modified.[163]

Despite the great interest of monolithic reactors in environmental applications, they show some shortcomings. Monolithic devices are virtually adiabatic, which limits the control of temperature.[171] The adiabatic temperature rise of monolithic medium-temperature WGS reactors operated at 20,000/h amounted to 68 °C when the catalyst runs at 300 °C, whereas it only amounts to 15 °C when operated at 280 °C and 10,000/h.[172] The heat exchange is a primary requirement in WGS in order to reach sufficiently low CO levels. The use of metallic monoliths, which are believed to improve the heat transfer inside the reactor, improves heat management. For instance, van Dijk et al.[173] developed a single-stage heat-integrated WGS reactor consisting of washcoated catalyst on two types of high-conductivity catalyst supports: Al metal foam and Al metal monolith. In comparison with the conventional adiabatic reactor, the use of metal monolith significantly allows simpler process control and lower risk to temporary increase of the CO content.

The specific interactions between gold and support determine the catalytic activity, and especially the stability, of gold catalysts;[174–178] shaping of the catalysts then becomes crucial. Rebrov et al.[179] reported gold supported on mesoporous titania films for application in microstructured reactors using titanium alloys as substrate for the simulated microreactor. The thin films prepared via evaporation-induced self-assembly process showed promising results in an idealized WGS mixture. Stabilization of the catalytic activity was found after the initial period in which 15% of the initial activity was lost.

Qi et al.[180] in an excellent review discussed the technological progress made in the field of development of integrated fuel processor for hydrogen production. They indicate that the extensive volume of the WGS catalysts, which is 6 times larger than that of the reforming catalyst, could be significantly collapsed by using a microchannel heat exchanger for optimizing the temperature profile and to reduce the amount of the catalysts by up to 50%. This approach is also implemented in microreactors where the catalyst is washcoated on inserts housed inside the microreactor channels.[181] Baier and Kolb[30] also demonstrated the volume reduction associated with single-stage WGS reactors. These authors modeled the replacement of the conventional two-step WGS process (HTS + LTS) with a temperature control unit between the reactors with a single-step process with a given temperature profile along the reactor. In their one-dimensional model, the single-step process is more compact as the total reactor length is shorter.

By imposing external temperature profiles in microreactor/heat exchanger devices, the CO conversion in the WGS may be substantially enhanced. Romero and Wilhite[182] developed a plug-flow model with an externally imposed temperature gradient to investigate the influence of thermal profiles on WGS conversion. This allowed them to conclude that an externally imposed linear profile is the most volume efficient, requiring the least increase in reactor size.

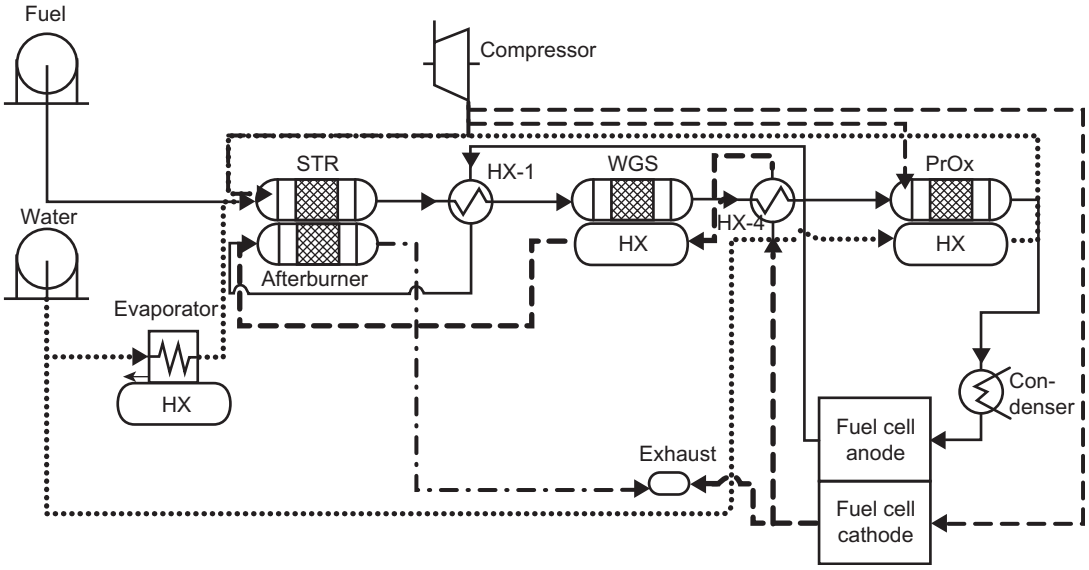

FIGURE 10.4 Flow scheme of a fuel processor prototype having a WGS reactor operated as a counter-current heat exchanger. The cathode off-gas of the FC was used as a coolant for imposing an external temperature profile. Straight lines, fuel; dashed lines, air/cathode off-gas; dotted lines, water/steam; dotted–dashed lines, afterburner off-gas. *Source: With permission from Kolb et al.*[4]

Kolb et al.[4,183] reported the development of a fuel processor prototype having a WGS reactor (Fig. 10.4) operated as a counter-current heat exchanger; for imposing an external temperature profile, the cathode off-gas of the FC was used as the coolant. A summary of the dimensions and characteristics of the WGS reactor are provided in Table 10.2.

The same group[10] developed microstructured WGS and PROX reactors for the cleanup section of a fuel processor/FC system running on isooctane and designed for an electrical output of 5 kW_{el}. The applied Pt/ceria catalysts revealed conversion close to the thermodynamic limit in a pilot scale test at a weight hourly space velocity (WHSV) of 17–41 $NL/h \cdot g_{cat}$. The performance and the fuel processor efficiency changed from 88% to 74% when the steam/carbon ratio was varied from 10 to 3.3.

TABLE 10.2 Summary of the WGS Reactor Dimensions and Operating Conditions[4]

Maximum operating temperature (°C)	**425**
Maximum operating pressure (bar)	2
Plate size (L × W × H) (mm)	145 × 75.8 × 0.6
Number of half channels per plate	60
Number of reformate channel levels	12
Channel dimensions (L × W × H) (mm)	125 × 1 × 0.65
Number of plates	36
Plate stack dimensions (mm)	145 × 75.8 × 35.2

In another relevant work of this research group,[6] a CO concentration as low as 0.78 vol.% (from reformate surrogate) was attained at the exit of the designed WGS reactor (Fig. 10.4). However, the catalyst degraded. This was attributed to the severe demands in terms of start-up and load change conditions.

Dubrovskiy et al.[31] studied Mo_2C/Mo coatings on a microreactor heat exchanger system for WGS reaction (Fig. 10.5). Two coolant side streams were required to

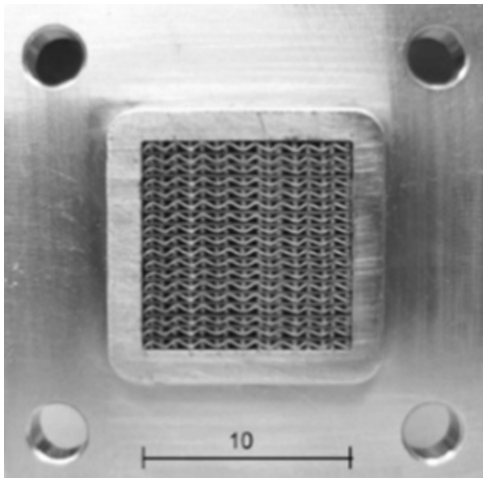

FIGURE 10.5 Section of the catalytic wall microreactor/heat exchanger produced by stacking flat and perforated metal plates that result in triangular-sectioned passages. Between perforated and flat plates metal wires are inserted splitting the large triangular channel into three smaller (equilateral triangles) channels. Mo_2C/Mo catalyst coats the plates. *Source: With permission from Dubrovskiy et al.*[31]

approach the optimal temperature profile and the highest rate of the reaction. They proposed the use of stacked three dimensional assembly in preference to large planar plate for microreactor construction in order to reduce the surface-to-volume ratio and thus the convective losses.

Microchannel-based micro heat exchangers may allow precise temperature control and, if adequately designed, may impose a temperature profile that maximizes CO conversion, allowing one to reach values at the reactor outlet close to the equilibrium ones. A catalytic wall device consisting of a stack of multiple metallic micromachined sheets allowing heat exchange between a refrigerating fluid (water) and the reformate gas has been described by Cho et al.[184] for operating the exothermic WGS reaction using a Pt-Re catalyst supported on CeO_2/ZrO_2.

In summary, the successful design of WGS reactor as a part of fuel processor/FC system for mobile or stationary applications depends mainly on the reduction of the size and/or number of reactors and on the careful control of the temperature. When mobile applications are targeted, the required reduction of size and volume could be achieved by a single step WGS reactor/heat exchanger system. For stationary application when the size is not a real constraint, two HTS and LTS microreactors or coated monoliths could be envisaged. Still there is a work to do concerning the catalyst stability and operation under start-up–shutdown conditions. The Cu-based LTS traditional catalyst, which is undesirable for mobile application because of its pyrophoricity, could be married with a microchannel reactor in which the inherent reactor safety and broader reaction conditions includes working into explosive regime.

Structured metallic foams have been proposed as support for the PROX catalysts; the turbulence provided by the foams to the gas flow improves the catalyst–reactant contact as well as the mechanical stability of the deposited catalyst.[185] The Pt–Fe/alumina catalyst deposition procedure includes a series of precise steps and maximum operational temperatures. Provided the preparation of the catalyst and the washcoating procedure were properly followed, the structured catalyst operated successfully in the CO preferential oxidation reaction at 90 °C and 20,000/h space velocity. In these conditions, the CO conversion was c. 99% and the final CO level was below 10 ppm for an O_2-to-CO molar ratio of 1. The addition of copper to this catalyst improves the catalyst performances, extending the operational window by avoiding the R-WGS.[186] Metallic monoliths washcoated with this catalyst can reduce the CO level below 10 ppm in realistic reformate mixtures when operated at 10,000/h and temperatures below 100 °C. Figure 10.6 presents the CO and O_2 concentration at the reactor outlet at a space velocity of 10,000/h.

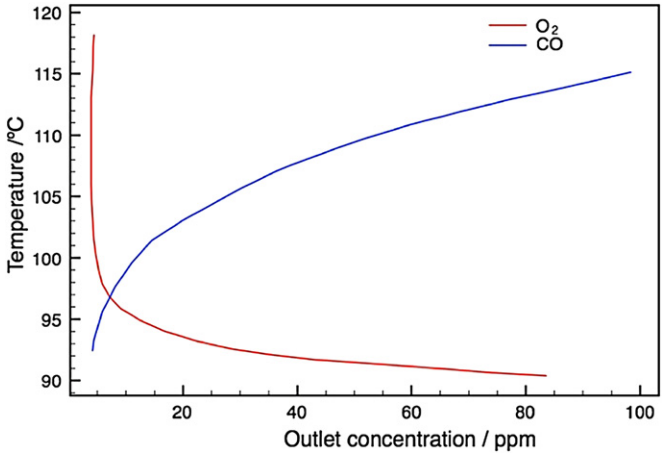

FIGURE 10.6 Outlet CO, for 10,000/h, and O_2, for 20,000/h, for a catalyst with 8% copper and 2% platinum supported on alumina. The reformate contained, on dry basis, 50% H_2, 15% CO_2, 0.3% CO, 0.48% O_2 and the remaining nitrogen. Steam was injected in the reformate at 25% v/v. (For color version of this figure, the reader is referred to the online version of this book.) *Source: Adapted from Shore, Farrauto et al.*[186]

Heat-transfer limitations during the PROX reaction are within the aims of the studies developed by Besser et al.[187] using Pt/Al_2O_3 catalysts, as in the previous work by Goerke et al. on WGS and PROX reactions.[148] Catalytic wall microreactors built by photolithography and deep reactive ion etching of silicon chips anodically bonded were compared to mini-packed-bed reactors (m-PBR) by these authors.[187–189] Both reactors consist of single channels with cross-sectional dimensions of $500 \times 470\ \mu m^2$ and 4.5 cm length; thickness in the range of 2–5 μm were tested in the case of the coated microreactor. The main difference between both reactors is the development of thermal gradients within the reactor. In the studied temperature range, thermal gradients are hardly observed for the microreactor, whereas considerable thermal gradients in both radial and axial directions are observed in m-PBR reactors under the experimental conditions evaluated in their study. The control of the reaction temperature is responsible for the improved selectivity of microreactors in the PROX reaction.[143] An inefficient temperature control favors temperature gradients along the reactor speeding up the R-WGS reaction[187,190] Besides this, efficient heat transfer in catalytic wall microreactors prevents hotspot formation, reducing the oxidation of hydrogen, and hence improves selectivity. The differences between the microreactors and m-PBR reactors may be expressed in terms of the effective interparticle heat conduction distance, being lower for the microreactor (catalytic thickness) than for the packed-bed reactor (reactor inner radius).

Moreover, start-up, stop-down and changes in the operation conditions take benefit of the small volume and weight of microreactors, shortening transient

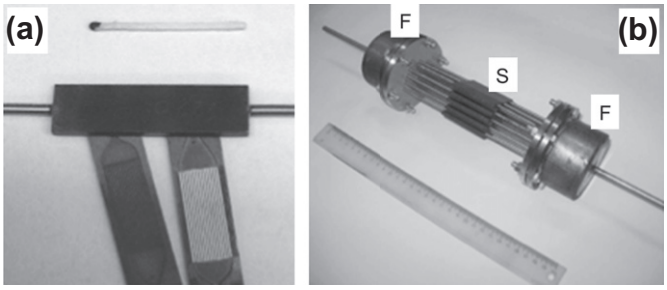

FIGURE 10.7 (a) Laser-welded microstructured reactor and platelets with 5 wt.% Cu/CeO_{2-x} (bottom left) and CeO_2 (bottom right) washcoats. (b) Array of 26 microreactors (S) with gas distribution fittings (F). *Source: With permission from Snytnikov et al.*[192]

periods; temperature gradients of up to 6400 K/s for microstructured heat exchangers on freezing are reported.[143] Using CO oxidation as a model, the suitability of this type of device for undergoing fast temperature cycling is demonstrated.[191]

Snytnikov et al. developed a microchannel reactor for the PROX reaction using a copper–cerium oxide catalyst (5 wt.% Cu/CeO_{2-x})[52,192,193] suitable for coupling to a WGS reactor by laser welding microplatelets to create a sandwich-type reactor, Fig. 10.7. The microreactor manufactured this way presented higher catalytic performances than the respective powder catalyst and the optimal temperature window for the maximum CO conversion was very close to that of the low-temperature WGS reaction keeping selectivity at very high levels. This facilitates the easy combination of serial PROX and WGS microreactors for cleaning H_2 flows. Piling up 26 of these microreactors was proposed for application with a 100 W_e FC system. (Fig. 10.7b)[192] The array was able to reduce the CO concentration in a realistic reformate out gas from 1.5 vol.% to 10 ppm and O_2/CO ratio of 1.5 within the temperature range of 230–240 °C, which is close to the operating temperature of a low-temperature WGS microreactor without the need of intermediate heat exchangers, confirming the results of single microreactor evaluation.[52]

By joining together micromilled ferritic stainless-steel plates using the transient liquid phase bonding process, Odriozola et al.[111] developed a catalytic wall microreactor for the PROX reaction also employing copper–cerium-oxide-based catalyst. This manufacturing process resulted in a microblock that was housed in Al-alloyed ferritic steel cases (Fig. 10.8). The studies carried out over this microreactor confirmed the improvement of the CO conversion and selectivity at lower temperatures compared to the powder catalyst. The catalytic data obtained with this block allowed to successfully validating a computational fluid dynamic (CFD) simulation model. The three-dimensional simulations have been carried out using ANSYS CFX software, which is based on the finite-volume method for spatial discretization of the Navier–Stokes equations. The model consisting of square parallel microchannels of 20 mm length and 0.70 mm side was previously developed and it has been successfully applied to study the steam reforming of methane and methanol.[194,195] This model has three main physical domains, two of them are fluidic and the third corresponds to the solid block (stainless steel). These domains were meshed using prismatic and hexahedral elements, resulting in dense computational unstructured grids as presented in Fig. 10.9.[194–196] CFD simulations were conducted at steady state and isothermal conditions, considering the microchannel walls as sources of products and sinks of reactants.[194–196] A reaction scheme including the oxidation of CO to CO_2, the oxidation of H_2 to H_2O and the

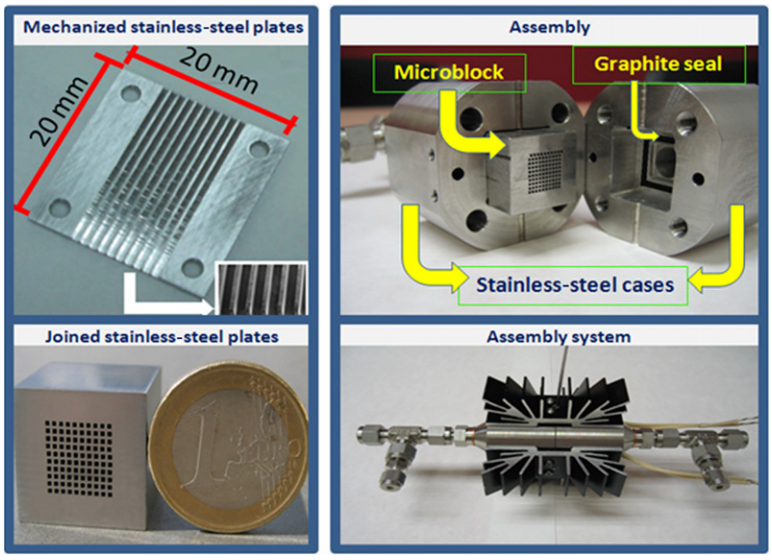

FIGURE 10.8 Assembling of a microchannel reactor for the CO-PROX reaction. (For color version of this figure, the reader is referred to the online version of this book.)*Source: With permission from Cruz et al.*[111]

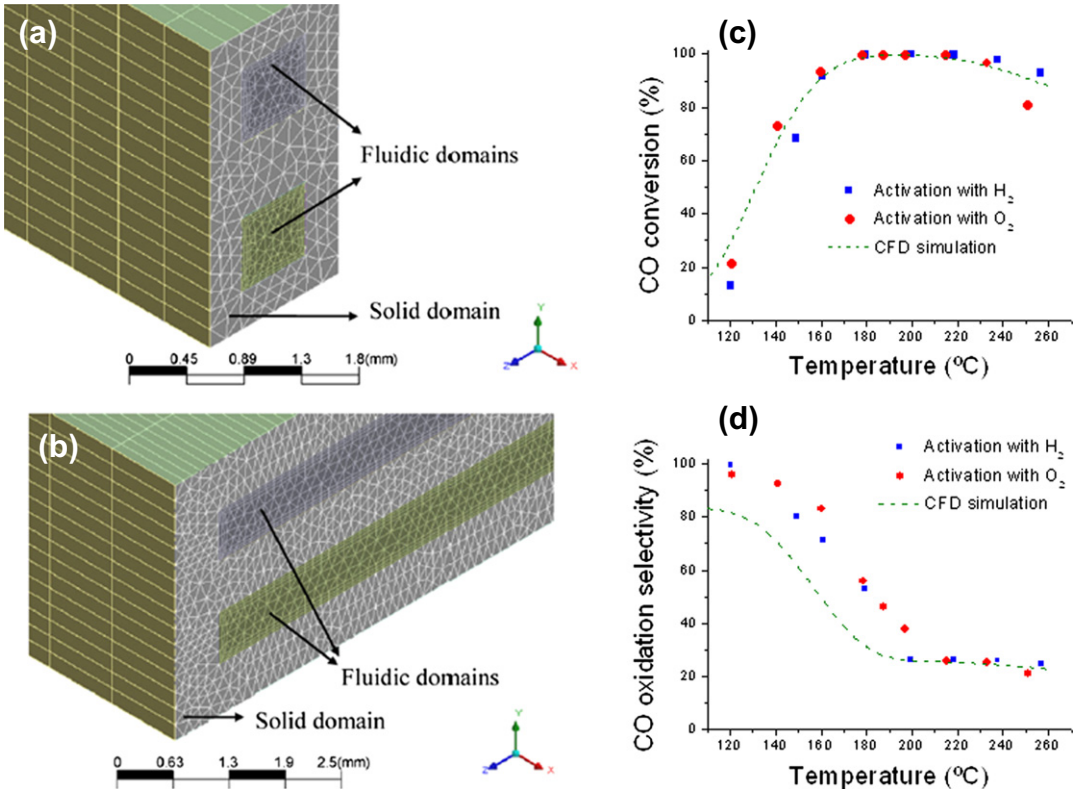

FIGURE 10.9 Meshes applied to the fluidic and solid domains of a microchannel (a) and microslit reactors (b). Effect of the activation pretreatment on the CO conversion (c) and selectivity (d) over a CuO_x/CeO_2 catalyst in the PROX reaction using an ideal PROX mixture. Points indicate experimental data and dashed lines denote the kinetic model fit. (For color version of this figure, the reader is referred to the online version of this book.)

R-WGS reaction was considered within the kinetic equations implemented in the code for the CFD simulations, employing a previous kinetic study carried out over the CuO_x/CeO_2 powder catalyst.[196]

According to our knowledge, this is the first time that a CFD model including the kinetic expressions for predicting the catalytic results of a microreactor as presented in Fig. 10.9b and c has been validated experimentally. There is an acceptable agreement between the experimental data and the simulated results considering that internal mass transport limitations have been considered negligible.

Within a wide study on selective oxidations in microstructured reactors, Kolb et al.[51] analyzed the PROX reaction and on the basis of Damköller numbers concluded that the heat transport properties of microreactors were superior compared to those of m-PBR. Again, the minimized heat-transport resistance of the thin-film catalyst is claimed to be responsible for the efficient suppression of the R-WGS. Ouyang and Besser[187] concluded that mass- and heat-transport resistance is negligible at low temperature for their Pt/Al_2O_3 but at temperatures above 220 °C mass transport limited the PROX reaction rate.

Using wall-coated silicon-etched microreactors, Srinivas et al.[197] came to similar conclusions on transport resistances in the PROX reaction. According to them, external mass transfer limitations are similar in wall-coated microreactors and m-PBR. The mass transfer limitations may arise by internal diffusion within the porous catalyst itself. Therefore, this would be a problem in designing the catalyst and not the reactor that can be overcome by achieving suited pore microstructures, which would be the same for the microreactor and packed-bed reactor. However, very recently, Laguna et al.[112] have shown that for CuO_x/CeO_2 wall-coated catalysts heat-transfer limitations may occur at temperatures as low as 100 °C.

In general, internal diffusion resistance is minimized using thin-coating catalysts. For the preferential oxidation of CO in microchannel reactor over a Pt/Al_2O_3 catalyst, the internal mass-transport limitations have been shown as negligible for thickness as small as 2–5 μm,[190] whereas for particles 360 μm in diameter, the internal effectiveness factor drops to 0.5 at 250 °C.[198]

To minimize mass-transfer limitations in order to provide the best process efficiency in the CO-PROX reaction, Potemkin et al.[193] analyzed the optimum catalyst

pellet diameter and catalytic coating thickness using the textural data of CuO_x/CeO_2 catalyst and reaction kinetics data for determining the effectiveness factor, η_{CO}, that characterizes the effect of internal mass-transfer limitations on the PROX reaction. The effectiveness factor depends on both reaction temperature and pellet radius R or coating thickness h for catalyst pellets or for catalyst deposited on the walls of microchannels, respectively. The effectiveness factor in the optimal reaction temperature window is higher than 0.8 (170−230 °C; $\eta_{CO} > 0.8$) provided the catalytic layer thickness does not exceed 20 μm. The η_{CO} was determined as the ratio of the rate of CO oxidation accounting for mass-transfer limitations to that calculated assuming absence of transfer limitations. The decrease of η_{CO} as a function of the catalytic layer thickness and temperature is clearly seen in Fig. 10.10. These results pointed out that if the thickness of the catalytic layer, which represents also the amount of loaded catalyst, is above a certain value, the positive effect of high heat transfer ability of microreactors can be counterbalanced by the mass transport limitations derived by the excess of catalyst.

In the case of the PROX reaction, there are not thermodynamic limitations to the oxidation of CO; therefore, kinetics favors CO oxidation at high temperatures. In fact, the reaction is usually very slow below a certain temperature, although the strong exothermicity of the process indicates that the reaction is thermodynamically favored at low temperatures. Unfortunately, the same is true for hydrogen oxidation, the process resulting in poorer selectivities as the temperature increases. The differences in H_2 and CO oxidation kinetics determine the operating window for every catalyst. Imposing temperature profiles to the reactor may optimize the CO abatement process, avoiding as much as possible the oxidation of H_2, the R-WGS or the methanation reactions.

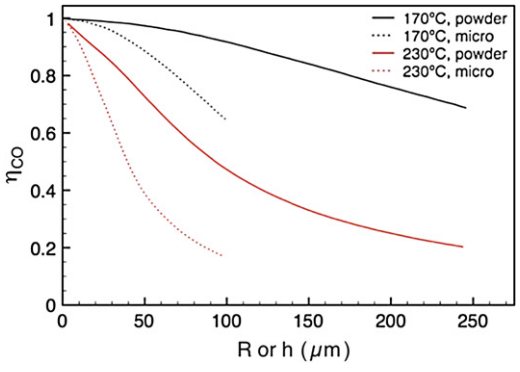

FIGURE 10.10 Effectiveness factor for CO as a function of temperature and pellet radius R or coating thickness h for catalyst pellets or for catalyst deposited on the walls of microchannels. (For color version of this figure, the reader is referred to the online version of this book.) *Source: Adapted from Potemkin et al.*[193]

Using a conventional 5% Pt/Al_2O_3 catalyst it is possible to reduce the CO content of a reformate gas from 1.5% to below 10 ppm by imposing a temperature profile in the reactor through multiple water injection at different points of the reactor length. A mesh- or foam-type high-surface-area metallic structure favors fast water evaporation helping in the control of the reactor temperature.[199] Other approaches for imposing temperature profiles include helical-type heat exchangers, with the catalyst deposited on fins surrounding the helical tube. The temperature gradient is generated through a two-phase steam−water system in such a way that water reaches its boiling temperature at a point close to the reactor outlet where the water exits the reactor.[200] Alternatively, the PROX reactor may consist of a catalytic wall microchannel cross-flow micro heat exchanger having micromachined plates with baffles in order to create a turbulent flow pattern as well as an increased catalyst deposition area.[200]

To date, PEMFC's continue to be extensively studied because they are promising suppliers of clean energy with high efficiency.[201] However, as discussed above, hydrogen storage for feeding these FCs has serious drawbacks concerning transport and process safety that make difficult the wide diffusion of such technology.

The alternative is to produce on demand the required H_2 in an attached unit from hydrogen-rich fuels. As described above, hydrogen production from hydrocarbon molecules implies the inclusion of purification stages complementary to a reformer in order to provide reformate gases clean enough (CO concentration at the parts per million level). Therefore, fuel processors must integrate reforming and purification processes (WGS and PROX or methanation) in a single unit for feeding a PEM cell.[7,9,145,180,183,202−204]

The design of PROX reactors for the purification stage of a fuel processor faces the same challenges described above: active and selective catalysts suitable for oxidizing CO from 1 to 0.5 vol.% to 50 ppm without consuming a large amount of H_2. The process temperature is usually between the outlet temperature of the WGS reactor and the inlet temperature of the FC in order to facilitate the coupling between the different processes.

In a review about fuel processing catalyst for H_2 production, Faur Ghenciu pointed out that the exothermic character of the oxidation reactions (of CO and H_2) requires multistage PROX systems with interstage cooling and/or water injection between stages.[201] In this sense, the need for a strict control of the reaction temperature confirms the promising viability of microreactors due to their high heat- and mass-transfer abilities, among other advantages as discussed above.

Moreover, once the adequate catalyst is selected, the architecture design of the microreactor is relevant. The geometrical configuration of the reactor and the effects of the main operating parameters on CO preferential oxidation performance have been extensively studied using 2D simulations by Cipitì et al.[205–208] The overall performance during CO removal strongly depends on the reactor geometrical configuration in single-stage multitubular PROX units. Besides this, the reactor performance depends on the O_2/CO molar ratio, GHSV (gas hourly space velocity) and inlet temperature.[208] These studies have led these authors to design a fuel processor prototype (HYGen II) using a multitubular PROX reactor[206] in which they use the reactor temperature profile modeled to maximize the performance of the PROX reactor through an adequate control of the heat transfer system.[205]

Delsman et al. reported the successful application of a microreactor for PROX in a portable fuel processor.[209,210] The authors described the design, modeling, simulation and experimental data of a microdevice for the PROX reaction that integrates two heat exchangers with the reactor (Fig. 10.11). The system allows reducing the CO concentration to 10 ppm with a high heat recovery efficiency of 90%. The design process started with the optimization of the geometry of the flow distribution chambers verifying that all microchannels presented the same temperature profiles. The experimental data were well described by the simulations. Then, a comparison was made between preferential oxidation heat exchanger (PROX-Heatex) reactors based on fixed bed technology and microreactor technology for system designed for 100 and 5 W_e power output.[211] The 100-W_e device is well suited for portable electronics applications, while the 5-W_e device is typical for APUs. As summarized by Kolb et al.,[51] the most relevant conclusion for these devices is that, whatever the scale, the microreactor designs outperform the conventional fixed bed ones, resulting in significantly lower reactor volumes and weights. However, reactor volume and reactor weight scaling factors are larger for the microreactor systems than for the fixed bed reactors, which indicates that at larger scales, the fixed bed reactors will ultimately outperform the microreactor designs.

A microstructured 5-kW complete isooctane fuel processor as a H_2 supply system for mobile APUs has been developed by Kolb et al.[10] Therefore, the fuel

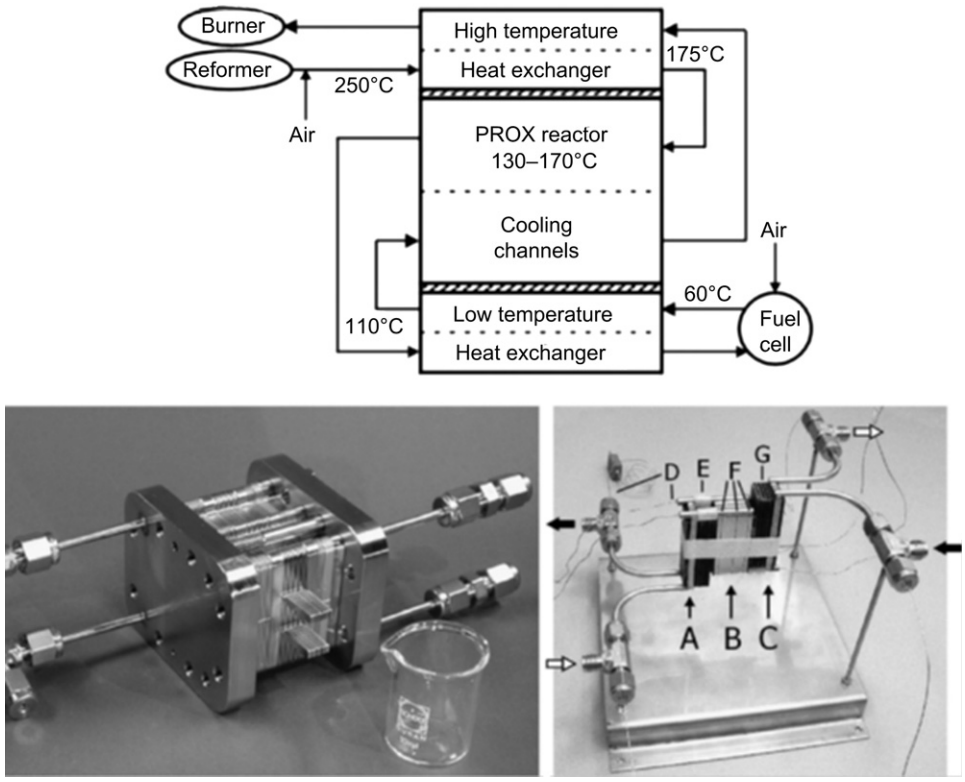

FIGURE 10.11 (Top) Schematic drawing of the integrated preferential CO oxidation heat exchanger microdevice (PROX-Heatex). The temperatures of the reformate and coolant gas streams are indicated. (Bottom left) First PROX-Heatex prototype. (Bottom right) Assembled second-generation PROX-Heatex microdevice consisting of a low-temperature heat exchanger (A), a preferential CO oxidation reactor (B) and a high temperature heat exchanger (C); thermocouples (D); tube connection (E); thermocouple channels (F) and insulating material (G). *Source: With permission from Kolb et al.*[51]

processor includes microreactors for the WGS and PROX reactions; the microreactors were built from microstructured stainless-steel foils using Pt on zeolite/alumina as catalyst on the PROX unit. To achieve a H_2 supply containing less than 50 ppm CO, a two-stage PROX reactor working at WHSV in the 48–97 NL/h·g_{cat} was designed. This PROX system converted up to 90% CO in the first-stage reactor and then, in the second stage, the CO content was decreased to less than 50 ppm. An isooctane autothermal reformer operated at a steam-to-carbon ratio of 3.3, and oxygen-to-carbon ratio of 0.67 delivered the primary hydrogen supply that after purification resulted in an overall efficiency of 74%.[10]

CO methanation, the alternative to PROX fine cleanup, is highly exothermic and, therefore, the control of the reaction temperature is also a mandatory task to avoid hotspots and to keep the high selectivity required. Thus, as in WGS and PROX reactions, microchannel reactors enhance the process efficiency by improving the heat transfer phenomena. The careful control of the reactor temperature in the methanation reactor is a fairly old story. Almost 30 years ago, Yoon designed a multitubular heat-exchange reactor for the methanation reaction. Unfortunately, no information is given on the nature or performances of the methanation catalysts.[212] Basic aspects for implementing the methanation process in microreactors lie in the development of very active, selective and stable catalysts as well as homogenous, stable and well-adhered coatings on the metal surface because of the difference in thermal expansion coefficients between the metallic substrate and the catalytic layer. Adequate washcoating procedures over a previously pretreated metallic substrates are used to solve the later issue.[12,129,149,213] Preliminary studies are usually carried out on monolithic devices whose preparation easiness and affordability are better than those of microreactors.[214,215] Alternatively, millichannel reactors have been built and tested in the methanation reaction. Zyryanova et al.[216] show that a millichannel reactor built by assembling alternate flat and corrugated metal gauzes allows triangular cross-section channels (3 mm × 3 mm × 5 mm) that after coating with a Ni/ceria catalyst reduces the CO concentration to less than 20 ppm in the realistic reformate generated by a methane steam reformer and the subsequent WGS reactor. A similar approach consisting of a channel flow reactor in which a metal plate coated with a commercial Ni/Al_2O_3 catalyst is placed and fixed at the bottom, the upper wall being a quartz glass plate. This embodiment allows an effective channel of 5 mm height, 50 mm width and 130 mm length.[217] These studies allowed optimization of the washcoating procedure[216] and a detailed investigation of the reaction kinetics of the exothermic CO methanation reaction with high initial CO partial pressure.[217]

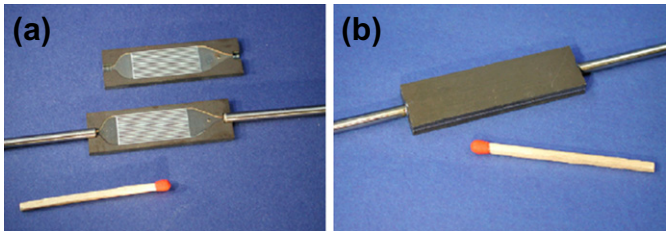

FIGURE 10.12 Sandwiched microchannel reactor for methanation reaction. (a) Coated platelets with capillary. (b) Laser-welded reactor. (For color version of this figure, the reader is referred to the online version of this book.) *Source: With permission from Men et al.*[133]

The focus on the PROX reaction for reducing CO levels in realistic reformate flows has resulted in few studies on the methanation reaction in microreactors in the open literature.

In a first screening for selective removal of CO with simulated reformates, Men et al.[133] tested a series of washcoated Ru and Ni catalysts in a microchannel reactor (Fig. 10.12). The aim of using microreactors was mainly to study the reaction pathway by varying feed composition and reaction temperature. A critical temperature of 250 °C was identified for the selective methanation of CO. Below this temperature, preferential CO methanation occurs, the methanation rate being diminished by the presence of steam. After the screening, they concluded that a Ni/CaO/Al_2O_3 catalyst operated at 300 °C allows efficient CO methanation with a relatively low CO_2 methanation activity.

Görke et al.[121] took benefits of all the advantages of the microreactor technology in studying the CO methanation reaction. They manufactured a microchannel reactor consisting of 27 stainless-steel foils, each of them having 17 etched microchannels (600 μm width × 150 μm height) assembled together with a clamping device (Fig. 10.13). A sol–gel procedure is used for coating the

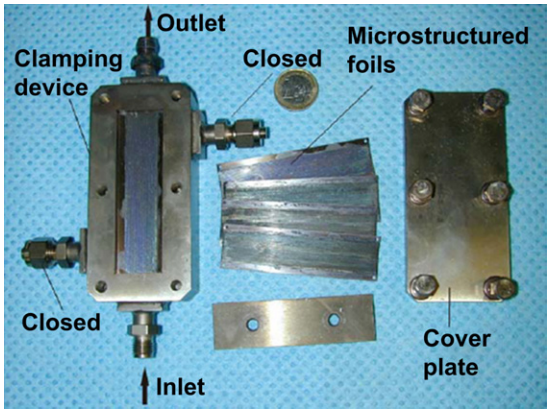

FIGURE 10.13 Microchannel reactor for methanation experiments with clamping device and coated foils. (For color version of this figure, the reader is referred to the online version of this book.) *Source: With permission from Görke et al.*[121]

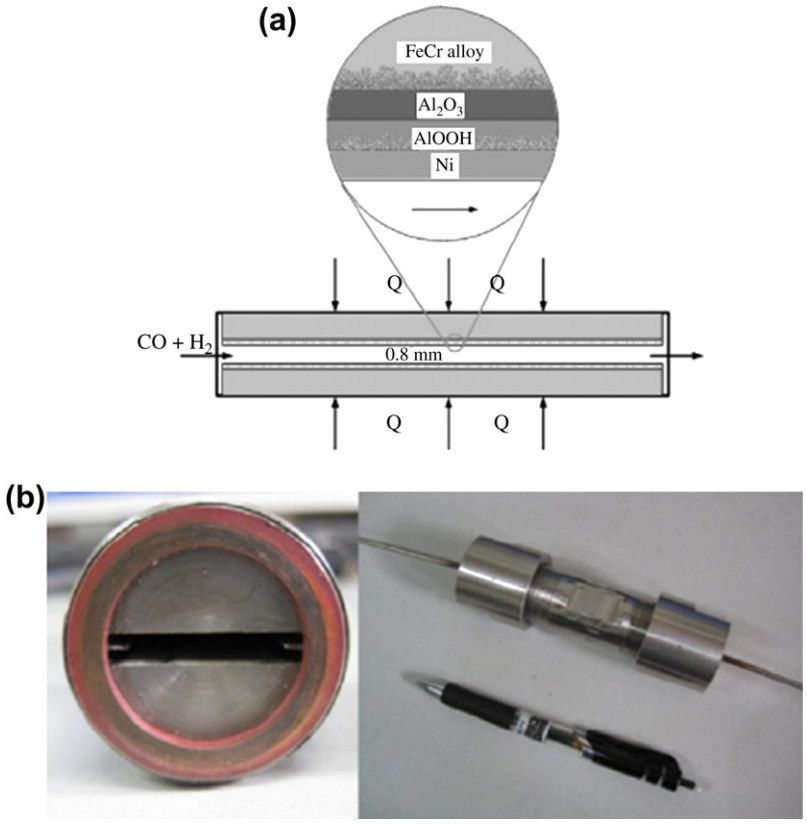

FIGURE 10.14 Schematic diagrams of (a) metal–ceramics complex substrate with catalyst coating and (b) microchannel reactor. (For color version of this figure, the reader is referred to the online version of this book.)*Source: With permission from Liu et al.*[219]

stainless-steel foils with either SiO_2 or Al_2O_3, which were used as supports of ruthenium catalysts prepared by wet impregnation. Due to its inner dimensions and the enhanced heat transfer coefficients, the device allowed a precise control of the reactor temperature and, therefore, maximized CO-to-CO_2 methanation rate ratio. The excellent temperature control of the microreactor allowed these authors to add oxygen to the reformate mixture. They showed that in the presence of oxygen the CO conversion is higher in the 140–200 °C temperature range since CO can be converted to CO_2. At higher temperatures (200–320 °C), H_2 oxidation is favored over CO oxidation and consumes most of the O_2. Temperature control in this process can be easily achieved in the microreactor because of its inner dimensions and improved heat transfer coefficients.

Galletti et al.[218] also studied the methanation of CO over a structured reactor constituted by a stack of six Fe–Cr–Ni plates (5 cm × 5 cm × 0.1 cm) loaded with 50 microchannels of 0.26 mm. The microreactor was loaded with 5 or 10 mg/cm^2 of a 3% Ru/Al_2O_3 catalyst. However, in this case, the catalytic activity and selectivity was poor, specifically the selectivity since CO_2 methanation was largely produced.

In a recent paper, Liu et al.[219] proposed a microreactor formed by ceramic plates inserted in a metallic housing. Using a new method called improved thermal spray, they manufactured a metal–ceramics complex substrate as catalyst support. The microreactor was prepared by inserting two 2 × 5.5-cm^2 sheets of the catalyst plates into the slits of microreactor separately; the space between the two plates forms the channel (1.8 × 5.5 × 0.08 cm^3), as shown in Fig. 10.14. With this device, they performed the total methanation of syngas over Ni/Al_2O_3 catalyst deposited in their microchannel reactor. Although the CO conversion (>98%) and selectivity (>92%) were high, their conclusions cannot be extrapolated to the fine cleanup process we are dealing with.

Acknowledgments

Financial support by the Spanish Ministry of Science and Innovation and Ministry of Economy and Competitiveness (ENE2009-14522-C04 and ENE2012-37,431-C03 grants, respectively) and Junta de Andalucía (POG-TEP01965) is gratefully acknowledged. S. Ivanova gratefully acknowledges the Spanish Ministry of Science and Innovation for her contract within the Ramon y Cajal Program. All contracts are cofunded by FEDER funds from the European Union.

References

1. Holladay, J. D.; Wang, Y.; Jones, E. *Chem. Rev.* **2004,** *104,* 4767–4789.
2. Hessel, V.; Knobloch, C.; Löwe, H. *Recent Pat. Chem. Eng.* **2008,** *1,* 1–16.

3. Protasova, L. N.; de Croon, M. H. J. M.; Hessel, V. *Recent Pat. Chem. Eng.* **2012,** *5,* 28−44.
4. Kolb, G.; Hofmann, C.; O'Connell, M.; Schürer, J. *Catal. Today* **2009,** *147,* S176−S184.
5. O'Connell, M.; Kolb, G.; Schelhaas, K. P.; Schuerer, J.; Tiemann, D.; Ziogas, A.; Hessel, V. *Int. J. Hydrogen Energy* **2009,** *34,* 6290−6303.
6. O'Connell, M.; Kolb, G.; Schelhaas, K. P.; Schuerer, J.; Tiemann, D.; Ziogas, A.; Hessel, V. *Int. J. Hydrogen Energy* **2010,** *35,* 2317−2327.
7. Holladay, J.; Jones, E.; Palo, D. R.; Phelps, M.; Chin, Y. H.; Dagle, R.; Hu, J.; Wang, Y.; Baker, E. Miniature Fuel Processors for Portable Fuel Cell Power Supplies. In Knauth, Philippe, Gasteiger, Hubert A., Eds., Vol. 756; Materials Research Society: Warrendale, PA, 2003; pp 429−434.
8. Lin, S.-T.; Chen, Y.-H.; Yu, C.-C.; Liu, Y.-C.; Lee, C.-H. *J. Power Sourc.* **2005,** *148,* 43−53.
9. Sopeña, D.; Melgar, A.; Briceño, Y.; Navarro, R. M.; Álvarez-Galván, M. C.; Rosa, F. *Int. J. Hydrogen Energy* **2007,** *32,* 1429−1436.
10. Kolb, G.; Baier, T.; Schürer, J.; Tiemann, D.; Ziogas, A.; Specchia, S.; Galletti, C.; Germani, G.; Schuurman, Y. *Chem. Eng. J.* **2008,** *138,* 474−489.
11. Ratnasamy, C.; Wagner, J. *Catal. Rev. − Sci. Eng.* **2009,** *51,* 325−440.
12. Sanz, O.; Echave, F. J.; Romero Sarria, F.; Odriozola, J. A.; Centeno, M. A. *Advances in Structured and Microstuctured Catalytic Reactors for Hydrogen Production*.
13. Rostrup-Nielsen, J. R.; Aasberg-Petersen, K. In Vielstich, W., Gasteiger, H. A., Lamm, A., Eds., Vol. 3; Wiley: Chichester, 2003; pp 159−176.
14. Djinovic, P.; Galletti, C.; Specchia, S.; Specchia, V. *Catal. Today* **2011,** *164,* 282−287.
15. Tabakova, T.; Idakiev, V.; Tenchev, K.; Boccuzzi, F.; Manzoli, M.; Chiorino, A. *Appl. Catal. B. Environ.* **2006,** *63,* 94−103.
16. Tabakova, T.; Idakiev, V.; Papavasiliou, J.; Avgouropoulos, G.; Ioannides, T. *Catal. Comm.* **2007,** *8,* 101−106.
17. Tabakova, T.; Idakiev, V.; Andreeva, D.; Mitov, I. *Appl. Catal. A. Gen.* **2000,** *202,* 91−97.
18. Tabakova, T.; Boccuzzi, F.; Manzoli, M.; Sobczak, J. W.; Idakiev, V.; Andreeva, D. *Appl. Catal. A. Gen.* **2006,** *298,* 127−143.
19. Jacobs, G.; Williams, L.; Graham, U.; Thomas, G. A.; Sparks, D. E.; Davis, B. H. *Appl. Catal. A. Gen.* **2003,** *252,* 107−118.
20. Boaro, M.; Vicario, M.; Llorca, J.; de Leitenburg, C.; Dolcetti, G.; Trovarelli, A. *Appl. Catal. B. Environ.* **2009,** *88,* 272−282.
21. Amieiro Fonseca, A.; Fisher, J.; Ozkaya, D.; Shannon, M.; Thompsett, D. *Top. Catal.* **2007,** *44,* 223−235.
22. Schönbrod, B.; Mariño, F.; Baronetti, G.; Laborde, M. *Int. J. Hydrogen Energy* **2009,** *34,* 4021−4028.
23. Martínez-Arias, A.; Hungría, A. B.; Munuera, G.; Gamarra, D. *Appl. Catal. B. Environ.* **2006,** *65,* 207−216.
24. Martínez-Arias, A.; Hungría, A. B.; Fernández-García, M.; Conesa, J. C.; Munuera, G. *J. Power Sourc.* **2005,** *151,* 32−42.
25. Martínez-Arias, A.; Gamarra, D.; Fernández-García, M.; Wang, X. Q.; Hanson, J. C.; Rodríguez, J. A. *J. Catal.* **2006,** *240,* 1−7.
26. Martínez-Arias, A.; Gamarra, D.; Fernández-García, M.; Hornés, A.; Bera, P.; Koppány, Z.; Schay, Z. *Catal. Today* **2009,** *143,* 211−217.
27. Mariño, F.; Descorme, C.; Duprez, D. *Appl. Catal. B. Environ.* **2005,** *58,* 175−183.
28. Bion, N.; Epron, F.; Moreno, M.; Mariño, F.; Duprez, D. *Top. Catal.* **2008,** *51,* 76−88.
29. Zalc, J. M.; Sokolovskii, V.; Löffler, D. G. *J. Catal.* **2002,** *206,* 169−171.
30. Baier, T.; Kolb, G. *Chem. Eng. Sci.* **2007,** *62,* 4602−4611.
31. Dubrovskiy, A. R.; Rebrov, E. V.; Kuznetsov, S. A.; Schouten, J. C. *Catal. Today* **2009,** *147* (Suppl.), S198−S203.
32. Giroux, T.; Hwang, S.; Liu, Y.; Ruettinger, W.; Shore, L. *Appl. Catal. B. Environ.* **2005,** *56,* 95−110.
33. Smith R J, B.; Loganathan, M.; Shantha, M. S. *Int. J. Chem. Reactor Eng.* **2010,** *8,* 1−28.
34. Hinrichsen, K.-O.; Kochloefl, K.; Muhler, M. In Ertl, G., Knotzinger, H., Weitkamp, J., Eds;., Vol. 6; VCH Verlagsgesellshaft mbH: Weinheim, 2008; chapter 13.12.
35. Farrauto, R.; Liu, Y.; Ruettinger, W.; Ilinich, O.; Shore, L.; Giroux, T. *Catal. Rev. − Sci. Eng.* **2007,** *49,* 141−196.
36. Andreeva, D.; Idakiev, V.; Tabakova, T.; Andreev, A.; Giovanoli, R. *Appl. Catal. A. Gen.* **1996,** *134,* 275−283.
37. Sakurai, H.; Ueda, A.; Kobayashi, T.; Haruta, M. *Chem. Comm.* **1997,** 271−272.
38. Andreeva, D.; Idakiev, V.; Tabakova, T.; Ilieva, L.; Falaras, P.; Bourlinos, A.; Travlos, A. *Catal. Today* **2002,** *72,* 51−57.
39. Venugopal, A.; Scurrell, M. S. *Appl. Catal. A. Gen.* **2003,** *245,* 137−147.
40. Fu, Q.; Saltsburg, H.; Flytzani-Stephanopoulos, M. *Science* **2003,** *301,* 935−938.
41. Burch, R. *Phys. Chem. Chem. Phys.* **2006,** *8,* 5483−5500.
42. Reina, T.R.; Xu, W.; Ivanova, S.; Centeno, M.Á.; Hanson, J.; Rodriguez, J.A.; Odriozola, J.A. *Catal. Today,* in press doi: http://dx.doi.org/10.1016/j.cattod.2012.1008.1004.
43. Panagiotopoulou, P.; Papavasiliou, J.; Avgouropoulos, G.; Ioannides, T.; Kondarides, D. I. *Chem. Eng. J.* **2007,** *134,* 16−22.
44. Panagiotopoulou, P.; Kondarides, D. I. *Catal. Today* **2006,** *112,* 49−52.
45. Panagiotopoulou, P.; Christodoulakis, A.; Kondarides, D. I.; Boghosian, S. *J. Catal.* **2006,** *240,* 114−125.
46. Jacobs, G.; Crawford, A.; Williams, L.; Patterson, P. M.; Davis, B. H. *Appl. Catal. A. Gen.* **2004,** *267,* 27−33.
47. Grenoble, D. C.; Estadt, M. M.; Ollis, D. F. *J. Catal.* **1981,** *67,* 90−102.
48. Basińska, A.; Kepiński, L.; Domka, F. *Appl. Catal. A. Gen.* **1999,** *183,* 143−153.
49. Hilaire, S.; Wang, X.; Luo, T.; Gorte, R. J.; Wagner, J. *Appl. Catal. A. Gen.* **2001,** *215,* 271−278.
50. Fodor, K.; Suru, G.; Erdohelyi, A. *Appl. Catal. A. Gen.* **1996,** *139,* 131−147.
51. Kolb, G.; Hessel, V.; Cominos, V.; Hofmann, C.; Löwe, H.; Nikolaidis, G.; Zapf, R.; Ziogas, A.; Delsman, E. R.; de Croon, M. H. J. M., et al. *Catal. Today* **2007,** *120,* 2−20.
52. Snytnikov, P. V.; Popova, M. M.; Men, Y.; Rebrov, E. V.; Kolb, G.; Hessel, V.; Schouten, J. C.; Sobyanin, V. A. *Appl. Catal. A. Gen.* **2008,** *350,* 53−62.
53. Echigo, M.; Tabata, T. *Appl. Catal. A. Gen.* **2003,** *251,* 157−166.
54. Igarashi, H.; Uchida, H.; Suzuki, M.; Sasaki, Y.; Watanabe, M. *Appl. Catal. A. Gen.* **1997,** *159,* 159−169.
55. Oh, S. H.; Sinkevitch, R. M. *J. Catal.* **1993,** *142,* 254−262.
56. Snytnikov, P. V.; Sobyanin, V. A.; Belyaev, V. D.; Tsyrulnikov, P. G.; Shitova, N. B.; Shlyapin, D. A. *Appl. Catal. A. Gen.* **2003,** *239,* 149−156.
57. Tanaka, H.; Ito, S.-i.; Kameoka, S.; Tomishige, K.; Kunimori, K. *Appl. Catal. A. Gen.* **2003,** *250,* 255−263.
58. Wörner, A.; Friedrich, C.; Tamme, R. *Appl. Catal. A. Gen.* **2003,** *245,* 1−14.
59. Chen, L.; Ma, D.; Zhang, Z.; Guo, Y.; Ye, D.; Huang, B. *Catal. Lett.* **2012,** 1−9.
60. Gu, X. K.; Ouyang, R.; Sun, D.; Su, H. Y.; Li, W. X. *ChemSusChem.* **2012,** *5,* 871−878.
61. Kim, Y. H.; Yim, S. D.; Park, E. D. *Catal. Today* **2012,** *185,* 143−150.
62. Kugai, J.; Moriya, T.; Seino, S.; Nakagawa, T.; Ohkubo, Y.; Nitani, H.; Daimon, H.; Yamamoto, T. A. *Int. J. Hydrogen Energy* **2012,** *37,* 4787−4797.
63. Lang, S.; Türk, M.; Kraushaar-Czarnetzki, B. *J. Catal.* **2012,** *286,* 78−87.
64. Liu, K.; Wang, A.; Zhang, T. *ACS Catal.* **2012,** *2,* 1165−1178.
65. Piccolo, L.; Nassreddine, S.; Morfin, F. *Catal. Today* **2012**.

66. Teschner, D.; Wootsch, A.; Paál, Z. *Appl. Catal. A. Gen.* **2012,** *411-412,* 31−34.
67. Xu, J.; Xu, X. C.; Ouyang, L.; Yang, X. J.; Mao, W.; Su, J.; Han, Y. F. *J. Catal.* **2012,** *287,* 114−123.
68. Laguna, O. H.; Romero Sarria, F.; Centeno, M. A.; Odriozola, J. A. *J. Catal.* **2010,** *276,* 360−370.
69. Sangeetha, P.; Chang, L. H.; Chen, Y. W. *Mat. Chem. Phys.* **2009,** *118,* 181−186.
70. Sangeetha, P.; Chen, Y. W. *Int. J. Hydrogen Energy* **2009,** *34,* 7342−7347.
71. Albonetti, S.; Bonelli, R.; Delaigle, R.; Gaigneaux, E. M.; Femoni, C.; Riccobene, P. M.; Scirè, S.; Tiozzo, C.; Zacchini, S.; Trifirò, F. *Stud. Surf. Sci. Catal.* **2010,** *175,* 785−788.
72. Desmond Ng, J. W.; Zhong, Z.; Luo, J.; Borgna, A. *Int. J. Hydrogen Energy* **2010,** *35,* 12724−12732.
73. Laguna, O. H.; Centeno, M. A.; Arzamendi, G.; Gandía, L. M.; Romero-Sarria, F.; Odriozola, J. A. *Catal. Today* **2010,** *157,* 155−159.
74. Liotta, L. F.; Di Carlo, G.; Pantaleo, G.; Venezia, A. M. *Catal. Today* **2010,** *158,* 56−62.
75. Yi, G.; Yang, H.; Li, B.; Lin, H.; Tanaka, K. I.; Yuan, Y. *Catal. Today* **2010,** *157,* 83−88.
76. Davran-Candan, T.; Demir, M.; Yildirim, R. *React. Kinet. Mechanisms Catal.* **2011,** 1−10.
77. Hammer, N.; Mathisen, K.; Zscherpe, T.; Chen, D.; Rønning, M. *Top. Catal.* **2011,** *54,* 922−930.
78. Ilieva, L.; Pantaleo, G.; Ivanov, I.; Zanella, R.; Sobczak, J. W.; Lisowski, W.; Venezia, A. M.; Andreeva, D. *Catal. Today* **2011,** *175,* 411−419.
79. Sakwarathorn, T.; Luengnaruemitchai, A.; Pongstabodee, S. *J. Ind. Eng. Chem.* **2011,** *17,* 747−754.
80. Tabakova, T.; Avgouropoulos, G.; Papavasiliou, J.; Manzoli, M.; Boccuzzi, F.; Tenchev, K.; Vindigni, F.; Ioannides, T. *Appl. Catal. B. Environ.* **2011,** *101,* 256−265.
81. Fonseca, J.; Royer, S.; Bion, N.; Pirault-Roy, L.; Rangel, M.d. C.; Duprez, D.; Epron, F. *Appl. Catal. B. Environ.* **2012**.
82. Gavril, D.; Georgaka, A.; Karaiskakis, G. *Molecules* **2012,** *17,* 4878−4895.
83. Scirè, S.; Crisafulli, C.; Riccobene, P. M.; Patanè, G.; Pistone, A. *Appl. Catal. A. Gen.* **2012,** *417−418,* 66−75.
84. Tu, Y.; Meng, M.; Sun, Z.; Zhang, L.; Ding, T.; Zhang, T. *Fuel Process. Tech.* **2012,** *93,* 78−84.
85. Avgouropoulos, G.; Ioannides, T.; Matralis, H. K.; Batista, J.; Hocevar, S. *Catal. Lett.* **2001,** *73,* 33−40.
86. Avgouropoulos, G.; Ioannides, T.; Papadopoulou, C.; Batista, J.; Hocevar, S.; Matralis, H. K. *Catal. Today* **2002,** *75,* 157−167.
87. Avgouropoulos, G.; Ioannides, T. *Appl. Catal. B. Environ.* **2006,** *67,* 1−11.
88. Caputo, T.; Lisi, L.; Pirone, R.; Russo, G. *Ind. Eng. Chem. Res.* **2007,** *46,* 6793−6800.
89. Chen, Y.-Z.; Liaw, B.-J.; Chang, W.-C.; Huang, C.-T. *Int. J. Hydrogen Energy* **2007,** *32,* 4550−4558.
90. Gamarra, D.; Hornés, A.; Koppány, Z.; Schay, Z.; Munuera, G.; Soria, J.; Martínez-Arias, A. *J. Power Sourc.* **2007,** *169,* 110−116.
91. Jung, C. R.; Kundu, A.; Nam, S. W.; Lee, H.-I. *Appl. Catal. A. Gen.* **2007,** *331,* 112−120.
92. Liu, Z.; Zhou, R.; Zheng, X. *J. Nat. Gas Chem.* **2007,** *16,* 167−172.
93. Papavasiliou, J.; Avgouropoulos, G.; Ioannides, T. *Appl. Catal. B. Environ.* **2007,** *69,* 226−234.
94. Avgouropoulos, G.; Papavasiliou, J.; Ioannides, T. *Catal. Comm.* **2008,** *9,* 1656−1660.
95. Chen, Y.-Z.; Liaw, B.-J.; Wang, J.-M.; Huang, C.-T. *Int. J. Hydrogen Energy* **2008,** *33,* 2389−2399.
96. Gómez-Cortés, A.; Márquez, Y.; Arenas-Alatorre, J.; Díaz, G. *Catal. Today* **2008,** *133−135,* 743−749.
97. Jung, C. R.; Kundu, A.; Nam, S. W.; Lee, H.-I. *Appl. Catal. B. Environ.* **2008,** *84,* 426−432.
98. Kim, K.-Y.; Han, J.; Nam, S. W.; Lim, T.-H.; Lee, H.-I. *Catal. Today* **2008,** *131,* 431−436.
99. Lee, H. C.; Kim, D. H. *Catal. Today* **2008,** *132,* 109−116.
100. Mariño, F.; Baronetti, G.; Laborde, M.; Bion, N.; Le Valant, A.; Epron, F.; Duprez, D. *Int. J. Hydrogen Energy* **2008,** *33,* 1345−1353.
101. Mariño, F.; Schönbrod, B.; Moreno, M.; Jobbágy, M.; Baronetti, G.; Laborde, M. *Catal. Today* **2008,** *133-135,* 735−742.
102. Moreno, M.; Baronetti, G. T.; Laborde, M. A.; Mariño, F. J. *Int. J. Hydrogen Energy* **2008,** *33,* 3538−3542.
103. Moretti, E.; Lenarda, M.; Storaro, L.; Talon, A.; Montanari, T.; Busca, G.; Rodríguez-Castellón, E.; Jiménez-López, A.; Turco, M.; Bagnasco, G.; Frattini, R. *Appl. Catal. A. Gen.* **2008,** *335,* 46−55.
104. Moretti, E.; Storaro, L.; Talon, A.; Patrono, P.; Pinzari, F.; Montanari, T.; Ramis, G.; Lenarda, M. *Appl. Catal. A. Gen.* **2008,** *344,* 165−174.
105. BalIkçI Derekaya, F.; Kutar, C.; Güldür, Ç *Mat. Chem. Phys.* **2009,** *115,* 496−501.
106. Gamarra, D.; Martínez-Arias, A. *J. Catal.* **2009,** *263,* 189−195.
107. Gurbani, A.; Ayastuy, J. L.; González-Marcos, M. P.; Herrero, J. E.; Guil, J. M.; Gutiérrez-Ortiz, M. A. *Int J Hydrogen Energy* **2009,** *34,* 547−553.
108. Kosmambetova, G. R.; Kriventsov, V. V.; Moroz, E. M.; Pakharukova, V. P.; Strizhak, P. E.; Zyuzin, D. A. *Nucl. Instrum. Methods Phys. Res. A. Accelerators, Spectrometers, Detectors and Associated Equipment* **2009,** *603,* 191−193.
109. Marbán, G.; López, I.; Valdés-Solís, T. *Appl. Catal. A. Gen.* **2009,** *361,* 160−169.
110. Bera, P.; Hornés, A.; Cámara, A. L.; Martínez-Arias, A. *Catal. Today* **2010,** *155,* 184−191.
111. Cruz, S.; Sanz, O.; Poyato, R.; Laguna, O. H.; Echave, F. J.; Almeida, L. C.; Centeno, M. A.; Arzamendi, G.; Gandía, L. M., et al. *Chem. Eng. J.* **2011,** *167,* 634−642.
112. Laguna, O.H.; Domínguez, M.I.; Oraá, S.; Navajas, A.; Arzamendi, G.; Gandía, L.M.; Centeno, M.A.; Montes, M.; Odriozola, J.A. *Catal. Today* **2013**, *203,* 182−187. doi: http://dx.doi.org/10.101.cattod.2012.2004.2021.
113. Laguna, O. H.; Ngassa, E. M.; Oraá, S.; Álvarez, A.; Domínguez, M. I.; Romero-Sarria, F.; Arzamendi, G.; Gandía, L. M.; Centeno, M. A.; Odriozola, J. A. *Catal. Today* **2012,** *180,* 105−110.
114. Shore, L.; Farrauto, R.J. Use of Radial Zone Coating to Facilitate a Two Stage PROX System with Single Air Injection, US Patent US2007/0028594 A1, 2007.
115. Gao, J.; Wang, Y.; Ping, Y.; Hu, D.; Xu, G.; Gu, F.; Su, F. *RSC Adv.* **2012,** *2,* 2358−2368.
116. Snel, R. *Ind. Eng. Chem. Res.* **1989,** *28,* 654−659.
117. Tada, S.; Kikuchi, R.; Urasaki, K.; Satokawa, S. *Appl. Catal. A. Gen.* **2011,** *404,* 149−154.
118. Panagiotopoulou, P.; Kondarides, D. I.; Verykios, X. E. *Appl. Catal. A. Gen.* **2008,** *344,* 45−54.
119. Dagle, R. A.; Wang, Y.; Xia, G.-G.; Strohm, J. J.; Holladay, J.; Palo, D. R. *Appl. Catal. A. Gen.* **2007,** *326,* 213−218.
120. Panagiotopoulou, P.; Kondarides, D. I.; Verykios, X. E. *Appl. Catal. B. Environ.* **2009,** *88,* 470−478.
121. Görke, O.; Pfeifer, P.; Schubert, K. *Catal. Today* **2005,** *110,* 132−139.
122. Choudhury, M. B. I.; Ahmed, S.; Shalabi, M. A.; Inui, T. *Appl. Catal. A. Gen.* **2006,** *314,* 47−53.
123. Xu, G.; Chen, X.; Zhang, Z.-G. *Chem. Eng. J.* **2006,** *121,* 97−107.
124. Chen, A.; Miyao, T.; Higashiyama, K.; Yamashita, H.; Watanabe, M. *Angewandte Chemie International Edition* **2010,** *49,* 9895−9898.
125. Eckle, S.; Anfang, H.-G.; Behm, R. J. *J. Phys. Chem. C* **2010,** *115,* 1361−1367.

126. Shore, L. Simplified Article for Carbon Monoxide Removal, US Patent 7837953 B2, 2010.
127. Gray, P. G.; Petch, M. I. *Platinum Met. Rev.* **2000,** *4,* 108–111.
128. Jiménez, V.; Sánchez, P.; Panagiotopoulou, P.; Valverde, J. L.; Romero, A. *Appl. Catal. A Gen.* **2010,** *390,* 35–44.
129. Zyryanova, M.; Snytnikov, P.; Amosov, Y.; Ven'yaminov, S.; Golosman, E.; Sobyanin, V. *Kinet. Catal.* **2010,** *51,* 907–913.
130. Seemann, M. C.; Schildhauer, T. J.; Biollaz, S. M. A. *Ind. Eng. Chem. Res.* **2010,** *49,* 7034–7038.
131. Kopyscinski, J.; Schildhauer, T. J.; Biollaz, S. M. A. *Chem. Eng. Sci.* **2011,** *66,* 924–934.
132. Kopyscinski, J.; Schildhauer, T. J.; Biollaz, S. M. A. *Ind. Eng. Chem. Res.* **2010,** *50,* 2781–2790.
133. Men, Y.; Kolb, G.; Zapf, R.; Hessel, V.; Löwe, H. *Catal. Today* **2007,** *125,* 81–87.
134. Zhao, A.; Ying, W.; Zhang, H.; Hongfang, M.; Fang, D. *J. Nat. Gas Chem.* **2012,** *21,* 170–177.
135. Choudhary, T. V.; Goodman, D. W. *J. Mol. Catal. A Chem.* **2000,** *163,* 9–18.
136. Duisberg, M.; Maier, W.F.; Kraemer, M. Metal-Doped Nickel Oxides as Catalysts for the Methanation of Carbon Monoxide, US Patent 2010/0168257 A1, 2010.
137. Eckle, S.; Augustin, M.; Anfang, H.-G.; Behm, R. J. *Catal. Today* **2012,** *181,* 40–51.
138. Urasaki, K.; Endo, K.-i.; Takahiro, T.; Kikuchi, R.; Kojima, T.; Satokawa, S. *Top. Catal.* **2010,** *53,* 707–711.
139. Dagle, R.A.; Wang, Y.; Xia, G. Selective CO Methanation Catalysis, US Patent 2007/0253893 A1, 2007.
140. Watanabe, M.; Yamashita, H.; Higashima, K.; Miyao, T.; Chen, A. Selective CO Methanation Catalyst Method of Producing the Same, and Apparatus Using the Same, US Patent 2012/0063963 A1, 2012.
141. Li, Z.; Mi, W.; Liu, S.; Su, Q. *Int. J. Hydrogen Energy* **2010,** *35,* 2820–2823.
142. Chein, R.; Chen, Y.-C.; Chen, J.-Y.; Chung, J. N. *Int. J. Hydrogen Energy* **2012,** *37,* 6562–6571.
143. Kiwi-Minsker, L.; Renken, A. *Catal. Today* **2005,** *110,* 2–14.
144. Utaka, T.; Takeguchi, T.; Kikuchi, R.; Eguchi, K. *Appl. Catal. A Gen.* **2003,** *246,* 117–124.
145. Kolb, G.; Cominos, V.; Hofmann, C.; Pennemann, H.; Schürer, J.; Tiemann, D.; Wichert, M.; Zapf, R.; Hessel, V.; Löwe, H. *Chem. Eng. Res. Des.* **2005,** *83,* 626–633.
146. Park, G.-G.; Yim, S.-D.; Yu, S.-P.; Lee, W.-G.; Yoon, Y.-G.; Um, S.; Kim, C.-S.; Eguchi, K.; Shul, Y.-G.; Hyun-Ku Rhee, I.-S. N.; Jong Moon, P. Development of a CO Remover Employing Microchannel Reactor for Polymer Electrolyte Fuel CellsStudies in Surface Science and Catalysis; Elsevier, 2006; pp 653–656.
147. Jensen, K. F. *Chem. Eng. Sci.* **2001,** *56,* 293–303.
148. Goerke, O.; Pfeifer, P.; Schubert, K. *Appl. Catal. A Gen.* **2004,** *263,* 11–18.
149. Avila, P.; Montes, M.; Miró, E. E. *Chem. Eng. J.* **2005,** *109,* 11–36.
150. Grabke, H. J.*Carburization. A High Temperature Corrosion Phenomenon;* Materials Technology Institute, 1998.
151. Grabke, H. J. *Materials and Corrosion* **1998,** *49,* 303–308.
152. Di Gabriele, F.; Bernstein, J. R.; Al-Qhatani, M. M.; Liu, Z.; Jordan, M. P.; Richardson, J. A.; Stott, F. H. *Materials and Corrosion* **2003,** *54,* 854–859.
153. Yin, R. *Oxidation of Metals* **2004,** *61,* 323–337.
154. Yin, R. C. *Mat. Sci. Eng. A* **2004,** *380,* 281–289.
155. Yin, R. *Mat. Sci. Eng. A* **2005,** *391,* 19–28.
156. Allam, I. M.; Gasem, Z. M. *Materials and Corrosion* **2007,** *58,* 245–253.
157. Grabke, H. J.; Muller-Lorenz, E. M.; Eltester, B.; Lucas, M.; Monceau, D. *Steel Res.* **1997,** *49,* 226.
158. Ramanarayanan, T. A.; Petkovic, R. A.; Mumford, J. D.; Ozekcin, A. *Materials and Corrosion* **1998,** *49,* 226–230.
159. Ganser, B.; Wynns, K. A.; Kurlekar, A. *Materials and Corrosion* **1999,** *50,* 700–705.
160. Klöwer, J. High Temperature Corrosion Behaviour of Iron Aluminides and Iron–Aluminium–Chromium Alloys. In *Oxidation of Intermetallics;* Grabke, H. J., Schütze, M., Eds.; Wiley-VCH: Berlin, 1998; pp 203–220.
161. Strauss, S.; Krajak, R.; Palm, M.; Grabke, H. J. *Materials and Corrosion* **1996,** *47,* 701–702.
162. Frías, D. M.; Nousir, S.; Barrio, I.; Montes, M.; Martínez, L. M.; Centeno, M. A.; Odriozola, J. A. *Appl. Catal. A Gen.* **2007,** *325,* 205–212.
163. Martínez, L. M.; Sanz, O.; Centeno, M. A.; Odriozola, J. A. *Chem. Eng. J.* **2010,** *162,* 1082–1090.
164. Tonkovich, A.L. Tailored and Uniform Coatings in Microchannel Apparatuts, US Patent 2005/094982 A2, 2005.
165. Yang, B.L.; Daly, F.P.; Watson, J.M.; Manzanec, T.; Fitzgerald, S.P.; Johnson, B.R.; Li, X.; Cao, C.; Chin, Y.H.; Tonkovich, A.L.; et al, Protected Alloy Surfaces in Microchannel Apparatus and Catalysts, Alumina Supported Catalysts, Catalysts Intermediates, and Methods of Forming Catalysts and Microchannel Apparatus, US Patent 2005/0271563 A1, 2005.
166. Ruettinger, W.; Ilinich, O.; Farrauto, R. J. *J. Power Sourc.* **2003,** *118,* 61–65.
167. Du, X.; Gao, D.; Yuan, Z.; Liu, N.; Zhang, C.; Wang, S. *Int. J. Hydrogen Energy* **2008,** *33,* 3710–3718.
168. Teo, J. S. K.; Teh, S. P.; Addiego, W. P.; Zhong, Z.; Borgna, A.; Truitt, R. E. *Int. J. Hydrogen Energy* **2011,** *36,* 5763–5774.
169. Casanovas, A.; de Leitenburg, C.; Trovarelli, A.; Llorca, J. *Catal. Today* **2008,** *138,* 187–192.
170. Casanovas, A.; de Leitenburg, C.; Trovarelli, A.; Llorca, J. *Chem. Eng. J.* **2009,** *154,* 267–273.
171. Xuan, J.; Leung, M. K. H.; Leung, D. Y. C.; Ni, M. *Renew. Sustain. Energy Rev.* **2009,** *13,* 1301–1313.
172. Dokupil, M.; Spitta, C.; Mathiak, J.; Beckhaus, P.; Heinzel, A. *J. Power Sourc.* **2006,** *157,* 906–913.
173. van Dijk, H. A. J.; Boon, J.; Nyqvist, R. N.; van den Brink, R. W. *Chem. Eng. J.* **2010,** *159,* 182–189.
174. Romero-Sarria, F.; Penkova, A.; Martínez T, L. M.; Centeno, M. A.; Hadjiivanov, K.; Odriozola, J. A. *Appl. Catal. B. Environ.* **2008,** *84,* 119–124.
175. Domínguez, M. I.; Romero-Sarria, F.; Centeno, M. A.; Odriozola, J. A. *Appl. Catal. B. Environ.* **2009,** *87,* 245–251.
176. Hernández, W. Y.; Romero-Sarria, F.; Centeno, M. A.; Odriozola, J. A. *J. Phys. Chem. C* **2010,** *114,* 10857–10865.
177. Laguna, O. H.; Centeno, M. A.; Boutonnet, M.; Odriozola, J. A. *Appl. Catal. B. Environ.* **2011,** *106,* 621–629.
178. Plata, J.; Márquez, A.; Sanz, J.; Avellaneda, R.; Romero-Sarria, F.; Domínguez, M.; Centeno, M. A.; Odriozola, J. A. *Top. Catal.* **2011,** *54,* 219–228.
179. Rebrov, E. V.; Berenguer-Murcia, A.; Johnson, B. F. G.; Schouten, J. C. *Catal. Today* **2008,** *138,* 210–215.
180. Qi, A.; Peppley, B.; Karan, K. *Fuel Process. Tech.* **2007,** *88,* 3–22.
181. Wang, Y. Tonkovich, A.L.Y. Catalysts Reactors and Methods of Producing Hydrogen via the Water-Gas Shift Reaction, US Patent 6652830 B2, 2003.
182. Romero, E. L.; Wilhite, B. A. *Chem. Eng. J.* **2011,** *175,* 433–442.
183. Kolb, G.; Schürer, J.; Tiemann, D.; Wichert, M.; Zapf, R.; Hessel, V.; Löwe, H. *J. Power Sourc.* **2007,** *171,* 198–204.
184. Cho, J.Y.; Choi, J.U.; Choe, J.H.; Park, K.C.; Rhee, C.H.; Bae, S.H.; Song, K.H. Micro Channel Reactor System, US Patent 2010/0015016 A1, 2010.
185. Korotkikh, O.; Farrauto, R.J.; McFarland, A. Method for Preparation of Catalytic Material for Selective Oxidation and Catalyst Members Thereof, US Patent 2003/0083196 A1, 2003.
186. Shore, L.; Farrauto, R.J. Preferential Oxidation Catalyst Containing Platinum, Copper and Iron, US Patent 2006/0276332 A1, 2006.

187. Ouyang, X.; Besser, R. S. *J. Power Sourc.* **2005,** *141,* 39−46.
188. Surangalikar, H.; Ouyang, X.; Besser, R. S. *Chem. Eng. J.* **2003,** *93,* 217−224.
189. Besser, R. S.; Shin, W. C. *J. Vac. Sc. Tech. B Microelectronics and Nanometer Structures* **2003,** *21,* 912−915.
190. Ouyang, X.; Bednarova, L.; Besser, R. S.; Ho, P. *AIChE J.* **2005,** *51,* 1758−1772.
191. Brandner, J. J.; Emig, G.; Liauw, M. A.; Schubert, K. *Chem. Eng. J.* **2004,** *101,* 217−224.
192. Snytnikov, P. V.; Potemkin, D. I.; Rebrov, E. V.; Sobyanin, V. A.; Hessel, V.; Schouten, J. C. *Chem. Eng. J.* **2010,** *160,* 923−929.
193. Potemkin, D. I.; Snytnikov, P. V.; Belyaev, V. D.; Sobyanin, V. A. *Chem. Eng. J.* **2011,** *176-177,* 165−171.
194. Arzamendi, G.; Diéguez, P. M.; Montes, M.; Centeno, M. A.; Odriozola, J. A.; Gandía, L. M. *Catal. Today* **2009,** *143,* 25−31.
195. Arzamendi, G.; Diéguez, P. M.; Montes, M.; Odriozola, J. A.; Sousa-Aguiar, E. F.; Gandía, L. M. *Chem. Eng. J.* **2009,** *154,* 168−173.
196. Arzamendi, G.; Uriz, I.; Diéguez, P. M.; Laguna, O. H.; Hernández, W. Y.; Álvarez, A.; Centeno, M. A.; Odriozola, J. A.; Montes, M.; Gandía, L. M. *Chem. Eng. J.* **2011,** *167,* 588−596.
197. Srinivas, S.; Dhingra, A.; Im, H.; Gulari, E. *Appl. Catal. A Gen.* **2004,** *274,* 285−293.
198. Kim, D. H.; Lim, M. S. *Appl. Catal. A Gen.* **2002,** *224,* 27−38.
199. van Keulen, A.N.J.; Reinkingh, J.G. Hydrogen Purification, US Patent 6403049 B1, June 2002.
200. Pollica, D.; Northrop, W.F.; Qi, C.; Hagan, M.R.; Smith, A.; Clawson, L.G. Preferential Oxidation Reactor Temperature Regulation, US Patent 2004/0037758 A1, 2004.
201. Faur Ghenciu, A. *Curr. Opin. Solid State Mat. Sci.* **2002,** *6,* 389−399.
202. Cutillo, A.; Specchia, S.; Antonini, M.; Saracco, G.; Specchia, V. *J. Power Sourc.* **2006,** *154,* 379−385.
203. De Lima, S. M.; Colman, R. C.; Jacobs, G.; Davis, B. H.; Souza, K. R.; De Lima, A. F. F.; Appel, L. G.; Mattos, L. V.; Noronha, F. B. *Catal. Today* **2009,** *146,* 110−123.
204. Men, Y.; Kolb, G.; Zapf, R.; Tiemann, D.; Wichert, M.; Hessel, V.; Löwe, H. *Int. J. Hydrogen Energy* **2008,** *33,* 1374−1382.
205. Cipitì, F.; Pino, L.; Vita, A.; Laganà, M.; Recupero, V. *Int. J. Hydrogen Energy* **2007,** *32,* 4040−4051.
206. Cipitì, F.; Pino, L.; Vita, A.; Laganà, M.; Recupero, V. *Int. J. Hydrogen Energy* **2008,** *33,* 3197−3203.
207. Cipitì, F.; Pino, L.; Vita, A.; Laganà, M.; Recupero, V. *IInt. J. Hydrogen Energy* **2009,** *34,* 4463−4474.
208. Cipitì, F.; Recupero, V. *Chem. Eng. J.* **2009,** *146,* 128−135.
209. Delsman, E. R.; de Croon, M. H. J. M.; Kramer, G. J.; Cobden, P. D.; Hofmann, C.; Cominos, V.; Schouten, J. C. *Chem. Eng. J.* **2004,** *101,* 123−131.
210. Delsman, E. R.; De Croon, M. H. J. M.; Pierik, A.; Kramer, G. J.; Cobden, P. D.; Hofmann, C.; Cominos, V.; Schouten, J. C. *Chem. Eng. Sci.* **2004,** *59,* 4795−4802.
211. Delsman, E. R.; Laarhoven, B. J. P. F.; De Croon, M. H. J. M.; Kramer, G. J.; Schouten, J. C. *Chem. Eng. Res. Des.* **2005,** *83,* 1063−1075.
212. Yoon, H. Monolith Reactor, US Patent 4378336, 1983.
213. Almeida, L. C.; Echave, F. J.; Sanz, O.; Centeno, M. A.; Odriozola, J. A.; Montes, M. *Stud. Surf. Sci. Catal.* **2010,** *175,* 25−33.
214. Komori, S.; Chen, A.; Miyao, T.; Higashima, K.; Yamashita, H.; Watanabe, M. *J. Jpn. Petrol. Inst.* **2011,** *54,* 50−51.
215. Papaioannou, E. I.; Souentie, S.; Hammad, A.; Vayenas, C. G. *Catal. Today* **2009,** *146,* 336−344.
216. Zyryanova, M. M.; Snytnikov, P. V.; Amosov, Y. I.; Kuzmin, V. A.; Kirillov, V. A.; Sobyanin, V. A. *Chem. Eng. J.* **2011,** *176−177,* 106−113.
217. Kopyscinski, J.; Schildhauer, T. J.; Vogel, F.; Biollaz, S. M. A.; Wokaun, A. *J. Catal.* **2010,** *271,* 262−279.
218. Galletti, C.; Specchia, S.; Specchia, V. *Chem. Eng. J.* **2011,** *167,* 616−621.
219. Liu, Z.; Chu, B.; Zhai, X.; Jin, Y.; Cheng, Y. *Fuel* **2012,** *95,* 599−605.

CHAPTER

11

Advances in Hydrogen Separation and Purification with Membrane Technology

Beatriz Zornoza [*], *Clara Casado* [†], *Alberto Navajas* [‡]

[*]Departamento de Ingeniería Química y Tecnologías del Medio Ambiente, Instituto de Nanociencia de Aragón, Universidad de Zaragoza, Zaragoza, Spain, [†]Departamento de Ingeniería Química y Química Inorgánica, E.T.S. Ingenieros Industriales y Telecomunicación, Universidad de Cantabria, Santander, Spain, [‡]Departamento de Química Aplicada, Universidad Pública de Navarra, Pamplona, Spain

OUTLINE

11.1 Introduction 245
11.1.1 Hydrogen Economy 245
11.1.2 Conventional Hydrogen Purification Processes 246
11.2 Membranes for Gas Separation 247
11.2.1 Performance Parameters 247
11.2.2 Hydrogen Separation Membranes: General Aspects 248
11.3 Polymeric Membranes 251
11.3.1 History of First Generation of Commercial Gas Separation Membranes 251
11.3.2 Polymer Membranes for Hydrogen Separation 252
11.4 Inorganic Membranes 253
11.4.1 Metal Membranes 254
11.4.2 Ceramic Membranes 256
11.4.3 Zeolite Membranes 256
11.5 Mixed Matrix Membranes 257
11.5.1 Factors Defining Mixed Matrix Membranes Performance 258
11.5.2 Mixed Matrix Membranes for Hydrogen Separation 259
11.6 Membrane Reactors 259
11.6.1 Membrane Reactors Design 259
11.6.2 Membrane Reactors for Hydrogen Production Processes 260
11.6.2.1 Steam Reforming 260
11.6.2.2 Water-Gas Shift 261
References 263

11.1 INTRODUCTION

11.1.1 Hydrogen Economy

The increasing demand for clean and efficient energy has resulted in an increased global willingness to embrace the so-called "hydrogen economy" as a potential long-term solution to the growing crisis. With global energy consumption predicted to nearly double by 2050, and our present fossil fuel reserves under increasingly urgent environmental, political and economic pressures, scientific and technological hurdles existing between the present state of hydrogen production, utilization and storage capabilities and those required for a competitive sustainable hydrogen economy should be overcome.[1] The hydrogen economy is a situation where hydrogen is used as the major carrier of energy. In the past few decades, the need to reduce atmospheric pollution and greenhouse gas emissions has led to the development of this concept. Although the potential of hydrogen has been known for almost two centuries, it was coal, and later petroleum, that have powered the world's engine so far.[2,3]

Nearly 2% or ~6 Exajoules ($1\ EJ = 10^{18}\ J$) of the world's primary energy is stored in the 41 millions of tons of H_2 produced industrially per year. Over 90% of this 0.85 trillion m^3/year is generated from fossil sources (mainly steam reforming of natural gas) while the remaining fraction (~8%) is produced through the electrolysis of water.[4] Many countries around the world are seriously considering the implications of a shift toward hydrogen economy. Hydrogen could help to solve one of the major challenges of the humanity, how to achieve energy independence while minimizing the environmental impact of economy activity. But before the potential for hydrogen as a future energy carrier can be realized, materials and processes have to be developed and subsequently implemented in new technology that is socially and economically acceptable. These are the key steps to the hydrogen energy transition. However, major challenges have to be met in materials development to enable cheap fuel cell technology, the production and stable supply of large quantities of hydrogen and the safe, efficient, and compact storage of the gas to give hydrogen energy a perceived advantage over oil- and coal-based energies.[5]

Proton exchange membrane fuel cells (PEMFCs) are some of the most interesting candidates to cover the necessity of new technologies that use hydrogen as fuel. PEMFCs are fueled by highly pure hydrogen, which is industrially produced as a hydrogen-rich stream mainly via steam reforming of natural gas[6,7]; it is then further purified to achieve the desired purity. Fuel cells could be one of the most promising technologies for applications in both large-scale stationary systems and small-scale portable power supplying devices.[7] In particular, PEMFCs transform the chemical energy produced by the electrochemical reaction between hydrogen and oxygen into electrical energy.

11.1.2 Conventional Hydrogen Purification Processes

Hydrogen is an attractive option as a sustainable fuel but it is mostly present in nature as a compound so it needs to be isolated or generated prior to use. These processes of generation or isolation are very energy intensive, so hydrogen production itself constitutes a major challenge for the hydrogen economy. Nowadays, hydrogen is industrially produced by steam methane reforming (SMR)[8,9] but there are more processes that can be industrially used, as water-gas shift (WGS) reaction,[10–13] and steam reforming of methanol,[14] ethanol,[15–18] bio-oil,[19] dimethyl ether,[20] glycerol (a subproduct of biodiesel industry),[17] and acetic acid.[21]

Hydrogen is typically being recovered from gas streams at refineries (from hydrocrackers), petrochemical plants (adjustment of syngas ratio, dehydrogenation), and from other streams where hydrogen is present, for example, ammonia plants. Syngas contains, in addition to H_2 and CO_2, impurities like N_2, CO_2, CH_4 and water. There may be a significant variation in the stoichiometric ratio of H_2/CO for the various chemical syntheses, and the adjustment of syngas ratio has to be performed by energy-intensive separation processes, such as pressure swing adsorption (PSA) and cryogenic systems, which are widely employed in hydrogen recovery applications over a large range of operating conditions.

PSA-based hydrogen plants have many technical advantages compared to traditional SMR technology, such as higher operating pressures/temperatures, higher hydrogen purity, and simpler operation. While PSA and fractional/cryogenic distillation systems are in commercial operation, they are generally not cost-effective and are quite energetically demanding for the separation and purification of H_2. In addition, none of these methods provides sufficient purity for the targeted applications in the hydrogen economy (such as fuel cells). Because of this, nowadays membrane-based processes are considered to be the most promising technologies for the production of high-purity hydrogen (Fig. 11.1).[6]

Therefore, to supply PEMFCs, hydrogen needs purification, and this can be carried out by means of further processes like WGS reaction, PSA and/or membrane separation. When hydrogen from reformed fuel is used

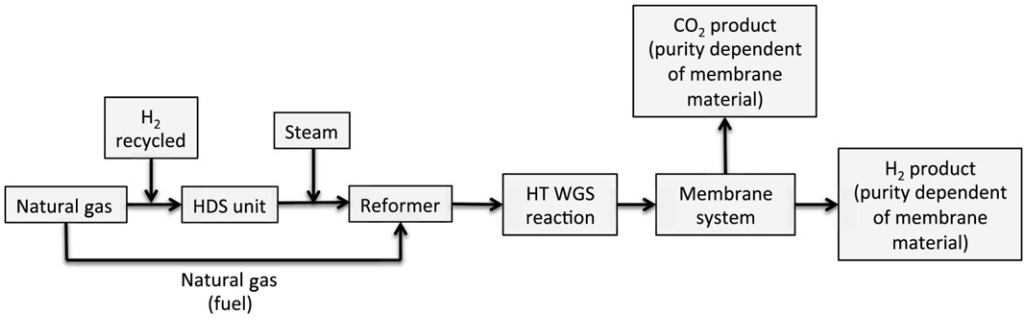

FIGURE 11.1 Hydrogen-modified production and membrane-based hydrogen purification.

in downstream catalytic process (PEMFC), the final CO concentration is well above the allowable levels (CO concentration ≈ 2 ppm for on-board vehicle applications—2007 Design Of Experiments Guidelines) due to the equilibrium-limited shift reaction.[22]

Hydrogen can also be purified via selective permeation through a membrane.[23,24] While PSA and cryogenic distillation processes are commercially available separation techniques but energy intensive,[23] membrane processes are considered to be some of the most promising techniques for the production of high-purity hydrogen.[25] In PSA systems, the gas separation mixture is subjected to high pressure (>10 MPa) in confined chambers containing molecular adsorbing beds to purify hydrogen. On the other hand, to achieve the separation, cryogenic distillation is needed to freeze the gas mixture by using the difference in gas boiling points. Membrane technology supplies a hydrogen-enriched gas mixture under pressure to one side of the membrane creating a driving force from the feed to the low pressure or permeate side. This process depends on the purity and the scale of production, but it is the preferred option, for instance, when selecting the optimal technique for hydrogen separation taking into account the conditions to which the hydrogen separation materials will be exposed to (temperature, impurities, pressure, etc.), flexibility, efficiency, cost and purity of the final product.[26] Actually, the membrane process is potentially more cost-effective, needs less energy and is simple in operation compared with the other two technologies, and with the possibility of continuous operation.

The majority of hydrogen production is used to supply the oil refining and fertilizer industries. The major applications of membranes for hydrogen separation comprise hydrogen purification, membrane reactor (MR) processes and fuel cell technology and include mainly recovery of hydrogen from hydrocarbon or ammonia streams and hydrogen composition adjustment in synthetic gases.[27]

11.2 MEMBRANES FOR GAS SEPARATION

The purification and separation stages are the most costly part of the hydrogen production processes. In order to attain the viability of the hydrogen economy, a special effort has to be done into membrane technology for hydrogen purification. As explained above, after hydrocarbons reforming and WGR, further purification steps are necessary in order to obtain the high-purity hydrogen stream required by PEMFCs. Typically, the resulting composition at the exit stream of the LT-WGS reactor is: 73.9% H_2, 17.7% CO_2, 6.9% CH_4, and 1.0% CO.[28,29]

In this context, membranes compete with the well-established processes discussed in the previous section and their industrial implementation has often been predicted due to their inherent advantages: high energy efficiency, easy intensification, simple operation, and low capital and operating costs, among other advantages.[30–33]

11.2.1 Performance Parameters

A membrane is a physical barrier allowing selective mass species transport, widely used for separation and purification in many industries.[2]

The most usual way of classification of membranes for H_2 separation is by composition: inorganic (ceramic oxides, carbon molecular sieves (CMSs), zeolites, metallic and metal alloys), purely organic materials (polymer membranes) and hybrids or composites, such as mixed matrix membranes (MMMs)[34]. Generally, metallic membranes are dense, polymeric membranes are found to be dense or porous, and inorganic membranes consist mainly of porous membranes, which, for an efficient H_2 gas separation, must be microporous ($d_p < 2$ nm).

The main role of a membrane layer is to control the transport of components between two adjacent fluid phases. The membrane action results in a fluid stream (retentate), which is depleted from some of its original components, and another fluid stream (permeate), which is concentrated in these components. The ability of a membrane to effect separation of mixtures is determined by two parameters—its permeability and selectivity. The permeability is defined as the flux (molar or volumetric flow per unit membrane area) through the membrane scaled with respect to the membrane thickness and driving force. The second important parameter is the membrane selectivity, which characterizes the ability of the membrane to separate two given molecular species, and which is, typically, defined as the ratio of the individual permeabilities for the two species. There are two more basic features that membranes have to respond to durability and mechanical strength. The relative importance of each of these requirements varies with the application. However, selectivity and permeation rate are the most basic properties of a membrane. In general, inorganic membranes favor applications under harsh temperature and chemical conditions, whereas polymeric ones have the advantage of being more economical and processable.

The basic parameters governing membrane performance are, therefore: *permeability* (P) of the gas and *selectivity* ($\alpha_{A/B}$) of one gas (A) over the other gas (B). P gives a measure of the overall inherent productivity of the membrane and is defined as the permeance Q (pressure- and area-normalized flux, N, through the membrane)

normalized by the thickness l. This parameter is commonly used with unsupported films where the selective layer thickness is well defined. The pure-gas permeability value is given by Eqn (11.1),

$$P = Q \cdot l = \frac{N \cdot l}{A \cdot \Delta p} \tag{11.1}$$

where A is the surface area of the membrane, and Δp is the driving force for separation, that is, the pressure difference across the membrane ($p_{\text{feed}} - p_{\text{permeate}}$). Units for the permeance (Q) are mol/m^2 s Pa or, more conveniently, gas permeation units (GPUs), where 1 GPU = 10^{-6} cm^3(STP)/cm^2 s cmHg, STP being standard temperature and pressure. Units for permeability (P) are usually given in mol m/m^2 s Pa or Barrer, where 1 Barrer = 10^{-10} cm^3(STP)/cm^2 s cmHg. Accordingly, a membrane with a permeability of 1 Barrer will have a permeance of 1 GPU if the thickness is 1 μm.

The pure-gas selectivity or ideal selectivity ($\alpha_{A/B}$) is an intrinsic measure of the effectiveness of a membrane to separate one individual gas, A, over another individual gas, B, in ideal conditions and is defined as follows:

$$\alpha_{A/B} = P_A/P_B = \frac{N_A \cdot (p_{\text{feed,B}} - p_{\text{permeate,B}})}{N_B \cdot (p_{\text{feed,A}} - p_{\text{permeate,A}})} \tag{11.2}$$

where P_A and P_B are the permeabilities of the gas A and gas B, respectively, N_A and N_B, the flow rate of the aforementioned gases.

However, concerning a mixture of gases instead of a pure gas going through the membrane, the partial pressure difference of the gas among the feed and the permeate is used. Therefore, mixed-gas permeability is defined as follows:

$$P_i = \frac{N \cdot x_{\text{permeate,i}} \cdot l}{A \cdot (p_{\text{feed}} \cdot x_{\text{feed,i}} - p_{\text{permeate}} \cdot x_{\text{permeate,i}})} \tag{11.3}$$

where P_i is the mixed-gas permeability coefficient of component i, and $x_{\text{feed,i}}$ and $x_{\text{permeate,i}}$ are the mole fractions of component i.

On the other hand, the mixed-gas selectivity or separation factor expresses the relative enrichment in the permeate stream with respect to the feed composition when a gas mixture is fed to the membrane system. This parameter accounts for the fact that a gas may influence the behavior of other gases in the mixture indicating the actual performance of the membrane module, what is important to meet the real gas separation mixtures for industrial requirements. It is calculated as follows:

$$\alpha_{A/B} = \frac{x_{\text{permeate,A}} \cdot (p_{\text{feed}} \cdot x_{\text{feed,B}} - p_{\text{permeate}} \cdot x_{\text{permeate,B}})}{x_{\text{permeate,B}} \cdot (p_{\text{feed}} \cdot x_{\text{feed,A}} - p_{\text{permeate}} \cdot x_{\text{permeate,A}})} \tag{11.4}$$

being x_A and x_B, in mixed-gas selectivity, the mole fractions of components A and B in the feed and permeate streams.

11.2.2 Hydrogen Separation Membranes: General Aspects

Membrane behavior is classified by the processability, maximum H_2 flux, permeability and selectivity of a given membrane material. In terms of hydrogen purification, an ideal membrane is the one that selectively separates the hydrogen from the rest of the gases (Fig. 11.2).

The separation processes can be attributed to one (or more) of the four gas separation mechanisms: (1) viscous flow (2) Knudsen flow, (3) micropore molecular sieving, (4) surface diffusion, and (5) solution-diffusion.[35]

Viscous flow takes place when there is a crack or a defect into membrane structure and gases can pass through the membrane without separation. In the Knudsen regime flow, separation depends on the inverse square root ratio of the molecular weights of species. Molecular sieving (or activated diffusion) separation is based on the much higher diffusion rates of the small molecules and it usually takes place in microporous or submicroporous systems. Adsorption capacities may be important factors for molecules with similar size. Surface diffusion occurs when there is competitive adsorption of the components of the feed mixture. Solution-diffusion regime separation is based on both solubility and mobility. The gas dissolves into the membrane material and then diffuses to the permeate side. This is the transport mechanism occuring in dense metallic and polymeric membranes are based, and it allows achieving the highest selectivities.

For hydrogen separation, ceramic (zeolites, silica, alumina…), metallic (Pd, Ta, V…), carbon, and polymer membranes have been extensively studied. In Table 11.1,[1]

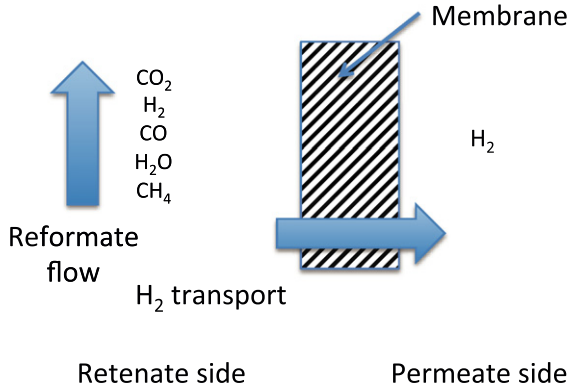

FIGURE 11.2 Hydrogen separation from methane steam reforming reaction products by membrane selective permeation. (For color version of this figure, the reader is referred to the online version of this book.)

TABLE 11.1 Comparison of Membrane Classes[1]

	Metallic: Pd, Ta, V, Nb, and alloys	**Ceramic: silica, alumina, zirconia, and zeolites**	**Carbon: porous, nanotubes**	**Polymer: polyesters, esters…**	
	Dense	**Microporous**	**Porous**	**Dense**	**Porous**
Temperature range (°C)	300−600	200−600	500−900	<100	
H_2 selectivity	>1000	5−139	4−20	Low	
H_2 flux (10^{-3} mol/m^2 s) at 1 bar					
Transport mechanism	Sol-diff.	Mol. siev.	Sol-diff., Mol. siev., Surf. Dif.	Sol-diff.	Mol. siev.
Stability issues	Phase transition	Stability in H_2O, stability in CO_2	Brittle	Swelling mechanical strength	Compaction, mechanical strength
Poisoning issues	H_2S, HCl, CO		Organic vapors	HCl, SO_x (CO_2)	
Development	Commerical (Johnson & Mattey); prototypes up to 60 cm	Tubular silica membranes up to 90 cm; other materials only small samples	Commercially, only small membrane modules for testing	Air Products, Linde, BOC, Air Liquide	

Sol-diff.: solution-diffusion, Mol. siev.: molecular sieving; surf-dif.: surface diffusion.

a comparison between the different membranes for hydrogen separation and their main features is presented.

Gas separation through polymer and metal membranes is described by the solution-diffusion mechanism. In this case, the gas molecules adsorb on the surface of the polymer, then dissolve into the bulk of the membrane material and finally diffuse across the membrane due to the chemical potential gradient from the feed to the product (permeate) stream. Figure 11.3 shows a scheme of a membrane that allows the transport of two fluids ($H_2 + CH_4$ feed) dropping down one component (H_2) against the other (CH_4) in a selective way by the action of the driving force ($p_{feed} - p_{permeate}$).

Generally, the higher the permeability, the smaller the membrane area required, thus the lower the capital cost of the membrane system. Besides, the higher the selectivity, more efficient is the process, the lower the partial pressure difference across the feed and permeate side (driving force), and then the lower operation costs of the system.

Gas transport through dense membranes can also be described by the two contributions to the flux density: (1) the solubility of the components in the membrane (sorption or solubility coefficient S), and (2) the kinetic mobility of the gaseous components through the membrane (diffusion coefficient D). The solubility (cm^3 (STP)/cm^3 cm Hg) measures the amount of gas adsorbed by the membrane when equilibrated at a given temperature and pressure.

Generally, gas solubility increases with decreasing volatility and when establishing more favorable physicochemical interactions between the gaseous components and the polymers, which in polymer membranes can be related to the fractional free volume (FFV) of the polymer. Nevertheless, the kinetic mobility increases by decreasing gas size, rising FFV, and increasing chain flexibility.[36]

Therefore, the variation in permeability and selectivity clearly indicates that the polymeric membranes based on the solution-diffusion transport mechanism are selective to certain gas molecules due to their chemical affinity, condensability and kinetic parameters, [37,38] as given in Table 11.2. It can be seen that H_2 has the lowest condensation temperature compared to those gases, indicating lower potential hydrogen solubility. In addition, hydrogen has the smallest kinetic diameters suggesting higher diffusivities.

The permeability P of a component i can be expressed as the product of the sorption and diffusion coefficients, as given by:

$$P_i = D_i \cdot S_i \tag{11.5}$$

When the permeability is defined through Eqn (11.5), the pure-gas selectivity (or ideal separation factor), $\alpha_{A/B}$, can be expressed simply by the ratio of two gases, A and B, being separated, as:

$$\alpha_{A/B} = \left[\frac{D_A}{D_B}\right] \cdot \left[\frac{S_A}{S_B}\right] = \alpha^D_{A/B} \cdot \alpha^S_{A/B} \tag{11.6}$$

where the ratio (D_A/D_B) refers to the diffusivity selectivity, $\alpha^D_{A/B}$, reflecting the difference in molecular size of the gases and the ratio (S_A/S_B) is the solubility selectivity, $\alpha^S_{A/B}$, emphasizing the preferential adsorption of some gases over the others.

Fick, in the mid-nineteenth century, and Knudsen, Barrer and James, in the mid-twentieth century, advanced in the field of permeation. The transport behavior of rubbery materials can be explained by using a simple solution-diffusion mechanism: Henry's law. Rubbery polymers do not contain any crystalline phase that could act as a complete barrier against the gas molecule. Nevertheless, gas transport through glassy polymers is more complicated, linked to the unrelaxed volume of the matrix when the materials are quenched below their glass transition temperature. In glassy

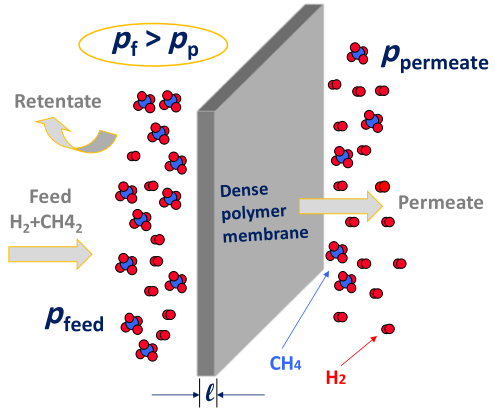

FIGURE 11.3 Scheme of a dense membrane for H_2 purification (i.e. H_2/CH_4 separation). (For color version of this figure, the reader is referred to the online version of this book.)

TABLE 11.2 Physical Properties of Gas Molecules that Influenced the Gas Transport through Membranes[134]

Gas	Normal condensation temperature (K)	Kinetic diameter (Å)
H_2	33.24	2.89
CO_2	304.21	3.30
O_2	154.6	3.46
N_2	126.2	3.64
CH_4	191.05	3.80

polymers, changes of gas permeability as a function of pressure are often dictated by the "dual-mode" model. This model was proposed by Paul and Koros as the sum of Henry''s law and Langmuir domains. In this model, the concentration of the component i, C_i, is explained in terms of Henry's law coefficient, k_D, and the sorption Langmuir parameters: the affinity constant, b, and the saturation constant (maximum sorption capacity), C'_H, as a function of the pressure p_i, as follows[39]

$$C_i = k_{D,i}p_i + \frac{C_{H,i}b_i p_i}{1 + b_i p_i} \tag{11.7}$$

11.3 POLYMERIC MEMBRANES

Polymeric membranes dominate traditional gas separations and are currently in an advanced stage of development[40] due to some main factors. First, because of their processability and low cost, they are compared with inorganic materials. Second, organic membranes in the shape of hollow fibers of flat sheets can be easily processed into hollow fiber or spiral-wound modules, being effortlessly scalable. Hollow fiber membranes are typically utilized for industrial applications due to their high surface area per unit volume. In fact, the commercial membrane technology units today are usually based on either polysulfone hollow fibers or spiral-wound cellulose acetate (CA) membranes.[41] In this sense, to compete with the aforementioned well-established conventional separation processes, ultrahigh permeance and high selective polymer membranes must be developed, that is, the membrane materials must be adapted to carry out the separation in the terms of size, shape and/or chemical properties of the gases to be separated.

The third issue is related to the stability of the membrane. An ideal membrane material must be chemically and physically stable under the usage conditions and have productivity and selectivity dictated by the volume and the process economy. Therefore, polymers for gas separation should meet different requirements: (1) good mechanical properties, (2) thermal and chemical resistance, and (3) plasticization resistance and physical aging tolerance, to ensure proper robustness and membrane lifetime.[42]

11.3.1 History of First Generation of Commercial Gas Separation Membranes

Organic polymers have a long, rich history which dated back to the 1840s with the breakthrough of nitrocellulose and vulcanization of polyisoprene (a natural rubber). It was not only until one century later when gas separation using polymer membranes became a reality in the industry. In 1961, Loeb and Sourirajan were the first to produce the concept of membrane-based gas separation with the fabrication of high-flux anisotropic membranes. Permea (now a division of Air Products), in the 1970s, successfully launched its polysulfone hollow-fiber membrane for the separation and purification of hydrogen from the purge-gas streams of ammonia plants, to adjust the hydrogen/carbon monoxide ratio in synthesis gas.[35] Later, this company developed its hydrogen-separating Prism membrane, the first large industrial application of gas separation membranes.[32] By the mid-1980s, the industrial implementation of polymer membranes broaden to other gas separations, such as hydrogen recovery from recycling refinery gas. Separex (part of UOP), Cynara (Natco) and GMS (Kvaerner) followed this high-performance membranes technology with large-surface-area membrane modules developing spiral-wound CA membranes for similar applications, including natural gas purification and dehydration.[43] Furthermore, Ube introduced a polyimide (PI) membrane with high heat- and solvent-resistance properties. At the same time, Generon, Medal and Praxair produced systems to separate nitrogen from air obtaining progressively custom polymers with O_2/N_2 selectivities of 6−8.[32] Although polymeric membranes can be used nowadays for separation of nearly all imaginable gas mixtures, large industrial applications have been found only for the following processes[32]: air separation (obtaining oxygen-enriched air or nitrogen of technical grade), hydrogen separations (separation of H_2/N_2, H_2/CH_4 and H_2/CO mixtures in refineries and petrochemical industry), separation of CO_2/CH_4 mixtures (natural gas sweetening) and CO_2/N_2 (treatment of flue gas, etc.), and vapor gas separations, which include numerous systems. In addition, although hundreds of polymers have been investigated so far, only some of them found also actual application in industrial gas separation plants, as can be seen in Table 11.3, together with the supplier company that is active in membrane gas separation. The materials are classified into rubbery and glassy polymers. The distinction is based on their temperature of formation relative to the glass transition temperature (T_g): those polymers formed at temperatures above the T_g are *rubbery*, whereas those formed below are referred to as *glassy*. Regarding gas separation performance, glassy polymers have relatively high selectivity and low flux, whereas rubbery membranes have increased flux, due to their more flexible chains, but lower selectivity. In absolute terms, both types present moderate fluxes and selectivities.[1]

TABLE 11.3 Summary of Gas Separation Mixtures and the Main Applications for the First-Generation of Commercial Polymeric Membranes[32,57,135]

Separation	Main application	Typical membranes	Supplier
Air separation (O_2/N_2)	N_2 generation O_2 enrichment	PSF	Permea (Air Products)
		PC	MG Generon (Messer)
		PI, PA	Medal (Air Liquide)
			UBE
			IMS (Praxair)
Hydrogen purification			
(H_2/HC's)	Refinery H_2 recovery	PSF	Air Products
(H_2/CO)	Syngas ratio adjustment	PI, PA	Air Liquide
(H_2/N_2)	Ammonia purge gas		Ube, Praxair
CO_2/CH_4 separation	Acid gas treating	CA, CTA	Cynara (Natco) Separex (UOP) GMS (Kvaerner)
	Enhanced oil recovery		
	Landfill gas upgrading	PSF	Air Products Ube
H_2S/HC	Sorn gas treatment	PI	
HC vapor separation		PDMS PMP	MTR GKSS Licensees
(HCs/air) (HCs from streams)	Pollution control, HC recovery Organic solvent recovery		

PSF (polysulfone), PC (polycarbonate), PI (polyimide), PA (polyaramide), CA (cellulose acetate), CTA (cellulose triacetate) and the rubbery polymers: PDMS (polydimethylsiloxane) and PMP (polymethylpentene).

11.3.2 Polymer Membranes for Hydrogen Separation

As mentioned before, the first industrially successful application of membrane gas separation system came in the 1970s for hydrogen purification. Hydrogen separation from highly supercritical gases, such as CO_2, CH_4 and N_2, is easy to accomplish due to the exceptionally high diffusion coefficient of hydrogen relative to all other molecules (except helium). Although solubility coefficient is not favorable for hydrogen, the diffusivity contribution dominates and provides overall high selectivities. An opposite scenario is attempting the separation of CO_2/H_2 mixtures by CO_2- selective membrane materials, given the difficulty to obtain high selectivity for H_2-selective polymer membranes (ref. 44). In this case the H_2 is concentrated in the retentate and the CO_2 passes through the membrane. The high flexibility provided by the ethylene oxide groups leads to weak size-sieving behavior and high diffusion coefficients contributing directly to high CO_2 permeability. Besides, a cross-linked organic–inorganic reverse-selective membrane fabricated by using functional oligomer (ED-2003) containing PEO and the epoxy-functional xilanes GOTMS (3-glycidyloxypropyltrimethoxysilane) demonstrated high CO_2 permeabilities of 367 Barrer with an attractive CO_2/H_2 selectivity of 8.95 at 3.5 atm and 35 °C.[45] In this case, although diffusion favors hydrogen permeation, competitive adsorption favors permeation of the other molecules.

There appears to be a trade-off between permeability and selectivity for polymer membranes, where a highly selective membrane tends to have low permeability and vice versa. This inverse permeability/selectivity behavior was illustrated by Robeson in 1991,[46] and updated in 2008 (ref. 47), in the graphs of the upper-bound curve beyond which a commercially attractive region can be plotted. In Fig. 11.4, the Robeson trade-off upper bound of some hydrogen gas separations (H_2/CH_4, H_2/N_2, and H_2/CO_2), including the position of some of the polymers most widely used for industrial gas separation, is depicted.

To purify hydrogen from a gaseous mixture stream, glassy polymers are generally preferred due to their effective separation based on small differences in molecular dimensions, being more size and shape selective than rubbery polymers.[33]

Glassy polymers such as PSF or PI (those most utilized for hydrogen separation as stated in Table 11.3) are a successful example of industrially applied polymers with relatively high gas permeability coefficients and separation factors coupled with excellent mechanical

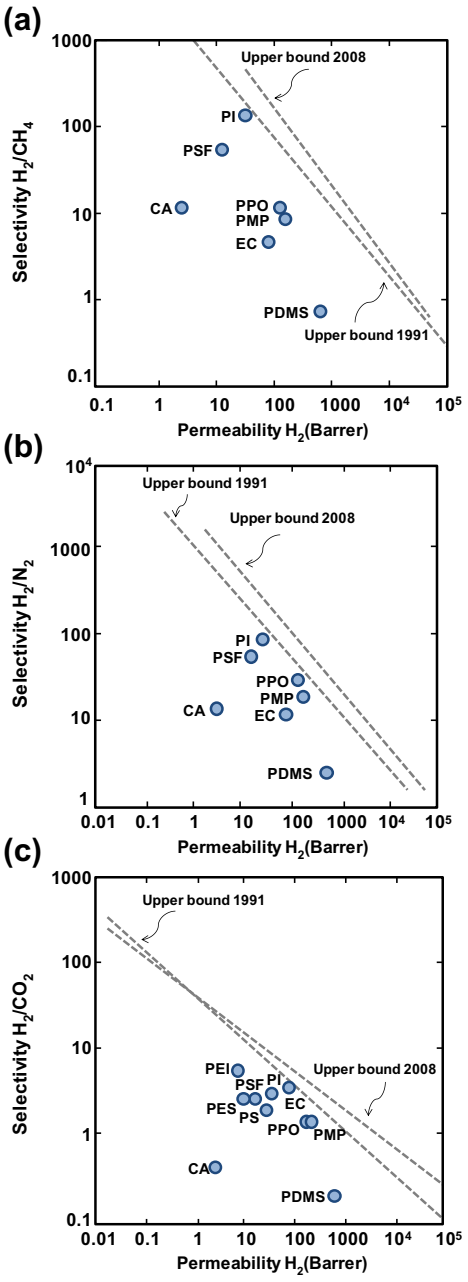

FIGURE 11.4 Robeson trade-off curves for the gas pairs: (a) H_2/CH_4, (b) H_2/N_2, and (c) H_2/CO_2,[46,47] where the permeability–selectivity pairs of different commercially used polymers are located (CA: cellulose acetate; EC: Ethyl cellulose; PDMS: polydimethylsiloxane, PI: polyimide, PMP: polymethylpentene, PPO: polyphenyleneoxide, PEI: polyetherimide, PS: polystyrene, PES: polyethersulfone, and PSF: polysulfone).[135] (For color version of this figure, the reader is referred to the online version of this book.)

properties, solubility in non-hazardous organic solvents and comercial availability.[48]

Generally, PIs are synthesized by polycondensation reactions of dianhydrides with diamines and a thermally stable polymer with good correlation between permeability and permselectivity.[49] A lab-scale membrane module, packed with more than 150 hollow fibers of P84® PI, was used for the separation of hydrogen mixtures.[48] P84® copolyimide (BTDA-TDI/MDI, 3,3′, 4,4′-benzophenone tetracarboxylic dianhydride, and 80% methylphenylene diamine + 20% methylene diamine) was reported to be one of the most selective glassy polymers with high heat resistance and excellent mechanical and chemical properties. Ideal membrane performance of H_2, N_2, CO, CO_2 and CH_4 together with H_2/N_2 and H_2/CO mixtures selectivities was tested, being the last two values of 78 and 60, respectively.

Asymmetric flat-sheet membrane composed of PI Matrimid® 5218 was developed for the separation of hydrogen from its mixtures with other gases resulting in a H_2/CH_4 selectivity higher than 100 and hydrogen permeability of 24 Barrer.[50] Besides, an asymmetric hollow fiber membrane composed of polybenzimidazole (PBI) was also reported for H_2/CO_2 separation at high temperature.[51] H_2 and CO_2 permeances showed an increment of approximately eightfold when increasing temperature from 100 to 400 °C, obtaining H_2 permeance of about 2.6 GPU and H_2/CO_2 selectivity of 27. Generally, commercial polymeric membranes have an asymmetric structure with a very thin selective layer supported on a thicker porous layer. This thin layer is responsible for higher gas fluxes through the membrane while the thick support layer allows for structural integrity.[52]

Moreover, by integration of a polymer blend constructed of the interpenetrated networks of PBI and Matrimid® by dual-layer hollow fiber spinning process, higher H_2/CO_2 ideal selectivity was achieved (6.1) than the pure constituents (3.9 using for pure Matrimid® and 3.8 for pure PBI), measured at 35 °C.[53] In addition, chemical cross-linking modification of those membranes with *p*-xylene diamine (PXDA) for a very short period of time was found effective increasing the diffusivity selectivity boosted up to about 14.5. The same research group found a H_2/CO_2 selectivity of about 26 when Matrimid/PBI (25/75 wt.%) blend membrane was cross-linked with PXDA.[27] This behavior was caused by the high-chain packing density and restrictions in the segmental mobility of polymer chains.

11.4 INORGANIC MEMBRANES

The hydrogen purification typically involves the separation of H_2 from small gas molecules, such as CO_2, CO, CH_4, H_2O and impurities such as H_2S. Physical adsorption becomes negligible at temperatures above 400 °C, thus separation is mainly based on molecular sieving and differences in molecular diffusivity.[54] Research on inorganic materials for membrane gas separation was motivated on their superior properties

regarding chemical, thermal and mechanical stability as compared to polymer membranes. However, inorganic membranes application in gas separation is limited so far. Still, interest keeps growing intermittently since novel materials are being developed for gas separation. Zeolite membranes have a very narrow pore-size distribution and ceramic membranes present robustness and relative ease of fabrication. Carbon materials are often classified as a special class of organic materials since they are prepared by pyrolysis of polymer membranes, so they offer a new concept of membranes for gas separation. Pure-metal and metal-alloy membranes offer 100% H_2 selective membrane materials via proton transport through the membrane, and proton electronic conducting membranes based on rare-earth oxides have been reported to produce rather pure H_2 from a CO_2-rich stream.[55]

The economic viability of inorganic membranes depends on the flux and selectivity as well as membrane lifetime, which is governed by the chemical and structural stability, especially in high-temperature atmospheres containing water vapor, acidic compounds and other corrosive impurities, which are the harsh conditions that could make the expensive inorganic membranes viable against the cheaper polymeric membranes.

The huge potential of inorganic membranes has led to a moderate collection of reviews appeared between 2000 and 2010 comparing the different kinds of inorganic membranes prepared for H_2 separation.[1,2,17,54,56,57] Table 11.4 collects permeation and preparation data of the most representative types of these inorganic membranes, whose advantages and drawbacks will be discussed in the following sections.

11.4.1 Metal Membranes

Dense-phase metallic or metal-alloyed membranes have attracted a great deal of attention mainly because they are commercially available, existing in various compositions and offering the possibility of large-scale production of continuous films on membrane modules, although the development of effective membranes for hydrogen separation is still limited.[2] Typically, H_2 permeates through the dense sheets or films in dissociated form, i.e. as protons, H^+, hydride ions, H^-, neutral atoms, or protons and electrons, by solution-diffusion mechanism. The selectivity to hydrogen is therefore very high since the fundamental mechanism involves the conduction of free electrons and the presence of specific catalytic surfaces to dissociate H_2 on the raw feed stream side and recombine the protons and electrons on the product side, thus preventing the passage of other molecules such as CO_2, CO, N_2 or CH_4. H_2 permeation through Pd-based membranes and alloys is usually described by Sievert's law from chemical potential of interstitial and gaseous species. Extended models based on density functional theories to consider the transition-state energies that define hops between adjacent sites have been attempted but predictions do not seem to agree with low-temperature experiments.[58]

The metal must satisfy four requirements: high hydrogen solubility, high diffusivity, catalytic activity of the surface to dissociate hydrogen molecules into atoms, and mechanical strength in a hydrogen atmosphere. The three former constitute the advantages of metallic membranes over other materials. The metals most suitable for H_2 separation membranes have high permeabilities, diffusivities or solubilities, such as tantalum, niobium, vanadium,[59] nickel,[60] which, unlike platinum and palladium, are abundant and not so expensive.

Metal membranes are commonly prepared by three methods: chemical vapor deposition (CVD),[61] physical sputtering or electroless plating, the last one being the most versatile.[2]

The transport mechanism through conventional palladium or platinum membranes for H_2 separation is a function of the underlying lattice structure and various types of lattice defects, such as vacancies, contaminant atoms, dislocations, and the reactivity of the material toward hydrogen. Thus, body centered cubic (bcc) lattices (Fe, V, Nb, Ta) provide high H_2 permeability, whereas face centered cubic lattices (Ni, Pd) show high permeation due to high solubility but low activation energy, thus total permeation is reduced due to increased hydride formation and risk of embrittlement.[1]

Hydrogen transport in metals has been long studied, and described as a series of steps: (1) external mass transfer of molecular hydrogen from the bulk of the gas phase to the vicinity of the metal surface on the high-pressure side, (2) reversible dissociative adsorption of hydrogen, (3) reversible dissolution of surface atomic hydrogen in the metal layer, (4) diffusion of atomic hydrogen inside this layer, (5) reversible movement of atomic hydrogen on the bulk metal layer to the low-pressure surface, and (6) recombinative desorption of hydrogen at the low-pressure surface. The H_2 flux is usually a function of the diffusivity coefficient of an H atom in the metal[62] and a Sievert's constant ($mol/m^3/Pa^{0.5}$) with the driving partial pressure raised to an n power that usually has a value of 0.5, approaching 1 when the process is limited by surface kinetics.[63] Palladium is usually affected by poisoning, so effort is being made in increasing the permeation flux in order to limit the importance of this phenomenon. Poisoning by H_2S, a ubiquitous contaminant present in many gas streams has been modeled as a function of thermal resistance

TABLE 11.4 Inorganic Membranes for Hydrogen Separation in the Literature

Membrane type	Preparation method	Active layer thickness (μm)	Experimental conditions		H_2 permeance (mol/m^2 s^1 Pa^1)	Ideal selectivity	Reference
			P (bar)	*T* (°C)			
Metal membranes							
Pd/Al_2O_3	MOCVD	2	1	500	0.1	1000	61
Pd/YSZ/SS	ELP	27.7	1–5	350–450	1.1×10^{-8}	100%	66
Pd/ceramic	ELP	2–5		300–400		99.5%	65
Zeolite membranes							
MFI/ceramic	Hydrothermal	3	0.1–0.4	25–300	$2–4 \times 10^{-4}$	12–278	136
MFI	Hydrothermal	3–5	1	450	1.86×10^{-7}	17.5	137
FAU	Hydrothermal, seeding-free	2.5			4.0×10^{-7}	6.5–11.1	138
Dense natural zeolite	Clinoptilolite + cement	1.2	1	500	5.2×10^{-7}	6–98	139
Ceramic membranes							
SiO_2/ceramic	Sol–gel		1	600	10^{-7}	1000	71
Co- & Ni-SiO_2	Sol–gel	0.5	0.3	500	1.8×10^{-7}	730	73
MTES–SiO_2	Sol–gel			100–200	$2.07–3.37 \times 10^{-9}$	6–24	140
$Al_{100}P_{60}O$				50	10^{-12}	16	141
SiO_2–ZrO_2	Sol–gel				10^{-6}	4.1	142
ZrO_2	Sol–gel				$2.8–3 \times 10^{-8}$	6	143
Ni–ceramic	Sol–gel			600	2.5×10^{-3}	28	72

YSZ: yttria-stabilized zirconia; MOCVD: metal organic chemical vapor deposition, ELP: electroless plating.

and long-term stability of Pd and Pd−Cu alloyed membranes.[58]

Dense palladium membranes are permeable only to hydrogen but they use expensive limited resources. Therefore, the metal membranes employed in industry up to date are made of palladium or palladium alloys. Metal membranes have been prepared using metal alloys of cheaper metals like Zr and Ni[64]; $Zr_{36}Ni_{64}$ membranes with no noble metals in their composition and similar H_2 separation performance to previous Pd membranes have been reported. Composite membranes have been largely studied by coating a Pd thin layer on the top of a commercial support as a means of reducing the Pd layer thickness without compromising the selectivity.[65] However, defects may arise upon heat treatment at temperatures of 400 °C because of the differences in thermal expansion coefficients existing between the support and active layer materials. These may be avoided by introducing intermediate layers of ceramic materials such as yttria-doped zirconia.[66]

H_2 environment usually turns the metal layer brittle. This is another reason why research is derived to develop stable materials, such as amorphous alloy membranes, that have been presented as their more economical substitutes. For example, the performance of four-membrane modules agreed with that expected from the results of a one-membrane module allowing to 82.7% recovery for a 31.7 mL (STP)/min permeation rate and 99.999% hydrogen purity in the permeate stream.[67] Alloys have been used to improve metal's physical characteristics, such as strength, durability, degradation and resistance, while maintaining a single-phase bcc structure. Another advantage of using an alloy of Pd and other metal is economical, of course. Pd and Ag alloy tubular membranes (23 wt%) of 60 μm thickness are commercialized by Johnson-Matthey for H_2/CO separation, with a CO content up to 30%, where the bulk diffusion rate is the determining step.[68] Alloying offers another way to improve the chemical resistance to poisoning by CO_2 or S-rich gas streams, which is a major problem in H_2 purification through Pd-based membranes.[58] With this purpose, especially at high temperatures, intermediate layers of thermally stable yttria-doped zirconia have also been applied.[66] Another alternative to reduce high membrane fabrication cost is the recycling of the ceramic support where the Pd layer is coated, thus avoiding the continuous purchase or fabrication of costly alumina tubular or flat supports.[69]

11.4.2 Ceramic Membranes

Ceramic membranes, mostly based on silica, are usually prepared by sol−gel or Chemical Vapor Deposition (CVD) methods. They are also promising membranes for H_2 purification because of their relatively easy fabrication, low cost of production and mechanical strength. Pore opening and shrinkage is a major issue in microporous membranes and silicon carbide membranes were studied as a means of controling the hardness of membrane material by its density and pore volume distribution.[70] The hydrogen fluxes obtained on silica-based membranes are usually higher than those traditionally obtained by metallic, carbon or zeolite membranes prepared on tubular alumina supports, mainly attributed to the small thickness of the active separation layer, which can reach values of 20−30 nm.[71]

The transport mechanism in silica-based membranes is usually molecular sieving or surface diffusion since the active separation layers possess so small pores that some authors refer to them as nonporous. This transport is usually described by the general Maxwell−Stefan model, which can be adapted to describe transient multicomponent permeation such as the real-gas stream that has to be treated in H_2 production systems.

One of the problems of the silica membranes is their instability against water. This drawback has been attempted to remove by different modification treatments, such as doping with transition metals such as nickel[72] or cobalt.[73]

The sol−gel is a versatile preparation method allowing to prepare continuous layers of other metallic oxides such as titania[74] or zirconia,[75] which are more stable in the presence of water vapor. Since the thickened sol that is deposited on the commercial support is prepared from liquid organometallic alkoxides at room temperature and pressure conditions, the morphology, tortuosity and porosity can be altered by adding functionalization agents such as organosilanes.[76]

Other ceramic membranes that have been largely studied for gas separation are carbon molecular sieve (CMS) membranes, which are often prepared by the pyrolysis of PI membranes.[77] Their major drawback is their brittleness. The stability at high temperature is necessary for hydrogen production applications. This feature has been recently improved by modifying the carbon material with mesoporous silica fillers prior to the pyrolysis treatment, obtaining higher fluxes without altering the selectivity.[78]

A novel class of ceramic membranes is protonic electronic-conducting membranes based on systems such as Nd_5LnWO_{12}, where the protons are transferred across the membrane due to chemical potential gradient with no external force applied. These have been reported to improve the stability in CO_2-rich environments, such as those encountered in IGCC processes.[79]

11.4.3 Zeolite Membranes

Zeolites are crystalline microporous aluminosilicates composed of TO_4 (T = Si, Al) building units with oxygen

atoms connecting the neighboring tetrahedrons and balanced by extraframework cations and H_2O inside the cavities. Zeolite membranes are polycrystalline thin films supported on strong rigid porous substrates of small mass transport resistance such as macroporous and mesoporous ceramic, stainless steel, and glass plates and tubes.[54] For H_2 separation, 8- or 10-member small pore zeolites are preferred because of the possibility to achieve high separation factors by activated diffusion mechanism.

Zeolite membranes have been studied for gas separations due to their molecular sized pores, adsorption properties and high thermal and chemical stabilities. Their ability to separate mixtures depends on the size and number of defects, which are intercrystalline pathways in these polycrystalline membranes that are larger than the zeolite pores and are thus nonselective. They are normally synthesized hydrothermally on a support, with Si/Al ratio varying from one to infinity. The chemical and structural stability of zeolite membranes can be modified by varying the Si/Al ratio. The Si-rich membranes such as MFI and DDR are the ones that show an acceptable performance in the presence of water vapor at temperatures above 400 °C.[54]

The orientation of the zeolite crystals in the active layer can be controlled by varying the precursor chemistry, seed layer and synthesis conditions, in order to enhance the membrane quality and reduce the presence of defects due to intercrystalline pores. By this way, very thin membranes[80] have been reported for zeolite X-supported membranes which give high fluxes. However, when these membranes were tested in the separation of ternary mixtures hydrogen/methanol/water as those encountered in methanol synthesis, H_2 permeation is usually depleted in the presence of water and methanol.[81] The stability of high silica MFI-type thin membranes in water vapor is a major issue that has been studied in the literature.[82]

Molecular layer deposition is another zeolite membrane synthesis technique to form ultrathin conformal coatings of inorganic–organic hybrid materials on a substrate,[80] in order to increase the productivity.

Transport mechanism is surface and activated diffusion, based on the competitive adsorption of the gas components in the zeolite pores and grain boundaries, since defect-free zeolite membranes are still very difficult to obtain.[83] Multicomponent mixtures have been modeled by an adsorption–diffusion model where the H_2 is the nonadsorbing component and the larger molecules such as hydrocarbons are the adsorbing ones.[54]

Recent efforts are directed to remove the non-zeolite pores by functionalization of the zeolite filling intercrystalline defects by amorphous materials such as has been done for natural zeolite membranes using cement,[84] so that only H_2 can go through the separation layer and selectivity is not lost. Another possibility that has been examined is the preparation of pure ZIF-8[85,86] and ZIF-7[87] membranes by solvothermal procedures, but the separation factors obtained or the preparation procedures still suffer from the same drawbacks as the zeolite membranes themselves.

11.5 MIXED MATRIX MEMBRANES

Attending to the limitations of pure polymer membranes to pass the upperbound trade-off curve proposed by Robeson[46,47] (Fig. 11.4), new membranes and morphologies are claimed to be developed to reach the commercially attractive region. Among the various strategies for the next generation membranes are (1) the synthesis of new polymers with improved performance, (2) the modification of the properties and structure of the existing polymers, (3) the combination of two polymers in a membrane (also called copolymer membranes), (4) preparation of polymer–molecular sieve or high-performance polymer–polymer asymmetric membranes, or (5) the preparation of mixed matrix membranes or MMMs. The latter strategy comprises embedding the properly specific "ingredients", usually nanostructured inorganic porous materials, within the polymer matrix with the aim of enhancing the permselectivity performance of the polymer. Figure 11.5 shows the scheme of the concept of a MMM.

The term "mixed matrix membrane" was introduced in 1988 by Kulprathipanja et al.[88] who propose the addition of silicates into a polymer matrix of CA, obtaining an enhancement in CO_2/H_2 selectivity from 0.77 to 5.15. MMMs have the advantage of combining the positive aspects of both phases: the superior transport properties and higher chemical and thermal stability of the inorganic fillers with the better mechanical properties, low cost and easy industrial processability of the polymers.[89] In this sense, the idea of mixing both phases, the organic and the inorganic ones, could lead to an increase in gas separation performance relative to the Robeson upperbound trade-off line,[89–91] considered as the reference frame for the improvement of membranes.

In economic terms, the price of a polymer membrane to separate gas mixtures may be around 80 €/m^2.[92] The

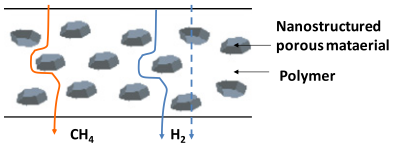

FIGURE 11.5 Mixed matrix membrane scheme comprising nanostructured porous materials and polymer as dispersed and continuous phases, respectively. (For color version of this figure, the reader is referred to the online version of this book.)

next generation of membranes for the same separations but with higher selectivity, performance could be the ones composed only by inorganic membranes. However, the price estimation of these membranes is from 10 to 1000 times higher than the equivalent polymeric ones.[32] In this regard, the estimated price for inorganic membranes was around 2500 €/m^2,[93] clearly outside of the commercial scope. Hereby, a MMMs generation with an intermediate cost position is needed, compromising, therefore, on the one hand, the price and on the other hand, the improvement in gas separation permselectivity.

The prediction of the gas transport mechanism in a MMM is essential to know the gas properties of the two constituent phases independently. In 1873, Maxwell developed a theoretical model governed by the electrical potential and the flow through the membrane. This model was later proposed to explain the gas transport through a MMM,[94] and defines the calculation of the effective permeability of an ideal MMM as follows:

$$P_{mm} = P_c\left[\frac{n\cdot P_d + (1-n)P_c - (1-n)\Phi_d(P_c - P_d)}{n\cdot P_d + (1-n)P_c + n\Phi_d(P_c - P_d)}\right] \tag{11.8}$$

where P_{mm} is the effective permeability of a gas in a MMM with a volume fraction Φ_d of the dispersed phase (d) in a continuous phase (c). P_c and P_d are, respectively, the permeabilities in the continuous and dispersed phases, and n is the shape factor of the dispersed phase that varies from 0 to 1. For spherical particles, this factor is 1/3 and the equation is known as "Maxwell model." Its mathematical expression is shown as follows:

$$P_{mm} = P_c\left[\frac{P_d + 2P_c - 2\Phi_d(P_c - P_d)}{P_d + 2P_c + \Phi_d(P_c - P_d)}\right] \tag{11.9}$$

This is the most common model in the literature and has been used by several researchers to predict the behavior of the MMMs.[95–97] It seems that the model describes well the permeability for ideal MMMs with $0 < \Phi_d < 0.2$. However, studies by Tsuru et al. proved that higher values of Φ_d produced significant deviation.[18] Furthermore, this model does not take into account either the particle size distribution or the particle shape or particle aggregation. Because of these limitations, Lewis–Nielsen model, initially applied to the elastic modulus of particulate composites, is also used:

$$P_{mm} = P_c\frac{1 + 2((\lambda_{dc} - 1)/(\lambda_{dc} + 2))\Phi_d}{1 - ((\lambda_{dc} - 1) + /(\lambda_{dc} + 2))\Phi_d\psi} \tag{11.10}$$

where

$$\psi = 1 + \left(\frac{1 - \Phi_{max}}{\Phi_{max}^2}\right)\Phi_d \tag{11.11}$$

λ_{dc} is the permeability ratio P_d/P_c and Φ_{max} is the volume fraction of maximum particles packing, being a parameter responsive to the morphology (Φ_{max} is 0.64 for a random uniform spheres packing). In addition, when Φ_{max} tends to 1 the Lewis–Nielsen model reduces to the Maxwell model. Between these two models, the former one is more attractive when using high loading rates since it covers wider range of Φ_d.[91] Petropoulos reported a comparison of various models for MMMs application.[98]

11.5.1 Factors Defining Mixed Matrix Membranes Performance

There are several important factors in the design of a successful MMM.[89] The first one is the selection of inorganic and organic phases: the appropriate filler and suitable polymer for a desired separation. Rubbery polymers, such as PDMS, have been shown to reduce the diffusion selectivity.[99] The higher mobility of their chain structures increases the diffusivity of all gaseous species. Since smaller molecules are highly movable, larger molecules benefit most from this chain mobility, which causes reductions in the diffusion selectivity. This is not a problem in glassy polymers because the low mobility of the polymer chains prevents any reduction in the diffusion selectivity.

Concerning the filler, one of the most important parameters is the pore structure, as mentioned in Section 11.4, and the particle size, related also to the desired membrane thickness. Generally, smaller particles provide larger interactions between the filler and the polymer as they present higher surface area/volume ratios, and therefore enhanced performance. Nevertheless, particle agglomeration and sedimentation can easily occur, especially at high loadings. Gaps between the phases can be created by obtaining nonselective defects in the MMM that leads to less effectiveness.

The last, but one of the most important parameters is the interaction between the polymer and the inorganic filler. In ideal MMMs, molecular adhesion of the polymer onto the solid surface and polymer flexibility during the membrane formation is required.[30] As mentioned above, the Maxwell model describes only the ideal case, the scenario in which the filler and the polymer are perfectly attached, assuming also a uniform distribution of the particles in the polymer matrix. Nevertheless, the adhesion between the phases sometimes presents a nonideal configuration what requires more complex mechanisms, taking into account not only the organic and inorganic phases but also a third phase related to the contact between them.[89,100] This interaction should be sufficient to eliminate any pinholes among the phases but not block the access to the pore surface and structure. Moore and Koros[100]

analyzed the influence of the interfacial interaction on the membrane properties. They categorized the interaction into different classes based on morphology, being the three more important: "sieve-in-a-cage-morphology" (the interfacial voids are larger than the penetrating molecules, so a by-pass around the particles is produced enhancing the permeability and reducing the selectivity), "leaky interface morphology" (the voids are of molecular scale providing an extra free volume with small decrease in selectivity and increase in permeability), and "matrix rigidification morphology" (where the reduction in free volume takes place near the particle surface, obtaining then lower permeability with an increase in selectivity).[89,100]

11.5.2 Mixed Matrix Membranes for Hydrogen Separation

Many polymers have been modified with the incorporation of inorganic fillers, such as zeolites,[101] porous titanosilicates,[102] ordered mesoporous silica,[101] nonporous silica,[40] CMSs,[103] and carbon nanotubes,[104] among others, to produce MMMs displaying gas separation performances that overpass the pure polymer.

Several reviews have been published studying the performance of MMMs for gas separation where the future direction and perspectives for further investigations, development and applications are included.[89,105,106] Going into detail, for instance, by adding loadings up to 38 vol.% of CMSs in polyeterimide Ultem® and PI Matrimid®, an enhancement of 45% in CO_2/CH_4 selectivity and 200% in CO_2 permeability was reached, postulating a polymer matrix rigidification phenomenon.[103] Another example of improving permselectivity performance over the pure polymer was using 10 vol.% of zeolite HSSZ-13 previously modified with a Grignard reagent, also in Ultem®. These membranes revealed an increase in CO_2/CH_4 selectivity of 25%, obtaining similar results or exceeded the theoretical Maxwell model.[107] In addition, 4–8 wt.% of hollow zeolite spheres embedded in polysulfone Udel® or PI Matrimid® matrix led to CO_2/N_2 and O_2/N_2 selectivity improvements of 35–50%. The spherical sieve structure minimizes agglomeration and hence improves dispersion and interaction with the polymer phase.[101]

Particular to hydrogen separation, some of the MMMs have already been used for that purpose. For instance, by incorporating 40 wt.% of zeolite 3A into polysulfone matrix, an enhancement of H_2/CO_2 selectivity from 1.53 for the bare polymer to 3.57 was found.[108] In those membranes, aminopropyltrimethoxylane was used as coupling agent to covalently link the zeolite particles with acrylate-modified polymer resulting in defect-free membranes. Moreover, adding 8 wt.% of ordered mesoporous silica spheres of 2–4 μm in diameter resulted in a selective membrane with an increase in H_2/CH_4 selectivity of 35 and 25%, for polysulfone and PI as a continuous phase, respectively.[109] Also, incorporating 4 wt.% of high aspect ratio delaminated titanosilicate UZAR-S1 to polysulfone, a similar enhancement was reached.[102]

In recent years, the research trend in MMMs has shift toward the utilization of metal-organic frameworks (MOFs), materials with extremely higher surface area and pore volume compared to zeolites used in MMMs. In those materials, the combination of organic and inorganic building blocks offers an almost infinite number of structures, high pore size and shape flexibility, and high potential of functionalization. Recently, MOF–MMMs have experienced a rapid growth[101,110] and the first example of industrial application is expected in the near future.[111] A detailed review on MOF-based MMMs can be found elsewhere.[112]

Regarding MOF–MMMs for hydrogen purification, hollow fiber MMMs of $Cu_3(BTC)_2$ and Matrimid® matrices have been developed for H_2/N_2, H_2/CO_2 and H_2/CH_4 separations.[113] In those membranes, SEM images revealed plastic deformation of the polymer matrix due to the strong affinity between the phases. An increase in H_2 permeance and selectivity with respect to the other gases, by 45% the permeance and two- to threefold the ideal selectivity when compared for pure PI membranes was reported. In addition, ZIF-8/Matrimid® MMMs were also fabricated for H_2/O_2, H_2/CO_2, and H_2/CH_4, among others.[114] Large improvements in the ideal selectivity at 40 wt.% loading along with a decrease at loadings higher than 50–60 wt.% due to MOF aggregation were reported. Besides, the incorporation of ZIF-7 into PBI polymer was also studied.[86] MMMs with ZIF-7 loadings as high as 50 wt % enhanced H_2 permeability without compromising the H_2/CO_2 selectivity compared to pure PBI membranes even at elevated temperatures (up to 180 °C).

11.6 MEMBRANE REACTORS

11.6.1 Membrane Reactors Design

Membrane-based reactive separation processes (also known as MR processes) are attracting attention in catalytic reactor applications. In these reactor systems, the membrane separation process is coupled with a catalytic reaction.

In the early stages of the MRs, engineers chose the simplest structure for the system (Fig. 11.6(a)), a membrane coupled just after the reactor in order to separate the target products. Reactants A and B enter into the reactor. Not converted reactants A and B exit

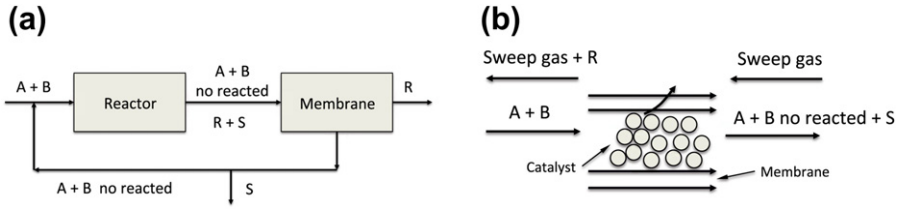

FIGURE 11.6 Membrane reactor configurations (a) separated and (b) coupled membrane and reactor.

with products R (aimed product) and S. Membrane purifies the exit reactor stream and produces a pure stream of R. But the evolution of the concept brought to the MR configuration is shown in Fig. 11.6(b). It is a single unit with the catalyst within the membrane. A and B react and R permeates at the same time through the membrane.

Many researchers have been working on MRs development and there are some reviews on the subject.[34,115–117] Main advantages of MRs compared with conventional reactors are that they allow to circumvent thermodynamic limitations of an equilibrium-controlled process and to operate at lower temperatures. In addition, lower operating temperatures reduce material cost as well as increase operation safety.

11.6.2 Membrane Reactors for Hydrogen Production Processes

In MRs, H_2 can be selectively removed from the reaction system and the thermodynamic equilibrium of hydrogen production reactions shifted to the products side, which allows obtaining higher conversion even at lower operating temperatures. The use of MRs makes possible to achieve: (1) higher conversion than traditional reactors working under the same operating conditions or (2) the same conversion as a conventional reactor, but working under milder operating conditions.[118] Finally, MRs simplify the process and reduce capital costs in order to produce hydrogen from hydrocarbons reforming for use in PEMFCs. In this regard, MRs could be applied in steam reforming and WGS reactions, as discussed in the following sections.

11.6.2.1 Steam Reforming

A membrane reformer is considered as a new type of reactor allowing both separation and reformer of hydrogen in only one unit. Ideally, a membrane with infinite hydrogen permselectivity would make unnecessary the WGS reactor and subsequent CO removal steps.

Although conventional polymeric and carbon membranes were not recommended due to the high temperaturas typical of steam reformers, research on the development of more robust materials continues, as has been outlined above. For this reason, dense metallic membranes and microporous membranes have been mainly considered for use in MRs because of their higher resistance at harsh conditions.

11.6.2.1.1 DENSE METALLIC MEMBRANES

There are a number of reviews on metallic and dense membranes for MRs.[6,8,119,120] Palladium is the most used material in membrane construction for hydrogen separation due to its selectivity. But pure Pd membranes have some drawbacks (hydrogen embrittlement,[121] CO and sulfur compounds poisoning) that together with Pd elevated prize, have limited their utilization, as stated in Section 11.4.1.[120] In order to apply dense membranes in MRs, the amount of metal used should be decreased by fabricating a film as thin as possible. Also, alloying Pd with Ag or Cu could minimize embrittlement effect. Porous alumina, zeolite, SiO_2, porous glass, and stainless steel have been used for many researchers for supporting thin palladium films. Table 11.5 shows the main published works on Pd films MRs for methane steam reforming and the results obtained. Generally, MRs increase CH_4 conversion by equilibrium shifting and reduce the temperature of reformer reactor.

Besides CH_4, alcohols, acetic acid, glycerol, etc. have been reformed using Pd MRs showing good performance. Some of these compounds have been obtained from renewable materials and not from fossil sources, contributing by this way to a sustainable hydrogen economy. Table 11.6 compiles some of these works. Iulianelli et al.[17] have recently published a review about the use of ethanol and bioethanol in steam reforming MRs.

There are some industrial plants for hydrogen production that use palladium MRs. De Falco et al.[8] have built up a hydrogen production plant by SMR by placing the palladium membrane outside the reactor. This configuration was chosen because it had been demonstrated that Pd membranes are not stable at temperatures above 500 °C. This limits the reaction temperature in MR. Kikuchi[9] described a membrane reformer used by Tokyo Gas and Mitsubishi Heavy Industries to produce hydrogen at large scale. They used Pd over glass porous supports membranes.

Besides, some papers described automotive applications of Pd MRs. Uemiya[120] described a demonstrative study of membrane reformer using town gas as a fuel for a hydrogen supply station for fuel cell vehicles. The membrane used was also Pd over porous support. Han et al.[122] described a methanol steam reforming

TABLE 11.5 Methane Conversion for Methane Steam Reforming Reaction with Palladium Membrane Reactors[8]

Membrane	T [°C]	$P_{reaction}$ [bar]	MR conversion [%]	Conventional reactor conversion [%]	References
Pd-SS	500	20.0 9.0	85 40	– 20	144
Pd/Al_2O_3	550	9.0	99	27	145
Pd/Al_2O_3	500–550	9.0	≈100	–	145
Pd dense	550	8.7	73.1	–	146
Pd-SS	550	1.0	90	50	147
Pd dense	600	2.0	97.8	77.7	148
Pd/25% Ag-Al_2O_3	150 300	1.0	15.4 16.5	12.7 16.5	149
Pd-SS	527	3.0	100	50	150
Pd-based	650	2.0–4.0	97	–	151

MR designed for a vehicle. They used a Pd–Cu dense membrane.

11.6.2.1.2 CERAMIC MEMBRANES

Lukyanov et al.[22] claimed that one of the main drawbacks of the known catalytic membranes for hydrogen production is their short operation lifetime. While reforming catalysts can operate for more than 1000 h, the best Pd membranes exhibit stable operation during several hundreds of hours. Furthermore, these membranes show insufficient mechanical strength and high cost.

Pd membranes have been researched for well over 50 years; in comparison, developments in molecular sieve silica (MSS) membranes are far more recent.[2] These ceramic materials are mechanically stable under thermal stresses up to 600 °C, but selectivities are generally lower than Pd, ranging from 9 to 1500. The main drawback of silica membranes is the water influence into their permeability and selectivity. Recently, researches have proposed material functionalization making hydrothermally stable membranes. Table 11.7 shows a short summary of studies using silica and ceramic membranes into methane steam reforming MRs. Ceramic membrane reactors improve methane conversions compared with conventional reactors but not as much as Pd membranes because of their lower hydrogen selectivities. Nevertheless, ceramic membranes (mainly SiO_2 membranes) offer high resistance and durability in thermal and chemical harsh conditions.

11.6.2.2 Water-Gas Shift

As explained before, WGS reaction is one of the most important processes in order to obtain pure hydrogen for PEMFCs. In addition, biomass gasification produces

TABLE 11.6 Steam Reforming of Bioethanol, Methanol, Glycerol and Acetic Acid with Palladium Membrane Reactors

H_2 source	Membrane	T [°C]	$P_{reaction}$ [bar]	MR conversion [%]	Conventional reactor conversion [%]	References
Bioethanol	Pd–SS	400	8.0–12.0	94	–	152
Bioethanol	Dense Pd–Ag	400	1.5	95	30	153
Bioethanol	Dense Pd–Ag	400	3.0	100	65	153
Methanol	Pd/23% Ag–Cu/ZnO	280	–	95	–	154
Methanol	$Pd/Ag–TiO_2/Al_2O_3$	450	–	100	–	155
Methanol	Pd–SS	350	12	100	–	156
Glycerol	Dense Pd/Ag	400	5.0	60	42	17
Acetic Acid	Dense Pd/Ag	400	4.0	100	–	157
Butane	Pd–Ag/SS	600	8.0	70	45	158

TABLE 11.7 Methane Conversion for Methane Steam Reforming Reaction in Ceramic Membrane Reactors

Membrane	T [°C]	$P_{reaction}$ [bar]	MR conversion [%]	Conventional reactor conversion [%]	References
$SiO_2-Al_2O_3$	500	1	70	44	159
SiO_2	750	–	86	–	160
$Al_2O_3/SiO_2/ZrO$	450–500	6	50	30	161
SiO_2	500	1	80	44	162
$SiO_2-Al_2O_3$	550	–	50	45	163

syngas that usually is converted into highly purified H_2 stream by WGS reaction. Conventionally, as the reforming reaction, the WGS reaction is limited by thermodynamic constrains. Therefore, conversion is limited but using MRs, it can be increased. In these reactors, hydrogen is separated, at the same time, the reaction takes place shifting it to the products side. Obviously, CO_2-selective membranes also allow shifting the WGS reaction. Huang et al.[123] have been working in the use of polymeric membranes to separate CO_2.

The CO conversion into H_2 requires lower temperatures than reforming reactions and because of this, many materials as metals and ceramics, and also carbon and polymers can be used as membrane into MRs. As a result, many studies have been devoted to the WGS MR development. Main results have been recently reviewed by Babita et al.[124] and Lu et al.[2]

11.6.2.2.1 METALLIC DENSE MEMBRANES

Palladium membranes have been extensively used in WGS MRs. Recently, Mendes et al.[118] and De Falco et al.[8] have reviewed these works. Table 11.8 includes some of the most relevant works with Pd membranes used in WGS MRs. Special interest has to be paid to the Brunetti et al. study,[125] where a WGS reactor with dense Pd–Ag membranes was coupled directly to a PEMFCs in order to produce electricity.

11.6.2.2.2 CERAMIC AND CARBON MEMBRANES

Palladium membranes have been extensively studied for WGS reactions; they provide 100% permselectivity to hydrogen though often suffer from steam embitterment and H_2S poisoning. Recent improvements in porous silica membrane's hydrostability, selectivity, and H_2 flux, have created new interest in their use for MR in the WGS field. The main drawback of MSS membranes is their hydrophilic nature of silica that leads to pore blocking and degradation of the membrane's selectivity. Battersby et al.[126] doped MSS with metal and achieved high selectivity and hydrostability for WGS MRs. Silica could be supported on alumina,[127] or zeolite.[128] Table 11.9 includes some of the works made on MSS for WGS MRs. MR conversions suggest that their use could be an option instead of the more expensive and less durable palladium membranes.

On the other hand, Abdollahi et al.[129] have recently developed a CMS membrane tested into a WGS MR with simulated syngas (containing NH_3 and H_2S) from biomass gasification. These common impurities of syngas from biomass gasification are known to adversely

TABLE 11.8 CO Conversion Data for Water-Gas Shift Reaction in Palladium Membrane Reactors[8]

Membrane	T [°C]	$P_{reaction}$ [bar]	MR conversion [%]	Conventional reactor conversion [%]	References
Pd/Vycor	400	1.0	92	76	164
Pd/γ-Al_2O_3	320	1.1	100	84	165
Pd/porous glass	400	1.0	98	75	166
Pd/SS	380	1.0	61	–	10
Dense Pd–Ag	290	1.0–6.0	75	–	125
Pd/ceramic	350	1.2	95	90	167
Pd–Ag/Al_2O_3	300	1.0	≈100	91	118
Pd/Al_2O_3	300	4.46	≈100	88	168

TABLE 11.9 CO Conversion Data for Water Gas Shift Reaction in Ceramic and Carbon Membrane Reactors

Membrane	T [°C]	$P_{reaction}$ [bar]	MR conversion [%]	Conventional reactor conversion [%]	References
SiO_2/SS	200–290	6.0	95	8	169
Hydrophobic SiO_2/Al_2O_3	290	–	99	90	127
Doped SiO_2/Al_2O_3	150–250	2.5	95	–	126
SiO_2/zeolite/Al_2O_3	550	–	81.7	62.5	128
Silicalite/Al_2O_3	500	–	75	–	170
CMS	300	3.0	90	70	129

affect Pd membranes, even at parts per million concentration levels. WGS MRs with CMR membranes and $Co/Mo/Al_2O_3$ catalyst show satisfactory stability in presence of impurities and deliver higher CO conversion and hydrogen purity than a conventional reactor.

Finally, a new concept of adsorbent-membrane reactor (HAMR) has been used during the last years by some researchers in order to separate and adsorb hydrogen and CO_2, respectively, in the WGS reactor. For example, Harale et al.[130] used a commercial hydrotalcite as adsorbent for the CO_2, and a nanoporous H_2-selective CMS membrane. Recently, a new study of this group[131] has demonstrated that the HAMR system is capable of delivering a hydrogen stream, which is ready for use in PEMFCs without the need for any additional downstream processing.

In conclusion, in the field of hydrogen production, the use of MRs has demonstrated to have great potential in order to reduce costs because they can eliminate successive steps of purification, decrease the energy consumed, and improve the hydrocarbon conversion (steam reforming reaction) or CO conversion (WGS reaction). According with Lu et al.,[2] catalytic membranes can be easily integrated with existing industrial plants but there is a lack of economic studies in this regard.[118] However, a few existing economic studies reiterate the importance of limiting the noble metal thickness on the membrane support when dense metals are used and the use of alternative membrane materials.[124] A complete economic study is very difficult because in the case of MR integration into hydrogen production for PEMFCs, should be considered many factors: the reactor configuration, catalyst and membrane performance, their lifetime and hydrogen purity, among others.

The lack of economic studies is partly due to the fact that MR technology is not still developed and there are some drawbacks that should be overcome before its implementation at larger scales. These drawbacks are related mainly with their durability, permeabilities and selectivities. Although a strong effort has been done during the last years in order to overcome these difficulties, the areas of high-temperature sealing and scaling-up have been neglected and should be studied more deeply.[132,133]

In the framework of a sustainable development of hydrogen economy, the following perspective on hydrogen MRs can be established:

- Although a strong effort has been done in the past to develop pilot plants of MRs, the scale-up of hydrogen membrane technologies is one of the most challenging and important tasks for future work.
- Cheaper and more durable membranes than that based on pure palladium have to be developed for MRs. MSS and CMS membranes are good candidates, but more research has to be done.
- In order to develop MRs for WGS reactors that process syngas from biomass gasification into pure hydrogen streams, more research has to be done to study the influence of some impurities as Hg, As, CN, etc.

References

1. Ockwig, N. W.; Nenoff, T. M. Membranes for Hydrogen Separation. *Chem. Rev.* **2007,** *107,* 4078–4110.
2. Lu, G. Q.; da Costa, J. C. D.; Duke, M.; Giessler, S.; Socolow, R.; Williams, R. H.; Kreutz, T. Inorganic Membranes for Hydrogen Production and Purification: A Critical Review and Perspective. *J. Colloid Interf. Sci.* **2007,** *314,* 589–603.
3. Bergh, J.v.d.; Tihaya, A.; Kapteijn, F. High Temperature Permeation and Separation Characteristics of an All-Silica DDR Zeolite Membrane. *Micropor. Mesopor. Mater.* **2010,** *132,* 137–147.
4. Palo, D. R.; Dagle, R. A.; Holladay, J. D. Methanol Steam Reforming for Hydrogen Production. *Chem. Rev.* **2007,** *107,* 3992–4021.
5. Mandal, T. K.; Gregory, D. H. Hydrogen: Future Energy Vector for Sustainable Development. *J. Mechanical Eng. Sci.* **2010,** *224.*
6. Barelli, L.; Bidini, G.; Gallorini, F.; Servili, S. Hydrogen Production through Sorption-Enhanced Steam Methane Reforming and Membrane Technology: A Review. *Energy* **2008,** *33,* 554–570.
7. Mulder, M. M. *Basic Principles of Membrane Technology,* 2nd ed. Kluwer Academic: Dordrecht, 1996.
8. De Falco, M.; Marrelli, L.; Iaquaniello, G. *Membrane Reactors for Hydrogen Production Processes;* Springer, 2011.

9. Kikuchi, E. Membrane Reactor Application to Hydrogen Production. *Catal. Today* **2000,** *56,* 97–101.
10. Sanchez, J. M.; Barreiro, M. M.; Marono, M. Hydrogen Enrichment and Separation from Synthesis Gas by the Use of a Membrane Reactor. *Biomass Bioenerg.* **2011,** *35,* 132–S144.
11. Tanksale, A.; Beltramini, J. N.; Lu, G. Q. M. A Review of Catalytic Hydrogen Production Processes from Biomass. *Renew. Sust. Energ. Rev.* **2010,** *14.*
12. Zhang, R. Q.; Brown, R. C.; Suby, A. Thermochemical Generation of Hydrogen from Switchgrass. *Energ. Fuel.* **2004,** *18,* 251–256.
13. Zhang, R. Q.; Cummer, K.; Suby, A.; Brown, R. C. Biomass-Derived Hydrogen from an Air-Blown Gasifier. *Fuel Proc. Technol.* **2005,** *86,* 861–874.
14. Sa, S.; Silva, H.; Brandao, L.; Sousa, J. M.; Mendes, A. Catalysts for Methanol Steam Reforming-A Review. *Appl. Catal. B-environ.* **2010,** *99,* 43–57.
15. Benito, M.; Sanz, J. L.; Isabel, R.; Padilla, R.; Arjona, R.; Daza, L. Bio-ethanol Steam Reforming: Insights on the Mechanism for Hydrogen Production. *J. Power Sources* **2005,** *151,* 11–17.
16. Dolgykh, L.; Stolyarchuk, I.; Deynega, I.; Strizhak, P. The Use of Industrial Dehydrogenation Catalysts for Hydrogen Production from Bioethanol. *Int. J. Hydrogen Energ* **2006,** *31,* 1607–1610.
17. Iulianelli, A.; Basile, A. Hydrogen Production from Ethanol via Inorganic Membrane Reactors Technology: A Review. *Catal. Sci. Technol.* **2011,** *1,* 366–379.
18. Tsuru, T.; Morita, T.; Shintani, H.; Yoshioka, T.; Asaeda, M. Membrane Reactor Performance of Steam Reforming of Methane Using Hydrogen Permselective Catalytic SiO_2 Membranes. *J. Membr. Sci.* **2008,** *316,* 53–62.
19. Czernik, S.; Evans, R.; French, R. Hydrogen from Biomass-Production by Steam Reforming of Biomass Pyrolysis Oil. *Catal. Today* **2007,** *129,* 265–268.
20. Gazsi, A.; Ugrai, I.; Solymosi, F. Production of Hydrogen from Dimethyl Ether on Supported Au Catalysts. *Appl. Catal. A: Gen.* **2011,** *391,* 360–366.
21. Thaicharoensutcharittham, S.; Meeyoo, V.; Kitiyanan, B.; Rangsunvigit, P.; Rirksomboon, T. Hydrogen Production by Steam Reforming of Acetic Acid Over Ni-Based Catalysts. *Catal. Today* **2011,** *164,* 257–261.
22. Lukyanov, B. N.; Andreev, D. V.; Parmon, V. N. Catalytic Reactors with Hydrogen Membrane Separation. *Chem. Eng. J.* **2009,** *154,* 258–266.
23. Sircar, S.; Rao, M. B. Nanoporous Carbon Membranes for Gas Separation. *Membr. Sci. Technol.* **2000,** *6,* 473–496.
24. Adhikari, S.; Fernando, S. Hydrogen Membrane Separation Techniques. *Ind. Eng. Chem. Res.* **2006,** *45,* 875–881.
25. Cheng, Y. S.; Peña, M. A.; Fierro, J. L.; Hui, D. C. W.; Yeung, K. L. Performance of Alumina, Zeolite, Palladium, Pd-Ag Alloy Membranes for Hydrogen Separation from Towngas Mixture. *J. Membr. Sci.* **2002,** *204,* 329–340.
26. Phair, J. W.; Badwal, S. P. S. Review of Proton Conductors for Hydrogen Separation. *Ionics* **2006,** *12,* 103–115.
27. Hosseini, S. S.; Teoh, M. M.; Chung, T. S. Hydrogen Separation and Purification in Membranes of Miscible Polymer Blends with Interpenetrating Networks. *Polymer* **2008,** *49,* 1594–1603.
28. Molburg, J.C.; Doctor, R.D. Hydrogen from Steam-Methane Reforming with CO_2 Capture In *20th Annual International Pittsburg Coal Conference*, Pittsburg, PA, 2003.
29. Ockwig, N. W.; Nenoff, T. M. Erratum: Membranes for Hydrogen Separation (Chemical Reviews (2007) 107, 4078). *Chem. Rev.* **2010,** *110,* 2573.
30. Koros, W. J.; Mahajan, R. Pushing the Limits on Possibilities for Large Scale Gas Separation: Which Strategies? *J. Membr. Sci.* **2000,** *175,* 181–196.
31. Fawas, E. P.; Kapantaidakis, G. C.; Nolan, J. W.; Mitropoulos, A. C.; Kanellopoulos, N. K. Preparation, Characterization and Gas Permeation Properties of Carbon Hollow Fiber Membranes Based on Matrimid (R) 5218 Precursor. *J. Mater. Process. Tech.* **2007,** *186,* 102–110.
32. Baker, R. W. Future Directions of Membrane Gas Separation Technology. *Ind. Eng. Chem. Res.* **2002,** *41,* 1393–1411.
33. Stern, S. A. Polymers for Gas Separations: The Next Decade. *J. Membr. Sci.* **1994,** *94,* 1–65.
34. Sanchez Marcano, J. G.; Tsotsis, T. T. *Catalytic Membranes and Membrane Reactors;* Wiley-VCH, 2002.
35. Koros, W. J.; Fleming, G. K. Membrane-Based Gas Separation. *J. Membr. Sci.* **1993,** *83,* 1–80.
36. Freeman, B. D. Basis of Permeability/Selectivity Tradeoff Relations in Polymeric Gas Separation Membranes. *Macromolecules* **1999,** *32,* 375–380.
37. Weller, S.; Steiner, W. A. Separation of Gases by Fractional Permeation through Membranes. *J. Appl. Phys.* **1950,** *21,* 279–283.
38. Park, H. B.; Lee, Y. M. Polymeric Membrane Materials and Potential Use in Gas Separation. *In Advanced Membrane Technology and Applications;* John Wiley & Sons, Inc, 2008; Chapter 12.
39. Koros, W. J.; Chern, R. T. Separation of Gaseous Mixtures Using Polymer Membranes. In *Handbook of Separation Process Technology;* Rousseau, R. W., Ed.; John Wiley and Sons: New York, 1987.
40. Merkel, T. C.; Freeman, B. D.; Spontak, R. J.; He, Z.; Pinnau, I.; Meakin, P.; Hill, A. J. Ultrapermeable, Reversible-Selective Nanocomposite Membranes. *Science* **2002,** *296,* 519–522.
41. Hägg, M.-B. Membranes in Gas Separation. In *Handbook of membrane separations;* CRC Press, Taylor & Francis: NW, USA, 2009; pp. 65–103.
42. Powell, C. E.; Qiao, G. G. Polymeric CO_2/N_2 Gas Separation Membranes for the Capture of Carbon dioxide from Power Plant Flue Gases. *J. Membr. Sci.* **2006,** *279,* 1–49.
43. Schell, W. J. Commercial Applications for Gas Permeation Membrane Systems. *J. Membr. Sci.* **1985,** *22,* 217–224.
44. Lin, H. Q.; Van Wagner, E.; Freeman, B. D.; Toy, L. G.; Gupta, R. P. Plasticization-Enhanced Hydrogen Purification Using Polymeric Membranes. *Science* **2006,** *311,* 639–642.
45. Lu, S.; Tai-Shung, C. In situ Fabrication of Cross-Linked PEO/Silica Reverse-Selective Membranes for Hydrogen Purification. *Int. J. Hydrogen Energy* **2009,** *34.*
46. Robeson, L. M. Correlation of Separation Factor versus Permeability for Polymeric Membranes. *J. Membr. Sci.* **1991,** *62,* 165–185.
47. Robeson, L. M. The Upper Bound Revisited. *J. Membr. Sci.* **2008,** *320,* 390–400.
48. Choi, S.-H.; Brunetti, A.; Drioli, E.; Barbieri, G. H_2 Separation from H_2/N_2 and H_2/CO Mixtures with Co-Polyimide Hollow Fiber Module. *Sep. Sci. Technol.* **2011,** *46,* 1–13.
49. Kapantaidakis, G. C.; Koops, G. H. High Flux Polyethersulfone-Polyimide Blend Hollow Fiber Membranes for Gas Separation. *J. Membr. Sci.* **2002,** *204,* 153–171.
50. Shishatskiy, S.; Nistor, C.; Popa, M.; Nunes, S. P.; Peinemann, K. V. Polyimide Asymmetric Membranes for Hydrogen Separation: Influence of Formation Conditions on Gas Transport Properties. *Adv. Eng. Mater.* **2006,** *8,* 390–397.
51. Kumbharkar, S. C.; Liu, Y.; Li, K. High Performance Polybenzimidazole Based Asymmetric Hollow Fibre Membranes for H_2/CO_2 Separation. *J. Membr. Sci.* **2011,** *375,* 231–240.
52. Iarikov, D.; Ted Oyama, S. Review of CO_2/CH_4 Separation Membranes*Membrane Science and Technology;* Elsevier, 2011; pp. 91–115; Chapter 5.
53. Hosseini, S. S.; Peng, N.; Chung, T. S. Gas Separation Membranes Developed through Integration of Polymer Blending and

Dual-Layer Hollow Fiber Spinning Process for Hydrogen and Natural Gas Enrichments. *J. Membr. Sci.* **2010,** *349,* 156−166.
54. Dong, J.; Lin, Y. S.; Kanezashi, M.; Tang, Z. Microporous Inorganic Membranes for High Temperature Hydrogen Purification. *J. Appl. Phys.* **2008,** *104,* 121301.
55. Escolástico, S.; Solís, C.; Serra, J. M. Hydrogen Separation and Stability Study of Ceramic Membranes Based on the System Nd_5LnWO_{12}. *Int. J. Hydrogen Energy* **2011,** *36,* 11946−11954.
56. Lin, Y. S. Microporous and Dense inorganic Membranes: Current Status and Prospective. *Sep. Purif. Technol.* **2001,** *23,* 39−55.
57. Bernardo, P.; Drioli, E.; Golemme, G. Membrane Gas Separation: A Review/State of the Art. *Ind. Eng. Chem. Res.* **2009,** *48,* 4638−4663.
58. Kamaroki, P.; Morreale, B. D.; Ciocco, M. V.; Howard, B. H.; Killmeyer, R. P.; Cugini, A. V.; Sholl, D. S. Prediction of Hydrogen Flux through Sulfur-Tolerant Binary Alloy Membranes. *Science* **2005,** *307,* 569−573.
59. Gade, S. K.; Chmelka, S. J.; Parks, S.; Way, J. D.; Wolden, C. A. Dense Carbide/Metal Composite Membranes for Hydrogen Separations Without Platinum Group Metals. *Adv. Mater.* **2011,** *23,* 3585−3589.
60. Ryi, S.-K.; Park, J.-S.; Kim, S.-H.; Hong, S.-C.; Kim, D.-W. Development of Porous Nickel Membrane Made by Uniaxial Pressing for Hydrogen Separation. *Desalination* **2006,** *200,* 213−215.
61. Yan, S.; Maeda, Hideaki; Kusakabe, K.; Morooka, S. Thin Palladium Membrane Formed in Support Pores by Metal-Organic Chemical Vapor Deposition Method and Application to Hydrogen Separation. *Ind. Eng. Chem. Res.* **1994,** *33,* 616−622.
62. Holleck, G. L. Diffusion and Solubility of Hydrogen in Palladium and Palladium-Silver Alloys. *J. Phys. Chem.* **1970,** *74,* 503−511.
63. Buxbaum, R. E.; Kinney, A. B. Hydrogen Transport through Tubular Membranes of Palladium-Coated Tantalum and Niobium. *Ind. Eng. Chem. Res.* **1996,** *35,* 530−537.
64. Hara, S.; Sakaki, K.; Itoh, N.; Kimura, H. M.; Asami, K.; Inoue, A. An Amorphous Alloy Membrane Without Noble Metals for Gaseous Hydrogen Separation. *J. Membr. Sci.* **2000,** *164,* 289−294.
65. David, E.; Kopac, J. Development of Palladium/Ceramic Membranes for Hydrogen Separation. *Int. J. Hydrogen Energy* **2011,** *36,* 4498−4506.
66. Sanz, R.; Calles, J. A.; Alique, D.; Furones, L.; Ordoñez, S.; Marín, P.; Corengia, P.; Fernandez, E. Preparation, Testing and Modelling of a Hydrogen Selective Pd/YSZ/SS Composite Membrane. *Int. J. Hydrogen Energy* **2011,** *36,* 15783−15793.
67. Ishitsuka, M.; Hara, S.; Mukaida, M.; Haraya, K.; Kita, K.; Kato, K. Hydrogen Separation from Dry Gas Mixtures Using a Membrane Module Consisting of Palladium-Coated Amorphous-Alloy. *Desalination* **2008,** *234,* 293−299.
68. Bernardo, P.; Algieri, C.; Barbieri, G.; Drioli, E. Hydrogen Purification from Carbon monoxide by Means of Selective Oxidation Using Zeolite Catalytic Membranes. *Sep. Purif. Technol.* **2008,** *62,* 629−635.
69. Hu, X.; Yu, J.; Song, J.; Wang, X.; Huang, Y. Toward Low-Cost Pd/Ceramic Composite Membranes for Hydrogen Separation: A Case Study on Reuse of the Recycled Porous Al_2O_3 Substrates in Membrane Fabrication. *Int. J. Hydrogen Energy* **2011,** *36,* 15794−15802.
70. Suda, H.; Yamauchi, H.; Uchimaru, Y.; Fujiwara, I.; Haraya, K. Preparation and Gas Permeation Properties of Silicon Carbide-based Inorganic Membranes for Hydrogen Separation. *Desalination* **2006,** *193,* 252−255.
71. Lee, D.; Zhang, L.; Oyama, S. T.; Niu, S.; Saraf, R. F. Synthesis, Characterization, and Gas Permeation Properties of a Hydrogen Permeable Silica Membrane Supported on Porous Alumina. *J. Membr. Sci.* **2004,** *231,* 117−126.
72. Kanezashi, M.; Asaeda, M. Hydrogen Permeation Characteristics and Stability of Ni-doped Silica Membranes in Steam at High Temperature. *J. Membr. Sci.* **2006,** *271,* 86−93.
73. Tsuru, T. Development of Metal-doped Silica Membranes for Increased Hydrothermal Stability and Their Applications to Membrane Reactors for Steam Reforming of Methane. *J. Jpn. Petrol. Inst.* **2011,** *5,* 277−286.
74. Ahmad, A. L.; Othman, M. R.; Mukhtar, H. H_2 Separation from Binary Gas Mixture Using Coated Alumina-titania Membrane by Sol-Gel Technique at High Temperature Region. *Int. J. Hydrogen Energy* **2004,** *29,* 817−828.
75. Casado-Coterillo, C.; Yokoo, T.; Yoshioka, T.; Tsuru, T.; Asaeda, M. Synthesis and Characterization of Microporous ZrO_2 Membrane for Gas Permeation at 200 °C. *Sep. Sci. Technol.* **2011,** *46,* 1224−1230.
76. Kanezashi, M.; Yada, K.; Yoshioka, T.; Tsuru, T. Design of Silica Networks Using Organic−Inorganic Hybrid Alkoxides for Highly Permeable Hydrogen Separation Membranes. *Ceram. Eng. Sci Proc.* **2010,** *30,* 229−239.
77. Fuertes, A. B.; Centeno, T. A. Preparation of Supported Asymmetric Carbon Molecular Sieve Membranes. *J. Membr. Sci.* **1998,** *144,* 105−111.
78. Tseng, H.-H.; Shiu, P.-T.; Lin, Y.-S. Effect of Mesoporous Silica Modification on the Structure of Hybrid Carbon Membrane for Hydrogen Separation. *Int. J. Hydrogen Energy* **2011,** *36,* 15352−15363.
79. Escolástico, S.; Solís, C.; Serra, J. M. Study of Hydrogen Permeation in (La5/6Nd1/6)5.5Wo12-d Membranes. *Solid State Ionics* **2011;**. http://dx.doi.org/10.1016/j.ssi.2011.11.004.
80. Sandström, L.; Palomino, M.; Hedlund, J. High Flux Zeolite X Membranes. *J. Membr. Sci.* **2010,** *354,* 171−177.
81. Sato, K.; Sugimoto, K.; Sekine, Y.; Takada, M.; Matsukata, M.; Nakane, T. Application of FAU-type Zeolite Membranes to Vapor/Gas Separation Under High Pressure and High Temperature up to 5 MPa and 180 °C. *Micropor. Mesopor. Mater.* **2007,** *101,* 312−318.
82. Wang, H.; Lin, Y. S. Synthesis and Modification of ZSM-5/Silicalite Bilayer Membrane with Improved Hydrogen Separation Performance. *J. Membr. Sci.* **2012,** *396,* 128−137.
83. Aoki, K.; Kusakabe, K.; Morooka, S. Gas Permeation Properties of A-Type Zeolite Membrane Formed on Porous Substrate by Hydrothermal Synthesis. *J. Membr. Sci.* **1998,** *141,* 197−205.
84. Shafie, A. H.; An, W.; Hejazi, S. A. H.; Sawada, J. A.; Kuznicki, S. M. Natural Zeolite-based Cement Composite Membranes for H_2/CO_2 Separation. *Sep. Purif. Technol.* **2011,** *88,* 24−28.
85. Bux, H.; Liang, F.; Li, Y.; Cravillon, J.; Wiebcke, M.; Caro, J. Zeolitic Imidazolate Framework Membrane with Molecular Sieving Properties by Microwave-Assisted Solvothermal Synthesis. *J. Am. Chem. Soc.* **2009,** *131,* 16000−16001.
86. Yang, T.; Xiao, Y.; Chung, T.-S. Poly-/Metal-Benzimidazole Nano-Composite Membranes for Hydrogen Purification. *Energy Environ. Sci.* **2011,** *4,* 4171−4180.
87. Li, Y.; Liang, F.; Bux, H.; Yang, W.; Caro, J. R. Zeolitic Imidazolate Framework ZIF-7 based Molecular Sieve Membrane for Hydrogen Separation. *J. Membr. Sci.* **2010,** *354,* 48−54.
88. Kulprathipanja, S; Neuzil, R.W; Li, N.N. Separation of Fluids by Means of Mixed Matrix Membranes, In: U.S. Patent (Ed.) U.S. Patent U.S., **1988**.
89. Chung, T.-S.; Jiang, L. Y.; Li, Y.; Kulprathipanja, S. Mixed Matrix Membranes (MMMs) Comprising Organic Polymers with Dispersed Inorganic Fillers for Gas Separation. *Prog. Polym. Sci.* **2007,** *32,* 483−507.
90. Moore, T. T.; Mahajan, R.; Vu, D. Q.; Koros, W. J. Hybrid Membrane Materials Comprising Organic Polymers with Rigid Dispersed Phases. *AIChE J* **2004,** *50,* 311−321.

91. Pal, R. Permeation Models for Mixed Matrix Membranes. *J. Colloid Interf. Sci.* **2008,** *317,* 191−198.
92. Ho, M. T.; Allinson, G.; Wiley, D. E. Comparison of CO_2 Separation Options for Geo-Sequestration: Are Membranes Competitive? *Desalination* **2006,** *192,* 288−295.
93. Caro, J.; Noack, M.; Kölsch, P.; Schäfer, R. Zeolite Membranes—State of Their Development and Perspective. *Micropor. Mesopor. Mater.* **2000,** *38,* 3−24.
94. Bouma, R. H. B.; hecchetti, A. C.; Chidichimo, G.; Drioli, E. Permeation through a Heterogeneous Membrane: The Effect of the Dispersed Phase. *J. Membr. Sci.* **1997,** *128,* 141−149.
95. Mahajan, R.; Koros, W. J. Factors Controlling Successful Formation of Mixed-Matrix Gas Separation Materials. *Ind. Eng. Chem. Res.* **2000,** *39,* 2692−2696.
96. Boom, J. P.; Pünt, I. G. M.; Zwijnenberg, H.; Boer, R.d.; Bargeman, D.; Smolders, C. A.; Strathmann, H. Transport through Zeolite Filled Polymeric Membranes. *J. Membr. Sci.* **1998,** *138,* 237−258.
97. Robeson, L. M.; Noshay, A.; Matzner, M.; Merriam, C. N. Physical Property Characteristics of Polysulfone-Poli-(Dimethylsiloxane) Block Copolymers. *Angewandte Makromolekulare Chemie* **1973,** *29-3,* 47−62.
98. Petropoulos, J. H. A Comparative Study of Approaches Applied to the Permeability of Binary Composite Polymeric Materials. *J. Polym. Sci., Part B: Polym. Phys.* **1985,** *23,* 1309−1324.
99. Merkel, T. C.; Gupta, R. P.; Turk, B. S.; Freeman, B. D. Mixed-Gas Permeation of Syngas Components in Poly(Dimethylsiloxane) and Poly(1-Trimethylsilyl-1-Propyne) at Elevated Temperatures. *J. Membr. Sci.* **2001,** *191,* 85−94.
100. Moore, T. T.; Koros, W. J. Non-Ideal Effects in Organic−Inorganic Materials for Gas Separation Membranes. *J. Mol. Struct.* **2005,** *739,* 87−98.
101. Zornoza, B.; Gorgojo, P.; Casado, C.; Téllez, C.; Coronas, J. Mixed Matrix Membranes for Gas Separation with Special Nanoporous Fillers. *Desal. Water Treat.* **2011,** *27,* 42−47.
102. Rubio, C.; Casado, C.; Gorgojo, P.; Etayo, F.; Uriel, S.; Téllez, C.; Coronas, J. Exfoliated Titanosilicate Material UZAR-S1 Obtained from JDF-L1. *Eur. J. Inorg. Chem.* **2010,** 159−163.
103. Vu, D. Q.; Koros, W. J.; Miller, S. J. Mixed Matrix Membranes Using Carbon Molecular Sieves: I. Preparation and Experimental Results. *J. Membr. Sci.* **2003,** *211,* 311−334.
104. Kim, S.; Chen, L.; Johnson, J. K.; Marand, E. Polysulfone and Functionalized Carbon Nanotube Mixed Matrix Membranes for Gas Separation: Theory and Experiment. *J. Membr. Sci.* **2007,** *294,* 147−158.
105. Aroon, M. A.; Ismail, A. F.; Matsuura, T.; Montzer-Rahmati, M. M. Performance Studies of Mixed Matrix Membranes for Gas Separation: A Review. *Sep. Purif. Technol.* **2010,** *75,* 229−242.
106. Goh, P. S.; Ismail, A. F.; Sanip, S. M.; Ng, B. C.; Aziz, M. Recent Advances of Inorganic Fillers in Mixed Matrix Membrane for Gas Separation. *Sep. Purif. Technol.* **2011,** *81,* 243−264.
107. Husain, S.; Koros, W. J. Mixed Matrix Hollow Fiber Membranes Made with Modified HSSZ-13 Zeolite in Polyetherimide Polymer Matrix for Gas Separation. *J. Membr. Sci.* **2007,** *288,* 195−207.
108. Khan, A. L.; Cano-Odena, A.; Gutiérrez, B.; Minguillón, C.; Vankelecom, I. F. J. Hydrogen Separation and Purification Using Polysulfone Acrylate-Zeolite Mixed Matrix Membranes. *J. Membr. Sci.* **2010,** *350,* 340−346.
109. Zornoza, B.; Irusta, S.; Téllez, C.; Coronas, J. Mesoporous Silica Sphere-Polysulfone Mixed Matrix Membranes for Gas Separation. *Langmuir* **2009,** *25,* 5903−5909.
110. Bae, T. H.; Lee, J. S.; Qiu, W.; Koros, W. J.; Jones, C. W.; Nair, S. A High-Performance Gas-Separation Membrane Containing Submicrometer-Sized Metal-Organic Framework Crystals. *Angewandte Chemie - International Edition* **2010,** *49,* 9863−9866.
111. Caro, J. Are MOF Membranes Better in Gas Separation Than Those Made of Zeolites? *Curr. Opin. Chem. Eng.* **2011,** *1,* 77−83.
112. Zornoza, B; Téllez, C; Coronas, J; Gascón, J; Kaptejin, F. Metal Organic Framework Based Mixed Matrix Membranes: An Increasingly Important Field of Research with a Large Application Potential, *Micropor. Mesopor. Mater.* **2012,** In Press.
113. Hu, J.; Cai, H.; Ren, H.; Wei, Y.; Xu, Z.; Liu, H.; Hu, Y. Mixed-Matrix Membrane Hollow Fibers of Cu3(BTC)2MOF and Polyimide for Gas Separation and Adsorption. *Ind. Eng. Chem. Res.* **2010,** *49,* 12605−12612.
114. Ordoñez, M. J. C.; Balkus, K. J., Jr.; Ferraris, J. P.; Musselman, I. H. Molecular Sieving Realized with ZIF-8/Matrimid Mixed Matrix Membranes. *J. Membr. Sci.* **2010,** *361,* 28−37.
115. Coronas, J.; Santamaria, J. Catalytic Reactors Based on Porous Ceramic Membranes. *Catal. Today* **1999,** *51,* 377−389.
116. Julbe, A.; Farrusseng, D.; Guizard, C. Porous Ceramic Membranes for Catalytic Reactors − Overview and New Ideas. *J. Membr. Sci.* **2001,** *181,* 3−20.
117. Basile, A.; Gallucci, F.; Téllez, C.; Menéndez, M. *Membranes for Membrane Reactors: Preparation, Optimization and Selection;* Wiley, 2011.
118. Mendes, D.; Mendes, A.; Madeira, L. M.; Iulianelli, A.; Sousa, J. M.; Basile, A. The Water-Gas Shift Reaction: From Conventional Catalytic Systems to Pd-Based Membrane Reactors − A Review. *Asia-Pac. J. Chem. Eng.* **2010,** *5,* 111−137.
119. Shigarov, A. B.; Meshcheryakov, V. D.; Kirillov, V. A. Use of Pd Membranes in Catalytic Reactors for Steam Methane Reforming for Pure Hydrogen Production. *Theor. Found. Chem. Eng.* **2011,** *45,* 595−609.
120. Uemiya, S. Brief Review of Steam Reforming Using a Metal Membrane Reactor. *Top. Catal.* **2004,** *29,* 79−84.
121. Hsieh, H. P. Inorganic Membranes Reactors − A Review. *AIChE Symp. Ser.* **1989,** *85,* 53−67.
122. Han, J.; Kim, I.-S.; Choi, K.-S. Purifier-Integrated Methanol Reformer for Fuel Cell Vehicles. *J. Power Sources* **2000,** *86,* 223−227.
123. Huang, J.; El-Azzami, L.; Ho, W. S. W. Modeling of CO_2-Selective Water Gas Shift Membrane Reactor for Fuel Cell. *J. Membr. Sci.* **2005,** *261,* 67−75.
124. Babita, K.; Sridhar, S.; Raghavan, K. V. Membrane Reactors for Fuel Cell Quality Hydrogen Through WGSR − Review of Their Status, Challenges and Opportunities. *Int. J. Hydrogen Energy* **2011,** *36,* 6671−6688.
125. Brunetti, A.; Barbieri, G.; Drioli, E. Integrated Membrane System for Pure Hydrogen Production: A Pd-Ag Membrane Reactor and a PEMFC. *Fuel Proc. Technol.* **2011,** *92,* 166−174.
126. Battersby, S.; Duke, M. C.; Liu, S.; Rudolph, V.; da Costa, J. C. D. Metal Doped Silica Membrane Reactor: Operational Effects of Reaction and Permeation for the Water Gas Shift Reaction. *J. Membr. Sci.* **2008,** *316,* 46−52.
127. Giessler, S.; Jordan, L.; da Costa, J. C. D.; Lu, G. Q. Performance of Hydrophobic and Hydrophilic Silica Membrane Reactors for the Water Gas Shift Reaction. *Sep. Purif. Technol.* **2003,** *32,* 255−264.
128. Tang, Z.; Kim, S.-J.; Reddy, G. K.; Dong, J.; Smirniotis, P. Modified Zeolite Membrane Reactor for High Temperature Water Gas Shift Reaction. *J. Membr. Sci.* **2010,** *354,* 114−122.
129. Abdollahi, M.; Yu, J.; Hwang, H. T.; Liu, P. K. T.; Ciora, R.; Sahimi, M.; Tsotsis, T. T. Process Intensification in Hydrogen Production from Biomass-Derived Syngas. *Ind. Eng. Chem. Res.* **2010,** *49,* 10986−10993.

130. Harale, A.; Hwang, H. T.; Liu, P. K. T.; Sahimi, M.; Tsotsis, T. T. Experimental Studies of a Hybrid Adsorbent-Membrane Reactor (HAMR) System for Hydrogen Production. *Chem. Eng. Sci.* **2007,** *62,* 4126−4137.
131. Harale, A.; Hwang, H. T.; Liu, P. K. T.; Sahimi, M.; Tsotsis, T. T. Design Aspects of the Cyclic Hybrid Adsorbent-Membrane Reactor (HAMR) System for Hydrogen Production. *Chem. Eng. Sci.* **2010,** *65,* 427−435.
132. Saracco, G.; Specchia, V. Catalytic Inorganic Membrane Reactors − Present Experience and Future Opportunities. *Catal. Rev.* **1994,** *36,* 305−384.
133. Saracco, G.; Versteeg, G. F.; Vanswaaij, W. P. M. Current Hurdles to the Success of High-Temperature Membrane Reactors. *J. Membr. Sci.* **1994,** *95,* 105−123.
134. Lin, H.; Freeman, B. D. Gas Solubility, Diffusivity and Permeability in Poly(Ethylene Oxide). *J. Membr. Sci.* **2004,** *239,* 105−117.
135. Nunes, S. P.; Ruffmann, B.; Rikowski, E.; Vetter, S.; Richau, K. Inorganic Modification of Proton Conductive Polymer Membranes for Direct Methanol Fuel Cells. *J. Membr. Sci.* **2001,** *203,* 215−225.
136. Dong, J.; Lin, Y. S. Multicomponent Hydrogen/Hydrocarbon Separation by MFI-Type Zeolite Membranes. *AIChE J.* **2000,** *46,* 1957−1967.
137. Gu, X.; Tang, Z.; Dong, J. On-stream Modification of MFI Zeolite Membranes for Enhancing Hydrogen Purification at High Temperature. *Micropor. Mesopor. Mater.* **2008,** *111,* 441−448.
138. Huang, A.; Wang, N.; Caro, J. Seeding-Free Synthesis of Dense Zeolite FAU Membranes on 3-Aminopropyltriethoxysilane-Functionalized Alumina Supports. *J. Membr. Sci.* **2012,** *389,* 272−279.
139. An, W.; Swenson, P.; Wu, L.; Waller, T.; Ku, A.; Kuznicki, S. M. Selective Separation of Hydrogen from C1/C2 Hydrocarbons and CO_2 Through Dense Natural Zeolite Membranes. *J. Membr. Sci.* **2011,** *369,* 414−419.
140. Moon, J.-H.; Bae, J.-H.; Bae, Y.-S.; Chung, J.-T.; Lee, C.-H. Hydrogen Separation from Reforming Gas Using Organic Templating Silica/Alumina Composite Membrane. *J. Membr. Sci.* **2008,** *318,* 45−55.
141. Sklari, S. D.; Zaspalis, V. T. A Novel System of $Al_{100}P_{60}O_z$ Microporous Ceramic Membrane for Hydrogen Separation from Hydrogen/Propane Mixtures. *Micropor. Mesopor. Mater.* **2007,** *99,* 176−180.
142. Fan, J.; Ohya, H.; Suga, T.; Ohashi, H.; Yamashita, K.; Tsuchiya, S.; Aihara, M.; Takeuchi, T.; Negishi, Y. High Flux Zirconia Composite Membrane for Hydrogen Separation at Elevated Temperature. *J. Membr. Sci.* **2000,** *170,* 113−125.
143. Gu, Y.; Kusakabe, K.; Morooka, S. Sulfuric Acid-Modified Zirconia Membrane for Use in Hydrogen Separation. *Sep. Purif. Technol.* **2001,** *24,* 489−495.
144. Lin, Y. M.; Liu, S. L.; Chuang, C. H.; Chu, Y. T. Effect of incipient removal of hydrogen through palladium membrane on the conversion of methane steam reforming - Experimental and modeling. *Catal. Today* **2003,** *82,* 127−139.
145. Chen, Y.; Wang, Y.; Xu, H.; Xiong, G. Efficient Production of Hydrogen from Natural Gas Steam Reforming in Palladium Membrane Reactor. *Appl. Catal. B-Environ.* **2008,** *81,* 283−294.
146. Mahecha-Botero, A.; Boyd, T.; Gulamhusein, A.; Comyn, N.; Lim, C. J.; Grace, J. R.; Shirasaki, Y.; Yasuda, I. Pure Hydrogen Generation in a Fluidized-Bed Membrane Reactor: Experimental Findings. *Chem. Eng. Sci.* **2008,** *63,* 2752−2762.
147. Tong, J.; Matsumura, Y. Pure Hydrogen Production by Methane Steam Reforming with Hydrogen-Permeable Membrane Reactor. *Catal. Today* **2006,** *111,* 147−152.
148. Gallucci, F.; Annaland, M. V. S.; Kuipers, J. A. M. Autothermal Reforming of Methane with Integrated CO_2 Capture in a Novel Fluidized Bed Membrane Reactor. Part 1: Experimental Demonstration. *Top. Catal.* **2008,** *51,* 133−145.
149. Basile, A.; Paturzo, L.; Vazzana, A. Membrane Reactor for the Production of Hydrogen and Higher Hydrocarbons from Methane Over Ru/Al2O3 Catalyst. *Chem. Eng. J.* **2003,** *93,* 31−39.
150. Tong, J. H.; Matsumura, Y. Effect of Catalytic Activity on Methane Steam Reforming in Hydrogen-Permeable Membrane Reactor. *Appl. Catal. A: Gen.* **2005,** *286,* 226−231.
151. Annaland, M. S.; Patil, C. S.; Kuipers, J. A. M. Fluidised Bed Membrane Reactor for Ultrapure Hydrogen Production via Methane Steam Reforming: Experimental Demonstration and Model Validation. *Chem. Eng. Sci.* **2007,** *62,* 4095−4111.
152. Seelam, P. K.; Liguori, S.; Iulianelli, A.; Pinacci, P.; Calabrò, V. Hydrogen Production from Bio-ethanol Steam Reforming Reaction in a Pd/PSS Membrane Reactor. *Catal. Today* **2012;**. http://dx.doi.org/10.1016/j.cattod.2012.01.008.
153. Iulianelli, A.; Basile, A. An Experimental Study on Bio-ethanol Steam Reforming in a Catalytic Membrane Reactor. Part I: Temperature and Sweep-Gas Flow Configuration Effects. *Int. J. Hydrogen Energy* **2010,** *35,* 3170−3177.
154. Arstad, B.; Venvik, H.; Klette, H.; Walmsley, J. C.; Tucho, W. M.; Holmestad, R.; Holmen, A.; Bredesen, R. Studies of Self-Supported 1.6 μm Pd/23 wt.% Ag Membranes During and After Hydrogen Production in a Catalytic Membrane Reactor. *Catal. Today* **2006,** *118,* 63−72.
155. Basile, A.; Tosti, S.; Capannelli, G.; Vitulli, G.; Iulianelli, A.; Gallucci, F.; Drioli, E. Co-Current and Counter-Current Modes for Methanol Steam Reforming Membrane Reactor: Experimental Study. *Catal. Today* **2006,** *118,* 237−245.
156. Lin, Y. M.; Rei, M. H. Study on the Hydrogen Production from Methanol Steam Reforming in Supported Palladium Membrane Reactor. *Catal. Today* **2001,** *67,* 77−84.
157. Iulianelli, A.; Longo, T.; Basile, A. CO-Free Hydrogen Production by Steam Reforming of Acetic Acid Carried Out in a Pd-Ag Membrane Reactor: The Effect of Co-Current and Counter-Current Mode. *Int. J. Hydrogen Energy* **2008,** *33,* 4091−4096.
158. Damle, A. S. Hydrogen Production by Reforming of Liquid Hydrocarbons in a Membrane Reactor for Portable Power Generation-Experimental Studies. *J. Power Sources* **2009,** *186,* 167−177.
159. Tsuru, T.; Shintani, H.; Yoshioka, T.; Asaeda, M. A Bimodal Catalytic Membrane Having a Hydrogen-Permselective Silica Layer on a Bimodal Catalytic Support: Preparation and Application to the Steam Reforming of Methane. *Appl. Catal. A: Gen.* **2006,** *302,* 78−85.
160. Prabhu, A. K.; Oyama, S. T. Highly Hydrogen Selective Ceramic Membranes: Application to the Transformation of Greenhouse Gases. *J. Membr. Sci.* **2000,** *176,* 233−248.
161. Tsuru, T.; Tsuge, T.; Kubota, S.; Yoshida, K.; Yoshioka, T.; Asaeda, M. Catalytic Membrane Reaction for Methane Steam Reforming Using Porous Silica Membranes. *Sep. Sci. Technol.* **2001,** *36,* 3721−3736.
162. Tsuru, T.; Yamaguchi, K.; Yoshioka, T.; Asaeda, M. Methane Steam Reforming by Microporous Catalytic Membrane Reactors. *AIChE J.* **2004,** *50,* 2794−2805.
163. Kurungot, S.; Yamaguchi, T.; Nakao, S. Rh/Gamma-Al_2O_3 Catalytic Layer Integrated with Sol-Gel Synthesized Microporous Silica Membrane for Compact Membrane Reactor Applications. *Catal. Lett.* **2003,** *86,* 273−278.
164. Kikuchi, E.; Uemiya, S.; Sato, N.; Inoue, H.; Ando, H.; Matsuda, T. Membrane Reactor Using Microporous Glass-Supported Thin-Film of Palladium. 1. Application to the Water Gas Shift Reaction. *Chem. Lett* **1989,** 489−492.
165. Basile, A.; Chiappetta, G.; Tosti, S.; Violante, V. Experimental and Simulation of Both Pd and Pd/Ag for a Water Gas Shift Membrane Reactor. *Sep. Purif. Technol.* **2001,** *25,* 549−571.

166. Uemiya, S.; Sato, N.; Ando, H.; Kikuchi, E. The Water Gas Shift Reaction Assisted by a Palladium Membrane Reactor. *Ind. Eng. Chem. Res.* **1991,** *30,* 585–589.
167. Bi, Y.; Xu, H.; Li, W.; Goldbach, A. Water-Gas Shift Reaction in a Pd Membrane Reactor Over $Pt/Ce_{0.6}Zr_{0.4}O_2$ Catalyst. *Int. J. Hydrogen Energy* **2009,** *34,* 2965–2971.
168. Abdollahi, M.; Yu, J.; Liu, P. K. T.; Ciora, R.; Sahimi, M.; Tsotsis, T. T. Ultra-Pure Hydrogen Production from Reformate Mixtures Using a Palladium Membrane Reactor System. *J. Membr. Sci.* **2012,** *390,* 32–42.
169. Brunetti, A.; Barbieri, G.; Drioli, E.; Granato, T.; Lee, K. H. A Porous Stainless Steel Supported Silica Membrane for WGS Reaction in a Catalytic Membrane Reactor. *Chem. Eng. Sci.* **2007,** *62,* 5621–5626.
170. Lin, J.Y.S. Zeolite. Membrane Reactor for Water-Gas-Shift Reaction for Hydrogen Production, In: FY2007 Annual Progress Report, FY2007 Annual Progress Report, 2007, pp. 83–89.

CHAPTER

12

Advances in Hydrogen Storage in Carbon Materials

Dolores Lozano-Castelló [*], *Fabián Suárez-García* [†], *Ángel Linares-Solano* [*], *Diego Cazorla-Amorós* [*]

[*]Departamento Química Inorgánica and Instituto de Materiales, Universidad de Alicante, Alicante, Spain,
[†]Instituto Nacional del Carbón, INCAR-CSIC, Oviedo, Spain

OUTLINE

12.1 Introduction 269

12.2 Carbon Materials 270
12.2.1 Carbon Nanotubes and Carbon Nanofibers 271
12.2.2 Activated Carbons and Activated Carbon Fibers 272
12.2.3 Other Porous Carbon Materials 273
12.2.3.1 Carbide-Derived Carbons 273
12.2.3.2 Templated Carbons: Zeolite-Templated Carbons and Ordered Mesoporous Carbons 273
12.2.3.3 Doped Carbons 274

12.3 Fundamentals of Gas Adsorption at High Pressure 274

12.4 Hydrogen Adsorption in Carbon Materials 276
12.4.1 State of the Art 276
12.4.2 Hydrogen Adsorption on "Classical" Carbon Materials 277
12.4.2.1 Hydrogen Adsorption at 298 K 278
12.4.2.2 Hydrogen Adsorption at 77 K 280

12.5 Hydrogen Storage Capacities 281
12.5.1 Hydrogen Adsorption on Volumetric Basis 281
12.5.2 Total Hydrogen Storage Capacity 282

12.6 Comparison with Other Porous Materials 283

12.7 Comments and Tendencies on Doped Carbons 286

12.8 Summary and Recommendations 286

Acknowledgments 287

References 287

12.1 INTRODUCTION

Hydrogen is a clean fuel, abundant, well distributed in the world and with a flexible and efficient energy conversion. Thus, it can be used in mobile applications (such as cars, buses, …) in conventional systems of internal combustion and/or in fuel cells, which results in a much more efficient conversion (60% versus 20% of the combustion engines). In addition, the versatility of the fuel cell will allow a wider use of hydrogen as fuel cells can be used in a variety of additional products, such as portable devices (like mobile phones, laptops, …), or to produce heat and electricity in stationary applications in domestic, industrial and energy sectors. However, there are two major drawbacks to the use of hydrogen as fuel, which are the production and storage. Hydrogen is not a primary source like coal or natural gas since it is mostly combined (<2% of hydrogen is as molecular hydrogen) and, hence, it has to be produced. However, hydrogen can be obtained through very different routes, using a wide range of technologies and primary energy sources, including fossil fuels, nuclear power and renewable energy.[1] Thus, hydrogen is near an ideal fuel and

TABLE 12.1 Gravimetric and Volumetric Targets for H_2 Storage Systems Established by the Department of Energy of USA (DOE) on "Weighted Average Corporate Vehicle" (WACV)[5] and "Light-Duty Vehicles"[6]

	WACV		Light-duty vehicle		Ultimate full
Target	**2010**	**2015**	**2010**	**2015**	**Fleet**
System gravimetric density	6 wt% 2.0 kWh/kg	9 wt% 3.0 kWh/kg	4.5 wt% 1.5 kWh/kg	5.5 wt% 1.8 kWh/kg	7.5 wt% 2.5 kWh/kg
System volumetric density	45 g H_2/l 1.5 kWh/l	81 g H_2/l 2.7 kWh/l	28 g H_2/l 0.9 kWh/l	40 g H_2/l 1.3 kWh/l	70 g H_2/l 2.3 kWh/l

energy carrier as it can be generated from a diverse number of feedstocks and be converted to a desired form of energy without releasing harmful emissions at the point of use, thus reducing the emissions of greenhouse gases and other pollutants and decreasing the dependence on fossil fuels.[1,2]

The second drawback is the hydrogen storage. This is especially crucial in the case of mobile and portable applications being storage one of the main problems for use in such applications as fuel.[1–4] Hydrogen has a chemical energy per mass (on a gravimetric basis) of 120 MJ/kg (33.3 kWh/kg), which is approximately three times greater than that of gasoline (44.4 MJ/kg or 12.4 kWh/kg). However, the energy density of hydrogen (on a volumetric basis) is very low compared to gasoline or other hydrocarbons. Thus, two examples are: (1) at room temperature and at atmospheric pressure, 1 kg of hydrogen occupies 11,250 l and (2) gasoline has a volumetric energy of 31.7 MJ/l (8.8 kWh/l) which is approximately six times more energy than hydrogen compressed at 70 MPa (4.7 MJ/l, 1.3 kWh/l). Therefore, great efforts have been carried out in order to increase the volumetric energy of hydrogen.

To be economically competitive with existing fuels, the hydrogen storage techniques for using in vehicles have to meet the provisional criteria established by Department of Energy (DOE, USA).[5,6] Table 12.1 shows the values of density storage required for gravimetric and volumetric on "weighted average corporate vehicle" (WACV) (including vans, light trucks, cars and sport utility vehicles/crossovers in proportion to their U.S. sales) whose average weight is 1740 kg[5] and recent values recalculated to "light-duty vehicles".[6] As seen in Table 12.1, the hydrogen storage targets in 2015 are, in volumetric and gravimetric density on system basis, 81 g H_2/l and 9 wt% for WACV, respectively, and 40 g H_2/l and 5.5 wt% for light-duty vehicles. Ultimate targets for full fleet are 70 g H_2/l and 7.5 wt% for volumetric and gravimetric density based on full system, respectively. It has to be recalled that these values refer to the whole storage system, including the material, the tank and the auxiliary systems (pipes, valves, gauges, …). Therefore, targets calculated with respect to the materials basis should be higher. In addition, other requirements to be met by storage system have been established: loading/unloading should be reversible below 80 °C, energy consumption <5% in the process of unloading and the loading must be rapid (<5 min).

Currently, different alternatives for developing efficient hydrogen storage systems are being investigated. These strategies are focused on increasing hydrogen density by pressuring up to very high pressures (e.g. 70 MPa), decreasing the temperature to cryogenic conditions, using chemicals or sorbents, or a combination of all of them. Four different methods to store hydrogen are currently available:[1,7] (1) compressed gas, (2) liquid hydrogen, (3) metal hydrides and (4) adsorption on different types of porous materials (carbon materials, zeolites, metal organic frameworks (MOFs)…).

Storage of hydrogen by compression involves very high pressures in order to achieve a reasonable amount of hydrogen. For example, it is necessary to pressurize up to 70 MPa to reach a hydrogen density of 39 g/l and, consequently, suitable materials to withstand these high pressures are necessary. Another possibility is to store hydrogen in liquid form, but hydrogen liquefies at very low temperature (20.39 K) and a high amount of energy is consumed during the liquation process. Other possibility for storing hydrogen is by the formation of metal hydrides. High volumetric capacities can be reached with metal hydrides, but, as it is based on an exothermal reaction, a considerable amount of heat is generated upon hydrogenation and, for hydrogen release, heating is necessary. Thus, a number of secondary devices are needed in order to manage the heats of hydrogenation and dehydrogenation. Finally, adsorption in porous material could be an alternative to solve these problems and research on hydrogen storage in porous materials has grown significantly over 2000–2010. Thus, in this chapter, we will review the state of the art in the field of hydrogen storage by adsorption in porous solids, focusing in the use of porous carbon materials.

12.2 CARBON MATERIALS

The extraordinary ability of the carbon element to combine with itself and other elements is the basis of organic chemistry and of life. The electronic configuration of the carbon atom $1s^2\,2s^2\,2p^2$ and its singular ability

to form sp^3, sp^2 and sp^1 hybrid bonds, as a result of electron promotion and orbital hybridization, gives rise to a very large variety of carbon forms. Carbon has four different allotropic forms with carbon atoms having different hybridizations:

1. Diamond is a metastable form of carbon at room temperature. It is most frequently found in a cubic form, in which each carbon atom is linked to four other carbon atoms by sp^3 σ-bonds in tetrahedral array. Diamond also exists in a hexagonal form with a wurtzite crystal structure.
2. Graphite is a well-established allotrope of carbon; the basic unit of the crystal structure of graphite is the graphene layer, i.e. an extended hexagonal array of carbon atoms with sp^2 σ-bonds and delocalized π bonds. Hexagonal compact is the most common crystal structure of graphite which consists of graphene layers in the stacking sequence ABA… The other crystalline form of graphite is rhombohedral with a stacking sequence ABCA…
3. Fullerene: The most common fullerene is the C_{60} molecule or Buckminsterfullerene, although other fullerenes with lower (C_{20}, C_{32}, …) or higher (C_{70}, C_{80},…) number of carbon atoms are known. The most stable one and the first to be discovered, C_{60} molecule, consists of 60 carbon atoms forming a nearly spherical cage, which contains 20 hexagons and 12 pentagons. In the C_{60} molecule, each carbon atom is bonded to other three. The hybridization of the carbon atoms is between sp^3 and sp^2.
4. Carbynes: Consist of chains of carbon atoms linearly bonded with sp^1 hybridization with π electrons forming alternative simple and triple bonds or conjugated bonds.

More information about carbon allotropic forms can be found easily in literature[8–14] and in specialty series of books, like *Chemistry and Physics of Carbon*.

Many other carbon materials are derived or based on the above commented allotropic forms where the presence of defects and/or heteroatoms gives different structures and properties. For example, carbon nanotubes (CNTs) are nanostructures that can be envisaged as a cylindrical rolled single layer of graphene, hollow and capped at each end by half of fullerene where the carbon atoms hybridization is similar to that in fullerene. The broadest family of materials is based on a more or less degree of defective graphite structure, which covers a number of substances consisting of the elemental carbon (>90 wt%) with more or less structural defects.[10,11,15] This large variety of carbon materials that includes, among others, carbon blacks, cokes, activated carbons (ACs), carbon fibers, or other carbonaceous residues, can be prepared from a huge variety of carbonaceous precursors and organic compounds. However, all of them are manufactured by few types of processes, such as chemical vapor deposition (CVD), pyrolysis/combustion, carbonization and activation.

The following section contains some details about carbon nanostructures like CNTs and carbon nanofibers (CNFs) because they have been extensively studied as hydrogen adsorbents. The subsequent one collects information about the preparation of ACs with controlled porous texture (i.e. surface area, pore size and pore size distribution) and activated carbon fibers (ACFs), also used for hydrogen storage. Section 12.2.3 includes a description of other types of recent nanostructured materials also used for hydrogen storage applications; i.e. carbide-derived carbons (CDCs) and templated carbons (both zeolite-templated carbons (ZTCs) and ordered mesoporous carbons (OMCs)).

12.2.1 Carbon Nanotubes and Carbon Nanofibers

CNTs were discovered in 1991 as a minor by-product of fullerene synthesis;[16] these nanotubes were multiwall carbon nanotubes (MWCNTs). Two years later (1993), single-wall carbon nanotubes (SWCNTs) were discovered.[17,18] From these discoveries and further reports about the experimental conditions for the synthesis of large quantities of CNT,[19,20] an intensive investigation in this field has been done. These materials show interesting electrical and mechanical properties and may have many potential applications in different fields.

There are two basic types of CNT: single-wall and multiwall. The first only has one graphene sheet, whereas the second contain more than one sheet. The graphene sheet of the SWCNT can be rolled into a tube in different ways and, depending on the chiral angle $\boldsymbol{\theta}$ (or "rolling direction"), "armchair", "zigzag" or "chiral" tubule can be differentiated.[9,21] This rolling direction determines the electrical (conductor or semiconductor) and mechanical properties of the material. SWCNTs have a diameter of around 1 nm and normally, they group together forming bundles of several nanotubes. The MWCNT is an arrangement of coaxial tubes of graphene sheets. MWCNTs can be formed from 2 to 50 sheets. The inner diameters can be from 1.5 to 15 nm and the outer diameters from 2.5 to about 100 nm.

CNTs are produced by evaporation of bulk carbon to generate carbon molecules and atoms by electric arc discharge, laser vaporization or CVD.[22–24] Journet et al.[25] have reported a highly efficient method for growing SWCNT arrays with a small distribution of nanotubes diameter using an Ni−Y catalyst by the carbon arc method. Laser vaporization method was reported by a group of Rice University (US).[26] This method utilizes a Co−Ni/graphite composite target operating in a furnace at 1473 K. Authors have reported

high yields of SWCNTs. If this method is carried out without metal catalyst, MWCNTs are produced. CVD with metal catalysts forms mainly MWCNTs and a smaller fraction of SWCNTs.[27]

CNFs are formed at high temperatures from a mixture of carbon-containing gases and hydrogen, or hydrocarbons alone, in the presence of Ni and Fe alloys as catalysts. Depending on the experimental conditions (catalyst, composition of the gases, temperature of reaction, etc.), different types of CNFs can be formed. Two primary production processes, which are differentiated on the initial state of the catalyst, can be distinguished: "fixed catalyst method" and "floating catalyst method".[23,24,28] In the fixed catalyst method, the metallic particles are fixed on a substrate, so that the resulting fiber is attached to the substrate. In the floating catalyst method, the catalyst, or a catalyst precursor, is injected in a heated gas flow into the furnace, where it nucleates and grows, in length and diameters, from nanotubes to nanofibers.

The steps in the nanofiber formation are the following: (1) hydrocarbons are adsorbed on the surface of catalysts particles, decomposed and carbon atoms diffuse to the interface, (2) CNF grows lengthwise and (3) CNF grows in thickness. In the second step, the core of the nanofiber is formed and it is principally constituted by ordered graphite platelets. The growth in thickness is normally not controlled by the catalyst and deposition of pyrolytic carbon takes place yielding outer layers less graphitic than the core. The CNFs have submicron diameters and lengths that vary from 5 to 100 μm. Depending on the orientation of the graphitic platelets with respect to the longitudinal axis of the fiber (which depends on geometry of the catalyst), different structures can be distinguished.[29]

12.2.2 Activated Carbons and Activated Carbon Fibers

To prepare ACs and ACFs, selection of the precursor and the method of preparation is necessary. Several precursors, such as wood, coals, pitches, polymers, residues with high carbon contents, and so on, as well as different experimental methods can be used for the preparation of ACs. These two factors have great importance as they determine the final porous structure of the AC. For obtaining ACFs, general purpose carbon fibers (obtained from coal tar or petroleum pitches or from synthetic polymeric fibers) are activated by different activation methods.[30,31]

The main stage determining the porous structure is the method of activation and the experimental conditions and variables used. The objective during the activation is both to increase the number of pores and to increase the size of the existing ones, so that the AC may have a high adsorption capacity. And, in relation to hydrogen storage application, the most important is to control the pore size distribution of the resulting activated material. The activation processes are usually divided into two different groups: chemical and the so-called "physical" activations.[32,33] The differences between both of them are the procedure and the activating agents used.

Chemical activation consists of mixing a carbonaceous precursor with a chemical activating agent, followed by a pyrolysis stage.[34,35] The material after this stage is richer in carbon content and presents, after the removal of the activating agent, a well-developed porous structure. In the literature,[33–39] there exist several activating agents used in the chemical activation process, including phosphoric acid, zinc chloride and hydroxides and carbonates of alkaline metals. Among the precursors used, there are two main types of sources for the production of ACs: lignocellulosic materials and coals. Depending on the raw material used for the preparation of the ACs, the activating agent chosen will be different.

Preparation of ACs by physical activation includes a controlled gasification of the carbonaceous material that usually has been previously carbonized although, occasionally, the activation of the precursor can be directly done. Thus, the samples are treated to 800−1000 °C with an oxidant gas, so that atoms are being removed selectively. Carbon dioxide and steam are the activating agents commonly used. The removal of the outer and less ordered carbon atoms of the graphitic microcrystals leads to the creation of new micropores and/or the widening of their size in the char, what results in an increase of its pore volume.

The chemical activation presents advantages over the physical one, that can be summarized as follows: (1) the chemical activation uses lower temperatures and pyrolysis times; (2) it usually consists of one stage; (3) the yields obtained are higher; (4) it produces highly microporous ACs; and v) it is a suitable method for applying it to materials with a high ash content, as is the case of coals.[33,36,37]

On the other hand, the chemical activation presents disadvantages as the need of a washing stage after the pyrolysis and the corrosiveness of the chemical agents used.

ACs with different porous texture for a very wide range of applications, e.g. liquid and gas phase treatments and energy storage, can be prepared by both activation processes. Knowledge of the effect of the different preparation variables in the porous texture (surface area, pore size and pore size distribution) is required. The porous texture of the resulting ACs can be controlled by an adequate selection of the preparation variables

(precursor, activation method, activation agent, temperatures, heating rates, gases flows, etc.).[32,33]

12.2.3 Other Porous Carbon Materials

12.2.3.1 Carbide-Derived Carbons

Selective etching of carbides is considered to be a promising technique for the synthesis of various carbon structures.[40] The carbon material produced by extraction of metals from metal carbides (MeCs) is called *carbide-derived carbon*. Leaching in supercritical water, high-temperature treatment in halogens, vacuum decomposition, and other methods can be used to remove metals from carbides, producing carbon coatings or bulk and powdered carbon materials.

A manufacturing process based on the reaction of silicon carbide with chlorine gas was reported in 1918 for the first time.[41] Hutchins patented a method for the production of silicon tetrachloride using the following reaction:

$$SiC + 2Cl_2 \rightarrow SiCl_4 + C$$

The reaction was conducted by passing dry chlorine over silicon carbide heated to a temperature of 1000 °C or above. The main product of the reaction, silicon tetrachloride vapor, passed through the outlet pipe into a condenser. Development of this method was patented in 1956.[42]

Treatment of other MeCs in chlorine gas has been used to produce the corresponding metal chlorides. Kinetics of chlorination of titanium and niobium carbides[43] and zirconium carbide[44] were studied. The reactions

$$MeC + x/2Cl_2 \rightarrow MeCl_x + C$$

(where $x = 4$ when Me = Ti, Zr; and $x = 5$ when Me = Nb) were conducted in a quartz-tube flow reactor in the temperature range 600–800 °C in the case of TiC and NbC, and 450–950 °C in the case of ZrC.

Selective removal of metals from MeCs generally results in the formation of porous carbon with a density lower than that of graphite. Porous structure and molecular sieve properties of CDC were first investigated by Boehm and Warnecke in 1975.[45] A mechanism of nanopore formation in carbon materials produced by the interaction of carbides with chlorine was proposed in Ref. 46. If the external parameters, the component fluxes, and the diffusion rates satisfy certain relations, a self-organization process can occur. This process results in the creation of a periodic nanoporous structure in the carbon material formed.

The size of pores in the CDC is influenced by the distribution of carbon atoms in the initial carbide, the CDC's atomic structure, the amounts of chloride and chlorine trapped in the CDC, the presence of catalytic particles as well as by the effect of optional posttreatments, such as activation,[47] or mild oxidation. Recently, it has been shown that the detailed nature of the porosity average size and size distribution, shape, and total specific surface area (SSA) can be tuned with high sensitivity by selection of precursor carbide (composition, lattice type)[48–50] and chlorination temperature.[48] Moreover, different starting carbides (B_4C, ZrC, TiC, and SiC) have been used to prepare materials with tailored porosity.[51]

12.2.3.2 Templated Carbons: Zeolite-Templated Carbons and Ordered Mesoporous Carbons

A template carbonization method consists in the carbonization of an organic compound in the nanospace of a template inorganic substance and the liberation of the resulting carbon material from the template. Such spatial regulation of the carbonization process by the nanospace makes it possible to control the structure of carbon material at nanometer level by changing either the size or the shape of the nanospace.

Zeolites have a regular porous structure because of its crystalline structure. If the pores in the zeolite are completely filled with carbon and then the carbon is extracted from the zeolite framework, one can expect the formation of porous carbon whose structure reflects the porosity of the original zeolite template. On the basis of this concept, Kyotani et al. used USY zeolite as a template to prepare a new type of porous carbon.[52] They adopted the CVD method for the introduction of carbon into the channels of USY zeolite. The CVD was carried out by exposing the zeolite to propylene at 700 or 800 °C and then the carbon was liberated from the zeolite framework by acid washing. Rodriguez-Mirasol et al. also reported the formation of a similar type of porous carbon by using Y zeolite as a template and, furthermore, they examined the oxidation behavior of this porous carbon.[53]

Later, Kyotani's group prepared long-range ordered microporous carbons with the structural regularity of zeolite Y.[54–57] Powdered zeolite Y (Na form, $SiO_2/Al_2O_3 = 5.6$) was impregnated with furfuryl alcohol, which was polymerized inside the zeolite channels. The resultant polyfurfuryl alcohol/zeolite composite was heated to 700 °C in N_2 and then propylene CVD was performed at this temperature for further carbon deposition (CVD period of 1 or 4 h). After the CVD, the composite was further heat-treated at 900 °C, under an N_2 flow. The resultant carbon was liberated from the zeolite framework by HF washing. This ZTC, characterized by a very uniform and ordered pore structure, is presumably the highest SSA carbon material ever reported (about 4000 m^2/g). Recently, several types of ZTCs with different surface areas, nitrogen-doped ZTC and ZTC loaded with Pt nanoparticles were prepared.[58–62]

In some applications, the presence of mesopores is required. A nanocasting method for the preparation of mesoporous carbons was firstly reported in 1999 by Ryoo et al.[63] as an extension of the templating concept used in the preparation of zeolites. But in this case, highly ordered mesoporous silica were employed as templates. Ordered porous silica materials, for instance, MCM-48, SBA-1 and SBA-15, are filled with an organic carbon precursor, the composite is carbonized and finally, the template is removed leading to a porous carbon with a pore structure that replicates the pore structure of the parent silica. Thus, the space once occupied by the host silica materials is transformed into pores in the carbon material. The resulting OMCs have a controllable mesopore structure, which can be accurately tuned by appropriate selection of the siliceous template and the infiltration conditions.

For the OMCs to be more efficiently used in some applications, some researchers have been focused on developing microporosity in OMCs trying to preserve the ordered mesoporous structure of the starting OMC. Several activation methods of the OMCs have been used, including the so-called "physical activation" using CO_2,[64–66] and chemical activation with KOH,[66–68] which successfully developed microporosity.

12.2.3.3 Doped Carbons

In order to improve hydrogen storage results in some of the above-mentioned porous carbons, two alternatives are being analyzed: (1) to dope them with heteroatoms like boron or nitrogen to increase the heat of hydrogen adsorption or (2) to increase the amount of hydrogen uptake by a spillover process of hydrogen using different metal nanoparticles that will dissociate the hydrogen molecules. As we will comment later, quite controversial results have been reported and, hence, a clear conclusion about the usefulness of these two alternatives cannot yet be deduced.

12.3 FUNDAMENTALS OF GAS ADSORPTION AT HIGH PRESSURE

In this section, some considerations and definitions about high-pressure adsorption under supercritical conditions and about the experimental procedure used to measure hydrogen adsorption isotherms are presented.

As it is known, the isotherm obtained experimentally in conventional gravimetric or volumetric systems is the excess adsorption isotherm or Gibbs isotherm, i.e. the amount of adsorbed gas whose density is greater than the density of the gas at the same pressure and temperature. Figure 12.1 gives a schematic representation of the Gibbs adsorption where the relation between excess adsorption and absolute adsorbed amounts are shown.

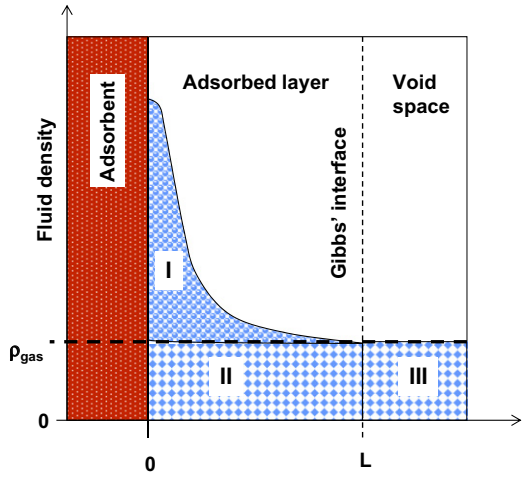

FIGURE 12.1 Schematic representation relating excess adsorption and absolute adsorbed amount. Region I represents the excess adsorption. Regions II and III represent the fluid with a density given by the conditions (P and T) inside and outside of the adsorption volume, respectively. Absolute adsorption is given by the sum of regions I and II. L is the thickness of the adsorbed phase. (For color version of this figure, the reader is referred to the online version of this book.)

The relationship between the excess, n_e (region I in Fig. 12.1), and the absolute adsorption amount, n_a (sum of region I and II), is given by the following equation:

$$n_e = n_a - \rho_{gas} V_{ad} \tag{12.1}$$

where ρ_{gas} is the gas density and V_{ad} is the volume of the adsorbed phase. Both n_e and ρ_{gas} are experimentally measurable parameters while n_a and V_{ad} cannot be directly measured.

Under subcritical conditions, it can be assumed that the density of the adsorbed phase, ρ_{ad}, is constant and equal to liquid or solid density of the adsorbate.[69] So, it is possible to obtain the absolute adsorption isotherm by introducing the following relations into Eqn (12.1):

$$\rho_{gas} = \frac{MP}{ZRT} \tag{12.2}$$

and

$$V_{ad} = \frac{n_a}{\rho_{ad}} \tag{12.3}$$

where, M is the molecular weight, Z is the compressibility factor, R is the gas constant, P is the pressure and T is the temperature. Therefore, Eqn (12.1) can be written as:

$$n_a = \frac{n_e}{1 - \dfrac{MP}{ZRT\rho_{ad}}} \tag{12.4}$$

In the case of adsorption at supercritical conditions, as it is the case of hydrogen adsorption at temperatures above 33.1 K, it is not possible to establish that the

adsorbed phase density (ρ_{ad}) is equal to liquid or solid adsorbate density because it cannot condense under supercritical conditions. There are different theoretical approaches to estimate the absolute adsorption isotherm. These models can be classified in a general way into two groups:[70] those which assume that the adsorbed phase density is constant and, therefore, use the Eqn (12.4) and those which consider that the adsorbed phase volume is constant and use Eqn (12.1).

However, to obtain the total amount of gas stored in a tank filled with an adsorbent, it is not necessary to calculate the absolute isotherm. A simple method to obtain the total storage capacities using only measurable parameters will be explained in Section 12.5.

Excess adsorption isotherms or Gibbs isotherms can be measured experimentally by different methods. Gravimetric and volumetric devices are the most extensively used.

In the gravimetric method, a degassed sample is introduced into a sample holder, which is situated inside a chamber, whose temperature remains constant and which can be pressurized. The chamber is pressurized with the gas (i.e. hydrogen) and the amount adsorbed is measured by reading the change of weight of the sample when thermodynamic equilibrium of adsorption is reached (the weight of the sample does not change anymore). The advantage of this method is that the weight change can be directly related to the amount of hydrogen that is adsorbed. The main error source is the buoyancy that the hydrogen gas has on the volume occupied by all mechanical parts connected to the balance, including the sample itself as well as the adsorbed phase. Thus, the buoyancy can be estimated by different ways.[71] After correcting the experimental data with the buoyancy due to the balance components, sample volume and sample holder, the excess or Gibbs isotherm is obtained.

Because the adsorption is directly measured by weighting, it is very important to use highly purified gases, especially in the case of hydrogen, because it is the lightest element. The presence of impurities was an error source in several works in this field as it will be presented next in Section 12.4.1.

The volumetric method (also called Sieverts method) is probably the most widely used to measure adsorption isotherms. In this case, the amount of gas adsorbed by the sample is determined indirectly by measuring the pressure variation in a given volume and using an appropriate gas equation of state (EOS). A typical device consists of two parts: the sample cell and the manifold. Both sample cell and manifold volumes are known and the temperature of the system is measured. The principle of this method is to expand gas from the manifold to the sample cell and measures the equilibrium pressure. There are different error sources in this method. One of them is the volume of the manifold. Since all calculations refer to this volume, it is very important to calibrate it with high accuracy. One of the main sources of error is due to the presence of leaks because a small leak could be interpreted as gas adsorption if the equilibrium time is larger than the rate of gas release due to the leak.

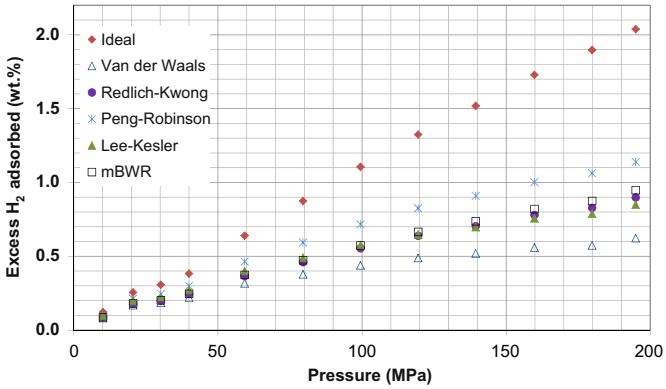

FIGURE 12.2 Excess hydrogen adsorption isotherms at 298 K and up to 200 bar (20 MPa) for an activated carbon obtained using different EOS. (For color version of this figure, the reader is referred to the online version of this book.)

Finally, a very common source of error, in both the gravimetric and volumetric method, is the incorrect data analysis. For example, the use of a suitable EOS is essential in the volumetric method. Different EOS can be used (Ideal, van der Waals, Redlich–Kwong,[72] Soave–Redlich–Kwong,[73] Peng–Robinson,[74] two equations based on the Benedict–Webb–Rubin equation: Lee–Kesler[75] and mBWR proposed by Younglove,[76] and Helmholtz equation[77]). The last two equations, mBWR proposed by Younglove[76] and Helmholtz,[77] give the best results for hydrogen and, hence, they are the equations recommended by the National Institute of Standards and Technology (www.nist.gov) of USA.

An example of the importance of the EOS used can be clearly seen in Fig. 12.2. The figure includes the same experimental hydrogen adsorption data (measured at 298 K and up to 20 MPa in a volumetric device) but treated with different EOS. The hydrogen adsorption capacity varies from 0.5 to 2 wt% depending on the EOS used. The highest value is obtained when the ideal EOS is used. Despite these great discrepancies, many authors dealing with hydrogen storage do not mention the EOS used in their publications or they use a nonsuitable EOS like ideal or Van der Waals EOS, as it occurred in a recent publication.[78]

In addition to the concepts discussed above regarding the experimental procedure for measuring and calculating the adsorption isotherms, several sample properties must be taken into account because they are necessary for a proper interpretation of results and because they will be used to determine the adsorption capacity on volumetric basis and for obtaining the total amount of hydrogen stored. Thus, different kinds of

sample densities are used in this field but, in some cases, they are erroneously used. Because of that, several density definitions are given next.

True density, also called skeletal density or Helium density (ρ_{He}), is defined as the solid mass divided by the volume occupied by the atoms of the sample. Thus, this density does not include the interparticle space volume neither the particle internal pore volume. True density is a relatively well-defined quantity as it is not dependent on the degree of compaction of the solid. True density is measured by Helium pycnometry.

Bulk density and tap density (ρ_{tap}) are defined as the solid mass divided by total volume occupied by the solid. These densities include the volume occupied by the solid atoms, the particle internal pore volume and the interparticle space volume. Bulk density has different values depending on whether it is measured in the freely settled or compacted state. Bulk density is determined by putting a solid mass in a container (e.g. in a burette) and measuring the volume it occupies. The sample can be subjected to a specified compaction, usually involving vibration of the container, from which the tap density is obtained.

Packing density ($\rho_{packing}$) refers also to a bulk density but in this case, the sample is subjected to a compression process by applying axial pressure in order to decrease the interparticle space. This density also includes the volume occupied by the solid atoms, the particle internal pore volume and the interparticle space volume. Packing density is determined by putting a solid mass in a container, applying pressure and measuring the volume occupied. The final pressure applied has a great effect on the density value obtained (in general, $\rho_{packing}$ increases with pressure).[79] Therefore, when packing density is used, the pressure applied for measuring has to be indicated. Furthermore, it must be checked that the applied pressure does not reduce the sample porosity. For example, MOFs do not support high compacting pressures and their porosity falls down.[79–81]

Finally, other packing density that is frequently and erroneously used by authors in the field of hydrogen storage in MOFs is the crystal density. Crystal density refers to the mass of solid divided by the volume occupied by the particle. This density includes the volume occupied by the solid atoms and the particle internal pore volume but does not include the interparticle space volume. Crystal density can be calculated from X-Ray diffraction (XRD) data for MOFs.

As expected from the previous definitions, the density of the materials increases following the sequence: bulk density < tap density < packing density < crystal density < true density. As it will be shown later, the density used will have a great influence in the amount of adsorbed hydrogen in volumetric basis and, hence, in the resulting total hydrogen storage capacity.

12.4 HYDROGEN ADSORPTION IN CARBON MATERIALS

12.4.1 State of the Art

Carbon materials created great expectation in the field of hydrogen storage due to the promising results reported by Dillon et al.,[82] who predicted a hydrogen adsorption capacity between 5 and 10 wt% for the SWCNTs in samples which contained <0.2 wt% of nanotubes. This high expectation was augmented by Chambers et al.[83] who reported a hydrogen adsorption capacity of 67.55 wt% on herringbone CNFs and a value of 53.68 wt% on platelet CNFs at room temperature and 11.2 MPa. Because of this, many of the initial work on hydrogen storage in carbon materials focused on the use of CNTs and CNFs.

An example about the values reported[83–106] for hydrogen adsorption at room temperature at different pressures on both CNTs and CNFs can be seen in Fig. 12.3. It plots the gravimetric hydrogen adsorption capacity versus the apparent BET surface area (calculated by the Brunauer-Emmett-Teller method) of the samples used. The two highest values in Fig. 12.3 correspond to those reported by Chambers et al.[83] As it has been previously indicated, these values belong to two types of CNFs (herringbone and platelet CNFs). Gupta et al.[95] had also reported a hydrogen adsorption capacity of 17 wt% at room temperature and 12 MPa, on graphite CNFs synthesized using Pd as catalyst. Many other authors had tried to reproduce these results, but all of them failed.[107,108] For example, same CNFs used by Chambers et al. were reproduced by Anh et al.[109] but <5 wt% of H_2 was obtained, and only when the sample was cooled below 100 K. Xu et al.[108]

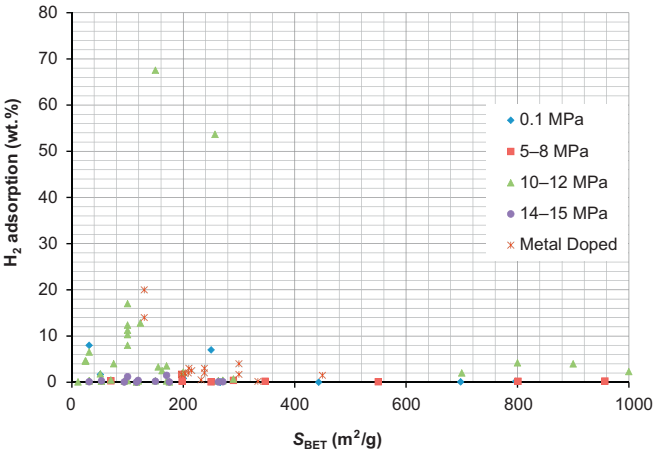

FIGURE 12.3 Hydrogen adsorption data found in the literature at room temperature and different pressures on gravimetric basis on different carbon nanotubes and nanofibers versus their apparent BET surface area. (For color version of this figure, the reader is referred to the online version of this book.)

also showed that graphitic CNFs adsorb <0.25 wt% of hydrogen at room temperature and 10 MPa.

Other outstanding values in this figure are those reported by Chen et al.,[92] corresponding to Li-doped CNTs (20 wt% of hydrogen) and to K-doped CNTs (14 wt% H_2), both at atmospheric pressure. These authors carried out the measurements with purified H_2 (99.99%) by using a thermogravimetric device. In 2000, Yang[110] demonstrated that the large amounts of hydrogen adsorbed were partially due to the moisture of the gas. In this case, "ultrahigh purity grade" hydrogen (>99.999%) and a series of traps for removing the water was used. The hydrogen adsorption capacity did not exceed 2.5 wt% for Li-doped CNT, and 1.8 wt % H_2 in K-doped CNT.

Besides these doubtful outstanding results, one can see in Fig. 12.3 that there is a large scatter in the reported values and that it does not exist any clear trend between the hydrogen adsorption capacity and the porosity (i.e. BET surface area) on CNTs and CNFs. This high dispersion on the results and low reproducibility of experimental measurements are mainly attributed to experimental errors (specially the small amount of sample used, the use of nonpurified hydrogen,…), the different purities and characteristics of the samples used due to their different synthesis methods (conditions and catalyst) as well as to the different purification methods used.[111–114]

Other more "classical" porous carbon materials have also been widely studied for hydrogen storage. Figure 12.4 compiles a selection of the hydrogen adsorption capacities values reported in the literature at room temperature, and at different pressures, on several ACs, ACFs, and ZTCs versus their apparent BET surface area.[58,115–119]

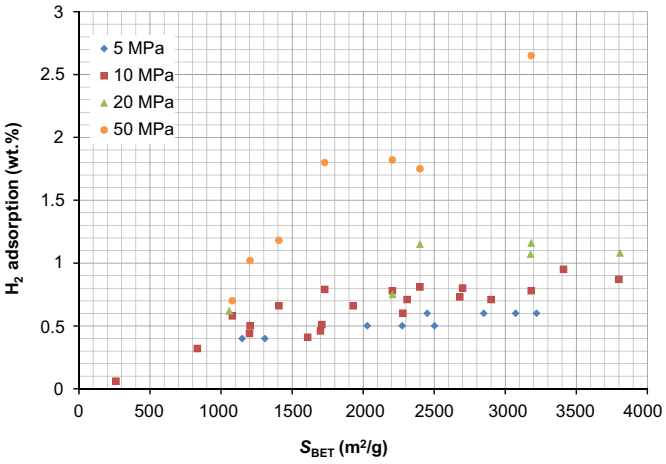

FIGURE 12.4 Hydrogen adsorption data found in the literature at room temperature and different pressures on gravimetric basis on ACs, ACFs and ZTCs versus their apparent BET surface area. (For color version of this figure, the reader is referred to the online version of this book.)

Contrary to what happened with CNTs and CNFs, a much clear relationship can be observed in these more "classical" porous carbons in which the hydrogen adsorption capacity increases reasonably well with the sample porosity (e.g. BET surface area). This relationship is apparently independent of the type of porous carbon material (AC, ACF, templated carbons…). And, as expected, the hydrogen adsorption capacity increases with the pressure used. These observations, indicative and characteristic of a physisorption process, are in agreement with theoretical and experimental works reporting heats of hydrogen adsorption on carbon materials between 4 and 8 kJ/mol[120,121] typical of a physisorption process.

A closer look to Fig. 12.4 shows that at 10 MPa, values close to 1 wt% of hydrogen are obtained with ZTCs.[58] At pressures of 20 MPa, the highest adsorption capacity is 1.15 wt% which corresponds to ACs prepared by chemical activation with KOH of an anthracite.[115] Very recently, [122] a 1.3 wt% has been reported at the same pressure using CNFs activated in CO_2. At 34 MPa, a value of 2.3 wt% has been obtained with a ZTC[58] (data not shown in Fig. 12.4). At 50 MPa, one of those KOH-activated samples presents a hydrogen adsorption of 2.65 wt%.[115]

From the comparison of Figs 12.3 and 12.4, it can be summarized that the former shows a much larger scattering in the values (in some cases with such unexpected very high hydrogen adsorption capacities). Such comparison confirms the influence of the previously commented different errors related with sample purity, hydrogen quality and technical problems during hydrogen adsorption experiments.[114] Although Fig. 12.4 shows for these "classical" porous carbon materials (ACs, ACFs, and templated carbons) less spectacular hydrogen adsorption values than Fig. 12.3, they are much more reproducible. Additionally, the hydrogen uptakes are related to the sample porosity, independently of the type of porous carbon material used.[114,115] In the following section, we will focus only on reproducible reported hydrogen results (on a gravimetric or volumetric basis) usually obtained with these "classical" porous carbons at different temperatures and pressures.

12.4.2 Hydrogen Adsorption on "Classical" Carbon Materials

Reproducible high-pressure adsorption of hydrogen on classical porous carbons has been widely and deeply studied and a huge number of published papers deal with hydrogen adsorption under different experimental conditions (i.e. temperatures and pressure). Nevertheless, although obtained data are reproducible, important discrepancies on the interpretation of the experimental data can be found in the literature. Thus, some researchers

have established that hydrogen adsorption capacity of porous carbons is directly related to the BET surface area and total micropore volume,[123,124] while others have not found a so clear relationship between those parameters;[125,126] however, other authors have found a linear trend between hydrogen adsorption and the narrow micropore volume (<0.7 nm),[127,128] determined by CO_2 adsorption at 273 K. In part, such discrepancies are due to the fact that hydrogen adsorption results are strongly dependent on both the temperature and pressure used, as well as on the sample characteristics.

In order to get insights into these discrepancies and trying to understand the adsorption process at high pressures, we are doing research in gas storage, including hydrogen storage, for more than 15 years. Such intense research carried out on high-pressure adsorption of hydrogen was focused on (1) experimental measurements of hydrogen adsorption at high pressures and different temperatures (298 and 77 K) in a wide variety of reproducible carbon materials (15 samples that include a series of ACs by KOH activation of different coals as raw materials (anthracite and bituminous coal), commercial ACs (Maxsorb-A and AX21), CNTs, CNFs, as well as their corresponding KOH-activated CNTs and CNFs and (2) providing an interpretation of the hydrogen adsorption data according to the properties of the carbon materials (SSA, pore size distribution, structure and packing density) and to the adsorption conditions (temperature and pressure), making use of the fundamentals of adsorption at supercritical conditions. A compilation of our hydrogen storage research can be found elsewhere.[115–117,129] From such study, it can be concluded that at 298 K, the hydrogen adsorption capacities up to 20 MPa depend on both the adsorption capacity of the sample (i.e. micropore volume or the apparent BET surface area) and on its micropore size distribution (MPSD). As the pressure decreases, the MPSD becomes more relevant being the key parameter at pressures <10 MPa. On the other hand, hydrogen adsorption capacity at 77 K and at pressures up to 4 MPa follows a good correlation with the total micropore volume of the samples. As the storage pressure decreases (e.g. at atmospheric pressure), the MPSD also becomes the most important sample parameter.

In this chapter, we will deepen into the conclusions obtained in our previous works[115–117,129] and we will extend the analysis to other types of carbon materials (such as, ZTCs, CDCs, metal doped nanotubes, boron- and nitrogen-doped nanotubes, and so on). Thus, in the following sections, the hydrogen adsorption values found in the literature for those materials at different temperatures and pressures conditions will be compared with our results obtained in a large series of porous carbons (e.g. activated coals, commercial ACs (Maxsorb-A and AX21),[80,81,115] ACFs,[130,131] CNTs, CNFs, activated CNTs[115–119] and activated CNFs[122,132]).

12.4.2.1 Hydrogen Adsorption at 298 K

A very wide range of hydrogen pressures (from atmospheric pressure up to even more than 50 MPa) have been used by different researchers to study the hydrogen adsorption at 298 K on many nanoporous carbons. As a summary, Fig. 12.5 includes the gravimetric amount of hydrogen adsorbed (weight percent) at four different pressures (5, 10, 20 and 50 MPa) versus the total micropore volume ($V_{\mu p}$) (pore size <2 nm; obtained from N_2 adsorption isotherms at 77 K) for many nanoporous carbons. These materials include KOH-activated coals, commercial ACs (Maxsorb-A and AX21), ACFs, CNTs, CNFs, KOH-activated CNTs, activated amorphous CNFs, and ZTCs.[58,115–119,122]

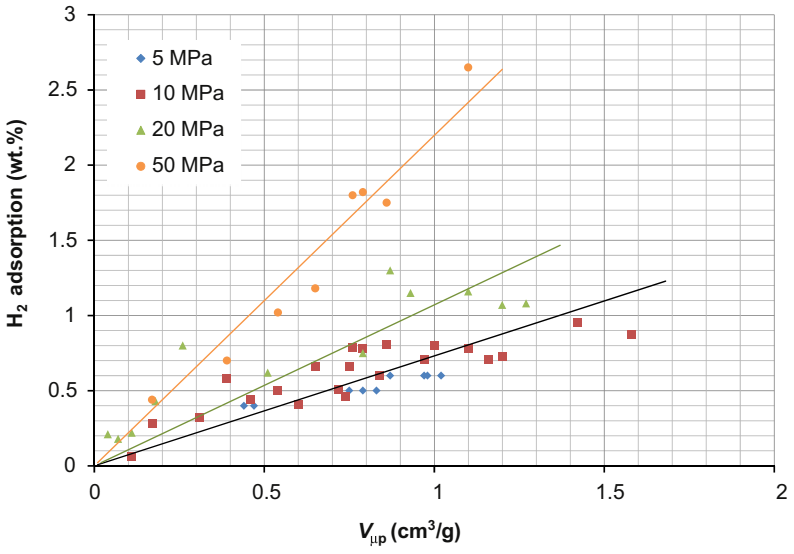

FIGURE 12.5 Amount of hydrogen adsorbed at 298 K and different pressures in a wide range of nanoporous carbons versus the total micropore volume. (For color version of this figure, the reader is referred to the online version of this book.)

A general trend, where hydrogen adsorption capacity increases with total micropore volume, is observed for all the pressures, being the best correlation, that obtained for hydrogen adsorption results at 50 MPa. The values obtained at that pressure follows a linear relationship with the total micropore volume which is better than those observed at 20 MPa, 10 and 5 MPa. The highest adsorption capacity corresponds to an AC prepared by KOH activation of an anthracite, reaching a value of 2.7 wt% at 50 MPa.[115] It should be remarked that that sample is the best among the KOH-ACs series specially prepared with tailored porosity.[33] This selected sample remarks the importance of developing materials with suitable porosity for hydrogen storage at room temperature.

At lower pressures (20, 10 and 5 MPa), some deviations to this general trend exist. It can be seen that the samples with the highest porosity development do not present the highest hydrogen adsorption capacity, but the highest hydrogen adsorption capacity at each pressure corresponds to samples with slightly lower micropore volume but with narrower MPSD. These results point out the importance of developing materials having both high micropore volume and narrow MPSD for the adsorption of hydrogen at room temperature and pressures up to 20 MPa. This conclusion agrees with that obtained in a previous paper, which showed that the optimum pore size for hydrogen adsorption on porous carbons at these conditions is close to 0.6 nm.[133]

Thus, as the pressure decreases, the hydrogen adsorption capacity correlates much better with the narrow micropore volume (<0.7 nm obtained from CO_2 adsorption at 273 K) than with total micropore volume used in Fig. 12.5. Figure 12.6 presents the hydrogen adsorption capacity values plotted versus the narrow micropore volume ($V_{\mu p}(CO_2)$). It can be observed that for lower pressures (20, 10 and 5 MPa), better linear correlations than that in Fig. 12.5 are obtained. This is important, and should be remarked, because it confirms that to maximize the hydrogen storage at room temperature and up to 20 MPa, adsorbents with narrow micropores should be designed. On the other hand, in the case of hydrogen adsorption at 50 MPa, a very high dispersion of the results is obtained using $V_{\mu p}(CO_2)$. These results can be explained considering the fundamentals of supercritical adsorption. H_2 has a critical pressure (P_c) equal to 1.315 MPa and a critical temperature (T_c) of 33.19 K. This means that at room temperature, hydrogen behaves as a supercritical fluid. Thus, there will not exist volume filling of the adsorbate and the density of the adsorbed phase will depend on both pressure and pore size.[134] However, it is possible to estimate a "saturation pressure" under supercritical conditions by using different empirical equations,[135] for example, the equation proposed by Dubinin ($P_S = P_C(T/T_C)^2$),[135,136] what is useful for a qualitative interpretation of the experimental data. This equation gives a value of $P_S = 106$ MPa for hydrogen at room temperature. Using this saturation pressure value, hydrogen adsorption isotherms can be expressed and compared as a function of their relative pressures (P_r). These two experimental conditions (20 and 50 MPa) give rise to a relative pressure of 0.19 at 20 MPa and of 0.47 at 50 MPa. Considering these values of relative pressures, it can be understood that at 0.47 (50 MPa), the contribution of the micropores to the total adsorption is important as shown in Fig. 12.5. Contrarily, at lower relative pressure (0.19; 20 MPa), the narrow micropore volume controls the hydrogen uptake, as shown in Fig. 12.6.

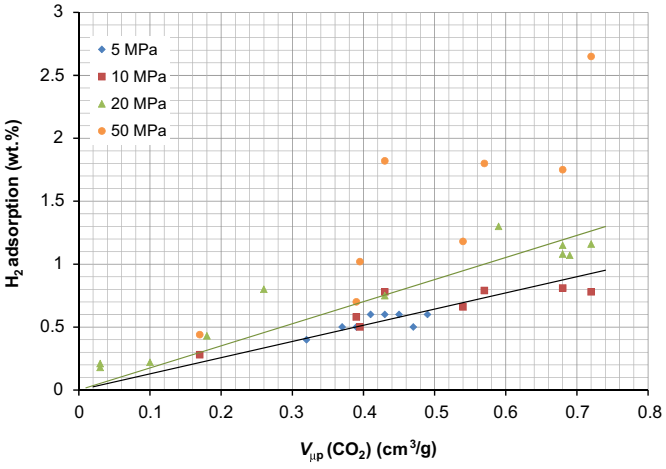

FIGURE 12.6 Amount of hydrogen adsorbed at 298 K and different pressures in a wide range of nanoporous carbons versus the narrow micropore volume. (For color version of this figure, the reader is referred to the online version of this book.)

To try to enhance the above commented hydrogen storage values at room temperature, other alternatives are under research by different research groups. As an example, we will mention two recent contributions carried out in our research group: (1) Using a controlled CO_2 activation process of amorphous CNFs (produced by the polymer blend technique), activated CNFs with moderate adsorption capacity but with well-controlled MPSD were prepared. The maximum H_2 uptake (room temperature and at 20 MPa) reached a value of 1.3 wt%.[122] (2) Enhancing the hydrogen storage by increasing the heat of adsorption of hydrogen (from 4 to 8 kJ/mol to 8–11 kJ/mol) by using pillared carbons. These pillared samples, obtained from graphite oxide silylated with methyltrichlorosilane, reach a maximum H_2 uptake (at room temperature and at 20 MPa) of 0.6 wt% in spite of their low micropore volume (about 0.2 cm^3/g measured by CO_2 adsorption at 273 K).[137]

To further increase the amount of hydrogen stored in a given porous sorbent, a quite suitable alternative is to

decrease the adsorption temperature. This means the use of cryogenic conditions (Section 12.4.2.2).

12.4.2.2 Hydrogen Adsorption at 77 K

Excess adsorption isotherms for hydrogen at 77 K and up to different pressures (0.1, 2, 4 and 6 MPa) on many types of nanoporous carbon materials have been published by different researchers, being the most widely used the adsorption at 0.1 MPa (due to the accessibility to low-pressure gas adsorption equipments). A compilation of these data is included in Fig. 12.7, where the amount of hydrogen adsorbed at 77 K and different pressures are plotted versus the total micropore volume for a wide spectrum of nanoporous carbon materials (ACs, ACFs, CDCs, ZTCs, OMCs, and among others).[51,58–60,62,64,65,67,80,89,100,115,116,121,123,126–128,131,132,138–158] Considering the large number of samples, the different authors and the fact that the total micropore volumes extracted from the literature have been estimated using different adsorption equations, the correlations found in Fig. 12.7 are acceptable. In general, they allow us to conclude that hydrogen adsorption at 77 K increases with the micropore volume of the samples and with the hydrogen pressure. Hence, as expected, the values of hydrogen adsorption at the lowest pressure used (0.1 MPa) are much lower. The quite close hydrogen adsorption values obtained for samples with similar porosity at 2 and 6 MPa can be easily explained. For these porous carbon materials, the excess adsorption isotherms of hydrogen at 77 K and up to 4 MPa are of Type I, as shown elsewhere,[116] reaching a maximum at around 2–4 MPa and decreasing at higher pressures.

As the hydrogen storage pressure decreases, the hydrogen adsorption capacity correlates much better with the narrow micropore volume (<0.7 nm obtained from CO_2 adsorption at 273 K) than with total micropore volume used in Fig. 12.7. This is clearly shown in Fig. 12.8 that plots the hydrogen adsorption capacity at 77 K and 0.1 MPa versus the narrow micropore volume ($V_{\mu p}$ (CO_2)) for samples in which their $V_{\mu p}$ (CO_2) have been reported. The hydrogen uptake data correlate quite well with the narrow micropore volumes, which indicates that at 77 K and at 0.1MPa, the narrow microporosity plays the most relevant role. Similar to the discussion done for the results obtained at room temperature, the saturation pressure of hydrogen at 77 K, estimated by Dubinin equation,[136] is 7 MPa. Thus, hydrogen relative pressure at 0.1 MPa is quite low ($P_r = 0.014$); hence, only the narrow micropores contribute in a larger extent to the hydrogen adsorption due to their higher adsorption potential.

As a summary, at 77 K and relatively high pressure (4 MPa), no effect of the MPSD on the hydrogen adsorption capacity is observed and samples with high micropore volumes are desired. On the other hand, and as it was already published by our research group with many different samples prepared in our laboratory,[115] at 77 K and low pressure (0.1 MPa), the narrow micropore volume controls the hydrogen uptake (analogously to hydrogen adsorption at room temperature and pressures up to 10–20 MPa). This strong correlation between the H_2 storage capacities at 77 K (0.1 MPa) and 298 K (10–20 MPa) and the narrow micropores has been also recently discussed by Yang et al.,[159] where H_2 adsorption was found to occur preferentially in ultrafine pores (diameters <1 nm) at both 77 K (≤0.1 MPa) and 298 K (10 MPa), irrespective of the adsorbent (MOFs and microporous carbons). They found an empirical correlation

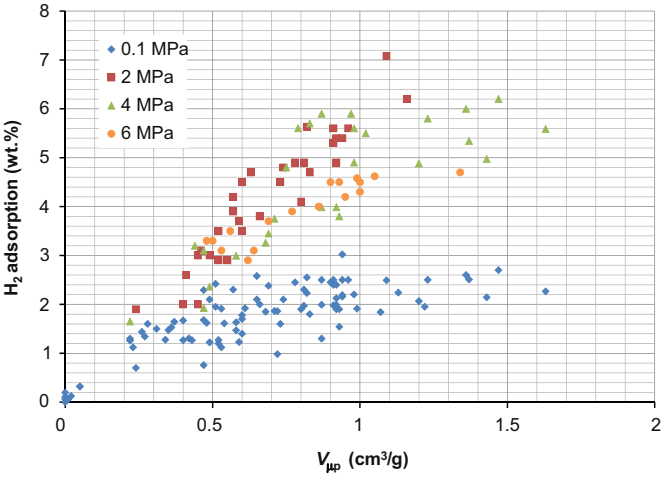

FIGURE 12.7 Amount of hydrogen adsorbed at 77 K and different pressures (0.1, 2, 4 and 6 MPa) on several types of nanoporous carbons (ACs, ACFs, CDCs, ZTCs and OMCs) versus the total micropore volume. (For color version of this figure, the reader is referred to the online version of this book.)

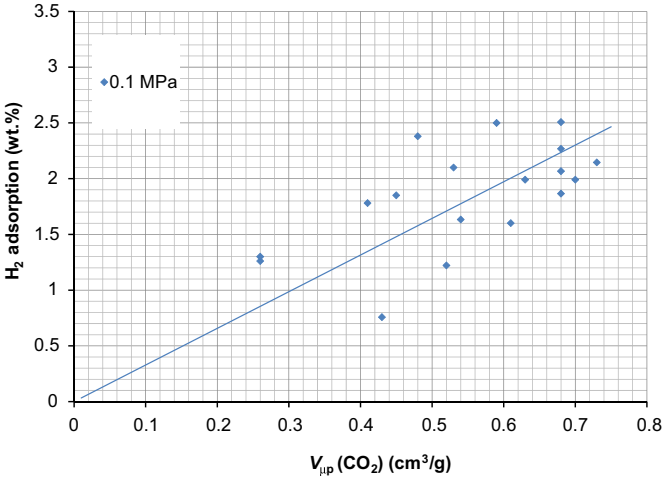

FIGURE 12.8 Amount of hydrogen adsorbed at 77 K and 0.1 MPa on several types of nanoporous carbons versus the narrow micropore volume. (For color version of this figure, the reader is referred to the online version of this book.)

between the H_2 adsorption capacities at 77 K (0.1 MPa) and 298 K (10 MPa). This correlation offers an easy method for predicting H_2 adsorption capacities under unapproachable conditions by many researchers (for example, 298 K and 10 MPa) of a given porous material.

12.5 HYDROGEN STORAGE CAPACITIES

12.5.1 Hydrogen Adsorption on Volumetric Basis

Adsorption isotherms are usually measured on gravimetric basis, i.e. amount of gas adsorbed per weight of sample. However, from a practical point of view, and also to make easier the comparison between different adsorbents, hydrogen adsorption capacities should be reported on a volumetric basis, which makes necessary to know and use a suitable sample density (see Section 12.3). Usually, in the literature reporting hydrogen adsorption, the data are expressed on gravimetric basis, and data on volumetric basis or density of the material are not reported.

The importance of expressing the amount of hydrogen adsorbed on volumetric basis was already remarked in 1994 by Chahine and Bose,[146] and later by Buczek et al.[139] and by Zhou et al.[150] Also, works from our research group highlighted the importance of the sample density on the field of gases storage.[80,81,115–117,129,132,160–162] Although these studies and others clearly demonstrate the importance of reporting the gas adsorption capacities on volumetric basis, unfortunately, it is not commonly found in the literature. Next, the effect of material density on the calculated hydrogen adsorption capacity on volumetric basis, will be pointed out.

As an example to discuss the effect of the density used for converting gravimetric values to volumetric ones, Fig. 12.9 contains the excess hydrogen adsorption isotherm at 77 K and up to 4 MPa for the commercial AC Maxsorb expressed on volumetric basis by using three different densities.

In Fig. 12.9, it is clearly observed that the density of the material used for calculating the isotherms on volumetric basis has a great effect on the obtained values. Hydrogen adsorption capacities from 19.2 to 25.6 g/l are obtained by using tap or crystal density, respectively. Here, we have used a calculated crystal density for this material, only for the purpose of demonstrating the great effect of the density, and because many works on hydrogen storage in MOFs mistakenly use this density. As it was indicated in Section 12.2, different material densities can be measured but only those that include the interparticle void space should be used for calculating hydrogen adsorption capacities on volumetric basis. Therefore, only bulk, tap or packing density must be used.

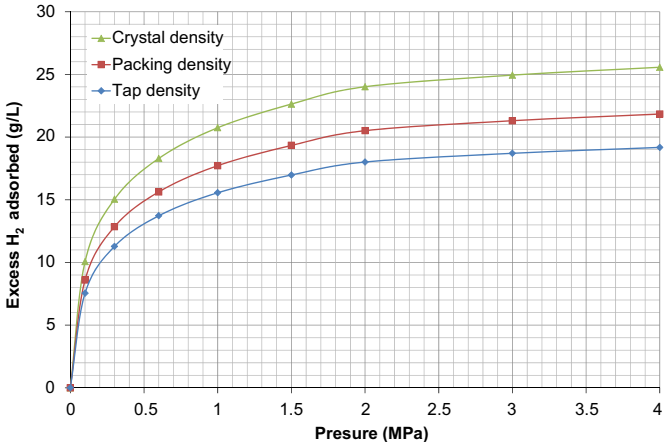

FIGURE 12.9 Excess hydrogen adsorption isotherm at 77 K and up to 4 MPa for commercial activated carbon Maxsorb expressed in volumetric basis by using different densities. (For color version of this figure, the reader is referred to the online version of this book.)

In general, bulk, tap and packing densities decrease with increasing material porosity (i.e. increase the internal pore volume). An example of the variation of tap and packing densities with the porosity is shown in Fig. 12.10 for a series of KOH-ACs.[116]

Packing density values in Fig. 12.10 were determined by pressing at 550 kg/cm^2 a given amount of AC in dry basis (1 g approximately) in a mould. From these results, it can be said that, in general, the higher the porosity development of the materials, the lower the tap and packing densities, following a linear trend. Packing densities for these materials are between 0.4 and 0.75 g/cm^3 and their tap densities vary between 0.3 and 0.66 g/cm^3. Due to this evolution, hydrogen adsorption on volumetric basis does not follow the same trend with the sample porosity as that shown in Section 12.4.2 for the adsorption of hydrogen in gravimetric basis.

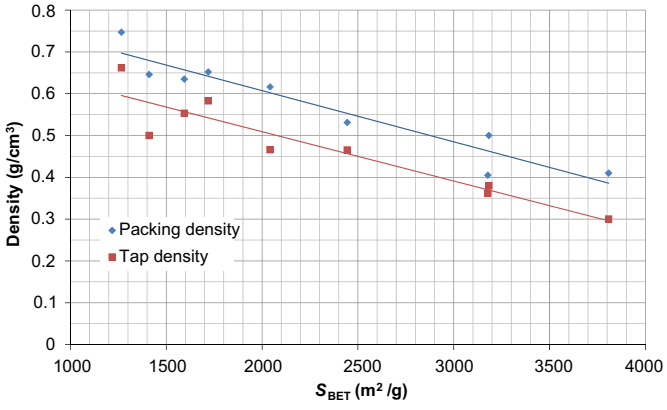

FIGURE 12.10 Packing and tap density of powder activated carbons versus their BET surface area. (For color version of this figure, the reader is referred to the online version of this book.) *Source: Data from Ref. 116.*

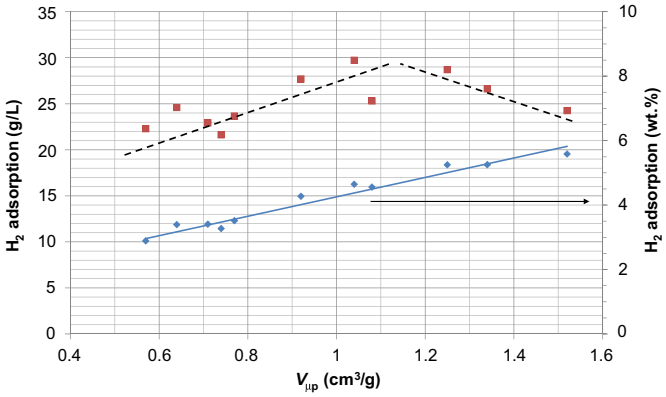

FIGURE 12.11 Hydrogen adsorption capacities at 77 K and 4 MPa on gravimetric basis (right-hand *y*-axis) and on volumetric basis (left-hand y-axis). (For color version of this figure, the reader is referred to the online version of this book.) *Source: Data from Ref. 116.*

This fact is illustrated in Fig. 12.11, where the hydrogen adsorption capacity for a series of ACs at 77 K and 4 MPa, both on gravimetric and volumetric basis, is shown. Values are extracted from Ref. 116 and packing density values from Fig. 12.10 were used for calculating capacities on volumetric basis. As it was explained in Section 12.4.2, hydrogen adsorption capacity on gravimetric basis at 77 K and 4 MPa follows a good correlation with the total micropore volume. Thus, the highest adsorption capacity value is obtained with the sample having the highest micropore volume. Noteworthy, for the data on volumetric basis, the maximum hydrogen adsorption does not correspond to the sample with the highest micropore volume, but to those samples that have a quite high porosity development and still present quite high packing density. Thus, according to these results, in order to get a maximum hydrogen adsorption capacity on volumetric basis, the best results will be obtained for materials with a good balance between porosity development and packing density.

Consequently, there is a need to increase the density of the porous carbon materials. One way to do it is first by a suitable selection of the carbon precursor, the activation method used and the variables of the activation process[33] followed by making pieces, pellets or monoliths of these selected ACs.[129] Additionally, from an application point of view, pieces have advantages regarding to powdered samples because they can present good mechanical properties, they are easier to handle than powder and appropriately prepared pieces, pellets or monoliths can give materials with high density. For example, Jordá-Beneyto et al.[116] prepared high-density monoliths from powder high-surface area AC by using a polymeric binder, submitted to hot pressing and to carbonization. The textural parameters of those carbon monoliths slightly decrease but their densities increase with respect to the starting powder ACs. The best value obtained on volumetric basis with a carbon monolith in that work was a hydrogen adsorption capacity of 29.7 g/l at 77 K and 4 MPa.[116] Similar strategy was used by other authors. Thus, Singer et al.[163] prepared peels and pellets from powder CDCs by using Polytetrafluoroethylene (PTFE) as binder. A hydrogen adsorption capacity on volumetric basis of 21 g/l at 77 K and 4 MPa was achieved. Later, other work from Gogotsi group[164] reported the synthesis of monolithic CDCs by chlorination of fully dense ceramic titanium carbide plates. The resulting materials had mainly micropores and exhibited enhanced volumetric hydrogen adsorption capacity compared to powder equivalents, achieving a hydrogen adsorption capacity of 35 g/l at 77 K and 6 MPa on a monolith with a density of 1 g/cm^3.

12.5.2 Total Hydrogen Storage Capacity

The most interesting parameter, from a practical point of view, is the total amount of gas stored. This is the amount of gas that can be introduced in a tank filled with an adsorbent. This parameter includes the amount of gas adsorbed in the porosity of the material plus the compressed gas in the space not occupied by atoms of the material, including the interparticle space but also the porosity of the sample, as it is discussed below. Therefore, the total gas in a tank is the sum of regions I, II and III represented in Fig. 12.1.

Attending to the definition of excess or Gibbs isotherm explained in Section 12.3 and shown in Fig. 12.1, what is measured experimentally is the amount of gas in region I. Therefore, to obtain the total amount of gas stored in a tank filled with an adsorbent, in addition to the excess adsorption isotherm, we need to know the space occupied by the skeleton of the material and how much material we can introduce inside the tank. The volume occupied by the skeleton of the material (V_S) can be measured experimentally by helium pycnometry (i.e. true density) as it is shown by Eqn (12.5):

$$V_s = \frac{1}{\rho_{He}} \tag{12.5}$$

and the amount of material (W) that we can put in the tank can be obtained from its bulk, tap or packing density:

$$W = V_{tank} \cdot \rho_a \tag{12.6}$$

where V_{tank} is the tank volume and ρ_a is the bulk, tap or packing density. Therefore, the free volume, V_f, or volume not occupied by the skeleton of the material in a tank is

$$V_f = V_{tank}\left(1 - \frac{\rho_a}{\rho_{He}}\right) \tag{12.7}$$

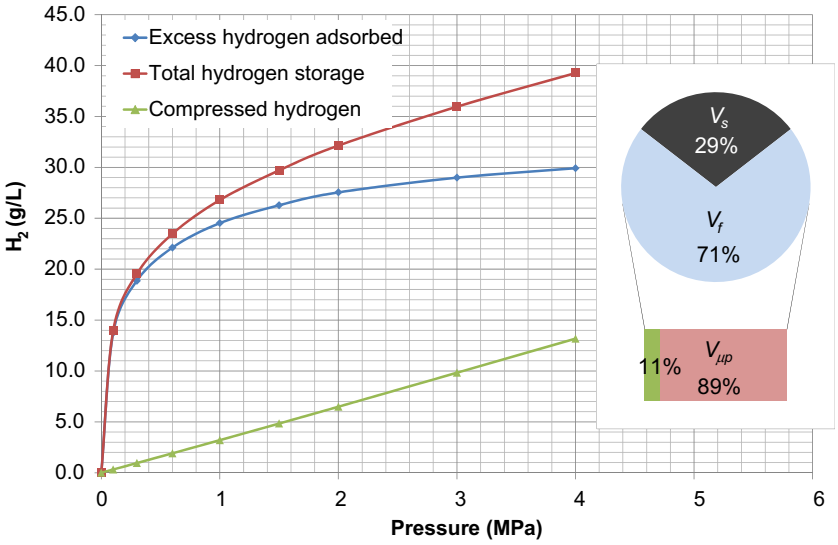

FIGURE 12.12 Hydrogen storage capacity in a tank of 1 l at 77 K and up to 4 MPa just by compression (green line), and filled with a carbon monolith:[116] adsorption excess data on volumetric basis (blue line) and total hydrogen storage capacity (red line). The insert represents an estimation of the distribution of the volume occupied by the skeleton of the material (V_S) and the free volume, V_f, available in a tank filled with this carbon monolith. The percentage of the V_f, which corresponds to the microporosity of the monolith (micropore volume $V_{\mu p}$), is of 89%. (For interpretation of the references to color in this figure legend, the reader is referred to the online version of this book.)

V_f corresponds to the volume of regions II and III in Fig. 12.1.

Finally, the total amount of gas stored (n_S) in a tank of 1 l is

$$n_S = n_e + \rho_{gas}\left(1 - \frac{\rho_a}{\rho_{He}}\right) \tag{12.8}$$

where n_S and n_e are on volumetric basis.

With this simple equation and using only experimentally measurable parameter, the total amount of gas stored can be obtained.

Figure 12.12 includes the amount of hydrogen stored in a tank with a volume of 1 l at 77 K and up to 4 MPa just by compression (triangles), the adsorption excess data on volumetric basis (diamonds), and the total hydrogen storage capacity (squares). These hydrogen isotherms, used as an example, correspond to an activated carbon monolith (ACM)[116] with a piece density of 0.61 g/cm^3, a ρ_{He} of 2.2 g/cm^3, an apparent surface area S_{BET} of 2374 m^2/g and a micropore volume $V_{\mu p}$ of 1.04 cm^3/g.

It can be seen that storage of hydrogen at 77 K achieves considerable enhancement due to both adsorption and compression. The total hydrogen storage capacity of a 1 l tank filled with this carbon monolith is 39.3 g H_2 at 77 K and 4 MPa, which is around three times the amount stored in the same container just by compression (13.2 g of H_2). This concept of total hydrogen storage is applicable to other adsorption conditions, such as 298 K, and on any type of porous carbon materials.[115]

The insert in Fig. 12.12 represents an estimation of the distribution of the volume occupied by the skeleton of the material (V_S, calculated from Eqn (12.5)) and the free volume (V_f, calculated from Eqn (12.7)) available in a tank filled with this carbon monolith. As it is shown in this figure, the carbon skeleton occupies 29% of the tank volume and about 71% corresponds to void volume where the gas adsorption and compression takes place. By using micropore volume ($V_{\mu p}$) and density of this monolith, the percentage of the V_f which corresponds to its microporosity was estimated. Thus, about 89% corresponds to micropores and only 11% corresponds to other voids, mainly due to the interparticle space. These values show the high compaction of this sample, where its interparticle space was highly reduced after preparing the monolith from the powder sample.

12.6 COMPARISON WITH OTHER POROUS MATERIALS

Hydrogen adsorption capacities on other types of porous materials, like zeolites,[126,165–174] MOFs[175–195] and covalent organic frameworks (COFs)[196,197] have been widely studied.

Zeolites are well-known inorganic crystalline materials containing pores in a three-dimensional disposition which pore diameters vary from 0.3 to 0.9 nm.[198] These materials are widely used in heterogeneous catalysts, catalysts supports and as ion exchangers.[199] The elemental composition of a zeolite is $M_{n/v}(Al_nSi_mO_{2(m+n)})\cdot wH_2O$, in which M is the counterbalancing cation, n is the number of Al atoms, v is the valence of M, m is the number of Si atoms in the framework and w is the number of hosted water molecules. The Si- and Al atoms are tetrahedrally coordinated by the oxygen atoms and are called the T atoms of the zeolite. Other elements (P, Ge, Ga, Ti, B, etc.) can be found as T atom. The counterbalancing cations are normally elements of the 1 and 2 groups.

Hydrogen adsorption in zeolites has been reported, both at 77 K[126,165] and at room temperature.[165,172,174] The amount of hydrogen adsorbed at room temperature by zeolites is <0.2–0.3 wt%.[165] At cryogenic temperatures, their hydrogen adsorption capacity follows a linear relationship with porosity. As it can be observed in Fig. 12.13, a good correlation is obtained between the amount of hydrogen adsorbed at 77 K and their BET surface area.[165] Values achieved by the zeolites are similar to those obtained by other porous materials with similar porosity (Fig. 12.13). However, the low development of porosity of zeolites (<1000 m^2/g) makes these materials not very attractive for this application compared with porous materials with higher porosity development.

MOFs are crystalline solids that are assembled by the connection of metal ions or clusters through molecular bridges.[184,185,192,193] Metals like Zn, Cu, Ni, Al, Cr, Mg, etc. are used as inorganic units. Carboxylic compounds based on phenyl and polyphenyl molecules are the organic units. Both parts (inorganic and organic) are linked through carboxylate groups. Recently, COFs have been synthesized.[196,197,200–202] These materials are synthesized by self-assembling based on the interaction between poly boronic acids and poly diol compounds forming boronate ester as linking bonds. Thus, the framework is formed by strong covalent bonds (C–C, C–O, B–O, …) rather than metal ions (as in the case of MOFs) to produce materials with high porosity (COFs with $S_{BET} > 3500\ m^2/g$ can be prepared). In both types of materials, the possibility of using different organic molecules, metals and ligands makes possible the preparation of MOFs and COFs with different porosities, geometries and properties.

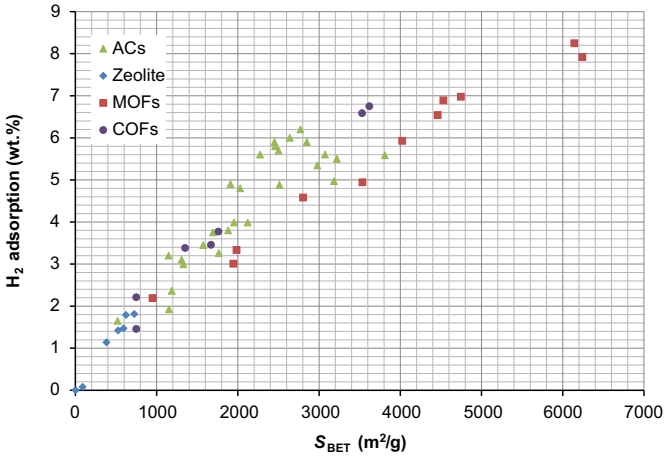

FIGURE 12.13 Hydrogen adsorption capacities on gravimetric basis at 77 K and 4 MPa on zeolites, carbon materials (ACs), MOFs and COFs. (For color version of this figure, the reader is referred to the online version of this book.)

These materials have been extensively studied for gas storage applications due to their exceptionally high porosity.[180] Thus, a large number of articles can be found in the literature. A detailed review of hydrogen adsorption in MOFs and COFs is out of the scope of this chapter since it focuses mainly on carbon materials. Extensive reviews on hydrogen storage in MOFs can be found elsewhere.[189–193] Some examples are included next to demonstrate that these materials behave like carbon materials in this application, and therefore, their hydrogen adsorption capacity is a function of their porosity.

Hydrogen adsorption capacities at 77 K and 4 MPa on zeolites,[165] carbon materials,[116,118,139,154,203] MOFs[180,187,194] and COFs[196] as a function of their S_{BET} have been plotted in Fig. 12.13. In the case of MOFs and COFs, hydrogen adsorption was recalculated to wt% (expressed as $(weight_{H2})/(weight_{sample} + weight_{H2})$) because authors had reported the hydrogen adsorption as $(weight_{H2})/(weight_{sample})$. Then, here, values are slightly smaller.

It can be seen that for all kinds of porous materials, the amount of hydrogen adsorbed for a given porosity is similar and, it increases almost linearly with the apparent BET surface area, which confirms that the hydrogen adsorption process is similar in those materials. In this gravimetric basis, we can observe that MOFs achieve higher values (8.2 wt%)[194] because they have higher surface areas (>4000 m^2/g), which is the current limit of porous carbons. In the case of COFs, hydrogen adsorption capacities of 7 wt% were achieved with COF-102.[196]

The similar behavior of the different kind of material suggests that hydrogen adsorption in MOFs and COFs follows the same mechanism as in carbon materials, i.e. physisorption. Hence, the heats of adsorption of hydrogen in MOFs and COFS are typically between 4 and 8 kJ/mol,[191,192,196] which are similar to the values reported for carbon materials.

As discussed in Section 12.5, hydrogen adsorption capacities should be reported on volumetric basis, which makes necessary to know the sample density. Unfortunately, most of the papers reporting hydrogen adsorption capacities of MOFs in volumetric basis used the crystal density of the materials, which is not suitable because it does not include the interparticle space. Due to that, authors claim very high hydrogen adsorption capacities in volumetric basis in MOFs (for example, values of 34 g/l and 43 g/l have been reported in[187] and,[195] respectively) and it is concluded that these values are close to DOE target. However, these capacities are not realistic from a practical point of view because, as previously mentioned, authors used MOFs' crystal density, which does not include the interparticle space.

Recently, we have compared the behavior of ACs and MOFs for gases (including H_2, CO_2 and CH_4) storage

under same experimental conditions.[80,81,129] In those works, we compared three samples (two ACs and MOF-5) with similar porosity, and therefore, with similar hydrogen adsorption capacities on gravimetric basis (as it is deduced from Fig. 12.13).

Figure 12.14 shows the excess hydrogen adsorption isotherms at 77 K and up to 4 MPa (data from Ref. 80) on a commercial AC Maxsorb,[204] an activated carbon (AC1) prepared by chemical activation with KOH of anthracite[115] and a commercial MOF, MOF-5.[205] Left-hand graph represents isotherm on gravimetric basis. As expected from their surface area, the three samples have very close isotherms and achieve similar hydrogen uptakes at 4 MPa.

Interestingly, when isotherms are represented on volumetric basis (right-hand graph), each sample achieves different uptakes. Now, ACs have much more hydrogen adsorption capacity on volumetric basis than MOF-5. This is due to the effect that the sample density has on the volumetric adsorption (as it was explained in Section 12.5). The tap densities of these materials are different; 0.36, 0.38 and 0.3 g/cm^3 for Maxsorb, AC1 and MOF-5, respectively. The value achieved here by MOF-5 (16.3 g H_2/l) is far below the one reported by Wong-Foy et al. (30.6 g H_2/l)[187] for the same material but using the crystal density.

In the above mentioned works,[80,81,129] we also analyzed the effect of increasing hydrogen adsorption capacity on volumetric basis, and therefore, the total hydrogen storage capacity, by increasing the materials density by applying increasing compacting pressures (i.e. increasing packing densities). As expected, by increasing the packing pressure, their volumetric hydrogen uptake capacities, and hence their total storage capacities, increase remarkably, and similarly, in the three samples. Increasing further the packing pressure will further increase their hydrogen storage as is the case of the two ACs used but, unfortunately, this is not the case for MOF-5. At compacting pressures >415 kg/cm^2, the porosity of MOF-5 fells down dramatically, indicating that its structure does not support such high compacting pressures. This fact was also reported by Alcañiz-Monge et al.[79]

Selecting, for the three samples, the highest pressure that MOF-5 can support (415 kg/cm^3), their maximum volumetric hydrogen storage capacities, as well as their maximum total hydrogen storage capacities, were compared. Under these best conditions, the hydrogen adsorption capacity on volumetric basis at 77 K and 4 MPa was quite similar for the two best samples; AC1 with 30.4 g/l and MOF-5 with 30.6 g/l. At 298 K and 20 MPa, the hydrogen adsorption capacity of sample AC-1 was higher than for MOF-5 (5.8 g/l against 4.8 g/l). Regarding their total hydrogen storage capacities, by use of Eqn (12.8) and the packing density obtained at the highest pressure than MOF-5 can support, we obtained at 77 K and 4 MPa, 33.3, 40.4 and 40.0 g/l for Maxsorb, AC1 and MOF-5, respectively. Values for AC1 and MOF-5 meet the 2015 DOE volumetric target on "Light-Duty vehicles".[6] At 298 K and 20 MPa, the total storage values obtained were 15.8, 16.8 and 15.2 g/l for Maxsorb, AC1 and MOF-5, respectively.

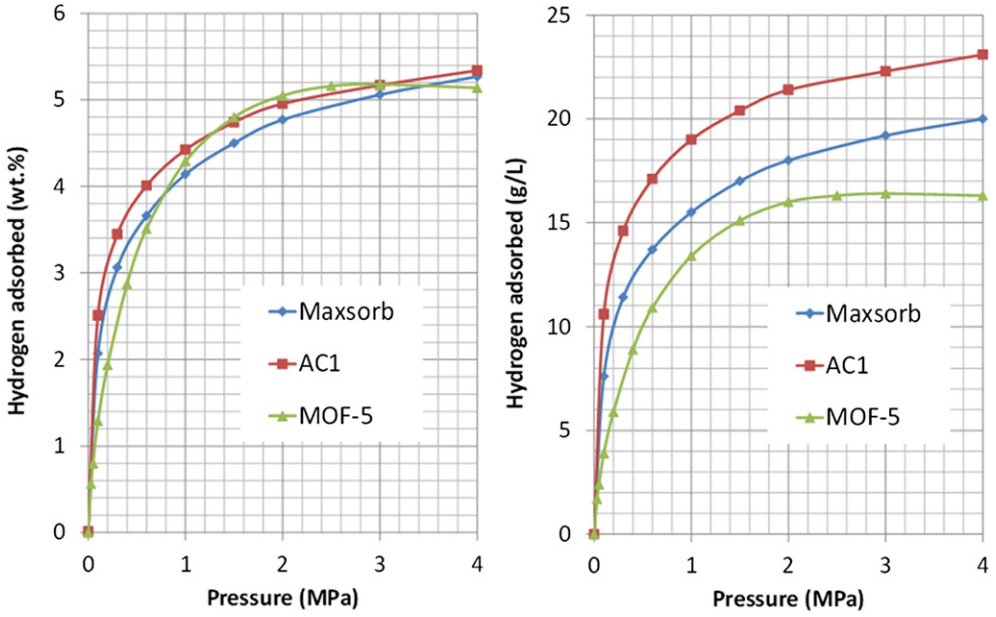

FIGURE 12.14 Hydrogen adsorption isotherms at 77 K and up to 4 MPa for a commercial AC Maxsorb, an activated carbon (AC1) and MOF-5. Left-hand graph is on gravimetric basis and right-hand graph is on volumetric basis using tap density of samples. (For color version of this figure, the reader is referred to the online version of this book.) *Source: Data from Ref. 80.*

Three additional comments merit to be made: (1) contrary to MOF-5, in the case of ACs, higher packing densities can be achieved at pressure >415 kg/cm^2 because they can support much higher pressures, and therefore, higher hydrogen storage capacities can be achieved; (2) our sample stability study, both with time and ambient humidity, shows in the case of ACs that they are fully stable with time (several years); however, MOF-5 degrades over time (after 2 years, its porosity fell dramatically) and after exposition to moisture (after 72 h at 70% of relative humidity), the sample was decomposed; and (3) these results show that MOF-5, in relation to carbon materials, does not present any of the advantages claimed in the literature.

12.7 COMMENTS AND TENDENCIES ON DOPED CARBONS

As commented above (Section 12.2.3), it has been proposed that hydrogen storage can be enhanced increasing the heat of adsorption by doping carbon materials with heteroatoms like boron or nitrogen or by a spillover process, adding catalytic nanoparticles that will dissociate the H_2 molecules. In the former case, theoretical studies[206–208] or experimental works[209,210] have reported that carbons doped with B can increase the strength of the interaction between hydrogen and the carbon material. Thus, Ferro et al.[207] reported that the adsorption energy of hydrogen atoms on graphite doped with boron could be improved by 4–5 times although Zhu et al.[206] reported a lower improvement (only between 10% and 20%). Experimentally, Chung et al.[209] proved a positive effect of boron on the heat of adsorption of hydrogen on a microporous carbon with an S_{BET} of 780 m^2/g and with a B content of 7.2 wt% (heat of adsorption had a value of 11 kJ/mol). However, the reported hydrogen uptake at 77 K and 6 MPa was only 3.2 wt%.

In the case of N-doped carbon materials, more literature can be found. Thus, different N-doped porous carbon materials, including CNTs, ACs, ZTCs, OMCs, graphene, and carbon nitride nanobells, were synthesized and their hydrogen adsorption capacities were studied.[61,78,211–218] The higher hydrogen adsorption capacity was reported by Bai et al. [211] who achieved 8 wt% at 573 K and ambient pressure on carbon nitride nanobells. Jiang et al.[214] have also reported very high adsorption capacities (2.21 wt% at room temperature and 8 MPa) on hollow nitrogen-containing carbon spheres prepared by CO_2 activation of OMC nitrides. Despite the results shown above, other authors have not found a clear benefit of nitrogen on the hydrogen adsorption.[61,212]

In summary, the effect of doping carbons with boron or nitrogen seems to be beneficial to enhance the heat of adsorption, but this occurs only for low hydrogen coverage (low hydrogen uptake). Nevertheless, there are reasonable doubts about the usefulness of doping with heteroatoms at high hydrogen uptake.[217]

Another approach to increase the hydrogen uptake at room temperature is by using metal nanoparticles which dissociate the hydrogen molecules followed by spillover. A summary of the research groups who have reported an enhancement in the amount of hydrogen uptake by this approach can be found in the recent review by Wang and Yang.[219] In that work, an extensive discussion about the effect of different factors on the hydrogen storage by spillover can be found. Due to the extensive review in this field, only some comments about this approach are included here.

Different transition metals (including Pd, Pt, Ni, Co, Ru, Rh) which dissociate hydrogen have been studied. CNTs, CNFs, ACs, ACFs, ZTCs, CDCs, and OCMs have been studied as support and receptor.[58,87,102,105,106,148,219–231] Three main factors affect the hydrogen uptake via spillover: the metal catalyst, the carbon material and the interaction between them.

The metal catalyst acts as active site for hydrogen molecules dissociation. Therefore, high metal dispersion would increase the hydrogen dissociation rate. Also, the amount and type of metal have a great effect on the hydrogen uptake.[105,231] The other important factor is the carbon material used as support and receptor. It is expected that high-surface area carbon materials would give better results. The third factor is the contact between the metal catalyst and the carbon material. A proper interaction between the two should allow adequate transfer of the hydrogen atoms from the metal nanoparticles to the carbon receptor. This positive effect has been observed in several works,[102,148,219,225] although, unfortunately, it is not so clear in many others. Such controversial results need clarification, and hence, more research is necessary to accept such approach.

12.8 SUMMARY AND RECOMMENDATIONS

Some considerations and definitions about high-pressure adsorption under supercritical conditions and about the experimental procedures used to measure excess hydrogen adsorption isotherms (mainly gravimetric and volumetric methods) are given in this chapter. Moreover, definitions of the different types of materials density are included, remarking the importance of properly measuring this parameter. This parameter has a great influence in the calculation of the amount of hydrogen adsorbed in volumetric basis and in the total hydrogen storage capacity and, then, in reporting hydrogen storage data.

Our conclusions obtained in previous works of hydrogen storage have been extended to other types of carbon materials (such as ZTCs, CDCs, metal-doped CNTs, boron- and nitrogen-doped CNTs, and so on). Thus, the hydrogen adsorption values found in the literature for those materials under different conditions are compared with our published results obtained for KOH-activated coals, commercial ACs (Maxsorb-A and AX21), CNTs, CNFs and KOH-activated CNTs,[80,81,115–119] ACFs,[130,131] and activated CNFs.[122,132]

As a summary of the comparison at room temperature, it can be said that the hydrogen adsorption values at 50 MPa follow a linear relationship with the total micropore volume, being this correlation better than the ones observed at 20, 10 and 5 MPa. The highest adsorption capacity corresponds to an AC prepared by KOH activation of an anthracite, reaching a value of 2.7 wt% at 50 MPa. On the other hand, hydrogen adsorption capacity values at lower pressures (20, 10 and 5 MPa) follow linear trends with the narrow micropore volume ($V_{\mu p}(CO_2)$). Thus, to maximize the hydrogen storage at room temperature and up to 20 MPa, adsorbents with narrow micropores should be designed.

Hydrogen adsorption at 77 K and up to different pressures (0.1, 2, 4 and 6 MPa) on many types of nanoporous carbon materials points out that at this temperature and at relatively high pressures (4–6 MPa), no effect of the MPSD on the hydrogen adsorption capacity is observed and samples with high micropore volumes are desired. On the other hand, and as it was already published by our research group with many different samples prepared in our laboratory,[115] at 77 K and low pressure (0.1 MPa), the narrow micropore volume controls the hydrogen uptake (analogously to hydrogen adsorption at room temperature and pressures up to 10–20 MPa). Thus, a strong correlation between the H_2 storage capacities at 77 K (0.1 MPa) and 298 K (10–20 MPa) exists.

It is also remarked that from an application point of view and also for comparison purposes between different types of porous materials, it is important to measure and report the packing density of the materials in order to obtain the hydrogen adsorption capacities in volumetric basis. Thus, the use of packing density for a series of chemically ACs together with their performance in hydrogen storage has been reviewed. These results point out the importance of developing materials having both high micropore volume and high packing density, in order to get a high hydrogen adsorption capacity in volumetric basis.

Taking into account the advantages of monoliths for hydrogen storage applications (easier to handle than powder, good mechanical properties and high density), ACMs having both high micropore volume and high density were prepared in our laboratory. The optimization of the preparation conditions allowed us to obtain an ACM with a total micropore volume of 1.04 cm^3/g and a piece density of 0.61 g/cm^3. This material presents a hydrogen adsorption capacity of 29.7 g H_2/l at 77 K and 4 MPa.[116] With the same objective, Gogotsi's group[164] reported the synthesis of monolithic CDCs by chlorination of fully dense ceramic titanium carbide plates, achieving a hydrogen adsorption of 35 g/l at 77 K and 6 MPa.

Finally, in this chapter, the results obtained at cryogenic conditions using ACs and ACMs are compared with those reported in the literature for other porous materials, such as zeolites, MOFs and COFs. This comparison points out that high-performance ACMs have a great potential as carriers of hydrogen since their storage density numbers at 4 MPa and 77 K are quite high and there is still some possibility of improvement by, for example, increasing the material density. Moreover, some data are presented comparing MOF and ACs. The data show that MOFs do not have clear advantages compared to carbon materials, and therefore, they do not have the qualities to store hydrogen claimed in the literature.

Acknowledgments

The authors would like to thank the Spanish Ministerio de Economía y Competitividad and PLAN E funds (projects MAT2009-11375, CTQ2012/31762 and CTQ2009-10813/PPQ) and Generalitat Valenciana and FEDER (PROMETEO/2009/047) for financial support.

References

1. Zuettel, A.; Remhof, A.; Borgschulte, A.; Friedrichs, O. *Phil. Trans. Math. Phys. Eng. Sci.* **2010,** *368* (1923), 3329–3342.
2. McWhorter, S.; Read, C.; Ordaz, G.; Stetson, N. *Curr. Opin. Solid State Mater. Sci.* **2011,** *15* (2), 29–38.
3. Zuttel, A. *Naturwissenschaften* **2004,** *91* (4), 157–172.
4. Pumera, M. *Energy Environ. Sci.* **2011,** *4* (3), 668–674.
5. DOE Targets. 2010 [cited; Available from: http://www1.eere.energy.gov/hydrogenandfuelcells/pdfs/freedomcar_targets_explanations.pdf].
6. DOE Targets Light-Duty vehicles. 2010 [cited; Available from: http://www1.eere.energy.gov/hydrogenandfuelcells/storage/pdfs/targets_onboard_hydro_storage_explanation.pdf].
7. Yartys, V. A.; Lototsky, M. V. An Overview of Hydrogen Storage Methods. In *Hydrogen Materials Science and Chemistry of Carbon Nanomaterials NATO Science Series II-Mathematics Physics and Chemistry;* Veziroglu, T. N., Zaginaichenko, S. Y., Schur, D. V., Baranowski, B., Shpak, A. P., Skorokhod, V., Eds.; pp 75–104.
8. Bottani, E. J., Tascon, J. M. D., Eds. *Adsorption by Carbons;* Elsevier: Amsterdam, 2008.
9. Dresselhaus, M. S.; Dresselhaus, G.; Eklund, P. *Science of Fullerenes and Carbon Nanotube: Their Properties and Applications;* Acadamic Press: San Diego, 1996.
10. Ertl, G.; Knözinger, H.; Weitkamp, J. *Handbook of Heterogeneous Catalysis;* Wiley-VCH: Weinheim, Germany, 1997.
11. Inagaki, M. *New carbons. Control of Structure and Functions;* Elsevier: Oxford, 2000.
12. Kelly, B. T. *Physics of Graphite;* Applied Science Publishers: London, 1981.

13. Marsh, H.; Rodriguez-Reinoso, F. *Science of Carbon Materials;* Publicaciones de la Universidad de Alicante: Alicante, Spain, 2000.
14. Yasuda, Ei, Inagaki, M., Kaneko, K., Endo, M., Oya, A., tanabe, Y., Eds. *Carbon alloys. Novel Concepts to Develop Carbon Science and Technology;* Elsevier: Amsterdam, 2003.
15. Fitzer, E.; Kochling, K. H.; Boehm, H. P.; Marsh, H. *Pure Appl. Chem.* **1995,** *67* (3), 473−506.
16. Iijima, S. *Nature* **1991,** *354* (6348), 56−58.
17. Iijima, S.; Ichihashi, T. *Nature* **1993,** *363* (6430), 603−605.
18. Bethune, D. S.; Kiang, C. H.; Devries, M. S.; Gorman, G.; Savoy, R.; Vazquez, J., et al. *Nature* **1993,** *363* (6430), 605−607.
19. Ebbesen, T. W.; Ajayan, P. M. *Nature* **1992,** *358* (6383), 220−222.
20. Ebbesen, T. W.; Hiura, H.; Fujita, J.; Ochiai, Y.; Matsui, S.; Tanigaki, K. *Chem. Phys. Lett.* **1993,** *209* (1−2), 83−90.
21. Dresselhaus, M. S.; Dresselhaus, G.; Saito, R. *Carbon* **1995,** *33* (7), 883−891.
22. Loiseau, A.; Loiseau, T.; Petit, P.; Roche, S.; Salvetat, J. P. *Understanding Carbon Nanotubes*. From basics to application; Springer: Berlin, 2006.
23. Harris, P. J. F. *Carbon Nanotubes and Related Structures. New Materials for the Twenty-First Century;* Cambridge University Press: Cambridge, 1999.
24. Tanaka, K.; Yambe, T.; Fukui, K. *The Science and Technology of Carbon Nanotubes;* Elsevier: Oxford, 1999.
25. Journet, C.; Maser, W. K.; Bernier, P.; Loiseau, A.; delaChapelle, M. L.; Lefrant, S., et al. *Nature* **1997,** *388* (6644), 756−758.
26. Thess, A.; Lee, R.; Nikolaev, P.; Dai, H. J.; Petit, P.; Robert, J., et al. *Science* **1996,** *273* (5274), 483−487.
27. Dupuis, A. C. *Prog. Mater. Sci.* **2005,** *50* (8), 929−961.
28. Burchell, T. D. *Carbon Materials for Advanced Technologies;* Pergamon: Amsterdam, 1999.
29. Rodriguez, N. M.; Chambers, A.; Baker, R. T. K. *Langmuir* **1995,** *11* (10), 3862−3866.
30. Donnet, J.; Bansal, R. C. *Carbon Fibers;* Marcel Dekker: New York, 1998.
31. Suzuki, M. *Carbon* **1994,** *32* (4), 577−586.
32. Bansal, R. C.; Donnet, J.; Stoeckli, F. *Active Carbon;* Dekker: New York, 1988.
33. Linares-Solano, A.; Lozano-Castelló, D.; Lillo-Ródenas, M. A.; Cazorla-Amorós, D. Carbon Activation by Alkaline Hydroxides: Preparation and Reactions, Porosity and Performance. In *Chemistry and Physics of Carbon;* Radovic, L. R., Ed.; CRC Press: Boca Raton, 2007; pp 1−62.
34. Illan-Gomez, M. J.; Garcia-Garcia, A.; Salinas-Martinez de Lecea, C.; Linares-Solano, A. *Energy Fuels* **1996,** *10* (5), 1108−1114.
35. Ahmadpour, A.; Do, D. D. *Carbon* **1996,** *34* (4), 471−479.
36. Lillo-Ródenas, M. A.; Lozano-Castelló, D.; Cazorla-Amorós, D.; Linares-Solano, A. *Carbon* **2001,** *39* (5), 751−759.
37. Lozano-Castelló, D.; Lillo-Ródenas, M. A.; Cazorla-Amorós, D.; Linares-Solano, A. *Carbon* **2001,** *39* (5), 741−749.
38. Puziy, A. M.; Poddubnaya, O. I.; Martinez-Alonso, A.; Suarez-Garcia, F.; Tascon, J. M. D. *Carbon* **2005,** *43* (14), 2857−2868.
39. Suarez-Garcia, F.; Martinez-Alonso, A.; Tascon, J. M. D. *Carbon* **2001,** *39* (7), 1111−1115.
40. Gogotsi, Y.; Kamyshenko, V.; Shevchenko, V.; Welz, S.; Ersoy, D. A.; McNallan, M. J. Nanostructured Carbon Coatings on Silicon Carbide: Experimental and Theoretical Study. In *NATO ASI on Functional Gradient Materials and Surface Layers Prepared by Fine Particles Technology;* Baraton, M. I., Uvarova, I., Eds.; Kluwer Academic: Dordrecht, 2001; pp 239−255.
41. Hutchins, O.; US Patent 1271713, 1918.
42. Andersen, J.N.; US Patent 2739041, 1956.
43. Kirillova, G. F.; Meerson, G. A.; Zelikman, A. N. *Izvestiya vuzov, Tsvetnaya Metallurgiya* **1960,** *3,* 90−96.
44. Orekhov, V. P.; Seryakov, G. V.; Zelikman, A. N.; Starobina, T. M.; Kahzanova, T. I.; Petrova, K. V., et al. *Zhurnal Prikladnoi Khimii* **1969,** *42* (2), 251−260.
45. Boehm, H. P.; Warnecke, H. H. *Carbon* **1975,** *13* (6), 548.
46. Gordeev, S. K.; Kukushkin, S. A.; Osipov, A. V.; Pavlov, Y. V. *Phys. Solid State* **2000,** *42* (12), 2314−2317.
47. Yeon, S.-H.; Osswald, S.; Gogotsi, Y.; Singer, J. P.; Simmons, J. M.; Fischer, J. E., et al. *J. Power Sources* **2009,** *191* (2), 560−567.
48. Gogotsi, Y.; Nikitin, A.; Ye, H. H.; Zhou, W.; Fischer, J. E.; Yi, B., et al. *Nat. Mater.* **2003,** *2* (9), 591−594.
49. Dash, R. K.; Yushin, G.; Gogotsi, Y. *Microporous Mesoporous Mater.* **2005,** *86* (1−3), 50−57.
50. Dash, R. K.; Nikitin, A.; Gogotsi, Y. *Microporous Mesoporous Mater.* **2004,** *72* (1−3), 203−208.
51. Gogotsi, Y.; Dash, R. K.; Yushin, G.; Yildirim, T.; Laudisio, G.; Fischer, J. E. *J. Am. Chem. Soc.* **2005,** *127* (46), 16006−16007.
52. Kyotani, T.; Nagai, T.; Inoue, S.; Tomita, A. *Chem. Mater.* **1997,** *9* (2), 609−615.
53. Rodriguez-Mirasol, J.; Cordero, T.; Radovic, L. R.; Rodriguez, J. J. *Chem. Mater.* **1998,** *10* (2), 550−558.
54. Ma, Z.; Kyotani, T.; Tomita, A. *Chem. Commun.* **2000,** *23,* 2365−2366.
55. Ma, Z.; Kyotani, T.; Liu, Z.; Terasaki, O.; Tomita, A. *Chem. Mater.* **2001,** *13* (12), 4413−4415.
56. Ma, Z. X.; Kyotani, T.; Tomita, A. *Carbon* **2002,** *40* (13), 2367−2374.
57. Matsuoka, K.; Yamagishi, Y.; Yamazaki, T.; Setoyama, N.; Tomita, A.; Kyotani, T. *Carbon* **2005,** *43* (4), 876−879.
58. Nishihara, H.; Hou, P. X.; Li, L. X.; Ito, M.; Uchiyama, M.; Kaburagi, T., et al. *J. Phys. Chem. C* **2009,** *113* (8), 3189−3196.
59. Alam, N.; Mokaya, R. *Energy Environ. Sci.* **2010,** *3* (11), 1773−1781.
60. Xia, Y.; Yang, Z.; Mokaya, R. *Chem. Vapor. Depos.* **2010,** *16* (10−12), 322−328.
61. Xia, Y. D.; Mokaya, R.; Grant, D. M.; Walker, G. S. *Carbon* **2011,** *49* (3), 844−853.
62. Almasoudi, A.; Mokaya, R. *J. Mater. Chem.* **2012,** *22* (1).
63. Ryoo, R.; Joo, S. H.; Jun, S. *J. Phys. Chem. B* **1999,** *103* (37), 7743−7746.
64. Xia, K. S.; Gao, Q. M.; Song, S. Q.; Wu, C. D.; Jiang, J. H.; Hu, J., et al. *Int. J. Hydrogen Energy* **2008,** *33* (1), 116−123.
65. Xia, K. S.; Gao, Q. M.; Wu, C. D.; Song, S. Q.; Ruan, M. L. *Carbon* **2007,** *45,* 1989−1996.
66. Enterría, M.; Suárez-García, F.; Martínez-Alonso, A.; Tascón, J. M. D. *Microporous Mesoporous Mater.* **2012,** *151,* 390−396.
67. Choi, M.; Ryoo, R. *J. Mater. Chem.* **2007,** *17,* 4204−4209.
68. Enterría, M.; Suárez-García, F.; Martínez-Alonso, A.; Tascón, J. M. D. *Carbon* **2012,** *50* (10), 3826−3835.
69. Rouquerol, F.; Rouquerol, J.; Sing, K. W. S. *Adsorption by Powders & Porous Solids. Principles, Methodology and Applications;* Academic Press: New York, 1999.
70. Murata, K.; El Merraoui, M.; Kaneko, K. *J. Chem. Phys.* **2001,** *114* (9), 4196−4205.
71. Sircar, S. *AICHE J.* **2001,** *47* (5), 1169−1176.
72. Redlich, O.; Kwong, J. N. S. *Chem. Rev.* **1949,** *44* (1), 233−244.
73. Soave, G. *Chem. Eng. Sci.* **1972,** *27* (6), 1197.
74. Peng, D.; Robinson, D. B. *Ind. Eng. Chem. Fund.* **1976,** *15* (1), 59−64.
75. Lee, B. I.; Kesler, M. G. *AICHE J.* **1975,** *21* (3), 510−527.
76. Younglove, B. A. *J. Phys. Chem. Ref. Data* **1982,** *11,* 1−353.
77. Leachman, J. W.; Jacobsen, R. T.; Penoncello, S. G.; Lemmon, E. W. *J. Phys. Chem. Ref. Data* **2009,** *38* (3), 721−748.
78. Parambhath, V. B.; Nagar, R.; Ramaprabhu, S. *Langmuir* **2012,** *28* (20), 7826−7833.
79. Alcañiz-Monge, J.; Trautwein, G.; Perez-Cadenas, M.; Roman-Martinez, M. C. *Microporous Mesoporous Mater.* **2009,** *126* (3), 291−301.
80. Juan-Juan, J.; Marco-Lozar, J. P.; Suarez-Garcia, F.; Cazorla-Amorós, D.; Linares-Solano, A. *Carbon* **2010,** *48* (10), 2906−2909.

81. Marco-Lozar, J. P.; Juan-Juan, J.; Suárez-García, F.; Cazorla-Amorós, D.; Linares-Solano, A. *Int. J. Hydrogen Energy* **2012,** *37* (3), 2370−2381.
82. Dillon, A. C.; Jones, K. M.; Bekkedahl, T. A.; Kiang, C. H.; Bethune, D. S.; Heben, M. J. *Nature* **1997,** *386* (6623), 377−379.
83. Chambers, A.; Park, C.; Baker, R. T. K.; Rodriguez, N. M. *J. Phys. Chem. B* **1998,** *102* (22), 4253−4256.
84. Tibbetts, G. G.; Meisner, G. P.; Olk, C. H. *Carbon* **2001,** *39* (15), 2291−2301.
85. Anson, A.; Benham, M.; Jagiello, J.; Callejas, M. A.; Benito, A. M.; Maser, W. K., et al. *Nanotechnology* **2004,** *15* (11), 1503−1508.
86. Anson, A.; Jagiello, J.; Parra, J. B.; Sanjuan, M. L.; Benito, A. M.; Maser, W. K., et al. *J. Phys. Chem. B* **2004,** *108* (40), 15820−15826.
87. Anson, A.; Lafuente, E.; Urriolabeitia, E.; Navarro, R.; Benito, A. M.; Maser, W. K., et al. *J. Phys. Chem. B* **2006,** *110* (13), 6643−6648.
88. Blackman, J. M.; Patrick, J. W.; Arenillas, A.; Shi, W.; Snape, C. E. *Carbon* **2006,** *44* (8), 1376−1385.
89. Kayiran, S. B.; Lamari, F. D.; Levesque, D. *J. Phys. Chem. B* **2004,** *108* (39), 15211−15215.
90. Browning, D. J.; Gerrard, M. L.; Lakeman, J. B.; Mellor, I. M.; Mortimer, R. J.; Turpin, M. C. *Nano Lett.* **2002,** *2* (3), 201−205.
91. Callejas, M. A.; Anson, A.; Benito, A. M.; Maser, W.; Fierro, J. L. G.; Sanjuan, M. L., et al. *Mater. Sci. Eng. B Adv. Funct. Solid State Mater.* **2004,** *108* (1−2), 120−123.
92. Chen, P.; Wu, X.; Lin, J.; Tan, K. L. *Science* **1999,** *285* (5424), 91−93.
93. Fan, Y. Y.; Kaufmann, A.; Mukasyan, A.; Varma, A. *Carbon* **2006,** *44* (11), 2160−2170.
94. Fan, Y. Y.; Liao, B.; Liu, M.; Wei, Y. L.; Lu, M. Q.; Cheng, H. M. *Carbon* **1999,** *37* (10), 1649−1652.
95. Gupta, B. K.; Tiwari, R. S.; Srivastava, O. N. *J. Alloys Compd.* **2004,** *381* (1−2), 301−308.
96. Hou, P. X.; Xu, S. T.; Ying, Z.; Yang, Q. H.; Liu, C.; Cheng, H. M. *Carbon* **2003,** *41* (13), 2471−2476.
97. Li, X. S.; Zhu, H. W.; Ci, L. J.; Xu, C. L.; Mao, Z. Q.; Wei, B. Q., et al. *Carbon* **2001,** *39* (13), 2077−2079.
98. Liu, C.; Fan, Y. Y.; Liu, M.; Cong, H. T.; Cheng, H. M.; Dresselhaus, M. S. *Science* **1999,** *286* (5442), 1127−1129.
99. Lupu, D.; Biris, A. R.; Misan, I.; Jianu, A.; Holzhuter, G.; Burkel, E. *Int. J. Hydrogen Energy* **2004,** *29* (1), 97−102.
100. Poirier, E.; Chahine, R.; Benard, P.; Cossement, D.; Lafi, L.; Melancon, E., et al. *Appl. Phys. A Mater. Sci. Process.* **2004,** *78* (7), 961−967.
101. Rzepka, M.; Bauer, E.; Reichenauer, G.; Schliermann, T.; Bernhardt, B.; Bohmhammel, K., et al. *J. Phys. Chem. B* **2005,** *109* (31), 14979−14989.
102. Singh, P.; Kulkarni, M. V.; Gokhale, S. P.; Chikkali, S. H.; Kulkarni, C. V. *Appl. Surf. Sci.* **2012,** *258* (8), 3405−3409.
103. Sudan, P.; Zuttel, A.; Mauron, P.; Emmenegger, C.; Wenger, P.; Schlapbach, L. *Carbon* **2003,** *41* (12), 2377−2383.
104. Wang, Q. K.; Zhu, C. C.; Liu, W. H.; Wu, T. *Int. J. Hydrogen Energy* **2002,** *27* (5), 497−500.
105. Wu, H.; Wexler, D.; Liu, H. *Int. J. Hydrogen Energy* **2011,** *36* (15), 9032−9036.
106. Wu, H.; Wexler, D.; Liu, H. *Int. J. Hydrogen Energy* **2012,** *37* (7), 5686−5690.
107. Hirscher, M.; Becher, M.; Haluska, M.; Quintel, A.; Skakalova, V.; Choi, Y. M., et al. *J. Alloys Compd.* **2002,** *330,* 654−658.
108. Xu, W. C.; Takahashi, K.; Matsuo, Y.; Hattori, Y.; Kumagai, M.; Ishiyama, S., et al. *Int. J. Hydrogen Energy* **2007,** *32* (13), 2504−2512.
109. Ahn, C. C.; Ye, Y.; Ratnakumar, B. V.; Witham, C.; Bowman, R. C.; Fultz, B. *Appl. Phys. Lett.* **1998,** *73* (23), 3378−3380.
110. Yang, R. T. *Carbon* **2000,** *38* (4), 623−626.
111. Orinakova, R.; Orinak, A. *Fuel* **2011,** *90* (11), 3123−3140.
112. Ioannatos, G. E.; Verykios, X. E. *Int. J. Hydrogen Energy* **2010,** *35* (2), 622−628.
113. Yurum, Y.; Taralp, A.; Veziroglu, T. N. *Int. J. Hydrogen Energy* **2009,** *34* (9), 3784−3798.
114. Strobel, R.; Garche, J.; Moseley, P. T.; Jorissen, L.; Wolf, G. *J. Power Sources* **2006,** *159* (2), 781−801.
115. Jordá-Beneyto, M.; Suarez-Garcia, F.; Lozano-Castelló, D.; Cazorla-Amorós, D.; Linares-Solano, A. *Carbon* **2007,** *45* (2), 293−303.
116. Jordá-Beneyto, M.; Lozano-Castelló, D.; Suarez-Garcia, F.; Cazorla-Amorós, D.; Linares-Solano, A. *Microporous Mesoporous Mater.* **2008,** *112* (1−3), 235−242.
117. Linares-Solano, A.; Jordá-Beneyto, M.; Kunowsky, M.; Lozano-Castelló, D.; Suarez-Garcia, F.; Cazorla-Amorós, D. Hydrogen Storage in Carbon Materials. In *Carbon Materials: Theory and Practice;* Terzyk, A. P., Gauden, P. A., Kowalczyk, P., Eds.; Research Signpost: Kerala, 2008; pp 245−281.
118. Suarez-Garcia, F.; Jorda-Beneyto, M.; Lozano-Castello, D.; Cazorla-Amoros, D.; Linares-Solano, A. Hydrogen Adsorption on Carbon Materials at High Pressures and Different Temperatures. In *Recent Advances in Adsorption Processes for Environmental Protection and Security;* Mota, J. P. L. S., Ed.; pp 165−175.
119. Linares-Solano, A.; Jorda-Beneyto, M.; Lozano-Castello, D.; Suarez-Garcia, F.; Cazorla-Amoros, D. High Density Carbon Materials for Hydrogen Storage. In *Materials Innovations in an Emerging Hydrogen Economy;* Wicks, G. G. S. J., Ed.; pp 77−90.
120. Schmitz, B.; Muller, U.; Trukhan, N.; Schubert, M.; Ferey, G.; Hirscher, M. *Chem. Phys. Chem.* **2008,** *9* (15), 2181−2184.
121. Yushin, G.; Dash, R.; Jagiello, J.; Fischer, J. E.; Gogotsi, Y. *Adv. Funct. Mater.* **2006,** *16* (17), 2288−2293.
122. Kunowsky, M.; Marco-Lozar, J. P.; Oya, A.; Linares-Solano, A. *Carbon* **2012,** *50* (3), 1407−1416.
123. Takagi, H.; Hatori, H.; Soneda, Y.; Yoshizawa, N.; Yamada, Y. *Mater. Sci. Eng. B Adv. Funct. Solid State Mater.* **2004,** *108* (1−2), 143−147.
124. Panella, B.; Hirscher, M.; Roth, S. *Carbon* **2005,** *43* (10), 2209−2214.
125. Strobel, R.; Jorissen, L.; Schliermann, T.; Trapp, V.; Schutz, W.; Bohmhammel, K., et al. *J. Power Sources* **1999,** *84* (2), 221−224.
126. Nijkamp, M. G.; Raaymakers, J. E. M. J.; van Dillen, A. J.; de Jong, K. P. *Appl. Phys. A Mater. Sci. Process.* **2001,** *72* (5), 619−623.
127. Texier-Mandoki, N.; Dentzer, J.; Piquero, T.; Saadallah, S.; David, P.; Vix-Guterl, C. *Carbon* **2004,** *42* (12−13), 2744−2747.
128. Gadiou, R.; Saadallah, S. E.; Piquero, T.; David, P.; Parmentier, J.; Vix-Guterl, C. *Microporous Mesoporous Mater.* **2005,** *79* (1−3), 121−128.
129. Linares-Solano, A.; Cazorla-Amoros, D.; Marco-Lozar, J. P.; Suarez-Garcia, F. High Pressure Gas Storage on Porous Solids; A Comparative Study of MOFs and Activated Carbons. In *Coordination Polymers and Metal Organic Frameworks: Properties, Types and Applications;* Ortiz, O. L., Ramírez, L. D., Eds.; Nova Science Publishers: New York, 2012; pp 197−224.
130. Kunowsky, M.; Suarez-Garcia, F.; Cazorla-Amoros, D.; Linares-Solano, A. Synthesis of Activated Carbon Fibers for High-Pressure Hydrogen Storage. In *Materials Innovations in an Emerging Hydrogen Economy;* Wicks, G. G. S. J., Ed.; pp 69−75.
131. Kunowsky, M.; Marco-Lozar, J. P.; Cazorla-Amoros, D.; Linares-Solano, A. *Int. J. Hydrogen Energy* **2010,** *35* (6), 2393−2402.
132. Suarez-Garcia, F.; Vilaplana-Ortego, E.; Kunowsky, M.; Kimura, M.; Oya, A.; Linares-Solano, A. *Int. J. Hydrogen Energy* **2009,** *34* (22), 9141−9150.
133. Casa-Lillo, M. A.; Lamari-Darkrim, F.; Cazorla-Amorós, D.; Linares-Solano, A. *J. Phys. Chem. B* **2002,** *106* (42), 10930−10934.

134. Wang, Q. Y.; Johnson, J. K. *J. Chem. Phys.* **1999,** *110* (1), 577−586.
135. Agarwal, R. K.; Schwarz, J. A. *Carbon* **1988,** *26* (6), 873−887.
136. Dubinin, M. M. Physical Adsorption of Gases and Vapors in Micropores. In *Progress in Surface and Membrane Science;* Cadenhead, D. A., Danielli, J. F., Rosenberg, M. D., Eds.; Academic Press: New York, 1975; pp 1−70.
137. Matsuo, Y.; Ueda, S.; Konishi, K.; Marco-Lozar, J. P.; Lozano-Castelló, D.; Cazorla-Amorós, D. *Int. J. Hydrogen Energy* **2012,** *37* (14), 10702−10708.
138. Poirier, E.; Chahine, R.; Bose, T. K. *Int. J. Hydrogen Energy* **2001,** *26* (8), 831−835.
139. Buczek, B.; Czepirski, L.; Zietkiewicz, J. *Adsorption* **2005,** *11,* 877−880.
140. Figueroa-Torres, M. Z.; Robau-S nchez, A.; De la Torre-S enz, L.; Aguilar-Elgu'zabal, A. *Microporous Mesoporous Mater.* **2007,** *98,* 89−93.
141. Furuya, Y.; Hashishin, T.; Iwanaga, H.; Motojima, S.; Hishikawa, Y. *Carbon* **2004,** *42* (2), 331−335.
142. Parra, J. B.; Ania, C. O.; Arenillas, A.; Rubiera, F.; Palacios, J. M.; Pis, J. J. *J. Alloys Compd.* **2004,** *379* (1−2), 280−289.
143. Rzepka, M.; Lamp, P.; Casa-Lillo, M. A. *J. Phys. Chem. B* **1998,** *102* (52), 10894−10898.
144. Shindo, K.; Kondo, T.; Sakurai, Y. *J. Alloys Compd.* **2004,** *379* (1−2), 252−255.
145. Gogotsi, Y.; Portet, C.; Osswald, S.; Simmons, J. M.; Yildirim, T.; Laudisio, G., et al. *Int. J. Hydrogen Energy* **2009,** *34* (15), 6314−6319.
146. Chahine, R.; Bose, T. K. *Int. J. Hydrogen Energy* **1994,** *19* (2), 161−164.
147. Kojima, Y.; Kawai, Y.; Koiwai, A.; Suzuki, N.; Haga, T.; Hioki, T., et al. *J. Alloys Compd.* **2006,** *421* (1−2), 204−208.
148. Lachawiec, A. J.; Qi, G. S.; Yang, R. T. *Langmuir* **2005,** *21* (24), 11418−11424.
149. Zhou, L.; Zhou, Y. P.; Sun, Y. *Int. J. Hydrogen Energy* **2004,** *29* (5), 475−479.
150. Zhou, L.; Zhou, Y. P.; Sun, Y. *Int. J. Hydrogen Energy* **2004,** *29* (3), 319−322.
151. Fierro, V.; Szczurek, A.; Zlotea, C.; Mareche, J. F.; Izquierdo, M. T.; Albiniak, A., et al. *Carbon* **2010,** *48* (7), 1902−1911.
152. Akasaka, H.; Takahata, T.; Toda, I.; Ono, H.; Ohshio, S.; Himeno, S., et al. *Int. J. Hydrogen Energy* **2011,** *36* (1), 580−585.
153. Schlichtenmayer, M.; Streppel, B.; Hirscher, M. *Int. J. Hydrogen Energy* **2011,** *36* (1), 586−591.
154. Sevilla, M.; Foulston, R.; Mokaya, R. *Energy Environ. Sci.* **2010,** *3* (2), 223−227.
155. Armandi, M.; Bonelli, B.; Karaindrou, E. I.; Arean, C. O.; Garrone, E. *Catal. Today* **2008,** *138* (3−4), 244−248.
156. Armandi, M.; Bonelli, B.; Bottero, I.; Arean, C. O.; Garrone, E. *Microporous Mesoporous Mater.* **2007,** *103* (1−3), 150−157.
157. Wang, H.; Gao, Q.; Hu, J. *J. Am. Chem. Soc.* **2009,** *131* (20), 7016−7022.
158. Sevilla, M.; Fuertes, A. B.; Mokaya, R. *Energy Environ. Sci.* **2011,** *4* (4), 1400−1410.
159. Yang, S. J.; Im, J. H.; Nishihara, H.; Jung, H.; Lee, K.; Kyotani, T., et al. *J. Phys. Chem. C* **2012,** *116* (19), 10529−10540.
160. Lozano-Castelló, D.; Alcañiz-Monge, J.; Casa-Lillo, M. A.; Cazorla-Amorós, D.; Linares-Solano, A. *Fuel* **2002,** *81* (14), 1777−1803.
161. Lozano-Castelló, D.; Cazorla-Amorós, D.; Linares-Solano, A. *Energy Fuels* **2002,** *16* (5), 1321−1328.
162. Lozano-Castelló, D.; Cazorla-Amorós, D.; Linares-Solano, A.; Quinn, D. F. *Carbon* **2002,** *40* (15), 2817−2825.
163. Singer, J. P.; Mayergoyz, A.; Portet, C.; Schneider, E.; Gogotsi, Y.; Fischer, J. E. *Microporous Mesoporous Mater.* **2008,** *116* (1−3), 469−472.
164. Yeon, S.-H.; Knoke, I.; Gogotsi, Y.; Fischer, J. E. *Microporous Mesoporous Mater.* **2010,** *131* (1−3), 423−428.
165. Langmi, H. W.; Walton, A.; Al Mamouri, M. M.; Johnson, S. R.; Book, D.; Speight, J. D., et al. *J. Alloy Compd.* **2003,** *356,* 710−715.
166. Darkrim, F.; Aoufi, A.; Malbrunot, P.; Levesque, D. *J. Chem. Phys.* **2000,** *112* (13), 5991−5999.
167. Efstathiou, A. M.; Borgstedt, E. V.; Suib, S. L.; Bennett, C. O. *J. Catal.* **1992,** *135* (1), 135−146.
168. Efstathiou, A. M.; Suib, S. L.; Bennett, C. O. *J. Catal.* **1990,** *123* (2), 456−462.
169. Fraenkel, D. J. *Chem. Soc., Faraday Trans.* **1981,** *77,* 2041−2052.
170. Fraenkel, D. J. *Chem. Soc., Faraday Trans.* **1981,** *77,* 2029−2039.
171. Fraenkel, D.; Shabtai, J. *J. Am. Chem. Soc.* **1977,** *99* (21), 7074−7076.
172. Kayiran, S. B.; Darkrim, F. L. *Surf. Interface Anal.* **2002,** *34* (1), 100−104.
173. Yoon, J. H. *J. Phys. Chem.* **1993,** *97* (22), 6066−6068.
174. Weitkamp, J.; Fritz, M.; Ernst, S. *Int. J. Hydrogen Energy* **1995,** *20* (12), 967−970.
175. Ferey, G. *Chem. Soc. Rev.* **2008,** *37* (1), 191−214.
176. Ferey, G.; Latroche, M.; Serre, C.; Millange, F.; Loiseau, T.; Percheron-Guegan, A. *Chem. Commun.* **2003,** *9* (24), 2976−2977.
177. Ferey, G.; Mellot-Draznieks, C.; Serre, C.; Millange, F. *Acc. Chem. Res.* **2005,** *38* (4), 217−225.
178. Latroche, M.; Surble, S.; Serre, C.; Mellot-Draznieks, C.; Llewellyn, P. L.; Lee, J. H., et al. *Angew. Chem. Int. Ed.* **2006,** *45* (48), 8227−8231.
179. Surble, S.; Millange, F.; Serre, C.; Duren, T.; Latroche, M.; Bourrelly, S., et al. *J. Am. Chem. Soc.* **2006,** *128* (46), 14889−14896.
180. Furukawa, H.; Ko, N.; Go, Y. B.; Aratani, N.; Choi, S. B.; Choi, E., et al. *Science* **2010,** *329* (5990), 424−428.
181. Furukawa, H.; Miller, M. A.; Yaghi, O. M. *J. Mater. Chem.* **2007,** *17* (30), 3197−3204.
182. Rowsell, J. L. C.; Millward, A. R.; Park, K. S.; Yaghi, O. M. *J. Am. Chem. Soc.* **2004,** *126* (18), 5666−5667.
183. Rowsell, J. L. C.; Spencer, E. C.; Eckert, J.; Howard, J. A. K.; Yaghi, O. M. *Science* **2005,** *309* (5739), 1350−1354.
184. Rowsell, J. L. C.; Yaghi, O. M. *Microporous Mesoporous Mater.* **2004,** *73* (1−2), 3−14.
185. Rowsell, J. L. C.; Yaghi, O. M. *Angew. Chem. Int. Ed.* **2005,** *44* (30), 4670−4679.
186. Sudik, A. C.; Millward, A. R.; Ockwig, N. W.; Cote, A. P.; Kim, J.; Yaghi, O. M. *J. Am. Chem. Soc.* **2005,** *127* (19), 7110−7118.
187. Wong-Foy, A. G.; Matzger, A. J.; Yaghi, O. M. *J. Am. Chem. Soc.* **2006,** *128* (11), 3494−3495.
188. Kaye, S. S.; Dailly, A.; Yaghi, O. M.; Long, J. R. *J. Am. Chem. Soc.* **2007,** *129* (46), 14176−14177.
189. Thomas, K. M. *Dalton Trans.* **2009,** *9,* 1487−1505.
190. Hu, Y. H.; Zhang, L. *Adv. Mater.* **2010,** *22* (20). E117−EE30.
191. Getman, R. B.; Bae, Y.-S.; Wilmer, C. E.; Snurr, R. Q. *Chem. Rev.* **2012,** *112* (2), 703−723.
192. Suh, M. P.; Park, H. J.; Prasad, T. K.; Lim, D.-W. *Chem. Rev.* **2012,** *112* (2), 782−835.
193. Sculley, J.; Yuan, D.; Zhou, H.-C. *Energy Environ. Sci.* **2011,** *4* (8), 2721−2735.
194. Farha, O. K.; Yazaydin, A. O.; Eryazici, I.; Malliakas, C. D.; Hauser, B. G.; Kanatzidis, M. G., et al. *Nat. Chem.* **2010,** *2* (11), 944−948.
195. Dinca, M.; Dailly, A.; Liu, Y.; Brown, C. M.; Neumann, D. A.; Long, J. R. *J. Am. Chem. Soc.* **2006,** *128* (51), 16876−16883.
196. Furukawa, H.; Yaghi, O. M. *J. Am. Chem. Soc.* **2009,** *131* (25), 8875−8883.
197. Sang, S. H.; Furukawa, H.; Yaghi, O. M.; Goddard, W. A., III *J. Am. Chem. Soc.* **2008,** *130* (35), 11580−11581.
198. Baerlocher, C.; Meier, W. M.; Olson, D. H. *Atlas of Zeolite Framework Types;* Elsevier Science: Amsterdam, 2001.
199. Corma, A. *Chem. Rev.* **1997,** *97* (6), 2373−2420.
200. Cote, A. P.; Benin, A. I.; Ockwig, N. W.; O'Keeffe, M.; Matzger, A. J.; Yaghi, O. M. *Science* **2005,** *310* (5751), 1166−1170.
201. El-Kaderi, H. M.; Hunt, J. R.; Mendoza-Cortes, J. L.; Cote, A. P.; Taylor, R. E.; O'Keeffe, M., et al. *Science* **2007,** *316* (5822), 268−272.

202. Tilford, R. W.; Gemmill, W. R.; zur Loye, H.-C.; Lavigne, J. J. *Chem. Mater.* **2006,** *18* (22), 5296−5301.
203. Kim, H. S.; Singer, J. P.; Gogotsi, Y.; Fischer, J. E. *Microporous Mesoporous Mater.* **2009,** *120* (3), 267−271.
204. Otowa, T.; Nojima, Y.; Miyazaki, T. *Carbon* **1997,** *35* (9), 1315−1319.
205. Eddaoudi, M.; Kim, J.; Rosi, N.; Vodak, D.; Wachter, J.; O'Keefe, M., et al. *Science* **2002,** *295* (5554), 469−472.
206. Zhu, Z. H.; Lu, G. Q.; Hatori, H. *J. Phys. Chem. B* **2006,** *110* (3), 1249−1255.
207. Ferro, Y.; Marinelli, F.; Jelea, A.; Allouche, A. *J. Chem. Phys.* **2004,** *120* (24), 11882−11888.
208. Kuchta, B.; Firlej, L.; Roszak, S.; .Pfeifer, P.; Wexler, C. *Appl. Surf. Sci.* **2010,** *256* (17), 5270−5274.
209. Chung, T. C. M.; Jeong, Y.; Chen, Q.; Kleinhammes, A.; Wu, Y. *J. Am. Chem. Soc.* **2008,** *130* (21), 6668−6669.
210. Sankaran, M.; Viswanathan, B. *Carbon* **2007,** *45* (8), 1628−1635.
211. Bai, X. D.; Zhong, D. Y.; Zhang, G. Y.; Ma, X. C.; Liu, S.; Wang, E. G., et al. *Appl. Phys. Lett.* **2001,** *79* (10), 1552−1554.
212. Giraudet, S.; Zhu, Z.; Yao, X.; Lu, G. *J. Phys. Chem. C* **2010,** *114* (18), 8639−8645.
213. Yang, Z. X.; Xia, Y. D.; Sun, X. Z.; Mokaya, R. *J. Phys. Chem. B* **2006,** *110* (37), 18424−18431.
214. Jiang, J.; Gao, Q.; Zheng, Z.; Xia, K.; Hu, J. *Int. J. Hydrogen Energy* **2010,** *35* (1), 210−216.
215. Sankaran, M.; Viswanathan, B. *Carbon* **2006,** *44* (13), 2816−2821.
216. Zhu, Z. H.; Hatori, H.; Wang, S. B.; Lu, G. Q. *J. Phys. Chem. B* **2005,** *109* (35), 16744−16749.
217. Xia, Y. D.; Walker, G. S.; Grant, D. M.; Mokaya, R. *J. Am. Chem. Soc.* **2009,** *131* (45), 16493−16499.
218. Yang, S. J.; Cho, J. H.; Oh, G. H.; Nahm, K. S.; Park, C. R. *Carbon* **2009,** *47* (6), 1585−1591.
219. Wang, L. F.; Yang, R. T. *Catal. Rev Sci. Eng.* **2010,** *52* (4), 411−461.
220. Giasafaki, D.; Bourlinos, A.; Charalambopoulou, G.; Stubos, A.; Steriotis, T. *Microporous Mesoporous Mater.* **2012,** *154,* 74−81.
221. Han, S. S.; Jung, H.; Jung, D. H.; Choi, S.-H.; Park, N. *Phys. Rev. B* **2012,** *85* (15).
222. Lueking, A.; Yang, R. T. *J. Catal.* **2002,** *211* (2), 565.
223. Lueking, A. D.; Yang, R. T. *Appl. Catal. A Gen.* **2004,** *265* (2), 259−268.
224. Reyhani, A.; Mortazavi, S. Z.; Mirershadi, S.; Moshfegh, A. Z.; Parvin, P.; Golikand, A. N. *J. Phys. Chem. C* **2011,** *115* (14), 6994−7001.
225. Singh, A. K.; Ribas, M. A.; Yakobson, B. I. *ACS. Nano.* **2009,** *3* (7), 1657−1662.
226. Yang, F. H.; Lachawiec, A. J.; Yang, R. T. *J. Phys. Chem. B* **2006,** *110* (12), 6236−6244.
227. Yoo, E.; Gao, L.; Komatsu, T.; Yagai, N.; Arai, K.; Yamazaki, T., et al. *J. Phys. Chem. B* **2004,** *108* (49), 18903−18907.
228. Zhan, L.; Zhang, R.; Wang, Y. L.; Liang, X. Y.; Li, K. X.; Lu, C. X., et al. *New Carbon Mater.* **2005,** *20* (1), 33−38.
229. Back, C. K.; Sandi, G.; Prakash, J.; Hranisavljevic, J. *J. Phys. Chem. B* **2006,** *110* (33), 16225−16231.
230. Lee, J. W.; Kim, H. S.; Lee, J. Y.; Kang, J. K. *Appl. Phys. Lett.* **2006,** *88* (14).
231. Wang, L.; Yang, R. T. *J. Phys. Chem. C* **2008,** *112* (32), 12486−12494.

CHAPTER

13

Progress in Hydrogen Storage in Complex Hydrides

Robert A. Varin *, *Zbigniew S. Wronski* *,†

*Department of Mechanical and Mechatronics Engineering, University of Waterloo, Waterloo, Canada N2L 3G1,
†Canmet ENERGY, Natural Resources Canada, Ottawa, Canada K1A 1M1

OUTLINE

13.1 Introduction 293

13.2 Alanates 296
13.2.1 Sodium Alanate ($NaAlH_4$) 296
13.2.2 Lithium Alanate ($LiAlH_4$) 301

13.3 Metal Borohydrides 316
13.3.1 The $LiBH_4$–$MnCl_2$ and $NaBH_4$–$MnCl_2$ Systems 316

13.4 Lithium Amides 320
13.4.1 The ($LiNH_2$–LiH) System 320
13.4.2 The ($LiNH_2$–MgH_2) System 323

13.5 Summary 327

Acknowledgments 329

References 329

13.1 INTRODUCTION

The last 300 years of technological developments in the industrialized world were based on burning fossil fuels. In the beginning of the industrial revolution, it was mainly coal, and later it became crude oil and natural gas. In particular, the exponential increase in the use of oil to power transportation and industry in the last 100 years led to a substantial depletion of oil fields in oil-rich countries. The remaining oil reserves will be most likely consumed within the next 50–70 years.[1–3] In addition, there is an on-going debate that the exponential consumption of fossil fuels leads to increasing levels of CO_2 (so-called "greenhouse gas") in the atmosphere, which in turn, may lead to the average temperature increase on the earth bringing about severe climate destabilization.[4]

This critical situation requires that alternative energy sources and fuels be developed to promote future world energy security. Among a number of available renewable energies (wind, solar, biomass, etc.), hydrogen has been perceived as a future energy carrier that may allow a gradual transformation from a fossil fuel-based economy to a hydrogen economy. One of a few obstacles to the implementation of hydrogen economy is safe and efficient storage of hydrogen, particularly for mobile/automotive applications where hydrogen gas will be supplied to fuel cells that, in turn, will power a variety of transport vehicles in a clean, inexpensive, safe, and efficient manner.[5] Obviously, the transportation sector (automobiles) provides the most intense driver for the hydrogen economy, but simultaneously it is the most challenging for basic research and a key factor in enabling the success of the hydrogen economy. Gaseous and liquid hydrogen storage techniques have been known for quite a long time, but they have a number of serious drawbacks, such as relatively low volumetric densities, substantial energy losses occurring during pressurizing, and liquefaction and various safety issues. Nevertheless, high-pressure (70 MPa) gaseous storage will, most likely, be a short-term solution for the automotive/transportation sector. For stationary, portable and off-road mobile

http://dx.doi.org/10.1016/B978-0-444-56352-1.00013-1

applications as well as for long-term automotive applications, a general consensus has emerged that a better interim option is solid state hydrogen storage in hydrides and their composite systems. However, solid state storage has its own serious constraints.

The first constraint is directly related with the technical specifications for a certain type of fuel cells.[6,7] The most common type of fuel cells is a high-power density proton exchange membrane fuel cell (PEMFC) (sometimes also named a polymer electrolyte fuel cell). It is the most suitable for automotive as well as a number of other applications in portable electronic devices, stationary auxiliary power systems, off-road vehicles, lawn mowers, air transportation, coastal and international shipping, bulk hydrogen storage, and many others.[4,8–12] For achieving a substantial amount of power, individual fuel cells must be connected into a fuel cell stack. As an example, advanced Andromeda™ HCS-575 fuel cell stack series from Nuvera Fuel Cells, Inc. (150-, 272-, and 384-cell architectures) generate the quantity of waste heat, which is able to rise a coolant temperature to ~70 °C and operate in 1.1–1.8 bar H_2 fuel pressure.[13] These technical specifications require that the suitable hydrogen storage material must desorb hydrogen in an H_2 pressure of at least 1 bar and exhibit desorption temperature at that pressure not much higher than 70 °C. In general, one can roughly say that the hydride materials that are of potential interest for solid-state hydrogen storage are only those that would desorb H_2 under 1 bar H_2 pressure at temperatures not higher than 100 °C. Therefore, it is crucially important to realize that a technical screening of potential candidate hydride materials for storage for supplying PEMFCs must always be conducted under, at least, 1 bar H_2 pressure. In this case, desorption tests in vacuum are of no practical value. As the reader can envisage, the desorption temperature corresponding to 1 bar H_2 pressure is only valid for a PEM fuel cell. Another type of fuel cell like, for example, a solid oxide fuel cell (SOFC) that operates at very high temperatures[6,7] can use solid hydrides exhibiting desorption temperatures much higher than 100 °C under 1 bar H_2 pressure. However, SOFCs due to their high operating temperatures and relative bulk are mostly suitable for stationary applications.

The second constraint is man-made and depends on the required travel distance for hydrogen-fueled transportation vehicles. The US Department of Energy (DOE) requires a distance of 300 miles (480 km). Based on this travel distance, the recently revised DOE-automotive targets for 2015 require a H_2 capacity of 5.5 wt% for the entire storage *system*, which includes storage medium, tank, and some auxiliary devices.[14] This translates into roughly ~10–11 wt% H_2 capacity for the solid hydride-based storage material. Obviously, all high-capacity hydrides must have very low densities, which require that their chemical compositions must include light metal/nonmetal elements such as Li, Al, B, N and possibly Mg and Na.[15] If it is required that the depleted storage tank should be replenished by simply pumping pressurized H_2 into it, then the depleted hydride storage material would have to easily absorb H_2 at a temperature not exceeding the waste heat temperature of a PEMFC or even better at the outside air room temperature (RT). So, the requirement for the reversibility/rehydrogenation of a hydride storage material under reasonable conditions of temperature (<100 °C) and H_2 pressure (<10–20 bar) brings about another complexity into the equation. Additional requirements such as relatively rapid rates of desorption/absorption (dehydrogenation/rehydrogenation) and low price of the storage material make the situation even more difficult. However, the relative importance of the latter two factors depends on a perceived application in a selected industrial sector.

In summary, these two important constraints, technical and man-made, require the potential hydrogen storage material for fueling a PEMFC to desorb at <100 °C under 1 bar H_2, have a practical achievable capacity ~10 wt% H_2, exhibit reversibility under reasonable conditions of pressure/temperature, desorb/absorb rapidly, and be relatively inexpensive.

A reader can now ask how we can carry out a preliminary screening of various hydrides from the standpoint of their suitability of desorbing H_2 under 1 bar pressure and at temperatures not exceeding 100 °C. This can be achieved by knowing a thermodynamic property of hydrides such as the enthalpy of decomposition/formation change, ΔH. If the natural logarithm of desorption/absorption H_2 pressure is plotted against wt% H_2 desorbed/absorbed at constant temperature then the so-called *pressure–composition–temperature* (PCT) curve is obtained, which usually exhibits plateau.[15] Then the equilibrium mid-plateau H_2 pressure for the hydrogen desorption/absorption plateau is related to temperature through the Van't Hoff equation[15]:

$$\ln(p/p_0) = -\Delta H/RT + \Delta S/R \qquad (13.1)$$

where p is the recorded pressure (atm/bar), p_0 is the atmospheric pressure (1 Atm/1 bar), ΔH and ΔS are the enthalpy and entropy changes in kJ/mol H_2 and J/mol H_2 K, respectively, R is the gas constant (8.314,472 J/mol K), and T is absolute temperature (K). This approach requires time-consuming measurements of pressure and corresponding H_2 capacity for one PCT and at least for three selected temperatures. More recently, we simplified this approach by using step-wise

desorption curves (pseudo-PCT curves) where we measure pressure vs desorption time at a constant temperature and then after obtaining satisfactory equilibrium plateau pressure, we rapidly ramp temperature to a higher value until equilibrium plateau is achieved and again temperature is ramped to yet higher value and equilibrium plateau pressure recorded. Then the term ln (p/p_0), where p is the equilibrium plateau pressure for each temperature, is plotted vs 1000/T according to Eqn (13.1). This method is shown in Fig. 13.1(a), (b) as applied to a ball-milled mixture of lithium amide ($LiNH_2$) and lithium hydride (LiH) in the molar ratio ($LiNH_2 + 1.2LiH$). A value of the dehydrogenation enthalpy obtained in Fig. 13.1(b) agrees well with the values quoted in the literature.[17] This complex hydride system will be discussed in more detail in one of the following sections.

Finally, it must be reminded that according to the Van't Hoff Eqn (13.1), a certain hydride (or a hydride composite system) will be thermodynamically capable of desorbing H_2 only if the selected desorption pressure (e.g. 1 bar) is *lower* than its equilibrium plateau pressure at selected desorption temperature. The larger the difference between the desorption pressure and the PCT equilibrium pressure, the larger the driving force for decomposition. However, these thermodynamic considerations do not tell us about the rapidity of H_2 release during dehydrogenation, which is a kinetic property.

The aim of this chapter is to make a brief review of the progress made in the past few years in the research on complex metal–nonmetal hydrides and their composites that have the greatest potential for being applied in the future hydrogen economy as a viable source of supplying hydrogen to fuel cells.

In the broadest sense, complex hydrides are composed of an anionic metal–hydrogen complex or nonmetal–hydrogen complex bonded to a cationic alkali or transition metal.[15,18,19] Thus, complex hydrides can be roughly subdivided into two categories: group I and II salts of $[AlH_4]^-$, $[NH_2]^-$, $[BH_4]^-$, i.e. alanates, amides, and borohydrides,[15,18,19] and transition metal (TM) complex hydrides that have anionic $(TMH_x)^-$ complexes such as $[FeH_6]^{4-}$ attached to a cationic light metal, e.g. Mg^{2+}, in Mg_2FeH_6.[15,18] Their bonding is usually an ionic–covalent mix.[19] Similar transition metal ternary complex hydrides exist in the Mg–Co, Mg–Ni and Mg–Mn systems forming Mg_2CoH_5, Mg_2NiH_4, and Mg_3MnH_7 (the latter was synthesized under 20 k bar H_2 at ~800 °C[15,20]). Some references classify certain complex hydrides, e.g. $NaBH_4$, as "chemical hydrides" because they can easily react with water solution of KOH or NaOH (or water steam) releasing hydrogen.[15]

The progress made up to 2008 has already been reported in our book "Nanomaterials for Solid State Hydrogen Storage".[15] In the present work, we will try to focus mostly on research results that have been reported after 2008. We will limit discussion to the complex hydride systems based on the lightest elements Li, Na, Al, N, and B since, as mentioned earlier, they have the lowest densities and as such the highest available gravimetric hydrogen capacities. This review concerns only tertiary metal/nonmetal complex hydrides, so the rapidly growing area of ammonia borane-based systems (NH_3BH_3) is not covered here.

Finally, it must be pointed out that as usual there is a bad news and good news. The good news is that a continuous progress on better understanding of the fundamental principles of hydrogen storage behavior of complex hydrides has been made in the past 5 years. The bad news is that a breakthrough has not been achieved yet and there is not even one hydride system that is close to commercialization for application as a storage medium for the most important automotive market. However, it is shown that, at least, a system based on $LiAlH_4$ with nanometric metal and other additives may be close near-commercialization for applications for disposable H_2 storage cartridges for long-duration, low-demand devices that use H_2.

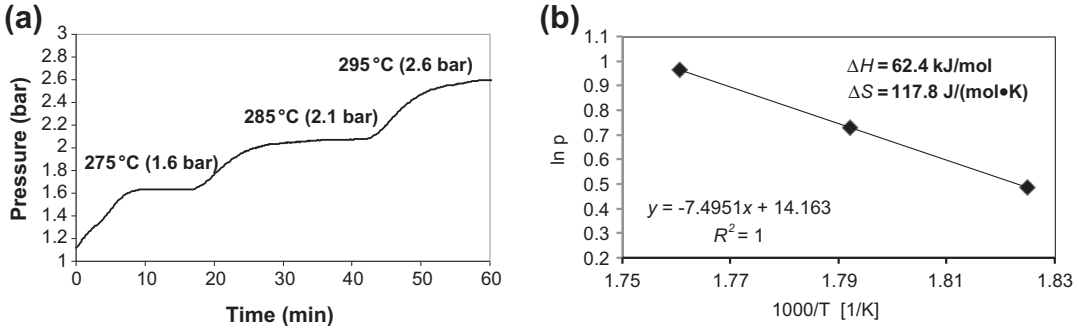

FIGURE 13.1 (a) Step-wise pseudo-PCT curves at varying temperatures and (b) corresponding Van't Hoff plot (Eqn (13.1)) for the ($LiNH_2 + 1.2LiH$) mixture milled for 25 h under a high-energy milling mode. *Source: Adapted from Ref. 16.*

13.2 ALANATES

The most important representatives in this family of complex hydrides are $NaAlH_4$, $LiAlH_4$, $Mg(AlH_4)_2$, and $Ca(AlH_4)_2$, among others, having the maximum theoretical gravimetric hydrogen capacities 7.5, 10.6, 9.3, and 7.9 wt%H_2, respectively, assuming 100% pure materials (Table 1.4 in[15]). Obviously, these values will be proportionally lower if a purity of real material obtained from a supplier is taken into account. However, the important problem is that all these alanate hydrides decompose and desorb H_2 in multistep reactions the last of which usually occurs at temperatures exceeding 300 °C. The practical maximum H_2 capacity (for a 100% pure material), which can be obtained up to roughly 250 °C for $NaAlH_4$, $LiAlH_4$, $Mg(AlH_4)_2$, and $Ca(AlH_4)_2$, is of the order of 5.6, 7.9, 7.0, and 5.9 wt%, respectively (Table 1.4 in[15]). In view of our earlier discussion regarding the DOE targets for automotive storage, none of these hydrides can be considered a potential candidate because they have lower practical gravimetric capacities than the targeted ~10 wt% H_2 for a storage *material* (5.5 wt% H_2 for a storage *system*). The two most interesting alanates are $NaAlH_4$ and $LiAlH_4$ because they are widely commercially available in contrast to $Mg(AlH_4)_2$ and $Ca(AlH_4)_2$ that require a complicated synthesis process usually using a mechanochemical activation synthesis (MCAS) by ball milling of a mixture of $NaAlH_4$ and $MgCl_2/CaCl_2$.[15] $NaAlH_4$ and $LiAlH_4$ have relatively high theoretical volumetric capacities of 97 and 74 kg h_2/m^3,[21] respectively, and low densities of 1.28 and 0.917 g/cm^3, respectively.[19]

13.2.1 Sodium Alanate ($NaAlH_4$)

For the first time, Bogdanović and Schwickardi[22,23] reported that the addition of Ti alkoxide/halide catalytic precursors (e.g. $Ti(OBu^n)_4$ or $TiCl_3$) reduced the dehydrogenation temperature of $NaAlH_4$ and rendered it reversible under relatively mild conditions of temperature and hydrogen pressure. Their findings were followed by a large number of research papers that have been reviewed until the end of 2008 in our recent book.[15] At present, the general consensus has emerged that during decomposition (dehydriding) of pristine $NaAlH_4$ as well as those containing a catalyst or catalytic precursor, the following reactions may take place[15,24–26]:

$$NaAlH_4(s) \leftrightarrow NaAlH_4(l) \quad (\Delta H = 23\,\text{kJ/mol}) \tag{13.2a}$$

$$NaAlH_4(l) \rightarrow \frac{1}{3}\alpha\text{-}Na_3AlH_6(s) + \frac{2}{3}Al(s) + H_2(g) \quad (\Delta H = 9\,\text{kJ/mol}) \tag{13.2′b}$$

$$NaAlH_4(s) \leftrightarrow \frac{1}{3}\alpha\text{-}Na_3AlH_6(s) + \frac{2}{3}Al(s) + H_2(g) \quad (\Delta H = 37\,\text{kJ/mol}\,H_2) \tag{13.2″b}$$

$$\alpha\text{-}Na_3AlH_6(s) \leftrightarrow \beta\text{-}Na_3AlH_6(s) \quad (\Delta H = 3.6\,\text{kJ/mol}\,H_2) \tag{13.2c}$$

$$\frac{1}{3}\beta\text{-}Na_3AlH_6(s) \leftrightarrow NaH(s) + \frac{1}{3}Al(s) + 0.5H_2(g) \quad (\Delta H = 47\,\text{kJ/mol}\,H_2) \tag{13.2d}$$

$$NaH(s) \rightarrow Na(l) + 0.5H_2 \quad (\Delta H = 57\,\text{kJ/mol}\,H_2) \tag{13.2e}$$

where ΔH is the enthalpy change of the reaction, and (s), (l), and (g) refer to "solid", "liquid", and "gas", respectively. Reactions (13.2′b) or (13.2″b), (13.2d), and (13.2e) proceed with maximum theoretical hydrogen releases of 3.7, 1.9, and 1.8 wt%, which in practical terms are slightly lower because hydrides are not 100% pure. Their approximate temperature ranges are 180, 270−300, and above 300 °C, respectively. As can be seen, hydrogen is desorbed in three major steps although Reaction (13.2e) is not accessible for practical storage purposes due to its high temperature (>300 °C). The hydrogen capacity, which can be theoretically obtained from two Reactions (13.2′b or 13.2″b) and (13.2d), is around 5.6 wt%. If isothermal dehydriding occurs below the melting point of $NaAlH_4$ (~180 °C[15,24,25]), then the first dehydriding Reaction is (13.2″b), which occurs in *solid state*. In addition, Claudy et al.[15,24] reported a phase transition of pseudocubic α-Na_3AlH_6 into face-centered cubic β-Na_3AlH_6 at about 252 °C (Reaction (13.2c)).

From the experimental Van't Hoff plot (Eqn (13.1)), it has been established[25] that the dehydrogenation of Ti-doped $NaAlH_4$ according to Reaction (13.2″b) and that of Ti-doped Na_3AlH_6 according to Reaction (13.2d) reaches ~30 °C and ~100 °C, respectively, at the pressure of 1 bar H_2 (atmospheric). Unfortunately, due to very sluggish kinetics, the Ti-doped $NaAlH_4$ hydride can operate only with a reasonable hydrogen desorption rate at temperatures >100 °C.[25] These are the temperature/pressure limits for any practical application of Ti-doped $NaAlH_4$. Experimental support for these temperature limits can be found in,[27] where it was reported that $NaAlH_4$ doped with 2 mol% $TiCl_3$ decomposed to a considerable degree to NaCl, Al, and Na_3AlH_6 at the only moderately elevated temperatures created during ball milling. This indicates that a decomposition of $TiCl_3$ adds, most likely, nanometric Ti component, which acts as a potent catalyst in the desorption process of $NaAlH_4$. The recent findings seem to confirm that the role of $TiCl_3$ is to form Ti, which alloys with Al and, in turn, forms an intermetallic compound whose local structure resembles Al_3Ti[26] according to the following reaction[26]:

$$3NaAlH_4 + TiCl_3 \leftrightarrow 3NaCl + Al_3Ti + 6H_2 \tag{13.3}$$

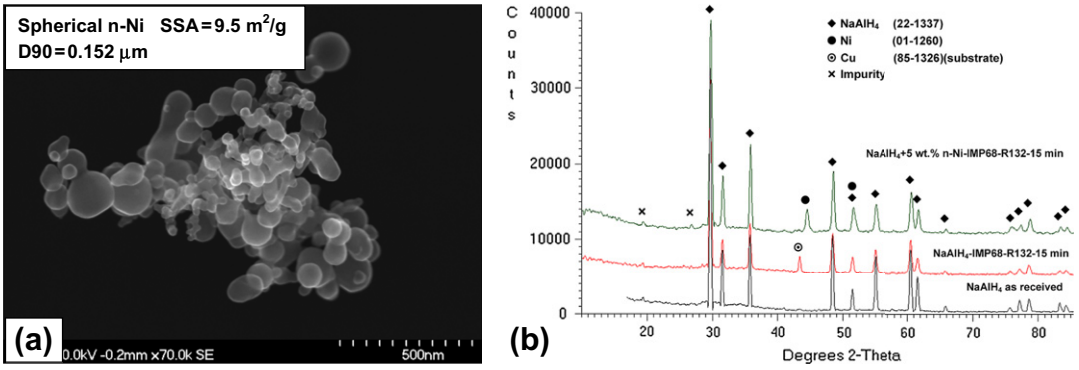

FIGURE 13.2 (a) Scanning electron micrograph of Vale Ltd nanometric Ni (n-Ni) with specific surface area (SSA) = 9.5 m^2/g. Secondary electrons (SE) contrast. (b) A comparison of the XRD patterns for as-received $NaAlH_4$, ball-milled $NaAlH_4$, and the ball-milled ($NaAlH_4 + 5$ wt% n-Ni) nanocomposite. ICDD file numbers are shown for phase identification. (For color version of this figure, the reader is referred to the online version of this book.) *Source: Adapted from Ref. 36.*

It was also reported that the plateau pressures of the $TiCl_3$-doped $NaAlH_4$ system, especially for the first dehydrogenation step (Reaction (13.2″b)), are markedly affected by the Ti content.[26] Bogdanović et al.[28] reported that $ScCl_3$ and $CeCl_3$ were even better catalytic precursors than $TiCl_3$ in particular for rehydrogenation. For example, $NaAlH_4$ doped with 4 mol% $ScCl_3$ was rehydrogenated at 90 °C in the 9th cycle under about 50 bar H_2 pressure within 70 min to achieve ~3.4 wt% H_2.[26] Furthermore, Wang et al.[29] have reported that there is a synergistic effect of codoping with $TiCl_3$, $ZrCl_4$, and $FeCl_3$ from which the combination of 3 mol% $TiCl_3$−1 mol% $FeCl_3$ exhibited the best synergistic performance. Xiao et al.[30] extended the studies on the synergistic effects of dopants to pure elemental metals such as Ti (particle size 54−70 μm) and Zr (particle size 50 μm).[30] Schmidt and Röntzsch[31] investigated the combined effect of metallic Zr (particle size 2−3 μm) and a $TiCl_3$ precursor. In turn, Bogdanović et al.[32] added colloidal titanium (Ti) nanoparticles (particle size unspecified) and the nanoparticles of titanium nitride (TiN)(size unspecified). Xueping et al.[33] investigated the catalyzing effects of pure metallic elements such as Ti, Co, and Ni of unspecified particle sizes together with $LaCl_3$ on hydrogen release of $NaAlH_4$. Fan et al.[34] used titanium carbide (TiC; particle size <4 μm) to catalyze the rate of desorption/absorption of $NaAlH_4$. A nonmetallic catalyst such as carbon of unspecified particle size was also used in the past by Zaluska et al.[35]

A disadvantage of catalytic precursors such as metal chlorides is such that they locally react (Reaction (13.3)) with $NaAlH_4$-forming metal salts and free elemental metals and/or intermetallic compounds of nanometric size that most likely act as effective catalysts, as discussed above. A by-product of a metal salt constitutes unnecessary "dead-weight" (ballast) for the microstructure and, in effect, reduces the total available hydrogen capacity. It would be better to find some effective nanometric metallic catalytic additives that directly influence the dehydrogenation/rehydrogenation properties of $NaAlH_4$ without exhibiting any unwanted reaction with the host matrix. Most recently, we investigated the catalytic effect of nanometric nickel (**n-Ni**) produced by Vale Ltd. (Ontario, Canada) on the desorption behavior of ball-milled $NaAlH_4$.[36]

Figure 13.2(a) shows the morphology of the n-Ni additive, which was added in the amount of 5 wt%. It exhibits a very spherical shape with the average equivalent circle diameter (ECD) = 76 ± 32 nm.[36] Figure 13.2(b) shows the X-ray diffraction (XRD) patterns for the as-received and ball-milled $NaAlH_4$ and the ball-milled ($NaAlH_4 + 5$ wt% n-Ni) nanocomposite. The principal phase, before and after ball milling, is $NaAlH_4$, and a minority phase in the doped nanocomposite is n-Ni. High-energy ball milling did not induce any phase transformations, e.g. reaction with nanonickel. Very small impurity peaks are also seen in Fig. 13.2(b), which tentatively were identified as either $Al_{29}(OH)_{78}Cl_9$ (ICDD file# 13-0320) or $AlCl_3 \cdot 6H_2O$ (ICDD# 08-0453&44-1473). It seems that the impurities in this technical purity $NaAlH_4$ may be some complex aluminum chlorides that point toward their origin in the production process of the powder.[36]

Figure 13.3(a), (b) and (c) show the differential scanning calorimetry (DSC) curves for the as-received and ball-milled $NAlH_4$, and ball-milled ($NaAlH_4 + 5$ wt% n-Ni), respectively. The first exotherm for the as-received $NaAlH_4$ at 174.3 °C in Fig. 13.3(a), 167.6 °C for milled $NaAlH_4$ in Fig. 13.3(b), and 165.7 °C for milled ($NaAlH_4 + 5$ wt% n-Ni) in Fig. 13.3(c), was attributed by Block and Gray,[37] who investigated the thermal decomposition of $LiAlH_4$, to the reaction of the surface aluminum-hydroxyl groups owing to the presence of impurities of the following type:

$$>\text{Al-OH} + \text{H-Al}< \rightarrow >\text{Al-O-Al}< + H_2 \qquad (13.4)$$

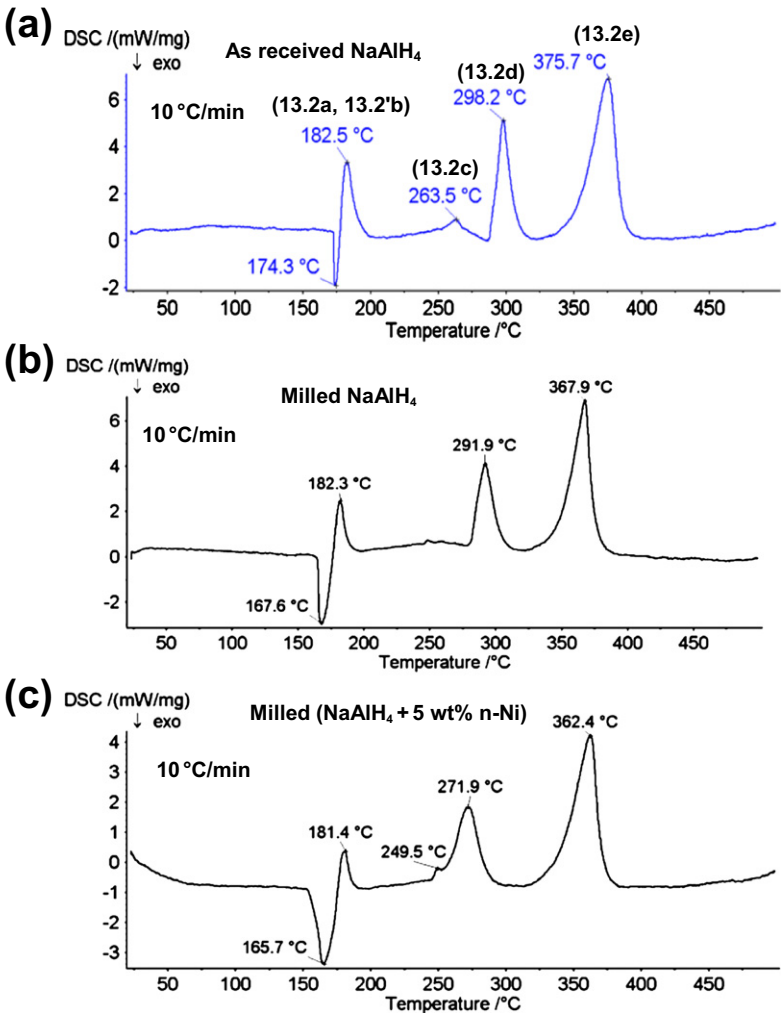

FIGURE 13.3 DSC curves for (a) as-received $NaAlH_4$, (b) ball-milled $NaAlH_4$, and (c) ball-milled ($NaAlH_4$ + 5 wt% n-Ni). Heating rate 10 °C/min; high-purity argon flow rate of 100 ml/min. (For color version of this figure, the reader is referred to the online version of this book.) *Source: Adapted from Ref. 36.*

Recently, Xiao et al.[30] attributed this peculiar peak to some microstructural arrangement including the release of residual stresses and recombination of dislocations in the ball-milled powder because they did not observe this exothermic peak for the unmilled/undoped $NaAlH_4$. However, as clearly shown in Fig. 13.3(a), the as-received $NaAlH_4$ also exhibits very well-developed exothermic peak.

The first endothermic peaks at 182.5, 182.3, and 181.4 °C in Fig. 13.3(a), (b) and (c), respectively, can be attributed to a simultaneous melting and decomposition of $NaAlH_4$ into Na_3AlH_6, Al, and H_2 according to Reactions (13.2a)and (13.2′b). The second weak endothermic peaks at 263.5−250 °C can be attributed to the allotropic transformation of Na_3AlH_6 according to Reaction (13.2c). The third strong endo peaks at 298.2, 291.9, and 271.9 °C in Fig. 13.3(a), (b) and (c), respectively, can be attributed to the decomposition of Na_3AlH_6 into NaH, Al, and H_2 according to Reaction (13.2d). The reactions attributed to these two endothermic peaks are in agreement with the interpretation reported in.[24,30,34,38,39] The fourth high-temperature endo peaks at 375.7, 367.9, and 362.4 °C in Fig. 13.3(a), (b) and (c), respectively, are most likely due to the decomposition of NaH into Na (liquid) and H_2 (Reaction (13.2e)). NaH is reported as decomposing at 425 °C.[40] The temperatures of the third high-temperature endo peak in Fig. 13.3 are approximately 50−60 °C lower than the quoted decomposition temperature of NaH. Dilts and Ashby[38] attributed this peak to the decomposition of NaH. Zaluski et al.[39] argued that the decomposition temperature of NaH may be significantly changed when NaH has been formed as a result of the decomposition of complex alanate like $NaAlH_4$. Figure 13.3 also shows that peaks (13.2d) and (13.2e) after ball milling are shifted to a slightly lower temperature range. The peak corresponding to the melting and decomposition of $NaAlH_4$ (Reactions (13.2a) and (13.2′b)) seems not to be affected by milling. Peaks (13.2d) and (13.2e) are additionally

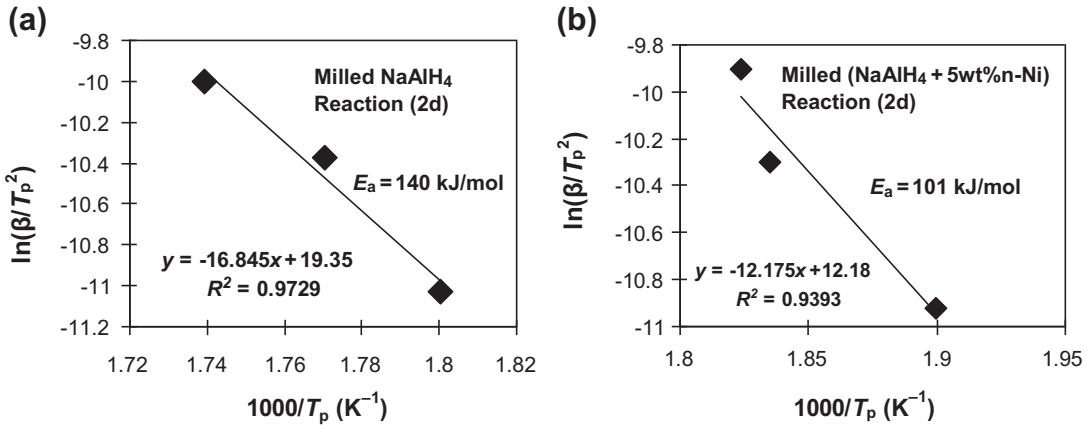

FIGURE 13.4 Examples of the Kissinger plots for the determination of the apparent activation energy of dehydrogenation (E_a) of ball-milled (a) $NaAlH_4$ and (b) ($NaAlH_4 + 5$ wt% n-Ni) for Reaction (13.2d) [$1/3\beta$-$Na_3AlH_6(s) \rightarrow NaH(s)+1/3Al(s) + 0.5H_2(g)$]. *Source: Adapted from Ref. 36.*

shifted to slightly lower temperatures after adding 5 wt% n-Ni. Even smaller temperature shifts were reported by Xiao et al.[30] after adding Ti + Zr elements.

The apparent activation energy of Reactions (13.2d) and (13.2e) were determined by the Kissinger method using DSC tests[15] at the heating rates of 5, 10, and 15 °C/min (DSC curves not shown here). An example of the Kissinger plot for ball-milled $NaAlH_4$ and ($NaAlH_4 + 5$ wt% n-Ni) for Reaction (13.2d) is shown in Figure 13.4(a) and (b), respectively. We were unable to determine the activation energy of Reaction (13.2a) and (13.2′b) because at the highest heating rate of 15 °C/min, the peak corresponding to Reaction (13.2a) and (13.2′b) was not present on a DSC curve for the ball-milled ($NaAlH_4 + 5$ wt% n-Ni).[36] It is possible that the elimination of melting of the ($NaAlH_4 + 5$ wt% n-Ni) nanocomposite is caused by the n-Ni catalytic additive, but it clearly appears only at the highest heating rate of 15 °C/min.[36] The apparent activation energy of the decomposition of Na_3AlH_6 (Reaction (13.2d)) is equal to ~140 and 101 kJ/mol for ball-milled $NaAlH_4$ and ($NaAlH_4 + 5$ wt% n-Ni), respectively. It is in agreement with the value of ~121 kJ/mol reported by Sandrock et al.[41] for $NaAlH_4$ ball milled for 3 h. The addition of n-Ni catalyst results in a substantial reduction of the apparent activation energy of the decomposition of Na_3AlH_6. The value of ~101 kJ/mol is comparable to the apparent activation energy of 97–98 kJ/mol for ball-milled $NaAlH_4$ doped with $TiCl_3$ catalytic precursors (0.9–6 mol%).[41] Surprisingly, the addition of 5 wt% n-Ni increased the apparent activation energy of the decomposition of NaH (Reaction (13.2e)) to ~226 kJ/mol from the value of ~143 kJ/mol for $NaAlH_4$ without any additive.[36] In this peculiar behavior, the catalytic n-Ni additive reduces the activation energy for the decomposition of Na_3AlH_6 while it acts in the opposite direction increasing the apparent activation energy of the decomposition of NaH. At the present moment, there is no clear explanation of this behavior.

The addition of n-Ni catalyst dramatically enhances the rate of hydrogen desorption at 170 °C for the ball-milled ($NaAlH_4 + 5$ wt% n-Ni) (Fig. 13.5(b)) as compared to the ball-milled $NaAlH_4$ without additive (Fig. 13.5(a)). It is characteristic that the desorption curve for the ball-milled ($NaAlH_4 + 5$ wt% n-Ni) nanocomposite in Fig. 13.5(b) clearly exhibits two stages of desorption, designated I and II. Stage I can be attributed to Reaction (13.2″b) in which $NaAlH_4$ decomposes in a solid state because the desorption temperature (170 °C) is lower than the melting temperature of $NaAlH_4$ (~180 °C in Fig. 13.3). Stage II is attributed to Reaction (13.2d) in which β-Na_3AlH_6 decomposes in solid state.

X-ray diffraction studies confirmed[36] that after desorption at 170 °C (Fig. 13.5(a)), the microstructure still contained quite a substantial amount of retained $NaAlH_4$ and a small amount of Na_3AlH_6, which agrees well with only ~2 wt% H_2 desorbed in Fig. 13.5(a). Apparently, for ball-milled $NaAlH_4$ without Ni additive, this temperature is too low for a completion of Reaction (13.2″b). The presence of two polymorphic forms of Na_3AlH_6, one cubic and the other one noncubic, was also confirmed.[36] As mentioned earlier, Claudy et al.[15,24] reported that this polymorphic transformation occurred at about 252 °C (Reaction (13.2c)). However, our results clearly show that the polymorphic transformation of Na_3AlH_6 can also occur isothermally at the temperature of 170 °C after relatively long dehydrogenation time. XRD pattern for ($NaAlH_4 + 5$ wt% n-Ni) after desorption at 170 °C (Figure 13.5(b)) showed the presence of both cubic and noncubic polymorphs of Na_3AlH_6, NaH, Al, and obviously the n-Ni additive.[36] This result is in excellent accord with desorption of ~5.2 wt% H_2 in Fig. 13.5(b), indicating that Reaction (13.2″b) was completed and Reaction (13.2d) is still in progress.

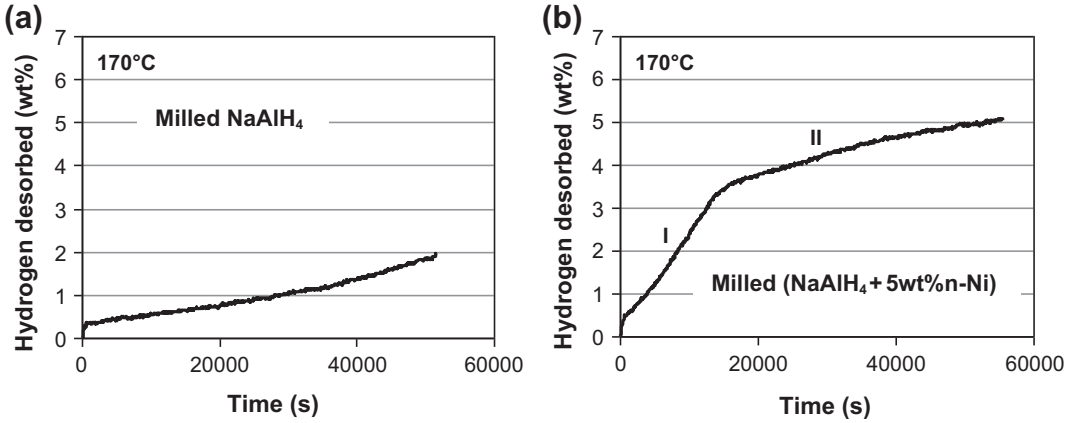

FIGURE 13.5 Volumetric desorption curves at 170 °C under 1 bar H_2 back pressure for ball milled (a) $NaAlH_4$ and (b) ($NaAlH_4 + 5$ wt% n-Ni). *Source: Adapted from Ref. 36.*

Table 13.1 shows a comparison of experimentally observed quantity of hydrogen desorbed at 170 °C within 18,000 s (5 h) from ball-milled ($NaAlH_4 + 5$ wt% n-Ni) observed in the present work with other catalytic precursors and metal catalysts used for $NaAlH_4$ desorbed at a similar temperature range.[36] The desorption duration of 18,000 s was so chosen because desorption tests in some references were carried out only up to this time duration. In one case in Table 13.1, the desorption temperature is 125 °C, which is much lower than the one in the present work to show a benefit of codoping with two catalytic additives.[31] It is clearly seen from Table 13.1 that the n-Ni catalyst used in the present work compares very favorably with other additives used for the enhancement of dehydrogenation of $NaAlH_4$. The present n-Ni catalyst results in a faster desorption rate than carbon used in[35] and is on par with micro-Ti[34] and liquid Ti and Zr alkoxides.[42] It should be noted that Xueping et al.[33] reported that the addition of 3 mol% of unspecified Ni to $NaAlH_4$ did not improve the desorption rate, which disagrees with the present results.

In general, slightly faster rates of desorption are observed for catalyzed $NaAlH_4$, which were synthesized by ball milling from NaH, Al, and a catalytic additive involving a long milling time such as in.[30,34] The best enhancement of desorption rate seems to occur by a codoping of $NaAlH_4$ (unpurified) with $TiCl_4$ and elemental Zr ball milled for 24 h.[31] It must be pointed out that at least two experimental parameters such as the content of n-Ni and ball-milling duration have not been optimized yet in the present work.

The effect of milling duration and resulting particle size on the dehydrogenation rate is not obvious. On the one hand, Bogdanović et al.[25] reported faster dehydrogenation of Ti-doped ($Ti(OBu)_4$) $NaAlH_4$ having smaller particle size. On the other hand, Sandrock et al.[42] reported that long-time ball milling did not result

TABLE 13.1 The Amount of Hydrogen Desorbed at 170 °C (under 1 bar H_2) within 18,000 s from the Ball-milled $NaAlH_4$ Containing Several Catalytic Precursors Observed in the Present Work as Compared with the Data Reported in the Literature[36]

Dehydriding temperature (°C)	Dehydriding pressure (bar)	Wt% H_2 desorbed after 18,000 s	Catalytic precursor/catalyst	Ball-milling time (h)	Ref.	Comment
170	1.0	3.7	n-Ni	0.25	This work	Unpurified $NaAlH_4$
180	1.0	4.0	Carbon	0.25	35	Unpurified $NaAlH_4$
165	1.0	4.2	Micro-TiC	48	34	Synthesized $NaAlH_4$
150–165	1.3	6.0 (1)* 3.0 (3–5)#	Liquid Ti and Zr alkoxides	A few minutes	42	Purified $NaAlH_4$
160	1.0	4.2	8% Ti + 2% Zr	12	30	Synthesized $NaAlH_4$
150	?	3.0	$LaCl_3$	0.17	33	Unpurified $NaAlH_4$
125	1.0	4.0	$TiCl_4 + Zr$	24	31	Unpurified $NaAlH_4$

Notes: (1)*—after first cycle, possibly impurities; (3–5)#—after cycles 3–5 with wt% normalized to the alanate only.

in much particle size reduction due to agglomeration, which we also observed for ball-milled $NaAlH_4$.[15] Therefore, it seems that the refinement of a particle size of $NaAlH_4$ is not a principal factor responsible for faster desorption after a long-term milling. It is likely more important that energetic ball milling would create a very homogeneous distribution of catalytic species within particles and on their surfaces and allow an intimate contact with the $NaAlH_4$ matrix.

Two mechanisms of enhancement of dehydrogenation properties of $NaAlH_4$ with added Ti and Zr were proposed by Xiao et al.[30] In the first mechanism called "superficial catalytic process", the active Ti-hydrides and Zr-hydrides that formed during ball milling would act as catalytic active sites on the surface of hydride matrix particles. In the second mechanism, called the "favorable thermodynamic modification", the Ti^{4+} and Zr^{4+} ions dissolve in the crystal lattice of $NaAlH_4$, partially substituting Al^{3+}, and forming $NaAl_{1-x}Ti_xH_4$ and $NaAl_{1-x}Zr_xH_4$ solid solutions. Since the ionic radii of Ti^{4+} and Zr^{4+} are larger than that of Al^{3+} [43] the lattice,expansion could lead to a lower decomposition enthalpy and the resulting destabilization of $NiAlH_4$. With respect to a n-Ni additive to $NiAlH_4$, the "superficial catalytic process" mechanism is not viable since Ni does not easily form hydride. However, lattice expansion of $NiAlH_4$ may be possible because the ionic radius of Ni^{2+} of 0.069 nm is much larger than 0.051 nm for Al^{3+}.[43] This mechanism seems even more credible since it will be shown in the following section on $LiAlH_4$ that our most recent results show that the lattice expansion of $LiAlH_4$ containing the n-Ni and Fe additives significantly increases during the highly energetic ball milling, most likely, due to diffusion of Ni and Fe ions into the $LiAlH_4$ crystal lattice.

In summary, $NiAlH_4$, even if it contains catalytic additives, is not a very attractive hydrogen storage material because its practical dehydrogenation capacity at temperatures <100 °C under 1 bar H_2 pressure is rather low, and despite that it is reversible, it still requires relatively high pressures in the range of 80−100 bar for rehydrogenation.

13.2.2 Lithium Alanate ($LiAlH_4$)

One of the most interesting hydrides for the solid-state hydrogen storage is a complex metal hydride $LiAlH_4$ (lithium alanate) since it can liberate a relatively large theoretical quantity of 7.9 wt% H_2 below 250 °C.[15] Graetz and Reilly[44] classified $LiAlH_4$ as belonging to a group of hydrides called "kinetically stabilized metal hydrides," which also include AlH_3, $Mg(AlH_4)_2$, and $Ca(AlH_4)_2$ among others. All these hydrides are characterized by an equilibrium H_2 pressure of their respective PCT curves at RT (298 K) much higher than 1 bar. As mentioned in Section 13.1, this feature alone creates a large driving force for decomposition. However, they are quite stable at near RT, most likely, due to kinetic limitations as their name indicates. The mechanisms responsible for their stable behavior are not well understood although slow/hydrogen metal diffusion and surface barriers that hinder the easy formation of molecular H_2 are quite likely.[44]

It is well established[15] that $LiAlH_4$ decomposes releasing H_2 in steps similar to the ones discussed for $NaAlH_4$ (Reactions (13.2)), which are as follows:

$$LiAlH_4(s) \rightarrow LiAlH_4(l) \tag{13.5a}$$

$$LiAlH_4(l) \rightarrow \frac{1}{3}Li_3AlH_6(s) + \frac{2}{3}Al(s) + H_2(g) \tag{13.5′b}$$

$$LiAlH_4(s) \rightarrow \frac{1}{3}Li_3AlH_6(s) + \frac{2}{3}Al(s) + H_2(g) \tag{13.5″b}$$

$$\frac{1}{3}Li_3AlH_6(s) \rightarrow LiH + \frac{1}{3}Al + 0.5H_2 \tag{13.5c}$$

$$LiH \rightarrow Li + 0.5H_2 \tag{13.5′d}$$

or

$$LiH + Al \rightarrow LiAl + 0.5H_2 \tag{13.5″d}$$

where s-solid, l-liquid, and g-gas. Reaction (13.5a) is endothermic, Reaction (13.5′b) or (13.5″b) is exothermic, and Reactions (13.5c) and (13.5d) are both endothermic reactions. Reactions (13.5′b) or (13.5″b), (13.5c), and (13.5d) proceed with theoretical hydrogen releases of 5.3, 2.6, and 2.6 wt%, respectively.[15] Obviously, these numbers will be lower for the purity-corrected capacity.

In contrast to $NaAlH_4$, the enthalpies of each step in Reactions (13.5) are not so well established as those for $NaAlH_4$. The experimentally observed enthalpy of Reaction (13.5′b) was reported as being equal to −14 kJ/mol H_2 (exothermic)[45] and −10 kJ/mol H_2 (exothermic).[19,37] The calculated values of 9.79 and 15.72 kJ/mol H_2, both endothermic, were reported for Reactions (13.5′b) and (13.5c), respectively.[46]

The PCT equilibrium plateau pressure for the decomposition of $LiAlH_4$ has been reported to be very high, which could make $LiAlH_4$ irreversible under practical conditions of temperature/pressure. The plateau pressure for Stage I dehydrogenation reaction of $LiAlD_4$, containing a catalytic precursor TiF_3, into Li_3AlD_6, Al, and H_2 (Reaction (13.5′b) or (13.5″b)) was reported by Brinks et al.[47] to be higher than 99 and 87 bar at 53 and 80 °C, respectively. Furthermore, Mulana and Nishimiya[48] estimated the enthalpy (ΔH) and entropy (ΔS) for Stage I dehydrogenation (Reaction (13.5′b) or (13.5″b)) and the second stage dehydrogenation Reaction (13.5c)

(Stage II) as being equal to $\Delta H = 17.5$ kJ/mol H_2 and $\Delta S = 121.6$ J/mol H_2 K, and $\Delta H = 11.1$ kJ/mol H_2 and $\Delta S = 62.6$ J/mol H_2 K, respectively. Assuming $\Delta H = 17.5$ kJ/mol H_2 and $\Delta S = 121.6$ J/mol H_2 K, the equilibrium pressure for Stage I dehydrogenation calculated from Eqn (13.1) would amount to 1.88×10^3 and 19.6×10^3 Atm at RT (24 °C = 297 K) and 170 °C (443 K), respectively. Apparently, the first dehydrogenation reaction appears to be completely irreversible due to extremely high pressures required for rehydrogenation. Assuming $\Delta H = 11.5$ kJ/mol H_2 and $\Delta S = 62.6$ J/mol H_2 K for Stage II in Eqn (13.1), it is calculated that at 170 °C the equilibrium H_2 pressure is around 82 Atm. This pressure level although still relatively high can be achieved for realizing reversibility under more practical conditions. On the other hand, the computed stability diagrams for $LiAlH_4/Li_3AlH_6/LiH$ show very high pressures of the order of 10^3 Atm at 170 °C needed for the rehydrogenation of LiH/Al into Li_3AlH_6.[15,49,50]

A reduction of dehydrogenation temperature for $LiAlH_4$ accompanied by increasing dehydrogenation rate can be achieved by incorporating catalytic precursors or catalytic additives. Catalytic precursors are mostly various halides such as metal chlorides $AlCl_3$, $NiCl_2$, $TiCl_3$, $TiCl_3 \cdot 1/3AlCl_3$, $TiCl_4$, VCl_3, $ZrCl_4$, $ZnCl_2$, and bromides VBr_3[15,51] Metal fluorides such as TiF_3[47,52] and NbF_5[53] were also tried as catalysts for $LiAlH_4$; the mechanism by means of which they act as catalytic additives is not fully elucidated. However, most papers report that they locally react with $LiAlH_4$ and form metal salts and free elemental metals or intermetallic compounds of nanometric sizes, which most likely act as effective nanometal catalysts.[15,46,51–53] This is a similar behavior as discussed earlier for $NaAlH_4$ (e.g. Reaction (13.3)). A disadvantage of metal halides is the formation of a metal salt by-product, which constitutes unnecessary ballast (dead-weight) for the microstructure and reduces the total available hydrogen capacity.

In general, a highly electronegative dopant halide anion, like Cl^- or F^-, may play a role in destabilizing $LiAlH_4$. The AlH_4^- complex is covalent. While Al has three valence electrons available for bonding H in charge-neutral AlH_3, a fourth H atom can be added, provided that an extra electron is donated from the alkali metal to satisfy the two-electron bond. In effect, the negatively charged AlH_4^- complex becomes stable while bonded to the positively charged Li^+. The halide anions have high affinity to Li^+ cations and by forming ionic bonds with lithium ions destabilize the AlH_4^- complex, which dissociates to H and the AlH_3 vacancy formed within $LiAlH_4$ crystalline lattice. Introducing a vacancy defect destabilizes a complex hydride. Theoretical calculations by density functional method of the creation of the hydrogen-related point defects in $NaAlH_4$ and their diffusion through the hydride point to a decisive role they play in hydrogenation reactions. Only recently, the role of vacancy diffusion in the decomposition reaction of complex hydrides has been highlighted in research papers[54] and also received a good review.[55] Again, an important feature of these defects is that they are charged, hence the vacancy-formation energy is strongly affected by the presence of electrically active dopant, like Cl^-.[56]

Crystal defects are known to play a role in chemical reactions and their presence profoundly affects mass transport and diffusion in solid phases.[57] Generation of defects by doping with halide catalysts seems to apply to most complex hydrides. Yet, there may be an alternative. Alanates are mixed ionic–covalent compounds, consisting of either alkali (group I) or alkaline-earth (group II) metal ions bonded with anion complexes (AlH_4^-) located on the lattice sites. There may also be a "mechanical" process in play to introduce defects in ionic–covalent crystals. This is to shear the crystal along the easy slip planes. This can be possible in certain complex hydrides but not in the others. In Mg alanate, $Mg(AlH_4)_2$, where metal cations occupy sites that belong to one crystallographic plane and complex anions belong to the other plane, mechanical shearing of crystals may result in proliferation of stacking faults. This profoundly improves kinetics of dehydrogenation in the ball-milling experiments and hydrogen becomes more mobile in the faulted structure of alanate.[58] On the other hand, this may also render a hydride unstable as it disproportionates during any prolonged milling; the effect, which may explain the limits to the reaction yield in synthesis of new hydrides in the ball-mill reactors. This mechanism would not apply to more strongly bonded ionic crystals and where no easy slip planes are present. For them, introducing point defects by catalytic additions is the only way to improve reaction kinetics.

It is perhaps worth to notice that the electrically active ion can be an impurity ion. The presence of chlorine ions is inherent to the process used in manufacturing $LiAlH_4$. Chlorine concentration may differ from one to the other producer. What is certain to be present in commercial-grade $LiAlH_4$ powders is OH^- impurity. The obvious source of hydroxyl ions is hydrolysis that almost always occurs on the surface of $LiAlH_4$ solids. X-ray photoelectron spectroscopy (XPS) surface analysis gives evidence to the reactive OH^- impurity (Fig. 13.6).[59] Concentration varies greatly with temperature and from powder to powder depending on the powder batch and storage conditions. It becomes apparent that the level of impurity not only affects dehydrogenation temperatures but can change dehydrogenation reactions pathways.

The rehydrogenation attempts of $LiAlH_4$ with catalytic precursors and catalytic additives have been

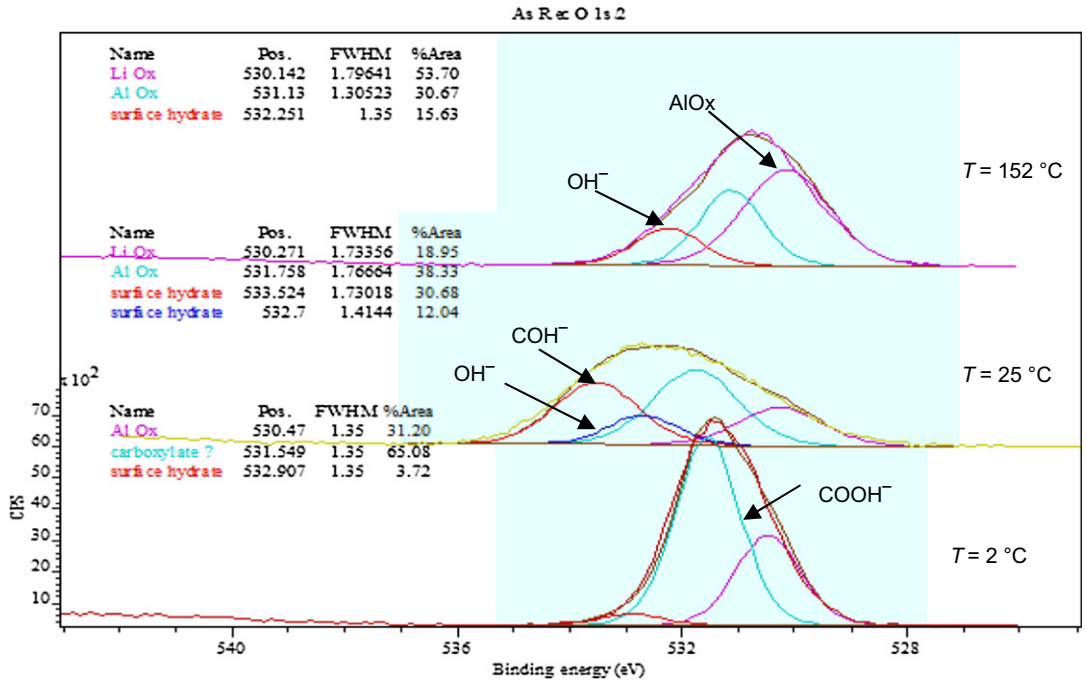

FIGURE 13.6 O1s X-ray photoelectron spectra at 25 °C, after cooling to 2 °C, and subsequent heating to 152 °C. (For color version of this figure, the reader is referred to the online version of this book.) *Source: Adapted from Ref. 59.*

reported. Chen et al.[60] investigated $LiAlH_4$ ball milled with the $TiCl_3 \cdot 1/3AlCl_3$ additive and showed reversibility of $(LiH + Al)$ into Li_3AlH_6 at 40 bar and ~175 °C with the achieved reversible H_2 capacity of 1.8 wt%. Recently, Rafi-ud-din et al.[61] reported that the ball-milled $LiAlH_4$ with 5 mol% TiC, dehydrogenated to $(LiH + Al)$ (Stage II), could be successfully rehydrogenated to Li_3AlH_6 at 165 °C and 95 bar H_2 pressure with the achieved reversible H_2 capacity of 1.9 wt%. These experimental results indicate that there is still a possibility of achieving at least a partial reversibility for $LiAlH_4$ containing catalytic additives using an appropriate window of temperature/pressure/time. It must also be added that it has recently been shown that $LiAlH_4$ doped with $TiCl_3$, TiN, and $LaNi_5$, and dehydrogenated to the $(LiH + Al)$ mixture can be nearly fully rehydrogenated back to $LiAlH_4$ at RT in low-boiling dimethyl ether under 100 bar H_2 pressure.[62–64]

The addition of metallic and especially nanometric size metal catalysts to $LiAlH_4$ has not been investigated so extensively. Balema et al.[65] reported that the elemental Fe as a catalytic additive was much less effective than $TiCl_4$, Al_3Ti, $Al_{22}Fe_3Ti_8$, and Al_3Fe. They also reported that ball milling of $LiAlH_4$ with 3 mol% $TiCl_4$ for 5 min caused decomposition of $LiAlH_4$ into Li_3AlH_6, Al and H_2 by a rapid reduction of $TiCl_4$ by $LiAlH_4$ forming a LiCl salt. They did not observe any accelerated decomposition of $LiAlH_4$ during ball milling with Fe.[65,66] A partial decomposition of $LiAlH_4$ during ball milling was also observed with the TiF_3[48] and $NiCl_2$[67] additives. Resan et al.[68] concluded that the addition of elemental Ti, Fe, and Ni did not cause the decomposition of $LiAlH_4$ during ball milling as did metal chlorides. Kojima et al.[69], besides metal chlorides and intermetallics, also added n-Ni as a catalyst to $LiAlH_4$. They found that both chlorides and n-Ni led to the decomposition of $LiAlH_4$ during ball milling for 24 h. More recently, Zheng et al.[70] reported the thermal behavior of $LiAlH_4$ with unspecified most likely micrometric-sized iron (Fe) and titanium (Ti) additives. They noticed slightly improved dehydrogenation properties although no isothermal dehydrogenation was carried out.

Recently, we thoroughly investigated the thermal behavior and volumetric dehydrogenation of the ball-milled $LiAlH_4$ without additives[71] and $LiAlH_4$ containing 5 wt% of n-Ni[72,73] and as well nanometric Fe (n-Fe).[74] In contrast to n-Ni, the XRD data showed that n-Fe also contains quite a large amount of about 15% Fe_3O_4.[74]

Figure 13.7 shows DSC curves for the ball-milled $LiAlH_4$ without any additive (Fig. 13.7(a)), $LiAlH_4$ mixed with 5 wt% n-Ni (Fig. 13.7(b)), $LiAlH_4$ ball milled with 5 wt% n-Ni) (Fig. 13.7(c)), and $LiAlH_4$ ball milled with 5 wt% n-Fe (Fig. 13.7(d)). Designations of DSC peaks in Fig. 13.7(a) correspond to a set of Reactions (13.5). The first exothermic peak at 143.8 °C in Fig. 13.7(a) is nearly identical to the first exothermic peak in the DSC curves of $NaAlH_4$ in Fig. 13.3. As discussed earlier, this peculiar peak was assigned by Block and Gray[37] to the reaction of the surface

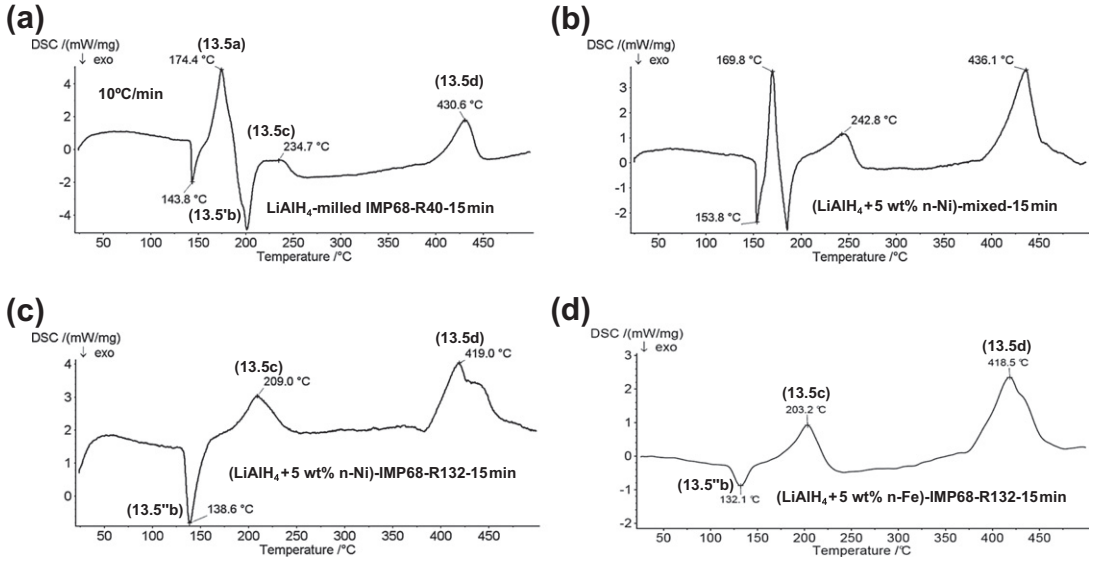

FIGURE 13.7 DSC curves for (a) ball-milled $LiAlH_4$ without any additive, (b) ($LiAlH_4 + 5$ wt% n-Ni) mixed without ball milling, (c) ($LiAlH_4 + 5$ wt% n-Ni) balled milled under a high-energy mode and (d) ($LiAlH_4 + 5$ wt% n-Fe) ball milled under a high-energy mode. IMP68—a high-impact energy mode of milling, R132-ball-to-powder-weight ratio = 132. *Source: Adapted from Refs 72,74.*

aluminum-hydroxyl groups owing to the presence of impurities according to Reaction (13.4). It is clearly seen in Fig. 13.7(b) that just a simple mixing of $LiAlH_4$ with a nanometric metallic additive, using mortar and pestle, does not change the DSC curve as compared to that for the ball-milled $LiAlH_4$ without additives (Fig. 13.7(a)). However, a highly energetic ball milling of $LiAlH_4$ with either the n-Ni or n-Fe additive completely eliminates melting of $LiAlH_4$, and the $LiAlH_4$ decomposition peak (13.5′b) in Fig. 13.7(a), (b) merges with the first peak for reaction of the surface aluminum-hydroxyl groups and becomes a single peak now corresponding to Reaction (13.5″b). This peak is now shifted to slightly lower temperatures (Fig. 13.7(c), (d)). Remarkably, this behavior is identical for both types of nanometric additive either n-Ni or n-Fe. The other two peaks corresponding to Reactions (13.5c) and (13.5d) appear unaffected except that they are shifted to slightly lower temperatures after high-energy ball milling with a nanometric metal additive (Fig. 13.7(c), (d)). The merging of peak attributed to surface hydroxyl reaction with the peak attributed to the decomposition of $LiAlH_4$ in Reaction (13.5′b) into one peak (13.5″b) for a solid-state decomposition is a very peculiar phenomenon and has never been reported in the literature. At this moment, it is unclear if this is just a coincidence or indeed, a new physical phenomenon. We hypothesized in[72,74] that reaction of the surface aluminum-hydroxyl groups may trigger a spontaneous decomposition of the ball-milled $LiAlH_4$ containing nanometric metallic additives at temperatures much lower than the melting point of either unmilled or ball milled $LiAlH_4$ without additives. However, it is still not clear whether the origin of the exothermic nature of the first peak in Fig. 13.7(a), (b) is related to the inherent exothermic nature of reaction of the surface aluminum-hydroxyl groups or indeed, Reaction (13.5″b) is simply exothermic in nature despite the fact that melting has been eliminated. It should also be pointed out that it is found[74] that ball milling of $LiAlH_4$ with *micrometric* size Fe additives does not lead to any special DSC curve changes, which are characteristic in Fig. 13.7(c), (d) for a nanometric additive, regardless of the intensity of milling.

In order to shed more light on the nature of the reactions occurring during a DSC test, the high-energy ball-milled ($LiAlH_4 + 5$ wt% n-Fe) nanocomposite powder was subjected to a thermal sectioning in DSC by stopping the test at predetermined temperatures, following the procedure outlined in.[71–73] After stopping the test at temperatures of 100, 140, 210, 300, 415, and 500 °C in Fig. 13.7(d) the powder sample was immediately extracted from a crucible for an XRD test. The corresponding XRD patterns are shown in Fig. 13.8. The microstructure of powder stopped at 100 °C before peak (13.5″b) consists of a principal phase $LiAlH_4$, a secondary phase Li_3AlH_6 most likely formed in Reaction (13.5″b), which occurs during a high-intensity ball milling, as will be discussed later in the text, Al (as received impurity[71–73] and possibly formed from Reaction (13.5″b) during ball milling), $LiOH \cdot H_2O$ (as received impurity), and Fe (additive). The microstructure of powder stopped at 210 and 300 °C, just after peak (13.5c) in the mid of the DSC plateau, consists of a principal phase Al and secondary phases LiOH and LiCl. A presence of LiH was also confirmed at this temperature.[74] Hence, LiOH may form as a result of

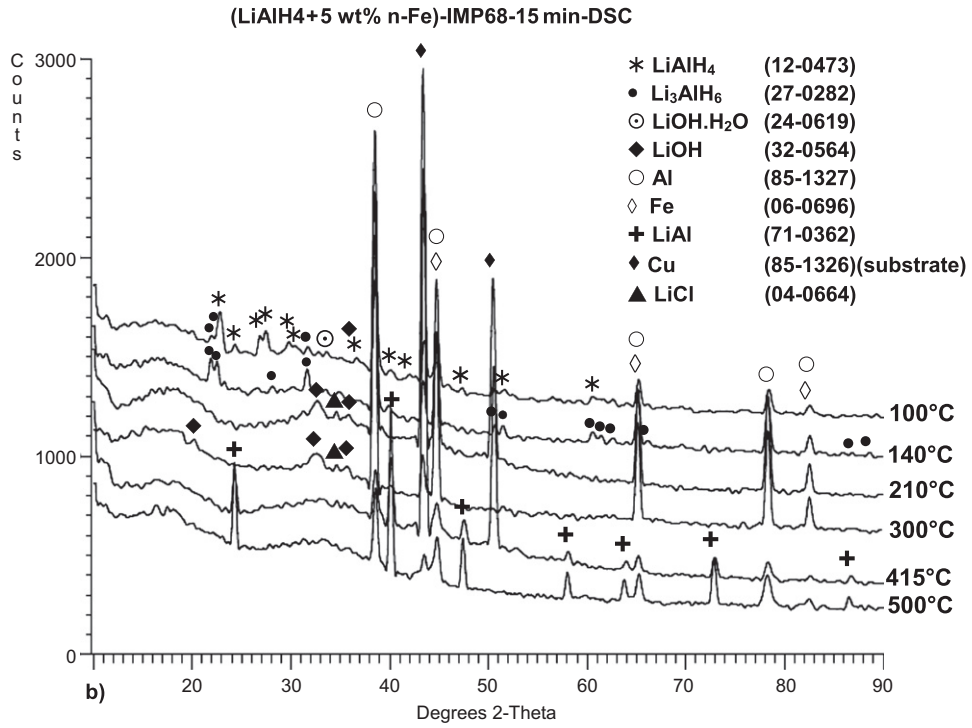

FIGURE 13.8 XRD patterns at thermal sectioning temperatures of a DSC curve for ball-milled ($LiAlH_4 + 5$ wt% n-Fe). IMP68—a high-impact energy mode of milling, R132-ball-to-powder-weight ratio = 132. ICDD file numbers are shown for peak identification. *Source: Adapted from Ref. 74.*

hydrolysis/oxidation of a fraction of LiH because the milled powder was transported to a DSC instrument in a glass vial filled with Ar and then quickly loaded into a DSC Al_2O_3 crucible. Usually this operation takes a short while, and for that period of time the powder could be in contact with air.[71–73] Alternatively, LiOH could be formed due to decomposition of the as-received $LiOH \cdot H_2O$ impurity. Most likely, LiCl is an as-received impurity arising from the industrial synthesis of $LiAlH_4$.[74]

At 415 and 500 °C just before and after peak (13.5d), an intermetallic compound LiAl appears in the microstructure, which indicates that peak (13.5d) can be attributed to reaction (13.5″d). Such reaction was also reported in Ref.[75] Note that the Reaction (13.5″d) can be reversible, as was found in experiments conducted at 500 °C and 0.26 Atm, which also confirmed the stoichiometry (Li/Al = 1) by electron energy-loss spectroscopy.[75]

It should be stressed out that the elimination of $LiAlH_4$ melting and simultaneous transformation of the $LiAlH_4$ decomposition reaction to solid state and shifting it to a lower temperature range, in the presence of a nanometric metal additive, occurs only after high-energy ball milling. A simple mixing is insufficient to induce such a profound change in its thermal behavior. At the first look, it seems that the only condition for this behavior is that the n-Ni and n-Fe additives must be very intimately embedded in the $LiAlH_4$ particles in order to be able to exert a potentially strong catalytic action on the alanate matrix in contrast to mixing where the potentially catalytic metal nanoparticles are just loosely distributed at the surfaces of $LiAlH_4$ powder particles. However, recent results on the effects of n-Fe on the dehydrogenation of the ball-milled $LiAlH_4$ clearly show that the mechanism of nanometal additive interaction with the $LiAlH_4$ during ball milling is more complicated.[74]

We have found that $LiAlH_4$ ball milled together with the n-Fe additive under a high-energy milling mode starts decomposing rapidly during milling, releasing large quantities of H_2 (Fig. 13.9(a)). Similar behavior was observed with metal chlorides[52,65,67,69] as additives to $LiAlH_4$ but has never been reported for the n-Fe additive. It must be stressed out that no H_2 desorption is observed during *low-energy* milling of $LiAlH_4$ containing n-Fe, for example, under a low-energy shearing mode (Fig. 13.9(a)). Similarly, no H_2 desorption occurs during high-energy ball milling for $LiAlH_4$ containing micrometric Fe (μ-Fe) and, for comparison, both the μ-Ni- and n-Ni additives. In order to identify reactions occurring as the milling progresses, the XRD patterns were obtained from the powders milled for 15 min, 1 h, and 5 h and are compared with the XRD for a mixed powder in Fig. 13.9(b). After only 15 min of milling, the diffraction

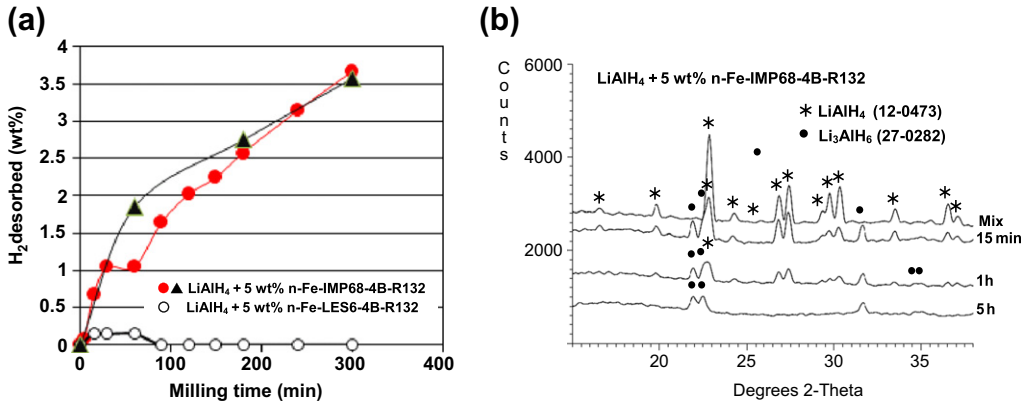

FIGURE 13.9 (a) The quantity of H_2 desorbed during ball milling under the high-impact energy (IMP68) mode and the low shearing energy (LES6) mode as a function of milling time. (b) XRD patterns after milling under high energy (IMP68) for various times. Milling under high-energy mode (IMP68) was repeated twice (solid circles and triangles). ICDD file numbers are shown for peak identification. 4B-four balls in the milling vial. Ball-to-powder weight ratio $R = 132$. For more details on ball milling in a magneto-mill, the reader is referred to Ref. 15. (For color version of this figure, the reader is referred to the online version of this book.) *Source: Adapted from Ref. 74.*

peaks of Li_3AlH_6 are clearly seen as opposed to the $LiAlH_4$ peaks observed for the mixed powders. The intensity of the Li_3AlH_6 peaks increases after 1 and 5 h (300 min) of milling while the intensity of $LiAlH_4$ peaks gradually decreases and they eventually disappear (Fig. 13.9(b)). Simultaneously, more H_2 is desorbed, as can be seen in Fig. 13.9(a). It is obvious that during high-energy milling, there is a gradual decomposition of $LiAlH_4$ in *solid-state* according to Reaction (13.5″b).

X-ray diffraction studies have shown that ball milling results in a varying degree of the lattice expansion of $LiAlH_4$ for both the n-Fe and n-Ni additives, as shown in Fig. 13.10. It seems that a volumetric lattice expansion larger than 1% triggers the accelerated decomposition of $LiAlH_4$ accompanied by continuous H_2 desorption during milling according to Reaction (13.5″b). It is hypothesized that the Fe and Ni ions are able to dissolve in the lattice of $LiAlH_4$ by the combined action of mechanical energy and chemical reaction as shown below, forming a substitutional solid solution of either the $LiAlFe_xH_4$- or $LiAlNi_xH_4$ type.[74] The ionic radius of 77 pm for Fe^{2+} is much larger than 53 pm for Al^{3+},[76] and the $LiAlH_4$ lattice expansion increases. In contrast, the ionic radius of Ni^{2+} is 69 pm[76] and the volumetric

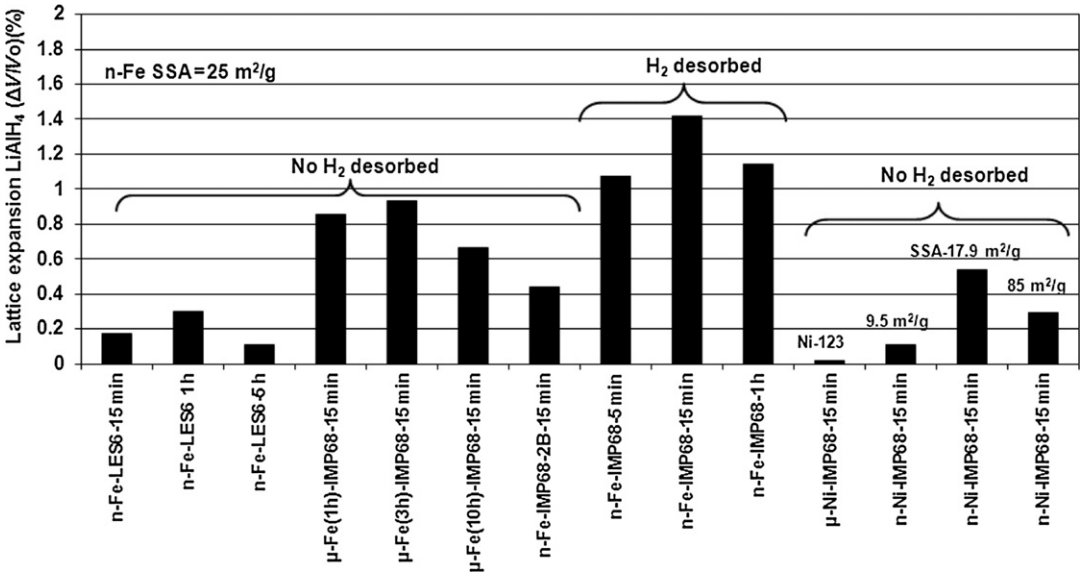

FIGURE 13.10 The correlation of the volumetric lattice expansion for $LiAlH_4$ with the type of Fe additive (μ-Fe n-and Fe), milling mode, and observed hydrogen desorption event during milling. For comparison, the results for μ-Ni and n-Ni are also shown. Milling conducted with four balls (4B) in the milling vial except where two balls (2B) are indicated; milling time duration is shown. Ball-to-powder weight ratio $R = 132$. IMP68-impact mode with two magnets, LES6-low energy shearing mode with one magnet (for more details on ball milling in a magneto-mill reader is referred to Ref. 15). SSA—specific surface area. μ-Fe-micrometric Fe additive: 1, 3, and 10 h—indicate the length of premilling time for the μ-Fe-additive. *Source: Adapted from Ref. 74.*

lattice expansion is smaller (Fig. 13.10). In addition, with reference to Fig. 13.9, it is observed that the quantity of dissolved metal ions depends primarily on the total energy of milling per unit mass of powder generated within a prescribed milling time. It also depends on the type of ions diffusing during ball milling, e.g. Fe vs Ni, because lattice expansion for n-Ni is smaller as compared to n-Fe for the same amount of total energy of milling (Fig. 13.10).

It is to be pointed out that the mechanism of accelerated mechanical decomposition of $LiAlH_4$ seems not to be a typical catalytic mechanism in which a catalyst is supposed to boost the surface formation of molecular H_2 from the atomic hydrogen escaping from the bulk. So far, the formation of Fe-ionic solid solution in $LiAlH_4$ and the resulting lattice expansion followed by its accelerated decomposition into Li_3AlH_6 during ball milling has never been reported in the literature although as discussed in Section 13.2.1 Xiao et al.[30] reported a lattice expansion for $NaAlH_4$ codoped with Ti and Zr both having much larger ionic radii than Al.[76]

Our experimental results show that n-Fe is more efficient in enhancing the dehydrogenation of lithium alanate during ball milling than n-Ni. This is a puzzling finding since, as it was said before, the Ni^{2+} ionic radius is smaller than size of the Fe^{2+} ion. However, incorporation of Ni ions into the ionic–covalent crystal of $LiAlH_4$ is less efficient than the Fe ions. To explain this peculiar phenomenon, one can take note that diffusion of metallic atoms/ions is different in a crystalline lattice of a host metal than in the lattice of an inorganic compound. A typical substitutional solid solution seems to be difficult to form as diffusivity of metal atoms/ions in an ionic covalent lattice of inorganic compounds is expected to be rather low. It was proposed in[77] that efficient incorporation of metal atoms/ions in the latter may be driven by chemical reactions with the use of oxide form of the alloying metal, instead of the metal itself. If so, the n-Fe that comes with much higher content of surface oxide (15 wt%) as reported in[74] than nanonickel (n-Ni) can be more efficient in enhancing the dehydrogenation reaction. Since the iron oxide associated with n-Fe is Fe_3O_4,[74] which, in essence, is a partly reduced form of Fe_2O_3 such as $Fe^{2+}O{\cdot}Fe^{3+}{}_2O_3$, the following reaction sequence can be postulated

$$(1+2x)LiAl^{3+}H_4 + xFe^{2+}O{\cdot}Fe^{3+}{}_2O_3 \rightarrow LiAl^{3+}Fe^{3+}{}_xH_4 + \{2xFe^{2+}O + 2xLiOH + (1+2x)AlH_3\} \quad (13.6a)$$

$$LiAl^{3+}Fe^{3+}{}_xH_4 \leftrightarrow \frac{1}{3}Li_3AlFe_xH_6 + \frac{2}{3}AlFe_x + H_2 \quad (13.6'b)$$

$$Li_3AlFe_xH_6 \leftrightarrow 3LiH + AlFe_x + \frac{3}{2}H_2 \quad (13.6''b)$$

This reduces the iron ions in Fe_3O_4 from Fe^{3+} to Fe^{2+} in Reaction (13.6a). Both the substituted $LiAlFe_xH_4$ and $Li_3AlFe_xH_6$ may be easier to dehydrogenate (Reaction 13.6′b). The Reaction (13.6a) can be difficult to reverse. The Reactions (13.6′b) and (13.6″b) can be reversible. In the reactions above, the catalytic additive is metal oxide Fe_3O_4. A part of atoms in Fe_3O_4 exhibit valence Fe^{3+}, the same as the valence of Al^{3+}. The ionic radius of Fe^{3+} of 63 pm is substantially smaller than that of Fe^{2+} i.e. 77 pm[76] so substitution of Fe for Al in the alanate lattice sites is more favorable. However, the driving force for Reaction (13.6a) is the oxidation–reduction potential, as Fe_3O_4 is the oxidizing agent and $LiAlH_4$ is a strong reducer. This reaction reduces the iron ions in Fe_3O_4 from Fe^{3+} to the metallic Fe atoms in solution with Al. However, reactions of incorporation of catalyst metal atoms into the lattice of complex hydride is even easier performed with halides than with use of oxides and are almost certain to occur with $MnCl_2$.

Figure 13.11(a) shows an example of volumetric dehydrogenation curves at varying temperatures for ($LiAlH_4$ + 5 wt% n-Fe) ball milled under a low-energy LES6 mode with four steel balls (4B) for 15 min during which there is no H_2 release (Fig. 13.8(a)). Dehydrogenation occurs in two stages of I and II as designated in Fig. 13.11(a), which correspond to Reactions (13.5″b) and (13.5c), respectively, as also confirmed by X-ray diffraction after completion of desorption at each temperature. Figure 13.11(b) shows a comparison of the effect of 5 wt% of n-Fe and milling mode obtained in this work and the n-Ni reported in[74] on the dehydrogenation behavior at 100 °C, which is a maximum temperature limit for a PEMFC stack. The dehydrogenation curves (two results) for the composite, containing n-Fe milled under the low-energy mode (LES6-4B) milling, exhibit slightly lower rate of H_2 dehydrogenation in both Stages I and II than their counterpart milled under the higher (IMP68-2B) energy mode. This difference could be related to a better structural refinement obtained under higher milling energy. It must be pointed out that under both modes, there was no desorption of H_2 during milling, and the volumetric lattice expansion is much less than 1% (Fig. 13.10). Also, it is observed in Fig. 13.11(b) that the dehydrogenation curves after milling under higher energy mode IMP68 for both additives n-Fe and n-Ni are close to one another, which indicates that at 100 °C, both nanometric metal additives provide nearly identical enhancement of dehydrogenation rate. Figure 13.11(c) and (b) shows a bar graph comparison of the apparent activation energies for ($LiAlH_4$ + 5 wt% μ-Fe/n-Fe) (μ-micrometric and

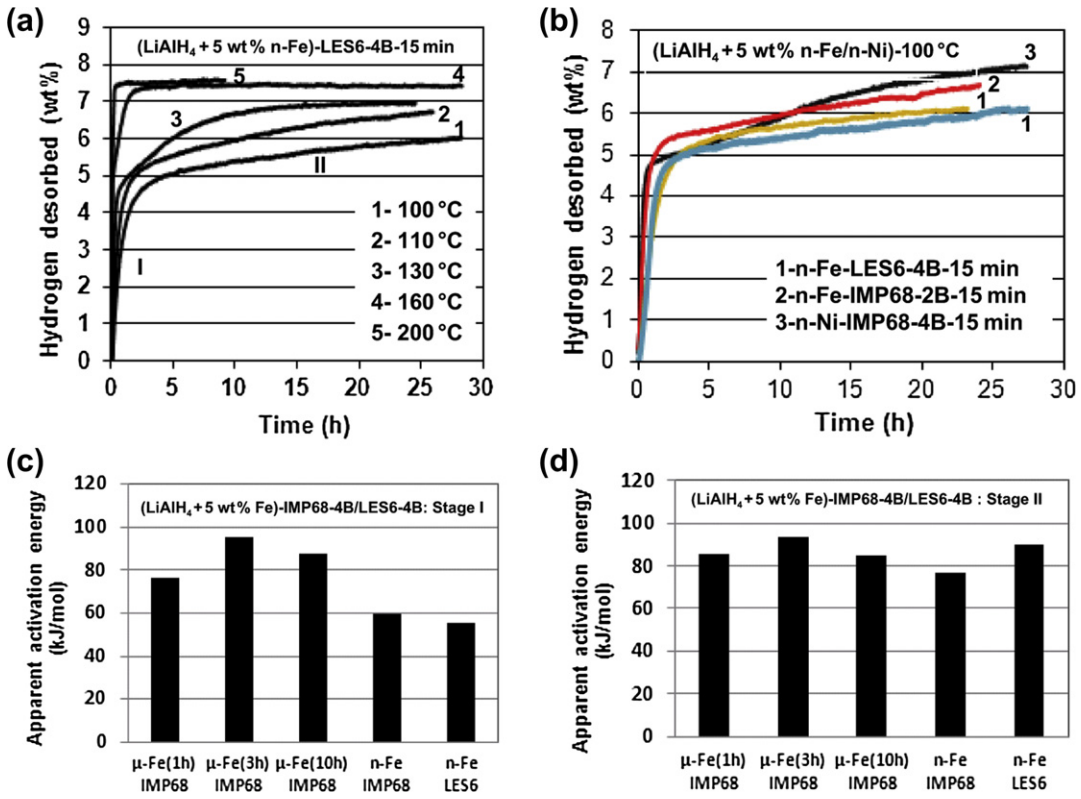

FIGURE 13.11 (a) Volumetric dehydrogenation curves at varying temperatures for ($LiAlH_4 + 5$ wt% n-Fe) ball milled under a low energy LES6 mode with four steel balls (4B) for 15 min, (b) a comparison of volumetric dehydrogenation curves at 100 °C for $LiAlH_4$ containing 5 wt% n-Fe ball milled for 15 min under a low (LES6-4B) and comparatively higher energy (IMP68-2B) mode as compared to the dehydrogenation curve for the 5 wt% n-Ni additive reported in Ref. 72. (c, d) bar graph comparison of the apparent activation energies for ($LiAlH_4 + 5$ wt% μ-Fe/n-Fe) ball milled for 15 min under (IMP68-4B) and (LES6-4B) milling modes for Stage I and Stage II (as designated in Figure 13.11(a)). Ball-to-powder weight ratio R = 132. IMP68-impact mode with two magnets, LES6-low energy shearing mode with one magnet, 2B-two balls and 4B-four balls in the milling vial (for more details on ball milling in a magneto-mill reader is referred to [15]). μ-Fe-micrometric Fe additive: 1, 3 and 10 h—indicate the length of premilling time for the μ-Fe-additive. (For color version of this figure, the reader is referred to the online version of this book.) *Source: Adapted from Ref. 74.*

n-nanometric Fe) ball milled for 15 min under (IMP68-4B) and (LES6-4B) milling modes, for Stage I and Stage II (as designated in Figure 13.11(a)). For Stage I (Reaction (13.5″b)), the n-Fe additive results in low activation energy of the order of 60 kJ/mol. For Stage II (Reaction (13.5c)), within the experimental error, the average apparent activation energy seems to fall within the range 77—93 kJ/mol, regardless of the Fe particle size (μ-Fe or n-Fe) and milling energy (an IMP68 or LES6 mode[74]). This clearly shows for the first time that for $LiAlH_4$ the catalytic additive is able to strongly reduce the apparent activation energy of Stage I dehydrogenation (but does not affect substantially the Stage II dehydrogenation). For comparison, for the ball-milled ($LiAlH_4 + 5$ wt% n-Ni) mixture, the apparent activation energies of Stages I and II equal ~70 and ~100 kJ/mol, respectively.[72] This can be compared with the apparent activation energy of the ball-milled undoped $LiAlH_4$ equaling about 90 kJ/mol for both Stages I and II, as reported in.[71]

Figure 13.12(a) shows that the ball-milled $LiAlH_4$ without additives is quite stable during storage up to 50 days at RT. In contrast, the ball-milled $LiAlH_4$ with 5 wt% n-Ni and n-Fe additives is able to self-discharge slowly large quantities of H_2 during storage at RTs, 40 and 80 °C (Fig. 13.12(b), (c) and (d)). The X-ray diffraction studies showed very clearly that a slow H_2 discharge during a long-term storage at RT and 40 °C proceeds through a solid-state decomposition of $LiAlH_4$ through Reaction (13.5″b).[72,74] When the storage temperature increases to 80 °C (Fig. 13.12(d)), the H_2 quantity discharged from the ball-milled ($LiAlH_4 + 5$ wt% n-Fe/n-Ni) reaches about 6 wt% after 15 days, which must have involved Reaction (13.5c). It is interesting that both nanometric catalysts n-Fe and n-Ni give nearly identical quantities of slowly discharged H_2.

Also recently, we have investigated the effect of a manganese chloride ($MnCl_2$) catalytic precursor on the hydrogen storage properties of $LiAlH_4$ for a wide range of molar ratios n in the ($nLiAlH_4 + MnCl_2$) system

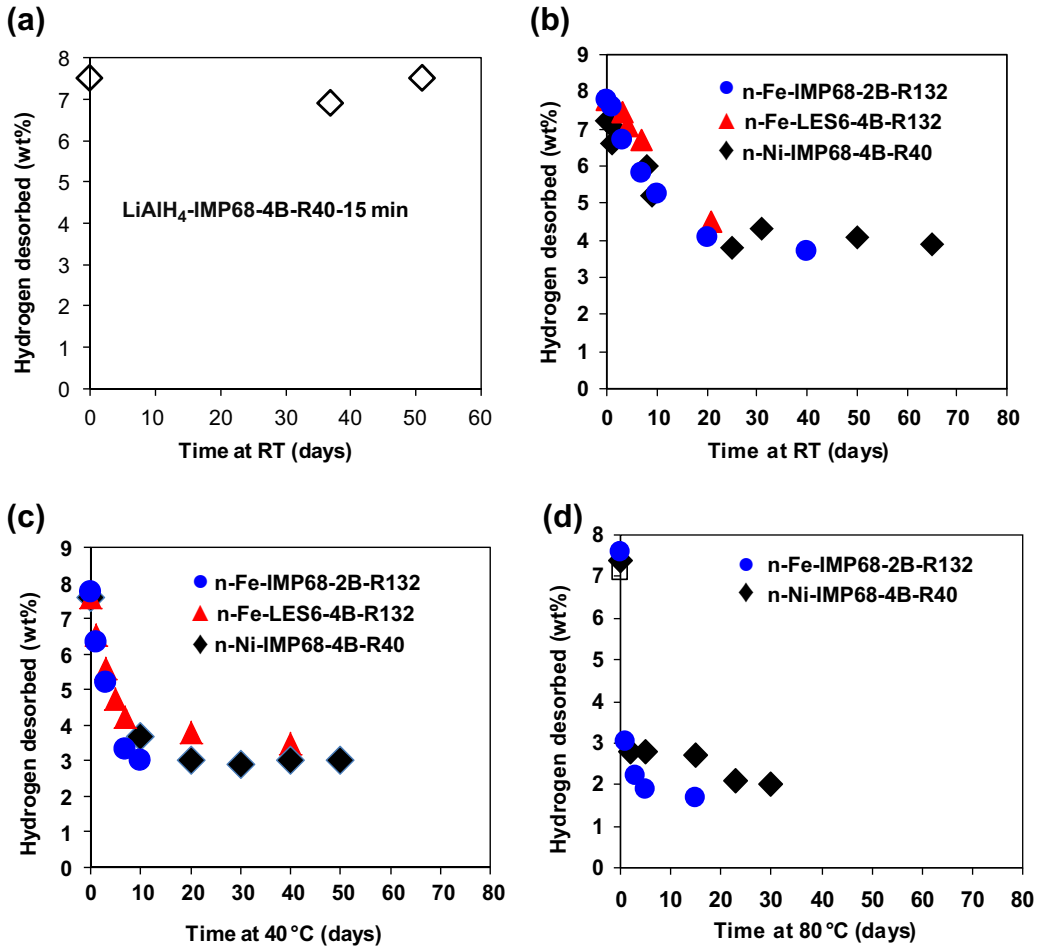

FIGURE 13.12 Plots of hydrogen desorbed vs. storage time in days (1 day = 24 h) for (a) ball-milled $LiAlH_4$; stored at room temperature (RT) under Ar; subsequently desorbed at 140 °C and ($LiAlH_4$ + 5 wt% n-Fe) compared with the data for the 5 wt% n-Ni additive extracted from Ref. 72, (b) stored at RT under Ar; subsequently desorbed at 250 °C for n-Fe and 140 °C for n-Ni, (c) stored at 40 °C under Ar; subsequently desorbed at 250 °C for n-Fe and 170 °C for n-Ni, (d) stored at 80 °C under Ar; subsequently desorbed at 250 °C for n-Fe and 170 °C for n-Ni. All desorptions carried out in 1 bar H_2 pressure. IMP68-impact mode with two magnets, LES6-low energy shearing mode with one magnet, 2B-two balls and 4B-four balls in the milling vial, R-ball-to-powder weight ratio (for more details on ball milling in a magneto-mill, reader is referred to Ref. 15). (For color version of this figure, the reader is referred to the online version of this book.) *Source: Adapted from Ref. 74.*

where $n = 1$, 3, 6, 8, 13, 30, and 63 (5 wt% $MnCl_2$).[78–80] This chloride is less volatile than those of Ti, V, and Zr metals. Figure 13.13(a) shows that for low molar ratios $n = 1$–13, the system releases substantial quantities of H_2 during ball milling with the maximum for $n = 3$. When the molar ratio n increases to 30 and 63, the quantity of released H_2 dramatically decreases. Figure 13.13(b) shows that for $n = 3$ ball milling up to barely 30 min results in nearly 4 wt% H_2 desorbed (remember that the H_2 released is referred to the whole mass of the solid). At the first look, this behavior is similar to that for ($LiAlH_4$ + 5 wt% n-Fe) shown in Fig. 13.9(a).

Figure 13.14 shows the XRD patterns of the mixtures with the molar ratio $n = 1$ and 3 after ball milling for 30 min. The peak of copper (Cu) in both patterns arises from a support plate of the XRD sample holder used.[71–74,78] In the $n = 1$ mixture, the principal diffraction peaks of the Li_2MnCl_4 compound are accompanied by minor peaks of LiCl, Al, and a very broadened Mn peak, which suggests that the Mn metal is heavily nanostructured. Li_2MnCl_4 is an inverse cubic spinel that has been extensively studied for its ionic conductivity as a potential solid electrolyte for lithium-ion batteries.[81–83] Its formation during ball milling in the ($nLiAlH_4 + MnCl_2$) system has never been reported in the literature. The presence of Li_2MnCl_4, Al, and Mn combined with the fact that about 2 wt%H_2 was desorbed within 30 min of ball milling (Fig. 13.13(a)) strongly suggests the following reaction that occurred during milling for the molar ratio $n = 1$:

$$LiAlH_4 + MnCl_2 \rightarrow 0.5Li_2MnCl_4 + 0.5Mn + Al + 2H_2 \quad (13.7)$$

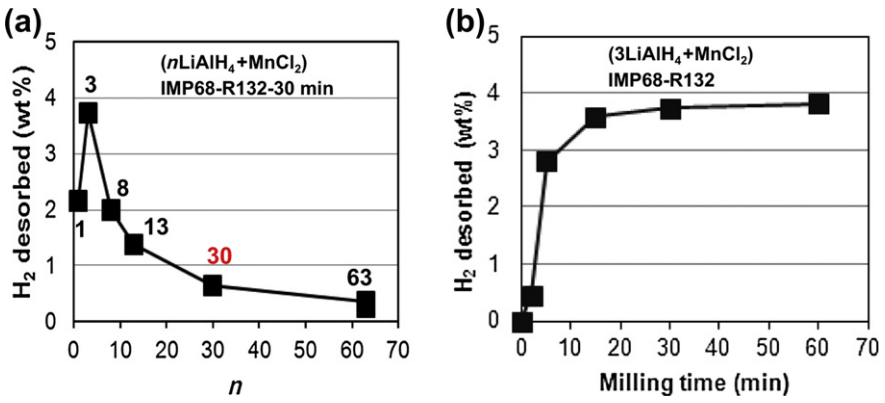

FIGURE 13.13 (a) The quantity of H_2 desorbed during ball milling of the (nLiAlH$_4$ + $MnCl_2$) mixture as a function of molar ratio n (shown by numbers) and (b) H_2 desorbed for $n = 3$ as a function of milling time. *Source: Adapted from Ref. 80.*

The total theoretical hydrogen capacity of Reaction (13.7) is 2.46 wt%. However, the presence of the LiCl peaks, which form doublets with the Li_2MnCl_4 peaks in Figure 13.14, also suggests that another reaction was taking place during ball milling:

$$2LiAlH_4 + MnCl_2 \rightarrow 2LiCl + 2Al + Mn + 4H_2 \quad (13.8)$$

Reaction (13.8) has a theoretical H_2 capacity of 4 wt%. It is not clear why this reaction occurred for the molar ratio $n = 1$. Normally, it should have occurred for the molar ratio $n = 2$. Perhaps, small-powder volumes during milling were locally enriched to the $n = 2$ ratio. Figure 13.13(a) shows that about 2 wt% H_2 was desorbed during milling for $n = 1$. That means that the principal reaction releasing H_2 was likely Reaction (13.7) with only a small fraction of H_2 released from Reaction (13.8).

As shown in Figure 13.14, ball milling of the $n = 3$ system for 30 min produced principal phases LiCl, Mn, Al, and a minority phase $LiAlH_4$. The observed weak peak of minor phase LiOH for $n = 3$ is an impurity commonly found in commercial $LiAlH_4$.[71–74] Apparently, the presence of these phases suggests the following reaction:

$$3LiAlH_4 + MnCl_2 \rightarrow LiAlH_4 + 2LiCl + 2Al + Mn + 4H_2 \quad (13.9)$$

The accessible theoretical capacity of this reaction is 3.4 wt% H_2. The quantity of H_2 desorbed within 30 min of milling for $n = 3$ in Fig. 13.13(b) is 3.7 wt%, which means that all H_2 from Reaction (13.9) was already desorbed during milling. The XRD patterns for the $n = 6$, 8, 13, 30, and 63 (5 wt% $MnCl_2$) molar ratios always show the same phases LiCl, Mn, Al, and $LiAlH_4$ after ball milling for 30 min (XRD patterns not shown here), associated with H_2 release (Fig. 13.13(a)).

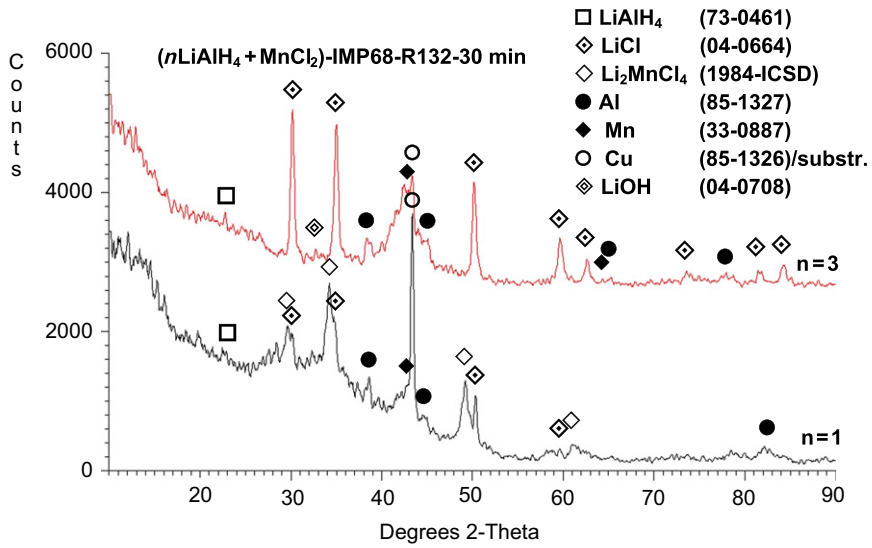

FIGURE 13.14 XRD patterns for the (nLiAlH$_4$ + $MnCl_2$) mixture where $n = 1$ and 3 ball milled for 30 min. ICDD file numbers are shown for peak identification. IMP68-high-energy impact mode, R132-ball-to-powder weight ratio = 132. (For color version of this figure, the reader is referred to the online version of this book.) *Source: Adapted from Ref. 80.*

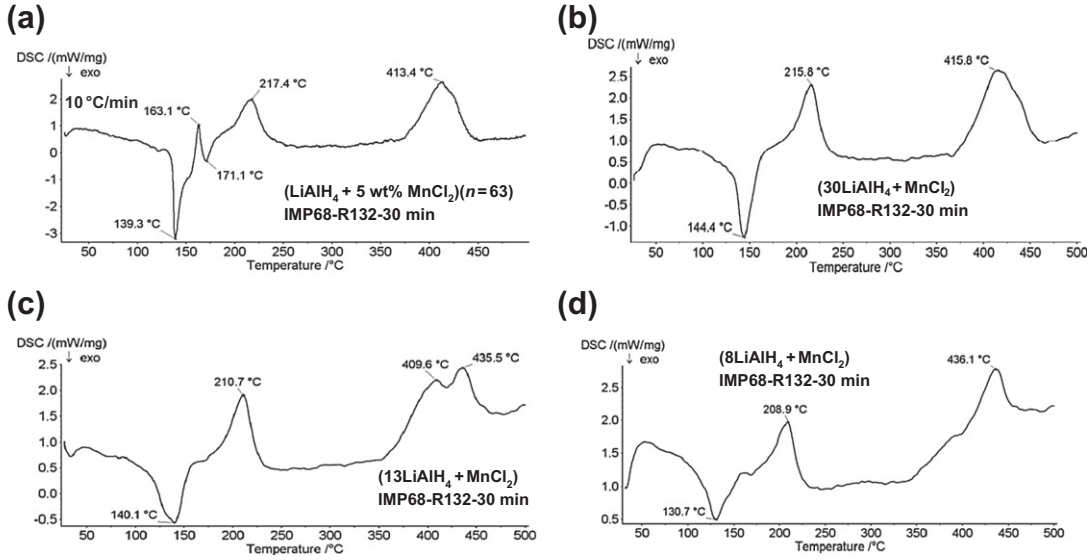

FIGURE 13.15 DSC curves for ball-milled (nLiAlH$_4$ + MnCl$_2$) mixtures with varying molar ratio n. (a) $n = 63$ (5 wt% MnCl$_2$),[72,73] (b) $n = 30$, (c) $n = 13$ and (d) $n = 8$. *Source: Adapted from Ref. 80.*

That means that Reaction (13.9) can be written in the following general form for $n \geq 2$:

$$n\text{LiAlH}_4 + \text{MnCl}_2 \rightarrow (n-2)\text{LiAlH}_4 + 2\text{LiCl} + 2\text{Al} + \text{Mn} + 4\text{H}_2 \quad (13.10)$$

Apparently, in this case, the H_2 desorption during ball milling occurs owing to simple chemical reaction in which LiAlH$_4$ is gradually consumed by reacting with MnCl$_2$ to produce LiCl, Al, possibly Mn in a nanostructured form and H_2.

Figure 13.15 shows DSC curves for the ball-milled (nLiAlH$_4$ + MnCl$_2$) mixtures with varying molar ratio n. All mixtures with the molar ratio $n = 8$, 13, 30, and 63 were ball milled for 30 min. For $n = 8$, 13 and 30, this milling duration led to the release of 2, 1.4, and 0.6 wt% H_2, respectively (Fig. 13.13(a)). The samples ball milled for 30 min with $n = 8$, 13, and 30 were still able to desorb at 250 °C, 3.6, 5.0, and 6.4 wt% H_2, respectively. It means that despite some H_2 desorption during milling for 30 min, these samples had still a large quantity of retained H_2 that resulted in very strong thermal peaks in Fig. 13.15. The first exothermic peak in Fig. 13.15(a) for the molar ratio $n = 63$ (5 wt% MnCl$_2$) is attributed to the partial decomposition of LiAlH$_4$ to Li$_3$AlH$_6$, Al, and H_2 in *solid state* according to Reaction (13.5″b), as discussed earlier for the (LiAlH$_4$ + 5 wt% n-Fe/n-Ni) system. However, in contrast to the LiAH$_4$/n-Fe/n-Ni system, the melting of LiAlH$_4$ is not completely eliminated since Reaction (13.5a) is incomplete and a small amount of retained LiAlH$_4$ was melting as evidenced by a weak endothermic peak at 163.1 °C and was decomposing to Li$_3$AlH$_6$, Al, and H_2 at exothermic peak at 171.1 °C. However, with decreasing molar ratios to $n = 30$, 13, and 8, the melting event disappears and LiAlH$_4$ decomposes to Li$_3$AlH$_6$ at the first exothermic peak around 130−140 °C in Fig. 13.15(b), (c), (d). The other peaks in Fig. 13.15 at the 200 and 400 °C range (Reactions (13.5c) and (13.5d)) are nearly identical to those in Fig. 13.7.

Figure 13.16 shows that a small quantity of the MnCl$_2$ catalytic precursor is not as effective in enhancing the rate of dehydrogenation at 100 °C as n-Ni. For LiAH$_4$ containing 5 wt% MnCl$_2$ dehydrogenation occurs in solid state but only through Stage I (Reaction (13.5″b)),

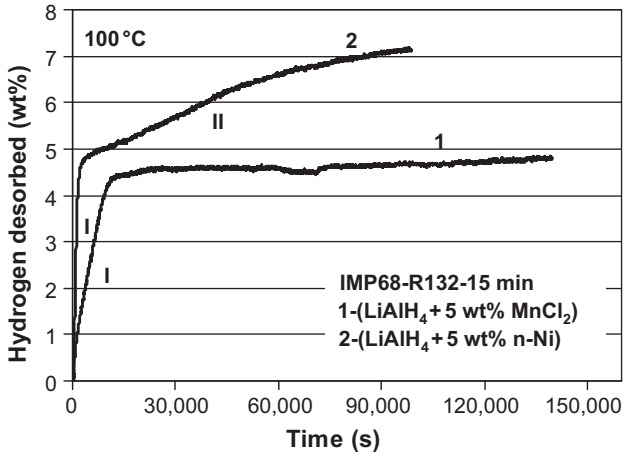

FIGURE 13.16 Comparison of volumetric desorption curves at 100 °C under 1 bar H_2 pressure for ball-milled 1-(LiAlH$_4$ + 5 wt% MnCl$_2$) (desorbed up to 140 ks). Adapted from Ref. 78. 2-(LiAlH$_4$ + 5wt% n-Ni) (desorbed up to 98 ks). Adapted from Ref. 72. IMP68-high-impact mode, R132-ball-to-powder weight ratio = 132.

whereas for the $LiAH_4$/n-Ni system within a similar time span, dehydrogenation occurs in solid state through both Stages I and II, Reactions (13.5″b) and (13.5c), respectively. After desorption of the ball-milled ($LiAlH_4 + 5$ wt% $MnCl_2$) at 100 °C for 140 ks, its XRD pattern (not shown here) exhibited the diffraction peaks of LiCl, Al, and Li_3AlH_6.[80] Apparently, during the $LiAlH_4$ decomposition besides Reaction (13.5″b) in Stage I producing Li_3AlH_6 and Al, second Reaction (13.10) producing LiCl (and again Al) must have occurred as discussed above. For 5 wt% $MnCl_2$, $n = 63$ so the exact reaction is as follows[78]:

$$63LiAlH_4 + MnCl_2 \rightarrow 61LiAlH_4 + 2LiCl + 2Al + Mn + 4H_2 \quad (13.11)$$

It should be pointed out that since no diffraction peaks of Mn were observed after desorption at 100 °C for 140 ks (39 h), most likely, elemental Mn, which to the extent could have catalyzed $LiAlH_4$ decomposition Reaction (13.5″b), is in an amorphous state.[78] The apparent activation energy of dehydrogenation of the ball-milled $LiAlH_4/MnCl_2$ system for Stage I is equal to ~80 kJ/mol ($R^2 = 1.0$)[78,79] as compared to ~70 kJ/mol for the $LiAlH_4$/n-Ni system.[72]

Very similar to the ($LiAlH_4 + 5$ wt% n-Ni/n-Fe) systems discussed earlier, the ball-milled system with 5 wt% $MnCl_2$ slowly self-discharges H_2 during a long-term storage at RT, 40, and 80 °C, as shown in Fig. 13.17. It can be seen that the ball-milled ($LiAlH_4 + 5$ wt% $MnCl_2$) system is able to desorb substantial quantities of H_2 at these low temperatures. At RT and 80 °C, the ball-milled ($LiAlH_4 + 5$ wt% $MnCl_2$) mixture slowly desorbs even slightly greater amount of H_2 than its ($LiAlH_4 + 5$ wt% n-Ni/n-Fe) counterparts within a comparable time span (Fig. 13.12(b), (d)), despite that at elevated temperatures, the apparent activation energy of the ($LiAlH_4 + 5$ wt% $MnCl_2$) decomposition in Stage I is slightly greater than the one for the n-Ni additive (~80 vs ~70 kJ/mol, respectively[71]). The XRD patterns after storage for 70 and 88 days at RT (the data point for 88 days is not shown in Fig. 13.17(a)) have shown principal peaks of Al, minor peaks of LiOH, and extremely weak 100% intensity peaks of $LiAlH_4$ and Li_3AlH_6 (XRD patterns not included here). The peaks of LiOH could be partially belonging to a typical impurity and/or arising from a partial hydrolysis/oxidation of LiH formed in Reaction (13.5c) discussed earlier. These XRD patterns suggest that a slow self-discharge occurred through Reactions (13.5″b) and (13.5c) However, since the quantity

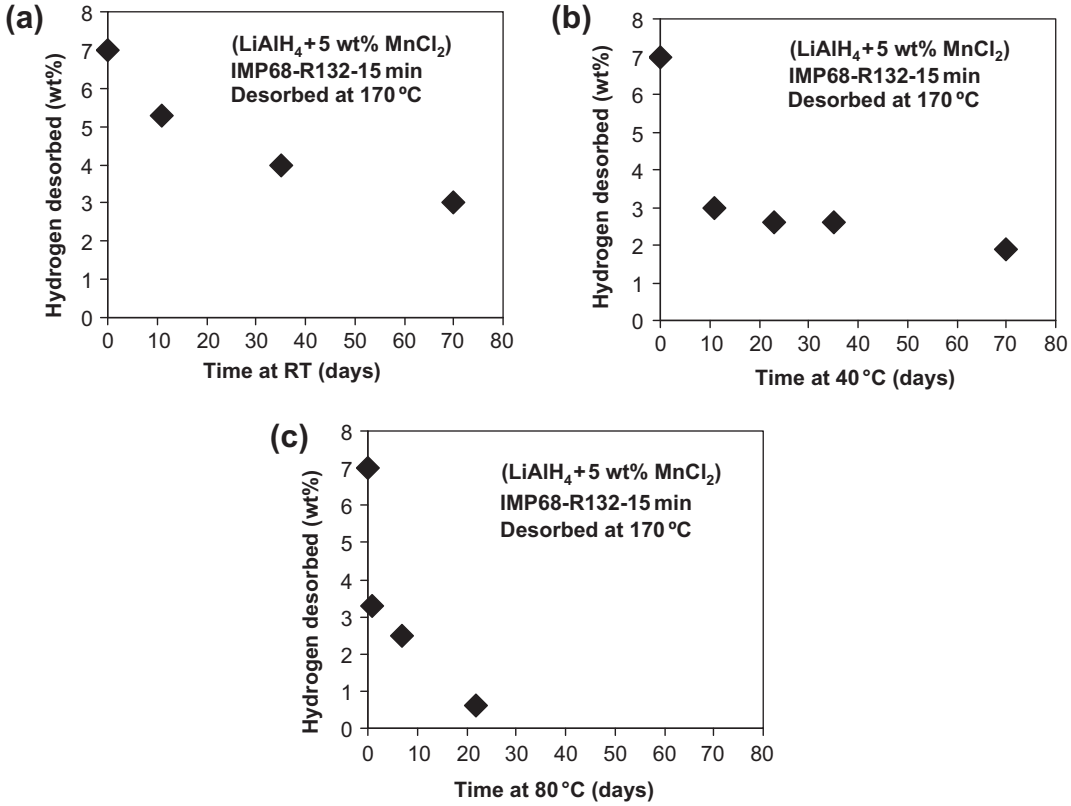

FIGURE 13.17 The quantities of hydrogen desorbed during the long-term storage of ball-milled ($LiAlH_4 + 5$ wt% $MnCl_2$)($n = 63$) at (a) room temperature (RT), (b) 40 °C, and (c) at 80 °C. *Source: Adapted from Ref. 79.*

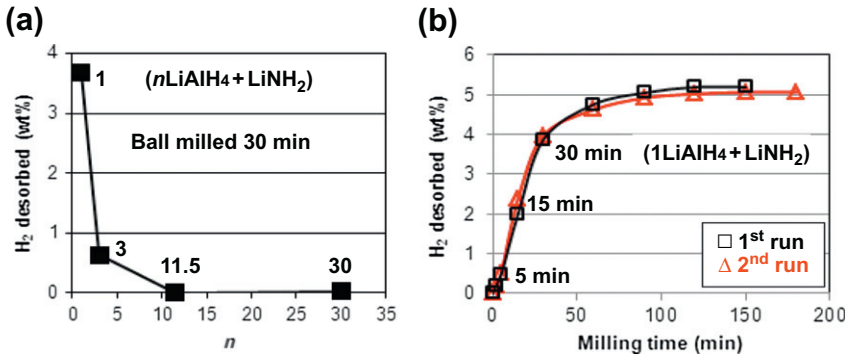

FIGURE 13.18 The quantity of H_2 desorbed during ball milling for the (nLiAlH$_4$ + LiNH$_2$) system as a function of (a) the molar ratio n (the numbers show the corresponding values of n) and (b) milling time for the composite with $n = 1$. IMP68 milling mode and an R132-ball-to-powder weight ratio. (For color version of this figure, the reader is referred to the online version of this book.) *Source: Adapted from Ref. 84.*

of self-discharged H_2 after 70 days in Fig. 13.17(a) is about 4 wt% then Reaction (13.5c) would not have to be involved because Reaction (13.5″b) could provide the amount of H_2 desorbed after 70 days. The XRD pattern (not shown here) after self-discharge at 80 °C for 22 days, corresponding to Fig. 13.17(c), shows principal peaks of Al, minor peaks of LiOH, weak 100% intensity peaks of Li_3AlH_6, and very weak 100% intensity peaks of LiCl and Mn. This pattern suggests that the nearly 7 wt% H_2 self-discharged at 80 °C after 22 days (Fig. 13.17(c)) was provided through Reactions (13.5″b) and (13.10). The XRD patterns after self-discharge at RT and 80 °C suggest slightly different paths of H_2 desorption.

The last hydride system we investigated containing $LiAlH_4$ is its combination with lithium amide ($nLiAlH_4 + LiNH_2$) where $n = 1$, 3, 11.5, and 30.[84] This system at the molar ratio $n = 1$ heavily decomposes during ball milling. Figure 13.18(a) shows the quantity of H_2 desorbed during ball milling, plotted as a function of the molar ratio n in (nLiAlH$_4$ + LiNH$_2$). It is observed that during ball milling up to 30 min, the composites with molar ratios $n = 1$ and 3 gradually release H_2. Figure 13.18(b) shows that for $n = 1$ further ball milling up to 100 min releases as much as 5 wt% H_2. We repeated the milling test in Fig. 13.18(b) twice (1st and 2nd run) to confirm that the results are reproducible. As can be seen, the hydrogen desorption during ball milling for the composite with $n = 1$ is perfectly reproducible and the quantity of desorbed H_2 is nearly almost the same for the 1st and 2nd runs. Also, Fig. 13.18(a) shows that the composites with $n = 11.5$ and greater do not release hydrogen during milling up to 30 min.

We carried out XRD tests to get more insight into the phase changes occurring during ball milling as a function of milling time and molar ratio. The samples were extracted after predetermined milling durations. For the $n = 1$ mixture after 15 min of milling, we observed the peaks of Li_3AlH_6 and the Al peak to become stronger, indicating that more Al was formed during milling.[84] The XRD patterns after 30 min, 1 h, and 3 h of milling for the molar ratio $n = 1$ are shown in Fig. 13.19. With increasing ball-milling time, the

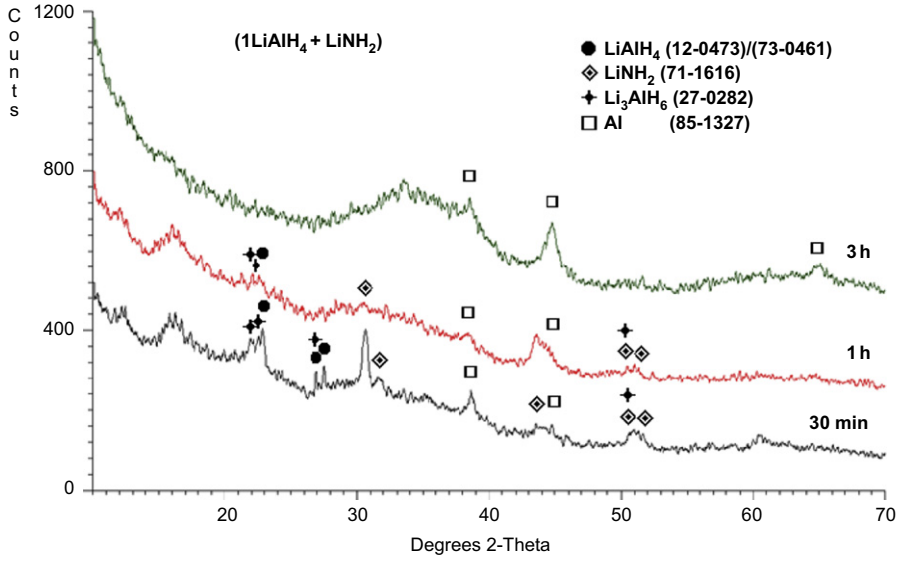

FIGURE 13.19 XRD patterns for ($1LiAlH_4 + LiNH_2$) after milling for 30 min, 1 h, and 3 h. IMP68 milling mode and an R132 ball-to-powder weight ratio. The ICDD file numbers for phase identification are shown. (For color version of this figure, the reader is referred to the online version of this book.) *Source: Adapted from Ref. 84.*

diffraction peaks become broadened and diffused as well as a pronounced rise in the baselines and the formation of a broad "hump" in the range of $2\theta = 30-40^\circ$ are observed, which can be attributed to heavy nanostructuring or even the existence of increasing quantities of amorphous structure(s).[84] The 100% intensity peaks of $LiAlH_4$, $LiNH_2$, and Li_3AlH_6 are still visible after 30 min and even after 1 h of milling although they become weaker. Also, there are clear peaks that can be assigned to Al. After 3 h of milling, the mixture with the molar ratio $n = 1$ released nearly 5 wt% H_2 (Fig. 13.18(b)). Theoretical H_2 capacities of Reactions (13.5″b) and (13.5c) are 5.3 and 2.6 wt%, respectively, which, for 97% pure $LiAlH_4$ used in this work, reduce to 5.14 and 2.52 wt%, respectively. The composite with the molar ratio of $n = 1$ ($1LiAlH_4 + LiNH_2$) corresponds to a weight ratio of 62.3 wt% $LiAlH_4$ and 37.7 wt% $LiNH_2$. Therefore, at this molar/weight ratio, fully completed Reactions (13.5″b) and (13.5c) should provide approximately purity-corrected 3.2 and 1.6 wt% H_2, respectively. Since ~5 wt% H_2 is released after 3 h of ball milling, both reactions must have occurred during ball milling. This observation is quite unexpected because in a thermal DSC test, Reaction (13.5″b) is exothermic and (13.5c) is endothermic (Fig. 13.7(c), (d)). That suggests that both types of reactions, thermodynamically opposite, have been realized during high-energy ball milling of hydride composites in the present work. However, since during ball milling the overall temperature increase in the milling vial is very small, then the question arises whether the thermodynamic character of both reactions, which are now induced by mechanical energy, remains the same as that at elevated temperatures in a DSC test.

Furthermore, it seems that the entire quantity of H_2 desorbed during ball milling for the molar ratio $n = 1$ can be easily provided by Reactions (13.5″b) and (13.5c) without invoking other reactions.[84] The fact that the diffraction peaks of $LiNH_2$ in Figure 13.19 persist throughout a long period of milling up to 3 h indicates that $LiNH_2$ does not react/decompose but most likely becomes heavily nanostructured or even partially amorphized, and in this capacity enhances the decomposition of $LiAlH_4$ during ball milling according to Reactions (13.5″b) and (13.5c). Interestingly, with decreasing molar content of $LiNH_2$ ($n = 3$ and larger), $LiNH_2$ gradually ceases to enhance the decomposition of $LiAlH_4$ during ball milling. At the molar ratio of $n = 11.5$ (5 wt% $LiNH_2$), no release of H_2 was observed.[84] However, at the moment, it is difficult to propose any detailed molecular mechanism by means of which $LiNH_2$ enhances decomposition of $LiAlH_4$ and H_2 release during ball milling and, furthermore, the dependence of that mechanism on the molar ratio of the composite. The changes in the lattice parameters of the unit cell of $LiAlH_4$ were not investigated.

Table 13.2 is a summary of the behavior of $LiAlH_4$ with various additives during ball milling. For the n-Fe additive, the mechanism of decomposition is, most likely, related to an excessive expansion of the $LiAlH_4$ unit cell, which is caused by the dissolved Fe^{2+} (or Fe^{3+}) ions, which are larger than Al^{3+} ions, and form a $LiAl_{1-x}Fe_xH_4$-type substitutional solid solution. In the case of $MnCl_2$, a simple chemical reaction between $LiAlH_4$ and $MnCl_2$ occurs during ball milling in which $LiAlH_4$ is gradually consumed producing LiCl, Al, most likely nanostructured Mn and H_2 (Reaction (13.10)). The most puzzling case is for the $LiNH_2$ in the exact molar ratio $n = 1$. In this case, there is no reaction during ball milling. Substitution of the Al ions in the $LiAlH_4$ lattice by the nonmetallic nitrogen ions seems to be rather unlikely. However, the $LiAlH_4$ lattice parameters were not investigated, so it is hard to draw a final conclusion.

We have already discussed that with use of n-Ni and n-Fe catalysts, the melting can be eliminated during discharge of hydrogen from $LiAlH_4$. Now, for the sake of completion, we must refer to our recent studies, which point to the role of thermal management and the critical role brought by achieving thermal equilibrium in dehydrogenation of $LiAlH_4$. We demonstrated that depending on the temperature history, the reaction-takes place either in the solid or in liquid phase after or during melting of the sample. And the reactions conducted in both cases can follow different reaction pathways. Namely, the DSC melting peak and the ubiquitous exothermic peak for Reactions (13.5a) and (13.5′b) can be completely eliminated. From several reports[85–86] and our own[87–88] solid-state 27 Al NMR

TABLE 13.2 Summary of the High-Energy Ball-Milling Behavior of Various $LiAlH_4$ Systems

$LiAlH_4$ system	$LiAlH_4$ lattice parameter change	Reaction between additive and the $LiAlH_4$ matrix and formation of metal/intermetallic product	H_2 desorption during ball milling
($LiAlH_4$ + 5 wt% n-Ni)	Moderate	No	No
($LiAlH_4$ + 5 wt% n-Fe)	Excessive	No	Yes
($n LiAlH_4 + MnCl_2$)	N/A	Yes	Yes
($LiAlH_4 + LiNH_2$)	Unknown	No	Yes

investigation of thermal decomposition of $LiAlH_4$, it has been clearly demonstrated that melting is not a prerequisite for the decomposition of $LiAlH_4$. However, in order to observe the solid-phase reaction, it is not enough to conduct experiments with low heating rates, but it is necessary to provide for a near-thermal equilibrium in the heated sample. In heating experiments, this means use of very low sample mass, as the thermal conductivities k of Li alanate powder samples are very low, and temperature gradients created are sufficient to start melting the powder, which otherwise can discharge H_2 from the solid. Since the deleterious, exothermic heat flow has been the common feature of H_2 release from this alanate, the new results showing that the $LiAlH_4$ solid can deliver almost 5 wt% H_2 in single endothermic reaction ca.150 °C, and another 2.5 wt% when heated below 250 °C (Fig. 13.20(a,b)) would be of interest.[88] The thermal decomposition of the catalyzed $LiAlH_4$ powder conducted in the near-perfect thermal equilibrium conditions gives evidence to a well-controlled endothermic heat flow that takes place in the narrow temperature range centered ca. 150 °C and is associated with a flow of 3 g H_2 per 4 min, at almost constant rate 0.75 g H_2/min (0.0125 g H_2/s) (Fig. 13.20(b)). In our power-compensating scanning calorimeter (Perkin–Elmer), the amplitude of H_2 release peak is directly measured in miliwatts per gram of powder and gives us the estimate of about 100 W/kg of alanate as being needed to produce the peak flow of 0.0125 g H_2/s/kg (obviously in absence of parasitic heat losses).

Comparing the drastically different reaction heat flows obtained from the power-compensating calorimeter (Figure 13.20) and the heat-flux calorimeter (all other DSC patterns in this chapter), one must conclude that the main driver toward good kinetics in $LiAlH_4$ (with or without catalyst) is good heat transfer to the active mass. This driver has been greatly overlooked.

Notwithstanding the poor understanding of this storage system, these authors are of the opinion that $LiAlH_4$ could be a near-commercial solid-state H_2 storage material in a number of applications other than automotive. With the additives such as n-Ni and n-Fe, it releases about 5 wt% H_2 at 100 °C with very reasonable flow rates, and up to 7.5 wt% at slow flow rates. With both metallic n-Ni and n-Fe additives, it can slowly self-discharge large quantities of H_2 during a long-term

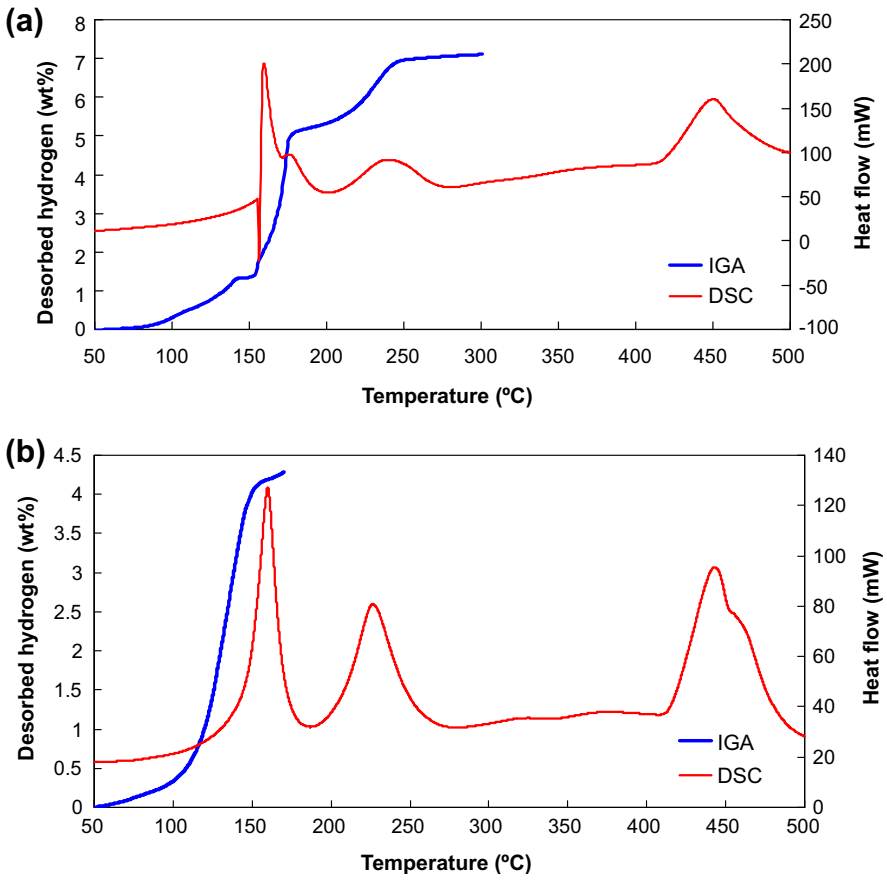

FIGURE 13.20 Heat flow (red) and hydrogen flow (blue) from non-catalyzed and catalyzed $LiAlH_4$ obtained under near-equilibrium conditions obtained the PE Model DSC7 power compensation scanning calorimeter and reproduced in the Hiden Model IGA001 hydrogen gravimetric analyzer; small samples mass few milligrams; heating rate 5° per min, and flow at 1 bar pressure. The lithium alanate is reagent grade (Alfa Aesar, Stock A1816), 99.7% purity mixed with 5 wt% n-Ni (Inco Special Products, now Vale Ltd.), SSA = 30.3 m^2/g; (a) mixed only and (b) high-energy ball-milled for 60 min. (For interpretation of the references to color in this figure legend, the reader is referred to the online version of this book.) *Source: Adapted from Ref. 88.*

storage under argon. This phenomenon has two aspects. One is purely scientific and clearly requires that the properties of $LiAlH_4$ with these additives must be investigated immediately after completion of ball milling because a longer storage may lead to erroneous results as the compound would be partially desorbed. The other is practical. Sandrock et al.[41,42] pointed out the practical significance of such a behavior for long-duration, low-demand devices that use H_2 such as low-power remote fuel cells or portable gas analyzers. These materials can also be used in a number of chemical processes where a continuously reducing atmosphere is needed for a completion of the process. They can also have an application in a military sector for long-term cartridges supplying hydrogen to portable devices for soldiers on a mission.[74]

13.3 METAL BOROHYDRIDES

13.3.1 The $LiBH_4$–$MnCl_2$ and $NaBH_4$–$MnCl_2$ Systems

Metal borohydrides are very interesting potential solid-state hydrogen storage materials due to their very high theoretical capacities of hydrogen.[15,19,89–93] Most of borohydrides crystallize in complex lattices that can be found in.[93] Two notable borohydrides, sodium borohydride ($NaBH_4$) and lithium borohydride ($LiBH_4$), are easily commercially available with theoretical gravimetric hydrogen capacities of 10.6 and 18.4 wt%, respectively. They also have quite high volumetric densities of hydrogen.[91] Unfortunately, their relatively high enthalpy change for dehydrogenation results in the dehydrogenation temperatures in excess of 400 °C.[91–93] Metal catalysts, for example, Ni[94] and nonmetal catalysts (e.g. fullerenes[95]) and metal chloride catalytic precursors ($FeCl_2$, $CoCl_2$ and $NiCl_2$[96]) accelerate the dehydrogenation rate of $LiBH_4$ but do not change its unfavorable thermodynamics. Also, it was reported in[96] that $CoCl_2$ led to the formation of diborane gas (B_2H_6) in contrast to both $NiCl_2$ and $FeCl_2$, which enabled complete hydrogen desorption without diborane. The authors suggested that the stronger the binding between the metal and boron, the less possible diborane is produced.[96]

The unfavorable thermodynamics of $LiBH_4$ can be overcome by converting it to another borohydride with better thermodynamics. Nakamori et al.[97,98] used the MCAS by ball milling of complex hydrides mixed with appropriate metal di- or trichlorides, MCl_n for synthesizing a large spectrum of new metal borohydrides. The reaction which occurs during the MCAS is a "metathesis reaction" that occurs in solid state similar to reaction that uses diethyl ether as a solvent.[15] Using metal chloride MCl_n and both $LiBH_4$ and $NaBH_4$, respectively, the proposed reaction would be as follows:

$$MCl_n + nLiBH_4 \rightarrow M(BH_4)_n + nLiCl \quad (13.12)$$

$$MCl_n + nNaBH_4 \rightarrow M(BH_4)_n + nNaCl \quad (13.13)$$

Nakamori et al.[97,98] reported that regardless of whether either $LiBH_4$ or $NaBH_4$ was used, the post-MCAS XRD patterns always showed the absence of the diffraction peaks of crystalline $M(BH_4)_n$, which could be taken as evidence of the "disordering" of the crystal structure of $M(BH_4)_n$. On the other hand, Raman spectra confirmed the presence of $M(BH_4)_n$ after MCAS. Furthermore, they reported that only the peaks of LiCl were observed when $LiBH_4$ was used as a reactant while when $NaBH_4$ was used with MCl_n where M = Cr, Mn, Ti, V, Zn then only the NaCl peaks shifted to lower diffraction angles were present. For the $NaBH_4$ and MCl_n (M = Ca, Sc and Al) mixtures, the diffraction peaks of $NaBH_4$ were still present after ball milling. Nakamori et al.[97,98] concluded that Reaction (13.12) with $LiBH_4$ was much easier than Reaction (13.13) with $NaBH_4$ due to similar ionic radii of Li^+ (0.076 nm) and Mn^{n+} in solid–solid cation exchange reaction as compared to that of Na^+ (0.102 nm). Later, Varin et al.[99] reported that the MCAS of the ($2NaBH_4 + MgCl_2$) mixture resulted in only partial synthesis of disordered magnesium borohydride $Mg(BH_4)_2$, accompanied by (Na, Mg)BH_4 solid solution and NaCl, which seems to confirm that $NaBH_4$ is not so effective as $LiBH_4$ in reacting with a metal chloride during MCAS. Nakamori et al.[97,98] also reported that the hydrogen desorption temperature, T_d, of disordered $M(BH_4)_n$ decreased with increasing values of the Pauling electronegativity χ_P of M in borohydride. They noted that the desorbed gas for M = Ca, Sc, Ti, V, and Cr ($\chi_P \leq 1.5$) was hydrogen only, while that for M = Mn, Zn, and Al ($\chi_P \geq 1.5$) contained a mix of borane and hydrogen.

In the further development, Choudhury et al.[100] reported that the MCAS of $LiBH_4$ with $MnCl_2$ in the ratio of 3:1 resulted in the synthesis of new complex metal borohydride $LiMn(BH_4)_3$. Based on the absence of any clear Bragg peaks except LiCl, they concluded that disordered $LiMn(BH_4)_3$ was synthesized. Varin et al.[101] also attempted to synthesize $LiMn(BH_4)_3$ by the MCAS of ($3LiBH_4 + MnCl_2$) with a presumption that $LiMn(BH_4)_3$ would indeed be synthesized. In contrast, Cerny et al.[102,103] and Severa et al.[104] reported that $Mn(BH_4)_2$ was always synthesized during the MCAS of the $LiBH_4$ and $MnCl_2$ constituents and not $LiMn(BH_4)_3$. Most recently, Liu et al.[105] reported limited studies of thermal decomposition behavior of 2 and 3 mol $LiBH_4$ mixed with $MnCl_2$ by ball milling using DSC and TG (thermogravimetric) analysis combined with XRD, Raman spectroscopy, and Fourier transform

infrared (FTIR) spectra. From these results, they deduced that dehydrogenation of $Mn(BH_4)_2$ occurs with the release of diborane (B_2H_6). They didn't conduct any isothermal dehydrogenation tests at 1 bar H_2 pressure.

In our studies,[101,106] we investigated a wide range of molar ratios in the mixture ($nLiBH_4 + MnCl_2$) where $n = 1$, 2, 3, 5, 9, and 23 with the objective of synthesizing $Mn(BH_4)_2$ whose theoretical H_2 capacity is close to 9.5 wt%. A very small quantity of H_2, not exceeding 0.2 wt%, was being released during ball milling for all molar ratios investigated.[106] In order to assess whether n-Ni produced by Vale Ltd, which was mentioned earlier, would be a suitable catalyst for the present system $LiBH_4$–$MnCl_2$, we compared the behavior of the mixture with the molar ratio $n = 3$ without any additive and with the additive of n-Ni having two different specific surface area (SSA) values of 9.5 m^2/g (Fig. 13.2(a)) and 60.5 m^2/g (Fig. 13.21(a)). Figure 13.21(b) shows the XRD pattern for the ($2LiBH_4 + MnCl_2$)($n = 2$) mixture after the MCAS by the high-energy ball milling. Only peaks of LiCl and $Mn(BH_4)_2$ are observed confirming that the following metathesis reaction occurred during milling:

$$2LiBH_4 + MnCl_2 \rightarrow Mn(BH_4)_2 + 2LiCl \qquad (13.14)$$

With increasing molar ratio $n \geq 2$, the reaction is modified to the following:

$$nLiBH_4 + MnCl_2 \rightarrow Mn(BH_4)_2 + 2LiCl + (n-2)LiBH_4 \quad (n = 2\text{–}23) \qquad (13.15)$$

A special case occurred for $n = 1$ where after the MCAS synthesis instead of LiCl an inverse cubic spinel ionic conducting compound Li_2MnCl_4 was formed according to the reaction:

$$LiBH_4 + MnCl_2 \rightarrow 0.5Mn(BH_4)_2 + 0.5Li_2MnCl_4 \quad (n = 1) \qquad (13.16)$$

This is the same compound, which was found in the $LiAlH_4$–$MnCl_2$ system formed according to the metathesis Reaction (13.7) discussed earlier. Apparently, whether the reacting hydride is lithium alanate ($LiAlH_4$) or lithium borohydride ($LiBH_4$) at the molar ratio $n = 1$ in the ball-milled mixture with $MnCl_2$ there is always formation of an inverse cubic spinel Li_2MnCl_4. Formation of a very similar inverse cubic spinel Li_2MgCl_4 was also reported for the $LiBH_4$–$MgCl_2$ system after ball milling for 36 h in a planetary ball mill.[107] This compound was formed together with $Mg(BH_4)_2$ hydride as a result of metathesis reaction. However, we carried out similar synthesis for the ($3LiBH_4 + MgCl_2$) mixture but instead of Li_2MgCl_4 regular salt LiCl was formed (unpublished results).

Synthesized $Mn(BH_4)_2$ is capable of desorbing at a low temperature of 100 °C (Fig. 13.22). In the presence of LiCl, which is a dead-weight product not taking part in dehydrogenation, $Mn(BH_4)_2$ desorbs about 4 wt% H_2. Since, for the molar ratios $n = 2$ and 3, the theoretical H_2 capacities of the respective mixtures are 4.76 and 4.2 wt%, it means that both mixtures dehydrogenated nearly full H_2 capacity at 100 °C (Fig. 13.22). Therefore, after extraction of LiCl, this would amount to at least of 9 wt% H_2 desorbed. This hydride seems to have the highest H_2 desorption capacity easily available at 100 °C among other borohydrides and alanates.

As reported in,[99] the activation energy for dehydrogenation of ($3LiBH_4 + MnCl_2$) without additive was 102 kJ/mol. This value is lower than the value of 131 kJ/mol reported by Choudhury et al.[100] The activation energies for the hydrogen desorption for the same mixture containing 9.5 and 60.5 m^2/g n-Ni were 98 and 92 kJ/mol, respectively. These values are also lower than 112 kJ/mol reported by Choudhury et al. for their mixture doped with a n-Ni.[100] It must, however, be pointed out that Choudhury et al. used the Kissinger method[15] for their estimate of the activation energy. Their methodology was different than the JMAK

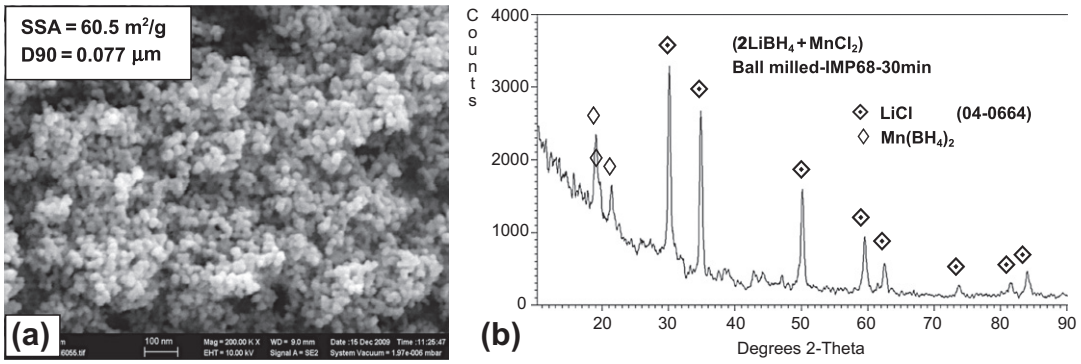

FIGURE 13.21 (a) Scanning electron micrograph of Vale Ltd. nanometric Ni (n-Ni) with specific surface area (SSA) = 60.5 m^2/g. Secondary electrons (SE) contrast. (b) The XRD pattern for the ($2LiBH_4 + MnCl_2$) mixture ball milled under IMP68-R132 mode for 0.5 h in H_2 gas; adapted from Ref. 99. Diffraction peaks of $Mn(BH_4)_2$ indexed after.[102–104]

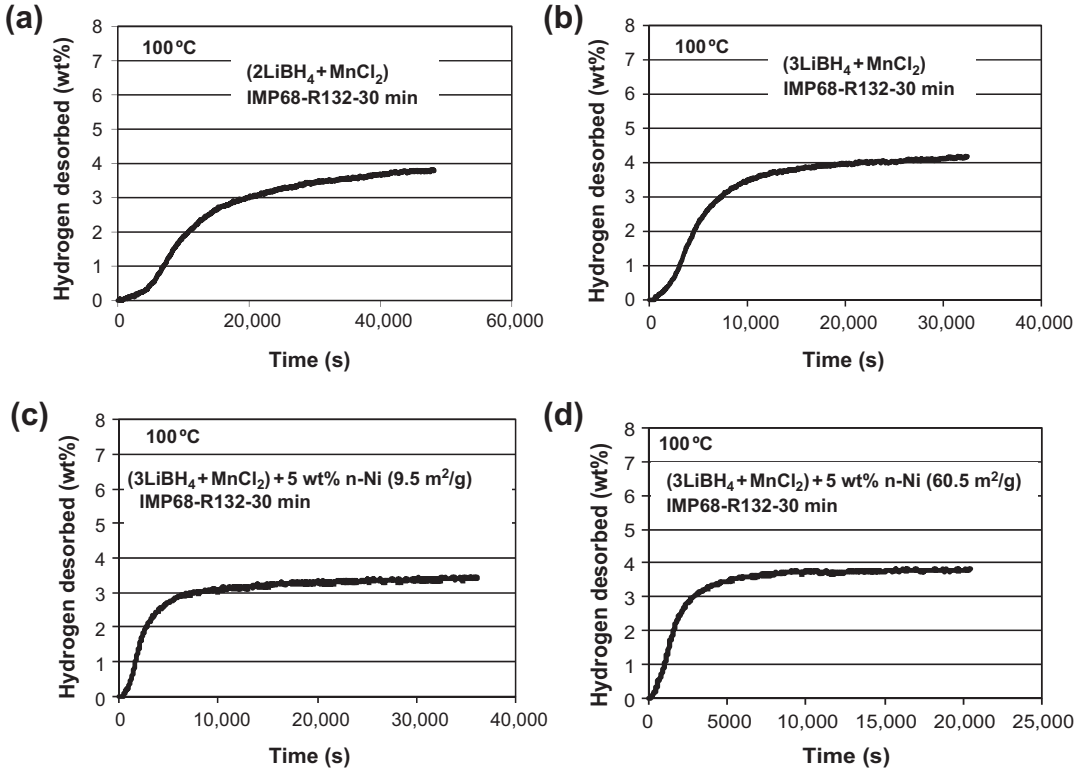

FIGURE 13.22 Volumetric desorption curves at 100 °C under 1 bar H_2 pressure for $Mn(BH_4)_2$ synthesized by ball milling of (a) $(2LiBH_4 + MnCl_2)$, (b) $(3LiBH_4 + MnCl_2)$, (c) $(3LiBH_4 + MnCl_2)$+5 wt% n-Ni (SSA = 9.5 m^2/g), and (d) $(3LiBH_4 + MnCl_2) + 5$ wt% n-Ni (SSA = 60.5 m^2/g). After ball milling, these mixtures contain $Mn(BH_4)_2$ and LiC the latter being just a dead-weight not taking part in the dehydrogenation of $Mn(BH_4)_2$. *Source: Adapted from Refs 101,106.*

(Johnson−Mehl−Avrami−Kolmogorov) method that we used in,[101] so one can expect slightly different results. In general, the agreement between both studies is quite reasonable. However, the possibly catalyzing effect of n-Ni is not very substantial.

Temperature programmed desorption gas desorption spectra combined with mass spectroscopy analysis for the ball-milled $n = 3$ and 5 composites showed the primary H_2 release peak from $Mn(BH_4)_2$ centered around 150 °C while a secondary smaller and very broad H_2 release peak from retained $LiBH_4$ occurred in a wide temperature range 300−450 °C.[106] In addition, around 150 °C, there was also a miniscule peak corresponding to the release of diborane B_2H_6, whose intensity increased with increasing heating rate from 2 to 10 °C/min but was 200−600 times smaller than the intensity of the primary H_2 peak.[106] The obtained results mean that the quantity of released diborane is negligibly small being barely on the verge of the resolution of the Hiden Sieverts apparatus-quadrupole mass spectrometric experimental system used in.[106] Therefore, neglecting minute quantities of B_2H_6 (if any), the decomposition reaction of $Mn(BH_4)_2$ can be written as follows:

$$Mn(BH_4)_2 \rightarrow Mn + 2B + 4H_2 \qquad (13.17)$$

A direct observation of the melting behavior of the $n = 2$ and 3 composites, according to Reactions (13.14) and (13.15), consisting of $(Mn(BH_4)_2 + LiCl)$ and $(Mn(BH_4)_2 + LiCl + LiBH_4)$, respectively, showed that up to 274 and 286 °C for the $n = 2$ and 3 composites, respectively, no melting was observed.[106] It has been reported in[93,102] that in a composite with LiCl, the $Mn(BH_4)_2$ hydride melted at about 177 °C (450 K). Apparently, the present experiments do not confirm such a low melting temperature of $Mn(BH_4)_2$, which is observed to be stable at least up to about 280 °C.

Figure 13.23 shows the quantities of H_2 desorbed at 140 °C after long storage at RT and 40 °C of samples without and with the catalytic additive of n-Ni. It is seen in Fig. 13.23(a), (b) that the $n = 3$ composite without any additive discharged only a small amount of ~0.7 and 1.4 wt% H_2 after storage for 70−80 days at RT and 40 °C, respectively. The addition of n-Ni does not measurably change the rate of self-discharge at RT (Fig. 13.23(c), (e)) although the n-Ni additive visibly accelerates it at 40 °C (Fig. 13.23(d), (f)). Particularly effective is n-Ni with SSA = 60.5 m^2/g, which allows discharge of ~2.5 wt% H_2 within 63 days of storage at 40 °C (Fig. 13.23(f)). XRD studies after slow discharge in Fig. 13.23 showed that it occurred by a slow

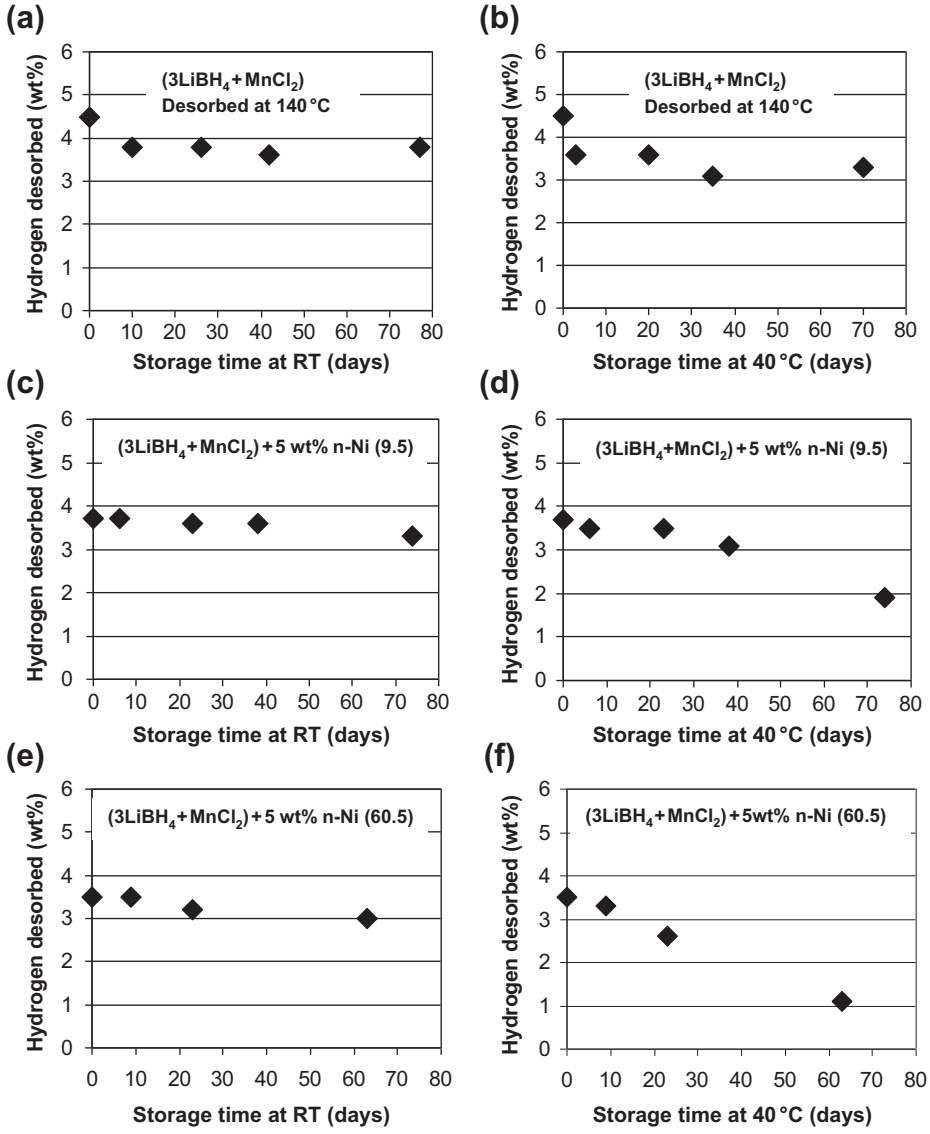

FIGURE 13.23 The quantities of hydrogen desorbed at 140 °C in 1 bar H_2 pressure after long-term storage of ball-milled $(3LiBH_4 + MnCl_2)$(microstructure consisting of $Mn(BH_4)_2 + 2LiCl + LiBH_4$) at low temperatures. (a) No additive; stored at room temperature (RT), (b) no additive; stored at 40 °C, (c) with 5 wt% n-Ni SSA = 9.5 m^2/g; stored at RT, (d) with 5 wt% n-Ni SSA = 9.5 m^2/g; stored at 40 °C, (e) with 5 wt% n-Ni SSA = 60.5 m^2/g; stored at RT, and (f) with 5 wt.% n-Ni SSA = 60.5 m^2/g; stored at 40 °C. SSA-specific surface area. Storage in a glass vial under high-purity argon. *Source: Adapted from Ref. 106.*

decomposition of $Mn(BH_4)_2$.[106] However, it should be pointed out that the rates of H_2 self-discharge observed for $LiAlH_4$ ball milled with n-Ni and Fe additives reported in[72–74] are much higher than that in Fig. 13.23(f) for $Mn(BH_4)_2$ containing n-Ni with SSA = 60.5 m^2/g. By the way of comparison, at 40 °C, the ball-milled ($LiAlH_4$+5wt.% n-Ni/n-Fe) mixture discharged about 4.7 wt% H_2 within 20 days of storage.

Rehydrogenation studies of the fully dehydrogenated $(3LiBH_4 + MnCl_2)$ mixture, containing most likely amorphous Mn and B, primary LiCl, and a small quantity of retained $LiBH_4$ (Reactions (13.15) and (13.17)) at 200 °C under 100 bar H_2 pressure for 12 h did not result in a measurable rehydrogenation.[101] At least under these rehydrogenation conditions, the dehydrogenated $(Mn + 2B + LiCl + LiBH_4)$ mixture seems to be irreversible. Similar results on a lack of reversibility of decomposed $Mn(BH_4)_2$ was reported by Liu et al.[105] However, the reversibility of extracted $Mn(BH_4)_2$, which dehydrogenates to just Mn and B and does not contain LiCl has not been investigated yet.

We also conducted some preliminary studies of the ball-milling behavior and subsequent dehydrogenation of the $(nNaBH_4 + MnCl_2)$ system where the molar ratios $n = 2$ and 3.[108] No desorption of H_2 was observed up to 30 min of ball milling under IMP68-high-energy impact mode with R132. The XRD patterns obtained after 30 min-ball milling show only principal diffraction peaks

of NaCl for the molar ratio $n = 2$ and NaCl and retained $NaBH_4$ peaks for the $n = 3$ molar ratio and nothing else. There is no evidence from XRD that $Mn(BH_4)_2$ is formed after ball milling. However, the ball-milled mixtures with the molar ratios $n = 2$ and 3 are able to desorb at 140 °C about 2.3 wt% H_2 after about 30 min. That shows that an amorphous hydride must have formed during ball milling. However, the mixtures desorb only small quantities of H_2 at temperatures lower than 140 °C. This is in total contrast to the desorption behavior of the $(nLiBH_4 + MnCl_2)$ system discussed above.

13.4 LITHIUM AMIDES

13.4.1 The ($LiNH_2$−LiH) System

From the view point of hydrogen capacity, a single-phase $LiNH_2$ is quite attractive since its theoretical gravimetric H_2 capacity is 8.8 wt.%. However, the major drawback is that a single-phase $LiNH_2$ decomposes releasing ammonia (NH_3) rather than H_2 according to reaction[15]:

$$2LiNH_2 \rightarrow Li_2NH + NH_3 \qquad (13.18)$$

NH_3 can be poisonous for the membrane of a conventional proton exchange membrane (PEM) fuel cell and its presence should be avoided in modern PEM fuel cells. However, an addition of LiH results in a very fast capture of NH_3 according to reaction:

$$NH_3 + LiH \rightarrow LiNH_2 + H_2 \qquad (13.19)$$

Therefore, it has been well documented[15] that the system of $LiNH_2$ and LiH is reversible according to

$$LiNH_2 + LiH \leftrightarrow Li_2NH + H_2 \qquad (13.20)$$

Shaw et al.[109] reported that that high-energy ball milling of the $(LiNH_2 + 1.1LiH)$ system, where the 10% excess of LiH was added to minimize the loss of NH_3 during dehydrogenation, resulted in the near-elimination of the escaping NH_3 at a heating rate of 5 °C/min and the 60% reduction in the apparent activation energy of Reaction (13.20). Nevertheless, despite such a fast rate of Reaction (13.19) in the ball-milled mixture, some escape of NH_3 was still observed.

We also investigated the effects of high-energy ball milling for a wide range of molar ratios in the $(LiNH_2 + nLiH)$ mixtures where $n = 1$, 1.2, and 1.4.[110] It was observed that the SSA of powder increased up to 25 h of milling duration and then decreased after milling for 100 h due to the excessive agglomeration of powder particles into lumps (Fig. 13.24(a)). Simultaneously, the

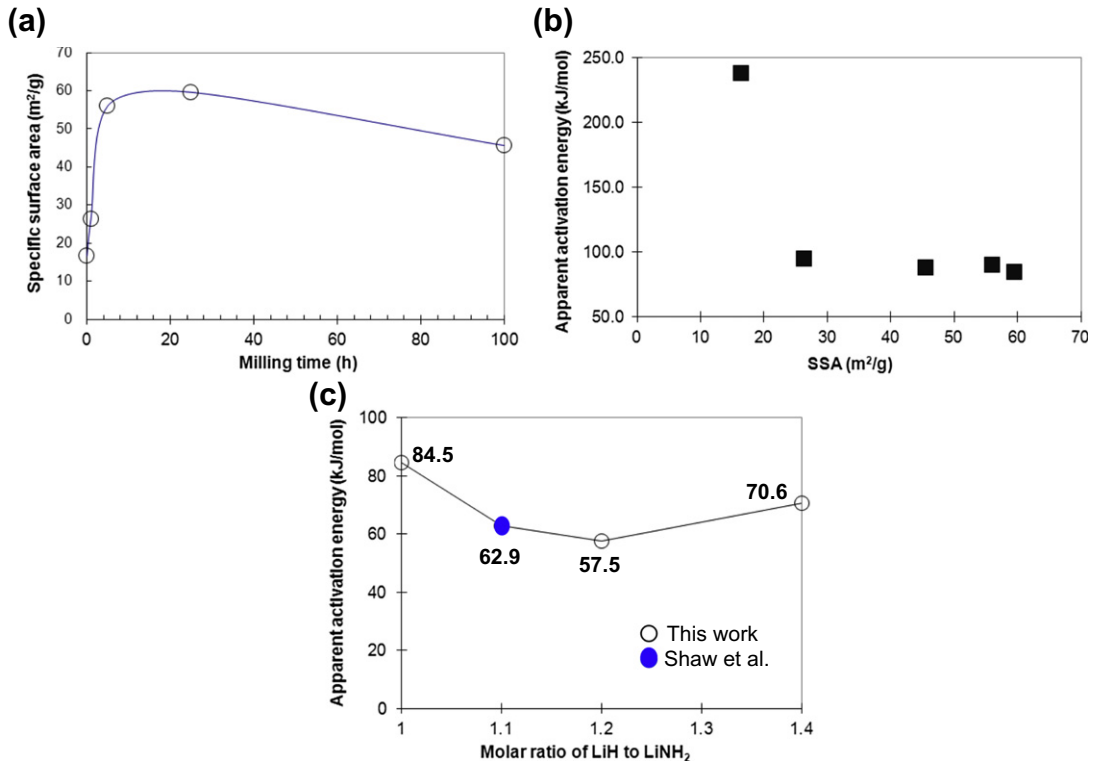

FIGURE 13.24 (a) Specific surface area (SSA) of the $(LiNH_2 + LiH)$ mixture vs milling time for the 1:1 molar ratio. (b) The apparent activation energy of Reaction (13.20) as a function of specific surface area (SSA) for the 1:1 molar ratio mixture $(LiNH_2 + LiH)$. (c) The apparent activation energy of Reaction (13.20) as a function of the molar ratio of LiH to $LiNH_2$ for the mixtures milled for 25 h (IMP68-R40). (For color version of this figure, the reader is referred to the online version of this book.) *Source: Adapted from Ref. 110 (Shaw et al. see Ref. 109).*

grain (crystallite) sizes of both $LiNH_2$ and LiH constituents decreased monotonically with increasing milling time.[110] It was confirmed that a single-phase $LiNH_2$ decomposed through melting and the release of ammonia (NH_3). Also, a just mixed ($LiNH_2 + nLiH$) mixture still decomposed through the melting of $LiNH_2$ and a release of NH_3.[110] For hydrogen to be effectively released from the mixture of ($LiNH_2 + nLiH$), a high-energy ball milling is necessary, which makes an intimate contact between both constituent particles. As shown in Fig. 13.24(b), the apparent activation energy for hydrogen desorption from the ball-milled mixture of ($LiNH_2 + nLiH$)($n = 1$) (Reaction (13.20)) dramatically decreases with increasing SSA of powders up to $\sim 26\ m^2/g$ and then levels off with further increase of SSA. For the ball-milled mixture of ($LiNH_2 + nLiH$), the lowest apparent activation energy is observed for the molar ratio $n = 1.2$ (Fig. 13.24(c)). This activation energy is still lower than that reported by Shaw et al.[109] for the molar ratio $n = 1.1$. Interestingly, increase of the molar ratio to 1.4 again increases the apparent activation energy (Fig. 13.24(c)). So, the ratio $n = 1.2$ seems to be optimal. We also observed that the hydrolysis/oxidation of the fraction of LiH into LiOH in the mixture made a fraction of LiH inactive in Reaction (13.19) created the major obstacle to the hydrogen desorption from the ball-milled mixture of ($LiNH_2 + nLiH$).[110]

In order to alleviate the problem of LiH hydrolysis/oxidation, 5 wt% of graphite was incorporated into the ($LiNH_2 + 1.2LiH$) system by ball milling in order to study its effect on the prevention of LiH from hydrolysis/oxidation, which leads to the escape of NH_3.[16] We anticipate that graphite after ball milling would be relatively evenly distributed as a thin coat/film around LiH particles. That could seal off the LiH particles from the effects of the environment/moisture. XRD studies showed that after ball milling graphite became amorphous. Typical DSC curves for ($LiNH_2 + 1.2LiH$) without graphite (G) and with 5 wt% G are shown in Fig. 13.25. The ball-milled mixture without graphite shows a very strong endothermic peak with the maximum at 227.6 °C related to Reaction (13.20) in which hydrogen is being released. The second smaller endothermic peak is observed at 396.2 °C, which is due to melting of retained $LiNH_2$ and desorption of some NH_3 (Reaction (13.18)). The presence of retained $LiNH_2$ is due to the fact that a part of LiH was hydrolyzed/oxidized, and there was not enough LiH to react with $LiNH_2$ in Reaction (13.20). DSC analysis in Fig. 13.25 clearly shows that for the mixture with 5 wt % G, the latter can prevent or at least substantially reduce the oxidation/hydrolysis of LiH since no melting peak of retained $LiNH_2$ is observed. The small exothermic peak at 470.9 °C for (($LiNH_2 + 1.2LiH$) + 5 wt% G) is related to the oxidation of graphite at high temperature.

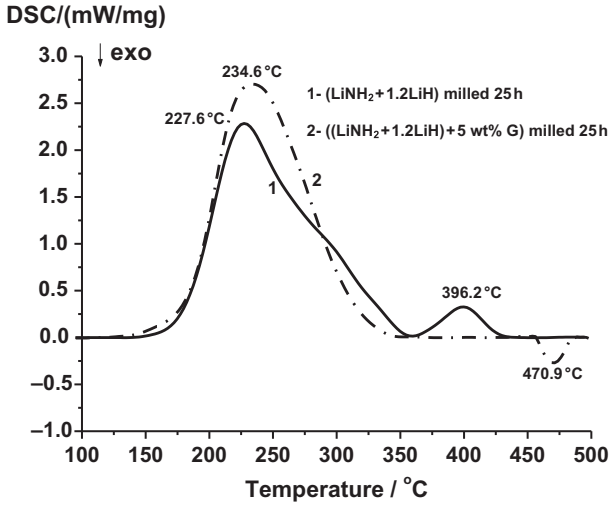

FIGURE 13.25 DSC curves at a heating rate of 10 °C/min for the ($LiNH_2 + 1.2LiH$) mixture without and with 5 wt% graphite (G) ball milled for 25 h (IMP68-R40). *Source: Adapted from Ref. 16.*

Examples of dehydrogenation curves at varying temperatures for ball milled ($LiNH_2 + 1.2LiH$) without and with 5 wt% G are shown in Fig. 13.26(a). At every temperature, the mixture with graphite desorbs a greater quantity of hydrogen than by its graphite-free counterpart. Particularly, large difference is observed at 275 °C. This is explained by less extensive hydrolysis/oxidation of LiH, which is covered by a thin film of graphite preventing any contact with remnants of moisture and more complete Reaction (13.20) with $LiNH_2$. The apparent activation energy of desorption (Reaction (13.20)) was estimated from both the DSC and Sieverts-type tests by the Kissinger and JMAK/Arrhenius methods, respectively. (For description of both methods, see Ref. 15). It is shown that the addition of graphite increases the apparent activation energy from the $\sim 57-58$ to $\sim 85-90$ kJ/mol range (Fig. 13.26(b)). Reversibility of both mixtures without and with 5 wt% G is very easy. An example of reversibility at 325 °C is shown in Fig. 13.27. A mixture without graphite is fully reversible at this temperature desorbing in 1 bar H_2 and reabsorbing in 11 bar H_2 pressure slightly less than 5 wt% H_2 (Fig. 13.27(a), (b)). A mixture with graphite desorbs/re-absorbs slightly more than 5 wt% H_2 under the same conditions (Fig. 13.27(c), (d)). Interestingly, for both mixtures, a lower absorption hydrogen pressure of 11 bar results in higher rate of re-absorption compared to that which occurs a higher hydrogen pressure of 35 bar (Fig. 13.27(b), (d)). It is hypothesized that hydrogen at a higher pressure of 35 bar reacts at a higher rate with the Li_2NH particles that were formed after dehydrogenation (Reaction (13.20)), and subsequently a layer of $LiNH_2$ is rapidly created on the particles' surface. This layer may block hydrogen from diffusing into the particle core,

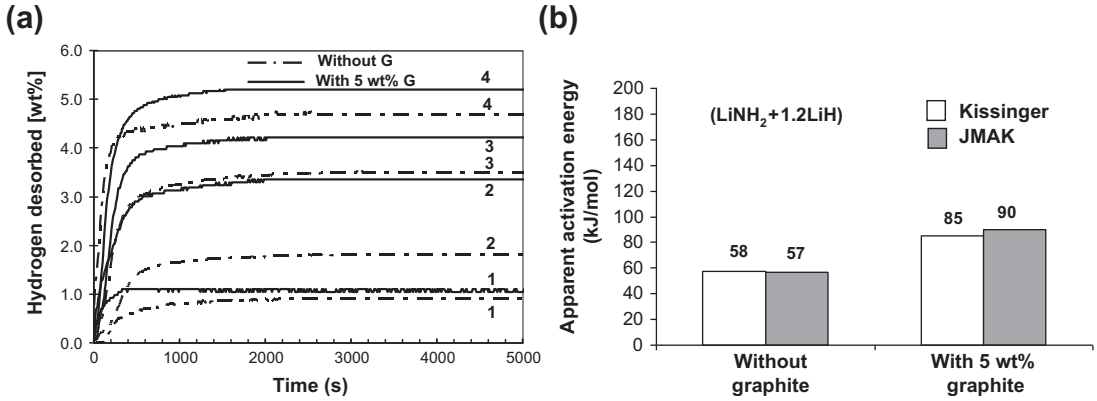

FIGURE 13.26 (a) Comparison of desorption curves under 1 bar H_2 pressure (atmospheric) for ball-milled ($LiNH_2 + 1.2LiH$) and (($LiNH_2 + 1.2LiH$) + 5 wt% G) (1—250 °C, 2—275 °C, 3—300 °C, 4—325 °C). (b) Comparison of apparent activation energies obtained from the Kissinger and JMAK/Arrhenius methods for the mixtures without and with 5 wt% G. Ball milled for 25 h under IMP68-R40 mode. *Source: Adapted from Ref. 16.*

which makes the re-absorption kinetics slower than those when using lower hydrogen pressure (11 bar).

Step-wise desorption tests (pseudo-PCT) shown in Figs 13.1(a), (b) and 13.28(a), (b) result in the enthalpy and entropy changes of reversible Reaction (13.20) equal to 62.4 and 61.0 kJ/mol H_2 and 117.8 and 115.8 J/mol K for the mixture without and with 5 wt% G, respectively. It shows that within the experimental error, there is no measurable effect of graphite additive on the thermodynamic properties. The Van't Hoff analysis with Eqn (13.1) shows that the equilibrium temperature at atmospheric pressure of hydrogen (1 bar H_2) is 256.8 and

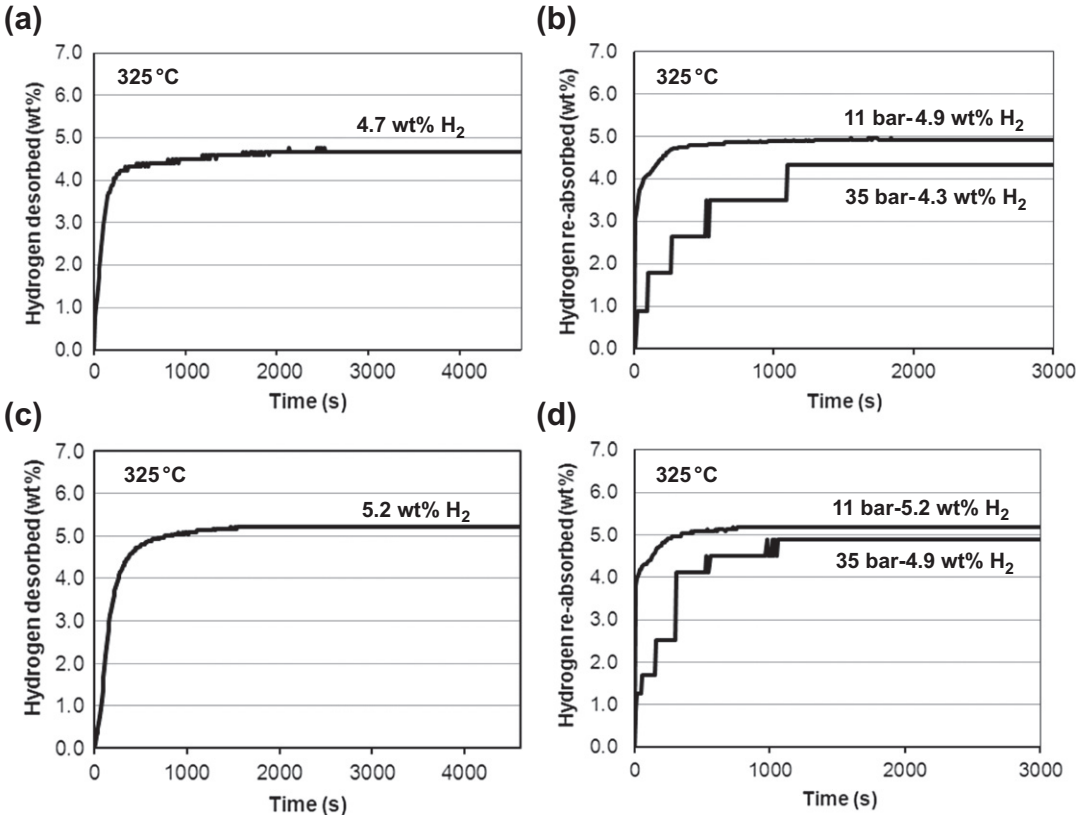

FIGURE 13.27 (a) Desorption curve at 325 °C under 1 bar H_2 pressure and (b) corresponding re-absorption curves at 325 °C under 11 and 35 bar H_2 pressure for the ($LiNH_2 + 1.2LiH$) mixture ball milled for 25 h. (c) Desorption curve at 325 °C under 1 bar H_2 pressure and (d) corresponding re-absorption curves at 325 °C under 11 and 35 bar H_2 pressure for the (($LiNH_2 + 1.2LiH$)+5wt% G) mixture ball milled for 25 h (IMP68-R40). *Source: Adapted from Ref. 16.*

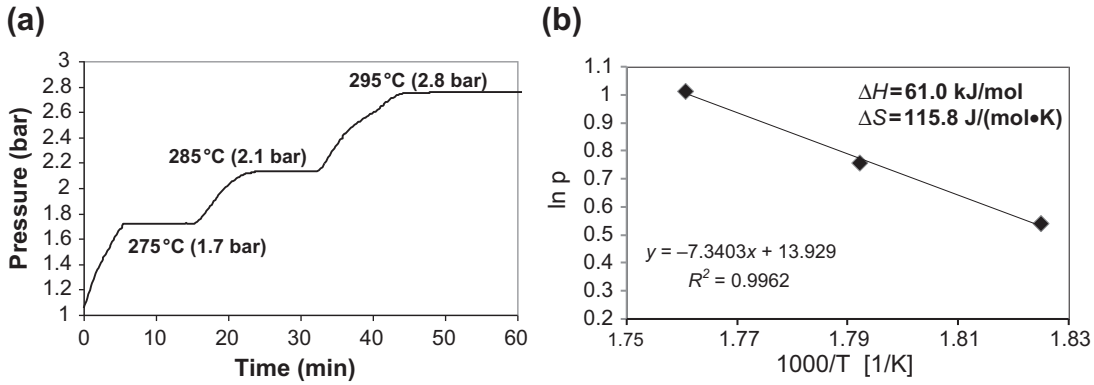

FIGURE 13.28 (a) Step-wise desorption curves (pseudo-PCT curves) at three temperatures and (b) corresponding Van't Hoff plot for the $((LiNH_2 + 1.2LiH) + 5$ wt% G) mixture. *Source: Adapted from Ref. 16.*

253.9 °C for the mixture without and with 5 wt% G, respectively. It is obvious then that with such high equilibrium temperatures both of this hydride system cannot be employed for hydrogen desorption/absorption below 100 °C as required by the DOE targets for the automotive hydrogen storage materials.

13.4.2 The ($LiNH_2$−MgH_2) System

As an alternative to the ($LiNH_2$−LiH) system, the ($LiNH_2$−MgH_2) system was proposed by Luo et al.[111–114] and Ichikawa et al.[115] Since then, the research on the ($LiNH_2$−MgH_2) system was pursued vigorously by other researchers.[116–125] Even more interest in this system was attracted by a paper by Alapati et al.[126] who theoretically predicted a direct reaction between $LiNH_2$ and magnesium hydride (MgH_2) having the reaction enthalpy ~32 kJ/mol H_2 as a result of which a new compound LiMgN was supposed to be formed releasing 8.2 wt% H_2. Unfortunately, this predicted reaction has never been observed experimentally and the quantities of H_2 released in the reactions occurring in this system are much less than 8 wt%. Another problem that clearly appears from the review of the pertinent literature[116–125] is a strong influence of various ball-milling conditions on the phase transformations occurring during ball milling in this system. There are conflicting results with respect to various hydride phases and their mixtures reported after ball milling by various authors. Obviously, the initial phase composition obtained after milling has a substantial influence on subsequent dehydrogenation at elevated temperatures.

We decided to undertake systematic studies of the effect of the milling energy on the phase transformations and subsequent thermal behavior of the ($LiNH_2$ + $nMgH_2$) system with a wide range of molar ratios $n = 0.5$, 0.7, 0.85, 0.9, 1.0, and 2.0.[127,128] Figure 13.29 is a summarizing plot-milling energy-phase content. The total injected energy of milling was calculated by theoretical approaches and experimental observations of the movement trajectories of steel balls in a milling cylinder/vial for each mode of milling as described in.[128] The lines E_1 and E_2 indicate the approximate minimum energy levels at which a new phase or the phase mixtures appear during the high-energy ball milling. It must be stressed that the E_1 and E_2 energy lines do not show the formation of only single-hydride phases. The phases/mixtures present in the delineated fields are labeled with the numbers explained in the legend. The phases and their mixtures were obtained from XRD and the Fourier transform-infra red (FTIR) spectroscopy investigations for each n after ball

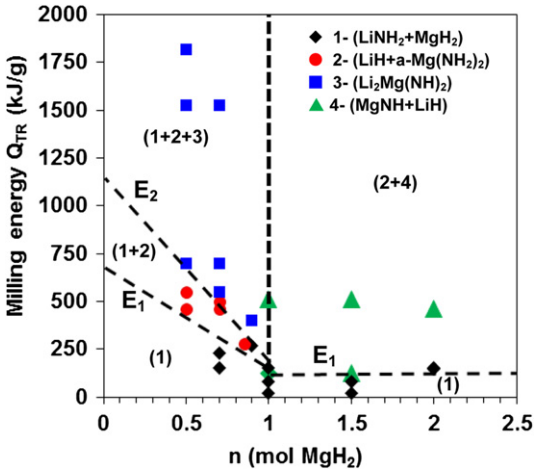

FIGURE 13.29 Injected milling energy (Q_{TR}) phase content diagram for the ($LiNH_2 + nMgH_2$) system for various molar ratios $n = 0.5$, 0.7, 0.85, 0.9, 1.0, and 2.0. The lines E_1 and E_2 indicate approximate minimum energy levels at which a new phase or the phase mixtures appear during high-energy ball milling. The thick vertical broken line delineates the phase fields for $n = 0.5$–0.9 and $n \geq 1$. (For color version of this figure, the reader is referred to the online version of this book.) *Source: Adapted from Ref. 128.*

milling.[127,128] For $n \geq 1$, the phase transformations substantially differ from those for $n = 0.5-0.9$. Therefore, a thick vertical broken line is used to clearly delineate the phase fields for $n = 0.5-0.9$ and $n \geq 1$ above the energy line E_1.

As shown by XRD studies (Fig. 13.30), two types of reactions between $LiNH_2$ and MgH_2 can occur during ball milling depending on the molar ratio and total milling energy. For the molar ratio $n = 0.5-0.9$ in the first step amorphous magnesium imide ($Mg(NH_2)_2$) is formed in the following reaction:

$$LiNH_2 + nMgH_2 \rightarrow 0.5Mg(NH_2)_2 + 1.0LiH + (n - 0.5)MgH_2 \quad (13.21a)$$

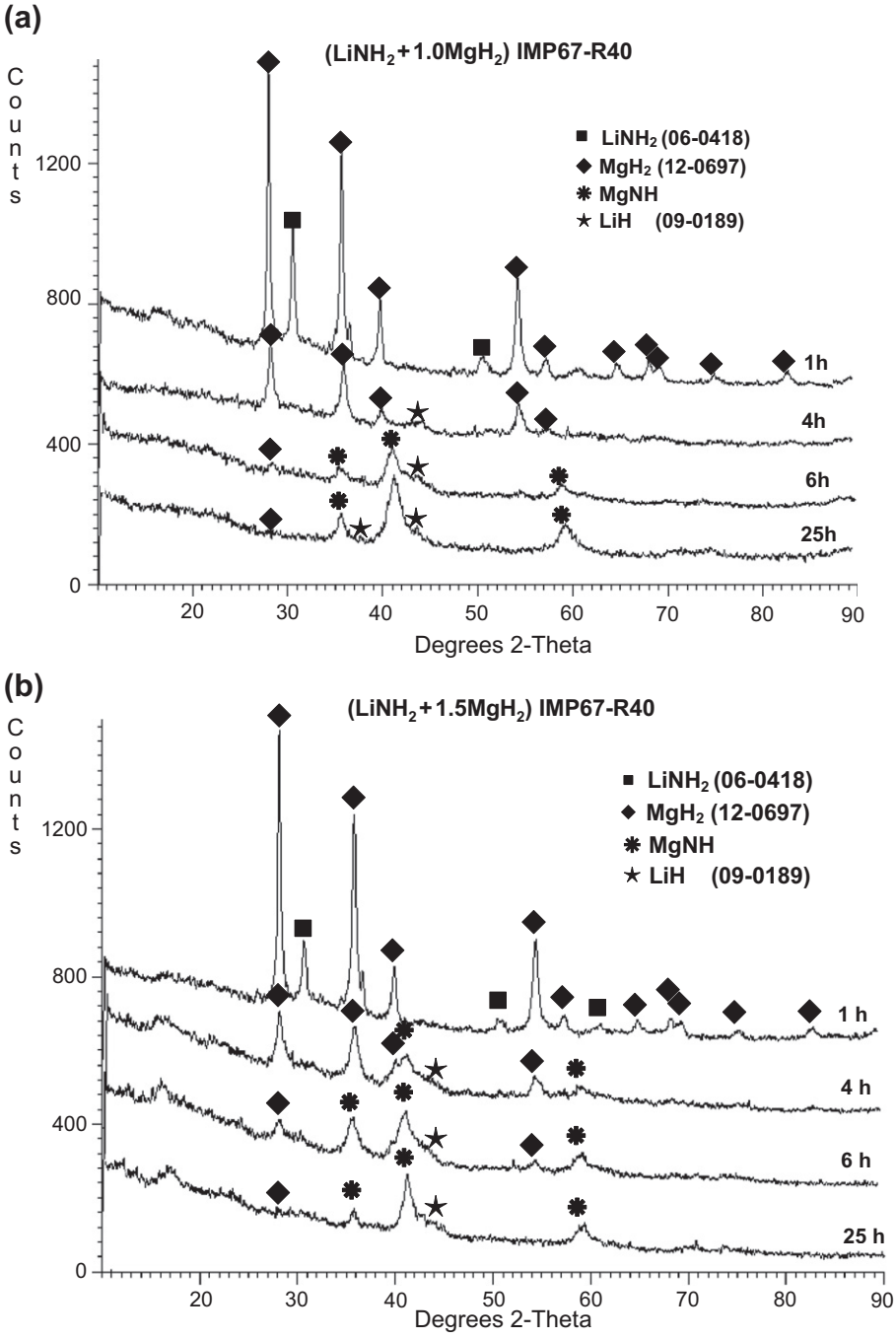

FIGURE 13.30 XRD patterns showing the evolution of microstructure as a function of milling time under IMP67-R40 mode for the ($LiNH_2 + nMgH_2$) mixture with (a) $n = 1.0$ and (b) $n = 1.5$. ICDD numbers for the phase identification are shown. The MgNH hydride was identified with our own standard XRD pattern. *Source: Adapted from Ref. 127.*

In the second step, $Mg(NH_2)_2$ reacts with LiH, forming $Li_2Mg(NH)_2$ and free hydrogen:

$$0.5Mg(NH_2)_2 + 1.0LiH + [(n-0.5)MgH_2] \leftrightarrow 0.5Li_2Mg(NH)_2 + [(n-0.5)MgH_2] + 1.0H_2 \quad (13.21b)$$

For $n = 0.5$, the theoretical total quantity of H_2 desorbed in Reaction (13.21b) is ~5.6 wt% and proportionally smaller for $n > 0.5$ because excess unreacted MgH_2 is retained in the microstructure and does not take part in reaction (designated in brackets). Taking into account purities of commercial hydrides, the purity-corrected H_2 quantities desorbed in Reaction (13.21b) will be slightly lower than the theoretical ones. Reaction (13.21b) can also occur at elevated temperatures and is fully reversible between $Li_2Mg(NH)_2$ and H_2.[116–125]

For $n \geq 1.0$, the first reaction step at lower total energy of milling (e.g. relatively short-milling time) can still occur according to Reaction (13.21a). However, with increasing energy of milling, Reaction (13.21b) does not occur anymore and another reaction starts taking place that has the following form:

$$0.5Mg(NH_2)_2 + 0.5MgH_2 + (n-1)MgH_2 + [1.0LiH] \rightarrow 1.0MgNH + (n-1)MgH_2 + [1.0LiH] + 1.0H_2 \quad (13.22)$$

In Reaction (13.22), the LiH in the square brackets does not take part in the reaction. For $n = 1.0$ the theoretical total quantity of H_2 desorbed in Reaction (13.22) is 4.1 wt% and is proportionally smaller for $n > 1.0$. Reaction (13.22) can also occur at elevated temperatures but is irreversible. It is also to be pointed out that Reactions (13.21) and (13.22) may remain incomplete desorbing only a fraction of the total theoretical H_2 quantity resulting from each reaction.

Since $Mg(NH_2)_2$ synthesized during ball milling according to Reaction (13.21a) is always amorphous, it is necessary to use the FTIR spectroscopy technique, which allows a clear identification of amorphous $Mg(NH_2)_2$. Since, according to Reaction (13.21a), $Mg(NH_2)_2$ is always synthesized together with LiH, the presence of LiH diffraction peaks in an XRD pattern means that amorphous $Mg(NH_2)_2$ is also present, which has been evidenced on numerous occasions. Figure 13.30(a) and (b) shows the XRD pattern of the $(LiNH_2 + 1.0MgH_2)$ and $(LiNH_2 + 1.5MgH_2)$ mixtures, respectively, as a function of milling time. In both mixtures, LiH and corresponding amorphous $Mg(NH_2)_2$ (also identified using the FTIR spectroscopy[125]) clearly appear after 4 h of milling indicating at least partial Reaction (13.21a). The diffraction peaks for MgNH appear for the mixtures $n = 1.0$ and 1.5 after 6 and 4 h of milling, respectively. It means that Reaction (13.22) starts occurring earlier (at a lower milling energy) in the $n = 1.5$ mixture (Fig. 13.29).

The mechanical dehydrogenation curves in Fig. 13.31(a), (b) correlate well with the identified microstructure for the mixtures with the $n = 1.0$ and 1.5 molar ratio in Figure 13.30(a), (b). Since H_2 is released in Reactions (13.21b) and (13.22), then during ball milling under high-energy mode, a continuously increasing quantity of H_2 is being desorbed with increasing milling time, as shown for the mixtures with the molar ratios $n = 1.0$ (Fig. 13.31(a)) and 1.5 (Fig. 13.31(b)). The calculated approximate total milling energy values per unit mass of powder (kJ/g), injected into the powder after 25 h of milling, are shown in Fig. 13.31. The energy values correspond to the maximum quantity of H_2 desorbed after 25 h of milling in Fig. 13.31. It is seen that the quantity of H_2 desorbed after 25 h of milling increases with increasing total milling energy injected into the powder. The $n = 1$ mixture in Fig. 13.31(a) desorbed around 2 wt% H_2 after 25 h corresponding to 520 kJ/g of total energy consumed. The MgNH starts appearing in this mixture

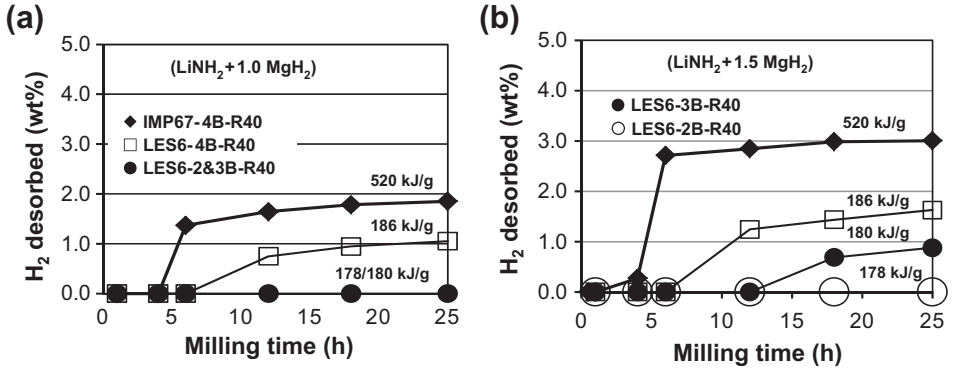

FIGURE 13.31 The quantity of H_2 desorbed during ball milling under high-energy impact (IMP67) and low energy-shearing (LES6) modes as a function of milling time for (a) $(LiNH_2 + 1.0MgH_2)$ composite and (b) $(LiNH_2 + 1.5MgH_2)$ composite. The numbers show the approximate total energy of milling per unit mass of powder injected into the powder after 25 h of milling. B-the number of steel balls in the milling vial. *Source: Adapted from Ref. 127.*

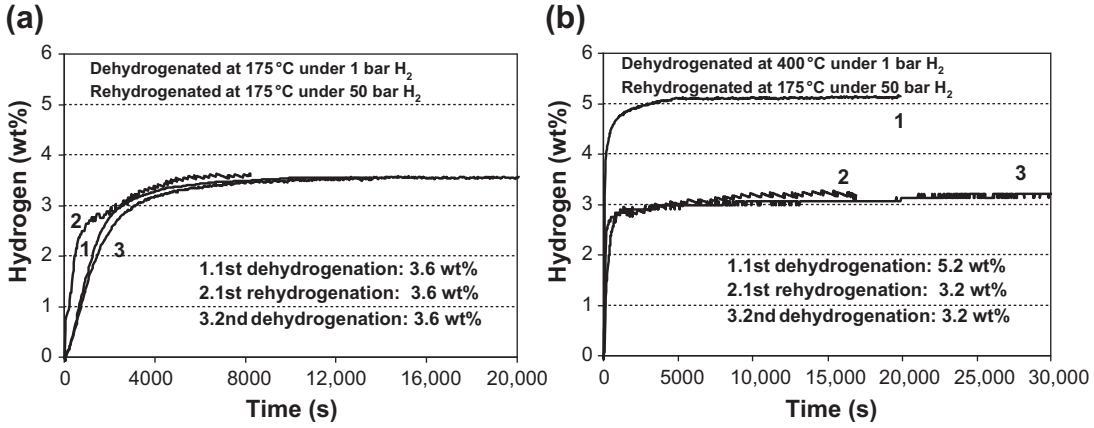

FIGURE 13.32 Volumetric dehydrogenation/rehydrogenation curves for the ($LiNH_2 + 0.7MgH_2$) mixture with 5 wt% n-Ni ball milled for 25 h (IMP67-R40)(total milling energy 520 kJ/g).

after 6 h (Fig. 13.30(a)). After 25 h of milling and the same 520 kJ/g total energy, the $n = 1.5$ mixture desorbed a larger quantity of H_2 equal to 3 wt%. In this mixture, the MgNH phase appears after only 4 h of milling, which means that Reaction (13.22) started earlier allowing much larger quantity of mechanically desorbed H_2. The $n = 1.5$ mixture starts desorbing even during milling under low shearing energy mode LES6-3B, which after 25 h provides only 180 kJ/g total energy (Fig. 13.31(b)). However, it should be pointed out that the maximum quantity of 3 wt% H_2 mechanically dehydrogenated from the $n = 1.5$ mixture after 25 h of milling (Fig. 13.31(b)) is still lower than the theoretical capacity of Reaction (13.22). That means that Reaction (13.22) is still incomplete after 25 h of ball milling.

The reversibility for n = 0.7 was investigated for ball-milled ($LiNH_2$–MgH_2) with 5 wt% n-Ni(SSA = 60.5 m^2/g), which was added as a possible catalytic additive. XRD analysis showed that the microstructure after milling for 25 h consisted of $LiNH_2$, MgH_2, and small quantities of LiH and $Mg(NH_2)_2$. The latter two phases were formed according to Reaction (13.21a). Figure 13.32 shows volumetric dehydrogenation/rehydrogenation curves. Dehydrogenation/rehydrogenation at 175 °C in Fig. 13.31(a) occurs according to Reaction (13.21a) modified for $n = 0.7$:

$$0.5Mg(NH_2)_2 + 1.0LiH + [0.2MgH_2] \leftrightarrow 0.5Li_2Mg(NH)_2 + [0.2MgH_2] + 1.0H_2 \quad (13.23)$$

The phase in brackets is retained. The full theoretical H_2 capacity of this reaction is 4.9 wt%. After correction for 95% and 98% purity of $LiNH_2$ and MgH_2, and the presence of 5 wt% n-Ni, the practical mixture capacity is roughly 4.5 wt% H_2. It is seen that at 175 °C, the mixture desorbs less than a full practical capacity due to the fact that its microstructure after ball milling is not exactly corresponding to the mixture at the left-hand side of Reaction (13.23). However, after rehydrogenation, the mixture returns to exactly the H_2 content that was dehydrogenated, which means that full practical reversibility is achieved. The situation changes when dehydrogenation is carried out at 400 °C, as shown in Fig. 13.32(b). At such a high-temperature, Reaction (13.23) still occurs but also another general reaction takes place, which was reported in the literature[116–125]:

$$0.5Li_2Mg(NH)_2 + 1.0MgH_2 \rightarrow 0.5Mg_3N_2 + 1.0LiH + 1.0H_2(\text{theoretical total 3.34 wt\% } H_2) \quad (13.24)$$

Since from Reaction (13.23) there is only 0.2 mol MgH_2 available for $n = 0.7$ then only a small molar fraction of $Li_2Mg(NH)_2$ produced in Reaction (13.23) will react with $0.2MgH_2$ according to:

$$0.1Li_2Mg(NH)_2 + 0.2MgH_2 \rightarrow 0.1Mg_3N_2 + 0.2LiH + 0.2H_2 \quad (13.25)$$

Theoretical capacity of this reaction is about 0.6 wt% H_2. As can be seen in Fig. 13.32(b) at 400 °C, the $n = 0.7$ mixture dehydrogenates close to the practical capacity of combined Reactions (13.23) and (13.25) but rehydrogenates only the retained molar fraction of $Li_2Mg(NH)_2$, which was not consumed in Reaction (13.25) according to the following:

$$0.4Li_2Mg(NH)_2 + [0.1Mg_3N_2] + [0.2LiH] + 0.8H_2 \rightarrow 0.4Mg(NH_2)_2 + 1.0LiH + [0.1Mg_3N_2] \quad (13.26)$$

In this reaction, magnesium nitride, Mg_3N_2, is an irreversible phase that leads to a loss of H_2 during

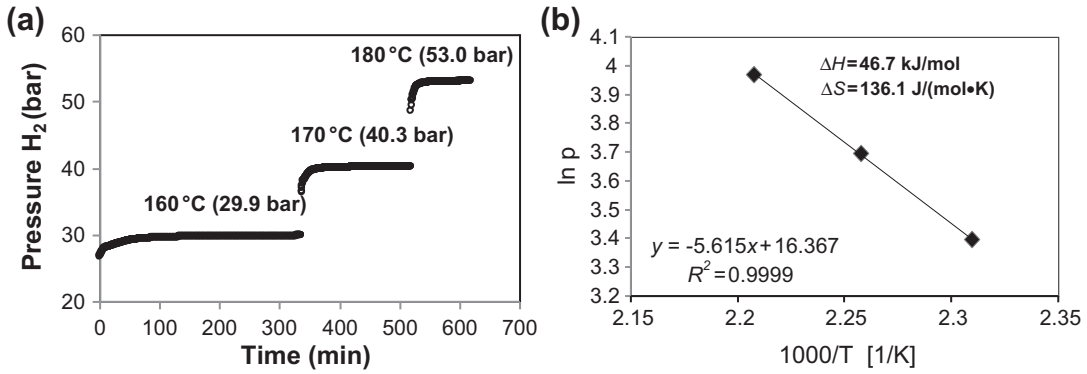

FIGURE 13.33 (a) Step-wise desorption curves at varying temperatures and (b) corresponding Van't Hoff plot for the ($LiNH_2 + 0.7MgH_2$) mixtures milled for 25 h (IMP67-R40) (total milling energy 520 kJ/g). Reaction (13.23).

rehydrogenation because the H_2 capacity of this reaction is slightly less than 4 wt%. Figure 13.32(b) shows that even this amount is not achieved after rehydrogenation (max. 3.2 wt%H_2).

Figure 13.33(a) shows step-wise desorption curves (pseudo-PCT) at varying temperatures and Fig. 13.33(b) shows corresponding Van't Hoff plot for the ($LiNH_2 + 0.7MgH_2$) mixture milled for 25 h (IMP67-R40)(total milling energy 520 kJ/g). The obtained value of ~47 kJ/mol H_2 for the reaction enthalpy change (Reaction (13.23)) is rather low and obviously much lower than that for ($LiNH_2 + n$LiH), as shown in Figs 1(b) and 28(b). It is also much lower than ~75 kJ/mol H_2 for MgH_2.[15] The obtained values of enthalpy/entropy change in Fig. 13.33(b) show that this system has a temperature of around 70 °C at 1 bar H_2 pressure. However, our recent attempts indicate that for the best combination of the molar ratio $n = 0.5$ and premilling of the $LiNH_2$ and MgH_2 constituents before final synthesis with only a short milling time, the mixture is able to desorb at 125 °C under 1 bar H_2 pressure a maximum of about 0.8 wt% H_2.

13.5 SUMMARY

The presented review shows that a substantial progress has been made in fundamental understanding of the thermodynamic and kinetic behavior of various complex hydrides and their composite systems. Unfortunately, no breakthrough has been made that would identify at least one complex hydride system as being reasonably close to commercial development.

From the group of alanates, the most attractive is $LiAlH_4$. With a catalytic additive, e.g. n-Ni or n-Fe, it is capable of discharging 6 wt% within 10 h at 100 °C (Fig. 13.11(b)). Most interestingly, its ability for a slow self-discharge at RT, 40, and 80 °C (Figs 13.12 and 13.17) makes it a pretty attractive candidate for usage in commercial disposable cartridges in application for long-duration, low-demand devices that use H_2 in both civilian and military sectors. Obviously, insufficient H_2 discharge capacity at 100 °C and irreversibility at reasonable combination of temperature and pressure are severe drawbacks for on-road automotive applications of $LiAlH_4$. However, it can be envisaged that by using larger disposable cartridges with catalyzed $LiAlH_4$, it would be feasible to power fuel cells in the off-road vehicles that do not require a substantial driving range and/or on-board reversibility. As recently reported in,[62–64] $LiAlH_4$ decomposed to LiH and Al could be regenerated back to $LiAlH_4$ in dimethyl ether at RT under a relatively low 100 bar H_2 pressure that is a quite mild condition for off-board rehydrogenation. Table 13.3 shows hydrogen flow and energy from hydride storage medium for ball-milled $LiAlH_4$ with 5% n-Ni, n-Fe catalytic additives, or $MnCl_2$ catalytic precursor. Specific usable energy is also compared in Table 13.3 to the DOE 2015 automotive targets and Li-ion batteries. It is clearly seen that at 100 °C, $LiAlH_4$ with n-Ni has very favorable specific usable energy as compared to the DOE target. Obviously, the comparison temperature of 100 °C is still slightly higher than that generated by a PEM fuel cell stack but the n-Ni additive works very well. Near 100 °C $LiAlH_4$ with n-Ni, n-Fe and $MnCl_2$ have even better specific usable energy than a Li-ion battery. The goal here would be to further reduce dehydrogenation temperature to a more usable range of 40–70 °C with the same dehydrogenation kinetics by improving the possibly catalytic behavior of additives. Furthermore, it should be mentioned that the main driver toward better kinetics in the most promising $LiAlH_4$ ternary complex hydride, notwithstanding the use of a catalyst, is a good heat transfer to the active mass. This is perhaps the single overlooked area that deserves better attention to be given from both materials scientists and system designers.

In the group of borohydrides, $LiBH_4$, which has a very high theoretical H_2 capacity regardless of a catalyst used,

TABLE 13.3 Hydrogen Flow and Energy from Hydride Storage Medium of Ball-milled $LiAlH_4$ with 5% n-Ni, n-Fe, or $MnCl_2$ Catalytic Additives (see notes)

Catalytic additive (5 wt%)	Dehydrogenation temperature (°C)	Flow time (min)	Gravimetric discharge capacity (kg H_2/kg)	Storable H_2 volume (SL/kg)	H_2 flow—volume (SL/min/kg)	H_2 flow—gravimetric (g H_2/s/kg)	Power—at this flow from a 70 g-cartridge (W)	Specific energy—usable (kWh/kg)
n-Ni (18 m^2/g)	100	35	0.052	582.4	16.6	0.025	58.1	1.66
n-Ni (9.5 m^2/g)	100	46	0.044	492.8	10.7	0.016	37.4	1.07
n-Ni (9.5 m^2/g)	80	2880	0.046	515.2	0.18	0.000 (10^{-4})	0.6	0.02
n-Ni (9.5 m^2/g)	40	10,080	0.033	369.6	0.04	0.000 (10^{-5})	0.1	0.00 (10^{-3})
n-Fe	100	55	0.047	526.4	9.57	0.014	33.4	0.96
n-Fe	80	4320	0.054	604.8	0.14	0.000 (10^{-4})	0.5	0.01
n-Fe	40	10,080	0.034	380.8	0.38	0.000 (10^{-5})	0.1	0.00 (10^{-3})
$MnCl_2$	140	21	0.044	492.8	23.6	0.04	82.6	2.36
$MnCl_2$	120	54	0.043	481.6	8.91	0.01	31.2	0.89
$MnCl_2$	100	150	0.038	425.6	2.85	0.00 (10^{-3})	9.9	0.28
2015 DOE target								1.80[129]
Li-ion battery (typical)								0.09[130]
Li-ion battery (record)+								0.4[131]

Notes: (1) All data calculated are as per 1 kg powder consisting of reagent grade $LiAlH_4$ milled with 5 wt% n-Ni additive and $MnCl_2$ catalytic precursor for 15 min under high-energy IMP68-4B-R132/R40 mode, and for n-Fe under low-energy LES6-4B and IMP68-2B both R132 (B-number of balls). (2) Flow calculations are from dehydrogenation curves obtained in 1 bar hydrogen pressure. Flow times and gravimetric discharge capacities used in these calculations are from the start of flow to the point it levels up, viz. maximum flow segment. The residual flow from the mostly discharged hydride is neglected. Hence, the flow and energy values are underestimated. The degree to which they are underestimated depends on the shape of the dehydrogenation curves. (3) The specific energy calculations are based on the definition of an ampere (A) and an equivalence of electrons: one equivalence of electrons is 1 g mol of electrons (Avogadro number of electrons) that produces the current charge equaling 96,487 coulombs (C) given by Faraday's constant. With one C/s equal to 1 A (A), this gives us a convenient factor 0.037,605 kg H_2 per kA.[132] (4) The speculative calculations of power to be delivered from a small lithium alanate hydrogen store (70 g) are based on 50% penalty for the weight of an empty cartridge.

has too high temperature of dehydrogenation. However, a $Mn(BH_4)_2$ derivative synthesized by the MCAS with a metathesis reaction is capable of desorbing 4 wt% H_2 at 100 °C in the mixture with a large quantity of LiCl, which is a dead-weight. It simply shows that after extraction of LiCl, this borohydride would be able to desorb the quantity of H_2 close to its theoretical quantity of 9.5 wt% at 100 °C. This value is near a lower limit of H_2 required for a storage material by D.O.E. targets as discussed in the Introduction. After the MCAS with appropriate ball milling parameters and with a catalyst additive, its decomposition occurs with a miniscule.desorption of borane gas (B_2H_6).[106] This hydride needs further vigorous studies, in particular, devoted to its capability of being rehydrogenated at some mild conditions of temperature and pressure or regenerated in a similar manner as $LiAlH_4$.

In the group of lithium amides, the ($LiNH_2$−MgH_2) system is able to dehydrogenate about 1 wt% H_2 at 125 °C, which is rather inadequate quantity for any practical application at that temperature. This system is still unable to desorb larger quantities of H_2 at 125 °C despite that this temperature is 55 °C higher than the theoretical temperature for desorption in 1 bar H_2, which is about 70 °C. This is either a thermodynamic constraint indicating that a further reduction of the reaction enthalpy change is needed or a kinetic constraint indicating that more effective catalysts must be sought for improving the hydrogen storage properties of this particular system.

Acknowledgments

This research was supported by the NSERC Hydrogen Canada (H2CAN) Strategic Research Network and NSERC Discovery grants which are gratefully acknowledged. A technical assistance in collecting some experimental data by Dr M. Jang, a former PhD student under supervision of Prof. Varin, is gratefully acknowledged.

References

1. http://www.oilcrisis.com.
2. Rath, B. B.; Marder, J. M. Does the Fuel Gage Read Empty? *Adv. Mater. Process.* **2007,** *165* (1), 28−29.
3. Ball, M.; Wietschelb, M. The Future of Hydrogen − Opportunities and Challenges. *Int. J. Hydrogen Energy* **2009,** *34,* 615−627.
4. Scott, D. S. *Smelling Land: The Hydrogen Defense Against Climate Catastrophe;* The Canadian Hydrogen Association. www.h2.ca. 2007.
5. Zimmer, R.; Welke, J. Let's Go Green with Hydrogen! The General Public's Perspective. *Int. J. Hydrogen Energy* **2012,** *37,* 17502−17508.
6. Steele, B. C. H.; Heinzel, A. Materials for Fuel-Cell Technologies. *Nature* **2001,** *414,* 345−352.
7. Haile, S. M. Fuel Cell Materials and Components. *Acta. Mater.* **2003,** *51,* 5981−6000.
8. Tüber, K.; Zobel, M.; Schmidt, H.; Hebling, C. A Polymer Electrolyte Membrane Fuel Cell System for Powering Portable Computers. *J. Power Sourc.* **2003,** *122,* 1−8.
9. Scott, D. S. Contrails Against an Azure Sky. *Int. J. Hydrogen Energy* **2004,** *29,* 1317−1325.
10. Yvon, K.; Lorenzoni, J.-L. Hydrogen-Powered Lawn Mower. *Int. J. Hydrogen Energy* **1993,** *18,* 345−348.
11. Yvon, K.; Lorenzoni, J.-L. Hydrogen-Powered Lawn Mower: 14 Years of Operation. *Int. J. Hydrogen Energy* **2006,** *31,* 1763−1767.
12. Andrews, J.; Shabani, B. Re-envisioning the Role of Hydrogen in a Sustainable Energy Economy. *Int. J. Hydrogen Energy* **2012,** *37,* 1184−1203.
13. www.nuvera.com.
14. Dillich, S. D. O. E. *Hydrogen Program 2009 Annual Progress Report; Technical Report for IV.0 Hydrogen Storage Sub-Program Overview;* U.S. Department of Energy: Washington, DC, May 2009.
15. Varin, R. A.; Czujko, T.; Wronski, Z. S. *Nanomaterials for Solid State Hydrogen Storage;* Springer Science & Business Media: New York, NY, USA, 2009.
16. Varin, R. A.; Jang, M. The Effects of Graphite on the Reversible Hydrogen Storage of Nanostructured Lithium Amide and Lithium Hydride ($LiNH_2 + 1.2LiH$) System. *J. Alloys Compd.* **2011,** *509,* 7143−7151.
17. Kojima, Y.; Kawai, Y. IR Characterizations of Lithium Imide and Amide. *J. Alloys Compd.* **2005,** *395,* 236−239.
18. Bogdanović, B.; Sandrock, G. Catalyzed Complex Metal Hydrides. *MRS Bull.* **2002,** *27* (9), 712−716.
19. Orimo, S.-I.; Nakamori, Y.; Eliseo, J. R.; Züttel, A.; Jensen, C. M. Complex Hydrides for Hydrogen Storage. *Chem. Rev.* **2007,** *107,* 4111−4132.
20. Bortz, M.; Bertheville, B.; Yvon, K.; Movlaev, E. A.; Verbetsky, V. N.; Fauth, F. Mg_3MnH_7, Containing the First Known Hexahydridomanganese (I) Complex. *J. Alloys Compd.* **1998,** *279,* L8−L10.
21. George, L.; Saxena, S. K. Structural Stability of Metal Hydrides, Alanates and Borohydrides of Alkali and Alkali- Earth Elements: A Review. *Int. J. Hydrogen Energy* **2010,** *35,* 5454−5470.
22. Bogdanović, B.; Schwickardi, M. Ti-Doped Alkali Metal Aluminium Hydrides as Potential Novel Reversible Hydrogen Storage Materials. *J. Alloys Compd.* **1997,** *253-254,* 1−9.
23. Bogdanović, B.; Schwickardi, M. Ti-Doped $NaAlH_4$ as a Hydrogen-Storage Material − Preparation by Ti-Catalyzed Hydrogenation of Aluminum Powder in Conjunction with Sodium Hydride. *Appl. Phys. A* **2001,** *72,* 221−223.
24. Claudy, P.; Bonnetot, B.; Chahine, G.; Letoffe, J. M. Etude du Comportement Thermique du Tetrahydroaluminate de Sodium $NaAlH_4$ et de L'hexahydroaluminate de Sodium Na_3AlH_6 de 298 a 600 K. *Thermochim. Acta* **1980,** *38,* 75−88.
25. Bogdanović, B.; Brand, R. A.; Marjanović, A.; Schwickardi, M.; Tölle, J. Metal-doped Sodium Aluminium Hydrides as Potential New Hydrogen Storage Materials. *J. Alloys Compd.* **2000,** *302,* 36−58.
26. Bogdanović, B.; Eberle, U.; Felderhoff, M.; Schüth, F. Complex Aluminum Hydrides. *Scripta Mater.* **2007,** *56,* 813−816.
27. Gross, K. J.; Sandrock, G.; Thomas, G. J. Dynamic In Situ X-Ray Diffraction of Catalyzed Alanates. *J. Alloys Compd.* **2002,** *330−322,* 691−695.
28. Bogdanović, B.; Felderhoff, M.; Pommerin, A.; Schüth, F.; Spielkamp, N. Advanced Hydrogen-Storage Materials Based on Sc-, Ce-, and Pr-Doped $NaAlH_4$. *Adv. Mater.* **2006,** *18,* 1198−1201.
29. Wang, J.; Ebner, A. D.; Zidan, R.; Ritter, J. A. Synergistic Effects of Co-dopants on the Dehydrogenation Kinetics of Sodium Aluminum Hydride. *J. Alloys Compd.* **2005,** *391,* 245−255.
30. Xiao, X.; Chen, L.; Wang, X.; Li, S.; Chen, C.; Wang, Q. Reversible Hydrogen Storage Properties and Favorable Co-doping Mechanism of the Metallic Ti and Zr Co-doped Sodium Aluminum Hydride. *Int. J. Hydrogen Energy* **2008,** *33,* 64−73.
31. Schmidt, T.; Röntzsch, L. Reversible Hydrogen Storage in Ti−Zr-Codoped $NaAlH_4$ Under Realistic Operation Conditions. *J. Alloys Compd.* **2010,** *496,* L38−L40.

32. Bogdanović, B.; Felderhoff, M.; Kaskel, S.; Pommerin, A.; Schlichte, K.; Schüth, F. Improved Hydrogen Storage Properties of Ti-Doped Sodium Alanate Using Titanium Nanoparticles as Doping Agents. *Adv. Mater.* **2003,** *15,* 1012−1015.
33. Xueping, Z.; Shenglin, L.; Donglin, L. The Effect of Additives on the Hydrogen Storage Properties of $NaAlH_4$. *Int. J. Hydrogen Energy* **2009,** *34,* 2701−2704.
34. Fan, X.; Xiao, X.; Hou, J.; Zhang, Z.; Liu, Y.; Wu, Z.; Chen, C.; Wang, Q.; Chen, L. Reversible Hydrogen Storage Behaviors and Microstructure of TiC-Doped Sodium Aluminum Hydride. *J. Mater. Sci.* **2009,** *44,* 4700−4704.
35. Zaluska, A.; Zaluski, L.; Ström-Olsen, J. O. Sodium Alanates for Reversible Hydrogen Storage. *J. Alloys Compd.* **2000,** *298,* 125−134.
36. Varin, R. A.; Zbroniec, L. Catalytic Effects of Nanometric Ni (n-Ni) on the Dehydrogenation of Ball Milled Sodium Alanate ($NaAlH_4$). *Nanosci. Nanotechnol. Lett.* **2012,** *4,* 149−159.
37. Block, J.; Gray, A. P. The Thermal Decomposition of Lithium Aluminum Hydride. *Inorg. Chem.* **1965,** *4,* 304−305.
38. Dilts, J. A.; Ashby, E. C. A Study of the Thermal Decomposition of Complex Metal Hydrides. *Inorg. Chem.* **1972,** *11,* 1230−1236.
39. Zaluski, L.; Zaluska, A.; Ström-Olsen, J. O. Hydrogenation Properties of Complex Alkali Metal Hydrides Fabricated by Mechano-Chemical Synthesis. *J. Alloys Compd.* **1999,** *290,* 71−78.
40. CRC Handbook of Chemistry and Physics, 91st Edition 2010−2011, Section 4: Properties of the Elements and Inorganic Compounds (Interactive Table).
41. Sandrock, G.; Gross, K.; Thomas, G. Effect of Ti-Catalyst Content on the Reversible Hydrogen Storage Properties of the Sodium Alanates. *J. Alloys Compd.* **2002,** *339,* 299−308.
42. Sandrock, G.; Gross, K.; Thomas, G.; Jensen, C.; Meeker, D.; Takara, S. Engineering Considerations in the Use of Catalyzed Sodium Alanates for Hydrogen Storage. *J. Alloys Compd.* **2002,** *330−332,* 696−701.
43. Askeland, D. R.; Fulay, P. P.; Wright, W. J. *The Science and Engineering of Materials;* Cengage Learning: Stamford, CT, 2011. pp. 891−892.
44. Graetz, J.; Reilly, J. J. Kinetically Stabilized Hydrogen Storage Materials. *Scripta Mater.* **2007,** *56,* 835−839.
45. Ares, J. R.; Aguey-Zinsou, K-F.; Porcu, M.; Sykes, J. M.; Dornheim, M.; Klassen, T.; Bormann, R. *Mater Res. Bull.* **2008,** *43,* 1263−1275.
46. Løvvik, O. M.; Opalka, S. M.; Brinks, H. W.; Hauback, B. C. Crystal Structure and Thermodynamic Stability of the Lithium Alanates $LiAlH_4$ and Li_3AlH_6. *Phys. Rev. B* **2004,** *69,* 134117-1−134117-9.
47. Brinks, H. W.; Fossdal, A.; Fonneløp, J. E.; Hauback, B. C. Crystal Structure and Stability of $LiAlD_4$ with TiF_3 Additive. *J. Alloys Compd.* **2005,** *397,* 291−295.
48. Mulana, F.; Nishimiya, N. Application of Mechanical Milling to Synthesize a Novel Quarterly Hydride. *J. Alloys Compd.* **2006,** *413,* 273−280.
49. Ke, X.; Chen, C. Thermodynamic Functions and Pressure-Temperature Phase Diagram of Lithium Alanates by *ab initio* Calculations. *Phys. Rev. B* **2007,** *76*, 024112-11.
50. Jang, J. W.; Shim, J. H.; Cho, Y. W.; Lee, B. J. Thermodynamic Calculation of $LiH \leftrightarrow Li_3AlH_6 \leftrightarrow LiAlH_4$ Reactions. *J. Alloys Compd.* **2006,** *420,* 286−290.
51. Ares Fernandez, J. R.; Aguey-Zinsou, K. F.; Elsaesser, M.; Ma, X. Z.; Dornheim, M.; Klassen, T.; Bormann, R. Mechanical and Thermal Decomposition of $LiAlH_4$ with Metal Halides. *Int. J. Hydrogen Energy* **2007,** *32,* 1033−1040.
52. Liu, S. S.; Sun, L. X.; Zhang, Y.; Xu, F.; Zhang, J.; Chu, H. L.; Fan, M. Q.; Zhang, T.; Song, X. Y.; Grolier, J. P. Effect of Ball Milling Time on the Hydrogen Storage Properties of TiF_3-doped $LiAlH_4$. *Int. J. Hydrogen Energy* **2009,** *34,* 8079−8085.
53. Ismail, M.; Zhao, Y.; Yu, X. B.; Dou, S. X. Effects of NbF_5 Addition on the Hydrogen Storage Properties of $LiAlH_4$. *Int. J. Hydrogen Energy* **2010,** *35,* 2361−2367.
54. Gunaydin, H.; Houk, K. N.; Ozolins, V. Vacancy-Mediated Dehydrogenation of Sodium Alanate. *Proc. Natl. Acad. Sci. U S A* **2008,** *105,* 3673−3677.
55. Parker, S. F. Spectroscopy and Bonding in Ternary Metal Hydride Complexes-Potential Hydrogen Storage Materials. *Coord. Chem. Rev.* **2010,** *254,* 215−234.
56. Wilson-Short, G.; Janotti, A.; Hoang, K.; Peles, A.; Van der Walle, C. G. First-Principles Study of the Formation and Migration of native Defects in $NaAlH_4$. *Phys. Rev. B* **2009,** *80,* 224102−224107.
57. Kroger, A. *The Chemistry of Imperfect Crystals;* North-Holland Publ.: Amsterdam, 1964.
58. Wronski, Z. S.; Varin, R. A.; Czujko, T. Mechanochemical Activation and Synthesis of Nanomaterials for Hydrogen Storage and Conversion in Electrochemical Power Sources. *J. Nanosci. Nanotechnol.* **2009,** *9,* 4048−4055.
59. Wronski, Z. S.; Pratt, A. *XPS Analysis and Valence Bands Study of LiAlH4 Hydride During the Early Stages of Hydrogen Discharge on Heating up to 152 °C. Unpublished manuscript;* CanmetENERGY: Ottawa, June 2011.
60. Chen, J., Kuriyama, N., Xu, Q., Takeshita, H.T., Sakai, T. Reversible hydrogen storage via titanium-catalyzed $LiAlH_4$ and Li_3AlH_6. J. Phys. Chem. B, **2001,** 105, 11214−11220.
61. Rafi-ud-din; Lin, Z.; Li, P.; Qu., X. Catalytic Effects of Nano-Sized TiC Additions on the Hydrogen Storage Properties of $LiAlH_4$. *J. Alloys Compd.* **2010,** *508,* 119−128.
62. Liu, X. F.; Sean McGrady, G.; Langmi, H. W.; Jensen, C. M. Facile Cycling of Ti-Doped $LiAlH_4$ for High Performance Hydrogen Storage. *J. Am. Chem. Soc.* **2009,** *131,* 5032−5033.
63. Liu, X. F.; Langmi, H. W.; Beattie, S. D.; Azenwi, F. F.; Sean McGrady, G.; Jensen, C. M. Ti-doped $LiAlH_4$ for Hydrogen Storage: Synthesis, Catalyst Loading, and Cyclic Performance. *J. Am. Chem. Soc.* **2011,** *133,* 15593−15597.
64. Azenwi, F. F.; Langmi, H. W.; Sean McGrady, G. Hydrogenation of LiH/Al catalyzed with TiN, $TiMn_2$ and $LaNi_5$. *Int. J. Hydrogen Energy* **2012,** *37,* 10210−10214.
65. Balema, V. P.; Wiench, J. W.; Dennis, K. W.; Pruski, M.; Pecharsky, V. K. Titanium Catalyzed Solid-State Transformations in $LiAlH_4$ During High-Energy Ball Milling. *J. Alloys Compd.* **2001,** *329,* 108−114.
66. Balema, V. P.; Pecharsky, V. K.; Dennis, K. W. Solid Phase Transformations in $LiAlH_4$ During High-Energy Ball-Milling. *J. Alloys Compd.* **2000,** *313,* 69−74.
67. Sun, T.; Huang, C. K.; Wang, H.; Sun, L. X.; Zhu, M. The Effect of Doping $NiCl_2$ on the Dehydrogenation Properties of $LiAlH_4$. *Int. J. Hydrogen Energy* **2008,** *33,* 6216−6221.
68. Resan, M.; Hampton, M. D.; Lomness, J. K.; Slattery, D. K. Effects of Various Catalysts on Hydrogen Release and Uptake Characteristics of $LiAlH_4$. *Int. J. Hydrogen Energy* **2005,** *30,* 1413−1416.
69. Kojima, Y.; Kawai, Y.; Masumoto, M.; Haga, T. Hydrogen Release of Catalyzed Lithium Aluminum Hydride by a Mechanochemical Reaction. *J. Alloys Compd.* **2008,** *462,* 275−278.
70. Zheng, X.; Li, P.; An, F.; Wang, G.; Qu, X. Effects of Ti and Fe Additives on Hydrogen Release from Lithium Alanate. *Rare Met. Mater. Eng.* **2008,** *37,* 0400−0403.
71. Varin, R. A.; Zbroniec, L. Decomposition Behavior of Unmilled and Ball Milled Lithium Alanate ($LiAlH_4$) Including Long-term Storage and Moisture Effects. *J. Alloys Compd.* **2010,** *504,* 89−101.
72. Varin, R. A.; Zbroniec, L. The Effects of Nanometric Nickel (n-Ni) Catalyst on the Dehydrogenation and Rehydrogenation Behavior of Ball Milled Lithium Alanate ($LiAlH_4$). *J. Alloys Compd.* **2010,** *506,* 928−939.

73. Varin, R. A.; Zbroniec, L.; Czujko, T.; Wronski, Z. S. The Effects of Nanonickel Additive on the Decomposition of Complex Metal Hydride $LiAlH_4$ (lithium alanate). *Int. J. Hydrogen Energy* **2011,** *36,* 1167−1176.
74. Varin, R. A.; Parviz, R. The Effects of the Micrometric and Nanometric iron (Fe) Additives on the Mechanical and Thermal Dehydrogenation of Lithium Alanate ($LiAlH_4$), its Self-Discharge at Low Temperatures and Rehydrogenation. *Int. J. Hydrogen Energy* **2012,** *37,* 9088−9102.
75. Graetz, J.; Reilly, J. J. Nanoscale Energy Storage Materials Produced by Hydrogen-Driven Metallurgical Reactions. *Adv. Eng. Mater.* **2005,** *7,* 597−601.
76. http://webelements.com.
77. Carpenter, G. J. C.; Wronski, Z. S. The Characterization of Nanostructured CVD Ni Powders Using Transmission Electron Microscopy. *J. Nanoparticle Res.* **2004,** *6,* 215−221.
78. Varin, R. A.; Zbroniec, L. Fast and Slow Dehydrogenation of Ball Milled Lithium Alanate ($LiAlH_4$) Catalyzed with Manganese Chloride ($MnCl_2$) as Compared to Nanometric Nickel Catalyst. *J. Alloys Compd.* **2011,** *509S,* S736−S739.
79. Varin, R. A.; Zbroniec, L.; Polanski, M.; Bystrzycki, J. A Review of Recent Advances on the Effects of Microstructural Refinement and Nano-Catalytic Additives on the Hydrogen Storage Properties of Metal and Complex Hydrides. *Energies* **2011,** *4,* 1−25.
80. Varin, R.A., Zbroniec, L. in preparation.
81. Van Loon, C. J. J.; De Jong, J. Some Chlorides with the Inverse Spinel Structure: Li_2TCl_4 (T = Mg, Mn, Fe, Cd). *Acta. Crystallogr. B* **1975,** *31,* 2549−2550.
82. Court-Castagnet, R.; Kaps, Ch.; Cros, C.; Hagenmuller, P. Ionic Conductivity-Enhancement of LiCl by Homogeneous and Heterogeneous Dopings. *Solid State Ionics* **1993,** *61,* 327−334.
83. Robertson, A. D.; West, A. R.; Ritchie, A. G. Review of Crystalline Lithium-Ion Conductors Suitable for High Temperature Battery Applications. *Solid State Ionics* **1997,** *104,* 1−11.
84. Varin, R. A.; Zbroniec, L. Mechanical and Thermal Dehydrogenation of Lithium Alanate ($LiAlH_4$) and Lithium Amide ($LiNH_2$) Hydride Composites. *Crystals* **2012,** *2,* 159−175.
85. Tarasov, V. P.; Bakum, S. I.; Kuznetsova, S. F. NMR Study of Thermal Decomposition of Lithium Tetrahydroaluminate. *Russ. J. Inorg. Chem.* **1997,** *42,* 694−701.
86. Wiench, J. W.; Balema, V. P.; Pecharsky, V. K.; Pruski, M. Solid-State 27 Al NMR Investigation of Thermal Decomposition of $LiAlH_4$. *J. Solid State Chem.* **2004,** *177,* 648−653.
87. Murdakovski, I., Wronski, Z.S. In-situ Heating 27 NMR Experiment of Thermal Dissociation of LiAlH4 in the Temperature Range 22 to173 °C. Unpublished manuscript. CanmetENERGY, Ottawa, September 2011.
88. Wronski, Z. S.; Czujko, T. Nanonickel Catalyst for Kinetic Destabilization of $LiAlH_4$ (Lithium Alanate) for Facile Discharge of Hydrogen. *Adv. Sci. Technol.* **2010,** *72,* 182−187.
89. Züttel, A.; Rentsch, S.; Fischer, P.; Wenger, P.; Sudan, P.; Mauron, Ph.; Emmenegger, Ch. Hydrogen Storage Properties of $LiBH_4$. *J. Alloys Compd.* **2003,** *356−357,* 515−520.
90. Orimo, S.; Nakamori, Y.; Kitahara, G.; Miwa, K.; Ohba, N.; Towata, S.; Züttel, A. Dehydriding and Rehydriding Reactions of $LiBH_4$. *J. Alloys Compd.* **2005,** *404-406,* 427−430.
91. Li, H-W.; Yan, Y.; Orimo, S-I.; Züttel, A.; Jensen, C. M. Recent Progress in Metal Borohydrides for Hydrogen Storage. *Energies* **2011,** *4,* 185−214.
92. Lang, J.; Gerhauser, A.; Filinchuk, Y.; Klassen, T.; Huot, J. Differential Scanning Calorimetry (DSC) and Synchrotron X-ray Diffraction Study of Unmilled and Milled $LiBH_4$: A Partial Release of Hydrogen at Moderate Temperatures. *Crystals* **2012,** *2,* 1−21.
93. Rude, L. H.; Nielsen, T. K.; Ravnsbæk, D. B.; Bösenberger, U.; Ley, M. B.; Richter, Bo; Arnbjerg, L. M.; Dornheim, M.; Filinchuk, Y.; Besenbacher, F.; Jensen, T. R. Tailoring Properties of Borohydrides: A Review. *Phys. Status Solidi* **2011,** *208,* 1754−1773.
94. Xia, G. L.; Guo, Y. H.; Wu, Z.; Yu, X. B. Enhanced Hydrogen Storage Performance of $LiBH_4$-Ni Composite. *J. Alloys Compd.* **2009,** *479,* 545−548.
95. Wellons, M. S.; Berseth, P. A.; Zidan, R. Novel Catalytic Effects of Fullerene for $LiBH_4$ Hydrogen Uptake and Release. *Nanotechnology* **2009,** *20,* 204022 (4 pp.).
96. Zhang, B. J.; Liu, B. H. Hydrogen Desorption from $LiBH_4$ Destabilized by Chlorides of Transition Metal Fe, Co, and Ni. *Int. J. Hydrogen Energy* **2010,** *35,* 7288−7294.
97. Nakamori, Y.; Miwa, K.; Ninomiya, A.; Li, H.-W.; Ohba, N.; Towata, S.; Züttel, A.; Orimo, S. Correlation Between Thermodynamical Stabilities of Metal Borohydrides and Cation Electronegativities: First Principle Calculations and Experiments. *Phys. Rev. B* **2006,** *74,* 045126 1-9.
98. Nakamori, Y.; Li, H.-W.; Kikuchi, K.; Aoki, M.; Miwa, K.; Towata, S.; Orimo, S. Thermodynamical Stabilities of Metal-Borohydrides. *J. Alloys Compd.* **2007,** *446-447,* 296−300.
99. Varin, R. A.; Chiu, Ch.; Wronski, Z. S. Mechano-Chemical Activation Synthesis (MCAS) of Disordered $Mg(BH_4)_2$ Using $NaBH_4$. *J. Alloys Compd.* **2008,** *462,* 201−208.
100. Choudhury, P.; Srinivasan, S. S.; Bhethanabotla, V. R.; Goswami, Y.; McGrath, K.; Stefanakos, E. K. Nano-Ni doped Li-Mn-B-H System as a New Hydrogen Storage Candidate. *Int. J. Hydrogen Energy* **2009,** *34,* 6325−6334.
101. Varin, R. A.; Zbroniec, L. The Effects of Ball Milling and Nanometric Nickel Additive on the Hydrogen Desorption from Lithium Borohydride and Manganese Chloride ($3LiBH_4 + MnCl_2$) Mixture. *Int. J. Hydrogen Energy* **2010,** *35,* 3588−3597.
102. Černý, R.; Penin, N.; Hagemann, H.; Filinchuk, Y. The First Crystallographic and Spectroscopic Characterization of a 3d-Metal Borohydride: $Mn(BH_4)_2$. *J. Phys. Chem. C* **2009,** *113,* 9003−9007.
103. Černý, R.; Penin, N.; D'Anna, V.; Hagemann, H.; Durand, E.; Růžička, J. $Mg_xMn_{(1-x)}(BH_4)_2$ (x = 0−0.8), A Cation Solid Solution in a Bimetallic Borohydride. *Acta Mater.* **2011,** *59,* 5171−5180.
104. Severa, G.; Hagemann, H.; Longhini, M.; Kaminski, J. W.; Wesolowski, T. A.; Jensen, C. M. *J. Phys. Chem. C* **2010,** *114,* 15516−15521.
105. Liu, R.; Reed, D.; Book, D. Decomposition Behaviour of $Mn(BH_4)_2$ Formed by Ball-Milling $LiBH_4$ and $MnCl_2$. *J. Alloys Compd.* **2012,** *515,* 32−38.
106. Varin, R.A., Zbroniec, L., Polanski, M., Filinchuk, Y., Černý, R. Mechano-Chemical Synthesis of Manganese Borohydride ($Mn(BH_4)_2$) and Inverse Cubic spinel (Li_2MnCl_4) in the ($n LiBH_4 + MnCl_2$) ($n = 1$, 2, 3, 5, 9 and 23) Mixtures and their Dehydrogenation Behavior. Int. J. Hydrogen Energy. **2012,** *37,* 16056−16069.
107. Chłopek, K.; Frommen, C.; Léon, A.; Zabara, O.; Fichtner, M. Synthesis and Properties of Magnesium Tetrahydroborate, $Mg(BH_4)_2$. *J. Mater. Chem.* **2007,** *17,* 3496−3503.
108. Varin, R.A., Zbroniec, L. Mechano-Chemical Activation Synthesis of amorphous (disordered) hydride in the sodium borohydride and Manganese chloride ($n NaBH_4 + MnCl_2$; $n = 2$, 3) Hydrogen Storage System and its Dehydrogenation Behavior. in preparation for publication.
109. Shaw, L. L.; Ren, R.; Markmaitree, T.; Osborn, W. Effects of Mechanical Activation on Dehydrogenation of the Lithium Amide and Lithium Hydride System. *J. Alloys Compd.* **2008,** *448,* 263−271.
110. Varin, R. A.; Jang, M.; Polanski, M. The Effects of Ball Milling and Molar Ratio of LiH on the Hydrogen Storage Properties of Nanocrystalline Lithium Amide and Lithium Hydride ($LiNH_2$ + LiH) System. *J. Alloys Compd.* **2010,** *491,* 658−667.

111. Luo, W. ($LiNH_2$−MgH_2): A Viable Hydrogen Storage System. *J. Alloys Compd.* **2004,** *381,* 284−287.
112. Luo, W. Corrigendum to ($LiNH_2$−MgH_2): A Viable Hydrogen Storage System. *J. Alloys Compd.* **2004,** *381,* 284−287. J Alloys Compd 385 (2004) 316.
113. Luo, W.; Rönnebro, E. Towards a Viable Hydrogen Storage System for Transportation Application. *J. Alloys Compd.* **2005,** *404−406,* 392−395.
114. Luo, W.; Sickafoose, S. Thermodynamic and Structural Characterization of the Mg−Li−N−H System. *J. Alloys Compd.* **2006,** *407,* 274−281.
115. Ichikawa, T.; Leng, H. Y.; Isobe, S.; Hanada, N.; Fujii, H. Recent Development on Hydrogen Storage Properties in Metal-N-H Systems. *J. Power Sourc.* **2006,** *159,* 126−131.
116. Chen, Y.; Wang, P.; Liu, C.; Cheng, H.-M. Improved Hydrogen Storage Performance of Li−Mg−N−H Materials by Optimizing Composition and Adding Single-Walled Carbon Nanotubes. *Int. J. Hydrogen Energy* **2007,** *32,* 1262−1268.
117. Lu, J.; Fang, Z. Z.; Choi, Y. J.; Sohn, H. Y. Potential of Binary Lithium Magnesium Nitride for Hydrogen Storage Applications. *J. Phys. Chem. C* **2007,** *111,* 12129−12134.
118. Shahi, R. R.; Yadav, T. P.; Shaz, M. A.; Srivastava, O. N. Effects of Mechanical Milling on Desorption Kinetics and Phase Transformation of $LiNH_2/MgH_2$ Mixture. *Int. J. Hydrogen Energy* **2008,** *33,* 6188−6194.
119. Liu, Y.; Zhong, K.; Gao, M.; Wang, J.; Pan, H.; Wang, Q. Hydrogen Storage in a $LiNH_2$−MgH_2 (1:1) System. *Chem. Mater.* **2008,** *20,* 3521−3527.
120. Liang, C.; Liu, Y.; Luo, K.; Li, B.; Gao, M.; Pan, H.; Wang, Q. Reaction Pathways Determined by Mechanical Milling Process for Dehydrogenation/Hydrogenation of the $LiNH_2/MgH_2$ System. *Chem. Eur. J.* **2010,** *16,* 693−702.
121. Dolotko, O.; Paulson, N.; Pecharsky, V. K. Thermochemical Transformations in $2MNH_2$−$3MgH_2$ Systems (M = Li or Na). *Int. J. Hydrogen Energy* **2010,** *35,* 4562−4568.
122. Pottmaier, D.; Dolci, F.; Orlova, M.; Vaughan, G.; Fichtner, M.; Lohstroh, W.; Baricco, M. Hydrogen Release and Structural Transformations in $LiNH_2$−MgH_2 Systems. *J. Alloys Compd.* **2011,** *509S,* S719−S723.
123. Price, C., Gray, J., Lascola R. Jr., Anton, D.L. The Effects of Halide Modifiers on the Sorption Kinetics of the Li−Mg−N−H System. 2012, 37 2742−2749.
124. Durojaiye, T.; Goudy, A. Desorption Kinetics of Lithium Amide/Magnesium Hydride Systems at Constant Pressure Thermodynamic Driving Forces. *Int. J. Hydrogen Energy* **2012,** *37,* 3298−3304.
125. Luo, W.; Stavila, V.; Klebanoff, L. E. New Insights into the Mechanism of Activation and Hydrogen Absorption of ($2LiNH_2$−MgH_2). *Int. J. Hydrogen Energy* **2012,** *37,* 6646−6652.
126. Alapati, S. V.; Johnson, J. K.; Sholl, D. S. Using First Principles Calculations to Identify New Destabilized Metal Hydride Reactions for Reversible Hydrogen Storage. *Phys. Chem. Chem. Phys.* **2007,** *9,* 1438−1452.
127. Varin, R. A.; Zbroniec, L.; Jang, M. Mechano-Chemical Synthesis of Nanostructured Hydride Composites Based on Li−Al−N−Mg for Solid State Hydrogen Storage. *Eng. Rev.* **2011,** *31,* 111−123.
128. Parviz, R.; Varin, R. A. Combined Effects of the Molar Ratio n in the Lithium Amide-Magnesium Hydride ($LiNH_2 + nMgH_2$) Composite and Ball Milling Energy on its Phase Transformations and Mechanical Dehydrogenation behavior. *Int. J. Hydrogen Energy.* submitted for publication.
129. http://www1.eere.energy.gov/hydrogenandfuelcells/storage/pdfs/targets_onboard_hydro_storage.pdf (DOE targets for onboard storage for light-duty vehicles).
130. Rao, Z.; Wang, Sh. A Review of Power Battery Thermal Energy Management. *Renew. Sustain. Energ. Rev.* **2011,** *15,* 4554−4571.
131. Press Release Envia Systems, Newark CA, 27 February 2012.
132. Hirshenhofer, J. H.; Stauffer, D. B.; Engleman, R. R.; Klett, M. G. *Fuel Cell Handbook*. DOE/FETC-99/1076; U.S. Department of Energy, November 1998.

CHAPTER

14

Electric Conditioning and Efficiency of Hydrogen Production Systems and Their Integration with Renewable Energies

Alfredo Ursúa, Pablo Sanchis, Luis Marroyo

Department of Electrical and Electronic Engineering, Public University of Navarre, Pamplona, Spain

OUTLINE

14.1 Introduction 333

14.2 Power Supplies for Electrolyzers 334
- *14.2.1 Introduction* 334
- *14.2.2 Power Electronic Systems: Fundamentals and Principal Power Converters* 334
- *14.2.3 Conditioning Factors for the Hydrogen Production Systems* 340
- *14.2.4 Electronic Conversion Systems for the Electrolyzer Power Supplies* 340

14.3 Energy Efficiency of Hydrogen Production Systems 344
- *14.3.1 Introduction* 344
- *14.3.2 Water Electrolyzer System for Hydrogen Production* 344
- *14.3.3 Efficiency of the Electrolyzer Based on the Power Supply* 347
- *14.3.4 Overall Efficiency of the Hydrogen Production System* 349

14.4 Renewable Hydrogen Production and Demonstration Projects 351
- *14.4.1 Integration of Hydrogen Production Units with Renewable Energies* 351
- *14.4.2 Demonstration Projects* 353
- *14.4.3 Operation of an Electrolyzer under Different Solar Operating Conditions* 354

14.5 Conclusions 357

Acknowledgments 358

References 358

14.1 INTRODUCTION

Traditionally, electrolyzer manufacturers have designed their equipment to cover a wide range of industrial applications such as ammonia and methanol production, the desulfurization of petroleum products, the generation of protective atmospheres for the production of steel, glass and electronic devices (semiconductors, photovoltaic cells, optics, etc.), the hydrogenation of fats and oils, and the cooling of high-capacity power generators. In these operating environments, alkaline electrolyzers are considered to be a mature technology, characterized as being grid-connected and for producing a stable hydrogen supply in the range established for each electrolysis unit. Despite the fact that electrolysis accounts for a very small percentage of the worldwide production of hydrogen, this production method is now arousing considerable interest for future developments, primarily due to the possibility of integrating it with renewable energies to create a sustainable and environmentally friendly source of fuel.

The cost of hydrogen produced by water electrolysis is primarily related to the cost of the electricity consumed. This can account for as much as 70–90% of the total electrolyzer-operating costs. Over the last few years, much headway has been made in the design of alkaline electrolyzers, directed at improving the overall energy efficiency whilst reducing energy consumption. These new innovations have focused on factors such as the development of new configurations for the electrolysis module, the improvement in electrode efficiency with new materials, shapes and designs, the improvement of the diaphragm properties, etc. However, few significant studies have been made on the relevance of the power supply on the overall efficiency of the hydrogen production system. Neither do the electrolyzer manufacturers nor the investigators have any clear and common criteria with regard to the most suitable power supply typology for delivering power to the electrolyzer.

The integration of renewable energy-based sources in hydrogen production systems places new demands on electrolyzers, not only relating to the study and analysis of their performance, but also with regard to the electrical requirements involved in the integration and also to the improvement of the energy efficiency of the complete system.

This chapter aims to describe the principal power electronic systems used to deliver power to alkaline electrolyzers, to analyze the impact of these power supplies on the energy efficiency of the electrolyzers, and to study how to integrate hydrogen production systems into renewable energy-based systems.

In particular, Section 14.2 presents the principal power electronic systems used to power the hydrogen production systems. After providing a generic description of the fundamentals of power electronics and the principal power electronic converters, the section goes on to discuss the specific conditioning factors governing the electrolytic systems and to study the electronic configurations most widely used in power supplies to electrolyzers, highlighting their advantages and drawbacks.

Based on a real system, Section 14.3 aims to demonstrate the influence of the power supply typology on the energy efficiency of the hydrogen production system as a whole. Following an in-depth description of an actual system, a study is made of the influence of the power supply typology on the system, by first looking at how the electric power profile supplied to the electrolyzer influences the energy efficiency and consumption of the electrolytic process. This electric power profile depends on the power supply used and, more specifically, on its electronic conversion topology, its current and voltage control, and the corresponding harmonic filters at the conversion stage output. Secondly, a study is made of the actual efficiency of the power supplies analyzed, leading on to the calculation of the overall efficiency for the system. The results obtained for both studies serve as a guide for the selection of the most appropriate power supply to maximize the energy efficiency of the entire hydrogen production system.

Finally, Section 14.4 focuses on the integration of electrolysis systems into renewable energy-based systems. Firstly, a description is given of the principal configurations possible for this integration, for grid-connected and stand-alone systems alike, with mention of the most representative demonstration projects. The section then goes on to analyze the integration potential of an actual electrolysis system into a photovoltaic system. By emulating real photovoltaic profiles, the performance of the hydrogen production system described in Section 14.3 is studied with a view to evaluating its performance and its potential for technological integration with the photovoltaic system.

14.2 POWER SUPPLIES FOR ELECTROLYZERS

14.2.1 Introduction

This section focuses on the power electronic systems used to transfer power to electrolyzers. It first discusses the fundamentals of power electronics and explains the main types of power converters used for medium- and high-power dc loads, such as the hydrogen production systems. These systems offer a series of characteristic conditioning factors, which will be discussed later on. Finally, an analysis is made of the principal conversion structures used in commercial electrolyzers as well as the different proposals that have been made at a research level and validated theoretically and experimentally.

14.2.2 Power Electronic Systems: Fundamentals and Principal Power Converters

A power electronic system, also termed a power electronic processor, makes it possible to exchange energy between two electrical systems of different characteristics, by conditioning and controlling the energy flow between these systems. As shown in Fig. 14.1, a power electronic system comprises basically a power conversion stage, which is connected between the input and the output electrical systems, and a control stage, which measures the electric variables of the system and sends suitable control signals to the conversion stage in order to make these variables, and therefore the power flow between the input and the output tracks the references previously defined. Although the fundamentals of power electronics are given in this subsection, there

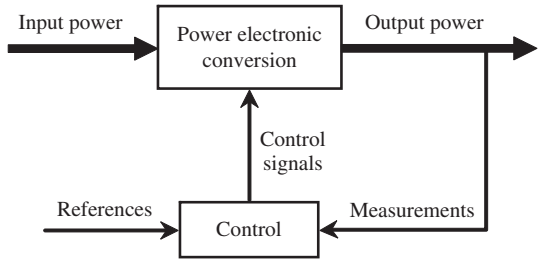

FIGURE 14.1 General scheme of a power electronic system.

are many academic and scientific books on this subject where more in-depth information can be found.[1–5]

The devices forming part of a power electronic system are called power electronic converters. Power electronic systems can include one or several electronic converters. When there is more than one electronic converter, then these are interconnected through passive components. Due to their high-performance qualities and wide range of rated powers, power converters are used today in many different applications, not only at an industrial level, but also in renewable energy systems and in household applications. Furthermore, power converters are an essential part of electric vehicle technology.

Normally, the actual electric grid is one of the two systems exchanging energy through the power electronic system, whilst the other system could be an electric load or an electricity generating system (typically photovoltaic or wind power). In the first case, the energy flow is established from the grid to the load, whilst the flow is reversed in the second case. There are also applications in which the energy flow is reversible depending on the operating conditions. The flow of electricity is controlled through regulation schemes that compare the electrical quantities of the power converter with the references imposed on it, in order to either reduce or eliminate the error and thereby obtain the desired electrical energy profile.

In order to achieve maximum performance, power converters use power semiconductors that act as electronic switches with a controlled on–off sequence in order to adapt the electrical quantities (voltage and current) to the desired reference values. Likewise, the semiconductors include coils and capacitors, in other words, passive energy-storage components that do not consume real power and which are used to filter the waveforms generated by the semiconductors.

Based on the type of input and output systems used for the energy exchange, the electronic power converters can be classified as follows:

- ac–dc power converters: These converters, also known as rectifiers, serve to convert an ac input into a dc output. They are generally used to transfer energy from an ac electric grid in order to supply power to dc loads. Electrolyzers are an example of this. This type of converter is also used as a first conversion stage in more complex electronic systems.
- dc–ac power converters: These converters, which are also termed inverters, transfer energy between a dc power supply and an ac output. Grid-connected photovoltaic systems are an example of this, whereby the dc energy generated by the PV modules needs to be converted to ac for delivery to the grid.
- dc–dc power converters: These converters transfer energy between two dc systems with different values.
- ac–ac power converters: These converters make it possible to transfer energy between two ac systems of a different amplitude and frequency.

As already mentioned, the converters indicated above may form part of conversion systems configured through a number of stages. The most common example can be seen in the ac–ac conversion systems, which can be based on an ac–dc and dc–ac converter combination.

Power semiconductors, also called power static switches, constitute the most important elements of a power converter and are largely responsible for determining its performance qualities. They are made from silicon substrates with different layers doped with P and N type materials (PN junctions). Switches are now also being developed based on SiC.

In order to achieve maximum efficiency, the operation of a power switch must be as close as possible to that of an ideal switch. The performance qualities of the semiconductor are determined by its operating states and its degree of controllability. There are four possible switch-operating states, two being static while the other two are dynamic. The first two are the on- and off-states, in which the switch is respectively closed (i.e. short-circuited) or open (i.e. in an open circuit). The dynamic states are the turn-on and turn-off states and represent the transition between the on- and off-states.

Losses in a power converter are primarily due to the operation of the semiconductors and to the internal resistance of the passive components, namely the inductors and capacitors. The semiconductor power losses are associated with the different operating states: off, on, turn-on and turn-off. Unlike the on-state losses, the off-state losses are generally considered to be negligible. On the other hand, the turn-on and turn-off power losses, also termed switching power losses, may be considerable, depending on the converter switching frequency.

With regard to the degree of controllability, semiconductors can be divided into three broad groups: uncontrollable (such as diodes); semicontrollable with a turn-on control (such as thyristors); and fully controllable with a turn-on and turn-off control (such as metal oxide field effect transistor (MOSFET), insulated gate bipolar transistor (IGBT), and gate turn-off thyristor (GTO). Figure 14.2 shows the symbols commonly used

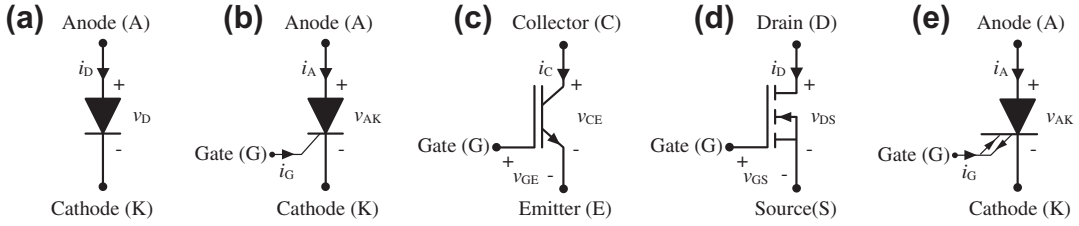

FIGURE 14.2 Main semiconductors: (a) diode, (b) thyristor, (c) IGBT, (d) MOSFET, and (e) GTO.

for the semiconductors mentioned as well as the names of their terminals.

Diodes are the simplest of all semiconductor devices. A diode begins conducting current i_D only if voltage v_D between anode and cathode exceeds a certain threshold voltage in the forward direction (a state in which the diode is said to be forward biased). When the diode is reverse biased, current i_D is virtually zero. Diodes form part of the great majority of power converters, either alone or connected in antiparallel to other semiconductors.

Thyristors are semiconductors that have large current-handling capability and low on-state losses, and that commutate at low frequencies. They can be switched on by applying a pulse of positive gate current i_G for a short duration provided that the device is forward biased. Once the thyristor begins to conduct, it behaves like a diode. It cannot be turned off by the gate and only when the anode i_A current tries to go negative, it turns off and the current goes to zero.

The IGBT is becoming the most important semiconductor for medium and large powers, and is the device of choice in most new applications. The device conducts the current i_C and approximates a closed switch when the gate-emitter voltage (v_{GE}) is above a threshold value, and requires the continuous application of this voltage v_{GE} to remain in the on-state with a small on-state voltage v_{CE}. When v_{GE} goes down below the threshold voltage, the device turns off and blocks the current i_C. Although they also have large current-handling capability, IGBTs do not achieve currents as high as those of the thyristors, but due to the fact that they have a turn-on and turn-off control, with switching times of the order of 1 μs, they can commutate at much higher frequencies, up to several kHz for applications ranging from medium power up to some MW. As a consequence, IGBT-based converters have higher switching losses but generate much lower harmonics at higher frequencies than those based on thyristors.

The turn-on and turn-off of MOSFETs are similar to those of IGBTs. As long as the voltage v_{GS} remains greater than a threshold value, the device is on; otherwise, it turns off and blocks the current i_D. In comparison with IGBTs, MOSFETs can be turned on and turned off much faster, but their on-state conduction losses are larger, especially in devices rated for higher blocking voltages (up to some hundreds volts). Therefore, they can operate at very high frequencies, higher than those of IGBTs, but with considerably lower current and power-handling capabilities.

Finally, the GTO is a thyristor that has been modified to make it possible to control it also at the turn-off. Like thyristors, GTOs can handle high currents and have low on-state losses, but on the contrary they can operate at higher frequencies thanks to their higher degree of controllability. Compared to IGBTs, the switching frequencies that can reach GTOs are not so high and the turn-on and turn-off are more complicated. Due to this and to the constant improvements in the commercial IGBTs, particularly with regard to the current and power-handling capability, IGBTs are gaining more and more ground on GTOs.

Power switches basically have two switching modes: forced commutation and natural commutation. Forced commutation is a controlled switching that is possible only for those switches having a control terminal. When turned on, the current increases and the voltage decreases, whilst the reverse happens when turned off. This joint presence of voltage and current during the commutation process generates switching losses that limit the converter switching frequency. Forced commutation is common in semiconductors such as MOSFET, IGBT and GTO. On the other hand, natural commutation, characteristic of diodes and thyristors, solely depends on the external circuit. In this switching process, the current (or voltage) is naturally canceled before the voltage (or current) starts to increase, leading to minimal switching losses.

Depending on the switch used, and on the type of commutation in particular, power converters can generically be divided into three broad groups: line frequency converters, switching converters, and resonant (and quasi-resonant) converters. The first group comprises those converters in which the semiconductors (diodes and thyristors) switch on and switch off naturally at the utility line frequency of 50 or 60 Hz. Whilst the switching converters comprise semiconductors with forced commutation, in other words, they are controlled at the turn-on and turn-off. This is the case of the IGBT and MOSFET. These devices are turned on and turned

off at frequencies that are far higher than the line frequency (up to tens of kilohertz), making it possible to considerably reduce the size of the filtering elements and the voltage and current harmonics. Finally, the third group is formed by resonant electronic converters in which controlled semiconductors are switched at zero voltage or current. The main advantage is that the switching losses are practically nonexistent, making it possible to reach high switching frequencies. However, the voltage and current resonant peaks may also be high, requiring semiconductors of a larger size.

With regard to the electronic converter configuration, there are many different power electronic conversion topologies to implement the conversion options (ac−dc, dc−dc, dc−ac and ac−ac). As water electrolyzers for hydrogen production are a dc load, these must be powered from either dc−dc or ac−dc converters. The principal topologies associated with both types of converter are detailed below.

As already mentioned, the dc−dc converters, often also termed switching dc power supplies, make it possible to supply a constant, controlled voltage to dc loads from a dc power supply that is either unsuited to the load or whose amplitude is uncontrolled. These converters provide a high-quality voltage supply. Furthermore, they generally use semiconductors with controlled turn-on and turn-off, together with diodes. Depending on the structure, they may include a transformer to provide galvanic isolation between the input supply and the output voltage. In these cases, the transformer is usually powered with high-frequency waves, making it possible to reduce its size and cost whilst increasing performance.

The principal non-insulated dc−dc converters are the buck (also termed step-down), the boost (also known as step-up) and the buck-boost (also termed step-down/step-up). The first one, which is described in detail below, is shown in Fig. 14.3, while the boost and buck-boost converters are shown in Fig. 14.4. In the graphs of the pictures that are shown along this section, v_i and i_i are, respectively, the input voltage and current, and v_o and i_o are the output voltage and current. The buck converter generates a controlled dc voltage that is lower than the input voltage, while the boost makes it possible to obtain an output voltage that is greater than the input voltage. Finally, the buck-boost generates an output dc voltage that can be either greater or less than the input voltage.

The operation of the buck converter is described now, in simple terms, as a representative example of the operation of the switched-mode converters. Figure 14.3a shows the general diagram for this type of converter, where S_1 and S_2 represent the power switches (the set of which is termed the commutation cell), v_s is the switched voltage at terminals S_2, and L and C are the inductor and capacitor, respectively. The choice of the type of semiconductor for the power switches depends on the converter operation. If it is assumed that the power flows solely from the input to the output, then the S_1 switch must be of the fully controllable type (for example IGBT), whilst for S_2 it is sufficient to have a diode. This is the case of the diagram shown in Fig. 14.3b, and also of the diagrams for the boost and buck-boost shown in Fig. 14.4. On the contrary, if the converter is to have a reversible power flow so that it can also flow from the output to the input, then both switches must allow the current to flow in both directions, and therefore both switches must be configured as a fully controllable switch together with an antiparallel diode.

For each switching period, switches S_1 and S_2 switch complementarily. Therefore, when S_1 is closed and S_2 is open, voltage v_s is equal to input voltage v_i. In contrast, when S_1 is open and S_2 is closed, voltage v_s is zero. In this way, voltage v_s is configured as a switched voltage at a frequency that is equal to the switching frequency and with a ratio between the pulse duration (t_{on}) and the switching period T_s that is constant and that is defined as the operating cycle D of the switching cell. Logically, the operating cycle always has values between 0 and 1. The coil (L) and the capacitor (C) filter the voltage v_s so that the output voltage v_o finally obtained is the mean value of v_s with a certain ripple that is practically negligible compared to the said mean value. At

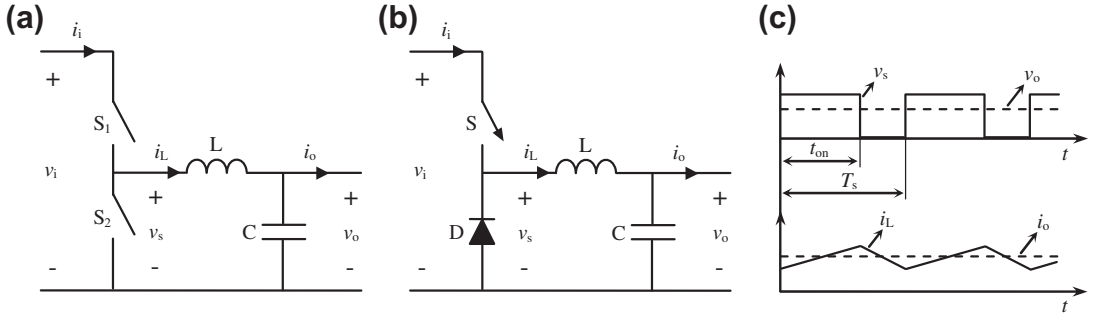

FIGURE 14.3 Buck dc−dc converter: (a) general configuration, (b) unidirectional configuration, and (c) main waveforms.

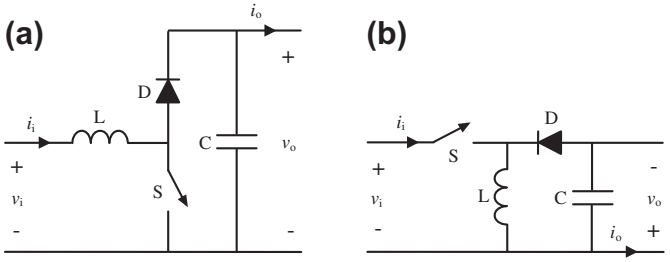

FIGURE 14.4 (a) Boost and (b) buck-boost dc–dc converters.

steady state, this resulting voltage is related to the input voltage through the operating cycle:

$$v_o = D\, v_i \tag{14.1}$$

For its part, the current through the coil i_L can be considered to be the sum of a mean value (equal to the output current i_o) and a ripple flowing through the capacitor. This ripple is a function of the actual inductor of the input voltage value and of the switching frequency. At steady state, the ratio between the input and output currents is inverse to that for the voltages:

$$i_o = \frac{1}{D} i_i \tag{14.2}$$

The dc–dc conversion topologies with isolation are necessary when galvanic isolation is required between the input and the output. In turn, the transformer winding-turns ratio offers greater versatility in the selection of input and output voltage ranges and the use of transformers with multiple windings offers the possibility of multiple output voltages. The principal dc–dc conversion topologies with isolation for medium and larger powers are the half and full-bridges and, to a lesser extent, the push-pull. The three of them are shown in Fig. 14.5. The choice of the converter depends on the specific application. The push-pull is generally used for lower power ratings than the other two. The full-bridge is more complicated than the half-bridge and requires more switches. On the other hand, it delivers an output power that is twice the power delivered by the half-bridge, with the same requirements of maximum voltage and current. Therefore, in large power ratings, it may be advantageous to use a full-bridge over a half-bridge converter. In addition, the push-pull can be of interest in low-voltage applications.

The ac–dc converters, commonly termed rectifiers, make it possible to supply dc power from an ac input. Based on the type of ac input, they can be either single or three-phase. Single-phase converters are used for low power outputs, up to approximately 5 kW, while the three-phase converters are used for higher power outputs. The ac input is typically the electric grid, although it may also be an electric generator in the case of stand-alone systems. In turn, a transformer may be included at the input, in order to condition the voltage values to others that are better suited to the

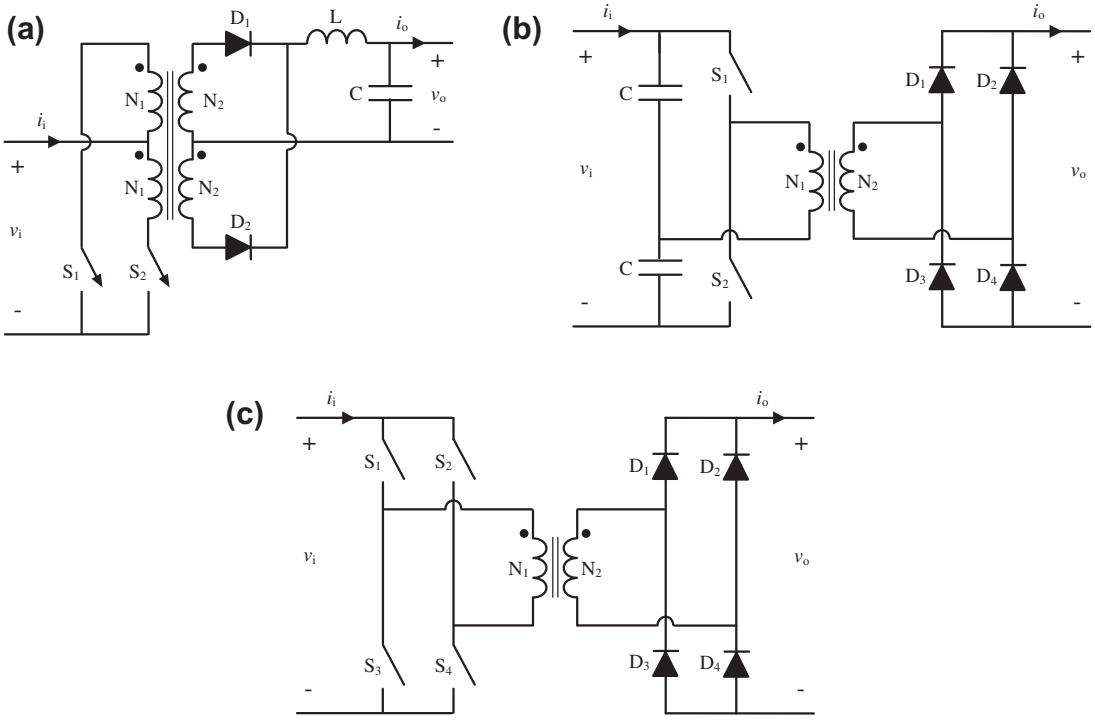

FIGURE 14.5 dc–dc converters with isolation: (a) push-pull, (b) half-bridge, and (c) full-bridge.

subsequent conversion stages. This transformer is of low frequency, being connected to the 50 or 60 Hz ac source.

There are two broad groups of ac–dc converters: natural commutation converters and forced commutation converters. Based on the degree of controllability of the semiconductor used, the naturally commutating converters can, in turn, be divided into two subgroups: uncontrolled and controlled rectifiers. Uncontrolled rectifiers use only diodes and generate an uncontrolled dc output voltage. It is not possible to reverse either the voltage or the current and, therefore, the power flow is unidirectional. Figure 14.6 shows the diagram for a three-phase full-bridge diode rectifier. The output voltage v_o is a dc voltage but with a considerable ripple, in this case six times the frequency of the input ac voltage. Assuming a continuous conduction mode, the mean value of this voltage (V_o) is also constant and depends on the root mean square (rms) value of line-to-line ac voltage V_{LL}:

$$V_o = \frac{3}{\pi}\sqrt{2}\,V_{LL} \tag{14.3}$$

The controlled rectifiers are based on thyristors. This allows them to generate a controlled dc output voltage, as it is possible to control the turn-on time through what is termed the delay or firing angle α. In turn, this makes it possible to reverse the direction of the voltage (and therefore the power flow). Figure 14.7 shows the diagram for a full-bridge thyristor rectifier. Assuming a continuous conduction mode, the delay angle α determines the mean output voltage value V_o based on the rms value of line-to-line ac voltage V_{LL}:

$$V_o = \frac{3\sqrt{2}}{\pi}V_{LL}\cos\ \alpha \tag{14.4}$$

For delay angles of less than 90°, the mean output voltage is positive and the converter delivers power to the load. On the contrary, for greater values, the mean voltage becomes negative and the converter starts to absorb mean power from the dc side.

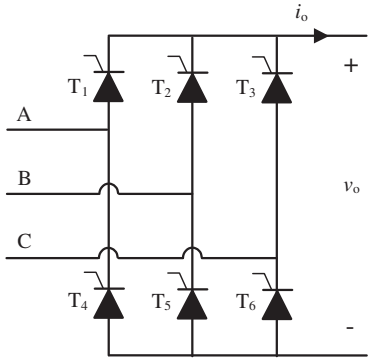

FIGURE 14.7 Three-phase full-bridge thyristor rectifier.

The semicontrolled rectifiers are an intermediate alternative, employing thyristors and diodes. These rectifiers make it possible to generate a controlled dc output voltage that is always greater than zero, in other words the voltage and, therefore, the power flow are not reversible.

The forced commutation ac–dc rectifiers make it possible to obtain a controlled dc voltage from an ac source. The voltage and current are reversible on the ac side, and it is therefore possible to reverse the power flow. This allows them to also operate as dc–ac inverters. They are widely used, principally operating as an inverter, in renewable electricity generating systems and in industrial applications, particularly in electrical drives. For these converters, the switches used are antiparallel-connected fully controllable semiconductors (mainly IGBTs) and diodes. Figure 14.8 shows a three-phase IGBT-based rectifier. Thanks to the control of the ac input current, these converters can establish any phase angle between this current and the ac voltage, allowing them to behave as rectifiers with a unit power factor. In their normal configuration, the dc output voltage must be higher than the ac input voltage peak. For loads requiring low dc voltages, it will therefore be necessary to include an additional subsequent dc–dc conversion stage, in order to adapt

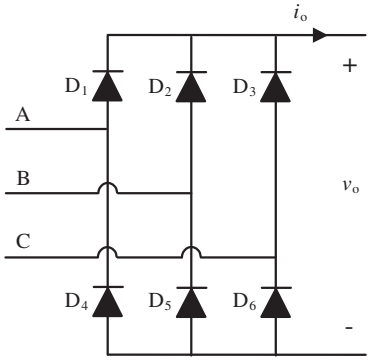

FIGURE 14.6 Three-phase full-bridge diode rectifier.

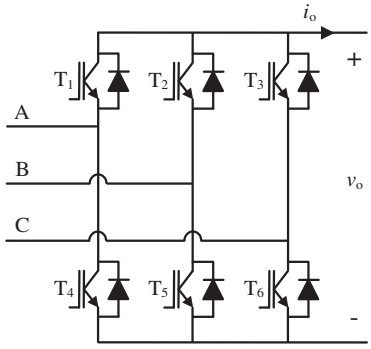

FIGURE 14.8 Three-phase IGBT-based rectifier.

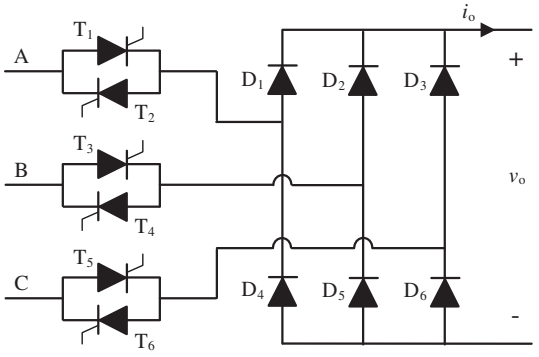

FIGURE 14.9 ac–dc conversion structure with a three-phase ac–ac voltage controller and a diode rectifier.

the dc voltage generated by the ac–dc rectifier to the values demanded by the load.

In addition to the converters described above, there is an ac–dc conversion structure that is of particular interest for powering considerable dc loads, such as large electrolyzers. This structure, shown in Fig. 14.9, comprises an initial ac–ac stage and a second ac-dc stage. The first stage is an ac–ac converter termed an ac–ac voltage controller. The second stage is a diode rectifier, as analyzed above. The ac–ac voltage controller is a converter that includes two antiparallel-connected thyristors in each ac line. By controlling the firing angle of the thyristors, an ac output voltage is generated whose rms value is proportional to the said angle. By contrast, the frequency remains the same as for the ac input voltage. It is therefore possible to obtain a variable ac output voltage from a fixed ac input voltage. This type of converter is generally used for the speed control of large induction motors, particularly at start-up. It is also used as a reactive power regulator in electric grids, as well as in heating and lighting systems. The second stage, comprising a three-phase diode bridge, makes it possible to rectify the ac voltage generated by the ac–ac voltage controller. Therefore, the dc voltage finally achieved at the output of the structure can be controlled through the ac–ac voltage controller firing angle.

14.2.3 Conditioning Factors for the Hydrogen Production Systems

Before selecting or designing a power electronic system for a specific load, it is first necessary to determine the load characteristics and, in particular, the conditioning factors imposed by the load on the power system. Due to the fact that hydrogen production systems are characterized by being dc loads that require high currents and low voltages, they are not of a conventional load for power electronic systems, both with regard to the dc energy demand profile and the required voltage and current values.

Despite the fact that electronic converters are designed for a wide range of power outputs, voltages, and currents, they are generally used for applications characterized by high voltages and low currents, such as electrical drives in the industrial sector. In turn, the electrical drives, which were initially in dc, are now mainly in ac. On the other hand, although there are a great number of applications in other fields requiring a dc supply, such as computing equipment, electronic devices, etc., their powers are far lower than those required by electrolyzers, and their current and voltage characteristics also differ considerably.

Due to these conditioning factors, a large proportion of the power electronics designed for hydrogen production systems is based on thyristors and diodes, as will be seen in the next subsection. Thyristors are semiconductor devices that can withstand high current levels and which are generally employed in medium- and high-powered dc electrical drives. In turn, thyristor-based converters generally require less passive components, leading to reduced cost and weight and improved efficiency. However, these converters are generally associated with a high rate of harmonic distortion. Given the fact that, without considering the losses, the hydrogen produced in the electrolyzers is directly proportional to the mean current supplied, the current harmonics make no contribution to the generation of more hydrogen. On the contrary, they cause a loss of efficiency that can become significant, as will be analyzed in Section 14.3. Likewise, these converters can inject excessive levels of harmonics into the electric grid they are connected to, which has also to be taken into account.

Another important factor in the hydrogen production systems is the earthing of the metal parts in order to avoid the risk of electrical discharges and the danger of explosions. If the live parts are earthed, then the electronic conversion system must include a galvanic isolation stage to isolate the hydrogen production system from the electric grid or input voltage.

All these conditioning factors must be taken into account when designing the power electronic system to power the electrolyzer.

14.2.4 Electronic Conversion Systems for the Electrolyzer Power Supplies

The dc electric current, required to ensure that the electrolysis process is correctly carried out, is generally supplied to the electrolyzer by an electric power supply. This section analyzes the various electronic conversion systems for the power supplies used for the production of hydrogen, at both a commercial and a research level. Some of these conversion structures are used to power electrolyzers from the electric grid, whilst others are

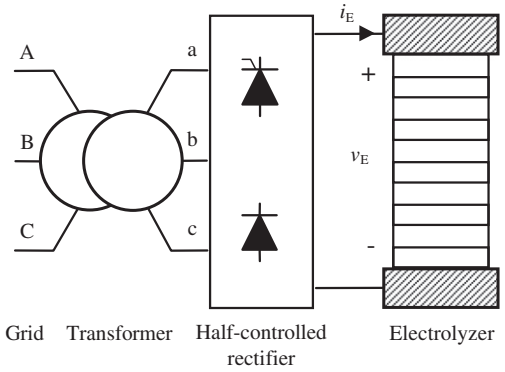

FIGURE 14.10 Electrolyzer power supply characteristic of the LFPS group: ac−dc conversion structure comprising a transformer and a three-phase half-controlled rectifier with thyristors and diodes.

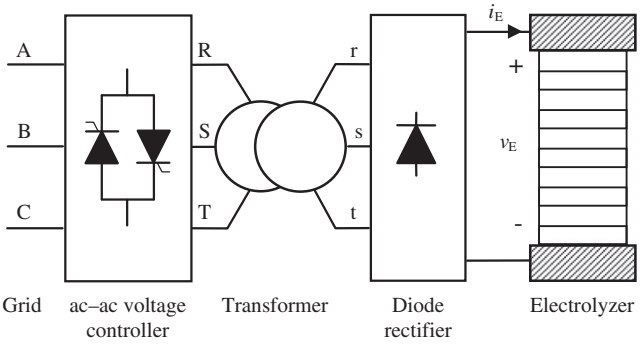

FIGURE 14.11 Electrolyzer power supply characteristic of the LFPS group: ac−dc conversion structure comprising a three-phase ac−ac voltage controller, a transformer, and three-phase diode rectifier.

based on renewable energy sources, such as solar and wind powers. Section 14.4 discusses in detail the integration of electrolyzers and renewable energies at an energy level, whilst this section focuses on the electronic conversion structures.

As indicated in Section 14.2.2, converters can be divided into three broad groups, based on whether the commutation is natural, forced, or through resonant circuits. Based on this classification, the electrolyzer power supplies can be classified in a similar way. Thus, the power supplies configured from line frequency converters shall from now onwards be termed LFPS (line frequency power supply). While those power supplies that include switching converters shall be identified as SPS (switching power supply). Finally, the supplies based on resonant converters shall be called RPS (resonant power supply).

With regard to conventional hydrogen production applications, the electrolysis units are generally operated through a connection to the electric grid, in other words with a 50 or 60 Hz ac current. The rectification of the grid voltages and currents to dc values suitable for the production of hydrogen in large electrolysis units is generally performed with LFPS sources. Figures 14.10 and 14.11 show two electrolyzer power supplies that are characteristic of this type. In these figures, as well as in the figures that will be shown below, v_E and i_E are the voltage and current supplied to the electrolyzer. The power units shown in Figs 14.10 and 14.11, or similar ones, are used by the leading electrolyzer manufacturers, such as Hydrogenics,[6] NEL Hydrogen,[7] Industrie Haute Technologie,[8] and Acca-Gen.[9] Figure 14.10 shows a power supply comprising a three-phase transformer and a half-controlled bridge rectifier, with thyristors at the top and diodes at the bottom, to convert the grid ac current into a suitable dc current to produce the desired hydrogen flow. On the other hand, Fig. 14.11 shows a power supply comprising a thyristor three-phase ac−ac voltage controller, a three-phase transformer connected to the voltage controller output, and a diode bridge rectifier which, based on the transformer ac current, provides a dc current whose value can be controlled through the firing of the voltage controller thyristors. In this way, the power source has control over the hydrogen production. This structure, already discussed in Section 14.2.2, is widely used in high-power electrolysis units. The function of the transformer in the structures shown in Figs 14.10 and 14.11 is, on the one hand, to galvanically isolate the electric grid from the electrolyzer and, on the other hand, to considerably reduce the grid voltages to adequate values for rectification and subsequent supply to the electrolyzer.

The LFPS-type power supplies comprise converters switching at grid frequency (50 or 60 Hz), leading to the introduction of a high harmonic content in the electric grid and in the power supplied to the electrolyzer. Specifically, the current and voltage supplied to the electrolyzer by these sources contain harmonics with a high amplitude and low frequency. In principle, the use of a filtering stage located at the conversion stage output could be considered as a solution for mitigating the harmonic distortion delivered to the electrolyzer. However, the filtering of low-frequency, high-amplitude harmonics entails considerable drawbacks, implying the use of large, heavy, and costly filters and, therefore, this use is generally ruled out.

Despite the fact that the LFPS power supplies are the most widely used for the production of hydrogen with grid-connected electrolyzers, power supplies of the SPS-type are also used, although, in this case, to supply electrolysis units requiring less power.[10–12] Figure 14.12 shows a power supply from the SPS group, formed by a three-phase transformer, a three-phase diode rectifier, and an IGBT-based buck dc−dc converter. The transformer galvanically isolates the grid from the electrolyzer and steps down the voltage; the diode rectifier provides a dc voltage and current at its output; and,

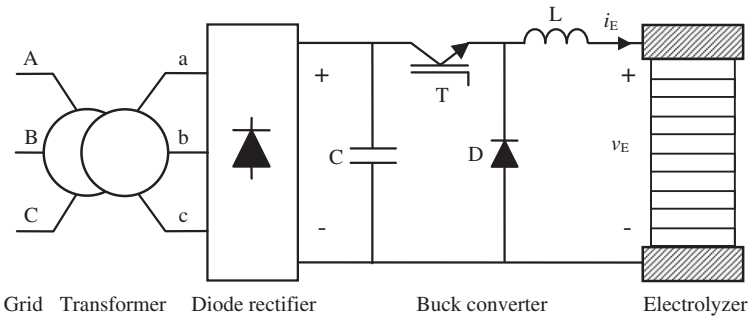

FIGURE 14.12 Electrolyzer power supply characteristic of the SPS group: ac–dc conversion structure formed by a transformer, a three-phase diode rectifier, and a buck converter.

finally, the buck converter is responsible for supplying a controlled electric current to the electrolyzer in order to produce the hydrogen desired at each moment in time. When this power source is used for electrolysis units of less than around 5 kW, then the transformer and, therefore, the rectifier, are single-phase instead of three-phase. Depending on the voltage and current levels, it is possible to replace the IGBT with MOSFET as the controlled power switch.

Figure 14.13 shows another conversion structure, namely an SPS-type power supply to power the electrolyzer from the electric grid. The power unit comprises a three-phase diode rectifier to provide the dc voltage to an IGBT-based three-phase inverter. This inverter generates a high-frequency, three-phase pseudo-sinusoidal voltage, whose level is dependent on the hydrogen flow desired. Subsequently, a high-frequency transformer reduces the voltage amplitude and a second diode rectifier bridge, with the aid of a filtering stage, finally generates an appropriate dc voltage and current for the electrolyzer.

Over the last few years, considerable interest has been aroused in the study and analysis of the integration of electrolyzers into renewable energy generating systems. The power supply to these electrolyzers is primarily made through SPS-type power supplies. The studies conducted, to date, range from solely theoretical or simulation analyzes to demonstration projects based on experimental facilities.

When the electrolyzers are powered from photovoltaic generators in stand-alone systems, then the SPS power supplies perform a dc–dc power conversion. In this scenario, the principal function of the system is to produce hydrogen. The buck converter is the most widely used conversion structure for the power supplies.[13–15] This converter was shown above in Fig. 14.3 of Section 14.2.2. Given the fact that in this converter, the input voltage is always greater that the output voltage, the photovoltaic generator voltage must always be greater than the rated voltage of the electrolyzer. The buck converter is responsible for executing the maximum power-point tracking of the PV generator, thereby obtaining the maximum benefit from the renewable resource and, consequently, achieving the maximum production of hydrogen. The connection of electrolyzers to PV generators can also be made through a buck-boost converter,[16] already shown in Fig. 14.4b of Section 14.2.2. The buck-boost converter makes it possible to supply the electrolyzer with voltages that can be higher or lower than the voltage provided by the PV generator at its input. In this way, the power supply covers a wide operating range for the PV generator and the electrolyzer alike. Yet again, the converter can be controlled to execute the maximum power-point tracking of the PV generator and thereby to maximize hydrogen production. Another electronic converter used in the generation of photovoltaic hydrogen is the push-pull.[17] This converter was shown in Fig. 14.5a

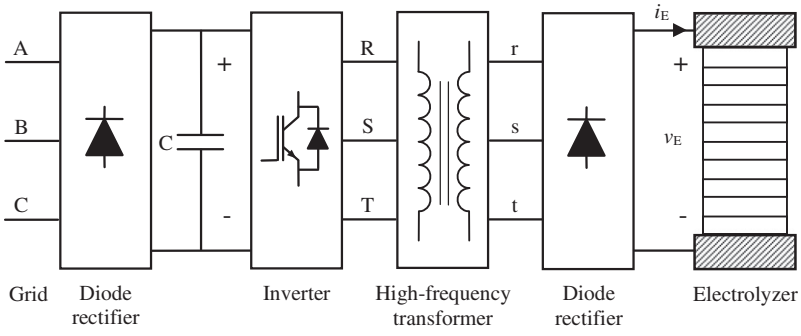

FIGURE 14.13 Electrolyzer power supply characteristic of the SPS group: ac–dc conversion structure formed by a first three-phase diode rectifier, an IGBT inverter, a high-frequency transformer, and a second three-phase diode rectifier.

within Section 14.2.2. This dc–dc power supply is characterized by the incorporation of a high-frequency transformer to provide galvanic isolation between the input and output, in other words, between the PV generator and the electrolyzer. In turn, the transformer-winding turns ratio makes it possible to obtain the most adequate relationship between the PV generator voltage and the electrolyzer voltage.

Electrolyzers can also be connected to wind turbines. In this case, this is done through ac–dc SPS power supplies, given the fact that the electric machines of the wind turbines operate with ac. In the stand-alone configurations, the primary objective is to produce hydrogen, in the same way as for the stand-alone PV systems. There are a number of proposals for conversion structures for this system.[18] The first is based on the power source already shown in Fig. 14.12, yet without including a transformer. In this case, the wind turbine output is connected to the three-phase diode rectifier in order to extract the maximum power through the buck converter and to maximize the production of hydrogen. The second conversion structure proposed is shown in Fig. 14.14. In this case, the power supply receives the ac current from the wind turbine and then converts it into a dc current through the IGBT three-phase rectifier. The rectifier generates an adequate power supply for the electrolyzer and, by controlling the power taken from the turbine, it maximizes the production of hydrogen.

Electrolyzers can also be used in the renewable stand-alone systems in which hydrogen is used to store energy in the medium- and long-term.[19,20] In these configurations, the electrolyzers are generally connected to a common dc bus that serves to connect the majority of the system components such as renewable generators, fuel cells, other storage devices, and the loads. The most widely used SPS supply for connecting the electrolyzer in these stand-alone scenarios is a buck converter. This converter controls the electric power supplied to the electrolyzer and, therefore, its production of hydrogen. Depending on the type of energy management for the stand-alone system, the converter can either receive set points directly from the system supervisor or take part in the control of the common dc bus through specific control algorithms.

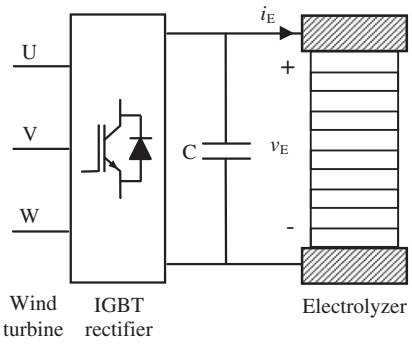

FIGURE 14.14 Electrolyzer power supply characteristic of the SPS group: ac–dc conversion structure formed by a three-phase IGBT rectifier.

Electrolyzers can also be used to support the integration of wind power into the electric grid.[21,22] In these cases, it is possible to control the electrolysis units in order to smooth the electrical power delivered to the grid by the wind turbines. For this purpose, the connection of the electrolyzer to the wind turbine or wind farm is generally made by an SPS power supply based on an ac–dc rectification stage and another dc–dc conversion stage. This makes it possible to control the profile of the power supplied to the electrolyzer. This profile is calculated so that it helps to ensure that the power finally delivered to the grid by the complete system (wind farm and electrolysis system) has some specific quality characteristics, predefined either by the wind farm or by the electric grid operator.

Unlike the LFPS supplies, the SPS ones are made up of forced commutation converters. As indicated in subsection 2.2, these converters operate on the basis of high-frequency switching techniques. One of the most common techniques is pulse width modulation (PWM) where each electronic switch can be turned on and off several 100 times in each grid frequency cycle. The high switching frequency permits the use of filtering stages at the converter output in order to reduce the harmonic content of the power supply to the electrolyzer. The current and voltage harmonics introduced by the SPS supplies into the electrolyzer are often negligible, due to their reduced amplitude and high frequencies.

Finally, before ending this section, mention should be made of the RPS power supplies for powering the electrolyzers. These power supplies are little used to power the electrolysis units.[23,24] However, compared to the conventional SPS structures, this option could be of interest, depending on the application in question. The advantage offered by the L–C resonant circuit in the RPS sources lies in the possibility of commutating the inverter stage in soft switching. By selecting adequate values for the passive resonant components and the inverter stage switching frequency, it is possible to achieve zero current switching (ZCS) or zero voltage switching (ZVS), thereby ensuring that switching losses are negligible. Soft switching therefore makes it possible to increase the operating frequency of the switches, given the fact that there is no limitation regarding switching losses, as is commonly found in forced commutation. This in turn makes it possible to use an intermediate high-frequency transformer, thereby considerably reducing the cost and size of the

transformer and, therefore, the cost of the overall system. In turn, soft switching reduces the level of electromagnetic interference of the power supply, as it avoids the considerable voltage and current drifts appearing when the switches are turned on and turned off. However, one of the key negative factors relates to the high values that can be achieved by the current resonance peak, which makes it necessary to use larger semiconductors and increases the conduction losses and those of the passive components. Likewise, the combination of a resonant circuit with a high-frequency transformer requires the use of a greater number of switches compared to the conventional SPS structures, due to the implementation of the additional inverter stage, which also makes it necessary to add a specific control system to generate the desired ac waveform for powering the resonant circuit. Despite this, RPS supplies offer an interesting potential in applications such as the production of electrolytic hydrogen.

14.3 ENERGY EFFICIENCY OF HYDROGEN PRODUCTION SYSTEMS

14.3.1 Introduction

This section describes in detail the operation of a real hydrogen production system and analyzes its energy efficiency based on two types of power supply: one of the LFPS-type and the other of the SPS-type.

As will be shown throughout the section, the energy efficiency of the electrolysis stage largely depends on the harmonic content in the current delivered by the power supply. The hydrogen produced by the electrolyzer is a function of the mean current supplied, whilst the internal losses depend on the rms value of the current. Considering the fact that any form of current with harmonics has an rms (root mean square) value that is higher than the mean, it can be seen that, for the same production of hydrogen, minimal losses are obtained with a harmonic-free current, in other words with a current that has an rms value that is equal to the mean value. In short, a greater harmonic content in the current supplied leads to higher electrolyzer losses and, therefore, lower efficiency.

Likewise, the calculation of the overall efficiency for the complete hydrogen production system must also include the actual power supply, given the fact that all the energy supplied to the electrolyzer first passes through the power supply.

Therefore, the correct design of a hydrogen production system should not only aim to optimize the electrolysis stage, but also the actual power supply. Any errors in the design of this supply could entail a considerable drop in the overall efficiency of the system, resulting in a more costly hydrogen production process. This is particularly important in the case of electrolyzers, due to the fact that this type of system requires high currents, which can provoke considerable losses in the passive components and semiconductors.

14.3.2 Water Electrolyzer System for Hydrogen Production

An electrolyzer, or an electrolytic hydrogen production plant in general, requires a number of sub-systems to guarantee the success of the process. Hydrogen and oxygen are generated in the electrolysis module as a result of the dc current delivered by the power supply. The gases produced are cooled, purified, compressed, and stored. Many facilities do not store the oxygen but discharge it into the atmosphere. Some electrolyzers operate at high pressure in order to eliminate the compression stage and thereby reduce the production and energy costs of the process. The excess heat generated in the electrolytic process is removed through an air-cooling system, in the case of very small units, or a water-cooled system for larger units. Finally, a supply stage is responsible for replenishing the water consumed during the process. The water is treated to ensure that it complies with the minimum purity requirements, thereby avoiding mineral deposits on the cells, the accelerated deterioration of the cell components, and potential undesirable collateral electrochemical reactions.

In general, electrolyzers are reliable devices that do not require continuous maintenance, having practically no moving parts. In turn, they are noiseless, highly modular devices, making them ideal for decentralized applications that are close to residential, commercial, and industrial areas. Currently, more than 15 recognized manufacturers worldwide offer commercial electrolyzers.[25] Despite the maturity of the electrolyzers, there is still a long way to go with regard to improvements in energy efficiency, given the fact that the cost of the hydrogen produced is very closely related to the consumption of electricity during the process.

The hydrogen production system analyzed in this section comprises an alkaline electrolyzer and two electric power sources, one of the LFPS-type and the other of the SPS-type (refer to Section 14.2.4). The electrolyzer, model H_2 IGen 300/1/25, was manufactured by Vandenborre Hydrogen Systems (now acquired by Hydrogenics) and is shown in Fig. 14.15. The device is of the advanced alkaline type and uses an aqueous solution of KOH at 30 wt% to maximize ionic conductivity at the rated operating temperature of 65 °C. The electrolysis module is formed by 22 circular cells, 300 cm^2 each, electrically connected in series to give a bipolar design (cell stack). The electrodes in each cell are separated by an

FIGURE 14.15 Interior view of the alkaline electrolyzer, model H2 IGEN 300/1/25, manufactured by the company Vandenborre (now named Hydrogenics). (For color version of this figure, the reader is referred to the online version of this book.)

FIGURE 14.16 Commercial power and control unit for the alkaline electrolyzer, model H2 IGEN 300/1/25. (For color version of this figure, the reader is referred to the online version of this book.)

inorganic ion-exchange membrane (IMET®). In turn, the various components in each cell are assembled and compacted in order to minimize the separation between the membranes and the electrodes, thereby achieving a zero-gap configuration. The hydrogen production rate is 1 Nm^3/h at a dc current of 120 A. The operating pressure can be adjusted between 4 and 25 bar. The water used in the process must have a conductivity of less than 5 μS/cm and its consumption is less than 1 L/Nm^3 of hydrogen produced. According to the manufacturer, the electrolysis module has an energy consumption of 4.2 kWh/Nm^3, whilst the overall consumption of the complete hydrogen production system, including the power supply, magnetic valves, instruments, and other peripherals, comes to 4.8 kWh/Nm^3.

As mentioned above, the hydrogen production system includes two power supplies. The first, shown in Fig. 14.16, is type LFPS, being the commercial power and control unit supplied with the electrolyzer. More specifically, it has a conversion structure equivalent to the one shown in Fig. 14.10 (Section 14.2.4). In turn, this unit is responsible for the control of the complete hydrogen production process. The second power supply, shown in Fig. 14.17, is type SPS and has been designed and constructed by the authors for the purpose of the characterization and modeling of the electrolyzer,[26] the emulation of operating conditions that are characteristic of photovoltaic and wind generators,[27–29] and the emulation of the electric power supply profiles of different power supply conversion topologies.[10]

The electrical performance of electrolyzers is commonly represented through their $I-V$ characteristic curves. However, these curves only make full sense when no current or voltage harmonics are introduced by the electric power supply. Due to the nonlinearity of the $I-V$ curves, the presence of harmonics in the current and voltage distorts these curves when they are calculated using the mean values of the said variables. Likewise, the harmonics in the current and voltage provide additional power to the cell that is not reflected in the graph for the $I-V$ curves. This additional power depends on the phase lags between the current and voltage harmonics of the same order, and on their rms values. In short, power sources that introduce harmonics in the cell should not be used to obtain the $I-V$ characteristic curves, given the fact that the information obtained is not correct. Figure 14.18 shows the $I-V$ curves for the alkaline electrolyzer being studied in this section. The curves were obtained from 0 to 120 A (rated current) at an operating pressure of 25 bar

FIGURE 14.17 Electric power supply designed and developed by the authors for the study and analysis of electrolyzers. (For color version of this figure, the reader is referred to the online version of this book.)

and for a temperature range of 15–65 °C. The curves were obtained with the SPS-type power supply, delivering harmonic-free currents and voltages to the electrolyzer. It can be seen that the $I-V$ curves show a highly linear relationship in the current interval from around 50–120 A. This is primarily due to the linear behavior

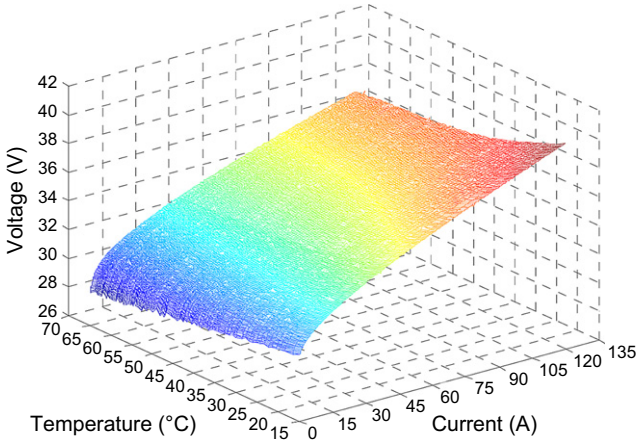

FIGURE 14.18 $I-V$ characteristic curves of the electrolyzer H2 IGEN 300/1/25 for a temperature range of 15–65 °C and an operating pressure of 25 bar. (For color version of this figure, the reader is referred to the online version of this book.)

of the ohmic overvoltage and to the fact that the activation overvoltage is relatively constant for high currents. The interval from 0 to 50 A shows a logarithmic nonlinear trend due to the considerable influence of the activation overvoltage in relation to the ohmic overvoltage for low currents. In turn, the graph shows that the increase in temperature leads to a reduction in the consumption of electricity by the electrolyzer, given the fact that, for the same current, the cell stack voltage drops, becoming more noticeable at low temperatures. This is primarily due to the increased activity of the redox semireactions and to the increased conductivity of the electrolyte and the diaphragm. At the rated current (120 A), the electrolyzer consumes approximately 8% more electricity when operating at 15 °C than at 65 °C, consuming 4836 W at 40.3 V and 4476 W at 37.3 V respectively. On the contrary, for this type of electrolyzer, the pressure variations in the process have little influence on the $I-V$ performance of the electrolyzer.

Ideally, the quantity of hydrogen produced in an electrolyzer is proportional to the quantity of charge involved in the process. The amount of hydrogen generated in the electrolysis process during a certain time interval corresponds to the mean value of the current flowing through the cell stack. This statement is true, regardless of the current profile, given the fact that the electric charge provided by the power supply solely depends on the mean value of the current and on the length of time. Therefore, the ideal hydrogen production rate in an electrolyzer is directly proportional to the transfer rate of the charge, in other words, to the electric current. On the other hand, the hydrogen production rate generated by the electrolyzer that is delivered to the user is less than the ideal. This is due to the various hydrogen losses occurring in the electrolyzer, such as the transfer of hydrogen to the oxygen compartments through the diaphragms, hydrogen drifts toward the safety sensors, etc. Figure 14.19 shows the hydrogen production for the alkaline electrolyzer studied in this section for a current range from 40 to 120 A, and for operating conditions of 55 °C and 25 bar. The graph shows the hydrogen production rate obtained by the user in the experimental tests, f_{H_2}. It can be seen that, for the 40 A current, the production rate is 0.31 Nm^3/h, while, for the 120 A current it is 0.95 Nm^3/h. The production value achieved at the rated point of 120 A is 5% lower than the rated flow provided by the manufacturer in the technical data sheet for the electrolyzer (1 Nm^3/h). In turn, the graph also shows the ideal hydrogen production rate, f_{ideal}, theoretically calculated from Faraday's first law of electrolysis. The ideal hydrogen production rate at 40 A is 0.37 Nm^3/h, while at 120 A it is 1.1 Nm^3/h. As it was previously explained, the hydrogen production rate is directly proportional to the current. Finally, the

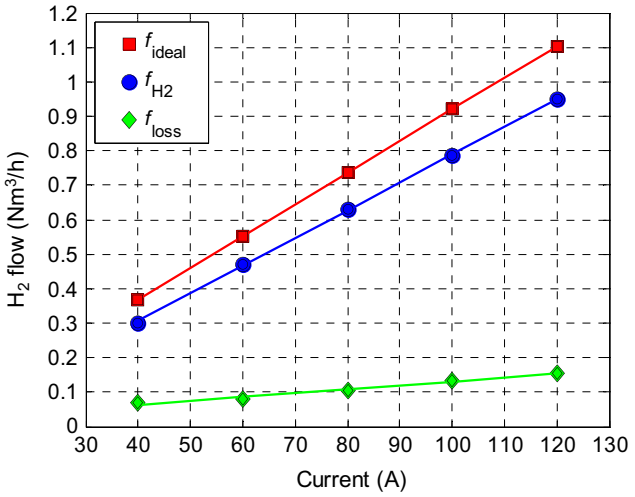

FIGURE 14.19 Hydrogen production rate: measured (f_{H_2}), ideal (f_{ideal}), and lost (f_{loss}) as a function of the current, for operating conditions of 55 °C and 25 bar. (For color version of this figure, the reader is referred to the online version of this book.)

graph also shows the total hydrogen production losses, f_{loss}, corresponding to each current point. These losses were obtained from the difference between the ideal hydrogen production rate and the experimentally measured production rate. Analyzing the losses in relation to the ideal production, it can be observed that the hydrogen production losses range from 18.4% at 40 A to 14.1% at 120 A; in other words, the hydrogen losses are greater, in percentage terms, as the electrolyzer current decreases.

Assuming that the energy required for the electrolysis process is completely supplied by the electric power supply, as is the case for the majority of commercial units, then the electrolyzer energy consumption (C_E) in Wh/Nm^3 for a time interval Δt can be calculated from the following expression:

$$C_E = \frac{\int_0^{\Delta t} I_E V_E \, dt}{\int_0^{\Delta t} f_{H_2} \, dt} \tag{14.5}$$

where I_E and V_E are the current and cell stack voltage and current, and f_{H_2} is the hydrogen production generated by the electrolyzer for the user. The electrolyzer manufacturers generally publish the energy consumption of their units, although they normally do not specify in detail the power supply used and the operating conditions established to obtain the consumption reported. The electrolyzer efficiency can be calculated from the higher heating value of hydrogen (3.5 kWh/Nm^3) and the energy consumption (C_E) as follows:

$$\eta_E = 100 \, \frac{\text{HHV of } H_2}{C_E} \tag{14.6}$$

The expression above provides the energy efficiency for the electrolysis process taking account of the losses caused by overvoltages and the hydrogen losses in the electrolyzer. On the other hand, it is important to emphasize that, in the hydrogen production systems, there are also energy losses and consumption in the peripherals and ancillary equipment forming part of the system, such as the magnetic valves, sensors, electrolyte cooling system, and the systems used to remove the oxygen and the humidity from the hydrogen produced.

14.3.3 Efficiency of the Electrolyzer Based on the Power Supply

In this section, an analysis and comparison of the consumption and energy efficiency of the H2 IGEN 300/1/25 electrolysis unit is made, when powered by the LFPS and SPS power supplies. Figure 14.20 shows the characteristics for the current (i_E) and the voltage (v_E) of the electrolysis stack when powered by the LFPS supply. The current and voltage are identified from now onward in lower case letters in order to show their instantaneous nature. In Fig. 14.20, the graph on the left shows the profile of i_E and v_E in relation to time, when a rated production of hydrogen is established from a mean current of 120 A. It can be seen that i_E is an extremely pulsating waveform with maximum values of up to 275 A and minimum values of 0 A, and therefore the LFPS supply is operating in a discontinuous conduction mode. This operating mode is primarily due to the electrical behavior of the electrolysis module, similar to that of a voltage supply, which represents the cell stack reversible voltage, with resistors and RC networks connected in series.[26] Voltage v_E has a similar profile to i_E, with peak values of some 43.2 V and valley values of some 31.6 V. However, this profile is slightly cushioned by the capacitive behavior (double layer effect) present in the electrolysis module. The frequency of both waveforms is 150 Hz given the fact that the LFPS power supply is connected to a 50 Hz electric grid.

The graph on the right in Fig. 14.20 shows the harmonic distribution of current i_E, observing a value of 120 A for the dc component. As was to be expected, there is a predominance of the low-frequency harmonics, such as the third order (150 Hz) with a peak amplitude of 155 A, the sixth order (300 Hz) with a peak of 18 A and the ninth order (450 Hz) with a peak of 22 A. Likewise, it can be seen that the harmonics above the eighteenth order (900 Hz) have little effect on the waveform i_E. The harmonic content of the dc waveforms can be quantified from the form

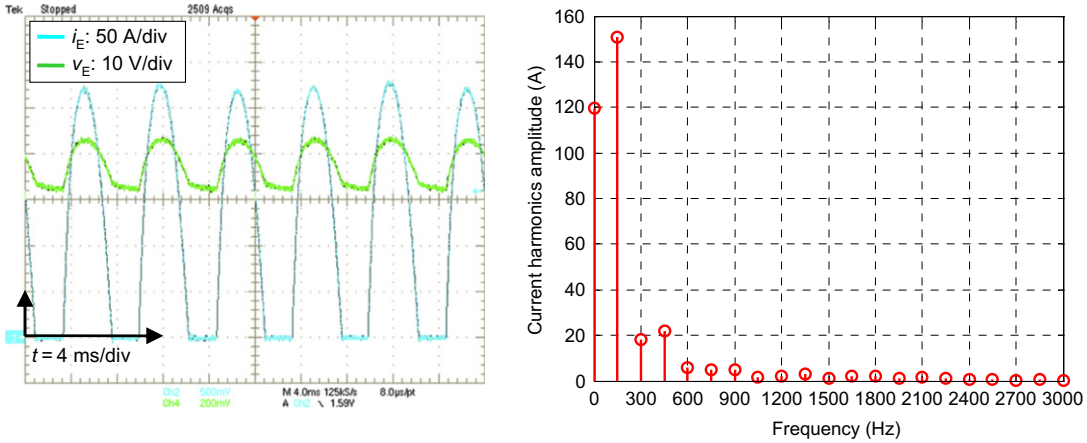

FIGURE 14.20 Electricity delivered by the LFPS power supply to the electrolyzer with a mean current value of 120 A. Electrolyzer operating conditions: 55 °C and 25 bar. Current and voltage waveforms (left) and harmonic distribution of the current waveform (right). (For color version of this figure, the reader is referred to the online version of this book.)

factor (FF). In the case of the current, the FF can be expressed as follows:

$$\mathrm{FF} = \frac{\sqrt{I_{\mathrm{dc}}^2 + \sum_{n=1}^{\infty}\left(\frac{i_n}{\sqrt{2}}\right)^2}}{I_{\mathrm{dc}}} \tag{14.7}$$

where i_n is the peak amplitude of the nth harmonic (n) of i_{E} (A), and I_{dc} is the dc component of the electrolyzer current (A), in other words, the mean value of i_{E}. The higher the value of FF in relation to the unit, the greater the influence of the harmonics on the waveform. Current i_{E} shown in Fig. 14.20 has a form factor of FF = 1.36. This high value reveals the great harmonic distortion present in the current through the electrolyzer.

Figure 14.21 shows the electricity delivered to the electrolyzer through the SPS power supply for the rated operating point, that is, a mean current of 120 A. The graph on the left shows that the i_{E} and v_{E} profiles over time have no oscillations. Both the mean values and the instantaneous values for the current and voltage are 120 A and 37.6 V, respectively.

Figure 14.21 also shows the harmonic distribution of current i_{E}, where it is possible to observe the value of 120 A for the dc component and practically negligible values for the entire harmonic spectrum. When quantifying the influence of the harmonic distortion on current i_{E} based on the form factor, a practically unitary value was obtained (FF = 1).

Once the electrical variables of the power delivered to the electrolyzer by the FLPS and SPS power supplies have been analyzed, an evaluation is made of the energy efficiency and consumption of the electrolysis system based on experimental tests, firstly using the LFPS supply and then the SPS. The tests with both supplies are conducted in the same electrolysis process-operating conditions, being 55 °C and 25 bar. Given the fact that, as discussed in the section above, the mean hydrogen production is

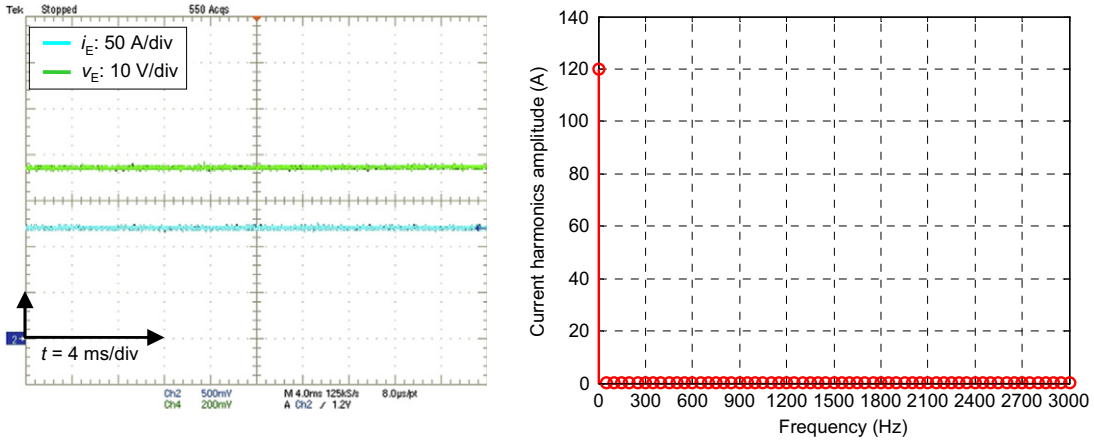

FIGURE 14.21 Electricity delivered by the SPS power supply to the electrolyzer with a mean current value of 120 A. Electrolyzer operating conditions: 55 °C and 25 bar. Current and voltage waveforms (left) and harmonic distribution of the current waveform (right). (For color version of this figure, the reader is referred to the online version of this book.)

independent of the harmonics contained in the electric current delivered by the power supply, the tests for both power supplies were made for the same mean dc current values, specifically 40, 60, 80, 100, and 120 A.

Figure 14.22 shows the energy consumption (top graph) and the energy efficiency (bottom graph) for the electrolyzer when powered by the LFPS and SPS supplies. The energy consumption (C_E) is obtained from the Eqn (14.5), where the numerator has been replaced by the electric energy consumed by the electrolyzer and the denominator by the amount of hydrogen produced by the electrolyzer. The energy efficiency (η_E) was calculated from the Eqn (14.6), that is, as the ratio between the higher heating value of hydrogen and C_E. The results obtained show that the minimum energy consumption and, therefore, the maximum efficiency occur with both power supplies when the mean current is at around 55 A. At this point, the electrolyzer consumes 4853 Wh/Nm^3 with the LFPS power supply and 4411 Wh/Nm^3 with the SPS, whilst the efficiencies are 73% and 80.3% respectively. On the other hand, the maximum energy consumption, in other words, the minimum efficiency, occurs with both power supplies when the electrolyzer is operating at its rated hydrogen production point (mean current of 120 A). In this case, the consumptions are 5233 Wh/Nm^3 with the LFPS and 4754 Wh/Nm^3 with the SPS, while the efficiencies are 67.7% and 74.5%, respectively. These consumption values are considerably higher than the consumption indicated by the manufacturer on the electrolyzer data sheet (4200 Wh/Nm^3) when operating in similar conditions. Specifically, it is exceeded by 1033 Wh/Nm^3 with the LFPS supply and by 554 Wh/Nm^3 with the SPS. On the other hand, comparing the electrolyzer consumption and efficiency with both power supplies, it can be seen that the power consumption can be as much as 495 Wh/Nm^3 more when using the LFPS compared to the SPS, whilst the efficiency is between 9.4 and 10.9% higher when using the SPS supply. The experimental results underscore the importance of the power supply typology on the electrolyzer energy efficiency.

14.3.4 Overall Efficiency of the Hydrogen Production System

After evaluating the efficiency of the electrolyzer based on the energy delivered by the LFPS and SPS power supplies in the subsections above, this subsection now goes on to analyze the overall energy balance of the system for each power supply. To do so, a study is first made of the actual efficiency of each power supply and then the overall efficiency of the entire hydrogen production system is subsequently obtained.

The two power supplies include a transformer and a number of electronic conversion stages. As indicated in Section 14.2, the electronic converter losses are primarily due to the semiconductors (on-state and switching losses) and to the passive components. In addition, the transformers also generate losses that have to be taken into account.

Depending on the length and cross section, the cables running from the power supply to the electrolyzer can also generate considerable losses in the hydrogen production systems, due to the high dc currents transmitted. In order to make the study as representative as possible, the loss calculation shown below does not take the cable losses into account.

The results for the overall energy balance for the LFPS and SPS power supplies are shown in Fig. 14.23, with the losses of the two supplies in the graph on the left and the

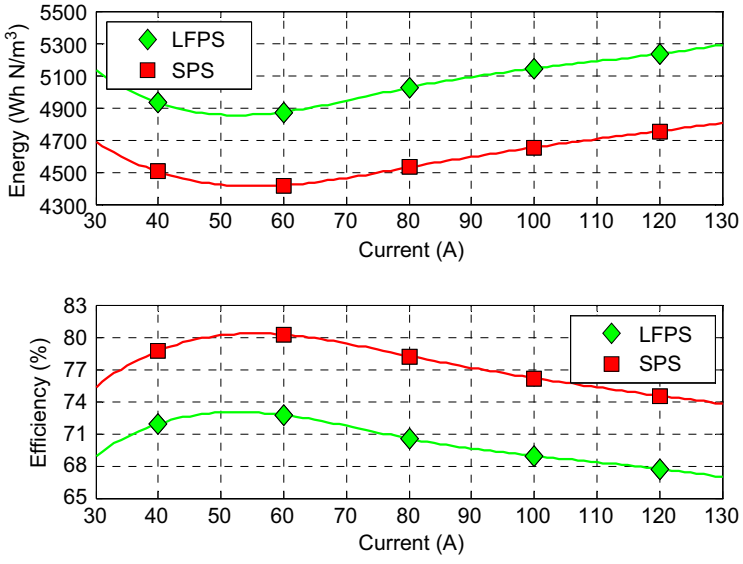

FIGURE 14.22 Energy consumption (top) and energy efficiency (bottom) of the electrolyzer when powered by the LFPS and SPS power supplies. Electrolyzer operating conditions: 55 °C and 25 bar. (For color version of this figure, the reader is referred to the online version of this book.)

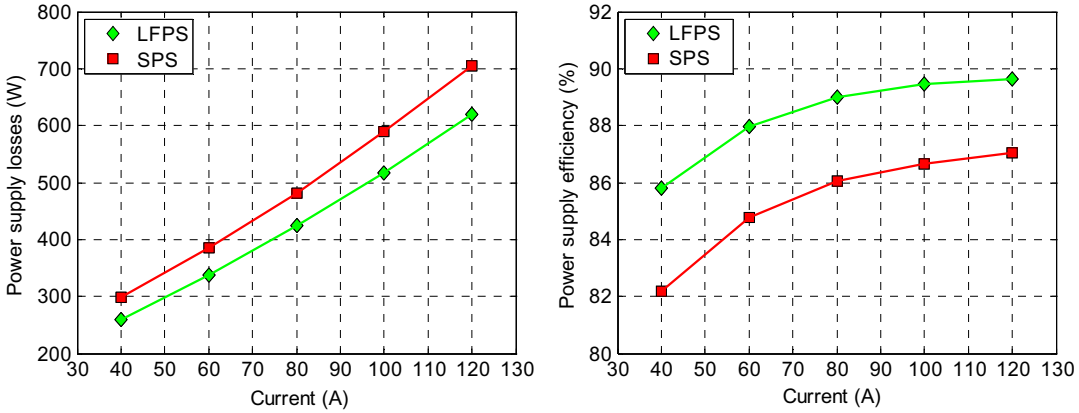

FIGURE 14.23 Power losses (left) and energy efficiency (right) for the LFPS and SPS power supplies. Electrolyzer operating conditions: 55 °C and 25 bar. (For color version of this figure, the reader is referred to the online version of this book.)

energy efficiencies in the one on the right. The results show that the losses for the SPS supply are greater for the entire electrolyzer current range. These losses range from 298 W at 40 A and 706 W at 120 A. With regard to the LFPS supply, the losses range from 259 W (40 A) up to 620 W (120 A). The graph on the right shows that the overall efficiency for the power supplies increases with the current, with values of 85.8% at 40 A and 89.6% at 120 A for the LFPS supply, and 82% at 40 A and 87% at 120 A for the SPS. Likewise, the LFPS supply has a higher efficiency than the SPS for the entire current range, which is 4.4% greater at 40 A and 3% greater at 120 A.

The results obtained are of particular interest, given the fact that the electrolyzer shows greater efficiency when powered by the SPS supply, and yet the efficiency of this power supply is lower than that of the LFPS. This serves to emphasize the fact that the efficiency analysis of a hydrogen production system should not only take into account the efficiency of the electrolyzer but also that of the power supply. Given the fact that the electric power flows through the power supply, the efficiency of the complete system will also depend on the supply, and not just on the electrolyzer. A well-designed electrolyzer will not be successful if its power supply is not designed correctly.

Figure 14.24 shows the energy consumption (top graph) and the energy efficiency (bottom graph) of the complete hydrogen production system for both power supplies, that is, the LFPS and the SPS. The system consumption in each test is obtained as the ratio between the energy consumed by the complete system, in other words, at the transformer input for each power supply, and the amount of hydrogen produced by the electrolyzer. The energy efficiency of the system is calculated from the ratio between the higher heating value of hydrogen and the consumption of the system. Similarly, the energy

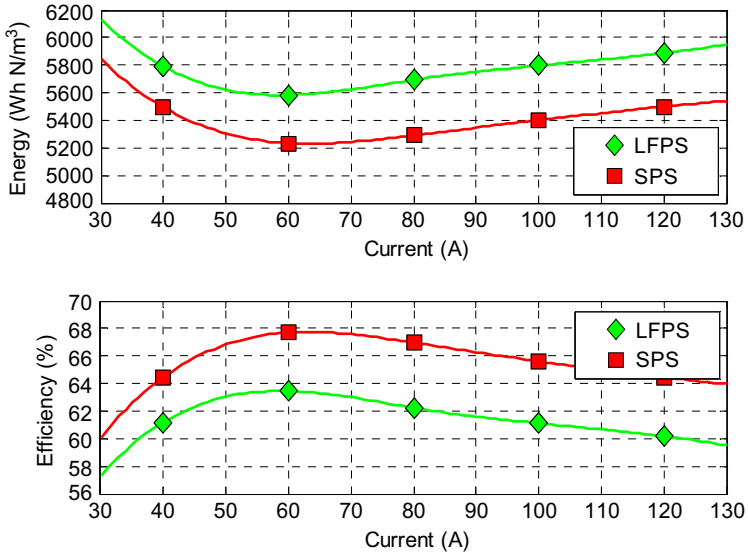

FIGURE 14.24 Energy consumption (top) and energy efficiency (bottom) for the complete hydrogen production system based on the LFPS and SPS supplies. Electrolyzer operating conditions: 55 °C and 25 bar. (For color version of this figure, the reader is referred to the online version of this book.)

efficiency of the system could also be obtained from the product between the efficiency of the electrolyzer and the efficiency of the power supplies, or as the ratio between the power of the useful hydrogen production and that of the input into the complete system.

The results show that the minimum energy consumption and, therefore, the maximum efficiency of the complete hydrogen production system occur with both power supplies at approximately 60 A. At this current point, the system consumes 5583 Wh/Nm^3 with the LFPS supply and 5233 Wh/Nm^3 with the SPS, while the efficiencies are at 63.4% and 67.7% respectively. In the electrolyzer operating range (from 40 to 120 A), the maximum energy consumption, in other words, the minimum efficiency occurs with both supplies when the mean electrolyzer current generates the rated hydrogen production (120 A). At this operating point, consumption is 5889 Wh/Nm^3 with the LFPS supply and 5499 Wh/Nm^3 with the SPS, whilst efficiencies are 60.2% and 64.4%, respectively. On the other hand, comparing the consumption and the efficiency of the hydrogen production system based on the power supplies, it can be seen that the energy consumption is up to 402 Wh/Nm^3 greater using the LFPS compared to the SPS, whilst the efficiency is between 5.3 (40 A) and 7.6% (80 A) greater using the SPS power supply.

The analysis made underscores the considerable influence that the power supply typology used in the hydrogen production systems exerts on consumption and energy efficiency, and the importance of correctly designing the power supply.

14.4 RENEWABLE HYDROGEN PRODUCTION AND DEMONSTRATION PROJECTS

14.4.1 Integration of Hydrogen Production Units with Renewable Energies

Hydrogen can be stored, transported, and used in a large number of applications in which fossil fuels are currently used.[30–37] However, hydrogen is not a source of energy, but an energy carrier that must be obtained by industrial and technological methods, given the fact that it cannot be found in a free natural state. From the point of view of sustainability, the synergy existing between hydrogen and renewable energy sources is of particular interest. Despite the fact that a number of methods are available for the production of hydrogen from renewable sources, the electrolysis of water is currently the best available method for obtaining hydrogen.[25,38–40]

Traditionally, renewable energies have made but a small contribution to meet the primary energy demand and to the generation of electricity. However, from the end of the twentieth century onward, governmental institutions have been responsible for strongly promoting these types of sustainable energy. Over the last few years, the development of renewable energies has been spectacular, in particular those directed at generating electricity. Thus, in 2009, the worldwide installed power capacity reached 1230 GW, representing a 7% increase over the previous year and accounting for almost 25% of the total installed electricity-generating capacity, estimated at close to 4800 GW. That year (2009), renewable energies supplied 18% of the global electricity production.[41] Furthermore, renewable energies, excluding large-scale hydropower, reached a total of 305 GW, 22% more than in 2008. China, the United States, Germany, Spain, and India were the principal installer countries.[41]

Among all the renewable energies, wind power accounted for the greatest new installed capacity in 2009, reaching 38 GW and bringing the total installed power capacity to 158 GW. The countries with the greatest installed wind power capacity were the United States (35 GW), China (25.8 GW), Germany (25.7 GW), and Spain (19 GW).[42] For its part, hydropower accounted for 15% of the global electricity production, according to figures from 2008. In 2009, new hydropower plants were installed for a total of 31 GW, the second greatest increase after the wind power systems. The global hydropower capacity, including large-scale hydropower, reached approximately 980 GW at the end of 2009, 60 GW of which corresponded to small hydropower.[41] Finally, the installed capacity for grid-connected photovoltaic systems was increased by 7.2 GWp in 2009, to reach 217.2 GWp, representing a year-on increase of 53%. For their part, the off-grid photovoltaic systems increased their installed power capacity by almost 4 GWp. Germany was the country with the greatest installed capacity, with 9.8 GWp, followed by Spain, with 3.5 GWp, Japan with 2.6 GWp, and the United States, which installed 1.6 GWp.[42]

Despite the fact that in subsequent years, there has been a reduction in the growth rates experienced by renewable energy sources, the growth targets for the forthcoming years continue to be extremely ambitious. Thus, at a European level, the 2011–2020 decade is to be marked by Directive 2009/28/EC of the European Parliament and of the Council, on the promotion of the use of energy from renewable sources.[43,44] Specifically, the Directive sets a target of a 20% minimum share of energy from renewable sources in the gross final consumption of energy in the European Union (EU), a 40% contribution of renewable energies to the production of electricity and a minimum share of 10% of energy from renewable sources in the energy consumption in the transport sector in each member state by year 2020. Directive 2009/28/EC is part of what is known as the

European Energy and Climate Change Package, establishing the basis to ensure that the EU achieves its targets for 2020: a 20% improvement in energy efficiency; a 20% contribution of renewable energies; and a 20% reduction in greenhouse gas emissions.

Likewise, within the electricity system, renewable energies represent new challenges with regard to the storage and use of excess energy, the operation of the system, the management of distributed generation, the security of the energy supply, and the future integration of electric vehicle.[45–47] Renewable energies can cause the grid to operate in extreme situations. One example of this is the Spanish electricity grid, which can experience wind power penetration peaks of 54% of the power demand (as occurred on the 9th November 2010) or days on which the wind power generation dropped to almost 1% (as occurred on the 26th June 2010).[48]

Hydrogen technologies can help to overcome these challenges, thereby contributing to the development of a new energy system.[21,37,49–50] The so-called hydrogen economy contemplates a future scenario in which hydrogen is produced through environmentally clean low-cost procedures, based on renewable sources, and in which fuel cells play a key role.[51–54] The support policies and the recent technological progress are contributing toward cost reductions, improved understanding, and social acceptance of hydrogen technologies.[36,37,55]

Hydrogen can be produced from the electricity generated by wind power and photovoltaic systems in a wide variety of applications.[25,38,39] Firstly, a stand-alone scenario can be contemplated whereby the electrolyzers and renewable systems are not connected to the electric grid. This scenario, which makes it possible to obtain completely renewable hydrogen, can primarily consider two configurations. In the first one, the wind power and photovoltaic systems are directly connected to the electrolyzers for the production of hydrogen.[14,24,56–63] In this configuration, there are considerable fluctuations to the electrolyzer operating conditions given the fact that they are imposed directly by the variability of the wind power and solar resources. The connection to the renewable system can be made through dc–dc power conversion stages for the photovoltaic systems and ac–dc or dc–dc for the wind power systems. These conversion stages make it possible to condition the currents and voltages generated by the renewable systems to some suitable values for the electrolyzers and, furthermore, to obtain the maximum power from these systems at all times. However, the high current and low voltage required for the operation of the electrolyzers, in addition to the wide power range due to the intermittency of the renewable resources, can lead to a significant reduction in the efficiency of the conversion stages. Therefore, a direct connection between the renewable systems and the electrolyzers can be considered, with no conversion stage. In the case of the photovoltaic systems, this implies designing the generator to ensure that its current–voltage characteristic curves are adapted to suit those of the electrolyzer. For the wind power systems, dc machines should be used so that direct coupling is possible.

The second configuration adopted by the stand-alone systems is the use of electrolyzers together with hydrogen storage and fuel cells, in order to achieve a configuration that is practically free from pollutant emissions.[19,64–72] This configuration is primarily directed at the supply of energy to remote areas where there is no connection to an electricity grid. The renewable systems are responsible for the supply of the electricity required for the loads, whilst any excess renewable energy is used to produce hydrogen. This hydrogen is stored for subsequent use in the fuel cells when the loads demand more power than can be supplied by the renewable sources. For these systems, it is also possible to consider the use of the residual heat produced, primarily from the fuel cells, in a cogeneration process (combined heat and power) in order to obtain, for example, hot water for sanitary use and domestic heating. In turn, excess hydrogen could be used in vehicles equipped with fuel cells. As far as the conversion stages are concerned, these must be correctly designed to ensure an adequate coupling between the renewable systems, the loads, the electrolyzers and the fuel cells, both with regard to the electric power conditioning (currents and voltages) and the energy management. Generally, this configuration comprises a combination of wind power and photovoltaic generators, given the fact that their complementary nature makes it possible to considerably increase the electricity generation capacity factor.

It is also possible to find electrolyzers and renewable systems integrated into the electric grid.[21,22,73–81] In this scenario, three configurations can be considered. In the first configuration, the electrolysers are connected to the electricity grid into which the renewable systems (principally wind farms and photovoltaic plants) deliver the energy produced. In this case, the electricity generated by the renewable systems is supplied directly to the grid, whilst the electrolyzers are able to operate continuously without having to depend on the variability of the wind speed or the solar irradiance. The electrolyzer capacity factor can be almost 100%, thereby reducing the hydrogen production costs. The hydrogen generated is not completely renewable given the fact that the electrolyzers may be operating when the renewable resources are practically at zero.

In the second grid-connected configuration, the electrolyzers operate solely from the electricity generated by the renewable systems. In this case, the hydrogen

produced is completely renewable. The wind farms or photovoltaic plants power the electrolyzers and the excess electricity is delivered to the grid. The operation of the electrolyzers is subject to the intermittent nature of the renewable energy generation and, therefore, full advantage is not taken of the net hydrogen production capacity of the electrolyzers.

The growing penetration of wind and photovoltaic power is bringing with it a new set of problems relating to the grid integration of a highly variable energy supply. From this point of view, the third configuration for a grid connection is perhaps of the greatest interest, given the fact that it helps to ensure the successful integration of the hydrogen generating systems with the renewable sources and the electric grid. In this configuration, the electrolyzers are actually or virtually connected to the renewable plant and to the electric grid. The electrolyzers are responsible for absorbing the energy derived from the imbalances between production and demand, in other words, between the variability of the renewable resources and the variability inherent in the electrical loads connected to the grid. In this way, the electrolyzers can help the renewable plants to carry out grid operating services such as primary regulation, in addition to other remunerated complementary services, such as secondary and tertiary regulation. In turn, the electrolyzers can also contribute to the improvement of compliance with the forecast for the quantity of renewable power generated. The use of fuel cells can improve this configuration, making the system completely manageable. In this configuration, the capacity factor for the electrolyzers and the generation of renewable hydrogen primarily depends on the management strategy implemented to support the operation of the electric grid.

Another scenario of interest that could be considered for the integration of electrolysis systems with renewable energies is the configuration of microgrids for the distributed generation of energy.[82–85] Microgrids can operate either independently of the grid, or with the support of weak networks that are connected to the main supply network. In this scenario, it makes complete sense to use the hydrogen storage and fuel cells to ensure that the complete hydrogen system can store energy and use it whenever necessary. Likewise, the microgrids may comprise a large number of additional elements, such as batteries, supercapacitors, gensets, microturbines, etc.

14.4.2 Demonstration Projects

Although, at a world level, there are but few demonstration projects on the integration of electrolytic hydrogen production systems with renewable energies, these last few years have seen the fledgling development of systems of this type in countries such as the United States, Canada, Germany, Italy, Norway, Finland, the United Kingdom, Japan, and Spain.[25,86,87] There are a number of reasons to justify this growing interest in the experimental investigation into the integration of hydrogen and renewable systems. On the one hand, there is increasingly widespread awareness in society of the need to develop a sustainable energy system. On the other hand, the problems arising from the storage of large quantities of energy are becoming increasingly evident due to the considerable increase in the number of plants generating electricity from renewable sources. Furthermore, the costs of generating electricity from renewable sources are getting progressively closer to those associated with fossil or nuclear based generation.

Most demonstration projects are based on a standalone scenario.[13,20,27,28,29,88–102] Photovoltaic solar energy is the principal renewable energy source used, although wind power is also used, as well as combinations of both power sources. The most-used electrolyzer typology is the alkaline one, although proton exchange membrane (PEM) electrolyzers are also used. The electrolyzers operate at atmospheric pressure, at medium pressure (4–30 bar) and at high pressure (448 bar), in addition to a wide range of power outputs (0.8–111 kW). The storage of hydrogen is also analyzed in a gaseous state, in a liquid state and forming metal hydrides. The most-used fuel cells are of the PEM type, although alkaline and phosphoric acid cells are also employed. The hydrogen produced is used in a number of applications, such as the electricity generation from fuel cells and also as a fuel to power electric vehicles based on fuel cells. In turn, the power stages used and their management vary considerably from one system to another. In the simplest cases, the conversion stages are omitted and the renewable sources are directly connected to the electrolyzers.

With regard to demonstration systems coming within the framework of electrolysis systems with renewable energies integrated into the electric grid, two projects should be highlighted. The first, entitled Wind2H2 and developed by the National Renewable Energy Laboratory, is focused on analyzing a number of configurations for the grid integration of wind and photovoltaic renewable energy sources, electrolyzers and fuel cells.[103] The project also analyzes the operation of different hydrogen technologies, comparing their efficiency with the variable conditions of the renewable resources. The second project is focused on the production of electrolytic hydrogen at the Sotavento wind farm (Galicia, Spain)[104]. The main objective is to analyze the use of hydrogen for energy storage in order to improve the coupling of a wind turbine to the electric grid. In this case, the electrolyzer makes use of part of the energy produced by the

wind turbine to convert it into hydrogen and subsequently deliver it to the grid via an internal combustion engine coupled to an electric generator.

Despite the theoretical studies and the demonstration projects, there is still little knowledge on the integration of the electrolytic hydrogen production systems with renewable energies. The electrolysis of water is currently considered to be a mature technology; however, the electrolyzers available on the market are designed to operate in stable operating systems, connected to the electric grid. For this reason, the manufacturers of these devices are starting to show an interest in the development of electrolysis units capable of being integrated with renewable power sources. They are currently trying to acquire the experience that will enable them to adapt their electrolyzers to this type of operation. However, the high investment cost required for this type of system is slowing down the development and integration of this technology with renewable energies.

14.4.3 Operation of an Electrolyzer under Different Solar Operating Conditions

After having discussed the various options for the integration of electrolyzers in renewable energy-based systems as well as the principal demonstration projects, a study will now be made of the operation of the 1 Nm^3/h and 5 kW electrolyzer described in Section 14.3, when subject to operating conditions that are characteristic of a stand-alone connection with a photovoltaic generator. Specifically, the operation is to be studied under two different solar operating conditions: with very stable irradiance on a clear day; and with extremely variable irradiance on a day with scattered clouds.

Figure 14.25 shows the diagram for the system to be studied. As can be observed, the alkaline electrolyzer described above is powered with an operating profile provided by a photovoltaic system comprising a PV array that is assumed to be connected to a dc–dc converter with maximum power point tracking (MPPT). The *PV* array is physically located on the campus of the Public University of Navarra (UPNa). The study procedure is as follows. The first step is to characterize the PV array and to calculate its expected operation under different irradiance and temperature profiles. This operating profile is subsequently emulated using the power unit designed by the authors and described in Section 14.3, and then used to power the electrolyzer.

The *PV* array is located on the roof of the building named Los Pinos, housing the Department of Electrical and Electronic Engineering of the UPNa. The array is south facing and tilted at an angle of some 30° relative to horizontal. The *PV* generator, with a peak power of 5100 W, comprises 60 BP585 modules. The PV array is a modular configuration comprising 20 strings of three series-connected modules each. The principal characteristics of the modules in standard conditions ($T_S = 25\ ^\circ C$ and $E_S = 1000\ W/m^2$) are as follows: peak power $P_{MS} = 85$ W with current $I_{MS} = 4.7$ A and voltage $V_{MS} = 18$ V, short circuit current $I_{SCS} = 5$ A, open circuit voltage $V_{OCS} = 22$ V, mean efficiency of 13.5%, and power variation coefficient with temperature $\gamma = -0.5\%/^\circ C$.

The analytical method was used to characterize the electrical performance of the PV generator.[105] This method makes it possible to model the $V-I$ curve of a module, by obtaining the five parameters appearing in the single-exponential based characteristic equation. Figure 14.26 shows the $V-I$ and $V-P$ characteristic curves of the BP585 module operating in standard conditions, after applying this method. The electrical characteristics obtained coincide with those provided by the manufacturer.

As mentioned in Section 14.3, the electrolyzer is model H2 IGen 300/1/25 manufactured by Hydrogenics. The nominal hydrogen flow rate is 1 Nm^3/h and is

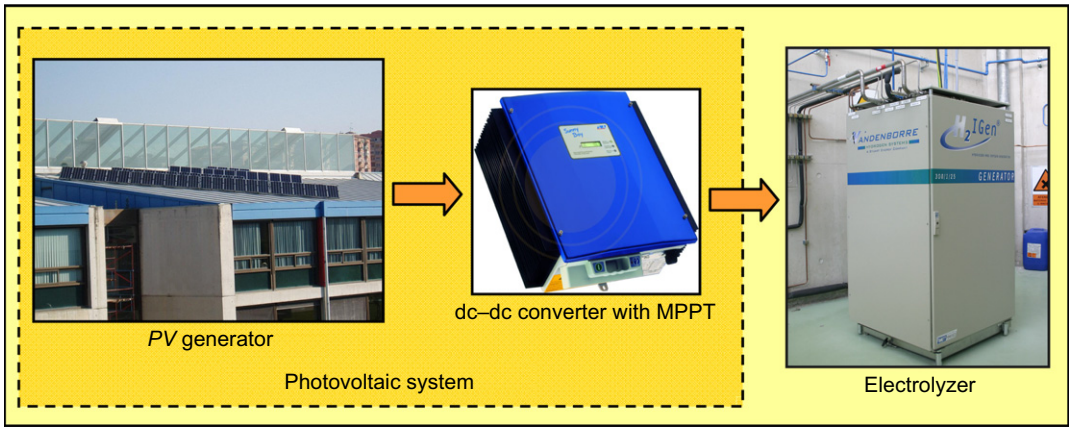

FIGURE 14.25 Diagram of the system studied. (For color version of this figure, the reader is referred to the online version of this book.)

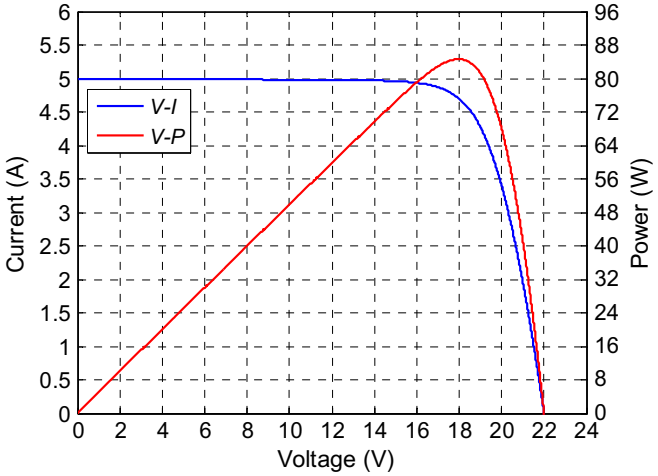

FIGURE 14.26 Characterization of the BP585 PV module: characteristic $V-I$ and $V-P$ curves in standard conditions. (For color version of this figure, the reader is referred to the online version of this book.)

equivalent to a dc current with a mean value of 120 A. The hydrogen production range is established between 25% (30 A in dc) and 100% (120 A in dc).

The initial input data for the *PV* emulation is the measurement of the incident irradiance on the *PV* generator. This variable is indirectly measured through short circuit current I_{SC} of a permanently short-circuited, precalibrated module, used as a reference standard. In this way, using digital power meter WT1600 and a database, the I_{SC} data are progressively stored over time at 1 s intervals. From I_{SC}, irradiance E is obtained at each moment in time:

$$E = \frac{I_{SC}E_S}{I_{SCS}} \tag{14.8}$$

Once the irradiance has been calculated, the next step is to obtain the maximum power P_M that the dc–dc converter with MPPT would have delivered to the electrolyzer. This requires the *PV* generator ambient temperature, synchronized in time with the irradiance data. This temperature is obtained from the ETSIA-UPNa meteorological station database. Now, the ambient temperature T_a and irradiance E are used to calculate the temperature T_m at which the generator *PV* modules would have been operating, through the following expression in which NOCT is the nominal operating cell temperature of the modules (47 °C):

$$T_m = T_a + \left(\frac{NOCT - 20\,^\circ\mathrm{C}}{800\ \mathrm{W/m^2}}\right)E \tag{14.9}$$

Finally, P_M is calculated from the following equation, which incorporates the effects of the irradiance and temperature on the power in standard conditions, whereby N_P is the number of *PV* generator modules, in this case 59, given the fact that one is used to measure the I_{SC}:

$$P_M = N_P P_{MS}\left(\frac{E}{E_S}\right)\left(\frac{100 + \gamma(T_M - T_S)}{100}\right) \tag{14.10}$$

For the PV emulation, the power unit needs to power the electrolyzer with the P_M obtained in Eqn (14.10). For this, it is necessary to calculate the corresponding current that the power unit must supply to the electrolyzer. The power characteristic equation of the electrolyzer can be expressed as[26]:

$$\begin{aligned} P_E &= V_E I_E \\ &= N_S[V_{rev} + r(T_E)I_E + s(T_E)\ln(t(T_E)I_E + 1) \\ &\quad + v(T_E)\ln(w(T_E)I_E + 1)]I_E \end{aligned} \tag{14.11}$$

where P_E, V_E and I_E are the electrical variables of the electrolysis stack, N_S is the number of series-connected electrolytic cells, and V_{rev} is the reversible voltage. The parameters r, s, t, v, and w are dependent on the process temperature (T_E), and are obtained by using nonlinear numerical analysis techniques to fit the model to the curves obtained for the static characterization of the electrolyzer (see Fig. 14.18 in Section 14.3). From here, the current that the power unit needs to supply to the electrolyzers (I_E) is obtained by equalizing the photovoltaic and electrolyzer power outputs ($P_E = P_M$), and solving Eqn (14.11) by numerical iteration.

The entire procedure described is programmed in the power unit microcontroller and is implemented in real time, based on the experimental vectors I_{SC} and T_a. This procedure is followed due to the fact that it is necessary to determine the real-time electrolyzer stack temperature (T_E) in order to obtain the reference current ($I_{ref} = I_E$) to be emulated at each instant in time.

In order to assess the different response of the electrolyzer under different *PV* generator operating conditions, two specific days in 2007 were emulated: namely the 11th March (day 1) and the 5th April (day 2). The experimental input data used for the emulations on both days (I_{SC} and T_a) were measured in the time interval from 7:00 until 20:00 h. Figure 14.27 shows the irradiance measured for both days. As can be observed, day 1 was selected for its high stability, while day 2 was chosen for the opposite reason, for being a day with high variability. On the one hand, it is possible to observe the logical trend of the irradiance based on the hours of sun, and, in the case of day 2, the high variability of the irradiance due to the presence of scattered clouds. These variations, throughout day 2, were as great as 800 $\mathrm{W/m^2}$ (changing from 300 $\mathrm{W/m^2}$ to 1100 $\mathrm{W/m^2}$) at around 12:30 h in times of less than a minute.

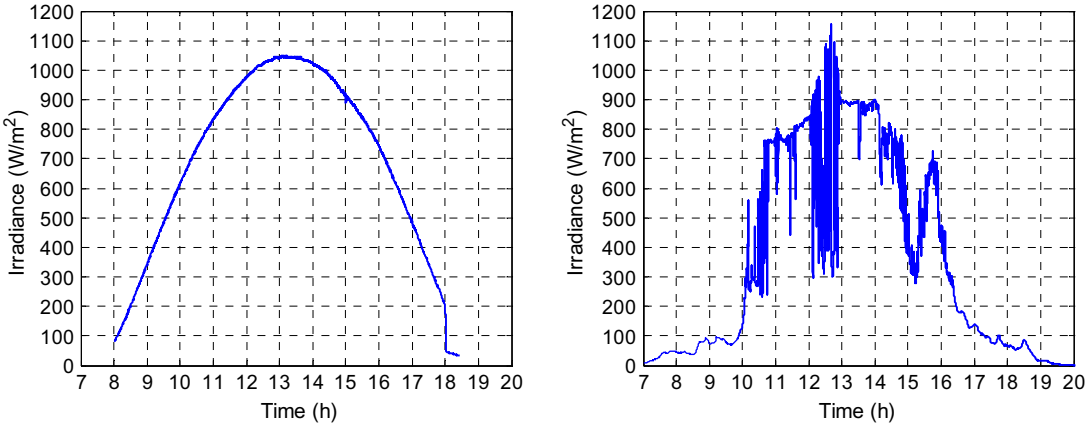

FIGURE 14.27 Evolution of the irradiance. Left: 11th March (day 1). Right: 5th April (day 2). (For color version of this figure, the reader is referred to the online version of this book.)

Figure 14.28 shows the electrical variables for the electrolyzer (I_E and V_E), and the evolution of the temperature T_E and pressure Pr_E of the electrolytic process during the tests on both days. Firstly, the graphs show that the *PV* emulation was conducted satisfactorily. Due to the limitation of the lower operating threshold of the electrolyzer (corresponding to $I_E = 30$ A), the electrolysis process produces hydrogen from 8:27 to 17:55 h for day 1, and from 10:03 to 16:27 h for day 2. Voltage V_E varies with a trend similar to the current due to the highly ohmic behavior of the electrolyzer. The pressure during the tests remained relatively stable at some 19.5 bar, with variations inherent in the process control (±1 bar); however, the evolution of the temperature is related to the current I_E (actually to the power), but with considerably slower dynamics.

Figure 14.29 shows the hydrogen flow produced (f_{H2}) during the PV emulation for both days, in addition to the purities of the hydrogen (OTH) and oxygen (HTO) generated in the electrolysis process. f_{H_2} can be observed to follow the current profile of Fig. 14.28, although with considerable variations in amplitude due to the constant opening and closing of the valves responsible for controlling the electrolyte level in the electrolyzer. Furthermore, by comparing Figs 14.28 and 14.29, it is possible to see that the dynamics of f_{H_2} are decoupled in relation to those of I_E, due to the fact that the electrical dynamics can be much faster than fluid dynamics. With regard to the purities of the gases produced, the trends of sensors OTH and HTO can be seen to be inversely proportional to the production of hydrogen. This is because, the greater the f_{H_2}, the faster the gases leave the electrolysis stack, remaining for less time in the anode and cathode compartments, leading to a lower degree of impurity due to a reduction in the rate of flow of the oxygen and hydrogen through the membranes. For day 1, the OTH range is 0.13−0.42 ppt (parts per thousand) while the HTO range is 0.52−1.1%. In turn, for day 2, the OTH is between 0.16 and 0.25 ppt and the HTO between 0.5 and 0.9%. By comparing these impurities on the same unit scale, it can be concluded that, throughout the tests, the HTO reached values that were around 40 times greater than

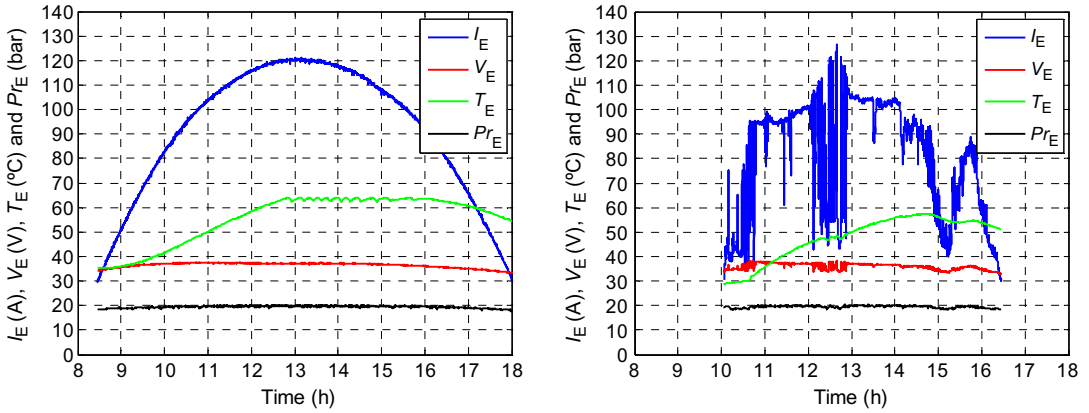

FIGURE 14.28 *PV* tests for both days (day 1 on the left; day 2 on the right): current (I_E) and voltage (V_E) of the electrolyzer stack, process temperature (T_E), and pressure (Pr_E). (For color version of this figure, the reader is referred to the online version of this book.)

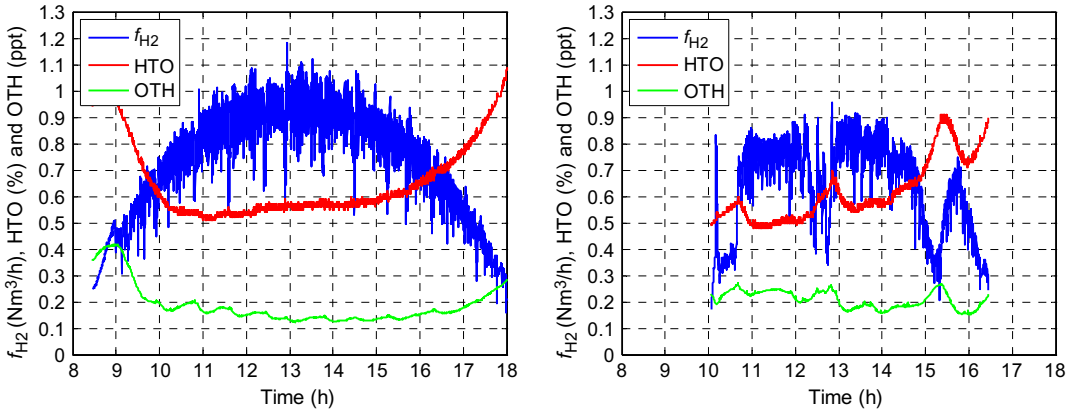

FIGURE 14.29 *PV* tests for both days (day 1 on the left; day 2 on the right): flow of hydrogen produced (f_{H_2}), oxygen purities (HTO), and hydrogen purities (OTH). (For color version of this figure, the reader is referred to the online version of this book.)

for the OTH on day 1 and around 30 times higher for day 2. This difference in purities is due to the fact that the flow of hydrogen through the membrane electrolysis stack to the oxygen compartments is much greater than that of oxygen, as hydrogen is a far lighter molecule (2 g/mol of hydrogen compared to 16 g/mol of oxygen).

Finally, the mean values for the energy consumption per Nm^3 (C_E) and performance (η_E) throughout the tests are given. These magnitudes are calculated from Eqns (14.5) and (14.6). The results obtained in the test corresponding to day 1, that is the day with minimal variability, are: $C_E = 4553$ Wh/Nm^3 and $\eta_E = 77.8\%$. With regard to day 2, the results reached values of $C_E = 4512$ Wh/Nm^3 and $\eta_E = 78.5\%$. Comparing both results, it can be concluded that the variability of the operating conditions does not negatively affect the performance of the electrolyzer, which dynamically adapts to the said variations with no loss of energy efficiency. The minimal difference between the efficiencies obtained is due to the differences in the electrolyzer efficiency as a function of the instantaneous current value applied. Finally, it should be pointed out that, in any case, a high efficiency was obtained in both tests. This serves to demonstrate the viability of integrating hydrogen production systems in renewable energy-based systems.

14.5 CONCLUSIONS

Over the last few years, hydrogen technologies have become key enablers in the medium- and long-term developments of a new energy model that offers greater sustainability and independence than the present-day one. Hydrogen, together with electricity, can play an important role as an energy carrier in an energy system primarily based on renewable energies. With regard to the different types of electrolyzers used for the production of hydrogen, alkaline electrolysis is the most developed and widely used technology in the industrial sector. For this reason, it is currently the best positioned for integration with renewable energies.

The high cost of electrolytic hydrogen production, basically associated with the electric energy consumption, justifies the effort to improve the overall energy efficiency, particularly considering their potential integration with renewable energies.

This chapter has described the main electronic conversion topologies used for power supplies to electrolyzers, and the tools have been provided to understand how these power supplies work. Specifically, topologies have been described based on natural commutation with semicontrollable semiconductors such as thyristors, and forced commutation with fully controllable semiconductors such as IGBT and MOSFET. Mention has also been made of the resonant converter topologies with a high- frequency transformer, pointing out their advantages and drawbacks.

The operation of a real hydrogen production system has also been described, analyzing the influence that the principal power supply typologies have on the energy efficiency of the system as a whole, and showing the efficiency results for the electrolyzer and also for the actual power supply. The results show that the design of the power supply plays a key role in the improvement of the efficiency of the complete system.

Finally, and in order to highlight the strengths, weaknesses, and room for improvement with regard to the integration of electrolysis systems and renewable energies, the principal configurations for the integration of grid-connected and stand-alone systems have been described. Furthermore, the performance of a real hydrogen production system has been evaluated when powered by emulating the operating conditions characteristic of a real photovoltaic system, on a clear day (low variability) and also on a day with scattered clouds (high variability). The experimentally obtained results serve to

demonstrate the correct performance of the electrolysis system in both situations.

Acknowledgments

We gratefully acknowledge the financial and ongoing support of the companies Acciona Energy and Ingeteam, and the Spanish Ministry of Economy and Competitiveness under grant DPI2010-21671-C02-01.

References

1. Mohan, N.; Undeland, T. M.; Robbins, W. P. *Power Electronics: Converters, Applications, and Design;* John Wiley & Sons, ISBN 0-471-22693-9; 2003.
2. Rashid, M. H. *Power Electronics: Circuits, Devices, and Applications;* Pearson/Prentice Hall, ISBN 0-13-101140-5; 2004.
3. Bose, B. K. *Power Electronics And Motor Drives: Advances and Trends;* Academic Press Inc, ISBN 0120884054; 2006.
4. Hart, D. W. *Power electronics;* McGraw-Hill, ISBN 0-07-338067-9; 2010.
5. Erickson, R. W. *Fundamentals of Power Electronics;* Springer, ISBN 0-79-237270-0; 2001.
6. http://www.hydrogenics.com.
7. http://www.nel-hydrogen.com.
8. http://www.iht.ch.
9. http://www.accagen.com.
10. Ursúa, A.; Marroyo, L.; Gubía, E.; Gandía, L. M.; Diéguez, P. M.; Sanchis, P. Influence of the Power Supply on the Energy Efficiency of an Alkaline Water Electrolyser. *Int. J. Hydrogen Energy* **2009,** *34,* 3221−3233.
11. http://www.h2nitidor.it/h2n.
12. Green, A. W. An ac−dc Power Supply. International Patent Application Nr. WO97/17753.
13. Brinner, A.; Bussmann, H.; Hug, W.; Seeger, W. Test Results of the HYSOLAR 10 kW PV-Electrolysis Facility. *Int. J. Hydrogen Energy* **1992,** *17,* 187−197.
14. Park, M.; Lee, D.; Yu, I. PSCAD/EMTDC Modelling and Simulation of Solar-Powered Hydrogen Production System. *Renew. Energy* **2006,** *31,* 2342−2355.
15. García-Valverde, R.; Miguel, C.; Martínez-Béjar, R.; Urbina, A. Optimized Photovoltaic Generator−Water Electrolyser Coupling through a Controller dc−dc Converter. *Int. J. Hydrogen Energy* **2008,** *33,* 5352−5362.
16. García, J. G.; Mantz, R. J.; De Battista, H. Hybrid Control of a Photovoltaic-Hydrogen Energy System. *Int. J. Hydrogen Energy* **2008,** *33,* 3455−3459.
17. Garrigós, A.; Blanes, J. M.; Carrasco, J. A.; Lizán, J. L.; Beneito, R.; Molina, J. A. 5 kW dc/dc Converter for Hydrogen Generation from Photovoltaic. *Int. J. Hydrogen Energy* **2010,** *35,* 6123−6130.
18. Oohara, S; Ichinose, M; Futami, M; Matsutake, M; Fujii, K; Ide, K; Itabashi, T; Tamura, J. Hydrogen Production System using Wind Turbine Generator. United States Patent Application Nr. 11/654684.
19. Kélouwani, S.; Agbossou, K.; Chahine, R. Model for Energy Conversion in Renewable Energy System with Hydrogen Storage. *J. Power Sourc.* **2005,** *140,* 392−399.
20. Ghosh, P. C.; Emonts, B.; Janben, H.; Mergel, J.; Stolten, D. Ten years of Operational Experience with a Hydrogen-Based Renewable Energy Supply System. *Sol. Energy* **2003,** *75,* 469−478.
21. Takahashi, R.; Kinoshita, H.; Murata, T.; Tamura, J.; Sugimasa, M.; Komura, A.; Futami, M.; Ichinose, M.; Ide, K. Output Power Smoothing and Hydrogen Production by Using Variable Speed Wind Generators. *IEEE Trans. Ind. Electron.* **2010,** *27,* 485−493.
22. Zhou, T.; Francois, B. Modelling and Control Design of Hydrogen Production Process for an Active Hydrogen/Wind Hybrid Power System. *Int. J. Hydrogen Energy* **2009,** *34,* 21−30.
23. Cavallaro, C.; Chimento, F.; Musumeci, S.; Sapuppo, C.; Santonocito, C. Electrolyser in H_2 Self-Producing Systems Connected to dc Link with Dedicated Phase Shift Converter. *International Conference on Clean Electrical Power* **2007,** 632−638.
24. Contreras, A.; Guirado, R.; Veziroglu, T. N. Design and Simulation of the Power Control System of a Plant for the Generation of Hydrogen via Electrolysis, using Photovoltaic Solar Energy. *Int. J. Hydrogen Energy* **2007,** *32,* 4635−4640.
25. Ursúa, A.; Gandía, L. M.; Sanchis, P. Hydrogen Production From Water Electrolysis: Current Status and Future Trends. *Proc. IEEE* **2012,** *100,* 410−426.
26. Ursúa, A; Sanchis, P. Static-Dynamic Modelling of the Electric Behaviour of a Commercial Advanced Alkaline Water Electrolyser. *Int. J. Hydrogen Energy* **2012**, *37*, 18598−18614.
27. Gandía, L. M.; Oroz, R.; Ursúa, A.; Sanchis, P.; Diéguez, P. M. Renewable Hydrogen Production: Performance of an Alkaline Water Electrolyzer Working under Emulated Wind Conditions. *Energy & Fuels* **2007,** *21,* 1699−1706.
28. Ursúa, A.; Gubía, E.; López, J.; Marroyo, L.; Sanchis, P. Electronic Device for the Emulation of Wind Systems and Analysis of Alkaline Water Electrolysers. *European Conf. on Power Electron. and Appl.* **2009,** 1−5.
29. Ursúa, A.; López, J.; Gubía, E.; Marroyo, L.; Sanchis, P. Photovoltaic Hydrogen Production with Commercial Alkaline Electrolysers. *World Hydrogen Energy Conference* **2010,** 119−128.
30. Conte, M.; Iacobazzi, A.; Ronchetti, M.; Vellone, R. Hydrogen Economy for a Sustainable Development: State-of-the-Art and Technological Perspectives. *J. Power Sourc.* **2001,** *100,* 171−187.
31. Dunn, S. Hydrogen Futures: Toward a Sustainable Energy System. *Int. J. Hydrogen Energy* **2002,** *27,* 235−264.
32. Elam, C. C.; Padró, C. E. G.; Sandrock, G.; Luzzi, A.; Lindblad, P.; Hagen, E. F. Realizing the Hydrogen Future: the International Energy Agency's Efforts to Advance Hydrogen Energy Technologies. *Int. J. Hydrogen Energy* **2003,** *28,* 601−607.
33. Barreto, L.; Makihira, A.; Riahi, K. The Hydrogen Economy in the 21st Century: A Sustainable Development Scenario. *Int. J. Hydrogen Energy* **2003,** *28,* 267−284.
34. Magdalena, M.; Veziroglu, T. N. The Properties of Hydrogen as Fuel Tomorrow in Sustainable Energy System for a Cleaner Planet. *Int. J. Hydrogen Energy* **2005,** *30,* 795−802.
35. Goltsov, V. A.; Veziroglu, T. N.; Goltsova, L. F. Hydrogen Civilization of the Future—A New Conception of the IAHE. *Int. J. Hydrogen Energy* **2006,** *31,* 153−159.
36. Jain, I. P. Hydrogen the Fuel for 21st Century. *Int. J. Hydrogen Energy* **2009,** *34,* 7368−7378.
37. Winter, C. J. Hydrogen Energy-Abundant, Efficient, Clean: A Debate over the Energy-System-of-Change. *Int. J. Hydrogen Energy* **2009,** *34,* S1−S52.
38. Barbir, F. PEM Electrolysis for Production of Hydrogen from Renewable Energy Sources. *Sol. Energy* **2005,** *78,* 661−669.
39. Sherif, S. A.; Barbir, F.; Veziroglu, T. N. Wind Energy and the Hydrogen Economy-Review of the Technology. *Solar Energy* **2005,** *78,* 647−660.
40. Zeng, K.; Zhang, D. Recent Progress in Alkaline Wáter Electrolysis for Hydrogen Production and Applications. *Prog. Energy Combust. Sci.* **2010,** *36,* 307−326.
41. REN21, Renewables 2010. Available: http://www.ren21.net.
42. Eurobserver Barometer. http://www.eurobserv-er.org.
43. http://www.idae.es/index.php/id.670/relmenu.303/mod.pags/mem.detalle. Plan de Energías Renovables en España 2011−2020. November 2011.

44. http://eur-lex.europa.eu/en/index.htm. Directive 2009/28/EC of the European Parliament and of the Council of 23 April 2009.
45. Xie, L.; Carvalho, P. M. S.; Ferreira, L. A. F. M.; Liu, J.; Krogh, B. H.; Popli, N.; Ilić, M. D. Wind Integration in Power Systems: Operational Challenges and Possible Solutions. *Proc. IEEE* **2011,** *99,* 214−232.
46. Varaiya, P. P.; Wu, F. F.; Bialek, J. W. Smart Operation of Smart Grid: Risk-Limiting Dispatch. *Proc. IEEE* **2011,** *99,* 40−57.
47. Carrasco, J. M.; Franquelo, L. G.; Bialasiewicz, J. T.; Galvan, E.; Portillo, R. C.; Prats, M. A. M.; León, J. I.; Moreno-Alfonso, N. Power-Electronic Systems for the Grid Integration of Renewable Energy Sources: A Survey. *IEEE Trans. Ind. Electron.* **2006,** *53,* 1002−1016.
48. Red Eléctrica de España. The Spanish Electricity System. Preliminary Report. 2010. http://www.ree.es/ingles.
49. Felder, F. A.; Hajos, A. Using Restructured Electricity Markets in the Hydrogen Transition: The PJM Case. *Proc. IEEE* **2006,** *94,* 1864−1879.
50. Shaw, S.; Peteves, E. Exploiting Synergies in European Wind and Hydrogen Sectors: A Cost-Benefit Assessment. *Int. J. Hydrogen Energy* **2008,** *33,* 3249−3263.
51. Rifkin, J. *The Hydrogen Economy;* Tarcher, 2003. ISBN: 978-1585422548.
52. Yeh, S.; Loughlin, D. H.; Shay, C.; Gage, C. An Integrated Assessment of the Impacts of Hydrogen Economy on Transportation, Energy Use, and Air Emissions. *Proc. IEEE* **2006,** *94,* 1838−1851.
53. Scott, J. H. The Development of Fuel Cell Technology for Electric Power Generation: From NASA's Manned Space Program to the Hydrogen Economy. *Proc. IEEE* **2006,** *94,* 1815−1825.
54. Veziroglu, A.; Macario, R. Fuel Cell Vehicles: State of the Art with Economic and Environmental Concerns. *Int. J. Hydrogen Energy* **2011,** *36,* 25−43.
55. Lee, J. Y.; Yoo, M.; Cha, K.; Lim, T. W.; Hur, T. Life Cycle Cost Analysis to Examine the Economical Feasibility of Hydrogen as an Alternative Fuel. *Int. J. Hydrogen Energy* **2009,** *34,* 4243−4255.
56. Contreras, A.; Carpio, J.; Molero, M.; Veziroglu, T. N. Solar Hydrogen: An Energy System for Sustainable Development in Spain. *Int. J. Hydrogen Energy* **1999,** *24,* 1041−1052.
57. Spinadel, E.; Gil, J.; Gamallo, F. Wind-Powered Electrolysis for Stand Alone Operation: An Approach to a Specific Wind Converter Design. *World Hydrogen Energy Conference* **2002**.
58. Vidueira, J. M.; Contreras, A.; Veziroglu, T. N. PV Autonomous Installation to Produce Hydrogen via Electrolysis and Its Use in FC Buses. *Int. J. Hydrogen Energy* **2003,** *28,* 927−937.
59. Roy, A. *Dynamic and Transient Modelling of Electrolysers Powered by Renewable Energy Sources and Cost Analysis of Electrolytic Hydrogen*. PhD Thesis; Loughborough University: UK, 2006.
60. De Battista, H.; Mantz, R. J.; Garelli, F. Power Conditioning for a Wind-Hydrogen Energy System. *J. Power Sourc.* **2006,** *155,* 478−486.
61. Paul, B.; Andrews, J. Optimal Coupling of PV Arrays to PEM Electrolysers in Solar-Hydrogen Systems for Remote Area Power Supply. *Int. J. Hydrogen Energy* **2008,** *33,* 490−498.
62. Clarke, R. E.; Giddey, S.; Ciacchi, S. F.; Badwal, S. P. S.; Paul, B.; Andrews, J. Direct Coupling of an Electrolyser to a Solar PV System for Generating Hydrogen. *Int. J. Hydrogen Energy* **2009,** 2531−2542.
63. Gibson, T. L.; Kelly, N. A. Predicting Efficiency of Solar Powered Hydrogen Generation using Photovoltaic−Electrolysis Devices. *Int. J. Hydrogen Energy* **2010,** *35,* 900−911.
64. Santarelli, M.; Calì, M.; Macagno, S. Design and Analysis of Stand-alone Hydrogen Energy Systems with Different Renewable Sources. *Int. J. Hydrogen Energy* **2004,** *29,* 1571−1586.
65. Khan, M. J.; Iqbal, M. T. Dynamic Modelling and Simulation of a Small Wind-Fuel Cell Hybrid Energy System. *Renew. Energy* **2005,** *30,* 421−439.
66. Miland, H.; Glockner, R.; Taylor, P.; Aaberg, R. J.; Hagen, G. Load Control of a Wind-Hydrogen Stand-alone Power System. *Int. J. Hydrogen Energy* **2006,** *31,* 1215−1235.
67. Bilodeau, A.; Agbossou, K. Control Analysis of Renewable Energy System with Hydrogen Storage for Residential Applications. *Int. J. Hydrogen Energy* **2006,** *162,* 757−764.
68. Onar, O. C.; Uzunoglu, M.; Alam, M. S. Dynamic Modelling, Design and Simulation of a Wind/Fuel Cell/Ultra-Capacitor-based Hybrid Power Generation System. *J. Power Sourc.* **2006,** *161,* 707−722.
69. Ipsakis, D.; Voutetakis, D.; Seferlis, P.; Stergiopoulos, F.; Elmasides, C. Power Management Strategies for a Stand-alone Power System using Renewable Energy Sources and Hydrogen Storage. *Int. J. Hydrogen Energy* **2008,** *34,* 7081−7095.
70. Aiche-Hamane, L.; Belhamel, M.; Benyoucef, B.; Hamane, M. Feasibility Study of Hydrogen Production from Wind Power in the Region of Ghardaia. *Int. J. Hydrogen Energy* **2009,** *34,* 4947−4952.
71. Hwang, J. J.; Lai, L. K.; Wu, W.; Chang, W. R. Dynamic Modelling of a Photovoltaic Hydrogen Fuel Cell Hybrid System. *Int. J. Hydrogen Energy* **2009,** *34,* 9531−9542.
72. Sopian, K.; Zamari, M.; Ramli, W.; Yusof, M.; Yatim, B.; Amin, N. Performance of a PV-Wind Hybrid System for Hydrogen Production. *Renew. Energy* **2009,** *34,* 1973−1978.
73. Zervas, P. L.; Sarimveis, H.; Palyvos, J. A.; Markatos, N. C. G. Model-Based Optimal Control of a Hybrid Power Generation System Consisting of Photovoltaic Arrays and Fuel Cells. *J. Power Sourc.* **2008,** *181,* 327−338.
74. Korpas, K.; Greiner, C. J. Opportunities for Hydrogen Production in Connection with Wind Power in Weak Grids. *Renew. Energy* **2008,** *33,* 1199−1208.
75. Zhou, T.; Francois, B.; el hadi Lebbal, M.; Lecoeuche, S. Modeling and Control Design of Hydrogen Production Process by Using a Causal Ordering Graph for Wind Energy Conversion System. *IEEE International Symposium on Industrial Electronics* **2007,** 3192−3197.
76. Troncoso, E.; Newborough, M. Implementation and Control of Electrolysers to Achieve High Penetrations of Renewable Power. *Int. J. Hydrogen Energy* **2007,** *32,* 2253−2268.
77. Mantz, R. J.; De Battista, H. Hydrogen Production from Idle Generation Capacity of Wind Turbines. *Int. J. Hydrogen Energy* **2008,** *33,* 4291−4300.
78. Jørgensen, C.; Ropenus, S. Production Price of Hydrogen from Grid Connected Electrolysis in a Power Market with High Wind Penetration. *Int. J. Hydrogen Energy* **2008,** *33,* 5335−5344.
79. García, J. G.; De Battista, H.; Mantz, R. J. Control of a Grid-Assisted Wind-Power Hydrogen Production System. *Int. J. Hydrogen Energy* **2010,** *35,* 5786−5792.
80. Gutiérrez-Martín, F.; Confente, D.; Guerra, I. Management of Variable Electricity Loads in Wind-Hydrogen Systems: The Case of a Spanish Wind Farm. *Int. J. Hydrogen Energy* **2010,** *35,* 7329−7336.
81. Sanchez, I.; Ursúa, A.; Marroyo, L.; Sanchis, P. Primary Regulation Strategies Applicable to Wind Farms Coupled with Hydrogen Production Systems. *International Conference on Clean Electrical Power* **2011,** 584−587.
82. Ntziachristos, L.; Kouridis, C.; Samaras, Z.; Pattas, K. A Wind-Power Fuel-Cell Hybrid System Study on the Non-interconnected Aegean Islands Grid. *Renew. Energy* **2005,** *30,* 1471−1487.
83. Li, X.; Song, Y.; Han, S. Frequency Control in Micro-grid Power System Combined with Electrolyzer System and Fuzzy PI Controller. *J. Power Sourc.* **2008,** *180,* 468−475.

84. Vachirasricirikul, S.; Ngamroo, I.; Kaitwanidvilai, S. Application of Electrolyzer System to Enhance Frequency Stabilization Effect of Microturbine in a Microgrid System. *Int. J. Hydrogen Energy* **2009,** *34,* 7131−7142.
85. Bagherian, A.; Tafreshi, S. M. M. A Developed Energy Management System for a Microgrid in the Competitive Electricity Market. *IEEE PowerTech.* **2009,** 1−6.
86. Schucan, T. *Case Studies of Integrated Hydrogen Systems. Hydrogen Implementing Agreement, Task 11: Integrated Systems, Subtask A: Case Studies;* International Energy Agency, 1999.
87. Ulleberg, Ø, et al. *Hydrogen Demonstration Project Evaluations. Hydrogen Implementing Agreement, Task 18: Integrated Systems Evaluation, Subtask B: Demonstration Project Evaluation;* International Energy Agency, 2007.
88. García-Conde, A. G.; Rosa, F. Solar Hydrogen Production: A Spanish Experience. *Int. J. Hydrogen Energy* **1993,** *18,* 995−1000.
89. Kauranen, P. S.; Lund, P. D.; Vanhanen, J. P. Development of a Self-Sufficient Solar-Hydrogen Energy System. *Int. J. Hydrogen Energy* **1994,** *19,* 99−106.
90. Lehman, P. A.; Chamberlin, C. E.; Pauletto, G.; Rocheleau, M. A. Operating Experience with a Photovoltaic-Hydrogen Energy System. *Int. J. Hydrogen Energy* **1997,** *22,* 465−470.
91. Szyszka, A. Ten years of Solar Hydrogen Demonstration Project at Neunburg Vorm Wald, Germany. *Int. J. Hydrogen Energy* **1998,** *23,* 849−860.
92. Hollmuller, P.; Joubert, J. M.; Lachal, B.; Yvon, K. Evaluation of a 5 kWp Photovoltaic Hydrogen Production and Storage Installation for a Residential Home in Switzerland. *Int. J. Hydrogen Energy* **2000,** *25,* 97−109.
93. Dutton, A. G.; Bleijs, J. A. M.; Dienhart, H.; Falchetta, M.; Hug, W.; Prischich, D.; Ruddell, A. J. Experience in the Design, Sizing, Economics, and Implementation of Autonomous Wind-Powered Hydrogen Production Systems. *Int. J. Hydrogen Energy* **2000,** *25,* 705−722.
94. Agbossou, K.; Chahine, R.; Hamelin, J.; Laurencelle, F.; Anouar, A.; St-Arnaud, J. M.; Bose, T. K. Renewable Energy Systems Based on Hydrogen for Remote Applications. *J. Power Sourc.* **2001,** *96,* 168−172.
95. Agbossou, K.; Kolhe, M.; Hamelin, J.; Bose, T. K. Performance of a Stand-alone Renewable Energy System Based on Energy Storage as Hydrogen. *IEEE Trans. Energy Convers.* **2004,** *19,* 633−640.
96. Gazey, R.; Salman, S. K.; Aklil-D'Halluin, D. D. A Field Application Experience of Integrating Hydrogen Technology with Wind Power in a Remote Island Location. *J. Power Sourc.* **2006,** *157,* 841−847.
97. Little, M.; Thomson, M.; Infield, D. Electrical Integration of Renewable Energy into Stand-alone Power Supplies Incorporating Hydrogen Storage. *Int. J. Hydrogen Energy* **2007,** *32,* 1582−1588.
98. Kelly, N. A.; Gibson, T. L. A Solar-Powered, High-Efficiency Hydrogen Fuelling System using High-Pressure Electrolysis of Water: Design and Initial Results. *Int. J. Hydrogen Energy* **2008,** *33,* 2747−2764.
99. Varkaraki, E.; Tzamalis, G.; Zoulias, E. Operational Experience from the RES2H2 Wind-Hydrogen Plant in Greece. *World Hydrogen Energy Conference* **2008,** 1−4.
100. Aprea, J. L. Hydrogen Energy Demonstration Plant in Patagonia: Description and Safety Issues. *Int. J. Hydrogen Energy* **2009,** *34,* 4684−4691.
101. Ulleberg, Ø; Nakken, T.; Eté, A. The Wind/Hydrogen Demonstration System at Utsira in Norway: Evaluation of System Performance using Operational Data and Updated Hydrogen Energy sysTem Modelling Tools. *Int. J. Hydrogen Energy* **2010,** *35,* 1841−1852.
102. Correas, L.; Aso, I. Task 24: Wind Energy and Hydrogen Integration. *World Hydrogen Energy Conference* **2010,** 419−427.
103. Harrison, K. W.; Martin, G. D.; Ramsden, T. G.; Kramer, W. E. The Wind-to-Hydrogen Project: Operational Experience, Performance Testing, and Systems Integration. NREL, Tech Rep. TP-550−44082; 2009.
104. Rey, M.; Aguado, M.; Garde, R.; Carretero, T. H_2 Production in Sotavento Windfarm. *World Hydrogen Energy Conference* **2010,** 45−52.
105. Phang, J. C. H.; Chan, D. S. H.; Phillips, J. R. Accurate Analytical Method for the Extraction of Solar Cell Model Parameters. *Electron. Lett.* **1984,** *20,* 406−408.

CHAPTER

15

Recent Advances in Fuel Cells for Transport and Stationary Applications

Antonio José Martín [*], *Aitor Hornés* [†], *Arturo Martínez-Arias* [†], *Loreto Daza* [†]

[*]**CIEMAT, Madrid, Spain,** [†]**Instituto de Catálisis y Petroleoquímica (CSIC), Madrid, Spain**

OUTLINE

15.1 Introduction 361

15.2 Transport Applications 362
- *15.2.1 Types of Mobile Applications* 362
  - 15.2.1.1 Auxiliary Power Units 362
  - 15.2.1.2 Motive Power 362
- *15.2.2 Required Features for Fuel Cell Systems* 363
  - 15.2.2.1 General Characteristics of Fuel Cell-based Automotive Systems 363
  - 15.2.2.2 Fuel Cell Systems Cost and Technical Objectives 365
- *15.2.3 Current Market Status* 366
  - 15.2.3.1 Materials Handling 366
  - 15.2.3.2 Fuel Cell Vehicles 366
  - 15.2.3.3 Fuel Cell Buses 366
  - 15.2.3.4 Other Applications 367
- *15.2.4 Market Prospective* 367

15.3 Stationary Applications 367
- *15.3.1 Types of Stationary Applications* 368
- *15.3.2 Technical Features for Stationary Applications* 368
  - 15.3.2.1 General Characteristics of Low-Temperature Fuel Cells 368
  - 15.3.2.2 General characteristics of High-Temperature Fuel Cells 369
  - 15.3.2.3 Fuel Cell Systems Cost and Technical Objectives 372
  - 15.3.2.4 Current R&D Guidelines 373
- *15.3.3 Current Market Status* 373
  - 15.3.3.1 Backup Power 374
  - 15.3.3.2 Combined Heat and Power 375
- *15.3.4 Market Prospective* 375

15.4 Fuel Cell Markets Supported by Governmental Programs 376
- *15.4.1 The United States* 376
- *15.4.2 Japan* 376
- *15.4.3 Europe* 377
- *15.4.4 South Korea* 377

15.5 Conclusions 377

References 378

15.1 INTRODUCTION

Fuel cells are one of the most promising technologies in terms of energy efficiency for high performance in operation. When hydrogen is used as fuel, the only emission is water. Fuel cells cover a wide range of applications for transportation and power generation to small and medium scale.

Main mobile applications for fuel cells include auxiliary power units (APUs), special vehicles such as forklifts, mainstream transportation and other niche applications. Proton exchange membrane fuel cells (PEMFCs) are used due to low-temperature operation, good performance and fast response. Analysts consider extensive adoption of fuel cell vehicles (FCVs) as necessary to cut greenhouse gas (GHG) emissions in the future.

http://dx.doi.org/10.1016/B978-0-444-56352-1.00015-5

Currently, cost and durability of fuel cells are the main obstacles to overcome even though significant improvements have been made during 2000–2010. Hydrogen infrastructure is also a key factor for widespread commercialization of FCVs. Supporting policies are currently in place through research projects and collaboration frameworks between manufacturers and research institutions, especially in the United States, Europe, Japan and South Korea. Analysts foresee a huge dependence on governmental policies in order to reach a significant presence of FCVs before 2050. Car companies continue to develop demonstration projects and aim to start commercialization of light-duty vehicles by 2015.

Regarding stationary applications, PEMFC and phosphoric acid fuel cell (PAFC) systems are among the first fuel cell products competing with conventional technologies. Due to their intrinsic characteristics, applications requiring fast response and few megawatts are most suitable. Backup power generation and combined heat and power (CHP) are the most developed applications nowadays. High-temperature fuel cells like solid oxide fuel cells (SOFCs) and molten carbonate fuel cells (MCFCs) operate typically at temperatures above 873 K, which allows use of the heat produced in further fuel processing and heat-generation systems. However, their high operating temperature disallows fast start-up and imposes important restrictions in terms of the type of structural or accessory materials employed, which should be able to resist such high thermal stress, as well as in terms of mutual compatibility between components. On the whole, such general characteristics make them the most useful for large-scale stationary energy generation, while mobile applications are certainly more limited. Nevertheless, an advantage of high-temperature fuel cells is their potential to be independent of a pure hydrogen infrastructure since they are generally able to operate with transitional fuels such as natural gas, syngas and biogas. A brief account of the general characteristics of this type of fuel cells including recent advances is given in this chapter.

"The issue is, now, cost, cost and cost. We need continued governmental support. In many cases each country tried to gain industrial pay out, but there is not enough international collaboration. Fuel cell industry has a bad reputation (nobody would like to work with the industry). The cost targets from the industry are not realistic for suppliers."[1]

15.2 TRANSPORT APPLICATIONS

Mobile applications include motive power for cars, buses and other fuel cell passenger vehicles, specialty vehicles, materials handling vehicles (e.g. forklifts) and APUs for highway as well as off-road vehicles or other niche applications.

15.2.1 Types of Mobile Applications

15.2.1.1 Auxiliary Power Units

PEMFCs can provide auxiliary power as an alternate source for portable, mobile on-road and off-road transportation applications such as trucks, locomotives, airplanes, boats, or military vehicles. They can provide electrical power for cooling, lighting, or other auxiliary power needs in more efficient and quieter conditions when the main internal combustion engine (ICE) is not operating. In addition, fuel cells do not produce either contaminating particles or NO_x, a key advantage for indoors use. PEM fuel cells for these applications can range in size from 3 to 30 kW and are expected to operate over lifetimes between 20,000 and 35,000 h.[2]

15.2.1.2 Motive Power

15.2.1.2.1 SPECIAL VEHICLES

PEM fuel cells offer clear advantages over batteries for special vehicles. While both can be used indoors due to pollutant-free operation, fuel cells show better productivity because refueling them takes shorter than changing batteries. Special vehicles application has emerged as the first niche of commercial success for automotive fuel cells fueled by hydrogen or methanol. Lift trucks (including forklifts and pallet trucks) powered by fuel cells are currently in use in commercial applications by several major global companies. Such vehicles usually require from 5 to 20 kW and operate indoors where ICEs cannot be used. PEM fuel cell forklifts help achieve better productivity and are less environmentally harmful because they (1) require minimal time for refueling (less than 3 min versus 15–30 min for changing batteries); (2) have significantly less maintenance than battery-powered forklifts, whose batteries must be regularly charged, refilled with water, and replaced; (3) reduce the energy consumption by up to 29% and their GHG emissions by up to 38%, when compared with lift trucks using conventional ICEs.[2,3] Ground support vehicles (GSVs) is another niche where FCVs are close to competing with incumbent technologies. Even though some mentioned advantages, PEM fuel cell GSVs are not as attractive as batteries, and specially ICEs on a total cost basis. In addition, batteries are not capable of providing the horsepower required to tow a large aircraft. Because fuel cells may outperform batteries with these heavier vehicles, the fact that fuel cells can support a wider variety of vehicles may provide a compelling case to be studied. A detailed description of forklifts and airport ground support

equipment requirements and market assessment can be found elsewhere.[4]

15.2.1.2.2 MAINSTREAM TRANSPORTATION

This is the main market where fuel cells are expected to play a major role in the future. Due to the unique characteristics (size, weight, and performance) required for these automotive systems, PEMFCs operating on pure hydrogen is the type of fuel cell used. Light-duty vehicles have proved system efficiencies from 53% to 59%. It represents more than twice the efficiency that can be expected from gasoline ICEs, and substantially higher than even hybrid electric power systems.[5] Figure 15.1 shows a chart comparing different automotive vehicles including hybrid ICE, pure electric, and fuel cell (FCVs) types according to duty cycle and driving range requirements. The FCV is the most flexible solution and is expected to be more appropriate for medium to large driving ranges and from medium to large duty cycles. It includes personal vehicles, fleet vehicles, transit buses, and short-haul trucks. Many automobile manufacturers around the world, and several transit bus manufacturers, are developing and demonstrating fuel cell electric vehicles today. The timeline for market readiness varies, but several companies have announced plans to commercialize by 2015.

The widespread commercialization of FCVs is a key requirement to accomplish the environmental challenge, even in the case of hydrogen being produced from fossil resources (natural gas). According to most studies,[2,6,7] plug-in hybrids and biofuels alone will not reach reductions of GHG emissions to a desired extent. Hydrogen-powered FCVs must be massively added to the global fleet of vehicles in order to achieve a large reduction. Figure 15.2 includes calculations about GHG emissions from future light-duty vehicles depending on the type of engine and origin of fuel.

15.2.1.2.3 OTHER TRANSPORT

Materials handling, buses and light-duty vehicles comprise the majority of fuel cell shipments to date.[3] Nevertheless, there are a number of projects in the transport sector including military uses such as unmanned aerial and underwater vehicles, or fuel cell scooters, assisted-pedaling bicycles, trains, and small boats.

15.2.2 Required Features for Fuel Cell Systems

15.2.2.1 General Characteristics of Fuel Cell-based Automotive Systems

FCVs share the most components with ICE cars, and are fairly similar to pure electric vehicles. Distinctive systems are the fuel cell stack and its associated control system as well as hydrogen storage or fuel conversion systems. PEM fuel cells present a series of features that make them suitable for use in mobile applications. They show a fast start from room temperature, adequate power-to-volume and power-to-weight ratios as well as high capacity to follow electrical load variations. On the other hand, they require both highly active catalysts and trace-level contaminated fuel (H_2). Nowadays it implies the use of expensive and scarce Pt-based catalysts and a costly fuel processing stage to be added when using hydrocarbons as the primary fuel.

The on-board storage of hydrogen is critical for the transport applications of FCVs and the most adopted solution by FCV manufacturers. A comparable driving

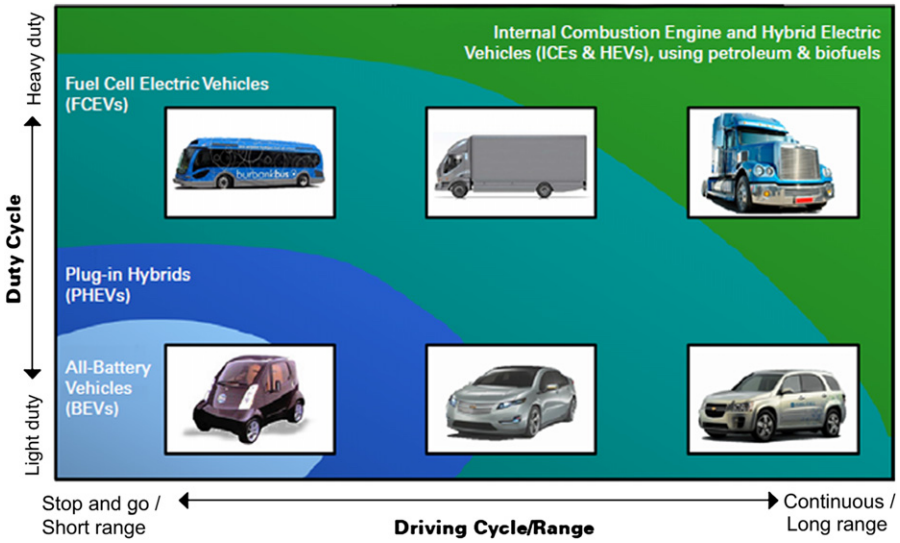

FIGURE 15.1 Most appropriate automotive vehicle solution depending on the duty cycle and driving cycle. (For color version of this figure, the reader is referred to the online version of this book.) *Source: US Department of Energy.*

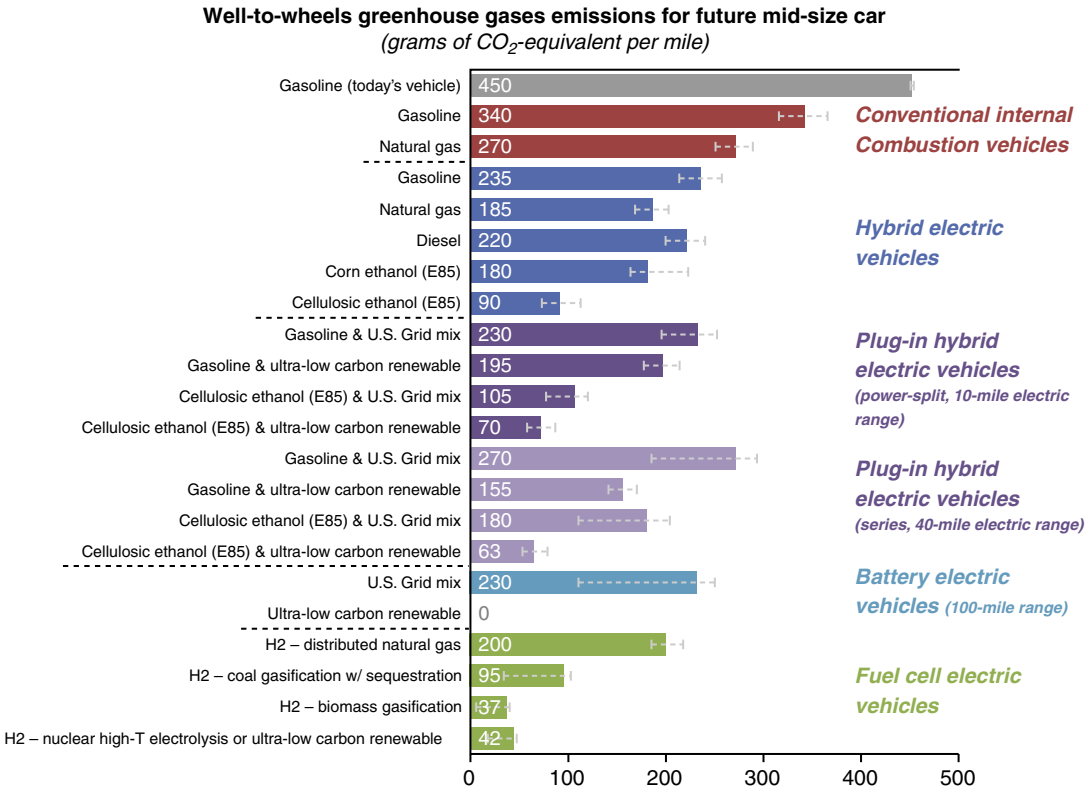

FIGURE 15.2 Analysis of GHG emissions for different types of light-duty vehicles. (For color version of this figure, the reader is referred to the online version of this book.) *Source: US Department of Energy (Well-to-Wheels Greenhouse Gas Emissions and Petroleum Use for Mid-Size Light-Duty Vehicles. US Department of Energy, October 2010).*

range with gasoline and diesel cars is mandatory for end users' adoption. Minimum storage volume, reduced weight and low cost are also highly desirable features for any on-board hydrogen storage system. Current hydrogen storage options do not allow a similar energy density when compared to gasoline (31.1 MJ/l). They include compressed hydrogen (2.8 MJ/l at 345 bar), liquid hydrogen (8.4 MJ/l) and metal hydrides (from 7 to 12 MJ/l).[2] Nevertheless, FCVs achieve acceptable driving ranges of about 450 km due to their higher global efficiency. Figure 15.3 contains a scheme of the main systems included in an FCV including a hydrogen storage system.

On-board fuel reforming is a more complex option designed to utilize the existing liquid hydrocarbon fuel infrastructure through on-board production of hydrogen. Therefore, on-board fuel reforming could be an intermediate solution while the establishment of

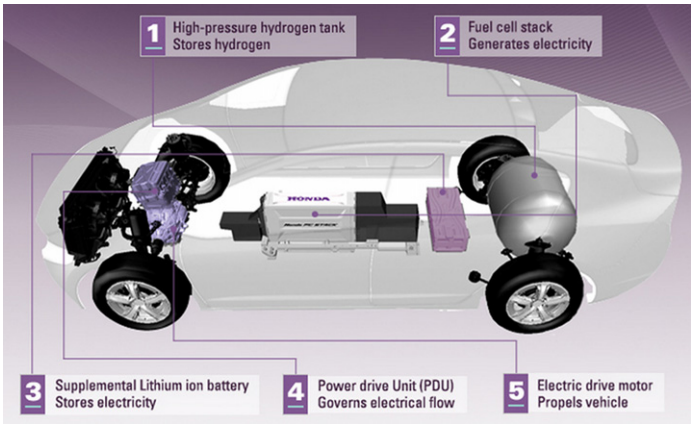

FIGURE 15.3 Main components of an automotive fuel cell system with hydrogen storage. (For color version of this figure, the reader is referred to the online version of this book.) *Source: Honda FCX Clarity (Available at http://automobiles.honda.com/fcx-clarity/).*

a hydrogen infrastructure is settled. Global reforming for automotive applications require catalytic processes such as reforming followed by hydrogen purification stages, namely, shift conversion and CO removal, due to high hydrogen purity requirements for PEM fuel cells. Catalytic partial oxidation (CPO, where fuel and air are mixed at the inlet of the reforming reactor) or autothermal reforming (similar to CPO but steam is also added) are the most common solutions for reforming. The on-board reforming system presents a number of technical and economical challenges including volume and weight targets and start-up requirements, among others.[8] System electrical efficiency reaches a maximum at partial loads (20–40%) followed by a slight decrease up to nominal power when fuel processing is present.[9] At partial loads, fuel cell efficiency is higher due to high voltages, but both fuel processing heat loses and parasitic loses in the power conditioning system are still high.[10] At full load, fuel cell efficiency decreases, while heat and parasitic power loses are minimum.

15.2.2.2 Fuel Cell Systems Cost and Technical Objectives

The remaining challenges for successful FCV commercialization are clearly identified by research institutions and manufacturers. They have become decisive criteria for research funds allocation from public sources, such as the US Department of Energy (DoE), Japanese New Energy and Industrial Development Organization (NEDO) project or European Framework Programmes. It is expected that overcoming such obstacles may help trigger the widespread commercialization of FCVs. A very informative chart reported by Japanese NEDO (Fig. 15.4) shows an image of both already overcome and remaining challenges for FCVs when compared to set milestones for 2015. It is remarkable that four of six have already been surpassed. Driving range, hydrogen refueling time and cold start have reached values comparable to ICE cars. However, durability and cost remain as major obstacles for light-duty FCV commercialization. Probably, the most outstanding parameter an FCV can provide compared to an ICE car is total efficiency; according to manufacturers' claims, under pure hydrogen, electrical efficiencies of state-of-the-art automotive PEM fuel cell systems amount to approximately 60% peak value when auxiliary batteries and hydraulic-regenerative cooperative braking systems are added, as recently reported for the paradigmatic Honda FCX Clarity.[11] This figure is more than three times higher than for a gasoline ICE and more than twice as high as that for a hybrid vehicle. Operation under reformate at partial loads surpasses 40% electrical for other FCVs.[10]

The US DoE has also set similar objectives regarding durability, efficiency and manufacturing cost (Table 15.1) for a middle-term time scale (up to 2020). The DoE's Technology Validation program continues to provide valuable real operation data. The program includes 152 FCVs that have accumulated 114,000 h and 4.5 million km under real end-user driving, demonstrating ranges of over 400 miles and fuel cell efficiencies of up to 59%.[12]

Demonstration projects focused on reliability, cost and durability continue to show the potential of fuel cell buses. Remarkable 7000-h durability with no fuel cell replacement in California is reported,[12] while Japan

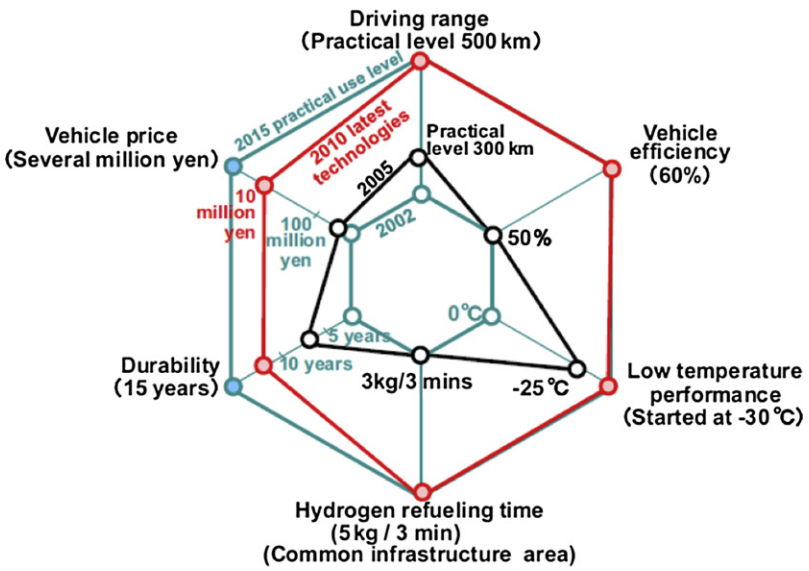

FIGURE 15.4 Evolution of some key features of FCVs compared to 2015 objectives as minimum requirements for commercialization. (For color version of this figure, the reader is referred to the online version of this book.) *Source: NEDO, Japan.*

TABLE 15.1 Technical and Cost Objectives for Transportation Applications up to 2020 Proposed by the US Department of Energy

Time scale	Objectives	Application
2017	Direct-H_2 fuel cell system manufactured at $30/kW, with 60% global efficiency and 5000-h durability	Transportation
	Developing and verification of on-board H_2 storage systems achieving capacity of 5.5% by weight and an energy density of 1300 Wh/l	
	Reduction of the high-volume cost of high-strength carbon fiber to ~$9/pound	
2020	Fuel cell system with 45 W/kg and power density of 40 W/l	APU

was especially active through its Hydrogen and Fuel Cell Demonstration Project (Japan Hydrogen and Fuel Cell (JHFC)), which finished its second phase in 2010 and is facing the precommercialization stage. JHFC accumulated 8 years of experience testing 135 passenger cars and 13 buses that added up about 1,500,000 km. JHFC reported bench test efficiencies of 60% and significant fuel economy for passenger cars.[13] Fuel cell bus fleets were also used at the 2010 Winter Olympics (20 buses), the 2010 Shangai Expo, and the 2012 Olympics in London. Europe has released a new project under the European Fuel Cell and Hydrogen Joint Technology Initiative, known as the "Clean Hydrogen in European Cities" (CHIC) project. It will deploy up to 28 hydrogen fuel cell buses in five major European cities. High cost is still a major drawback for this application, even though some remarkable approaches are in progress, like the modular approach taken by Daimler. Its Citaro bus system is based on two of its B-class automotive F-CELL units. Compared with diesel, a fleet of fuel cell buses may achieve a 60% better fuel economy, an 80% reduction in maintenance costs, and a 43% reduction in GHG emissions.[14]

15.2.3 Current Market Status

15.2.3.1 Materials Handling

Fuel cell-based forklifts are the first successful business case for sales without the need for subsidies. The materials handling market shows a steady improvement, with increasing sales volumes, cost reductions, and a strong track record of operating success. As evidence, half of all shipments in the transport sector for 2010 were for materials handling vehicles. Leader companies such as Plug Power achieve close to 1000 sold units per year. Encouragingly, Nissan, Wal-Mart and Coca Cola consistently report operational advantages when using fuel cell forklifts.[3,12] As a growing alternative for specific applications, direct methanol fuel cells, which use liquid fuel, are hybridized with the existing battery technology to operate as range extenders for smaller fleets in a single shift operation.

15.2.3.2 Fuel Cell Vehicles

Fuel cell cars continue to make substantial gains in performance and cost reduction. Eight of the world major car manufacturers signed a memorandum of understanding (MoU) in 2009 signaling the intent to commercialize FCVs by 2015. Manufacturers have confirmed it at regular intervals up to date. Another MoU was signed in 2011 between Hyundai–Kia Motors and Sweden, Denmark, Iceland and Norway to provide FCVs and develop the necessary hydrogen refueling infrastructure in the region. Most manufacturers are currently demonstrating FCV prototypes throughout the world. Daimler, Honda, Toyota or Hyundai are among them. FCVs are currently available through leasing in selected places like California or Japan as a private fleet of vehicles for institutional purposes such as police, big public events, universities, and others.[3] Projected high-volume transportation fuel cell system costs have decreased 80% since 2002 and are currently below $50/kW, which is close to the $30/kW objective (Table 15.1). These reductions are largely due to R&D efforts that enabled reduced platinum group metal content, increased power density, and simplified balance of plant (BoP).[12]

15.2.3.3 Fuel Cell Buses

As one of the most interesting automotive fuel cell markets, there is a continuous effort for demonstrating fuel cell buses. There are currently a number of projects with outstanding reliability and low maintenance records. Some relevant examples are AC Transit reported in the United States over 400,000 km operation for 7000 h with a 65% average higher fuel economy when compared with diesel fueled buses. In Canada, buses powered by fuel cells from Ballard Power Systems reached 480 km operating range. Other projects to coordinate the purchase of fuel cell buses are trying to leverage economies of scale, but these are limited to regions where funding is available.[3] In Europe, the current CHIC project is building upon previous work

by the Clean Urban Transport for Europe (CUTE), while HyFleet:CUTE projects aim to facilitate staged introduction of hydrogen fuel cell bus fleets, supporting infrastructure in Europe.

15.2.3.4 *Other Applications*

In Europe, fuel cell APUs are being sold as an optional accessory to power electronics in "caravans", or campers, when parked in remote locations or campsites.[12] Additional promising applications are APUs in trucks and recreational vehicles, and in marine applications.[15] Fuel cells are replacing batteries in unmanned aerial vehicles, setting new performance and durability records in electric-powered flight.

15.2.4 Market Prospective

Extensive use of automotive fuel cells for light to heavy-duty vehicles will likely be the dominant long-term solution to automotive applications, since pure electric vehicles may not be suitable for all transportation requirements (Fig. 15.1) and oil-derived fuels are expected to become scarcer over the next decades. In addition, the environmentally friendly mobility provided by hydrogen as a fuel will likely be a key mainstay of the global fight against global climate change.[6] It therefore seems that automotive fuel cells may gain market penetration up to becoming the leading technology in the future. This is the common view among automotive market studies that can be found in the literature. The automotive industry agrees on the importance of FCV business in the near future and is currently very active on fuel cell applied research. In 2011, 17 patents were awarded in the United States connected to automotive fuel cell systems.[16] Auto companies that signed an MoU committing to start fuel cell cars commercialization by 2015 are currently developing demonstration programs and periodically confirm the original timeline. As some examples, Hyundai signed that it intends to take the lead in commercializing fuel cell electric vehicle by 2015 to be offered at a cost below $50,000; General Motors restated its plan to introduce a commercial vehicle by 2015 at a rate of tens of thousands of vehicles by 2015–2017; Toyota plans to introduce a fuel cell sedan in 2015, priced to sell at $50,000; BMW showcased a new hybrid electric vehicle that uses a 5-kW UTC Power fuel cell system to supplement a battery and traditional gasoline engine, while Honda has recently released a cutting edge version of its fuel cell car called FCX Clarity, although only available through leasing.[3,12]

There are clear divergences among different authors regarding the rate of market penetration for FCVs. Simulations include very complex models including tens of estimated parameters with clear uncertainty and that are very sensitive to the short-term evolution of the market (up to 2025). In spite of the apparent commitment to develop FCVs market by auto companies, the US DoE foresees no significant change to FCVs before 2050 even in a favorable scenario with high oil prices and CO_2 taxes in place if not supporting policy is applied: "In case of no governmental supporting policy (…) even with technology success, high world oil prices, and a CO_2 tax in place, market forces alone will not drive a market shift to hydrogen powered vehicles until, perhaps, well after 2050. The market barriers and industry investments for FCVs are too large to overcome and advanced gasoline and diesel hybrid vehicles (which do not face the same market barriers) will dominate."[17]

Based on different evolutions of supporting policies, technical improvements, and hydrogen infrastructure development, estimations vary from 2 to 10 million FCVs by 2025 as representative figures for significant changeover to FCVs.[17] The initial commercialization of FCVs is expected to be on the order of tens of thousands of vehicles from 2015, with the majority of these being adopted by return-to-base fleets, under limited hydrogen infrastructure present at that time. It is noticeable that even a tiny success by three of the major automakers in achieving their goals by 2015 would lead to a dramatic increase in global fuel cell shipments.[3]

The same applies to fuel cell buses application. The worldwide market for fuel cell buses is currently very small. Even though both decreasing costs and increasing durability are required, encouraging public transport and the implementation of low-emission zones in major cities may be driving forces to increase the demand from public institutions.

Summarizing, directed policies of cost sharing and tax credits, continuous performance and cost improvements of FCVs, together with the required hydrogen infrastructure are required over a decade in order to help auto companies to bring competitive FCVs and obtain general public acceptance. The US DoE calculates a cumulative cost of $10–$45 billion for the federal government over the entire period.[17]

15.3 STATIONARY APPLICATIONS

Fuel cell-based systems are suitable for a vast majority of stationary applications, since they show a wide variety of technical solutions and can be coupled to cover from a few watts to several megawatt requirements. PAFCs and PEMFCs are more appropriate for applications requiring fast response up to 200 kW.

From 200 kW up to a few megawatts, MCFC and SOFCs are the most suitable technologies.

15.3.1 Types of Stationary Applications

Such applications currently are the following:

- **As unique power source.** Of critical importance in isolated places, where electrical energy supply is mandatory, like telecommunication sites or remote human settlements.[18] This category primarily comprises of fuel cell systems above 50 kW and includes mainly high-temperature or alternatively PAFC. PEMFC systems are rarely used for this purpose (see ClearGenTM multi MW systems by Ballard).[19]
- **As part of combined systems with nonpredictable renewable energy sources.** Wind/solar power sources and electric vehicles forthcoming penetration may jeopardize the electric grid stability. Hydrogen production systems from renewable sources coupled to fuel cells may provide necessary support as part of a smart grid. Integrated renewable hydrogen systems provide a pathway for the expanded use of distributed intermittent renewable sources or, at a larger scale, a solution for inherent mismatching between electrical production and consumption for wind farms or large solar plants. At the present stage of development, such a solution is a viable case only in some places for large wind farms with high capacity factors.[20] However, economical assumptions strongly depend on third-party factors such as local technical regulations, feed-in tariffs, long-term interest rates, etc.
- **As backup for emergency power generation.** According to the US DoE, telecommunication and data centers are the most sensitive facilities to power outages, followed by the commercial market, where long outages are very disruptive and may imply significant economic loses. Reliability is identified as one of the most critical factors when selecting backup power systems in commercial segments.[5] Besides, premium applications are good candidates for PEMFC and PAFC systems, like army applications.[21,22] For example, hurricane Katrina caused severe power outages and emergency supplies interruption across the Gulf Coast for some days. As a consequence, many hospitals and other critical emergency services could not use backup diesel generators due to lack of fuel or mechanical failure. In contrast, the New York Police Department's Central Park Station kept running during the big blackout of 2003 supported by a fuel cell backup system.[5] Pure hydrogen must be used for a quick response to avoid fuel processing or the use of significant energy reserve through batteries or supercapacitors.
- **As CHP supply.** CHP facilities are generally concentrated on large-scale plants including chemicals, paper, refining, food processing and metals production (e.g. 88% in the United States) The most common fuel is natural gas followed by coal and process waste.[23] Nevertheless, energy consumption data show that about 50% of the final energy is used by private households and 65% of it is due to room and water heating.[24,25] PEMFC systems are mainly manufactured for micro (below 1 kW) and small (10–200 kW) applications, while PAFC systems usually cover small applications. High-temperature fuel cells (MCFCs, SOFCs) cover medium-scale stationary energy generation (to a few milliwatts). These sizes include chiefly residential and small commercial. The electric power produced competes with the grid-based electricity, while the waste heat does with gas-fired boilers. Since the value of electric power is superior, the higher the electrical efficiency, the higher the net value achieved. Fuel cells show better electrical efficiencies than thermal machines driven by Stirling or Rankine cycles and are only exceeded by high-temperature fuel cells.[26] Electrical plus thermal combined efficiency is close to 85–90%, markedly higher than conventional systems. Among stationary applications, CHP will probably become the main fuel cells market.[9]

15.3.2 Technical Features for Stationary Applications

15.3.2.1 General Characteristics of Low-Temperature Fuel Cells

This section describes the current status of PAFC and PEMFC systems for stationary applications and key remaining challenges to eliminate commercialization barriers. Today, there are clear cost and technological objectives, mainly established by governmental institutions, that when overcome, will transform fuel cell stationary systems into a full competitive alternative to the market.

PAFCs and PEMFCs present a series of features that make them suitable for use in stationary applications. They share many characteristics since they work under identical anodic and cathodic reactions and at relatively low temperatures. They show some desirable features such as fast start from room temperature and high capacity to follow electrical load variations. On the other hand, low-temperature operation requires both highly active catalysts and trace-level contaminated fuel (H_2). To date, these imply the use of expensive and scarce Pt-based catalysts and a costly fuel processing stage to be added when using hydrocarbons as the primary fuel. Waste heat utilization is constrained to liquid or

gas heating below 343 K, since, due to Carnot limitations, its low temperature practically prevents additional electricity production through a subsequent thermal cycle. These features do not apply to high-temperature fuel cells.

PAFCs operate at higher temperatures than PEMFCs (473 and 333–353 K, respectively), which facilitates a better utilization of waste heat, and is less sensitive to CO poisoning (1% versus some parts per million in the anodic inlet[27]), which allows a simpler fuel processing. Besides, PAFCs have a slightly better efficiency.[27] On the other hand, catalyst stability becomes a central issue and due to the corrosive nature of phosphoric acid, the stack must be made of expensive materials. High-temperature PEMFCs (HT-PEMFC) work from 393 to 443 K, which overcomes some of the above-mentioned problems. They show similar CO-poisoning resistance to PAFCs, require inexpensive membrane materials and simplified water management compared to low-temperature PEMFCs. There is an increasing interest in developing these fuel cells nowadays, but durability appears as a major challenge. In spite of being at an early stage of development, extensive experimental work is currently in progress to assess stationary power prototypes in the kilowatt scale.[28–30]

According to manufacturers' claims, under pure hydrogen, electrical efficiencies of state-of-the-art PEMFC and PAFC systems amount to approximately 50%, and close to 100% if waste heat is utilized. Operation under reformate at partial loads reaches approximately 40% electrical and 90% total. System electrical efficiency reaches a maximum at loads between 20% and 40% followed by a slight decrease up to nominal power when fuel processing is present. The reason is that, at extreme partial loads, the fuel cell does not generate enough heat to keep an adequate working temperature, while fuel processing heat loses and parasitic loses in the power conditioning system are high. At partial loads, fuel cell efficiency is higher due to high voltages, but both fuel processing heat loses and parasitic loses in the power conditioning system are still high.[9,10] At full load, fuel cell efficiency decreases while heat and parasitic power loses are minimum. If heat plus electricity are considered, total efficiency of such systems steadily increases up to the nominal power.[31]

15.3.2.2 General characteristics of High-Temperature Fuel Cells

15.3.2.2.1 SOLID OXIDE FUEL CELLS

SOFCs use as electrolyte a dense nonporous oxide solid in either planar or tubular configuration. They can reach efficiency close to 60% in chemical to electrical energy conversion, which on the whole can be increased to 85% when employing cogeneration systems. They operate at high temperatures typically between 973 K and 1273 K. This provides advantages and drawbacks in comparison with other fuel cell technologies. Thus, such high operating temperatures allow employment of nonnoble metal formulations in electrodes catalysts while internal reforming of hydrocarbon fuels becomes feasible, both facts favoring cost reduction. In turn, SOFCs are the most resistant to poisoning by sulfur or CO, allowing an important versatility in terms of fuel use (including even solid carbonaceous fuel directly derived from coal or biomass).[32]

The first report on the employment of a solid electrolyte is attributed to the work of J-M. Gaugain; in 1853, which employed two contacting glass tubes through which air and alcohol vapor were flown.[33] At the end of the nineteenth century, the term "solid electrolyte" appeared in numerous reports.[34] By that time, W. Nernst pointed out the increase in conductivity of mixed oxides with respect to pure oxides, analyzing multiple ZrO_2-based binary and ternary oxides at temperatures between 1073 K and 1673 K and developing a bulb that is considered as the first gas cell with solid electrolyte.[35] Some years later F. Haber reported the first patent on a solid electrolyte fuel cell.[36] Then, before 1950, it can be highlighted the work by E. Baur on solid electrolytes; the first ceramic SOFC (with Y- or Mg-doped ZrO_2 as electrolyte and electrodes based on Fe-C or Fe_3O_4; H_2 or CO was used as fuel and air as oxidant) was operated, at relatively low current density as a consequence of internal resistance, by Baur and Preis.[37] Then, the development of advanced techniques and theories for solid analysis allowed an important development of SOFC before 1970, as collected in the review work by Etsell and Flengas.[38] Problems related to the cathode as well as interconnector materials and the making of thin electrolyte layer were later analyzed by Rohr et al.[39] New manufacturing methods like electrochemical vapor deposition allowed an important development in this field at that time, in any case related to tubular SOFC configurations.[40] Planar configurations were developed later along with the availability of new preparation technologies like tape casting, screen printing, plasma spray, etc.[41] During the past years, most of the research done in the SOFC field has been dedicated to decreasing production cost, increasing components lifetime and process efficiency as well as decreasing the cell size or operating temperature to so-called intermediate temperature (say 773–973 K), the latter also focusing on reducing the cost of SOFC component materials.[42,43] However, lowering the temperature leads also to a more relevant role of electrode polarization, which imposes more strict requisites to electrode materials, as recently reviewed[44,45]; in turn, decreasing the operating temperature requires the use of high conductivity electrolytes as well as generally lowering its thickness, as collected in a recent report.[46]

Most of the materials currently employed for SOFC manufacturing were collected in the review work by Wincewicz and Cooper and are displayed in Table 15.2.[47] A brief summary of specific characteristics of these components as a function of the type of material employed is provided hereafter.

Electrolytes should generally accomplish the following properties[48]: (1) high ionic conductivity, (2) electronic isolator, (3) high thermal stability, (4) high chemical stability in oxidizing or reducing ambient, (5) high gas impermeability, (6) high mechanical stability, and (7) thermal and chemical compatibility with electrode materials. So far, the most promising properties in this sense are achieved by oxides with fluorite structure like Y-doped ZrO_2 (YSZ) and CeO_2 doped with Gd or Sm, while perovskites, brownmillerites, and hexagonal structured oxides have also recently shown interesting characteristics.[47]

Stabilization of the fluorite structure of ZrO_2 along with the generation of oxygen vacancies leading to maximum ionic conductivity level is achieved upon doping typically with about 5–10% of di- or trivalent cations like Ca^{2+}, Mg^{2+}, Y^{3+}, Sc^{3+} or some rare earth cations.[49,50] Maximum ionic conductivity is generally achieved when the dopant amount is close to minimum required for stabilizing the ZrO_2 fluorite structure in order to avoid vacancies association phenomena.[38,51–53] In turn, the size of the dopant cation appears also relevant in this respect—the lower the difference between zirconium and dopant cation sizes, the higher the ionic conductivity.[38,54,55] In this sense, YSZ has become the most widely employed SOFC electrolyte material with Y doping level between 3% and 8% depending on the balance between the maximum ionic conductivity degree (achieved at 8% doping) and mechanical stability (achieved at 3% doping).[56] This is also motivated by thermal and chemical properties of YSZ as well as its low electronic conductivity even at very low oxygen partial pressure.[49] Thus, the generalized use of YSZ is motivated by the balance of such factors. Indeed, Sc-doped ZrO_2 (SSZ) at 8–12% doping level yields higher ionic conductivity, although structural stability is lower than that of YSZ, while Sc availability is lower and its price higher.

Electrolytes based on stabilized Bi_2O_3 display much higher ionic conductivity (one to two orders of magnitude) than ZrO_2-based electrolytes. However, they are prone to becoming reduced under low oxygen partial pressure, which strongly favors short circuits upon appearance of electronic conductivity.[57] Such an effect

TABLE 15.2 Materials Employed for SOFC Components

Electrolytes	Anodes	Cathodes	Interconnects	Seals
ZrO_2-based	**Ni-based**	**La materials**	**Metals**	Glass or glass–ceramic materials
YSZ/TZP	Ni-YSZ	LSM/LSF/LSC	*Base materials*	
SSZ	Ni-SSZ	LSCF/LSMC/LCM	Cr alloys	Mica-based composites
CaSZ	Ni-GDC	LSMCr	Ferritic or austenitic stainless steel	
CeO_2-based	Ni-YDC	LSCu		
GDC	**Cu-based**	LSFN	Fe super alloys	
SDC	Cu–CeO_2-YSZ	LNF	Ni super alloys	
YDC	Cu-YSZ	LSCN	**Coatings**	
CDC	Cu-YTZ	LBC	LSM	
La_2O_3-based	Cu-CeO_2-SDC	LNC	LCM	
LSGM	**La_2O_3-based**	LSAF	LSC	
LSGMC	$La_{1-x}Sr_xCrO_3$ (LSC)	LSCNCu	LSFeCo	
LSGMF	LSCM	LSFNCu	LSCr	
LSGMCF	LST	LNO	$LaCoO_3$	
$LaAlO_3$-based	LAC	**Gd materials**	**Ceramics**	
Other	**Other**	GSC	La chromites	
BCY	CeO_2-GDC	GSM		
YSTh	TiO_2-YSZ	**Pr materials**		
YSTa	Co-based	PCM		
Bi_2O_3-based	Pt-based	PSM		
$X_2Y_2O_7$-based	Ru-YSZ	PBC		
$A_2B_2O_5$-based		**Sr materials**		
		SSC		
		NSC		
		BSCCu		
		Y_2O_3 materials		
		YSCF		
		YCCF		
		YBCu		

appears also when dealing with doped CeO_2 electrolytes, although to a much lower extent. Nevertheless, the relatively high ionic conductivity of the latter at 773–973 K at which such reduction effect becomes more limited makes them promising candidates for electrolytes in intermediate temperature SOFC (IT-SOFC). Among possible different dopants, Sm or Gd at 10–20% doping degree is considered the most interesting based on the ionic conductivity level achieved.[58,59] The latter (Gd-doped ceria or GDC) has in turn shown good chemical compatibility with stainless steel interconnects as well as many employed cathodic materials.[42]

On the other hand, perovskite electrolytes based on $LaGaO_3$ also display higher ionic conductivity than ZrO_2-based ones. The maximum conductivity in $LaGaO_3$-based electrolytes is achieved upon partial substitution in A and B positions of the perovskite with Sr^{2+} and Mg^{2+} (other dopants being also considered[60]), respectively.[61] The main drawback of this type of electrolyte is related to their relatively poor thermal stability as a consequence of Ga_2O_3 volatilization above about 1073 K leading to chemical reactions with electrode components as well as poor mechanical stability and Ga cost. They can, however, be considered promising materials for intermediate temperature operation.

Other compounds examined as electrolytes include ThO_2, HfO_2 and pyrochlores as well as Ba, In and Sr brownmillerites or apatite-structured materials.[47,61–63] Another promising electrolyte compound for intermediate temperature operation is $BaZr_{0.1}Ce_{0.7}Y_{0.2-x}Yb_xO_{3-\delta}$ (BZCYYb), which has displayed high ionic conductivity along with excellent resistance toward deactivation by sulfur and carbon.[64]

On the other hand, compounds where oxygen diffuses via an interstitial rather than a vacancy mechanism are receiving increasing attention.[45] Apatite structure electrolytes and La_2NiO_{4+x} or $CeMO_{4+x}$ (M = V, Nb, Ta) materials are examples of the latter.[45]

Concerning cathode materials, they must in principle fulfill the following general requisites[65,66]: (1) high electronic and ionic conductivities, (2) chemical and thermal compatibility with the electrolyte along with high chemical stability under oxidizing atmosphere, (3) high porosity along with mechanical resistance allowing correct gas and current distribution, and (4) high oxygen reduction catalytic activity. A recent review on SOFC cathode materials can be found elsewhere.[67] Among all cathode materials collected in Table 15.2, $La_{0,8}Sr_{0,2}MnO_3$ (LSM), $La_{0,8}Sr_{0,2}FeO_3$ (LSF) and $Sm_{0,5}Sr_{0,5}CoO_3$ (SSC) are the most employed ones. LSM perovskite (in some cases also with Ca^{2+} as A position dopant[68]), usually combined with YSZ in order to increase Three-Phase Boundary (TPB) area, which decreases electrode polarization,[69] is the most typical choice when ZrO_2-based electrolytes are used due to good compatibility in thermal and chemical terms. LSF substituted in B positions with Co, Ni or Mn has also shown interesting properties in terms of chemical stability and current density,[70] while the La-deficient LSF perovskite could apparently present lower electrical resistance than the stoichiometric perovskite formulation.[71]

An alternative cathode material is $La_{1-x}Sr_xCoO_3$ (LSC), which generally displays higher conductivity than LSM at low temperatures and high power density when using LSGM ($La_{1-x}Sr_xGa_{1-y}Mg_yO_{3-0.5(x+y)}$) as the electrolyte.[55] However, care must be taken when dealing with cobalt due to its high diffusivity leading to phase separation.[55] In turn, other alternatives based on Sr oxides are also most interesting as SOFC cathodes. These include SSC, $Nd_{0.6}Sr_{0.4}CoO_{3-\delta}$ (NSC) and $Bi_2Sr_2CaCu_2O_8$ (BSCCu). Thus, SSC has shown ionic conductivity higher than that of LSM and better overall electrochemical performance than LSCF (lanthanum strontium cobalt ferrite).[72] Some drawbacks of SSC are its high chemical reactivity with YSZ or SSZ electrolytes above 1173 K as well as the high price of Sm.[72] Other general concerns with SOFC cathode materials are related to their poisoning with chromium when chromium-containing alloys are employed in the interconnect (as considered for IT-SOFC application).[67] Extensive work is accordingly being currently carried out to develop new chromium-tolerant cathodes for such types of applications and $LaNi_{0.6}Fe_{0.4}O_3$ (LNF) appears as the most promising in this sense.[67]

With respect to anode materials, they must basically fulfill the same requisites as cathodes concerning chemical and thermal compatibility properties. Since they are exposed to reducing atmosphere, they must be stable under such ambience, while in general they should be resistant to poisons in fuels (typically S) or formed upon fuel partial oxidation processes (typically coke). In addition, they should be resistant to water presence as well as present good hydrocarbon reforming activity when using hydrocarbon–water mixtures as fuel.

The first SOFC anode materials employed were constituted by a single phase (graphite, iron oxide, transition metals or Pt as well as conducting ceramics). However, such materials were generally poorly resistant to corrosion or other degradation processes, while thermal expansion coefficient (TEC) values were not generally compatible with YSZ and their ionic conductivity was generally low. As an alternative, the use of hybrid porous materials combining metal and ceramic, the so-called cermet, was established. The role of the cermet ceramic component is basically structural, supporting the dispersal of the active metallic phase as well as allowing minimizing the thermal stress as a consequence of mismatch in TEC values with that of the electrolyte; it also provides ionic conductivity, which enhances the overall electrochemical behavior of the cell.

Cermets with fluorite structure in the ceramic component include those formed by the combination of different metals with YSZ, CeO_2, GDC or SDC (samaria doped ceria). Among them, Ni−YSZ (with about 40−60% Ni in order to exceed the percolation limit[73]) has been widely employed because of its relatively low cost and good electrochemical characteristics, although it displays relatively poor sulfur tolerance (<10 ppm[74]) and Ni is a very efficient catalyst for hydrocarbon cracking favoring carbon deposition; the latter is typically solved by feeding with reforming mixtures. It is also chemically not compatible with LSGM electrolyte, although this can be minimized by using CeO_2, GDC or SDC intermediate layers in order to protect both components.[75] On the other hand, Ni-GDC cermets show enhanced properties with respect to Ni-YSZ in terms of conductivity as well as catalytic activity and stability, which could allow employing lower H_2O/CH_4 ratios in the feeding fuel.[76] During the past, research has focused on enhancing the properties of nickel in terms of chemical stability and/or resistance to catalytic poisons. An important concern in this respect is related to poison by sulfur.[77] Apart from precious metal alternatives, undesirable for economical reasons, cermets based on combination of nickel with BZCYYb apparently display superior sulfur and carbon tolerance,[77] as pointed out above. Other interesting alternatives are related to formation of alloys with copper, which could allow decreasing hydrocarbon decomposition activity and formation of coke deposits.[78,79] Indeed, an interesting property of Cu-containing cermets is related to their low hydrocarbon cracking activity. This led to the development of direct hydrocarbon oxidation (i.e. without including water in the reactant mixture) in SOFCs basically using Cu-CeO_2 combinations as anode (the ceria providing the catalytic activity in this case), which are able to employ a large diversity of hydrocarbon fuels presenting also interesting properties in terms of sulfur resistance.[80,81]The main drawback of Cu cermets is the relatively high volatility of copper (melting point about 1356 K) and its relatively low catalytic activity toward hydrocarbon oxidation or decomposition, the latter being also enhanced upon including Ni and forming CuNi alloys.[32,79,82]

Other alternative SOFC anode materials include perovskite-like doped chromites, Sr and Y titanates, Sr vanadate, doped lanthanum ferrites, Sr-Co ferrites, galates and niobates.[83−89] In turn, rutile-structured Nb or Nb-Ti oxide, W-bronces, pyrochlores and spinels have also displayed interesting properties as SOFC anodes.[49,90−92]

15.3.2.2.2 MOLTEN CARBONATE FUEL CELLS

The origin of this type of fuel cells dates back to the 1950s when following limitations shown at that time by solid oxide electrolytes, Broers and Ketelaar centered their work on molten carbonate salts.[93] MCFCs employ an electrolyte composed by a molten carbonate salt suspended in a porous chemically inert matrix of $LiAlO_2$. Carbonate ions circulate through such electrolyte from cathode (at present based on porous nickel, which becomes in situ oxidized and lithiated by the electrolyte Li−K carbonates to form a Li−Ni mixed oxide[94]) to anode (typically porous nickel, strengthened with aluminum and chromium[94]) operating at temperatures above 923 K and at pressures between 1 and 10 atm. Such high operating temperatures allow the use of non-noble metal electrodes (like Ni-based ones) and can achieve energy efficiency close to that of SOFCs, being in any case higher than that of PAFCs. MCFCs allow internal reforming of fuel with higher energy density than hydrogen while CO can also be used as a fuel. Typically CO_2 produced in the anode is recycled and taken to the cathode where it is consumed.

The main drawback of current MCFCs is related to their durability. High operating temperatures and pressures and the corrosivity of the electrolyte strongly favor degradation of the cells, which constitutes the main drawback of MCFC technology. Main advances in this field are accordingly related to the analysis of new corrosion-resistant and dimensionally stable materials. Another factor to consider is possible dissolution of cathode nickel in the electrolyte, while MCFCs are generally intolerant to sulfur and other poisons in the fuel, which can be improved by intermixing the nickel-based anode with ceramic oxides,[94] and require preheating prior to start-up. Nevertheless, MCFC constitutes a promising technology for stationary applications in coal and natural gas thermal power stations as well as industrial and military applications.

15.3.2.3 Fuel Cell Systems Cost and Technical Objectives

Cost and technical objectives for stationary FC systems are largely driven by economic factors. These systems must compete with reliable and inexpensive settled technologies and should be easily handled by users with low technical background. Governmental Research Frameworks in the United States, Europe or Japan have established clear objectives regarding remaining challenges for some stationary applications, mainly CHP and backup power as early markets (Table 15.3). Briefly, the main identified barriers for a wide commercialization scenario are cost and durability.

Cost evolution forecasts carried out some years ago have been exceeded by real cost reductions achieved by manufacturers. Data for 2010 indicate that PEM stack costs had declined from roughly $4000/kW to $1000/kW in 5 years. The cost of 1-kW backup systems had been reduced by a factor of four, while the cost of 5-kW units had come down from about $55,000 to $22,000.

TABLE 15.3 Proposed Objectives for Several Stationary Applications According to Main National or Regional Research Programs

Framework	Durablity (h)	Retail cost (kW)	Efficiency (%)	Objective year
FP7 (Europe)*,†	40,000 (CHP)	2000 € (micro-CHP) 1000 € (small CHP)	45+ (electrical) 80+ (total)	2020
FCTP (USA)‡,§	40,000 (H2+CHP) 60,000 (micro CHP)	$450/kW (stack factory cost)	40 (electrical[a]) 45+ (electrical[b])	[a]2014 [b]2020
NEDO (Japan)**,¶	90,000	$3500 (micro-CHP)	40 (electrical)	2020–2030

* *Hydrogen Energy and Fuel Cells. A Vision of Our Future. European Commission, 2003.*
** *Annual Report 2011, NEDO Activity Report, New Energy and Industrial Technology Development Organization, Japan, September 2011.*
†*Annual Implementation Plan, Fuel Cells and Hydrogen Joint Undertaking (FCH JU), December 2011.*
‡*Hydrogen, Fuel Cells and Infrastructure Technologies Program. Multi-Year Research, Development and Demonstration Plan, US Department of Energy, February 2012.*
§*The Department of Energy Hydrogen and Fuel Cells Program Plan, US Department of Energy, September 2011.*
¶*Kerry-Ann Adamson, Stationary Fuel Cells: an Overview. Elsevier, 2007.*

Japanese fuel cell manufacturers participating in Japan's ENE-FARM program for small-scale CHP also claim a fourfold cost reduction from 2005 to 2009.[95] Manufacturers believe further cost reduction of 40–50% is necessary to compete with alternative technologies.[5,96]

The largest PAFC system manufacturer, UTC Power, has recently released some statements about components sensitive to further cost reductions, namely, the stack, fuel processing, power conditioning and BoP. Remarkably, they did not identify a clear pathway leading to power plant costs below $2000/kW[97]:

- An increase in PAFC power density is needed. The main barrier is currently the anion adsorption problem at the cathode. Its solution would bring about a 20% increase in power density and the concomitant decrease in cost.
- The fuel processing system significantly burdens cost reductions for their 400-kW stationary system. The natural gas reformer cost approximately amounts to that of the stack.
- BoP components need a cost reduction effort mainly hindered by low production rates (20 units in 2010), leading to a business not attractive enough so as to trigger a real supplier's competition.

Manufacturers believe that durability issue surmounting is less complex than cost.[5] PEM stacks today operate under real conditions for 5000–10,000 h in backup power applications and 40,000–50,000 h in CHP applications. ENE-FARM systems (1-kW CHP applications) have been operating for 20,000 h in Japanese homes and are guaranteed for 40,000 h. Large-scale (>300 kW) PAFC CHP and stationary power already exceed 40,000 h before requiring replacement.

15.3.2.4 Current R&D Guidelines

Since cost and durability are central issues for all types of fuel cells, extensive funding and researching efforts by private and governmental institutions are devoted to new manufacturing pathways, system analysis and new materials, including electrocatalysts, membranes, bipolar plates, gas diffusion layers, etc. Stationary applications present additional challenges as a result of the integration of the stack into the BoP. There is a growing understanding of the need for further optimization and development of BoP as opposed to simply cell and stack. The BoP, i.e. fuel processing, power conditioning, air and fuel movement and circulation and heat exchangers greatly influences the overall efficiency, reliability and durability of such systems. Research projects have shown that nonoptimized BoP exacerbates cell and stack issues such as degradation.[98] For instance, both the European Commission[99] and The US DoE[100] are currently supporting projects in order to gain a better insight into components coupling and optimization. Main objectives are to (1) develop low-cost BoP components for low- and high-temperature systems (air/fuel/thermal) that meet performance and durability requirements and, (2) develop other subsystems, such as fuel processors, to meet cost, performance, durability and output fuel quality requirements; this includes fuel flexibility and gas cleanup for contaminants from biogas and other fuels. Governmental support is still active for new stationary PEM systems demonstrations worldwide, especially in Europe, while the US DoE favors patent awards through an intensive evaluation and support program.[16]

15.3.3 Current Market Status

Stationary fuel cell products are currently attempting to penetrate a reduced number of markets. These markets have been geographically located in those areas with strong governmental support to R&D and incentives for end users (the United States, Europe and Japan). Nevertheless, new markets in developing countries have recently emerged. Fuel cell stationary systems are still very rarely capable of competing with

conventional technologies without incentives. With regard to market prospective, even though many analysts foresee a high worldwide potential and favorable prospects, accurate middle-term forecasts are extremely difficult to achieve.

PEMFC systems cover a wide variety of stationary applications below 200 kW. Today, an increasing number of manufacturers are competing with similar performance systems. Table 15.4 includes the main manufacturers of stationary products including specific applications, kilowatt-range products and manufacturing capability.

The stationary PAFC market has been virtually dominated by UTC Power's 200-kW CHP plant and its recent upgrading up to 400 kW called PureCell™. Outstanding 10-year stack and 20-year product life are offered, recently achieved through thermal profile optimization of the stack, minimization of acid loss and reduced Pt particles sintering in the electrodes.[101] When fueled with natural gas, a 42% electrical and 90% total efficiencies are claimed. Nevertheless, Fuji Electric Company has recently launched a new 100-kW CHP product, FP-100i, with 40% and 90% efficiencies and beyond 60,000 h durability.[102]

For further information, the Fuel Cell and Hydrogen Energy Association provides a comprehensive and continuously updated database of fuel cell and hydrogen products.[103]

Commercial PEMFC systems are focused on backup, uninterruptible power (especially for telecommunications) and micro-CHP applications. Most manufacturers have reduced the available range of products and specialized in order to gain efficiency and increase sales volumes per product during 2007–2012. PA's main markets comprise larger scale applications, like grid-independent stationary power and CHP. Both are still competing at a cost disadvantage against established technologies. For stationary fuel cells in backup power, the cost and availability of hydrogen is a significant impediment to commercial success. While diverse programs have provided important incentives for purchasing fuel cells worldwide, supplying low-cost hydrogen onsite remains as a major barrier.[5] A more detailed insight into these markets follows, mainly extracted from extensive market research conducted by Mahadesan et al.[5] and Green et al.[26] for the US DoE.

15.3.3.1 *Backup Power*

Systems are replaced over a 15- to 20-year life so that new systems are purchased at a rate of about 15,000–20,000 per year for the 4- to 8-kW systems in the US market.[26] This market leads the US industry in total shipments (around 1200 in 5-kW-unit equivalents) and has achieved roughly a fivefold increase over 2007 production levels. In backup power applications for emergency response radio towers, PEMFCs are competitive with battery-generator systems from a lifecycle cost perspective either when short runtimes are required (i.e. 1–3 days) or when operating in harsh environments, which shorten the lifetime of batteries. However, PEMFCs are much less attractive than alternatives when longer backup power runtimes are required (i.e. 1 week or more) due to the high cost of hydrogen storage and use.[5] Table 15.5 summarizes a comparison between some technological solutions. Developing countries,

TABLE 15.4 Main Companies Selling Final Products Based on PEM Fuel Cells for Stationary Applications

Manufacturer	Product applications	Manufacturing capability per year	Product range (kW)
Ballard	Backup and supplemental power, and distributed generation	20,000 stacks	2–500
Hydrogenics	Renewable energy storage, backup power	160 MW	2–200
Ida Tech	Backup power for telecommunication	5000 units	2–5
Panasonic	Residential	–	0.75
Toshiba	Residential	–	0.7
Clear Edge Power	Residential and small commercial	6000 units	5
MicroCell	Stationary power, CHP	3 MW	1–100 kW
Protonex	Remote power	–	0.01–1
ReliOn	Backup power	–	0.05–20
Trenergi	CHP	–	1–5
UTC Power	Backup power	–	5

Based on manufacturers' public information and 2010 Fuel Cell Technologies Market Report, US Department of Energy, June 2011.

TABLE 15.5 Comparison for Backup Power for Response Radio Towers between Conventional Technologies and an Average Fuel Cell System

Technology	FC (5 kW)	Batteries (30 kWh)	Diesel generator (15 kW)
Unit cost (k$)	12–15	6	25
Retail price (k$)	22–24	10	30–35
Operation (hours)	9–12	10	Days
Working life (years)	12–15*	6–7	>20

* *Not yet proven.*

whose grids are usually less reliable, have also increased the use of fuel cells for backup and remote power. India and Indonesia telecommunication companies purchased more than 350 units in 2010, adding to the more than 100 fuel cell systems already installed across Indonesia for telecommunications backup power.[12]

15.3.3.2 Combined Heat and Power

15.3.3.2.1 MICRO-CHP

These systems market is the main current market for stationary fuel cell systems and has a large potential for residential and small commercial applications. Manufacturing has also been increased up to 250 5-kW-unit equivalents in the United States, largely supported by the California Self Generation Incentive Program (SGIP), while approximately a total of 7000 units of 1 kW were sold in Japan by Toshiba, Panasonic and ENEOS in 2011,[26] as a result of the ENE-FARM program. There are a number of commercial products available as well as prototype demonstrations worldwide in progress for such systems. Table 15.6 includes some commercial systems and their retail prices both for fuel cells and established competing technologies.

15.3.3.2.2 SMALL CHP

Larger (>100 kW) fuel cells for CHP and independent power have also increased significantly in the past years up to 80 units in 2010, including PAFC and MCFC as dominating technologies. Emerging markets are in California, US Northeast states and South Korea, where subsidies for clean energy technologies and relatively high electricity prices make them an attractive alternative. For these applications, recently published data reveal a widespread cost, from roughly $300–$5000/kW special sensitivity these applications have to a number of factors such as fuel, location (distance from fuel source), technology used or size.[26]

This market is largely dominated by UTC Power 400-kW plant, an upgraded version of the previous 200 kW, launched in 2009 and already under operation for combined 200,000 h. Markets served include supermarkets/retail, industrial, bottling, health care, hospitality, mixed-use/residential and educational institutions.[104] The company completed in 2011 two remarkable 4.8-MW projects in New York City and South Korea.

15.3.4 Market Prospective

Fuel cell-related markets were systematically overvalued before 2000, when hydrogen technologies rush suggested this technology was at a precommercialization stage. For instance, Vaillant foresaw in 2001 a 2500 M€ market for 2010,[24] whereas Allied Business Intelligence forecasted 15,000 MW installed by 2011 for stationary fuel cell systems.[105] It is an idiosyncratic market still strongly influenced by external factors such as pending technical breakthroughs and governmental support, which makes any market model extremely sensitive to small variations. This section briefly describes some public expectations by relevant market players, both

TABLE 15.6 Comparison for Some Micro-CHP Products in the Market

Product	Region	Technology	Power (kW)	Price ($/kW)
FreeWatt®	United States	Engine	1.2	10,800
Marathon™	United States and Europe	Engine	4.7	7400
ClearEdge	Worldwide	Fuel cell (PEM)	5	10,500 (7100*)
Toshiba	Japan	Fuel cell (PEM)	0.7	47,100 (28,500**)
Panasonic	Japan	Fuel cell (PEM)	1	48,000 (22,500**)
CleanTech	South Korea	Fuel cell (PEM)	1	40,300 (8000***)
EcoCute	Japan	Heat pump (heat only)	1 (thermal)	5000

* *Including US tax credit.*
** *Including Japanese government subsidy for 2011.*
*** *Including South Korea government subsidy.*

governmental and manufacturers. Some economic models forecast a growth for the PEMFC industries after 2015, especially backup power, the years from 2010 to 2015 being very challenging if current policy supports are removed.[5,26,106]

The annual total market value of the worldwide stationary fuel cell sector could reach $9.5 billion by 2017, surpassing 1.2 million units shipped annually.[107] A technical focus on durability, reliability, and reducing the cost of PEMFCs will also be critical for market adoption.[5] Some manufacturers believe that telecommunications market is the next opportunity, especially in Asia, where grid outages are more frequent. Payback under favorable conditions is as short as 3 years compared to standard backup solutions according to the manufacturer. To date, this solution is only viable under some assumptions: sites where diesel generators are costly or difficult to site, or site upgrades where additional batteries are problematic (rooftop).[22,108] New regulations in Asia are favoring this vision, e.g. the aggressive directive issued by the Telecom Regulatory Authority of India in 2011 requiring 50% of all rural telecom base station towers and 33% of all urban towers in the country to be powered by hybrid solutions within 5 years. A rapid growth is therefore expected with global shipments matching 422,000 units by 2017.[107]

As for CHP, the US DoE estimates a 40–60 GW potential for commercial and institutional applications only in the United States, to be covered by fewer than 5-MW plants. The micro-CHP industry may suffer a downturn immediately after the expiration of the tax credit in the United States after 2016, but sales would begin to steadily improve after 2018.However, the volume of sales may not be large enough to support more than one manufacturer at an economical scale of production through 2025.[26]

15.4 FUEL CELL MARKETS SUPPORTED BY GOVERNMENTAL PROGRAMS

Europe (especially Germany), the United States and Japan have been largely supporting hydrogen and fuel cell technologies through structured multiyear programs including basic research, validation and demonstration subprograms, among others. Their continuous large economic support has facilitated an incipient fuel cell penetration into these areas and its industry associate. As a result, these regions show most developed markets. A brief description of the contribution of fuel cell programs to stationary applications market is described below. Other countries like Australia[109] or South Korea have recently showed a new interest in hydrogen-related technologies.

15.4.1 The United States

The US DoE leads and coordinates research national efforts regarding fuel cells through its annually reviewed "Hydrogen and Fuel Cells Program Plan".[110] The American Recovery and Reinvestment Act (ARRA) program has been the decisive driver for fuel cell market penetration in the materials handling market as well as for stationary application since 2010 (Fig. 15.5). ARRA allocated $41.9 million for fuel cell commercialization activities and attracted $54 million in cost share. The success of the program has far surpassed expectations, doubling its target installations in 2010, with 24 telecommunications backup systems and 206 lift trucks. There are also state programs aiming to promote fuel cells as clean energy systems including automotive power and stationary applications; the main one is developed by California through a new clean vehicle rebate program, offering up to $5000 to purchase or lease new, zero-emission or plug-in hybrid electric vehicles.

Regarding stationary applications, the US government provides significant incentives. It offers an investment tax credit of 30% for qualified fuel cell property or $3000/kW (whichever is less). In addition, it features a credit of 10% for CHP purchase. The expected end year is 2016. The Fuel Cell Technologies Program accelerated the commercialization and deployment of fuel cells through the Recovery Act funding. It supported the deployment of nearly 1000 fuel cell systems in emergency backup power, material handling and CHP applications: Individual states also offer incentives, such as California's SGIP, which includes fuel cells as an emerging technology and is also expected to continue until 2016. Included incentives for emerging technologies decline 10% annually. For projects that are larger than 30 kW, the SGIP pays 50% of the incentive up front and the remaining 50% is covered under a performance-based incentive.[111]

15.4.2 Japan

The NEDO launched a very ambitious Fuel Cell and Hydrogen project under the Energy area. Cooperation between manufacturers, energy companies and the national Japanese Government is outstanding in this context. Thirteen Japanese companies (three automakers and 10 energy companies) formed a partnership in 2010 to develop a hydrogen station network. The companies plan to build 50–100 filling stations by 2015 in four major Japanese cities. Japanese companies claim they are committed to lead the world in FCV deployment by 2025 and are strongly supported by the government. One of the Fuel Cell and Hydrogen projects, called the Japan Hydrogen and Fuel Cell (JHFC), has collected extensive FCVs real operation data, with figures similar

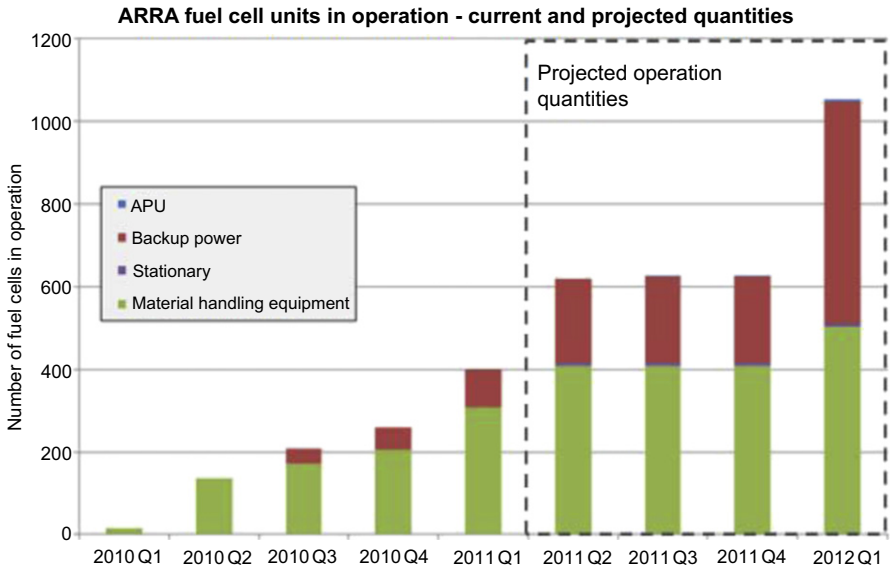

FIGURE 15.5 American Recovery and Reinvestment Act results for fuel cells shipments. (For color version of this figure, the reader is referred to the online version of this book.) *Source: US Department of Energy.*

to those obtained by the American DoE and is currently into a precommercialization stage.

Three companies, Toshiba, JX Energy, and Panasonic, account for nearly Japan's entire stationary fuel cell program, which is focused on small, 1-kW, PEM CHP units chiefly for single-family homes under the name of ENE-FARM. The government has already spent more than $12.5 million on fuel cell demonstrations. Government subsidy has come down over the years up to $13,150/kW in 2011. Market size was 9000 units in 2011.[112] After the 2011 earthquake and Fukushima nuclear disaster, demand sharply increased and secured budget run out temporarily.[113]

15.4.3 Europe

Europe also shows organized fuel cell and hydrogen initiatives lead by the European Commission under successive Framework Programs. Private companies and research institutions collaborate within the Fuel Cells and Hydrogen Joint Undertaking. This entity runs a €68M budget for 2012 mostly devoted to fund strategic call for proposals in order to achieve technical and economical milestones reflected on the strategic objectives list. Among transportation applications, off-road transport with an emphasis on industrial and material handling vehicles are of primary interest.[3,14]

The German Government's hydrogen organization (The National Organisation Hydrogen and Fuel Cell technology (NOW)) is leading a 1- to 5-kW CHP demonstration project (Callux) as an intermediate step for wide commercialization for residential applications. Callux project includes subsidies, tax reduction efficiency incentives and R&D grants. The goal is to deploy 800 units by 2012. Most of them are PEMFCs with a significant portion of SOFCs.[114]

15.4.4 South Korea

The Korean Fuel Cell and Hydrogen demonstration program between 2006 and 2009 tested 30 FCVs served by seven hydrogen fueling stations. The current demonstration program (2012–2014) includes deployment up to 1000 vehicles per year. Year 2015 is expected to be the onset of commercial production of 10,000 vehicles per year.[115] The Korean car manufacturer Hyundai-Kia plays a key role on the national transport fuel cells research program. It developed proprietary stacks for light duty and buses between 2000 and 2010.

South Korea has one of the most supportive policy environments for fuel cells. The residential fuel cell demonstration program that started in 2010 offered a subsidy of 80% of the cost of stationary fuel cells through 2012 and a 50% subsidy from 2013 to 2015. The program calls for an installation of 500 units in 2012.[115,116]

15.5 CONCLUSIONS

The fuel cell technology has a promising future in the coming decades. This technology, combined with the use of hydrogen, will play an important role in transport applications to be environmentally friendly. FCVs using hydrogen from renewable energy sources are needed to decarbonize the transportation sector. Regarding stationary applications, its use will become very interesting in distributed power generation and off-grid applications. Hydrogen produced from renewable power sources is needed to stabilize the power grid.

The main problem of fuel cells is the high cost. Cost and hydrogen production/delivery issues are main key barriers for commercialization. Unfortunately, fund's priority is making money not saving the planet. In a time of crisis like this it does not seem that fuel cells have much future. However, it is precisely at this time when we have to face the challenges. As Albert Einstein said, "Let's not pretend that things will change if we keep doing the same things. A crisis can be a real blessing to any person, to any nation. For all crises bring progress. Creativity is born from anguish, just like the day is born form the dark night. It's in crisis that inventive is born, as well as discoveries, and big strategies."

We need new technologies, new investment and new regulatory policies. Over the next decades, no simple power train satisfies all key criteria for economics, energy demand and environmental. Governmental incentives have played a central role on market early development and need to be maintained over the next years. Hydrogen and fuel cells may be the key in the energy scenario.

References

1. John Lughhead, UK Energy Research Centre. 4th IPHE Workshop Stationary Fuel Cells REPORT. September 2011.
2. *The Department of Energy Hydrogen and Fuel Cells Program Plan;* U.S. Department of Energy, September 2011.
3. *Fuel Cell Today Industry Review*, 2011. Available at www.fuelcelltoday.com.
4. Schoenung, S. Economic Analysis of Large-Scale Hydrogen Storage for Renewable Utility Applications, Sandia National Laboratory Report, August 2011.
5. Mahadesan, K.; Judd, K.; Stone, H.; Zewatsky, J.; Thomas, A.; Mahy, H.; Paul, D. *Identification and Characterization of Near-Term Direct Hydrogen Proton Exchange Membrane Fuel Cell Markets;* U.S. Department of Energy, 2007.
6. Thomas, S. Simulation Data available at www.cleancaroptions.com
7. Analysis of the Transition to Hydrogen Fuel Cell Vehicles and The Potential Hydrogen Energy Infrastructure Requirements. Oak Ridge Laboratory Report under Reference ORNL/TM 2008/30, 2008, U.S. Department of Energy.
8. van den Oosterkamp, P.F.; Kraaij, G.J.; van der Laag, P.C.; Stobbe, E.R.; Wouters, D. The Development of Fuel Cell Systems for Mobile Applications, WHEC16 Conference, Lyon, France, 13–16 June 2006.
9. Garche, J.; Jörissen, L. PEMFC Fuel Cell Systems. In *Hand Book of fuel Cells;* Vielstich, W., Lamm, A., Gasteiger, H. A., Eds.; Vol. 4, J. Wiley & Sons: Chichester, England, 2003; pp 1233–1259.
10. Barbir, F. System Design for Stationary Power Generation. In *Hand Book of fuel Cells;* Vielstich, W., Lamm, A., Gasteiger, H. A., Eds.; Vol. 4, J. Wiley & Sons: Chichester, England, 2003; pp 683–692.
11. Matsunaga, M.; Fukushima, T.; Ojima, K. Powertrain System of Honda FCX Clarity Fuel Cell Vehicle. Presented at EVS24 International Battery, Hybrid and Fuel Cell Electric Vehicle Symposium, Stanvanger, Norway, 2009.
12. 2010 Fuel Cell Technologies Market Report, U.S. Department of Energy, June 2011.
13. Available at www.jari.or.jp/jhfc/e
14. Fuel Cells and Hydrogen Joint Undertaking (FCH JU), Annual Implementation Plan 2012.
15. Available at: www.fuelcells.org
16. *Pathways to Commercial Success: Technologies and Products Supported by the Fuel Cell Technologies Program;* U.S. Department of Energy, September 2011.
17. *Analysis of the Transition to Hydrogen Fuel Cell Vehicles & the Potential Hydrogen Energy Infrastructure Requirements;* Oak Ridge National Laboratory, 2008. under reference ORNL/TM-2008/30.
18. Himri, Y.; Stambouli, A. B.; Draoui, B.; Himri, S. Techno-economical Study of Hybrid Power System for a Remote Village in Algeria. *Energy* **2008,** *33,* 1128–1136.
19. Available at http://www.ballard.com/fuel-cell-products/cleargen-multi-mw-systems.aspx
20. Schoenung., S. Economic Analysis of Large-Scale Hydrogen Storage for Renewable Utility Applications. *Sandia National Laboratory* August 2011. report.
21. Spitznagel, K. *Demonstration of PEM Backup Fuel Cell Systems in Mission-Critical Applications, Book of abstracts of Fuel Cell Seminar and Exposition*. Orlando, Florida, U.S.A.
22. DOE-DOD PEM Hammill, S.; Josefik, N. M.; Devlin, P.; Logan, S. *Fuel Cell Emergency Back-Up Power Field Demonstration, Book of abstracts of Fuel Cell Seminar and Exposition*. Orlando, Florida, U.S.A.
23. Available at http://www.eea-inc.com/chpdata
24. Klinder, K. The Vaillant Residential Fuel Cell Solution. Book of Abstracts of the FC-Meeting, Luzern, Switzerland, pp 117–132, 2001.
25. Lipman, T.; Sperling, D. Market Concepts, Competing Technologies and Cost Challenges for Automotive and Stationary Applications. In *Hand Book of fuel Cells;* Vielstich, W., Lamm, A., Gasteiger, H. A., Eds.; Vol. 4, J. Wiley and Sons: Chichester, England, 2003; pp 1318–1328.
26. Greene, D. L.; Duleep, K. G.; Upreti, G. *Status and Outlook for the U.S. Non-Automotive Fuel Cell Industry: Impacts of Government Policies and Assessment of Future Opportunities;* U.S. Department of Energy, May 2011.
27. *Seventh Fuel Cell Handbook;* U.S. Department of Energy, 2004.
28. Colella, W. G.; Dillon, H.; Timme, R.; King, D.; Holladay, J. *Independent Evaluation of Measured Performance Data from Stationary Combined Heat and Power (CHP) Fuel Cell Systems (FCSs) Installed in Light Commercial Buildings, Book of abstracts of the Fuel Cell Seminar and Exposition*. Orlando, Florida, U.S.A.
29. Falcucci, G.; Minutillo, M.; Jannelli, E.; Ubertini, S. Experimental Analysis of a High-Temperature PEM Fuel Cell Stack, Book of Abstracts of the European Fuel Cell Conference and Exhibition, Rome, Italy, 2011.
30. Zuliani, N.; Taccani, R.; Radu, R. Effects of Control Strategies on the Transient Performance of a HTPEM Fuel Cell System Fuelled with Propane, Book of abstracts of the European Fuel Cell Conference and Exhibition, Rome, Italy, 2011.
31. Landsman, D. A.; Luczak, F. J. Experience with 200 kW PC25 Fuel Cell Power Plant. In *Hand Book of Fuel Cells;* Vielstich, W., Lamm, A., Gasteiger, H. A., Eds.; Vol. 4, J. Wiley and Sons: Chichester, England, 2003; pp 832–846.
32. Gorte, R. J.; Vohs, J. M. *Curr. Opin. Coll. Interf. Sci.* **2009,** *14,* 236.
33. Gaugain, J.-M.; Séances, C. R. *Acad. Sci.* **1853,** *37,* 584.
34. Wiedemann, G. *Die Lehre von der Elektricität*, 2a; Vieweg: Braunschweig, 1893, 98.
35. (a) Nernst, W. *Z. Elektrochem.* **1899,** *6,* 41. (b) Nernst, W. USA Patent. n° 685 730, 1899.
36. Haber, F. Austria Patent n° 27 743, 1905.
37. (a) Baur, E.; Preis, H. *Z. Elektrochem.* **1937,** *43,* 727. (b) Baur, E.; Preis, H. *Z. Elektrochem.* **1938,** *44,* 695. (c) Baur, E. *Brennstoff-chemie* **1939,** *20,* 385. (d) Baur, E. *Ber. Ges. Kohlentechn* **1940,** *5,* 99.
38. Etsell, T. H.; Flengas, S. N. *Chem. Rev.* **1970,** *70,* 339.
39. (a) Fischer, W.; Kleinschmager, H.; Rohr, F. J.; Steiner, R.; Eysel, H. H. *Chem. Ing. Tech.* **1972,** *44,* 726. (b) . Rohr, F. J.Hagenmuller, P., van Gool, W., Eds.; Academic Press: NY, 1978; p 431.

40. (a) Feduska, W.; Isenberg, A. O. *J. Power Sourc.* **1983,** *10,* 89. (b) Reichner, P.; Makiel, J. M. *Fuel Cell Sem. Abs.* **1986**. Courtesy Associates, Washington DC (1986) 32.
41. Brown, J. T. Solid Oxide Fuel Cells. In *High Conductivity Solid Ionic Conductors;* Takahashi, T., Ed.; World Scientific: Singapore, 1989; p 630.
42. Steele, B. C. H.; Heinzel, A. *Nature* **2001,** *414,* 345.
43. Tucker, M. C. *J. Power Sourc.* **2010,** *195,* 4570.
44. Tsipis, E. V.; Kharton, V.,V. *J. Sol. St. Electrochem.* **2011,** *15,* 1007.
45. Jacobson, A. J. *Chem. Mater.* **2010,** *22,* 660.
46. Evans, A.; Bieberle-Hütter, A.; Rupp, J. L. M.; Gauckler, L. J. *J. Power Sourc.* **2009,** *194,* 119.
47. Wincewicz, K. C.; Cooper, J. S. *J. Power Sourc.* **2005,** *140,* 280.
48. Singhal, S. C. *Solid State Ionics* **2000,** *135,* 305.
49. Tao, S.; Irvine, J. T. S. *Chem. Rec.* **2004,** *4,* 83.
50. Minh, N. Q. *J. Am. Ceram. Soc.* **1993,** *76,* 563.
51. Kharton, V. V.; Naumovich, E. N.; Vecher, A. A. *J. Solid State Electrochem.* **1999,** *3,* 61.
52. Yamamoto, O.; Arachi, Y.; Sakai, H.; Takeda, Y.; Imanishi, N.; Mizutani, Y.; Kawai, M.; Nakamura, Y. *Ionics* **1998,** *4,* 403.
53. Badwal, S. P. S. *Solid State Ionics* **1992,** *52,* 23.
54. Arachi, Y.; Sakai, H.; Yamamoto, O.; Takeda, Y.; Imanishai, N. *Solid State Ionics* **1999,** *121,* 133.
55. Yamamoto, O. *Electrochim. Acta* **2000,** *45,* 2423.
56. Ivers-Tiffée, E.; Weber, A.; Herbstritt, D. *J. Eur. Ceram. Soc.* **2001,** *21,* 1805.
57. Takahashi, T.; Esaka, T.; Iwahara, H. *J. Appl. Electrochem.* **1977,** *7,* 303.
58. Balazs, G. B.; Glass, R. S. *Solid State Ionics* **1995,** *76,* 155.
59. Kharton, V. V.; Figueiredo, F. M.; Navarro, L.; Naumovich, E. N.; Kovalevsky, A. V.; Yaremchenko, A. A.; Viskup, A. P.; Carneiro, A.; Marques, F. M. B.; Frade, J. R. *J. Mater. Sci.* **2001,** *36,* 1105.
60. (a) Ishihara, T.; Shibayama, T.; Honda, M.; Nishiguchi, H.; Takita, Y. *Mater. Res. Soc. Symp. Proc.* **2001,** *575,* 283. (b) Ishihara, T.; Shibayama, T.; Ishikawa, S.; Hosoi, K.; Nishiguchi, H.; Takita, Y. *J. Eur. Ceram. Soc.* **2004,** *24,* 1329.
61. Kharton, V. V.; Marques, F. M. B.; Atkinson, A. *Solid State Ionics* **2004,** *174,* 135.
62. Molenda, J.; Świerczek, K.; Zajac, W. *J. Power Sourc.* **2007,** *173,* 657.
63. Kharton, V. V.; Shaula, A. L.; Patrakeev, M. V.; Waerenborgh, J. C.; Rojas, D. P.; Vyshatko, N. P.; Tsipis, E. V.; Yaremchenko, A. A.; Marques, F. M. B. *J. Electrochem. Soc.* **2004,** *151,* A1236.
64. Yang, L.; Wang, S.; Blinn, K.; Liu, M.; Liu, Z.; Cheng, Z.; Liu, M. *Science* **2009,** *326,* 126.
65. Maguire, E.; Gharbage, B.; Marques, F. M. B.; Labrincha, J. A. *Solid State Ionics* **2000,** *127,* 329.
66. Ralph, J. M.; Schoeler, A. C.; Krumpelt, M. *J. Mater. Sci.* **2001,** *36,* 1161.
67. Sun, C.; Hui, R.; Roller, J. *J. Sol. St. Electrochem.* **2010,** *14,* 1125.
68. Badwal, S. P. S.; Foger, K. *Mater. Forum* **1997,** *21,* 187.
69. Yoon, S. P.; Han, J.; Nam, S. W.; Lim, T.-H.; Oh, I.-H.; Hong, S.-A.; Yoo, Y.-S.; Lim, H. C. *J. Power Sourc.* **2002,** *106,* 160.
70. Simmer, S. P.; Bonnet, J. F.; Canfield, K. D.; Meinhardt, K. D.; Shelton, J. P.; Sprenkle, V. L.; Stevenson, J. W. *J. Power Sourc.* **2003,** *113,* 1.
71. Krumpelt, M. *SECA Core Technology Review;* SECA: Sacramento, 2003.
72. Fukunaga, H.; Koyama, M.; Takahashi, N.; Wen, C.; Yamada, K. *Solid State Ionics* **2000,** *132,* 279.
73. Dees, D. W.; Claar, T. D.; Easler, T. E.; Fee, D. C.; Mrazek, F. C. *J. Electrochem. Soc.* **1987,** *134,* 2141.
74. Ralph, J. M.; Kilner, J. A.; Steele, B. C. H. *Mater. Res. Soc. Symp. Proc.* **1999,** *575,* 309.
75. Zhang, X.; Ohara, S.; Maric, R.; Mukai, K.; Fukui, T.; Yoshida, H.; Nishimura, M.; Inagaki, T.; Miura, K. *J. Power Sourc.* **1999,** *83,* 170.
76. Marina, O.; Bagger, C.; Primdahl, S.; Mogensen, M. *Solid State Ionics* **1999,** *123,* 411.
77. Cheng, Z.; Wang, J.-H.; Choi, Y.; Yang, L.; Lin, M. C.; Liu, M. *Ener. Env. Sci.* **2011,** *4,* 4380.
78. Lee, S.-I.; Vohs, J. M.; Gorte, R. J. *J. Electrochem. Soc.* **2004,** *151,* A1319.
79. Hornés, A.; Bera, P.; Fernandez-Garcia, M.; Guerrero-Ruiz, A.; Martínez-Arias, A. *Appl. Catal. B* **2012,** *111–112,* 96.
80. Craciun, R.; Park, S.; Gorte, R. J.; Vohs, J. M.; Wang, C.; Worrell, W. L. *J. Electrochem. Soc.* **1999,** *146,* 4019.
81. McIntosh, S.; Gorte, R. J. *Chem. Rev.* **2004,** *104,* 4845.
82. Hornés, A.; Gamarra, D.; Munuera, G.; Fuerte, A.; Valenzuela, R. X.; Escudero, M. J.; Daza, L.; Conesa, J. C.; Bera, P.; Martínez-Arias, A. *J. Power Sourc.* **2009,** *192,* 70.
83. Atkinson, A.; Barnett, S.; Gorte, R. J.; Irvine, J. T. S.; McEvoy, A. J.; Mogensen, M.; Singhal, S. C.; Vohs, J. *Nat. Mater.* **2004,** *3,* 17.
84. Tao, S.; Irving, J. T. S. *J. Electrochem. Soc.* **2004,** *151,* A252.
85. Mukundan, R.; Brosha, E. L.; Garzon, F. H. *Electrochem. Solid State Lett.* **2004,** *7,* A5.
86. Hui, S. Q.; Petric, A. *J. Euro. Ceram. Soc.* **2002,** *22,* 1673.
87. Hui, S.; Petric, A. *Solid State Ionics* **2001,** *143,* 275.
88. Hartley, A.; Sahibzada, M.; Weston, M.; Metcafe, I. S.; Mantzavinos, D. *Catal. Today* **2000,** *55,* 197.
89. Tomita, A.; Hibino, T.; Sano, M. *Electrochem. Solid State Lett.* **2005,** *8,* A333.
90. Reich, C. M.; Kaiser, A.; Irving, J. T. S. *Fuel Cells* **2001,** *1,* 249.
91. Holtappels, P.; Bradley, J.; Irvine, J. T. S.; Kaiser, A.; Mogensen, M. *J. Electrochem. Soc.* **2001,** *148,* A923.
92. Flot, D. M.; Irvine, J. T. S. *Solid State Ionics* **2000,** *135,* 513.
93. Broers, G. H. J.; Ketelaar, J. A. A.; Young, G. J., Ed., Vol. 1; University of Amsterdam: NY, 1960.
94. McPhail, S. J.; Aarva, A.; Devianto, H.; Bove, R.; Moreno, A. *Int. J. Hydrogen Energy* **2011,** *36,* 10337.
95. Greene, D. L.; Duleep, K. G. *Bootstrapping a Sustainable North American PEM Fuel Cell Industry: Could a Federal Acquisition Program Make a Difference?* ORNL/TM-2008/183; Oak Ridge National Laboratory: Oak Ridge, TN, U.S.A, 2008.
96. Upretia, G.; Greeneb, D. L.; Duleepd, K. G.; Sawhneya, R. Fuel Cells for Non-Automotive Uses: Status and Prospects. *Int. J. Hydrogen Energy* **2012**. http://dx.doi.org/10.1016/j.ijhydene.2012.01.060.
97. Remick, R.; Wheeler, D. Molten Carbonate and Phosphoric Acid Stationary Fuel Cells: Overview and Gap Analysis, Technical Report, NREL/TP-560–49072, September 2010.
98. European Funded Research on Hydrogen and Fuel Cells, Hydrogen and Fuel Cell Review Days, Brussels, 10–11 October 2007.
99. STAYERS Project. available at http://cordis.europa.eu/search.
100. Project Summaries available at http://www.hydrogen.energy.gov/annual_progress11.html
101. Kanuri, S. *Shattering 10 year Durability Barrier for Fuel Cells. UTC Power, Books of abstracts of Fuel Cell Seminar and Exposition*. Orlando, Florida, USA, 2011.
102. Kuroda, K. Present and Future of PAFC at Fuji Electric, Presentation at the 4th IPHE Workshop—Stationary Fuel Cells, Tokyo, Japan, 2011.
103. Available at FCHEA web page: http://www.fchea.org/index.php?id=86.
104. Available at http://www.utcpower.com/products/purecell400
105. Allied Business Intelligence. *Stationary Fuel Cells: US Global Early Market Opportunities*.
106. Cottrella, C. A.; Grasmana, S. E.; Thomasa, M.; Martina, K. B.; Sheffieldb, J. W. Strategies for Stationary and Portable Fuel Cell Markets. *Int. J. Hydrogen Energy* **2011,** *36* (13), 7969–7975.
107. *Stationary Fuel Cells;* Pike Research, 2011.
108. Smarter Solutions for a Clean Energy Future. *Ballard Power Systems, Books of Abstracts of Fuel Cell Seminar and Exposition*. Orlando, Florida, USA, 2011.
109. *Towards Development of an Australian Scientific Roadmap for the Hydrogen Economy;* Australian Academy of Science, 2008.
110. Available at http://www1.eere.energy.gov/hydrogenandfuelcells/

111. Available at http://energycenter.org/index.php/incentive-programs/self-generation-incentive-program/program-overview
112. Available at http://www.fuelcelltoday.com/news-events/news-archive/2012/january/japanese-ene-farm-production-ramping-up-as-customer-demand-grows
113. Available at http://www.fuelcelltoday.com/news-events/news-archive/2011/october/japanese-ene-farm-subsidies-proving-popular,-fund-depleting-rapidly
114. Garche, J.; Bonhoff, K.; Ehret, O.; Tillmetz, W. The German National Innovation Programme Hydrogen and Fuel Cell Technology. *Fuel Cells* **2009,** *9,* 192–196.
115. Butler, J. 2010 Survey of Korea. *Fuel Cell Today* **2010**.
116. Cleantech Group, LLC. South Korea Plans Fuel Cell subsidy for 2010, Technical Report, 2009.

CHAPTER

16

Update on the Progress of Hydrogen-Fueled Internal Combustion Engines

Sebastian Verhelst [*], *Joachim Demuynck* [*], *Roger Sierens* [*], *Riccardo Scarcelli* [†], *Nicholas S. Matthias* [†], *Thomas Wallner* [†]

[*]Ghent University, Department of Flow, Heat and Combustion Mechanics, Sint-Pietersnieuwstraat 41. 9000 Gent, Belgium, [†]Energy Systems Division, Argonne National Laboratory, Building 362, 9700 South Cass Avenue, Argonne, IL 60439-4815, USA

OUTLINE

16.1 Introduction 381
- *16.1.1 H_2-Internal Combustion Engine vs. Fuel Cell* 381
- *16.1.2 H_2 Properties Relevant for ICE* 382
- *16.1.3 Definition of State of the Art and Advanced Technology Hydrogen Engines* 384

16.2 State of the Art Hydrogen Engine Technology 384
- *16.2.1 Mixture Formation* 384
- *16.2.2 Load Control Strategy* 385
- *16.2.3 Abnormal Combustion* 386
- *16.2.4 Demonstration Vehicles* 386

16.3 Advanced Technology Hydrogen Engines 387
- *16.3.1 Cryogenic PFI* 387
- *16.3.2 Direct Injection* 387
- *16.3.3 Realizing Ideal Mixture Stratification* 390

16.4 Assessment of Present Challenges and Future Potential 393
- *16.4.1 Analysis of Heat Transfer in Hydrogen Engines* 393
- *16.4.2 Analysis of Efficiency Losses in a DI Hydrogen Engine* 395
- *16.4.3 Evaluating Performance and Emissions of DI Hydrogen Vehicles* 396

16.5 Conclusions 397

Acknowledgments 398

References 398

16.1 INTRODUCTION

16.1.1 H_2-Internal Combustion Engine vs. Fuel Cell

The interest in hydrogen as an energy carrier or buffer is explained in detail throughout this book. A significant research effort has gone into the development of the hydrogen-fueled fuel cells for stationary or transport applications as also discussed elsewhere. Fuel cells are attractive for their high efficiency potential throughout the load range with their high efficiency at part-load operation being of particular interest to transportation applications. Furthermore, they are relatively quiet and only emit water vapor as the reaction product. Much less attention has been devoted to internal combustion engines (ICEs) using hydrogen as fuel. The ICE is often readily dismissed as a future prime mover, for its low efficiency (particularly at part load), and pollutant emissions. However, as discussed in this chapter, because of hydrogen's unique

Renewable Hydrogen Technologies
http://dx.doi.org/10.1016/B978-0-444-56352-1.00016-7

properties, it is possible to substantially increase the ICE's efficiency when operated on hydrogen. When using high-temperature oxidation of fuel to produce power, i.e. combustion, the formation of oxides of nitrogen (NO and NO_2, collectively termed NO_X) is possible, which is a disadvantage compared to the low-temperature oxidation in fuel cells. Again, the unique properties of hydrogen allow the emission of NO_X to be ultralow if adequate measures are taken, as explained below.

ICEs have the very interesting feature of being able to operate on different fuels. This "flex-fuel" ability is an advantage for introducing hydrogen vehicles to the marketplace. First, this can assist with the gradual buildup of a hydrogen fueling infrastructure, and second, this can alleviate the on-board storage challenge, with a second fuel (e.g. gasoline) essentially serving as a "range extender". The much lower cost of a hydrogen-fueled ICE compared to a fuel cell is another advantage that can help with setting up demonstration fleets, etc., with the HyNor project vehicle fleet being a prime example (see http://hynor.no). The lower cost applies not only to the ICE itself but also to the fuel; the ICE can handle lower purity hydrogen without any problems.

The hydrogen-fueled ICE has thus been recognized as being a compelling bridging technology to introduce hydrogen as an energy carrier for transportation.[1] However, it has also been advanced as a sustainable and scalable technology, as the ICE is made from abundantly available and recyclable materials,[2] which might not be the case for fuel cells, which require relatively large amounts of platinum.

In the following, hydrogen's properties as an engine fuel are reviewed, the current state of the art in hydrogen engines and hydrogen ICE-equipped vehicles is presented; the present research on H_2 ICEs is described and an outlook on where the development is headed is given.

16.1.2 H_2 Properties Relevant for ICE

Since hydrogen is a gas at ambient conditions, its properties are significantly different from conventional liquid fuels. Table 16.1 shows a comparison of relevant properties of hydrogen, methane (as the main constituent of natural gas) and iso-octane (representative of gasoline fuel). Although some properties of hydrogen, namely, laminar flame speed and flammability range, are advantageous for ICEs, other properties pose challenges for the design of a hydrogen-fueled vehicle. As an example, the density of hydrogen at ambient conditions is almost one order of magnitude lower than methane. This presents a challenge for storing sufficient amounts of the gaseous fuel on-board a vehicle even under compressed or liquefied conditions. The low density also negatively affects the power density of hydrogen engines with external mixture formation.

TABLE 16.1 Properties of Hydrogen Compared to Methane and Iso-octane

Property	Hydrogen	Methane	Iso-octane
Molecular weight (g/mol)	2.016	16.043	114.236
Density gaseous (kg/m^3)	0.08	0.65	–
Density liquefied (kg/m^3)	71	430–470	692
Minimum ignition energy (mJ)	0.02	0.28	0.28
Minimum quenching distance (mm)	0.64	2.03	3.5
Lower heating value (MJ/kg)	120	50	44.3
Stoichiometric air/fuel ratio (kg/kg)	34.2	17.1	15
Flammability limits in air (vol%)	4–75	5–15	1.1–6
Flammability limits (λ^*) (–)	10–0.14	2–0.6	1.51–0.26
Flammability limits ($\varphi^\dagger$) (–)	0.1–7.1	0.5–1.67	0.66–3.85

* *Relative air/fuel ratio.*
† *Fuel/air equivalence ratio.*

As far as combustion is concerned, the minimum ignition energy of hydrogen is more than an order of magnitude lower than that of methane or iso-octane suggesting that hydrogen is easy to ignite. While the ignitability decreases with leaner air/fuel mixtures, its low level at stoichiometric conditions presents a challenge due to the occurrence of combustion anomalies at high engine loads. The significantly lower minimum quenching distance results in hydrogen flames to burn closer to the combustion chamber walls potentially decreasing engine efficiency due to increased wall heat losses. The mass-specific lower heating value as well as the stoichiometric air demand of hydrogen is significantly higher than for methane or iso-octane. These two factors in combination with the density determine the mixture calorific value, which is discussed in a subsequent section. The flammability limits of hydrogen are extremely wide compared to other fuels and hydrogen is ignitable in a range from 4 to 75 vol%.

Figure 16.1 graphically compares the flammability limits of hydrogen to diesel, gasoline and methane. These wide flammability limits are the key to the application of lean-burn combustion strategies with hydrogen as a fuel. Another factor making hydrogen very suitable for lean-burn combustion concepts is

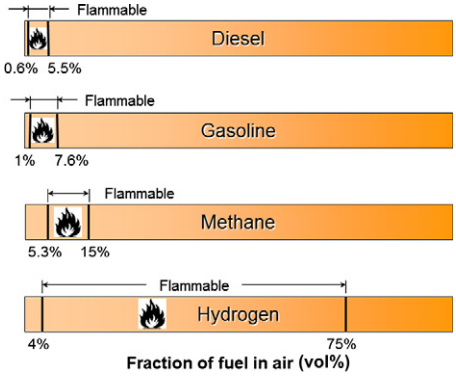

FIGURE 16.1 Comparison of flammability limits of typical engine fuels. (For color version of this figure, the reader is referred to the online version of this book.)

the high flame speeds even under lean conditions. Figure 16.2 compares the laminar flame speeds of hydrogen−, iso-octane− and methane−air mixtures as a function of relative air/fuel ratio (AFR) λ, defined here as the AFR relative to the air/fuel ratio in a stoichiometric mixture (AFR_{st}). Relative AFR λ and fuel/air equivalence ratio Φ are calculated using the following equations:

$$\mathrm{AFR} = \frac{m_{\mathrm{air}}}{m_{\mathrm{fuel}}} \tag{16.1}$$

$$\mathrm{AFR}_{\mathrm{st}} = \left(\frac{m_{\mathrm{air}}}{m_{\mathrm{fuel}}}\right)_{\mathrm{st}} \tag{16.2}$$

$$\lambda = \frac{\mathrm{AFR}}{\mathrm{AFR}_{\mathrm{st}}} \tag{16.3}$$

$$\phi = \frac{\mathrm{AFR}_{\mathrm{st}}}{\mathrm{AFR}} \tag{16.4}$$

Engine combustion is a highly turbulent event with flame speeds that are an order of magnitude higher than the laminar flame speed. Nonetheless the laminar flame speed can be used as an indicator for in-cylinder combustion velocity suggesting extremely short combustion durations for stoichiometric hydrogen−air mixtures. Furthermore, hydrogen−air mixtures at a relative AFR λ of 2 still burn about as fast as stoichiometric iso-octane− or methane−air mixtures.

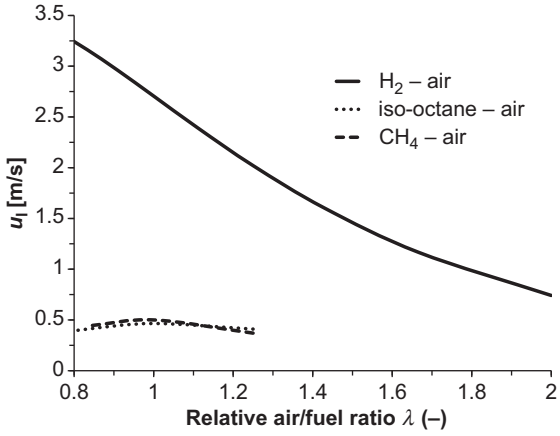

FIGURE 16.2 Laminar flame speed of hydrogen compared to gasoline and methane.[3–6]

The significance of lean combustion is its positive effect on engine efficiency. Under idealized conditions, the engine efficiency (η) can be estimated based on the engine's compression ratio (r_c) and the isentropic coefficient (γ), which is a function of the AFR, using the following equation[7]:

$$\eta = 1 - \frac{1}{r_c^{\gamma-1}} \tag{16.5}$$

The theoretical engine efficiency can therefore be increased by a lean-burn strategy (lean mixtures have higher γ than stoichiometric mixtures), allowed by the wide flammability range of hydrogen.

Another critical property of combustion engine fuels is their resistance to knock, an abnormal combustion event caused by autoignition of the end gases resulting in extremely high pressure oscillations. Research and Motor Octane Numbers (RON and MON) are used to express the resistance of liquid, spark-ignition engine fuels to knocking combustion. While a determination of RON and MON for gaseous fuels is not applicable, research suggests that the knock resistance of hydrogen strongly depends on the AFR.[8] While stoichiometric mixtures are prone to knock, engines have been operated knock-free under high load conditions using lean-burn strategies. Accordingly, lean mixtures can also afford higher compression ratios than stoichiometric mixtures, and this can further improve the theoretical engine efficiency, as shown in the equation above.

As far as pollutants are concerned, hydrogen combustion engines only produce trace amounts of carbon dioxide, carbon monoxide and hydrocarbon emissions. Due to the lack of carbon in the fuel, these small traces have been attributed to lube oil combustion.[9] However, oxides of nitrogen (NO_X) emissions are a result of high in-cylinder temperatures and can occur in hydrogen engines. Figure 16.3 shows a typical NO_X emissions trend of a hydrogen engine as a function of the relative AFR. Due to reduced combustion temperatures, lean homogeneous hydrogen−air mixtures in excess of $\lambda = 2$ burn without forming NO_X emissions. However, engine operation at relative AFRs of $1 < \lambda < 2$ can result in high NO_X emissions levels that can exceed those of conventional gasoline engines. A typical NO_X emissions curve for homogeneous hydrogen combustion peaks around $\lambda = 1.3$ and decreases when approaching stoichiometric conditions due to reduced oxygen availability.

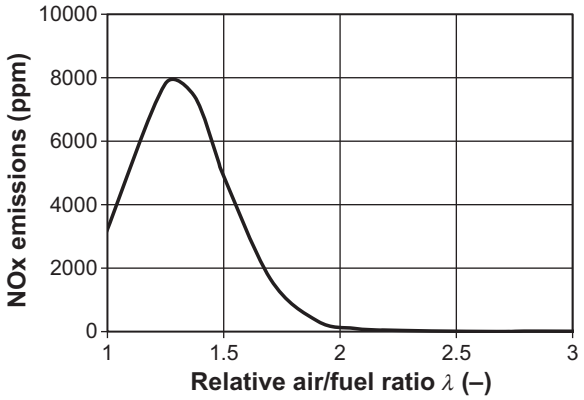

FIGURE 16.3 NO_X emissions trend for homogeneous hydrogen air mixtures as a function of relative air/fuel ratio.[10–13]

16.1.3 Definition of State of the Art and Advanced Technology Hydrogen Engines

In the following sections hydrogen engines are categorized either as state of the art or advanced technology. While the number of hydrogen vehicles and engines in the field is negligible compared to conventionally fueled engines, the term state of the art is used nonetheless to define engine technology that has been demonstrated in prototype fleets. On the other hand, mixture formation concepts that have so far been limited to research engines or to single prototype vehicles are considered advanced technology. A differentiation of hydrogen mixture formation concepts can be done by (1) location of the mixture formation equipment and (2) temperature of the introduced hydrogen. Injection or carburetion in the intake manifold or intake pipe of ambient temperature hydrogen has been widely used for demonstration vehicles and is therefore considered state of the art technology. As shown in Fig. 16.4, this mixture formation concept is very similar to conventional gasoline engine technology, while both injection of cryogenic (very low temperature) hydrogen into the intake system and direct injection (DI) of hydrogen into the combustion chamber are considered advanced technologies. These three hydrogen mixture formation concepts differ in terms of engine performance and emissions behavior, current state of development and dissemination, and complexity and are further discussed in the following sections.

16.2 STATE OF THE ART HYDROGEN ENGINE TECHNOLOGY

16.2.1 Mixture Formation

Because of its physical and chemical properties, hydrogen is mostly used in spark-ignited engines. Therefore, a conventional gasoline engine is used as baseline. In a gasoline engine, fuel is injected in the intake manifold, where it evaporates and mixes with air to form a homogeneous mixture by the time it is compressed in the cylinder. The injection of the fuel in the intake manifold is indicated by the term port fuel injection (PFI).

Figure 16.4 compares the theoretical maximum power output from a PFI gasoline and a hydrogen engine per unit of engine displacement. The achievable power output of a hydrogen engine is reduced compared to that of its gasoline counterpart due to the low volumetric density of hydrogen. Hydrogen occupies a larger

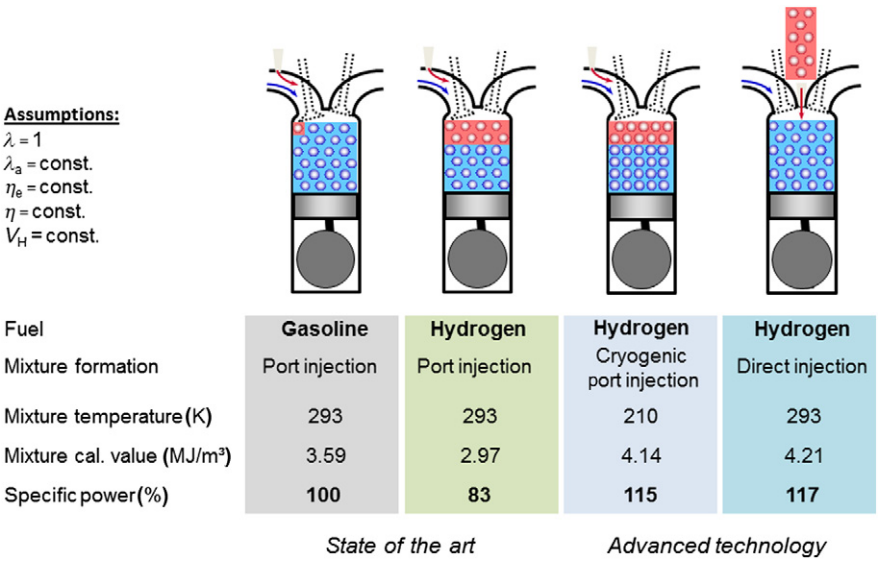

FIGURE 16.4 Comparison of specific power density of hydrogen mixture formation concepts. (For color version of this figure, the reader is referred to the online version of this book.)

amount of the available space in the engine, which reduces the amount of air that can be aspirated into the cylinder. This negative effect is partially compensated by the higher heating value (more released energy per unit of mass) and AFR_{st} (less fuel needed per unit of air), but it still theoretically results in a 17% lower achievable power output. Despite the lower theoretical power output compared to other mixture formation systems, PFI is the only mixture formation system used in demonstration vehicles because of its relative simplicity and availability of injection equipment.

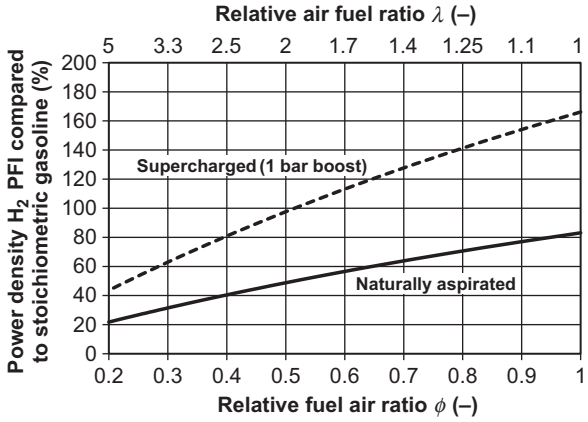

FIGURE 16.5 Theoretical power density of a PFI H_2 engine compared to stoichiometric gasoline operation as a function of relative air/fuel ratio λ or fuel/air equivalence ratio ϕ and charging strategy.

16.2.2 Load Control Strategy

In a conventional gasoline engine, a throttle valve is used in the intake manifold to reduce the power output for part-load operation. Varying the throttle position (TP) controls the amount of mixture (air + fuel) inside the engine, while the AFR is kept constant. Since the quantity of the mixture is controlled, it is also referred to as "quantitative" load control strategy. Using a throttle valve results in poor part-load efficiency, because the partially closed valve represents a resistance for the flow (pumping losses), which requires work from the engine.

The wide flammability limits of hydrogen are an advantage for the load control strategy, since they allow a "qualitative" load control strategy, which avoids throttling in the intake manifold and the corresponding pumping losses. Here, the AFR is increased to reduce the power output for part-load operation like in a diesel engine. Operating the engine with ultralean mixtures also has the advantage of reducing the engine-out NO_X emissions as shown in Fig. 16.3.

Recirculation of exhaust gases back to the intake of the engine is another way to reduce the power output for part-load operation without throttling. The presence of the inert exhaust gases also reduces the amount of air and fuel inside the engine. Hydrogen allows stable engine operation with higher amounts of exhaust gas recirculation (EGR) compared to gasoline because of the wider flammability limits and faster flame propagation.

The maximum achievable power output per unit of engine displacement can be increased by increasing the pressure in the intake manifold of the engine. Figure 16.5 demonstrates that the same power output of the reference gasoline engine can be achieved with hydrogen if the intake pressure is boosted by 1 bar and a relative AFR of around two is used. The compressor that boosts the intake pressure can be driven mechanically (supercharging) or by a turbine that recovers the remaining energy in the exhaust gases (turbocharging). From an efficiency standpoint, turbocharging is considered the preferred option. However, reduced throttle response and reduced exhaust energy with hydrogen compared to conventional fuel operation make the implementation of a turbocharged hydrogen engine more challenging.

Applying one of the load control strategies mentioned above leads to a compromise either in terms of power density (for qualitative, lean-burn approach) or engine efficiency (for quantitative, stoichiometric approach). A potential solution to this trade-off is combining lean-burn and stoichiometric operating strategies.[12–15] At low engine loads, the engine is operated at variable lean AFRs, resulting in good engine efficiencies and extremely low engine-out emissions. Once a certain engine power demand is exceeded, the operating strategy is switched to throttled stoichiometric operation. The NO_X emissions critical operating regime at relative AFRs of $1 < \lambda < 2$ is avoided and a conventional aftertreatment system can be used to reduce NO_X emissions in stoichiometric operation.

The engine performance provided by the load control strategy mentioned above is shown in the map in Fig. 16.6, as a result of the intensive research carried out on a single-cylinder engine at BMW.[16] This result was later scaled to the 12 cylinders case, for implementation in a demonstration vehicle. The map is characterized by an island of peak performance between 4 and 6 bar indicated mean effective pressure (IMEP) with an indicated thermal efficiency (ITE) of 42%. This peak efficiency along with much of the map showing ITE values greater than 38% demonstrates promising engine performance using state of the art engine technology. Unfortunately, it can also be seen in Fig. 16.6 that the peak torque is approximately 10.3 bar IMEP meaning the power density is low relative to comparable gasoline engines. This load limit is largely the result of low intake charge density and partly the result of combustion limitations associated with abnormal combustion.

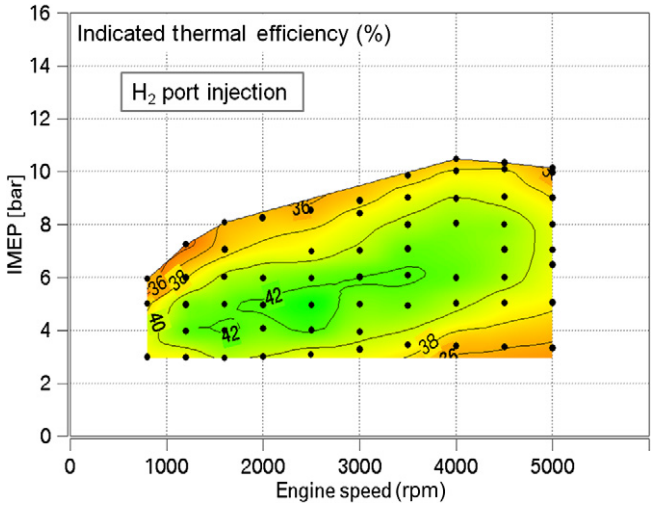

FIGURE 16.6 Efficiency map of a PFI hydrogen engine developed by BMW.[16] (For color version of this figure, the reader is referred to the online version of this book.)

16.2.3 Abnormal Combustion

The wide flammability limits and high flame speeds, combined with low required ignition energy, are beneficial for the efficiency of hydrogen engines, as explained above. However, these properties can also result in undesirable combustion phenomena. Much of the early work on hydrogen engines was targeted at trying to avoid these phenomena.

The most frequently cited phenomenon is called "backfire", which is the early ignition of the hydrogen–air mixture during the intake stroke. This results in a combustion event in the intake, which could be damaged as a consequence. To avoid this premature ignition, care must be taken to prevent unwanted ignition sources such as hot spark plug electrodes, exhaust valves, etc., which implies some hardware modifications to the engine. Avoiding the presence of ignitable mixtures when there might be an ignition source, is another means to prevent backfire. Here, variable valve timing and carefully controlled injection timing have been used to avoid backfire occurrence by allowing a cooling phase with fresh air while limiting the presence of hydrogen during the early intake phase.[17,18]

Unwanted ignition before the spark plug is fired can also occur when the intake valves are already closed. This undesired phenomenon is called "preignition". As the valves are closed and the cylinder charge is being compressed, this can lead to very high pressures and severe damage.

Finally, autoignition of the unburned mixture (knock) can occur like in any spark-ignition engine. As explained in the introduction, compared to conventional gasoline engines, knock is less likely to occur in a hydrogen engine. However, the effect could be more severe, because of the high burning velocity of hydrogen mixtures.

FIGURE 16.7 Quantum hydrogen prius. (For color version of this figure, the reader is referred to the online version of this book.)

16.2.4 Demonstration Vehicles

PFI of hydrogen is the state of the art technology, already being implemented in several demonstration vehicles. The first category of vehicles includes those that have been converted from existing vehicles. The second category is for dedicated vehicles that have been fully developed for hydrogen operation.

The changes that have to be made to an existing vehicle in order to convert it to operate on hydrogen are limited to the fuel system (from storage to injection) and the engine control unit programming. Quantum Tecstar has converted over 30 vehicles to hydrogen operation using the Toyota Prius hybrid as a platform (Fig. 16.7). Two tanks with compressed hydrogen replace the conventional gasoline tank, leaving the interior of the vehicle unchanged. The converted Prius engine is turbocharged in order to increase the power output on hydrogen operation. With similar drivability to the gasoline version, the Quantum Hydrogen Prius has an estimated range of 100–130 km, while meeting Super Ultra Low Emissions Vehicle (SULEV II) emissions standards.[19]

Developing a dedicated hydrogen vehicle requires a higher number of considerations concerning the hardware.[20] With approximately 100 units built, the BMW Hydrogen 7 (Fig. 16.8) is likely the hydrogen vehicle with the highest number of vehicles produced. The vehicle is equipped with a bifuel system allowing for operation on hydrogen or gasoline. On hydrogen, the car employs the combination of a variable AFR lean-burn strategy at low and medium loads and a throttled stoichiometric strategy at high engine loads, which was described above. Approximately 8 kg of hydrogen are stored on the vehicle in a cryogenic tank that is located in the trunk, which allows a range of 200 km on

FIGURE 16.8 BMW hydrogen 7. (For color version of this figure, the reader is referred to the online version of this book.)

hydrogen. Emissions tests of a dedicated monofuel version of the Hydrogen 7 vehicles showed the low emissions potential of hydrogen-powered vehicles. With a dedicated aftertreatment design featuring two catalysts (one for stoichiometric operation and one for reducing NO_X peaks that occur when switching from lean to stoichiometric operation) the vehicle achieved drive-cycle NO_X emissions that were approximately 0.0008 g/mi, which is equal to 3.9% of the SULEV II limit.[21]

16.3 ADVANCED TECHNOLOGY HYDROGEN ENGINES

16.3.1 Cryogenic PFI

Cryogenic PFI is similar to conventional PFI in terms of location of the mixture formation equipment. However, rather than introducing hydrogen at ambient temperature, the fuel is supplied at low, cryogenic temperatures, typically available when hydrogen is stored in its liquid form at approximately 20 K. The low temperature of the introduced hydrogen leads to the reduction in the temperature of the intake air when mixing and ultimately leads to increased charge density. While conventional hydrogen PFI suffers from reduced power density compared to gasoline, hydrogen engine operation with cryogenic injection theoretically exceeds the power density of a comparable gasoline engine under stoichiometric conditions, as shown in Fig. 16.4.

The performance benefits associated with cryogenic port injection include not only higher power density but also improved efficiency. The ITE map in Fig. 16.9 is taken from the same single-cylinder research engine at BMW as the PFI map in Fig. 16.6. With the use of cryogenic PFI, the peak torque is increased by 25% to approximately 12.8 bar IMEP at the same engine speed.[16] Furthermore, greater charge density while using

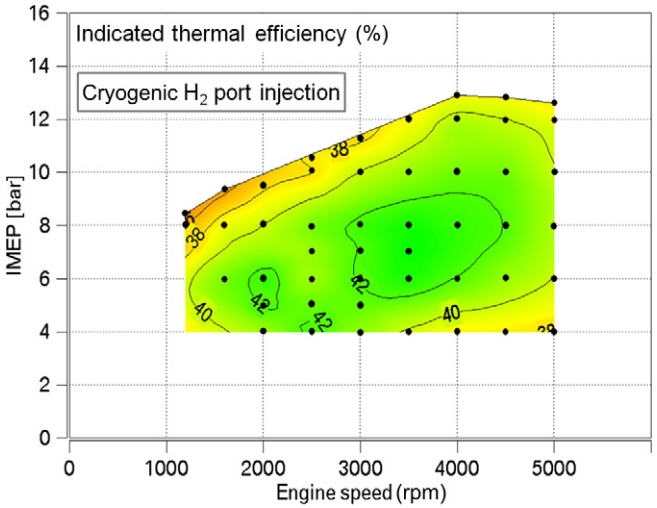

FIGURE 16.9 Efficiency map of a cryogenic hydrogen port injection engine developed by BMW.[16] (For color version of this figure, the reader is referred to the online version of this book.)

a qualitative load control strategy results in proportionally higher IMEP throughout the engine operating range. This effectively expands the 42% ITE operating range because AFR is a key factor impacting efficiency in this engine.[18] Another benefit of using cryogenic PFI is improved knock resistance, which allows spark timing to be optimized where it was previously limited by knock, namely, during high load operation.[16] Improved spark timing results in higher ITE along the full load line at the top of the map in Fig. 16.9.

While the increased power density, as well as the improved engine efficiency, makes cryogenic PFI a promising concept, there are still several remaining challenges. Application of cryogenic injection is only sensible in combination with liquid hydrogen on-board storage, a concept that has been proven to be feasible; however, cost and complexity of liquid on-board storage are significantly higher than compressed storage. Furthermore, injector performance and durability under cryogenic conditions needs to be investigated. Finally, introduction of cryogenic hydrogen into the intake manifold can lead to freezing of humidity contained in the intake air and can ultimately cause ice buildup around the injector.

16.3.2 Direct Injection

As shown in Fig. 16.4, a promising approach to increase the engine performance consists in injecting the fuel directly into the combustion chamber during the compression stroke, when the intake valves are closed. In the particular case of a fuel like hydrogen, the DI approach allows overcoming the loss of volumetric efficiency due to the gas phase fuel displacing

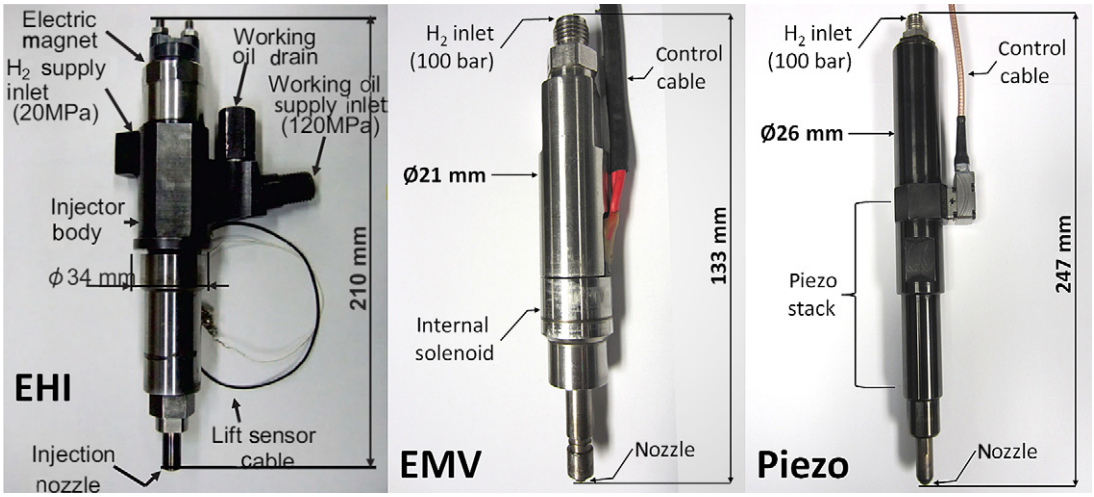

FIGURE 16.10 Comparison of electrohydraulic, electromagnetic, and piezo injectors. (For color version of this figure, the reader is referred to the online version of this book.)

air in the intake manifold. Accordingly, hydrogen DI engines can provide the same or higher power density than conventional gasoline engines. In order to perform the fuel injection during the compression stroke, the fuel injection pressure has to be higher than in the case of PFI. To accomplish injection at late crank angles (against the high in-cylinder pressure) and to ensure the highest mass flow rate (occurring under sonic conditions), hydrogen DI injectors typically operate between 25 and 200 bar. Higher injection pressure leads to higher mass flow rate; however, in a real vehicle this would potentially also reduce the range, since the hydrogen pressure in the tank would progressively decrease. Typically, an injection pressure of 100 bar represents a good compromise. Due to the high pressure, DI injectors require advanced and robust technology. Injectors are usually classified based on the actuator technology. The actuator commands the motion of the needle, thus regulating the fuel flow through the injector nozzle. In Fig. 16.10, three injector generations (electrohydraulic injectors (EHI), electromagnetic valve (EMV) injectors, and piezo injectors) used in DI engines are shown. The main differences in the working principle of the three injectors can be summarized as follows:

- EHI injector. Uses an actuator (usually a solenoid) and a hydraulic oil servo system to lift the needle and inject the fuel. The needle valve is closed again through the hydraulic oil servo system (ON/OFF control).
- EMV injector. Uses a solenoid actuator and a collapsing magnetic field to lift the needle and inject the fuel. The needle valve is closed by a spring (ON/OFF control).
- Piezo injector. Uses a piezoelectric actuator to directly convert a voltage signal into needle lift. The lift is proportional to the applied voltage (analog control).

The EHI shown here was developed at Tokyo City University,[22] while the solenoid (EMV) and piezo injectors were manufactured by Westport[23,24] and extensively tested at Argonne National Laboratory. The piezoelectric element represents the latest generation of injector actuators and ensures higher performance, in particular faster response, than the solenoid actuator because there is no need to generate a collapsing magnetic field. Accordingly, the piezo injector is capable of delivering higher average fuel mass flow than a solenoid injector.

Table 16.2 shows the main characteristics of the three examined injectors. Despite the lowest maximum

TABLE 16.2 Characteristics and Performance of the Examined Injectors: EHI,[19] EMV and Piezo

Injector	EHI	EMV	Piezo
Control method	ON/OFF	ON/OFF	Analog
Maximum injection pressure (bar)	200	150	250
Maximum needle lift (mm)	0.87	0.25	0.1
Start of injection (SOI) delay (ms)	0.375	0.3	0.05
Opening transient duration (ms)	1.42	0.4	0.5
Rate of needle lift during opening (m/s)	0.61	0.62	0.2
Average mass flow rate at 100 bar (g/s)	5.91	2.24	3.94
Average mass flux at 100 bar ($kg/m^2 \cdot s$)	1607	1750	5184
Maximum mass flow rate at 100 bar (g/s)	10.25	2.93	6.22
Mass flow rate increase during transient (g/s·CAD*)	0.79	0.73	1.24

* *CAD, crank angle degree.*

needle lift and the lowest rate of needle lift during the injector opening, piezo injectors show the highest average mass flux, generally due to lower injection delay and faster fuel flow transient than EMV and EHI injectors. The EHI injector shows the highest maximum lift and flow area; however, the extremely slow transients (due to the inertia of the hydraulic servo system) condemn it to be characterized by the lowest performance in terms of fuel mass delivered in a certain amount of time.

The EMV injector is characterized by fast needle lift but the response is overall still slow due to the initial delay. Therefore, it is clear that a piezo injector allows injecting a certain amount of fuel in much shorter time than a solenoid injector, for the same injection pressure. Moreover, piezo injectors can manage higher injection pressures (up to 250 bar) than EMV injectors.

The piezo actuator technology significantly improved the durability of high-pressure gaseous injectors. Nonetheless development of hydrogen injectors is particularly challenging due to a variety of factors:

- The low density of hydrogen significantly reduces the internal damping effect, which helps reducing the needle oscillation, especially during the transients (opening and closing).
- The low viscosity of hydrogen reduces the hydrodynamic lift effect, which helps to keep the injector internal parts separated and prevents shear stresses.
- Hydrogen is usually delivered as totally free of lubricant traces and is much drier than natural gas; thus, relative motion between the sealing elements is detrimental to hydrogen injectors.
- Hydrogen potentially degrades epoxy resins used to coat the piezo stack.

As a result, compared to liquid fuels or compressed natural gas, extreme precision has to be ensured for the opening and closing operations. The piezo injector offers several benefits in terms of needle lift control. Piezoelectric material is characterized by a well-known relationship between voltage and expansion; thus, the lift control is much more precise than in solenoid injectors. This not only ensures excellent repeatability but also allows modifying the waveform to provide the desired lift profile, depending on the engine operating condition. The lift and acceleration profile can be optimized to improve the needle seating, reduce the seat impact, and control the needle bouncing, thus improving the injector durability.

The current generation of piezo injectors offers higher injection pressure and higher mass flow along with better repeatability and durability than the previous EHI or EMV injectors. It is also suitable for multiple injections, due to the fast response and high precision. Nonetheless, research is still required to face remaining challenges concerning durability, control, size and cost. In particular, hydrogen may cause embrittlement of the injector materials and can chemically attack the oxide layer of the metallic surfaces, thus leading to fracture and wear, respectively. Research in the proper coatings and materials as well as in reducing friction and impact wear can improve the injector durability.

In some cases, modified versions of the solenoid injector (dual solenoid[25]) can achieve almost the same performance of piezo injectors, but with half the size and much lower cost. Therefore, depending on the scope (research or series production), required performance (mass flow rate, number of injections) and cost and size constraints, the old-generation solenoid injectors may still be more desirable than new-generation piezo-actuated injectors. The latter technology has yet to overcome limiting issues concerning high production costs and large size of the piezo stack.

Independently of the injector technology, DI offers higher flexibility than PFI in defining the proper strategy to achieve high thermal efficiency. This also means higher number of degrees of freedom since injection timing, number of injections, injector location, and nozzle geometry significantly influence the final stratification of the charge around the spark plug at the time of spark ignition. Figure 16.11 shows the basic strategies for DI, defined on a timescale where the ignition timing is represented by the spark symbol. High load conditions require a large amount of hydrogen injected. Accordingly, in a single-injection approach, the injection cannot be started too close to the top dead center (TDC), since the end of injection has to occur before the spark timing. To increase stratification around the spark plug at the ignition timing, a multiple injection strategy can be adopted, where hydrogen is injected immediately before and during the combustion event.

In general, the main goals and challenges in a DI strategy can be defined as follows:

1. Perform late injection: Late injection allows increasing the thermal efficiency due to decreased compression work. It also allows providing highly stratified mixtures, since there is not enough time for complete mixing of the fuel with air.
2. Properly stratify the mixture at the spark timing (see Fig. 16.12): The ideal mixture stratification consists of a stoichiometric or rich mixture around the spark plug at spark timing and an ultralean mixture close to the cylinder walls. The engine efficiency benefits from such a configuration due to increased combustion efficiency and reduced losses from heat transfer to the cylinder walls.

Pollutant emissions are influenced by the mixture stratification as well. Figure 16.1 shows that hydrogen

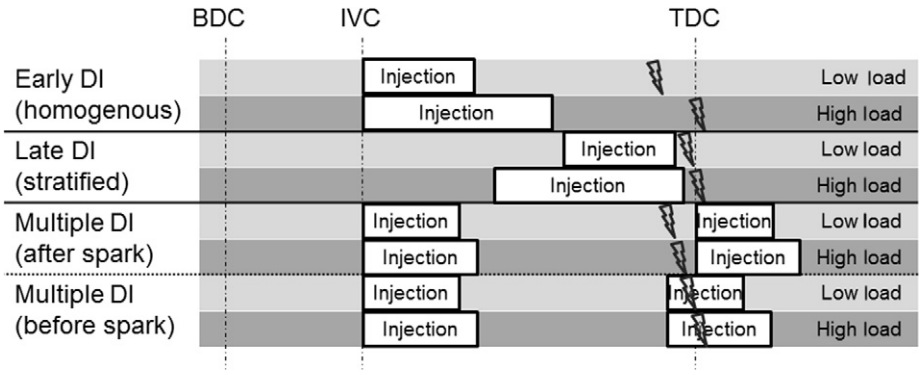

FIGURE 16.11 Typical hydrogen direct injection strategies.

can still be burned efficiently in ultralean mixtures ($\lambda > 2$) and Fig. 16.3 shows that at these lean conditions the NO_X emissions are extremely low. At the same time, when mixtures are highly stratified, richer zones may exist thus increasing NO_X emissions even if the mixture is lean overall.

It becomes evident that the injection timing (start of injection, SOI) is not the only parameter to be controlled in order to optimize performance and emissions in a DI hydrogen engine. In order to pursue the ideal mixture stratification shown in Fig. 16.12, nozzle geometry, injector location, piston shape and combustion chamber design become very important parameters. At Argonne National Laboratory, computational fluid dynamics (CFD) is being used to support engine testing. CFD numerical simulations provide deep insight into the mixture formation process and are used as an effective development tool, with the final goal of pursuing the ideal mixture stratification.

CFD results have been extensively validated against particle image velocimetry and planar laser-induced fluorescence data from an optically accessible engine[26,27] and have been subsequently used to optimize the injector nozzle geometry. As shown through the CFD results in Fig. 16.13, even in the case of extremely simple chamber geometry (pent roof with flat piston) the mixture stratification is significantly affected by the nozzle configuration.

Hydrogen jets not only interact with the cylinder walls and the existing flow field, but also interact with each other, due to the Coanda effect.[28] The number and diameter of holes in the injector nozzle greatly influence the evolution of each jet. However, in order to maximize the mass flow rate, the total flow area cannot be larger than the critical area between the needle valve and its seat. Accordingly, the nozzle geometry is the main factor responsible for an efficient stratification at the time of ignition. Conversely, as far as the injection duration is concerned, the actual bottle neck is represented by the actuator characteristics (nominal injection pressure, needle response, maximum needle lift and flow area).

16.3.3 Realizing Ideal Mixture Stratification

Currently, research is taking place to realize ideal hydrogen mixture stratification in an ICE to demonstrate its potential for high efficiency and low emissions.

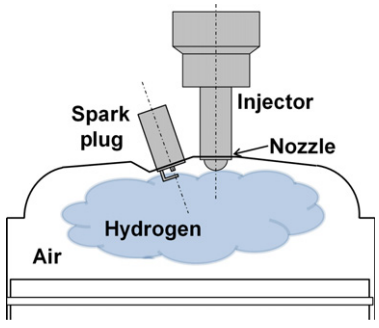

FIGURE 16.12 Schematic of ideal mixture distribution. (For color version of this figure, the reader is referred to the online version of this book.)

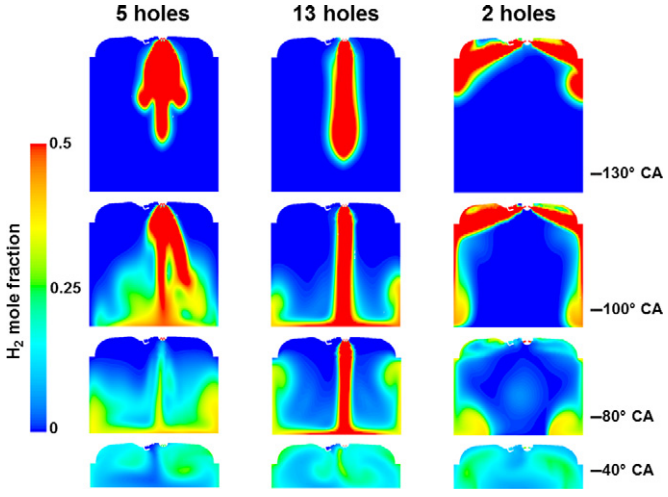

FIGURE 16.13 Influence of nozzle design on mixture formation (CFD results). (For color version of this figure, the reader is referred to the online version of this book.)

Multiple engine concepts have been developed to realize ideal mixture stratification.

One recent example is the work of Heindl et al.[29] in which a diesel like engine concept was developed to perform stratified, diffusive combustion of hydrogen jets in a ω-shaped piston bowl. One focus of the work was to locate the injector nozzles and design the piston bowl such that the hydrogen jets would have the maximum possible time for combustion before impinging the combustion chamber walls. The idea is to ignite the injected hydrogen immediately upon entering the combustion chamber to prevent combustion from taking place in close proximity to the combustion chamber walls. This concept requires a very high injection pressure in order to overcome the in-cylinder pressure near TDC, especially when the mixture is combusting during injection and at higher engine loads where more fuel is required.

A key consideration in order to effectively perform stratified, diffusive combustion is ignition timing. Heindl et al. explored various ignition methods including a pilot injection to facilitate ignition of a homogeneous mixture by which the main injection would be ignited. Compression ignition of the homogeneous charge was possible with the use of intake air heating but more stable combustion resulted from using a spark plug to ignite the homogeneous mixture. An ITE based only on the high pressure part of the cycle (ITE_hp) of 44% was achieved.[29] It is worth noting that ITE_hp overestimates the ITE, which is otherwise calculated based on the entire cycle. Comparable efficiency and combustion stability were also demonstrated using a glow plug mounted close to the injector in order to directly ignite the hydrogen jets. In this case a pilot injection was not possible because it would be subject to uncontrolled ignition by the glow plug, so the entire charge was subject to stratified, diffusive combustion and ignition timing was dependent on injection timing.

A similar engine concept using a diesel like combustion chamber but with a spark plug mounted near the injector nozzle has been studied by Tanno et al.[30] The engine concept used a hydraulically actuated injector, which was centrally located in the combustion chamber in order to aim multiple hydrogen jets into a ω-shaped piston bowl. This study highlighted the importance of jet penetration because the location of the stratified mixture at ignition timing depends on how quickly the jets travel through the combustion chamber. Jet penetration is dictated by injector nozzle design and injection pressure (in this case the injector is rated to 300 bar). Using injection pressure to control mixture stratification, an injection pressure of 100 bar allowed the engine to operate with a peak ITE of 52% at 2000 rpm, 2.5 bar IMEP.[30] Using 100 bar injection pressure limited the amount of fuel that could be delivered because injection was taking place near TDC; thus, the engine was limited to low load in this case. Injection pressure was increased at medium to high loads to the detriment of ideal mixture stratification resulting in an ITE of 43.8% at 2000 rpm, 8 bar IMEP.[30] EGR was used to mitigate NO_X at this operating point and the resulting NO_X emissions were 0.35 g/kWh for this condition.[30] Future work on this diesel like engine concept is intended to expand the operating range while managing jet penetration for improved efficiency, possibly through a different nozzle design, and continued use of EGR to mitigate NO_X.

Research at Argonne National Laboratory focused on the development of a partially stratified combustion system based on a typical Spark Ignition (SI) combustion chamber design. Using a pent roof head and flat piston top, the mixture formation process is controlled using injector nozzle geometry coupled with injection timing. The engine configuration is shown in Fig. 16.12 with a centrally located injector nozzle and a spark plug mounted near the nozzle. An example of the mixture formation process is depicted in Fig. 16.13, which shows that injector nozzle geometry is critical to achieving ideal mixture stratification. Recent developments, based on collaborative engine testing and multidimensional CFD engine modeling, have led to a four-hole injector nozzle operated at SOI times from 60 to 120 crank angle before top dead center (°CA BTDC) at engine speeds from 1000 to 3000 rpm, respectively. SOI can be delayed as engine speed decreases while still allowing sufficient time for mixture formation. SOI was optimized as a function of engine speed based on a series of SOI sweeps at different operating speeds. The resulting SOI trend is a 15 °CA delay per 500 rpm decrease in engine speed.

The results for engine performance shown in Figs 16.14 and 16.15 are presented in terms of brake engine values. This requires a friction assumption since the single-cylinder research engine is understood to have inherently greater friction than a multicylinder counterpart. Since the engine geometry (89 mm bore and 105.8 mm stroke) is representative of a light-duty automotive engine, friction values from a similar multicylinder engine have been applied to the measured single-cylinder results.[31] Brake engine values as shown in subsequent engine maps are based on the estimated work output from the engine through the crankshaft to the rest of the powertrain.

The partially stratified concept provides promising results not only for peak efficiency but also over an operating range that is relevant for vehicle applications. The engine operates above 35% brake thermal efficiency (BTE) over approximately 80% of the tested operating range from 1000 to 3000 rpm and from 1.7 to 14.3 bar Brake Mean Effective Pressure (BMEP).[31] The peak efficiency point occurs at 2000 rpm and 13.5 bar BMEP with a BTE value of 45.5% as specified on the map in

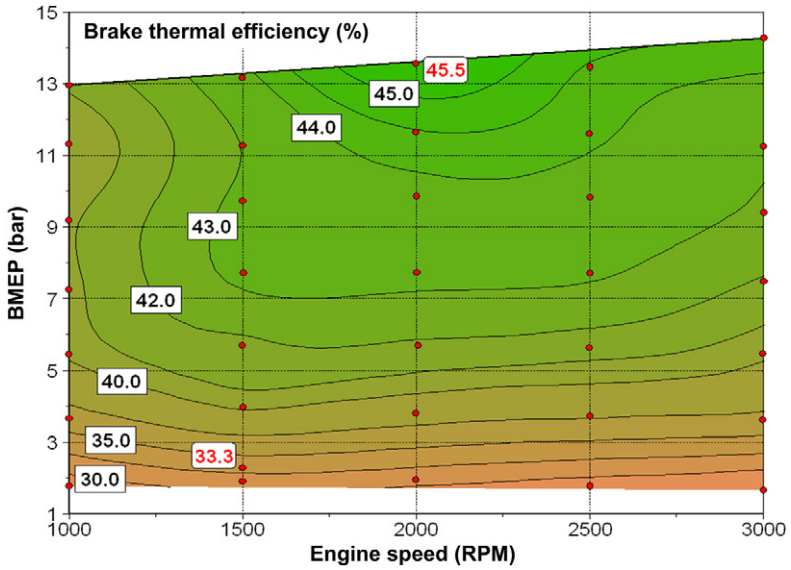

FIGURE 16.14 Brake thermal efficiency map of an optimized hydrogen DI engine.[31] (For color version of this figure, the reader is referred to the online version of this book.)

Fig. 16.14.[31] The other specified operating point with a BTE of 33.3% is 1500 rpm and 2.3 bar BMEP,[31] which represents a typical part-load operating point.

Compared to engine maps for PFI and cryogenic PFI mixture formation strategies (Figs 16.6 and 16.9, respectively) the operating range for the DI engine is limited by 3000 rpm maximum speed but includes a broader range of engine loads. Within the comparable operating range, the partially stratified H_2-DI engine concept shows a substantial improvement in thermal efficiency (note that friction losses have been included in Fig. 16.14 and not in the previous maps) and the peak efficiency is observed at higher load. The peak torque is also increased reaching a maximum of 14.3 bar BMEP. The preconceived benefit of DI to increase charge density (Fig. 16.4) is only partially responsible for the higher peak torque because simulated turbocharging was also used on the optimized DI engine.

A constant relative AFR ($\lambda = 3.3$) control strategy was employed whenever possible[31] over the tested operating range. This was done through variable injection durations for fuel metering and simulated turbocharging for AFR control. To simulate turbocharging the exhaust back pressure was set as a function of intake pressure. This function was validated to ensure that simulated turbocharging was in-line with the capability of a real

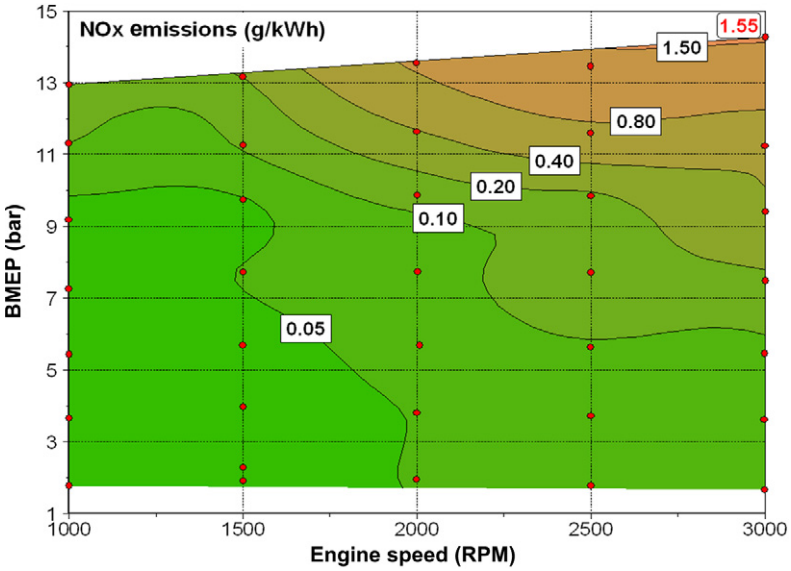

FIGURE 16.15 NO_X emissions map of optimized hydrogen DI engine.[31] (For color version of this figure, the reader is referred to the online version of this book.)

turbocharger.[31] The constant $\lambda = 3.3$ strategy was chosen because it was found to be sufficiently rich in providing flame speeds conducive to ideal combustion phasing while sufficiently lean to mitigate NO_X formation. It is interesting to note that λ may be further optimized especially in conjunction with different injector nozzle designs and mixture formation concepts. The aforementioned benefits of using $\lambda = 3.3$ were determined experimentally for the given engine configuration.

An engine map of NO_X emissions corresponding to the efficiency map in Fig. 16.14 is shown in Fig. 16.15. Results show that the partially stratified mixture formation concept coupled with the overall lean control strategy provides relatively low NO_X emissions. Although no aftertreatment is used, the map is dominated by NO_X emissions less than 0.10 g/kWh with lower NO_X emissions observed at lower engine load. Despite a peak NO_X of 1.55 g/kWh at 3000 rpm and high load, lower engine loads are more relevant to engine operation in vehicular applications. The map of engine-out emissions therefore provides promising results for evaluation of hydrogen vehicle emissions, which is discussed in a later section.

16.4 ASSESSMENT OF PRESENT CHALLENGES AND FUTURE POTENTIAL

The previous sections have highlighted the enormous potential of hydrogen engines in achieving high thermal efficiency and low impact on the environment. Nevertheless, challenges still remain to be addressed in order to increase the efficiency even further. Heat transfer to the cylinder walls is the largest efficiency loss within the cylinder–piston thermodynamic system. In a PFI strategy, this loss is mainly a function of the fuel properties and of the AFR. With a DI strategy, it also depends on the stratification of the charge. This section first investigates the heat transfer to the walls in detail for state of the art (PFI) and advanced (DI) technologies. Then, other contributions to the total efficiency loss are discussed for the advanced (DI) technology. Finally, the potential application of the advanced technology to a real light-duty vehicle is evaluated by means of a simulation tool and an estimate of performance in terms of fuel consumption and emissions is provided.

16.4.1 Analysis of Heat Transfer in Hydrogen Engines

The investigation of heat transfer inside ICEs has always been a topic of interest in the search for higher power output, higher engine efficiency and lower emissions. However, only a few research groups have investigated it in hydrogen engines, because measuring the instantaneous heat loss during the combustion cycle is challenging.

Extensive research has been performed by teams working at Graz University of Technology and BMW. They focused on the investigation of combustion concepts for hydrogen engines. Heat transfer measurements were an important part of the research program to examine the effect of the heat loss on thermal efficiency. Wimmer et al.[32] compared the heat loss of hydrogen and gasoline combustion and concluded that the peak and total cycle heat transfer was higher for hydrogen. They investigated both injection strategies discussed above (PFI and DI). Both peak and total cycle heat losses were higher for DI than for PFI, because the injection process during the compression stroke augments the in-cylinder turbulence and consequently the heat transfer. Eichlseder et al.,[33] however, showed lower total cycle heat losses with stratified DI concepts. Both studies showed that the heat loss is an important factor for efficiency optimization in hydrogen engines. Michl et al.[34] measured heat flux on the cylinder head and piston at a total of 29 positions. They concluded that the AFR and the amount of EGR have a large influence on the heat loss. It would be beneficial to operate the engine on lean mixtures or with high amounts of EGR to reduce the heat loss. Shudo et al.[35–37] have also done research on the heat loss in hydrogen engines to increase the thermal efficiency, first with PFI and later with DI. They investigated the influence of ignition timing and AFR and compared hydrogen to methane combustion, concluding that hydrogen combustion results in higher heat losses. However, the engine loads of the operating points were not published, so it is not clear whether the measurements on both fuels resulted in similar engine loads. The thermal efficiency increased with increasing the relative AFR λ because of lower heat losses, confirming the results of Michl et al.[34] Based on measurements in a constant volume chamber, Shudo et al.[36] found stratified DI to be the best strategy to increase the thermal efficiency of hydrogen engines, which agrees with the conclusions of Eichlseder et al.[33] Wei et al.[38] investigated the heat transfer in a hydrogen engine with dual injection (PFI at low loads and DI at high loads), comparing it to gasoline. The peak of the heat flux was 2.5 times larger for hydrogen under the same engine speed and load.

Based on the literature described above, it could be concluded that the heat loss of hydrogen is always higher than that of any other fuel. However, the comparisons were not done in a wide range of similar engine loads. Therefore, this section compares the heat loss in a PFI engine operated on hydrogen and methane in a range of similar indicated power outputs at a constant speed of 600 rpm. A detailed description of the measurement setup

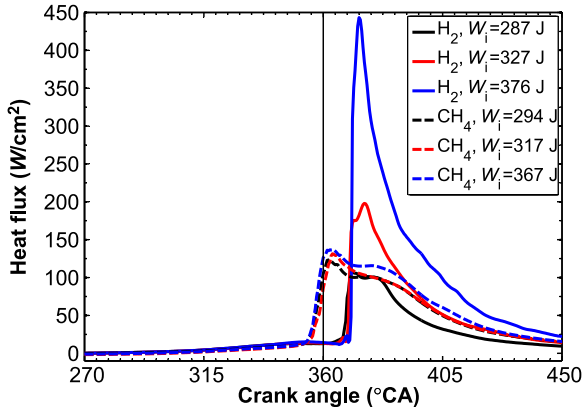

FIGURE 16.16 Varying the engine load by 23% results in a variation of 80% in the heat transfer of hydrogen and only 13% in that of methane. (For color version of this figure, the reader is referred to the online version of this book.)

and method can be found elsewhere.[39] The power output for hydrogen was controlled by varying the relative AFR. In contrast, a throttle was used in the intake manifold for methane ($\lambda = 1$). The ignition was always at Minimum spark advance for Best Torque (MBT)-timing.

Three different relative AFRs were selected for hydrogen (λ = 2, 1.5 and 1), which resulted in an indicated work output (W_i) of 287, 327 and 376 J, respectively. The corresponding engine IMEPs were 4.7, 5.3 and 6.1 bar. The comparable three indicated power outputs on methane were 294 J (TP at 77°), 317 J (TP at 76°) and 367 J (TP at 74°). The heat flux measurements at a certain position on the cylinder liner are plotted in Fig. 16.16, those of hydrogen with a solid line and those of methane with a dotted line. The lowest, middle and highest engine load are in black, red and blue, respectively.

The initial increase in the heat flux traces is caused by the flame passage over the measurement position. Although the flame speed is slower for the leanest hydrogen measurements (black), the initial rise occurs at the same instant of the stoichiometric measurement (blue) due to the advanced ignition timing.

For hydrogen, the fast and short combustion of the stoichiometric measurement generates a high peak in the heat flux trace. This peak greatly reduces if the engine is operated on a lean mixture. The peak in the heat flux trace is reduced by 80% when λ is changed from 1 to 2. The resulting power output decreases by 23%. In contrast, the heat flux traces of methane remain almost identical. Reducing the in-cylinder mass has a large effect on the resulting power output, but not on the heat loss. The heat transfer does decrease when the load is reduced, but not as much as expected. The AFR on the other hand has a great influence on the heat transfer process. The peak in the stoichiometric heat flux trace of hydrogen is three times higher compared to methane, but it is smaller if λ is equal to 2.

The difference in the heat transfer process is reflected in the indicated efficiency of the engine. To demonstrate this, an estimate of the total cycle heat loss is calculated assuming that the heat flux at the measurement position represents the heat flux over the entire cylinder wall. The most important data of the measurements are summarized in Table 16.3. For hydrogen, the total cycle heat loss decreases from 597 to 235 J if the power output is reduced from 367 to 294 J, which is a reduction by 61%. The heat loss through the cylinder walls for methane reduces from 386 to 343 J, which is only a reduction by 11%.

For the highest power output, the indicated efficiency for hydrogen is lower (23%) compared to that for methane (26%) due to the higher heat loss. The indicated efficiencies for both fuels are almost the same for the middle power output and that of hydrogen becomes higher at the lowest engine load, 29% compared to 25% for methane. Although there is a difference of 10% in the total cycle heat loss between hydrogen and methane at the highest engine load, there is only a difference of 3% in the indicated efficiency. The higher combustion efficiency caused by the fast combustion process of hydrogen partially counters the high amount of heat loss through the cylinder walls. The results of Shudo et al.[35] showed a similar trend. The difference

TABLE 16.3 The Effect of the Heat Loss is Reflected in the Indicated Efficiency, which Drops from 29% to 23% for Hydrogen Going from Low to High Load

Fuel	Ignition (°CA BTDC)	λ	Throttle	W_i (J)	IMEP (bar)	ITE (%)	Heat loss (J)	Heat loss (%)
Hydrogen	4	2	WOT*	287	4.7	29	235	24
Methane	23	1	77°	294	4.8	25	343	29
Hydrogen	−2	1.5	WOT*	327	5.3	26	353	28
Methane	23	1	76°	317	5.2	25	329	26
Hydrogen	−6	1	WOT*	376	6.1	23	597	37
Methane	23	1	74°	367	6	26	386	27

** Wide Open Throttle*

in heat loss between hydrogen and methane was around 20%, whereas the difference in indicated efficiency was only around 5%.

The results presented here, combined with the findings in the literature, demonstrate that a hydrogen engine should be operated with a lean mixture to obtain high engine efficiency. EGR in combination with supercharging could be used to achieve high engine loads without increasing the high heat losses. A remaining challenge is the development of a heat transfer model for ICEs that is capable of predicting the large variation in the heat loss for operation on hydrogen, since it has been shown that current models are not suitable.[40,41]

16.4.2 Analysis of Efficiency Losses in a DI Hydrogen Engine

This section provides a comprehensive analysis and quantification of the efficiency loss contributions in a DI engine. The efficiency analysis begins with a theoretical maximum efficiency of the engine based on the engine geometry and properties of the air–fuel mixture. This efficiency of an ideal engine with real charge is termed ηIRC and is labeled on the y-axis in Fig. 16.17. Consider, for example, a compression ratio of 12:1 and a relative AFR of $\lambda = 2$ on the plot in Fig. 16.17; ηIRC is approximately 55% meaning the greatest achievable engine efficiency will always be less than that value. From this plot it could be concluded that continually increasing the compression ratio will result in continually increasing engine efficiency; however, this is not the case because many partial losses also increase with the compression ratio resulting in a trade-off between ηIRC and partial losses with respect to compression ratio.

The difference between air aspirating and mixture aspirating operation takes into account the added work required to compress hydrogen during the compression stroke. For PFI operation ηIRC is based on mixture aspirating operation because hydrogen is present during the entire compression stroke while in DI engines hydrogen is added during the compression stroke. The ideal cycle for DI operation would therefore be an instantaneous addition of hydrogen at TDC. The equation and terminology used for the analysis of losses are as follows.[42]

BTE = ηIRC − ΔICS − ΔIC − ΔRC − ΔWH − ΔGE − ΔF	
BTE	brake thermal efficiency
ηIRC	efficiency of ideal engine with real charge
ΔICS	losses due to injection during compression
ΔIC	losses due to incomplete combustion
ΔRC	losses due to real combustion
ΔWH	losses due to wall heat
ΔGE	gas exchange losses
ΔF	friction losses (multicylinder counterpart)

ΔICS is specific to DI engines and accounts for the fact that the real injection process is not an instantaneous addition of hydrogen at TDC. Rather it is an addition of hydrogen of finite duration with an SOI time that has to allow the proper amount of time for ideal mixture stratification. ΔICS monotonically decreases with delayed SOI but in the case of the partially stratified engine concept SOI time is optimized between 60 and 120 °CA BTDC depending on engine speed. This results in an efficiency loss of nearly 1.6% (Fig. 16.18).

ΔIC accounts for hydrogen that escapes combustion typically by being compressed into the crevice volume or flame quenching zone of the combustion chamber.

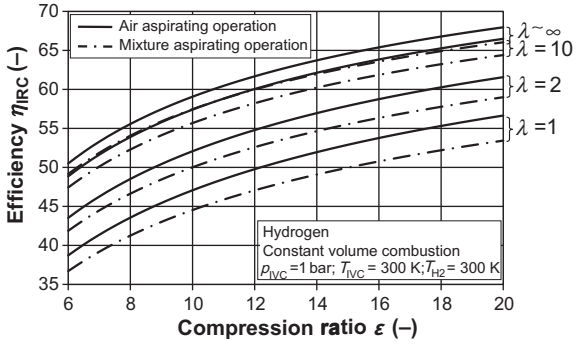

FIGURE 16.17 Theoretical efficiency potential of hydrogen engines as a function of compression ratio and A/F ratio.

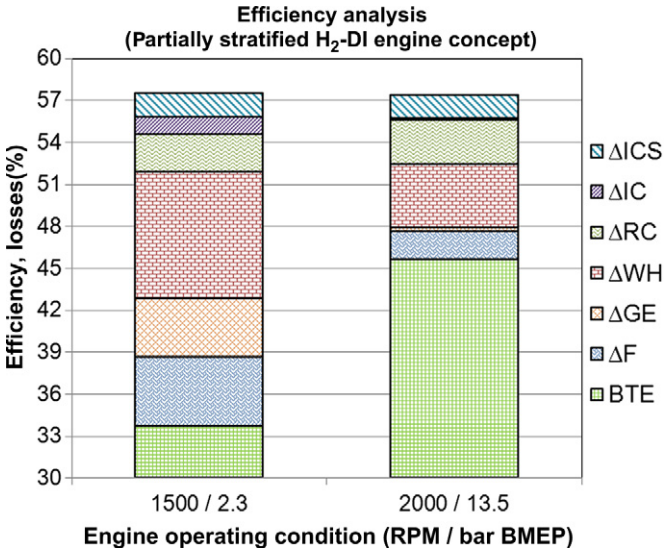

FIGURE 16.18 Efficiency analysis at low and high load points.[31] (For color version of this figure, the reader is referred to the online version of this book.)

ΔIC is a small loss under normal conditions unless the mixture formation process leaves substantial quantities of hydrogen in the crevice or quenching zones.

Losses due to real combustion, ΔRC, account for the real heat release profile in the engine. While ηIRC assumes constant volume combustion at TDC, real combustion requires a finite period of time with the majority of heat release taking place after TDC. The fast laminar flame speed of hydrogen mixtures, albeit a function of the local AFR, provides relatively short combustion durations, which serve to minimize ΔRC. Moreover, proper mixture stratification around the spark plug reduces the ignition delay and allows combustion phasing to be optimized which also serves to minimize ΔRC. From the evaluation of ΔRC in the partially stratified H_2-DI engine it can be seen that this is a significant efficiency loss. These results along with the other partial losses are shown in Fig. 16.18. ΔRC equates to 2.7% and 3.2% losses in efficiency at the low and high load operating conditions, respectively.

Efficiency losses due to wall heat, ΔWH, are 9.1% and 4.6%, which for both operating conditions is the most significant loss mechanism. The general trend in ΔWH is that it increases at lower engine speeds because there is more time per cycle for the combustion gases to interact with the combustion chamber walls. A trade-off exists between ΔWH increasing with lower engine speed and other partial losses that tend to decrease and this trade-off results in the peak efficiency being observed at 2000 rpm (Fig. 16.14).[31] In terms of engine load, one would expect ΔWH to increase with increasing load because the in-cylinder temperatures are higher. However, the trend is reversed when ΔWH is considered as a percentage of the total heat release as it is in Fig. 16.18. The 1500 rpm low load operating condition exhibits almost twice the efficiency losses due to wall heat compared to 2000 rpm high load. This is because the heat losses increase with the load but the total heat release increases as well.

In the previous section the typical trend was an increase in ΔWH with increasing engine load even when calculated as a percentage of efficiency loss. At the same time, the effect of heat transfer losses on the indicated efficiency is a complex function of engine speed, load, and load-regulating strategy. As an example, in Table 16.3 the hydrogen engine load is regulated by the relative AFR λ ranging from one (high load) to two (low load). Accordingly, the cylinder temperature during combustion at high load is expected to be higher than for the low load and this increases the heat transfer to the walls.

A further reduction in ΔWH is possible with a DI strategy. As discussed earlier in the Direct Injection section, the optimal stratification of the mixture within the cylinder has been the main goal of collaborative experimental and numerical efforts. With ideal mixture stratification (Fig. 16.12), it would be possible to simultaneously reduce the heat transfer (ΔWH) and real combustion (ΔRC) losses. Furthermore, as discussed in the same section, achieving ideal stratification with late injection would also reduce the compression losses (ΔICS). Therefore, a DI strategy not only provides higher performance but also offers higher potential in further improving such performance, due to the high flexibility in optimizing the mixture preparation process.

Gas exchange losses, ΔGE, are the result of pumping work that is required to exhaust spent gases and intake a fresh charge. The amount of pumping work required largely depends on the load control strategy being employed and whether it requires throttling or not. The wide flammability limits of hydrogen generally allow less throttling providing an inherent efficiency benefit. In the case of the partially stratified H_2-DI engine with the prescribed $\lambda = 3.3$ control strategy, throttling was only required for loads less than 4 bar BMEP. The effect of throttling can be seen in Fig. 16.18 where ΔGE is a 4.2% loss at low load and a negligible loss at high load. The high load operating point was run using simulated turbocharging with a 1.0 bar boost (2.0 bar absolute) and 0.2 bar differential pressure between the intake and exhaust manifolds.

The final loss mechanism being considered is friction, ΔF, and it is important to note that the friction values are taken from a multicylinder engine that is similar in geometry to the single-cylinder research engine. Similar to ΔWH, the trend in efficiency loss in terms of percentage is counterintuitive because friction is expected to increase with both engine speed and load. The expected trend is true in terms of absolute energy loss but ΔF still makes up a lesser percentage of the total heat release at the high load operating condition in Fig. 16.18.

16.4.3 Evaluating Performance and Emissions of DI Hydrogen Vehicles

Thus far, only state of the art hydrogen engines have been evaluated by their intended use in light-duty vehicles and advanced hydrogen engines by definition have not yet been implemented in vehicles for on-road testing. Vehicle simulations are used in lieu of experimental data in order to evaluate the future potential of advanced hydrogen engines. Having shown efficiency and emissions maps as well as an efficiency analysis (Figs 16.14, 16.15, and 16.18, respectively) from the partially stratified H_2-DI engine concept, this example will be carried forward for the subsequent vehicle simulation results.

Vehicle simulations are carried out using the Autonomie vehicle simulation tool.[43] The hydrogen engine under consideration is intended for light-duty automotive applications so the simulated vehicle is a midsize sedan with a five-speed automatic transmission. The vehicle mass is 1553 kg, it has a footprint of 4.42 m^2 (the footprint in square feet is used for calculating Corporate Average Fuel Economy (CAFE) fuel economy), and it has a conventional (nonhybrid) powertrain.[44] The engine parameters were scaled to 2.0-, 2.5-, and 3.0-l displacements based on the results from the 0.68-l research engine. City fuel economy is based on the Urban Dynamometer Driving Schedule (UDDS) driving cycle, highway fuel economy is based on the Highway Fuel Economy Driving Schedule (HWFET) driving cycle, and combined fuel economy is based on a weighted average (55% city and 45% highway). These are evaluated in miles per gallon (mpg) of gasoline based on equivalent energy consumption.

Vehicle simulation results are presented in Fig. 16.19 in the context of yearly CAFE fuel economy standards and US Environmental Protection Agency (EPA) NO_X emissions categories. CAFE fuel economy standards are based on the vehicle footprint and it is important to note that unadjusted EPA values are used to provide a meaningful comparison to CAFE standards. Likewise, CAFE credits for alternative fuels are not considered in calculating the fuel economy. It follows from the promising engine efficiency values that the vehicle fuel economy exceeds 2016 CAFE standards even with a larger engine. The effect of engine downsizing is improved fuel economy because the engine is being pushed into its higher load-operating regime where peak efficiency is observed. Vehicle fuel economy increases from 38.9 to 45.4 mpg when the hydrogen engine is downsized from 3.0 to 2.0 l.[44]

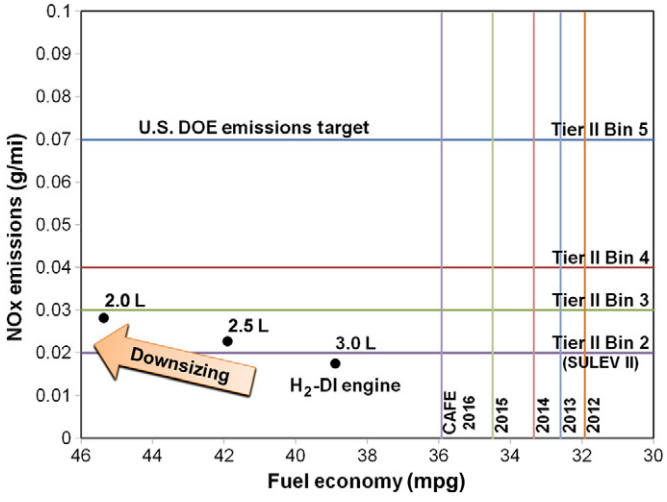

FIGURE 16.19 Fuel economy and emissions behavior of a simulated hydrogen DI engine vehicle.[44] (For color version of this figure, the reader is referred to the online version of this book.)

There is clearly a trade-off between fuel economy and NO_X emission that comes with engine downsizing. As the engine is pushed into its higher efficiency operating regime this is also a higher NO_X operating regime. The 2.0-l hydrogen engine emits 0.028 g/mi of NO_X,[44] which is well within the US Department of Energy (DOE) emissions target of Tier II Bin 5 (0.07 g/mi[45]) for hydrogen-powered vehicles.[46] With the larger 3.0-l engine the NO_X emissions are significantly less with a value of 0.017 g/mi, which falls within the SULEV II category.[44] This estimate comes from engine-out emissions data meaning hydrogen engines have the potential to achieve SULEV II emissions levels without the need for any exhaust after treatment.

16.5 CONCLUSIONS

Hydrogen is a promising fuel for ICEs. However, its physical and chemical properties pose significant challenges for the design of hydrogen engines and vehicles. In particular, low density (low storage and power density), low ignition energy (combustion anomalies), low quenching distance and high flame temperature (high efficiency losses for heat transfer to the cylinder walls), significantly affect hydrogen vehicles in terms of performance, range and safety. Nonetheless, the chemical structure of hydrogen and its wide flammability range allow efficient and clean combustion, since high compression ratio and ultralean mixtures can be used, the latter also reducing the only significant pollutant produced (NO_X) during the combustion of hydrogen.

Because of its properties, hydrogen is mostly used in spark-ignited engines. Compared to conventional gasoline spark-ignition engines, hydrogen engines are affected by the loss of volumetric efficiency. Even though hydrogen has a higher heating value than gasoline, PFI hydrogen engines are theoretically doomed to deliver 17% lower power density than gasoline engines. Nevertheless, by combining lean-burn (low load) and stoichiometric (high load) strategies, peak indicated efficiency of 42% could be reached together with a peak IMEP of 10.3 bar. State of the art (PFI) technology has already been implemented in several demonstration vehicle prototypes that can be classified in converted (e.g. Quantum Hydrogen Prius, 130 km maximum range and NO_X emissions meeting the SULEV II limits) and dedicated (e.g. BMW Hydrogen 720 km range and NO_X emissions well below the SULEV II limits) vehicles.

Cryogenic PFI can be considered as one of the advanced hydrogen engine technologies. It has the potential to increase the power density (even higher

than in conventional gasoline engines) through the injection of hydrogen at cryogenic temperatures, thus reducing the temperature of the intake air and increasing the volumetric efficiency. Cryogenic PFI has demonstrated to be able to provide higher peak torque (12.8 bar IMEP) and to expand the 42% indicated efficiency to a broader range of operating conditions compared to standard PFI.

DI is another advanced hydrogen engine technology that aims at injecting hydrogen directly into the cylinder at elevated pressures (typically around 100 bar), after the intake valves close. DI increases the power density of hydrogen engines to levels potentially higher than in conventional gasoline engines. Furthermore, it provides high flexibility for optimizing the mixture formation process, which significantly affects combustion. Today, the new generation of piezo-actuated injectors allows providing high injection pressure (up to 250 bar), large fuel flow rate, fast response, remarkable repeatability, and precise control of the needle lift. The later also allows reducing the needle seating impact and bouncing, thus improving the durability with respect to the previous generations of solenoid-actuated injectors. The large flow rate delivered through a piezo injector can help performing late injection, which leads to a benefit in terms of ITE. In addition, advanced research in injector geometries and mixture formation concepts can help realizing ideal mixture stratification, consisting of the stratification of hydrogen around the spark plug and far from the cylinder walls.

With a dedicated injector nozzle and an optimized DI strategy, adjusting the injection timing on the basis of engine speed and load, a single-cylinder research DI hydrogen engine delivered 45.5% peak BTE (almost 48% ITE) and a BTE higher than the peak value for gasoline engines over 80% of the tested operating range, from 1000 to 3000 rpm and from 1.7 to 14.3 bar BMEP. Compared to cryogenic PFI, the range of tested engine speed is narrower but the DI engine shows a higher peak load (14.9 bar IMEP). Furthermore, most of the operating conditions were turbocharged with a relative AFR λ of 3.3, which provided extremely low NO_X emissions.

Current performance and emissions from hydrogen engines are already at a very good level, especially if compared to those provided by conventional spark-ignition gasoline engines. Nonetheless, this chapter also focuses on the remaining challenges and provides an estimate of future potential of hydrogen engines in terms of performance and emissions. A comprehensive analysis of the heat transfer in a hydrogen engine is mandatory because it is the largest efficiency loss for state of the art and advanced technology engines at a majority of the tested operating conditions. In the particular case of hydrogen, it has been demonstrated that the relative AFR λ plays a key role in the high heat flux measured on the cylinder walls, caused by the high temperature during combustion. Generally, lean hydrogen/air mixtures produce low heat transfer to the walls, and thus lower efficiency loss.

The analysis of the efficiency losses can be expanded in case of the DI strategy, since through the injection strategy it is also possible to simultaneously reduce more than one contribution to the total efficiency loss. Future research on DI hydrogen engines should aim at performing late injection and pursuing the concept of ideal stratification. As a result, the efficiency losses due to compression work, real combustion, and heat transfer to the wall can be reduced.

The vehicle simulation tool Autonomie was used in order to provide an estimate of performance and emissions delivered by an advanced DI engine when applied to a real light-duty vehicle. Results show that with a 3.0-l engine it is possible to achieve a combined fuel economy of 38.9 mpg and NO_X emissions of 0.017 g/mi (below the SULEV II limit). If the engine is downsized to 2.0 l, the vehicle fuel economy increases to 45.4 mpg. NO_X emissions increases as well, 0.028 g/mi, just above the SULEV II limit but well below the target set by the US DOE (Tier II Bin 5, 0.07 g/mi).

Even though the vehicle results are only predictions based on vehicle simulations, fuel economy and NO_X emissions estimates demonstrate the enormous potential of hydrogen as a fuel for ICEs especially since it was estimated that the SULEV II limits can be met without the need for any aftertreatment device.

Acknowledgments

Parts of the submitted manuscript have been created by UChicago Argonne, LLC, Operator of Argonne National Laboratory (''Argonne''). Argonne, a US Department of Energy Office of Science laboratory, is operated under Contract No. DE-AC02-06CH11357. The US Government retains for itself, and others acting on its behalf, a paid-up nonexclusive, irrevocable worldwide license in said article to reproduce, prepare derivative works, distribute copies to the public, and perform publicly and display publicly, by or on behalf of the Government.

Research referenced in this manuscript was partially funded by DOE's FreedomCAR and Vehicle Technologies Program, Office of Energy Efficiency and Renewable Energy. R. Scarcelli, N. Matthias and T. Wallner wish to thank Gurpreet Singh and Lee Slezak, program managers at DOE, for their support.

References

1. *U.S. Department of Energy office of Energy Efficiency and Renewable Energy. "FreedomCAR and Fuel Partnership Plan".* <http://www1.eere.energy.gov/vehiclesandfuels/pdfs/program/fc_fuel_partnership_plan.pdf>, (accessed 5 April 2011).
2. Abbott, D. Keeping the Energy Debate Clean: How Do We Supply the World's Energy Needs? *Proc. IEEE* **2010,** *98* (1), 42–66.

3. Bradley, D.; Hicks, R. A.; Lawes, M.; Sheppard, C. G. W.; Woolley, R. The Measurement of Laminar Burning Velocities and Markstein Numbers for Iso-Octane–Air and Iso-Octane–n-Heptane–Air Mixtures at Elevated Temperatures and Pressures in an Explosion Bomb. *Combust. Flame* **1998,** *115,* 126–144.
4. Gu, X. J.; Haq, M. Z.; Lawes, M.; Woolley, R. Laminar Burning Velocity and Markstein Lengths of Methane–Air Mixtures. *Combust. Flame* **2000,** *121,* 41–58.
5. Verhelst, S. A Study of the Combustion in Hydrogen-Fuelled Internal Combustion Engines. Ph.D. Thesis, Ghent University, 2005. <http://hdl.handle.net/1854/3378>.
6. Knop, V.; Benkenida, A.; Jay, S.; Colin, O. Modelling of Combustion and Nitrogen Oxide Formation in Hydrogen-Fuelled Internal Combustion Engines within a 3D CFD Code. *Int. J. Hydrogen Energy* **2008,** *33,* 5083–5097.
7. Heywood, J. B. *Internal Combustion Engine Fundamentals;* McGraw-Hill, 1988.
8. Verhelst, S; Sierens, R; Verstraeten, S. *A Critical Review of Experimental Research on Hydrogen Fueled SI Engines*. SAE Paper No. 2006-01-0430, 2006.
9. Rottengruber, H.; Wiebicke, U.; Woschni, G.; Zeilinger, K. Wasserstoff-Dieselmotor mit Direkteinspritzung, hoher Leistungsdichte und geringer Abgasemission. Teil 3: Versuche und Berechnungen am Motor. *MTZ (Motortechnische Zeitschrift)* **1999,** *61*.
10. Wallner, T; Nande, A; Naber, J. *Evaluation of Injector Location and Nozzle Design in a Direct-Injection Hydrogen Research Engine*. SAE Paper No. 2008-01-1785, 2008.
11. Tang, X; Stockhausen, W. F; Kabat, D. M; Natkin, R. J; Heffel, J. W. *Ford P2000 Hydrogen Engine Dynamometer Development*. SAE Paper No. 2002-01-0242.
12. Eichlseder, H.; Wallner, T.; Freymann, R.; Ringler, J. *The Potential of Hydrogen Internal Combustion Engines in a Future Mobility Scenario*. SAE Paper No. 2003-01-2267.
13. Enke, W.; Gruber, M.; Hecht, L.; Staar, B. Der Bivalente V12-Motor Des BMW Hydrogen 7. *MTZ* **June 2007,** *68* (6), 446–453.
14. Rottengruber, H.; Berckmüller, M.; Elsässer, G.; Brehm, N.; Schwarz, C. *Operation Strategies for Hydrogen Engines with High Power Density and High Efficiency;* 15th Annual U.S. Hydrogen Conference: Los Angeles, California, 2004.
15. Verhelst, S.; Maesschalck, P.; Rombaut, N.; Sierens, R. Efficiency Comparison between Hydrogen and Gasoline, on a Bi-fuel Hydrogen/Gasoline Engine. *Int. J. Hydrogen Energy* **2009,** *34* (5), 2504–2510.
16. Verhelst, S.; Wallner, T.; Eichlseder, H.; Naganuma, K.; Gerbig, F.; Boyer, B.; Tanno, S. Electricity Powering Combustion: Hydrogen Engines. *Proc. IEEE* **2012,** *100* (2).
17. Liu, X.-H.; Liu, F.-S.; Zhou, L.; Sun, B.-G.; Schock, H. J. Backfire Prediction in a Manifold Injection Hydrogen Internal Combustion Engine. *Int. J. Hydrogen Energy* **2008,** *33* (14), 3847–3855.
18. Abele, A. Quantum Hydrogen Prius. In *ARB ZEV Technology Symposium*, Sacramento, California, 2006.
19. Verhelst, S.; Wallner, T. Hydrogen-Fueled Internal Combustion Engines. *Prog. Energy Combust. Sci.* **2009,** *35* (6), 490–527.
20. Wallner, T.; Lohse-Busch, H.; Gurski, S.; Duoba, M.; Thiel, W.; Martin, D.; Korn, T. Fuel Economy and Emissions Evaluation of a BMW Hydrogen 7 Mono-Fuel Demonstration Vehicle. *Int. J. Hydrogen Energy* **2008,** *33* (24), 7607–7618.
21. Heller, K; Ellgas, S. *Optimization of Hydrogen Internal Combustion Engine with Cryogenic Mixture Formation. Presented at the 1st Int Symp on Hydrogen Internal Combustion Engines*, Graz, Austria, September 28–29, 2006; pp 49–58.
22. Yamane, K.; Nogami, M.; Umemura, Y.; Oikawa, M.; Sato, Y.; Goto, Y. Development of High Pressure H_2 Gas Injectors, Capable of Injection at Large Injection Rate and High Response Using a Common-Rail Type Actuating System for a 4-Cylinder, 4.7-Liter Total Displacement, Spark Ignition Hydrogen Engine SAE Paper 2011-01-2005, 2011.
23. Mumford, D.; Welch, A.; Bartunek, B. Development of H_2 Direct Injection Technology for High Efficiency/High BMEP Engines, 1st International Symposium on Hydrogen Internal Combustion Engines, Graz, Austria, September 28–29, 2006.
24. Welch, A.; Mumford, D.; Munshi, S.; Holbery, J.; Boyer, B.; Younkins, M.; Jung, H. *Challenges in Developing Hydrogen Direct Injection Technology for Internal Combustion Engines*. SAE Paper 2008-01-2379.
25. Steinrueck, P.; Ranegger, G. *Timed Injection of Hydrogen for Fuel Cells and Internal Combustion Engines, 1st International Symposium on Hydrogen Internal Combustion Engines*, Graz, Austria, September 28–29, 2006.
26. Scarcelli, R.; Wallner, T.; Salazar, V. M.; Kaiser, S. A. CFD and Optical Investigations of Fluid Dynamics and Mixture Formation in a DI-H_2ICE, ICEF2010-35084, ASME 2010 Internal Combustion Engines Division Fall Technical Conference (ICEF), San Antonio, TX, USA, September 12–15, 2010.
27. Scarcelli, R.; Wallner, T.; Matthias, N.; Salazar, V.; Kaiser, S. Mixture Formation in Direct Injection Hydrogen Engines: CFD and Optical Analysis of Single- and Multi-Hole Nozzles. *SAE Int. J. Engines* **August 2011,** *4* (2), 2361–2375.
28. Tritton, D. J. *Physical Fluid Dynamics, Section 22.7, "The Coanda Effect";* Van Nostrand Reinhold, 1977 (reprinted 1980).
29. Heindl, R.; Eichlseder, H.; Spuller, C.; Gerbig, F.; Heller, K. *New and Innovative Combustion Systems for H_2-ICE: Compression Ignition and Combined Processes*. SAE Paper 2009-01-1421.
30. Tanno, S.; Ito, Y.; Michikawauchi, R.; Nakamura, M.; Tomita, H. *High-Efficiency and Low-NO_x Hydrogen Combustion by High Pressure Direct Injection*. SAE Paper 2010-01-2173.
31. Matthias, N. S.; Wallner, T.; Scarcelli, R. *A Hydrogen Direct Injection Engine Concept that Exceeds U.S. DOE Light-Duty Efficiency Targets*. SAE Paper 2012-01-0653.
32. Wimmer, A.; Wallner, T.; Ringler, J.; Gerbig, F. *H_2-Direct Injection: a Highly Promising Combustion Concept*. SAE Paper 2005-01-0108.
33. Eichlseder, H.; Grabner, G.; Gerbig, F.; Heller, K. *Advanced Combustion Concepts and Development Methods for Hydrogen IC Engines;* FISITA 2008 World Automotive Congress: Munich, Germany, 2008.
34. Michl, J.; Schenk, M.; Rottengruber, H.; Huhn, W. *Thermal Boundary Conditions in a Stoichiometric Operating Hydrogen Engine;* FISITA 2008 World Automotive Congress: Munich, Germany, 2008.
35. Shudo, T.; Nabetani, S. *Analysis of Degree of Constant Volume and Cooling Loss in a Hydrogen Fuelled SI Engine*. SAE Paper 2001-01-3561.
36. Shudo, T. Improving Thermal Efficiency by Reducing Cooling Losses in Hydrogen Combustion Engines. *Int. J. Hydrogen Energy* **2007,** *32* (17), 4285–4293.
37. Shudo, T.; Nakajima, Y.; Futakuchi, T. Thermal Efficiency Analysis in a Hydrogen Premixed Combustion Engine. *JSAE Review* **2000,** *21* (2), 177–182.
38. Wei, S. A Study on Transient Heat Transfer Coefficient of In-Cylinder Gas in the Hydrogen Fueled Engine. In *KHES and HESS, the 6th Korea–Japan Joint Symposium on Hydrogen Energy,* 2001.
39. Demuynck, J.; De Paepe, M.; Huisseune, H.; Vancoillie, J.; Sierens, R.; Verhelst, S. Investigation of the Influence of Engine Settings on the Heat Flux in a Hydrogen – and Methane-Fuelled Spark Ignition Engine. *Appl. Therm. Eng.* **2011,** *31,* 1220–1228.

40. Demuynck, J.; De Paepe, M.; Huisseune, H.; Sierens, R.; Vancoillie, J.; Verhelst, S. On the Applicability of Empirical Heat Transfer Models for Hydrogen Combustion engines. *Int. J. Hydrogen Energy* **2011,** *36* (1), 975–984.
41. Shudo, T.; Suzuki, H. Applicability of Heat Transfer Equations to Hydrogen Combustion. *JSAE Review* **2002,** *23* (3), 303–308.
42. Pischinger, R.; Klell, M.; Sams, T. *Thermodynamik der Verbrennungskraftmaschine;* Springer Verlag, 2002.
43. Rousseau, A; Wallner, T.; Pagerit, S.; Lohse-Busch, H. *Prospects on Fuel Economy Improvements for Hydrogen Powered Vehicles*. SAE Paper 2008-01-2378.
44. Wallner, T.; Matthias, N. S.; Scarcelli, R.; Kwon, J. C. Evaluation of Efficiency and Drive Cycle Emissions for a Hydrogen Direct Injection Engine. In *Proceedings of the IMechE Part D Journal of Automobile Engineering, Special Issue on Vehicle Fuel Economy: High Efficiency Engines and Hybrid Powertrains*, 2012.
45. *DieselNet. "Emissions Standards: USA: Cars and Light-Duty Trucks – Tier 2".* <http://www.dieselnet.com/standards/us/ld_t2.php>, (accessed 5 April 2011).
46. *U.S. Department of Energy office of Energy Efficiency and Renewable Energy. Vehicle Technologies Program Multi-Year Program Plan 2011–2015.* <http://www1.eere.energy.gov/vehiclesandfuels/pdfs/program/vt_mypp_2011-2015.pdf>, (accessed 5 April 2011).

CHAPTER

17

Computational Fluid Dynamics as a Tool for Designing Hydrogen Energy Technologies

Irantzu Uriz, Gurutze Arzamendi, Pedro M. Diéguez, Luis M. Gandía

Escuela Técnica Superior de Ingenieros Industriales y de Telecomunicación, Universidad Pública de Navarra, Campus de Arrosadía, E-31006 Pamplona, Spain

OUTLINE

17.1 Introduction 401

17.2 CFD Basics 402
- *17.2.1 Problem and Physical Model Definition* 402
- *17.2.2 Mathematical Modeling* 402
- *17.2.3 Computational Domains and Initial and Boundary Condition Definition* 405
- *17.2.4 Discretization and Numerical Solution* 405
  - 17.2.4.1 Discretization 405
  - 17.2.4.2 Numerical Solution. Finite Volume Method 407
- *17.2.5 Results Interpretation* 409

17.3 CFD for Designing Hydrogen Production Technologies 410
- *17.3.1 Reforming of Gaseous Fuels* 411
  - 17.3.1.1 Fixed-Bed Reactors 411
  - 17.3.1.2 Fluidized-Bed Reactors 414
  - 17.3.1.3 Catalytic Wall Microreactors 416
- *17.3.2 Conversion of Solid or Liquid Fuels* 423
  - 17.3.2.1 Gasification and Pyrolysis 424
  - 17.3.2.2 Anaerobic Fermentation 425
- *17.3.3 Water Electrolysis* 425

17.4 CFD for Investigating Hydrogen Energy End-Use Applications 426
- *17.4.1 Fuel Cells* 426
  - 17.4.1.1 Proton-Exchange Membrane Fuel Cells 426
  - 17.4.1.2 Solid Oxide Fuel Cells 427
- *17.4.2 H_2-Fueled Internal Combustion Engines (H_2-ICEs)* 429

17.5 Conclusions 431

Acknowledgments 431

References 431

17.1 INTRODUCTION

Computational fluid dynamics (CFD) is a computer simulation tool that allows modeling the dynamics of fluids, that is, a numerical tool for predicting the pressure and velocity fields, and the temperature and concentration profiles on physical systems that may include chemical transformations.[1,2] At present, CFD is a highly developed discipline from the academic and practical points of view. Excellent monographs and reviews have been published on the subject.[2–16]

The first CFD computer codes were developed in the 1960s but their capacities were greatly limited by the poor power of the computers available at that time. The first commercial software appeared in the 1980s, and since then, there has been a rapid development parallel to the exponential increase of the calculation capacity of modern computers. The aerospace, nuclear energy, and automotive industries were the first in using these tools and still continue making large benefits from their simulation capacities. Currently, CFD can be considered as a tool of general interest for the most diverse fields: biomechanics and biomedical engineering, conventional

http://dx.doi.org/10.1016/B978-0-444-56352-1.00017-9

energy production and renewables, environmental and civil engineering, architecture, meteorology, oceanography, etc.

As for the chemical processes, it is becoming increasingly frequent the application of CFD to process equipment analysis and design, particularly for scaling-up purposes because it allows simulating the behavior of the systems under operating conditions that are difficult to reproduce on a pilot scale.[1,17] Thus, CFD is starting to be employed for the analysis and design of chemical reactors (fixed, fluidized, and transported catalytic beds; bubble columns; and microchannel reactors and microreactors), stirred tanks, cyclones, drying systems, combustion chambers, solids handling systems, heat exchangers, and pipe networks, among other applications. A very comprehensive review on CFD models for the analysis and design of chemical reactors has been performed by Fox.[18]

In this chapter, an updated overview of the possibilities of commercial CFD codes for the analysis and design of technologies relevant to the hydrogen energy field is provided. These technologies are grouped into two broad categories according to their interest for hydrogen production or for energetic or other hydrogen applications. Previously, a section is devoted to the fundamentals of CFD. The active field of CFD application for risks analysis associated with hydrogen distribution, storage, and use is presented in the last chapter of this book.

17.2 CFD BASICS

The study of a physical system through CFD simulations is a process involving the following stages[2]:

- Problem and physical model (geometry) definition
- Mathematical modeling
- Computational domains and initial and boundary conditions definition
- Discretization
- Numerical solution
- Analysis and interpretation of the results

These stages are frequently grouped as *preprocessing* (geometry definition, mathematical modeling, initial and boundary conditions definition, and discretization), *solver* (numerical solution), and *postprocessing* (result analysis and interpretation). This classification makes reference to the structure of the most common CFD software packages. In the next subsections, we will describe briefly the basic features of the simulation stages.

17.2.1 Problem and Physical Model Definition

CFD is not very different from other more conventional computer simulation tools in that much of the computational effort necessary and the final success depends on a careful and rigorous definition of the problem. This implies starting by establishing the precision with which it is necessary to know the solution, setting the simplifications and assumptions that can be made, and determining the temporal and spatial scales of the phenomena involved in the system under study. It will be also necessary to take into account the main model features (e.g. steady state/transient model, turbulence model, compressible or incompressible flow, multiphase flow, porous media, heat transfer characteristics, chemical kinetics).

The physical model, that is, the system geometry, has to be defined also at this stage of the simulation model development. The commercial CFD software packages include especially dedicated tools for the creation (drafting) of the system to be simulated. At present, these tools are normally compatible with most of the computer-aided design software that are routinely used by engineers, so it is relatively easy to incorporate a previously designed system/device into a CFD code. This feature is essential for an easier introduction of CFD in the industrial practice. When creating the geometry it is important to reach a satisfactory compromise between the level of detail and the basic description of the main defining characteristics of the system in order to guarantee obtaining a sufficiently accurate solution with a reasonable computational effort. It will be important to consider at this point if a three-dimensional (3D) model is necessary or if a simpler two-dimensional (2D) one could be enough. In this regard, the analysis of the possible system symmetries and periodicities will help in the suitable definition of the physical model.

17.2.2 Mathematical Modeling

The basic equations of any CFD model are the balances of momentum and total mass, which determine the velocity, pressure, and density fields in a physical system. Depending on the problem characteristics these balances are complemented with energy balances and balances of individual species if changes of composition are produced. Additional equations are needed to describe phenomena such as turbulence or multiphase flow.

The extensive properties (mass, energy, momentum) are subjected to conservation laws, so that it is possible to apply balances on them in order to understand the changes undergone by a physical system. The so-called transport equations can be derived from the property balances and consist of differential equations describing the spatial and temporal distribution of intensive quantities instead of the extensive ones.[19] These quantities may be referred to the mass (molar or mass fractions, specific energy) or the volume (density and molar concentration), so they are property concentrations,

a transport magnitude that in the most general case we will denote in this chapter by Φ. Under these conditions we can write the general transport equation as follows:

$$\frac{\partial \Phi}{\partial t} = -\mathrm{div}(\vec{v}\cdot\Phi) - \mathrm{div}\vec{J_\Phi} + S_\Phi \qquad (17.1)$$

where t is time and $\frac{\partial \Phi}{\partial t}$ the rate of increase of the transport magnitude; $\vec{v}$ is the velocity and the term $-\mathrm{div}(\vec{v}\cdot\Phi)$ represents the net rate of property concentration entry by convection; $\vec{J_\Phi}$ is the flux of property due to molecular transport and $-\mathrm{div}\vec{J_\Phi}$ is the net rate of property concentration entry associated with that transport mechanism. Finally, S_Φ is a *source* term (net rate of property generation) that in the case of momentum transport corresponds to external forces, for the transport of energy to the exchange between forms of energy and for the transport of mass to the consumption or formation of species due to chemical reactions.

The total mass conservation is expressed by the continuity equation in which the transport magnitude is the density, ρ:

$$\frac{\partial \rho}{\partial t} = -\mathrm{div}(\vec{v}\cdot\rho) \qquad (17.2)$$

On the other hand, the equation of motion is the principle of the conservation of momentum, which is a balance of forces in which the transport magnitude is the momentum per unit volume, $\rho\vec{v}$:

$$\frac{\partial \rho\vec{v}}{\partial t} = -\mathrm{div}(\rho\vec{v}\cdot\vec{v}) - \mathrm{div}\,\tau - \mathrm{grad}\,p + \rho\vec{g} \qquad (17.3)$$

This is a key equation in CFD because the ultimate purpose is very often describing the fluid dynamics. τ is the shear stress tensor and grad p is the gradient of pressure, which may be considered as a source term (as expressed in Eqn (17.3)) or being treated as a stress, in which case it is included in τ. The combined terms $-\mathrm{div}\ \tau - \mathrm{grad}\ p$ in Eqn (17.3) represent the net rate of momentum increase per unit volume due to molecular transport. Finally, the action of gravity forces appears as a source term $(\rho\vec{g})$. Solving this equation is particularly complex for two main reasons: The first one is the nonlinear structure of the convective term $(-\mathrm{div}(\rho\vec{v}\cdot\vec{v}))$. Indeed, while for the mass or thermal energy transport the velocity can be treated as a parameter, in the equation of motion it is the unknown. The second reason lies in the term grad p because there is no transport equation for pressure. For compressible flow, the use of an equation of state allows calculating the pressure from the density field derived from the continuity equation. For incompressible flow, the density is constant and the pressure cannot be calculated in such a way, as explained in Section 17.2.4.2.

A case of particular interest is the flow of Newtonian fluids with constant density and viscosity (μ), for which Eqns (17.2) and (17.3) adopt the following expressions:

$$\mathrm{div}\,\vec{v} = 0 \qquad (17.4)$$

$$\rho\frac{\partial \vec{v}}{\partial t} = -\rho\vec{v}\cdot\mathrm{grad}\ \vec{v} + \mu\cdot\nabla^2\vec{v} - \mathrm{grad}\,p + \rho\vec{g} \qquad (17.5)$$

Equations (17.4) and (17.5) are the so-called Navier–Stokes equations, whose validity is limited to the conditions indicated although they provide a reasonable first approach in many cases.

The continuity equation arises from a total mass balance. For multicomponent systems it is necessary to determine the concentration of the different chemical species involved so, apart from the continuity equation, a number of concentration equations has to be written:

$$\frac{\partial c_j}{\partial t} = -\mathrm{div}\left(c_j\cdot\vec{v}\right) + \mathrm{div}\left(D_j\cdot\mathrm{grad}\ c_j\right) + S_{c_j} \qquad (17.6)$$

c_j is the concentration of species j ($j = 1, 2, \ldots, n-1$; n being the total number of components) and D_j its molecular diffusion coefficient. S_{c_j} is the source term associated with the chemical reactions, it is given by chemical kinetics. This term normally includes nonlinear expressions dependent on the temperature and concentration of the rest of species, which greatly complicates the resolution.

As regards the energy equation, the transport equation for the specific internal energy (u) is included in the CFD models to calculate the temperature fields. Internal energy includes the kinetic energy of atoms and molecules, the potential energy of atomic interactions, the energy associated with chemical bonds, and the nuclear energy. This equation can be expressed as follows:

$$\begin{aligned}\frac{\partial \rho u}{\partial t} = &-\mathrm{div}(\rho u\cdot\vec{v}) - \mathrm{div}\,\vec{q} \\ &-(\tau:\mathrm{grad}\ \vec{v}) - p(\mathrm{div}\,\vec{v}) + S_u\end{aligned} \qquad (17.7)$$

where $-\mathrm{div}(\rho u\cdot\vec{v})$ is the net rate of internal energy increase per unit volume by convection, $\vec{q}$ is the flux of energy due to molecular transport (conduction), $-(\tau:\mathrm{grad}\ \vec{v})$ represents the net increase of energy by viscous dissipation, $-p(\mathrm{div}\,\vec{v})$ the increase by compression, and S_u is the source term. An interesting case is when the source comes only from the enthalpy change associated with a chemical reaction (S_{hr}); if it is also possible to neglect the viscous dissipation and heat transfer by radiation, the temperature equation can be written as follows:

$$\frac{\partial \rho c_p T}{\partial t} = -\vec{v}\cdot\mathrm{grad}\left(\rho c_p T\right) - \mathrm{div}\left(\lambda\cdot\mathrm{grad}\left(\rho c_p T\right)\right) + S_{hr} \qquad (17.8)$$

where c_p is the specific heat and λ the thermal conductivity.

CFD calculations present special complications and require additional models to describe the transport of properties when the flow regime is turbulent. The characteristic fluctuations of the properties values require an extremely fine description of the computational domains as well as applying very short time intervals, resulting in very time consuming simulations. Van den Akker has reviewed the simulation capabilities of CFD for studying phenomena such as mixing under turbulent conditions.[20] The approaches most frequently used for turbulent flow modeling available in commercial CFD codes are

- Reynolds-averaged Navier–Stokes (RANS)
- Large-eddy simulations (LES)

The RANS model is based on averages of all the transport properties that allow using relatively coarse meshes for the computational domains thus increasing the computation speed. This method has allowed commercial CFD software to become a reliable tool for simulating turbulent flows.[20] RANS simulations usually use some k–ε turbulence model with the aim of obtaining information on the average flow field. These models include the concept of eddy viscosity (μ_t) according to Eqn (17.9), where k is the turbulent kinetic energy and ε the velocity at which this energy is dissipated.

$$\mu_t = 0.09 \cdot \rho \cdot \frac{k^2}{\varepsilon} \tag{17.9}$$

The LES model provides a much more precise description of turbulence compared with the RANS one but it requires powerful computing capacities incorporating parallelization. This model accepts that the flow is not fully resolved because the turbulent eddies smaller than the grid spacing of the computational domain are not solved explicitly although they contribute to the redistribution of momentum.[20] All eddies larger than the grid size are resolved explicitly; therefore, using very fine grids is required to take full advantage of this concept.

Another issue of considerable practical interest is the modeling of multiphase systems that are characterized by the presence of interfaces across which the extensive properties are transported. The best approach to address this problem depends on the structure of the system, that is, if it can be considered dispersed as in the cases of solid or fluid particles (droplets or bubbles) of a small size compared with the whole system. The particles form the dispersed phase while the other is called the continuous phase. These systems are modeled considering that the properties in both phases are distributed in a continuous manner while for each particle mean values of the transport properties are considered.

A very important parameter for dispersed systems is the volume fraction of each phase. In some cases (e.g. dragged particles which do not alter the velocity field of the continuous phase), these fractions can be managed as if they were concentrations. Obviously, the particle size distribution is also essential because it affects, for example, the buoyancy forces and the rate of transport across the interface. The simplest case is a monodisperse system, but if it is polydisperse, there is a size distribution and the particle size becomes another additional independent variable that significantly complicates the situation, making necessary the resolution of population balances. This happens when the size varies during the process (nucleation, precipitation, flocculation, boiling, etc.).

Sometimes it is not possible to identify a dispersed phase because the extension of all the phases is large; these are the so-called discontinuous multiphase systems. These situations are modeled by treating each phase as a continuum, using the interface as a boundary condition. As at the interface the properties cannot be accumulated, the condition used is that the flux of property on each side must be the same.

The computational methods most frequently used for the description of multiphase systems are the following:

- Euler–Euler. Transport equations for each phase are written as if they were continuous and fully interpenetrating media. Weight factors are applied to take into account the volume fraction of each phase and the source terms include the interactions between the phases. Conservation equations for each phase are derived to obtain a set of equations, which have a similar structure for all phases. This method is applicable for a wide range of volume fractions and turbulence is easily incorporated. Applications of this approach include the simulations of stratified flows and free-surface flows, particle-laden flows with low loading, bubbly flows, sedimentation, cyclone separators, bubble columns, risers, particle suspensions, and fluidized beds.
- Euler–Lagrange. The fluid phase is treated as a continuum while the dispersed phase is solved by tracking a large number of particles, bubbles, or droplets through the calculated flow field. The dispersed phase can exchange momentum, mass, and energy with the fluid phase and it is modeled defining a number of regions that are distributed to match the corresponding volume fraction. The path and velocity of each region are individually set by ordinary differential equations. A collision model is included to handle the energy dissipation caused by nonideal interactions. As each computational grid cell cannot contain more than one of the defined regions, this method is often used when the volume of the

dispersed phase is very small. This makes the approach suitable for the modeling of dusty gases, spray dryers, combustion of fuel sprays such as liquid fuel or powdered solid (coal, biomass, etc.), and some particle-laden flows, but inappropriate for the modeling of any application where the volume fraction of the dispersed phase cannot be neglected.

Modern commercial CFD codes incorporate a variety of tools to complete the mathematical models such as vapor–liquid equilibrium data, flow through filtering media, radiation heat transfer, kinetic models for the combustion of several fuels.

17.2.3 Computational Domains and Initial and Boundary Condition Definition

After creating the system geometry and the mathematical model, it is necessary to establish the physical domains and determine the initial (for time) and boundary (for space) conditions. As regards the computational domains, it is obviously essential to distinguish between the fluid and solid regions as well as to assign the correct materials nature and composition. Commercial CFD software includes materials libraries that allow selecting the components (fluid, solid, or mixture) as well as selecting the equations to evaluate its thermophysical properties. New materials and their properties can be also incorporated by the user if needed.

As for the initial conditions it is necessary to provide values of the transport properties (Φ) at a given time, usually the initial time ($t = 0$). As concerns the boundary conditions, it is necessary to set at least two of them and may consist of the value of Φ (Dirichlet condition) or one of its derivatives with respect to the spatial coordinates (Newman condition) or a combination of the above (Cauchy condition) in the system boundaries. Some of the most commonly used boundary conditions in CFD are

- Inlet and outlet. The entry conditions are assumed to be known so the values of all the transport properties at the inlet boundary are usually provided. As concerns the outlet, it is common practice to set the value of mass flow rate to ensure the conservation of mass. As it is usually difficult to establish velocity values, another option is to set the value of the pressure at the outlet. Inlet and outlet conditions are essential to establish flow directionality.
- Wall. Most of the physical systems of interest are limited, at least in part, by solid walls that can be static or mobile. A wall is a boundary that does not allow mass transfer whereas may or may not be allowed. Regarding the velocity, under nonslip flow conditions the fluid velocity tangential to the wall is that of the wall, and therefore zero if the wall is static. In the case of slip flow, the gradient of the tangential component of the fluid velocity in the direction perpendicular to the wall is zero. The slip or nonslip character of the flow can be evaluated through the Knudsen number (Kn):

$$Kn = \frac{\lambda_{\mathrm{mfp}}}{l} \tag{17.10}$$

where λ_{mfp} is the mean molecular free path and l the characteristic dimension of the system. If Kn is <0.001 the fluid is considered as a continuous medium. For values of Kn between 0.001 and 0.1 slip flow is considered. Values between 0.1 and 10 correspond to the transition regime. Above 10, free molecular flow in which the interactions (collisions) of the molecules with the walls dominate is considered.[21] For a simple gas, the mean molecular free path can be calculated in the framework of the kinetic theory as follows[22]:

$$\lambda_{\mathrm{mfp}} = \frac{\kappa \cdot T}{\sqrt{2} \cdot \pi \cdot d_{\mathrm{m}}^2 \cdot p} \tag{17.11}$$

where d_{m} is the molecular diameter and κ the Boltzmann constant. From these equations it follows that the slip flow is favored, besides decreasing the characteristic dimension, by increasing temperatures and decreasing molecular size and pressure.

For the heat flow, the wall can be considered adiabatic, that is, a temperature gradient of zero in the direction perpendicular to the wall, or it can set a constant value at the wall.

- Symmetry. Sometimes, physical systems studied show symmetry, which is very useful for reducing the size of the physical model and computational domains thus saving computational power. Obviously, the symmetry must be not only geometric, it should affect all the transport properties.

17.2.4 Discretization and Numerical Solution

17.2.4.1 Discretization

Due to the complexity and coupled character of the partial differential equations included in the mathematical model, they must be solved numerically through iterative methods for the cases of practical interest. This involves replacing differential equations in partial derivatives over space and time on a continuous basis by a system of algebraic equations that provide solutions for the transport properties only at certain discrete points. The algebraic equations are the so-called discretized equations.

Time is discretized in a simple way adopting ranges whose value must respond to a compromise between the stability and reliability of the results and the corresponding computational effort. The discretization of space offers many more possibilities. The two methods

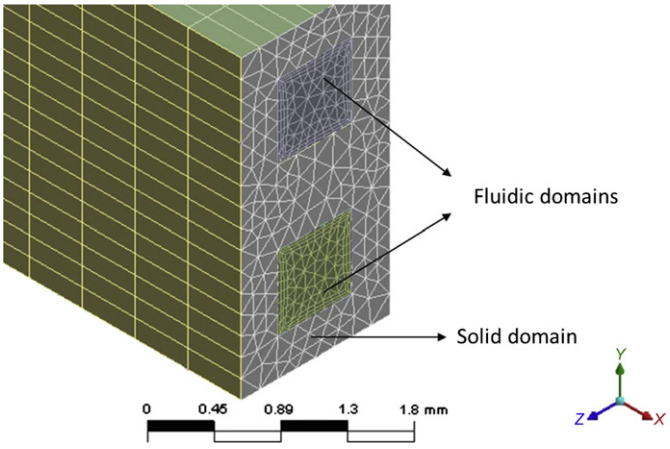

FIGURE 17.1 Meshes of three computational domains corresponding to a solid block with two square parallel microchannels of a 0.7-mm side. (For color version of this figure, the reader is referred to the online version of this book.)

most frequently used in CFD, the finite volume and the finite element methods, require the subdivision of the space in a number of computational cells that should not overlap. The set of cells is a mesh. As an illustrative example, the meshes of three different computational domains are shown in Fig. 17.1. Two of the domains are fluidic and consist of parallel square microchannels with a 0.7-mm side in a solid domain. This is a simplified physical model used by our research group to simulate the performance of catalytic wall microreactors.[23–27]

It is important that the meshes meet the following requirements:

- Geometrical: cell edges should be suitably adjusted to the limits of the physical domains in order to set the boundary conditions at the correct points.
- Physical: cell density should be greater at locations with abrupt changes of the properties, for example, at the interfaces, as can be seen in Fig. 17.1 for the fluidic domains near the walls (where a thin catalyst layer is located), or, for example, in regions where the fluid regime is turbulent. By contrast, those areas with smooth variations of the properties admit coarser meshes composed of larger cells.
- Numerical: abrupt changes in cell size must be avoided as well as using cells with a very small volume-to-surface ratio (cell degeneration).

Meshing of the computational domains is a key step of any CFD simulation study. During the model resolution, the numerical algorithms will provide values of the transport properties within the cells (e.g. at their center) or at the nodes connecting them. Obviously, the higher the number of cells, the higher is the precision in the system description; however, a compromise should be reached for not to arrive at extreme situations virtually impossible to solve with a reasonable computing power.

There are two types of meshes, structured and unstructured. The first ones are regular, and the cells are entirely constituted by hexahedrons; they are easy to generate and adapt well to simple geometries without curvatures. The unstructured meshes are more flexible and can be adapted to complex geometries, with curvatures and sharp angles. They consist of combinations of hexahedrons and tetrahedral cells, and in some cases polyhedrons. The meshes shown in Fig. 17.1 are unstructured. These meshes are more difficult to create so modern commercial CFD software incorporates mesh generators that build up the meshes automatically; nevertheless, it is always necessary a careful examination of the resulting mesh to evaluate if all the requirements are fulfilled. There are also software packages that allow the user the complete creation of the mesh. Some problems require the adaptation of the mesh during the simulations. This is the case when moving parts are involved, as for example, in a stirred tank or the piston in a cylinder of an internal combustion engine. This is also the case of mobile interfaces in multiphase systems.

As a general rule, a mesh is suitable when grid independence has been achieved, that is, when the simulation result does not depend on the mesh type or cells density. Grid independence requires the generation of meshes of varying degrees of refinement, followed by the model resolution under similar or identical conditions until results independent on the mesh are achieved. This allows reaching a satisfactory solution without an excessive mesh refinement that would otherwise increase unnecessarily the computational time and costs. As an illustrative example, Fig. 17.2 shows the results obtained in CFD simulation of the methane steam reforming reaction on a catalytic wall square channel reactor with a 50-mm side and a 500-mm length. The reaction conditions were as follows: 850 °C, 1 atm, gas-hourly space velocity (GHSV) of 5000 h^{-1}, feed stream with H_2O/CH_4 molar ratio of 2. The applied reaction kinetics over a nickel-based catalyst and model details can be found in Ref. 27. Three types of meshes were considered: regular structured mesh with all the elements of the same size (Fig. 17.2(a)), nonregular (stretched) structured mesh with smaller cells, that is, higher cells density, near the channel wall (Fig. 17.2(b)), and unstructured mesh with inflation layers consisting of very small cells near the channel wall (Fig. 17.2(c)). The results shown are the steady-state mean methane conversion at the section corresponding to the channel outlet and the error in the methane conversion defined with respect to the converged value (0.31) obtained with a sufficiently high number of mesh elements. It can be seen that when the number of elements is <10,000, large errors, >10%, are produced. The error rapidly decreases as the number of cells increases and for a number >1,000,000, an almost

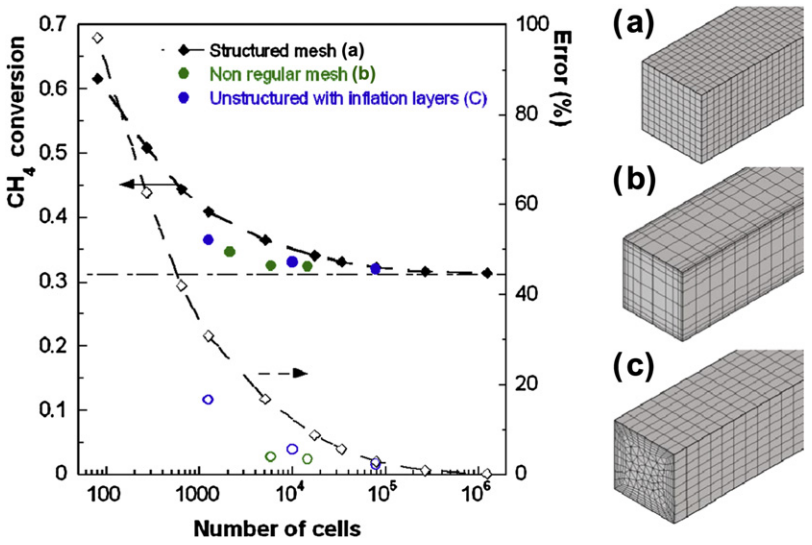

FIGURE 17.2 Mean methane steam reforming conversion at the reactor outlet and associated error for three types of meshes: regular structured (a), stretched structured (b), and unstructured with inflation layers (c). (For color version of this figure, the reader is referred to the online version of this book.)

exact solution for methane conversion is obtained; however, the computing power required significantly exceeds that of personal computers. In this example, between 10,000 and 100,000 cells offer a convenient solution depending on the mesh structure. In this regard, the structured regular mesh provokes the greatest errors. Both the structured stretched mesh and the unstructured mesh with inflation layer near the wall give similar and more satisfactory results because of their good resolution of the region close to the wall, where the reactions take place. Nevertheless, this does not mean that other regions of the fluidic domain are not important. In this case, due to the laminar nature of the flow inside the channel, a sufficiently high cells density is also required far from the walls to accurately describe the velocity profile. These 3D CFD simulations were performed using ANSYS® CFX software on a Dell Precision PWS690 workstation running MS Windows XP® × 64 with an available random-access memory of 16.0 GB.

17.2.4.2 *Numerical Solution. Finite Volume Method*

The finite volume method (FVM) is the most commonly applied in the CFD software.[2,5] It is based on considering a number of cells or control elements in which all the physical parameters and system characteristics are assumed to be constant. The balances are integrated for each element transforming the volume integrals to surface integrals through the divergence theorem that, for example, for the flow by molecular transport of the property Φ can be written as follows:

$$\iiint_V \mathrm{div}\vec{J_\Phi}\cdot \mathrm{d}V = \oiint_S \vec{J_\Phi}\cdot\vec{n}\cdot \mathrm{d}S \tag{17.12}$$

where V is the volume of the cell or the element, S is its outer surface, and $\vec{n}$ a unit vector normal to the surface. The surface integrals are solved taking into account that the physical properties are considered also constant along each cell face. The properties values are constant within each cell but change unsteadily at the cell faces. Consider for example a 2D system at steady state. The velocity field and the general coefficient of molecular transport Γ are assumed to be known. In such conditions, the general transport equation (Eqn (17.1)) for the transport of the property Φ can be written as follows:

$$0 = -v_x\frac{\partial\Phi}{\partial x} - v_y\frac{\partial\Phi}{\partial y} + \frac{\partial}{\partial x}\left(\Gamma\frac{\partial\Phi}{\partial x}\right) + \frac{\partial}{\partial y}\left(\Gamma\frac{\partial\Phi}{\partial y}\right) + S_\Phi \tag{17.13}$$

For the sake of simplicity, the mesh shown in Fig. 17.3 is considered. As the system is 2D, the integration volume V becomes a face, and the integration surface A, a line. In this mesh, the nodes are named with capital letters and the shaded cell (with the center at P) is that of interest. The points at the faces (lines) are identified by lowercase letters.

Application of the divergence theorem to Eqn (17.13) leads to

$$0 = -\int_A \vec{n}\,v_x\Phi\,\mathrm{d}A - \int_A \vec{n}\,v_y\Phi\,\mathrm{d}A + \int_A \vec{n}\left(\Gamma\frac{\partial\Phi}{\partial x}\right)\mathrm{d}A + \int_A \vec{n}\left(\Gamma\frac{\partial\Phi}{\partial y}\right)\mathrm{d}A + \int_V S_\Phi\,\mathrm{d}A \tag{17.14}$$

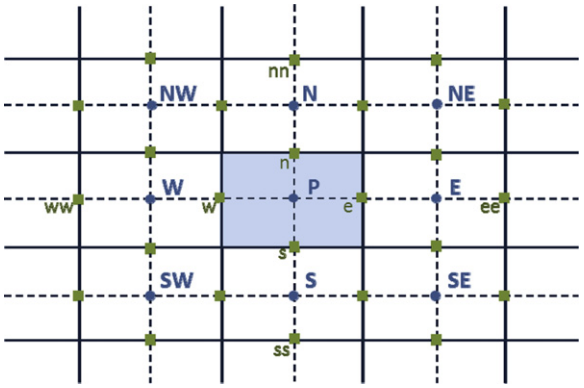

FIGURE 17.3 The 2D regular mesh showing the notation used for the development of the general transport equation. (For color version of this figure, the reader is referred to the online version of this book.) *Source: Adapted from Ref. 2.*

$$0 = -(v_x A\Phi)_e + (v_x A\Phi)_w - (v_y A\Phi)_n + (v_y A\Phi)_s + \left(\Gamma A\frac{\partial\Phi}{\partial x}\right)_e - \left(\Gamma A\frac{\partial\Phi}{\partial x}\right)_w + \left(\Gamma A\frac{\partial\Phi}{\partial y}\right)_n - \left(\Gamma A\frac{\partial\Phi}{\partial y}\right)_s + \overline{S}\cdot V \tag{17.15}$$

The derivatives are calculated based on the values of Φ at the nodes, for example:

$$\left(\Gamma A\frac{\partial\Phi}{\partial x}\right)_w = \Gamma_w\cdot A_w\cdot\left(\frac{\Phi_P-\Phi_W}{\delta x_{WP}}\right) \tag{17.16}$$

where δx_{WP} is the distance between points W and P. To express the values of Φ it is possible to follow different procedures:

- Upwind Differencing Scheme (UDS). The procedure is simple and mathematically very stable although the numerical error is relatively large; there is also some tendency to smooth the properties profiles (numerical diffusion). Some authors, as Ferziger and Perić recommend not using this first-order scheme due to its inaccuracy, especially in 3D simulations with unstructured meshes.[7] According to the UDS,

$$\Phi_w = \Phi_W \tag{17.17}$$

- Central Differencing Scheme (CDS). It is more appropriate to describe pronounced changes in the properties but the results tend to show numerical oscillations that sometimes difficult reaching convergence. This scheme shows the best performance for systems in which molecular diffusion is the governing mechanism. CDS is the simplest scheme of second-order accuracy and offers a good compromise among accuracy, simplicity, and efficiency.[7] According to the CDS,

$$\Phi_w = \frac{\delta x_{Ww}\Phi_W + \delta x_{wP}\Phi_P}{\delta x_{WP}} \tag{17.18}$$

- Quadratic Upstream Interpolation for Convective Kinetics. In this case, a parabolic function instead of a linear one is used to describe the property profiles so it is slightly more accurate than the CDS. Although this interpolation scheme has third-order truncation errors, the overall approximation is still of a second-order accuracy.[7] Numerical oscillations are not as marked as for the CDS. Due to its structure it is better suited for convective transport, so it presents limitations for systems with a strong diffusive component. According to this scheme,

$$\Phi_w = -\frac{1}{8}\cdot\Phi_{WW} + \frac{6}{8}\cdot\Phi_W + \frac{3}{8}\cdot\Phi_P \tag{17.19}$$

There are also higher order, such as the fourth-order CDS, and other interpolation and differentiation methods.[7] High-order schemes oscillate if the mesh is relatively coarse but converge more rapidly to accurate solutions than low-order schemes when the grid is suitably refined.

As for the source term, it is common practice using a linear relationship as follows:

$$\overline{S}\cdot V = S_0 + S_1\cdot\Phi \tag{17.20}$$

For transient cases, in addition to space, it is also necessary to discretize time:

$$\frac{\partial\Phi}{\partial t} = -v_x\frac{\partial\Phi}{\partial x} - v_y\frac{\partial\Phi}{\partial y} + \frac{\partial}{\partial x}\left(\Gamma\frac{\partial\Phi}{\partial x}\right) + \frac{\partial}{\partial y}\left(\Gamma\frac{\partial\Phi}{\partial y}\right) + S_\Phi \tag{17.21}$$

$$\int_V\int_t^{t+\Delta t}\frac{\partial\Phi}{\partial t}\cdot dt\cdot dV = V\cdot\left(\Phi_P^{t+\Delta t} - \Phi_P^t\right) \tag{17.22}$$

In addition, the following expression also holds:

$$\int_t^{t+\Delta t}\Phi\cdot dt = [f\cdot\Phi^{t+\Delta t} + (1-f)\cdot\Phi^t]\cdot\Delta t \tag{17.23}$$

where f is a weight factor whose value gives rise to the following methods:

- Explicit method ($f=0$). Obviously, it is very simple numerically given the linear character of the resulting equations. It is suitable for cases in which transport is dominated by convection.
- Implicit method ($f=1$). It is very stable numerically so it can be used when the application of relatively long time intervals is necessary.
- Crank–Nicolson method ($f=0.5$). This is appropriate when a high accuracy is required.

There are a series of issues that make the solution of the Navier–Stokes equations particularly complex: the fact that momentum is a vector transport property, the nonlinearity of the momentum transport equation, the lack of an independent equation for the pressure whose gradient contributes to the momentum equation, and the fact that the continuity equation does not contain the pressure and is reduced to a kinematic constraint on the velocity field. This problem is most commonly addressed by combining the momentum and continuity equations resulting in a Poisson equation for the pressure that can be solved by numerical methods. For example, the SIMPLE (Semiimplicit Method for Pressure Linked Equations) algorithm is very popular as its accuracy and efficiency have been widely demonstrated for incompressible flows; this method has been described in detail by Ferziger and Perić.[7] Essentially, the velocity and pressure are obtained separately and then coupled through corrected values. Initially, a velocity field is obtained that does not satisfy the continuity equation. A correction is introduced in these values of the velocity assuming that the velocity corrections are only determined by corrections in pressure in order that the continuity equation is satisfied. Solving of the pressure–correction equation allows correcting the pressure and velocities. The corrected velocities satisfy the continuity equation to certain accuracy but they do not satisfy the nonlinear momentum equation so an iterative process is established until the equations are satisfied to the desired tolerance. If necessary, the turbulence models are solved at the end of each step.

17.2.5 Results Interpretation

The discretized transport equations are solved by numerical iterative procedures. A number of iterations are required to reach a solution according to the established convergence criteria. During the progress of CFD simulations, it is strongly recommended to continuously monitor the evolution with the number of iterations of the residuals for the transport properties of interest in order to be able to detect possible anomalies and save computation time and power.

The interpretation of the results has to start by evaluating their significance. The main sources of errors that must be considered when evaluating the quality of the results are the following:

- Modeling errors. They refer to the differences between the actual values of the properties in a system and those resulting from an exact solution of the mathematical model. As not all physical or chemical phenomena can be formulated with accuracy, nor the transport equations can always be solved exactly, it is necessary to introduce simplifications that imply errors. For example, errors associated to the models of turbulence, the dependence of the thermophysical properties of the substances with temperature or pressure, nonideal behavior or the proper assignment of the boundary conditions. It is practically impossible to quantify these errors whose importance is usually evaluated through the experience gained in previous studies.
- Discretization errors. Numerical methods provide approximate solutions for the transport equations. In the most general case, these solutions correspond only to the nodes along a series of steps or time intervals. To understand these errors, it is convenient to consider the finite difference method for the sake of simplicity.[2] According to this method the derivatives are expressed in terms of Taylor series for which only the first terms are considered. The remaining terms provide the discretization error; in particular the first term neglected. This term is proportional to the size of the mesh elements raised to a power that is known as the order of accuracy so discretization errors are reduced when working with fine meshes. One can include within this group the errors associated with the meshing procedure. As mentioned in Section 17.2.4.1 a mesh is suitable when the results do not depend on the mesh type or cell density.
- Truncation errors. The discretized algebraic equations are solved with iterative procedures that provide a solution when the convergence criteria are reached. These criteria are most commonly based on the residuals of significant variables such as the temperature, pressure, and composition. One way to define them is by the difference between the values of the solution between two consecutive iterations. It is easily calculated but has the problem that when the convergence is slow, the difference between iterations is very small even being far from the correct solution.

These errors are usually additive, and very frequently, the main sources of error are the model and the computational grid.

The volume of results provided by CFD simulations is enormous. There are also many possibilities for representing them graphically. This includes color plots showing the fields of transport properties in lines, surfaces, or volumes, streamlines representation and even animations. Figure 17.4 shows as an illustrative example, the results of one of the simulations on methane steam reforming performed during the study of grid independence (Section 17.2.4.1). The concentration of one of the reactants (methane) expressed as molar fraction is shown along two planes within the channel reactor. The plane parallel to the flow direction allows visualizing how methane is being gradually consumed along the reactor. It can be seen that the methane

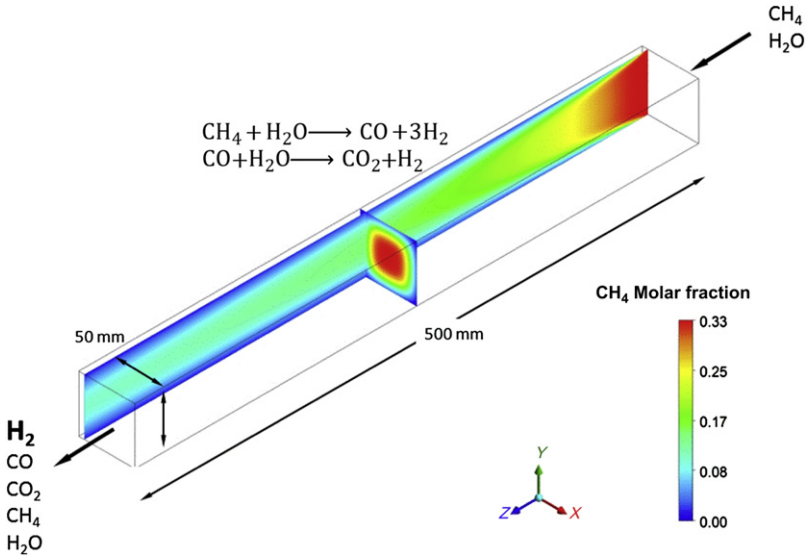

FIGURE 17.4 Evolution of the fraction molar of methane along two planes of a catalytic wall microchannel reactor for the steam reforming of methane. (For color version of this figure, the reader is referred to the online version of this book.)

concentration is very low near the wall where methane reacts over the catalyst layer thus generating a concentration profile along the side. This is better shown by the plane perpendicular to the flow direction; the concentration of methane is maximal at the channel center and gradually decreases when approaching the walls.

The interpretation of the results should be always very cautious. It is frequently necessary to reconsider and modify the mathematical model and adapt the mesh before one can be confident about the significance of the results. Moreover, it is very important to bear in mind that by no means can CFD be considered a substitute of experimentation. The best results are obtained when CFD is the complement of a properly designed experimental program. A CFD model will be useful only if it has been validated previously and a good accordance between the simulation and the experimental results has been demonstrated.

17.3 CFD FOR DESIGNING HYDROGEN PRODUCTION TECHNOLOGIES

After describing the basic aspects of CFD, in this section, a review of the application of commercial CFD codes for studying and designing the most common technologies involved in the processes utilized for the production of hydrogen is presented.

Figure 17.5 includes a simplified scheme of the main technologies involved in the thermochemical conversion of fuels into hydrogen. As can be seen, a first classification can be made as a function of the physical state of the fuel. Solid fuels such as coal, biomass, and some solid wastes are first processed by gasification or pyrolysis to produce gaseous and liquid streams that, after cleaning and pretreatment steps (e.g. desulfurization, hydrotreatments, prereforming), are subjected to some type of reforming (steam reforming, autothermal reforming, or partial oxidation). In contrast, gaseous and liquid fuels such as natural gas, biogas, biooil, diesel, bioethanol, glycerine, can be fed to the reforming step after less demanding pretreatments as compared with solid fuels. The reformate is the gaseous stream produced in the reforming step. This stream mainly contains hydrogen, methane, carbon oxides (CO and CO_2), nitrogen, and steam and is suitable for feeding high-temperature fuel cells such as the solid oxide fuel cells (SOFCs) and molten carbonate fuel cells. However, low-temperature fuel cells and other applications (e.g. food industry, semiconductors, industrial gases) require high-purity hydrogen. In this case, the hydrogen yield is first increased through the water–gas shift reaction in one or two stages, and then, the gaseous stream has to be subjected to a series of separation and purification processes until obtaining a product of the required quality. Among these new steps, the most outstanding ones are pressure-swing adsorption (PSA), membrane separation, methanation, and preferential oxidation of CO (PROX). Another option is processing the reformate to produce syngas (a mixture of H_2 and CO) in order to subsequently obtain synthetic liquid fuels through the Fischer–Tropsch synthesis, methanol, or other valuable chemicals.

CFD work on the technologies involved in thermochemical processes has focused on two main areas: the reforming of gaseous fuels and the conversion of solid or liquid fuels through gasification/pyrolysis or anaerobic fermentation. These research areas will be reviewed in the following subsections. The case of fixed-bed reactors is discussed with more detail due to the outstanding

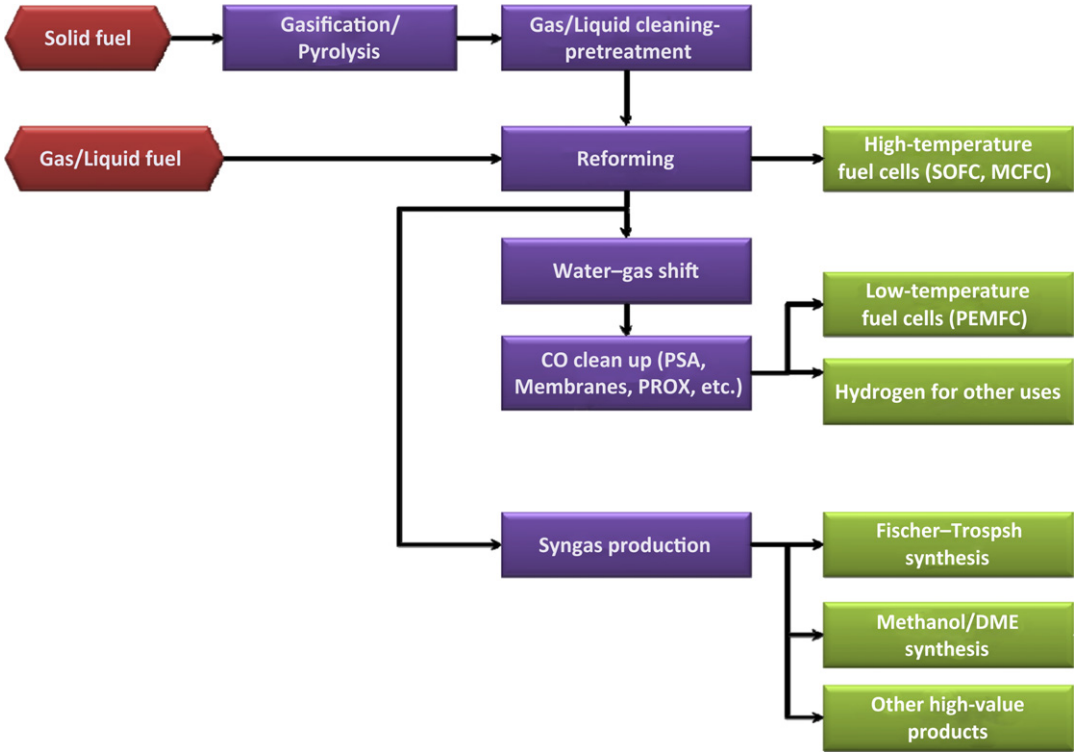

FIGURE 17.5 Scheme of the main technologies involved in the thermochemical conversion of fuels into hydrogen. (For color version of this figure, the reader is referred to the online version of this book.)

importance of this technology for hydrogen production. It should not be forgotten that, apart from the thermochemical processes, water electrolysis allows the production of high-purity hydrogen and a relatively easy integration of renewables (Chapters 1 and 2) in the hydrogen production routes. CFD work carried out on water electrolysis will be considered at the end of this section.

17.3.1 Reforming of Gaseous Fuels

17.3.1.1 Fixed-Bed Reactors

Hydrogen is principally produced via the steam reforming of methane in fixed-bed catalytic reactors. In order to model these reactors, it is important to realize that there are many important factors affecting the process, including the type of catalyst, reformer characteristics, and heat transfer, mass transport and drop pressure issues. CFD studies have been carried out by several researchers considering the analysis of some of these parameters in order to improve the reactor and process design.

Dixon et al. have highlighted the potential and also the challenges of CFD for obtaining a detailed description of the flow fields and scalar transport information in fixed-bed reactors.[28,29] According to these authors, models for heterogeneous reactors have traditionally been based on a number of simplifying assumptions driven by the need for a relatively easy mathematical resolution and the difficulties for describing the complex structure of random packed beds of catalyst particles. Among these simplifications, perhaps the most critical affects the description of the fluid flow because, many often plug flow is assumed, or at the most, fluid flow with a single velocity component that varies in the radial direction. However, regions of stagnant and reverse flow exist in packed beds which contribute to poor heat exchange performance near the tube wall so it is essential to have realistic information about the fluid flow in packed beds for a proper design of these reactors.

An important parameter of the fixed-bed reactors is the reactor tube-to-catalyst particle diameter ratio (N). A reasonably flat velocity profile can be assumed for values of $N > 30$, with a maximum deviation of 20%.[30] This criterion is usually fulfilled except for the small-diameter reactors, such as the ones used in the steam reforming of methane (N between 4 and 8) because the reaction is strongly endothermic and requires the use of narrow tubes in order that heat may be supplied rapidly. Narrow tubes are also used in reactors for partial oxidation although in this case, of course, heat has to be efficiently removed. On the other hand, the interest for reducing compressor costs implies low-pressure drop in the bed so the catalyst particles cannot be too small. These constraints lead to reformers with

low values of N that are very difficult to model due to the presence of strong wall effects that affect the whole bed inducing radial heterogeneities. The void fraction in unstructured beds is larger near the wall, which also results in fluid flow channeling in these regions. Theoretical models fail to predict wall-to-fluid heat transfer when N is low; however, the CFD modeling of heat transfer in fixed beds is also particularly challenging due to the need for solving both convection in the voids and conduction in the solid particles.

Modeling of packed bed reactors with CFD has been carried out usually considering the bed of solid particles as an effective continuum so both fluid and solids are modeled as fully interpenetrating continua according to an Eulerian–Eulerian (EE) approach. Main disadvantages of this procedure are that lumped transport parameters are used to represent dispersion phenomena and heat transfer and the necessity of introducing the concept of an effective viscosity for the solid bed. Another more recent approach consists in not introducing simplifications at the level of the bed geometry in such a manner that the 3D interstitial fluid flow between the particles is solved.[29] Evidently, the geometry and mesh creation steps become much more complex and the computational power demand required increases remarkably. For these reasons, this approach is feasible only for small periodic regions of the packed bed. In spite of this limitation, the knowledge gained from this more rigorous method can be very useful for guiding the simplifications introduced in approaches of the pseudocontinuum type. Dixon et al. have reviewed the CFD approaches used to solve the interstitial flow in fixed beds.[29] Although there are a growing number of papers dealing with CFD simulations of fixed-bed behavior, there are few modeling studies relating the nature of the fluid flow with that of the bed structure in complete beds of particles. Much of the studies have focused in the pressure drop, comparing the results of the CFD simulations with that of experiments or the predictions obtained from well-known correlations such as Ergun's equation for a random bed of particles. A relevant work on this subject is that of Calis et al.[31] These authors found a constant pressure gradient across the bed of spherical particles and periodical flow streamlines ($N = 1$), concluding that a short bed of about six particle diameters is representative of a much longer bed (N of 1–2), at least regarding pressure drop. The local velocity profiles predicted by CFD simulations performed with the commercial CFX-5.3 code agreed well with the profiles measured by laser-Doppler anemometry. CFD simulations were performed at fully laminar and turbulent regimes in order to determine the parameters of Ergun's correlation. This allowed estimating pressure drops with an average error of about 10% that was considered acceptable for design purposes. Two turbulence models were used, a $k-\varepsilon$ model due to its wide utilization and a Reynolds-stress model that a priori seemed more appropriate for the curvature of the bed geometry; nevertheless, both models gave almost the same results. Regarding the mesh, the author indicate that a grid-independent solution required up to 3 million cells for a packed bed containing 16 spheres.[31] This figure gives a good idea on how extremely computational power demanding can be the modeling and simulation of packed beds.

Dixon and coworkers have devoted great effort to the 3D CFD modeling and simulation of heat transfer in fully packed beds and bed segments with emphasis on flow patterns and heat transfer in the proximity of the reactor tube wall.[28,29] The first works by this group modeled a packed bed as two layers of four spheres with the limitation that contact points between the particles and the tube wall and between the particles themselves were not included in the geometry. Subsequently, a model for a bed containing 10 spheres ($N = 2.43$) was developed considering both particle–particle and wall–particle contact points and incorporating spherical dead volumes around those points.[32] The geometry consisted of four layers of spheres that were meshed with up to 252,000 tetrahedral elements whose size was much smaller near the particles and tube wall. Simulations were performed with the commercial software ANSYS/FLOTRAN® using a standard $k-\varepsilon$ model for turbulence and considering cooling and heating from the wall with and without heat generation from the spheres. Velocity fields from simulations with Reynolds numbers (Re) of 3344 showed the formation of eddies near the wall–particle contact points that improved locally heat transfer near the wall. This phenomenon was not observed at $Re < 182$. Flow around the contact points showed stagnant zones due to high shear of the solid surfaces. Marked gradients of velocity in the radial direction were observed between two layers of spheres thus indicating that heat transfer is increased within the bed.[32] The number of spheres in the bed was increased to 44 ($N = 2$) in a later paper by Nijemeisland and Dixon.[33] This work highlighted the importance of constructing a CFD geometry model as close as possible to the experimental setup in order to obtain good fits between simulations and experimental results for low-N packed beds. It was also found that contact points significantly complicate the solution of the turbulence model. Subsequently, a simpler geometry called wall segment model of a reduced size was created on the basis that, for example, for a reactor with N of 4, 75% of the particles are in contact with the tube wall. The model consisted in a 120-degree slice containing a fully symmetrical layout of particles.[34] Extensive checks were performed comparing simulations with the wall segment model and a full bed with 72 spherical

particles ($N = 4$) resulting in no significant or systematic differences in the flow fields obtained.[35] The kinetics of the methane steam reforming over a commercial Ni/α-Al_2O_3 catalyst was included neglecting internal diffusion and mass transfer limitations. This is a reasonable simplification in order to avoid the computational burden of a more rigorous approach. It is well known that for this reaction under industrial practice conditions the activity is proportional to the external geometric surface area rather than the internal surface. This indicates that the catalyst particle behaves as an egg-shell type with the reaction taking place mainly in a thin layer near the catalyst external surface. This fact justifies the approximation of modeling the chemical reactions involved as surface reactions confined to the external surface of the particles. However, regarding heat transfer, it was essential to incorporate the full energy balances to account for heat conduction across the particles internals, whereas axial conduction in the bed was shown to have little effect. This study concluded that the catalyst particles located close to the tube wall do not show symmetric internal temperature fields, whereas the remaining ones were nearly isothermal.[34] The wall segment model was subsequently applied to the methane steam reforming in packed beds of cylindrical particles including solid cylinders and cylinders with one, three, and four longitudinal holes.[36–38] It was found that the internal voids affect the flow patterns near the wall resulting in regions with improved or worse heat transfer compared with the flow patterns nearby. In the absence of a chemical reaction, as the number of holes increases, there is a lesser displacement of the flow toward the wall thus decreasing the heat transfer effectiveness. When the thermal effects of the steam reforming reaction were included, the temperature profiles changed significantly resulting in complex interactions between heat transfer, fluid flow and chemical reaction. At a constant pressure drop, the solid particles give the highest bed and tube wall temperatures followed by the 1-hole particles and then the multihole particles. Little difference was observed between particles with three or four holes and the influence of the hole size was comparatively small. This implies that the multihole particles are more convenient from the point of view of prolonging the reactor tube life but at the cost of slightly less efficient heat transfer into the packed bed. The wall segment model was further improved with the explicit inclusion of intraparticle transport effects (heat conduction and species diffusion) and chemical reaction for the steam reforming of methane.[39] In this case, simulations were performed with the commercial software Fluent® using the $k-\varepsilon$ Renormalization group turbulence model. The catalyst particles were modeled as porous regions incorporating sinks/sources defined by the user for heat and chemical species. Binary molecular diffusion coefficients corrected with the particle tortuosity and an effective thermal conductivity calculated from the values for the alumina support and gas phase and considering the particle voids fraction were used. The results showed strong temperature and species gradients within the particles in contact with the reactor wall. This fact should be taken into account for proper reactor design regarding tube lifetime and catalyst deactivation by coking.

As mentioned previously, meshing is a crucial step of any CFD model. This is particularly true for fixed beds because the simultaneous solution of heat and mass transfer coupled to chemical reaction requires very fine meshes near the particles surface and reactor tube wall. This issue is being systematically studied by Dixon et al. under conditions relevant for industrial steam reformers and partial oxidation reactors ($500 < Re < 10{,}000$; $2-4 < N < 8$). These authors have also reviewed the literature on this subject.[40,41] In general, regarding the velocity fields, pressure drop, and heat transfer, it is recommended replacing the contact points with bridges. This method gives good results for the drag coefficient and heat transfer if a suitable effective thermal conductivity for the bridge material is defined. Another possibility with poorer results is a global reduction of the particles sizes, which leads to the creation of small gaps.

In recent works by Dixon's group, it has been satisfactorily achieved the experimental validation of a CFD model for studying heat transfer in a pilot-scale fixed-bed reactor for the steam reforming of methane operated under conditions typical of industrial practice.[42,43] The mesh refinement analysis carried out indicated that an unstructured mesh with cell sizes of $d_p/20$, being d_p the catalyst particle diameter, and without boundary layers was sufficiently precise for a good description of the radial temperature profiles in the bed. The authors stated that the need for finer meshes and boundary layers should be determined for each case as part of a tradeoff against more realistic models including a larger number of bed particles. Very small differences between the treatment of contact points introducing gaps or bridges were found as the result of a series of compensatory effects taking place in large packed beds. Several bed geometries were considered in the CFD models, for example, 1000 spheres in a bed with $N = 5.45$ and a 0.72-m length and 1250 particles with $N = 7.44$ and a 0.35-m length. The spheres were generated with a code developed by the authors and each bed took approximately 24 h on a standard workstation. Turbulence was modeled according to the RANS method with the $k-\varepsilon$ Realizable model with enhanced wall treatment. In general, the simulations underpredicted the temperatures at the bed center, which was attributed to uncertainty in the particles thermal conductivity although some contribution to

this disagreement of the experimental error in the measuring temperature could not be discarded.

Apart from the extensive work by Dixon and coworkers, there are also other relevant CFD studies on low-*N* fixed-bed reactors; nevertheless an exhaustive literature review is beyond the scope of this chapter. One might note however the hydrodynamic study by Magnico.[44] Due to the moderate *Re* numbers considered (between 7 and 200) the author used direct numerical simulation (DNS) based on the FVM with a collocated structured mesh under stationary conditions. The bed geometries considered included between 80 and 620 spherical particles with *N* within the 5−7.8 range. A good agreement was found between the predicted velocity fields and experimental data reported in the literature. A layer of a width of about one-fourth of the particle diameter was observed at the reactor wall in which the flow is both longitudinal and tangential. A second layer along the spheres in contact with the wall was also detected. The mass transport in these layers is dominated by molecular diffusion. As *Re* increases the layers tend to disappear, whereas numerous eddies are formed that improve significantly the radial mass transfer. In a subsequent paper extending this work it has been reported that the temperature fields reveal that the two phases are not at thermal equilibrium along the wall over a layer whose depth is a particle diameter. In spite of the good results obtained by DNS at low-temperature gradients, the structured mesh used was not suitable for an accurate description of the solid surfaces and contact points.[45] Among the studies concerned with the operation under conditions of industrial interest, Sadeghi and Molaei have simulated using 3D CFD an industrial methane steam reformer. The model has been successfully validated against the results of a hydrogen plant at a refinery.[46] The results show that it is essential in industrial steam reforming furnaces to have a suitable axial temperature distribution in order to create appropriate thermal conditions for the reactions. In the reactor considered in this study, the first 2 m of a total length of 11.6 m did not contribute to the methane conversion due to its low temperature. An optimum value of the steam-to-carbon ratio was found. Values >4 did not affect the conversion leading to higher operating costs but lower ratios led to an increased production of CO. De Wilde and Froment have applied 3D CFD to the analysis and design of a new reactor concept for the steam reforming of methane, the ZoneFlow™ reactor.[47] This concept optimizes heat transfer near the wall due to relatively high velocities and by directing the flow toward and away from the reactor wall resulting in a superior performance compared to that of conventional fixed-bed reactors.

Whereas methane is the dominating raw material for hydrogen production via reforming routes, there is a rapidly increasing interest in other fuels as the simpler alcohols, methanol, and ethanol (bioethanol). However, there are still a few studies dealing with CFD simulations of the steam reforming of these feedstocks in fixed-bed reactors. The main issues from the point of view of the reactor simulation and design are essentially the same as that with methane because the steam reforming of alcohols is also strongly endothermic although the reaction temperatures are significantly lower, especially for the case of methanol. Fukahori et al. investigated the performance of a structured Cu/ZnO catalyst for the steam reforming of methanol. The study included a CFD analysis to demonstrate the positive effects of thermal conductivity and the shape of the catalyst layer resulting in rapid heat transfer and small temperature gradients that reduced the formation of CO. 2D CFD simulations of reactor with a 330-mm length and a 33.6-mm diameter were carried out with Fluent® software.[48] Arteaga et al. studied through CFD simulations the steam reforming of ethanol in a fixed-bed multitube reformer (114-cm length and 150 tubes). It was found that most of the ethanol conversion is reached near the reactor inlet whereas in the rest of the reactor the steam reforming of methane takes place at nearly isothermal conditions.[49]

17.3.1.2 *Fluidized-Bed Reactors*

Compared with the fixed-bed reactors, the fluidized-bed ones are more difficult to model via CFD. Nevertheless, CFD remains a useful tool for the analysis and design of these heterogeneous fluid−solid reactors for which understanding their complex hydrodynamics is crucial for formulating suitable predictive models. As a matter of fact, CFD for describing fluidization has reached some maturity.[50] The fluid is most frequently a gas and the solid particles can be the catalyst (as will be considered in this Section) or a reactant (Section 17.3.2.1) in which case the situation becomes even more complex because the reaction is accompanied by changes of the particles sizes. Much of the interest in these reactors lies in the fact that the intense mixing associated with fluidization allows operating at a more homogeneous and controllable temperature, which is very positive as regards reaction selectivity, catalyst stability, and safety.

When a fluid flows at a given superficial velocity through a bed of particles with a given size and density, the following contact regimes can be distinguished[51,52]: packed bed, bubbling fluidized bed (BFB), and circulating fluidized bed (CFB). CFB includes three additional regimes: turbulent fluidized, fast fluidized and pneumatic transport. In a packed bed the particles are static, whereas in the BFB the solid particles move chaotically ascending and descending but without actually leaving the bed; gas bubbles are also observed.

BFB requires particles of a small size, typically <100 μm, and a suitable fluid velocity (above the minimum fluidizing velocity) for provoking the particles to become suspended. When the fluid velocity exceeds the so-called terminal velocity, individual particles are blown out of the bed and have to be replaced with new solids (e.g. regenerated catalyst particles, recycled unconverted and make-up solid reactant). In this regime, the bubbling action becomes very violent; the bubbles coalesce and become large giving rise to the turbulent CFB. At increasing fluid velocities, the fluid bubbles expand forming a core space in the center of the tube, whereas a higher concentration of solids is present near the tube walls; this is known as the fast fluidizing CFB regime. Finally, at even higher fluid velocities, the wall region with solids becomes very thin when the system reaches the pneumatic conveying regime. These regimes lead to very different fluid−solid contact efficiencies and pressure drops, so each case should be carefully analyzed for finding the most convenient range of particle sizes and hydrodynamic conditions.[52]

According to Fox, two types of fluid−solid systems can be distinguished from the perspective of CFD modeling[18]: fine particles that follow the fluid exactly and can be treated as a transported scalar field, and systems with particles velocities different from that of the fluid. In the second case, the solid phase has its own momentum equation that requires many modeling assumptions to describe all possible flow regimes. On the other hand, dilute fluid−solid systems such as those encountered in CFB, which are dominated by fluid turbulence, are easier to model than dense systems such as the BFB. Indeed, turbulence models for dense systems are still not well developed, so CFD simulations of BFBs are usually carried out without turbulence models and require fine meshes to be able to describe the flow characteristics. This needs a very high computational effort, which makes the simulation of industrial-scale BFB reactors intractable.

Elnashaie and Adris first proposed in 1989 the use of a BFB steam reformer using powdered catalyst, which allowed achieving effectiveness factors of 1, in contrast with the very low values found in conventional packed-bed reformers (as low as 0.01). An improved concept was subsequently developed by incorporating composite permselective membranes within the reactor that allowed producing very pure hydrogen (>99.99%). This eliminated the need for additional downstream purification (e.g. PSA), improved the yield by shifting toward the products the steam reforming equilibrium, facilitated operation at lower temperatures and reduced compression costs.[53,54] Another interesting feature was that autothermal operation can be reached and maintained by feeding oxygen directly into a fluidized bed methane steam reformer thus improving the thermal efficiency.[55]

Later, Prasad and Elnashaie proposed a novel integrated fluidized-bed membrane steam reformer for the production of hydrogen that consisted of two connected subsystems: a CFB membrane reformer and a reactor-regenerator.[56] The steam reforming takes place in the CFB whereas the CO_2 in the reformate stream is used for the dry reforming of additional fuel in the other unit. Thermal integration, regeneration, and recirculation of the steam and dry reforming catalysts, and shifting of the steam reforming equilibrium with the aid of CO_2 capture with recirculating calcium oxide are contemplated. This concept was proposed to circumvent the limitations of the BFB membrane reactor. On the one hand, using the bubbling fluidized regime limits the feed stream flow rate; on the other hand, these reactors do not have any provision for handling extensive catalyst deactivation by coking. In the integrated reformer, the CFB operates under the fast fluidizing regime that allows processing very high flow rates and hence increases the hydrogen production capacity.

Prasad and Elnashaie modeled the fast fluidizing CFB reformer assuming that both gas and catalyst are in the plug flow regime and have the same velocity, and that the volume fraction of solids remains constant along the reactor.[56] The model was used to perform a parametric sensitivity analysis that showed that a significant increase in the hydrogen productivity can be obtained compared with previous generations of reformers. A model of the complete system was developed in a subsequent paper.[57] Plug flow was also assumed by Adris et al. for a fluidized-bed membrane reactor for the steam reforming of methane.[58] The model was based on the two-phase bubbling bed model, solved numerically, and validated against data from a pilot-scale unit. A low influence of the hydrodynamic conditions on the reactor performance was found mainly due to the relatively low superficial velocities considered (up to about six times the minimum fluidization velocity) and the dominant role of the reaction thermodynamics and selective permeation through the membranes.

Mousa et al.[59] performed a CFD modeling study of the internally circulating fast fluidizing CFB membrane reformer proposed by Xie et al. for autothermal operation using air as oxidant.[60] This reactor operates in the core-annular flow regime in which solids circulate downwards near the column walls and are reentrained at the column bottom by the feed stream gases (methane, steam, and air) that flow upward mainly through the central zone of the riser, so the core is very dilute whereas the annulus is dense. Mousa et al. adopted an EE approach and the kinetic theory of granular flow (KTGF) for describing the solids rheological properties.[59] The KTGF can be applied to both dilute and dense two-phase flows.[61] It is based on a granular temperature that gives a measure of the kinetic energy oscillation due

to collisions and fluctuating motions of the particles; its role is similar to that of absolute temperature in the kinetic theory of gases. When solids are modeled as a separate pseudocontinuum phase following an Eulerian approach, model magnitudes such as the pressure or viscosity can be obtained from the granular temperature according to KTGF.[50,62] Mousa et al. conducted 2D axisymmetric simulations with Fluent® software using the standard $k-\varepsilon$ turbulence model and a structured stretched mesh with a higher cells density near the tube walls.[59] It was found that for proper reformer performance, the riser should be operated under high density (inlet void fraction <85%) and high solids flux conditions.

Lindborg and Jakobsen performed 2D simulations of a BFB reactor for the sorption enhanced steam reforming of methane.[63] The authors used and validated for chemical reactive flow an in-house CFD code based on the finite-volume method developed by Lindborg et al. for dense gas–solid flows in fluidized beds.[61] Due to the high particle loading an EE approach was adopted, and the standard $k-\varepsilon$ turbulence model was applied for describing influence of the continuous phase turbulence in dilute zones such as the gas bubbles. Kinetic equations for the methane steam reforming over $Ni/MgAl_2O_4$ and CO_2 adsorption over Li_2ZrO_3 were incorporated into the CFD code. The positive effect of the CO_2 adsorption on hydrogen concentration was evidenced, resulting in hydrogen yields very close to 100%. It was also found that wide reactors are the most favorable choice for obtaining high mass throughputs since changes in the bed diameter had minor effects on the hydrogen production. This CFD study was subsequently extended to 3D simulations with CO_2 adsorption over CaO during the steam reforming of methane in a BFB and regeneration of the adsorbent in a separate CFB.[64]

Apart from methane, the steam reforming of glycerol in fluidized-bed reactors for hydrogen production has been also investigated through CFD simulations. Dou et al.[65] and Dou and Song[66] considered an EE approach and the KTGF with Fluent® software. A heterogeneous structure of the bed was observed and it was claimed that short residence times allowed obtaining high glycerol conversions although coke formation reactions were not considered in the kinetic scheme.

17.3.1.3 *Catalytic Wall Microreactors*

The interest and potential of microreaction technology for the production of hydrogen have been reviewed in Chapter 9. Microreactors, together with membrane and plasma reformers, constitute the most important recent developments in the field of fuels reforming for hydrogen and syngas production.[67] In contrast to conventional steam reforming in packed-bed reactors that has been highly successful in the large-scale hydrogen production, microreactors (microreformers) are suitable for the increasingly important noncentralized small-scale portable and mobile applications. This is mainly due to their higher flexibility, compactness, easier startup, and improved temperature control. Microreactors have characteristic dimensions typically below 1 mm that lead to very high surface-to-volume ratios. This fact and the very short transport distances allow achieving high heat and mass transfer rates that enable fully exploiting the intrinsic activity of the catalysts and operating the reactor at very high space velocities. This is of great interest for chemical reactions that are accompanied by intense thermal effects, such as the strongly endothermic reactions involved in the reforming of fuels for obtaining hydrogen and syngas. Moreover, due to the reduced transport distances, thermal integration is more easily implemented in microreactors. In this way, the endothermic reforming reactions can be thermally coupled within the same microdevice with exothermic reactions such as the combustion of part of the fuel thus improving the thermal efficiency of the process. Heat transfer is very rapid across the walls (most frequently metallic) that separate the chambers where the reactions take place. In most of the cases the catalyst is deposited onto the inner walls of microducts or microchannels with square, rectangular or hemispherical section. Therefore, heat is readily available at the point where it is needed in thermally integrated catalytic wall microdevices.

In the recent years, numerous studies have appeared dealing with the use of microreaction technology in reformers for fuels such as methane and methanol, principally, but also ethanol, gasoline, diesel, liquefied petroleum gas, as well as in multifuel reformers.[68] Compared with the previously discussed technologies, that is, packed and fluidized catalytic beds, the number of papers devoted to the CFD modeling of microreactors is much higher. This is in great part due to the interest provoked by this novel technology. However, another important factor is that the flow regime in microchannels is typically laminar, which remarkably simplifies the development of the mathematical model and the geometry meshing and reduces the computational power requirements. A selection of studies on the reforming of methane and other fuels in microreactors that include CFD modeling and simulation is compiled in Tables 17.1 and 17.2, respectively.

As can be deduced from Table 17.1, much attention has been paid to the steam and autothermal reforming of methane while the partial oxidation of methane in catalytic wall microchannels has been much less investigated through CFD simulations. Rectangular or square microchannels, microslits, and micromonoliths are the reactor geometries most frequently considered. As

TABLE 17.1 Selection of Studies on the Reforming of Methane in Microreactors Including CFD Modeling and Simulation

Reaction system	Reactor and CFD model features	Main findings/conclusions	References
Steam reforming of methane over $Rh/Mg/Al_2O_3$ supported on microstructured catalyst based on felts.	Two engineered catalysts are considered: parallel and corrugated felts. 3D simulations included first-order kinetics and were carried out with FEMLAB software.	Experiments and simulations validated the concept of process intensification applied to the steam reforming of methane that was carried out at very high GHSV of up to 3,600,000 h^{-1}.	69
Steam reforming of methane over $Ni/Mg-Al_2O_3$ catalyst.	Rectangular reaction ducts of 10×5 mm with only a face exposed to the catalyst. 3D simulations included chemical kinetics, diffusion in the catalyst layer (4 mm thick), and effective thermal conductivity and specific heat.	Maximum reaction rates are observed within a thin porous region close to the interface between the gas phase and the porous catalytic layer at the entrance region.	70
Methane steam reforming on Rh/Al_2O_3 coupled with propane or hydrogen combustion on Pt catalyst.	Parallel plate microreactors with a 50-mm length and characteristic dimensions of 0.3 and 0.2 mm for the steam reforming and combustion ducts, respectively. Reactions take place on the opposite sides of a wall. 2D simulations of the adiabatic microreactor were performed with Fluent software.	This set of studies includes a wide parametric sensitivity analysis. Cocurrent flow configuration gives a better overlap of reaction zones and minimizes hot spots. The steam reforming is controlled by chemical kinetics at the microscale and can be carried out at submillisecond contact times. Reactor stability improves as the catalyst load and the reactivity of the combustion fuel increase.	71–73
Methane steam reforming on Ni/Al_2O_3 coupled with methane combustion on Pd/Al_2O_3 catalyst.	Parallel square microchannels and microslits with a 20-mm length and characteristic dimensions of 0.35, 0.70, 1.4, and 2.8 mm. Catalytic reactions are modeled considering the inner walls as sources of products and sinks of reactants. Internal diffusion effects are neglected due to the small thickness of the catalyst layers. 3D simulations of adiabatic microreactor were performed with ANSYS CFX software.	A wide parametric sensitivity analysis is performed. It is possible to achieve methane conversions >96% at 930–1000 °C and high GHSV. The temperature in the solid metallic block is very homogeneous, especially for the cocurrent flow arrangement. Little differences exist between the performances of square microchannels and microslits. Reactor performance improves as the characteristic dimension decreases. For the biggest dimension considered (2.80 mm) external transport limitations are significant.	24,27
Methane steam reforming on Ni/Al_2O_3 catalyst.	Micromonolith with square channels of about 0.75-mm side and a 30-mm length. 2D simulations were performed with Fluent software. Two approaches were considered for implementing the chemical reactions in the CFD code: surface reaction model assuming that reaction takes place at the walls and volume-based model considering a catalyst layer 0.07 mm thick.	Simulations of individual channels were compared with the experimental results obtained with the micromonolith. Predictions of the surface reaction model were in better agreement with the experimental results. One problem with the volume-based model is the uncertainty in obtaining the effective diffusion coefficients.	74
Methane steam reforming on Rh coupled with methane combustion on Pt catalyst.	Parallel microslits of a 10-mm length and width and a 0.5-mm height. 2D simulations were performed with Fluent software and included elementary reaction kinetics for the steam reforming and global kinetics for the combustion reactions.	A parametric sensitivity analysis is included considering among other variables the effect of the thermal conductivity of the catalyst layer. A ratio of about 0.7 between the volumetric flow rates of the fuel and reforming streams was found suitable.	75
Methane steam reforming on $Ni/MgO-\alpha Al_2O_3$ coupled with methane combustion on the $Pt/\alpha Al_2O_3$ catalyst.	Parallel microslits of a 50-mm length, a 10-mm width, and a 1 and 2-mm height for the combustion and reforming ducts, respectively. Heat and mass transfer in the catalysts layers (0.2 mm thick) are considered. 2D and 3D simulations were performed with COMSOL Multiphysics software.	Very small temperature gradients are established and extremely high heat fluxes are achieved. A better performance of the microreactor is found under countercurrent flow arrangement. Thicknesses of the catalyst layer >0.5 mm are useless for enhancing reactor performance.	76

(*Continued*)

TABLE 17.1 Selection of Studies on the Reforming of Methane in Microreactors Including CFD Modeling and Simulation—cont'd

Reaction system	Reactor and CFD model features	Main findings/conclusions	References
High-temperature partial oxidation of methane over Pt gauze.	Gauze consisting of two rows of six parallel Pt wires with an opening of about 0.6 mm. 3D simulations were performed with Fluent software. Codes included both Pt-surface and homogeneous gas-phase reactions kinetics by means of external subroutines.	Simulation results were found to be in perfect agreement with experiments reported in the literature. For typical reaction conditions the heterogeneous catalytic reactions govern the reactor performance.	77
Autothermal reforming of methane over the Rh catalyst.	Micromonoliths with characteristic dimension of 1 mm. 2D simulations included chemical kinetics and were performed with CFD-ACE software.	Axial wall conduction strongly influences the reformer performance due to its influence on the catalyst layer temperature, which in turn affects the partial oxidation and steam reforming.	78
Autothermal reforming of methane over Ni/Al_2O_3.	Square microchannels with a 1-mm side, a 40-mm length, and zigzag arrangement including up to five side feed streams. 3D simulations of the adiabatic microreactor were performed with Fluent software. The model included pseudohomogeneous chemical kinetics and a porous domain to simulate a fixed bed.	Hot spots were found near the microchannel entry due to the combustion of methane. Air distribution along the duct length allows solving this problem and increases the yield of hydrogen.	79
Autothermal reforming of methane over Ni catalyst.	Square microchannel of a 0.34-mm side and a 8.5-mm length. Reactions are assumed to take place on the inner walls. 3D simulations were performed with an in-house CFD code based on the finite-volume method incorporating chemical kinetics.	Virtually isothermal operation can be achieved. A parametric sensitivity analysis allowed determining suitable operating conditions for maximizing the production of hydrogen while reducing the CO molar fraction to about 5% (dry basis).	80
Autothermal reforming of methane over Ni catalyst.	Microchannel reformer integrated with hydrogen permselective membrane. The characteristic dimension of the reaction duct was 1.2 mm, and the thickness of the catalyst layer 0.3 mm. The Darcy–Brinkman–Forchheimer equation was used to describe the flow in the catalytic layer (Fluent software).	A remarkable intensification of the process is obtained by combining the short transport distances characteristic of microreactors with the rapid removal of hydrogen from the reaction microchannel. Permeation greatly enhances mass transport within the catalyst layer.	81

concerns the catalyst, micropacked beds are modeled as homogeneous porous media, while in catalytic wall configurations, reaction at the wall surface is usually adopted, neglecting the influence of the catalyst coating due to its small thickness. In some cases, however, transport limitations within the catalyst layer are taken into account by introducing effectiveness factors. In the case of methane steam reforming, thermal integration is considered through the coupling of the reforming reaction with the catalytic combustion of a fuel (e.g. methane, hydrogen or propane) in neighboring microducts. There are a few examples in which the simulation results are validated against experimental data obtained in catalytic microreactors. In general, the agreement between experimental and simulation results is satisfactory. Parametric sensitivity analyses through CFD simulations evidence the effectiveness of microreaction technology for intensifying the processes of hydrogen and syngas production from the reforming of fuels. It is also worth noting the extremely uniform temperatures that are present within microreactors making possible a virtually isothermal operation in spite of the intense thermal effects associated with the chemical reactions involved. Nevertheless, a careful adjustment of the reforming and fuel flow rates and proper selection of the inlet temperatures and flow arrangement (cocurrent, countercurrent, or crossflow) is required; CFD is very useful in this regard. It should be noted that most of the published studies have dealt with adiabatic systems. Although still very scarce, there are some reports that highlight the critical influence of heat losses to the environment on the microreactor's performance. It is necessary to pay more attention to this issue as well as to a more in-depth description of the transport phenomena within the catalyst layer in order to suitably improve the available CFD models of catalytic wall microreactors.

Apart from methane, methanol is another fuel that has been widely adopted in investigations on hydrogen production in catalytic wall microreactors. This interest mainly arises from the facts that methanol is a liquid

TABLE 17.2 Selection of Studies on the Reforming of Methanol, Ethanol, and Logistic Fuels in the Microreactors Including CFD Modeling and Simulation

Reaction system	Reactor and CFD model features	Main findings/conclusions	References
Methanol steam reforming on $Pd/ZnO/Al_2O_3$ coupled with methanol combustion.	Integrated microfuel processor with a total volume of 0.3 cm^3. The device incorporates the steam reforming catalyst particles (0.2-mm diameter) in an annular bed. A 3D pseudohomogeneous model including chemical kinetics and effective transport coefficients is developed with FEMLAB software.	Heat losses to the environment were found to be critical for such a small system. Simulations allowed optimizing the thermal insulation thickness and the reactor configuration to maximize hydrogen production and reduce the CO content incorporating a methanation section.	82
Methanol steam reforming on $Cu/ZnO/Al_2O_3$ catalyst.	Silicon-based microreactor incorporating a thin film heater and a serpentine catalyst coated microchannel 333 mm long, 0.6 mm wide, and 0.4 mm deep. CFD simulations were performed with STREAM software.	CFD simulations were conducted to investigate pressure drop and temperature fields. Pressure drops <2052 Pa were found as well as excellent temperature uniformity. Concentration was also very uniform in the radial direction.	83
Methanol steam reforming coupled with methanol combustion on $Cu/ZnO/Al_2O_3$ catalyst.	Parallel square microchannels of a 20-mm length and a 0.35-, 0.70-, and 1.4-mm side. Catalytic reactions are modeled considering the inner walls as sources of products and sinks of reactants. Internal diffusion effects are neglected due to the small thickness of the catalyst layers. 3D simulations of the adiabatic microreactor were performed with ANSYS CFX software.	A wide parametric sensitivity analysis is performed that allowed establishing suitable ratios between the fuel and reforming gases flow rates. This was important to ensure complete methanol reforming while avoiding overheating that increases the formation of CO. Cocurrent flow arrangement provided a very uniform temperatures compared with the countercurrent and crossflow configurations.	23
Methanol steam reforming on $Cu/ZnO/Al_2O_3$ catalyst.	Catalyst particles of a 0.025-mm diameter are arranged forming micropacked beds or layers (referred to as wall-coated reformer). The bed is modeled as a homogeneous porous medium with a given porosity and permeability. Simulations including chemical kinetics were performed with COMSOL Multiphysics software.	If heat is supplied across the wall, higher reforming temperature, methanol conversion, and CO production are achieved with the wall-coated configuration, with a maximum when the catalyst layer thickness is 90% of the reformer radius. An important influence of the wall thickness and thermal conductivity was found.	84–86
Methanol steam reforming on $Cu/ZrO_2/CeO_2$ coupled with methanol combustion.	Microchannels with a characteristic dimension of 0.45 mm. The catalyst layers (0.05 mm thick) are modeled as porous media. 3D simulations were performed with Fluent software.	A serpentine flow arrangement improves the reactor performance compared with straight-parallel flow configuration. The highest methanol conversion is obtained with the countercurrent flow disposition.	87–91
Methanol steam reforming on $Zn–Cr/CeO_2–ZrO_2$; heat is provided by hot air.	Microreformer with 8 nonparallel channels; the section of some of them is not constant and increases or decreases gradually along their length. The microchannels height is 3 mm and their length 20 mm. The effect of the catalyst layer thickness is taken into account by means of a geometrical factor. The layer is modeled as a porous medium with homogeneous porosity and permeability. 3D simulations were performed with Fluent software.	It is claimed that the proposed microchannel configuration guarantees flow distribution uniformity that can increase methanol conversion compared with the use of parallel microchannels. A higher conversion rate is obtained with catalytic wall reformers compared with packed-bed reactors. An optimal catalyst layer exists due to the opposite effect of the increase of the thickness on the methanol conversion and hydrogen selectivity.	92
Ethanol steam reforming on $Rh/CeO_2/Al_2O_3$; heat is provided by cocurrent flow of a hot gas in adjacent channels.	Parallel microchannels of a 60-mm length, a 0.4-mm depth, and a 0.5-mm width separated by 0.3 mm. Diffusional effects in the catalyst layer are neglected due to its small thickness (<0.03 mm). This assumption was supported by the	Ethanol conversion and axial and transverse temperature profiles depend on heating gas space velocity and temperature, channel width, catalyst loading as well as inlet temperature and velocity of the reforming gas stream. Suitable values for these	93

(*Continued*)

TABLE 17.2 Selection of Studies on the Reforming of Methanol, Ethanol, and Logistic Fuels in the Microreactors Including CFD Modeling and Simulation—cont'd

Reaction system	Reactor and CFD model features	Main findings/conclusions	References
	fulfillment of the Weisz–Prater criteria. 2D simulations were performed with COMSOL Multiphysics software.	variables are obtained from the simulations with a view of obtaining a high methanol conversion and a suitable axial temperature profile for satisfactory selectivity.	
Ethanol steam reforming on Co_3O_4–ZnO.	Silicon microreactor with square parallel microchannels of a 20-mm length and a 0.10-, 0.35-, and 0.70-mm side. Catalytic reactions were modeled considering the microchannels walls as sources of products and sinks of reactants. Homogeneous heat generation inside the Si block was adopted to emulate the presence of heating cartridges. 3D simulations of the adiabatic microreactor were performed with ANSYS CFX software.	Simulations reveal that high reforming temperatures should be avoided because under these conditions the decomposition of ethanol competes with the formation of acetaldehyde, which is the key intermediate of the reaction over the considered catalyst and results in an increased content of CO. Using microchannels of 0.10–0.35 mm of a characteristic dimension allows achieving an almost isothermal flow and an effective control of the temperature that preserves high hydrogen yield.	26
Light fuel oil and diesel fuel steam reforming coupled with hydrogen combustion.	Catalytic wall microchannel heat exchanger with parallel channels The thickness of the catalyst layer was 0.025 mm. After discarding the application of the dusty gas model for describing transport within the porous layer due to its small thickness, the effectiveness factor concept was applied. Simulations of adiabatic systems were performed with ANSYS CFX software.	CFD simulations were validated against experimental results of the temperature distribution and used to optimize the reformer geometry design and investigate the influence of the flow disposition. It was found that an inlet temperature of only 500 °C is feasible due to the superheating reformer capacity. Cocurrent flow with lateral inlets and suitable channel size meet the demands.	94
Partial oxidation of isooctane over Rh/Al_2O_3 catalyst.	Cordierite micromonolith of a 10-mm length, 19-mm diameter, and 900 cells per square inch. A single channel is modeled as representative of the whole reactor due to the virtual absence of radial temperature gradients given the thermal insulation an effectiveness factor is introduced to account for transport limitations in the catalyst layer. 2D simulations were carried out with an in-house CFD code.	Very high hydrogen and carbon monoxide selectivity was found at stoichiometric conditions, whereas at fuel lean conditions more total oxidation occurred. A very powerful code has been developed that incorporates detailed homogeneous (noncatalytic) and heterogeneous (catalytic) chemical kinetics. Up to 800 chemical species are considered for describing the isooctane conversion.	95,96
Hydrogen production from NH_3 decomposition on the Ru catalyst coupled with the homogeneous combustion of propane.	Alternate parallel channels 600 and 300 μm wide for the propane combustion and ammonia decomposition, respectively. 2D simulations of adiabatic microreactors included chemical kinetics and were performed with Fluent software.	Similar results were found between cocurrent and countercurrent flow configurations of the two streams due to the use of highly conductive materials. Working at very short contact times is feasible but the flow rates should be carefully adjusted.	97,98

under ambient conditions, which greatly contributes to settle the issues associated with fuel storage and the relatively mild temperatures required by methanol reforming compared with methane. As a result, alcohols, and particularly methanol, are the fuels of choice for small portable energy systems. It can be seen in Table 17.2 that CFD studies on methanol reforming in microreactors are mainly concerned with the steam reforming route. The reaction products, hydrogen and carbon dioxide, can further react through the reverse water–gas shift reaction to form CO, which is detrimental for the quality of the reformate stream in view of its use in low-temperature fuel cells. In this case, predictive CFD simulations combined with the ability of microreactors for controlling the reaction temperature constitute a very effective means for minimizing the production of CO from methanol steam reforming. Thermal integration can be also accomplished coupling the reforming reaction with the catalytic combustion of hydrogen or methanol. CFD modeling details and capabilities are similar to the ones commented before for methane. The importance of heat losses on the reactor performance and the application of CFD for designing its thermal insulation have been reported by Cao et al.[82]

Due to the opposite effect of the catalyst loading on the methanol conversion and the selectivity to hydrogen, the existence of an optimal layer thickness for maximal hydrogen production has been found. CFD studies concerned with the reforming of higher alcohols such as ethanol in catalytic wall microreactors are much less abundant. In passing from methanol to ethanol requires the use of remarkably higher reforming temperatures. Moreover, the reforming of ethanol is more challenging from the point of view of the reaction selectivity because the decomposition of the alcohol is also favored as the temperature increases. CFD simulations are powerful tools for optimizing the reaction conditions, especially the temperature, in order to maximize the yield of hydrogen. Logistic fuels such as light fuel oil or diesel are also of interest to be used in catalytic wall microreactors for hydrogen production. CFD simulation studies have been conducted to assist the design of these microreactors, as indicated in Table 17.2.

Our research group has been studying from several years ago through CFD simulations the use of catalytic wall microreactors for the production of syngas and hydrogen from methanol,[23] ethanol,[26] and methane[24,27] conversion. We have also investigated the preferential oxidation of CO (CO-PROX) in catalytic microreactors for hydrogen conditioning prior to its use in fuel cells.[25] The simulations corresponding to CO-PROX in a microchannel reactor coated with a CuO_x/CeO_2 catalyst have been validated satisfactorily against experimental results.[99] These studies included relatively broad parameter sensitivity analyses that allowed investigating the influence on the microreactor's performance of the most relevant operating variables such as reforming and fuel space velocities, reaction temperature, feed stream composition, catalyst load, and characteristic dimension of the microducts (square microchannels or microslits). Rate equations included in the CFD codes were obtained after a kinetic analysis of the experimental data obtained with the catalyst under consideration or taken from the literature. As a representative example, Fig. 17.6 shows the mean outlet methane conversion reached as a function of the feed stream weight-hourly space velocity (WHSV) and the characteristic dimension (d) of square microchannels and microslits for the steam reforming of methane over a nickel catalyst. The length (L) of the microducts was 20 mm; additional details on the geometries and CFD models can be found in Ref. 27. It is important to realize that as the catalyst is located on the inner walls of the microducts, the use of the WHSV instead of the volumetric space velocity (GHSV) allows comparing the results irrespective of the significant change of the surface-to-volume ratio that takes place as d varies. As can be seen, high methane conversions, >80%, can be obtained even at high space velocities. This illustrates the effectiveness of microreactors for process intensification. It is also apparent that for the two geometries considered, at a given space velocity, the reactor performance improves as the characteristic dimension decreases within the 2.8- to 0.35-mm range. This result is a good example of the advantages associated with a reduction of the transport distances in chemical reactors. Indeed, Fig. 17.7 shows the evolution of the normalized fraction molar of methane (y/y_{entry}) referred to its value at the microreactor entry ($y_{entry} = 0.33$) along the dimensionless transverse position in the microchannels cross-section. The molar fraction profiles are shown for two characteristic dimensions (0.70 and 2.8 mm) at three positions along the microchannel length ($L/8$, $L/2$, and the outlet L). It can be seen that for the largest value of d, significant transverse concentration profiles develop, particularly near the microchannel entry. The increased effect of the diffusional transport limitations is thus responsible for the decrease of methane conversion as d increases. The fraction molar profiles are more pronounced near the reactor entry due to the higher reaction rate; it should be noted that methane is consumed at the inner walls of the microducts. Similar graphs are included in Fig. 17.8 for the microslits. In this case, two dimensions, the width and length, are above the millimeter scale thus strengthening the effect of transport limitations, which explains the poorer performance of the microslits in comparison with the microchannels.

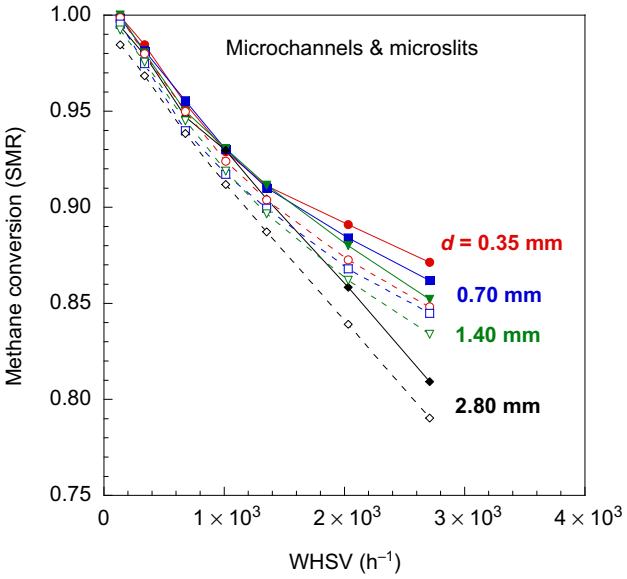

FIGURE 17.6 Mean methane conversion as a function of the feed stream WHSV and the characteristic dimension (d) of square microchannels and microslits for the steam reforming of methane over a nickel catalyst. (For color version of this figure, the reader is referred to the online version of this book.)

Another aspect of the catalytic wall microreactors for hydrogen production investigated by our research group has been thermal integration. Figure 17.9 shows the

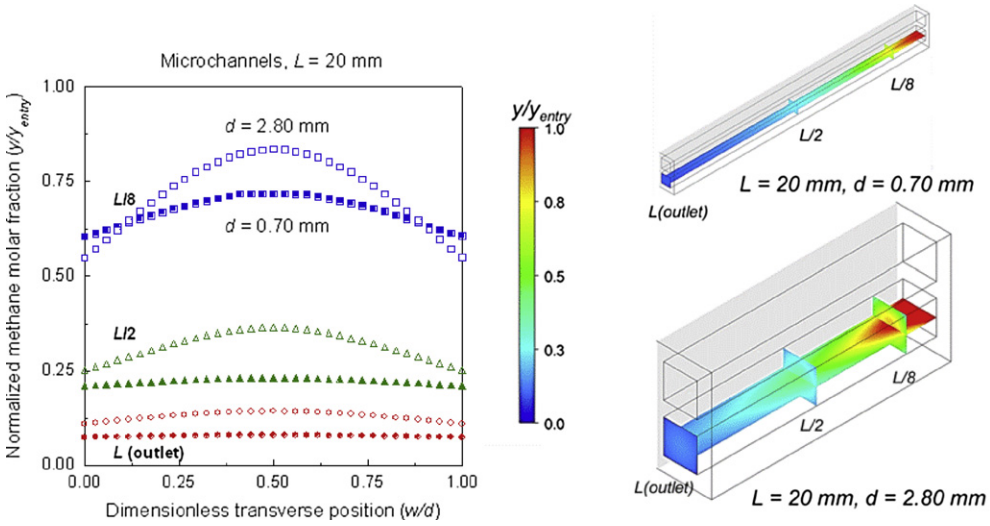

FIGURE 17.7 Evolution of the normalized fraction molar of methane along the dimensionless transverse position and several planes of two square catalytic wall microchannels with a characteristic dimension of 0.7 and 2.8 mm. (For color version of this figure, the reader is referred to the online version of this book.)

temperature fields in two plates containing 10 square microchannels each. Methanol steam reforming takes place in one of the plates and methanol combustion with air in the other. The plates are arranged in parallel cocurrent (Fig. 17.9, top), parallel countercurrent (Fig. 17.9, middle), and crossflow (Fig. 17.9, bottom). More details can be found in Ref. 23. The positions at which 85% methanol steam reforming conversion is reached are also indicated in Fig. 17.9 with arrows in the reforming microchannels. As can be seen, the parallel cocurrent configuration provides a very uniform temperature. The system is almost isothermal with a maximum variation of the temperature within the solid (steel) block of only 3 °C. This behavior is due to the very short heat transfer distances and a good overlap of the zones where heat is consumed (reforming) and produced (combustion) at the highest rates (microchannels entry). Regarding the parallel countercurrent flow arrangement, the temperature is also considerably uniform although the maximum variation of temperature (7 °C) is slightly higher than for the parallel cocurrent configuration. Finally, the crossflow arrangement gives rise to the highest difference of temperature within the block albeit it continues being small (12 °C) taking into account that the mean temperature is about 300 °C. In this case, it is apparent that the block is hotter near the combustion microchannel's entry. It can be seen also that in the reforming channels that are closer to this zone the

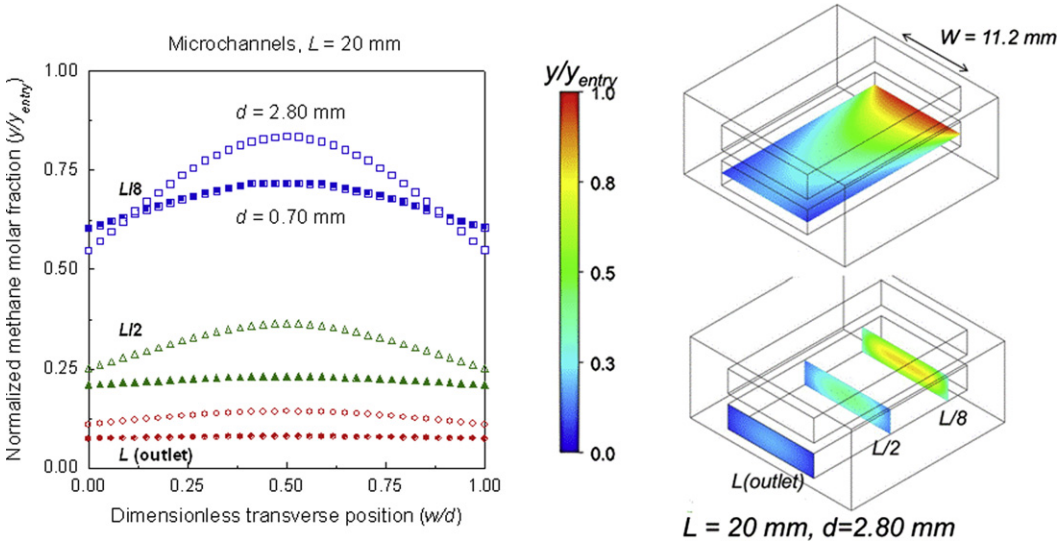

FIGURE 17.8 Evolution of the normalized fraction molar of methane along the dimensionless transverse position and several planes of two catalytic wall microslits with a characteristic dimension of 0.7 and 2.8 mm. (For color version of this figure, the reader is referred to the online version of this book.)

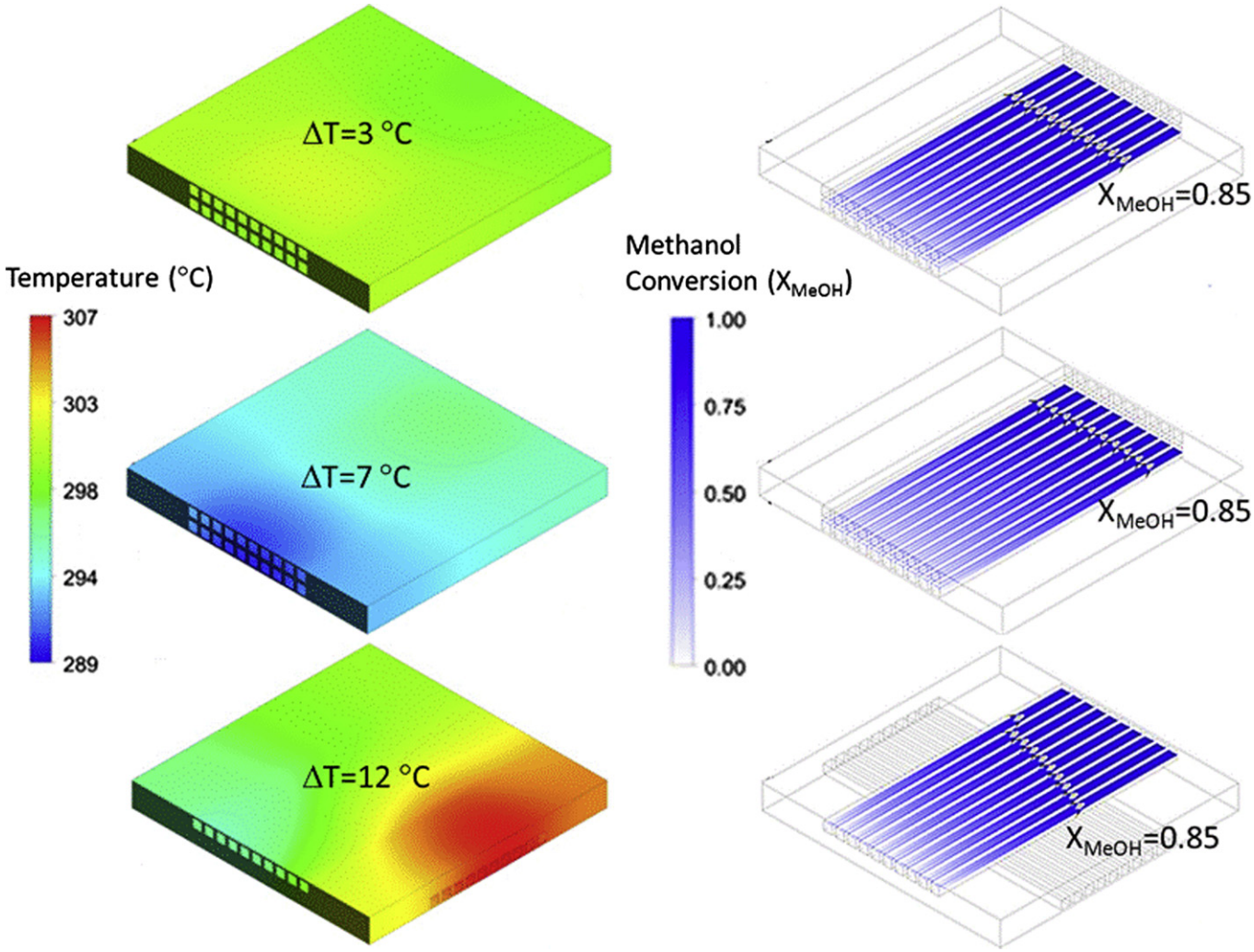

FIGURE 17.9 Temperature fields in two microchannels plates integrating the methanol steam reforming and combustion reactions for three flow arrangements: parallel cocurrent (top), parallel countercurrent (middle), and crossflow (bottom). On the right, the positions at which 85% methanol steam reforming conversion is reached are indicated in the reforming microchannels with arrows. (For color version of this figure, the reader is referred to the online version of this book.)

methanol reforming conversion increases more rapidly, that is, higher values are present at points closer to the channel entry. In contrast, in the parallel arrangements, all the channels behave similarly due to the more homogeneous temperature distribution.

17.3.2 Conversion of Solid or Liquid Fuels

Biomass is typically present in solid form. Depending on its characteristics and the desired products, thermochemical conversion by pyrolysis or gasification and biochemical conversion by fermentation or anaerobic digestion are the main conversion technologies employed. Very frequently liquid and gaseous streams are first produced that require further processing for obtaining hydrogen. Due to the complex structure of biomass, a great number of interacting physical and chemical processes take place simultaneously in the biomass conversion reactors. This makes particularly challenging the modeling and simulation of these devices through CFD. Nevertheless, once appropriate simplifying assumptions are established, this simulation tool is very useful for assisting the analysis and design of the biomass conversion reactors. As a matter of fact, there is a rapid increase of the studies devoted to the CFD modeling of the biomass conversion technologies.[100] One of the largest applications of CFD modeling to biomass utilization has been in biomass combustion or cofiring with coal in boilers and furnaces.[101–108] In these applications there is considerable interest on the analysis of the temperature profiles, and the formation of

pollutants as NO_x and unburned carbon. This interesting topic is outside the scope of this section that focuses on technologies for hydrogen production.

17.3.2.1 Gasification and Pyrolysis

Biomass gasification is a proven technology to produce satisfactory yields of hydrogen and syngas, as well as fuel gas with low to medium energetic value for direct firing in several applications (kilns, boilers, and gas turbines).[109] The products of the gasification process are the so-called producer gas (a mixture of CO, H_2, CH_4, CO_2, N_2, H_2O, and hydrocarbons) and the unconverted solids or char. Tar is an undesired product consisting of condensable hydrocarbons sometimes present in the producer gas when the gasifier operates at unsuitably low temperatures. The conversion processes during gasification initially include drying and devolatilization, then the oxidation of volatiles and char and finally the gasification of char with CO_2 and H_2O.[110] These processes can take place at different points of the gasifier depending on the operating conditions, reactor configuration, and biomass and oxidant-feeding mode. In contrast to coal gasification, which is dominated by entrained flow technology, in the case of biomass gasification a wider range of technologies is being considered (fixed-bed, fluidized-bed, or entrained flow). Nevertheless, the preferred technology for nearly all medium- to large-scale gasification plants has been the atmospheric CFB reactor.[109]

As concerns pyrolysis, it consists in the thermal degradation of biomass in the absence of oxygen. In the recent years, fast pyrolysis of biomass at moderate temperatures of around 500 °C and short residence times of up to 2 s has become of considerable interest because the process directly gives high yields of liquids, of up to 75 wt.%.[111] These liquids are known as condensable volatiles or tars and can be used in a variety of applications, for example, they can be reformed to hydrogen or syngas. Other primary products of pyrolysis are the in the form of solids, or char, and the noncondensable volatiles such as H_2, CO, CO_2, and C_1–C_2 hydrocarbons. Relatively low process temperatures and long residence times favor the production of char whereas high temperatures are suitable to increase the production of gases. Fluidized beds are the most widely used type of reactor for fast pyrolysis due to the high heat transfer rates and the good homogeneity and controllability of the temperature they offer.[112]

From the point of view of CFD modeling, most studies reported in the literature correspond to entrained flow,[113–116] and, especially, fluidized-bed[110,117–119] gasifiers, and fast-pyrolysis reactors. The application of CFD to the modeling of fluidized-bed reactors has been discussed with some detail in Section 17.3.1.2. Hydrodynamics and reaction studies are the two aspects that have attracted more attention. Regarding hydrodynamics, an EE approach has been frequently adopted that consists in applying a continuum approach for both gas and solid phases. Source terms are introduced in order to account for the interactions between the phases (Section 17.2.2). More recently, Eulerian–Lagrangian (EL) approaches have been introduced that consider the fluid as a continuum and describe the solid phase by means of discrete particle methods. In the case of biomass processing, the EL approach is particularly interesting because it allows describing variable- and time-dependent particle sizes in a natural way by tracking each individual particle with its physical properties.[110] It should be noted that the size of biomass particles is subjected to changes due to the effect of chemical reactions and also as a consequence of collisions, friction, thermal stresses, and internal pressures caused by volatile and gaseous products. Change of size affects the conversion rate and the hydrodynamics so it is essential to take it into account for a suitable design of biomass thermochemical conversion technologies. Very recently, Xie et al. have reported on a novel form of the EL approach based on the so-called multiphase particle-in cell method where the effects of fluid drag, gravity, particle collision stress, static–dynamic friction, and other forces on each particle are considered. The model has been satisfactorily validated against gasification experimental data and allows predicting the composition of the producer gas and the carbon conversion efficiency.[120]

A key aspect of the CFD models for biomass conversion reactors refers to the rate of the chemical reactions taking place. Here a tradeoff has to be attained between reliability and computation power demand in order to handle kinetic models that describe the essential chemistry of the biomass transformation using a reasonable number of adjustable kinetic parameters and with acceptable simulation lengths until convergence is reached. In this regard, several approaches can be found in the literature.[121] For biomass pyrolysis, Boateng and Mtui[118] (Eqn (17.24)) and Sun et al.[116] (Eqn (17.25)) considered a single global reaction with a constant distribution of products and stoichiometric coefficients and/or mass fractions of volatiles taken from the literature or experimental studies:

$$\text{Biomass} \xrightarrow{k} \alpha_1\text{char} + \alpha_2\text{Bioil} + \alpha_3\text{H}_2\text{O} + \alpha_4\text{H}_2 + \alpha_5\text{CO} + \alpha_6\text{CO}_2 + \alpha_7\text{CH}_4 \tag{17.24}$$

$$\text{Biomass} \xrightarrow{k} \text{Char} + \text{Volatiles}\,(\text{Tar} + \gamma_1\text{CO} + \gamma_2\text{CO}_2 + \gamma_3\text{CH}_4 + \gamma_4\text{H}_2 + \gamma_5\text{C}_2\text{H}_4) \tag{17.25}$$

Papadakis et al.,[115] on the other hand, considered a more complex two-stage semiglobal model:

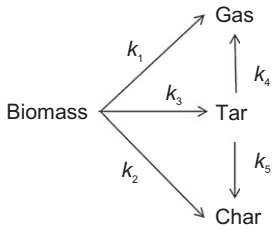

(17.26)

In the presence of a limited amount of an oxidizing agent as is the case of gasifiers, the species resulting from biomass cracking will further react to form new volatiles. Thus, in the CFD models of gasifiers, the following sets of homogeneous (gas phase) and heterogeneous (involving solids and gases) reactions are usually considered[113,122,123]:

Homogeneous reactions:

$$H_2 + \frac{1}{2}O_2 \rightarrow H_2O \quad (17.27)$$

$$CO + \frac{1}{2}O_2 \rightarrow CO_2 \quad (17.28)$$

$$CH_4 + 2O_2 \rightarrow CO_2 + 2H_2O \quad (17.29)$$

$$CH_4 + H_2O \rightarrow CO + 3H_2 \quad (17.30)$$

$$CO + H_2O \leftrightarrow CO_2 + H_2 \quad (17.31)$$

Heterogeneous reactions:

$$C + CO_2 \rightarrow 2CO \quad (17.32)$$

$$C + \frac{1}{2}O_2 \rightarrow CO \quad (17.33)$$

$$C + H_2O \rightarrow CO + H_2 \quad (17.34)$$

17.3.2.2 Anaerobic Fermentation

Biohydrogen production through anaerobic fermentation of organic substrates has been reviewed in Chapter 8. Its production is a complex combination of chemical, biological, and physical processes with numerous internal interactions between the gas, liquid, and solid phases that are present in the bioreactor. CFD is being increasingly used in this field because the information provided through process simulation about the velocity fields, distribution of shear stresses, turbulence, and volume fraction of each phase is crucial regarding the microbial activity and settling rate of the activated sludge. For example, Wang et al. have extensively studied by CFD different aspects of the hydrodynamics and kinetics of biohydrogen production in continuous stirred-tank reactors (CSTR) and expanded granular sludge beds (EGSB) in order to scale up and optimize these bioreactors.[124–127] An Eulerian–Eulerian multiphase approach was adopted to describe the behavior of the different phases. In the case of the CSTR, it was assumed that the water-activated sludge mixture is the continuous phase, whereas the biogas spherical bubbles constitute the dispersed phase. It was found that the geometry and speed of the reactor impeller affected the hydrogen yield. Although the uniformity of velocity distribution in the reactor is improved with the increase of impeller speed, the average yield of hydrogen does not continually increase because the shear strain stress and biogas volume fraction also increase and cause damage to microorganism cells and sludge flocs. For EGSB, the authors considered that both biogas bubbles and sludge granules/particulates were dispersed phases. The results indicated that an appropriate hydraulic retention time (HRT) is crucial to maximize biohydrogen production. At long HRTs a core-annulus structure is developed within the bed with back mixing and internal circulation. When the HRT is short, the high liquid upflow velocity and the lifting action of the biogas makes the flow pattern highly turbulent. As a result, sludge particle clusters were dragged, following the biogas bubbles, leading to lower biohydrogen yields.

17.3.3 Water Electrolysis

As discussed in Chapter 2, hydrogen can be produced by direct water electrolysis. Alkaline and proton-exchange membrane (PEM) technologies are commercially available whereas solid oxide electrolysis cells (SOEC) still need development mainly as regards long-term durability. Much of the work performed on CFD modeling of water electrolysis has focused on SOEC.

Hawkes et al.[128] have developed an electrochemical CFD model to investigate the high-temperature steam electrolysis in SOEC stacks constituted in the early work by 10 planar cells and extended later on to 60 planar cells. Simulations provided detailed temperature profiles, Nernst potentials, composition of the gases evolved at the electrodes, and current densities for different operating voltages. CFD predictions of the stack temperatures showed a net cooling effect of operating voltages lower than the thermoneutral one, and a net heating effect for higher voltages. Ni[129] investigated the effects of operating/structural parameters on heat/mass transfer and the electric characteristics of a planar SOEC. The effects of other factors such as gas

velocity and electrode microstructure (porosity, pore size) on SOEC performance were investigated. The electrode porosity showed small effect on SOEC performance. High electrode porosity facilitates the transport of gaseous species, tending to decrease the Nernst potential and thus increase current density. However, an increase in current density tends to increase the molar fractions of hydrogen and oxygen, which in turn limits the increase in local current density. The combined effects result in a small dependence of current density on electrode porosity. Accordingly, the temperature and velocity fields of the SOEC do not vary significantly with a change in electrode porosity. Laurencil et al.[130] have developed a 2D CFD model to investigate the performance of SOEC stacks. This model encompasses a combined electrochemical and thermal description of the water electrolyzer. Simulations showed that thermal equilibrium of the stack is strongly dependent on radiation heat losses. It was found that in order to avoid a too high-temperature increase, an operating condition close to the thermoneutral voltage is necessary.

17.4 CFD FOR INVESTIGATING HYDROGEN ENERGY END-USE APPLICATIONS

Fuel cells constitute the most important and promising energetic application of hydrogen. However, as discussed in this book (see Chapters 1 and 16), hydrogen-fueled internal combustion engines (H_2-ICEs) can be also relevant in some transportation sectors such as heavy-duty vehicles, mainly as transitional technology. Given the interest of these end-use applications, an overview of the potential of CFD for the analysis and design of fuel cells and H_2-ICEs is provided in this section.

17.4.1 Fuel Cells

The proton-exchange membrane fuel cell (PEMFC) and the SOFC are well-known technologies to generate electricity. As for the PEMFC the electrolyte is a polymeric membrane whereas in the SOFC it is a ceramic material or solid oxide. SOFC can sustain high operating temperatures and consequently may provide a high reaction rate and high conversion efficiency. Moreover, there is great interest in using high-temperature reformate streams generated from thermochemical conversion processes directly as fuel of SOFCs thus avoiding costly separation and purification steps. On the other hand, PEMFCs present the advantages of low operating temperatures (50−100 °C), lower cost and volume, and easier startup that make it more suitable for use in electric vehicles and portable devices.

CFD modeling and simulation of PEMFCs and SOFCs are being carried out in order to better understand the fundamental processes taking place and optimize fuel cell designs. The mathematical models describing fuel cells performance have to include the electrochemical reactions on the corresponding electrodes, the transport of active species through the porous electrolyte or polyelectrolyte membrane and gaseous diffusion layers (GDLs), and the equations for mass, energy, and momentum conservation.[131] The complexity of some of the phenomena involved requires that some simplifications have to be made. As concerns the electrochemical model, due to the internal resistance and polarization, the cell voltages are lower than the ideal ones. One can account for the anode and cathode activation polarizations using the Butler−Volmer equation. The CFD studies existing in the literature usually consider that some polarizations losses can be neglected, although in some cases they are completely neglected. Gas transport through porous media or layers is important because at the high operating current densities the performance of fuel cells can be limited by mass transport. The diffusion of chemical species through porous electrodes is described adopting one of the following approaches: (1) the Fick law model. It is the simplest diffusion model and is used for dilute or binary systems; (2) the Stefan−Maxwell model, which is more commonly used in multicomponent systems for the calculation of species fluxes; (3) the Dusty Gas model. It is an extension of the Stefan−Maxwell model and constitutes the most complete diffusion model considering molecule−molecule and molecule−wall interactions in the porous media. It also takes into account Knudsen diffusion phenomena. Darcy's equation has been used by several researchers to calculate the pressure drop in porous media. Pressure drops in both the anode and cathode sides were neglected by some authors. With respect to heat transfer, the majority of the studies on PEMFCs assumed isothermal conditions, whereas in the case of SOFCs, heat management becomes a key factor.

17.4.1.1 Proton-Exchange Membrane Fuel Cells

The electrochemical model has to account for the generation of protons from the hydrogen at the anode that are transferred through the electrolyte membrane to the cathode where they react with oxygen producing water, which in the majority of studies is considered to be present as vapor. The presence of the so-called GDLs limit the transport of reactants and products. In what follows we will refer to some representative CFD studies published in the open literature.

Ferng and Su have investigated the effects of different flow channel designs on the performance of PEMFCs through 3D CFD simulations.[132] The channel designs included parallel and serpentine flow arrangements,

single-path and multipath flow channels, and uniform depth and stepwise depth flow channels. The performance of a PEMFC with the serpentine flow channel is superior to that with the parallel flow channel. In addition, the behavior of a PEMFC with the parallel flow channel is significantly influenced by the channel design. In this regard, the performance of a fuel cell with channels of stepwise depths is superior to that of a uniform depth. The simulation results were confirmed experimentally.

Rismannchi and Akbari have developed a 3D model of a PEMFC that allowed reproducing the experimental cell behavior (e.g. polarization curves) over a range of operating conditions, varying some parameters closely linked to gaseous reactant diffusion in both GDL.[133] The numerical results rightfully indicate that by decreasing the cell voltage, current density will increase and reach a limit produced by the resistance to reactant diffusion through the gas diffusion and catalyst layers. Kamarajugadda and Mazumder focused their study on the agglomerates formed in the catalyst.[134] A generalized flooded agglomerate model that was implemented into CFD codes founding that when cathodes are comprised of agglomerates of intersecting spheres result in a better overall fuel cell performance than cathodes comprised of agglomerates of individual spheres of the same equivalent volume. This is a manifestation of the improvement in the oxygen reduction rate at the agglomerate scale due to an increased surface-area-to-volume ratio. Su et al. have developed a 3D nonisothermal CFD model to predict polarization curves and local data to be acquired with microsensors.[135] A good agreement between experimental and simulated values was found. The ionic conductivity increases with the water content of the membrane, thus enhancing the cell performance. The positive effect of inlet fuel humidity on the cell performance found experimentally was also captured by the CFD simulation model.

Water management is a key factor of PEMFC operation that determines cell performance. During operation, the anode side of the membrane is dehydrated by the electroosmotic drag (EOD), while the cathode side is flooded by the EOD and water generation from the oxidation–reduction reaction. Eventually, it becomes necessary to prevent dehydration at the anode and flooding at the cathode in order to preserve high proton conductivity and the clearance of liquid water from the fuel passage to the catalytic surface. In the past years some works taking into account the saturation of water and its transport have been published. For example, Berning et al. modeled the water transport across the membrane as a constant EOD with a diffusion coefficient of water in the electrolyte phase.[136] It was found that the overall water balance can depend strongly on the specific surface area of the electrolyte in the catalyst layers. The net drag coefficient alone defines which side of the electrolyte membrane becomes dehydrated. On the other hand, the membrane water content was not always at its maximum when both gases enter the cell fully humidified. Anode liquid water was found only at high current densities and for high values of the specific surface area of the electrolyte in the catalyst layers. The comparison between multiphase and multispecies models reveals that flooding effects are important to estimate cell performance, especially at high current density where transport issues become more evident.[137]

Yung et al. have reported on a very interesting and novel CFD study taking into account the three-phase water transport.[138] Two parametric studies are presented and discussed in detail: (1) varying compositions in the catalyst layer, and (2) varying channel-to-shoulder ratios (CSRs) in the flow-field design. Regarding the catalyst layer, the Nafion loaded in catalyst formulation was increased, showing that the mass transport limitation is anticipated because of the decreased porosity in the layer. The catalyst layer thickness was also varied using different coating methods worsening the cell performance because of the lowered porosity. An increase of the Pt content was accompanied by little performance improvement. As concerns the CSR, when it was increased, the mass transport limitations were alleviated because improved supply of oxygen. Cell designs with a high CSR had a better liquid water removal performance. On the other hand, it should be taken into account that a high CSR can also cause increased ohmic losses. In a recent work by Chiu et al. it was considered that water produced at the cathode could condense in the porous catalytic layer having consequences on cell performance.[139] The authors found that the interdigitated flow was most effective on liquid water removal and cell performance than serpentine or parallel flow fields.

17.4.1.2 *Solid Oxide Fuel Cells*

SOFCs are generally more tolerant to contaminants than other fuel cells and the possibility to internally (as well as externally) reform the hydrocarbon fuels make them interesting for renewable energy resources. Besides that, the advantages of this class of fuel cells include high efficiency, fuel flexibility, and relatively low cost. The largest disadvantage is the high operating temperature, which results in longer startup times and mechanical and chemical compatibility issues. Validated models are necessary to understand various transport processes and reactions for improving the cell performance. Since the species and temperature distributions within the cell are not easy to measure, numerical simulations are being increasingly employed to understand the experimental evidence and to steer cell optimization. It should be noted that CFD models make it possible to reduce the amount of experimental tests needed for cell development.

With respect to the electrochemical model it is necessary to consider that at the cathode side oxide anions (O^{2-}) are generated that migrate through the crystal lattice. Hydrogen and/or carbon monoxide in the fuel stream react at the anode with oxide ions from the electrolyte to produce water or CO_2. Due to the high operating temperatures, water is in the gaseous state and is much more easily removed than in PEMFCs. It is also essential to develop heat transfer models that could account for various heat effects in both the solid structure and flow channels. However, many researchers have assumed isothermal operation in their studies. Temperature strongly affects the fuel cell system. Under nonisothermal conditions the voltage response is slow in comparison with isothermal operation. Heat management clearly plays an important role to minimize the temperature gradients and the hot spots within the SOFC. The temperature distribution is not easy to determine experimentally; therefore, the availability of a reliable numerical tool becomes very useful.

Studies of 2D or 3D models with various configurations and geometries have been published for the distribution of temperatures in either tubular or planar cell types.

For instance, a model has been applied to study the temperature field in an SOFC and its components along and across the cell at different loads.[140] Qu et al. predicted the temperature distribution within an anode-supported planar SOFC with corrugated bipolar plates.[141] They found critical locations in the cell where current density and electric potential are at the local minimum. Furthermore, the temperature gradients at these locations are the highest and structural analyses should be carried out to reveal their implications regarding materials and cell degradation. Therefore, it is strongly recommended to perform thermal structural analyses when designing SOFC stacks. Peksen performed a 3D thermomechanical analysis of a 36-layer planar SOFC stack.[142] The locations susceptible to mechanical stress within the fuel stack could be determined.

Serincan et al. presented a parametric sensitivity analysis of a microtubular SOFC to investigate the effects of operating parameters such as temperature, flow rate, fuel composition, and pressure of the gas chambers on the fuel cell performance.[143] The most significant effects of the operating temperature are on the kinetics of the reactions and the ionic conductivity of the electrolyte. Also an increase of the gas diffusion coefficients is produced. The performance of the cell also improves with the temperature. The properties for the cell components were taken from an experimental microtubular cell composed of Gd-doped CeO_2 electrolyte. A common problem with ceria-based electrolytes is that they can be reduced under fuel cell operating conditions, consequently becoming electronically conductive, which results in electron transfer from the anode to the cathode through the electrolyte. As a result the cell is short circuited and a drop in open circuit voltage is observed. This phenomenon is referred to as the "internal current leak", and the model is capable of capturing this behavior of the system that is more important at high temperatures.

García-Camprubí et al. developed an in-house algorithm implemented in an open-source CFD platform to investigate the anode-supported microtubular SOFC.[144] This is one of the promising new cell design offering high thermal shock resistance, rapid startup, lower operating temperatures, higher power densities, and simpler seal requirements. It was found that mass transport and heat management become critical during the operation of such microtubular cells, since the high power density enhances Joule heating and the thick anode hinders the supply of the reactants to the reaction sites.

In the majority of CFD studies, the contribution of radiation to thermal effects is not taken into account. VanderSteen and Pharoah found that radiation contribution reduces the peak and gradients of temperature in the planar fuel cells.[145] This results in a fairly uniform temperature field within the fuel cell system. The effect of radiation was likely to be more important in tubular geometries.

SOFCs enable internal reforming of hydrocarbons with relatively short carbon chains. Vakouftsi et al. developed a 3D CFD model for a planar SOFC fueled by biogas/steam mixtures.[146] Janardhanan and Deutschmann presented a chemical and electrochemical analysis of an internally reforming anode-supported SOFC fueled by humidified CH_4 (3% H_2O)[147] and Huang et al. presented an interesting study on flow uniformity provided by various interconnects in a planar SOFC fed by syngas.[148]

Andersson et al. investigated the influence of the ion and electron transport resistance within the anode and cathode by solving a fully coupled CFD model including the governing equations for heat, mass, momentum, ion and electron transport as well as chemical kinetics of the internal reforming reactions of the fuel and the electrochemical reactions involved in an intermediate temperature SOFC single cell.[149] Heat generated within the cell can be used for the internal steam reforming reaction within the anode and/or outside the cell for external reforming and preheating of the fuel and air. The cell current density can be increased by increasing the operating temperature; however, a too high maximum temperature or temperature gradient decreases the cell lifetime.

Recently, Kattke et al. have performed an interesting study of an integrated tubular SOFC system with an output power range of 500−1000 W for small mobile applications.[150] The system includes a tubular SOFC stack (66 tubes), catalytic partial oxidation (CPOx) for

fuel reforming and tail-gas combustor (TGC). Submodels for the CPOx, TGC, and electrochemical tubular cell were defined and integrated in the CFD model through user-defined functions. Stack cooling predominately occurred at the external surface of the tubes where radiation accounted for 66–92% of heat transfer. Nonuniformities within the stack led to power differences among cells (from 7.6 to 10.8 W). It was therefore recommended that tubular stacks should be configured in such a way that the variation of the view factors from individual cells to the stack surroundings is minimal.

17.4.2 H_2-Fueled Internal Combustion Engines (H_2-ICEs)

The current status of H_2-ICEs has been reviewed in Chapter 16. CFD simulations are one of the most interesting tools to analyze complex processes such as the in-cylinder combustion. In the recent years, CFD has started to be used in the study of diesel and spark-ignition engines, mostly in relation to the development of combustion models. One of the first CFD applications was performed by Johnson.[151] Models of the different aspects of the engine cycle are proposed based on previous models used in traditional internal combustion engines, and are compared to experimental data, with quite a good agreement. Modeling of the nitrogen oxides (NO_x) formation is also included, using the standard Zeldovich model, which is still the most applied for describing NO_x formation in combustion processes. The aim of the study was to apply those models and validate them. Liu et al. proposed a similar approximation to the problem and focused on backfire and preignition of the mixture, two of the main issues of H_2-ICEs.[152] Some relevant results were found, such as the dependence of backfire on the residual hydrogen concentration at the intake ports. A very interesting study was carried out by Knop et al. in which a new combustion model was proposed and compared with previous approaches in order to establish possible ways for reducing NO_x formation.[153] On the other hand, recent works by Rakopoulos et al. have considered the development and evaluation of combustion and heat transfer models, NO_x emissions and exhaust gas recirculation (EGR).[154–156] These papers show interesting results, such as the high efficiency achieved by the H_2-ICE or that under high EGR rates, up to 50%, the combustion becomes much slower. It can be concluded that although some work has been carried out that includes CFD simulations for the development of H_2-ICEs, there are still many areas where the application of this tool can achieve a significant impact regarding safety, engine performance, and pollution reduction.

The density of hydrogen is much smaller than that of air, which has important implications from the point of view of the formation of combustible mixtures. Various CFD studies have revealed that due to the fact that hydrogen combustion is very sensitive to the composition, the hydrogen injection procedures have critical effects on the quality of the hydrogen/air mixtures and then on the engine performance, having consequences on combustion spreading, laminar flame speed, temperature profiles, and NO_x formation.[153,157]

Our research group is also working on the adaptation of internal combustion engines to run on hydrogen.[158–160] CFD simulations have been conducted in order to establish the hydrogen content of the stream entering the cylinder in a naturally aspirated gaseous port hydrogen injection system. The port fuel injection system considered was that of the Volkswagen Polo 1.4 vehicle in which the gasoline injectors were substituted by hydrogen injectors. The aim of the study was to investigate the effect of the engine speed (ω), air-to-hydrogen equivalence ratio (λ) and injection timing (θ, crank angle or advance angle referred to the top dead center). Figure 17.10(a) shows the geometry of the fluidic domain,

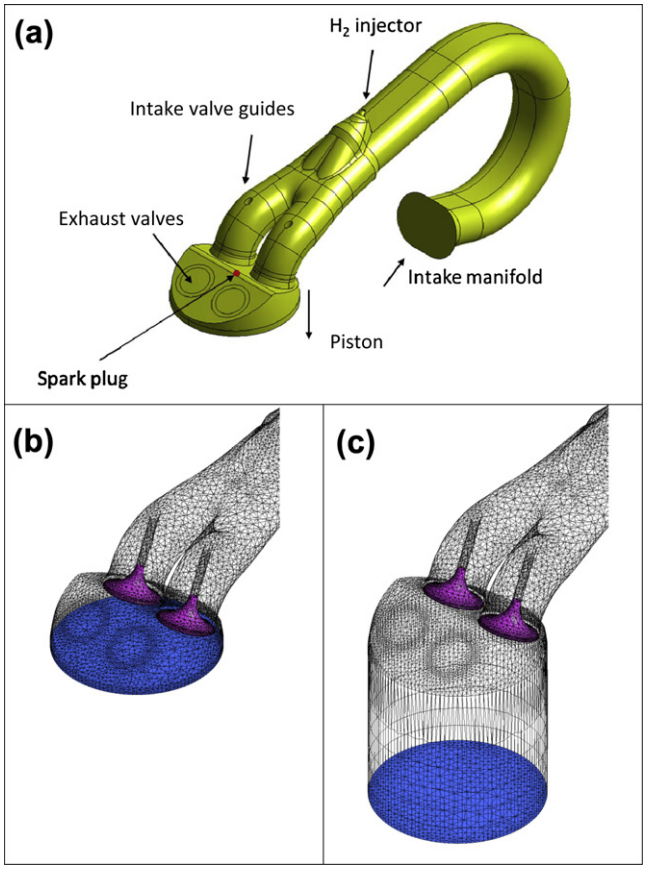

FIGURE 17.10 Geometry of the fluidic domain of a spark ignition engine port fuel injection system (a), and meshes of the geometry with the piston at the top dead center (b), and in motion (c). (For color version of this figure, the reader is referred to the online version of this book.)

including the intake manifold and intake valves guides; the positions of the spark plug, hydrogen injector, and valves are also indicated. One of the characteristics of this CFD model is that the meshes should be mobile in order to describe the piston and valves motion (Figs 17.10(b) and (c)). During the intake stroke, the piston descends and the valves complete an opening and closing cycle. Representative results are shown in Fig. 17.11 that shows the evolution of the hydrogen mass fraction in the hydrogen/air mixture. The amount of hydrogen injected in this case was 3.9 mg, corresponding to $\lambda = 1.7$, and the injector started to open at $\theta = 16°$. The results shown cover 18.06 ms, corresponding to 195° of crank angle at $\omega = 1800$ rpm. It can be seen that the hydrogen concentration is much higher near the injection point. The hydrogen concentration decreases as

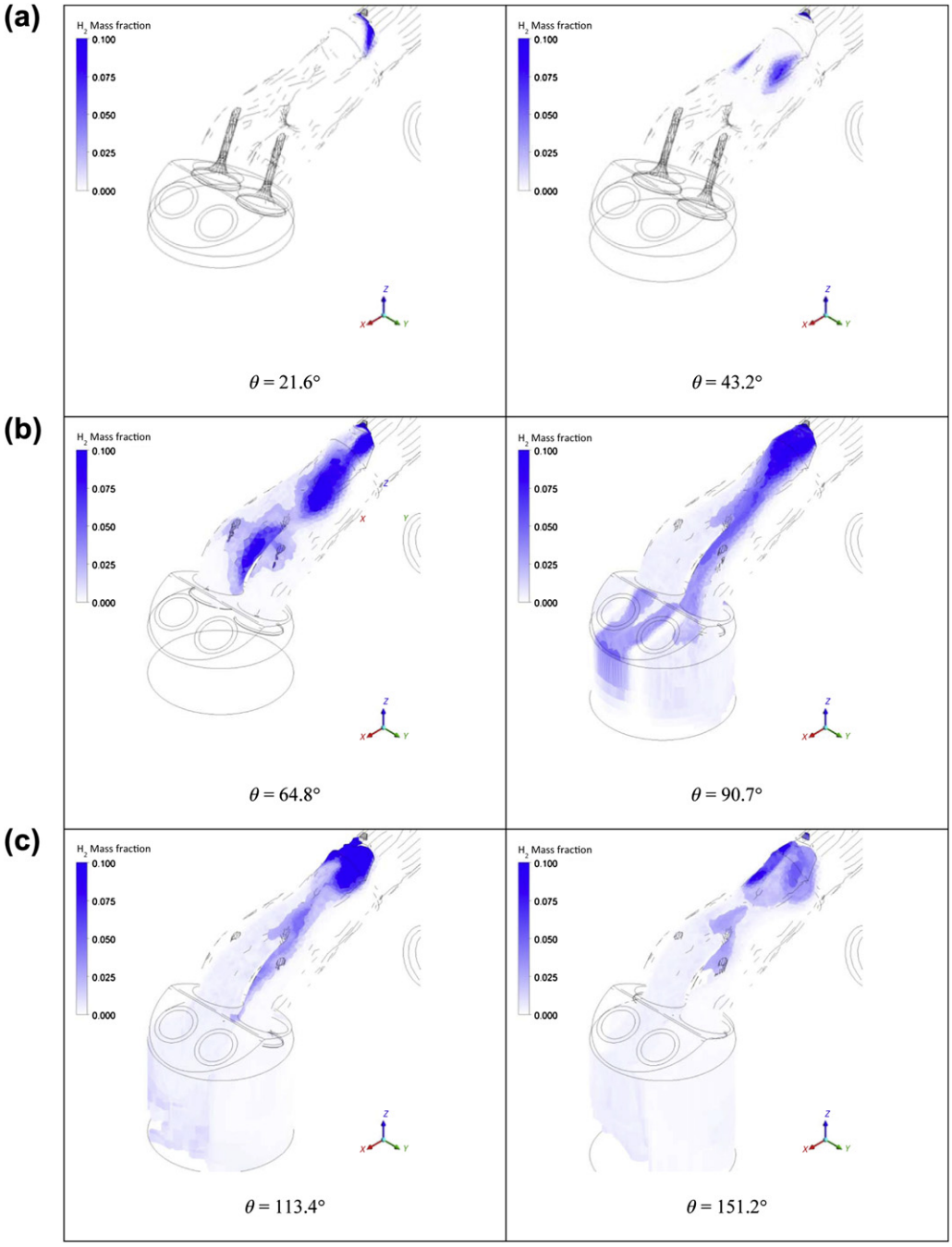

FIGURE 17.11 Geometry of the fluidic domain of a port fuel injection system (a) and meshes of the geometry with the piston at top dead center (b) and in motion (c). (For color version of this figure, the reader is referred to the online version of this book.)

mixing with air takes place until achieving a relatively homogeneous composition. These simulations are useful to establish injection strategies that improve the engine performance.

17.5 CONCLUSIONS

This chapter has tried to evidence the enormous potential of CFD for making a valuable contribution to the development of hydrogen technologies. Emphasis has been put on hydrogen production through thermochemical conversion processes and hydrogen end use in fuel cells and internal combustion engines because these areas are the subject of the majority of the work published in the open literature. Nevertheless, the use of CFD in other relevant fields such as hydrogen storage or hydrogen production through biological routes, thermal and photocatalytic water splitting, and water electrolysis is now starting and it can be expected that will become significant in the coming years.

CFD is a modeling and simulation tool useful for the analysis, design, optimization, and scaleup of process equipment. The number of commercially available CFD codes is high, which is contributing to the spread of its use in both the academia and the industry. CFD is also helpful for assisting the understanding of the behavior of the physical system under study. It is important to bear in mind that CFD cannot replace experimentation. Moreover, a CFD model is useful only if it has been fully validated against high-quality experimental results. In this regard, it should be also noted that although commercial codes reliably solve the transport equations, they have a number of limitations as regards the description of chemical and biological transformations and the physics of complex systems such as the multiphase flow. On the other hand, there are also capacity limits so a tradeoff has to be permanently maintained between the depth of the system description and the computational power demand. For these reasons, it is important not only to expand the range of CFD applications but also revise and improve the existing models and develop more robust codes capable of better capturing the physics and chemistry of the several phenomena of general technological interest.

Acknowledgments

The financial support by the Spanish Ministry of Science and Innovation and Ministry of Economy and Competitiveness (ENE2009-14522-C04 and ENE2012-37431-C03 grants, respectively) is gratefully acknowledged. I. Uriz gratefully acknowledges the fellowships granted by the Innovation Department of the Navarre Government and the Spanish Ministry of Science and Innovation (program FPI, BES-2010-030021).

References

1. Bakker, A.; Haidari, A. H.; Oshinowo, L. M. Realize Greater Benefits from CFD. *Chem. Eng. Prog.* **March 2001,** 45.
2. Paschedag, A. R. *Computational Fluid Dynamics in Ullmann's Modeling and Simulation;* Wiley-VCH: Weinheim, 2007.
3. Fletcher, C. A. J. *Computational Techniques for Fluid Dynamics;* Springer-Verlag: Berlin, 1991.
4. Anderson, J. D., Jr. *Computational Fluid Dynamics;* McGraw-Hill: New York, 1995.
5. Versteeg, H. K.; Malalasekera, W. *An Introduction to Computational Fluid Dynamics;* Pearson Education Ltd.: Harlow, UK, 1995.
6. Tannehill, J. C.; Anderson, D. A.; Pletcher, R. H. *Computational Fluid Mechanics and Heat Transfer;* Taylor & Francis: Philadelphia, PA, 1997.
7. Ferziger, J. H.; Perić, M. *Computational Methods for Fluid Dynamics;* Springer: Berlin, 2002.
8. Chung, T. J. *Computational Fluid Dynamics;* Cambridge University Press: Cambridge, UK, 2002.
9. Lomax, H.; Pulliam, T. H.; Zingg, D. W. *Fundamentals of Computational Fluid Dynamics;* Springer-Verlag: Berlin, 2003.
10. Blazek, J. *Computational Fluid Dynamics: Principles and Applications;* Elsevier: Amsterdam, 2005.
11. Cebeci, T.; Shao, J. P.; Kafyeke, F.; Laurendeau, E. *Computational Fluid Dynamics for Engineers;* Springer: Long Beach, CA, 2005.
12. Date, A. W. *Introduction to Computational Fluid Dynamics;* Cambridge University Press: New York, 2005.
13. Madenci, E.; Guven, I. *The Finite Element method and Applications in Engineering Using ANSYS®;* Springer: New York, 2006.
14. Prosperetti, A.; Tryggvason, G. *Computational Methods for Multiphase Flow;* Cambridge University Press: Cambridge, 2007.
15. Moaveni, S. *Finite Element Analysis. Theory and Application with ANSYS;* Pearson Education International: Upper Saddle River, NJ, 2008.
16. Tu, J.; Yeoh, G. H.; Liu, Ch. *Computational Fluid Dynamics. A Practical Approach;* Elsevier: Amsterdam, 2008.
17. Bakker, A.; Haidari, A. H.; Marshall, E. M. Design Reactors via CFD. *Chem. Eng. Prog.* **December 2001,** 30.
18. Fox, R. O. CFD Models for Analysis and Design of Chemical Reactors. *Adv. Chem. Eng.* **2006,** *31,* 231.
19. Bird, R. B.; Stewart, W. E.; Lightfoot, E. N. *Transport Phenomena;* John Wiley & Sons: Hoboken, NJ, 2002.
20. Van den Akker, H. E. A. The Details of Turbulent Mixing Process and Their Simulation. *Adv. Chem. Eng.* **2006,** *31,* 151–229.
21. Wang, M.; Lan, X.; Li, Z. Analyses of Gas Flows in Micro- and Nanochannels. *Int. J. Heat Mass Transfer* **2008,** *51,* 3630.
22. Bird, G. A. *Molecular Gas Dynamics and the Direct Simulation of Gas Flows;* Oxford Science Publications: Oxford, UK, 1994.
23. Arzamendi, G.; Diéguez, P. M.; Montes, M.; Centeno, M. A.; Odriozola, J. A.; Gandía, L. M. Integration of Methanol Steam Reforming and Combustion in a Microchannel Reactor for H_2 Production: A CFD Simulation Study. *Catal. Today* **2009,** *143,* 25.
24. Arzamendi, G.; Diéguez, P. M.; Montes, M.; Odriozola, J. A.; Falabella Sousa-Aguiar, E.; Gandía, L. M. Methane Steam Reforming in a Microchannel Reactor for GTL Intensification: A Computational Fluid Dynamics Simulation Study. *Chem. Eng. J.* **2009,** *154,* 168.
25. Arzamendi, G.; Uriz, I.; Diéguez, P. M.; Laguna, O. H.; Hernández, W. Y.; Álvarez, A.; Centeno, M. A.; Odriozola, J. A.; Montes, M.; Gandía, L. M. Selective CO Removal over Au/CeFe and CeCu Catalysts in Microreactors Studied through Kinetic Analysis and CFD Simulations. *Chem. Eng. J.* **2011,** *167,* 588.
26. Uriz, I.; Arzamendi, G.; López, E.; Llorca, J.; Gandía, L. M. Computational Fluid Dynamics Simulation of Ethanol Steam Reforming in Catalytic Wall Microchannels. *Chem. Eng. J.* **2011,** *167,* 603.

27. Arzamendi, G.; Uriz, I.; Navajas, A.; Diéguez, P. M.; Gandía, L. M.; Montes, M.; Centeno, M. A.; Odriozola, J. A. A CFD Study on the Effect of the Characteristic Dimension of Catalytic Wall Microreactors. *AIChE J.* **2012,** *58,* 2785.
28. Dixon, A. G.; Nijemeisland, M. CFD as a Design Tool for Fixed-Bed Reactors. *Ind. Eng. Chem. Res.* **2001,** *40,* 5246.
29. Dixon, A. G.; Nijemeisland, M.; Stitt, E. H. Packed Tubular Reactor Modeling and Catalyst Design Using Computational Fluid Dynamics. *Adv. Chem. Eng.* **2006,** *31,* 307.
30. Rase, H. F. *Fixed-Bed Reactor Design and Diagnostics;* Butterworth Publishers: Stoneham, MA, 1990.
31. Calis, H. P. A.; Nijenhuis, J.; Paikert, B. C.; Dautzenberg, F. M.; van den Bleek, C. M. CFD Modelling and Experimental Validation of Pressure Drop and Flow Profile in a Novel Structured Catalytic Reactor Packing. *Chem. Eng. Sci.* **2001,** *56,* 1713.
32. Logtenberg, S. A.; Nijemeisland, M.; Dixon, A. G. Computational Fluid Dynamics Simulations of Fluid Flow and Heat Transfer at the Wall−Particle Contact Points in a Fixed-Bed Reactor. *Chem. Eng. Sci.* **1999,** *54,* 2433.
33. Nijemeisland, M.; Dixon, A. G. Comparison of CFD Simulations to Experiment for Convective Heat Transfer in a Gas−Solid Fixed Bed. *Chem. Eng. J.* **2001,** *82,* 231.
34. Dixon, A. G.; Nijemeisland, M.; Stitt, E. H. CFD Simulation of Reaction and Heat Transfer Near the Wall of a Fixed Bed. *Int. J. Chem. React. Eng.* **2003,** *1,* A22.
35. Nijemeisland, M.; Dixon, A. G. CFD Study of Fluid Flow and Wall Heat Transfer in a Fixed Bed of Spheres. *AIChE J.* **2004,** *50,* 906.
36. Nijemeisland, M.; Dixon, A. G.; Stitt, E. H. Catalyst Design by CFD for Heat Transfer and Reaction in Steam Reforming. *Chem. Eng. Sci.* **2004,** *59,* 5185.
37. Dixon, A. G.; Taskin, M. E.; Nijemeisland, M.; Stitt, E. H. Wall-to-Particle Heat Transfer in Steam Reformer Tubes: CFD Comparison of Catalyst Particles. *Chem. Eng. Sci.* **2008,** *63,* 2219.
38. Taskin, M. E.; Dixon, A. G.; Nijemeisland, M.; Stitt, E. H. CFD Study of the Influence of Catalyst Particle Design on Steam Reforming Reaction Heat Effects in Narrow Packed Tubes. *Ind. Eng. Chem. Res.* **2008,** *47,* 5966.
39. Dixon, A. G.; Taskin, M. E.; Stitt, E. H.; Nijemeisland, M. 3D CFD Simulations of Steam Reforming with Resolved Intraparticle Reaction and Gradients. *Chem. Eng. Sci.* **2007,** *62,* 4963.
40. Dixon, A. G.; Taskin, M. E.; Nijemeisland, M.; Stitt, E. H. Systematic Mesh Development for 3D CFD Simulation of Fixed Beds: Single Sphere Study. *Comput. Chem. Eng.* **2011,** *35,* 1171.
41. Dixon A. G.; Nijemeisland M.; Stitt E. H. Systematic Mesh Development for 3D CFD Simulation of Fixed Beds: Contact Points Study, *Comput. Chem. Eng.* DOI:10.1016/j.compchemeng.2012.08.011.
42. Dixon, A. G.; Walls, G.; Stannes, H.; Nijemeisland, M.; Stitt, E. H. Experimental Validation of High Reynolds Number CFD Simulations of Heat Transfer in a Pilot-Scale Fixed Bed Tube. *Chem. Eng. J.* **2012,** *200−202,* 344.
43. Behnam, M.; Dixon, A. G.; Wright, P. M.; Nijemeisland, M.; Stitt, E. H. Comparison of CFD Simulations to Experiment under Methane Steam Reforming Reaction Conditions. *Chem. Eng. J.* **2012,** *207−208,* 690.
44. Magnico, P. Hydrodynamic and Transport Properties of Packed Beds in Small Tube-to-Sphere Diameter Ratio: Pore-Scale Simulation Using and Eulerian and a Lagrangian Approach. *Chem. Eng. Sci.* **2003,** *58,* 5005.
45. Magnico, P. Pore-Scale Simulations of Unsteady Flow and Heat Transfer in Tubular Fixed Beds. *AIChE J.* **2009,** *55,* 849.
46. Sadeghi, M. T.; Molaei, M. CFD Simulation of a Methane Steam Reforming Reactor. *Int. J. Chem. React. Eng.* **2008,** *6,* A50.
47. De Wilde, J.; Froment, G. F. Computational Fluid Dynamics in Chemical Reactor Analysis and Design: Application to the ZoneFlow™ Reactor for Methane Steam Reforming. *Fuel* **2012,** *100,* 48.
48. Fukahori, S.; Koga, H.; Kotaoka, T.; Nakamura, M.; Wariishi, H. Steam Reforming Behavior of Methanol Using Paper-Structured Catalysts: Experimental and Computational Fluid Dynamic Analysis. *Int. J. Hydrogen Energy* **2008,** *33,* 1661.
49. Arteaga, L. E.; Peralta, L. M.; Casas, Y.; Castro, D. Optimal Design, Modeling and Simulation of an Ethanol Steam Reforming Reactor. *Int. J. Chem. React. Eng* **2009,** *7,* A59.
50. Neri, A.; Gidaspow, D. Riser Hydrodynamics: Simulation Using Kinetic Theory. *AIChE J.* **2000,** *46,* 52.
51. Lim, K. S.; Zhu, J. X.; Grace, J. R. Hydrodynamics of Gas−Solid Fluidization. *Int. J. Multiphase Flow* **1995,** *21,* 141.
52. Kunii, D.; Levenspiel, O. Circulating Fluidized-Bed Reactors. *Chem. Eng. Sci.* **1997,** *52,* 2471.
53. Adris, A. M.; Elnashaie, S. S. E. H.; Hughes, R. A Fluidized Bed Membrane Reactor for the Steam Reforming of Methane. *Can. J. Chem. Eng.* **1991,** *69,* 1061.
54. Adris A. M.; Boyd T.; Bereton C.; Grace J. R.; Lim C. J.; Wolfs W. Production of Pure Hydrogen by the Fluidized Bed Membrane Reactor. In *Proc. 14th World Hydrogen Energy Conference*, Montreal, 2002.
55. Roy, S.; Pruden, B. B.; Adris, A. M.; Grace, J. R.; Lim, C. J. Fluidized-Bed Steam Methane Reforming with Oxygen Input. *Chem. Eng. Sci.* **1999,** *54,* 2095.
56. Prasad, P.; Elnashaie, S. S. E. H. Novel Circulating Fluidized-Bed Membrane Reformer for the Efficient Production of Ultra-clean Fuels from Hydrocarbons. *Ind. Eng. Chem. Res.* **2002,** *41,* 6518.
57. Chen, Z.; Elnashaie, S. S. E. H. Bifurcation Behavior and Efficient Hydrogen Production for Fuel Cells Using a Novel Autothermic Membrane Circulating Fluidized-Bed (CFB) Reformer: Sequential Debottlenecking and the Contribution of John Grace. *Ind. Eng. Chem. Res.* **2004,** *43,* 5449.
58. Adris, A. M.; Lim, C. J.; Grace, J. R. The Fluidized-Bed Membrane Reactor for Steam Methane Reforming: Model Verification and Parametric Study. *Chem. Eng. Sci.* **1997,** *52,* 1609.
59. Mousa, M. B. M.; Fateen, S.-E. K.; Ibrahim, E. A. Hydrodynamic Characteristics of a Novel Circulating Fluidized Bed Steam Reformer Operating in the Fast Fluidization Regime. *Int. J. Chem. React. Eng.* **2011,** *9,* A104.
60. Xie, D.; Lim, C. J.; Grace, J. R.; Adris, A.-E. M. Gas and Particle Circulation in an Internally Circulating Fluidized Bed Membrane Reactor Cold Model. *Chem. Eng. Sci.* **2009,** *64,* 2599.
61. Lindborg, H.; Lysberg, M.; Jakobsen, H. A. Practical Validation of the Two-Fluid Model Applied to Dense Gas−Solid Flows in Fluidized Beds. *Chem. Eng. Sci.* **2007,** *62,* 5854.
62. Goldschmidt, M. J. V.; Beetstra, R.; Kuipers, J. A. M. Hydrodynamic Modelling of Dense Gas-Fluidised Beds: Comparison and Validation of 3D Discrete Particle and Continuum Models. *Powder Technol.* **2004,** *142,* 23.
63. Lindborg, H.; Jakobsen, H. A. Sorption Enhanced Steam Methane Reforming Process Performance and Bubbling Fluidized Bed Reactor Design Analysis by Use of a Two-Fluid Model. *Ind. Eng. Chem. Res.* **2009,** *48,* 1332.
64. Wang, Y.; Chao, Z.; Jakobsen, H. A. CFD Modelling of CO_2 Capture in the SE-SMR Process in the Fluidized Bed Reactors. *Chem. Eng. Trans.* **2010,** *21,* 601.
65. Dou, B.; Dupont, V.; Williams, P. T. Computational Fluid Dynamics Simulation of Gas−Solid Flow during Steam Reforming of Glycerol in a Fluidized Bed Reactor. *Energy Fuels* **2008,** *22,* 4102.
66. Dou, B.; Song, Y. A CFD Approach on Simulation of Hydrogen Production from Steam Reforming of Glycerol in a Fluidized Bed Reactor. *Int. J. Hydrogen Energy* **2010,** *35,* 10271.

67. Subramani, V.; Sharma, P.; Zhang, L.; Liu, K. Catalytic Steam Reforming Technology for the Production of Hydrogen and Syngas. In *Hydrogen and Syngas Production and Purification Technologies;* Liu, K., Song, C., Subramani, V., Eds.; AIChE — John Wiley & Sons: Hoboken (NJ), 2010; p 109.
68. Kolb, G. *Fuel Processing for Fuel Cells;* Wiley-VCH: Weinheim, 2008.
69. Cao, C.; Wang, Y.; Rozmiarek, R. T. Heterogeneous Reactor Model for Steam Reforming of Methane in a Microchannel Reactor with Microstructured Catalysts. *Catal. Today* **2005,** *110,* 92.
70. Yuan, J.; Ren, F.; Sundén, B. Analysis of Chemical-Reaction-Coupled Mass and Heat Transport Phenomena in a Methane Reformer Duct for PEMFCs. *Int. J. Heat Mass Transfer* **2007,** *50,* 687.
71. Stefanidis, G. D.; Vlachos, D. G. Millisecond Methane Steam Reforming via Process and Catalyst Intensification. *Chem. Eng. Technol.* **2008,** *31,* 1201.
72. Stefanidis, G. D.; Vlachos, D. G.; Kaisare, N. S.; Maestri, M. Methane Steam Reforming at Microscales: Operation Strategies for Variable Power Output at Millisecond Contact Times. *AIChE J.* **2009,** *55,* 180.
73. Mettler, M. S.; Stefanidis, G. D.; Vlachos, D. G. Enhancing Stability in Parallel Plate Microreactor Stacks for Syngas Production. *Chem. Eng. Sci.* **2011,** *66,* 1051.
74. Irani, M.; Alizadehdakhel, A.; Pour, A. N.; Hoseini, N. CFD Modeling of Hydrogen Production Using Steam Reforming of Methane in Monolith Reactors: Surface or Volume-Base Reaction Model? *Int. J. Hydrogen Energy* **2011,** *36,* 15602.
75. Zhai, X.; Ding, S.; Cheng, Y.; Jin, Y.; Cheng, Y. CFD Simulation with Detailed Chemistry of Steam Reforming of Methane for Hydrogen Production in an Integrated Micro-Reactor. *Int. J. Hydrogen Energy* **2010,** *35,* 5383.
76. Vaccaro, S.; Malangone, L.; Ciambelli, P. Modelling of a Catalytic Micro-Reactor Coupling Endothermic Methane Reforming and Combustion. *Int. J. Chem. React. Eng.* **2010,** *8,* A51.
77. Quiceno, R.; Pérez-Ramírez, J.; Warnatz, J.; Deutschmann, O. Modeling the High-Temperature Catalytic Partial Oxidation of Methane over Platinum Gauze: Detailed Gas-Phase and Surface Chemistries Coupled with 3D Flow Field Simulations. *Appl. Catal. A* **2006,** *303,* 166.
78. Stutz, M. J.; Poulikakos, D. Effects of Microreactor Wall Heat Conduction on the Reforming Process of Methane. *Chem. Eng. Sci.* **2005,** *60,* 6983.
79. Fazeli, A.; Behnam, M. CFD Modeling of Methane Autothermal Reforming in a Catalytic Microreactor. *Int. J. Chem. React. Eng.* **2007,** *5,* A93.
80. Akbari, M. H.; Ardakani, A. H. S.; Tadbir, M. A. A Microreactor Modelling, Analysis and Optimization for Methane Autothermal Reforming in Fuel Cell Applications. *Chem. Eng. J.* **2011,** *166,* 1116.
81. Xuan, J.; Leung, D. Y. C.; Leung, M. K. H.; Ni, M.; Wang, H. Chemical and Transport Behaviors in a Microfluidic Reformer with Catalytic-Support Membrane for Efficient Hydrogen Production and Purification. *Int. J. Hydrogen Energy* **2012,** *37,* 2614.
82. Cao, C.; Wang, Y.; Holladay, J. D.; Jones, E. O.; Palo, D. R. Design of Micro-Scale Fuel Processors Assisted by Numerical Modeling. *AIChE J.* **2005,** *51,* 982.
83. Kawamura, Y.; Ogura, N.; Yamamoto, T.; Igarashi, A. A Miniaturized Methanol Reformer with Si-Based Microreactor for a Small PEMFC. *Chem. Eng. Sci.* **2006,** *61,* 1092.
84. Chein, R.-Y.; Chen, L.-C.; Chen, Y.-C.; Chung, J. N. Heat Transfer Effects on the Methanol—Steam Reforming with Partially Filled Catalyst Layers. *Int. J. Hydrogen Energy* **2009,** *34,* 5398.
85. Chein, R.-Y.; Chen, Y.-C.; Chung, J. N. Thermal Resistance Effect on Methanol—Steam Reforming Performance in Micro-Scale Reformers. *Int. J. Hydrogen Energy* **2012,** *37,* 250.
86. Chein, R.; Chen, Y.-C.; Chung, J. N. Axial Heat Conduction and Heat Supply Effects on Methanol—Steam Reforming Performance in Micro-Scale Reformers. *Int. J. Heat Mass Transfer* **2012,** *55,* 3029.
87. Chen, F.; Chang, M.-H.; Kuo, C.-Y.; Hsueh, C.-Y.; Yan, W.-M. Analysis of a Plate-Type Microreformer for Methanol Steam Reforming Reaction. *Energy Fuels* **2009,** *23,* 5092.
88. Hsueh, C.-Y.; Chu, H.-S.; Yan, W.-M. Numerical Study on Micro-Reformer Performance and Local Transport Phenomena of the Plate Methanol Steam Micro-Reformer. *J. Power Sources* **2009,** *187,* 535.
89. Hsueh, C.-Y.; Chu, H.-S.; Yan, W.-M.; Chen, C.-H. Numerical Study of Heat and Mass Transfer in a Plate Methanol Steam Micro Reformer with Methanol Catalytic Combustor. *Int. J. Hydrogen Energy* **2010,** *35,* 6227.
90. Hsueh, C.-Y.; Chu, H.-S.; Yan, W.-M.; Chen, C.-H. Transport Phenomena and Performance of a Plate Methanol Steam Reformer with Serpentine Flow Field Design. *Appl. Energy* **2010,** *87,* 3137.
91. Hsueh, C.-Y.; Chu, H.-S.; Yan, W.-M.; Leu, G.-C.; Tsai, J.-I. Three-Dimensional Analysis of a Plate Methanol Steam Micro-Reformer and a Methanol Catalytic Combustor with Different Flow Channel Designs. *Int. J. Hydrogen Energy* **2011,** *36,* 13575.
92. Hao, Y.; Du, X.; Yang, L.; Shen, Y.; Yang, Y. Numerical Simulation of Configuration and Catalyst-Layer Effects on Micro-Channel Steam Reforming of Methanol. *Int. J. Hydrogen Energy* **2011,** *36,* 15611.
93. Rao Peela, N.; Kunzru, D. Steam Reforming of Ethanol in a Microchannel Reactor: Kinetic Study and Reactor Simulation. *Ind. Eng. Chem. Res.* **2011,** *50,* 12881.
94. Grote, M.; Maximini, M.; Yang, Z.; Engelhardt, P.; Köhne, H.; Lucka, K.; Brenner, M. Experimental and Computational Investigations of a Compact Steam Reformer for Fuel Oil and Diesel Fuel. *J. Power Sources* **2011,** *196,* 9027.
95. Hartmann, M.; Maier, L.; Minh, H. D.; Deutschmann, O. Catalytic Partial Oxidation of Iso-Octane over Rhodium Catalysts: An Experimental, Modeling, and Simulation Study. *Combust. Flame* **2010,** *157,* 1771.
96. Hartmann, M.; Maier, L.; Deutschmann, O. Hydrogen Production by Catalytic Partial Oxidation of Iso-Octane at Varying Flow Rate and Fuel/Oxygen Ratio: From Detailed Kinetics to Reactor Behavior. *Appl. Catal. A* **2011,** *391,* 144.
97. Deshmukh, S. R.; Vlachos, D. G. Effect of Flow Configuration on the Operation of Coupled Combustor/Reformer Microdevices for Hydrogen Production. *Chem. Eng. Sci.* **2005,** *60,* 5718.
98. Deshmukh, S. R.; Vlachos, D. G. CFD Simulations of Coupled, Countercurrent Combustor/Reformer Microdevices for Hydrogen Production. *Ind. Eng. Chem. Res.* **2005,** *44,* 4982.
99. Laguna, O. H.; Ngassa, E. M.; Oraá, S.; Álvarez, A.; Domínguez, M. I.; Romero-Sarria, F.; Arzamendi, G.; Gandía, L. M.; Centeno, M. A.; Odriozola, J. A. Preferential Oxidation of CO (CO-PROX) over CuO_x/CeO_2 Coated Microchannel Reactor. *Catal. Today* **2012,** *180,* 105.
100. Ahmed, T. Y.; Ahmad, M. M.; Yusup, S.; Inayat, A.; Khan, Z. Mathematical and Computational Approaches for Design of Biomass Gasification for Hydrogen Production: A Review. *Renew. Sustain. Energy Rev.* **2012,** *16,* 2304.
101. Jones, J. M.; Pourkashanian, M.; Williams, A.; Hainsworth, D. A comprehensive biomass combustion model. *Renew. Energy* **2000,** *19,* 229.
102. Miltner, M.; Miltner, A.; Harasek, M.; Friedl, A. Process Simulation and CFD Calculations for the Development of an Innovative Baled Biomass-Fired Combustion Chamber. *Appl. Therm. Eng.* **2007,** *27,* 1138.

103. Chaney, J.; Liu, H.; Li, J. An Overview of CFD Modelling of Small-Scale Fixed-Bed Biomass Pellet Boilers with Preliminary Results from a Simplified Approach. *Energy Convers. Manag.* **2012,** *63,* 149.
104. Ghenaia, C.; Janajreh, I. CFD Analysis of the Effects of Co-firing Biomass with Coal. *Energy Convers. Manag.* **2010,** *51,* 1694.
105. Hermansson, S.; Thunman, H. CFD Modelling of Bed Shrinkage and Channelling in Fixed-Bed Combustion. *Combust. Flame* **2011,** *158,* 988.
106. Rosendahl, L. A.; Yin, C.; Kær, S. K.; Friborg, K.; Overgaard, P. Physical Characterization of Biomass Fuels Prepared for Suspension Firing in Utility Boilers for CFD Modelling. *Biomass Bioenergy* **2007,** *31,* 318.
107. Ma, L.; Jones, J. M.; Pourkashanian, M.; Williams, A. Modelling the Combustion of Pulverized Biomass in an Industrial Combustion Test Furnace. *Fuel* **2007,** *86,* 1959.
108. Collazo, J.; Porteiro, J.; Patiño, D.; Granada, E. Numerical Modeling of the Combustion of Densified Wood under Fixed-Bed Conditions. *Fuel* **2012,** *93,* 149.
109. Kirkels, A. F.; Verbong, G. P. J. Biomass Gasification: Still Promising? A 30-Year Global Overview. *Renew. Sustain. Energy Rev.* **2011,** *15,* 471.
110. Gómez-Barea, A.; Leckner, B. Modeling of Biomass Gasification in Fluidized Bed. *Prog. Energy Combust. Sci.* **2010,** *36,* 444.
111. Bridgwater, A. V. Review of Fast Pyrolysis of Biomass and Product Upgrading. *Biomass Bioenergy* **2012,** *38,* 68.
112. Papadikis, K.; Gu, S.; Bridgwater, A. V. CFD Modelling of the Fast Pyrolysis of Biomass in Fluidised Bed Reactors. Part B Heat, Momentum and Mass Transport in Bubbling Fluidized Beds. *Chem. Eng. Sci.* **2009,** *64,* 1036.
113. Fletcher, D. F.; Haynes, B. S.; Christo, F. C.; Joseph, S. D. A CFD Based Combustion Model of an Entrained Flow Biomass Gasifier. *Appl. Math. Model.* **2000,** *24,* 165.
114. Fan, J.; Zhang, Z.; An, Q.; Lou, T. Investigation on the Aerodynamic Field Distribution in an Entrained-Flow Gasifier by Two-Stage Oxygen. *Ind. Eng. Chem. Res.* **2012,** *51,* 12488.
115. Papadikis, K.; Gu, S.; Bridgwater, A. V.; Gerhauser, H. Application of CFD to Model Fast Pyrolysis of Biomass. *Fuel Process. Technol.* **2009,** *90,* 504.
116. Sun, S.; Tian, H.; Zhao, Y.; Sun, R.; Zhou, H. Experimental and Numerical Study of Biomass Flash Pyrolysis in an Entrained Flow Reactor. *Bioresour. Technol.* **2010,** *101,* 3678.
117. Xue, Q.; Heindel, T. J.; Fox, R. O. A CFD Model for Biomass Fast Pyrolysis in Fluidized-Bed Reactors. *Chem. Eng. Sci.* **2011,** *66,* 2440.
118. Boateng, A. A.; Mtui, P. L. CFD Modeling of Space-Time Evolution of Fast Pyrolysis Products in a Bench-Scale Fluidized-Bed Reactor. *Appl. Therm. Eng.* **2012,** *33*−*34,* 190.
119. Xue, Q.; Dalluge, D.; Heindel, T. J.; Fox, R. O.; Brown, R. C. Experimental Validation and CFD Modeling Study of Biomass Fast Pyrolysis in Fluidized-Bed Reactors. *Fuel* **2012,** *97,* 757.
120. Xie, J.; Zhong, W.; Jin, B.; Shao, Y.; Liu, H. Simulation on Gasification of Forestry Residues in Fluidized Beds by Eulerian−Lagrangian Approach. *Bioresour. Technol.* **2012,** *121,* 36.
121. Wang, Y.; Yan, L. CFD Studies on Biomass Thermochemical Conversion. *Int. J. Mol. Sci.* **2008,** *9,* 1108.
122. Sofialidis, D.; Faltsi, O. Simulation of Biomass Gasification in Fluidized Beds Using Computational Fluid Dynamics Approach. *Therm. Sci.* **2001,** *5,* 95.
123. Wang, Y.; Yan, L. CFD Modeling of a Fluidized Bed Sewage Sludge Gasifier for Syngas. *Asia*−*Pac. J. Chem. Eng.* **2008,** *3,* 161.
124. Ding, J.; Wang, X.; Zhou, X.-F.; Ren, N.-Q.; Guo, W.-Q. CFD Optimization of Continuous Stirred-Tank (CSTR) Reactor for Biohydrogen Production. *Bioresour. Technol.* **2010,** *101,* 7005.
125. Wang, X.; Ding, J.; Guo, W.-Q.; Ren, N.-Q. Scale-Up and Optimization of Biohydrogen Production Reactor from Laboratory-Scale to Industrial-Scale on the Basis of Computational Fluid Dynamics Simulation. *Int. J. Hydrogen Energy* **2010,** *35,* 10960.
126. Wang, X.; Ding, J.; Guo, W.-Q.; Ren, N.-Q. A Hydrodynamics-Reaction Kinetics Coupled Model for Evaluating Bioreactors Derived from CFD Simulation. *Bioresour. Technol.* **2010,** *101,* 9749.
127. Wang, X.; Ding, J.; Ren, N.-Q.; Liu, B.-F.; Guo, W.-Q. CFD Simulation of an Expanded Granular Sludge Bed (EGSB) Reactor for Biohydrogen Production. *Int. J. Hydrogen Energy* **2009,** *34,* 9686.
128. Hawkes, G.; O'Brien, J.; Stoots, C.; Hawkes, B. 3D CFD Model of a Multi-Cell High-Temperature Electrolysis Stack. *Int. J. Hydrogen Energy* **2009,** *34,* 4189.
129. Ni, M. Computational Fluid Dynamics Modeling of a Solid Oxide Electrolyzer Cell for Hydrogen Production. *Int. J. Hydrogen Energy* **2009,** *34,* 7795.
130. Laurencin, J.; Kane, D.; Delette, G.; Deseure, J.; Lefebvre-Joud, F. Modelling of Solid Oxide Steam Electrolyser: Impact of the Operating Conditions on Hydrogen Production. *J. Power Sources* **2011,** *196,* 2080.
131. Hajimolana, S. A.; Hussain, M. A.; Wan Daud, W. M. A.; Soroush, M.; Shamiri, A. Mathematical Modeling of Solid Oxide Fuel Cells: A Review. *Renew. Sustain. Energy Rev.* **2011,** *15,* 1893.
132. Ferng, Y. M.; Su, A. A Three-Dimensional Full-Cell CFD Model Used to Investigate the Effects of Different Flow Channel Designs on PEMFC Performance. *Int. J. Hydrogen Energy* **2007,** *32,* 4466.
133. Rismanchi, B.; Akbari, M. H. Performance Prediction of Proton-Exchange Membrane Fuel Cells Using a Three-Dimensional Model. *Int. J. Hydrogen Energy* **2008,** *33,* 439.
134. Kamarajugadda, S.; Mazumder, S. Generalized Flooded Agglomerate Model for the Cathode Catalyst Layer of a Polymer Electrolyte Membrane Fuel Cell. *J. Power Sources* **2012,** *208,* 328.
135. Su, A.; Ferng, Y. M.; Chen, W. T.; Cheng, C. H.; Weng, F. B.; Lee, C. Y. Investigating the Transport Characteristics and Cell Performance for a Micro PEMFC through the Micro Sensors and CFD Simulations. *Int. J. Hydrogen Energy* **2012,** *37,* 11321.
136. Berning, T.; Odgaard, M.; Kær, S. K. Water Balance Simulations of a Polymer-Electrolyte Membrane Fuel Cell Using a Two-Fluid Model. *J. Power Sources* **2011,** *196,* 6305.
137. Cordiner, S.; .Lanzani, S. P.; Mulone, V. 3D Effects of Water-Saturation Distribution on Polymeric Electrolyte Fuel Cell (PEFC) Performance. *Int. J. Hydrogen Energy* **2011,** *36,* 10366.
138. Jung, C.-Y.; Park, C.-H.; Lee, Y.-M.; Kim, W.-J.; Yi, S.-C. Numerical Analysis of Catalyst Agglomerates and Liquid Water Transport in Proton Exchange Membrane Fuel Cells. *Int. J. Hydrogen Energy* **2010,** *35,* 8433.
139. Chiu, H.-C.; Jang, J.-H.; Yan, W.-M.; Li, H.-Y.; Liao, C.-C. A Three-Dimensional Modeling of Transport Phenomena of Proton Exchange Membrane Fuel Cells with Various Flow Fields. *Appl. Energy* **2012,** *96,* 359.
140. Jeon, D. H. A Comprehensive CFD Model of Anode-Supported Solid Oxide Fuel Cells. *Electrochim. Acta* **2009,** *54,* 2727.
141. Qu, Z.; Aravind, P. V.; Boksteen, S. Z.; Dekker, N. J. J.; Janssen, A. H. H.; Woudstra, N.; Verkooijen, A. H. M. Three-Dimensional Computational Fluid Dynamics Modeling of Anode-Supported Planar SOFC. *Int. J. Hydrogen Energy* **2011,** *36,* 10209.
142. Peksen, M. A Coupled 3D Thermofluid−Thermomechanical Analysis of a Planar Type Production Scale SOFC Stack. *Int. J. Hydrogen Energy* **2011,** *36,* 11914.
143. Serincan, M. F.; Pasaogullari, U.; Sammes, N. M. Effects of Operating Conditions on the Performance of a Micro-Tubular Solid Oxide Fuel Cell (SOFC). *J. Power Sources* **2009,** *192,* 414.
144. García-Camprubí, M.; Jasak, H.; Fueyo, N. CFD Analysis of Cooling Effects in H_2-Fed Solid Oxide Fuel Cells. *J. Power Sources* **2011,** *196,* 7290.

145. VanderSteen, J. D. J.; Pharoah, J. G. Modeling Radiation Heat Transfer with Participating Media in Solid Oxide Fuel Cells. *J. Fuel Cell Sci. Technol.* **2006,** *3,* 62.
146. Vakouftsi, E.; Marnellos, G. E.; Athanasiou, C.; Coutelieris, F. CFD Modeling of a Biogas Fuelled SOFC. *Solid State Ionics* **2011,** *192,* 458.
147. Janardhanan, V. M.; Deutschmann, O. CFD Analysis of a Solid Oxide Fuel Cell with Internal Reforming: Coupled Interactions of Transport, Heterogeneous Catalysis and Electrochemical Processes. *J. Power Sources* **2006,** *162,* 1192.
148. Huang, C. M.; Shy, S. S.; Lee, C. H. On Flow Uniformity in Various Interconnects and Its Influence to Cell Performance of Planar SOFC. *J. Power Sources* **2008,** *183,* 205.
149. Andersson, M.; Yuan, J.; Sundén, B. SOFC Modeling considering Electrochemical Reactions at the Active Three Phase Boundaries. *Int. J. Heat Mass Transfer* **2012,** *55,* 773.
150. Kattke, K. J.; Braun, R. J.; Colclasure, A. M.; Goldin, G. High-Fidelity Stack and System Modeling for Tubular Solid Oxide Fuel Cell System Design and Thermal Management. *J. Power Sources* **2011,** *196,* 3790.
151. Johnson N. L. Hydrogen as a Zero-Emission, High-Efficiency Fuel: Uniqueness, Experiments and Simulation. In *3rd International Conference on Internal Combustion Engines: Experiments and Modeling. ICE97,* Naples, 1997.
152. Liu, X.; Liu, F.; Zhou, L.; Suna, B.; Schockb, H. J. Backfire Prediction in a Manifold Injection Hydrogen Internal Combustion Engine. *Int. J. Hydrogen Energy* **2008,** *33,* 3847.
153. Knop, V.; Benkenida, A.; Jay, S.; Coiln, O. Modelling of Combustion and Nitrogen Oxide Formation in Hydrogen-Fuelled Internal Combustion Engines within a 3D CFD Code. *Int. J. Hydrogen Energy* **2008,** *33,* 5083.
154. Rakopoulos, C. D.; Kosmadakis, G. M.; Pariotis, E. G. Evaluation of a Combustion Model for the Simulation of Hydrogen Spark-Ignition Engines Using a CFD Code. *Int. J. Hydrogen Energy* **2010,** *35,* 12545.
155. Rakopoulos, C. D.; Kosmadakis, G. M.; Demuynck, J.; De Paepe, M.; Verhelst, S. A Combined Experimental and Numerical Study of Thermal Processes, Performance and Nitric Oxide Emissions in a Hydrogen-Fueled Spark-Ignition Engine. *Int. J. Hydrogen Energy* **2011,** *36,* 5163.
156. Kosmadakis, G. M.; Rakopoulos, C. D.; Demuynck, J.; De Paepe, M.; Verhelst, S. CFD Modelling and Experimental Study of Combustion and Nitric Oxide Emissions in Hydrogen-Fuelled Spark-Ignition Engine Operating in a Very Wide Range of EGR Rates. *Int. J. Hydrogen Energy* **2012,** *37,* 10917.
157. Zhenzhong, Y.; Aiguo, S.; Fei, W.; Nan, G. Research into the Formation Process of Hydrogen−Air Mixture in Hydrogen Fueled Engines Based on CFD. *Int. J. Hydrogen Energy* **2010,** *35,* 3051.
158. Sopena, C.; Diéguez, P. M.; Sáinz, D.; Urroz, J. C.; Guelbenzu, E.; Gandía, L. M. Conversion of a Commercial Spark Ignition Engine to Run on Hydrogen: Performance Comparison Using Hydrogen and Gasoline. *Int. J. Hydrogen Energy* **2010,** *35,* 1420.
159. Sáinz, D.; Diéguez, P. M.; Urroz, J. C.; Sopena, C.; Guelbenzu, E.; Pérez-Ezcurdia, A.; Benito-Amurrio, M.; Marcelino-Sádaba, S.; Arzamendi, G.; Gandía, L. M. Conversion of a Gasoline Engine-Generator Set to a Bi-Fuel (Hydrogen/Gasoline) Electronic Fuel-Injected Power Unit. *Int. J. Hydrogen Energy* **2011,** *36,* 13781.
160. Sáinz, D.; Diéguez, P. M.; Sopena, C.; Urroz, J. C.; Gandía, L. M. Conversion of a Commercial Gasoline Vehicle to Run Bi-fuel (Hydrogen−Gasoline). *Int. J. Hydrogen Energy* **2012,** *37,* 1789.

CHAPTER

18

Hydrogen Hazards and Risks Analysis through CFD Simulations

Pedro M. Diéguez, Javier López-San Martín, Iñigo Idareta, Irantzu Uriz, Gurutze Arzamendi, Luis M. Gandía

Escuela Técnica Superior de Ingenieros Industriales y de Telecomunicación, Universidad Pública de Navarra, Campus de Arrosadía, E-31006 Pamplona, Spain

OUTLINE

18.1 Introduction 437

18.2 Hydrogen Hazards 439
- *18.2.1 Physiological Hazards* 440
- *18.2.2 Physical Hazards: Embrittlement* 441
- *18.2.3 Chemical Hazards: Ignition and Explosion* 441

18.3 Hydrogen Leaks and Dispersion Studied through CFD Simulations 443
- *18.3.1 Transport Phenomena* 443
- *18.3.2 CFD Modeling of Hydrogen Leaks* 445

18.4 Hydrogen Combustion Phenomena Studied through CFD Simulations 446
- *18.4.1 Combustion Modeling for Deflagration Processes* 446
- *18.4.2 Combustion Modeling for Detonation Processes* 447

18.5 Conclusions 450

Acknowledgments 451

References 451

18.1 INTRODUCTION

Safety is recognized as a key issue for the development, commercialization and implementation of hydrogen technologies. This is a feature common to any technological innovation. The identification and control of possible hazardous consequences is an ethical requirement in any case. Moreover, the risk of a large-scale accident with fatalities could have sufficient impact on our modern information society as to throw a new technology backward for many years.[1,2] Whereas there is long experience on the safe use of hydrogen mainly by the chemical/petrochemical and aerospace industries, much of the existing information has proprietary character or cannot be directly transferred to a series of scenarios in which the general public is in contact with hydrogen instead of engineers or specifically formed personnel. It is therefore of the outmost importance to continue gaining theoretical and experimental information on the safety aspects of the whole hydrogen energy chain to fill the existing knowledge gaps[3] and develop suitable regulations allowing the commercialization and safe use of hydrogen technologies.

An effective legal framework is indispensable to promote capital investments and national and international trade as well as to improve the public confidence and acceptance of hydrogen. As hydrogen is at a very early stage as a consumer fuel, demonstration programs are very important and useful because they greatly contribute to increase the experience and familiarity of the general public. The experience is a key factor by which attitudes can change, so a combination of controlled exposure and handling and education should be implemented to improve the understanding of the

http://dx.doi.org/10.1016/B978-0-444-56352-1.00018-0

benefits and limitations of hydrogen.[4] The introduction of hydrogen as an energy carrier will be successful only under a climate of positive institutional and general public attitudes. However, in spite of the existing initiatives, much remains to be done in this respect. Recent studies show that public awareness and knowledge of hydrogen, the associated technologies such as fuel cells and of specific demonstration projects is, in general, very low.

Ricci et al. indicated that thoughts associated with the word "hydrogen" are generally neutral which contrasts with a recurrent assumption usually made by a sector of the hydrogen community that people have a negative opinion about hydrogen.[5] In general, the lack of sufficient knowledge leads to a low level of concern about hydrogen safety. Safety is considered a prerequisite and it is expected that hydrogen technologies and infrastructures would be engineered to be safe for use by inexperienced consumers. This is a logical attitude but big efforts are required to avoid that it leads to an excessive relaxation. Within this context, inherently safer design (ISD) should play a very important role in the development of hydrogen energy technologies and infrastructures. ISD principles are based on the underlying chemistry and physics of materials and processing technologies, therefore, the issue of materials hazards is directly addressed. ISD concepts combined with suitable safety systems including detection have been recommended by Rigas and Amyotte[1] for dealing with hydrogen safety aspects.

A number of national and international programs have been undertaken to improve the current understanding of the hazards and risks associated with the hydrogen energy.[6,7] The International Energy Agency Hydrogen Implementing Agreement (IEA HIA) was established in 1977 and is the first and world's largest collaborative program for hydrogen research and development and information exchange.[8,9] The participants include 21 countries, the European Commission (EC) and the United Nations Industrial Development Organization. IEA HIA Task 19 devoted to hydrogen safety was accomplished during the period 2004−2010 with the objectives of developing testing methodologies and collecting information on hydrogen components and systems failures. Several subtasks were considered: risk management, experimental testing, and information dissemination. Now the IEA HIA is developing a strategic plan for 2009−2015 with the aim of expanding its commitment to analysis and outreach to advance introduction and commercialization of hydrogen energy technologies. Within this new framework, hydrogen safety is tackled by Task 31 under the theme devoted to hydrogen awareness, understanding and acceptance. The main objective is to provide a technically sound and credible basis for establishing risk informed codes and standards for stationary and mobile hydrogen energy systems. The subtasks include the investigation of phenomena related with gaseous and liquid hydrogen leakage, dispersion and ignition as well as the development of quantitative tools. The safety issues of the storage systems and materials are also addressed.

In 2003, the U.S. Department of Energy (DOE) and U.S. Department of Transportation promoted the formation of the International Partnership for Hydrogen and Fuel Cells in the Economy (IPHE) to foster international cooperation on hydrogen and fuel cell research and development, common codes and standards, and information sharing on infrastructure development.[7,10] Nowadays, IPHE has 18 partners, including Australia, Brazil, Canada, China, the EC, India, Japan, New Zealand, Republic of Korea, Russian Federation, Republic of South Africa and the United States. IPHE coordinates multinational deployment programs with the aim of advancing the introduction of hydrogen and fuel cell technologies on a global scale. Some relevant projects dealing with safety issues recognized by IPHE are Fundamental Safety Testing and Analysis of Hydrogen Storage Materials & Systems led by the U.S., and HySafe—Safety of Hydrogen as an Energy Carrier led by Germany.

The U.S. DOE Hydrogen and Fuel Cells Program experienced a strong acceleration in 2004.[11] Since then, the program works in partnership with industry, academia, laboratories, federal and international agencies to overcome technical barriers through research and development of hydrogen production, delivery, and storage technologies, as well as fuel cell technologies for transportation, distributed stationary power, and portable power applications. The Safety subprogram develops and promotes safe practices and protocols in all activities across the program and also participates in the U.S. DOE collaborations with the IEA HIA and the IPHE. It is highlighted by this initiative that the continued safe operation, handling and use of hydrogen and related systems require comprehensive safety management. This task is accomplished in collaboration with the Hydrogen Safety Panel of the Pacific Northwest National Laboratory (PNNL) and experts from the insurance, fire safety, fuel provider, automaker, aerospace, engineering and other industries that provide recommendations on safety and hazard mitigation. The objectives include helping to identify safety concerns and determining the current status of regulations, policies, codes, standards and guidelines. Another area of interest is the necessity of additional data for the commercial use of hydrogen beyond its conventional industrial use. It is necessary to work in the development of the scientific basis to promote the adoption of hydrogen regulations that facilitate its use as a fuel, as

is done with other common fuels such as gasoline. In addition, safety-related information, often corresponding to company-specific processes and handling procedures, has been treated as proprietary. Therefore, the widespread availability and communication of safety-related information will be crucial to ensure safe operation of future hydrogen fuel systems.

The EC has created and funded the Network of Excellence (NoE) HySafe—Safety of Hydrogen as an Energy Carrier to facilitate the safe introduction of hydrogen energy and to remove safety-related obstacles.[1,12,13] The network, coordinated by the Forschungszentrum Karlsruhe (Germany), started its activities in 2004 and consisted of 25 partners including research organizations, governmental agencies, universities and industry from 12 countries: Germany (5 partners), France (3), Norway (3), United Kingdom (3), Netherlands (2), Spain (2), Denmark, Greece, Italy, Poland, Sweden, Russian Federation and Canada. During the 5 years duration of the project, the network has worked in four main research areas: Basic Research, Risk Management, Dissemination and Management. Three internal projects have also been accomplished: InsHyde—Hydrogen Releases in Confined and Partially Confined Spaces, HyTunnel, focused on hydrogen dispersion, fire and explosion modeling studies relevant to tunnels, and HyQRA, with the aim of developing a reference quantitative risk assessment (QRA) methodology for hydrogen technologies. In 2009, the HySafe participants founded the International Association for Hydrogen Safety (IA HySafe).[14] This association aims to maintain the network's activities for the further development and dissemination of knowledge and for the coordination of research in the field of hydrogen safety. The IA HySafe is also responsible for the organization of the International Conference on Hydrogen Safety.[15,16]

It has been shown in this section that hydrogen safety is a very active field of research, development and international collaboration. Due to the importance, but also the difficulties and risks associated to the experimentation with hydrogen in situations relevant from the safety point of view, computational fluid dynamics (CFD) has become an almost indispensable tool for studying complex scenarios through computer simulation. Obviously, a key issue is the previous validation against a range of relevant experiments of the mathematical models developed in order to establish the confidence levels and range of validity of the simulation results.[17] Almost all the above-mentioned initiatives and research programs dealing with hydrogen safety include tasks or subprojects, in which the focus is on the use of CFD.

The aim of this chapter is to provide an overview of the main hazards of hydrogen and of the potential and range of applications of CFD as a modern tool for investigating safety aspects relevant to the use of hydrogen as a commercial fuel.

18.2 HYDROGEN HAZARDS

The physicochemical properties of hydrogen define the main hazards associated with this fuel. The specific properties are, in general, very well-known and can be found in the literature.[1,18–20] Hydrogen is colorless, odorless and tasteless making impossible its detection by human senses. It is nontoxic but there is the risk of asphyxiation if its presence in air leads to an oxygen-deficient atmosphere. The high diffusivity associated to the small molecular size and low molecular weight, the extremely low density of the gas under normal conditions and the wide range of compositions in air within the flammability limits are among the most relevant features of hydrogen from the safety point of view. Leakages from valves, flanges, storage containers, gaskets, seals, fittings and distribution pipelines constitute a risk more serious than in the case of natural gas or liquid hydrocarbon fuels. Any released hydrogen will rapidly mix with air through a combination of molecular diffusion and convection transport mechanisms, in which inertial and buoyancy forces play very important roles. In confined or partially confined areas, a flammable mixture can be formed with the risk of deflagration or explosion in the event of ignition. In open and well-ventilated areas, the hazards associated to leakages are obviously limited by the rapid dilution of hydrogen in air.

Whereas the density of gaseous hydrogen is very low, about 14 times lower than that of air under normal pressure and temperature, this is not the case of saturated vapor which is denser than air. This fact is relevant in the case of spills of liquid hydrogen because a cloud of very cold saturated vapor will be formed that will initially remain near the spillage point. The cloud can move horizontally or even downward until the temperature increases allowing hydrogen to disperse. Liquid hydrogen is a common form of storage and additional hazards should be taken into account such as frostbite burns, ice formation that may block vents and valves, contamination with solidified air, excessive overpressure generation and losses by continuous evaporation.[1]

Hydrogen hazards associated to deflagration and detonation phenomena constitute another important category. As a matter of fact, the principal hazard of hydrogen is the formation of a flammable or explosive mixture with air. A flame originated by the combustion of hydrogen in oxygen or air is almost invisible in daylight. Therefore, there is an obvious risk of being inadvertently exposed to the flame and suffering severe burns. The flame emits mainly infrared (IR) and

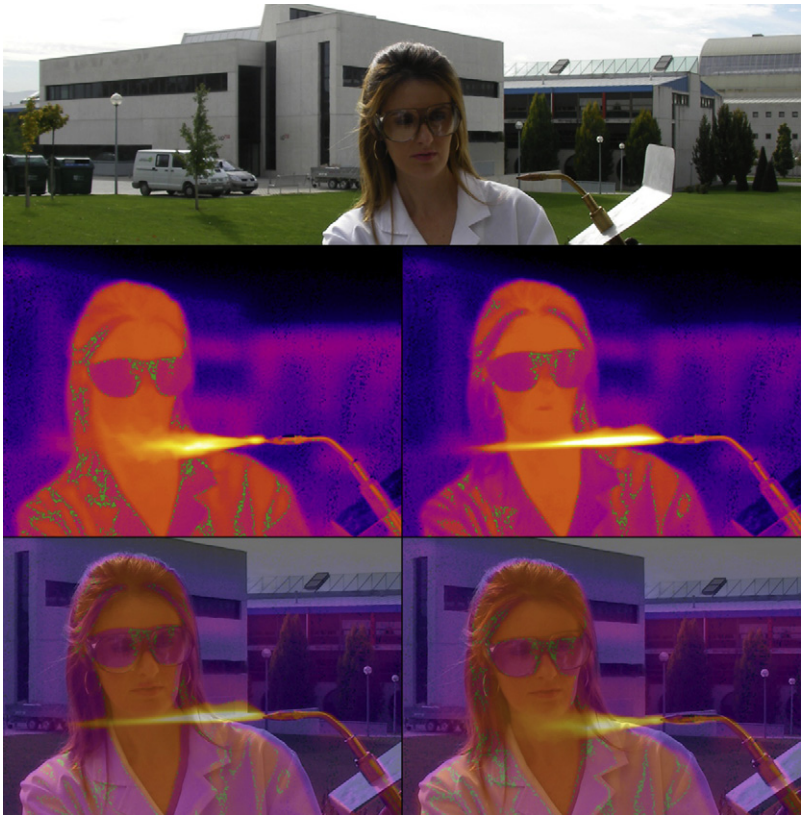

FIGURE 18.1 Photographs showing the combustion in a burner of hydrogen premixed with air. The flame is visible using an infrared camera (AGEMA Thermovision 570). (For color version of this figure, the reader is referred to the online version of this book.)

ultraviolet (UV) radiation. This is illustrated in Fig. 18.1, where the combustion in a burner of a mixture of hydrogen and air is shown. The flame cannot be appreciated with a naked eye but it is visible using an IR camera; these flames are also visible at dark. Nevertheless, large hydrogen fires are more easily detectable in daylight due to the effects of the intense thermal radiation produced. The burning velocity of hydrogen in air is very high (2.7−3.5 m/s), that is, about an order of magnitude higher than the burning velocity of methane. This gives an idea of the difficulty of confining or controlling hydrogen fires.

The Hydrogen Incident and Accident Database has been created within the framework of the HySafe NoE as a repository of data describing incidents or accidents related to hydrogen.[21] It is an open web-based information system serving purposes such as data source for lessons learned, risk communication and partly for some stages of the risk assessment process. Another important online knowledge tool is the Hydrogen Safety Best Practices database that fosters sharing of the worldwide experience gained with the use of hydrogen in a wide variety of applications.[22,23] Best practices were compiled from diverse sources such as the safety plan and project reviews carried out by the PNNL Hydrogen Safety Panel.

The hazards associated with hydrogen are usually classified into three main categories: physiological, physical and chemical. In the following subsections, these hazards will be described in more detail.

18.2.1 Physiological Hazards

According to Rigas and Amyotte, this category includes asphyxiation, thermal and cryogenic burns, hypothermia and injury by blast waves.[1] The hazard of respiratory ailment or asphyxiation is obviously non-hydrogen-specific; it exists whenever a gas such as hydrogen, helium or nitrogen displaces the air in an area. Several stages of asphyxiation have been established depending on the concentration of oxygen. The most critical event leading to death in a few minutes appears for oxygen concentrations below 8 vol. %; nevertheless, early symptoms may appear in sensitive persons at oxygen concentrations just below 19.5 vol. %. Thermal burns are produced through the absorption by the organism of radiation produced by a flame or fire. Harm provoked by the IR radiation is higher than that of the UV one. First-degree burns start to appear for IR and UV radiation doses of 80 and 260 kW/m^2, respectively. Third-degree burns may appear for doses above 870 kW/m^2 (IR) or 1220 kW/m^2 (UV). The lethal

dose of IR radiation to 50% of individuals (LD50) is of the order of 2000 kW/m^2. Obviously, the effects of thermal radiation depend on the flux of energy that is received but also on the exposition time. In the case of hydrogen, one of the main problems is, as mentioned above, the great difficulty for detecting the flame in daylight. However, as the water produced by the combustions absorbs an important fraction of the heat, and also due to the absence of carbon compounds, a hydrogen flame generates significantly less radiant heat compared to the flames originated by the combustion of hydrocarbon fuels. Another type of burns, cryogenic burns or frostbite, is produced through contact with liquid hydrogen or the surface of recipients containing it if they are not conveniently thermally insulated. Injuries from first to fourth degree can be produced depending on the depth of the frostbitten zone, which in turn depends on the temperature and contact duration. Hypothermia is a hazard also associated to liquid hydrogen spills and is produced when the body temperature is below 35 °C.

Finally, severe physiological injury may be produced by the overpressure associated to blast waves from hydrogen explosions.[1,19] Both direct and indirect effects are distinguished. Direct effects are those produced by the sudden rise of pressure, mainly affecting ears and lungs. An overpressure of 13.8 kPa is the threshold for eardrum rupture, whereas a value of 103.4 kPa constitutes a 90% probability of eardrum rupture and the threshold for lung hemorrhage. Immediate fatalities can be caused by the internal injuries produced due to overpressures above 483 kPa. The indirect effects refer to the injury caused by the impact on a person of fragments, shrapnel and debris from a hydrogen explosion and also the impact of the body against a hard surface if a violent displacement is provoked by an explosion.

18.2.2 Physical Hazards: Embrittlement

Main physical hydrogen hazards arise as consequence of its interaction with the multitude of materials used to build the hydrogen systems consisting of pipelines, storage vessels, vacuum jackets, valve bodies and seats, electrical and thermal insulation, gaskets, seals, lubricants, adhesives, etc. Selecting a material for hydrogen applications implies considering a number of requirements such as compatibility with the operating environment, availability of appropriate test data, corrosion resistance, toxicity, resistance to hydrogen embrittlement, thermal contraction properties and behavior at cryogenic temperatures.[1,19,24]

Hydrogen can provoke an important deterioration in the mechanical properties of metals; this effect is referred to as *hydrogen embrittlement*. This phenomenon is influenced by many factors such as the temperature and pressure, the purity and hydrogen concentration, exposure time, and material properties and conditions (stress state, surface conditions, microstructure, crack front nature). Hydrogen embrittlement can occur in one or as a combination of the following forms[19]:

- Environmental embrittlement observed in metals and alloys plastically deformed in contact with gaseous hydrogen. The deformations produced lead to increased cracks that start at the surface, loss in ductility and decrease in fracture stress.
- Internal embrittlement produced by absorbed hydrogen. Small amounts of hydrogen may cause premature failures with little or no warning. In this case, cracks start internally.
- Reaction embrittlement takes place when absorbed hydrogen reacts with a metallic element to form a brittle hydride. In the case of carbon steels, the formation of methane has been reported.

Metals with face-centered cubic structure are in general suitable for hydrogen systems. This is the case austenitic stainless steels with nickel content above 7% (304, 304L, 308, 316, 321, 347), titanium and its alloys, aluminum and its alloys and copper and its alloys such as brass, bronze and copper−nickel. These metals are suitable for service with both gaseous and liquid hydrogen; nevertheless, some of the nonstabilized austenitic steels of the 300 series make martensitic conversion if stressed above the yield stress point at low temperature and loss ductility. Nickel and nickel-based alloys (Inconel®, Monel®, and steels such as 2.25, 3.5, 5 and 9% nickel) constitute notable exceptions because they suffer from severe embrittlement and ductility loss. Ordinary carbon steels lose their ductility at the liquid hydrogen temperature and are considered too brittle for low-temperature operation. Neither can be used in hydrogen systems iron, low-alloy steels, chromium, molybdenum, niobium, zinc and most metals with body-centered crystal structure.[19]

Regarding nonmetallic materials, most elastomers and plastics are compatible with gaseous hydrogen; this is the case of Neoprene®, Viton®, Mylar®, Buna-N®, Nylon®, Kel-F®, and Teflon®, but only the last two are compatible with liquid hydrogen. Nevertheless, due to contraction or shrinkage, filled Teflon® or Kel-F® are preferred to Teflon® for use in liquid hydrogen service. In general, the use of these materials should be limited in gasketing, packing or other sealing elements, in which failure as a result of fire can cause hydrogen leakage.[19]

18.2.3 Chemical Hazards: Ignition and Explosion

Chemical hydrogen hazards are principally associated to the deflagration and detonation phenomena

that can be produced when a flammable or explosive mixture of hydrogen and an oxidant is ignited. The minimum energy for the ignition of gaseous hydrogen in air at atmospheric pressure is only 0.02 mJ; this explains the fact that hydrogen leaks are very easily ignited. The majority of the industrial hydrogen accidents are caused by undetected leaks, off-gassing and equipment (piping and pressure vessels) rupture. Ignition sources responsible for these incidents mainly were electrical short circuits and sparks and static charges.[1,19,25]

Mixtures of hydrogen with air, oxygen or other oxidants are highly flammable over a wide range of compositions. The flammability limits are expressed as percentage by volume (vol. %) of hydrogen and establish the composition range over which fuel gases or vapors will ignite when exposed to an ignition source of sufficient energy. The flammability limits of hydrogen in dry air at 101.3 kPa and ambient temperature are 4.1 vol. % (lower flammability level, LFL) and 74.8 vol. % (upper flammability level, UFL). The LFL in air rises to about 9 vol. % at pressures above 10.3 MPa. Using a strong ignition source, the lowest pressure for which ignition of hydrogen takes place in air is as low as 0.117 kPa. As concerns the effect of temperature, at 673 K and atmospheric pressure, the flammable mixtures in air range from 6.3 to 81.5 vol. % hydrogen. In the case of mixtures with oxygen, LFL and UFL at 101.3 kPa and ambient temperature are 4.1 and 94 vol. % hydrogen, respectively. At elevated pressures, the LFL does not change up to values of 12.4 MPa and the UFL increases to 95.7 vol. % hydrogen at 1.52 MPa. Water vapor is the most effective diluent in reducing the flammability range for hydrogen in air.[19]

The worst event resulting from the release of any form of hydrogen into the ambient environment is mixing of hydrogen with an oxidant (most frequently air) to form a detonable mixture and its subsequent ignition. The term *explosion* corresponds to a sudden energy release and pressure rise; it is sometimes used in the literature for referring to any type of violent pressure rise such as in the cases of deflagration and detonation. As a matter of fact in most cases, explosions involve some kind of wave such as a deflagration or detonation wave.[1] However, deflagration and detonation are different phenomena. Deflagration is the movement of a flame front through a flammable mixture as a subsonic wave with respect to the unreacted medium. The terms deflagration, flash fire, combustion, flame and burn are frequently used interchangeably. Detonation takes place when the flame front propagates through a detonable mixture in the form of a supersonic wave with respect to the unreacted medium. The energy released by the combustion reaction sustains the shock wave, which in turn compress the unreacted mixture to sustain the chemical reaction. Consequently, a detonation propagates much faster than a deflagration resulting in much higher pressure increases. This can be shown in Tables 18.1 and 18.2, where the pressures and temperatures resulting after deflagrations and detonations, respectively, are indicated as functions of the composition of hydrogen/air and hydrogen/oxygen mixtures.[19] In the case of detonations of hydrogen/oxygen mixtures, a pressure 5–19 times higher than the initial one (101.3 kPa) can be reached. For hydrogen/air mixtures, the detonation pressure increase is less dependent on composition and ranges between values 12.1–14.6 times higher. In the

TABLE 18.1 Deflagration Temperatures (T_f) and Pressures (P_f) for Mixtures of Hydrogen and Air or Oxygen*

Vol. % hydrogen	T_f/T_0	P_f/T_0	T_f (K)	P_f (kPa)
Hydrogen/air				
5	2.4	2.3	707.9	234.7
25	7.3	6.3	2159.2	643.8
50	6.5	5.8	1937.9	590.0
75	3.9	3.7	1165.7	375.6
Hydrogen/oxygen				
5	2.3	2.2	694.2	230.1
25	7.2	6.3	2134.5	639.1
50	9.8	8.0	2913.0	808.5
75	10.1	8.3	3003.4	837.5
90	6.4	5.7	1899.2	581.4
95	3.8	3.6	1132.8	365.9

* *Initial conditions:* $T_0 = 298$ K; $P_0 = 101.3$ kPa.

TABLE 18.2 Detonation Temperatures (T_d) and Pressures (P_d) for Mixtures of Hydrogen and Air or Oxygen*

Vol. % hydrogen	T_d/T_0	P_d/P_0	T_d (K)	P_d (kPa)
Hydrogen/air				
18.3	7.7	12.1	2281.8	1231.2
25	9.3	14.6	2758.6	1479.5
50	8.7	13.7	2594.4	1389.1
75	7.7	12.1	2288.0	1230.2
Hydrogen/oxygen				
5	3.1	4.9	929.16	494.34
25	9.0	14.3	2692.1	1447.5
50	11.6	17.9	3470.5	1808.9
75	12.1	18.7	3609.1	1891.4
90	8.6	13.6	2555.6	1376.1

* *Initial conditions:* $T_0 = 298$ K; $P_0 = 101.3$ kPa.

case of deflagrations, the pressure increase can reach values 10.1 and 7.3 times higher than the initial pressure for hydrogen mixtures with oxygen and air, respectively. Temperature increases are very important also in both phenomena. Temperatures as high as 3600 and 2760 K can be reached in the detonation of hydrogen/oxygen and hydrogen/air mixtures, respectively.

A highly energetic source such as a shock wave can start a detonation, whereas a low-strength source such as a flame or a spark will typically initiate a deflagration. It should be noted, however, that there is the possibility of the occurrence of a deflagration-to-detonation transition.[1] The expansion of the combustion gases can generate compression waves perturbing the gas ahead the front flame of a deflagration. Successive compression waves propagating through precompressed and adiabatically heated gas can finally transform into a shock wave resulting in a detonation.

The detonation limits establish the range of concentrations of a fuel in an oxidant for the occurrence of a stable detonation. These limits depend on many factors, among them the volume and geometry of the enclosure, so values reported in the literature should be carefully used.[19] Detonability limits of hydrogen in air under normal pressure and temperature conditions of 18.3–59.0 and 13.5–70 vol. % hydrogen have been reported. As can be seen, these limits are narrower than the flammability limits. The worst case during a hydrogen release is reaching a near-stoichiometric mixture (29.5 vol. % hydrogen in air) and encountering an ignition source with sufficient energy that will result in a detonation. The fact that the range of concentrations within the detonability limits for hydrogen in air is very broad makes relatively ease the formation of detonable mixtures compared to other fuels such as methane (6.3–13.5 vol. %) or gasoline (1.1–3.3 vol. %).

18.3 HYDROGEN LEAKS AND DISPERSION STUDIED THROUGH CFD SIMULATIONS

The main risk related to hydrogen systems is the uncontrolled burning or explosion of an accidental leakage. Due to its low density, gaseous hydrogen will rise and accumulate near the ceiling of an enclosed area during the transitory period as a result of a leak. Afterward, hydrogen, as any other gas, will tend to homogenize its concentration within the enclosure through molecular diffusion. The scales of time associated to these phenomena are very different. Initially and near the leakage point, a buoyancy- and momentum-dominated regime is established that is characterized by a very rapid transport of hydrogen. In contrast, once the leakage has been controlled or far from the leakage point, the gas is almost static and the transport becomes slow. This is relevant regarding the location of the hydrogen safety sensors that should activate the corresponding alarms and the venting, decontamination or inertization systems. These sensors are key elements of any reliable safety system that should guarantee the rapid detection of hydrogen releases.[26,27] If detection is delayed, the risk of the occurrence of a severe accident will increase, whereas the decontamination of the enclosure will become more complicated because the extension of the affected area is higher. However, if the sensors are capable of detecting the leak during the first moment, the transition regime, hydrogen venting will be faster and more effective. Obviously, there are many factors affecting the relevance of a hydrogen incident and it is necessary to analyze each scenario individually since the optimal solution mainly depends on the leakage type, its rate, location and duration, and the geometry and dimensions of the enclosure. CFD is a powerful tool for analyzing hydrogen safety scenarios that can help to design the decontamination systems and define the number and location of the hydrogen sensors.[28]

18.3.1 Transport Phenomena

After any release, hydrogen moves rapidly toward locations above the leaking point due to the momentum gained from the containing pipe or vessel and the buoyancy forces originated by the great difference between hydrogen and air densities. The hydrogen density relative to air is 0.0695 under normal pressure and temperature conditions and the ascensional speeds of hydrogen may vary from 1.2 to 9 m/s. In the absence of restriction on the rise, that is, in open spaces, hydrogen would disperse quickly in the air. This process could be strongly favored by the atmospheric conditions, especially turbulences and transport associated to wind. This scenario is not possible indoors, where there is restriction to the vertical movement of hydrogen that will accumulate under the ceiling, creating hydrogen accumulations that can be potentially explosive.

The study of hydrogen diffusion in enclosed spaces is especially important from the point of view of safety because useful information can be gained for defining the optimal ventilation or inertization strategies. Three relevant stages can be distinguished in this regard:

- Leak. A hydrogen plume is formed that rises up to the ceiling wall from where it tends to expand and disperse. The concentration in the plume depends mainly on the leak mass flow rate and the distance from the leaking point to the ceiling. In this phase, the hydrogen is concentrated mainly on the ceiling and in the plume, whose position depends on the leaking

point. During this period, the hydrogen transport is momentum- and/or buoyancy-driven.

- Stratification. This stage covers the period of time between the end of the leak and the moment, in which the concentration of hydrogen only depends on the vertical position. The hydrogen concentration shows a fully stratified pattern after this stage mainly as a result of buoyancy and molecular diffusion.
- Homogenization. During this period, molecular diffusion is the sole relevant transport phenomena involved as far as the air within the enclosure is static. The concentration of hydrogen in each point tends asymptotically toward a homogeneous mean value (C_∞) that will be achieved once a long time has passed. It can be calculated as the ratio of the volume of hydrogen released at the mean enclosure pressure and temperature to the enclosure volume. It is important to compare both the local and C_∞ concentrations with the LFL of hydrogen in air (4.1 vol. %) to establish the areas where a deflagration can occur in the case of unintended ignition.

Figure 18.2 shows different moments of a hydrogen leak in an enclosure simulated through CFD that illustrate the above-described stages. The leakage takes 1000 s at a constant flow-rate of 1 m^3/h in an enclosure of 27 m^3 being $C_\infty = 1$ vol. %. The leak occurs in a corner of the enclosure at the ground level. In the sequence of images, the colored contours indicate the hydrogen concentration as molar or volume fraction. The red color identifies areas where the concentration of hydrogen is equal to or greater than 2 vol. %. Under the conditions of this example, these areas are present only during the leak stage and they are restricted to the vertical

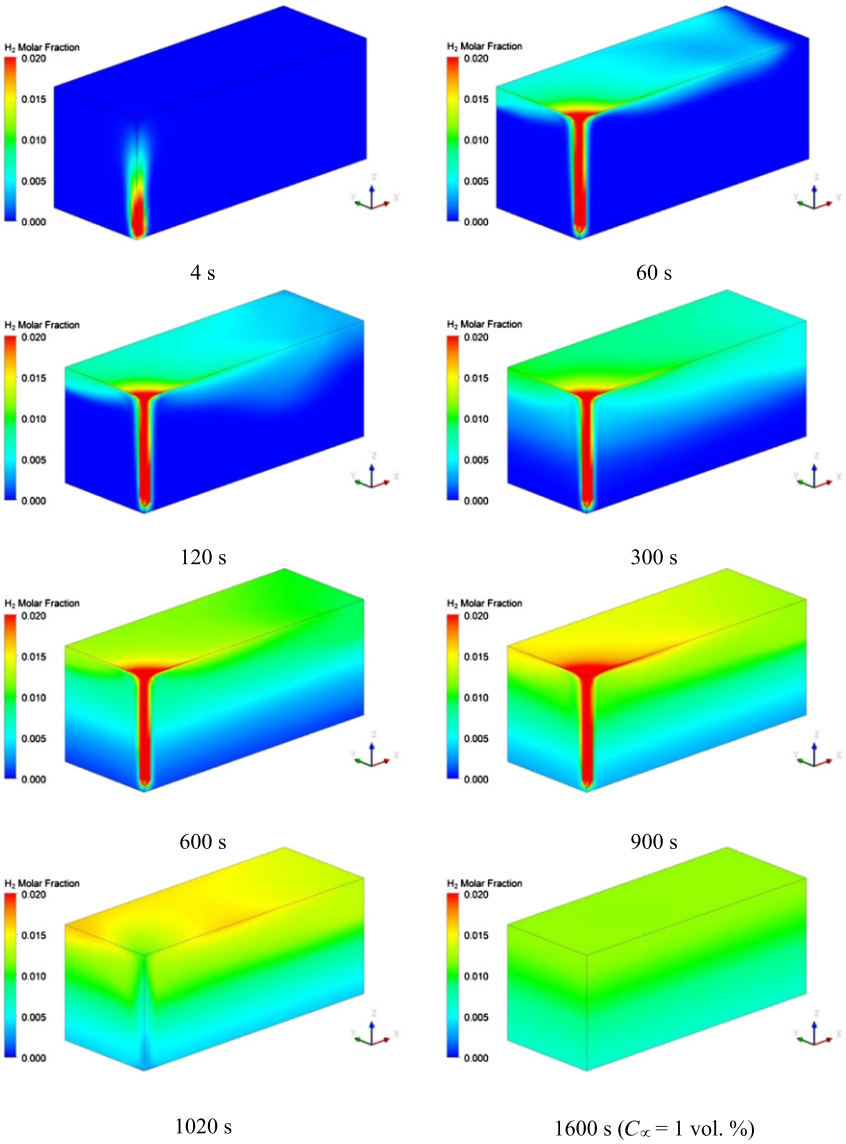

FIGURE 18.2 CFD simulation showing different moments of a hydrogen leak (1000 s at 1 $NPTm^3$/h) in an enclosure of 27 m^3 (1 vol. %). (For color version of this figure, the reader is referred to the online version of this book.)

above the leaking point due to the confinement of the hydrogen plume by the enclosure walls. Twenty seconds after the end of the leak, a stratification of the hydrogen concentration can be appreciated. The last image, corresponding to 600 s after the leak has stopped, shows a significant level of homogenization of the hydrogen concentration.

Obviously, the leak stage is very influenced by the location of the leaking point and the leak rate, while at the end of the stratification stage, the main variable is the vertical position. The mathematical description of the first two phases (leakage and stratification) is complex mainly because the turbulent nature of the flow regime. During the last stage, the homogenization, the transport equations can be solved analytically. Nevertheless, most times, CFD is needed to simulate the evolution of the different leakage stages.

18.3.2 CFD Modeling of Hydrogen Leaks

CFD basics were summarized in the preceding chapter. In essence, the computational space is divided in a series of control volumes or cells. Cells in contact with the domain limits will have boundary conditions that impose fixed values for some of the variables. Then, the solution method will start from some initial values and an iterative numerical process is applied until the residuals for each variable reach sufficiently low values.

Modeling of turbulence is an essential element of the CFD model for describing fluid dynamics and mass transport. The phenomenon is very complex and it is still not fully understood. Theoretically, if there would be the possibility of dividing a fluid domain in sufficiently small control volumes and defining the boundary conditions with enough resolution, there would be no need of turbulence models for solving the Navier–Stokes equations through CFD, which would give satisfactory solutions. However, computational capacities are still too low to be able to solve problems of this nature involving multiple scale lengths without the help of approximate models. There is a vast variety of turbulence models, some of them even developed for specific applications.[29] The purpose of these models is to give a value to the turbulence existing inside the volume cells with a length-scale lower than the grid scale. Most of the models introduce a new set of transport equations to represent values like the turbulence kinetic energy or the turbulence eddy dissipation rate. The standard $k-\varepsilon$ model has been one of the most employed in industry and research due to its good performance and ease implementation and it is still the most used for diffusion and mass transfer problems.[30] Other models such as the $k-\omega$ and large eddy simulation (LES) are also frequently considered.[31,32] There has also been proposed and applied with satisfactory results the change of turbulence model at some point of the simulations, usually favoring a laminar model of the fluid motion after hydrogen leak periods, offering faster calculations and more accuracy in the results obtained.[33]

There exists the possibility that the pressure inside a hydrogen storage vessel is high and the jet velocity at the leaking point becomes supersonic. This would require modeling compressible flow of hydrogen. This leads to an increase of the complexity of the CFD models and in the calculation times, so incompressible flow condition is sometimes kept and corrections are introduced through experimental coefficients.

There is an extensive literature on the simulation and analysis of hydrogen leaks using CFD.[17,30,33–51] Special mention deserves in this regard the theoretical and experimental work carried out by the HySafe network.[12,13] As it could be expected, simulation of hydrogen leaks in enclosures is the focus of most studies because they constitute the most hazardous scenarios. Comparatively, there are few reports on CFD modeling of liquid hydrogen spills.

Experiments on an enclosure (20.046 m^3) with a subsonic release of hydrogen from a vessel were performed by Shebeko et al.[34] The enclosure contained initially quiescent air at 293 K and 101.3 kPa. A hydrogen release of 4.5 l in 60 s was provoked and concentrations were measured during a period of 250 min after the leakage. Up to 11 research centers, companies and universities took part in this benchmark exercise, proposing different codes, models and simulation characteristics. It was found that the most important aspect was turbulence modeling. In this case, the flow was initially turbulent but soon changed to laminar, so the model must be able to describe both phenomena. However, even if the performance of some models was better, a clear correlation between the turbulence models and the accuracy of the results was not found. This suggested that other issues such as the resolution of the computational grid could be as important as the turbulence model itself.

The Institut National de l' Environnement Industriel et des Risques (INERIS, France) performed experiments on a roughly rectangular facility with dimensions $7.2 \times 3.78 \times 2.88$ m.[35] Hydrogen was released through a circular orifice on the top surface of the facility at a flow rate of 1 g/s for 240 s. Different hydrogen concentration sensors were distributed at different locations and results were obtained for more than 5000 s after the beginning of the experiment. The authors also concluded that the turbulence was a key issue of the CFD model. It was found that the standard $k-\varepsilon$ model tended to overestimate the concentration values, so it was recommended to employ small time steps and

a higher order convective scheme. In contrast, the LVEL turbulence models [36] underestimated the concentrations.

An interesting analysis was performed at the Sandia National Laboratories (USA) where Houf et al.[39] analyzed possible leakages from fuel-cell vehicles inside a tunnel through CFD simulations. Wilkening and Baraldi studied accidental hydrogen and methane releases from pipelines in an open environment.[40] The simulations offered some interesting conclusions, such as the smaller accumulation of hydrogen in the regions near the ground due to stronger buoyancy effects and the higher sonic speed of hydrogen. However, the amount of hydrogen forming flammable areas was higher than in the case of methane, so the authors were not able to assess which of the two fuels presented higher risks.

Salva et al.[41] analyzed a hydrogen leak in a fuel-cell vehicle with closed windows. The results allowed establishing the best placements of the hydrogen sensors and even the design of an optimized ventilation system. A similar case was analyzed by Liu and Schreiber.[42] Modifications to the ventilation system demonstrate to be capable of evacuating most of the hydrogen.

18.4 HYDROGEN COMBUSTION PHENOMENA STUDIED THROUGH CFD SIMULATIONS

CFD is a very valuable tool for investigating deflagration and detonation phenomena in relation with hydrogen safety aspects. However, modeling of these processes is challenging due to their complexity because they involve simultaneously turbulence, heat transport and chemical reactions (combustion and NO_x formation).

The most critical aspects are the modeling of the combustion propagation and turbulence. The importance of the latter has been highlighted in the preceding section and it is also a key issue in the case of the combustion processes, mainly concerning deflagration. Turbulence is responsible for the corrugation of the flame front in the case of a premixed fuel, thus enlarging the flame area. Although detonation also involves turbulence, this process is much less influenced by this phenomenon. Regarding combustion modeling for CFD, in the following subsections, a selection of the most representative models used for simulating hydrogen combustion for deflagration and detonation processes will be presented.

18.4.1 Combustion Modeling for Deflagration Processes

The UU model was proposed by the HySAFER Center at the University of Ulster (UU).[52,53] An LES model is used for turbulence description, and a gradient method-based combustion model characterized by the following source term:

$$S_c = \rho \cdot S_t \cdot |\nabla \tilde{c}| \tag{18.1}$$

where ρ is the density of the unburnt gases, $\tilde{c}$ is the reaction progress (Favre averaged) and S_t is the turbulent flame velocity. This turbulent velocity is defined as proposed by Yakhot[54]:

$$S_t = S_u \exp\left(\frac{u'}{S_t}\right) \tag{18.2}$$

where u' is the subgrid fluid velocity of the LES turbulence model and S_u is the laminar flame velocity. The model proposes a definition of the laminar flame speed based on the concept of wrinkling, which allows enlarging the flame front and an acceleration of the flame speed due to turbulence. It also defines a critical radius centered on the ignition point that separates the inner area where turbulence has little effect and the area over this critical radius where turbulence effects become relevant.

The JRC model was developed by the Joint Research Center, The Netherlands.[55] It is based on the standard $k-\varepsilon$ turbulence model and the eddy dissipation concept combustion model,[56] a modified standard eddy dissipation model. JRC employs an expression for the mass burning rate as follows:

$$\begin{aligned} \dot{m} &= -c_f \frac{\varepsilon}{k} \rho \cdot Y_{lim} \quad \text{if } \tau_{ch}/\tau_{tu} < D_{ie} \\ \dot{m} &= 0_{lim} \quad \text{if } \tau_{ch}/\tau_{tu} \geq D_{ie} \end{aligned} \tag{18.3}$$

where ε (turbulence kinetic energy) and k (turbulence dissipation velocity) are the parameters of the turbulence model, and Y_{lim} is the mass fraction of the limiting reactant. The definition of c_f, the scale factor, is more complex than the corresponding one in the standard eddy dissipation model, where a constant value is used. In the JRC is defined according to:

$$c_f = c_{f0}\left(1 + \frac{4.4}{1 + 3.2\sqrt{k}/S_{lam}}\right) \tag{18.4}$$

where c_{f0} is the constant value depending on the air–fuel ratio and S_{lam} is the laminar flame velocity of the mixture.

The KI model was developed by the Kurchatov Institute (Russia).[57,58] The effect of viscosity is neglected, so there is no need of modeling turbulence effects. The combustion model includes a burning rate defined by the relation:

$$\frac{\partial Y_f}{\partial t} = \frac{K_0}{\Delta x} \tag{18.5}$$

where Y_f is the fuel mass fraction and Δx is the size of the control volume. K_0 is the burning rate constant, estimated through the following expression:

$$K_0 = S_u\{a\cdot\exp[b(p-c)^2] + d\cdot\arctan[e(p-f)]\} \quad (18.6)$$

where a, b, c, d, e and f are empirical constants and S_u, the laminar burning velocity.

18.4.2 Combustion Modeling for Detonation Processes

Hydrogen detonations are complex processes and their analysis and modeling need experimental data, which are difficult to obtain. However, there have been some studies that propose models describing this kind of processes. It is a common practice to neglect both turbulence and heat losses because of the very fast dynamics.

The UU model for detonation[59] is based on the deflagration one and introduced as the main change in the substitution of the turbulent burning velocity by the detonation velocity (D) in the source term, which is usually assumed constant:

$$S_c = \rho\cdot D\cdot|\nabla\tilde{c}| \quad (18.7)$$

The Kurchatov Institute Eulerian explicit solver (KI model) has also been modified in order to simulate hydrogen detonation processes.[60] Defined as a new code, it has some advantages because of the wide use of Eulerian explicit solvers in the study of explosive detonations. Equation (18.5) is now written as

$$\frac{\partial C}{\partial t} = \rho K_0 \exp(-E_a/T) \quad (18.8)$$

where C is the mass fraction of the components, K_0, the pre-exponential factor and E_a, the activation energy.

The Forschungszentrum Karlsruhe (Germany) employs COM3D, a finite differences CFD tool for deflagration and detonation modeling (FZK model).[60] The combustion model implemented for the detonation description is the Heaviside Detonation model, emulating an Arrhenius-like chemical reaction rate (R_r) expression:

$$\Delta y_{H_2} = 100\cdot Cf\cdot\frac{\Delta t}{\Delta x}\cdot y_{H_2}\cdot R_r \quad (18.9)$$

Groethe et al. reported on several large-scale hydrogen deflagration and detonation experiments, including the effect of obstacles and the performance of barrier walls.[61,62] The results of one of them have been used by our group to validate the hydrogen combustion models that we have developed in ANSYS® CFD codes. It consists in the detonation of an almost stoichiometric mixture containing 30 vol. % hydrogen in air enclosed in a 300 m^3 hemispherical polyethylene balloon placed in the ground. The detonation was initiated using 10 g of C-4 explosive and was filmed using high-speed cameras. Figure 18.3 includes several video frames corresponding to the first microseconds of the event showing the propagation of the flame front. The experimental results are compared with the CFD simulations and it can be seen that the agreement is very good. From these results, a detonation velocity of 1980 m/s could be estimated.[61]

Our group has also developed CFD models that describe the behavior of both hydrogen diffusion and premixed flames. This is illustrated in Fig. 18.4 where a series of images of hydrogen flames taken with an IR camera (AGEMA Thermovision 570) are compared with the contour lines for temperature obtained through CFD simulations. Both diffusion (Fig. 18.4a and c) and premixed (Fig. 18.4b and d) flames are shown in vertical and horizontal disposition. As can be seen, the contour lines delimit reasonably well the flame fronts. In the case of the horizontal flames (Fig. 18.4c and d), the effects of buoyancy and the turbulence are clearly seen, particularly for the diffusion flame (Fig. 18.4c). In Fig. 18.5, the temperature values obtained from the CFD simulations are compared with the temperatures measured with a thermocouple in the vertical flames at different position above the burner outlet. As can be seen, the CFD simulations lead to overestimated temperature values; nevertheless, the maximum errors (10–15%) seem acceptable, especially in the case of the premixed flame and also taking into account the high temperatures reached.

Experiments on hydrogen deflagrations in a tunnel have been performed by Groethe et al.[61] They constitute very interesting and useful data sources that can be used for the validation of CFD codes. A 78.5 m long tunnel was manufactured, with an inner diameter of 2.4 m and a cross-sectional area of 3.74 m^2. Homogeneous mixtures ranging from 9.5 to 30 vol. % hydrogen in air were contained within a volume of 37 m^3 at the tunnel center using plastic film barriers, which were cut prior to spark ignition. The facility was provided with pressure gauges at various points. A total of six participants took part in the benchmark exercises. Some of them have described in detail their models and the different aspects they have taken into account while studying this case.[39,53] After analyzing the different results, the authors indicated that the different codes achieved a notably accurate capture of the pressure peaks and of the propagation speed. These results confirm that CFD codes are well suited to represent the phenomena related to a deflagration process in closed environments. Overpredicted values

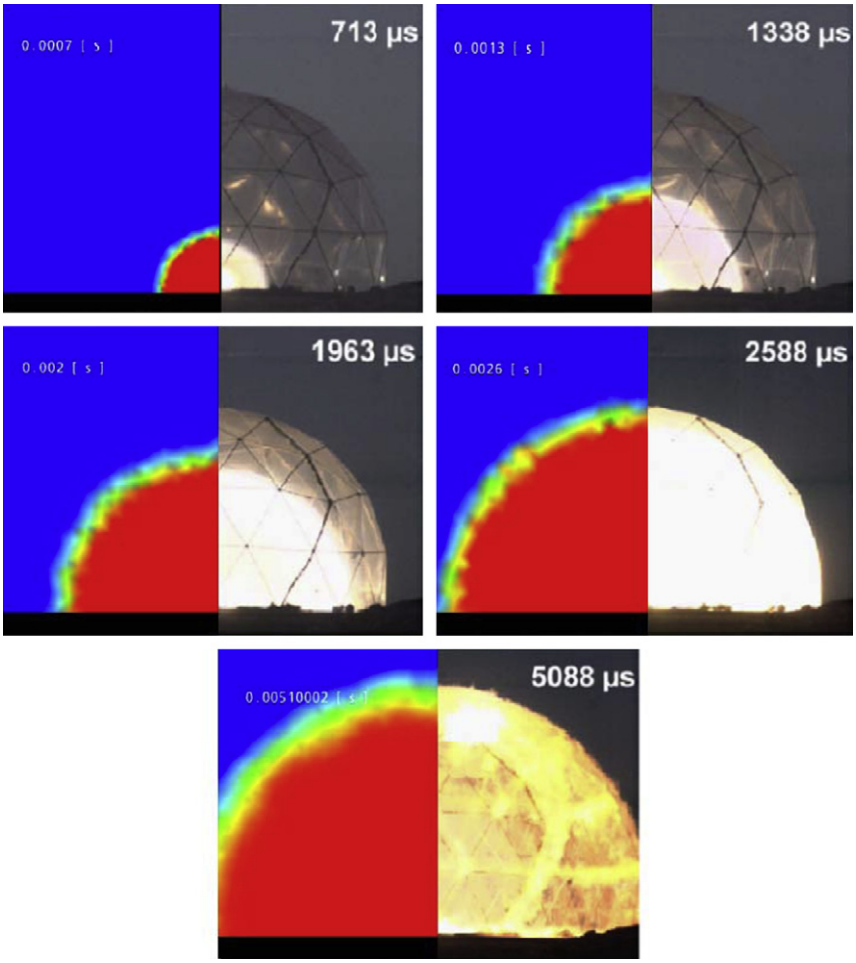

FIGURE 18.3 Detonation of a 300 m^3 hemispherical polyethylene balloon containing a mixture of 30 vol. % hydrogen in air. High-speed video frames showing the propagation of the flame front are compared with the CFD simulations performed by the Hydrogen Group of the Universidad Pública de Navarra. (For color version of this figure, the reader is referred to the online version of this book.) *Source: Images were taken from Ref. 61 with permission from the International Association for Hydrogen Energy.*

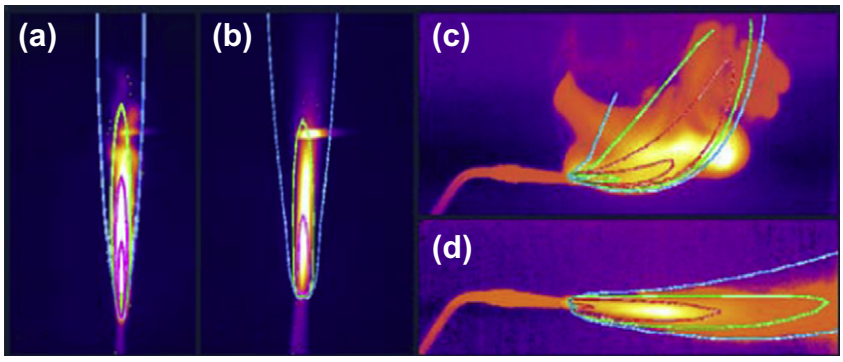

FIGURE 18.4 Images of hydrogen flames in air taken with an infrared camera. Temperatures calculated through CFD simulations are indicated by the colored lines: 373 K (blue), 1023 K (green), and 1773 K (red). Images (a) and (c) show diffusion flames and images (b) and (d) premixed flames. (For interpretation of the references to color in this figure legend, the reader is referred to the online version of this book.)

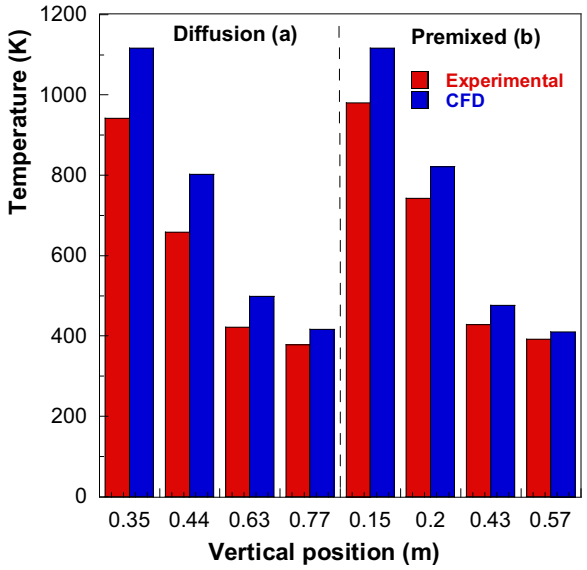

FIGURE 18.5 Comparison between the experimental temperatures and the values obtained through CFD simulation for the vertical flames shown in Fig. 18.4a and b. (For color version of this figure, the reader is referred to the online version of this book.)

were explained, at least in part, by the noninclusion of heat transfer models. Figure 18.6 shows some examples of the results obtained by our group through CFD simulations showing the evolution of the pressure rise and the propagation of the hydrogen combustion reaction for this case. A combustion model analogous to the UU one but using the standard $k-\varepsilon$ turbulence model was implemented in ANSYS®. It was found that overpressures close to 150 kPa can be achieved in accordance with the experimental data. An interesting application of these results is the evaluation of possible physiological injuries associated to overpressure as described in Section 18.2.1. Figure 18.7 compares the overpressures developed in the tunnel experiment with the thresholds for eardrum (Fig. 18.7a) and lung (Fig. 18.7b) injuries. As can be seen, the simulation results indicate that eardrum damages will probably be present in the victims, but severe lung damage is not expected in this particular scenario.

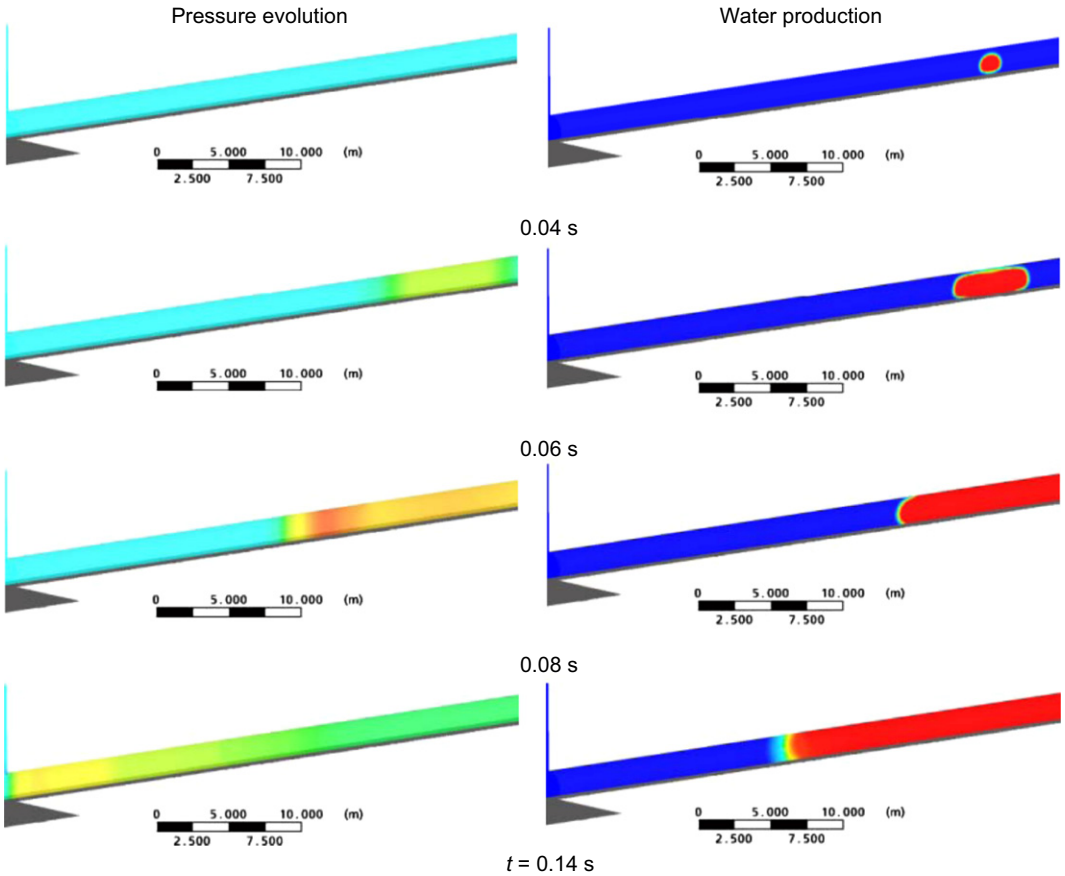

FIGURE 18.6 Examples of the results of CFD simulations showing the evolution of the pressure rise and the propagation of the hydrogen combustion reaction for the deflagration in a tunnel described by Groethe et al.[61] (For color version of this figure, the reader is referred to the online version of this book.)

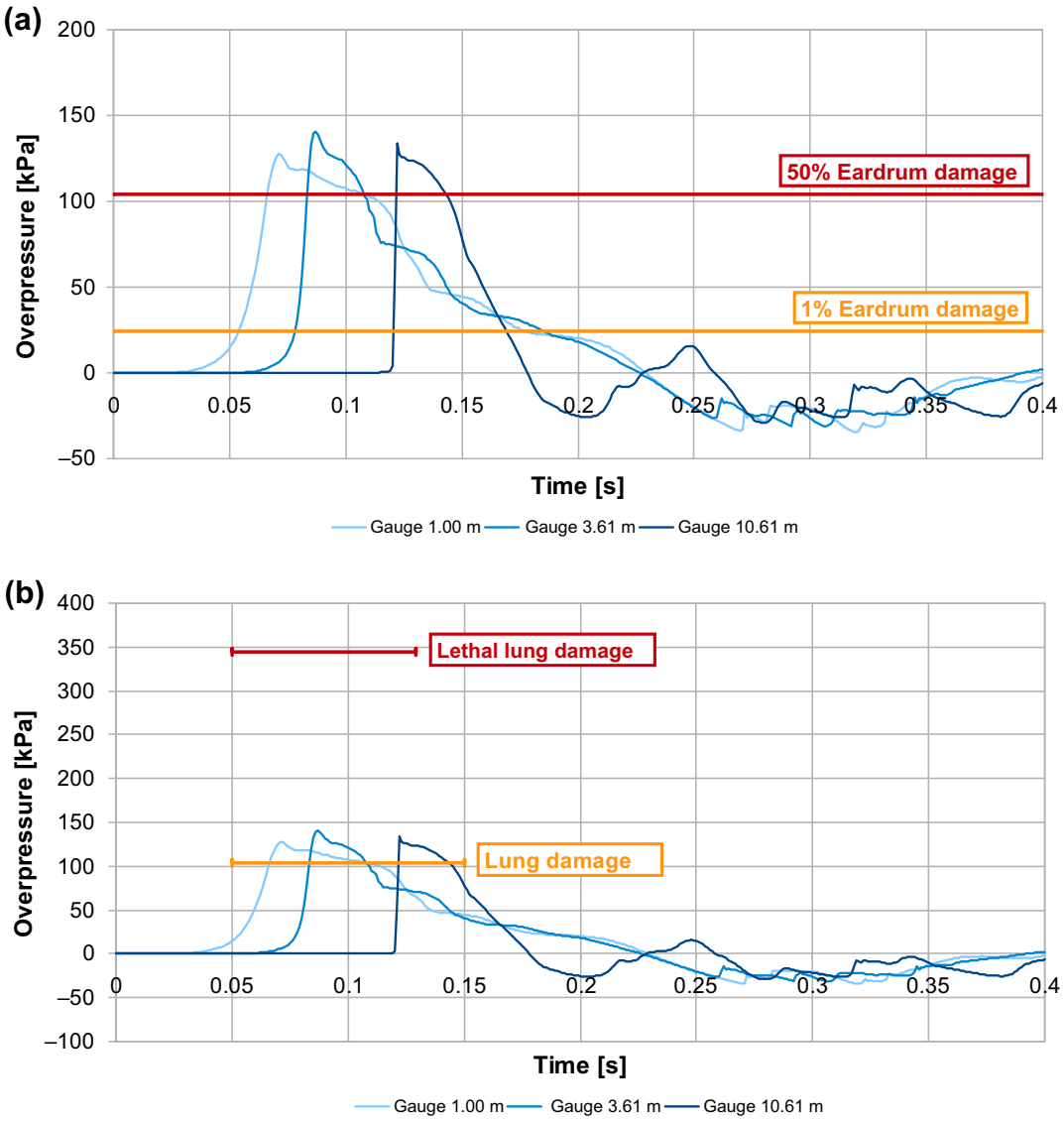

FIGURE 18.7 Comparison of the overpressures obtained through CFD simulations for the deflagration in a tunnel described by Groethe et al.[61] with the thresholds for eardrum (a) and lung (b) injuries.

18.5 CONCLUSIONS

Hydrogen safety is a very active field of research and international collaboration because it is widely recognized that safety is a key issue for the development and commercialization of hydrogen technologies. There is strong evidence that the hazards associated to the use of hydrogen as a fuel are not greater to those of the use of natural gas or gasoline; they are simply different. The reasons for this difference rely on the physicochemical properties of this element, mainly its very low density in gaseous state, very wide limits of flammability and detonability in air, easy ignition and its interaction with some materials leading to their embrittlement. All these issues can be conveniently managed through codes, regulations, standards and preventive safety programs.

CFD allows simulating the evolution of relevant scenarios from the safety point of view such as leakages, fires and explosions. Conclusions can be drawn regarding possible physiological injuries. As a result, almost all the international initiatives concerned with the safety of hydrogen have adopted CFD as a tool for analyzing safety systems, including the location of hydrogen sensors, and the design of ventilation and inertization systems. The main advantage of CFD is its ability of solving complex models describing mass, energy and momentum transport coupled with chemical reactions. A number of examples are described in the literature showing good agreement between CFD

simulations and experimentation for a variety of situations of special interest such as leakages in enclosures, from pipelines or storage vessels, in tunnels, garages or vehicles. Nevertheless, it is still necessary to improve the confidence on the existing models. The main areas of interest in this regard are the modeling of turbulence and hydrogen combustion as well as the experimentation under realistic conditions in order to suitably validate the CFD models.

Acknowledgments

Financial support by the Spanish Ministry of Science and Innovation and Ministry of Economy and Competitiveness (ENE2009-14522-C04 and ENE2012-37431-C03 grants, respectively) is gratefully acknowledged. I. Uriz gratefully acknowledges the fellowships granted by the Innovation Department of the Navarre Government and the Spanish Ministry of Science and Innovation (program FPI, BES-2010-030021). The authors wish to acknowledge Susana Berdonces for the images of Figure 18.1.

References

1. Rigas, F.; Amyotte, P. *Hydrogen Safety;* CRC Press, Taylor & Francis Group: Boca Raton, FL, 2013.
2. Pasman, H. J. Challenges to Improve Confidence Levels of Risk Assessment of Hydrogen Technologies. *Int. J. Hydrogen Energy* **2011,** *36,* 2407.
3. Tchouvelev, A. V. *Knowledge Gaps in Hydrogen Safety. A White Paper. International Energy Agency Hydrogen Implementing Agreement Task 19 − Hydrogen Safety.* Available from: http://ieahia.org/pdfs/Task19/Knowledge%20Gaps_White%20Paper_R1.pdf, 2008.
4. Schulte, I.; Hart, D.; van der Vorst, R. Issues Affecting the Acceptance of Hydrogen Fuel. *Int. J. Hydrogen Energy* **2004,** *29,* 677.
5. Ricci, M.; Bellaby, P.; Flynn, R. What Do We Know about Public Perceptions and Acceptance of Hydrogen? A Critical Review and New Case Study Evidence. *Int. J. Hydrogen Energy* **2008,** *33,* 5868.
6. Royle, M.; Willoughby, D. The Safety of the Future Hydrogen Economy. *Process Saf. Environ. Prot.* **2011,** *89,* 452.
7. Pasman, H. J.; Rogers, W. J. Safety Challenges in View of the Upcoming Hydrogen Economy: An Overview. *J. Loss Prev. Process Ind.* **2010,** *23,* 697.
8. http://ieahia.org/.
9. de Valladares, M. R.; Jensen, J. K. IEA HIA Research & Analysis that enable H_2 energy solutions. *Energy Procedia* **2012,** *29,* 128.
10. http://www.iphe.net/.
11. http://www.hydrogen.energy.gov/.
12. Jordan, T., et al. Achievements of the EC Network of Excellence HySafe. *Int. J. Hydrogen Energy* **2011,** *36,* 2656.
13. http://www.hysafe.net/.
14. http://www.hysafe.org/IAHySafe.
15. Carcassi, M. N. ICHS-2005: The First International Conference on Hydrogen Safety. *Int. J. Hydrogen Energy* **2007,** *32,* 2105.
16. Wen, J. X. Editorial for Special Issues on Hydrogen Safety. *Int. J. Hydrogen Energy* **2012,** *37,* 17350.
17. Hansen, O. R.; Middha, P. CFD-Based Risk Assessment for Hydrogen Applications. *Process Saf. Prog.* **2008,** *27,* 29.
18. Häussinger, P.; Lohmüller, R.; Watson, A. M. *Hydrogen*; In: *Ullmann's Encyclopedia of Industrial Chemistry.* 5th ed., Vol. A 13; VCH Verlagsgesellschaft: Weinheim, Germany, 1989; p 299.
19. *National Aeronautics and Space Administration (NASA), Safety Standard for Hydrogen and Hydrogen Systems, Document NSS 1740.16*, Washington DC, 1997.
20. Molkov, V. *Fundamentals of Hydrogen Safety Engineering;* Ventus Publishing ApS. Available from: http://bookboon.com/.
21. Galassi, M. C.; Papanikolau, E.; Baraldi, D.; Funnemark, E.; Håland, E.; Engebø, A.; Haugom, G. P.; Jordan, T.; Tchouvelev, A. V. HIAD − Hydrogen Incident and Accident Database. *Int. J. Hydrogen Energy* **2012,** *37,* 17351.
22. Weiner, S. C.; Fassbender, L. L.; Quick, K. A. Using Hydrogen Safety Best Practices and Learning from Safety Events. *Int. J. Hydrogen Energy* **2011,** *36,* 2729.
23. Weiner, S. C.; Fassbender, L. L. Lessons Learned from Safety Events. *Int. J. Hydrogen Energy* **2012,** *37,* 17358.
24. Louthan, M. R.; Caskey, G. R. Hydrogen Transport and Embrittlement in Structural Metals. *Int. J. Hydrogen Energy* **1976,** *1,* 291.
25. Mirza, N. R.; Degenkolbe, S.; Witt, W. Analysis of Hydrogen Incidents to Support Risk Assessment. *Int. J. Hydrogen Energy* **2011,** *36,* 12068.
26. Buttner, W. J.; Post, M. B.; Burgness, R.; Rivkin, C. An Overview of Hydrogen Safety Sensors and Requirements. *Int. J. Hydrogen Energy* **2011,** *36,* 2462.
27. Buttner, W. J.; Burgness, R.; Rivkin, C.; Post, M. B.; Boon-Brett, L.; Black, G.; Harskamp, F.; Moretto, P. Inter-Laboratory Assessment of Hydrogen Safety Sensors Performance under Anaerobic Conditions. *Int. J. Hydrogen Energy* **2012,** *37,* 17540.
28. Legg, S. W.; Benavides-Serrano, A. J.; Siirola, J. D.; Watson, J. P.; Davis, S. G.; Bratteteig, A.; Laird, C. D. A Stochastic Programming Approach for Gas Detector Placement using CFD-Based Dispersion Simulations. *Comput. Chem. Eng.* **2012,** *47,* 194.
29. Menter, F. R.; Langtrey, R.; Völker, S. Transition Modelling for General Purpose CFD Codes. *Flow Turbul. Combust.* **2006,** *77,* 277.
30. Gallego, E.; Migoya, E.; Martín-Valdepeñas, J. M.; Crespo, A.; García, J.; Venetsanos, A.; Papanikolau, E.; Kumar, S.; Studer, E.; Dagba, Y.; Jordan, T.; Jahn, W.; Høiset, S.; Makarov, D.; Piechna, J. An Intercomparison Exercise on the Capabilities of CFD Models to Predict Distribution and Mixing of H_2 in a Closed Vessel. *Int. J. Hydrogen Energy* **2007,** *32,* 2235.
31. Walters, D. K.; Cokljat, D. A Three-Equation Eddy-Viscosity Model for Reynolds-Averaged Navier−Stokes Simulations of Transitional Flow. *J. Fluids Eng.* **2008,** *30,* 121401−121402.
32. Koutsourakis, N.; Venetsanos, A. G.; Bartzis, J. G. LES Modelling of Hydrogen Release and Accumulation within a Non-ventilated Ambient Pressure Garage using the ADREA-HF CFD Code. *Int. J. Hydrogen Energy* **2012,** *37,* 17426.
33. Venetsanos, A. G.; Papanikolau, A.; Delichatsios, M.; Garcia, J.; Hansen, O. R.; Heitsch, M.; Huser, A.; Jahn, W.; Jordan, T.; Lacome, J.-M.; Ledin, H. S.; Makarov, D.; Middha, P.; Studer, E.; Tchouvelev, A. V.; Teodorczyk, A.; Verbecke, F.; Van der Voort, M. M. An Inter-comparison Exercise on the Capabilities of CFD Models to Predict the Short and Long Term Distribution and Mixing of Hydrogen in a Garage. *Int. J. Hydrogen Energy* **2009,** *34,* 5912.
34. Shebeko, Y. N.; Keller, V. D.; Yeremenko, O. Y.; Smolin, L. M.; Serkin, M. A.; Korolchenko, A. Y. Regularities of Formation and Combustion of Local Hydrogen−Air Mixtures in a Large Volume (In Russian). *Chem. Ind.* **1988,** *21−24,* 728.
35. Lacome, J. M.; Dagba, Y.; Jamois, D.; Perrette, L.; Proust, C. Large Scale Hydrogen Release in an Isothermal Confined Area. In *2nd International Conference on Hydrogen Safety*; San Sebastián, Spain, 2007.

36. http://www.cham.co.uk/phoenics/d_polis/d_enc/turmod/enc_t312.htm.
37. Prasad, K.; Yang, J. Vertical Release of Hydrogen in a Partially Enclosed Compartment: Role of Wind and Buoyancy. *Int. J. Hydrogen Energy* **2011,** *36,* 1094.
38. Venetsanos, A. G.; Papanikolaou, E.; Hansen, O. R.; Middha, P.; Garcia, J.; Heitsch, M.; Baraldi, D.; Adams, P. HySafe Standard Benchmark Problem SBEP-V11: Predictions of Hydrogen Release and Dispersion from a CGH2 bus in an Underpass. *Int. J. Hydrogen Energy* **2010,** *35,* 3857.
39. Houf, W. G.; Evans, G. H.; Merilo, E.; Groethe, M.; James, S. C. Releases from Hydrogen Fuel-Cell Vehicles in Tunnels. *Int. J. Hydrogen Energy* **2012,** *37,* 715.
40. Wilkening, H.; Baraldi, D. CFD Modelling of Accidental Hydrogen Release from Pipelines. *Int. J. Hydrogen Energy* **2007,** *32,* 2206.
41. Salva, J. A.; Tapia, E.; Iranzo, A.; Pino, F. J.; Cabrera, J.; Rosa, F. Safety Study of a Hydrogen Leak in a Fuel Cell Vehicle using Computational Fluid Dynamics. *Int. J. Hydrogen Energy* **2012,** *37,* 5299.
42. Liu, H.; Schreiber, W. The Effect of Ventilation System Design on Hydrogen Dispersion in a Sedan. *Int. J. Hydrogen Energy* **2008,** *33,* 5115.
43. Heitsch, M.; Huhtanen, R.; Téchy, Z.; Fry, C.; Kotska, P.; Niemi, J.; Schramm, B. CFD Evaluation of Hydrogen Risk Mitigation Measures in a VVER-440/213 Containment. *Nuclear Eng. Des.* **2010,** *240,* 385.
44. Venetsanos, A. G.; Bartzis, J. G. CFD Modeling of Large-Scale LH2 Spills in Open Environment. *Int. J. Hydrogen Energy* **2007,** *32,* 2171.
45. Middha, P.; Hansen, O. R. CFD Simulation Study to Investigate the Risk from Hydrogen Vehicles in Tunnels. *Int. J. Hydrogen Energy* **2009,** *34,* 5875.
46. Ichard, M.; Hansen, O. R.; Middha, P.; Willoughby, D. CFD Computations of Liquid Hydrogen Releases. *Int. J. Hydrogen Energy* **2012,** *37,* 17380.
47. Venetsanos, A. G.; Papanikolaou, E.; Bartzis, J. G. The ADREA-HF CFD Code for Consequence Assessment of Hydrogen Applications. *Int. J. Hydrogen Energy* **2010,** *35,* 3908.
48. Kikukawa, S. Consequence Analysis and Safety Verification of Hydrogen Fueling Stations using CFD Simulation. *Int. J. Hydrogen Energy* **2008,** *33,* 1425.
49. Papanikolaou, E.; Venetsanos, A. G.; Cerchiara, G. M.; Carcassi, M.; Markato, N. CFD Simulations on Small Hydrogen Releases Inside a Ventilated Facility and Assessment of Ventilation Efficiency. *Int. J. Hydrogen Energy* **2011,** *36,* 2597.
50. Middha, P.; Ichard, M.; Arntzen, B. J. Validation of CFD Modelling of LH2 Spread and Evaporation Against Large-Scale Spill Experiments. *Int. J. Hydrogen Energy* **2011,** *36,* 2620.
51. Venetsanos, A. G.; Papanikolaou, E.; Cariteau, B.; Adams, P.; Bengaouer, A. Hydrogen Permeation from CGH2 Vehicles in Garages: CFD Dispersion Calculations and Experimental Validation. *Int. J. Hydrogen Energy* **2010,** *35,* 3848.
52. Molkov, V.; Makarov, D.; Schneider, H. Hydrogen−Air Deflagrations in Open Atmosphere: Large Eddy Simulation Analysis of Experimental Data. *Int. J. Hydrogen Energy* **2007,** *32,* 2198.
53. Molkov, V.; Verbecke, F.; Makarov, D. LES of Hydrogen−Air Deflagrations in a 78.5 m Tunnel. *Combust. Sci. Technol.* **2008,** *180,* 769.
54. Yakhot, V. Propagation Velocity of Premixed Turbulent Flames. *Combust. Sci. Technol.* **1988,** *60,* 191.
55. Baraldi, D.; Wilkening, H. CFD Simulations of Hydrogen Combustion in a Simplified EPR Containment with CFX and REACFLOW. *Nuclear Eng. Des.* **2007,** *237,* 1668.
56. Magnussen, B. F. On the Structure of Turbulence and a Generalized Eddy Dissipation Concept for Chemical Reaction in Turbulent Flow. 19th American Institute of Aeronautics and Astronautics Aerospace Science Meeting, 1981.
57. Baraldi, D.; Kotchourko, A.; Lelyakin, A.; Yáñez, J.; Middha, P.; Hansen, O. R.; Gavrikov, A.; Efimenko, A.; Verbecke, F.; Makarov, D.; Molkov, V. An Inter-comparison Exercise on CFD Model Capabilities to Simulate Hydrogen Deflagrations in a Tunnel. *Int. J. Hydrogen Energy* **2009,** *34,* 7862.
58. Makarov, D.; Verbecke, F.; Molkov, V.; Kotchourko, A.; Lelyakin, A.; Yáñez, J.; Baraldi, D.; Heitsch, M.; Efimenko, A.; Gavrikov, A. An Intercomparison of CFD Models to Predict Lean and Non-uniform Hydrogen Mixture Explosions. *Int. J. Hydrogen Energy* **2010,** *35,* 5754.
59. Zbikowski, M.; Makarov, D.; Molkov, V. LES Model of Large Scale Hydrogen−Air Planar Detonations: Verification by the ZND Theory. *Int. J. Hydrogen Energy* **2008,** *33,* 4884.
60. Yáñez, J.; Kotchourko, A.; Lelyakin, A.; Gavrikov, A.; Efimenko, A.; Zbikowski, M.; Makarov, D.; Molkov, V. A Comparison Exercise on the CFD Detonation Simulation in Large-Scale Confined Volumes. *Int. J. Hydrogen Energy* **2011,** *36,* 2613.
61. Groethe, M.; Merilo, E.; Colton, J.; Chiba, S.; Sato, Y.; Iwabuchi, H. Large-Scale Hydrogen Deflagrations and Detonations. *Int. J. Hydrogen Energy* **2007,** *32,* 2125.
62. Houf, W.; Schefer, R.; Evans, G.; Merilo, E.; Groethe, M. Evaluation of Barrier Walls for Mitigation of Unintended Releases of Hydrogen. *Int. J. Hydrogen Energy* **2010,** *35,* 4758.

RENEWABLE HYDROGEN TECHNOLOGIES

PRODUCTION, PURIFICATION, STORAGE, APPLICATIONS AND SAFETY

Edited by

LUIS M. GANDÍA
Escuela Técnica Superior de Ingenieros Industriales y de Telecomunicación, Universidad Pública de Navarra, Campus de Arrosadía, Pamplona, Spain

GURUTZE ARZAMENDI
Escuela Técnica Superior de Ingenieros Industriales y de Telecomunicación, Universidad Pública de Navarra, Campus de Arrosadía, Pamplona, Spain

PEDRO M. DIÉGUEZ
Escuela Técnica Superior de Ingenieros Industriales y de Telecomunicación, Universidad Pública de Navarra, Campus de Arrosadía, Pamplona, Spain

ELSEVIER

AMSTERDAM • BOSTON • HEIDELBERG • LONDON
NEW YORK • OXFORD • PARIS • SAN DIEGO
SAN FRANCISCO • SYDNEY • TOKYO

List of Contributors

María Consuelo Alvarez-Galván, Grupo de Energía y Química Sostenibles, Instituto de Catálisis y Petroleoquímica (CSIC), Marie Curie 2, Madrid, Spain

Javier Arenales, Grupo de Energía y Química Sostenibles, Instituto de Catálisis y Petroleoquímica (CSIC), Marie Curie 2, Madrid, Spain

Gurutze Arzamendi, Escuela Técnica Superior de Ingenieros Industriales y de Telecomunicación, Universidad Pública de Navarra, Campus de Arrosadía, E-31006 Pamplona, Spain

Clara Casado, Departamento de Ingeniería Química y Química Inorgánica, E.T.S. Ingenieros Industriales y Telecomunicación, Universidad de Cantabria, Santander, Spain

Diego Cazorla-Amorós, Departamento Química Inorgánica and Instituto de Materiales, Universidad de Alicante, Alicante, Spain

Miguel Ángel Centeno, Department of Inorganic Chemistry and Institute of Materials Science of Seville, University of Sevilla-CSIC, Sevilla, Spain

De Chen, Department of Chemical Engineering, Norwegian University of Science and Technology, Trondheim, Norway

Alfonso Cornejo, Dept. Química Aplicada, Universidad Pública de Navarra, Pamplona, Spain

Vicente Cortés Corberán, Institute of Catalysis and Petroleumchemistry (ICP), Spanish Council for Scientific Research (CSIC), Marie Curie 2, Madrid, Spain

Loreto Daza, Instituto de Catálisis y Petroleoquímica (CSIC), Madrid, Spain

Joachim Demuynck, Ghent University, Department of Flow, Heat and Combustion Mechanics, Sint-Pietersnieuwstraat 41. 9000 Gent, Belgium

Pedro M. Diéguez, Escuela Técnica Superior de Ingenieros Industriales y de Telecomunicación, Universidad Pública de Navarra, Campus de Arrosadía, E-31006 Pamplona, Spain

Núria J. Divins, Institute of Energy Technologies, Technical University of Catalonia—BarcelonaTECH, Barcelona, Spain

Francisco J. Echave, Novargi-Nova-Synergy Industrial Solutions S.L, Vitoria-Gasteiz, Spain

Asier Eleta, NOVARGI-Nova Synergy Industrial Solutions, Vitoria-Gasteiz, Spain

José Luis García Fierro, Grupo de Energía y Química Sostenibles, Instituto de Catálisis y Petroleoquímica (CSIC), Marie Curie 2, Madrid, Spain

Raquel Olivera Fraile, Institute of Catalysis and Petroleumchemistry (ICP), Spanish Council for Scientific Research (CSIC), Marie Curie 2, Madrid, Spain

Luis M. Gandía, Escuela Técnica Superior de Ingenieros Industriales y de Telecomunicación, Universidad Pública de Navarra, Campus de Arrosadía, E-31006 Pamplona, Spain

María José Gil, Dept. Química Aplicada, Universidad Pública de Navarra, Pamplona, Spain

Sergey Grigoriev, National Research Center "Kurchatov Institute", Moscow, Russian Federation

Li He, Department of Chemical Engineering, Norwegian University of Science and Technology, Trondheim, Norway

Aitor Hornés, Instituto de Catálisis y Petroleoquímica (CSIC), Madrid, Spain

Anis Houaijia, Deutsches Zentrum für Luft und Raumfahrt e.V., Institute of Solar Research, Linder Höhe, Köln, Germany

Iñigo Idareta, Escuela Técnica Superior de Ingenieros Industriales y de Telecomunicación, Universidad Pública de Navarra, Campus de Arrosadía, E-31006 Pamplona, Spain

Svetlana Ivanova, Department of Inorganic Chemistry and Institute of Materials Science of Seville, University of Sevilla-CSIC, Sevilla, Spain

Oscar Hernando Laguna, Department of Applied Chemistry, UFI11/53, University of the Basque Country, UPV/EHU, San Sebastian, Spain

Ángel Linares-Solano, Departamento Química Inorgánica and Instituto de Materiales, Universidad de Alicante, Alicante, Spain

Jordi Llorca, Institute of Energy Technologies, Technical University of Catalonia—BarcelonaTECH, Barcelona, Spain

Javier López-San Martín, Escuela Técnica Superior de Ingenieros Industriales y de Telecomunicación, Universidad Pública de Navarra, Campus de Arrosadía, E-31006 Pamplona, Spain

Dolores Lozano-Castelló, Departamento Química Inorgánica and Instituto de Materiales, Universidad de Alicante, Alicante, Spain

Luis Marroyo, Department of Electrical and Electronic Engineering, Public University of Navarre, Pamplona, Spain

Antonio José Martín, CIEMAT, Madrid, Spain

Arturo Martínez-Arias, Instituto de Catálisis y Petroleoquímica (CSIC), Madrid, Spain

Víctor Martínez-Merino, Dept. Química Aplicada, Universidad Pública de Navarra, Pamplona, Spain

Nicholas S. Matthias, Energy Systems Division, Argonne National Laboratory, Building 362, 9700 South Cass Avenue, Argonne, IL 60439-4815, USA

Pierre Millet, University of Paris (XI), France

Nathalie Monnerie, Deutsches Zentrum für Luft und Raumfahrt e.V., Institute of Solar Research, Linder Höhe, Köln, Germany

Mario Montes, Department of Applied Chemistry, UFI11/53, University of the Basque Country, UPV/EHU, San Sebastian, Spain

Alberto Navajas, Departamento de Química Aplicada, Universidad Pública de Navarra, Pamplona, Spain

Rufino Manuel Navarro Yerga, Grupo de Energía y Química Sostenibles, Instituto de Catálisis y Petroleoquímica (CSIC), Marie Curie 2, Madrid, Spain

José Antonio Odriozola, Department of Inorganic Chemistry and Institute of Materials Science of Seville, University of Sevilla-CSIC, Sevilla, Spain

Martin Roeb, Deutsches Zentrum für Luft und Raumfahrt e.V., Institute of Solar Research, Linder Höhe, Köln, Germany

Francisca Romero-Sarria, Department of Inorganic Chemistry and Institute of Materials Science of Seville, University of Sevilla-CSIC, Sevilla, Spain

Pablo Sanchis, Department of Electrical and Electronic Engineering, Public University of Navarre, Pamplona, Spain

Oihane Sanz, Department of Applied Chemistry, UFI11/53, University of the Basque Country UPV/EHU, San Sebastian, Spain

Christian Sattler, Deutsches Zentrum für Luft und Raumfahrt e.V., Institute of Solar Research, Linder Höhe, Köln, Germany

Riccardo Scarcelli, Energy Systems Division, Argonne National Laboratory, Building 362, 9700 South Cass Avenue, Argonne, IL 60439-4815, USA

Roger Sierens, Ghent University, Department of Flow, Heat and Combustion Mechanics, Sint-Pietersnieuwstraat 41. 9000 Gent, Belgium

Fabián Suárez-García, Instituto Nacional del Carbón, INCAR-CSIC, Oviedo, Spain

Elena Taboada, Institute of Energy Technologies, Technical University of Catalonia—BarcelonaTECH, Barcelona, Spain

Dennis Thomey, Deutsches Zentrum für Luft und Raumfahrt e.V., Institute of Solar Research, Linder Höhe, Köln, Germany

Irantzu Uriz, Escuela Técnica Superior de Ingenieros Industriales y de Telecomunicación, Universidad Pública de Navarra, Campus de Arrosadía, E-31006 Pamplona, Spain

Alfredo Ursúa, Department of Electrical and Electronic Engineering, Public University of Navarre, Pamplona, Spain

Fernando Vaquero, Grupo de Energía y Química Sostenibles, Instituto de Catálisis y Petroleoquímica (CSIC), Marie Curie 2, Madrid, Spain

Robert A. Varin, Department of Mechanical and Mechatronics Engineering, University of Waterloo, Waterloo, Canada N2L 3G1

Sebastian Verhelst, Ghent University, Department of Flow, Heat and Combustion Mechanics, Sint-Pietersnieuwstraat 41. 9000 Gent, Belgium

Thomas Wallner, Energy Systems Division, Argonne National Laboratory, Building 362, 9700 South Cass Avenue, Argonne, IL 60439-4815, USA

Zbigniew S. Wronski, Department of Mechanical and Mechatronics Engineering, University of Waterloo, Waterloo, Canada N2L 3G1; Canmet ENERGY, Natural Resources Canada, Ottawa, Canada K1A 1M1

Jia Yang, Department of Chemical Engineering, Norwegian University of Science and Technology, Trondheim, Norway

Beatriz Zornoza, Departamento de Ingeniería Química y Tecnologías del Medio Ambiente, Instituto de Nanociencia de Aragón, Universidad de Zaragoza, Zaragoza, Spain

Elsevier
Radarweg 29, PO Box 211, 1000 AE Amsterdam, The Netherlands
The Boulevard, Langford Lane, Kidlington, Oxford, OX5 1GB, UK
225 Wyman Street, Waltham, MA 02451, USA

British Library Cataloguing in Publication Data
A catalogue record for this book is available from the British Library

Library of Congress Cataloging-in-Publication Data
A catalog record for this book is available from the Library of Congress

ISBN: 978-0-444-56352-1

Printed and bound in Poland
13 14 15 16 17 10 9 8 7 6 5 4 3 2 1

Preface

Public awareness on energy security, climate change and other environmental problems is continuously growing and does exert pressure on policymakers and governments to adopt urgent and convenient solutions. Within this context, never has been more necessary than today to claim hydrogen as a key element of a long-awaited sustainable energy model. End use of hydrogen releases the energy stored in it producing water as the sole product with minimal impacts on the environment. However, to be really sustainable, hydrogen has to be produced from renewable sources. This is the central point of this book: a comprehensive update of the main routes for producing hydrogen from water and biomass using renewable energy sources.

In the recent years, the field of hydrogen energy, and the concept of "Hydrogen Economy" itself, have evolved considerably. The several aspects covered by these topics are reaching high levels of specialization making them true individual disciplines. This is the case of hydrogen production and, more specifically, renewable hydrogen production, a subject that has not been treated according to a unified approach by previous books. In the present work, the reader will find in the same volume the latest technological advances on hydrogen production from water and biomass. This includes photocatalytic and solar thermal water splitting as well as water electrolysis. As concerns biomass, its sources as feedstock for hydrogen production, and the advances in thermochemical and biological hydrogen production are described. On the other hand, hydrogen purification and storage, continue being key challenges that could limit the future use of hydrogen irrespective of its source. For this reason the advancements in purification of hydrogen with membrane technology and its storage in "solid" form using new hydrides and carbon materials are addressed.

The emergence and great impulse acquired by microreactors and micro process engineering for distributed and portable energy generation have led us to the inclusion of two chapters with the aim of showing the interest and the new perspectives open by these technologies in the fields of hydrogen production and purification.

Other novelties of this book include the analysis of suitable power supplies to make the integration of water electrolysers and renewable energy-based systems possible with the maximum energy efficiency. Also the use of modern simulation tools such as computational fluid dynamics (CFD) for designing hydrogen technologies and the assessment of hydrogen safety issues. Finally, the recent advances in fuel cells and hydrogen-fueled internal combustion engines are presented.

The several chapters that constitute this book have been written by recognized specialists that have compiled, organized and discussed the most recent information available resulting in a practical and updated reference volume. The book is primarily aimed at professionals from both the academia and industry but it will be found useful equally by interested public and postgraduate students of environmental sciences, chemistry, physics and engineering as well as policymakers and consultants.

We would like to thank all the authors and the reviewers of the book proposal for their very valuable contributions and critical feedback. We also thank our editors from Elsevier, Kostas Marinakis, Anita Koch and Louisa Hutchins for their advice, help and patience. Our families have also had a lot of patience with us; special thanks to them for their support and time.

Luis M. Gandía (lgandia@unavarra.es),
Gurutze Arzamendi (garzamendi@unavarra.es),
Pedro M. Diéguez (pmde@unavarra.es)
Public University of Navarre, Pamplona

Index

Note: Page numbers with "f" denote figures; "t" tables.

A

ac-ac converters, 335
ac-dc converters, 335
  groups of, 339
    controlled rectifiers, 339
    uncontrolled rectifiers, 339
  single-phase, 338–339
  three-phase, 338–339
ACFs. *See* Activated carbon fibers
ACs. *See* Activated carbons
Activated carbon fibers (ACFs), 272–273
Activated carbons (ACs), 272–273
Alanates
  lithium, 301–316
  sodium, 296–301
Alkaline water electrolysis
  advances, 28–29
  cell components and, 26
  limitations, 28–29
  PEM water electrolysis compared with, 32–33, 33t
  performances, 26
  perspectives, 28–29
  principles, 25
  stack structure and, 26
  technology developments and applications, 26–27
Andromeda HCS-575 fuel cell, 294
Anisotropic photocatalysts, 56–57
Annual Report on World Progress in Hydrogen (PATH), 15–16
Aqueous phase reforming, 121–122
  hydrogen production, 102–103
Argonne National Laboratory, 3–4
Autothermal oxidation, 150
Autothermal reforming, ethanol, 151–155
  catalytic systems, 154–155
  nickel catalysts, 152–154
  noble metal catalysts, 151–152
Auxiliary power units, 334–340

B

Band gap engineering
  approaches to
    cation or anion doping, 50–52
    composite systems, 52
    solid solutions, 52–54
  photocatalyst visible response strategies, 50–54
BEE project. *See* Biomass Energy Europe project
Biodiesel hydrogen production, 213
Bioethanol
  definition of, 135–136
  hydrogen production, 216
  manufacture, 136
Biofuels, hydrogen production, 209–217
  biodiesel, 213
  bioethanol, 216
  biogas, 215
  bioglycerol, 213–215
  biomethanol, 211–213
  bio-oil, 217
  dimethyl ether, 210–211
  producer gas, 215–216
Biogas
  biomass-derived chemicals, sorption-enhanced reforming of, 124
  hydrogen production, 215
Bioglycerol hydrogen production, 213–215
Biomass. *See also* Feedstocks
  carbohydrates derived from, 88
  composition and properties, 89–92
  hydrogen production from, 87–89, 111–113, 129
    aqueous phase reforming, 102–103
    bio-oil and, 101–102
    fast pyrolysis, 101–102
    microbial conversion, 104–105
    thermochemical gasification, 98–101
    transformations, 103–104
  microbial conversion of, 104–105
    dark fermentation, 104–105
    photofermentation, 105
  resource potential, 92–94
  supercritical water-mediated transformations of, 103–104
  thermal chemical conversion of, CO_2 acceptor in, 126
Biomass Energy Europe (BEE) project, 93
Biomass gasification, hydrogen production
  catalysts, 127–128
  sorption-enhanced, 128
  sorption-enhanced water gas shift reaction, 128–129
Biomass-derived chemicals
  sorption-enhanced reforming of, 123–126
    biogas, 124
    bio-oil, 125–126
    catalyst, 126
    CO_2 acceptor and, 126
    ethanol, 124–125
    hydrogen production, 123–124
    polyols, 124–125
    sugars, 125
  steam reforming of, 113–121
    biomass-derived oxygenates and, 116–119
    bio-oil, 115–116
    carbohydrates, 114–115
    challenges in, 113–114
    coke formation in, 119–120
    ethanol, 114–115
    fast pyrolysis and, 115–116
    reactors for, 121
    thermal efficiency of, 120–121
Biomethanol
  hydrogen production, 211–213
  membranes, 212
  microfibrous networks, 212–213
Bio-oil
  aqueous phase of, 125–126
  biomass, hydrogen production, 101–102
  biomass-derived, steam reforming of, 115–116
  biomass-derived chemicals, sorption-enhanced reforming of, 125–126
  hydrogen production, 217
Biophotolysis
  CO_2 emissions reduced by, 194
  cyanobacteria, 190–193
    photobioreactors and operating conditions of, 193
    substrate, 191–193
  green algae, 187–190
    photobioreactors and operating conditions of, 189–190
    substrate, 187–189
Bioreactors, 176–177
BMW, 386–387, 387f
Burns
  cryogenic, 440–441
  thermal, 440–441

C

Carbide-derived carbons, 273
Carbohydrates, biomass-derived
  definition of, 88
  steam reforming of, 114–115
Carbon
  activated, 272–273
  carbide-derived, 273
  doped, 274
  fibers, 272–273
  forms, 270–271

Carbon (*Continued*)
carbynes, 271
diamond, 271
fullerene, 271
graphite, 271
materials, 270–274
hydrogen adsorption in, 276–281
porous, 273–274, 283–286
nanofibers, 271–272
nanotubes, 271–272
templated
ordered mesoporous, 273–274
zeolite, 273–274
Carbon materials, 270–274
hydrogen adsorption, 276–281
porous
carbide-derived, 273
porous materials compared with, 283–286
templated, 273–274
Carbon membranes, 262–263
Carbon tax, 5
Carbynes, 271
Catalysts
biomass gasification, hydrogen production, 127–128
biomass-derived chemicals, sorption-enhanced reforming of, 126
cobalt, 145–147
ethanol, autothermal reforming of, 154–155
hydrogen production routes of, 136–138
nickel, 143–145, 152–154
noble metal, 141–143, 148–149, 151–152
structured, 149–150
structured substrate coating, 205–209
dip coating, 206–208
surface growing, 208–209
Catalytic membrane reactors, 155–158
Catalytic wall microreactors, CFD for reforming of gaseous fuels, 416–423
CDS. *See* Central Differencing Scheme
Cell components
alkaline water electrolysis and, 26
high-temperature water electrolysis, 37
PEM water electrolysis, 29f, 30–31, 35–36
Central Differencing Scheme (CDS), 408
Ceramic membranes, 256
steam reforming, 261
WGS, 262–263
CFD. *See* Computational fluid dynamics
CHP. *See* Combined heat and power
Climate change
decarbonization and, 4–6
energy security and, 1–6
international energy outlook and, 2–4
CO_2 emissions, 3–4
electricity, 3–4
natural gas and coal, 3–4
oil and liquid fuels, 2–3
CO cleanup
fine cleanup
PROX, 227–229
selective methanation, 227–229
fundamentals, 226–229
structured reactors for, 229–230
WGS as first stage of, 226–227
CO_2 acceptor
biomass-derived chemicals and, sorption-enhanced reforming of, 126
in thermal chemical conversion, of biomass, 126
CO_2 emissions
biophotolysis reducing, 194
energy international outlook, 4
increases in, 4
Cobalt
catalysts, 145–147
steam reforming, ethanol, 145–147
Co-cultivation, 183–184
Coke formation, in steam reforming, of biomass-derived chemicals, 119–120
Combined heat and power (CHP), 375
micro-, 375
small, 375
Combustion, 217–218
abnormal, 386
backfire, 386
knock, 386
preignition, 386
hydrogen, CFD, 446–449
Complex hydrides, hydrogen storage in, 293–295, 327–329
alanates, 296–316
lithium amides, 320–327
metal borohydrides, 316–320
Computational fluid dynamics (CFD), 401–402, 431
basics, 402–410
boundary condition, 405
computational domains, 405
discretization, 405–407
initial condition, 405
mathematical modeling, 402–405
numerical solution, 407–409
problem and physical model definition, 402
results interpretation, 409–410
boundary conditions, 405
for conversion of solid or liquid fuels
anaerobic fermentation, 425
gasification and pyrolysis, 424–425
deflagration modeling, 446–447
hydrogen combustion, 446–449
deflagration process modeling, 446–447
detonation process modeling, 447–449
for hydrogen energy end-use applications, 426–431
fuel cells, 426–429
hydrogen engines, 429–431
hydrogen leaks and dispersion, 443–446
modeling, 445–446
transport phenomena, 443–445
for hydrogen production technologies design, 410–426
for reforming of gaseous fuels, 411–423
catalytic wall microreactors, 416–423
fixed-bed reactors, 411–414
fluidized-bed reactors, 414–416
safety investigated by, 439
symmetry influencing, 405
for water electrolysis, 425–426
Controlled rectifiers, 339
Copper-chlorine cycle, 78–80
electrolysis step in, 79
hydrogen production step in, 79
hydrolysis step in, 79
oxygen production step in, 79
Costs
fuel cell systems, 365–366
mobile application, 365–366
stationary application, 372–373
hydrogen production, Life Cycle Assessment and, 105–107
water electrolysis, 334
Crank-Nicholson method, 408
CRISTINA process, 74
Cryogenic burns, 440–441
Cryogenic PFI, 387
CUTE. *See* Clean Urban Transport for Europe
Cyanobacteria
biophotolysis
photobioreactors and operating conditions, 193
substrate, 191–193
photobioreactors, biophotolysis, 193

D

d^{10} metal oxides, photocatalysts, 48
Dark fermentation, 173–178
biomass, microbial conversion, 104–105
bioreactor type, 176–177
coupled processes to
co-cultivation technologies, 183–184
sequential cultivation technologies, 184
hydrogen production, biological, 173–178
operational parameters, 177–178
substrate, 175–176
dc-ac converters, 335
dc-dc converters, 335
operation of, 337
types of, 337
Decarbonization
climate change and, 4–6
EIA and, 4–5
energy security and, 4–6
IEA and, 4–5
milestones, 5
Deflagration
CFD modeling, 446–447
characteristics of, 439–440
conditions for, 441–442
detonation compared with, 442–443
detonation initiated by, 443
temperatures and pressures, 442t
Demonstration vehicles, 386–387
Quantum Prius, 386, 386f
Department of Energy, U.S.
Hydrogen and Fuel Cells Program, 15
hydrogen requirements of, 294
Nuclear Hydrogen Initiative, 75
Technology Validation Program, 365
Detonation
deflagration compared with, 442–443
deflagration initiating, 443

description of, 442–443
temperatures and pressures, 442–443, 442t
Dimethyl ether hydrogen production, 210–211
Diodes, 335–336
operation of, 336
Dip coating
procedure
channel size and shape, 207
dipping and withdrawing velocity, 207
drying, 208
slurry excess elimination, 208
substrate surface, 207
viscosity, 207–208
slurry properties of
catalyst particle size, 206
viscosity, 206
Direct injection, 387
Direct water splitting, 64–65
separation
at high temperature, 65
at low temperature, 65
Directive 2009/28/EC, 351–352
Directive on the Promotion of the Use of Energy from Renewable Sources (EU), 5–6
Discretization, 405–407
errors, 409
Doped carbons, 274–286
Drying
pretreatment, 95
in washcoating procedure, 208
Dye sensitization, photocatalysts visible response strategies, 54–55

E

EC. *See* European Commission
ECF. *See* European Climate Foundation
EIA. *See* Energy Information Administration, U.S.
Electric grid, 9–11
in Europe, 5
wind power connected to, 343
Electricity
EIA on, 4
energy international outlook, 4
world net generation of, 4
Electrolyzer Company, 27
Electrolyzers, 333–334, 343, 357–358
power supplies, 334–344
electronic conversion systems, 340–344
power electronic systems, 334–340
solar operating condions influencing, 354–357
wind power connected to grid by, 343
wind turbines connected to, 343
Energy
for high-temperature water electrolysis, 81–83
international outlook on
CO_2 emissions, 4
electricity, 4
fossil fuels, 2–4
natural gas and coal, 3–4
oil and liquid fuels, 2–3
primary consumption of, 5f
for water splitting, 45–46
Energy carrier
in hydrogen economy and, 6–7, 15–16
Energy efficiency
energy carrier and, 7–9
in hydrogen engine, 395–396
hydrogen production systems, 344–351
overall, 349–351
water electrolyzer, 344–349
of power semiconductors, 335
power supply influencing, 347–349
Energy Information Administration, U.S. (EIA)
decarbonization and, 4–5
on electricity, 4
on international energy outlook, 2
on natural gas and coal, 3–4
on oil and liquid fuels, 2–3
Energy security
climate change and, 1–6
decarbonization and, 4–6
international energy outlook and, 2–4
CO_2 emissions, 4
electricity, 4
natural gas and coal, 3–4
oil and liquid fuels, 2–3
Ethanol
autothermal reforming of, 151–155
catalytic systems, 154–155
nickel catalysts, 152–154
noble metal catalysts, 151–152
biomass-derived, steam reforming of, 114–115
biomass-derived chemicals, sorption-enhanced reforming of, 124–125
hydrogen from, 135–141, 161
photocatalytic production, 159–161
partial oxidation, 147–150
autothermal oxidation, 150
noble metal catalysts, 148–149
non-noble metals, 149–150
preliminary overview, 147
reaction mechanism, 147–148
structured catalysts, 149–150
reaction pathways of, 138–141
reforming
in catalytic membrane reactors, 155–158
in miniaturized systems, 158–159
steam reforming of
cobalt catalysts, 145–147
nickel catalysts, 143–145
noble metal catalysts, 141–143
thermodynamics, 138–141
ETH-Caltech solar reactor, 72, 72f
EU. *See* European Union
European Climate Foundation (ECF), 5
European Commission (EC), 5–6, 15
European Commission Joint Research Council (JRC-Ispra), 74
European Energy and Climate Change Package, 351–352
Explicit method, 408
Explosion, 442–443

F

Fast pyrolysis, 101–102
FCVs. *See* Fuel cell vehicles
Feedstocks, pretreatment of, 94–97
biological, 97
chemical, 95–97
physical and thermal, 94–95
Finite volume method (FVM), 407–409
Fixed-bed reactors, 411–414
Fluidized-bed reactors, 414–416
Forced commutation, 336
converters, 339
Fossil fuels
energy, international outlook on, 2–4
greenhouse gases increased by, 293
hydrogen production from, 12
Fuel cell vehicles (FCVs)
buses, 366–367
commercialization of, 334–335, 363
cost, 365–366
in Europe, 5
general characteristics of, 363–365
GHG emissions cut by, 361–362
market prospective, 367
on-board fuel reforming of, 364–365
required features for, 363–366
technical objectives, 365–366
Fuel cells, 7–10, 225–226, 361–362, 377–378
Andromeda HCS-575, 294
automotive systems, 363–365
buses, 366–367
cost
for mobile applications, 365–366
for stationary applications, 372–373
governmental programs influencing, 376–377
high-temperature, 369–372
molten carbonate, 372
solid oxide, 369–372
hydrogen storage influenced by, 294
ICE compared with, hydrogen, 381–384
low-temperature, 368–369
in mainstream transportation, 363
materials handling, 366
mobile applications
auxiliary power units, 362
motive power, 362–363
other applications for, 367
other transport powered by, 363
special vehicles powered by, 362–363
stationary applications, 367–376
backup power, 374–375
combined heat and power, 375
market prospective, 375–376
market status, 373–375
as power backup, 368
power source, 368
R&D guidelines for, 373
renewable energy source part, 368
technical features, 368–373
types, 368

Fuel cells (*Continued*)
technical objectives, 365–366
transport applications
market prospective, 367
market status, 366–367
required features, 363–366
types, 362–363
vehicles, 366
FVM. *See* finite volume method

G

G8. *See* Group of Eight
GA. *See* General Atomics
Gas adsorption, 274–276
Gas separation, membranes, 247–251
commercial, 251
performance parameters, 247–248
Gate turn-off thyristor (GTO), 335–336
IGBT compared to, 336
operation of, 336
Gemasolar solar power tower, 82, 82f
GHGs. *See* Greenhouse gases
Graphite, 271
Green algae
biophotolysis, 187–190
photobioreactors and operating conditions, 189–190
substrate, 187–189
photobioreactors, biophotolysis, 189–190
Greenhouse gases (GHGs)
FCVs cutting emissions of, 361–362
fossil fuels increasing, 293
reducing, 4–6
GTO. *See* Gate turn-off thyristor

H

High-temperature fuel cells, 369–372
molten carbonate, 372
solid oxide, 369–372
High-temperature water electrolysis, 80–83
advances, 39
cell components, 37
energy sources, 81–83
limitations, 39
operation modes, 83
performances, 37–38
perspectives, 39
principles, 36–37
technology developments and applications, 38–39
thermodynamics of, 80–81
electrolyzer configuration, 80–81
electrolyzer materials, 81
HOGEN S Series, 32f
Hydrogen. *See also* Nonrenewable hydrogen; Renewable hydrogen
electric grid contributed to by, 9–11
from ethanol, 135–141, 161
photocatalytic production, 159–161
as fuel, 269–270
legal framework for, 437–438
liquid, 439
properties, ICE, relevant for, 382–383
public awareness of, 437–438
purification, 246–247
safety as key issue for, 437
sunlight converted into, 43–44
transport phenomena, 443–445
homogenization stage, 444
leak stage of, 443–444
stratification stage of, 444
transportation contributed to by, 9–11
Hydrogen adsorption
carbon materials, 276–281
classical, 277–281
state of the art, 276–277
hydrogen storage capacities
Hydrogen and Fuel Cell Demonstration Project, 365–366
Hydrogen and Fuel Cells Program Plan (DoE), 15
Hydrogen combustion
deflagration process of, CFD modeling, 446–447
detonation process of
CFD modeling, 447–449
injuries sustained from, 441
Hydrogen economy, 245–246
energy carrier and, 6–7, 15–16
Hydrogen embrittlement, 441
Hydrogen engines
advanced technology, 387–393
cryogenic PFI, 387
definition of, 384
direct injection, 387–390
ideal mixture in, 390–393
CFD for, 429–431
direct injection
efficiency losses in, 395–396
emissions of, 396–397
performance of, 396–397
energy efficiency in, 395–396
heat transfer in, 393–395
state of the art, 384–387
abnormal combustion, 386
definition of, 384
demonstration vehicles, 386–387
load control strategy, 385
mixture formation, 384–385
Hydrogen explosion
definition of, 442–443
injuries sustained from, 441
Hydrogen hazards, 437–443
chemical
explosion, 441–443
ignition, 441–443
physical, embrittlement, 441
physiological, 440–441
programs for, 438
Hydrogen Incident and Accident Database, 440
Hydrogen leaks and dispersion
experiments on
HySafe NoE, 445
INERIS, 445–446
Sandia National Laboratories, 446
modeling
CFD, 445–446
of turbulence, 445
stages of
homogenization, 444
leak, 443–444
stratification, 444
transport phenomena, CFD, 443–445
Hydrogen Posture Plan (DoE), 15
Hydrogen production, 201–202
biofuels
biodiesel, 213
bioethanol, 216
biogas, 215
bioglycerol, 213–215
biomethanol, 211–213
bio-oil, 217
dimethyl ether, 210–211
producer gas, 215–216
biological, 171–172, 195
dark fermentation, 173–178, 183–184
LCA of, 193–195
photofermentation, 178–182
WGS reaction, 185–186
from biomass, 87–89, 111–113, 129
aqueous phase reforming, 102–103
bio-oil and, 101–102
fast pyrolysis, 101–102
microbial conversion, 104–105
thermochemical gasification, 98–101
transformations, 103–104
biomass gasification
catalysts, 127–128
sorption-enhanced, 128
sorption-enhanced water gas shift reaction, 128–129
biomass-derived chemicals, sorption-enhanced reforming of, 123–124
catalytic routes to, 136–138
CFD for, 410–426
conditioning factors for, 340
costs, Life Cycle Assessment and, 105–107
demonstration projects and renewable, 351–357
energy efficiency, 344–351
overall, 349–351
water electrolyzer, 344–349
ethanol, photocatalytic, 159–161
from fossil fuels, 12
membranes, reactors, 260–263
pathways
nonrenewable hydrogen, 11–13
renewable hydrogen, 13–14
reactors, membranes, 260–263
reforming catalysts for, 117–119
renewables and, 14–15, 351–353
from solar energy, 63–64
steam reforming, membrane reactors, 260–261
technologies, CFD, 410–426
WGS and, 98–101
Hydrogen safety, 437–439, 450–451
Hydrogen Safety Best Practices database, 440
Hydrogen separation
membranes

general aspects, 248–251
mixed matrix, 259
polymeric membranes for, 252–253
Hydrogen storage
capacities
hydrogen adsorption and, 281–282
total, 282–283
in complex hydrides, 293–295, 327–329
alanates, 296–316
lithium amides, 320–327
metal borohydrides, 316–320
fuel cells influencing, 294
hydrogen economy influenced by, 293–294
summary and recommendations, 286–287
HyS cycle, 77–78
HySafe Network of Excellence (NoE), 439
HySTAT, 29f
HyWays (EC), 15

I

IA HySafe. *See* International Association for Hydrogen Safety
IAHE. *See* International Association for Hydrogen Energy
ICE. *See* Internal combustion engine
Idriss, H., 141–142, 147, 160–161
IEA. *See* International Energy Agency
IEA HIA. *See* International Energy Agency Hydrogen Implementing Agreement
IGBT. *See* Insulated gate bipolar transistor
INERIS. *See* Institut National de l' Environnement Industriel et des Risques
Inorganic membranes, 253–257
metal, 254–256
Institut National de l' Environnement Industriel et des Risques (INERIS), 445–446
Institute for Microtechnology Mainz, 229
Institute of the High Temperature Electrochemistry, 37–38, 38f
Insulated gate bipolar transistor (IGBT), 335–336
Integrated Laboratory Scale experiment, 75
Intergovernmental Panel on Climate Change, 1–2
Internal combustion engine (ICE)
hydrogen, 397–398
challenges for, 393–397
emissions of, 396–397
fuel cell compared with, 381–384
performance of, 396–397
potential of, 393–397
hydrogen properties relevant for, 382–383
International Association for Hydrogen Energy (IAHE), 16
International Association for Hydrogen Safety (IA HySafe), 439
International Conference on Hydrogen Safety, 439
International Energy Agency (IEA)
International Energy Agency Hydrogen Implementing Agreement (IEA HIA), 438
International Partnership for Hydrogen and Fuel Cells in the Economy (IPHE), 15–16
IPHE. *See* International Partnership for Hydrogen and Fuel Cells in the Economy
IPHE Renewable Hydrogen Report (IPHE), 15–16

J

JRC-Ispra. *See* European Commission Joint Research Council

K

Kinetics, water electrolysis, 22
Knock, 386
Kurchatov Institute, 33f

L

LCA. *See* Life Cycle Assessment
LFPS. *See* Line frequency power supply
Life Cycle Assessment (LCA), hydrogen production, 193–195
Line frequency converters, 336–337
Line frequency power supply (LFPS), 341
operation of, 341
Lithium alanate, 301–316
Lithium amides
$LiNH_2$-LiH system, 320–323
$LiNH_2$-MgH_2 system, 323–327
Low-temperature fuel cells, 368–369

M

Market
fuel cells
stationary applications, 373–376
transportation, 366–367
oil and liquid fuels' share of, 2–3
Materials handling, 366
MCFCs. *See* Molten carbonate fuel cells
Membrane reactors, 259–263
hydrogen production, 260–263
steam reforming, 260–261
WGS, 261–263
Membranes
biomethanol, 212
gas separation, 247–251
commercial, 251
performance parameters of, 247–248
hydrogen separation
general aspects of, 248–251
mixed matrix, 259
inorganic
ceramic, 256
metal, 254–256
zeolite, 256–257
mixed matrix, 257–259
hydrogen separation, 259
performance factors of, 258–259
Metal borohydrides
$LibH_4$-$MnCl_2$ system, 316–320
$NaBH_4$-$MnCl_2$ system, 316–320
Metal oxide field effect transistor (MOSFET), 335–336
operation of, 336
Metallic membranes, 254–256
steam reforming, 260
WGS, 262
Microbial conversion
biomass
dark fermentation, 104–105
hydrogen production, 104–105
photofermentation, 105
dark fermentation, 104–105
photofermentation, 104–105
Microfibrous networks, biomethanol, 212–213
Microstructured reactors, 202–203
substrate materials for, 203–205
Mixed matrix membranes, 257–259
for hydrogen separation, 259
performance factors of, 258–259
Molten carbonate fuel cells (MCFCs), 372
MOSFET. *See* Metal oxide field effect transistor

N

Nanodesign
photocatalysts, 56–57
photogenerated charge separation improved by, 55–57
structures, 56–57
synthesis approaches, 55–56
National Energy Technology Laboratory (NETL), 213
National Renewable Energy Laboratory, 353–354
Natural gas and coal
EIA on, 3–4
energy international outlook, 3–4
world consumption of, 3–4
NEL Hydrogen, 27, 28f
NETL. *See* National Energy Technology Laboratory (NETL)
Nickel
catalysts, 143–145, 152–154
steam reforming, ethanol, 143–145
Niobates
doped, 51
photocatalysts, under UV irradiation, 48
Noble metals
autothermal reforming, ethanol, 151–155
catalysts, 141–143, 148–149, 151–152
steam reforming, ethanol, 141–143
Non-noble metals, ethanol partial oxidation, 149–150
Nonoxide materials, photocatalysts under UV irradiation, 48
Nonrenewable hydrogen, pathways hydrogen production, 11–13
Nuclear power, 5

O

Oil and liquid fuels
energy international outlook, 2–3
market share of, 2–3
monthly average prices of, 3f
WTI, 2–3
On-board fuel reforming, 364–365
Ordered mesoporous carbons, 273–274

Organization for Economic Cooperation and Development (OECD), in international energy outlook, 2
Oxides
  photocatalysts under visible irradiation, 48–49
  solid solutions, 53
Oxygenates, biomass-derived reforming reactions of, 116–119

P
Pacific Northwest National Laboratory (PNNL), 215
PAFC. *See* Phosphoric acid fuel cell
Partial oxidation, ethanol
  autothermal oxidation, 150
  noble metal catalysts, 148–149
  non-noble metals, 149–150
  preliminary overview of, 147
  reaction mechanism of, 147–148
  structured catalysts, 149–150
Partnership for Advancing the Transition to Hydrogen (PATH), 15–16
PATH. *See* Partnership for Advancing the Transition to Hydrogen
PEM water electrolysis. *See* Proton-exchange membrane water electrolysis
PEMFCs. *See* Proton exchange membrane fuel cells
Phosphoric acid fuel cell (PAFC), 362
  efficiency, 369
  features of, 368–369
  at full load, 369
  operating temperatures, 369
  at partial load, 369
  in stationary applications, 368–369
Photobioreactors
  cyanobacteria biophotolysis, 190–193
  green algae biophotolysis, 189–190
  operating conditions and, 189–190, 193
  in photofermentation, 181–182
Photofermentation, 178–182
  biomass microbial conversion, 105
  hydrogen production, biological, 178–182
  operational parameters, 182
  photobioreactor type, 181–182
  substrate, 180–181
Photogenerated charge separation, strategies to improve
  co-catalyst loading, 57–58
  nanodesign, 55–57
Photo-semiconductor catalysts
  anisotropic, 56–57
  challenges and opportunities, 58–59
  co-catalysts of, 57–58
  electrochemical properties of, 46–47
  nanodesign, 56–57
  semiconducting properties of, 46–47
  under UV irradiation, 47–48
    d^{10} metal oxides, 48
    niobates, 48
    nonoxide materials, 48
    tantalates, 48
    TiO_2, 47–48
    titanates, 47–48
  under visible irradiation, 48–49
    materials, 49
    oxides, 48–49
    sulfides, 49
  visible response strategies for, 49–55
    band gap engineering, 50–54
    dye sensitization, 54–55
  water splitting on, 44–49
Platinum group metals (PGM), in PEM water electrolysis, 33–34
PNNL. *See* Pacific Northwest National Laboratory
Polymeric membranes
  commercial gas separation membranes and, 251
  for hydrogen separation, 252–253
Polyols, sorption-enhanced reforming of biomass-derived chemicals, 124–125
Power electronic converters
  classifications of, 335
  groups of
    line frequency, 336–337
    resonant, 336–337
    switching, 336–337
  in power electronic systems, 335
  power semiconductors in, 335
Power electronic systems, 334–340
  definition of, 334–335
  power electronic converters in, 335
Power semiconductors, 335
  controllability of, 335–336
  energy efficiency of, 335
  groups of, 335–336
    diodes, 335–336
    GTOs, 335–336
    IGBTs, 335–336
    MOSFETs, 335–336
    thyristors, 335–336
  operating states of, 335
  performance qualities of, 335
  power electronic converters influenced by, 335
  switching modes of
    forced commutation, 336
    natural commutation, 336
Power supplies
  electrolyzer
    electronic conversion systems, 340–344
    power electronic systems, 334–340
  energy efficiency influenced by, 347–349
Preignition, 386
Pretreatment
  acidic, 95–96
  alkali, 96
  ammonia, 96
  drying, 95
  feedstocks
    biological, 97
    chemical, 95–97
    physical and thermal, 94–95
  IL, 96–97
  irradiation, 94
  liquid hot water, 95
  particle size reduction, 94
  steam, 95
Primary energy consumption, 5f
ProAlcohol program, 136
Producer gas hydrogen production, 215–216
Proton exchange membrane fuel cells (PEMFCs), 361–362
  for backup power, 374–375
  batteries at disadvantage to, 362–363
  efficiency, 369
  features of, 368–369
  forklifts, 362–363
  at full load, 369
  high-temperature, 369
  manufacturers, 374t
  operating temperatures, 369
  at partial load, 369
  in stationary applications, 368–369
Proton OnSite, 32f
Proton-exchange membrane (PEM) water electrolysis
  Alkaline water electrolysis compared with, 32–33, 33t
  cell components of, 29f, 30–31
  limitations, recent advances, and perspectives, 32–36
    cell components, 35–36
    lifetime of operation, 36
    non-PGM catalysts, 33–34
    operating current densities, 35
    operating temperature, 35
    PGM contents, 33–34
  operating pressure, 35
  performances, 31
  principles, 29–30
  technology developments and applications, 31–32
PROX reaction, 227–229
Pulse width modulation (PWM), 343
PureCell, 374
PWM. *See* Pulse width modulation

Q
Quadratic Upstream Interpolation for Convective Kinetics, 408

R
Reactors
  biomass, steam reforming, 121
  design, for WGS, 186
  hydrogen production, membrane, 260–263
  membrane, hydrogen production, 260–263
  operating conditions, for WGS, 186
  for steam reforming, of biomass, 121
Redox cycles, 65–73
Reforming catalysts, 117–119
Reforming reactions, 116–117
Renewable Energy Policy Network for the 21st Century (REN21), 15
Renewable hydrogen, production, 13–14
Renewables
  hydrogen production and, 14–15, 351–353
Resonant converters, 336–337
Resonant power supply (RPS), 341, 343–344

Roadmap 2050: a practical guide to a prosperous, low-carbon Europe (ECF), 5–6
RPS. *See* Resonant power supply

S
Safety
  CFD investigating, 439
  as hydrogen key issue, 437
Sandia National Laboratories, 446
Selective methanation reactions, 227–229
Semicontrolled rectifiers, 339
Sequential cultivation, 184
Shale gas, 3–4
Sodium alanate, 296–301
SOFCs. *See* Solid oxide fuel cells
Solar energy
  hydrogen production from, 63–64
  in visible spectrum, 43–44
Solar fuel, 63–64
Solid oxide fuel cells (SOFCs), 369–372
Solid solutions
  band gap engineering approach, 52–54
  metal (oxy)nitride, 53
  metal oxide, 53
  sulfide, 53
Sorption-enhanced reforming, of biomass-derived chemicals
  biogas, 124
  bio-oil, 125–126
  catalyst, 126
  CO_2 acceptor and, 126
  ethanol, 124–125
  hydrogen production, 123–124
  polyols, 124–125
  sugars, 125
SPS. *See* Switching power supply
Stack structure, 26
Steam, feedstocks pretreatment, 95
Steam reforming, 260–261
  of biomass-derived chemicals, 113–121
    biomass-derived oxygenates and, 116–119
    bio-oil, 114–115
    carbohydrates, 114–115
    challenges, 113–114
    coke formation in, 119–120
    ethanol, 114–115
    fast pyrolysis and, 115–116
    reactors for, 121
    thermal efficiency of, 120–121
  ceramic membranes, 261
  of ethanol
    cobalt catalysts, 145–147
    nickel catalysts, 143–145
    noble metal catalysts, 141–143
  hydrogen production, membrane reactors, 260–261
  metallic membranes, 260
  thermal efficiency, 120–121
Structured catalysts, 202
  ethanol, 149–150
  substrate materials for, 203–205
Structured reactors, for CO cleanup, 229–230
Structured substrate, catalyst coating, 205–209
  dip coating, 206–208
  surface growing, 208–209
Substrate
  of biological WGS, 185
  biophotolysis
    cyanobacteria, 191–193
    green algae, 187–189
  dark fermentation, 175–176
  microstructured reactors, materials, 203–205
  photofermentation, 180–181
  structured catalysts, materials, 203–205
Sugars, sorption-enhanced reforming of, 125
Sulfides
  doped, 52
  photocatalysts under visible irradiation, 49
  solid solutions, 53
Sulfur-based cycles, 73–78
  copper-chlorine cycle, 78–80
    electrolysis step in, 79
    hydrogen production step in, 79
    hydrolysis step in, 79
    oxygen production step in, 79
  HyS cycle, 77–78
  other, 78–80
  sulfuric acid decomposition and, 73–75
  sulfur-iodine cycle, 75–77
Sulfuric acid
  solar decomposition of, 73–75
  sulfur-based cycles and decomposition of, 73–75
Sulfur-iodine cycle, 75–77
Sunlight, hydrogen converted from, 43–44
Supercritical reforming, 123
Switching converters, 336–337
Switching power supply (SPS), 341
  operation of, 341–343
  studies based on, 342

T
Tantalates
  doped, 51
  photocatalysts, under UV irradiation, 48
Technologies
  alkaline water electrolysis, 26–27
  co-cultivation, dark fermentation coupled to, 183–184
  high-temperature water electrolysis, 38–39
  hydrogen production, CFD for designing, 410–426
  PEM water electrolysis, 31–32
  sequential cultivation, dark fermentation coupled to, 184
  water electrolysis, 22–25, 24t, 25f
Templated carbons, 273–274
Thermal burns, 440–441
Thermal efficiency, steam reforming, 120–121
Thermochemical cycles
  redox cycles, 65–73
  sulfur-based cycles, 73–78
Thermochemical gasification
  biomass, hydrogen production from, 98–101
  WGS coupled with, 98–101
Thermodynamics
  ethanol, 138–141
  high-temperature electrolysis, 80–81
    electrolyzer configuration, 80–81
    electrolyzer materials, 81
  water electrolysis, 20–21
Thyristors, 335–336
  operation of, 336
TiO_2
  doped, 51
  photocatalysts, under UV irradiation, 48
Titan electrolyzer, 29f
Titanates
  doped, 51
  photocatalysts, under UV irradiation, 47–48
Total hydrogen storage capacity, 282–283
Transportation
  fuel cells
    market prospective, 367
    market status, 366–367
    required features, 363–366
    types, 362–363
  hydrogen contribution to, 9–11
  mainstream, 363

U
UDS. *See* Upwind Differencing Scheme
UN. *See* United Nations
Uncontrolled rectifiers, 339
United Nations (UN)
  Climate Change Conference 2011, 2
  Intergovernmental Panel on Climate Change, 1–2
  fuel cells influenced by, 376
  oil and liquid fuel growth contribution of, 2–3
Upwind Differencing Scheme (UDS), 408
UTC Power, 373–374
UV irradiation, photocatalysts active under
  d^{10} metal oxides, 48
  niobates, 48
  nonoxide materials, 48
  tantalates, 48
  TiO_2, 47–48
  titanates, 47–48

V
Visible irradiation, photocatalysts under
  materials, 49
  oxides, 48–49
  sulfides, 49
Visible spectrum, solar energy in, 43–44

W
Water electrolysis, 39–40
  biophotolysis
    cyanobacteria, 190–193
    green algae, 187–190
  CFD for, 425–426
  costs, 334

Water electrolysis (*Continued*)
historical review of, 19–20
kinetics and efficiencies, 22
technologies, 22–25, 24t, 25f
thermodynamics, 20–21
Water splitting, 83–84. *See also* Direct water splitting
concept, 44–45
energy requirements, 45–46
on photocatalysts, 44–49
Water-gas shift (WGS), 230–239
biological
reactor design and operating conditions for, 186
substrate of, 185
as CO cleanup's first stage, 226–227
high-temperature reaction, 119
hydrogen production, 98–101
membrane reactors, 261–263
sorption-enhanced, 128–129
thermochemical gasification coupled with, 98–101
West Texas Intermediate (WTI) crude oils, 2–3
WGS. *See* Water-gas shift
Wind power, 343
Wind turbines, 343
Wind2H2, 353–354
WTI crude oils. *See* West Texas Intermediate (WTI) crude oils

Z

Zeolite
membranes, 256
templated carbons, 273–274